

**School of Earth and Planetary Science
Faculty of Science and Engineering**

**Geochemical Records Linking Plate Tectonics with Mantle
Dynamics: Neoproterozoic and Beyond**

Hamed Mohammed Abdel Ghany Mansour Gamal El Dien

0000-0003-3656-1240

**This thesis is presented for the Degree of
Doctor of Philosophy
of
Curtin University**

November 2020

Declaration

To the best of my knowledge and belief, this thesis contains no material previously published by any other person except where due acknowledgment has been made. I have obtained permission from the copyright owners to use any of my own published work in which the copyright is held by another party.

This thesis contains no material which has been accepted for the award of any other degree or diploma in any university.

Signature:

Date: 11/11/2020

“Dedicated to

My beautiful wife, SALMA,

And

My two little boys, HAMZA and RAHEM”

Abstract

Plate tectonics has shaped Earth's surface and crust, and the continents that we now live on; it also impacted the evolution of life. Plate tectonic activities on the Earth are also responsible for the formation of mineral and energy resources. With the mantle being the largest of the Earth's three layers (crust, mantle, and core), the study of feedback mechanisms between plate tectonics and mantle dynamics, and the composition of the mantle, forms the backbone of understanding the evolution and inner workings of the Earth.

The Earth evolved, from the Hadean to the present, through major changes in Earth processes. These processes mainly comprise (1) an extensive differentiation and generation of the crust (continental crustal growth), (2) plate tectonics, including the generation of a global subduction system, (3) global geochemical cycles causing mantle heterogeneities, and (4) the assembly and breakup of supercontinents and their feedback on deep mantle processes such as the formation of superplumes. This Ph.D. thesis aims to investigate Earth's dynamic evolution through geological time by addressing possible linkages between the evolution of the Earth's mantle and crustal growth, plate tectonics, and superplume-supercontinental cycles. This is achieved through deciphering the geochemical records of mantle-derived/related rocks that characterised the Earth's mantle evolution and processes at global-, regional- and micro- to nano-scales. This thesis consists of three main parts, each including multiple chapters. The major outcomes and findings of this Ph.D. thesis are summarised below.

Part 1: Crustal growth from the Neoproterozoic mantle: an Egyptian Nubian Shield example

In this part, I report the discovery of the largest known plagiogranitic pluton on Earth (~5,000 km²) and bimodal volcanic province (80 km x 35 km and >10 km-thick) from the Eastern Desert of Egypt as part of the Arabian-Nubian Shield (ANS). These are interpreted to have formed through the remelting of a juvenile continental crust (i.e., accreted oceanic slabs) during the break-up of Rodinia and possibly linked to a mantle plume. This result argues against the widely held belief that Neoproterozoic crustal growth in the ANS was primarily driven by arc magmatism; instead, rift- and plume-related magmatism may also have played important roles. I also demonstrate that Neoproterozoic crustal growth in the

Eastern Desert is characterised by a protracted and episodic nature, involving extensive reworking, through three major magmatic episodes with peaks at ~730 Ma, ~ 700 Ma, and ~ 600 Ma, respectively.

Part 2: Mantle partial melting and metasomatism: Geochemical cycling and subduction polarity implications

In this part, I demonstrate that the composition of Cr-spinel in mantle rocks is not a good petrogenetic indicator, as widely assumed; instead, it is a tracer for metasomatic processes and a potential carrier for bringing fluid-mobile elements deep into the lower mantle. I further report that temperature is the main controlling factor for the release of trace elements from subducted slabs into arc magmatism, and the resulting cross-arc geochemical variation trend can help to determine the subduction polarity of ancient arcs.

Part 3: Geochemical records linking mantle plumes, supercontinent cycles, and plate tectonics

In this part, I use global geochemical analyses (data mining) to explore two major questions: (a) how plate tectonics interact with mantle processes and influence the first-order mantle structure? (b) what was the starting time of global plate tectonics on Earth?. I demonstrate evidence for a possible dynamic coupling between supercontinent and superplume events. My work also suggests a ca. 3.2 Ga onset time for a global mantle re-enrichment/refertilization event, interpreted to be a consequence of global deep subduction and thus plate tectonics.

Acknowledgements

I would like to thank many people for helping me to accomplish this work, without them this thesis would not have been possible:

Firstly, I would like to express my deepest gratitude to Prof. Zheng-Xiang Li, my principal supervisor, for his very kind supervision, great help, valuable suggestions, assistance during fieldwork, and advice during the progress of this work. His unlimited encouragement incredible help me in so many different ways. He successfully transfers me from a normal geochemist and petrologist working on a small scale to be a mantle geodynamist addressing global-scale first-order questions in geoscience. He gives me a lot of freedom to design my project and kept up push me to aim for high standards in thinking and publishing my work. Above all of that, I am truly grateful to him for his always social support and advice.

I am greatly indebted to Dr. Luc-Serge Doucet, my co-supervisor, for his cooperation, faithful help, continuous encouragement, discussion, and providing great scientific support and editing, and also being a great friend.

Special thanks to Dr. Josh Beardmore and Prof. Brendan Murphy for their great support for me through scientific discussion and proofreading mostly all of this thesis.

I would like to thank Prof. Simon Wilde, the chairperson of my thesis committee, for his kind and nice support and for the usual interesting discussion about the geology of the Arabian-Nubian Shield.

I owe a great deal of gratitude to Dr. Tamer Abu-Alam for helping me in thermodynamic modelling, as well as Prof. Youngwoo Kill for helping in the LA-ICP-MS analyses of Cr-spinel. Prof. Noreen Evans and Mr. Brad McDonald are thanked for assistance with LA-ICP-MS analyses of zircon and data reduction. Thanks to Prof. Xiaoping Xia for assistance with SIMS analyses of zircon, Dr. Allen Kennedy and Mr. Hao Gao for helping in operating the SHRIMP and data reduction, and Ms Elaine Miller for assisting with CL imaging. And thanks to Prof. Steven M. Reddy, Dr. Denis Fougereuse, and Dr. David W. Saxey for assistance with EBSD and ATP analyses. I am greatly indebted to Prof. Mohamed Abu-Anbar and Prof. Mohamed Hamdy for their assistance during fieldwork.

Also, I would like to thank all my friends, staff members, and my colleagues of the Earth Dynamic Research group who helped me directly or indirectly during this work.

This thesis has never been completed without the help and support of my mother and all member of my family.

Most importantly, my beautiful wife, SALMA, is the superb source of joy in all my life and a great source of encouragement, kind patience, and motivation. She is not only shiny my life but also the closest friend who takes my hand through a lot of difficult times and if I was still doing great and rising high because you are in my life, I love you.

Last, my two little boys, HAMZA and RAHEM, you are my life and the life that push me looking high and fly.

List of Publications during the course of this thesis

Peer-reviewed journal articles as the first author:

1. [Gamal El Dien, H., Arai, S., Doucet, L., Li, Z.-X., Kil, Y., Fougereuse, D., Reddy, S.M., Saxey, D.W., and Hamdy, M., 2019, Cr-spinel records metasomatism not petrogenesis of mantle rocks: *Nature Communications*, p. 5103, doi:10.1038/s41467-019-13117-1.](#)
2. [Gamal El Dien, H., Li, Z.-X., Kil, Y., and Abu-Alam, T., 2019, Origin of arc magmatic signature: A temperature-dependent process for trace element \(re\)-mobilization in subduction zones: *Scientific Reports*, v. 9, p. 7098, doi:10.1038/s41598-019-43605-9.](#)
3. [Gamal El Dien, H., Doucet, L.S., Li, Z.-X., Cox, G., and Mitchell, R., 2019, Global geochemical fingerprinting of plume intensity suggests coupling with the supercontinent cycle: *Nature Communications*, v. 10, p. 5270, doi:10.1038/s41467-019-13300-4.](#)
4. [Gamal El Dien, H., Doucet, L.S., Murphy, J.B., and Li, Z.-X., 2020, Geochemical evidence for a widespread mantle re-enrichment 3 . 2 billion years ago : implications for global-scale plate tectonics: *Scientific Reports*, p. 1–7, doi:10.1038/s41598-020-66324-y.](#)

Other relevant co-authored publications:

5. [Doucet, L.S., Li, Z.-X., Gamal El Dien, H., et al. 2020. Hemispheric geochemical differences reflect distinct histories for deep mantle domains: *Nature Geoscience*, DOI:10.1038/s41561-020-0599-9](#)
6. [Doucet, L.S., Li, Z., Ernst, R.E., Kirscher, U., Gamal El Dien, H., and Mitchell, R.N., 2020, Coupled supercontinent – mantle plume events evidenced by oceanic plume record: *Geology*, v. 48, p. 1–5, doi:10.1130/G46754.1/4906660/g46754.pdf.](#)
7. [Wang, C., Peng, P., Li, Z.-X., Pisarevsky, S., Denyszyn, S., Liu, Y., Gamal El Dien, H., and Su, X., 2020, The 1.24-1.21 Ga Licheng large igneous province in the North China Craton: Implications for paleogeographic reconstruction: *Journal of Geophysical Research: Solid Earth*, p. e2019JB019005, doi:10.1029/2019JB019005.](#)

Contents

<i>Declaration</i>	iii
<i>Abstract</i>	vii
<i>Acknowledgements</i>	ix
<i>List of Publications</i>	xi
<i>List of Figures</i>	xvii
<i>List of Tables</i>	xxxiv

Chapter 1 Introduction	1
1.1 Mantle record of Earth's dynamic evolution	2
1.1.1 Earth's mantle laying	2
1.1.2 Earth's continental crust and crustal growth	7
1.1.3 Earth's dynamic evolution and key scientific questions for this research	9
1.2 Thesis structure and outlines	13
1.3 References	18
Chapter 2 Methodology	27
2.1 Field work	27
2.2 Laboratory work, including geochemical analyses	27
2.2.1 Microscopic examination	29
2.2.2 TIMA-phase maps	30
2.2.3 Whole-rock major and trace element geochemistry	30
2.2.4 Whole-rock Sr-Nd isotopes	32
2.2.5 Zircon mount preparation	33
2.2.6 SHRIMP U-Pb zircon analyses	34
2.2.7 LASS zircon U-Pb, Lu-Hf isotopes and trace elements analyses	35
2.2.8 SIMS zircon O-isotope analyses	40
2.3 Data-mining approach	42
2.4 References	43
Appendix A	46

Part I: Crustal growth from the Neoproterozoic mantle: an Egyptian Nubian Shield example

Chapter 3 <i>The El-Shadli plutonic complex of Eastern Desert: The largest plagiogranite on Earth formed by re-melting of juvenile continental crust</i>	61
Abstract	61
3.1 Introduction	62
3.2 Geological setting	63
3.2.1 General geological background	63
3.2.2 Field and age relationships	68
3.2.3 Sample description and petrography	70
3.3 Analytical methods	75
3.4 Results	75
3.4.1 Whole-rock geochemical data	75
3.4.2 Whole-rock Sr-Nd isotope data	80
3.4.3 Zircon U-Pb-Hf-O isotopes and trace elements	81

3.4.3.1	Diorite sample R10-1	81
3.4.3.2	Trondhjemite sample R11-1	82
3.4.3.3	Trondhjemite sample S01-1a	83
3.4.3.4	Trondhjemite sample S14	84
3.5	Discussion	89
3.5.1	El-Shadli plagiogranites: mineralogical, petrological and geochemical evidence	89
3.5.2	Nature of the parental magma and magma source	91
3.5.3	Petrogenesis of the El-Shadli plagiogranites	94
3.5.4	Geodynamic context and formation mechanism for the El-Shadli plutonic complex	99
3.6	References	107
	Appendix B	120
Chapter 4 <i>The El-Shadli bimodal volcanics, Eastern Desert, Egypt: Record of a 700 Ma rifting event during Rodinian break up</i>		133
	Abstract	133
4.1	Introduction	135
4.2	Geological setting	136
4.2.1	Geological background	136
4.2.2	Field observations and petrography	140
4.3	Analytical methods	144
4.4	Results	145
4.4.1	Whole-rock geochemical data	145
4.4.2	Whole-rock Sr-Nd isotopic data	150
4.4.3	Zircon U-Pb-Hf-O isotopes and trace elements	152
4.4.3.1	Rhyolite sample S02-5	152
4.4.3.2	Andesitic sample S16	153
4.5	Discussion	154
4.5.1	Was the El-Shadli bimodal volcanic province formed at a convergent margin, or was it rift-related?	154
4.5.2	Origin of the El-Shadli bimodal suite	163
4.5.2.1	Nature of the parental magma and magma source	163
4.5.2.2	Petrogenesis	164
4.5.3	Petrogenesis of the El-Shadli intermediate rocks	167
4.5.4	Formation mechanism and tectonic implications	169
4.6	References	176
	Appendix C	186
Chapter 5 <i>Nature of Neoproterozoic crustal growth in the Egyptian Nubian Shield: Geochronological and isotopic constraints</i>		203
	Abstract	203
5.1	Introduction	204
5.2	Previous geochronological data of granitoid and volcanic rocks in the Eastern Desert	208
5.3	Description and sample localities of the Genina Gharbia pluton	210
5.4	Analytical techniques	212
5.5	Results	212
5.5.1	Whole-rock geochemical and Sr-Nd isotopic data	212
5.5.2	Zircon U-Pb-Hf-O isotopes and trace elements	217

5.6	Discussion	220
5.6.1	Petrogenesis of the Genina Gharbia pluton.....	220
5.6.2	Crustal growth of the Eastern Desert of Egypt: juvenile vs recycled/reworked nature.....	222
5.6.3	Episodic magmatism during the growth of the Eastern Desert crust..	226
5.6.4	Transition of Neoproterozoic tectonic and magmatic styles: implications for the crustal evolution of the Eastern Desert.....	231
5.7	References	239
	Appendix D	248

Part II: Mantle partial melting and metasomatism: Geochemical cycling and subduction polarity implications

Chapter 6	<i>Cr-spinel records metasomatism not petrogenesis of mantle rocks</i>	253
	Abstract	253
6.1	Introduction	254
6.2	Methods	255
6.2.1	Bulk rock chemical analysis	255
6.2.2	Electron probe micro analyses (EMPA)	256
6.2.3	X-ray mapping of Cr-Spinel	256
6.2.4	Electron back-scattered diffraction (EBSD)	257
6.2.5	Laser ablation-inductively coupled plasma-mass spectrometry (LA-ICP-MS) micro analysis	257
6.2.6	Atom probe tomography (APT)	258
6.2.7	Filter criteria for Cr-spinel data	259
6.3	Results	259
6.3.1	Al-Cr reverse zoning in spinel: An example from the Arabian-Nubian Shield	259
6.3.2	A re-evaluation of Al-Cr heterogeneity in Cr-spinel from previous studies	268
6.4	Discussion	272
6.5	References	275
	Appendix E	282
Chapter 7	<i>Origin of arc magmatic signature: A temperature-dependent process for trace element (re)-mobilization in subduction zones</i>	299
	Abstract	299
7.1	Introduction	300
7.2	Geological background and sample description	301
7.3	Methods	302
7.3.1	Raman Spectroscopy analysis	302
7.3.2	Bulk rock chemical analysis	303
7.3.3	Electron probe micro analysis (EMPA)	305
7.3.4	Laser ablation-inductively coupled plasma-mass spectrometry (LA-ICP-MS) micro analysis	305
7.3.5	Thermodynamic modelling	306
7.4	Results	307
7.4.1	Geochemical composition	307
7.4.2	Thermodynamic modelling	309

7.5	Discussion	311
7.5.1	Origin of the protolith	311
7.5.2	Two-stage serpentinization and geochemical consequences	313
7.5.3	Carbonates formation and trace elements budget	316
7.5.4	Implications for arc magmatism and subduction polarity geochemical fingerprinting	318
7.6	References	322
	Appendix F	330

Part III: Geochemical records linking mantle plumes, supercontinent cycles, and plate tectonics

Chapter 8	<i>Global geochemical fingerprinting of plume intensity suggests coupling with the supercontinent cycle</i>	356
	Abstract	356
8.1	Introduction	357
8.2	Methods	358
8.2.1	Database compilation	358
8.2.2	Data bootstrap resampling	359
8.3	Results	360
8.3.1	Ni and Cr as tracers for mantle plume products	360
8.4	Discussion	364
8.4.1	Time variations in mantle plume intensity	364
8.4.2	Implications for mantle dynamics coupled with the supercontinent cycle	366
8.5	References	369
	Appendix G	373
Chapter 9	<i>Geochemical evidence for a widespread mantle re-enrichment 3.2 billion years ago: implications for global-scale plate tectonics</i>	380
	Abstract.....	380
9.1	Introduction	381
9.2	Geochemical tracer for crustal recycling	382
9.3	Methods	383
9.4	Results	384
9.5	Discussion	389
9.6	References	392
	Appendix H	398
Chapter 10	<i>Summary and future perspective: Geochemical records of the Earth's Mantle evolution from global- to nano-scale</i>	407
10.1	Mantle re-fertilization and the start of global subduction at ~3.2 Ga.....	408
10.2	Plate tectonics and superplumes-supercontinental coupling.....	409
10.3	Crustal evolution of the Egyptian Nubian Shield	411
10.4	Sub-arc mantle geochemical cycle and subduction polarity: implication for temperature control on trace elements (re)-mobilization	413
10.5	Mantle melting and metasomatism: Cr-spinel a new tool to decipher the mantle heterogeneity	414
10.6	Future work	415

10.7	References	417
	Attribution statements and copyright information.....	421

List of Figures

Figure 1.1:	The Earth's interior structure showing the major subdivision zones of the Earth (crust, mantle, and core). The figure is modified after Winter (2014). TZ= transition zone.	3
Figure 1.2:	A schematic diagram illustrating the evolution of the Earth's Mantle. Hadean primitive mantle at > 4.4 Ga (a) and formation of the Hadean depleted mantle and proto-crust at ~ 4.4 Ga (b) modified after Saji <i>et al.</i> (2018). (c) A simplified diagram showing the present-day Earth's mantle structure.	5
Figure 1.3:	The present-day lower mantle structure. (a) The configuration of the two equatorial African and Pacific LLSVPs (modified after Li <i>et al.</i> (2019) and Doucet <i>et al.</i> (2020)). (b) Earth's seismic map of the LLSVPs. Seismic shear-wave velocity anomalies (δV_s) are those of the mean S-wave tomography model s5mean. This figure is modified after Doucet, Li, Gamal El Dien, <i>et al.</i> (2020).	6
Figure 2.1:	Geological map of the Eastern Desert showing the ages and distribution of the main rock units. Eastern Desert terranes boundaries are after Stern and Hedge (1985). The map is modified after Johnson <i>et al.</i> (2011).	28
Figure 2.2:	An example of a granite sample G04–1 (Genina Gharbia) thin section imaging to petrographic description under polarizing light (a), crossed light (b) and TIMA-phase mapping (c).	30
Figure 2.3:	Primitive mantle (McDonough and Sun, 1995) normalized trace elements (including rare earth element) patterns of the reference materials used during ICP-MS analytical sessions. The measured values are compared with recommended values to show the precision of the measurements.	32
Figure 2.4:	Cathodoluminescence (CL) images of zircon from different rock types such as granite (sample R11–1a; El-Shadli area-W. Ranga) and rhyolite (sample S02–5; El-Shadli volcanics).	34
Figure 2.5:	U-Pb data for reference materials used during the LASS-ICPMS analytical session.	37
Figure 2.6:	Lu-Hf data for reference materials used during the LASS-ICPMS analytical session.	39
Figure 2.7:	Stable isotopic ratios ($^{178}\text{Hf}/^{177}\text{Hf}$ and $^{180}\text{Hf}/^{177}\text{Hf}$) of the all analyses during the LASS-ICPMS analytical session.	40
Figure 2.8:	O isotopic data for Qinghu zircon reference material used during the SIMS analytical session. The error bars are quote at the 95% confidence interval (2SD).	41
Figure 3.1:	(a) Gondwana at 500 Ma with both pre-Neoproterozoic cratons and Gondwana-forming orogens modified after Fitzsimons (2016), Daczko <i>et al.</i> (2018), and Olierook <i>et al.</i> (2019). (b) a schematic geological map	65

of the Arabian-Nubian Shield showing the distribution of Neoproterozoic terranes and their contact with pre-Neoproterozoic blocks modified after Johnson *et al.* (2011) and Pease and Johnson (2013).

- Figure 3.2:** Geological map of the Eastern Desert showing the ages and distribution of the main Precambrian crustal basement rock units. Eastern Desert terrene boundaries are after Stern and Hedge (1985). The map is modified after Johnson *et al.* (2011) 67
- Figure 3.3:** Detailed geological map of the studied El-Shadli area showing the ages and distribution of the main rock units: the El-Shadli bimodal volcanic rocks, the El-Shadli granite (plagiogranites)-diorite-gabbro assemblage, the W. Ghadir ophiolitic assemblage, the W. Hafafit core complex, post-collision alkaline granites, and post-collisional volcanics. Age data are from Stern, Kröner, and Rashwan (1991), Kröner *et al.* (1992), Kroner, Kruger, and Rashwan (1994) and this study. The map is modified after the geologic map of Jabal Hamatah quadrangle (GSE, 1997). 69
- Figure 3.4:** Field photos of the El-Shadli plagiogranites and associated gabbros. (a) Mafic dykes (likely related to the El-Shadli bimodal volcanics of ~700 Ma) intruding the studied plagiogranites (sample S01-1a, 729 ± 7 Ma). (b-d) Magmatic mixing zone. The large mafic enclaves in the mixing zone show no obvious chilled margin and have irregular boundaries with the plagiogranites. (e-g) Centimetre-size mafic enclaves within gabbroic diorites and plagiogranites. (h-j) Close up views of samples S14 (trondhjemite), R10 (diorite), and S12 (gabbro), showing medium- to coarse-grained hypidiomorphic-granular textures. 71
- Figure 3.5:** Photomicrographs of the El-Shadli plagiogranites and associated gabbros. (a-c) Crossed-polarized light images of the plagiogranites showing medium- to coarse-grained hypidiomorphic-granular texture and quartz-plagioclase intergrowths such as graphic and vermicular textures. The rocks consist mainly of plagioclase (pl) and quartz (qz). (d) Crossed-polarized light image of the gabbro showing the development of ophitic and sub-ophitic textures between plagioclase, clinopyroxene (cpx) and amphiboles (amph). 73
- Figure 3.6:** Harker plots showing the whole-rock major element compositions of the El-Shadli plagiogranites and associated gabbros. The previously published data are form Gharib and Ahmed (2012) and Maurice *et al.* (2013). 77
- Figure 3.7:** Chemical classification diagrams using the whole-rock major and trace element compositions of El-Shadli plagiogranites and associated gabbros. (a) A plot of data over the total alkali-silica diagram (TAS) of Middlemost (1994). (b) The Ab-An-Or diagram (O'Connor, 1965; Barker, 1979). (c) SiO_2 versus K_2O plot (Peccerillo and Taylor, 1976). Fields for oceanic plagiogranites (OP), island arc granitoids (IAG), continental arc granitoids (CAG), continental collision granitoids (CCG), post-orogenic granitoids (POG), rift-related granitoids (RRG), and continental epeirogenic uplift granitoids (CEUG) are after Maniar and Piccoli (1989). (d) Ternary diagram of $\text{Al}_2\text{O}_3/(\text{FeOT} + \text{MgO}) - 3*\text{CaO} - 5*(\text{K}_2\text{O}/\text{Na}_2\text{O})$ after Laurent *et al.* (2014) showing that the studied plagiogranites were likely derived from a low-K mafic magma 78

source. (e, f) Tectonic setting plots of Pearce, Harris, and Tindle (1984) and Pearce (1996). Data sources used: previous reported plagiogranites — as references through the text; arc-granitoids — GeoRoc (<http://georoc.mpch-mainz.gwdg.de/georoc/>); Archean trondhjemite-tonalite-granodiorite (TTG) — Moyen (2011); other ANS I- and A-type granitoids — Robinson *et al.* (2014, 2017), Farahat *et al.* (2007), Katzir *et al.* (2007), Moussa *et al.* (2008), El-Bialy and Streck (2009), Ali, Moghazi, *et al.* (2012), Eliwa *et al.* (2014), Ali *et al.* (2015), and Zoheir *et al.* (2020).

- Figure 3.8:** Chondrite-normalized REE patterns (Anders and Grevesse, 1989) of the El-Shadli plagiogranites and associated gabbros. MORB pattern is after Sun and McDonough (1989). Sources of other published data for comparison are the same as for Figure 3.7. 79
- Figure 3.9:** NMORB-normalized (Sun and McDonough, 1989) trace element diagram of the El-Shadli plagiogranites and associated gabbros. 80
- Figure 3.10:** Sr-Nd isotopes of the El-Shadli plagiogranites and associated gabbros. The ANS N-MORB ophiolite data are those from W. Gerf in the south of the study area (Zimmer *et al.*, 1995) and W. Ghadir in the north of the study area (Basta *et al.*, 2011). 81
- Figure 3.11:** SHRIMP geochronological data and CL images of the El-Shadli plagiogranites. Zircon U-Pb SHRIMP Concordia diagrams show the $^{206}\text{Pb}/^{238}\text{U}$ ages of the analysed zircons with 1 sigma errors. Weight means relative probability diagrams of $^{206}\text{Pb}/^{238}\text{U}$ age and representative CL images are shown for each sample. The red circles on the CL images mark the place for SHRIMP, LASS, and SIMS spot analyses for the U-Pb age, Hf and O isotopes, and trace element data, respectively. 86
- Figure 3.12:** LA-SS-ICPMS geochronological data and chondrite-normalized zircon trace element data of the El-Shadli plagiogranites. Zircon U-Pb Concordia diagrams show the $^{206}\text{Pb}/^{238}\text{U}$ ages of the studied zircons with 1 sigma errors. Chondrite-normalized zircon REE patterns (Anders and Grevesse, 1989) of each sample are shown. Oceanic and continental zircon fields are from Grimes *et al.* (2007). 87
- Figure 3.13:** Zircon trace elements tectono-magmatic classification of the El-Shadli plagiogranites using the classification fields of Grimes *et al.* (2015). 88
- Figure 3.14:** Age, Hf, and O isotopic data of zircons from the El-Shadli plagiogranites. (a) The calculated $\epsilon\text{Hf}(t)$ values of each analysis and the sample weighted mean. (b) $\epsilon\text{Hf}(t)$ vs $^{206}\text{Pb}/^{238}\text{U}$ age plot against the Chondritic uniform reservoir (CHUR) and depleted mantle (DM; Griffin *et al.*, 2002) lines. Hf isotopic data of ANS arc-related I- and A-type granitoids (e.g., Morag *et al.*, 2011, 2012; Robinson *et al.*, 2014) are used for comparison. (c) The plot of individual $\delta^{18}\text{O}$ values and sample weighted means. The zircon $\delta^{18}\text{O}$ value of oceanic ophiolitic plagiogranites (4.9 ± 0.6 ‰) is from Grimes *et al.* (2013), and that of mantle zircons (5.3 ± 0.3 ‰) is from Valley *et al.* (1998, 2005). (d) The plot of $\delta^{18}\text{O}$ vs $\epsilon\text{Hf}(t)$ for the studied zircons. Old upper and lower crust trends are from Kemp *et al.* (2007) and Wang *et al.* (2016). 89
- Figure 3.15:** Whole-rock petrogenetic discrimination diagrams. (a) Ternary diagram of TiO_2 - $\text{SiO}_2/50$ - K_2O modified after France *et al.* (2010) based on 99

experimental work to evaluate the composition of plagiogranitic melts resulted from fractional crystallization of MORB (e.g., Dixon-Spulber and Rutherford, 1983; Berndt, Koepke and Holtz, 2005) and from partial melting of hydrated oceanic crust (i.e., gabbros, amphibolites, and basalts; Beard and Lofgren, 1991; Thy, Leshner and Mayfield, 1999; Koepke et al., 2004; France et al., 2010, 2014). (b) TiO₂ vs. SiO₂ diagram after Koepke *et al.* (2007) showing the lower limit for plagiogranitic melts resulted from fractional crystallization of MORB. (c) TiO₂ (WR) vs. δ¹⁸O (zr) diagram after Grimes *et al.* (2013) showing the field of plagiogranites produced by fractional crystallization of MORB. (d) La vs. SiO₂ diagram was modified after Brophy (2009), suggesting a partial melting origin for the studied rocks.

- Figure 3.16:** A proposed tectonic model for the genesis of the El-Shadli plutonic complex. (a) Oceanic spreading and ridge magmatism, and possible subduction at a continental arc during ~830–750 Ma with hydrothermal fluids circulating and altering the lower crust section of the oceanic crust near MOR. (b) Accretion of oceanic slabs along the subduction zone during ~750–730 Ma, forming a juvenile accreted terrane. (c) Formation of the El-Shadli plagiogranites and associated gabbros above asthenosphere upwelling possibly driven by a mantle plume at ~730–720 Ma by partial melting the lower crust of the accreted oceanic slabs. 103
- Figure B.1:** Crossed-polarized images and TIMA phase maps for the El-Shadli plagiogranites and associated gabbroic rocks. 121
- Figure B.2:** CL images for the studied zircon showing the location of spot used during the SHRIMP, LASS, and SIMS analyses. 123
- Figure B.3:** Plot of δ¹⁸O versus U content (a) and Th/U ratio (b) for zircon crystals of the studied samples. 124
- Figure 4.1:** Geological map of the Eastern Desert showing the ages and distribution of the main Precambrian crustal basement rock units. Eastern Desert terrane boundaries are after Stern and Hedge (1985). The map is modified after Johnson *et al.* (2011). 138
- Figure 4.2:** Detailed geological map of the studied El-Shadli area showing the ages and distribution of the main rock units: the El-Shadli bimodal volcanic rocks, the El-Shadli granite (plagiogranites)-diorite-gabbro assemblage, the W. Ghadir ophiolitic assemblage, the W. Hafafit core complex, post-collision alkaline granites, and post-collisional volcanics. Age data are from Stern, Kröner, and Rashwan (1991), Kröner et al. (1992), Kroner, Kruger, and Rashwan (1994) and this study. The map is modified after the geologic map of Jabal Hamatah quadrangle (GSE, 1997). 139
- Figure 4.3:** Field photos for the El-Shadli bimodal volcanic suite showing the cyclic intercalations between mafic and felsic rocks. 141
- Figure 4.4:** Field photos showing the field relationships between the surrounding plagiogranites (~730 Ma) and mafic and felsic dykes related to the bimodal volcanic suite (~700 Ma). 142

- Figure 4.5:** Field photos for the El-Shadli bimodal volcanic suite. (a) Pyroclastic layers intercalation with mafic rocks. (b) Pillow basalts of the mafic end-member. (c-e) intermediate rocks intruding the mafic rocks. (d) Associated agglomerates. 142
- Figure 4.6:** Photomicrographs of the El Shadli bimodal suite and associated intermediate rocks. (a-f) Crossed-polarized light images of the mafic rocks showing the porphyritic, ophitic, and sub-ophitic textures. The primary mineral (plagioclase and clinopyroxene) assemblage are well preserved. (g-j) Crossed-polarized light images of the felsic rocks showing porphyritic textures. The phenocrysts include quartz, plagioclase, and potash feldspar. (k-L) Crossed-polarized light images of the intermediate rocks showing porphyritic textures and phenocrysts include quartz, plagioclase, and biotite. Plagioclase= pl, clinopyroxene= cpx, quartz= qz, amphiboles= amph, potash feldspar= kf, biotite= Bi and chlorite= ch. 144
- Figure 4.7:** Harker plots showing the whole-rock major elements composition of the El-Shadli bimodal volcanic province. The previously published data are form Stern, Kröner, and Rashwan (1991) and Faisal *et al.* (2020). 146
- Figure 4.8:** Chemical classification diagrams using the whole-rock major and trace element composition of the El-Shadli bimodal volcanic province. (a) Total alkali-silica diagram (TAS) of Middlemost (1994). (b) Zr/Ti versus Nb/Y of Winchester and Floyd (1976). (c-f) geochemical affinities plots including AFM diagram, SiO₂ versus K₂O relationship of Peccerillo and Taylor (1976), Co-Th diagram of Hastie *et al.* (2007) and Th/Yb versus Zr/Y diagram of Ross and Bédard (2009) showing that the El-Shadli bimodal suite belongs to the tholeiitic series and the intermediate rocks calc-alkaline series. 148
- Figure 4.9:** Chondrite-normalized REE patterns (Anders and Grevesse, 1989) and NMORB-normalized (Sun and McDonough, 1989) trace element diagram of the El-Shadli bimodal suite and intermediate rocks. MORB pattern is after Sun and McDonough (1989). Data of arc-basalts and granitoids are from GeoRoc (<http://georoc.mpch-mainz.gwdg.de/georoc/>). The previously published data are form Stern, Kröner, and Rashwan (1991) and Faisal *et al.* (2020). 150
- Figure 4.10:** Sr-Nd isotopes of the El-Shadli bimodal volcanic province. MORB and OIB fields are after Hofmann (2013). 151
- Figure 4.11:** SHRIMP and LA-SS-ICPMS geochronological data and CL images of the El-Shadli volcanic province . (a, c) Zircon U-Pb SHRIMP Concordia diagrams showing the ²⁰⁶Pb/²³⁸U ages of the analysed zircons with 1 sigma errors. Weighted means, relative probability diagrams of ²⁰⁶Pb/²³⁸U ages and representative CL images are shown for each sample. The red circles on the CL images mark the place for SHRIMP, LASS, and SIMS spot analyses for the U-Pb age, Hf and O isotopes, and trace element data, respectively. (b, d) Zircon U-Pb LASS Concordia diagrams showing the ²⁰⁶Pb/²³⁸U ages of the analysed zircons with 1 sigma errors. Weighted means and relative probability diagrams of ²⁰⁶Pb/²³⁸U age are shown for each sample. 155

- Figure 4.12:** Zircon Chondrite-normalized REE patterns (Anders and Grevesse, 1989) and trace element composition tectono-magmatic classification of the El-Shadli volcanic province using the classification fields of Grimes *et al.* (2007, 2015). 156
- Figure 4.13:** Age, Hf, and O isotopic data of zircon from the El-Shadli volcanic province. (a) $\epsilon\text{Hf}(t)$ vs $^{206}\text{Pb}/^{238}\text{U}$ age plot against the Chondritic uniform reservoir (CHUR) and depleted mantle (DM; Griffin *et al.*, 2002) lines. Hf isotopic data of ANS arc-related magmatism (e.g., Morag *et al.*, 2011, 2012; Robinson *et al.*, 2014) are used for comparison. (b) Plot of $\delta^{18}\text{O}$ vs $\epsilon\text{Hf}(t)$ for the studied zircons. Old upper and lower crust trends are from Kemp *et al.* (2007) and Wang *et al.* (2016). The zircon $\delta^{18}\text{O}$ mean value for ophiolitic plagiogranites ($4.9 \pm 0.6\text{‰}$) is from Grimes *et al.* (2013) and that of typical mantle zircon ($5.3 \pm 0.3\text{‰}$) is from Valley *et al.* (1998, 2005). 157
- Figure 4.14:** Density and histogram of silica contents of the El-Shadli bimodal volcanic province compared to that of the other Eastern Desert volcanics and well-studied arc- and rift-related volcanics. (a) The El-Shadli bimodal volcanic province data include that of this study, and of previous work (Shukri and Mansour, 1980; Khudeir, Ali and El Habaak, 1988; Stern, Kröner and Rashwan, 1991; Faisal *et al.*, 2020). (b-d) Data of other Eastern Desert volcanics including ophiolite-related volcanics (Stern, 1981; El-Sayed, Furnes and Mohamed, 1999; Abd El-Rahman, Polat, Yildirim Dilek, *et al.*, 2009; Abd El-Rahman, Polat, Yildirim Dilek, *et al.*, 2009; Basta *et al.*, 2011), arc-related volcanics (Ali *et al.*, 2009) and the Dokhan volcanics (Eliwa, Kimura and Itaya, 2006; Eliwa, El-Bialy, and Murata, 2014) (Figure 4.14a-d). (e) Global database (after GeoRoc: <http://georoc.mpch-mainz.gwdg.de/georoc/>) of oceanic arc (IBM) and continental arc (Andean arc) volcanics and rift-related volcanics (the East-African rift). 160
- Figure 4.15:** Tectonic discrimination diagrams for the El-Shadli mafic and intermediate rocks: (a) V versus Ti (Shervais, 1982; X.-C. Wang *et al.*, 2016); (b) ternary Sm-Ti-V (Vermeesch, 2006); (c) Th/Yb versus Nb/Yb (Pearce, 2008); and (d) TiO_2/Yb versus Nb/Yb (Pearce, 2008). The mafic rocks from the El-Shadli volcanic province plot in the MORB field similar to that of the Basin-and-Range rift-related basalts (X.-C. Wang *et al.*, 2016), and intermediate rocks plot in the arc-related volcanics field. 161
- Figure 4.16:** Tectonic discrimination diagrams for the El Shadli felsic rocks. (a) Ga/Al versus FeO_T/MgO ratio (Whalen, Currie, and Chappell, 1987) and (b) SiO_2 versus $\text{FeO}_T/(\text{FeO}_T + \text{MgO})$ ratio (Frost *et al.*, 2001), where the felsic rocks show similarity to A-type granites. (c-d) Rb vs. Y + Nb and Nb vs. Y of Pearce, Harris, and Tindle, (1984) and Pearce (1996); the El Shadli felsic rocks are similar to ocean ridge granites (ORG) and show a slight overlap with within-plate granites (WPG), thus supporting a rift-related origin. 162
- Figure 4.17:** Whole-rock petrogenetic discrimination diagrams. (a) $\epsilon\text{Nd}(t)$ vs. MgO (wt. %) after W. X. Li, X. H. Li, and Z. X. Li (2005) and (b) La/Yb vs. La showing that the El-Shadli bimodal volcanic suite represents a coherent magmatic series fractionated from MORB-Like melts. (d) La 168

vs. SiO₂ (wt. %) diagram modified after Brophy (2009) that suggests a partial melting origin.

- Figure 4.18:** A proposed tectonic model for the genesis of the El-Shadli plutonic complex and bimodal volcanic province. (a) Oceanic spreading and ridge magmatism, and possible subduction at a continental arc during ~830–750 Ma with hydrothermal fluids circulating and altering the lower crust section of the oceanic crust near MOR. (b) Accretion of oceanic slabs along the subduction zone during ~750–730 Ma, forming a juvenile accreted terrane. (c) Formation of the El-Shadli plagiogranites and associated gabbros above asthenosphere upwelling possibly driven by a mantle plume at ~ 730–720 Ma by partial melting the lower crust of the accreted oceanic slabs. (d) Rifting and formation of the bimodal volcanic province from further remelting of the same (but slightly more depleted) lower crustal source at ~ 700 Ma. 172
- Figure C.1:** Binary plots showing the relationship between the LOI and whole-rock major elements composition of the El-Shadli bimodal volcanic province. 187
- Figure C.2:** Binary plots showing the relationship between the LOI and trace element composition of the El-Shadli bimodal volcanic province. 188
- Figure C.3:** Harker plots showing the differences between the whole-rock major elements composition of the rift-related volcanics (East-African rift) and arc volcanics (the Izu-Bonin-Marian (IBM) arc and the Andean arc). Data are form global database Georoc (<http://georoc.mpch-mainz.gwdg.de/georoc/>). 189
- Figure 5.1:** Geological map of the Eastern Desert showing the ages and distribution of the main rock Precambrian crustal basement rock units. Eastern Desert terranes boundaries are after Stern and Hedge (1985). The map is modified after Johnson *et al.*, (2011). 207
- Figure 5.2:** Timeline chart of the magmatic activities in the Eastern Desert crust. 208
- Figure 5.3:** (a) Geological map of the Genina Gharbia area modified after Helmy *et al.* (2014) showing the major rock units. (b) The field photo displays the contact relationship between the granites and gabbros. (c) Close up view for sample G04-2. 211
- Figure 5.4:** Mineralogical composition of the Genina Gharbia pluton including the crossed polar image (left) and TIMA phase map (right). 213
- Figure 5.5:** Chemical classification diagrams for whole-rock major and trace element compositions of the Genina Gharbia pluton. (a) Total alkali-silica diagram (TAS) of Middlemost (1994). (b) The Ab-An-Or diagram (O'Connor, 1965; Barker, 1979). (c, d) Ga/Al ratio versus Na₂O + K₂O and Y plots (Whalen, Currie, and Chappell, 1987). (e) the plot of Shand's index A/NK (molar Al₂O₃/(NaO + K₂O)) versus A/CNK (molar Al₂O₃/(CaO + Na₂O + K₂O)) (Maniar and Piccoli, 1989). (f) SiO₂ versus K₂O relationship (Peccerillo and Taylor, 1976). 215

- Figure 5.6:** Chondrite-normalized REE patterns (Anders and Grevesse, 1989) and PM-normalized (McDonough and Sun, 1995) trace elements diagram of the Genina Gharbia pluton. I-and A-type granites database of the Eastern Desert used for comparison (e.g., Farahat *et al.*, 2007; Katzir *et al.*, 2007; Moussa *et al.*, 2008; Ali *et al.*, 2012a; Eliwa *et al.*, 2014; Ali *et al.*, 2015; Zoheir *et al.*, 2020). Arc-granitoids after GeoRoc (<http://georoc.mpch-mainz.gwdg.de/georoc/>) and MORB after Sun and McDonough (1989). 216
- Figure 5.7:** Sr-Nd isotopic data of the Eastern Desert magmatic activities (including the Genina Gharbia pluton and the El-Shadli plutonic complex-bimodal volcanic-intermediate rocks). The compiled data from the Egyptian Nubian Shield (ENS) after Zimmer *et al.* (1995), Katz *et al.* (2004), Moussa *et al.* (2008), Ali *et al.* (2009, 2012a, 2015), Be'eri-Shlevin *et al.* (2010), Liégeois and Stern (2010), Eyal *et al.* (2010), Basta *et al.* (2011), Eliwa *et al.* (2014), Sami *et al.* (2018) and Stern *et al.* (2020). Depleted mantle evolution curve after DePaolo (1981; DM(D81)) and Goldstein, O'Nions, and Hamilton (1984; DM (G84)). Panel (b) represents the density plot for all the data in panel (a). 216
- Figure 5.8:** Zircon geochronological data of sample G04-2 from the Genina Gharbia pluton. (a) Zircon U-Pb SHRIMP Concordia diagrams show the $^{206}\text{Pb}/^{238}\text{U}$ ages of the analysed zircons with 1 sigma errors. Weight means relative probability diagrams of $^{206}\text{Pb}/^{238}\text{U}$ age and representative CL images are shown. The red circles on the CL images mark the place for SHRIMP, LASS, and SIMS spot analyses for the U-Pb age, Hf and O isotopes, and trace element data, respectively. (b) Zircon U-Pb Concordia diagrams show the $^{206}\text{Pb}/^{238}\text{U}$ ages of the studied zircons with 1 sigma errors (left) and zircon chondrite-normalized REE patterns (Anders and Grevesse, 1989) (right). 218
- Figure 5.9:** Trace element tectono-magmatic classification of the Genina Gharbia pluton including data from the El-Shadli plutonic complex-bimodal volcanics-intermediate rocks. Zircon fields after Grimes *et al.* (2007, 2015). The 600-615 Ma post-collision magmatism of the Eastern Desert (A-type granites and Dokhan alkaline volcanics) after El-Bialy and Ali (2013). 219
- Figure 5.10:** Age, Hf, and O isotopic data of the Eastern Desert magmatic activities (including the Genina Gharbia pluton and the El-Shadli plutonic complex-bimodal volcanics-intermediate rocks). ENS zircon Hf and O isotopic data used for comparison after Ali *et al.* (2013, 2014, 2015, 2016), Morag *et al.* (2011), Be'eri-Shlevin, Katzir, and Valley, (2009), Be'eri-Shlevin *et al.* (2010) and Stern *et al.* (2020). Chondritic uniform reservoir (CHUR), depleted mantle (DM; Griffin *et al.*, 2002), and new crust form at the island-arc (NC: Dhuime, Hawkesworth, and Cawood, 2011) lines are plotted. Panel (b) and (d) are density plots for panel (a) and (b), respectively. 220
- Figure 5.11:** Chemical and isotopic compositions of the Genina Gharbia pluton. (a) Ternary diagram of $\text{Al}_2\text{O}_3/(\text{FeOT} + \text{MgO})-3*\text{CaO}-5*(\text{K}_2\text{O}/\text{Na}_2\text{O})$ after Laurent *et al.* (2014). (b, c) Granitoids source and tectonic setting plots of Pearce, Harris, and Tindle (1984). I and A-type granites database of the Eastern Desert used for comparison (e.g., Farahat *et al.*, 2007; Katzir *et al.*, 2007; Moussa *et al.*, 2008; Ali *et al.*, 2012a; Eliwa *et al.*, 2014; Ali *et al.*, 2015; Zoheir *et al.*, 2020). (d) The plot of $\delta^{18}\text{O}$ vs $\epsilon\text{Hf}(t)$ of 222

sample G04-2 zircons from the Genina Gharbia pluton. Old upper and lower crust trends are from Kemp *et al.* (2007) and Wang *et al.* (2016). The $\delta^{18}\text{O}$ value of mantle zircons ($5.3 \pm 0.3 \text{ ‰}$) is from Valley *et al.* (1998, 2005) and ϵHf value (13.2 ± 1.1) of new crust form at the island-arc (NC) after Dhuime, Hawkesworth, and Cawood (2011).

- Figure 5.12:** Histogram and Kernel density estimation for the Eastern Desert magmatic activities. 229
- Figure 5.13:** Geochronological map of the magmatic activities in the Eastern Desert crust. The age data was used to construct this map found in Table 5.1. The Eastern Desert terranes boundaries (dashed dark-red lines) are after Stern and Hedge (1985). 230
- Figure 5.14:** Histogram and Kernel density estimation for the Eastern Desert pre-collision magmatism and collision-related magmatism. 234
- Figure 5.15:** A proposed tectonic model for the evolution/growth of the Eastern Desert crust. 235
- Figure 6.1:** X-ray elemental map of the studied Cr-Spinel. (a) Backscattered electron (BSE) image of a Cr-spinel grain with a homogenous core surrounded by a small magnetite rim. Al (b) and Cr (c) X-ray map for the same grain show reverse zoning for Al and Cr. Asymmetrical and heterogeneous distribution of Al-Cr within the core (d) and gradual increase of Al-Cr from core to rim (b, c, e, f) of three different Cr-spinel grains. White arrows point to Al halos around inclusions within the Cr-spinel grains (d) and high Al content in small grains with tightly curved rims (b-e). The results of the Atom probe tomography (APT) specimens for the core (M8 and M10) and rim (M5 and M6) are shown in Figures 8.5. Mag = magnetite, Srp = serpentine, IC = inner core and R= rim. 261
- Figure 6.2:** Plots of the studied Cr-Spinel chemical composition for different zones within the grains. (a) Cr# (Cr/Cr+ Al) vs. Mg# (Mg/Mg+ Fe⁺²) plot of all the raw datasets for Cr-spinel grains in the studied rocks. Such data are usually not published in previous literature. The data span between recommended fields used in previous literature for abyssal peridotites (Dick and Bullen, 1984) and fore arc (FA)-peridotites (Ishii *et al.*, 1992; Parkinson and Pearce, 1998). (b) Representative/average Cr-spinel data for each sample. Such sample-average data are usually used in previous mantle petrology studies. This plot shows that our samples had a fore arc origin. (c) Al₂O₃ vs Cr₂O₃ and (d) Cr# vs Mg# plots of the studied Cr-spinel grains with low Al₂O₃ and high Cr₂O₃ and Cr# in their cores, and high Al₂O₃ and Low Cr₂O₃ and Cr# in their rims (reverse zoning). Partial melting trend and the brown line between abyssal peridotites (Cr# <0.60) and FA-peridotites (Cr# > 0.60) are from Dick and Bullen (1984). (e) All datasets have trends parallel to both the melting trend and our newly defined metasomatism trend. (f) Datasets of different zones (from core to rim) from four grains from a single sample (sample # A4D) that show large Al-Cr heterogeneity. The data span across the whole range between abyssal peridotites and FA- peridotites. (g) Plots of the studied Cr-spinel grains compared with the compositions of both modified spinel/rims and non-modified spinel/cores of published mantle 263

peridotite xenoliths (Franz *et al.*, 2002; Ishimaru *et al.*, 2007; Ishimaru and Arai, 2009; Ionov, B enard and Plechov, 2011).

- Figure 6.3:** Trace elements concentration of different zones in the studied Cr-Spinel. (a- d) Covariation between Al₂O₃ (wt %) content and fluid-mobile elements (FME: Li, Rb, Sr and Cs). All the elements show positive a correlation with Al content and an increase from core to rim. (e) FME and transition elements normalized to primitive mantle (McDonough and Sun, 1995) compare with the average content of subduction inputs including altered oceanic crust (AOC) (Staudigel, 2013), global subducted sediments (GLOSS II) (Plank, 2013) and marine sediments (Li and Schoonmaker, 2013), melt inclusions in Cr-spinel from Avacha peridotite xenoliths (Ionov, B enard and Plechov, 2011), and spinel in refractory/depleted peridotites (Szilas *et al.*, 2018). The Cr-spinel show high enrichment in FME, attributed to slab-derived fluid/melt interaction with host peridotites. 265
- Figure 6.4:** EBSD microstructural data from two Cr-spinel grains from sample A4D. Images comprise greyscale image of EBSD pattern quality overlain by misorientation maps measured relative to the orientation of spinel lattice at the position shown by the white cross. For grain (a) total misorientation is 10 , for (b) the total misorientation is 15 . The change in misorientation in each grain corresponds to presence of late fractures seen in the pattern quality image. Total misorientation within individual fracture-bound regions of the grain is <1 , indicating that there is no plastic deformation within the grains. 267
- Figure 6.5:** Atom probe tomography results. Atom maps of Mg, Cr, Al and Fe are presented for needle-shaped specimens from the core (M8 and M10) and the rim (M5 and M6). The specimens were extracted from sample A4D and their location is indicated on figure.1b. The composition in atomic % is indicated for each specimen (See Supplementary Data 2). The composition of the core is enriched in Cr and depleted in Al compared to the rim. 268
- Figure 6.6:** Spinel Cr# and Mg# for the forearc peridotites. (a) Cr-spinel database from arc-peridotites including forearc settings (composed of mantle wedge xenoliths (e.g., the Kamchatka arc) (Ishimaru *et al.*, 2007; Ionov, 2010) and dredged samples from present-day oceanic arcs (e.g., the Izu-Bonin-Mariana arc) (Ishii *et al.*, 1992; Parkinson and Pearce, 1998)) and back arc- peridotites (i.e., Mariana Trough) (Ohara *et al.*, 2002, 2003). (b) Cr-spinel database from abyssal/ Mid-ocean ridge (MOR) peridotites. See Supplementary Data 3 for the arc and MOR-Cr-spinel datasets. All the arc and MOR-peridotites dataset plot within the Cr-spinel from mantle wedge peridotites (Arai and Ishimaru, 2008). (c) All arc peridotite Cr-spinel datasets (without filtering) plotted against MOR-peridotite one, showing their overlapping fields. (d) Filtered dataset for both arc- and MOR-peridotite are still completely overlapping. For filter details, see the methods. The shaded area in (c, d) marks the overlapping range of Cr# (0.15-0.65) between the arc-peridotite and MOR-peridotite fields. 274
- Figure E.1:** Samples location of peridotite rocks that have modified spinel. The map shows the distribution of mid-ocean ridge (MOR) and arc-peridotites whole dataset used in this study and ones that have Al-Cr reverse zoning 283

in spinel and modified spinel that passed our filter. In addition to some examples of on-land ophiolites and mantle xenoliths that also have modified Cr-spinel. Only a small proportion of the original authors clearly stated spinel heterogeneity. The on-land ophiolites samples have ages ranging from Archean to the Present. See Supplementary Data 1 for more details about this record. Our compilation is certainly not an exhaustive one of all results on modified spinel as such features have commonly been ignored in previous studies, but it does illustrate how widespread such a feature is, and forms a base for future data addition.

- Figure E.2:** Simplified geological maps of the Eastern Desert region in Egypt and study area with sampling locations. (a) Distribution of ophiolitic rocks in the Eastern Desert of Egypt (Johnson *et al.*, 2011). (b) Geological map of the Wadi Alam serpentinitized peridotites (Hamdy and Gamal El Dien, 2017). (c) Partially serpentinitized peridotites showing lensoidal bodies. (d) Olivine (Ol) relics forming mesh texture and bastite texture, with oriented magnetite grains along cleave planes (e) Olivine cracked crystals dissected by antigorite (Atg) serpentine network. (f-h) Orthopyroxene (Opx) bastite texture has small magnetite (Mgt) grains distributed along original pyroxene cleavage. Carb = Carbonates. 284
- Figure E.3:** Whole-rock Al_2O_3 (wt %) vs. selected major, trace and rare earth elements variation of the studied peridotites. Fields of abyssal peridotites (Deschamps *et al.*, 2013; Peters *et al.*, 2017), forearc peridotites (Parkinson and Pearce, 1998), Oman peridotites (Le Mée, Girardeau and Monnier, 2004), mantle wedge peridotites (Deschamps *et al.*, 2013) and mantle xenoliths (Ionov, 2010). Composition of primitive mantle (McDonough and Sun, 1995) and depleted MORB mantle (DMM) (Workman and Hart, 2005) is plotted for comparison. 285
- Figure E.4:** Primitive mantle-normalized (McDonough and Sun, 1995) multielement and rare earth element patterns normalized to chondrite (Anders and Grevesse, 1989) of the studied peridotites. (a) Estimation of degree of partial melting for the studied rocks by using the non-modal fractional melting model of a source of depleted MORB mantle (DMM) (Workman and Hart, 2005), with melting curves based on an assumed source of DMM composition in the spinel stability field (De Hoog *et al.*, 2009). (b-c) A comparison our studied rocks with that of different tectonic settings and metasomatized peridotites from Arabian-Nubian Shield (ANS; after Hamdy *et al.* (2013)). (e) Primitive mantle normalized elements for the studied rock showing a gradual increase from rare earth elements to high field strength elements and high enrichment in Mo. 286
- Figure E.5:** A determination of the degree of partial melting of the studied rocks based on bulk-rock chemistry. The plots of Yb (ppm) vs. Sc ppm (a) and V ppm (b) are for residual peridotites according to Lee *et al.* (2003), with annotated degrees of mantle melting (in %). Diagrams contain fractional melting trends for different oxygen fugacities. FMM = Fertile MORB mantle. Vanadium behaves as a moderately incompatible element while melting under reducing conditions (QFM-1; this refers to $\log f\text{O}_2$ (QFM) = log units relative to quartz-fayalite-magnetite buffer), resulting in low depletion of V; under oxidizing conditions (QFM+1), the ratio of $\text{V}^{3+}/(\text{V}^{4+}+\text{V}^{5+})$ is low and partition coefficients are high. Thus vanadium as a highly incompatible element is readily depleted in the mantle during partial melting. Legends for symbols are the as in Figure E.3. 287

Figure E.6:	Variation diagrams of LOI (wt%) vs. selected major, trace and rare earth elements of bulk composition of the studied peridotites. The plots show no correlation between LOI and the selected elements.	288
Figure E.7:	Co-variation of HFSE and LREE. (a) Nb vs Σ LREE and (b) Th vs Σ LREE. The plots show the melt-rock interaction and fluid-rock interaction (serpentinization-related) trends (Paulick <i>et al.</i> , 2006). The studied peridotites have been affected by post melting melt/rock interactions process that led to HFSE enrichments. Legends for symbols are the as in Figure E.3.	289
Figure E.8:	Al-Cr-Fe-Mg X-ray elemental maps for the studied Cr-Spinel. The maps show heterogeneity in Al-Cr content distribution within the grains, but relatively homogenous Fe and Mg distribution between the cores and the rims.	290
Figure E.9:	Binary plots of Al ₂ O ₃ (wt %) vs. transition elements for the studied Cr-spinel. Sc shows negative relation, Ti and Ni show positive relation, V, Mn, Co and Zn show a V-shape relation, whereas Cu and Ga show no relation.	291
Figure E.10:	Binary plots of Fe ³⁺ /(Fe ³⁺ + Fe ²⁺) ratio vs Al ₂ O ₃ (wt %) and FME (ppm) for the studied Cr-spinel. The plot shows that Fe ³⁺ /(Fe ³⁺ + Fe ²⁺) ratio has a constant value between the Cr-spinel cores and rims and has no relationship with Al and FME.	292
Figure E.11:	Compositional variation for Cr-spinel in the global datasets for abyssal peridotites. The plots show Cr-spinel Cr# and Mg# in different mid-ocean ridges peridotites and defined as residual and non-residual peridotites. Red dash line represents melting trend from Dick and Bullen (1984). EPR= East Pacific Rise, CIR= Central Indian Ridge, MAR= Mid-Atlantic Ridge, AAR= American-Antarctic Ridge, SWIR= Southwest Indian Ridge and Arctic including Gakkel ridge, Lena trough and Molloy ridge.	293
Figure E.12:	LA-ICP-MS ablation profiles of the counting vs time (s) for trace element analyses for the studied Cr-spinel. All the calculated peaks area do not have any significant positive peaks for ²⁹ Si and ⁵⁷ Fe which indicated that there are no silicate inclusions and/or magnetite measured.	294
Figure E.13:	Atom probe mass spectrum of the studied Cr-spinel. The cations are present as different molecular species with singly-charged to triply-charged ions. For example, Cr is present as Cr ⁺ , Cr ⁺⁺ , CrO ⁺ , CrO ⁺⁺ , CrO ₂ ⁺ , CrO ₂ ⁺⁺ , CrO ₃ ⁺ and Cr ₂ O ₃ ⁺ ; and Al is present as Al ⁺ , Al ⁺⁺ , Al ⁺⁺⁺ , AlO ⁺ , AlO ⁺⁺ , AlO ₂ ⁺ , Al ₂ O ⁺⁺ , and AlCrO ₃ ⁺⁺ .	296
Figure 7.1:	Photomicrographs of the studied serpentinites. (a-c) Interpenetrating texture of antigorite (Atg). (d) Magnesite (Mgs) clast containing antigorite relics. (e) Raman spectra of fine (F) and coarse (C)-grained antigorites in the studied serpentinites in low frequency (0–1500 cm ⁻¹) and OH stretching (3350–3900 cm ⁻¹) ranges. Antigorite shows discrete peaks at 232, 377, 688 and 1044 cm ⁻¹ in the low wavenumber region and	304

3686 and 3702 cm^{-1} in the OH-band region. The Raman spectra of magnesite show peaks at 229, 332 and 1099 cm^{-1} in the low wavenumber region.

- Figure 7.2:** Mineral chemistry of antigorites from the studied samples. (a) Si/(Si+Al) vs. Mg/(Mg+Fe). The variation of Mg/(Mg+Fe) indicates different bulk chemistry of the rocks while the variation of Si/(Si+Al) is due to increase in the metamorphic grade. (b) NiO vs. Cr_2O_3 (wt %). Data used to create olivine and orthopyroxene fields collected from Kodolányi et al. (2012). 308
- Figure 7.3:** Primitive mantle (McDonough and Sun, 1995) normalized multielement and rare earth element patterns normalized to chondrite (Anders and Grevesse, 1989) of the studied antigorite and magnesite. 309
- Figure 7.4:** T-X pseudosections. The two pseudosections constructed at pressure 8 kbar (a) and 1 kbar (b) in the chemical system FMCASH- CO_2 using the activity models cited in the methods section. The x-axes represent a range of the bulk composition in wt% where 0 is equivalent to bulk of: FeO: 4.157, MgO: 47.13, CaO: 0.001, Al_2O_3 : 0.715, SiO_2 : 40.524, H_2O : 8.89, CO_2 : 0.001, and 1 is equivalent to bulk of: FeO: 7.00, MgO: 35.00, CaO: 0.04, Al_2O_3 : 3.00, SiO_2 : 50.00, H_2O : 18.00, CO_2 : 0.8. The red isochemical lines represent the chlorite-in boundaries. The studied mineral assemblages are stable to right-side of the chlorite-in boundaries. The yellow line shows the anthophyllite-in boundary. The studied assemblages are stable to the lower temperature part of the anthophyllite-in boundaries. 310
- Figure 7.5:** P-T-X pseudosection showing the shift of the anthophyllite-in boundaries toward higher temperature conditions when the pressure increases. The yellow area represents the anthophyllite-in boundaries at pressure of ca. 4 kbar which is equivalent to the peak metamorphic pressure of the volcanic arc assemblages of the Arabian-Nubian Shield (Abu-Alam *et al.*, 2014). The pressure represents a combination of lithostatic and hydrostatic pressures. The vertical isochemical solid lines show the shifting in the chlorite-in boundary with pressure change. Contour lines are the Si/(Si+Al) ration of the antigorite chemistry in the T-X space. The solid black arrow represents the P-T-X path of the studied rocks. The red dots along the P-T-X path represent some of the analysed antigorites (CA at the low temperature conditions) and (FA at the high temperature conditions).
The right hand plots shows the variations of Li and Rb (b) B, Sr and As (c) contents of the two group antigorites with the temperature changing along the P-T-X path. The x-axes represents temperature and Si/(Si+Al). 312
- Figure 7.6:** The average contents of fluid-mobile element and light rare earth element patterns of the studied serpentinites and rock forming minerals (antigorite and magnesite) normalized to the Primitive Mantle (McDonough and Sun, 1995). (a, b) plotted against the composition of hydrothermal fluids (Logatchev, Rainbow, Snake Pit) (Schmidt *et al.*, 2007) and the contents of subduction inputs including altered oceanic crust (AOC) (Staudigel, 2013), global subduction sediments (GLOSS II) (Plank, 2013) and marine sediments pattern (Li and Schoonmaker, 2013) 320

are reported for comparison; (c) plotted against the average compositions of arc-related basalts, plume-related basalts and mid ocean ridge basalts (MORB) after Georoc repository (<http://georoc.mpch-mainz.gwdg.de/georoc/>).

- Figure 7.7:** A cross-section sketch of a subduction zone complex showing the position of the first serpentinization stage (Serp-1) and formation of coarse antigorites (Atg) at 200–250 °C, the second serpentinization stage (Serp-2) and formation of fine antigorites at 425–475 °C and magnesite formation (Mgs). 321
- Figure F.1:** (a) Distribution of the ophiolites in the Arabian-Nubian Shield (modified after Vail (1983)). (b) Location of the studied serpentinite masses and their relations, with the major structural trends and younger metamorphic and magmatic core complexes (MCC, Meatiq and SCC, Sibai) in the East-African Orogen, central Eastern Desert of Egypt (major structures are after Fritz et al. (2013) and Abd El-Wahed and Kamh (2010)). (c) Geologic map of the Muweilih serpentinites in the Wadi Muweilih area (modified after El Bahariya (2012)). 331
- Figure F.2:** (a, b) Field photos showing a tectonic melange consisting of highly sheared serpentinites and schists. Photomicrographs of the studied serpentinites. (c) Carbonates (Carb) veins crosscut the antigorite (F-Atg and C-Atg) groundmass, indicating a later formation age after antigorite. (d) Magnesite (Mgs) veins with small amounts of talc (Tlc). (e) Chlorite aggregates disseminated in the antigorite groundmass. 332
- Figure F.3:** Variation diagrams of LOI (wt%) vs. selected major, trace and rare earth elements of bulk composition of the serpentinites. 335
- Figure F.4:** Primitive mantle (McDonough and Sun, 1995) normalized multielement and rare earth element patterns normalized to chondrite (Anders and Grevesse, 1989) of the studied serpentinites. Fields of Abyssal peridotites are from Niu (2004) , supra subduction zone (SSZ; Izu-Bonin-Mariana) peridotites from Parkinson and Pearce (1998) and Subducted and mantle wedge serpentinites from Deschamps et al. (2013). The non-modal fractional melting model of a depleted MORB mantle (DMM)source (Workman and Hart, 2005) is used, with melting curves assumed of a of DMM source in the spinel stability field (De Hoog *et al.*, 2009). 336
- Figure F.5:** Whole-rock Yb (ppm) vs. selected major, trace and rare earth elements variation of the studied serpentinites. Fields of abyssal peridotites are from Niu (2004), and supra subduction zone (SSZ; Izu-Bonin-Mariana) peridotites from Parkinson and Pearce (1998). Compositions of the primitive mantle (McDonough and Sun, 1995) and depleted MORB mantle (DMM) (Workman and Hart, 2005) is plotted for comparison.. Determination of the degree of partial melting was based on bulk-rock chemistry showing in figures (c, d) according to the bivariate of Yb (ppm) vs. Cr and V (ppm) for residual peridotites, according to Lee et al. (2003), with annotated degrees of mantle melting (in %). Fractional melting trends for different oxygen fugacities are also shown. FMM = fertile MORB mantle. Vanadium behaves as a moderately incompatible 337

element when melting occurs under reducing conditions (QFM–1; this refers to $\log fO_2$ (QFM) = log units relative to quartz–fayalite–magnetite buffer), resulting in low depletion of V. Under oxidizing conditions (QFM+1), the ratio of $V^{3+}/(V^{4+}+V^{5+})$ become lower whereas partition coefficients are higher causing vanadium to become a highly incompatible element and readily depleted in the mantle during partial melting. The melt/rock interaction trend in (b) after Deschamps et al. (2013) Depletion trends are after Uysal et al. (2016) and Gamal El Dien et al. (2016).

Figure F.6: Binary plots of B and various trace elements in the studied antigorites showing the different contents between the two antigorites groups. All concentrations are in ppm. 338

Figure F.7: A T-X pseudosection at 2 kbar shows the stability range of the spinel mineral up to > 670 °C. This indicates that the observed spinel in the studied samples are a metastable phase with respect to the surrounding low-grade assemblage. The x-axis is the bulk composition which is similar to that in Figures. 4 and 5 in the main text with the exception of reducing the system to FMASH. 339

Figure 8.1: Density plot of Ni, Cr, and Mg# for different basaltic magmatism types. Panels a, b and c are density plots of plume-related basalts (PRB) for Ni (ppm) vs. Cr (ppm) and Mg# ($100 \cdot MgO / (MgO + FeO)$) vs. Ni (ppm) and Cr (ppm), respectively. Panels d-f are density plots for mid-ocean ridge basalts (MORB) and g-i panels are for arc-related basalts. Data sources: Georoc and EarthChem (see Methods and Supplementary Data 1). Black contours define the data density values from high density (blue) to low density (red). The white contour represents 70% of PRB data. 362

Figure 8.2: Density plot of Fe/Mn vs. Mg# for different basaltic types. (a) Plume-related basalts (PRB); (b) mid-ocean ridge basalts (MORB); (c) arc-related basalts. Data sources: Georoc and EarthChem (see Methods). Black contours define the data density values from high density (blue) to low density (red). The white contour represents 70% of PRB data. 363

Figure 8.3: Time evolution of global mean MgO, Ni and Cr contents after a bootstrap resampling of the selected basaltic database. The blue dashed lines in a–c are regression lines for data between 0 to 3.0 Ga that reveal first-order secular decreases. Error bars in a–c show 2-s.e.m. (standard error of the mean) uncertainties. (d) Secular cooling of Earth’s mantle based on non-arc basalts (Herzberg, Condie and Korenaga, 2010) and thermal modelling (Korenaga, 2008). Urey ratios (Ur) are shown: 0.08 (upper curve), 0.23 (middle curve) and 0.38 (lower curve). 365

Figure 8.4: Variability of global mean MgO, Ni and Cr in basalts after detrending the linear secular decreases. The linear secular decreases used are those shown with blue dash lines in Figure 8.3. The plot shows major positive peaks at ~2.8–2.3 Ga, ~1.6–1.3 Ga, ~1.0–0.7 Ga, and ~0.3–0.0 Ga, broadly consistent with the tenures and break-up times of post-2 Ga supercontinents. The durations of supercontinent tenure (Evans, Li and Murphy, 2016; Pourteau *et al.*, 2018) are marked with solid green 368

vertical bars, e.g., at ca. 320–170 Ma (Pangea), 900–700 Ma (Rodinia), 1600–1300 Ma (Nuna), but the occurrence of Kenorland during 2700–2300 Ma is highly uncertain (thus shown in faded green). The assembly and break-up of supercontinents are generally prolonged and multistage processes, which are marked by gradual green shading.

- Figure G.1:** Covariation of MgO vs Ni, Cr, Ni/Co and Cr/Zn for different mantle magmatic products (komatiites, picrites and basalts). Data source: Georoc and EarthChem. 374
- Figure G.2:** Covariation plots of Mg# ($100 \times \text{MgO} / (\text{MgO} + \text{FeO})$) vs. Ni with the size of the symbol proportional to Cr content in each samples for plume-related basalts (PRB) (a), mid-ocean ridge basalts (MORB) (b) and arc-related basalts (c). Data sources: Georoc and EarthChem. 375
- Figure G.3:** Geographic distribution map of basaltic datasets used for bootstrap resembling and the plots in Figures 3a-c and 4. The basaltic datasets have an age range of 3.8 to 0 Ga, sourced from the Georoc and EarthChem community data repositories. 376
- Figure G.4:** Variability of global mean of bootstrap data of MgO, Cr and Ni in basalts from the global database (left hand plots), and plots of the same dataset after detrending the linear secular decreases (dashed lines) (right hand plots). 377
- Figure 9.1:** $^{143}\text{Nd}/^{144}\text{Nd}$ ratio (represented as ϵNd) vs. age for Archaean and Proterozoic basaltic rocks and komatiites (data from Spencer *et al.* (2018)). Brown circles represent individual samples. Red dots represent the median of samples with the same age, and the associated error bars spans across the middle 50% of the data, called the median data range here. The red field represents the envelope for the median range. The large variation in the mean ϵNd values after ~ 3.2 – 3.0 Ga suggests an isotopic shift in the mantle source of the basaltic rocks and the komatiites. The depleted mantle curves are shown for comparison (DePaolo, 1981; Goldstein, O’Nions and Hamilton, 1984). 386
- Figure 9.2:** Time evolution of fluid-mobile-elements/immobile-elements in the basaltic rock datasets. Ba/La (a), Ba/Nb (b), U/Nb (c), and Pb/Nd (d). All ratios show an abrupt increase at ~ 3.25 Ga. Dotted horizontal lines are the primitive mantle values (PM; Ba/La = 10.81, Ba/Nb = 10.03, U/Nb = 0.03, Pb/Nd = 0.12) (McDonough and Sun, 1995). Error bars in a–d show the 2-standard errors of the means. 388
- Figure 9.3:** Time evolution of fluid-mobile-elements/immobile-elements in the komatiite datasets.. Ba/La (a), Ba/Nb (b), U/Nb (c), and Pb/Nd (d). All ratios show an abrupt increase at ~ 3.15 Ga. Dotted horizontal lines are the primitive mantle values (PM; Ba/La = 10.81, Ba/Nb = 10.03, U/Nb = 0.03, Pb/Nd = 0.12) (McDonough and Sun, 1995). Error bars show 2-standard error of the mean. 388
- Figure H.1:** Sample locations of basaltic rocks and komatiites used in this study. The map shows that the samples covered all the continents. This map created 399

using ArcGIS Desktop 10.7 final-Curtin university licenced version (<https://www.arcgis.com/home/index.html>).

- Figure H.2:** 2D Pie-charts show that the distribution of the studied samples of basaltic rocks and komatiites is representative for all continents and cratons. 399
- Figure H.3:** 2D Pie-charts show that the distribution of the studied basalt samples is representative of all the cratons for the time range of 3.8–2.4 Ga. 400
- Figure H.4:** 2D Pie-charts show that the distribution of the studied komatiite samples is representative of all the cratons for the time range of 3.8–2.0 Ga. 401
- Figure H.5:** Time evolution of Pb/Ce ratios for basaltic rocks (a) and komatiites (b). Pb/Ce ratio shows an abrupt increase after ~3.25 Ga for basalts and after ~3.15 Ga for komatiites. Error bars show the 2-s.e.m. (standard error of the mean) uncertainties. 402
- Figure H.6:** Plots of Th/Yb vs Ba/La (a), Ba/Nb (b), U/Nb (c), Pb/Nd (d), and Pb/Ce (e) for basaltic rocks and TTGs. The basalts datasets are split into two age ranges <3.25–2.4 Ga and >3.8–3.25 Ga. Th/Yb is significantly higher for TTGs than for basalts, indicating no crustal contamination in the basalts. 402
- Figure H.7:** Plots of Th/Yb vs Ba/La (a), Ba/Nb (b), U/Nb (c), Pb/Nd (d), and Pb/Ce (e) for komatiites. The datasets are split into two ranges as <3.15–2.0 and >3.8–3.15 Ga. Th/Yb is significantly higher in TTGs than in komatiites, indicating no crustal contamination in the komatiites. 403
- Figure H.8:** Nb/Yb-Th/Yb plots Pearce (2008) for the studied basalts (a, b), komatiites (c, d) and TTGs. The primitive mantle value is from McDonough and Sun (1995), and the modern-arc basalts datasets are collected from Georoc. The basalt and komatiite datasets define a trend (bold blue arrows) parallel to the oceanic mantle array (grey field), as do modern arc-basalts. In contrast, TTGs have an oblique trend (bold green arrow). Moreover, the Th/Yb ratios of the TTGs are significantly higher than that of the basalts and komatiites, indicating no crustal contamination. 404
- Figure H.9:** Plots of selected fluid-mobile/immobile elements ratios of tonalite-trondjemite-granodiorite (TTG) rocks. Ba/La (a), Ba/Nb (b), U/Nb (c), Pb/Nd (d), and Pb/Ce. Grey dots represent the entire data compiled from Johnson et al. (2019). Red dots represent the medians using 50 Myr windows, and vertical bars span across the middle 50% of the data, called here the median data range. The rectangular shades of different colours represent the median data range before and after ~3.3–3.2 Ga. Solid horizontal lines are the average of medians for data within each rectangular shade. For Pb/Nd and Pb/Ce, datasets from the Kaapvaal and San-Francisco cratons show abnormal increase at 3.55 and 3.4 Ga which we take as representing local events. All but the U/Nb ratios show a step change to a higher value after ~3.3–3.2 Ga. 405

List of Tables

Table 2.1:	Sr and Nd isotopic ratios for BHVO–2 reference sample obtained by TIMS.	33
Table A.1:	Whole-rock trace and rear earth elements results of the standard references materials from ICP-MS analyses. All the concentrations in ppm.	47
Table A.2:	U-Pb data of the standard zircon references materials from LASS analyses.	53
Table A.3:	Lu-Hf data of the standard zircon references materials from LASS analyses.	56
Table A.4:	O isotopic data for Qinghu zircon standard reference material from SIMS analyses.	60
Table 3.1:	Whole-rock major and trace elements and Sr-Nd isotopes of the El-Shadli plagiogranites and associated gabbros.	104
Table B.1:	Zircon U-Pb data of the studied rocks generated by SHRIMP.	125
Table B.2:	Zircon U-Pb-Hf-O and Trace element data of the studied rocks generated by LASS and SIMS.	127
Table 4.1:	Whole-rock major and trace element and Sr-Nd isotopes of El-Shadli bimodal volcanic province.	173
Table C.1:	Zircon U-Pb age data of the studied rocks using SHRIMP.	190
Table C.2:	Zircon U-Pb-Hf-O and Trace element data of the studied rocks generated using LASS and SIMS.	193
Table 5.1:	List of all previously published U-Pb and Pb-Pb zircon/monazite geochronological data from granitoid and volcanic rocks of the Eastern Desert.	236
Table D.1:	Whole-rock major and trace elements and Sr-Nd isotopes of the Genina Gharbia granitoids.	249
Table D.2:	Zircon U-Pb of sample G04-2 generated by SHRIMP.	250
Table D.3:	Zircon U-Pb-Hf-O and trace element data of sample G04-2 generated by LASS and SIMS.	251

Table F.1:	Major oxides (anhydrous) and trace elements (including REEs) compositions of the studied serpentinites.	340
Table F.2:	EMP data of the studied antigorites.	342
Table F.3:	EMP data of the studied carbonates.	348
Table F.4:	<i>In situ</i> LA-ICP-MS data of the studied antigorites and carbonates.	350
Table G.1:	The average bootstrapped values used to create Figures 8.3 and 8.4 and the normalized values to the secular decrease.	378

Chapter 1:

Introduction

Earth is considered as a complex planetary system and has been evolving since its formation, ~4.56 billion years ago (Ga) (Patterson, 1956; McDonough, 2014; Condie, 2016). As a product of planetary differentiation (McDonough, 2014; Palme and O'Neill, 2014), Earth's interior is subdivided into three major well-defined zones: the crust and mantle, two silicate zones, and the metallic core (Figure 1.1). These zones were identified through seismic discontinuities (Helffrich, 2000; Helffrich and Wood, 2001; Winter, 2014). They reflect sudden changes in the physical properties across the zonal boundaries, including pressure, temperature, mineralogy, chemical composition, water content, and degree of partial melting (Winter, 2014; Condie, 2016). There are three first-order seismic discontinuities that divide the Earth, from top down, the Mohorovicic discontinuity or Moho (the crust-mantle boundary), the Gutenberg discontinuity at ~2900 km (the mantle-outer core boundary), and the Lehmann discontinuity at ~5200 km (the outer core-inner core boundary). The Earth's crust is a thin silicate shell and accounts for less than ~1% of Earth's volume. The mantle (between the crust and the core; Figure 1.1) is the largest of the Earth's three zones representing ~82% of the Earth's volume and ~65% of its mass (Helffrich and Wood, 2001; Bennett, 2003). The core comprises about ~16% of Earth's volume and ~32% of its mass (Winter, 2014; Condie, 2016). This PhD thesis aims to investigate Earth's dynamic evolution through geological time by studying the geochemical record of mantle-derived/related rocks.

1.1 Mantle record of Earth's dynamic evolution

1.1.1 Earth's mantle laying

The Earth's mantle is mainly composed of Fe- and Mg-rich silicate minerals (Ringwood, 1962). Structurally, the present-day mantle is essentially composed of two layers: the upper and lower mantle. The upper mantle extends from the Moho until 660-km depth, and includes the lower part of the lithosphere (the strong outer layer of the Earth that includes the crust and the top layer of the mantle, i.e. the plates, 50–300 km thick) and the asthenosphere (the ductile, highly viscous and mechanically weak region, that extends from the base of the lithosphere to, at some places, 660-km). The region between 410 km and 660 km depth is also called the transition zone (TZ) (Figures 1.1 and 1.2c) (Winter, 2014; Condie, 2016). The transition zone is defined by successive mineral phase changes which start from olivine, through wadsleyite at 410 km, and then to magnesiowüstite and perovskite at 660 km (Ringwood, 1962, 1991; Ringwood and Irifune, 1988; Helffrich and Wood, 2001). This 660-km discontinuity is also characterized by an increase in both density and seismic velocities (Ringwood and Irifune, 1988; Ringwood, 1991; Bina and Helffrich, 2014; Winter, 2014; Condie, 2016). The lower mantle is the thickest layer of the mantle and extends from 660-km to the Gutenberg discontinuity at ~2900 km, at the core-mantle boundary (Ringwood and Irifune, 1988; Condie, 2016) (Figures 1.1 and 1.2c). At the boundary between the lower mantle and the core is a ~200 km thick layer, the D'' layer (not shown in Figure 1.1), which exhibits ambiguous seismic velocities (Weber and Davis, 1990; Ringwood, 1991; Lay, Williams, and Garnero, 1998; Mao *et al.*, 2005) (Figure 1.2c). This layer displays lateral chemical heterogeneity and a thermal structure that distinguishes it from the overlaying mantle (Helffrich and Wood, 2001).

Seismic tomography has unveiled the presence of two antipodal large low shear velocity provinces (LLSVPs) in the lower mantle under the Pacific ocean and Africa (Dziewonski, 1984; Li and Zhong, 2009; Dziewonski, Lekic and Romanowicz, 2010) (Figures 1.2c and 1.3). These two LLSVPs are also known as the African and Pacific superplumes (Anderson, 1994; Anderson and Natland, 2005; Zhong *et al.*, 2007; Li and Zhong, 2009). It has been suggested that most mantle plumes are generated in the lower mantle and might be linked to these LLSVPs (e.g.,

Hill *et al.*, 1992; Courtillot *et al.*, 2003; Koppers, 2011). This is supported by the present-day observation, and reconstructed locations, of hotspots (i.e., oceanic island basalts; OIBs) and flood basalts (i.e., large igneous provinces; LIPs) occurring on the margins of the two LLSVPs (Burke *et al.*, 2008; Burke, 2011). Seismic topography has also demonstrated that subducted slabs can descend down to the lower mantle and stagnate at the core-mantle boundary (van der Hilst, Widiyantoro and Engdahl, 1997) (Figures 1.2c and 1.3a). Geodynamic modelling suggests that these deep, cold, stagnant subducted slabs can lead to an upward return flow that could potentially trigger the formation of the LLSVPs (Li, Evans and Zhang, 2004; Zhong *et al.*, 2007; Li and Zhong, 2009; Zhang *et al.*, 2010).

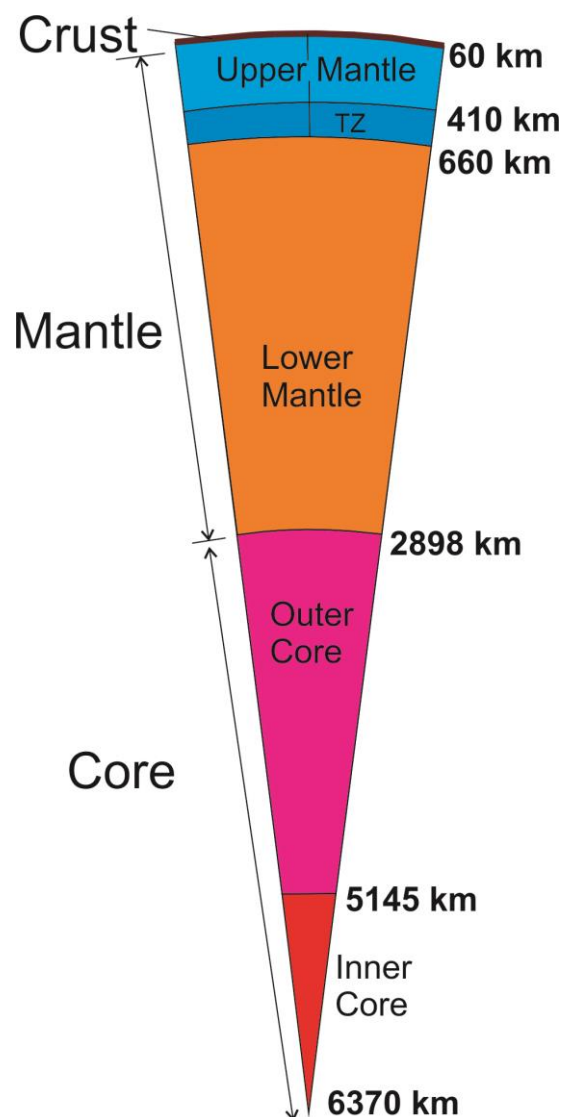


Figure 1.1: The Earth's interior structure showing the major subdivision zones of the Earth (crust, mantle, and core). The figure is modified after Winter (2014). TZ= transition zone.

Basalts formed by melting of the mantle at mid-ocean ridges (i.e., MORBs) and hotspots (OIBs) show that, chemically, the present-day Earth's mantle is composed of various reservoirs that have distinct geochemical and isotopic compositions, that may reflect long-lived and large-scale heterogeneity in the mantle (Zindler and Hart, 1986; Sun and McDonough, 1989; McDonough and Sun, 1995; Helffrich and Wood, 2001). There are three major reservoirs: primitive mantle (PM), depleted mantle (DM), and enriched mantle (EM) (Zindler and Hart, 1986; Sun and McDonough, 1989; McDonough and Sun, 1995; Helffrich and Wood, 2001; Hofmann, 2014; White, 2015). The PM reservoir, or Bulk Silicate Earth (BSE) (McDonough and Sun, 1995; Hofmann, 2014; White, 2015), is the initial composition of the mantle after the segregation of the core, that had not yet been depleted by the extraction of the continental crust (Palme and O'Neill, 2014). The DM reservoir is the mantle that has been depleted by the extraction of the continental crust and typically represents the source of mid-ocean ridge basalts (MORBs) (Hofmann, 1997, 2014). The EM reservoir, typically the source for OIBs, is composed of three enriched sources: HIMU, which exhibits high U/Pb components; EM1, and EM2, that reflect long-term enrichment of the source by different terrestrial materials (Zindler and Hart, 1986; Hofmann, 1997, 2014; White, 2015).

The evolution of the Earth's mantle, from the Hadean (Figure 1.2a, b) to the present-day (Figures 1.2c and 1.3) reflect major changes in processes that govern mantle dynamics (Bennett, 2003; Condie, 2016). These processes mainly comprise: (1) an extensive differentiation and generation of the crust (continental crustal growth, and crustal recycling; Kemp and Hawkesworth, 2014; Hawkesworth, Cawood and Dhuime, 2020), (2) plate tectonics including the generation of global subduction (Korenaga, 2013; Cawood *et al.*, 2018), (3) the effect of subduction zones on the mantle geochemical cycle and its heterogeneities (Poli and Schmidt, 2002; Stern, 2002a; Hofmann, 2014), and (4) the assembly and breakup of supercontinents and their feedback on deep mantle processes and the shape and formation of superplumes (Li and Zhong, 2009; Li *et al.*, 2019).

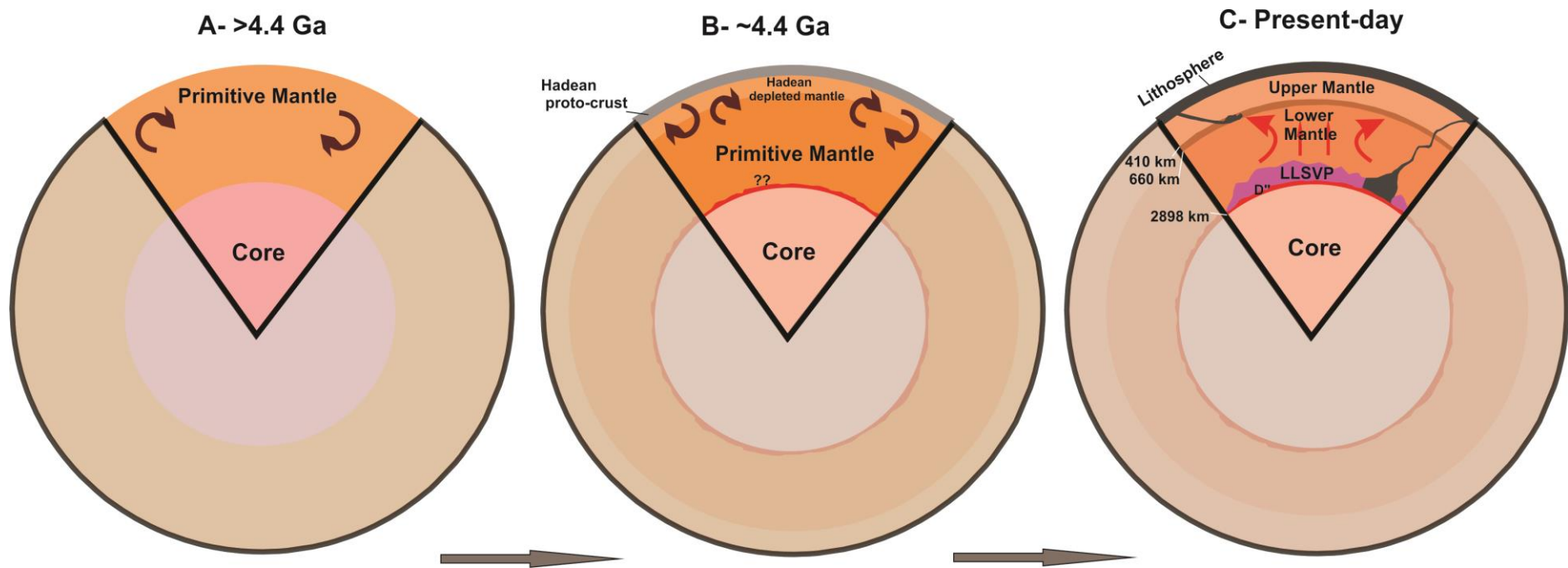


Figure 1.2: A schematic diagram illustrating the evolution of the Earth's Mantle. Hadean primitive mantle at > 4.4 Ga (a) and formation of the Hadean depleted mantle and proto-crust at ~ 4.4 Ga (b) modified after Saji *et al.* (2018). (c) A simplified diagram showing the present-day Earth's mantle structure.

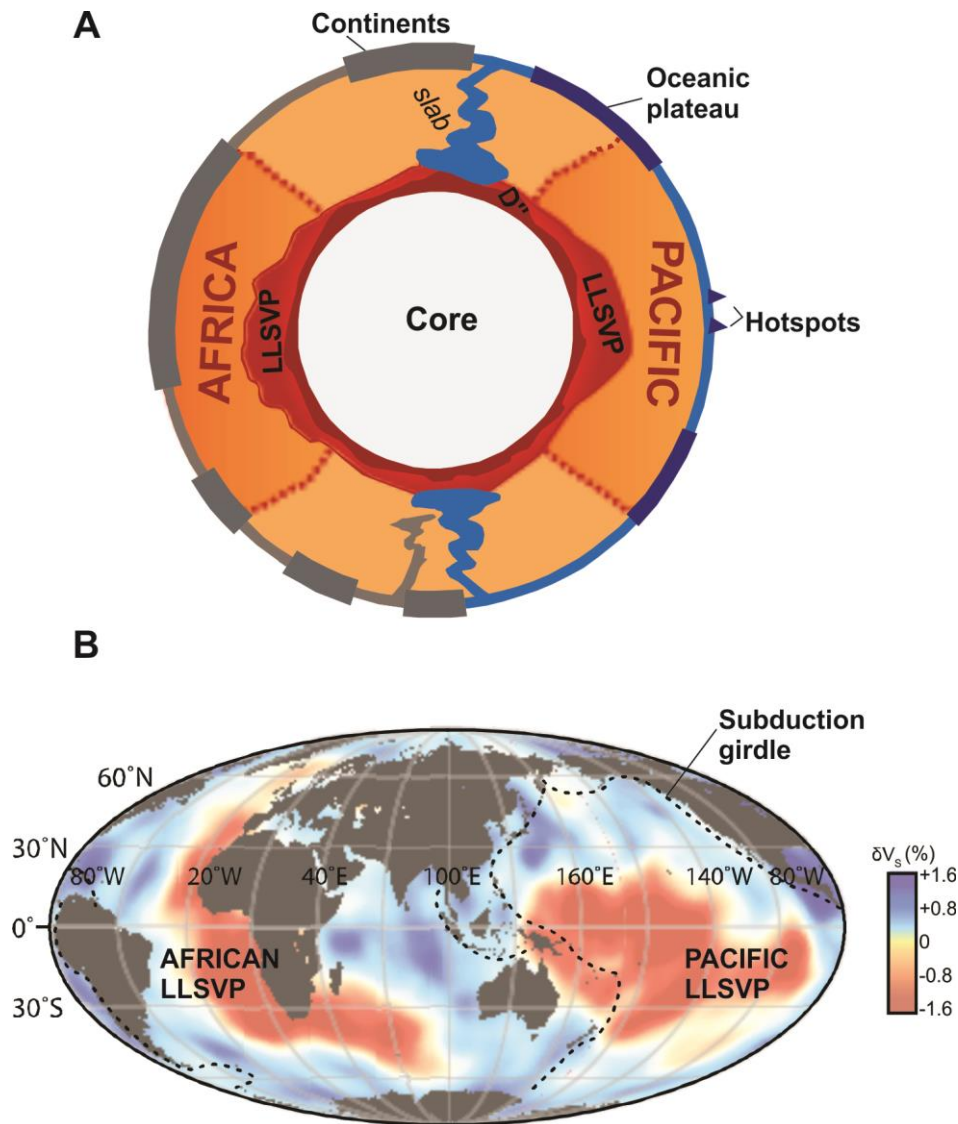


Figure 1.3: The present-day lower mantle structure. (a) The configuration of the two equatorial African and Pacific LLSVPs (modified after Li *et al.* (2019) and Doucet *et al.* (2020)). (b) Earth's seismic map of the LLSVPs. Seismic shear-wave velocity anomalies (δV_s) are those of the mean S-wave tomography model s5mean. This figure is modified after Doucet, Li, Gamal El Dien, *et al.* (2020).

During the first two eons of Earth's history (Hadean ~4.56–4.0 Ga and Archean 4.0–2.5 Ga), several processes fundamentally changed the interior and surface of the Earth. Such processes include core-mantle and mantle-crust differentiation, and continental crust formation. During the Hadean eon, >4.4 Ga, separation of the early Earth's mantle from the core, by a process called differentiation, lead to the formation of the Hadean primitive mantle (Hofmann, 2014; McDonough, 2014; Palme and O'Neill, 2014; Saji *et al.*, 2018) (Figure 1.2a). The composition of this primitive mantle was controlled by the chemical behaviour

of the elements (McDonough, 2014; Palme and O'Neill, 2014). As the mantle constitutes the main bulk silicate part of the Earth, its chemical composition would have been enriched in the lithophile elements (e.g., Mg, Si, Al, and Ca) and more depleted in siderophile elements (e.g., Ni, Fe, W, S, and Os), with the latter being retained in the core during its formation (Helfrich and Wood, 2001; Palme and O'Neill, 2014). Some recent studies have shown that the Hadean primitive mantle had a distinct isotopic and trace element composition, and some may have survived to the present-day and can potentially be sampled by young volcanism such as the Ontong Java plateau (Jackson *et al.*, 2010; Jackson and Carlson, 2011).

1.1.2 Earth's continental crust and crustal growth

The formation of the early Earth's crust during the Hadean potentially led to the first depletion of the mantle in incompatible elements, such as Na, K, and P which would be taken up by the crust (Bennett, 2003; Palme and O'Neill, 2014; Rudnick and Gao, 2014), forming a Hadean depleted upper mantle and its complementary proto-crust (Bennett, 2003; Saji *et al.*, 2018) (Figure 1.2b). This Hadean depleted upper mantle has been identified through ^{142}Nd systematics of Eoarchean Isua amphibolites, that suggest a formation age of the Isua depleted mantle reservoir at ~ 4.4 Ga (Saji *et al.*, 2018). The oldest known zircons (ca. 4.4 Ga) are found in the Jack Hills and Mt. Narryer in 3.3 Ga old metasedimentary rocks from Western Australia, and have been interpreted as remnants of the differentiated Hadean proto-crust, potentially the first continental crust (Wilde *et al.*, 2001; Cavosie, Valley and Wilde, 2019). Thus, the generation/extraction of continental crust, i.e. the crustal growth process, plays an important role in the chemical evolution of the Earth's mantle through time and the evolution of the Earth in general (Patterson, 1956; Rudnick and Gao, 2014).

The oldest, uncontroversial, zircon dated terrestrial rocks (continental crust) on Earth are from the Acasta gneiss complex in Canada (ca. 4.03 Ga; Bowring and Williams, 1999) marking the transition between the Hadean and the Archean. Archean rocks (4.0–2.5 Ga) represent the major component of the old core “cratons” of many present-day continents, i.e. continental crust (Condie, 2019). However, these rocks only represent about 5% of the exposed present-day continental crust, and less

than 1% of the studied Archean crust is older than 3.5 Ga (Nutman and Bennett, 2019). It had been proposed that a large proportion of Archean crust might have been recycled back into the mantle (Kemp and Hawkesworth, 2014; Condie, 2019; Johnson *et al.*, 2019). The preserved Archean continental crust is dominantly composed of deformed and metamorphosed mantle-related tonalite-trondhjemite-granodiorite rocks (TTGs; juvenile granitoids) (Johnson *et al.*, 2017, 2019; Condie, 2019). Those granitoids/TTGs were produced by partial melting of relatively hydrated basaltic rocks and represent the first-generation of continental crust (Foley, Tiepolo and Vannucci, 2002; Johnson *et al.*, 2014, 2019). Although there is a general consensus about the source rocks of these granitoids (i.e., hydrated mafic rocks), the mechanism(s) responsible for the generation of such continental crust and the processes linked to the crustal growth (including the geodynamic settings and melting of subducted slabs, and/or re-working of plateau-like mafic crust) remains debated, which hampers a comprehensive understanding of the early Earth and mantle evolution (Foley, Tiepolo and Vannucci, 2002; Bennett, 2003; Bédard, 2006; Hawkesworth and Kemp, 2006; Arndt, 2013; Kemp and Hawkesworth, 2014; Martin *et al.*, 2014; Johnson *et al.*, 2017; Bédard, 2018; Moyen and Laurent, 2018; Johnson *et al.*, 2019).

Also, the continuous or episodic nature of crustal growth, and the number of stages involved (from magma generation to stabilization/cratonization) remain controversial (Armstrong, 1981; Taylor and McLennan, 1995; Condie, 1998; Bennett, 2003; Hawkesworth and Kemp, 2006; Cawood *et al.*, 2009; Bradley, 2011; Dhuime, Chris J. Hawkesworth, *et al.*, 2012; Arndt, 2013; Arndt and Davaille, 2013; Kemp and Hawkesworth, 2014; Johnson *et al.*, 2017; Hawkesworth, Cawood and Dhuime, 2018; Johnson *et al.*, 2019; Hawkesworth, Cawood and Dhuime, 2020). Whether the crustal growth is a continuous process or episodic is related to the geodynamic setting of crustal generation on the early Earth (Taylor and McLennan, 1995; Arndt, 2013; Arndt and Davaille, 2013). Stein and Hofmann (1994) suggested that episodic crustal growth might be linked to mantle plume-related magmatism and the accretion of oceanic plateaus, whereas continuous growth is thought to be more likely controlled by slab subduction and juvenile addition in magmatic arcs (Taylor and McLennan, 1995; Arndt, 2013; Spencer, Roberts and Santosh, 2017). It is generally considered that, at present, the most important mechanism of crustal growth

is by arc magmatism at subduction zones; whereas the contribution of mantle plumes or rift-related magmatism is limited (Hawkesworth and Kemp, 2006; Cawood *et al.*, 2009; Dhuime, Hawkesworth and Cawood, 2011; Hawkesworth, Cawood and Dhuime, 2013; Cawood *et al.*, 2016). However, regarding the early Earth, it is still unclear what mechanism (arc magmatism or plume-related magmatism or both or another process) best explain the origin of the oldest continental crust.

Outcrops of the Archean rocks are not always easily accessible and are generally restricted to high-grade metamorphic terranes, where in most cases deformation and metamorphism have almost completely modified the original compositions and the primary structures. These complications have led to the search for younger analogues of juvenile crustal generation/growth to address in detail the above-mentioned questions and debates. The Arabian-Nubian Shield (ANS) forms one of the largest exposures of the Neoproterozoic juvenile continental crust on Earth (Pease and Johnson, 2013), and its crustal generation and cratonization/stabilization represent one of the major event of continental crustal growth since the Archean (Benton, 1985; Stern, 1994). The ANS crust is generally well exposed, and the low degrees of metamorphism make it one of the best areas to study continental crust formation. Hence, the ANS provides unique opportunities to study the evolution of the Earth's mantle and the formation of its complementary continental crust.

1.1.3 Earth's dynamic evolution and key scientific questions for this research

It is generally considered that continental crust (at least 60-70% of the continental crust) was mostly formed by the end of the Archean (2.5 Ga) (Taylor and McLennan, 1995; Belousova *et al.*, 2010; Dhuime, Chris J. Hawkesworth, *et al.*, 2012; Arndt, 2013; Dhuime *et al.*, 2018; Hawkesworth, Cawood and Dhuime, 2020). However, the specific timing of the growth and differentiation of continental crust is still debated. As mentioned above, continental crustal growth is typically linked to the tectonic and geodynamic settings. As such, examining whether global subduction and plate tectonics initiated during the Archean or not is a fundamental question.

Petrological estimation of mantle potential temperature using non-arc basalts (Herzberg, Condie and Korenaga, 2010), as well as Earth's secular cooling predicted by parameterized convection models (Korenaga, 2008), show that the Archean mantle potential temperature was 150–250 °C higher than the present-day ambient mantle. These conditions led some scholars to believe that plate tectonics did not exist in the early Archean or were of a different style from those prevalent in the present day (Bédard, 2006, 2018; van Hunen and Moyen, 2012). The start of plate tectonics is still an ongoing debate, with some recent studies proposing the onset of modern-style plate tectonics by the end of the Archean (Shirey and Richardson, 2011; Dhuime, Hawkesworth, *et al.*, 2012; Naeraa *et al.*, 2012; Laurent *et al.*, 2014), while others believe that it started in the Neoproterozoic (Stern, 2005). The resolution of this debate is fundamental to our understanding of the evolution of the Earth system. Most previous estimates of when plate tectonics commenced were based on crustal observations (Dhuime, Chris J Hawkesworth, *et al.*, 2012; Naeraa *et al.*, 2012; Nagel, Hoffmann and Münker, 2012; Tang, Chen and Rudnick, 2016; Reimink *et al.*, 2019), which are only indirectly related to mantle processes and its evolution, and may intrinsically have a preservation bias and/or reflect regional rather than global processes (Furnes *et al.*, 2007; Shirey and Richardson, 2011; Naeraa *et al.*, 2012; Komiya *et al.*, 2014; Turner *et al.*, 2014; Blichert-Toft *et al.*, 2015; Kaczmarek *et al.*, 2016; Sobolev *et al.*, 2019).

As stated above, the mantle-crust differentiation processes led to the formation of a depleted mantle and a continental crust enriched in highly incompatible elements (e.g. Ba, Pb, Rb, Cs, Sr, and U) (Figure 1.2b). It is commonly believed that before the plate tectonics regime, a chemically stratified Earth had a relatively homogeneous mantle composition (Condie, 2018; Moyen and Laurent, 2018). This is due to the lack of large and global-scale recycling of terrestrial materials into the upper and lower mantle, that was already depleted in highly incompatible elements (Hofmann, 1988). Crustal recycling has been proposed to be driven mainly by subduction (Stern, 2002b; van Hunen and Moyen, 2012; Moyen and Laurent, 2018) or to a lesser degree by delamination (Bédard, 2006, 2018). However, delamination of dense residue after TTG formation would have facilitated the refertilization of the upper mantle only with crust-like chemical and isotopic signatures (Bédard, 2018; Moyen and Laurent, 2018), but would have had less

influence on the composition of the lower mantle (Bédard, 2018; Condie, 2018). Re-enrichment/re-fertilization of Earth's upper and lower mantle can occur when continental crustal materials begin to founder into the mantle, mainly through subduction, profoundly affecting the mantle's trace element compositions (Stern, 2002a; Willbold and Stracke, 2010; Sobolev and Brown, 2019). As one of the key processes of plate tectonics is widespread subduction (Clift and Vannucchi, 2004; Sobolev and Brown, 2019), a globally-detectable large change in mantle heterogeneity (Hofmann, 1997, 2014; Bennett, 2003), caused by the refertilization/re-enrichment of the mantle in incompatible and fluid mobile elements, could identify the onset of global-scale subduction and thus plate tectonics. This could be achieved through investigating the composition of the mantle directly, through its derived magmatism, by examining the global database of Archean-Proterozoic basalts (to track upper mantle composition) and komatiites (to track lower mantle composition), focusing on geochemical tracers that are sensitive to crustal recycling.

Subduction zones recycle terrestrial materials back into Earth's mantle as the subducting slab sinks and re-equilibrates within Earth's interior. They could therefore have a profound impact on the Earth's mantle geochemical cycle and its heterogeneity (Stern, 2002a; Clift and Vannucchi, 2004; Willbold and Stracke, 2010). Fluids and melts released from sediments and crustal materials in the vicinity of the subducting slab cause enrichment/metasomatism of the sub-arc mantle (i.e., peridotites) and also facilitate melting of the upper mantle wedge, creating arc basalts with specific trace element signatures (such as elevated large ion lithophile elements (LILE): Ba, Pb, U, Sr, As, B, and Cs) (Poli and Schmidt, 2002; Gamal El Dien *et al.*, 2019). However, the factors and mechanisms that control the transfer of the trace elements from subducting slabs to the sub-arc mantle (i.e., mantle wedge), and to subsequent arc magmatism, are still unclear. Thus, deciphering the dehydration/devolatilization processes of subducting slabs represents a critical challenge in understanding trace element geochemical cycles in subduction zones and their feedback on the mantle processes, chemistry, and its geochemical and isotopic heterogeneity. In addition, if there is variability of the release of these trace elements along the length of the subducting slab, the resulting cross-arc geochemical variation will affect the resulting arc magmatism and can help to determine the subduction polarity of ancient arcs, particularly in accretionary orogens, i.e. ongoing

subductions. As the ANS represents a typical arc-accretion orogen (Stern, 1994; Stern *et al.*, 2004) and the ongoing subductions during this orogen would affect the geochemical cycle of the sub-arc mantle, the ANS provides an opportunity to investigate these effects through examining the mantle section rocks (i.e., peridotites).

The subducting slabs can also invade the deeper mantle and potentially stagnate at the core-mantle boundary (van der Hilst, Widiyantoro and Engdahl, 1997) (Figures 1.2c and 1.3a). Moreover, Li and Zhong (2009) suggest that the sinking of subducted slabs might be responsible for the formation of mantle superplumes (i.e. LLSVPs), modifying the lower mantle structure, and such events mantle structures might have been linked to the supercontinent cycle. Thus, the Earth's mantle structure, composition, and dynamics are potentially controlled by plate tectonics and subduction (Bennett, 2003; Condie, 2016), and even 600 Ma supercontinent (Li and Zhong, 2009) and super-ocean (Li *et al.*, 2019) cycles . However, such dynamic models remain to be tested using multidisciplinary approaches.

There are new three well-known supercontinents, called Nuna, Rodinia, and Pangea (Evans, Li, and Murphy, 2016; Nance and Murphy, 2018; Pastor-Galán *et al.*, 2018; Li *et al.*, 2019). The episodic assembly, tenure, and breakup (termed the supercontinent cycle), and the transition from one supercontinent to another, are closely related to plate tectonics and mantle dynamics (Zhong *et al.*, 2007; Li *et al.*, 2008, 2019; Li and Zhong, 2009; Torsvik *et al.*, 2014; Torsvik, 2019). It is now well established that the African LLSVP was located underneath the supercontinent Pangaea ca. 200 Ma (Burke and Torsvik, 2004; Burke *et al.*, 2008; Torsvik *et al.*, 2014), and there was a close link between mantle plumes and Pangaea breakup (Courtillot *et al.*, 1999). Geodynamic modelling suggests that the upward return flow of the LLSVPs (superplumes) could potentially lead to the breakup of the supercontinent (Zhong *et al.*, 2007; Li and Zhong, 2009; Zhang *et al.*, 2010). However, the nature and evolution histories of these LLSVPs, including how long the LLSVPs have been present, how such LLSVPs interact with tectonic plates through Earth history, and whether they are fixed in the deep mantle (Dziewonski, Lekic, and Romanowicz, 2010; Torsvik *et al.*, 2010, 2014) or part of a dynamic system associated with the supercontinent cycle since at least the Proterozoic (Zhong *et al.*, 2007; Li *et al.*, 2008, 2019; Li and Zhong, 2009), remain topics of debate. Thus,

tracking mantle plume activities and their geochemical signatures throughout Earth's history is fundamental to answering those questions. A direct relationship between increase in the intensity of plume magmatism and the supercontinent cycle would support a dynamic coupling between LLSVPs and plate tectonics. This hypothesis can be tested through detecting the mantle plume magmatism signatures (for example, an increase in the mantle temperature) from mantle-derived basalts through the Earth's history.

To sum up, the study of the Earth's mantle composition and evolution forms the backbone of understanding the evolution of the dynamic Earth. The geochemical composition of the Earth's mantle, particularly the upper mantle, can be studied directly by sampling mantle xenoliths brought to the surface by volcanic activity (Arai and Ishimaru, 2008; Pearson and Wittig, 2014), by analysing abyssal peridotites dredged from the oceanic floor (Bodinier and Godard, 2014), or by studying ophiolitic successions (Dilek and Furnes, 2011). In addition, the mantle can be studied indirectly by analysing MORBs that track the upper mantle composition, and OIBs and komatiites that potentially track the lower mantle composition (Hofmann, 1997, 2014; Bennett, 2003; Arndt, Leshner and Barnes, 2008). Another indirect approach is to study juvenile (mantle-derived) granites (Kemp and Hawkesworth, 2003, 2014). Hence, the study of those mantle-derived/related rocks will facilitate a better understanding of processes related to the dynamic evolution of the Earth.

This Ph.D. project aims to address the above-mentioned questions, debates, and hypotheses. Topics discussed will include crustal growth, the generation of a global subduction system and the start of the plate tectonics, and feedbacks between plate tectonics and the first-order mantle structure, superplumes, and supercontinent cycles. This will be achieved through deciphering the geochemical records of mantle-related rocks that characterised the Earth's mantle evolution and processes at global-, regional- and micro- to nano-scales.

1.2 Thesis structure and outlines

Following the introduction (this chapter), the thesis contains a methodology section (Chapter 2), seven main chapters that represent the core of the thesis (Chapter 3 to Chapter 9), and a final summary and future perspective chapter (Chapter 10).

Chapter 1 (Introduction) reviews the background about the structure and composition of the Earth's mantle, highlights the main relevant processes, raise the main relevant science questions, and provide a thesis outline. Chapter 2 (Methodology) details the utilised research methods, including field and laboratory work. Chapters 3 to 9 begin with a detailed introduction highlighting the background of the topics discussed in each chapter as well as the aims of each chapter. Each of the seven chapters (3 to 9) include the results and an interpretation/discussion of the significance of the results. Chapter 10 (summary and future perspective) summarises the major outcomes and findings of this research.

The text and figures of the published works (Chapters 6–9), and works still in-preparation for publication (Chapters 3–5), are reproduced in full but have been reformatted for consistency in the thesis. There is some unavoidable repetitions between Chapters 3, 4, and 5, particularly regarding the geological background and methods.

The following is a brief introduction to the contents of Chapters 3 to 9.

Part 1: Crustal growth from the Neoproterozoic mantle: an Egyptian Nubian Shield example

The Neoproterozoic Arabian-Nubian Shield (ANS) consists of continental crust formed prior to and during the collision between East and West Gondwana. The Eastern Desert of Egypt (i.e., Egyptian Nubian Shield) constitutes the north-western part of the ANS. Island-arc accretion during the assembly of Gondwana has been recognized to be the main mechanism for the Neoproterozoic crustal growth in the ANS (Stern, 1994; Fritz *et al.*, 2013), a typical example of continental crustal generation. The size of the ANS crust and its Neoproterozoic growth rate significantly exceeds that of the present-day addition of juvenile mantle materials to arcs along subduction margins (Reymer and Schubert, 1986). Mantle plume-related magmatism has been proposed to represent an important alternative mechanism for the evolution of the ANS crust (Stein and Goldstein, 1996). However, although Neoproterozoic plume and/or rifting magmatism is widely distributed during the fragmentation of the supercontinent Rodinia, there is yet no direct record of such magmatism in all ANS terranes. Also, the lack of adequate precise geochronological

and isotopic constraints of the magmatic activities hampered a comprehensive understanding of the crustal growth possible mechanisms.

In this section, I report the occurrence of the largest known plagiogranitic pluton on Earth (the El-Shadli plutonic complex) (~5,000 km²) (**Chapter 3**) and the El-Shadli bimodal volcanic suite (80 km x 35 km and >10 km-thick) (**Chapter 4**), discovered in the southern Eastern Desert of Egypt. Geochemical and geological data suggest that both the El-Shadli plagiogranites and the overlaying bimodal volcanic suite formed by extensive partial melting of a juvenile continental crust (i.e., accreted oceanic slabs), and is interpreted to have occurred during the break-up of Rodinia, possibly linked to a mantle plume. This result argues against the widely held belief that Neoproterozoic crustal growth in the ANS was primarily driven by arc magmatism; instead, magmatism formed in other tectonic settings such as mantle plume and continental rifting may also have played important roles. In **Chapter 5**, based on a compilation of all previously published whole-rock Nd-Sr isotopes and zircon U-Pb-Hf-O and trace elements of granitoids and volcanic rocks from the Eastern Desert, together with new isotopic datasets obtained from the Genina Gharbia granitoids in the south Eastern Desert, I show that the Eastern Desert crust is characterised by juvenile crustal growth with extensive reworking. I demonstrate that the Eastern Desert crust evolved through three episodes of crustal growth/reworking with peaks ~730 Ma, ~ 700 Ma, and ~ 600 Ma, respectively. The process involved a fundamental transition in tectonic and magmatic style around ~650 Ma, from pre-collisional (~800–650 Ma, oceanic lithosphere-related magmatism, accretion, arc magmatism, and possibly plume-reworking) to collision- to post-collisional (~650–550 Ma). The geochemical, isotopic, and geochronological data suggest that the crustal growth of the Eastern Desert crust has a protracted and episodic nature.

Part 1 includes Chapters 3, 4, and 5:

Chapter 3: The El-Shadli plutonic complex of Eastern Desert: The largest plagiogranite on Earth formed by re-melting of juvenile continental crust

Chapter 4: The El-Shadli bimodal volcanics, Eastern Desert, Egypt: Record of a 700 Ma rifting event during Rodinian break-up

Chapter 5: Nature of Neoproterozoic crustal growth in the Egyptian Nubian Shield: Geochronological and isotopic constraints

Part 2: Mantle partial melting and metasomatism: Geochemical cycling and subduction polarity implications

Partial melting and metasomatism, both along subduction zones and in the mantle away from subduction zones, directly impact on the geochemical cycling between the crust and the mantle, and thus the evolution of both the crust and the mantle. Cr-spinel in mantle peridotites has been widely used for determining mantle partial melting processes (Irvine, 1967; Dick and Bullen, 1984; Hellebrand *et al.*, 2001). In **Chapter 6**, I demonstrate that the composition of Cr-spinel in mantle rocks is not a good petrogenetic indicator as was widely assumed. Instead, it is a tracer for metasomatic processes and a potential carrier for bringing fluid-mobile elements deep into the lower mantle. In **Chapter 7**, I report the role of antigorite (a serpentine mineral phase) in the transportation of fluid-mobile elements (FME) and light rare earth elements (LREE) from the subducted slab to arc-related magma during subduction. The results show that temperature is the main controlling factor for the release of FME and LREE from subducted slabs into arc magmatism. As the liberation of these elements varies along the length of the slab at different depths, the resulting cross-arc geochemical variation trend can help to determine the subduction polarity of ancient arcs.

Part 2 includes Chapters 6 and 7:

Chapter 6 published as [Gamal El Dien, H., Arai, S., Doucet, L., Li, Z., Kil, Y., Fougerouse, D., Reddy, S.M., Saxey, D.W., and Hamdy, M., 2019, Cr-spinel records metasomatism not petrogenesis of mantle rocks: *Nature Communications*, p. 5103, doi:10.1038/s41467-019-13117-1.](#)

Chapter 7 published as [Gamal El Dien, H., Li, Z.-X., Kil, Y., and Abu-Alam, T., 2019, Origin of arc magmatic signature: A temperature-dependent process for trace element \(re\)-mobilization in subduction zones: *Scientific Reports*, v. 9, p. 7098, doi:10.1038/s41598-019-43605-9.](#)

Part 3: Geochemical records linking mantle plumes, supercontinent cycles, and plate tectonics

In this part, I use global geochemical analyses (data mining) to discuss two major questions: (a) how plate tectonics interact with mantle processes and influence

the first-order mantle structure? (**Chapter 8**), and (b) the starting time of global plate tectonics on Earth (**Chapter 9**). Plate tectonics shaped the Earth as we know it today, and influenced the Earth's environment and the evolution of life. In **Chapter 8**, a global analysis demonstrates that transition elements (Ni, Cr, and Fe/Mn) in basaltic rocks can be used to trace plume-related magmatism through Earth's history. A statistical analysis shows the presence of a direct relationship between the intensity of plume magmatism and the supercontinent cycle, suggesting a possible dynamic coupling between supercontinent and superplume events. In **Chapter 9** I document the onset of a mantle re-enrichment/refertilization from ca. 3.2 billion years ago (Ga) through comparing the abundances of petrogenetically significant isotopic values (Nd isotopes) and key ratios between highly incompatible elements and lithophile elements (i.e., Ba/La, Ba/Nb, U/Nb, Pb/Nd and Pb/Ce) in Archean to Early-Proterozoic mantle-derived melts (i.e., basalts and komatiites). The new observations are interpreted to be a consequence of global deep subduction via plate tectonics.

Part 3 includes Chapters 8 and 9:

Chapter 8 published as [Gamal El Dien, H., Doucet, L.S., Li, Z.-X., Cox, G., and Mitchell, R., 2019, Global geochemical fingerprinting of plume intensity suggests coupling with the supercontinent cycle: *Nature Communications*, v. 10, p. 5270, doi:10.1038/s41467-019-13300-4.](#)

Chapter 9 published as [Gamal El Dien, H., Doucet, L.S., Murphy, J.B., and Li, Z.-X., 2020, Geochemical evidence for a widespread mantle re-enrichment 3.2 billion years ago : implications for global-scale plate tectonics: *Scientific Reports*, p. 1–7, doi:10.1038/s41598-020-66324-y.](#)

1.3 References

- Anderson, D. L. (1994) 'Superplumes or supercontinents?', *Geology*. GeoScienceWorld, 22(1), p. 39. doi: 10.1130/0091-7613(1994)022<0039:SOS>2.3.CO;2.
- Anderson, D. L. and Natland, J. H. (2005) 'A brief history of the plume hypothesis and its competitors: Concept and controversy', in *Special Paper 388: Plates, plumes and paradigms*. Geological Society of America, pp. 119–145. doi: 10.1130/0-8137-2388-4.119.
- Arai, S. and Ishimaru, S. (2008) 'Insights into Petrological Characteristics of the Lithosphere of Mantle Wedge beneath Arcs through Peridotite Xenoliths : a Review', *JOURNAL OF PETROLOGY*, 49(4), pp. 665–695. doi: 10.1093/petrology/egm069.
- Armstrong, R. L. (1981) 'Radiogenic isotopes: the case for crustal recycling on a near-steady-state no-continental-growth Earth', *Philosophical Transactions of the Royal Society of London. Series A, Mathematical and Physical Sciences*. The Royal Society, 301(1461), pp. 443–472. doi: 10.1098/rsta.1981.0122.
- Arndt, N. and Davaille, A. (2013) 'Episodic Earth evolution', *Tectonophysics*. Elsevier B.V., 609, pp. 661–674. doi: 10.1016/j.tecto.2013.07.002.
- Arndt, N., Leshner, C. M. and Barnes, S. J. (2008) *Komatiite*. Cambridge: Cambridge University Press. doi: 10.1017/CBO9780511535550.
- Arndt, N. T. (2013) 'Formation and evolution of the continental crust', *Geochemical Perspectives*. European Association of Geochemistry, 2(3). doi: 10.7185/geochempersp.2.3.
- Bédard, J. H. (2006) 'A catalytic delamination-driven model for coupled genesis of Archaean crust and sub-continental lithospheric mantle', *Geochimica et Cosmochimica Acta*. Pergamon, 70(5), pp. 1188–1214. doi: 10.1016/J.GCA.2005.11.008.
- Bédard, J. H. (2018) 'Stagnant lids and mantle overturns: Implications for Archaean tectonics, magmagenesis, crustal growth, mantle evolution, and the start of plate tectonics', *Geoscience Frontiers*. Elsevier, 9(1), pp. 19–49. doi: 10.1016/J.GSF.2017.01.005.
- Belousova, E. A. *et al.* (2010) 'The growth of the continental crust: Constraints from zircon Hf-isotope data', *Lithos*. Elsevier, 119(3–4), pp. 457–466. doi: 10.1016/J.LITHOS.2010.07.024.
- Bennett, V. C. (2003) 'Compositional Evolution of the Mantle', *Treatise on Geochemistry*. Pergamon, pp. 493–519. doi: 10.1016/B0-08-043751-6/02013-2.
- Bentor, Y. K. (1985) 'The crustal evolution of the Arabo-Nubian Massif with special reference to the Sinai Peninsula', *Precambrian Research*. Elsevier, 28(1), pp. 1–74. doi: 10.1016/0301-9268(85)90074-9.
- Bina, C. R. and Helffrich, G. (2014) 'Geophysical Constraints on Mantle Composition', in *Treatise on Geochemistry*. Elsevier, pp. 41–65. doi: 10.1016/B978-0-08-095975-7.00202-3.
- Blichert-Toft, J. *et al.* (2015) 'Hf and Nd isotope systematics of early Archean komatiites from surface sampling and ICDP drilling in the Barberton Greenstone Belt, South Africa', *American Mineralogist*. Walter de Gruyter GmbH, 100(11–12), pp. 2396–2411. doi: 10.2138/am-2015-5325.
- Bodinier, J.-L. and Godard, M. (2014) 'Orogenic, Ophiolitic, and Abyssal Peridotites', in

- Treatise on Geochemistry*. 3rd edn. Elsevier, pp. 103–167. doi: 10.1016/B978-0-08-095975-7.00204-7.
- Bowring, S. A. and Williams, I. S. (1999) ‘Priscoan (4.00–4.03 Ga) orthogneisses from northwestern Canada’, *Contributions to Mineralogy and Petrology*, 134(1), pp. 3–16. doi: 10.1007/s004100050465.
- Bradley, D. C. (2011) ‘Secular trends in the geologic record and the supercontinent cycle’, *Earth-Science Reviews*. Elsevier B.V., 108(1–2), pp. 16–33. doi: 10.1016/j.earscirev.2011.05.003.
- Burke, K. *et al.* (2008) ‘Plume Generation Zones at the margins of Large Low Shear Velocity Provinces on the core-mantle boundary’, *Earth and Planetary Science Letters*, 265(1–2), pp. 49–60. doi: 10.1016/j.epsl.2007.09.042.
- Burke, K. (2011) ‘Plate Tectonics, the Wilson Cycle, and Mantle Plumes: Geodynamics from the Top’, *Annual Review of Earth and Planetary Sciences*, 39, pp. 1–29. doi: 10.1146/annurev-earth-040809-152521.
- Burke, K. and Torsvik, T. H. (2004) ‘Derivation of Large Igneous Provinces of the past 200 million years from long-term heterogeneities in the deep mantle’, *Earth and Planetary Science Letters*, 227(3–4), pp. 531–538. doi: 10.1016/j.epsl.2004.09.015.
- Cavosie, A. J., Valley, J. W. and Wilde, S. A. (2019) ‘The Oldest Terrestrial Mineral Record’, in *Earth’s Oldest Rocks*. Elsevier, pp. 255–278. doi: 10.1016/b978-0-444-63901-1.00012-5.
- Cawood, P. A. *et al.* (2009) ‘Accretionary orogens through Earth history’, *Geological Society Special Publication*, 318, pp. 1–36. doi: 10.1144/SP318.1.
- Cawood, P. A. *et al.* (2016) ‘Linking collisional and accretionary orogens during Rodinia assembly and breakup: Implications for models of supercontinent cycles’, *Earth and Planetary Science Letters*. Elsevier, 449, pp. 118–126. doi: 10.1016/J.EPSL.2016.05.049.
- Cawood, P. A. *et al.* (2018) ‘Geological archive of the onset of plate tectonics’, *Philosophical Transactions of the Royal Society A: Mathematical, Physical and Engineering Sciences*, 376(2132), p. 20170405. doi: 10.1098/rsta.2017.0405.
- Clift, P. and Vannucchi, P. (2004) ‘Controls on tectonic accretion versus erosion in subduction zones: Implications for the origin and recycling of the continental crust’, *Reviews of Geophysics*. John Wiley & Sons, Ltd, 42(2), p. RG2001. doi: 10.1029/2003RG000127.
- Condie, K. C. (1998) ‘Episodic continental growth and supercontinents: A mantle avalanche connection?’, *Earth and Planetary Science Letters*, 163(1–4), pp. 97–108. doi: 10.1016/S0012-821X(98)00178-2.
- Condie, K. C. (2016) *Earth as an Evolving Planetary System*. Elsevier. doi: 10.1016/C2015-0-00179-4.
- Condie, K. C. (2018) ‘A planet in transition: The onset of plate tectonics on Earth between 3 and 2 Ga?’, *Geoscience Frontiers*, 9(1), pp. 51–60. doi: 10.1016/j.gsf.2016.09.001.
- Condie, K. C. (2019) ‘Earth’s Oldest Rocks and Minerals’, in *Earth’s Oldest Rocks*.

Elsevier, pp. 239–253. doi: 10.1016/b978-0-444-63901-1.00011-3.

Courtillot, V. *et al.* (1999) ‘On causal links between flood basalts and continental breakup’, *Earth and Planetary Science Letters*, 166(3–4), pp. 177–195. doi: 10.1016/S0012-821X(98)00282-9.

Courtillot, V. *et al.* (2003) ‘Three distinct types of hotspots in the Earth’s mantle’, *Earth and Planetary Science Letters*. Elsevier, 205(3–4), pp. 295–308. doi: 10.1016/S0012-821X(02)01048-8.

Dhuime, B., Hawkesworth, Chris J., *et al.* (2012) ‘A change in the geodynamics of continental growth 3 billion years ago.’, *Science (New York, N.Y.)*. American Association for the Advancement of Science, 335(6074), pp. 1334–6. doi: 10.1126/science.1216066.

Dhuime, B., Hawkesworth, Chris J., *et al.* (2012) ‘A change in the geodynamics of continental growth 3 billion years ago’, *Science*, 335(6074), pp. 1334–1336. doi: 10.1126/science.1216066.

Dhuime, B. *et al.* (2018) ‘Rates of generation and destruction of the continental crust: Implications for continental growth’, in *Philosophical Transactions of the Royal Society A: Mathematical, Physical and Engineering Sciences*. Royal Society Publishing. doi: 10.1098/rsta.2017.0403.

Dhuime, B., Hawkesworth, C. and Cawood, P. (2011) ‘When Continents Formed’, *Science*, 331(6014), pp. 155–156. doi: 10.1126/science.1200643.

Dick, H. J. B. and Bullen, T. (1984) ‘Chromian spinel as a petrogenetic indicator in abyssal and alpine-type peridotites and spatially associated lavas’, *Contributions to Mineralogy and Petrology*, 86(1), pp. 54–76. doi: 10.1007/BF00373711.

Dilek, Y. and Furnes, H. (2011) ‘Ophiolite genesis and global tectonics: Geochemical and tectonic fingerprinting of ancient oceanic lithosphere’, *Bulletin of the Geological Society of America*, 123(3–4), pp. 387–411. doi: 10.1130/B30446.1.

Doucet, L. S., Li, Z., Ernst, R. E., *et al.* (2020) ‘Coupled supercontinent – mantle plume events evidenced by oceanic plume record’, *Geology*, 48, pp. 1–5. doi: 10.1130/G46754.1/4906660/g46754.pdf.

Doucet, L. S., Li, Z., Gamal El Dien, H., *et al.* (2020) ‘Distinct formation history for deep-mantle domains reflected in geochemical differences’, *Nature Geoscience*. Springer US, 13(July). doi: 10.1038/s41561-020-0599-9.

Dziewonski, A. M. (1984) ‘Mapping the lower mantle: Determination of lateral heterogeneity in *P* velocity up to degree and order 6’, *Journal of Geophysical Research: Solid Earth*. Wiley-Blackwell, 89(B7), pp. 5929–5952. doi: 10.1029/JB089iB07p05929.

Dziewonski, A. M., Lekic, V. and Romanowicz, B. A. (2010) ‘Mantle Anchor Structure: An argument for bottom up tectonics’, *Earth and Planetary Science Letters*. Elsevier B.V., 299(1–2), pp. 69–79. doi: 10.1016/j.epsl.2010.08.013.

Evans, D. A. D., Li, Z. X. and Murphy, J. B. (2016) ‘Four-dimensional context of Earth’s supercontinents’, in Li, Z., Evans, David A.D., and Murphy, J. B. (eds) *Geological Society Special Publication*. Geological Society of London, pp. 1–14. doi: 10.1144/SP424.12.

Foley, S., Tiepolo, M. and Vannucci, R. (2002) ‘Growth of early continental crust

- controlled by melting of amphibolite in subduction zones', *Nature*. Nature Publishing Group, 417(6891), pp. 837–840. doi: 10.1038/nature00799.
- Fritz, H. *et al.* (2013) 'Orogen styles in the East African Orogen: A review of the Neoproterozoic to Cambrian tectonic evolution', *Journal of African Earth Sciences*. Elsevier Ltd, 86, pp. 65–106. doi: 10.1016/j.jafrearsci.2013.06.004.
- Furnes, H. *et al.* (2007) 'A Vestige of Earth ' s Oldest Ophiolite', *Science (New York, N.Y.)*, 315(March), pp. 2001–2004. doi: 10.1126/science.1139170.
- Gamal El Dien, H. *et al.* (2019) 'Origin of arc magmatic signature: A temperature-dependent process for trace element (re)-mobilization in subduction zones', *Scientific Reports*, 9(1), p. 7098. doi: 10.1038/s41598-019-43605-9.
- Hawkesworth, C., Cawood, P. A. and Dhuime, B. (2018) 'Rates of generation and growth of the continental crust', *Geoscience Frontiers*. Elsevier. doi: 10.1016/J.GSF.2018.02.004.
- Hawkesworth, C., Cawood, P. and Dhuime, B. (2013) 'Continental growth and the crustal record', *Tectonophysics*. Elsevier B.V., 609, pp. 651–660. doi: 10.1016/j.tecto.2013.08.013.
- Hawkesworth, C. J., Cawood, P. A. and Dhuime, B. (2020) 'The Evolution of the Continental Crust and the Onset of Plate Tectonics', *Frontiers in Earth Science*. Frontiers, 8, p. 326. doi: 10.3389/feart.2020.00326.
- Hawkesworth, C. J. and Kemp, A. I. S. (2006) 'Evolution of the continental crust', *Nature*, 443(7113), pp. 811–817. doi: 10.1038/nature05191.
- Helfrich, G. (2000) 'Topography of the transition zone seismic discontinuities', *Reviews of Geophysics*, 38(1), pp. 141–158. doi: 10.1029/1999RG000060.
- Helfrich, G. R. and Wood, B. J. (2001) 'The Earth's mantle', *Nature*. Nature Publishing Group, pp. 501–507. doi: 10.1038/35087500.
- Hellebrand, E. *et al.* (2001) 'Coupled major and trace elements as indicators of the extent of melting in mid-ocean-ridge peridotites', *Nature*, 410(6829), pp. 677–681. doi: 10.1038/35070546.
- Herzberg, C., Condie, K. and Korenaga, J. (2010) 'Thermal history of the Earth and its petrological expression', *Earth and Planetary Science Letters*. Elsevier B.V., 292(1–2), pp. 79–88. doi: 10.1016/j.epsl.2010.01.022.
- Hill, R. I. *et al.* (1992) 'Mantle plumes and continental tectonics', *Science*, 256(5054), pp. 186–193. doi: 10.1126/science.256.5054.186.
- van der Hilst, R. D., Widiyantoro, S. and Engdahl, E. R. (1997) 'Evidence for deep mantle circulation from global tomography', *Nature*. Nature Publishing Group, 386(6625), pp. 578–584. doi: 10.1038/386578a0.
- Hofmann, A. W. (1988) 'Chemical differentiation of the Earth: the relationship between mantle, continental crust, and oceanic crust', *Earth and Planetary Science Letters*. Elsevier, 90(3), pp. 297–314. doi: 10.1016/0012-821X(88)90132-X.
- Hofmann, A. W. (1997) 'Mantle geochemistry: the message from oceanic volcanism', *Nature*. Nature Publishing Group, 385(6613), pp. 219–229. doi: 10.1038/385219a0.

- Hofmann, A. W. (2014) ‘Sampling Mantle Heterogeneity through Oceanic Basalts: Isotopes and Trace Elements’, in *Treatise on Geochemistry*. Elsevier, pp. 67–101. doi: 10.1016/B978-0-08-095975-7.00203-5.
- van Hunen, J. and Moyen, J.-F. (2012) ‘Archean Subduction: Fact or Fiction?’, *Annual Review of Earth and Planetary Sciences*, 40(1), pp. 195–219. doi: 10.1146/annurev-earth-042711-105255.
- Irvine, T. N. (1967) ‘Chromian Spinel As a Petrogenetic Indicator: Part 2. Petrologic Applications’, *Canadian Journal of Earth Sciences*, 4(1), pp. 71–103. doi: 10.1139/e67-004.
- Jackson, M. G. *et al.* (2010) ‘Evidence for the survival of the oldest terrestrial mantle reservoir’, *Nature*. Nature Publishing Group, 466(7308), pp. 853–856. doi: 10.1038/nature09287.
- Jackson, M. G. and Carlson, R. W. (2011) ‘An ancient recipe for flood-basalt genesis’, *Nature*. Nature Publishing Group, 476(7360), pp. 316–319. doi: 10.1038/nature10326.
- Johnson, T. E. *et al.* (2014) ‘Delamination and recycling of Archaean crust caused by gravitational instabilities’, *Nature Geoscience*. Nature Publishing Group, 7(1), pp. 47–52. doi: 10.1038/ngeo2019.
- Johnson, T. E. *et al.* (2017) ‘Earth’s first stable continents did not form by subduction’, *Nature*. Nature Publishing Group, 543(7644), pp. 239–242. doi: 10.1038/nature21383.
- Johnson, T. E. *et al.* (2019) ‘Secular change in TTG compositions: Implications for the evolution of Archaean geodynamics’, *Earth and Planetary Science Letters*. Elsevier, 505, pp. 65–75. doi: 10.1016/J.EPSL.2018.10.022.
- Kaczmarek, M. A. *et al.* (2016) ‘Earth’s oldest mantle fabrics indicate Eoarchaean subduction’, *Nature Communications*. Nature Publishing Group, 7(1), pp. 1–7. doi: 10.1038/ncomms10665.
- Kemp, A. I. S. and Hawkesworth, C. J. (2003) ‘Granitic Perspectives on the Generation and Secular Evolution of the Continental Crust’, in *Treatise on Geochemistry*. Elsevier, pp. 349–410. doi: 10.1016/B0-08-043751-6/03027-9.
- Kemp, A. I. S. and Hawkesworth, C. J. (2014) ‘Growth and Differentiation of the Continental Crust from Isotope Studies of Accessory Minerals’, in *Treatise on Geochemistry*. Elsevier, pp. 379–421. doi: 10.1016/B978-0-08-095975-7.00312-0.
- Komiya, T. *et al.* (2014) ‘Geology of the Eoarchean, >3.95 Ga, Nulliak supracrustal rocks in the Saglek Block, northern Labrador, Canada: The oldest geological evidence for plate tectonics’, *Tectonophysics*. Elsevier B.V., 662, pp. 40–66. doi: 10.1016/j.tecto.2015.05.003.
- Koppers, A. A. P. (2011) ‘Mantle plumes persevere’, *Nature Geoscience*. Nature Publishing Group, 4(12), pp. 816–817. doi: 10.1038/ngeo1334.
- Korenaga, J. (2008) ‘Urey Ratio and the Structure and Evolution of Earth’s Mantle’, *American Geophysical Union*, (2007), pp. 1–32. doi: 10.1029/2007RG000241.1.
- Korenaga, J. (2013) ‘Initiation and Evolution of Plate Tectonics on Earth: Theories and Observations’, *Annual Review of Earth and Planetary Sciences*, 41(1), pp. 117–151. doi: 10.1146/annurev-earth-050212-124208.

- Laurent, O. *et al.* (2014) ‘The diversity and evolution of late-Archean granitoids: Evidence for the onset of “modern-style” plate tectonics between 3.0 and 2.5 Ga’, *Lithos*. Elsevier, 205, pp. 208–235. doi: 10.1016/J.LITHOS.2014.06.012.
- Lay, T., Williams, Q. and Garnero, E. J. (1998) ‘The core-mantle boundary layer and deep Earth dynamics’, *Nature*, pp. 461–468. doi: 10.1038/33083.
- Li, Z. X. *et al.* (2008) ‘Assembly, configuration, and break-up history of Rodinia: A synthesis’, *Precambrian Research*, 160(1–2), pp. 179–210. doi: 10.1016/j.precamres.2007.04.021.
- Li, Z. X. *et al.* (2019) ‘Decoding Earth’s rhythms: Modulation of supercontinent cycles by longer superocean episodes’, *Precambrian Research*. Elsevier, 323, pp. 1–5. doi: 10.1016/J.PRECAMRES.2019.01.009.
- Li, Z. X., Evans, D. A. D. and Zhang, S. (2004) ‘A 90° spin on Rodinia: possible causal links between the Neoproterozoic supercontinent, superplume, true polar wander and low-latitude glaciation’, *Earth and Planetary Science Letters*. Elsevier, 220(3–4), pp. 409–421. doi: 10.1016/S0012-821X(04)00064-0.
- Li, Z. X. and Zhong, S. (2009) ‘Supercontinent-superplume coupling, true polar wander and plume mobility: Plate dominance in whole-mantle tectonics’, *Physics of the Earth and Planetary Interiors*, 176(3–4), pp. 143–156. doi: 10.1016/j.pepi.2009.05.004.
- Mao, W. L. *et al.* (2005) ‘Iron-rich silicates in the earth’s D” layer’, *Proceedings of the National Academy of Sciences of the United States of America*. National Academy of Sciences, 102(28), pp. 9751–9753. doi: 10.1073/pnas.0503737102.
- Martin, H. *et al.* (2014) ‘Why Archean TTG cannot be generated by MORB melting in subduction zones’, *Lithos*. Elsevier, 198–199(1), pp. 1–13. doi: 10.1016/j.lithos.2014.02.017.
- McDonough, W. . and Sun, S. –. (1995) ‘The composition of the Earth’, *Chemical Geology*, 120, pp. 223–252. doi: doi.org/10.1016/0009-2541(94)00140-4.
- McDonough, W. F. (2014) ‘Compositional Model for the Earth’s Core’, in *Treatise on Geochemistry*. Elsevier, pp. 559–577. doi: 10.1016/B978-0-08-095975-7.00215-1.
- Moyen, J. F. and Laurent, O. (2018) ‘Archean tectonic systems: A view from igneous rocks’, *Lithos*. Elsevier B.V., 302–303, pp. 99–125. doi: 10.1016/j.lithos.2017.11.038.
- Naeraa, T. *et al.* (2012) ‘Hafnium isotope evidence for a transition in the dynamics of continental growth 3.2 Gyr ago’, *Nature*. Nature Publishing Group, 485(7400), pp. 627–630. doi: 10.1038/nature11140.
- Nagel, T. J., Hoffmann, J. E. and Münker, C. (2012) ‘Generation of Eoarchean tonalite-trondhjemite-granodiorite series from a thickened mafic arc crust’, *Geology*. GeoScienceWorld, 40(4), pp. 375–378. doi: 10.1130/G32729.1.
- Nance, R. D. and Murphy, J. B. (2018) ‘Supercontinents and the case for Pannotia’, *Geological Society, London, Special Publications*, p. SP470.5. doi: 10.1144/SP470.5.
- Nutman, A. P. and Bennett, V. C. (2019) ‘The 3.9–3.6 Ga Itsaq Gneiss Complex of Greenland’, in *Earth’s Oldest Rocks*. Elsevier, pp. 375–399. doi: 10.1016/b978-0-444-63901-1.00017-4.

- Palme, H. and O'Neill, H. S. C. (2014) 'Cosmochemical Estimates of Mantle Composition', in *Treatise on Geochemistry*. Elsevier, pp. 1–39. doi: 10.1016/B978-0-08-095975-7.00201-1.
- Pastor-Galán, D. *et al.* (2018) 'Supercontinents: myths, mysteries, and milestones', *Geological Society, London, Special Publications*. Geological Society of London, 470, p. SP470.16. doi: 10.1144/SP470.16.
- Patterson, C. (1956) 'Age of meteorites and the earth', *Geochimica et Cosmochimica Acta*. Pergamon, 10(4), pp. 230–237. doi: 10.1016/0016-7037(56)90036-9.
- Pearson, D. G. and Wittig, N. (2014) 'The Formation and Evolution of Cratonic Mantle Lithosphere – Evidence from Mantle Xenoliths', in *Treatise on Geochemistry*. Elsevier, pp. 255–292. doi: 10.1016/B978-0-08-095975-7.00205-9.
- Pease, V. and Johnson, P. R. (2013) 'Introduction to the JEBEL volume of Precambrian Research', *Precambrian Research*, 239, pp. 1–5. doi: 10.1016/j.precamres.2013.10.003.
- Poli, S. and Schmidt, M. W. (2002) 'Petrology of Subducted Slabs', *Annual Review of Earth and Planetary Sciences*, 30(1), pp. 207–235. doi: 10.1146/annurev.earth.30.091201.140550.
- Reimink, J. R. *et al.* (2019) 'Onset of new, progressive crustal growth in the central Slave craton at 3.55 Ga', *Geochem. Persp. Lett.*, 10, pp. 8–13. doi: 10.7185/geochemlet.1907.
- Reymer, A. and Schubert, G. (1986) 'Rapid growth of some major segments of continental crust', *Geology*. GeoScienceWorld, 14(4), p. 299. doi: 10.1130/0091-7613(1986)14<299:RGOSMS>2.0.CO;2.
- Ringwood, A. E. (1962) 'Mineralogical constitution of the deep mantle', *Journal of Geophysical Research*. Wiley-Blackwell, 67(10), pp. 4005–4010. doi: 10.1029/JZ067i010p04005.
- Ringwood, A. E. (1991) 'Phase transformations and their bearing on the constitution and dynamics of the mantle', *Geochimica et Cosmochimica Acta*, 55(8), pp. 2083–2110. doi: 10.1016/0016-7037(91)90090-R.
- Ringwood, A. E. and Irifune, T. (1988) 'Nature of the 650-km seismic discontinuity: Implications for mantle dynamics and differentiation', *Nature*, 331(6152), pp. 131–136. doi: 10.1038/331131a0.
- Rudnick, R. L. and Gao, S. (2014) 'Composition of the Continental Crust', in *Treatise on Geochemistry*. Elsevier, pp. 1–51. doi: 10.1016/B978-0-08-095975-7.00301-6.
- Saji, N. S. *et al.* (2018) 'Hadean geodynamics inferred from time-varying $^{142}\text{Nd}/^{144}\text{Nd}$ in the early Earth rock record', *Geochemical Perspectives Letters*. European Association of Geochemistry, 7, pp. 43–48. doi: 10.7185/geochemlet.1818.
- Shirey, S. B. and Richardson, S. H. (2011) 'Start of the Wilson cycle at 3 Ga shown by diamonds from subcontinental mantle.', *Science (New York, N.Y.)*. American Association for the Advancement of Science, 333(6041), pp. 434–6. doi: 10.1126/science.1206275.
- Sobolev, A. V. *et al.* (2019) 'Deep hydrous mantle reservoir provides evidence for crustal recycling before 3.3 billion years ago', *Nature*. Nature Publishing Group, p. 1. doi: 10.1038/s41586-019-1399-5.

- Sobolev, S. V. and Brown, M. (2019) ‘Surface erosion events controlled the evolution of plate tectonics on Earth’, *Nature*. Nature Publishing Group, 570(7759), pp. 52–57. doi: 10.1038/s41586-019-1258-4.
- Spencer, C. J., Roberts, N. M. W. and Santosh, M. (2017) ‘Growth, destruction, and preservation of Earth’s continental crust’, *Earth-Science Reviews*. Elsevier B.V., pp. 87–106. doi: 10.1016/j.earscirev.2017.07.013.
- Stein, M. and Goldstein, S. L. (1996) ‘From plume head to continental lithosphere in the Arabian–Nubian shield’, *Nature*, 382, pp. 773–778. Available at: <https://doi.org/10.1038/382773a0>.
- Stein, M. and Hofmann, A. W. (1994) ‘Mantle plumes and episodic crustal growth’, *Nature*. Nature Publishing Group, 372(6501), pp. 63–68. doi: 10.1038/372063a0.
- Stern, R. J. (1994) ‘ARC Assembly and Continental Collision in the Neoproterozoic East African Orogen: Implications for the Consolidation of Gondwanaland’, *Annual Review of Earth and Planetary Sciences*, 22(1), pp. 319–351. doi: 10.1146/annurev.ea.22.050194.001535.
- Stern, R. J. (2002a) ‘Subduction zones’, *Reviews of Geophysics*, 40(4). doi: 10.1029/2001RG000108.
- Stern, R. J. (2002b) ‘Subduction zones’, *Reviews of Geophysics*. John Wiley & Sons, Ltd, 40(4), pp. 1–38. doi: 10.1029/2001RG000108.
- Stern, R. J. *et al.* (2004) ‘Neoproterozoic Ophiolites of the Arabian-Nubian Shield’, *Developments in Precambrian Geology*, 13(C), pp. 95–128. doi: 10.1016/S0166-2635(04)13003-X.
- Stern, R. J. (2005) ‘Evidence from ophiolites, blueschists, and ultrahigh-pressure metamorphic terranes that the modern episode of subduction tectonics began in Neoproterozoic time’, *Geology*, 33(7), pp. 557–560. doi: 10.1130/G21365.1.
- Sun, S. -s. and McDonough, W. . (1989) ‘Chemical and isotopic systematics of oceanic basalts: implications for mantle composition and processes’, *Geological Society, London, Special Publications*, 42, pp. 313–345. doi: doi: 10.1144/GSL.SP.1989.042.01.19.
- Tang, M., Chen, K. and Rudnick, R. L. (2016) ‘Archean upper crust transition from mafic to felsic marks the onset of plate tectonics’, *Science*, 351(6271), pp. 372–375. doi: 10.1126/science.aad5513.
- Taylor, S. R. and McLennan, S. M. (1995) ‘The geochemical evolution of the continental crust’, *Reviews of Geophysics*, 33(2), p. 241. doi: 10.1029/95RG00262.
- Torsvik, T. H. *et al.* (2010) ‘Diamonds sampled by plumes from the core-mantle boundary’, *Nature*. Nature Publishing Group, 466(7304), pp. 352–355. doi: 10.1038/nature09216.
- Torsvik, T. H. *et al.* (2014) ‘Deep mantle structure as a reference frame for movements in and on the Earth’, *Proceedings of the National Academy of Sciences*, 111(24), pp. 8735–8740. doi: 10.1073/pnas.1318135111.
- Torsvik, T. H. (2019) ‘Earth history: A journey in time and space from base to top’, *Tectonophysics*. Elsevier B.V., 760, pp. 297–313. doi: 10.1016/j.tecto.2018.09.009.

- Turner, S. *et al.* (2014) ‘Heading down early on? Start of subduction on earth’, *Geology*. Geological Society of America, 42(2), pp. 139–142. doi: 10.1130/G34886.1.
- Weber, M. and Davis, J. P. (1990) ‘Evidence of a laterally variable lower mantle structure from P- and S-waves’, *Geophysical Journal International*. Oxford Academic, 102(1), pp. 231–255. doi: 10.1111/j.1365-246X.1990.tb00544.x.
- White, W. (2015) ‘Probing the Earth’s Deep Interior Through Geochemistry’, *Geochemical Perspectives*, 4(2), pp. 95–251. doi: 10.7185/geochempersp.4.2.
- Wilde, S. A. *et al.* (2001) ‘Evidence from detrital zircons for the existence of continental crust and oceans on the Earth 4.4 Gyr ago’, *Nature*. Nature Publishing Group, 409(6817), pp. 175–178. doi: 10.1038/35051550.
- Willbold, M. and Stracke, A. (2010) ‘Formation of enriched mantle components by recycling of upper and lower continental crust’, *Chemical Geology*. Elsevier, 276(3–4), pp. 188–197. doi: 10.1016/J.CHEMGEO.2010.06.005.
- Winter, J. D. (2014) *Principles of Igneous and Metamorphic Petrology: Second Edition*, Pearson Education Limited. doi: 10.1016/0016-7037(91)90355-9.
- Zhang, N. *et al.* (2010) ‘A model for the evolution of the Earth’s mantle structure since the Early Paleozoic’, *Journal of Geophysical Research*, 115(B6), p. B06401. doi: 10.1029/2009JB006896.
- Zhong, S. *et al.* (2007) ‘Supercontinent cycles, true polar wander, and very long-wavelength mantle convection’, *Earth and Planetary Science Letters*, 261(3–4), pp. 551–564. doi: 10.1016/j.epsl.2007.07.049.
- Zindler, A. and Hart, S. (1986) *CHEMICAL GEODYNAMICS*, *Ann. Rev. Earth Planet. Sci.* Available at: www.annualreviews.org (Accessed: 25 September 2018).

“Every reasonable effort has been made to acknowledge the owners of copyright material. I would be pleased to hear from any copyright owner who has been omitted or incorrectly acknowledged.”

Chapter 2:

Methodology

This research project involved field, laboratory, and data-mining approaches for data acquisition. These approaches are described below as three consecutive sections.

2.1 Field work

Geological fieldwork to the Eastern Desert region of Egypt at the Arabian-Nubian Shield (ANS) (Figure 2.1) was carried out during two field seasons: on in April, 2018 for three weeks, and another in November-December, 2019 for two weeks. The target areas were ophiolitic sections, serpentinites, granitoids, and volcanics from Wadi (W, which is the Arabic word for ephemeral water courses) Um Seleimat, W. Muweilih, W. El Fawakhir, W. Um Khargia-W. Alam belt, W. Ranga, El-Shadli area, and Gabal (G, mountain in Arabic language) Genina Gharbia (Figure 2.1). Tasks for the fieldwork include rough stratigraphic logging, structural measurements, and collecting a large variety of ultramafic-mafic and felsic rock samples. Field relations and observations were described and photographed (more than 500 photographs were taken). A total of 92 rock samples were collected for geochemical and geochronological analyses to investigate the crustal growth of the ANS and deciphering the upper and lower Neoproterozoic mantle reservoir beneath the ANS.

2.2 Laboratory work, including geochemical analyses

Laboratory work includes whole-rock scale, mineral-scale, and atomic-scale sample preparation and analyses. At the whole-rock scale, laboratory work include samples crushing, thin-sections preparation, microscopic observations, whole-rock mineral phase distribution mapping by TESCAN Integrated Mineral Analyser (TIMA), whole-rock major element analysis by X-ray Fluorescence (XRF), trace element analysis by Inductively Coupled Plasma Mass Spectrometry (ICP-MS), and

Sr-Nd isotopes by Thermal Ionisation Mass Spectrometry (TIMS). Each method will be discussed in details in the following sections.

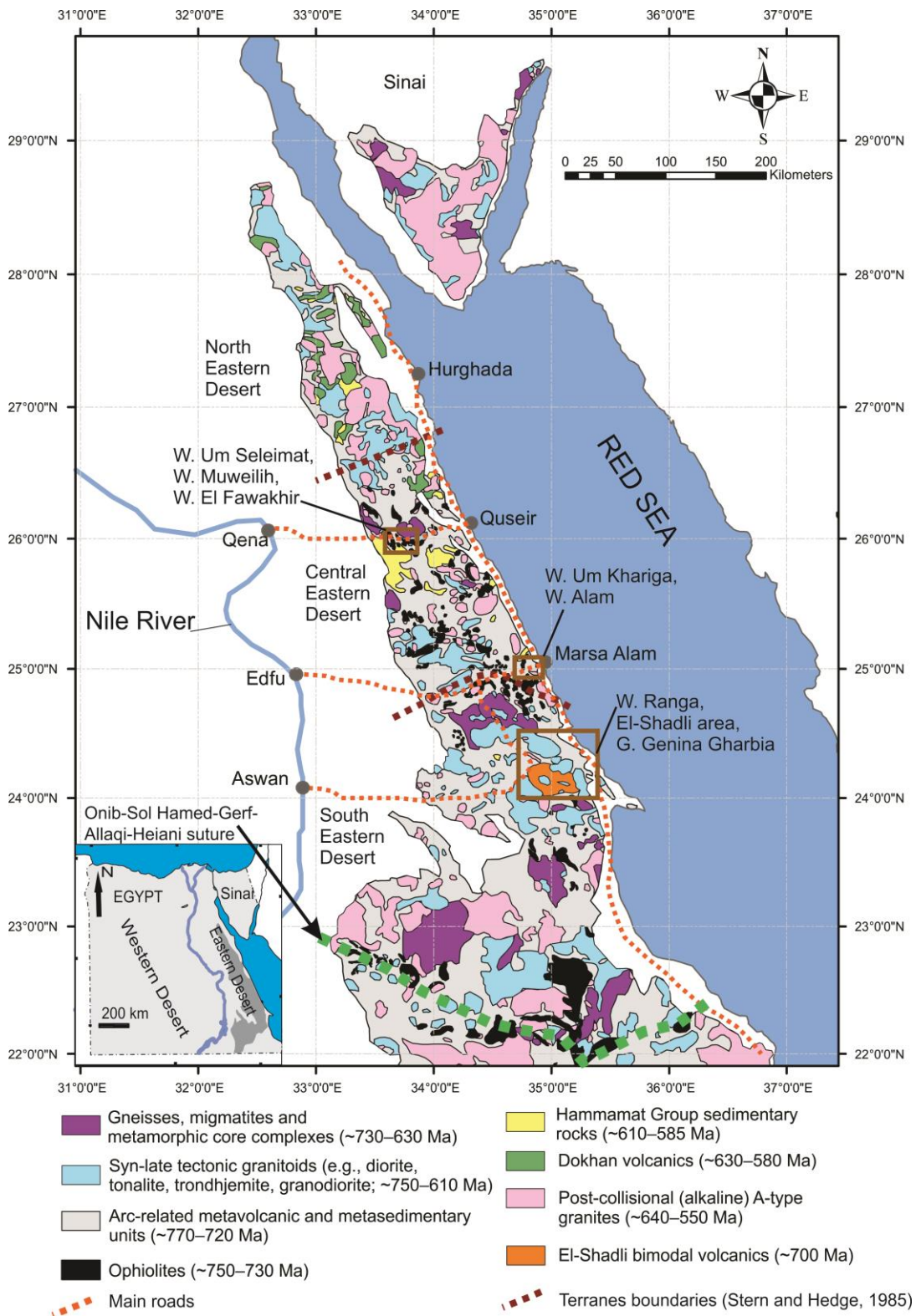


Figure 2.1: Geological map of the Eastern Desert showing the ages and distribution of the main rock units. Eastern Desert terranes boundaries are after Stern and Hedge (1985). The map is modified after Johnson *et al.* (2011).

At the mineral scale, the study involves zircon mineral separation, mount preparation, optical microscopic observations under both reflect-light and transmitted-light, cathodoluminescence (CL) imaging by Tescan MIRA3 scanning electron microscope (SEM), Sensitive High Resolution Ion Microprobe (SHRIMP) zircon U-Pb dating, zircon U-Pb, Lu-Hf isotopes and trace elements by laser ablation split stream inductively coupled plasma mass spectrometry (LA-SS-ICPMS), zircon O isotopes by Cameca IMS 1280-HR at high-precision secondary ion mass spectrometry (SIMS). In addition to zircon studies, silicate such as serpentine minerals, chromian-spinel (Cr-spinel) and carbonate minerals were investigated using Raman Spectroscopy, X-ray elemental mapping, electron microprobe (EMP), *in-situ* laser-ablation inductively coupled plasma mass spectrometry (LA-ICPMS), electron backscattered diffraction (EBSD), and atom probe tomography (APT) at atom-scale particularly for Cr-spinel. Furthermore, theoretical thermodynamic modelling including investigation of the temperature-pressure condition of serpentine and carbonate minerals was carried out for serpentinite rocks from W. Muweilih through collaboration. Detailed laboratory and geochemical analytical procedures and facilities used in chapters 3 to 5 of the thesis are described below. Analytical methods related to published chapters 6 and 7 are given in “the method sections” of those chapters.

2.2.1 Microscopic examination

Thin sections of the rock samples were cut and polished with progressively finer grades of diamond paste (9–1 μ m thick) by service provider Yu'neng Petrology and Mineral Service Company, China. The relative abundance of minerals (both transparent and opaque ones) and their textural relationships were analysed on a Nikon Eclipse optical microscope using transmitted and reflected lights at Curtin University. In addition, whole thin sections images were collected for some samples using a Zeiss Axio Imager M2m Imaging System at 5x magnification under transmitted and reflected light (Figure 2.2a, b) at Curtin University.

2.2.2 TIMA-phase maps

Phase mineral distribution maps of 11 granitoids samples (from El-Shadli and Genina Gharbia areas) were acquired using a TESCAN Integrated Mineral Analyser (TIMA) housed at the John de Laeter Centre, Curtin University. The analysis were performed on the carbon-coated whole thin sections using Liberation analysis in “Dot Mapping” mode adopting 3µm dot spacing for backscattered electron (BSE) images and 27 µm for X-ray acquisition operating at 25kV acceleration voltage, 15 mm working distance and a magnification of 185 times. Data processing (include calculation of modal composition) was performed with the TESCAN TIMA version 1.6.71 software (Figure 2.2c).

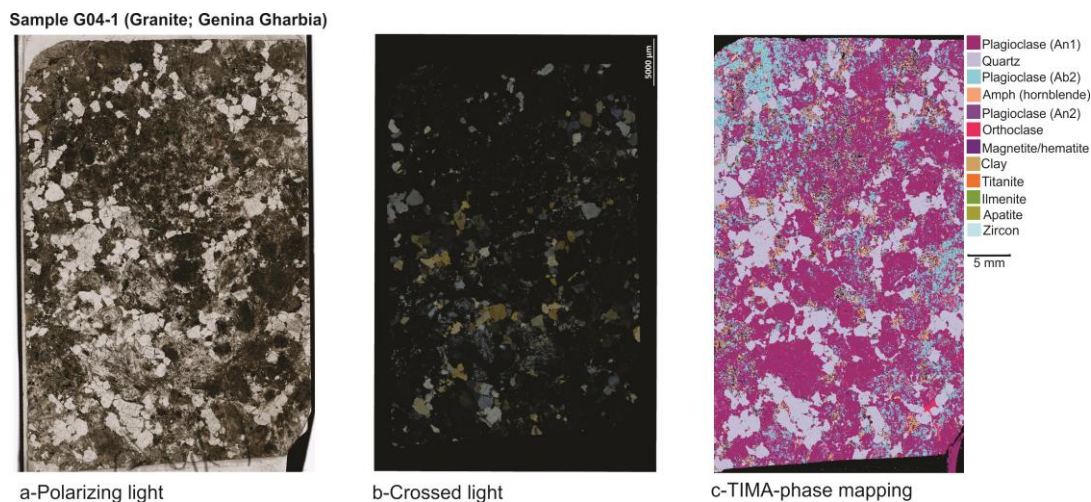


Figure 2.2: An example of a granite sample G04–1 (Genina Gharbia) thin section imaging to petrographic description under polarizing light (a), crossed light (b) and TIMA-phase mapping (c).

2.2.3 Whole-rock major and trace element geochemistry

Rock samples were examined first by optical microscopy. Selected rock samples were crushed with a polyethylene-wrapped hammer into <0.5 cm small chips, ultrasonically cleaned in distilled water, and subsequently dried and handpicked to avoid altered pieces and visible contamination. The samples were then grounded with ethyl alcohol in an agate ring mill to grain sizes below 50 µm, and the resulting powders were used for the analyses of major and trace elements, and Sr-Nd isotopes.

Whole-rock major element oxides were determined by XRF at Bureau Veritas Lab, Perth, Western Australia. Each whole-rock sample was pulverised in a vibrating

disc pulveriser. Then, the sample powder was ignited at 1,000 °C for 2 hours to determine the loss on ignition (LOI) using a robotic TGA system. Subsequently, the sample was cast using a 66:34 flux with 4% Lithium nitrate to prepare it into a glass pill (fuse bead) by melting at 1,080 °C. The major oxides (Al₂O₃, Cr₂O₃, Fe₂O₃, K₂O, MgO, MnO, Na₂O, P₂O₅, SiO₂, and TiO₂) were determined using XRF on the oven-dried (105 °C) fuse bead sample.

The trace and rare-earth elements (REE) of the samples were analysed using an Agilent 7500 quadrupole ICP-MS at Macquarie (MQ) GeoAnalytical lab, Macquarie University. Acid digestion with hydrofluoric acid (HF) was routinely used to digest geological materials for the trace-element determination. Powdered samples of 100 mg each were weighed into 15 mL Savillex Teflon beakers. The samples were first refluxed in 1.5 mL of conc. HF (Merck Suprapur grade) + 1.5 mL of Teflon distilled HNO₃ at 130°C overnight, then ultrasonicated and dry. This process was repeated once more. 10 drops of conc. HClO₄ (Merck Suprapur) and 2 mL of conc. HF (Merck Suprapur) were then added and evaporated to incipient dry at 170°C before adding 5 drops of conc. HClO₄. The sample beakers were tightly capped and placed on a hot plate for 24 hours at 190 °C and then cooled to room temperature. Samples were finally refluxed in 2 mL of 6N distilled HCl at 150°C for 3h and dried down at 190°C and then reflux again 2 mL of 6N distilled HNO₃ at 150°C for 3h. For trace element analyses, the samples were diluted in 100 mL of 2% HNO₃ + 0.5% HF, at 80°C until a clear solution resulted. Reference materials BCR-2 (basalts), BHVO-2 (basalt), BIR-1 (basalt), and GSP-2 (granodiorite) were analysed at the beginning and end of each analytical session and their measured values agree with recommended GeoRem (<http://georem.mpch-mainz.gwdg.de>) and USGS values (Figure 2.3; Table A1). The precision of the measurements by repeated analyses of reference samples is better than ±5% for trace elements and REEs.

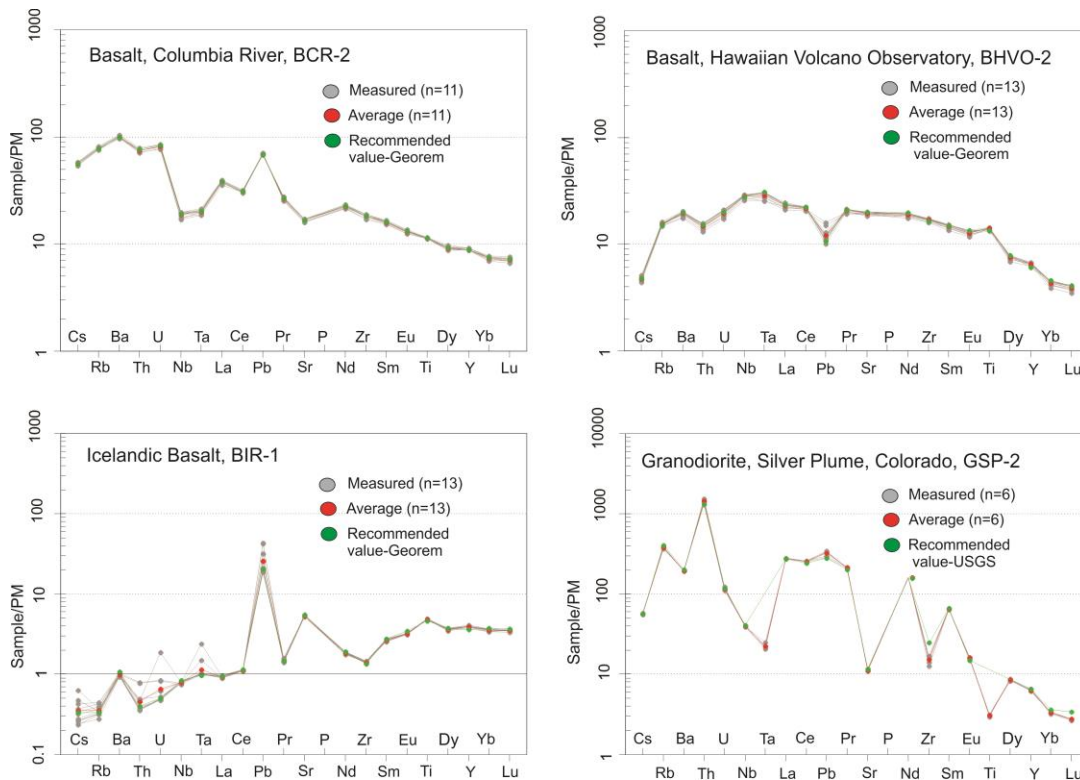


Figure 2.3: Primitive mantle (McDonough and Sun, 1995) normalized trace elements (including rare earth element) patterns of the reference materials used during ICP-MS analytical sessions. The measured values are compared with recommended values to show the precision of the measurements.

2.2.4 Whole-rock Sr-Nd isotopes

Sr and Nd isotopic ratios were obtained by thermal ionization mass spectrometry (TIMS) on a Thermo Finnigan Triton system at Macquarie (MQ) GeoAnalytical lab, Macquarie University. Analytical procedures including cleaning and column preparation, sample digestion, chromatographic separation to collect Sr and Nd, and sample loading on Re filament and data collection from TIMS are detailed in Tilhac *et al.*, (2017). The BHVO-2 reference sample was first measured in each analytical session to check instrument status and sensitivity for Sr and Nd and then followed by unknown samples. Sr isotopic data were collected during seven analytical sessions; whereas Nd isotopic data were collected during five analytical sessions. Ratios were normalized to $^{86}\text{Sr}/^{88}\text{Sr} = 0.1194$ and $^{146}\text{Nd}/^{144}\text{Nd} = 0.7219$ to correct for mass fractionation. The BHVO-2 reference sample yielded $^{87}\text{Sr}/^{86}\text{Sr}$ ratios ranging between 0.703449 ± 0.000290 (2σ) and 0.703486 ± 0.000464 (2σ) and $^{143}\text{Nd}/^{144}\text{Nd}$ between 0.512952 ± 0.000346 (2σ) and 0.512993 ± 0.000106 (2σ) (Table

2.1). These values are within the range of GeoRem preferred values for BHVO-2 ($^{87}\text{Sr}/^{86}\text{Sr} = 0.703469 \pm 0.000034$; $^{143}\text{Nd}/^{144}\text{Nd} = 0.512979 \pm 0.000014$). Blanks were below 1000 pg for Sr and 80 pg Nd. $^{87}\text{Rb}/^{86}\text{Sr}$ and $^{147}\text{Sm}/^{144}\text{Nd}$ were calculated using the elemental ratios measured by solution ICP-MS for whole rock.

Table 2.1: Sr and Nd isotopic ratios for BHVO–2 reference sample obtained by TIMS.

	$^{87}\text{Sr}/^{86}\text{Sr}$	$\pm 2\sigma$
BHVO-2X1	7.03486E-01	4.65E-04
BHVO-2X2	7.03487E-01	3.35E-04
BHVO-2X3	7.03461E-01	4.36E-04
BHVO-2X4	7.03449E-01	2.91E-04
BHVO-2X5	7.03458E-01	3.37E-04
BHVO-2X6	7.03460E-01	4.86E-04
BHVO-2X7	7.03477E-01	6.30E-04
	$^{143}\text{Nd}/^{144}\text{Nd}$	$\pm 2\sigma$
BHVO-2X1	5.129930E-01	1.06E-03
BHVO-2X2	5.129857E-01	7.38E-04
BHVO-2X3	5.129827E-01	7.21E-04
BHVO-2X4	5.129520E-01	2.49E-03
BHVO-2X5	5.129760E-01	3.46E-04

The initial $^{87}\text{Sr}/^{86}\text{Sr}$ and $^{143}\text{Nd}/^{144}\text{Nd}$ ratios were calculated using $\lambda^{87}\text{Rb} = 1.42 \times 10^{-11}$ and $\lambda^{147}\text{Sm} = 6.55 \times 10^{-12}$ and the assigned U-Pb zircon ages were collected from SHRIMP and LASS for each sample. The $^{143}\text{Nd}/^{144}\text{Nd}$ isotopic ratios are given as epsilon (ϵ) notations relative to chondritic uniform reservoir (CHUR) ($^{143}\text{Nd}/^{144}\text{Nd} = 0.512630$ and $^{147}\text{Sm}/^{144}\text{Nd} = 0.196$; Bouvier, Vervoort and Patchett, 2008):

$$\epsilon\text{Nd}_T = [({}^{143}\text{Nd}/{}^{144}\text{Nd}_{\text{i sample}})/({}^{143}\text{Nd}/{}^{144}\text{Nd}_{\text{i CHUR}}) - 1] \times 10000.$$

2.2.5 Zircon mount preparation

Zircon grains were separated from crushed rock samples (1–5 kg/each) using standard method of Frantz magnetic separator and heavy liquids at Yu'neng Petrology and Mineral Service Company, China. Best-quality grains characterized by homogenous transparency, colour, and fluorescence were handpicked and mounted in a 24 mm diameter epoxy resin discs and polished to expose the interior of the grains. Zircon grains from each sample are mounted along with zircon standards for age calibration (Plešovice) and O isotopes (Penglai and Qinghu) in Guangzhou

Institute of Geochemistry, Chinese Academy of Sciences (GIGCAS). The zircon crystals were characterised by cathodoluminescence (CL) imaging using a Tescan MIRA3 scanning electron microscope (SEM) in the Microscopy and Microanalysis Facility (MMF), John de Laeter Centre, Curtin University (Figure 2.4) using the setting of 12 kV, spot size 6 and working distance ~15 mm. In the CL images, high-U regions appear as dark regions, and low-U regions appear as brightly regions (Figure 2.4). Analytical spots, selected through CL imaging, were transparent, smooth, and without obvious inclusions. The polished mounts were cleaned in high-purity ethanol using an ultrasonic bath, and then vacuum-coated with high-purity gold prior to the SHRIMP and SIMS analyses.

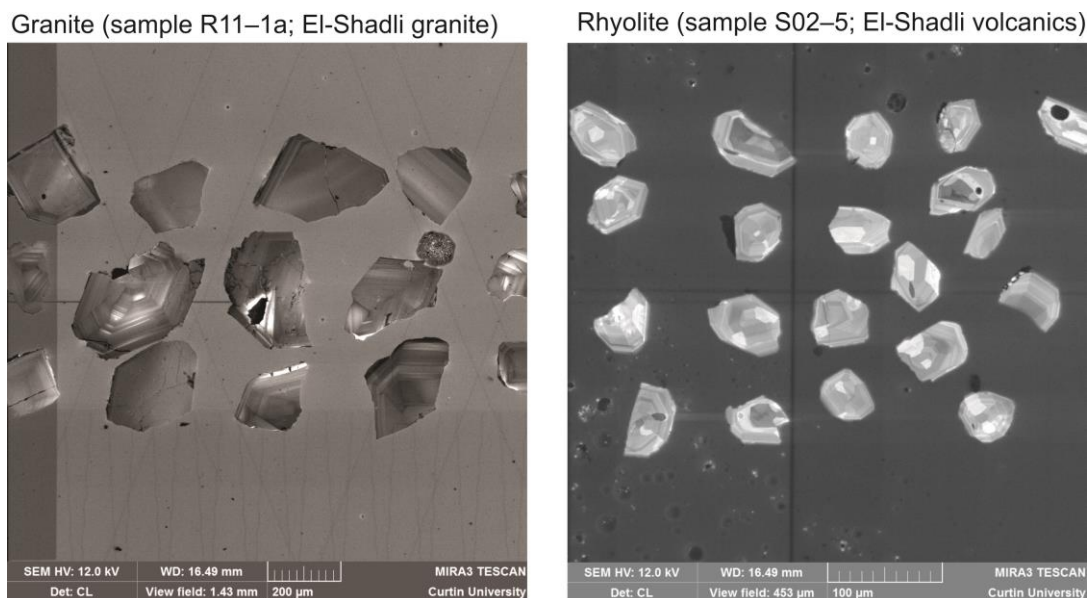


Figure 2.4: Cathodoluminescence (CL) images of zircon from different rock types such as granite (sample R11-1a; El-Shadli area-W. Ranga) and rhyolite (sample S02-5; El-Shadli volcanics).

2.2.6 SHRIMP U-Pb zircon analyses

Zircon U-Pb isotope measurements were done on the Sensitive High Resolution Ion Microprobe (SHRIMP) II instrument at the John de Laeter Centre, Curtin University. Full SHRIMP isotopic and trace elemental data sets for the studied samples are given in chapters 3, 4, and 5 (part I of the thesis). Curtin ion-microprobe SHRIMP II analytical procedures broadly followed those described by Compston et al., (1984) and Williams (1998). A 25–30 µm diameter spot size was used for all the

analysed grains with a primary beam current of 2.5–3.0 nA, mass resolution of ~5000 and analysis sensitivity of ~18 cps ppm⁻¹ nA⁻¹. Data for each spot were collected in sets of 6 scans through the mass range of ¹⁹⁶ZrO⁺, ²⁰⁴Pb⁺, background, ²⁰⁶Pb⁺, ²⁰⁷Pb⁺, ²⁰⁸Pb⁺, ²³⁸U⁺, ²⁴⁸ThO⁺, ²⁵⁴UO⁺. The measured isotopic ratios were corrected for common Pb based on the measured ²⁰⁴Pb and using the 2 stage common Pb evolution curve of Stacey and Kramers (1975) to get the common Pb compositions. Multiple standard analyses were interspersed between analyses during each session (once every four unknowns). Pb/U ages were normalized to a recommended value of 337.1 Ma determined by conventional U-Pb analysis of Plešovice zircon standard (Sláma *et al.*, 2008). The measurement of ²⁰⁶Pb/²³⁸U and ²⁰⁷Pb/²³⁵U ages requires normalization to results of the standard analyses, and the reported results were corrected for the uncertainties associated with the measurements of the Plesovice standard. The correction formula for Pb/U fractionation is $^{206}\text{Pb}^{+}/^{238}\text{U}^{+} = a(^{238}\text{U}^{16}\text{O}^{+}/^{238}\text{U}^{+})^b$ (Claoué-Long *et al.*, 1995) using the parameter values of Black *et al.* (2003). All isotopic measurements were reduced, processed and interpreted using SQUID II, Isoplot and Isoplot R programs (Ludwig, 2003, 2009; Vermeesch, 2018). The errors associated with individual analyses are 1σ uncertainties and include errors from U-Pb calibration based on the reproducibility of U-Pb standard measurements, counting statistics and the common-Pb correction. The weighted mean ages are quoted at the 95% confidence interval (2SD). The ages used through the text are ²⁰⁶Pb/²³⁸U ages which are more precise than ²⁰⁷Pb/²⁰⁶Pb ages for Neoproterozoic zircons due to the lower content of ²⁰⁷Pb in these zircons (Spencer, Kirkland and Taylor, 2016).

2.2.7 LASS zircon U-Pb, Lu-Hf isotopes and trace elements analyses

Zircon U-Pb, Lu-Hf isotopes and trace elements abundances were measured using laser ablation split stream inductively coupled plasma mass spectrometry (LASS-ICPMS) in the GeoHistory Facility at the John de Laeter Centre, Curtin University. The analyses were conducted on the same grain as the SHRIMP analysis, commonly over the same spots. Additional LASS-ICPMS spots were targeted based on cathodoluminescence images. The measured U-Pb and Lu-Hf isotopes and trace element data were collected simultaneously using an excimer laser (Resonetics S-155-LR 193 nm) coupled to a Nu Plasma II multicollector ICPMS (MC-ICPMS) and

Agilent 7700s quadrupole mass spectrometer. The laser spot diameter was 50 μm , with 3 J cm^{-2} on-sample laser fluence, repetition rate of 10 Hz, ablation time of 40 seconds and ~45 seconds of total baseline acquisition.

U-Pb and trace elements data were collected from the split stream on an Agilent 7700s quadrupole mass spectrometer. Analyses of unknowns were bracketed by blocks of primary and secondary zircon reference materials such as 91500, GJ1, Plešovice, and R33 to monitor and correct for mass fractionation and instrumental drift. Zircon standard 91500 (1062.4 ± 0.4 Ma; Wiedenbeck *et al.*, 2004) was utilized as the primary zircon reference age standard in this study. Standards GJ-1 (608.5 ± 01.5 Ma; Jackson *et al.*, 2004), Plešovice (337.13 ± 0.37 Ma; Sláma *et al.*, 2008) and R33 (419.26 ± 0.39 Ma; Black *et al.*, 2004) were analysed as secondary age standards and treated as unknowns to monitor data accuracy and precision, and were corrected for mass bias and fractionation based on measured isotopic ratios of the primary reference material. During the analytical session, 91500 gave a $^{206}\text{Pb}/^{238}\text{U}$ age of 1062.33 ± 3.33 Ma (mean square of weighted deviates [MSWD] = 0.09, $p = 1.00$, $n = 29$, self-normalized); GJ-1 yielded a $^{206}\text{Pb}/^{238}\text{U}$ age of 602.29 ± 1.16 Ma (MSWD = 0.89, $p = 0.65$, $n = 30$); Plešovice yielded a $^{206}\text{Pb}/^{238}\text{U}$ age of 337.46 ± 1.00 Ma (MSWD = 0.44, $p = 0.96$, $n = 15$); and R33 yielded a $^{206}\text{Pb}/^{238}\text{U}$ age of 416.99 ± 1.52 Ma (MSWD = 0.91, $p = 0.61$, $n = 31$) (Figure 2.5; Table A2). Accuracy on individual analyses was typically within 1% of the accepted value. Trace element data were collected simultaneously and raw data was reduced against GJ-1 using ^{91}Zr as the internal reference isotope standard, assuming 43.14% Zr in zircon.

Lu-Hf isotopic data were collected on a Nu Plasma II MC-ICPMS. Measurements of ^{172}Yb , ^{173}Yb , ^{175}Lu , $^{176}\text{Hf}+\text{Yb}+\text{Lu}$, ^{177}Hf , ^{178}Hf , ^{179}Hf and ^{180}Hf masses were made simultaneously on the Faraday array. The correction for the isobaric interference of Yb and Lu on ^{176}Hf was made following the method detailed in Spencer *et al.* (2020). The assessment of the resultant corrected $^{176}\text{Hf}/^{177}\text{Hf}$ ratio (and ϵHf) is facilitated through an evaluation of the correlation between $^{176}\text{Hf}/^{177}\text{Hf}$ and $^{176}\text{Yb}/^{177}\text{Hf}$ or $^{176}\text{Lu}/^{177}\text{Hf}$, and a range of reference materials with varying $^{176}\text{Lu}/^{177}\text{Hf}$ and $^{176}\text{Yb}/^{177}\text{Hf}$ ratios were also analysed to validate the isobaric interference corrections (Spencer *et al.*, 2017, 2020).

U-Pb Reference Materials analysed by LA-MC-ICPMS

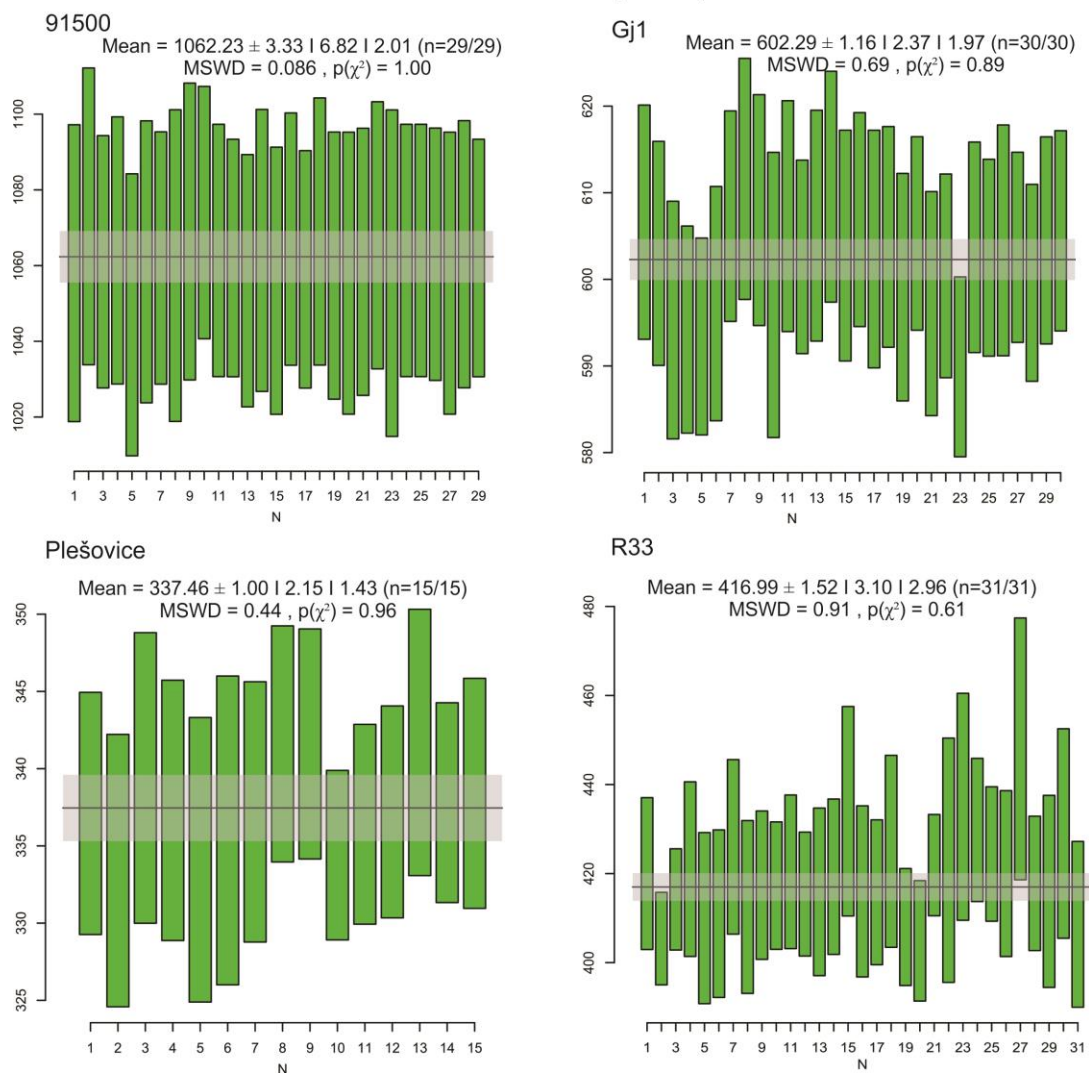


Figure 2.5: U-Pb data for reference materials used during the LASS-ICPMS analytical session.

Standard-sample-standard bracketing was applied using Mud Tank ($^{176}\text{Hf}/^{177}\text{Hf} = 0.282505 \pm 0.000044$; Woodhead and Hergt, 2005) as the primary reference material. 91500 ($^{176}\text{Hf}/^{177}\text{Hf} = 0.282306 \pm 0.000008$; Woodhead and Hergt, 2005), R33 ($^{176}\text{Hf}/^{177}\text{Hf} = 0.282749 \pm 0.000046$; Fisher *et al.*, 2014), GJ-1 ($^{176}\text{Hf}/^{177}\text{Hf} = 0.282000 \pm 0.000005$; Morel *et al.*, 2008), Plešovice ($^{176}\text{Hf}/^{177}\text{Hf} = 0.282482 \pm 0.000012$; Sláma *et al.*, 2008) and FC1 ($^{176}\text{Hf}/^{177}\text{Hf} = 0.282184 \pm 0.000018$; Woodhead and Hergt, 2005) were used as secondary standards to monitor accuracy of internal Hf isotope corrections for all Lu-Hf analyses. During the analytical session, the following corrected $^{176}\text{Hf}/^{177}\text{Hf}$ weighted average ratios were obtained on the standards: Mud Tank ($^{176}\text{Hf}/^{177}\text{Hf} = 0.282507 \pm 0.000006$, MSWD =

0.012, $p = 1.00$, $n = 31$), 91500 ($^{176}\text{Hf}/^{177}\text{Hf} = 0.282295 \pm 0.000011$, MSWD = 0.56, $p = 0.97$, $n = 29$), R33 ($^{176}\text{Hf}/^{177}\text{Hf} = 0.282739 \pm 0.000009$, MSWD = 0.41, $p = 1.00$, $n = 28$), GJ-1 ($^{176}\text{Hf}/^{177}\text{Hf} = 0.281999 \pm 0.000008$, MSWD = 0.54, $p = 0.98$, $n = 31$), Plešovice ($^{176}\text{Hf}/^{177}\text{Hf} = 0.282489 \pm 0.000018$, MSWD = 0.47, $p = 0.96$, $n = 16$), and FC1 ($^{176}\text{Hf}/^{177}\text{Hf} = 0.282161 \pm 0.000022$, MSWD = 0.79, $p = 0.69$, $n = 16$) (Figure 2.6; Table A3). Additionally, stable isotopic ratios ($^{178}\text{Hf}/^{177}\text{Hf}$ and $^{180}\text{Hf}/^{177}\text{Hf}$) can provide a powerful indication of instrument stability and the accuracy of mass bias corrections; the weighted average of stable $^{178}\text{Hf}/^{177}\text{Hf}$ and $^{180}\text{Hf}/^{177}\text{Hf}$ ratios for all analyses was 1.46733 and 1.88686, respectively, within the expected range of those ratios (Spencer *et al.*, 2020) (Figure 2.7). Data were reduced in Iolite (Paton *et al.*, 2011) and in-house Excel macros.

The $\epsilon\text{Hf}(t)$ values were calculated for all data using the ^{176}Lu decay constant = $1.865 \times 10^{-11} \text{ yr}^{-1}$ set out by Scherer, Münker and Mezger (2001). Chondritic values are after (Bouvier, Vervoort and Patchett, 2008): $^{176}\text{Hf}/^{177}\text{Hf}$ CHUR = 0.282785 and $^{176}\text{Lu}/^{177}\text{Hf}$ CHUR = 0.0336, where CHUR indicates chondritic uniform reservoir. Depleted mantle values are after Griffin *et al.* (2002): $^{176}\text{Hf}/^{177}\text{Hf}$ = 0.28325 and $^{176}\text{Lu}/^{177}\text{Hf}$ = 0.0384 and the new crust values are after Dhuime, Hawkesworth and Cawood (2011): $^{176}\text{Hf}/^{177}\text{Hf}$ = 0.283145 and $^{176}\text{Lu}/^{177}\text{Hf}$ = 0.0375. Two-stage Hf model ages (T_{DM} Crustal) were calculated from the measured Lu-Hf isotopes and U-Pb ages of the zircons; whereas the calculated initial $^{176}\text{Hf}/^{177}\text{Hf}$ ratio of the zircons is projected back to the depleted mantle growth curve assuming $^{176}\text{Lu}/^{177}\text{Hf}$ value of 0.015 for the average continental crust (Griffin *et al.*, 2002). Two-stage Hf model ages for new crust formed at island-arcs (T_{NC} Crustal) were calculated assuming $^{176}\text{Lu}/^{177}\text{Hf}$ value of 0.0113 (Dhuime, Hawkesworth and Cawood, 2011).

$$^{176}\text{Hf}/^{177}\text{Hf}_z(T) = ^{176}\text{Hf}/^{177}\text{Hf}_z(0) - ^{176}\text{Lu}/^{177}\text{Hf}_z \times (e^{\lambda T} - 1).$$

$$^{176}\text{Hf}/^{177}\text{Hf}_{\text{CHUR}(T)} = ^{176}\text{Hf}/^{177}\text{Hf}_{\text{CHUR}(0)} - ^{176}\text{Lu}/^{177}\text{Hf}_{\text{CHUR}} \times (e^{\lambda T} - 1).$$

$$^{176}\text{Hf}/^{177}\text{Hf}_{\text{DM}(T)} = ^{176}\text{Hf}/^{177}\text{Hf}_{\text{DM}(0)} - ^{176}\text{Lu}/^{177}\text{Hf}_{\text{DM}} \times (e^{\lambda T} - 1).$$

$$\epsilon\text{Hf}(T) = [^{176}\text{Hf}/^{177}\text{Hf}_z(T) / ^{176}\text{Hf}/^{177}\text{Hf}_{\text{CHUR}(T)} - 1] \times 10000.$$

$$T_{DM} = (1/\lambda) \times \ln[1 + ({}^{176}\text{Hf}/{}^{177}\text{Hf}_{DM} - {}^{176}\text{Hf}/{}^{177}\text{Hf}_Z) / ({}^{176}\text{Lu}/{}^{177}\text{Hf}_{DM} - {}^{176}\text{Lu}/{}^{177}\text{Hf}_Z)].$$

$$T_{DM}^C = T_{DM} - (T_{DM} - T) \times [(f_C - f_Z) / (f_C - f_{DM})].$$

$$T_{NC} = (1/\lambda) \times \ln[1 + ({}^{176}\text{Hf}/{}^{177}\text{Hf}_{NC} - {}^{176}\text{Hf}/{}^{177}\text{Hf}_Z) / ({}^{176}\text{Lu}/{}^{177}\text{Hf}_{NC} - {}^{176}\text{Lu}/{}^{177}\text{Hf}_Z)].$$

$$T_{NC}^C = T_{NC} - (T_{NC} - T) \times [(f_C - f_Z) / (f_C - f_{NC})].$$

$$f_{Lu/Hf} = {}^{176}\text{Hf}/{}^{177}\text{Hf} / {}^{176}\text{Lu}/{}^{177}\text{Hf}_{CHUR} - 1.$$

Where, f_C , f_Z , f_{DM} and f_{NC} are the $f_{Lu/Hf}$ values of the continental crust, zircon sample, the depleted mantle and the new (primitive) crust, respectively. Subscript Z = analyzed zircon sample, CHUR = chondritic uniform reservoir; DM = depleted mantle; NC = new (primitive) crust.

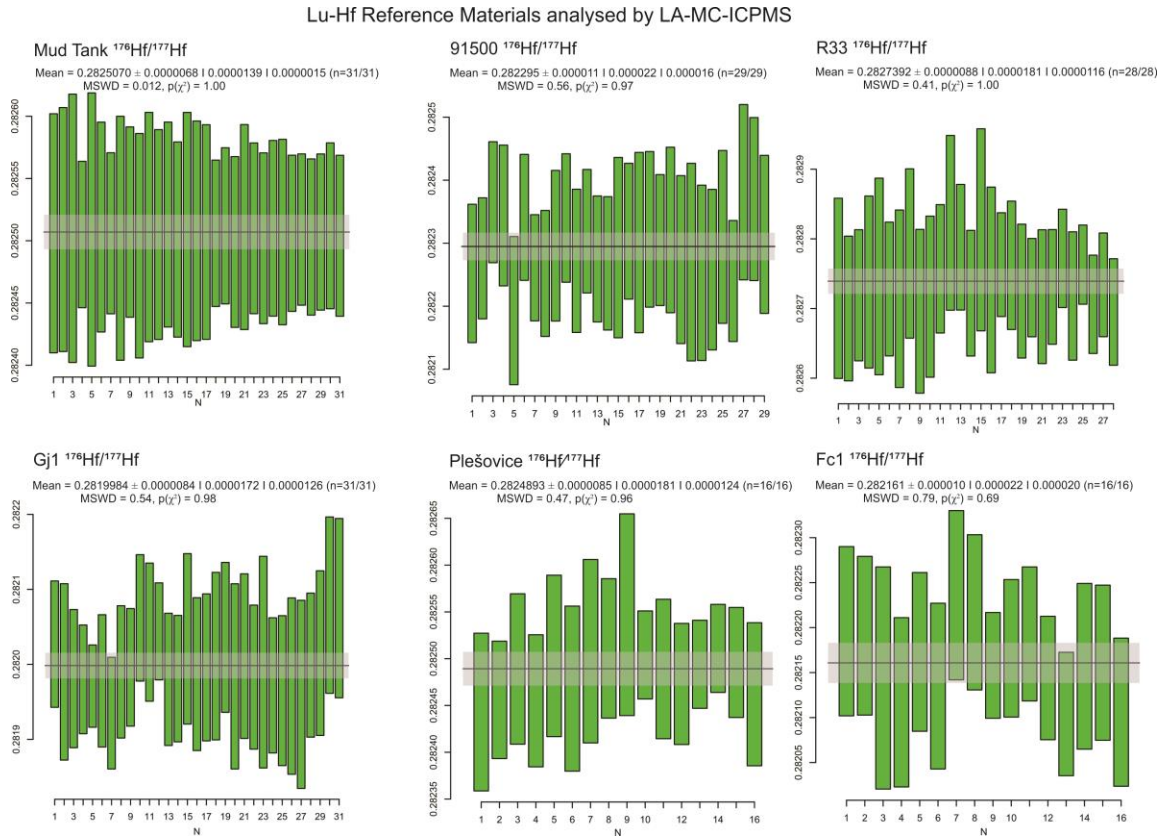


Figure 2.6: Lu-Hf data for reference materials used during the LASS-ICPMS analytical session.

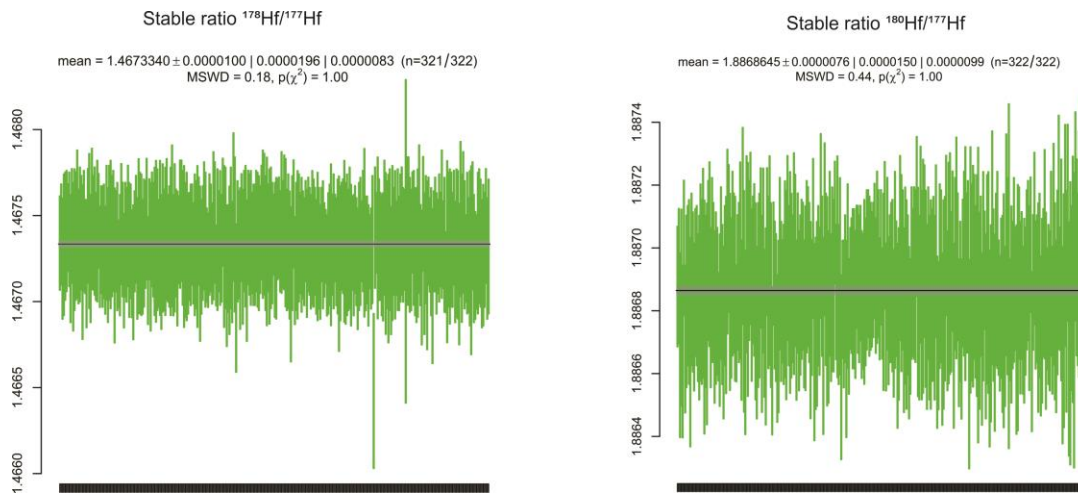


Figure 2.7: Stable isotopic ratios ($^{178}\text{Hf}/^{177}\text{Hf}$ and $^{180}\text{Hf}/^{177}\text{Hf}$) of the all analyses during the LASS-ICPMS analytical session.

2.2.8 SIMS zircon O-isotope analyses.

Zircon O isotopic compositions were measured using a Cameca IMS 1280–HR at the high–precision secondary ion mass spectrometry (SIMS) Laboratory of the Guangzhou Institute of Geochemistry, Chinese Academy of Sciences (GIGCAS), following the analytical procedures of Yang *et al.* (2018). Cs^+ primary ions beam was used to sputter oxygen ion from unknown zircon samples which accelerated at 10 kV and ~ 2 nA in intensity, with the mass resolution being ~ 2500 . The target area is ~ 20 μm in diameter which includes 10 μm being the spot diameter and an extra 10 μm the raster diameter. ^{16}O and ^{18}O isotopes were measured in multi-collector mode using two off–axis Faraday cups.

Qinghu and Penglai reference zircons (Li *et al.*, 2010, 2013) have been used to evaluate the precision (reproducibility) and accuracy. Penglai zircons were used as an external reference material to calibrate the instrumental mass fractionation (IMF). Qinghu zircons were treated as an unknown sample, which yielded a precision of $5.45 \pm 0.03\%$ (2SD; MSWD = 0.58) that is consistent with the recommended value of $5.4 \pm 0.2\%$ (2SD; (Li *et al.*, 2013) (Figure 2.8; Table A4). During each session, one Penglai zircon analysis was conducted with every five unknown spots (including a Qinghu zircon standard as an unknown). The measured $^{18}\text{O}/^{16}\text{O}$ ratios were normalized to the Vienna Standard Mean Ocean Water (VSMOW $^{18}\text{O}/^{16}\text{O} = 0.0020052$; Baertschi, 1976) and expressed on the $\delta^{18}\text{O}$ -scale.

A recommended value of $\delta^{18}\text{O} = 5.31 \pm 0.10\%$ (2SD) for the Penglai zircon standard was used in this study (Li *et al.*, 2010), and then corrected for the IMF as follows:

$$\delta^{18}\text{O}_M = \left(\frac{\left(\frac{^{18}\text{O}}{^{16}\text{O}} \right)_M}{0.0020052} - 1 \right) \times 1000(\text{‰}),$$

$$\text{IMF} = \delta^{18}\text{O}_M(\text{standard}) - \delta^{18}\text{O}_R(\text{standard})$$

$$\delta^{18}\text{O sample} = \delta^{18}\text{O}_M - \text{IMF}$$

whereas $(^{18}\text{O}/^{16}\text{O})_M$ is the raw value measured by SIMS, $(\delta^{18}\text{O})_M$ the normalized $(^{18}\text{O}/^{16}\text{O})_M$ by the value of VSMOW ($^{18}\text{O}/^{16}\text{O} = 0.0020052$), $(\delta^{18}\text{O})_M(\text{standard})$ the measured result of standard sample, $(\delta^{18}\text{O})_R(\text{standard})$ the recommended value of the Penglai standard, and $\delta^{18}\text{O}_{\text{sample}}$ the corrected sample value.

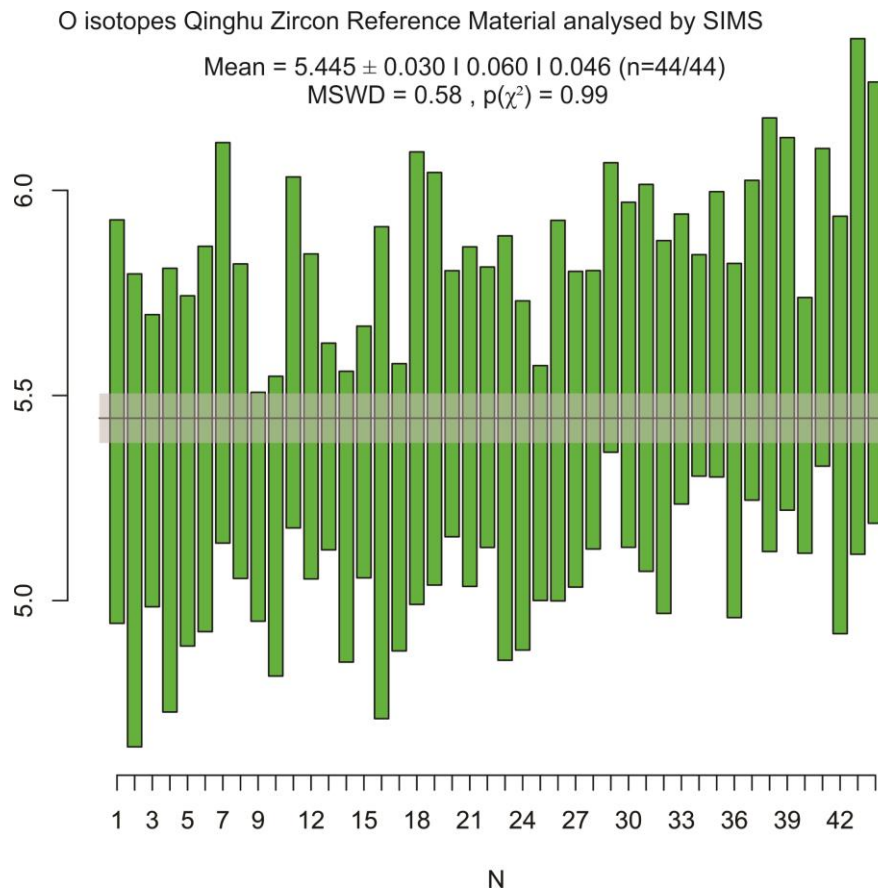


Figure 2.8: O isotopic data for Qinghu zircon reference material used during the SIMS analytical session. The error bars are quote at the 95% confidence interval (2SD).

2.3 Data-mining approach

Data-mining in this study involved the extraction, filtering and analyses of global mafic-ultramafic rock (basalts, picrites and komatiites) datasets from global database for the entire Earth history. This work, presented in part III of the thesis, aims to decipher the relationship between mantle dynamics, supercontinent cycles and plate tectonics. The two main databases used are the Georoc (<http://georoc.mpch-mainz.gwdg.de/georoc/>) and EarthChem (<https://www.earthchem.org/>). Major- and trace elements data were first extracted from the databases, and then manually double-checked when necessary (Chapter 9) for data quality against the original literature. Data selection was carried out using the following compositional cut-offs: basaltic composition (45–53 wt % SiO₂ , MgO < 12 wt% and total alkali (K₂O+Na₂O)<5 wt); picrite (>12 wt% MgO, SiO₂ <52 wt% and total alkali (K₂O+Na₂O) <3 wt%); and komatiite (>18 wt% MgO, SiO₂ <52 wt% and total alkali (K₂O+Na₂O) <2 wt%) (Le Bas, 2000; Herzberg *et al.*, 2007; Arndt *et al.*, 2008; Condie *et al.*, 2016). In addition, for Chapter 9, every sample was cross-checked against the original reference to verify its magmatic age and location (continent, craton and rock formation). To minimize sampling and preservation bias and the effect of uneven age distribution, the selected datasets were resampled using the weighted bootstrap method of Keller and Schoene (2012; Matlab MIT open-source code available at <https://github.com/brenhinkeller/StatisticalGeochemistry>).

2.4 References

- Arndt, N., Leshner, C. M. and Barnes, S. J. (2008) *Komatiite*. Cambridge: Cambridge University Press. doi: 10.1017/CBO9780511535550.
- Baertschi, P. (1976) 'Absolute ^{18}O content of standard mean ocean water', *Earth and Planetary Science Letters*. Elsevier, 31(3), pp. 341–344. doi: 10.1016/0012-821X(76)90115-1.
- LE BAS, M. J. (2000) 'IUGS Reclassification of the High-Mg and Picritic Volcanic Rocks', *Journal of Petrology*. Oxford University Press, 41(10), pp. 1467–1470. doi: 10.1093/petrology/41.10.1467.
- Black, L. P. *et al.* (2003) 'TEMORA 1: a new zircon standard for Phanerozoic U–Pb geochronology', *Chemical Geology*. Elsevier, 200(1–2), pp. 155–170. doi: 10.1016/S0009-2541(03)00165-7.
- Black, L. P. *et al.* (2004) 'Improved $^{206}\text{Pb}/^{238}\text{U}$ microprobe geochronology by the monitoring of a trace-element-related matrix effect; SHRIMP, ID-TIMS, ELA-ICP-MS and oxygen isotope documentation for a series of zircon standards', *Chemical Geology*. Elsevier, 205(1–2), pp. 115–140. doi: 10.1016/j.chemgeo.2004.01.003.
- Bouvier, A., Vervoort, J. D. and Patchett, P. J. (2008) 'The Lu–Hf and Sm–Nd isotopic composition of CHUR: Constraints from unequilibrated chondrites and implications for the bulk composition of terrestrial planets', *Earth and Planetary Science Letters*. Elsevier, 273(1–2), pp. 48–57. doi: 10.1016/J.EPSL.2008.06.010.
- Brenhin Keller, C. and Schoene, B. (2012) 'Statistical geochemistry reveals disruption in secular lithospheric evolution about 2.5Gyr ago', *Nature*. Nature Publishing Group, 485(7399), pp. 490–493. doi: 10.1038/nature11024.
- Claoué-Long, J. C. *et al.* (1995) 'Two Carboniferous Ages: A Comparison of Shrimp Zircon Dating with Conventional Zircon Ages and $^{40}\text{Ar}/^{39}\text{Ar}$ Analysis', in *Geochronology, Time Scales, and Global Stratigraphic Correlation*. SEPM (Society for Sedimentary Geology), pp. 3–21. doi: 10.2110/pec.95.04.0003.
- Compston, W., Williams, I. S. and Meyer, C. (1984) 'U-Pb geochronology of zircons from lunar breccia 73217 using a sensitive high mass-resolution ion microprobe', *Journal of Geophysical Research*, 89(S02), p. B525. doi: 10.1029/JB089iS02p0B525.
- Condie, K. C., Aster, R. C. and Van Hunen, J. (2016) 'A great thermal divergence in the mantle beginning 2.5 Ga: Geochemical constraints from greenstone basalts and komatiites', *Geoscience Frontiers*. Elsevier Ltd, 7(4), pp. 543–553. doi: 10.1016/j.gsf.2016.01.006.
- Dhuime, B., Hawkesworth, C. and Cawood, P. (2011) 'When Continents Formed', *Science*, 331(6014), pp. 155–156. doi: 10.1126/science.1200643.
- Fisher, C. M., Vervoort, J. D. and DuFrane, S. A. (2014) 'Accurate Hf isotope determinations of complex zircons using the "laser ablation split stream" method', *Geochemistry, Geophysics, Geosystems*. John Wiley & Sons, Ltd, 15(1), pp. 121–139. doi: 10.1002/2013GC004962.
- Griffin, W. . *et al.* (2002) 'Zircon chemistry and magma mixing, SE China: In-situ analysis

of Hf isotopes, Tonglu and Pingtan igneous complexes', *Lithos*. Elsevier, 61(3–4), pp. 237–269. doi: 10.1016/S0024-4937(02)00082-8.

Herzberg, C. *et al.* (2007) 'Temperatures in ambient mantle and plumes: Constraints from basalts, picrites, and komatiites', *Geochemistry, Geophysics, Geosystems*, 8(2). doi: 10.1029/2006GC001390.

Jackson, S. E. *et al.* (2004) 'The application of laser ablation-inductively coupled plasma-mass spectrometry to in situ U-Pb zircon geochronology', *Chemical Geology*. Elsevier, 211(1–2), pp. 47–69. doi: 10.1016/j.chemgeo.2004.06.017.

Johnson, P. R. *et al.* (2011) 'Late Cryogenian-Ediacaran history of the Arabian-Nubian Shield: A review of depositional, plutonic, structural, and tectonic events in the closing stages of the northern East African Orogen', *Journal of African Earth Sciences*. Elsevier Ltd, 61(3), pp. 167–232. doi: 10.1016/j.jafrearsci.2011.07.003.

Li, X.-H. *et al.* (2010) 'Penglai Zircon Megacrysts: A Potential New Working Reference Material for Microbeam Determination of Hf-O Isotopes and U-Pb Age', *Geostandards and Geoanalytical Research*. John Wiley & Sons, Ltd (10.1111), 34(2), pp. 117–134. doi: 10.1111/j.1751-908X.2010.00036.x.

Li, X. H. *et al.* (2013) 'Qinghu zircon: A working reference for microbeam analysis of U-Pb age and Hf and O isotopes', *Chinese Science Bulletin*. Springer, 58(36), pp. 4647–4654. doi: 10.1007/s11434-013-5932-x.

Ludwig, K. R. (2003) *Isoplot 3.0. A geochronological toolkit for Microsoft Excel: Berkeley Geochronology Center Special Publication*.

Ludwig, K. R. (2009) *SQUID II., a user's manual: Berkeley Geochronology Center, Special Publication*.

McDonough, W. . and Sun, S. -. (1995) 'The composition of the Earth', *Chemical Geology*, 120, pp. 223–252. doi: doi.org/10.1016/0009-2541(94)00140-4.

Morel, M. L. A. *et al.* (2008) 'Hafnium isotope characterization of the GJ-1 zircon reference material by solution and laser-ablation MC-ICPMS', *Chemical Geology*. Elsevier, 255(1–2), pp. 231–235. doi: 10.1016/j.chemgeo.2008.06.040.

Paton, C. *et al.* (2011) 'Iolite: Freeware for the visualisation and processing of mass spectrometric data', *Journal of Analytical Atomic Spectrometry*. Royal Society of Chemistry, 26(12), pp. 2508–2518. doi: 10.1039/c1ja10172b.

Scherer, E., Münker, C. and Mezger, K. (2001) 'Calibration of the lutetium-hafnium clock', *Science*. American Association for the Advancement of Science, 293(5530), pp. 683–687. doi: 10.1126/science.1061372.

Sláma, J. *et al.* (2008) 'Plešovice zircon — A new natural reference material for U–Pb and Hf isotopic microanalysis', *Chemical Geology*. Elsevier, 249(1–2), pp. 1–35. doi: 10.1016/J.CHEMGEO.2007.11.005.

Spencer, C. J. *et al.* (2017) 'Evidence for melting mud in Earth's mantle from extreme oxygen isotope signatures in zircon', *Geology*. GeoScienceWorld, 45(11), pp. 975–978. doi: 10.1130/G39402.1.

- Spencer, C. J. *et al.* (2020) ‘Strategies towards robust interpretations of in situ zircon Lu–Hf isotope analyses’, *Geoscience Frontiers*. Elsevier B.V., 11(3), pp. 843–853. doi: 10.1016/j.gsf.2019.09.004.
- Spencer, C. J., Kirkland, C. L. and Taylor, R. J. M. (2016) ‘Strategies towards statistically robust interpretations of in situ U–Pb zircon geochronology’, *Geoscience Frontiers*. Elsevier, 7(4), pp. 581–589. doi: 10.1016/J.GSF.2015.11.006.
- Stacey, J. S. and Kramers, J. D. (1975) ‘Approximation of terrestrial lead isotope evolution by a two-stage model’, *Earth and Planetary Science Letters*. Elsevier, 26(2), pp. 207–221. doi: 10.1016/0012-821X(75)90088-6.
- Stern, R. J. and Hedge, C. E. (1985) ‘Geochronologic and isotopic constraints on late Precambrian crustal evolution in the Eastern Desert of Egypt’, *American Journal of Science*, 285, pp. 97–127. doi: 10.2475/ajs.285.2.97.
- Tilhac, R. *et al.* (2017) ‘Sources and timing of pyroxenite formation in the sub-arc mantle: Case study of the Cabo Ortegal Complex, Spain’, *Earth and Planetary Science Letters*. Elsevier B.V., 474, pp. 490–502. doi: 10.1016/j.epsl.2017.07.017.
- Vermeesch, P. (2018) ‘IsoplotR: A free and open toolbox for geochronology’, *Geoscience Frontiers*. Elsevier, 9(5), pp. 1479–1493. doi: 10.1016/J.GSF.2018.04.001.
- Wiedenbeck, M. *et al.* (2004) ‘Further Characterisation of the 91500 Zircon Crystal’, *Geostandards and Geoanalytical Research*, 28, pp. 9–39.
- Williams, I. S. (1998) ‘U–Th–Pb Geochronology by Ion Microprobe’, in *Applications of Microanalytical Techniques to Understanding Mineralizing Processes*. Society of Economic Geologists, pp. 1–35. doi: 10.5382/Rev.07.01.
- Woodhead, J. D. and Hergt, J. M. (2005) ‘A Preliminary Appraisal of Seven Natural Zircon Reference Materials for In Situ Hf Isotope Determination’, *Geostandards and Geoanalytical Research*, 29(2), pp. 183–195. doi: 10.1111/j.1751-908x.2005.tb00891.x.
- Yang, Q. *et al.* (2018) ‘An evaluation of precision and accuracy of SIMS oxygen isotope analysis’, *Solid Earth Sciences*. Guangzhou Institute of Geochemistry, 3(3), pp. 81–86. doi: 10.1016/j.sesci.2018.05.001.

“Every reasonable effort has been made to acknowledge the owners of copyright material. I would be pleased to hear from any copyright owner who has been omitted or incorrectly acknowledged.”

Appendix A:
Supplementary materials to Chapter 2

Table A.1: Whole-rock trace and rear earth elements results of the standard references materials from ICP-MS analyses. All the concentrations in ppm.

Element	BCR-2x1	BCR-2x2	BCR-2x3	BCR-2x4	BCR-2x5	BCR-2x6	BCR-2x7	BCR-2x8
Li	7.93	7.79	7.90	8.02	7.90	7.99	6.50	7.51
Be	2.88	2.79	2.66	2.33	2.66	2.58	2.83	2.77
Sc	35.32	34.62	33.86	34.71	33.86	34.16	32.73	33.99
Ti	13496.65	13466.81	13595.45	13812.72	13595.45	13603.26	13357.55	13411.46
V	391.88	389.86	396.47	400.52	396.47	395.76	385.22	388.03
Cr	17.19	17.13	16.69	16.43	16.69	16.52	17.79	17.42
Mn	1524.59	1512.50	1520.00	1554.03	1520.00	1523.13	1521.21	1513.92
Co	37.80	37.18	36.45	36.30	36.45	36.02	35.64	36.74
Ni	14.33	13.71	13.46	12.94	13.46	13.20	14.12	13.75
Cu	26.96	27.01	27.23	27.99	27.23	27.59	27.41	27.41
Zn	135.90	129.32	125.43	127.26	125.43	125.43	129.97	123.48
Ga	20.80	20.60	21.15	21.76	21.15	21.17	20.08	20.15
Rb	46.45	46.17	46.42	48.76	46.42	48.09	45.33	46.11
Sr	316.96	320.13	329.13	339.03	329.13	340.86	316.75	320.47
Y	37.37	37.37	38.00	39.31	38.00	39.17	37.31	37.23
Zr	184.50	191.29	192.39	197.92	192.39	197.08	177.01	190.28
Nb	11.59	12.26	12.64	12.99	12.64	12.95	11.14	11.33
Mo	245.89	246.55	251.74	235.60	251.74	255.12	244.32	243.36
Cd	0.32	0.35	0.38	0.39	0.38	0.40	0.35	0.37
Cs	1.14	1.14	1.19	1.21	1.19	1.21	1.13	1.15
Ba	652.36	638.56	658.68	686.31	658.68	682.34	650.68	639.00
La	23.91	24.53	24.76	25.58	24.76	25.41	22.92	24.27
Ce	50.55	50.32	51.73	53.38	51.73	52.93	50.68	51.12
Pr	6.45	6.54	6.83	7.07	6.83	6.96	6.43	6.59
Nd	26.68	27.25	28.32	29.09	28.32	28.56	26.62	27.37
Sm	6.25	6.39	6.59	6.80	6.59	6.65	6.18	6.38
Eu	1.90	1.97	2.04	2.11	2.04	2.08	1.93	1.98
Tb	1.02	1.04	1.07	1.12	1.07	1.10	1.01	1.04
Gd	6.44	6.52	6.80	7.02	6.80	6.88	6.43	6.62
Dy	5.95	6.04	6.28	6.54	6.28	6.38	5.88	6.04
Ho	1.24	1.26	1.31	1.37	1.31	1.33	1.23	1.26
Er	3.46	3.52	3.66	3.81	3.66	3.71	3.42	3.53
Yb	3.10	3.20	3.28	3.41	3.28	3.35	3.08	3.21
Lu	0.47	0.47	0.49	0.51	0.49	0.50	0.45	0.47
Hf	4.53	4.61	4.76	4.96	4.76	4.83	4.44	4.59
Ta	0.70	0.72	0.75	0.78	0.75	0.76	0.69	0.72
Pb	10.43	10.57	10.32	10.33	10.32	10.44	10.40	10.54
Th	5.77	5.91	6.10	6.36	6.10	6.17	5.65	5.94
U	1.54	1.60	1.67	1.72	1.67	1.66	1.55	1.62

Table A.1: continue.

	BCR-2x9	BCR-2x10	BCR-2x11	Avg	Georem	BHVO-2x1	BHVO-2x2	BHVO-2x3
Li	7.83	8.00	8.00	7.76	7.90	5.22	3.91	3.86
Be	2.65	2.64	2.64	2.67	2.66	1.20	1.18	1.13
Sc	34.12	35.20	35.20	34.34	33.86	34.61	34.15	33.40
Ti	13639.34	13887.00	13887.00	13613.88	13595.45	16723.71	16851.09	16962.98
V	403.57	404.00	404.00	395.98	396.47	305.42	309.11	312.11
Cr	17.69	17.50	17.50	17.14	16.69	327.49	331.14	324.34
Mn	1520.50	1547.00	1547.00	1527.63	1520.00	1353.07	1349.71	1347.95
Co	37.56	36.70	36.70	36.69	36.45	45.94	45.43	44.21
Ni	13.29	13.60	13.60	13.59	13.46	133.57	130.66	125.77
Cu	27.78	27.30	27.30	27.38	27.23	163.64	160.67	154.79
Zn	126.44	128.00	128.00	127.70	125.43	120.11	106.03	102.64
Ga	21.29	21.70	21.70	21.05	21.15	20.21	20.30	20.77
Rb	45.96	47.60	47.60	46.81	46.42	9.13	9.23	9.43
Sr	330.36	338.00	338.00	328.98	329.13	377.96	382.50	390.79
Y	38.17	39.00	39.00	38.18	38.00	27.88	28.07	28.29
Zr	192.75	197.00	197.00	191.78	192.39	170.26	177.93	178.43
Nb	12.52	12.71	12.71	12.32	12.64	17.36	18.51	18.82
Mo	255.41	254.00	254.00	248.88	251.74	2.58	2.95	3.10
Cd	0.38	0.38	0.38	0.37	0.38	0.23	0.22	0.21
Cs	1.20	1.20	1.20	1.18	1.19	0.10	0.10	0.10
Ba	664.26	672.00	672.00	661.35	658.68	123.61	126.52	130.62
La	24.55	25.20	25.20	24.64	24.76	14.46	14.94	15.27
Ce	51.26	52.70	52.70	51.74	51.73	35.89	36.17	36.38
Pr	6.77	6.90	6.90	6.75	6.83	5.00	5.12	5.29
Nd	27.97	28.50	28.50	27.93	28.32	22.51	23.26	23.90
Sm	6.56	6.60	6.60	6.51	6.59	5.73	5.85	6.03
Eu	1.97	2.00	2.00	2.00	2.04	1.86	1.93	1.99
Tb	1.05	1.07	1.07	1.06	1.07	0.89	0.91	0.94
Gd	6.59	6.79	6.79	6.70	6.80	5.73	5.95	6.07
Dy	6.08	6.28	6.28	6.18	6.28	4.80	5.02	5.12
Ho	1.26	1.30	1.30	1.29	1.31	0.94	0.95	0.98
Er	3.58	3.64	3.64	3.60	3.66	2.37	2.41	2.51
Yb	3.22	3.30	3.30	3.25	3.28	1.81	1.88	1.94
Lu	0.48	0.49	0.49	0.48	0.49	0.26	0.26	0.27
Hf	4.63	4.75	4.75	4.69	4.76	3.95	4.09	4.23
Ta	0.73	0.75	0.75	0.74	0.75	1.00	1.06	1.10
Pb	10.10	10.34	10.34	10.38	10.32	2.39	1.82	1.68
Th	5.94	5.95	5.95	5.99	6.10	1.12	1.15	1.20
U	1.62	1.62	1.62	1.63	1.67	0.36	0.38	0.39

Table A.1: continue.

	BHVO- 2x4	BHVO- 2x5	BHVO- 2x6	BHVO- 2x7	BHVO- 2x8	BHVO- 2x9	BHVO- 2x10	BHVO- 2x11
Li	3.80	3.40	3.73	3.77	4.34	4.29	4.08	4.08
Be	1.21	1.13	1.12	1.08	1.14	1.18	1.28	1.28
Sc	31.94	33.80	33.26	33.23	33.20	33.57	33.40	33.40
Ti	16902.10	16799.49	17145.22	16780.93	16671.51	16966.79	16868.00	16868.00
V	309.04	307.80	310.61	308.10	313.13	311.89	309.00	309.00
Cr	326.20	336.93	333.32	322.98	241.05	224.02	217.10	217.10
Mn	1369.45	1346.77	1347.18	1350.38	1308.06	1308.28	1332.00	1332.00
Co	44.21	44.82	44.60	44.26	45.13	44.43	44.80	44.80
Ni	134.30	133.45	130.69	124.66	128.90	130.22	126.00	126.00
Cu	161.20	161.06	155.95	155.64	150.71	151.55	144.00	144.00
Zn	116.33	102.37	102.16	102.94	102.87	105.16	102.00	102.00
Ga	20.00	19.87	20.97	20.69	20.60	20.96	20.70	20.70
Rb	8.85	8.86	9.07	9.74	9.32	9.45	9.42	9.42
Sr	376.09	377.26	386.71	396.91	388.03	383.08	388.00	388.00
Y	26.89	28.00	27.99	28.72	28.42	28.23	28.00	28.00
Zr	166.93	176.98	179.45	181.65	179.35	179.13	177.00	177.00
Nb	16.90	18.44	18.93	19.12	18.61	18.69	18.78	18.78
Mo	2.34	2.78	2.97	3.10	4.66	4.59	4.25	4.25
Cd	0.21	0.20	0.20	0.21	0.08	0.08	0.08	0.08
Cs	0.09	0.10	0.10	0.10	0.10	0.10	0.10	0.10
Ba	115.57	119.12	128.66	134.33	130.85	130.32	131.00	131.00
La	13.56	14.10	15.04	15.78	15.33	15.32	15.10	15.10
Ce	33.94	35.98	36.25	37.16	36.67	37.39	37.20	37.20
Pr	4.89	5.02	5.23	5.35	5.36	5.38	5.40	5.40
Nd	21.96	22.53	23.54	24.10	24.14	24.20	24.40	24.40
Sm	5.47	5.73	5.94	6.10	6.14	6.13	6.20	6.20
Eu	1.80	1.88	1.95	2.02	1.99	1.98	1.97	1.97
Tb	0.85	0.88	0.92	0.96	0.95	0.94	0.95	0.95
Gd	5.65	5.83	6.03	6.28	6.19	6.15	6.21	6.21
Dy	4.60	4.80	5.05	5.24	5.14	5.22	5.19	5.19
Ho	0.90	0.92	0.96	1.00	0.98	0.97	0.99	0.99
Er	2.24	2.32	2.45	2.57	2.54	2.51	2.54	2.54
Yb	1.70	1.80	1.89	1.98	1.96	1.94	1.95	1.95
Lu	0.24	0.25	0.26	0.28	0.27	0.27	0.27	0.27
Hf	3.71	3.90	4.14	4.33	4.25	4.25	4.31	4.31
Ta	0.95	1.01	1.07	1.12	1.12	1.12	1.12	1.12
Pb	2.25	1.74	1.65	1.75	1.76	1.75	1.61	1.61
Th	1.04	1.09	1.16	1.24	1.25	1.24	1.24	1.24
U	0.35	0.36	0.39	0.41	0.41	0.41	0.42	0.42

Table A.1: continue.

	BHVO- 2x12	BHVO- 2x13	Avg	Georem	BIR-1X1	BIR-1X2	BIR-1X3	BIR-1X4
Li	3.88	4.13	4.04	4.80	3.06	2.76	3.06	2.99
Be	1.29	1.24	1.19	1.00	0.13	0.12	0.10	0.10
Sc	33.34	31.69	33.31	32.00	47.14	46.03	44.45	45.01
Ti	17137.38	16043.83	16824.69	16300.00	5785.61	5903.93	5887.99	5825.66
V	313.10	293.56	308.61	317.00	310.05	316.87	314.64	313.91
Cr	224.48	247.47	282.59	280.00	370.19	371.75	365.19	366.01
Mn	1348.15	1265.10	1335.24		1362.74	1366.45	1349.53	1358.08
Co	45.02	42.87	44.65	45.00	54.60	54.20	50.91	51.57
Ni	131.87	124.61	129.28	119.00	192.14	187.68	178.85	177.42
Cu	167.79	153.39	155.72	127.00	154.14	149.10	139.19	139.53
Zn	100.96	95.68	104.71	103.00	96.34	75.81	66.43	64.18
Ga	20.75	19.65	20.47	22.00	14.64	14.79	14.42	14.70
Rb	9.37	8.96	9.25	9.11	0.27	0.24	0.20	0.21
Sr	395.41	363.01	384.13	396.00	105.07	106.13	105.60	110.50
Y	28.71	27.03	28.02	26.00	16.59	17.06	16.98	17.46
Zr	182.07	169.85	176.62	172.00	14.97	15.00	14.96	15.14
Nb	18.99	17.87	18.45	18.10	0.51	0.52	0.53	0.53
Mo	4.48	3.51	3.50	4.00	0.00	0.00	0.00	0.01
Cd	0.09	0.09	0.15	0.06	0.14	0.12	0.10	0.10
Cs	0.11	0.10	0.10	0.10	0.01	0.01	0.01	0.01
Ba	131.63	125.67	127.61	131.00	6.84	6.52	6.30	6.40
La	15.35	14.44	14.91	15.20	0.61	0.60	0.60	0.60
Ce	37.04	35.11	36.34	37.50	1.84	1.86	1.87	1.89
Pr	5.37	5.09	5.23	5.35	0.36	0.37	0.37	0.37
Nd	24.23	23.09	23.56	24.50	2.20	2.24	2.30	2.32
Sm	6.14	5.83	5.96	6.07	1.05	1.04	1.08	1.08
Eu	2.06	1.92	1.95	2.07	0.48	0.49	0.50	0.50
Tb	0.96	0.90	0.92	0.92	0.35	0.35	0.35	0.36
Gd	6.36	5.90	6.04	6.24	1.78	1.82	1.86	1.88
Dy	5.31	4.95	5.05	5.31	2.34	2.39	2.46	2.48
Ho	1.02	0.94	0.96	0.98	0.59	0.56	0.56	0.57
Er	2.59	2.41	2.46	2.54	1.57	1.60	1.64	1.66
Yb	1.97	1.83	1.89	2.00	1.50	1.54	1.56	1.59
Lu	0.28	0.25	0.26	0.27	0.24	0.24	0.24	0.24
Hf	4.33	4.79	4.20	4.36	0.54	0.55	0.55	0.56
Ta	1.09	0.93	1.06	1.14	0.04	0.04	0.04	0.04
Pb	1.92	1.50	1.80	1.60	3.85	6.37	2.93	2.94
Th	1.23	1.17	1.18	1.22	0.06	0.04	0.03	0.03
U	0.41	0.39	0.39	0.40	0.02	0.01	0.01	0.01

Table A.1: continue.

	BIR-1X5	BIR-1X6	BIR-1X7	BIR-1X8	BIR-1X9	BIR-1X10	BIR-1X11	BIR-1X12
Li	1.32	2.22	2.93	3.24	3.17	2.90	2.90	2.62
Be	0.11	0.10	0.09	0.11	0.11	0.12	0.12	0.11
Sc	46.16	45.87	44.74	45.33	44.92	45.00	45.00	43.73
Ti	5767.24	5883.67	5923.77	5876.39	5869.01	5792.00	5792.00	5744.82
V	307.77	314.40	315.27	316.33	315.65	313.00	313.00	313.45
Cr	364.08	381.86	375.78	277.20	258.78	255.00	255.00	287.45
Mn	1357.77	1374.59	1368.75	1358.07	1353.83	1342.00	1342.00	1328.70
Co	52.85	53.52	51.02	53.19	51.74	51.30	51.30	50.10
Ni	189.76	192.23	183.56	185.01	185.00	177.00	177.00	181.81
Cu	146.64	146.97	139.68	137.93	137.87	130.00	130.00	149.58
Zn	91.84	72.57	62.74	68.34	68.71	63.50	63.50	68.57
Ga	14.27	14.54	14.44	14.82	15.03	14.90	14.90	14.31
Rb	0.25	0.22	0.19	0.19	0.19	0.21	0.21	0.23
Sr	104.14	105.69	105.07	107.13	106.93	107.00	107.00	104.51
Y	16.00	16.96	16.94	17.13	17.62	17.00	17.00	16.84
Zr	14.43	14.44	14.40	15.24	15.25	15.00	15.00	14.69
Nb	0.49	0.51	0.51	0.53	0.53	0.53	0.53	0.52
Mo	0.00	0.00	-0.04	0.02	0.03	0.02	0.02	0.42
Cd	0.13	0.10	0.09	0.08	0.07	0.08	0.08	0.18
Cs	0.01	0.01	0.00	0.01	0.01	0.01	0.01	0.01
Ba	6.57	6.32	6.14	6.51	6.58	6.59	6.59	7.05
La	0.59	0.58	0.59	0.61	0.63	0.62	0.62	0.61
Ce	1.83	1.82	1.84	1.88	1.92	1.90	1.90	1.88
Pr	0.37	0.37	0.37	0.38	0.38	0.40	0.40	0.37
Nd	2.24	2.27	2.33	2.32	2.39	2.40	2.40	2.32
Sm	1.05	1.06	1.10	1.10	1.11	1.10	1.10	1.09
Eu	0.48	0.49	0.50	0.49	0.50	0.49	0.49	0.50
Tb	0.34	0.35	0.35	0.35	0.36	0.35	0.35	0.35
Gd	1.81	1.84	1.89	1.86	1.89	1.85	1.85	1.91
Dy	2.36	2.41	2.51	2.46	2.53	2.50	2.50	2.51
Ho	0.58	0.57	0.58	0.56	0.58	0.58	0.58	0.58
Er	1.56	1.61	1.67	1.65	1.71	1.65	1.65	1.69
Yb	1.49	1.56	1.61	1.55	1.63	1.58	1.58	1.61
Lu	0.24	0.24	0.24	0.24	0.25	0.24	0.24	0.24
Hf	0.54	0.55	0.56	0.55	0.57	0.56	0.56	0.57
Ta	0.04	0.04	0.04	0.04	0.04	0.04	0.04	0.09
Pb	3.92	6.45	3.03	2.81	2.89	4.78	4.78	3.19
Th	0.06	0.04	0.03	0.03	0.03	0.03	0.03	0.04
U	0.02	0.01	0.01	0.01	0.01	0.01	0.01	0.04

Table A.1: continue.

	BIR-1X13	Avg	Georem	GSP-2x1	GSP-2x2	GSP-2x3	GSP-2x4	GSP-2x5	GSP-2x6	Avg	USGS
Li	3.03	2.78	3.20	27.13	26.74	27.30	27.30	27.54	24.51	26.75	36.00
Be	0.11	0.11	0.12	1.50	1.48	1.64	1.64	1.43	1.57	1.54	1.50
Sc	44.31	45.21	43.00	6.40	6.50	6.40	6.40	6.01	6.15	6.31	6.30
Ti	5748.21	5830.79	5600.00	3706.01	3694.76	3749.00	3749.00	3767.74	3537.24	3700.63	
V	306.53	313.14	319.00	47.26	46.63	48.00	48.00	47.47	44.89	47.04	52.00
Cr	325.20	327.19	391.00	20.17	18.63	20.00	20.00	16.37	18.17	18.89	20.00
Mn	1296.89	1350.72		298.55	292.83	301.00	301.00	304.36	285.05	297.13	320.00
Co	50.31	52.05	52.00	6.83	6.68	6.80	6.80	6.66	6.52	6.71	7.30
Ni	181.73	183.78	166.00	16.50	16.67	16.50	16.50	16.52	16.06	16.46	17.00
Cu	141.80	141.72	119.00	48.13	49.17	47.00	47.00	54.90	52.08	49.71	43.00
Zn	65.17	71.36	72.00	100.11	101.14	100.00	100.00	102.69	98.03	100.33	110.00
Ga	14.88	14.66	15.30	24.02	23.82	24.00	24.00	24.03	22.79	23.78	22.00
Rb	0.16	0.21	0.20	224.29	222.62	233.00	233.00	230.93	224.62	228.08	245.00
Sr	103.63	106.03	109.00	222.33	219.43	230.00	230.00	222.48	217.56	223.63	230.00
Y	16.77	16.95	15.60	27.27	27.44	28.00	28.00	26.78	26.37	27.31	28.00
Zr	14.76	14.87	14.00	162.00	164.68	178.00	178.00	133.56	148.29	160.76	550.00
Nb	0.52	0.52	0.55	25.70	26.07	27.00	27.00	25.96	25.53	26.21	27.00
Mo	-0.17	0.02	0.07	2.05	2.03	2.20	2.20	2.17	1.84	2.08	
Cd	0.08	0.10	0.10	0.08	0.08	0.08	0.08	0.10	0.10	0.09	
Cs	0.01	0.01	0.01	1.18	1.19	1.21	1.21	1.19	1.19	1.20	1.20
Ba	6.17	6.51	7.14	1289.72	1291.35	1297.00	1297.00	1285.37	1303.87	1294.05	1340.00
La	0.57	0.60	0.62	177.62	180.00	181.00	181.00	177.24	180.60	179.58	180.00
Ce	1.82	1.87	1.92	421.82	430.66	432.00	432.00	428.38	433.41	429.71	410.00
Pr	0.35	0.37	0.37	53.13	54.76	55.00	55.00	54.22	54.09	54.37	51.00
Nd	2.20	2.30	2.38	198.63	201.36	202.00	202.00	204.06	202.88	201.82	200.00
Sm	1.04	1.08	1.12	25.91	26.39	26.40	26.40	26.18	26.66	26.33	27.00
Eu	0.48	0.49	0.53	2.40	2.47	2.50	2.50	2.46	2.52	2.48	2.30
Tb	0.34	0.35	0.36	1.59	1.64	1.71	1.71	1.57	1.63	1.64	
Gd	1.79	1.85	1.87	13.28	13.72	14.40	14.40	13.52	13.61	13.82	12.00
Dy	2.39	2.45	2.51	5.55	5.68	5.75	5.75	5.75	5.85	5.72	
Ho	0.54	0.57	0.56	0.91	0.95	0.96	0.96	0.98	0.97	0.96	1.00
Er	1.59	1.63	1.66	2.59	2.68	2.76	2.76	2.56	2.66	2.67	
Yb	1.49	1.56	1.65	1.42	1.46	1.48	1.48	1.43	1.49	1.46	1.60
Lu	0.22	0.24	0.25	0.18	0.18	0.19	0.19	0.18	0.19	0.19	0.23
Hf	0.99	0.59	0.58	3.70	3.75	3.92	3.92	3.21	3.92	3.74	14.00
Ta	0.06	0.04	0.04	0.80	0.83	0.81	0.81	0.93	0.77	0.82	
Pb	2.92	3.91	3.10	43.54	45.23	49.70	49.70	51.09	51.90	48.53	42.00
Th	0.03	0.04	0.03	109.80	113.55	113.00	113.00	120.43	124.53	115.72	105.00
U	0.01	0.01	0.01	2.22	2.26	2.27	2.27	2.38	2.49	2.31	2.40

Table A.2: U-Pb data of the standard zircon references materials from LASS analyses.

Standard	$^{207}\text{Pb}/^{235}\text{U}$	$\pm 2\sigma$	$^{206}\text{Pb}/^{238}\text{U}$	$\pm 2\sigma$	$^{206}\text{Pb}/^{238}\text{U}$ Age (Ma)	$\pm 2\sigma$	$^{207}\text{Pb}/^{206}\text{Pb}$ Age (Ma)	$\pm 2\sigma$
Primary reference standard								
91500 - 1	1.76	0.1	0.1795	0.0034	1064	19	990	120
91500 - 2	1.964	0.091	0.178	0.0033	1056	18	1160	110
91500 - 3	1.85	0.11	0.1801	0.0031	1067	17	990	120
91500 - 4	1.78	0.12	0.1786	0.0029	1059	16	920	140
91500 - 5	1.78	0.14	0.1804	0.0034	1069	18	880	160
91500 - 6	1.86	0.12	0.1789	0.0033	1060	18	1100	140
91500 - 7	1.81	0.11	0.1785	0.0034	1058	19	1090	120
91500 - 8	1.94	0.11	0.1789	0.0032	1061	18	1160	120
91500 - 9	1.84	0.12	0.1797	0.0031	1068	18	1020	140
91500 - 10	1.8	0.13	0.1785	0.0041	1058	22	920	160
91500 - 11	1.92	0.12	0.1796	0.0032	1064	17	1110	130
91500 - 12	1.87	0.11	0.1791	0.0033	1064	17	1060	120
91500 - 13	1.8	0.12	0.1794	0.0031	1063	17	940	120
91500 - 14	1.777	0.095	0.1785	0.0035	1058	19	950	130
91500 - 15	1.88	0.11	0.1794	0.0032	1063	18	1050	130
91500 - 16	1.93	0.13	0.1792	0.0029	1062	16	1030	150
91500 - 17	1.9	0.1	0.1786	0.0037	1058	20	1150	110
91500 - 18	1.79	0.12	0.1812	0.0036	1073	20	990	140
91500 - 19	1.83	0.11	0.1786	0.0032	1061	17	990	130
91500 - 20	1.77	0.13	0.1795	0.0033	1064	18	970	150
91500 - 21	1.88	0.13	0.1764	0.0035	1047	19	1090	120
91500 - 22	1.79	0.11	0.1791	0.0035	1061	19	930	140
91500 - 23	2.03	0.11	0.1792	0.0032	1062	17	1220	110
91500 - 24	1.88	0.12	0.1788	0.0038	1060	21	1090	130
91500 - 25	1.8	0.1	0.1804	0.0036	1069	20	950	130
91500 - 26	1.87	0.12	0.1814	0.0032	1074	17	1000	140
91500 - 27	1.85	0.12	0.1791	0.003	1064	17	1020	140
91500 - 28	1.81	0.11	0.1792	0.0029	1062	16	1010	140
91500 - 29	1.86	0.11	0.178	0.003	1056	17	1040	130
Secondary reference standards								
GJ1 - 1	0.812	0.028	0.0987	0.0012	606.6	6.9	623	72
GJ1 - 2	0.777	0.033	0.0981	0.0011	603	6.6	472	94
GJ1 - 3	0.793	0.032	0.0968	0.0012	595.3	7	579	89
GJ1 - 4	0.793	0.034	0.0966	0.001	594.2	6.1	549	88
GJ1 - 5	0.788	0.033	0.09643	0.00099	593.4	5.8	557	86
GJ1 - 6	0.776	0.028	0.0971	0.0012	597.2	6.9	489	81
GJ1 - 7	0.811	0.035	0.0988	0.0011	607.3	6.2	586	93
GJ1 - 8	0.851	0.036	0.0995	0.0012	611.6	7.1	666	90
GJ1 - 9	0.825	0.029	0.0989	0.0012	608	6.8	600	83
GJ1 - 10	0.844	0.038	0.0973	0.0014	598.2	8.4	647	91
GJ1 - 11	0.844	0.033	0.0988	0.0012	607.3	6.8	611	81

GJ1 - 12	0.852	0.036	0.09799	0.00096	602.6	5.7	678	78
GJ1 - 13	0.867	0.032	0.0986	0.0012	606.2	6.8	658	76
GJ1 - 14	0.852	0.036	0.0994	0.0012	610.7	6.8	629	89
GJ1 - 15	0.856	0.035	0.0982	0.0012	603.9	6.8	623	88
GJ1 - 16	0.838	0.035	0.0987	0.0011	606.9	6.3	637	97
GJ1 - 17	0.819	0.033	0.0982	0.0012	603.5	7	650	89
GJ1 - 18	0.856	0.026	0.0984	0.0011	604.9	6.5	752	69
GJ1 - 19	0.834	0.028	0.0974	0.0011	599.1	6.7	691	79
GJ1 - 20	0.818	0.036	0.09845	0.00097	605.3	5.7	616	92
GJ1 - 21	0.828	0.027	0.0971	0.0011	597.2	6.6	641	77
GJ1 - 22	0.866	0.035	0.0976	0.001	600.4	6	736	77
GJ1 - 23	0.843	0.034	0.09584	0.00089	589.9	5.3	657	88
GJ1 - 24	0.809	0.032	0.0982	0.0011	603.7	6.2	539	96
GJ1 - 25	0.831	0.03	0.09798	0.00098	602.5	5.8	593	79
GJ1 - 26	0.823	0.033	0.0983	0.0012	604.5	6.8	589	89
GJ1 - 27	0.878	0.032	0.09819	0.00096	603.7	5.6	728	84
GJ1 - 28	0.824	0.033	0.09749	0.00098	599.6	5.8	674	85
GJ1 - 29	0.839	0.037	0.0983	0.001	604.5	6.1	669	94
GJ1 - 30	0.812	0.03	0.0985	0.001	605.6	5.9	635	80
Plešovice-1	0.369	0.019	0.05369	0.00066	337.1	4	230	120
Plešovice-2	0.419	0.026	0.05308	0.00074	333.4	4.5	420	130
Plešovice-3	0.396	0.028	0.05396	0.00076	339.4	4.8	320	150
Plešovice-4	0.37	0.021	0.05372	0.0007	337.3	4.3	230	130
Plešovice-5	0.397	0.022	0.05319	0.00076	334.1	4.7	330	120
Plešovice-6	0.409	0.028	0.05352	0.00083	336	5.1	310	150
Plešovice-7	0.399	0.023	0.0537	0.0007	337.2	4.3	280	120
Plešovice-8	0.422	0.022	0.05443	0.00064	341.6	3.9	490	120
Plešovice-9	0.43	0.018	0.05442	0.00062	341.6	3.8	508	94
Plešovice-10	0.389	0.016	0.05324	0.00046	334.4	2.8	303	91
Plešovice-11	0.393	0.019	0.05357	0.00054	336.4	3.3	270	100
Plešovice-12	0.396	0.016	0.0537	0.00057	337.2	3.5	271	92
Plešovice-13	0.392	0.019	0.05444	0.00072	341.7	4.4	260	99
Plešovice-14	0.393	0.019	0.0538	0.00054	337.8	3.3	290	110
Plešovice-15	0.392	0.019	0.05382	0.00061	338.4	3.8	330	110
R33 - 1	0.457	0.039	0.0667	0.0016	416	9.8	300	170
R33 - 2	0.529	0.031	0.0667	0.0014	415.8	8.3	460	130
R33 - 3	0.474	0.059	0.0682	0.0018	425	11	110	250
R33 - 4	0.516	0.036	0.0653	0.0011	408	6.7	440	140
R33 - 5	0.524	0.033	0.0648	0.0011	404.9	6.9	460	150
R33 - 6	0.484	0.031	0.06764	0.00095	421.9	5.8	290	130
R33 - 7	0.469	0.066	0.0678	0.0023	423	14	260	280
R33 - 8	0.497	0.051	0.0699	0.0021	435	13	280	210
R33 - 9	0.502	0.041	0.069	0.0014	429.8	8.2	290	180
R33 - 10	0.495	0.035	0.0681	0.0013	424.4	7.7	290	160

R33 - 11	0.521	0.042	0.0673	0.0016	420	9.5	410	180
R33 - 12	0.686	0.067	0.072	0.0025	448	15	820	180
R33 - 13	0.526	0.049	0.067	0.0013	417.8	7.7	350	180
R33 - 14	1.08	0.1	0.0732	0.0017	455	10	1720	170
R33 - 15	0.552	0.06	0.0668	0.0018	416	11	460	220
R33 - 16	0.549	0.075	0.0689	0.002	429	12	420	260
R33 - 17	0.504	0.045	0.0655	0.0016	408.6	9.5	310	200
R33 - 18	0.553	0.039	0.0673	0.0014	420	8.7	530	150
R33 - 19	0.534	0.028	0.06492	0.00087	405.4	5.3	570	110
R33 - 20	0.536	0.027	0.06637	0.00095	414.2	5.8	570	110
R33 - 21	0.5	0.05	0.0675	0.0017	421	10	420	210
R33 - 22	0.531	0.052	0.0657	0.0016	410	9.8	440	210
R33 - 23	0.496	0.074	0.0659	0.0016	411	9.6	160	280
R33 - 24	0.471	0.054	0.0684	0.0017	426	10	120	220
R33 - 25	0.504	0.045	0.0661	0.0016	412.5	9.9	330	180
R33 - 26	0.481	0.046	0.0669	0.0014	417.4	8.5	150	190
R33 - 27	0.502	0.034	0.0669	0.0012	417.3	7.3	330	140
R33 - 28	0.543	0.047	0.0674	0.0015	420.4	8.8	570	170
R33 - 29	0.531	0.033	0.0666	0.0012	415.4	7.1	480	140
R33 - 30	0.503	0.051	0.0667	0.0016	415.9	9.6	340	210
R33 - 31	0.522	0.05	0.0672	0.0015	419.3	8.9	400	200
R33 - 32	0.522	0.058	0.0697	0.002	434	12	370	220

Table A.3: Lu-Hf data of the standard zircon references materials from LASS analyses.

Standard	$^{178}\text{Hf}/^{177}\text{Hf}$	$\pm 2\sigma$	$^{180}\text{Hf}/^{177}\text{Hf}$	$\pm 2\sigma$	$^{176}\text{Hf}/^{177}\text{Hf}$	$\pm 2\sigma$	$^{176}\text{Lu}/^{177}\text{Hf}$	$\pm 2\sigma$
Primary reference standard								
Mud Tank - 1	1.46729	0.0002	1.88673	0.00012	0.282506	0.000049	0.00001991	7.9E-07
Mud Tank - 2	1.46737	0.0002	1.88683	0.00015	0.282509	0.00005	0.0000171	1.1E-06
Mud Tank - 3	1.46739	0.00019	1.88687	0.00013	0.28251	0.000055	0.00002447	3.9E-07
Mud Tank - 4	1.46735	0.00024	1.88678	0.00015	0.282505	0.00003	0.00002438	3.3E-07
Mud Tank - 5	1.46737	0.00017	1.88691	0.00012	0.282509	0.000056	0.00002363	3.5E-07
Mud Tank - 6	1.46739	0.00016	1.88688	0.00016	0.282511	0.000043	0.00002483	3.5E-07
Mud Tank - 7	1.46745	0.00015	1.886811	0.000089	0.282506	0.000033	0.00002401	3.8E-07
Mud Tank - 8	1.46732	0.00017	1.8869	0.00013	0.282502	0.00005	0.00002168	2.7E-07
Mud Tank - 9	1.46733	0.00016	1.88675	0.0001	0.282515	0.000039	0.00002339	3.5E-07
Mud Tank - 10	1.4674	0.00013	1.88697	0.00017	0.282496	0.000046	0.00002418	3.3E-07
Mud Tank - 11	1.46738	0.00018	1.88677	0.00014	0.282511	0.000047	0.00002413	3.2E-07
Mud Tank - 12	1.46738	0.00012	1.8869	0.00013	0.282505	0.000043	0.00002462	3.8E-07
Mud Tank - 13	1.46745	0.0002	1.88687	0.00013	0.282513	0.000042	0.0000221	3.3E-07
Mud Tank - 14	1.46738	0.00021	1.88694	0.00014	0.282501	0.00004	0.00002239	2.7E-07
Mud Tank - 15	1.46741	0.00018	1.88687	0.00018	0.282509	0.000048	0.00002079	3.8E-07
Mud Tank - 16	1.46739	0.00014	1.88677	0.00015	0.282508	0.000045	0.00002249	3.7E-07
Mud Tank - 17	1.46734	0.00012	1.88681	0.00011	0.282507	0.000044	0.00002137	2.8E-07
Mud Tank - 18	1.467324	0.000096	1.88682	0.00011	0.282506	0.00003	0.00002188	2.9E-07
Mud Tank - 19	1.46737	0.00013	1.887	0.00012	0.282512	0.000032	0.00002115	2.5E-07
Mud Tank - 20	1.46731	0.00012	1.88676	0.00011	0.282499	0.000035	0.00002108	2.9E-07
Mud Tank - 21	1.467423	0.000083	1.88701	0.00011	0.282511	0.000042	0.00002138	6.6E-07
Mud Tank - 22	1.46739	0.00014	1.88689	0.0001	0.28251	0.000035	0.0000046	3E-07
Mud Tank - 23	1.46729	0.00014	1.88678	0.00013	0.282502	0.000035	0.0000143	7.9E-07
Mud Tank - 24	1.467348	0.000085	1.88681	0.00011	0.28251	0.000036	0.00002024	3E-07
Mud Tank - 25	1.467294	0.000097	1.886901	0.000095	0.282507	0.000038	0.00002034	3.6E-07
Mud Tank - 26	1.46731	0.00013	1.88696	0.00013	0.282506	0.000032	0.00002035	2.5E-07
Mud Tank - 27	1.46738	0.00011	1.88689	0.00011	0.282509	0.000031	0.00000436	3.1E-07
Mud Tank - 28	1.467333	0.000082	1.88684	0.0001	0.282503	0.000032	0.00000548	5E-07
Mud Tank - 29	1.467301	0.000096	1.88683	0.00012	0.282507	0.000032	0.00002206	2.8E-07
Mud Tank - 30	1.467347	0.000099	1.88683	0.00011	0.282512	0.000034	0.00002155	2.5E-07
Mud Tank - 31	1.46739	0.00013	1.88685	0.00012	0.282504	0.000033	0.00002077	2.6E-07
Secondary reference standards								
91500 - 1	1.46749	0.00016	1.88703	0.00016	0.282293	0.000073	0.0003063	6.7E-07
91500 - 2	1.46729	0.0002	1.88666	0.00016	0.282319	0.000055	0.00030594	8.2E-07
91500 - 3	1.46729	0.00015	1.88683	0.00019	0.282301	0.000073	0.00030137	7.9E-07
91500 - 4	1.46741	0.0002	1.88669	0.00014	0.282322	0.000063	0.00030508	7.8E-07
91500 - 5	1.4674	0.00021	1.88685	0.00015	0.282305	0.000053	0.00030533	7.5E-07
91500 - 6	1.46736	0.00027	1.88688	0.00014	0.282321	0.000067	0.00029938	6.7E-07
91500 - 7	1.46751	0.00021	1.88704	0.0002	0.282274	0.000068	0.00029956	6.8E-07
91500 - 8	1.4674	0.0002	1.88695	0.00018	0.28227	0.00008	0.00029888	7.2E-07
91500 - 9	1.46732	0.00019	1.88689	0.00022	0.282253	0.000071	0.00030032	6.5E-07
91500 - 10	1.46742	0.00017	1.887	0.0002	0.282258	0.000065	0.00030107	7.5E-07
91500 - 11	1.46738	0.00024	1.88677	0.00018	0.28231	0.00007	0.00030186	7.5E-07

91500 - 12	1.46743	0.00019	1.88687	0.0002	0.28224	0.000049	0.00030169	7.3E-07
91500 - 13	1.46736	0.00017	1.88674	0.0002	0.282381	0.000071	0.00030262	8E-07
91500 - 14	1.46736	0.00019	1.88676	0.00021	0.28237	0.000066	0.00030125	8E-07
91500 - 15	1.46724	0.00019	1.88693	0.00019	0.282314	0.000064	0.0003004	7.7E-07
91500 - 16	1.46732	0.00012	1.8868	0.00019	0.282252	0.000056	0.0002393	1.2E-06
91500 - 17	1.46732	0.00012	1.88708	0.00015	0.282276	0.000049	0.0002694	1.1E-06
91500 - 18	1.46736	0.00014	1.88692	0.00017	0.282365	0.000049	0.00025225	8.8E-07
91500 - 19	1.46737	0.00013	1.88678	0.00016	0.282344	0.000057	0.00028111	6.3E-07
91500 - 20	1.46726	0.00011	1.88705	0.00014	0.282193	0.00006	0.0002651	1.3E-06
91500 - 21	1.46734	0.00016	1.88687	0.00013	0.282341	0.000051	0.0002733	6.5E-07
91500 - 22	1.46732	0.0001	1.88695	0.00014	0.282261	0.000043	0.00027529	4.5E-07
91500 - 23	1.4673	0.00012	1.88682	0.00014	0.282252	0.000051	0.00027487	6.1E-07
91500 - 24	1.46734	0.00015	1.88692	0.00013	0.282296	0.000061	0.00026119	8.8E-07
91500 - 25	1.46725	0.0001	1.8868	0.00012	0.28234	0.000052	0.00027299	7E-07
91500 - 26	1.46736	0.00013	1.88677	0.00015	0.282272	0.000058	0.00027227	8.5E-07
91500 - 27	1.46726	0.00013	1.8869	0.00017	0.282319	0.00005	0.00027976	7.8E-07
91500 - 28	1.46738	0.00011	1.88676	0.00012	0.282275	0.000051	0.00027948	6.3E-07
91500 - 29	1.46726	0.00011	1.8868	0.0002	0.282268	0.000054	0.00027401	6.5E-07
R33 - 1	1.4673	0.00017	1.88672	0.00014	0.282729	0.000066	0.0017736	6.4E-06
R33 - 2	1.46741	0.00021	1.88684	0.00017	0.2827	0.000053	0.0019337	5.5E-06
R33 - 3	1.46729	0.00022	1.88682	0.00015	0.282719	0.000048	0.0006704	6.8E-06
R33 - 4	1.46737	0.00016	1.88705	0.00015	0.282738	0.000063	0.00275	0.000078
R33 - 5	1.46725	0.00016	1.88693	0.00017	0.282746	0.000072	0.002463	0.000017
R33 - 6	1.4673	0.00021	1.88687	0.00017	0.282728	0.000049	0.001119	0.000014
R33 - 7	1.46733	0.00021	1.88693	0.00014	0.282714	0.000065	0.001134	0.00002
R33 - 8	1.46733	0.00025	1.8868	0.00013	0.282779	0.000062	0.001159	0.000054
R33 - 9	1.46744	0.00018	1.886954	0.000099	0.282696	0.00006	0.001116	0.000024
R33 - 10	1.46731	0.00018	1.88691	0.00014	0.282717	0.000059	0.001508	0.000066
R33 - 11	1.46719	0.00019	1.8868	0.00016	0.282757	0.000047	0.000861	0.000037
R33 - 12	1.4674	0.00017	1.88683	0.00017	0.282823	0.000064	0.000642	0.00002
R33 - 13	1.46733	0.00015	1.88694	0.00012	0.282788	0.000046	0.000795	0.000017
R33 - 14	1.467326	0.000097	1.88691	0.00014	0.282722	0.000046	0.002404	0.000054
R33 - 15	1.46728	0.00013	1.88692	0.00013	0.282813	0.000074	0.00525	0.000085
R33 - 16	1.46733	0.00015	1.88686	0.00014	0.282741	0.000068	0.00483	0.00011
R33 - 17	1.4673	0.000093	1.88668	0.00012	0.282763	0.000038	0.001273	0.000042
R33 - 18	1.4673	0.00011	1.88687	0.00012	0.282762	0.000047	0.0014	0.0001
R33 - 19	1.46734	0.00013	1.88692	0.00019	0.282725	0.000049	0.001201	0.00006
R33 - 20	1.46731	0.00011	1.88704	0.00012	0.28273	0.000036	0.001165	0.000013
R33 - 21	1.46733	0.0001	1.8868	0.00014	0.282717	0.000049	0.001918	0.000025
R33 - 22	1.467334	0.000092	1.88688	0.00011	0.282731	0.000042	0.001036	0.000011
R33 - 23	1.467209	0.000096	1.8868	0.00012	0.282772	0.000036	0.000894	0.000034
R33 - 24	1.46733	0.00012	1.88694	0.00015	0.282718	0.000047	0.001456	0.000086
R33 - 25	1.46732	0.00011	1.88688	0.00011	0.282763	0.000029	0.0009553	5.7E-06
R33 - 26	1.467267	0.000073	1.886815	0.000088	0.282706	0.000036	0.0007313	9.5E-06
R33 - 27	1.46733	0.00011	1.88688	0.00016	0.282734	0.000038	0.00179	0.00011
R33 - 28	1.46727	0.00013	1.88685	0.00013	0.282695	0.000039	0.000663	0.000012

GJ1 - 1	1.46748	0.00017	1.88686	0.00016	0.282034	0.000058	0.00029871	6.6E-07
GJ1 - 2	1.46748	0.0002	1.8868	0.00018	0.281987	0.000052	0.00027905	6E-07
GJ1 - 3	1.46734	0.00016	1.88697	0.00017	0.281996	0.00005	0.00029737	6.1E-07
GJ1 - 4	1.46743	0.0002	1.88676	0.00013	0.282011	0.000057	0.00029582	4.8E-07
GJ1 - 5	1.46743	0.00019	1.88671	0.00017	0.282036	0.000051	0.00028407	7.6E-07
GJ1 - 6	1.46728	0.00017	1.88677	0.00017	0.281984	0.000063	0.00029281	5.4E-07
GJ1 - 7	1.46739	0.00019	1.8872	0.00016	0.282011	0.000056	0.0002766	1.2E-06
GJ1 - 8	1.46738	0.00017	1.88702	0.00019	0.281983	0.000049	0.00029159	6.1E-07
GJ1 - 9	1.46729	0.0002	1.88679	0.00017	0.282003	0.000072	0.0002894	6.5E-07
GJ1 - 10	1.46733	0.00015	1.88667	0.0002	0.281972	0.000046	0.00029035	8.8E-07
GJ1 - 11	1.46748	0.00018	1.88676	0.00016	0.281965	0.000051	0.00029675	4.6E-07
GJ1 - 12	1.46726	0.0002	1.88662	0.00018	0.281971	0.00006	0.00026317	8.6E-07
GJ1 - 13	1.46733	0.00017	1.88697	0.00018	0.28196	0.000064	0.00029256	8.6E-07
GJ1 - 14	1.46742	0.00016	1.88687	0.00016	0.281999	0.000049	0.00028154	7.8E-07
GJ1 - 15	1.46735	0.00018	1.88679	0.00017	0.282015	0.000056	0.00028741	7E-07
GJ1 - 16	1.46738	0.00015	1.88679	0.00016	0.282079	0.00006	0.0002683	0.000001
GJ1 - 17	1.46739	0.00017	1.88658	0.00014	0.282075	0.000061	0.00029194	6.7E-07
GJ1 - 18	1.46729	0.00013	1.88683	0.00015	0.282027	0.000043	0.00028967	5.5E-07
GJ1 - 19	1.46741	0.00012	1.88696	0.00016	0.28199	0.00006	0.00028937	6.2E-07
GJ1 - 20	1.46741	0.00012	1.88698	0.00013	0.281981	0.000047	0.00029504	4.9E-07
GJ1 - 21	1.46736	0.00014	1.88696	0.0001	0.28198	0.000037	0.00028315	4.1E-07
GJ1 - 22	1.4673	0.00013	1.8869	0.00014	0.281971	0.000028	0.00029089	6.6E-07
GJ1 - 23	1.467354	0.000089	1.88687	0.00016	0.281978	0.000045	0.00028847	5.4E-07
GJ1 - 24	1.46731	0.00012	1.88714	0.00016	0.281935	0.000038	0.00029597	5.1E-07
GJ1 - 25	1.46733	0.000098	1.8869	0.00013	0.28199	0.000045	0.00028449	5.6E-07
GJ1 - 26	1.46737	0.00012	1.88696	0.00012	0.281996	0.00004	0.00029305	3.9E-07
GJ1 - 27	1.46726	0.00012	1.8868	0.00017	0.282062	0.000043	0.00028997	5.9E-07
GJ1 - 28	1.46734	0.00012	1.88695	0.00015	0.282043	0.000047	0.00029303	6E-07
GJ1 - 29	1.46733	0.00015	1.8869	0.00014	0.282044	0.000033	0.00028507	5.1E-07
GJ1 - 30	1.46733	0.00011	1.88685	0.00012	0.28198	0.000045	0.0002897	5.1E-07
GJ1 - 31	1.4673	0.00012	1.88684	0.00013	0.281981	0.000043	0.00028243	5.1E-07
Plešovice-1	1.46733	0.00023	1.88679	0.00013	0.282443	0.000043	0.000071	6.5E-06
Plešovice-2	1.46735	0.00018	1.88681	0.00015	0.282456	0.000032	0.0000757	6.9E-06
Plešovice-3	1.4673	0.00021	1.88687	0.00012	0.282489	0.000041	0.00005888	6.9E-07
Plešovice-4	1.46742	0.00015	1.88687	0.00012	0.282455	0.000036	0.0000663	1.5E-06
Plešovice-5	1.46744	0.00018	1.88693	0.00011	0.282503	0.000044	0.00006078	6.9E-07
Plešovice-6	1.46738	0.00017	1.88682	0.00011	0.282468	0.000045	0.0000683	1.7E-06
Plešovice-7	1.46734	0.00021	1.88684	0.00013	0.282508	0.00005	0.00006211	9.3E-07
Plešovice-8	1.46741	0.00019	1.88684	0.00014	0.282511	0.000038	0.00006098	5.5E-07
Plešovice-9	1.4673	0.00021	1.88682	0.00012	0.282547	0.000055	0.00004895	6.2E-07
Plešovice-10	1.46727	0.00013	1.88683	0.00011	0.282504	0.000024	0.00005906	2.8E-07
Plešovice-11	1.46737	0.00011	1.88697	0.00013	0.282489	0.000038	0.00006029	2.9E-07
Plešovice-12	1.46726	0.00012	1.88674	0.00012	0.282473	0.000033	0.00005823	2.5E-07
Plešovice-13	1.467247	0.000086	1.88684	0.0001	0.282494	0.000024	0.00005602	2.5E-07
Plešovice-14	1.46741	0.00011	1.88692	0.00012	0.282511	0.000024	0.00005608	4.6E-07

Plešovice-15	1.46726	0.0001	1.88664	0.00012	0.282496	0.00003	0.00006331	2.5E-07
Plešovice-16	1.467404	0.000087	1.88689	0.0001	0.282462	0.000039	0.00005693	2.8E-07
FC1 - 1	1.46729	0.0002	1.88672	0.00011	0.282196	0.000048	0.00143081	8E-07
FC1 - 2	1.46731	0.00022	1.88675	0.00014	0.282191	0.000045	0.0013047	1.5E-06
FC1 - 3	1.46735	0.00027	1.88679	0.00015	0.282144	0.000063	0.001141	0.000019
FC1 - 4	1.46747	0.00017	1.88694	0.00016	0.282117	0.000048	0.00080588	8.1E-07
FC1 - 5	1.46736	0.00014	1.88695	0.00014	0.282173	0.000045	0.000729	0.000014
FC1 - 6	1.46734	0.00016	1.8869	0.00014	0.282135	0.000047	0.000913	0.000034
FC1 - 7	1.4674	0.00019	1.88684	0.00011	0.282236	0.000048	0.0011832	8.5E-06
FC1 - 8	1.46718	0.00016	1.88684	0.00013	0.282217	0.000044	0.0014692	4.2E-06
FC1 - 9	1.46731	0.00011	1.88675	0.0001	0.282158	0.00003	0.001193	0.000012
FC1 - 10	1.46738	0.00016	1.8869	0.00013	0.282177	0.000039	0.001245	0.000011
FC1 - 11	1.467281	0.000096	1.88683	0.00012	0.282193	0.000038	0.001238	0.00001
FC1 - 12	1.467413	0.000087	1.886911	0.000085	0.282144	0.000035	0.001238	0.00001
FC1 - 13	1.46733	0.000088	1.88704	0.00011	0.282104	0.000035	0.0012407	9.6E-06
FC1 - 14	1.46723	0.00011	1.88692	0.00011	0.282157	0.000047	0.001464	0.000015
FC1 - 15	1.46729	0.00013	1.88697	0.00012	0.282161	0.000044	0.0020113	7.1E-06
FC1 - 16	1.467301	0.000098	1.88701	0.00012	0.282106	0.000042	0.0003663	1.8E-06

Table A.4: O isotopic data for Qinghu zircon standard reference material from SIMS analyses.

Standard	$^{18}\text{O}/^{16}\text{O}$	$\pm \sigma$	$\delta^{18}\text{O}$ not corrected	IMF	$\delta^{18}\text{O}$ corrected	$\pm 2\sigma$
Qinghu1-1	0.002014	0.012543	4.36	-1.07	5.44	0.25
Qinghu1-2	0.002014	0.014703	4.15	-1.07	5.22	0.29
Qinghu1-3	0.002014	0.009083	4.27	-1.07	5.34	0.18
Qinghu1-4	0.002014	0.013795	4.19	-1.07	5.27	0.28
Qinghu1-5	0.002014	0.01089	4.24	-1.07	5.32	0.22
Qinghu1-6	0.002014	0.011979	4.32	-1.07	5.39	0.24
Qinghu1-7	0.002014	0.01245	4.55	-1.07	5.63	0.25
Qinghu1-8	0.002014	0.00978	4.36	-1.07	5.44	0.20
Qinghu1-9	0.002014	0.007118	4.15	-1.07	5.23	0.14
Qinghu1-10	0.002013	0.00932	4.11	-1.07	5.18	0.19
Qinghu1-11	0.002014	0.010913	4.53	-1.07	5.60	0.22
Qinghu2-1	0.002015	0.010106	4.65	-0.80	5.45	0.20
Qinghu2-2	0.002014	0.006427	4.57	-0.80	5.38	0.13
Qinghu2-3	0.002014	0.00904	4.40	-0.80	5.20	0.18
Qinghu2-4	0.002014	0.007827	4.56	-0.80	5.36	0.16
Qinghu2-5	0.002014	0.015294	4.51	-0.80	5.31	0.31
Qinghu2-6	0.002014	0.008932	4.42	-0.80	5.23	0.18
Qinghu2-7	0.002015	0.014067	4.74	-0.80	5.54	0.28
Qinghu2-8	0.002015	0.012825	4.74	-0.80	5.54	0.26
Qinghu2-9	0.002015	0.008272	4.68	-0.80	5.48	0.17
Qinghu2-10	0.002015	0.010556	4.64	-0.80	5.45	0.21
Qinghu2-11	0.002015	0.008718	4.67	-0.80	5.47	0.17
Qinghu3-1	0.002014	0.013194	4.23	-1.14	5.37	0.26
Qinghu3-2	0.002014	0.010857	4.17	-1.14	5.31	0.22
Qinghu3-3	0.002014	0.007305	4.15	-1.14	5.29	0.15
Qinghu3-4	0.002014	0.011832	4.32	-1.14	5.46	0.24
Qinghu3-5	0.002014	0.009815	4.28	-1.14	5.42	0.20
Qinghu3-6	0.002014	0.008655	4.33	-1.14	5.47	0.17
Qinghu3-7	0.002014	0.009	4.58	-1.14	5.71	0.18
Qinghu3-8	0.002014	0.010727	4.41	-1.14	5.55	0.21
Qinghu3-9	0.002014	0.012029	4.40	-1.14	5.54	0.24
Qinghu3-10	0.002014	0.01159	4.28	-1.14	5.42	0.23
Qinghu3-11	0.002014	0.009014	4.45	-1.14	5.59	0.18
Qinghu4-1	0.002015	0.006885	4.91	-0.66	5.57	0.14
Qinghu4-2	0.002015	0.008871	4.99	-0.66	5.65	0.18
Qinghu4-3	0.002015	0.011009	4.73	-0.66	5.39	0.22
Qinghu4-4	0.002015	0.009941	4.97	-0.66	5.63	0.20
Qinghu4-5	0.002015	0.013481	4.99	-0.66	5.65	0.27
Qinghu4-6	0.002015	0.011584	5.01	-0.66	5.67	0.23
Qinghu4-7	0.002015	0.00795	4.77	-0.66	5.43	0.16
Qinghu4-8	0.002015	0.009875	5.05	-0.66	5.71	0.20
Qinghu4-9	0.002015	0.012978	4.77	-0.66	5.43	0.26
Qinghu4-10	0.002015	0.016029	5.08	-0.66	5.74	0.32
Qinghu4-11	0.002015	0.013718	5.07	-0.66	5.73	0.27

Part 1:

**Crustal growth from
the Neoproterozoic
mantle: an Egyptian
Nubian Shield
example**

Chapter 3:

The El-Shadli plutonic complex of Eastern Desert: The largest plagiogranite on Earth formed by remelting of juvenile continental crust

Abstract

Plagiogranites are felsic leucocratic rocks ranging from diorite to trondhjemite in composition. They consist of plagioclase (>40 %), quartz, and ferro-magnesium minerals, and are produced either by fractional crystallization or partial melting. Plagiogranites represent less than 1 vol. % of the oceanic lithosphere. They generally occur as meter- to kilometre- sized granitic intrusions, or as dykes of millimeters to kilometers wide, in the lower crust and mantle sections of oceanic lithosphere. Here, we report the occurrence of the largest known plagiogranitic complex on Earth (up to 5,000 km²), discovered in the Arabian-Nubian Shield in the Eastern Desert of Egypt. The El-Shadli plagiogranites are typically low in K₂O (<1 wt.%), high in Na₂O (>3.5 wt.%), and are characterized by flat rare earth element (REE) chondrite-normalized patterns with REE contents typically 5 to 40 times that of chondrite. These characteristics are shared by the spatially associated gabbroic rocks. Zircon U-Pb ages (using SHRIMP and LA-SS-ICPMS methods) of the El-Shadli plagiogranites range from 730 ± 7 to 722 ± 7 Ma. Hafnium isotopic data of zircon give weighted mean $\epsilon\text{Hf}(t)$ values ranging from +10.82 ± 0.17 to +11.56 ± 0.51, indicating that these rocks were derived from a juvenile depleted mantle source. SIMS oxygen isotope data for zircon show that the magmatic zircon has low- $\delta^{18}\text{O}$ values with sample weighted means ranging from 4.52 ± 0.14 to 4.83 ± 0.09 ‰. These values are lower than typical mantle values, indicating that the parental magma interacted with hydrothermal fluids. Collectively, field observations coupled with whole-rock petrological, geochemical,

and isotopic data and zircon U-Pb-Hf-O-trace element data suggest that the El-Shadli plagiogranites were produced by partial melting of the gabbroic oceanic lower crust. The El-Shadli plagiogranitic complex is interpreted to have formed by extensive partial melting of juvenile continental crust (i.e., accreted oceanic slabs) during the break-up of Rodinia that might be related to a mantle plume.

3.1 Introduction

Deciphering the petrogenesis of granitic rocks has important implications for our understanding of the growth of continental crust (Kemp and Hawkesworth, 2014). In contrast to widespread continental granitic rocks, plagiogranite is a rare leucocratic granite that primarily occurs in normal oceanic crust and is most commonly found in accreted ophiolite complexes (Coleman and Peterman, 1975; Coleman and Donato, 1979). Plagiogranites are composed of plagioclase (>40 %), quartz, and ferro-magnesium minerals (<10 %, e.g. hornblende:), with compositions ranging from diorite through trondhjemite to tonalite (Coleman and Peterman, 1975; Coleman and Donato, 1979). They are characterized by very low K₂O (<1 wt.%), low Rb/Sr (<0.2), high Na₂O (>3 wt.%), and flat REE chondrite-normalized patterns with enriched REE contents 10–100 times that of chondrite, distinguishing these trondhjemitic and tonalitic rocks from their continental equivalents.

Plagiogranites most commonly occur in modern and ancient oceanic settings such as mid-ocean ridges (MOR) and ophiolites (Aldiss, 1981; Amri, Benoit and Ceuleneer, 1996; Dick *et al.*, 2000; Rollinson, 2009; Grimes *et al.*, 2011, 2013; Freund *et al.*, 2014; Whattam *et al.*, 2016; Wang *et al.*, 2016; Haase *et al.*, 2016; Marien *et al.*, 2019). They are typically found as late intrusions into the gabbroic lower crustal (Koepke *et al.*, 2007; Grimes *et al.*, 2013) and/or the mantle (residual peridotite) sections (Amri, Benoit, and Ceuleneer, 1996; Rollinson, 2014; Xu *et al.*, 2017). Two main competing, but not mutually exclusive models have been proposed regarding the genesis of plagiogranites: (1) late-stage fractional crystallization of basaltic magma at low pressures and (2) partial melting of pre-existing gabbroic oceanic crust. The first model implies that plagiogranites represent late-stage, highly differentiated felsic melts formed in the lower oceanic crust by the differentiation of parental MORB melt (Coleman and Peterman, 1975; Aldiss, 1981; Pallister and Hopson, 1981; Floyd,

Yaliniz and Goncuoglu, 1998). The second model involves the generation of plagiogranitic melts through hydrous partial melting of the gabbroic crustal section triggered by the deep penetration of hydrothermal fluids into the oceanic crust along shear zones/detachment faults, i.e. melting of a hydrothermally altered oceanic lower crustal rocks (Gerlach, Leeman and Avé Lallemand, 1981; Flagler and Spray, 1991; Stakes and Taylor, 2003; Koepke *et al.*, 2004, 2007; Brophy, 2009; France *et al.*, 2010).

Volumetrically, plagiogranites do not exceed 1 vol. % of the oceanic crust, and range from dikes/veins a few millimeters to centimeters wide in MORs or ophiolites (Aldiss, 1981; Amri, Benoit and Ceuleneer, 1996; Dick *et al.*, 2000; Grimes *et al.*, 2011; Freund *et al.*, 2014; Haase *et al.*, 2016), to large granite bodies several hundred meters to kilometers in width such as the Wadi Suhaylay plagiogranite in the Oman ophiolite that has dimensions of 10 km x 8 km (Stakes and Taylor, 2003; Rollinson, 2008, 2009; Grimes *et al.*, 2013). No plagiogranite larger than that of the Wadi Suhaylay plagiogranite has been discovered.

Here, I report the largest plagiogranitic complex (~5,000 km²), discovered in the Eastern Desert of Egypt in the Arabian-Nubian Shield. We discuss in detail its petrogenesis and tectonic setting based on whole-rock geochemical and Sr-Nd isotope data, and integrated U-Pb-Hf-O isotope and trace element data from zircons. I propose that such an unusually large plagiogranite complex produced by partial melting of the juvenile crust during Rodinia break-up/rifting that might be induced by a mantle plume.

3.2 Geological setting

3.2.1 General geological background

Between the late Neoproterozoic and early Cambrian, Gondwana formed through the closure of multiple oceanic realms (Hoffman, 1991; Collins and Pisarevsky, 2005; Li *et al.*, 2008). Three main orogens were involved during the assembly of Gondwana (Figure 3.1a): (i) the Brasiliano-West African Orogen that peaked around 650-530 Ma but local remained active until ~490 Ma (Meert and Lieberman, 2008), (ii) the East African Orogen (EAO) that represents the largest orogen, peaked at around ~650 Ma (Stern, 1994; Fritz *et al.*, 2013; Merdith *et al.*,

2017), and (iii) the ~590–530 Ma Kuungan Orogen (Meert, 2003; Collins and Pisarevsky, 2005; Fritz *et al.*, 2013). Amongst them, the EAO consists of multiple zones of accretion and collision between East and West Gondwana, with the Neoproterozoic Arabian-Nubian Shield (ANS) located at its northern end (Stern, 1994; Johnson and Woldehaimanot, 2003; Johnson *et al.*, 2011; Pease and Johnson, 2013) (Figure 3.1a, b). The southern section of the EAO, the Mozambique Belt, represents a pre-Neoproterozoic crust overprinted by the early Cambrian tectonothermal event (Fritz *et al.*, 2013). At around 600 Ma, oceans were still present between Eastern Africa, Kalahari, East Antarctica-Australia, and India (Meert, 2003; Collins and Pisarevsky, 2005).

The ANS forms one of the largest exposures of Neoproterozoic juvenile continental crust on Earth (Figure 3.1b; Pease and Johnson, 2013). The ANS is divided into different terranes by arc-arc sutures marked by ophiolite belts (Figure 3.1b; Johnson *et al.*, 2011). The Eastern Desert of Egypt is the north-western terrane of the ANS (Figure 3.1b). It is bounded to the south by the Onib-Sol Hamed-Gerf-Allaqi-Heiani suture (an ophiolitic belt; Figure 3.2), which was formed between ~810 and 720 Ma (Ali *et al.*, 2010; Johnson *et al.*, 2011). The crustal basement of the Eastern Desert is composed of the following distinct rock assemblies (Figure 3.2): (1) ~750–730 Ma dismembered ophiolites (Kröner *et al.*, 1992; Stern *et al.*, 2004; Ali *et al.*, 2010); (2) ~770–720 Ma arc-related metavolcanic and metasedimentary rocks (Stern and Hedge, 1985; Kröner *et al.*, 1992; Ali *et al.*, 2009; Bühler *et al.*, 2014; Abd El-Rahman *et al.*, 2017); (3) ~740–610 Ma granitoid rocks including diorites, tonalites, trondhjemites and granodiorites (Stern and Hedge, 1985; Moussa *et al.*, 2008; Eliwa *et al.*, 2014; Abdel-Rahman, 2018; this study); (4) ~730–630 gneisses, migmatites and metamorphic core complexes (Stern and Hedge, 1985; Kroner *et al.*, 1994; Andresen *et al.*, 2009; Lundmark *et al.*, 2012; Augland *et al.*, 2012; Ali *et al.*, 2012a, 2015); (5) ~700 Ma pre-orogenic El-Shadli bimodal volcanics (this study); (6) ~640–550 Ma alkaline A-type granites (Moussa *et al.*, 2008; Ali *et al.*, 2012b, 2013; Eliwa *et al.*, 2014; Lehmann *et al.*, 2020); (7) ~630–580 Ma post-orogenic Dokhan (alkaline) volcanics (Wilde and Youssef, 2000; Breitkreuz *et al.*, 2010; this study); and (8) ~610–585 Ma Hammamat molasse-type sedimentary rocks (Wilde and Youssed, 2002; Abd El-Rahman *et al.*, 2019).

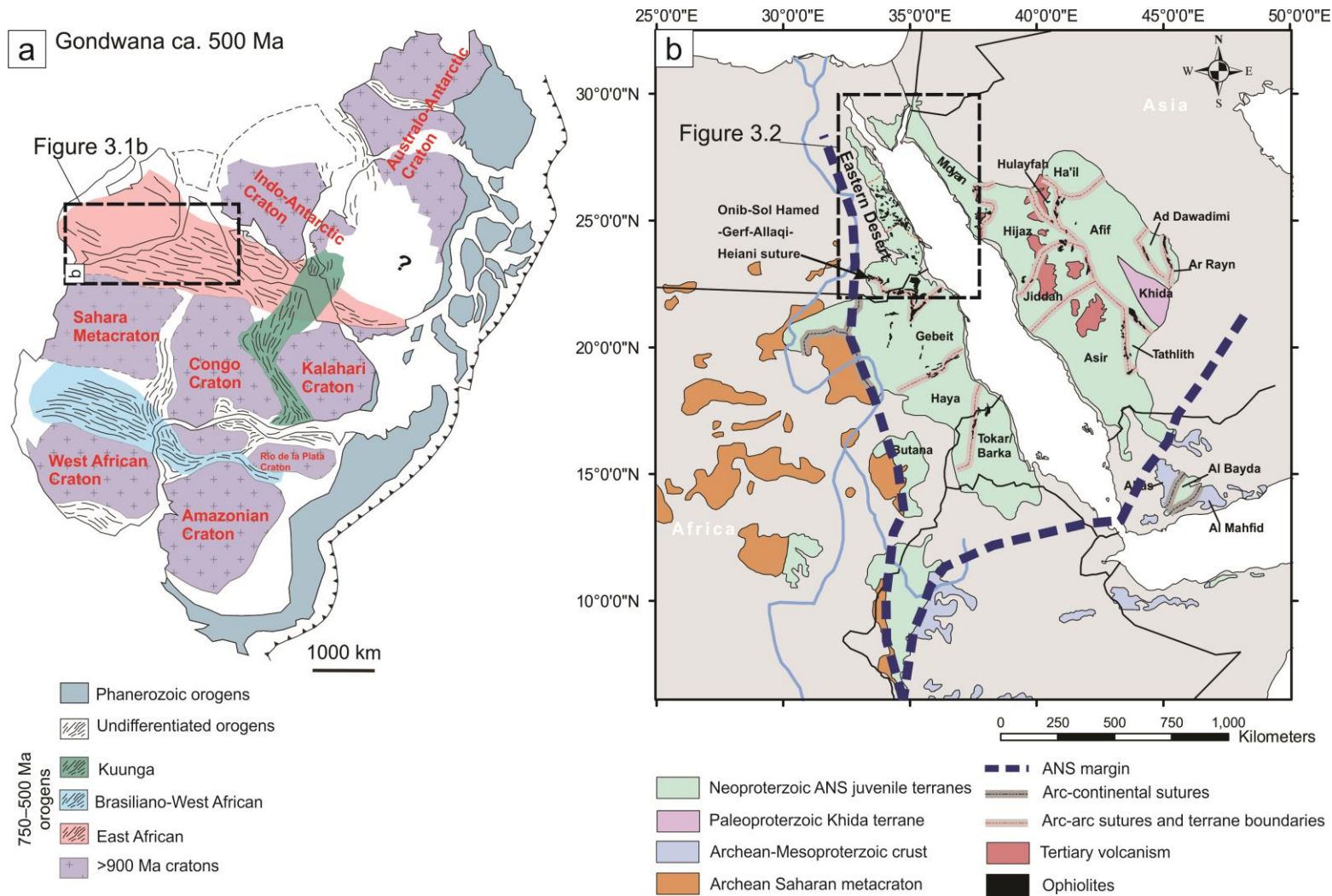


Figure 3.1: (a) Gondwana at 500 Ma with both pre-Neoproterozoic cratons and Gondwana-forming orogens modified after Fitzsimons (2016), Daczko *et al.* (2018), and Olierook *et al.* (2019). (b) a schematic geological map of the Arabian-Nubian Shield showing the distribution of Neoproterozoic terranes and their contact with pre-Neoproterozoic blocks modified after Johnson *et al.* (2011) and Pease and Johnson (2013).

Arc accretion has been proposed to be the main mechanism for crustal growth in the ANS (Kröner *et al.*, 1991; Stern, 1994, 2002; Johnson and Woldehaimanot, 2003; Johnson *et al.*, 2011; Fritz *et al.*, 2013). Bentor (1985) proposed that the evolution of the ANS involved four magmatic episodes. The first was the formation of oceanic assemblages including thick oceanic tholeiitic basalts and gabbro cumulates formed around >900–850 Ma. The second is represented by island arc calc-alkaline magmatism (such as andesites, dacites, diorites, and tonalities) with an age range of from >900 Ma to as young as ~650 Ma. The third episode produced calc-alkaline and silica-rich magmatism including rhyolites, ignimbrites, minor andesites, and their plutonic equivalents formed around ~640–590 Ma. The last phase (~590–540 Ma) is mainly represented by alkaline to per-alkaline magmatism such as rhyolites and A-type granites. More recently, Fritz *et al.* (2013) re-classified the ANS crustal evolution into the stages of (1) continental rifting between ~900 and ~860 Ma; (2) oceanic spreading during ~860–830 Ma; (3) subduction producing oceanic arcs and arc-related basins between ~830–700 Ma; (4) accretion of island arcs and closure of basins (~750–650 Ma); and (5) intracontinental collision-related magmatism (~640–550 Ma).

Reymer and Schubert (1986), Stein and Goldstein (1996), and Stein (2003) argued that the growth rate of the ANS significantly exceeds the rate of the present-day addition of juvenile mantle materials along subduction margins. Therefore, these authors suggested that the large volume of magmas formed during the early stage of ANS crustal growth (within the Mozambique Ocean) may be related to mantle plume magmatism. Testing this hypothesis requires reliable age data and detailed modern petrogenetic and tectonic studies. Such studies are scarce in the ANS, and so documentation of the timing, scale, and potential plume influence on magmatism and crustal growth and evolution of the ANS has not been attempted.

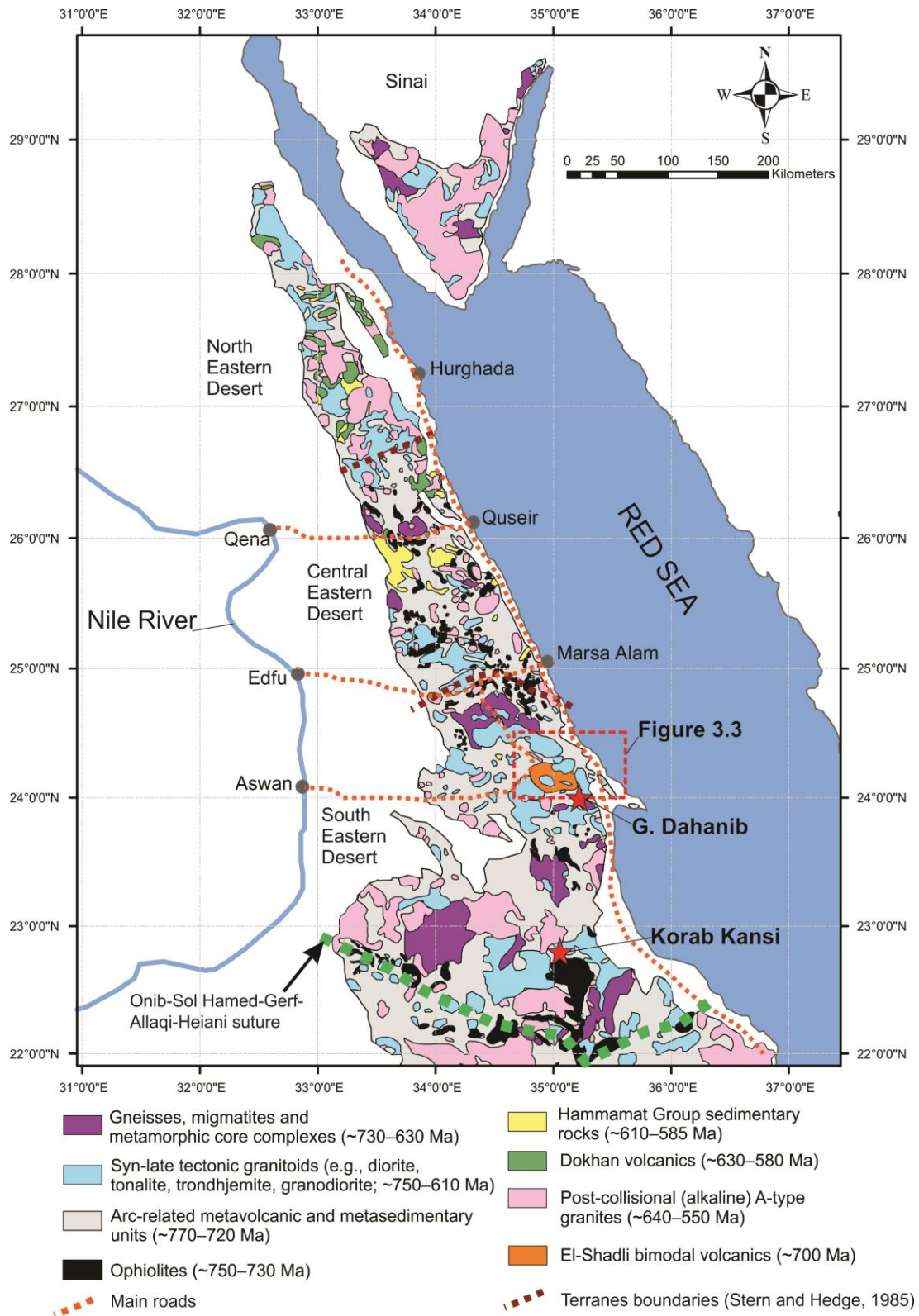


Figure 3.2: Geological map of the Eastern Desert showing the ages and distribution of the main Precambrian crustal basement rock units. Eastern Desert terrane boundaries are after Stern and Hedge (1985). The map is modified after Johnson *et al.* (2011)

3.2.2 Field and age relationships

The study area is located in the southern Eastern Desert region (Figures 3.2 and 3.3). Rocks exposed in this area include the El-Shadli bimodal volcanic rocks, the El-Shadli granite-diorite-gabbro assemblage, the Wadi (W) Ghadir ophiolitic assemblages, the W. Hafafit core complex, post-collisional alkaline granites, and post-collisional volcanics (Figure 3.2). The El-Shadli volcanic rocks represent the largest bimodal suite in the Eastern Desert of Egypt (80 km x 35 km) (Stern, Kröner, and Rashwan, 1991), and occur in a WNW-ESE trending belt flanked by granite-diorite-gabbro rocks (Figure 3.2). The mafic end-member of the El-Shadli bimodal volcanic rocks consists of massive to pillow basaltic lava flows and dike swarms that intrude the granitoid rocks (Figure 3.4a). The felsic end-member consists of massive rhyolitic lava flows. The El-Shadli bimodal volcanic rocks have an Rb-Sr isochron age of $\sim 710 \pm 24$ Ma (Stern, Kröner and Rashwan, 1991) and the new SHRIMP/LA-SS-ICPMS U-Pb zircon analysis of this study yields ~ 700 Ma crystallization age (see Chapter 4 for a detailed data and interpretation). The El-Shadli bimodal volcanic rocks are interpreted as pre-orogenic rift-related (Stern, Kröner, and Rashwan, 1991).

Post-collisional volcanic rocks occur around W. Ranga (W. Ranga volcanics) in the eastern part of the study area. The outcrops consist of alkaline volcanic rocks and their pyroclastic equivalents (Figure 3.3) consisting of two slightly metamorphosed volcanic sequences: (i) intermediate-mafic lava flows (andesites, basaltic andesites, and basalts) in the north near Gabal (G) El-Sarobi, and (ii) felsic rocks (rhyolitic and dacitic lava flows) in the south. Previously undated, these volcanic rocks have been interpreted as either post-orogenic young volcanics (Gharib and Ahmed, 2012), or pre-orogenic intra-oceanic arc volcanics (Maurice, Basta, and Khiamy, 2012). Most previous work (Gharib and Ahmed, 2012; Maurice, Basta, and Khiamy, 2012; Maurice *et al.*, 2013) inferred that the W. Ranga volcanic rocks were intruded by the El-Shadli granite-diorite-gabbro assemblage, although the contact relationship is unclear in the field. New SHRIMP/LA-SS-ICPMS U-Pb zircon analysis presented in this study gives an age of 585 ± 10 Ma to these volcanics, showing that they are significantly younger than the El-Shadli granite-diorite-gabbro assemblage (730 ± 7 to 722 ± 7 Ma; this study).

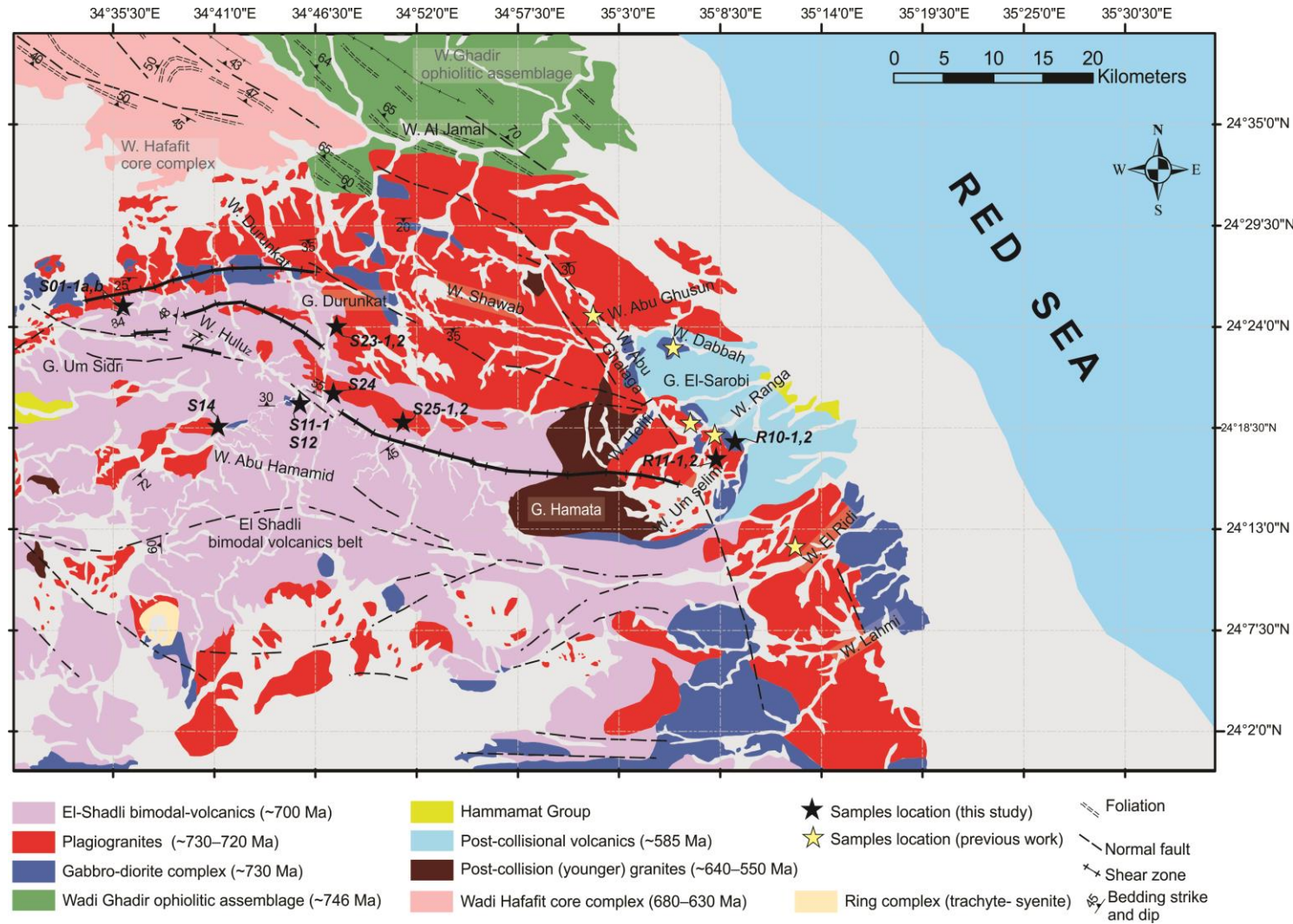


Figure 3.3: Detailed geological map of the studied El-Shadli area showing the ages and distribution of the main rock units: the El-Shadli bimodal volcanic rocks, the El-Shadli granite (plagiogranites)-diorite-gabbro assemblage, the W. Ghadir ophiolitic assemblage, the W. Hafafit core complex, post-collision alkaline granites, and post-collisional volcanics. Age data are from Stern, Kröner, and Rashwan (1991), Kröner *et al.* (1992), Kroner, Kruger, and Rashwan (1994) and this study. The map is modified after the geologic map of Jabal Hamatah quadrangle (GSE, 1997).

The El-Shadli granite-diorite-gabbro assemblage (the El-Shadli granitoids) crop out over much of the study area (Figure 3.3). These granitoids have an almost continuous, arch-shaped map pattern in the central-south eastern part of the study region, but are also exposed sporadically beneath the younger volcanic cover sequence, suggesting the possibility of a large and continuous plutonic complex under much of the region (Figure 3.3). The estimated dimension of such a plutonic complex is ca. ~100 km x 50 km.

In the northern part of the study area, the El-Shadli granitoids intrude the W. Ghadir ophiolitic assemblages ($\sim 746 \pm 19$ Ma: Kröner *et al.*, 1992). This ophiolitic assemblage has a dominantly NW-trending foliation that is truncated by the El-Shadli granitoids (Abdel El-Wahed *et al.*, 2019) (Figure 3.3), consistent with such an intrusive relationship.

3.2.3 Sample description and petrography

The El-Shadli granitoids occur as massive batholiths. Magmatic mixing zones have been found, where 1 x 1 m to 5 x 2 m gabbroic-diorite enclaves are found in granites, representing over 50% of the outcrop area (Figure 3.4b-d). The enclaves show no obvious chilled margins and have irregular shapes with the granites (Figure 3.4d). Such contacts are typical of mingling between two contemporaneous magmas (Rollinson, 2009). The interpreted co-magmatic origin is supported by geochronological data presented in this study (see below). A similar magmatic mixing zone has been described in the Oman ophiolite plagiogranitic suite (Rollinson, 2009). Smaller (centimeters size) mafic enclaves occur within the studied gabbroic diorite rocks and granites (Figure 3.4e-f).



Figure 3.4: Field photos of the El-Shadli plagiogranites and associated gabbros. (a) Mafic dykes (likely related to the El-Shadli bimodal volcanics of ~700 Ma) intruding the studied plagiogranites (sample S01-1a, 729 ± 7 Ma). (b-d) Magmatic mixing zone. The large mafic enclaves in the mixing zone show no obvious chilled margin and have irregular boundaries with the plagiogranites. (e-g) Centimetre-size mafic enclaves within gabbroic diorites and plagiogranites. (h-j) Close up views of samples S14 (trondhjemite), R10 (diorite), and S12 (gabbro), showing medium- to coarse-grained hypidiomorphic-granular textures.

Rock samples were collected along W. Ranga (samples R10-1, 2 and R11-1, 2), the entrance of W. Huluz (samples S01-1a, b), W. Durunkat (samples S23-1, 2, S24 and S25-1, 2), and W. Abu Hammamid (sample S14) (Figure 3.3). Samples from previous work (Gharib and Ahmed, 2012; Maurice *et al.*, 2013) covered the areas of W. El Ridi, W. Ranga, W. Abu Ghalaga, W. Dabbah, and W. Abu Ghusun (Figure 3.3). Both previous and the current studied samples include tonalites, trondhjemites, diorite, quartz diorite, and hornblende gabbro (Figure 3.4). A tonalite-trondhjemite-diorite-gabbro rock association is typical of ophiolitic plagiogranite suites (Coleman and Donato, 1979; Amri, Benoit and Ceuleneer, 1996; Floyd, Yaliniz and Goncuoglu, 1998; Rollinson, 2009; Grimes *et al.*, 2011, 2013; Freund *et al.*, 2014; Whattam *et al.*, 2016; Wang *et al.*, 2016; Haase *et al.*, 2016; Marien *et al.*, 2019).

The El-Shadli granite samples range from fine- to coarse-grained hypidiomorphic-granular rocks, consisting of zoned plagioclase (50–55%), quartz (35–40%), and ferromagnesium minerals (<5%) (Figures 3.4, 3.5a and Figure B.1). Typical plagiogranitic quartz-plagioclase intergrowths such as graphic and vermicular textures described by Coleman and Donato (1979) are reported in the studied granites (Figure 3.5b, c). Actinolite, sericite and clay, and chlorite represent the main secondary minerals. Fe-Ti oxides and zircon are common accessory minerals (Figure B.1). Detailed petrographic description and modal composition for all the studied samples are provided below (Figure B.1).

Diorite samples R10-1 and R10-2 are massive, fine- to medium-grained, and greenish-greyish black in colour (Figure 3.4i). They are made of hypidiomorphic grains of plagioclase (55%), quartz (25%), and amphibole (<5%) (Figure B.1). Accessory minerals include opaque minerals (<8%), apatite (1%), titanite and zircon (<1 %). Sericite, clay minerals, chlorite, and calcite represent secondary minerals (<0.5%). Plagioclase occurs as a medium to coarse subhedral to euhedral grains with elongate to granular shapes and simple/albite twinning and normal zoning (Figure B.1). Plagioclase grains are slightly altered to darkish yellow sericite and clay minerals. Quartz is a subhedral fine to medium interstitial grains between plagioclase groundmass (Figure B.1). Amphibole is mainly prismatic to elongate hornblende and actinolite. Opaque minerals include magnetite/hematite (6%) and ilmenite (1.7%) and are fine to medium subhedral grains distributed randomly in the groundmass.

Gabbro samples S11-1 and S12 are massive, medium- to coarse-grained, and greenish in colour (Figure 3.4j). They have subhedral to euhedral laths of plagioclase

that are sericitized and display ophitic and sub-ophitic textures with the pyroxene and hornblende (Figure B.1). Hornblendes are found as elongate crystals that replace primary pyroxene (Figure 3.5d). Chlorite, epidote, and clay minerals are other secondary phases. Opaque minerals of Fe-Ti oxides commonly count up to 10 % and are disseminated within the groundmass.

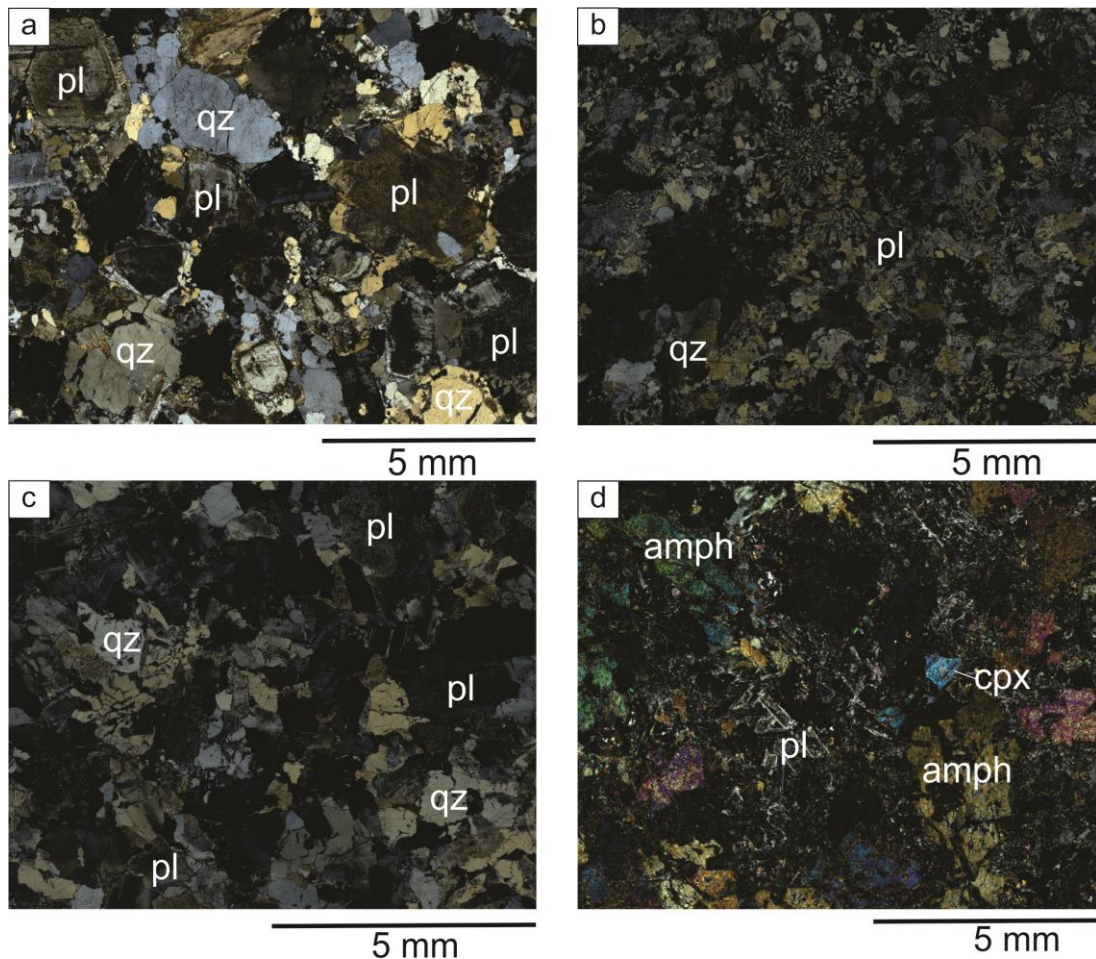


Figure 3.5: Photomicrographs of the El-Shadli plagiogranites and associated gabbros. (a-c) Crossed-polarized light images of the plagiogranites showing medium- to coarse-grained hypidiomorphic-granular texture and quartz-plagioclase intergrowths such as graphic and vermicular textures. The rocks consist mainly of plagioclase (pl) and quartz (qz). (d) Crossed-polarized light image of the gabbro showing the development of ophitic and sub-ophitic textures between plagioclase, clinopyroxene (cpx) and amphiboles (amph).

Trondhjemite samples R11-1 and R11-2 are medium- to coarse-grained, massive, and yellowish-grey and contain small dark mafic enclaves (Figure 3.4f). They have a hypidiomorphic coarse-grained texture, and are made of plagioclase (55%), quartz (36%), and amphiboles (<2%) (Figures 3.5 and Figure B.1). Opaque minerals (1%), titanite, and zircon (<1%) are accessory minerals. Secondary minerals

include chlorite, sericite, and clay minerals. Plagioclase occurs as a large subhedral, equant, and zoned grains that are altered to sericite and clay (Figure B.1). Quartz forms medium to coarse subhedral to anhedral grains between plagioclase grains and shows simple to complex undulose extinction patterns. Minor orthoclase forms small prismatic interstitial grains. Amphiboles include actinolite with minor amounts of hornblende. Chlorite occurs as small fibrous secondary grains partially pseudomorphing hornblende. Opaque minerals consist of magnetite, hematite, and ilmenite stacked as fine anhedral grains in the groundmass.

Trondhjemite samples S01-1a and S01-1b are fine- to medium-grained and greyish pink (Figure 3.4a). They exhibit a weak foliation defined by preferred orientations of quartz grains (Figure B.1). They have interlocking hypidio- to allotriomorphic (massive to porphyritic) textures and are composed of plagioclase (54%), quartz (40%), amphiboles (<1%), and orthoclase (<1%) (Figure B.1). Accessory minerals include opaques minerals (<1%), titanite, zircon, and apatite (<1%). Sericite, chlorite, and clay minerals represent secondary minerals (<0.5%). Plagioclase and quartz grains range in size from fine groundmass to deformed large grains. Plagioclase is platy, subhedral, and is locally zoned and sericitized. Amphiboles occur as finely disseminated hornblende grains in the groundmass. Magnetite, hematite, and ilmenite (opaque minerals) are very fine-grained and sparsely distributed.

Trondhjemite sample S14 is massive, medium-grained, and greyish black (Figure 3.4h). It is hypidiomorphic fine- to medium-grained comprised of 50% plagioclase, 40% quartz, and 1% amphibole. Magnetite/hematite (<1%), zircon, titanite, and apatite (<1%) represent the accessory minerals. Clay minerals (4%) and calcite (<1%) are secondary minerals. Plagioclase is subhedral to anhedral and exhibits minor alteration to sericite and clay alteration. Quartz is fine to medium grained and is a common constituent of the matrix. Magnetite/hematite are disseminated grains between the other minerals.

Trondhjemite samples S23-2 and S25-1 are massive, medium- to coarse-grained, and greyish. They are hypidiomorphic medium- to coarse-grained, composed of 52% plagioclase, 40% quartz, and <0.5% amphiboles for sample S23-2, and 53% plagioclase, 38% quartz, and <0.5% amphiboles for sample S25-1 (Figure 3.5 and Figure B.1). Opaque minerals (<2%), titanite, zircon, and apatite (<1%) are accessory minerals. Secondary minerals include clay minerals, chlorite, and sericite. Plagioclase

is large, subhedral to euhedral, and is mostly twinned and zoned. Quartz ranges from medium to coarse-grained, and forms in interstitial aggregates and as intergrowths with plagioclase. Opaque minerals consist of magnetite, hematite, and ilmenite that are disseminated between other minerals.

Tonalite samples S23-1, S24, and S25-2 are massive, hypidiomorphic, fine- to medium-grained, and dark greyish. Sample S23-1 is composed of 57% plagioclase, 39% quartz, and <0.5% amphiboles, sample S24 contains 52% plagioclase, 34% quartz, and <0.5% amphiboles and sample S25-2 is comprised of 54% plagioclase, 36% quartz, and <0.5% amphiboles (Figure 3.5 and Figure B.1). Plagioclase forms subhedral that are partially altered, quartz occurs is subhedral, medium to coarse, and interstitial between plagioclase groundmass. Titanite, zircon, and apatite (<1%) are accessory minerals. Opaque minerals consist of ilmenite, magnetite, and hematite are disseminated within the matrix.

3.3 Analytical methods

Phase mineral distribution maps for samples R10-1, R11-1, S01-1a, S14, S23-1, S23-2, S24, S25-1, and S25-2 were acquired using a TESCAN Integrated Mineral Analyser (TIMA) housed at the John de Laeter Centre, Curtin University (Figure B.1). Whole-rock major elements were determined using X-ray fluorescence at the Bureau Veritas Lab, Perth (Table 3.1). Whole-rock trace elements and Sr-Nd isotope data were determined using ICP-MS and TIMS, respectively, at the Macquarie (MQ) GeoAnalytical Lab, Macquarie University (Table 3.1). For samples R10-1, R11-1, S01-1a, and S14, zircon U-Pb dating was carried out using SHRIMP II at Curtin University (Table B.1). Zircon Hf isotope and trace element data were acquired using LASS-ICPMS at Curtin University (Table B.2); zircon O isotope data were acquired using SIMS at Guangzhou Institute of Geochemistry, China (Table B.3). Analytical techniques are given in detail in Chapter 2 (Methodology).

3.4 Results

3.4.1 Whole-rock geochemical data

Samples of the El-Shadli granitoids are fresh with minor alteration/weathering, as indicated by low loss on ignition (LOI) (typically below 1.2 wt.%, Table 3.1). Such

low LOI values indicate that the samples experienced no significant alteration of its primary geochemical composition that would affect petrogenetic-indicating high field strength element (HFSE) and rare earth elements (REE). The compositional range of the El-Shadli granitic (including dioritic) samples are: SiO₂ (60.3–78.5 wt.%), Al₂O₃ (11.8–15.5 wt.%), Fe₂O₃^T (1.29–10.9 wt.%), TiO₂ (0.14–1.43 wt.%) and MgO (0.14–1.67 wt.%) (Figure 3.6; Table 3.1). Gabbroic samples S11-1 and S12 have a composition of SiO₂ = 45.8–47.5 wt.%, Al₂O₃ = 15.6–18.5 wt %, Fe₂O₃^T = 8.6–12.2 wt.%, TiO₂ = 0.75–1.37 wt.% and MgO = 7.9–15.6 wt.% (Figure 3.6; Table 3.1). All the studied samples have very low K₂O (<1 wt.%) and total alkali contents (K₂O + Na₂O = 4.0–6.5 wt.%) (Figure 3.7; Table 3.1).

The studied samples also show a distinct flat-like REE pattern with a slightly LREE negative slope. The El-Shadli granites (including diorite samples) show MORB-like REE patterns with 5–40 times enrichments relative to that of the chondrite (Anders and Grevesse, 1989), and with slightly negative Eu anomalies [(Eu/Eu*)_{CI} = 0.28–0.95, where Eu* = $\sqrt{(\text{Sm} \times \text{Gd})}$] (Figure 3.8a). The associated gabbroic rocks mimic and completely overlap the REE pattern [(La/Sm)_{CI} <0.47 and (Yb/Gd)_{CI} <0.84] of the granite rocks [(La/Sm)_{CI} = 0.56–1.22 and (Yb/Gd)_{CI} = 0.71–1.29] (Figure 3.8a). On the N-MORB-normalized trace-element diagram (Sun and McDonough, 1989) (Figure 3.9a), all the samples exhibit flat MORB-like patterns, except for some samples with negative Ti and Nb anomalies and slightly positive Pb anomalies. Large ion lithophile elements (LILE) such as Cs, Rb, Ba, Th, and U show some enrichment relative to N-MORB (Sun and McDonough, 1989).

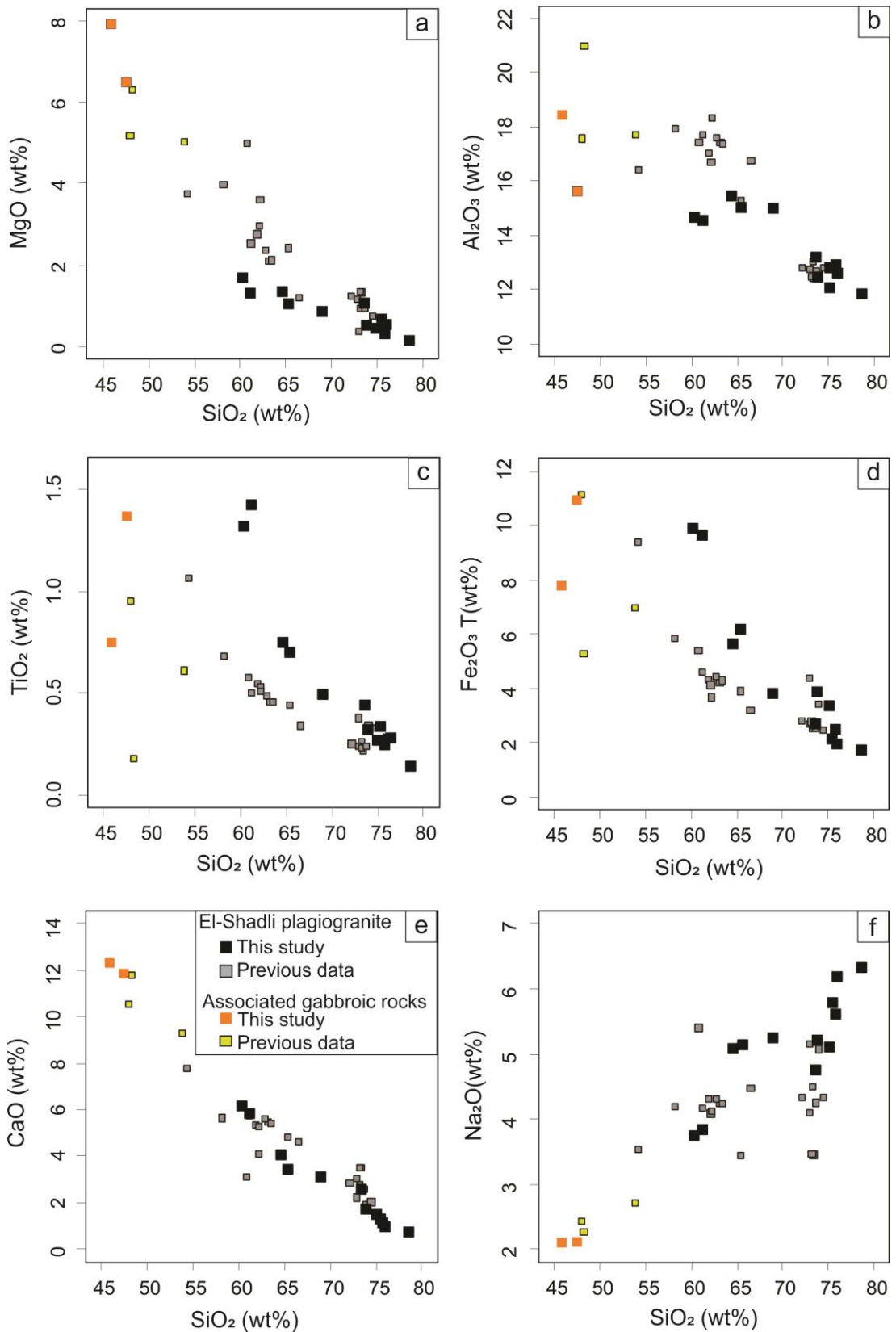


Figure 3.6: Harter plots showing the whole-rock major element compositions of the El-Shadli plagiogranites and associated gabbros. The previously published data are from Gharib and Ahmed (2012) and Maurice *et al.* (2013).

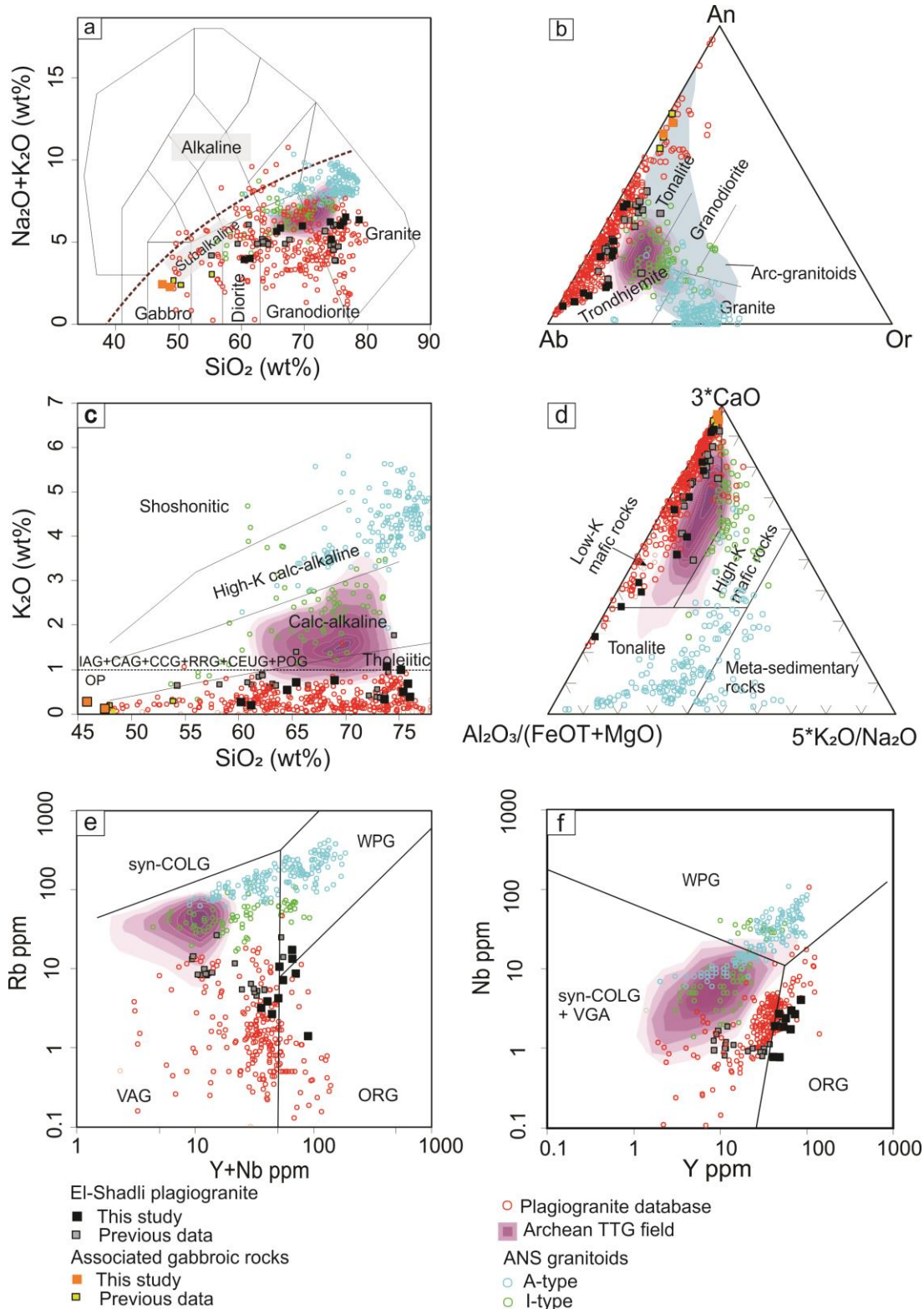


Figure 3.7: Chemical classification diagrams using the whole-rock major and trace element compositions of El-Shadli plagiogranites and associated gabbros. (a) A plot of data over the total alkali-silica diagram (TAS) of Middlemost (1994). (b) The Ab-An-Or diagram (O'Connor, 1965; Barker, 1979). (c) SiO_2 versus K_2O plot (Peccerillo and Taylor, 1976). Fields for oceanic plagiogranites (OP), island arc granitoids (IAG), continental arc granitoids (CAG), continental collision granitoids (CCG), post-orogenic granitoids (POG), rift-related granitoids (RRG), and continental epeirogenic uplift granitoids (CEUG) are after Maniar and Piccoli (1989). (d) Ternary diagram of

$Al_2O_3/(FeOT + MgO) - 3 * CaO - 5 * (K_2O/Na_2O)$ after Laurent *et al.* (2014) showing that the studied plagiogranites were likely derived from a low-K mafic magma source. (e, f) Tectonic setting plots of Pearce, Harris, and Tindle (1984). Data sources used: previous reported plagiogranites — as references through the text; arc-granitoids — GeoRoc (<http://georoc.mpch-mainz.gwdg.de/georoc/>); Archean trondhjemite-tonalite-granodiorite (TTG) — Moyen (2011); other ANS I-and A-type granitoids — Robinson *et al.* (2014, 2017), Farahat *et al.* (2007), Katzir *et al.* (2007), Moussa *et al.* (2008), El-Bialy and Streck (2009), Ali, Moghazi, *et al.* (2012), Eliwa *et al.* (2014), Ali *et al.* (2015), and Zoheir *et al.* (2020).

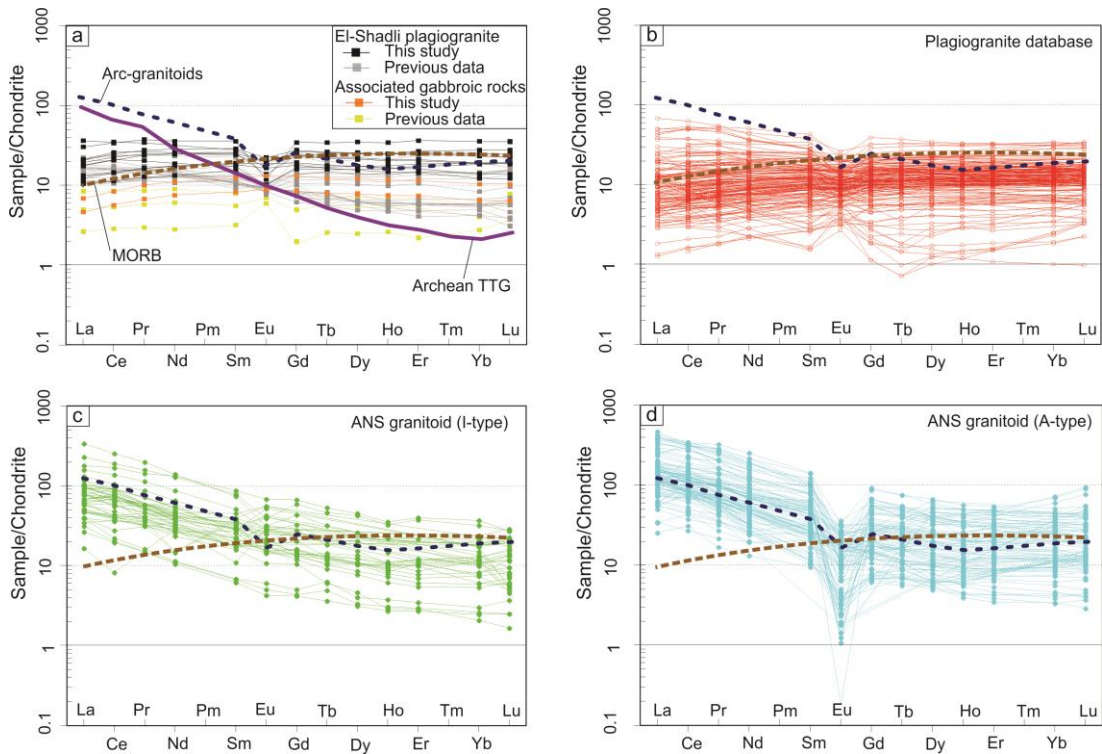


Figure 3.8: Chondrite-normalized REE patterns (Anders and Grevesse, 1989) of the El-Shadli plagiogranites and associated gabbros. MORB pattern is after Sun and McDonough (1989). Sources of other published data for comparison are the same as for Figure 3.7.

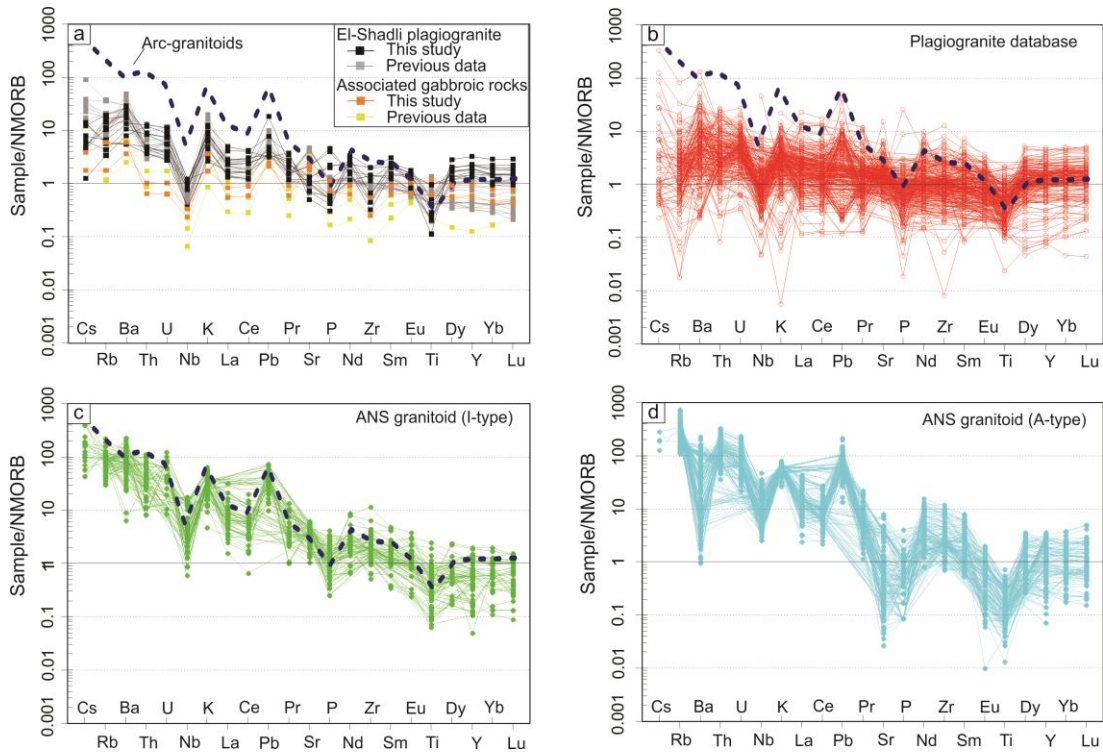


Figure 3.9: NMORB-normalized (Sun and McDonough, 1989) trace element diagram of the El-Shadli plagiogranites and associated gabbros.

3.4.2 Whole-rock Sr-Nd isotope data

All the studied rocks have low Sr (43.29–207.92 ppm) and low Rb (1.03–13.45 ppm) concentrations, with $^{87}\text{Sr}/^{86}\text{Sr}$ ratios ranging between 0.702637 ± 0.000002 and 0.708406 ± 0.000007 (Table 3.1). They also have low concentrations of Nd (4.42–26.61 ppm) and Sm (1.60–8.65 ppm) with the measured ratios of $^{143}\text{Nd}/^{144}\text{Nd} = 0.512871 \pm 0.000001 - 0.513165 \pm 0.000012$ (Table 3.1). The calculated initial ratios of $^{87}\text{Sr}/^{86}\text{Sr}$ have a range of $0.702027 \pm 0.000004 - 0.703401 \pm 0.000003$, and the $^{143}\text{Nd}/^{144}\text{Nd}$ ratios have a range of $0.511973 \pm 0.000002 - 0.512111 \pm 0.000003$ (Figure 3.10 and Table 3.1). The calculated $\epsilon\text{Nd}(t)$ values range from +5.55 to +8.18 (Figure 3.10), with the corresponding T_{DM} model ages ranging from 0.78 Ga to 1.2 Ga (Goldstein, O’Nions and Hamilton, 1984; Bouvier, Vervoort and Patchett, 2008).

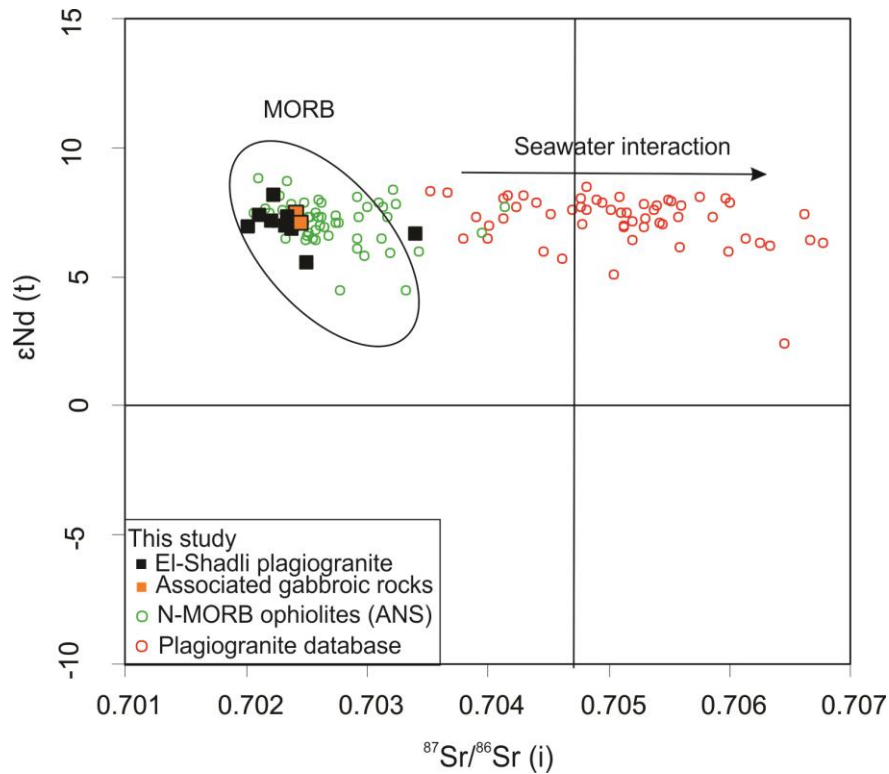


Figure 3.10: Sr-Nd isotopes of the El-Shadli plagiogranites and associated gabbros. The ANS N-MORB ophiolite data are those from W. Gerf in the south of the study area (Zimmer *et al.*, 1995) and W. Ghadir in the north of the study area (Basta *et al.*, 2011).

3.4.3 Zircon U-Pb-Hf-O isotopes and trace elements

3.4.3.1 Diorite sample R10-1

Zircon grains from sample R10-1 have equant to sub-rounded morphology and a size range of 100–>200 μm (Figure 3.11a and Figure B.2). In cathodoluminescence (CL) images, some zircon grains show relatively subhedral to euhedral rims with clear concentric oscillatory zoning (Figure 3.11a, Figure B.2) but a majority have anhedral corroding rims with oscillatory, convolute, or completely convoluted/mottled zoning patterns (Figure 3.11a and Figure B.2). We carefully excluded from our analysis grains with either mottled or convolute zones.

Fourteen U-Pb SHRIMP analyses for sample R10-1 were conducted on 14 grains. These analyses have variable U (142–680 ppm) and Th (69–1310 ppm) contents and Th/U ratios (0.48–4.42) (Table B.1). The high Th/U ratios are typical of zircons crystallized from low SiO_2 melts *i.e.*, gabbro-diorite rocks (Kirkland *et al.*, 2015). These U-Pb isotopic analyses yield a weighted mean $^{206}\text{Pb}/^{238}\text{U}$ age of 733 ± 7

Ma (± 95 % conf., MSWD = 0.76, N = 13; Figure 3.11a), which is interpreted as the crystallization age of the gabbro-diorite complex.

Eighteen laser ablation split stream (LASS) analyses on the same sample were conducted on 18 grains including the same 14 spots as the SHRIMP analyses, plus other 4 analyses. These analyses yield a similar $^{206}\text{Pb}/^{238}\text{U}$ age of 732 ± 5 Ma (± 95 % conf., MSWD = 1.4, N = 18; Figure 3.12a). Chondrite (CI)-normalized (Anders and Grevesse, 1989) REE patterns of the zircons show a negative slope from middle to heavy REE with $(\text{Yb}/\text{Gd})_{\text{CI}} = 29\text{--}42$, and limited variations in their negative Eu anomalies [$(\text{Eu}/\text{Eu}^*)_{\text{CI}} = 0.13\text{--}0.28$], a feature that is characteristic of unaltered magmatic zircons (Belousova *et al.*, 2002; Grimes *et al.*, 2015) (Figure 3.12a). Zircon grains have variable hafnium (7843–10390 ppm) and niobium (0.59–2.46 ppm) contents, and U/Yb ratios (0.06–0.23) (Figure 3.13 and Table B.2).

The Lu-Hf isotopic analyses of these 18 spots yield $^{176}\text{Lu}/^{177}\text{Hf}$ ratios of $0.004320 \pm 0.000340 - 0.008358 \pm 0.000099$ and $^{176}\text{Hf}/^{177}\text{Hf}_{(t)}$ ratios of $0.282596 \pm 0.000064 - 0.282760 \pm 0.000077$ (Table B.2). The calculated $\epsilon\text{Hf}_{(t)}$ values range from $+9.70 \pm 0.96$ to $+13.43 \pm 1.16$, with a weighted mean of $+11.56 \pm 0.51$ (MSWD = 1.12) (Figure 3.14), corresponding to two-stage Hf model ages (T_{DM} crustal) of 0.77 – 1.02 Ga. Whereas, spot R10-1-15 has $\epsilon\text{Hf}_{(t)} = 15.21 \pm 1.16$ and T_{DM} crustal = 0.66 Ga, the young T_{DM} crustal of this spot compared to the crystallization age of the sample suggests recent Pb loss. As a result, the data from this spot was not included in the $\epsilon\text{Hf}_{(t)}$ weighted mean calculations. The T_{DM} crustal calculation assumes a $^{176}\text{Lu}/^{177}\text{Hf}$ value of 0.015, an average value for the continental crust (Griffin *et al.*, 2002). The same eighteen spots were also analysed by SIMS for O isotopic data, and yield $\delta^{18}\text{O}$ values in the range of $4.33 \pm 0.29\text{--}5.09 \pm 0.24$ ‰ with a weighted mean of 4.73 ± 0.1 ‰ (MSWD = 1.09) (Figure 3.14 and Table B.2).

3.4.3.2 Trondhjemite sample R11-1

Zircon grains from sample R11-1 are commonly > 200 μm in length, and are equant to prismatic with euhedral rims. These grains show homogenous textures. Some grains display well-developed oscillatory zoning in CL images, but other grains show only faint and broad zoning (Figure 3.11b, Figure B.2).

Sixteen U-Pb SHRIMP analyses for this sample were conducted on 16 grains. The analysed grains have variable U (135–1241 ppm) and Th (53–703 ppm) contents,

and Th/U ratios of 0.37–0.66 (Table B.1) signifying their magmatic origin and crystallization from a high-SiO₂ magma (Kirkland *et al.*, 2015). The 16 analyses form a tight cluster that yields a weighted mean ²⁰⁶Pb/²³⁸U age of 733 ± 3 Ma (±95 % conf., MSWD = 0.11, N = 16; Figure 3.11b), which is interpreted to be the crystallization age of the Trondhjemite.

Thirty-eight LASS analyses were conducted on 38 grains from the same sample. These analyses include the same 16 grains that were analysed by SHRIMP, commonly over the same spots. The additional 22 new LASS analyses were conducted on 22 new grains. These 38 LASS analyses together yield a ²⁰⁶Pb/²³⁸U age of 730 ± 3 Ma (±95 % conf., MSWD = 0.87; Figure 3.12b and Table B.2) which is comparable within an uncertainty of the SHRIMP age. CI-normalized (Anders and Grevesse, 1989) zircon REE patterns are similar to that of sample R10-1, and are characterized by a negative slope from the middle to heavy REE [(Yb/Gd)_{CI} = 15–28] and by high negative Eu anomalies [(Eu/Eu*)_{CI} = 0.06–0.12] that are characteristic of unaltered magmatic zircons (Belousova *et al.*, 2002; Grimes *et al.*, 2015) (Figure 3.12b and Table B.2). Zircon grains have Hf contents of 7873–13098 ppm, Nb 1.01–17.8 ppm, and U/Yb ratios 0.06–0.22 (Figure 3.13 and Table B.2).

The Lu-Hf isotopes of these 38 spots yield ¹⁷⁶Lu/¹⁷⁷Hf ratios of 0.00272 ± 0.00011 – 0.01162 ± 0.00020 and ¹⁷⁶Hf/¹⁷⁷Hf_(t) ratios of 0.282570 ± 0.000086 – 0.282710 ± 0.0000680 (Table B.2). The calculated εHf_(t) values range from +8.66 ± 1.01 to +13.39 ± 0.80 and give a weighted mean of +10.82 ± 0.17 (MSWD = 1.01) (Figure 3.14), corresponding to T_{DM} crustal ages of 0.77–1.07 Ga. Twenty O isotope analyses of these zircons yield δ¹⁸O values ranging from 4.38 ± 0.15 ‰ to 4.88 ± 0.16 ‰ with a weighted mean of 4.57 ± 0.04 ‰ (MSWD = 0.51) (Figure 3.14 and Table B.2).

3.4.3.3 Trondhjemite sample S01-1a

Zircon grains from sample S01-1a are prismatic and euhedral with sizes < 200 μm. These grains commonly have well-developed concentric oscillatory zoning, although some have unzoned homogenous cores (Figure 3.11c, Figure B.2).

Twenty U-Pb SHRIMP analyses were conducted on 19 grains from this sample. The analysed spots have relatively low U (28–153 ppm) and Th (13–257 ppm) contents, and Th/U ratios of 0.38–0.65 (Table B.1) indicating a magmatic origin. Spot

#S01-1@2 has a high common ^{206}Pb (6.9%), and this analysis is not included in the age calculations. The remaining 19 analyses yield a weighted mean $^{206}\text{Pb}/^{238}\text{U}$ age of 729 ± 7 Ma (± 95 % conf., MSWD = 0.37, N = 19; Figure 3.11c), which is interpreted as the crystallization age of this Trondhjemite sample.

Thirty LASS analyses were conducted on 30 grains from the same sample. Twenty analyses were from the same 20 spots as the SHRIMP analyses, commonly over the SHRIMP spots, plus 10 additional LASS spots on 10 grains. The 30 analyses give a $^{206}\text{Pb}/^{238}\text{U}$ age of 728 ± 4 Ma (± 95 % conf., MSWD = 0.69, N = 27; Figure 3.12c and Table B.2) that overlaps with the SHRIMP age. CI-normalized (Anders and Grevesse, 1989) zircon REE patterns show variations in middle to heavy REE negative slopes [(Yb/Gd)_{CI} = 10-41], negative Eu anomalies [(Eu/Eu*)_{CI} = 0.06–0.12] and variable Ce anomalies [(Ce/Ce*)_{CI} = 0.4–16, where $\text{Ce}^* = \sqrt{(\text{La} \times \text{Pr})}$]. These patterns are typical of unaltered magmatic zircons (Belousova *et al.*, 2002; Grimes *et al.*, 2015) (Figure 3.12c and Table B.2). These zircon grains have Hf contents of 8182–9859 ppm, Nb contents of 0.73–3.06 ppm, and U/Yb ratios of 0.04–0.12 (Figure 3.13 and Table B.2).

The Lu-Hf isotopes of these 30 spots yield $^{176}\text{Lu}/^{177}\text{Hf}$ ratios of 0.001548 ± 0.00002 – 0.00668 ± 0.00020 and $^{176}\text{Hf}/^{177}\text{Hf}_{(t)}$ ratios of 0.282566 ± 0.000038 – 0.282725 ± 0.000043 (Table B.2). The calculated $\epsilon\text{Hf}_{(t)}$ values range from $+8.51 \pm 0.59$ to $+14.40 \pm 0.83$ and yield a weighted mean of $+11.00 \pm 0.12$ (MSWD = 4.3) (Figure 3.14 and Table B.2), corresponding to T_{DM} crustal ages of 0.72–1.09 Ga. Twenty O isotope spot analyses have $\delta^{18}\text{O}$ values ranging between 4.32 ± 0.24 ‰ and 5.09 ± 0.20 ‰ with a weighted mean of 4.83 ± 0.09 ‰ (MSWD = 0.97) (Figure 3.14 and Table B.2).

3.4.3.4 Trondhjemite sample S14

Zircon grains from sample S14 are equant to sub-rounded. They have euhedral rims and lengths ranging from 50 to 150 μm . In CL images, zircon grains are commonly homogenous and show oscillatory zoning, but some display unzoned homogenous cores (Figure 3.11d, Figure B.2).

For sample S14, nineteen U-Pb SHRIMP analyses were conducted on 19 grains. These analyses have U and Th contents of 48–937 ppm and 20–1451 ppm, respectively, and Th/U ratios of 0.31–1.55 (Table B.1) demonstrating a magmatic

origin. Seventeen of the 19 U-Pb isotopic analyses yield a weighted mean $^{206}\text{Pb}/^{238}\text{U}$ age of 722 ± 7 Ma (± 95 % conf., MSWD = 0.41, N = 17; Figure 3.11d), which is interpreted as the crystallization age of Trondhjemite sample S14.

Nineteen LASS analyses on the same sample, located over the same 19 SHRIMP spots, give a $^{206}\text{Pb}/^{238}\text{U}$ age of 722 ± 11 Ma (± 95 % conf., MSWD = 3.5, N = 19; Figure 3.12d and Table B.2) which is identical within error to the SHRIMP age. All the zircons have REE patterns with negative slopes [$(\text{Yb}/\text{Gd})_{\text{CI}} = 14\text{--}29$], negative Eu anomalies [$(\text{Eu}/\text{Eu}^*)_{\text{CI}} = 0.12\text{--}0.52$], and highly variable Ce anomalies [$(\text{Ce}/\text{Ce}^*)_{\text{CI}} = 1.06\text{--}114$], characteristics typical of unaltered magmatic zircons (Belousova *et al.*, 2002; Grimes *et al.*, 2015) (Figure 3.12d and Table B.2). These zircon grains have Hf contents of 8515–11322 ppm, Nb contents of 0.80–9.37 ppm, and U/Yb ratios of 0.07–0.47 (Figure 3.13 and Table B.2).

The Lu-Hf isotopes of the same 19 spots give $^{176}\text{Lu}/^{177}\text{Hf}$ ratios of 0.000936 ± 0.000009 – 0.011387 ± 0.000083 and $^{176}\text{Hf}/^{177}\text{Hf}_{(t)}$ ratios of 0.282577 ± 0.000041 – 0.282724 ± 0.000045 (Table B.2). The calculated $\epsilon\text{Hf}_{(t)}$ values range from $+9.39 \pm 0.62$ to $+13.19 \pm 1.08$ and give a weighted mean of $+11.38 \pm 0.56$ (MSWD = 3.3) (Figure 3.14 and Table B.2), corresponding to T_{DM} crustal ages of 0.78–1.05 Ga. These 19 spots have $\delta^{18}\text{O}$ values of 4.06 ± 0.17 – 4.93 ± 0.25 ‰ with a weighted mean of 4.52 ± 0.14 ‰ (MSWD = 2.4) (Figure 3.14 and Table B.2).

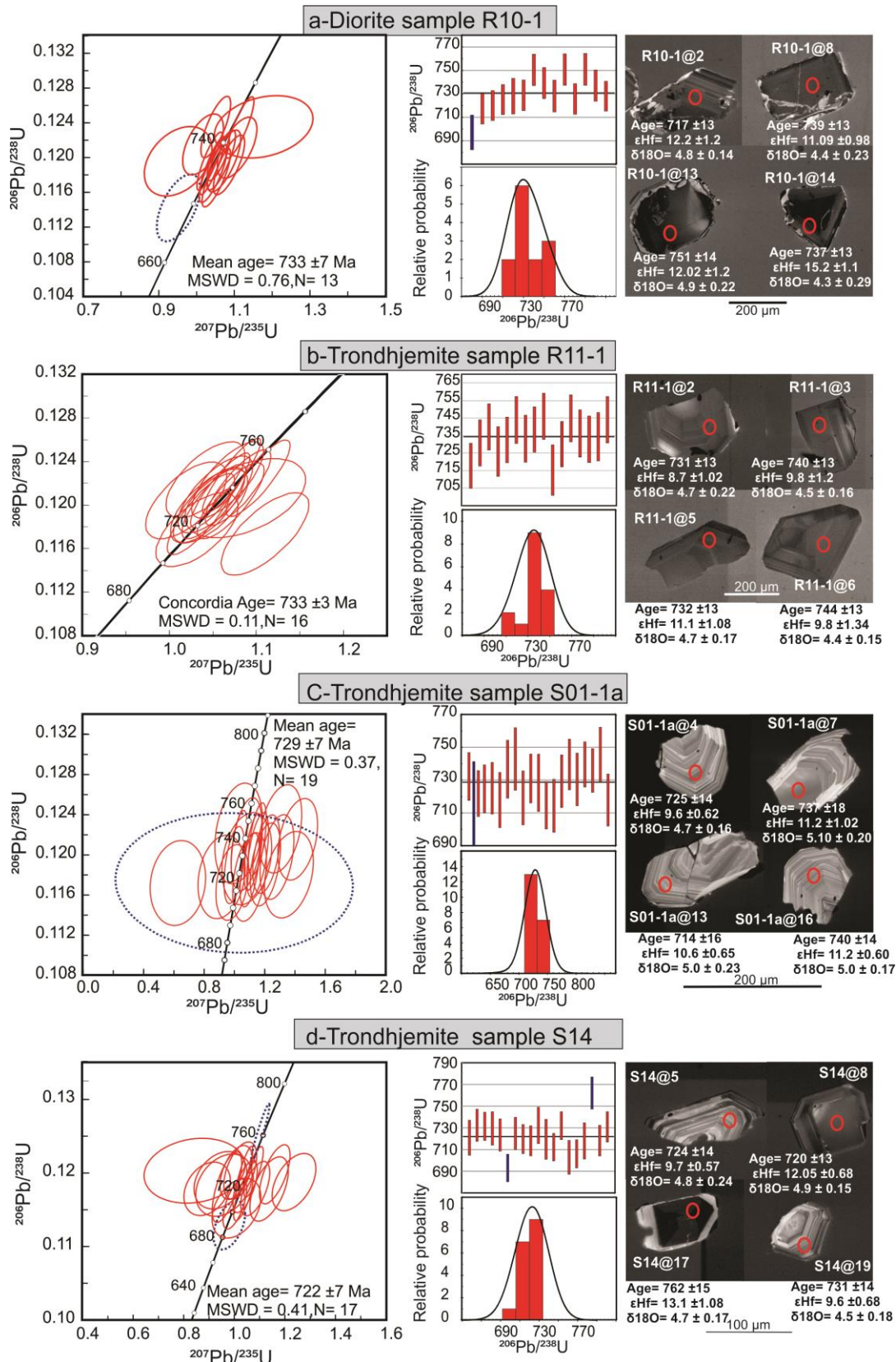


Figure 3.11: SHRIMP geochronological data and CL images of the El-Shadli plagiogranites. Zircon U-Pb SHRIMP Concordia diagrams show the $^{206}\text{Pb}/^{238}\text{U}$ ages of the analysed zircons with 1 sigma errors. Weight means relative probability diagrams of $^{206}\text{Pb}/^{238}\text{U}$ age and representative CL images are shown for each sample. The red circles on the CL images mark the place for SHRIMP, LASS, and SIMS spot analyses for the U-Pb age, Hf and O isotopes, and trace element data, respectively.

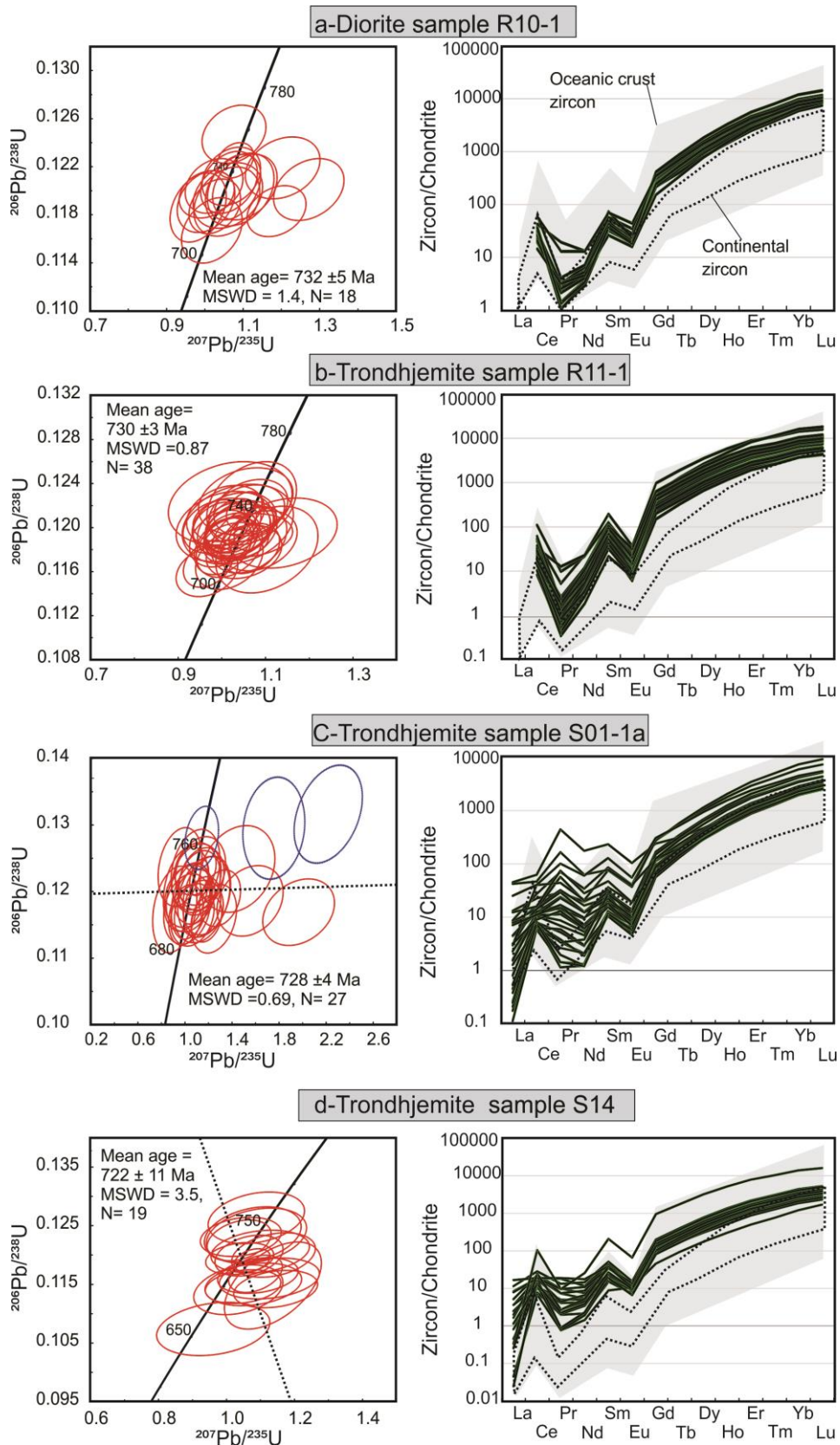


Figure 3.12: LA-SS-ICPMS geochronological data and chondrite-normalized zircon trace element data of the El-Shadli plagiogranites. Zircon U-Pb Concordia diagrams show the $^{206}\text{Pb}/^{238}\text{U}$ ages of the studied zircons with 1 sigma errors. Chondrite-normalized zircon REE patterns (Anders and Grevesse, 1989) of each sample are shown. Oceanic and continental zircon fields are from Grimes *et al.* (2007).

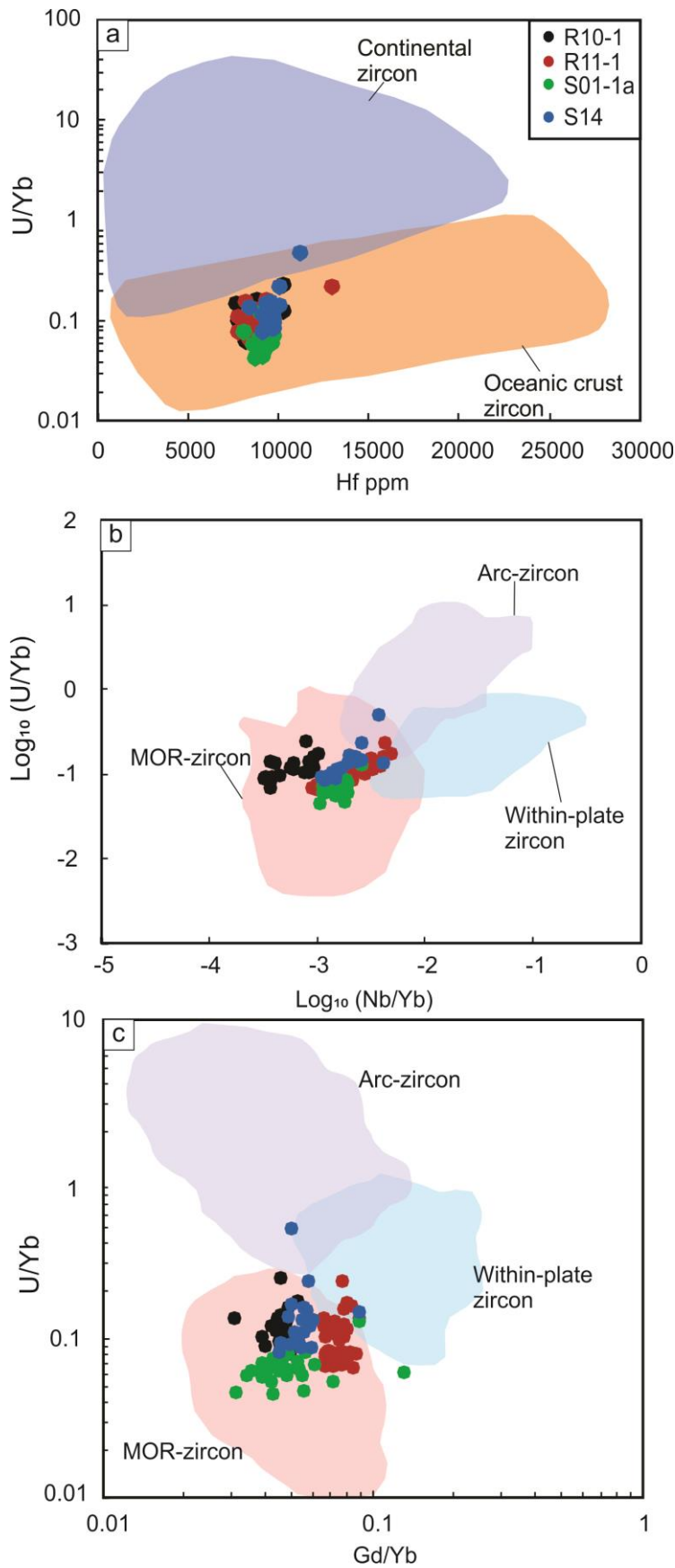


Figure 3.13: Zircon trace elements tectono-magmatic classification of the El-Shadli plagiogranites using the classification fields of Grimes *et al.* (2015).

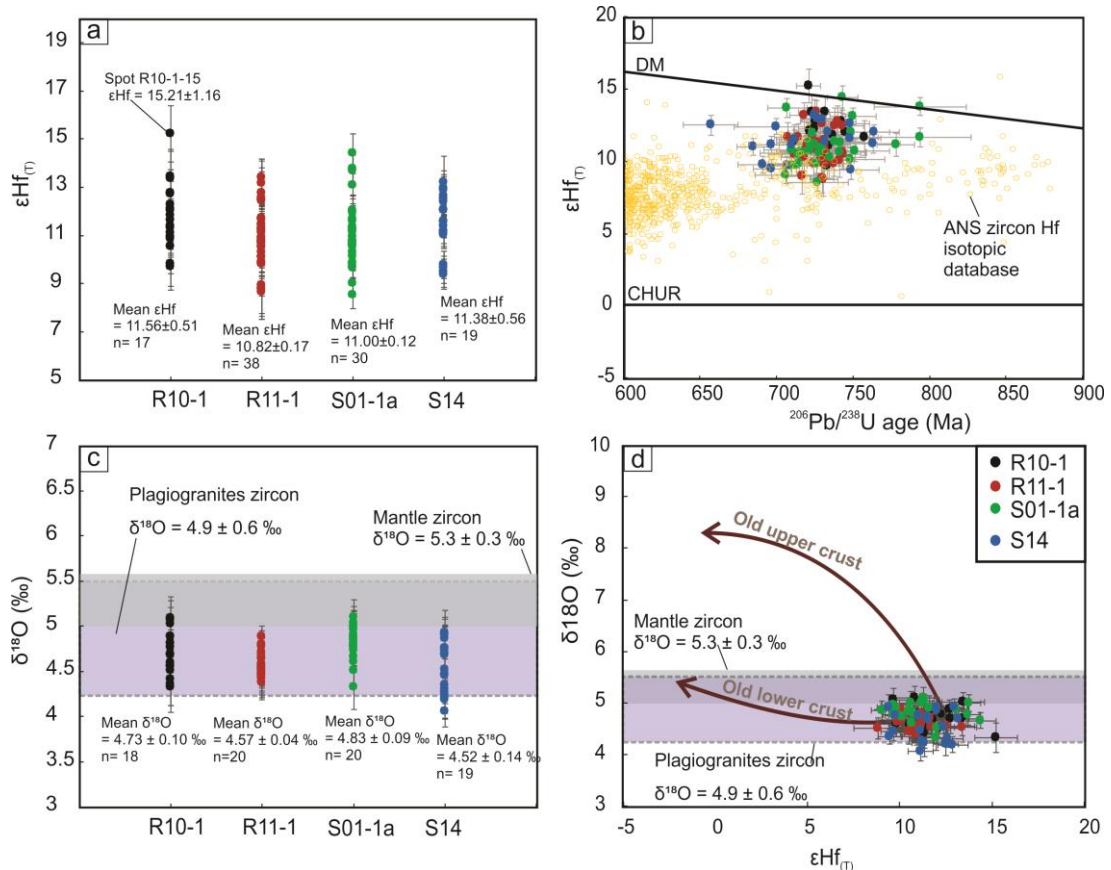


Figure 3.14: Age, Hf, and O isotopic data of zircons from the El-Shadli plagiogranites. (a) The calculated $\epsilon\text{Hf}(t)$ values of each analysis and the sample weighted mean. (b) $\epsilon\text{Hf}(t)$ vs $^{206}\text{Pb}/^{238}\text{U}$ age plot against the Chondritic uniform reservoir (CHUR) and depleted mantle (DM; Griffin *et al.*, 2002) lines. Hf isotopic data of ANS arc-related I- and A-type granitoids (e.g., Morag *et al.*, 2011, 2012; Robinson *et al.*, 2014) are used for comparison. (c) The plot of individual $\delta^{18}\text{O}$ values and sample weighted means. The zircon $\delta^{18}\text{O}$ value of oceanic ophiolitic plagiogranites (4.9 ± 0.6 ‰) is from Grimes *et al.* (2013), and that of mantle zircons (5.3 ± 0.3 ‰) is from Valley *et al.* (1998, 2005). (d) The plot of $\delta^{18}\text{O}$ vs $\epsilon\text{Hf}(t)$ for the studied zircons. Old upper and lower crust trends are from Kemp *et al.* (2007) and Wang *et al.* (2016).

3.5. Discussion

3.5.1 El-Shadli plagiogranites: mineralogical, petrological and geochemical evidence

Plagiogranites are commonly distinguished from other granite types by mineralogical and geochemical criteria (Coleman and Peterman, 1975; Coleman and Donato, 1979; Pearce, 1996). The modal mineralogy (plagioclase (>50%), quartz, and amphiboles (<10%)) and textures (quartz-plagioclase graphic and vermicular intergrowth textures) of the El-Shadli granite are typical features of plagiogranites

(Coleman and Donato 1979; Figure 3.5 and Figure B.2) and plot as trondhjemites and tonalites on the low-pressure field of the Ab-An-Or diagram (Figure 3.7b) (O'Connor, 1965; Barker, 1979) (Figure 3.7a, b). The rock association of the El-Shadli complex including trondhjemite, tonalite, diorite, and gabbro is a typical rock assemblage of plagiogranites found in MOR and ophiolites (Coleman and Donato, 1979; Amri, Benoit and Ceuleneer, 1996; Floyd, Yaliniz and Goncuoglu, 1998; Rollinson, 2009; Grimes *et al.*, 2011, 2013; Freund *et al.*, 2014; Haase *et al.*, 2016; Marien *et al.*, 2019) (Figure 3.7a, b).

Geochemically, the El-Shadli granitoids have a tholeiitic affinity with very low K₂O contents (<1 wt.%), similar to known plagiogranite rock suites worldwide (Figure 3.7c) and suggest a low-K mafic parental source (Figure 3.7d) (Laurent *et al.*, 2014). On granite discrimination diagrams of Rb vs. Y + Nb and Nb vs. Y (Pearce, Harris and Tindle, 1984; Pearce, 1996), the El-Shadli granites have compositions similar to that of plagiogranites (Figure 3.7e, f). In addition to their high contents of Y (38–98 ppm), and Nb (0.78–2.83 ppm), they are low in Rb contents (a fluid-mobile element (FME)) (2.06–13.45 ppm; average = 6.5 ppm) indicating derivation from a depleted mantle source and/or absence of interaction with (and contamination by) continental crust materials. These geochemical features are typical of the mid-ocean ridge- and/or oceanic plume-related granites (Pearce, Harris and Tindle, 1984; Pearce, 1996) (Figure 3.7e, f).

The flat REE patterns are also typical of plagiogranites (Coleman and Peterman, 1975; Coleman and Donato, 1979; Amri, Benoit and Ceuleneer, 1996; Floyd, Yaliniz and Goncuoglu, 1998; Grimes *et al.*, 2011, 2013; Freund *et al.*, 2014; Haase *et al.*, 2016; Marien *et al.*, 2019). In addition, the El-Shadli granitoids have low Sr (43–200 ppm), low Rb/Sr (0.02–0.21), low Sr/Y ratios (0.44–5.29) which are similar to plagiogranites (Coleman and Peterman, 1975; Coleman and Donato, 1979; Amri, Benoit and Ceuleneer, 1996; Floyd, Yaliniz and Goncuoglu, 1998; Whattam *et al.*, 2016) (Figure 3.7e, f). Their low abundance of LILE such as Cs, Rb, Ba, Th, and U also differentiate them from arc-related granitoids and demonstrates a lack of interaction between the parental magma and subducting crustal and sedimentary materials (Pearce, Harris and Tindle, 1984; Pearce, 1996) (Figure 3.9). Taken together, these overall geochemical features indicate that the El-Shadli granitoids have a

different origin and geodynamic setting from other known ANS granitoids (Figures 3.7–9).

Trace element contents from zircon are a powerful tool for tracking the origin of the granites and for distinguishing between the different granitic types (Belousova *et al.*, 2002; Grimes *et al.*, 2007, 2015). Chondrite-normalized REE patterns of the El-Shadli zircons plot in the ocean-crust zircon field (as defined by zircons from oceanic crust plagiogranites and gabbroic rocks; Grimes *et al.*, 2007) (Figure 3.12). Also, the low U/Yb and Gd/Yb of the El-Shadli zircons are similar to mid-ocean ridge (MOR) plagiogranite zircons (Grimes *et al.*, 2015) (Figure 3.13). The El-Shadli zircons have $\delta^{18}\text{O}$ values of $4.52 \pm 0.14 - 4.83 \pm 0.09$ ‰. They extend ~ 1 ‰ below the value of the typical mantle zircon (5.3 ± 0.3 ‰; Valley *et al.*, 1998, 2005) and are comparable to that of plagiogranites (Figure 3.14c, d) which range from 3.9 to 5.6 ‰ (average = 4.9 ± 0.6 ‰; Grimes *et al.*, 2013)

In conclusion, the mineralogical, petrological, and geochemical characteristics of the El-Shadli granites indicate that they are plagiogranites, and clearly distinguish them from other known ANS I- and A-type granites (e.g., Robinson *et al.*, 2014, 2017), Archean trondhjemite-tonalite-granodiorite (TTG) (Moyen, 2011), and arc-related granitoids (Pearce, Harris and Tindle, 1984; Pearce, 1996) (Figures 3.7–9 and 3.13–14).

3.5.2 Nature of the parental magma and magma source

It is widely accepted that plagiogranites are generated from depleted mantle sources, and have MOR-like tholeiitic parental magma compositions (Coleman and Peterman, 1975; Coleman and Donato, 1979; Pearce, Harris and Tindle, 1984; Amri, Benoit and Ceuleneer, 1996; Pearce, 1996; Floyd, Yaliniz and Goncuoglu, 1998; Grimes *et al.*, 2011, 2013; Freund *et al.*, 2014; Haase *et al.*, 2016; Marien *et al.*, 2019). The El-Shadli plagiogranites show geochemical affinities with tholeiitic parental magma include its metaluminous composition, very low K_2O (Figure 3.7 and Table 3.1), and flat-like CI-normalized (except for sample R11-1) REE patterns with slight LREE depletion relative to HREE [$(\text{La}/\text{Yb})_{\text{N}} = 0.41-0.88$], (Coleman and Donato, 1979; Gerlach, Leeman, and Avé Lallemant, 1981; Pearce, 1996; Haase *et al.*, 2016; Zhang *et al.*, 2017; Marien *et al.*, 2019) (Figure 3.8). The low initial $^{87}\text{Sr}/^{86}\text{Sr}$ ratios

and highly positive $\epsilon\text{Nd}(t)$ of the El-Shadli plagiogranites and associated gabbros (Figure 3.10) indicate a juvenile nature of the parental magma extracted from a depleted MOR-like mantle source. The Sr-Nd isotopic data of the El-Shadli plagiogranites and associated gabbros are comparable to the nearby ~750 Ma W. Gerf and W. Ghadir N-MORB ophiolites (Zimmer *et al.*, 1995; Basta *et al.*, 2011) (Figure 3.10). Taken together, the whole-rock geochemical and isotopic compositions of the El-Shadli plagiogranites and associated gabbros are consistent with derivation from a depleted MOR-like mantle source instead of the arc-related source. The enrichments in some LILE (Cs, Rb, Ba, Th, and U) in the El-Shadli plagiogranites and associated gabbros relative to N-MORB are likely an inherited feature and could be related to hydrothermal alteration of their mafic source in the oceanic crust (Gillis and Coogan, 2002; Koepke *et al.*, 2004; Koepke, Feig and Snow, 2005; France, Ildefonse and Koepke, 2009; France *et al.*, 2010, 2014; Fischer *et al.*, 2016; Currin *et al.*, 2018; Zihlmann *et al.*, 2018; Tao *et al.*, 2020).

U-Pb analyses of the El-Shadli plagiogranite zircons indicate a lack pre-Neoproterozoic inherited cores or zircon xenocrysts (Figures 3.11 and 3.12), implying no interaction with old crustal materials (Grimes *et al.*, 2013), consistent with the juvenile composition of the parental magma (i.e. a depleted mantle source). Tetravalent cations such as Hf and U are readily incorporated into the zircon crystal structure as a substitution for Zr (Hoskin and Schaltegger, 2003; Grimes *et al.*, 2007). Hf is highly compatible in zircon due to its comparable charge and similar ionic radius to Zr, whereas U is less compatible and larger than Hf and HREE (i.e., Yb). U is normally highly enriched in continental crust relative to MORB; for example, U/Yb ratio for the bulk continental crust is 0.7 (Rudnick and Gao, 2014) compared with 0.02 for MORB (White and Klein, 2014). Variations of U/Yb in zircon reflect variations in the melt at the time of zircon crystallization (Grimes *et al.*, 2007). The low U/Yb (mainly < 0.1) of the El-Shadli zircons is similar to modern ocean crust zircons from a depleted mantle-source with MOR-like magma, and contrast with continental and arc zircons (Grimes *et al.*, 2007, 2015; Carley *et al.*, 2014) (Figure 3.13). The low Nb/Yb and Gd/Yb ratios of the El-Shadli zircons are also well-defined features of zircon extracted from a depleted MOR-like source (Grimes *et al.*, 2015) (Figure 3.13b, c).

Hf and O isotopes in zircons can distinguish the recycled versus juvenile nature of granitic magmatism (Hawkesworth and Kemp, 2006; Kemp and Hawkesworth, 2014). As Hf is more incompatible than Lu during mantle partial melting processes, it is therefore highly enriched in the continental crust, leading to a depleted mantle source that becomes more radiogenic (i.e. high Lu/Hf and higher $^{176}\text{Hf}/^{177}\text{Hf}$ with time) and a complementary unradiogenic crust (low Lu/Hf and lower $^{176}\text{Hf}/^{177}\text{Hf}$ with time) continental crust (Patchett *et al.*, 1981; Patchett, 1983; Kinny, Compston and Williams, 1991). As Hf strongly partitions into zircon, Hf contents in zircon are high (0.5–2 %) and the Lu/Hf ratio is very low (<0.001) (Patchett, 1983; Kemp and Hawkesworth, 2014). Therefore, zircon preserves the near initial $^{176}\text{Hf}/^{177}\text{Hf}$ ratio of the source magma at the time of crystallization (Vervoort and Blichert-Toft, 1999; Hawkesworth and Kemp, 2006) and is sensitive to the evolution of the source magma as well as the potential presence of mixed source components from the older continental crust and depleted mantle of different ages (Kinny, Compston and Williams, 1991; Vervoort and Blichert-Toft, 1999; Griffin *et al.*, 2002; Kinny and Maas, 2003; Kemp *et al.*, 2006; Belousova *et al.*, 2010; Kemp and Hawkesworth, 2014). The highly positive $\epsilon\text{Hf}(t)$ values (weighted mean from $+10.82 \pm 0.17$ to $+11.56 \pm 0.51$) of the El-Shadli plagiogranite zircons (Figure 3.14) indicate a juvenile source with no involvement of the old continental crust (Hawkesworth and Kemp, 2006; Belousova *et al.*, 2010). These data support derivation from a highly depleted mantle source composition that contrasts with all other ANS granitoids of similar ages (e.g., Morag *et al.*, 2011, 2012; Robinson *et al.*, 2014; Ali *et al.*, 2015), indicating a different origin (Figure 3.14b).

O isotopic values in zircon track contamination of the source magma by continental and sedimentary materials (Valley, 2003). Typical $\delta^{18}\text{O}$ values in zircon of mantle-derived magma have a narrow range (5.3 ± 0.3 ‰), lower values are attributed to interactions with hydrothermal fluids, and higher values reflect contamination of source rocks by sedimentary or crustal recycling (Valley *et al.*, 1998, 2005b; Valley, 2003; Hawkesworth and Kemp, 2006).

The uniform $\delta^{18}\text{O}$ values (weighted mean from 4.52 ± 0.14 to 4.83 ± 0.09 ‰) of the El-Shadli plagiogranite zircons are lower than that of mantle $\delta^{18}\text{O}$ value (5.3 ± 0.3 ‰; Valley *et al.*, 1998, 2005), demonstrating that either their source had undergone interactions with high-temperature hydrothermal fluids, or the plagiogranites

experienced post magmatic fluid-rock interaction (Grimes *et al.*, 2013; Wang *et al.*, 2016) (Figure 3.14c, d). Typically, zircon resists post-magmatic modification, and well-crystallized zircon with oscillatory zoning should preserve primary magmatic signatures such as U and Th contents and Hf and O isotopic ratios (Valley, 2003; Kemp and Hawkesworth, 2014). In contrast, metamictization process can lead to porous zircons having very low Th/U ratios (<0.4), high U contents, and discordant U-Pb ages (Yakymchuk, Kirkland and Clark, 2018). The El-Shadli zircons preserve clear igneous magmatic features such as crystal shapes with oscillatory zoning (Figure 3.11 and Figure B.2), having Th/U mostly >0.4 (Yakymchuk, Kirkland and Clark, 2018), U contents mostly < 1000 ppm (Kirkland *et al.*, 2015; Yakymchuk, Kirkland and Clark, 2018) (Figure B.3 and Table B.2), no correlation between Th/U and U vs $\delta^{18}\text{O}$ (Figure B.3), and concordant to nearly concordant U-Pb ages (Figures 3.11 and 3.12). All these features indicate that the El-Shadli zircons preserve primary magmatic characteristics, indicating their lower $\delta^{18}\text{O}$ compositions may be attributed to hydrothermal fluid contamination of their mantle source (Grimes *et al.*, 2013; Wang *et al.*, 2016) instead of post-magmatic alteration processes.

In summary, the whole-rock petrological, geochemical, and isotopic data and zircon U-Pb-Hf-O-trace element data suggest that the El-Shadli plagiogranites were derived from a MOR-like parental magma extracted from a highly depleted mantle-derived mafic source which had undergone hydrothermal alterations in an oceanic- and/or ridge/rift-related setting.

3.5.3 Petrogenesis of the El-Shadli plagiogranites

Field observations indicate the presence of magmatic mixing zones which consists of irregular shaped enclaves of gabbroic blocks within the plagiogranite (Figure 3.4b-d) and imply the presence of two contemporaneous melts. This interpretation is confirmed by the overlapping ages for the two rock types (Figures 3.11 and 3.12). Variations in geochemical composition between the El-Shadli gabbroic rocks and plagiogranites are continuous, but not linear (Figures 3.6 and 3.7), consistent with crystallization from the same parental melt (Peccerillo *et al.*, 2003). In addition, a co-magmatic relationship between El-Shadli plagiogranite and associated gabbro is supported by (1) the overlap between their major, trace, and REE elemental

abundances (Figures 3.6-3.9), (2) similar Sr-Nd isotopic compositions (Figure 3.10), and (3) common and uniform zircon trace element contents and Hf-O isotopic compositions in both rock types (Figures 3.12 and 3.13). In addition, the negative Eu anomalies in the El-Shadli plagiogranites reflect the removal of plagioclase from a basaltic melt in the early stage (Coleman and Donato, 1979) (Figure 3.8). This interpretation is supported by the positive Sr anomalies, higher Al₂O₃, and slightly positive Eu anomalies of the El-Shadli gabbros which suggest complementary plagioclase accumulation (Sawyer, 2001; Haase *et al.*, 2016; Zhang *et al.*, 2017) (Figures 3.6 and 3.8). Also, the low Ti content and negative Ti anomalies of the El-Shadli plagiogranite compared to the gabbro have indicates fractionation of Ti-Fe oxides in the early magmatic stage (Koepke *et al.*, 2004; Zhang *et al.*, 2017) (Figure 3.9 and Table 3.1).

Thus, the El-Shadli plagiogranites and associated gabbroic rocks are interpreted to have fractionated through a complementary melt segregation process (i.e., a coherent magmatic series) from the same parental magma which had a MORB-like tholeiitic composition. This parental magma was either (1) a direct mantle-derived basaltic melt that fractionated to yield gabbro and plagiogranite compositions types (i.e., a one-stage process with fractionation of a primary mantle melt) (Coleman and Peterman, 1975; Aldiss, 1981; Pallister and Hopson, 1981; Floyd, Yaliniz and Goncuoglu, 1998) or (2) the product of partial melting of a hydrothermally altered depleted mafic lower oceanic crust (i.e., a two-stage formation process after primary mantle partial melting) (Gerlach, Leeman, and Avé Lallemant, 1981; Pedersen and Malpas, 1984; Flagler and Spray, 1991; Stakes and Taylor, 2003; Koepke *et al.*, 2004, 2007; Brophy, 2009; France *et al.*, 2010, 2014; Wolff, Koepke and Feig, 2013; Grimes *et al.*, 2013).

Experiments show that the composition of plagiogranitic melts resulting from fractional crystallization of MORB (e.g., Dixon-Spulber and Rutherford, 1983; Berndt, Koepke and Holtz, 2005) differ markedly from plagiogranite melts generated by partial melting of gabbros and amphibolites of lower oceanic crust and oceanic crustal basalts (Beard and Lofgren, 1991; Thy, Leshner and Mayfield, 1999; Koepke *et al.*, 2004; France *et al.*, 2010, 2014), particularly in their TiO₂, SiO₂ and K₂O contents (Figure 3.15a). The El-Shadli plagiogranites have a compositional range that overlaps with melts produced by hydrous partial melting of gabbroic and amphibolitic rocks of

the lower oceanic crust (Figure 3.15a). The TiO_2 content of plagiogranitic melts derived by fractionation from tholeiitic magmas is controlled by source composition and redox conditions (Berndt, Koepke, and Holtz, 2005; Koepke *et al.*, 2007). Experiments on tholeiitic primitive MORB melts (Berndt, Koepke, and Holtz, 2005) show that Fe-Ti oxides are generally stable under oxidizing conditions, and so SiO_2 -enriched felsic melts produced by having significantly lower Ti contents. On the other hand, under reducing conditions, the felsic melts produced by fractionation are characterized by high TiO_2 and FeO contents. As the differentiation of the MORB melts typically occurs under more reducing conditions, the resultant felsic melts should have high Ti contents (Berndt, Koepke, and Holtz, 2005; Koepke *et al.*, 2007). In contrast, gabbros in the lower oceanic crust are highly depleted in Ti, and partial melting of them generally occurs under hydrous (i.e. oxidizing) conditions. The resulting felsic melts should therefore have very low Ti contents (Koepke *et al.*, 2004). Thus, Koepke *et al.* (2004, 2007) proposed that the TiO_2 content of plagiogranites is a powerful indicator for discriminating between the more acidic plagiogranitic melts generated from anatexis of oceanic lower crustal gabbroic rocks ($\text{TiO}_2 < 1$ wt.%) and those generated by fractionation of MORB melts ($\text{TiO}_2 > 1$ wt.%). The El-Shadli trondhjemitic and tonalitic rocks have TiO_2 concentrations below the lower limit for experimental melts resulted from MORB fractionation, again supporting an origin by partial melting of mafic (gabbroic) crust (Figure 3.15b, c).

Based on theoretical modelling, Brophy (2009) proposed that plagiogranitic melts formed by hydrous partial melting should (1) yield a flat or slightly decreasing REE with increasing SiO_2 content, and (2) show slightly higher and/or overlap REE patterns with coexisting mafic rocks. On the other hand, plagiogranitic melts produced through fractional crystallization show a positive correlation between REE and SiO_2 over the entire mafic to the felsic range (Brophy, 2009). The El-Shadli plagiogranites and associated gabbroic rocks share the same REE contents. They have similar and overlapping flat-like REE patterns (Figure 3.8) and a consistent flat-like correlation between La and SiO_2 , again demonstrating a hydrous partial melting origin (Figure 3.15d). This process contrasts with that of the Iceland lavas, which display a positive correlation of La with SiO_2 between the mafic to felsic end-members and are thought to be related by fractional crystallization (Brophy, 2009).

Koepke and co-workers (Koepke *et al.*, 2004, 2007; Wolff, Koepke and Feig, 2013) proposed that hydrous partial melting of pre-existing gabbros produces a

plagiogranitic melts with amphibole as residual phase (Olivine + clinopyroxene + plagioclase (A) + H₂O = amphibole + orthopyroxene + plagioclase (B) + plagiogranitic melt). As REE abundances (particular LREE to MREE) are very sensitive to the presence of amphiboles that are in the residue, the resultant melt should be depleted in LREE, and the fractionated mafic and felsic rocks from this a melt should have similar LREE contents (Brophy, 2009; Brophy and Pu, 2012). This is indeed the case for the El-Shadli plagiogranites and associated gabbroic rocks (Figure 3.15d). Such a model also explains the notable negative Nb anomalies in the studied rocks (Figure 3.9) as amphibole is a residual phase after a high degree of partial melting of a hydrated gabbroic lower crust (Koepke *et al.*, 2004, 2007; Rollinson, 2009; Xiong *et al.*, 2011; France *et al.*, 2014). The lack of HREE depletion indicates the absence of residual garnet implying partial melting occurred in a low-pressure environment (i.e., in plagioclase stability field).

Zircon $\delta^{18}\text{O}$ values can distinguish between plagiogranitic rocks generated by fractional crystallization (typical mantle-like $\delta^{18}\text{O}$ values of 5.2 ± 0.5 ‰; Grimes *et al.*, 2011) and those generated by re-melting of hydrothermal altered gabbroic lower oceanic crust ($\delta^{18}\text{O} = 4.9 \pm 0.6$ ‰; Grimes *et al.*, 2013). The El-Shadli zircons have low $\delta^{18}\text{O}$ values ranging between 4.52 ‰ and 4.83 ‰ (Figure 3.14c). These low $\delta^{18}\text{O}$ values could be explained by either re-melting of hydrothermally altered source rocks, or by assimilation of magma with hydrothermally altered wall rock during magma emplacement (Grimes *et al.*, 2013; Wang *et al.*, 2016). If the plagiogranitic magma underwent the assimilation process, however, it should have zircon xenocrysts and Hf-O isotopic data with upper crustal compositions (Kemp *et al.*, 2007; Wang *et al.*, 2016), neither of which have been observed in the studied rocks (Figure 3.14d). Also, typical $\delta^{18}\text{O}$ depth profiles of normal oceanic crust show $\delta^{18}\text{O}$ values for the gabbroic lower crust as low as 2 ‰, reflecting an interaction with high-temperature seawater-derived/hydrothermal fluids (Eiler, 2001; Stakes and Taylor, 2003; Bindeman, 2008; Grimes *et al.*, 2013). Systematic low $\delta^{18}\text{O}$ values shown by global ophiolitic plagiogranites indicate that these values are primary signatures and reflect partial melting of the lower oceanic crust without overprinting by late, low-temperature fluids (Grimes *et al.*, 2013). Thus the above observations support an origin for the El-Shadli plagiogranites by the re-melting of altered gabbroic lower oceanic crust. On the plot of TiO₂ (WR) vs $\delta^{18}\text{O}_{\text{Zr}}$ (Figure 3.15c), the El-Shadli plagiogranites also plot outside of the field characterizing plagiogranites of fractional crystallization origin but overlap

with known plagiogranites of partial melting origin from the Oman and Troodos ophiolites (Grimes *et al.*, 2013).

It has been demonstrated that high-temperature hydrothermal fluids (i.e., seawater) can circulate into, and interact with, the oceanic gabbroic lower crust and even down to the upper mantle (Tao *et al.*, 2020). The circulation of such hydrothermal fluids has been recognized through seawater signatures such as high radiogenic $^{87}\text{Sr}/^{86}\text{Sr}$ values and high Chlorine and Boron contents in basaltic glass from MOR and secondary amphibole in the gabbroic section of ophiolites (Bosch *et al.*, 2004; Koepke *et al.*, 2004, 2007, 2011; Koepke, Feig and Snow, 2005; France, Ildefonse and Koepke, 2009; France *et al.*, 2010, 2014; Gillis *et al.*, 2014; Currin *et al.*, 2018; Zihlmann *et al.*, 2018; Tao *et al.*, 2020). The penetration of such hydrothermal fluids is facilitated by high-temperature shear zones/detachment fault systems in the oceanic crust (Koepke *et al.*, 2004; Zihlmann *et al.*, 2018; Tao *et al.*, 2020).

Collectively, the whole-rock petrological, geochemical, and isotopic data and zircon Hf-O isotopes support the partial melting of the gabbroic lower oceanic crust as the origin for the El-Shadli plagiogranites. Some 'arc-like' trace-element patterns, such as Nb and Ti negative anomalies, and LILE enrichment, can be interpreted as the results of (1) the source rocks underwent hydrothermal fluids contaminations and/or (2) a two-stage process (i.e., re-melting of highly depleted source) for the production of the plagiogranitic melt.

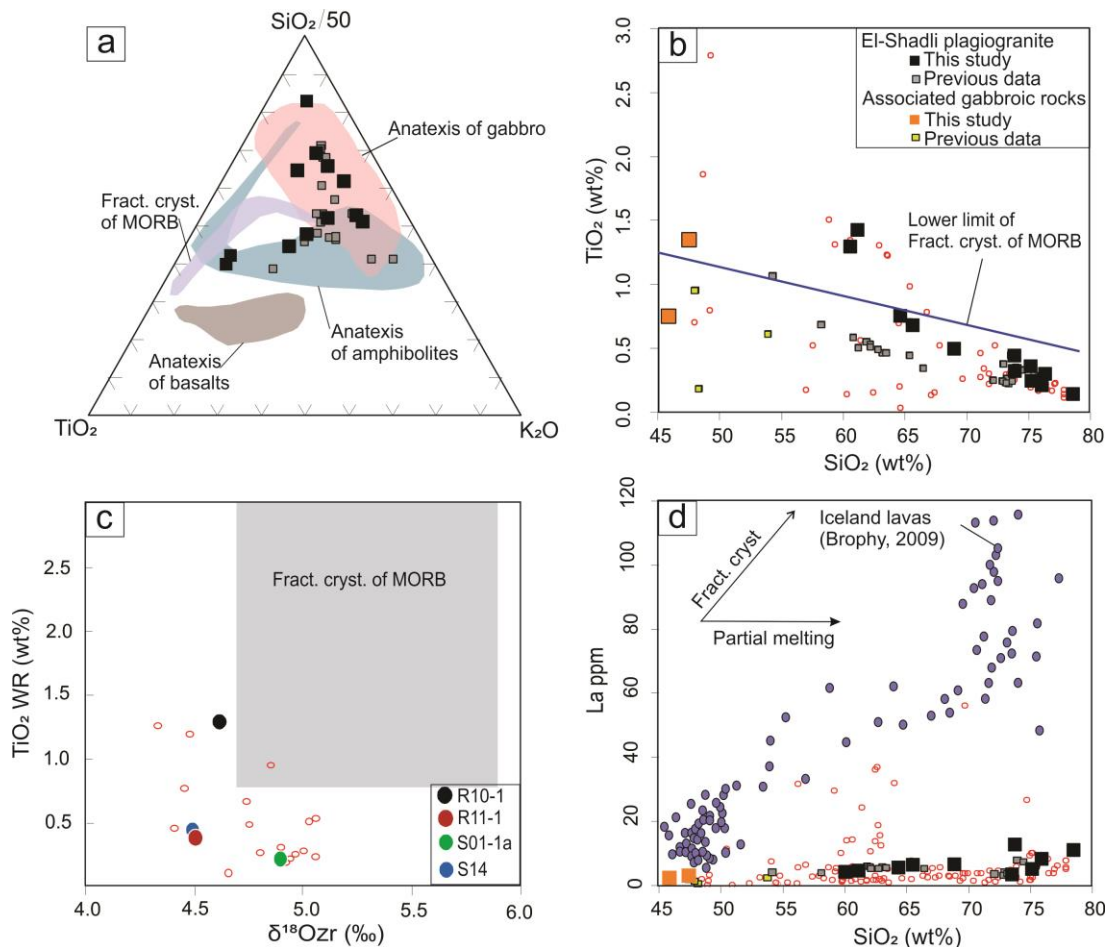


Figure 3.15: Whole-rock petrogenetic discrimination diagrams. (a) Ternary diagram of TiO_2 – $\text{SiO}_2/50$ – K_2O modified after France et al. (2010) based on experimental work to evaluate the composition of plagiogranitic melts resulted from fractional crystallization of MORB (e.g., Dixon-Spulber and Rutherford, 1983; Berndt, Koepke and Holtz, 2005) and from partial melting of hydrated oceanic crust (i.e., gabbros, amphibolites, and basalts; Beard and Lofgren, 1991; Thy, Leshner and Mayfield, 1999; Koepke et al., 2004; France et al., 2010, 2014). (b) TiO_2 vs. SiO_2 diagram after Koepke et al. (2007) showing the lower limit for plagiogranitic melts resulted from fractional crystallization of MORB. (c) TiO_2 (WR) vs. $\delta^{18}\text{O}$ (Zr) diagram after Grimes et al. (2013) showing the field of plagiogranites produced by fractional crystallization of MORB. (d) La vs. SiO_2 diagram was modified after Brophy (2009), suggesting a partial melting origin for the studied rocks.

3.5.4 Geodynamic context and formation mechanism for the El-Shadli plutonic complex

The petrological and geochemical characteristics of magmatic rocks are intrinsically linked to the magma sources and tectonic settings of the magmatic events (Pearce, 1996). The geochemical and isotopic data distinguish the El-Shadli plagiogranites from other arc-related granitoids (Figures 3.7-3.9, 3.12, and 3.13) and suggest a formation in a ridge/within-plate tectonic environment (Figure 3.7e, f). Geologically, the El-Shadli plutonic complex (plagiogranites and associated gabbros)

intrude strongly deformed and/or metamorphosed older ophiolitic complexes, as shown by their cross-cutting relationships with the strongly foliated ophiolitic country rocks (Figure 3.3). This suggests that these plutonic rocks formed post the accretion of the ophiolitic complexes. The absence of significant deformation and metamorphism of the El-Shadli plutonic complex is consistent with an emplacement within a relatively stable environment i.e., a within-plate/continental rift-related tectonic setting. Also, the El-Shadli plutonic complex is overlain by the rift-related, within-plate, and slightly younger (~700 Ma; this study) bimodal volcanics (Stern, Kröner and Rashwan, 1991; this study) (Figure 3.3, see Chapter 4 for the origin of these bimodal volcanics). This further supports a post-accretional within-plate/rifting tectonic setting for the El-Shadli plutonic complex, i.e. continental rifting environment. Geochemical and isotopic data of the El-Shadli plagiogranites and associated gabbros suggest an origin involving the anataxis of a hydrated gabbroic lower oceanic crust. Their highly depleted nature and juvenile origin indicate that the parental magma was likely derived from partial melting of a juvenile continental crust (i.e., accreted oceanic slabs) during a rifting event. The timing of the magmatism is consistent with that of global continental rifting and the break-up of the supercontinent Rodinia (~825–680 Ma; Li *et al.*, 2008; Li, Evans and Halverson, 2013).

It has been suggested that the volume of plagiogranites relates to the formation process (fractional crystallization vs partial melting) (Koepke *et al.*, 2004). Fractional crystallization of basaltic magma normally produces small amounts of plagiogranites in MOR environments (Aldiss, 1981; Koepke *et al.*, 2004; Grimes *et al.*, 2013). On the other hand, larger volumes of plagiogranitic melts can be generated by the partial melting process in MOR and more likely in preserve in ophiolites (Koepke *et al.*, 2004; Grimes *et al.*, 2013). Such a partial melting process is made possible by high H₂O activities and possibly with an excess heat source. The H₂O could be provided through penetration of hydrothermal fluids from the ocean via high-temperature detachment fault systems/shear zones at MOR (Koepke *et al.*, 2004; Koepke, Feig and Snow, 2005; Tao *et al.*, 2020). The excess heat source is generally believed to be provided by the underlying melt lenses at MOR (Koepke *et al.*, 2004; France, Ildefonse and Koepke, 2009; Rollinson, 2009; France *et al.*, 2014), but Amri, Benoit, and Ceuleneer (1996) suggested an upwelling mantle diapir as a heat source for the formation of the largest plagiogranites (up to 8 km in outcrop dimension) within the Oman ophiolites. As the El-Shadli plagiogranites formed after the terrane accretion instead of at a MOR

environment, the heat source can be related to mantle upwelling is driven by the continental rifting, i.e. Rodinia break-up.

Given that the El-Shadli plagiogranites form post-accretion, the mantle upwelling during the rifting of Rodinia could be induced by either slab break-off (Cawood *et al.*, 2009, 2016) or a mantle plume formed above the Rodinia superplume (Li *et al.*, 2008; Li and Zhong, 2009). The magmatism associated with the slab break-off proposed to show an arc-like signatures (Hildebrand, Whalen and Bowring, 2018), which not the case for the El-Shadli plutonic complex. Thus, the plume-induced model is slightly preferred based on the following arguments.

Given this exceptional large volume with a lateral dimension of ca. ~100 km x 50 km, a plume is needed here mainly to provide the enormous heat required to remelt the mafic lower crust to generate both the super-large El-Shadli plagiogranites and the overlying bimodal volcanics (80 km x 35 km and thickness of > 10 km; Shukri and Mansour, 1980; Khudeir, Ali and El Habaak, 1988; Stern, Kröner and Rashwan, 1991). In addition to the presence of other evidence for mantle plume activity in the region at that time include: (a) 741 ± 24 Ma Korab Kansi ferropicritic layered mafic-ultramafic intrusions (Figure 3.2; Khedr *et al.*, 2020) found in the southern part of the El-Shadli plutonic complex and (b) slightly younger 710 ± 7 Ma G. Dahanib komatiitic layered mafic-ultramafic intrusions (Figure 3.2; Dixon, 1981) located at the southern edge of the El-Shadli plutonic complex. This is in agreement with the proposed paleogeographic position of the ANS over the edge of the Rodinia superplume during the break-up/continental rifting of the supercontinent Rodinia between 825 and 680 Ma (Li *et al.*, 2008; Li, Evans and Halverson, 2013). Similar plume-related magmatism at that time, including granitoids, mafic-ultramafic dikes, and rift-related bimodal volcanics are also found in South China, Australia, Southern Africa, and Laurentia (e.g., Heaman, LeCheminant, and Rainbird, 1992; Li *et al.*, 1999, 2008; Frimmel, Zartman and Späth, 2002; X. H. Li *et al.*, 2003; Z. X. Li *et al.*, 2003; Zhang *et al.*, 2006). The proposed plume-induced model for the El-Shadli plutonic complex (~730–720 Ma) is coeval with the global plume/rift-related magmatism such as the well-known Franklin large igneous provinces event (~727–720 Ma) in Laurentia (Heaman, LeCheminant, and Rainbird, 1992; Li *et al.*, 2008) that extend until ~712 Ma (Denyszyn *et al.*, 2009), and the Gannakouriep event (~720 Ma) in South Africa and Namibia (Frimmel, Hartnady, and Koller, 1996).

In summary, this study proposes that the El-Shadli plutonic complex was formed by partial melting of accreted oceanic slabs during Rodinia break-up that might be linked to the mantle plume. The preferred tectonic model (Figure 3.16) has implications for the crustal growth of the ANS. Most previous models focused on arc accretion (Stern, 1994; Fritz *et al.*, 2013) although mantle plume and rift related-magmatism has been suggested to also have played an important role in the crustal evolution (Reymer and Schubert, 1986; Stein and Goldstein, 1996; Stein, 2003; Li *et al.*, 2008).

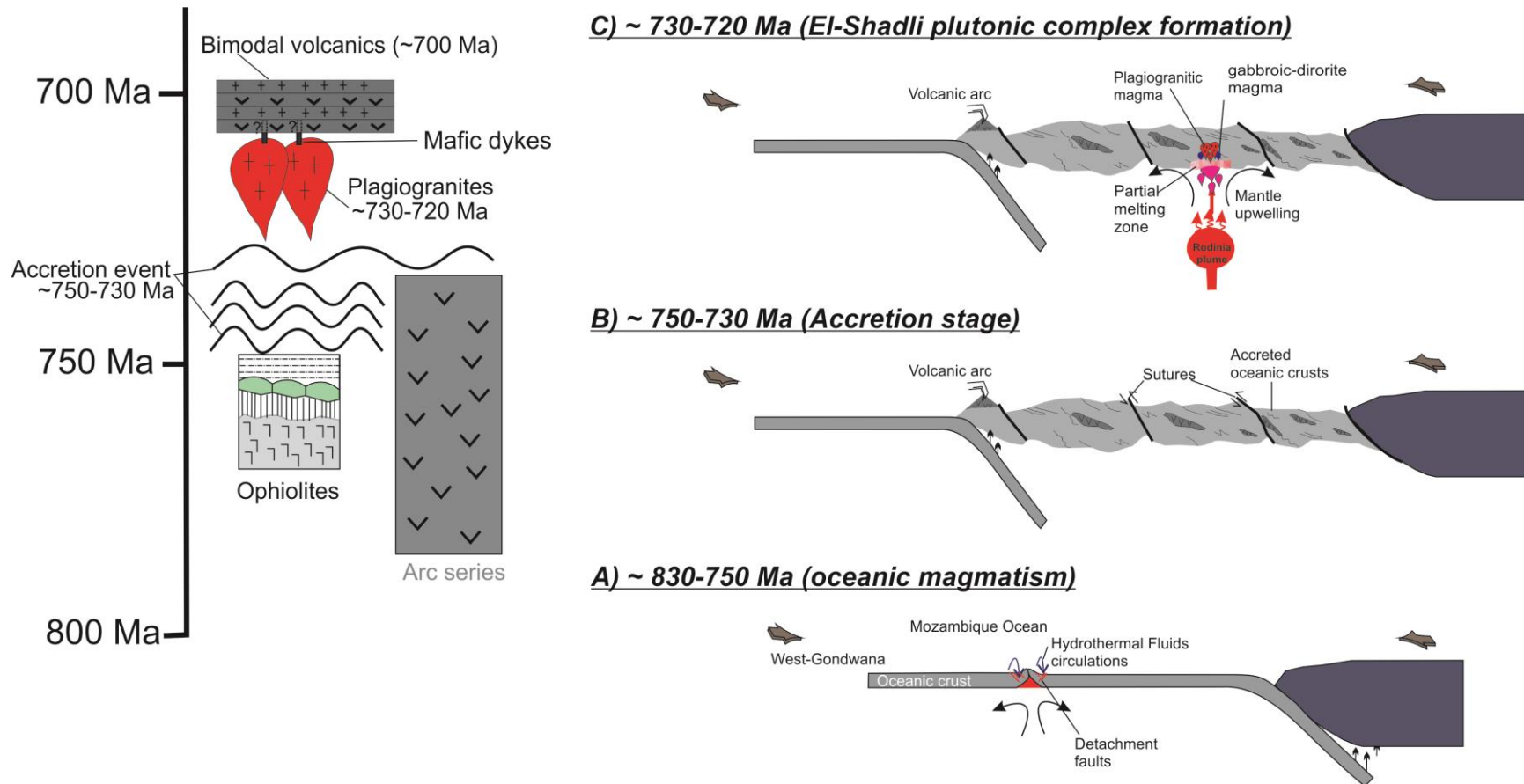


Figure 3.16: A proposed tectonic model for the genesis of the El-Shadli plutonic complex. (a) Oceanic spreading and ridge magmatism, and possible subduction at a continental arc during ~830–750 Ma with hydrothermal fluids circulating and altering the lower crust section of the oceanic crust near MOR. (b) Accretion of oceanic slabs along the subduction zone during ~750–730 Ma, forming a juvenile accreted terrane. (c) Formation of the El-Shadli plagiogranites and associated gabbros above asthenosphere upwelling possibly driven by a mantle plume at ~730–720 Ma by partial melting the lower crust of the accreted oceanic slabs.

Table 3.1: Whole-rock major and trace elements and Sr-Nd isotopes of the El-Shadli plagiogranites and associated gabbros.

Sample	R10-1 Diorite	R10-2 Diorite	S11-1 gabbro	S12 gabbro	R11-1 Troj	R11-2 Troj*	S01-1a Troj
Lat.	24°18'17"	24°18'17"	24°20'03"	24°20'00"	24°18'13"	24°18'13"	24°25'17"
Long.	35°08'15"	35°08'15"	34°45'05"	34°45'00"	35°08'07"	35°08'07"	34°35'38"
Major elements (wt %)							
SiO ₂	60.32	61.16	45.83	47.51	73.85	75.14	75.49
TiO ₂	1.32	1.43	0.75	1.37	0.32	0.34	0.27
Al ₂ O ₃	14.66	14.57	18.47	15.65	12.48	12.09	12.80
MgO	1.67	1.32	7.93	6.49	0.53	0.43	0.59
Fe ₂ O ₃	10.99	10.72	8.65	12.16	4.31	3.72	2.33
CaO	6.17	5.83	12.33	11.85	1.73	1.49	1.29
Na ₂ O	3.75	3.83	2.10	2.11	5.21	5.10	5.79
K ₂ O	0.25	0.21	0.29	0.13	1.08	1.00	0.51
MnO	0.11	0.11	0.14	0.20	0.14	0.13	0.08
Cr ₂ O ₃		0.00	0.06	0.02	0.00	0.00	
P ₂ O ₅	0.60	0.51	0.08	0.13	0.06	0.06	0.06
LOI	0.42	0.23	3.03	2.29	0.54	0.49	0.84
Total	100.25	99.91	99.66	99.91	100.25	99.98	100.04
Trace element (ppm)							
Li	5.87	5.37	6.07	4.92	3.52		0.35
Be	0.70	0.65	0.28	0.42	1.27		0.94
Sc	26.05	25.53	37.07	57.41	14.08		6.74
Ti	7181.21	7226.44	4464.05	9189.21	1912.58		1578.83
V	113.50	147.85	189.27	407.64	17.81		20.26
Cr	9.52	8.04	479.92	183.07	7.68		6.28
Mn	693.84	784.75	1064.17	1663.95	1021.70		311.19
Co	13.03	14.81	31.96	40.56	2.81		2.06
Ni	1.40	1.82	79.57	51.73	2.69		1.62
Cu	6.23	5.51	14.61	89.91	6.38		6.06
Zn	28.57	32.30	46.19	85.06	91.67		30.70
Ga	18.33	17.55	13.87	18.26	17.27		11.86
Rb	3.87	3.51	3.77	1.03	13.45		2.68
Sr	201.46	201.30	207.92	166.13	63.87		90.31
Y	40.60	38.04	16.00	26.50	64.86		42.57
Zr	31.68	21.92	16.98	38.78	43.94		107.00
Nb	0.78	0.79	0.49	0.71	1.74		1.92
Mo	0.41	0.00	bdl	0.03	0.11		0.05
Cd	0.03	0.03	0.04	0.10	0.15		0.06
Cs	0.12	0.12	0.03	0.01	0.10		0.05
Ba	39.24	39.89	42.09	25.25	206.01		78.02
La	4.02	4.43	1.31	2.06	13.88		6.17
Ce	12.30	12.68	4.26	6.70	34.37		19.19
Pr	2.13	2.12	0.76	1.21	4.97		2.75
Nd	11.81	11.57	4.43	6.93	23.01		12.70
Sm	4.15	3.95	1.60	2.55	6.55		3.77
Eu	1.55	1.34	0.67	1.04	1.61		0.77
Gd	5.71	5.19	2.21	3.63	8.18		4.60
Tb	0.95	0.87	0.38	0.62	1.44		0.84
Dy	6.18	5.45	2.50	4.11	9.51		5.62
Ho	1.35	1.18	0.54	0.90	2.13		1.31
Er	3.72	3.29	1.53	2.54	6.35		4.04

Yb	3.23	2.78	1.34	2.31	6.20		4.41
Lu	0.48	0.41	0.20	0.35	0.92		0.69
Hf	1.08	0.73	0.58	1.17	2.01		3.13
Ta	0.07	0.12	0.03	0.05	0.13		0.15
Pb	1.10	1.63	0.78	0.68	2.65		1.12
Th	0.66	0.48	0.08	0.12	1.19		1.18
U	0.19	0.14	0.03	0.05	0.29		0.40
Sr-Nd isotopic data**							
⁸⁷ Sr/ ⁸⁶ Sr	0.702983	0.703023	0.702974	0.702637	0.708406		0.704296
⁸⁷ Rb/ ⁸⁶ Sr	0.055595	0.050490	0.052451	0.017997	0.609653		0.085891
⁸⁷ Sr/ ⁸⁶ Sr (i)	0.702401	0.702495	0.702426	0.702448	0.702027		0.703401
¹⁴³ Nd/ ¹⁴⁴ Nd	0.513076	0.512964	0.513115	0.513121	0.512871		0.512891
¹⁸⁷ Sm/ ¹⁴⁴ Nd	0.212331	0.206266	0.218705	0.222669	0.171980		0.179300
¹⁴³ Nd/ ¹⁴⁴ Nd (i)	0.512056	0.511973	0.512065	0.512051	0.512044		0.512033
εNd (t)	7.182224	5.558700	7.354958	7.089065	6.962900		6.658317
<hr/>							
Sample	S01-1b	S14	S23-1	S23-2	S24	S25-1	S25-2
	Trodj*	Trodj	Tonalite	Trodj	Tonalite	Trodj	Tonalite
Lat.	24°25'17"	24°18'45"	24°22'46"	24°22'46"	24°20'32"	24°17'50"	24°17'50"
Long.	34°35'38"	34°41'49"	34°47'29"	34°47'29"	34°47'00"	34°50'32"	34°50'32"
<hr/>							
Major elements (wt %)							
SiO ₂	75.99	73.61	64.61	78.59	68.97	75.80	65.35
TiO ₂	0.28	0.44	0.75	0.14	0.49	0.25	0.70
Al ₂ O ₃	12.61	13.22	15.46	11.86	15.01	12.85	15.04
MgO	0.54	1.06	1.35	0.14	0.86	0.31	1.03
Fe ₂ O ₃	2.17	2.99	6.27	1.92	4.26	2.76	6.89
CaO	0.96	2.57	4.06	0.72	3.10	1.14	3.45
Na ₂ O	6.19	4.75	5.08	6.32	5.25	5.61	5.14
K ₂ O	0.39	0.36	0.56	0.13	0.77	0.68	0.72
MnO	0.07	0.03	0.18	0.03	0.11	0.03	0.16
Cr ₂ O ₃	0.00		0.01	0.00	0.00	0.00	0.00
P ₂ O ₅	0.06	0.07	0.27	0.03	0.14	0.05	0.25
LOI	0.70	1.04	1.26	0.18	1.07	0.50	1.21
Total	99.96	100.14	99.86	100.07	100.03	99.98	99.94
<hr/>							
Trace element (ppm)							
Li		1.72	1.75	0.32	2.34	1.12	3.21
Be		0.93	1.02	1.28	1.14	1.46	1.06
Sc		9.89	12.60	5.18	10.16	6.57	17.26
Ti		2865.66	3779.53	739.23	2817.39	1404.68	4114.83
V		40.40	26.90	3.28	23.55	5.79	8.24
Cr		11.28	4.40	3.71	5.07	4.87	4.27
Mn		231.55	1103.58	175.33	819.53	200.77	1265.55
Co		6.38	6.64	1.55	5.21	1.88	5.16
Ni		4.40	1.16	0.30	1.27	0.71	0.76
Cu		118.43	3.96	2.64	3.75	2.06	3.56
Zn		17.90	61.17	13.23	69.33	21.96	78.83
Ga		11.75	18.11	14.92	17.15	16.11	18.62
Rb		4.26	6.78	2.06	9.42	7.40	11.11
Sr		108.58	116.38	43.30	97.52	61.49	121.36
Y		47.69	55.50	98.37	53.44	67.74	65.87
Zr		109.14	47.46	153.97	32.44	153.29	84.91
Nb		2.76	1.96	2.83	2.47	2.47	2.64
Mo		0.20	0.00	0.00	0.00	0.00	0.09

Cd	0.05	0.04	0.05	0.07	0.04	0.07
Cs	0.06	0.04	0.01	0.04	0.03	0.04
Ba	100.64	127.26	58.23	162.03	232.42	139.57
La	3.43	6.06	11.31	6.79	7.47	7.34
Ce	9.44	18.93	33.14	20.71	24.43	22.88
Pr	1.60	3.26	5.43	3.40	3.73	3.89
Nd	8.49	17.33	26.62	17.26	18.22	20.44
Sm	3.29	5.71	8.65	5.51	5.83	6.74
Eu	0.78	1.68	0.93	1.42	1.10	1.90
Gd	4.83	7.27	11.10	6.96	7.30	8.56
Tb	0.90	1.27	2.03	1.21	1.36	1.48
Dy	6.20	8.14	13.81	7.81	9.32	9.71
Ho	1.45	1.78	3.10	1.70	2.16	2.13
Er	4.40	5.10	9.50	4.90	6.73	6.21
Yb	4.58	4.69	9.44	4.54	7.09	5.75
Lu	0.70	0.70	1.41	0.67	1.07	0.85
Hf	3.26	1.45	4.91	1.41	4.91	2.38
Ta	0.29	0.12	8.70	0.14	0.18	0.15
Pb	1.27	1.19	1.02	6.70	1.15	1.33
Th	1.81	0.48	1.70	0.60	1.23	0.65
U	0.61	0.15	0.48	0.16	0.39	0.21
Sr-Nd isotopic data**						
⁸⁷ Sr/ ⁸⁶ Sr	0.703551	0.703866	0.703784	0.705077	0.705854	0.704966
⁸⁷ Rb/ ⁸⁶ Sr	0.113423	0.168644	0.137865	0.279597	0.348232	0.264876
⁸⁷ Sr/ ⁸⁶ Sr (i)	0.702382	0.702109	0.702348	0.702163	0.702225	0.702206
¹⁴³ Nd/ ¹⁴⁴ Nd	0.513165	0.513024	0.512991	0.512984	0.513037	0.513013
¹⁸⁷ Sm/ ¹⁴⁴ Nd	0.234588	0.199257	0.196537	0.192807	0.193461	0.199358
¹⁴³ Nd/ ¹⁴⁴ Nd (i)	0.512054	0.512071	0.512051	0.512061	0.512111	0.512059
εNd (t)	6.879977	7.402992	7.014280	7.214755	8.187514	7.173352

-*Blanks = not measured.

-**The initial ⁸⁷Sr/⁸⁶Sr and ¹⁴³Nd/¹⁴⁴Nd ratios were calculated using $\lambda^{87}\text{Rb} = 1.42 \times 10^{-11}$ and $\lambda^{147}\text{Sm} = 6.55 \times 10^{-12}$ and the assigned U-Pb zircon ages were collected from SHRIMP and LASS for each sample. The ¹⁴³Nd/¹⁴⁴Nd isotopic ratios are given as epsilon (ε) notations relative to chondritic uniform reservoir (CHUR) (¹⁴³Nd/¹⁴⁴Nd = 0.512630 and ¹⁴⁷Sm/¹⁴⁴Nd = 0.196; Bouvier, Vervoort and Patchett, 2008):

$$\epsilon\text{Nd}_T = [({}^{143}\text{Nd}/{}^{144}\text{Nd}_{\text{sample}})/({}^{143}\text{Nd}/{}^{144}\text{Nd}_{\text{CHUR}}) - 1] \times 10000.$$

3.6 References

Abd El-Rahman, Y. *et al.* (2017) 'The South Um Mongul Cu-Mo-Au prospect in the Eastern Desert of Egypt: From a mid-Cryogenian continental arc to Ediacaran post-collisional appinite-high Ba-Sr monzogranite', *Ore Geology Reviews*. Elsevier, 80, pp. 250–266. doi: 10.1016/J.OREGEOREV.2016.06.004.

Abd El-Rahman, Y. *et al.* (2019) 'The evolution of the Arabian-Nubian Shield and survival of its zircon U-Pb-Hf-O isotopic signature: A tale from the Um Had Conglomerate, central Eastern Desert, Egypt', *Precambrian Research*. Elsevier, 320, pp. 46–62. doi: 10.1016/J.PRECAMRES.2018.10.011.

Abdel-Rahman, A.-F. M. (2018) 'Geochemistry, age and origin of the Mons Claudianus TTG batholith (Egypt): insight into the role of Pan-African magmatism in uniting plates of Gondwana', *Geological Magazine*. Cambridge University Press, pp. 1–20. doi: 10.1017/S0016756818000304.

Abdel El-Wahed, M. *et al.* (2019) 'Transpressive Structures in the Ghadir Shear Belt, Eastern Desert, Egypt: Evidence for Partitioning of Oblique Convergence in the Arabian-Nubian Shield during Gondwana Agglutination', *Acta Geologica Sinica - English Edition*. Wiley-Blackwell Publishing Asia, 93(6), pp. 1614–1646. doi: 10.1111/1755-6724.13882.

Aldiss, D. T. (1981) 'Plagiogranites from the ocean crust and ophiolites', *Nature*, 289(5798), pp. 577–578. doi: 10.1038/289577a0.

Ali, K. A. *et al.* (2009) 'Geochemistry, Nd isotopes and U-Pb SHRIMP zircon dating of Neoproterozoic volcanic rocks from the Central Eastern Desert of Egypt: New insights into the ~750 Ma crust-forming event', *Precambrian Research*, 171(1–4), pp. 1–22. doi: 10.1016/j.precamres.2009.03.002.

Ali, K. A. *et al.* (2010) 'Age constraints on the formation and emplacement of Neoproterozoic ophiolites along the Allaqi-Heiani Suture, South Eastern Desert of Egypt', *Gondwana Research*, 18(4), pp. 583–595. doi: 10.1016/j.gr.2010.03.002.

Ali, K. A., Moghazi, A.-K. M., *et al.* (2012) 'Composition, age, and origin of the ~620 Ma Humr Akarim and Humrat Mukbid A-type granites: no evidence for pre-Neoproterozoic basement in the Eastern Desert, Egypt', *International Journal of Earth Sciences*. Springer-Verlag, 101(7), pp. 1705–1722. doi: 10.1007/s00531-012-0759-2.

Ali, K. A., Andresen, A., *et al.* (2012) 'U–Pb zircon dating and Sr–Nd–Hf isotopic evidence to support a juvenile origin of the ~ 634 Ma El Shalul granitic gneiss dome, Arabian–Nubian Shield', *Geological Magazine*. Cambridge University Press, 149(5), pp. 783–797. doi: 10.1017/S0016756811000975.

Ali, K. A. *et al.* (2013) 'Hf isotopic composition of single zircons from Neoproterozoic arc volcanics and post-collision granites, Eastern Desert of Egypt: Implications for crustal growth and recycling in the Arabian-Nubian Shield', *Precambrian Research*. Elsevier B.V., 239, pp. 42–55. doi: 10.1016/j.precamres.2013.05.007.

Ali, K. A. *et al.* (2015) 'U–Pb zircon geochronology and Hf–Nd isotopic systematics of Wadi Beitan granitoid gneisses, South Eastern Desert, Egypt', *Gondwana Research*. Elsevier, 27(2), pp. 811–824. doi: 10.1016/J.GR.2013.11.002.

- Amri, I., Benoit, M. and Ceuleneer, G. (1996) 'Tectonic setting for the genesis of oceanic plagiogranites: Evidence from a paleo-spreading structure in the Oman ophiolite', *Earth and Planetary Science Letters*. Elsevier B.V., 139(1–2), pp. 177–194. doi: 10.1016/0012-821x(95)00233-3.
- Anders, E. and Grevesse, N. (1989) 'Abundances of the elements: Meteoritic and solar', *Geochimica et Cosmochimica Acta*. Pergamon, 53(1), pp. 197–214. doi: 10.1016/0016-7037(89)90286-X.
- Andresen, A. *et al.* (2009) 'U-Pb TIMS age constraints on the evolution of the Neoproterozoic Meatiq Gneiss Dome, Eastern Desert, Egypt', *International Journal of Earth Sciences*, 98(3), pp. 481–497. doi: 10.1007/s00531-007-0276-x.
- Augland, L. E., Andresen, A. and Boghdady, G. Y. (2012) 'U–Pb ID-TIMS dating of igneous and metaigneous rocks from the El-Sibai area: time constraints on the tectonic evolution of the Central Eastern Desert, Egypt', *International Journal of Earth Sciences*. Springer-Verlag, 101(1), pp. 25–37. doi: 10.1007/s00531-011-0653-3.
- Barker, F. (1979) 'Trondhjemite: Definition, Environment and Hypotheses of Origin', *Developments in Petrology*. Elsevier, 6, pp. 1–12. doi: 10.1016/B978-0-444-41765-7.50006-X.
- Basta, F. F. *et al.* (2011) 'Neoproterozoic contaminated MORB of Wadi Ghadir ophiolite, NE Africa: Geochemical and Nd and Sr isotopic constraints', *Journal of African Earth Sciences*. Pergamon, 59(2–3), pp. 227–242. doi: 10.1016/j.jafrearsci.2010.10.008.
- Beard, J. S. and Lofgren, G. E. (1991) 'Dehydration Melting and Water-Saturated Melting of Basaltic and Andesitic Greenstones and Amphibolites at 1, 3, and 6. 9 kb', *Journal of Petrology*. Oxford Academic, 32(2), pp. 365–401. doi: 10.1093/PETROLOGY/32.2.365.
- Belousova, E. *et al.* (2002) 'Igneous zircon: trace element composition as an indicator of source rock type', *Contributions to Mineralogy and Petrology*. Springer-Verlag, 143(5), pp. 602–622. doi: 10.1007/s00410-002-0364-7.
- Belousova, E. A. *et al.* (2010) 'The growth of the continental crust: Constraints from zircon Hf-isotope data', *Lithos*. Elsevier, 119(3–4), pp. 457–466. doi: 10.1016/J.LITHOS.2010.07.024.
- Bentor, Y. K. (1985) 'The crustal evolution of the Arabo-Nubian Massif with special reference to the Sinai Peninsula', *Precambrian Research*. Elsevier, 28(1), pp. 1–74. doi: 10.1016/0301-9268(85)90074-9.
- Berndt, J., Koepke, J. and Holtz, F. (2005) 'An Experimental Investigation of the Influence of Water and Oxygen Fugacity on Differentiation of MORB at 200 MPa', *Journal of Petrology*. Oxford Academic, 46(1), pp. 135–167. doi: 10.1093/PETROLOGY/EGH066.
- Bindeman, I. (2008) 'Oxygen isotopes in mantle and crustal magmas as revealed by single crystal analysis', *Reviews in Mineralogy and Geochemistry*, 69, pp. 445–478. doi: 10.2138/rmg.2008.69.12.
- Bosch, D. *et al.* (2004) 'Deep and High-temperature Hydrothermal Circulation in the Petrological and Isotopic Evidence', *Journal of Petrology*, 45(6), pp. 1181–1208. doi: 10.1093/petrology/egh010.

- Bouvier, A., Vervoort, J. D. and Patchett, P. J. (2008) 'The Lu–Hf and Sm–Nd isotopic composition of CHUR: Constraints from unequilibrated chondrites and implications for the bulk composition of terrestrial planets', *Earth and Planetary Science Letters*. Elsevier, 273(1–2), pp. 48–57. doi: 10.1016/J.EPSL.2008.06.010.
- Breitkreuz, C. *et al.* (2010) 'Neoproterozoic SHRIMP U–Pb zircon ages of silica-rich Dokhan Volcanics in the North Eastern Desert, Egypt', *Precambrian Research*. Elsevier, 182(3), pp. 163–174. doi: 10.1016/J.PRECAMRES.2010.06.019.
- Brophy, J. G. (2009) 'La-sio₂ and Yb-SiO₂ systematics in mid-ocean ridge magmas: Implications for the origin of oceanic plagiogranite', *Contributions to Mineralogy and Petrology*, 158(1), pp. 99–111. doi: 10.1007/s00410-008-0372-3.
- Brophy, J. G. and Pu, X. (2012) 'Rare earth element-SiO₂ systematics of mid-ocean ridge plagiogranites and host gabbros from the Fournier oceanic fragment, New Brunswick, Canada: A field evaluation of some model predictions', *Contributions to Mineralogy and Petrology*, 164(2), pp. 191–204. doi: 10.1007/s00410-012-0732-x.
- Bühler, B. *et al.* (2014) 'New insights into the accretion of the Arabian-Nubian Shield: Depositional setting, composition and geochronology of a Mid-Cryogenian arc succession (North Eastern Desert, Egypt)', *Precambrian Research*. Elsevier B.V., 243, pp. 149–167. doi: 10.1016/j.precamres.2013.12.012.
- Carley, T. L. *et al.* (2014) 'Iceland is not a magmatic analog for the Hadean: Evidence from the zircon record', *Earth and Planetary Science Letters*. Elsevier, 405, pp. 85–97. doi: 10.1016/j.epsl.2014.08.015.
- Cawood, P. A. *et al.* (2009) 'Accretionary orogens through Earth history', *Geological Society Special Publication*, 318, pp. 1–36. doi: 10.1144/SP318.1.
- Cawood, P. A. *et al.* (2016) 'Linking collisional and accretionary orogens during Rodinia assembly and breakup: Implications for models of supercontinent cycles', *Earth and Planetary Science Letters*. Elsevier, 449, pp. 118–126. doi: 10.1016/J.EPSL.2016.05.049.
- Coleman, R. G. and Donato, M. M. (1979) *Oceanic plagiogranite revisited*, *Developments in Petrology*. ELSEVIER SCIENTIFIC PUBLISHING COMPANY. doi: 10.1016/B978-0-444-41765-7.50010-1.
- Coleman, R. G. and Peterman, Z. E. (1975) 'Oceanic plagiogranite', *Journal of Geophysical Research*, 80(8), pp. 1099–1108. doi: 10.1029/jb080i008p01099.
- Collins, A. S. and Pisarevsky, S. A. (2005) 'Amalgamating eastern Gondwana: The evolution of the Circum-Indian Orogens', *Earth-Science Reviews*. Elsevier, 71(3–4), pp. 229–270. doi: 10.1016/J.EARSCIREV.2005.02.004.
- Currin, A. *et al.* (2018) 'Chlorine-rich amphibole in deep layered gabbros as evidence for brine/rock interaction in the lower oceanic crust: A case study from the Wadi Wariyah, Samail Ophiolite, Sultanate of Oman', *Lithos*. Elsevier B.V., 323, pp. 125–136. doi: 10.1016/j.lithos.2018.09.015.
- Denyszyn, S. W. *et al.* (2009) 'Paleomagnetism and U-Pb geochronology of Franklin dykes in High Arctic Canada and Greenland: a revised age and paleomagnetic pole constraining block rotations in the Nares Strait region 1', *Canadian Journal of Earth Sciences*, 46, pp.

155–167. doi: 10.1139/E09-042.

Dick, H. J. B. *et al.* (2000) ‘A long in situ section of the lower ocean crust: Results of ODP Leg 176 drilling at the Southwest Indian Ridge’, *Earth and Planetary Science Letters*, 179(1), pp. 31–51. doi: 10.1016/S0012-821X(00)00102-3.

Dixon-Spulber, S. and Rutherford, M. J. (1983) ‘The Origin of Rhyolite and Plagiogranite in Oceanic Crust: An Experimental Study’, *Journal of Petrology*. Oxford Academic, 24(1), pp. 1–25. doi: 10.1093/PETROLOGY/24.1.1.

Dixon, T. H. (1981) ‘Gebel Dahanib, Egypt: A Late Precambrian Layered Sill of Komatiitic Composition T.H.’, *Contribution to Mineralogy and Petrology Mineral Petrol*, 76, pp. 42–52.

Eiler, J. M. (2001) ‘Oxygen isotope variations of basaltic lavas and upper mantle rocks’, *Reviews in Mineralogy and Geochemistry*. Mineralogical Society of America, 43(1), pp. 319–364. doi: 10.2138/gsrmg.43.1.319.

El-Bialy, M. Z. and Streck, M. J. (2009) ‘Late Neoproterozoic alkaline magmatism in the Arabian–Nubian Shield: the postcollisional A-type granite of Sahara–Umm Adawi pluton, Sinai, Egypt’, *Arabian Journal of Geosciences*. Springer-Verlag, 2(2), pp. 151–174. doi: 10.1007/s12517-008-0025-x.

Eliwa, H. A. *et al.* (2014) ‘SIMS zircon U–Pb and mica K–Ar geochronology, and Sr–Nd isotope geochemistry of Neoproterozoic granitoids and their bearing on the evolution of the north Eastern Desert, Egypt’, *Gondwana Research*. Elsevier, 25(4), pp. 1570–1598. doi: 10.1016/J.GR.2013.06.006.

Farahat, E. S. *et al.* (2007) ‘Origin of I- and A-type granitoids from the Eastern Desert of Egypt: Implications for crustal growth in the northern Arabian–Nubian Shield’, *Journal of African Earth Sciences*. Pergamon, 49(1–2), pp. 43–58. doi: 10.1016/J.JAFREARSCI.2007.07.002.

Fischer, L. A. *et al.* (2016) ‘Trace element evidence for anatexis at oceanic magma chamber roofs and the role of partial melts for contamination of fresh MORB’, *Lithos*. Elsevier B.V., 260, pp. 1–8. doi: 10.1016/j.lithos.2016.05.001.

Flagler, P. A. and Spray, J. G. (1991) ‘Generation of plagiogranite by amphibolite anatexis in oceanic shear zones’, *Geology*, 19(1), pp. 70–73. doi: 10.1130/0091-7613(1991)019<0070:GOPBAA>2.3.CO;2.

Floyd, P. A., Yaliniz, M. K. and Goncuoglu, M. C. (1998) ‘Geochemistry and petrogenesis of intrusive and extrusive ophiolitic plagiogranites, Central Anatolian Crystalline Complex, Turkey’, *Lithos*, 42(3–4), pp. 225–241. doi: 10.1016/s0024-4937(97)00044-3.

France, L. *et al.* (2010) ‘Hydrous partial melting in the sheeted dike complex at fast spreading ridges: Experimental and natural observations’, *Contributions to Mineralogy and Petrology*, 160(5), pp. 683–704. doi: 10.1007/s00410-010-0502-6.

France, L. *et al.* (2014) ‘Contamination of MORB by anatexis of magma chamber roof rocks: Constraints from a geochemical study of experimental melts and associated residues’, *Lithos*. Elsevier, 202–203, pp. 120–137. doi: 10.1016/j.lithos.2014.05.018.

- France, L., Ildefonse, B. and Koepke, J. (2009) 'Interactions between magma and hydrothermal system in Oman ophiolite and in IODP Hole 1256D: Fossilization of a dynamic melt lens at fast spreading ridges', *Geochemistry, Geophysics, Geosystems*. John Wiley & Sons, Ltd, 10(10). doi: 10.1029/2009GC002652.
- Freund, S. *et al.* (2014) 'Constraints on the formation of geochemically variable plagiogranite intrusions in the Troodos Ophiolite, Cyprus', *Contributions to Mineralogy and Petrology*. Springer Verlag, 167(2), pp. 1–22. doi: 10.1007/s00410-014-0978-6.
- Frimmel, H. E., Hartnady, C. J. H. and Koller, F. (1996) 'Geochemistry and tectonic setting of magmatic units in the Pan-African Gariep Belt, Namibia', *Chemical Geology*. Elsevier B.V., 130(1–2), pp. 101–121. doi: 10.1016/0009-2541(95)00188-3.
- Frimmel, H. E., Zartman, R. E. and Späth, A. (2002) 'The Richtersveld Igneous Complex, South Africa: U-Pb Zircon and Geochemical Evidence for the Beginning of Neoproterozoic Continental Breakup', *The Journal of Geology*, 109(4), pp. 493–508. doi: 10.1086/320795.
- Fritz, H. *et al.* (2013) 'Orogen styles in the East African Orogen: A review of the Neoproterozoic to Cambrian tectonic evolution', *Journal of African Earth Sciences*. Elsevier Ltd, 86, pp. 65–106. doi: 10.1016/j.jafrearsci.2013.06.004.
- Gerlach, D. C., Leeman, W. P. and Avé Lallemant, H. G. (1981) 'Petrology and geochemistry of plagiogranite in the Canyon Mountain ophiolite, Oregon', *Contributions to Mineralogy and Petrology*. Springer-Verlag, 77(1), pp. 82–92. doi: 10.1007/BF01161505.
- Gharib, M. E. and Ahmed, A. H. (2012) 'Late Neoproterozoic volcanics and associated granitoids at Wadi Ranga, south Eastern Desert, Egypt: A transition from subduction related to intra-arc magmatism', *Lithos*. Elsevier B.V., 155, pp. 236–255. doi: 10.1016/j.lithos.2012.09.004.
- Gillis, K. M. *et al.* (2014) 'Primitive layered gabbros from fast-spreading lower oceanic crust', *Nature*. Nature Publishing Group, 505(7482), pp. 204–207. doi: 10.1038/nature12778.
- Gillis, K. M. and Coogan, L. A. (2002) 'Anatectic Migmatites from the Roof of an Ocean Ridge Magma Chamber', *Journal of Petrology*. Oxford Academic, 43(11), pp. 2075–2095. doi: 10.1093/petrology/43.11.2075.
- Goldstein, S. L., O'Nions, R. K. and Hamilton, P. J. (1984) 'A Sm-Nd isotopic study of atmospheric dusts and particulates from major river systems', *Earth and Planetary Science Letters*. Elsevier, 70(2), pp. 221–236. doi: 10.1016/0012-821X(84)90007-4.
- Griffin, W. . *et al.* (2002) 'Zircon chemistry and magma mixing, SE China: In-situ analysis of Hf isotopes, Tonglu and Pingtan igneous complexes', *Lithos*. Elsevier, 61(3–4), pp. 237–269. doi: 10.1016/S0024-4937(02)00082-8.
- Grimes, C. B. *et al.* (2007) 'Trace element chemistry of zircons from oceanic crust: A method for distinguishing detrital zircon provenance', *Geology*, 35(7), pp. 643–646. doi: 10.1130/G23603A.1.
- Grimes, C. B. *et al.* (2011) 'Uniformly mantle-like $\delta^{18}\text{O}$ in zircons from oceanic plagiogranites and gabbros', *Contributions to Mineralogy and Petrology*, 161(1), pp. 13–33. doi: 10.1007/s00410-010-0519-x.

- Grimes, C. B. *et al.* (2013) ‘Perspectives on the origin of plagiogranite in ophiolites from oxygen isotopes in zircon’, *Lithos*, 179, pp. 48–66. doi: 10.1016/j.lithos.2013.07.026.
- Grimes, C. B. *et al.* (2015) “‘Fingerprinting’ tectono-magmatic provenance using trace elements in igneous zircon’, *Contributions to Mineralogy and Petrology*. Springer Verlag, 170(5–6), pp. 1–26. doi: 10.1007/s00410-015-1199-3.
- Haase, K. M. *et al.* (2016) ‘Constraints on the magmatic evolution of the oceanic crust from plagiogranite intrusions in the Oman ophiolite’, *Contributions to Mineralogy and Petrology*. Springer Verlag, 171(5). doi: 10.1007/s00410-016-1261-9.
- Hawkesworth, C. J. and Kemp, A. I. S. (2006) ‘Using hafnium and oxygen isotopes in zircons to unravel the record of crustal evolution’, *Chemical Geology*. Elsevier, 226(3–4), pp. 144–162. doi: 10.1016/j.chemgeo.2005.09.018.
- Heaman, L. M., LeCheminant, A. N. and Rainbird, R. H. (1992) ‘Nature and timing of Franklin igneous events, Canada: Implications for a Late Proterozoic mantle plume and the break-up of Laurentia’, *Earth and Planetary Science Letters*. Elsevier, 109(1–2), pp. 117–131. doi: 10.1016/0012-821X(92)90078-A.
- Hildebrand, R. S., Whalen, J. B. and Bowring, S. A. (2018) ‘Resolving the crustal composition paradox by 3.8 billion years of slab failure magmatism and collisional recycling of continental crust’, *Tectonophysics*. Elsevier, 734–735, pp. 69–88. doi: 10.1016/J.TECTO.2018.04.001.
- Hoffman, P. F. (1991) ‘Did the breakout of laurentia turn gondwanaland inside-out?’, *Science (New York, N.Y.)*. American Association for the Advancement of Science, 252(5011), pp. 1409–12. doi: 10.1126/science.252.5011.1409.
- Hoskin, P. W. O. and Schaltegger, U. (2003) ‘The Composition of Zircon and Igneous and Metamorphic Petrogenesis’, *Reviews in Mineralogy and Geochemistry*. GeoScienceWorld, 53(1), pp. 27–62. doi: 10.2113/0530027.
- Johnson, P. R. *et al.* (2011) ‘Late Cryogenian-Ediacaran history of the Arabian-Nubian Shield: A review of depositional, plutonic, structural, and tectonic events in the closing stages of the northern East African Orogen’, *Journal of African Earth Sciences*. Elsevier Ltd, 61(3), pp. 167–232. doi: 10.1016/j.jafrearsci.2011.07.003.
- Johnson, P. R. and Woldehaimanot, B. (2003) ‘Development of the Arabian-Nubian Shield: perspectives on accretion and deformation in the northern East African Orogen and the assembly of Gondwana’, *Geological Society, London, Special Publications*, 206(1), pp. 289–325. doi: 10.1144/GSL.SP.2003.206.01.15.
- Katzir, Y. *et al.* (2007) ‘Interrelations between coeval mafic and A-type silicic magmas from composite dykes in a bimodal suite of southern Israel, northernmost Arabian–Nubian Shield: Geochemical and isotope constraints’, *Lithos*. Elsevier, 97(3–4), pp. 336–364. doi: 10.1016/J.LITHOS.2007.01.004.
- Kemp, A. I. S. *et al.* (2006) ‘Episodic growth of the Gondwana supercontinent from hafnium and oxygen isotopes in zircon’, *Nature*. Nature Publishing Group, 439(7076), pp. 580–583. doi: 10.1038/nature04505.
- Kemp, A. I. S. *et al.* (2007) ‘Magmatic and crustal differentiation history of granitic rocks

- from Hf-O isotopes in zircon.’, *Science (New York, N.Y.)*. American Association for the Advancement of Science, 315(5814), pp. 980–3. doi: 10.1126/science.1136154.
- Kemp, A. I. S. and Hawkesworth, C. J. (2014) ‘Growth and Differentiation of the Continental Crust from Isotope Studies of Accessory Minerals’, in *Treatise on Geochemistry*. Elsevier, pp. 379–421. doi: 10.1016/B978-0-08-095975-7.00312-0.
- Khedr, M. Z. *et al.* (2020) ‘Petrogenesis of the ~740 Korab Kansi mafic-ultramafic intrusion, South Eastern Desert of Egypt: Evidence of Ti-rich ferropicritic magmatism’, *Gondwana Research*. Elsevier Inc., 82, pp. 48–72. doi: 10.1016/j.gr.2019.12.013.
- Khudeir, A., Ali, M. and El Habaak, G. (1988) ‘The metavolcanics at Um Samiuku area, Egypt’, *Bulletin Faculty of Science, Assuit University*, 17, pp. 73–101.
- Kinny, P. D., Compston, W. and Williams, I. S. (1991) ‘A reconnaissance ion-probe study of hafnium isotopes in zircons’, *Geochimica et Cosmochimica Acta*. Pergamon, 55(3), pp. 849–859. doi: 10.1016/0016-7037(91)90346-7.
- Kinny, P. D. and Maas, R. (2003) ‘Lu-Hf and Sm-Nd isotope systems in zircon’, *Reviews in Mineralogy and Geochemistry*. GeoScienceWorld, 53(1), pp. 327–341. doi: 10.2113/0530327.
- Kirkland, C. L. *et al.* (2015) ‘Zircon Th/U ratios in magmatic environs’, *Lithos*. Elsevier, 212–215, pp. 397–414. doi: 10.1016/j.lithos.2014.11.021.
- Koepke, J. *et al.* (2004) ‘Petrogenesis of oceanic plagiogranites by partial melting of gabbros: An experimental study’, *Contributions to Mineralogy and Petrology*, 146(4), pp. 414–432. doi: 10.1007/s00410-003-0511-9.
- Koepke, J. *et al.* (2007) ‘The formation of SiO₂-rich melts within the deep oceanic crust by hydrous partial melting of gabbros’, *Contributions to Mineralogy and Petrology*, 153(1), pp. 67–84. doi: 10.1007/s00410-006-0135-y.
- Koepke, J. *et al.* (2011) ‘Gabbros from IODP Site 1256, equatorial Pacific: Insight into axial magma chamber processes at fast spreading ocean ridges’, *Geochemistry, Geophysics, Geosystems*. Blackwell Publishing Ltd, 12(9). doi: 10.1029/2011GC003655.
- Koepke, J., Feig, S. T. and Snow, J. (2005) ‘Hydrous partial melting within the lower oceanic crust’, *Terra Nova*, 17(3), pp. 286–291. doi: 10.1111/j.1365-3121.2005.00613.x.
- Kröner, A. *et al.* (1991) ‘Evolution of Pan-African island arc assemblages in the southern Red Sea Hills, Sudan, and in southwestern Arabia as exemplified by geochemistry and geochronology’, *Precambrian Research*. Elsevier, 53(1–2), pp. 99–118. doi: 10.1016/0301-9268(91)90007-W.
- Kröner, A. *et al.* (1992) ‘Dating of late Proterozoic ophiolites in Egypt and the Sudan using the single grain zircon evaporation technique’, *Precambrian Research*, 59(1–2), pp. 15–32. doi: 10.1016/0301-9268(92)90049-T.
- Kroner, A., Kruger, J. and Rashwan, A. A. A. (1994) ‘Age and tectonic setting of granitoid gneisses in the Eastern Desert of Egypt and south-west Sinai’, *Geologische Rundschau*. Springer-Verlag, 83(3), pp. 502–513. doi: 10.1007/BF00194157.

- Laurent, O. *et al.* (2014) ‘The diversity and evolution of late-Archean granitoids: Evidence for the onset of “modern-style” plate tectonics between 3.0 and 2.5 Ga’, *Lithos*. Elsevier, 205, pp. 208–235. doi: 10.1016/J.LITHOS.2014.06.012.
- Lehmann, B. *et al.* (2020) ‘Monazite and cassiterite U Pb dating of the Abu Dabbab rare-metal granite, Egypt: Late Cryogenian metalliferous granite magmatism in the Arabian-Nubian Shield’, *Gondwana Research*. Elsevier. doi: 10.1016/j.gr.2020.03.001.
- Li, X. H. *et al.* (2003) ‘Neoproterozoic granitoids in South China: Crustal melting above a mantle plume at ca. 825 Ma?’, *Precambrian Research*, 122(1–4), pp. 45–83. doi: 10.1016/S0301-9268(02)00207-3.
- Li, Z. . *et al.* (1999) ‘The breakup of Rodinia: did it start with a mantle plume beneath South China?’, *Earth and Planetary Science Letters*. Elsevier, 173(3), pp. 171–181. doi: 10.1016/S0012-821X(99)00240-X.
- Li, Z. X. *et al.* (2003) ‘Geochronology of Neoproterozoic syn-rift magmatism in the Yangtze Craton, South China and correlations with other continents: Evidence for a mantle superplume that broke up Rodinia’, *Precambrian Research*, 122(1–4), pp. 85–109. doi: 10.1016/S0301-9268(02)00208-5.
- Li, Z. X. *et al.* (2008) ‘Assembly, configuration, and break-up history of Rodinia: A synthesis’, *Precambrian Research*, 160(1–2), pp. 179–210. doi: 10.1016/j.precamres.2007.04.021.
- Li, Z. X., Evans, D. A. D. and Halverson, G. P. (2013) ‘Neoproterozoic glaciations in a revised global palaeogeography from the breakup of Rodinia to the assembly of Gondwanaland’, *Sedimentary Geology*. Elsevier B.V., 294, pp. 219–232. doi: 10.1016/j.sedgeo.2013.05.016.
- Li, Z. X. and Zhong, S. (2009) ‘Supercontinent-superplume coupling, true polar wander and plume mobility: Plate dominance in whole-mantle tectonics’, *Physics of the Earth and Planetary Interiors*, 176(3–4), pp. 143–156. doi: 10.1016/j.pepi.2009.05.004.
- Lundmark, A. M. *et al.* (2012) ‘Repeated magmatic pulses in the East African Orogen in the Eastern Desert, Egypt: An old idea supported by new evidence’, *Gondwana Research*. International Association for Gondwana Research, 22(1), pp. 227–237. doi: 10.1016/j.gr.2011.08.017.
- Maniar, D. and Piccoli, M. (1989) ‘Tectonic discrimination of granitoids’, *Geological Society of America Bulletin*. GeoScienceWorld, 101(5), pp. 635–643. doi: 10.1130/0016-7606(1989)101<0635:TDOG>2.3.CO;2.
- Marien, C. S. *et al.* (2019) ‘Petrogenesis of plagiogranites from the Troodos Ophiolite Complex, Cyprus’, *Contributions to Mineralogy and Petrology*. Springer Verlag, 174(4). doi: 10.1007/s00410-019-1569-3.
- Maurice, A. E. *et al.* (2013) ‘Geochemistry of gabbros and granitoids (M- and I-types) from the Nubian Shield of Egypt: Roots of Neoproterozoic intra-oceanic island arc’, *Precambrian Research*. Elsevier B.V., 224, pp. 397–411. doi: 10.1016/j.precamres.2012.10.012.
- Maurice, A. E., Basta, F. F. and Khiamy, A. A. (2012) ‘Neoproterozoic nascent island arc volcanism from the Nubian Shield of Egypt: Magma genesis and generation of continental

- crust in intra-oceanic arcs', *Lithos*. Elsevier B.V., 132–133, pp. 1–20. doi: 10.1016/j.lithos.2011.11.013.
- Meert, J. G. (2003) 'A synopsis of events related to the assembly of the eastern Gondwana', *Tectonophysics*. Elsevier B.V., 362(1–4), pp. 1–40. doi: 10.1016/S0040-1951(02)00629-7.
- Meert, J. G. and Lieberman, B. S. (2008) 'The Neoproterozoic assembly of Gondwana and its relationship to the Ediacaran–Cambrian radiation', *Gondwana Research*. Elsevier, 14(1–2), pp. 5–21. doi: 10.1016/J.GR.2007.06.007.
- Merdith, A. S. *et al.* (2017) 'A full-plate global reconstruction of the Neoproterozoic', *Gondwana Research*. International Association for Gondwana Research, 50, pp. 84–134. doi: 10.1016/j.gr.2017.04.001.
- Middlemost, E. A. K. (1994) 'Naming materials in the magma/igneous rock system', *Earth-Science Reviews*. Elsevier, 37(3–4), pp. 215–224. doi: 10.1016/0012-8252(94)90029-9.
- Morag, N. *et al.* (2011) 'Crustal evolution and recycling in the northern Arabian-Nubian Shield: New perspectives from zircon Lu–Hf and U–Pb systematics', *Precambrian Research*. Elsevier, 186(1–4), pp. 101–116. doi: 10.1016/J.PRECAMRES.2011.01.004.
- Morag, N. *et al.* (2012) '1000–580 Ma crustal evolution in the northern Arabian-Nubian Shield revealed by U–Pb–Hf of detrital zircons from late Neoproterozoic sediments (Elat area, Israel)', *Precambrian Research*. Elsevier, 208–211, pp. 197–212. doi: 10.1016/J.PRECAMRES.2012.04.009.
- Moussa, E. M. M. *et al.* (2008) 'SHRIMP zircon dating and Sm/Nd isotopic investigations of Neoproterozoic granitoids, Eastern Desert, Egypt', *Precambrian Research*, 160(3–4), pp. 341–356. doi: 10.1016/j.precamres.2007.08.006.
- Moyen, J. F. (2011) 'The composite Archaean grey gneisses: Petrological significance, and evidence for a non-unique tectonic setting for Archaean crustal growth', *Lithos*, 123(1–4), pp. 21–36. doi: 10.1016/j.lithos.2010.09.015.
- O'Connor, J. T. (1965) 'A classification of quartz rich igneous rock based on feldspar ratios.', *US Geological Survey*, 525B, pp. B79–B84. Available at: [https://www.scirp.org/\(S\(i43dyn45teexjx455qlt3d2q\)\)/reference/ReferencesPapers.aspx?ReferenceID=531502](https://www.scirp.org/(S(i43dyn45teexjx455qlt3d2q))/reference/ReferencesPapers.aspx?ReferenceID=531502) (Accessed: 3 September 2019).
- Pallister, J. S. and Hopson, C. A. (1981) 'Pallister and Hopson (1981) - Samail ophiolite plutonic suite - field relations, phase variation, cryptic variation and layering, and a model of a spreading ridge magma chamber.pdf', 86.
- Patchett, P. J. *et al.* (1981) 'Evolution of continental crust and mantle heterogeneity: Evidence from Hf isotopes', *Contributions to Mineralogy and Petrology*. Springer-Verlag, 78(3), pp. 279–297. doi: 10.1007/BF00398923.
- Patchett, P. J. (1983) 'Importance of the Lu-Hf isotopic system in studies of planetary chronology and chemical evolution', *Geochimica et Cosmochimica Acta*. Pergamon, 47(1), pp. 81–91. doi: 10.1016/0016-7037(83)90092-3.
- Pearce, J. (1996) 'Sources and settings of granitic rocks', *Episodes*, 19(4), pp. 120–125. doi: 10.18814/epiiugs/1996/v19i4/005.

- Pearce, J. A., Harris, N. B. W. and Tindle, A. G. (1984) 'Trace Element Discrimination Diagrams for the Tectonic Interpretation of Granitic Rocks', *Journal of Petrology*. Narnia, 25(4), pp. 956–983. doi: 10.1093/petrology/25.4.956.
- Pease, V. and Johnson, P. R. (2013) 'Introduction to the JEBEL volume of Precambrian Research', *Precambrian Research*, 239, pp. 1–5. doi: 10.1016/j.precamres.2013.10.003.
- Peccerillo, A. *et al.* (2003) 'Relationships between Mafic and Peralkaline Silicic Magmatism in Continental Rift Settings: a Petrological, Geochemical and Isotopic Study of the Gedemsa Volcano, Central Ethiopian Rift', *Journal of Petrology*. Oxford Academic, 44(11), pp. 2003–2032. doi: 10.1093/petrology/egg068.
- Peccerillo, A. and Taylor, S. R. (1976) 'Geochemistry of eocene calc-alkaline volcanic rocks from the Kastamonu area, Northern Turkey', *Contributions to Mineralogy and Petrology*. Springer-Verlag, 58(1), pp. 63–81. doi: 10.1007/BF00384745.
- Pedersen, R. B. and Malpas, J. (1984) 'The origin of oceanic plagiogranites from the karmoy ophiolite, western Norway', *Contributions to Mineralogy and Petrology*. Springer-Verlag, 88(1–2), pp. 36–52. doi: 10.1007/BF00371410.
- Reymer, A. and Schubert, G. (1986) 'Rapid growth of some major segments of continental crust', *Geology*. GeoScienceWorld, 14(4), p. 299. doi: 10.1130/0091-7613(1986)14<299:RGOSMS>2.0.CO;2.
- Robinson, F. A. *et al.* (2014) 'Arabian Shield magmatic cycles and their relationship with Gondwana assembly: Insights from zircon U-Pb and Hf isotopes', *Earth and Planetary Science Letters*. Elsevier B.V., 408, pp. 207–225. doi: 10.1016/j.epsl.2014.10.010.
- Robinson, F. A. *et al.* (2017) 'A discussion on the tectonic implications of Ediacaran late- to post-orogenic A-type granite in the northeastern Arabian Shield, Saudi Arabia', *Tectonics*. John Wiley & Sons, Ltd, 36(3), pp. 582–600. doi: 10.1002/2016TC004320.
- Rollinson, H. (2008) 'Ophiolitic trondhjemites: A possible analogue for Hadean felsic "crust"', *Terra Nova*, 20(5), pp. 364–369. doi: 10.1111/j.1365-3121.2008.00829.x.
- Rollinson, H. (2009) 'New models for the genesis of plagiogranites in the Oman ophiolite', *Lithos*, 112(3–4), pp. 603–614. doi: 10.1016/j.lithos.2009.06.006.
- Rollinson, H. (2014) 'Plagiogranites from the mantle section of the Oman Ophiolite: Models for early crustal evolution', *Geological Society Special Publication*, 392(1), pp. 247–261. doi: 10.1144/SP392.13.
- Rudnick, R. L. and Gao, S. (2014) 'Composition of the Continental Crust', in *Treatise on Geochemistry*. Elsevier, pp. 1–51. doi: 10.1016/B978-0-08-095975-7.00301-6.
- Sawyer, E. W. (2001) 'Melt segregation in the continental crust: Distribution and movement of melt in anatectic rocks', *Journal of Metamorphic Geology*. John Wiley & Sons, Ltd, 19(3), pp. 291–309. doi: 10.1046/j.0263-4929.2000.00312.x.
- Shukri, N. M. and Mansour, M. S. (1980) 'Lithostratigraphy of Um Samuiki District, Eastern Desert, Egypt', *Institute Applied Geology, University of Jeddah Bulletin*, 4, pp. 83–93. doi: 10.1016/b978-0-08-024481-5.50012-1.

- Stakes, D. S. and Taylor, H. P. (2003) 'Oxygen isotope and chemical studies on the origin of large plagiogranite bodies in northern Oman, and their relationship to the overlying massive sulphide deposits', *Geological Society Special Publication*, 218(1), pp. 315–351. doi: 10.1144/GSL.SP.2003.218.01.17.
- Stein, M. (2003) 'Tracing the plume material in the Arabian-Nubian Shield', *Precambrian Research*, 123(2–4), pp. 223–234. doi: 10.1016/S0301-9268(03)00069-X.
- Stein, M. and Goldstein, S. L. (1996) 'From plume head to continental lithosphere in the Arabian–Nubian shield', *Nature*, 382, pp. 773–778. Available at: <https://doi.org/10.1038/382773a0>.
- Stern, R. J. (1994) 'ARC Assembly and Continental Collision in the Neoproterozoic East African Orogen: Implications for the Consolidation of Gondwanaland', *Annual Review of Earth and Planetary Sciences*, 22(1), pp. 319–351. doi: 10.1146/annurev.earth.22.050194.001535.
- Stern, R. J. (2002) 'Crustal evolution in the East African Orogen: a neodymium isotopic perspective', *Journal of African Earth Sciences*. Pergamon, 34(3–4), pp. 109–117. doi: 10.1016/S0899-5362(02)00012-X.
- Stern, R. J. *et al.* (2004) 'Neoproterozoic Ophiolites of the Arabian-Nubian Shield', *Developments in Precambrian Geology*, 13(C), pp. 95–128. doi: 10.1016/S0166-2635(04)13003-X.
- Stern, R. J. and Hedge, C. E. (1985) 'Geochronologic and isotopic constraints on late Precambrian crustal evolution in the Eastern Desert of Egypt', *American Journal of Science*, 285, pp. 97–127. doi: 10.2475/ajs.285.2.97.
- Stern, R. J., Kröner, A. and Rashwan, A. A. (1991) 'A late Precambrian (~ 710 Ma) high volcanicity rift in the southern Eastern Desert of Egypt', *Geologische Rundschau*, 80(1), pp. 155–170. doi: 10.1007/BF01828773.
- Sun, S. -s. and McDonough, W. . (1989) 'Chemical and isotopic systematics of oceanic basalts: implications for mantle composition and processes', *Geological Society, London, Special Publications*, 42, pp. 313–345. doi: 10.1144/GSL.SP.1989.042.01.19.
- Tao, C. *et al.* (2020) 'Deep high-temperature hydrothermal circulation in a detachment faulting system on the ultra-slow spreading ridge', *Nature Communications*. Springer US, 11(1), pp. 1–9. doi: 10.1038/s41467-020-15062-w.
- Thy, P., Leshner, C. E. and Mayfield, J. D. (1999) *Low-pressure melting studies of basalt and basaltic andesite from the southeast Greenland continental margin and the origin of dacites at site 917, Proceedings of the Ocean Drilling Program*.
- Valley, J. W. *et al.* (1998) 'Zircon megacrysts from kimberlite: oxygen isotope variability among mantle melts', *Contributions to Mineralogy and Petrology*. Springer Berlin Heidelberg, 133(1–2), pp. 1–11. doi: 10.1007/s004100050432.
- Valley, J. W. (2003) 'Oxygen Isotopes in Zircon', *Reviews in Mineralogy and Geochemistry*. GeoScienceWorld, 53(1), pp. 343–385. doi: 10.2113/0530343.
- Valley, J. W. *et al.* (2005a) '4.4 billion years of crustal maturation: oxygen isotope ratios of

magmatic zircon', *Contributions to Mineralogy and Petrology*. Springer-Verlag, 150(6), pp. 561–580. doi: 10.1007/s00410-005-0025-8.

Valley, J. W. *et al.* (2005b) '4.4 billion years of crustal maturation: oxygen isotope ratios of magmatic zircon', *Contributions to Mineralogy and Petrology*. Springer-Verlag, 150(6), pp. 561–580. doi: 10.1007/s00410-005-0025-8.

Vervoort, J. D. and Blichert-Toft, J. (1999) 'Evolution of the depleted mantle: Hf isotope evidence from juvenile rocks through time', *Geochimica et Cosmochimica Acta*. Pergamon, 63(3–4), pp. 533–556. doi: 10.1016/S0016-7037(98)00274-9.

Wang, H. *et al.* (2016) 'Continental growth through accreted oceanic arc: Zircon Hf-O isotope evidence for granitoids from the Qinling orogen', *Geochimica et Cosmochimica Acta*. Elsevier Ltd, 182, pp. 109–130. doi: 10.1016/j.gca.2016.03.016.

Whattam, S. A. *et al.* (2016) 'Origin of plagiogranites in oceanic complexes: A case study of the Nicoya and Santa Elena terranes, Costa Rica', *Lithos*. Elsevier B.V., 262, pp. 75–87. doi: 10.1016/j.lithos.2016.06.017.

White, W. M. and Klein, E. M. (2014) 'Composition of the Oceanic Crust', *Treatise on Geochemistry*. Elsevier, pp. 457–496. doi: 10.1016/B978-0-08-095975-7.00315-6.

Wilde, S. A. and Youssed, K. (2002) 'A re-evaluation of the origin and setting of the Late Precambrian Hammamat Group based on SHRIMP U–Pb dating of detrital zircons from Gebel Umm Tawat, North Eastern Desert, Egypt', *Journal of the Geological Society*, 159(5), pp. 595–604. doi: 10.1144/0016-764901-081.

Wilde, S. A. and Youssef, K. (2000) 'Significance of SHRIMP U-Pb dating of the Imperial Porphyry and associated Dokhan Volcanics, Gebel Dokhan, north Eastern Desert, Egypt', *Journal of African Earth Sciences*. Pergamon, 31(2), pp. 403–413. doi: 10.1016/S0899-5362(00)00096-8.

Wolff, P. E., Koepke, J. and Feig, S. T. (2013) 'The reaction mechanism of fluid-induced partial melting of gabbro in the oceanic crust', *European Journal of Mineralogy*, 25(3), pp. 279–298. doi: 10.1127/0935-1221/2013/0025-2314.

Xiong, X. *et al.* (2011) 'Partitioning of Nb and Ta between rutile and felsic melt and the fractionation of Nb/Ta during partial melting of hydrous metabasalt', *Geochimica et Cosmochimica Acta*. Pergamon, 75(7), pp. 1673–1692. doi: 10.1016/j.gca.2010.06.039.

Xu, Y. *et al.* (2017) 'Petrogenesis and tectonic implications of gabbro and plagiogranite intrusions in mantle peridotites of the Myitkyina ophiolite, Myanmar', *Lithos*. Elsevier B.V., 284–285, pp. 180–193. doi: 10.1016/j.lithos.2017.04.014.

Yakymchuk, C., Kirkland, C. L. and Clark, C. (2018) 'Th/U ratios in metamorphic zircon', *Journal of Metamorphic Geology*. John Wiley & Sons, Ltd (10.1111), 36(6), pp. 715–737. doi: 10.1111/jmg.12307.

Zhang, C. *et al.* (2017) 'Felsic Plutonic Rocks from IODP Hole 1256D, Eastern Pacific: Implications for the Nature of the Axial Melt Lens at Fast-Spreading Mid-Ocean Ridges', *Journal of Petrology*, 58(8), pp. 1535–1566. doi: 10.1093/petrology/egx064.

Zhang, C. L. *et al.* (2006) 'Neoproterozoic bimodal intrusive complex in the southwestern

Tarim Block, northwest China: Age, geochemistry, and implications for the rifting of Rodinia', *International Geology Review*. Taylor & Francis Group , 48(2), pp. 112–128. doi: 10.2747/0020-6814.48.2.112.

Zihlmann, B. *et al.* (2018) 'Hydrothermal fault zones in the lower oceanic crust: An example from Wadi Gideah, Samail ophiolite, Oman', *Lithos*. Elsevier B.V., 323, pp. 103–124. doi: 10.1016/j.lithos.2018.09.008.

Zimmer, M. *et al.* (1995) 'The Gabal Gerf complex: A precambrian N-MORB ophiolite in the Nubian Shield, NE Africa', *Chemical Geology*. Elsevier, 123(1–4), pp. 29–51. doi: 10.1016/0009-2541(95)00018-H.

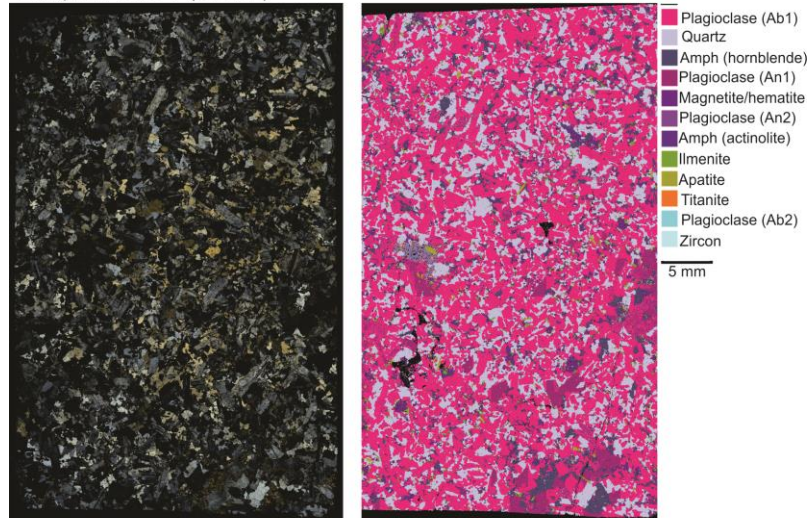
Zoheir, B. *et al.* (2020) 'Geochemical and geochronological characteristics of the Um Rus granite intrusion and associated gold deposit, Eastern Desert, Egypt', *Geoscience Frontiers*. Elsevier B.V., 11(1), pp. 325–345. doi: 10.1016/j.gsf.2019.04.012.

“Every reasonable effort has been made to acknowledge the owners of copyright material. I would be pleased to hear from any copyright owner who has been omitted or incorrectly acknowledged.”

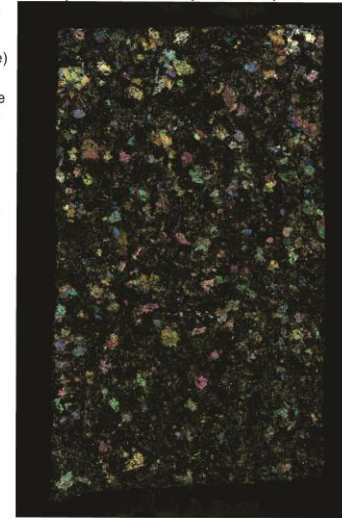
Appendix B:

Supplementary materials to Chapter 3

Sample # R10-1 (Diorite)



Sample # S11-1 (Gabbro)



Sample # S12 (Gabbro)

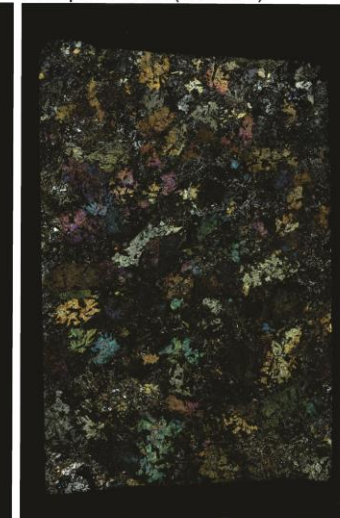
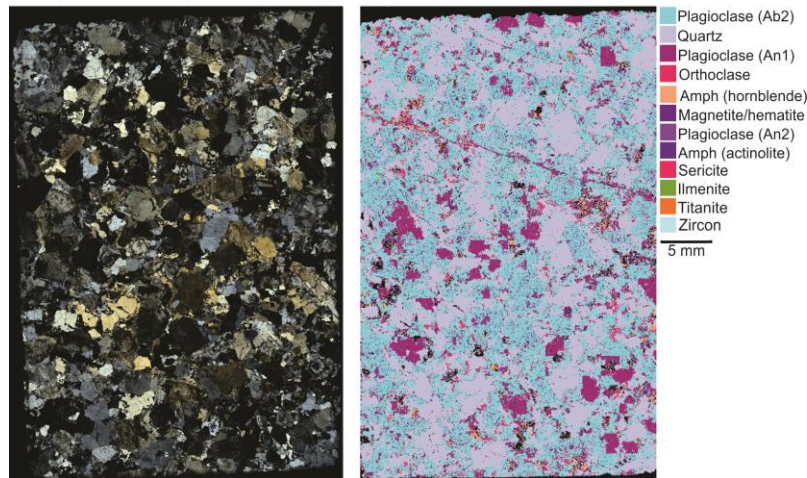
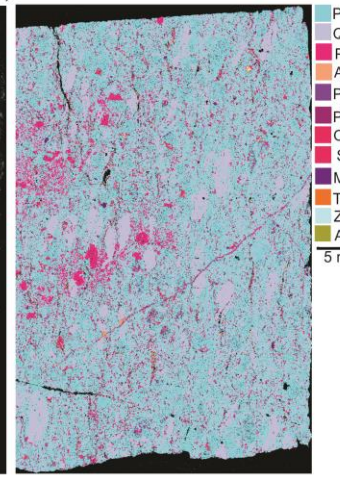
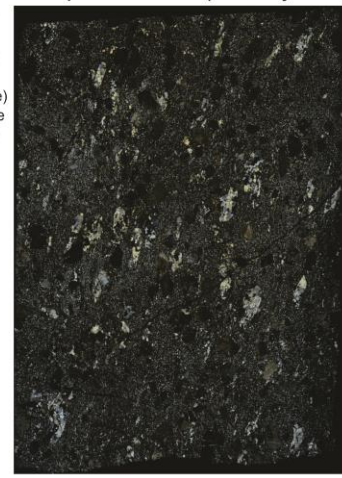


Figure B.1:
Crossed-polarized images and TIMA phase maps for the El-Shadli plagiogranites and associated gabbroic rocks.

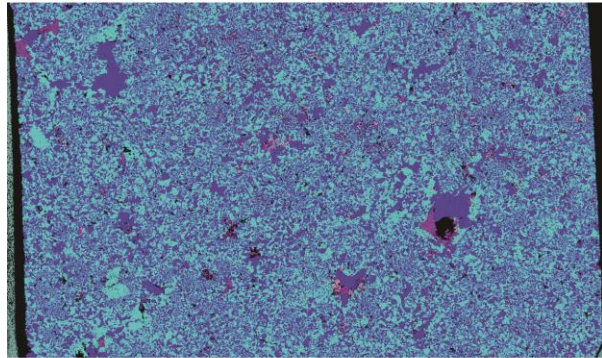
Sample # R11-1 (Trondhjemite)



Sample # S01-1a (Trondhjemite)

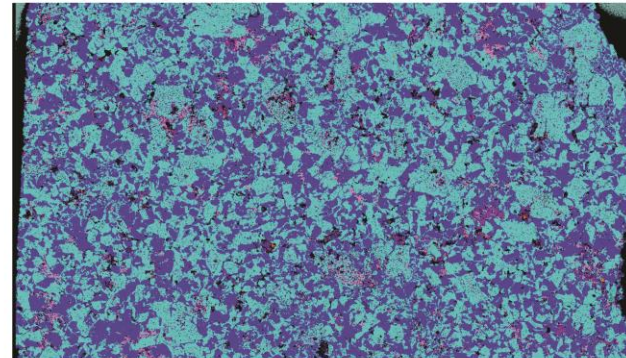


S23-2 (Trondhjemite)



- Albite
- Quartz
- Anorthite
- Hematite /Magnetite
- Sericite
- Unclassified

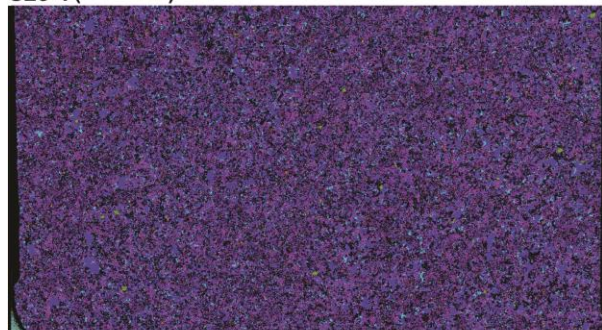
S25-1 (Trondhjemite)



- Albite
- Quartz
- Anorthite
- Hematite /Magnetite
- Plagioclase
- Sericite
- Unclassified

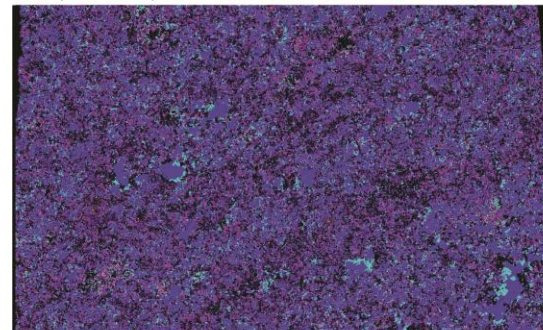
Figure B.1:
Continue

S23-1 (Tonalite)



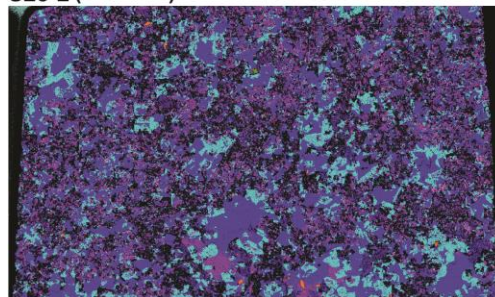
- Anorthite
- Albite
- Quartz
- Plagioclase
- Sericite
- Apatite
- Ilmenite
- Titanite
- Unclassified

S24 (Tonalite)



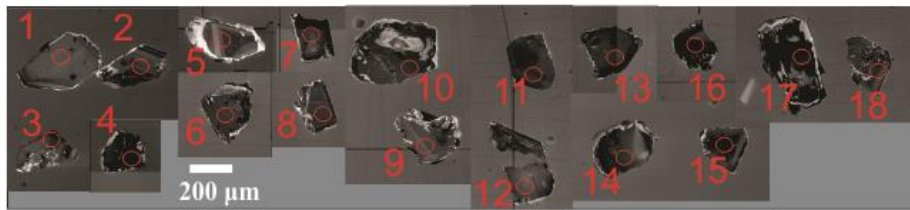
- Anorthite
- Albite
- Quartz
- Plagioclase
- Sericite
- Titanite
- Unclassified

S25-2 (Tonalite)

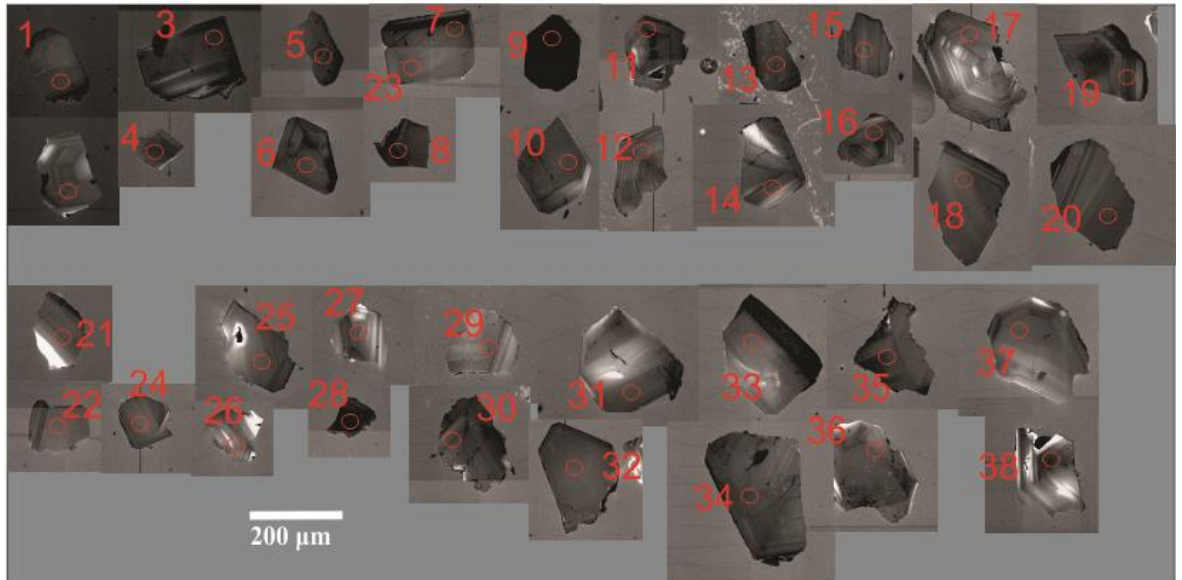


- Anorthite
- Albite
- Quartz
- Plagioclase
- Sericite
- Apatite
- Titanite
- Hematite /Magnetite
- Unclassified

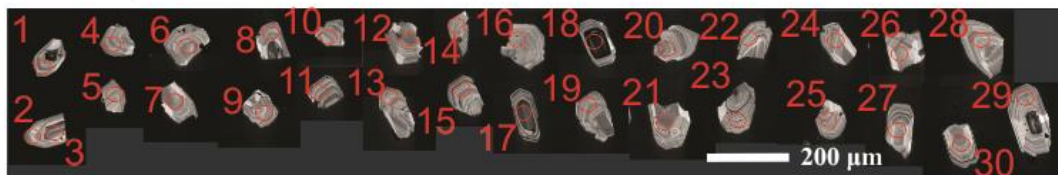
Sample # R10-1



Sample # R11-1



Sample # S01-1a



Sample # S14



Figure B.2: CL images for the studied zircon showing the location of spot used during the SHRIMP, LASS, and SIMS analyses.

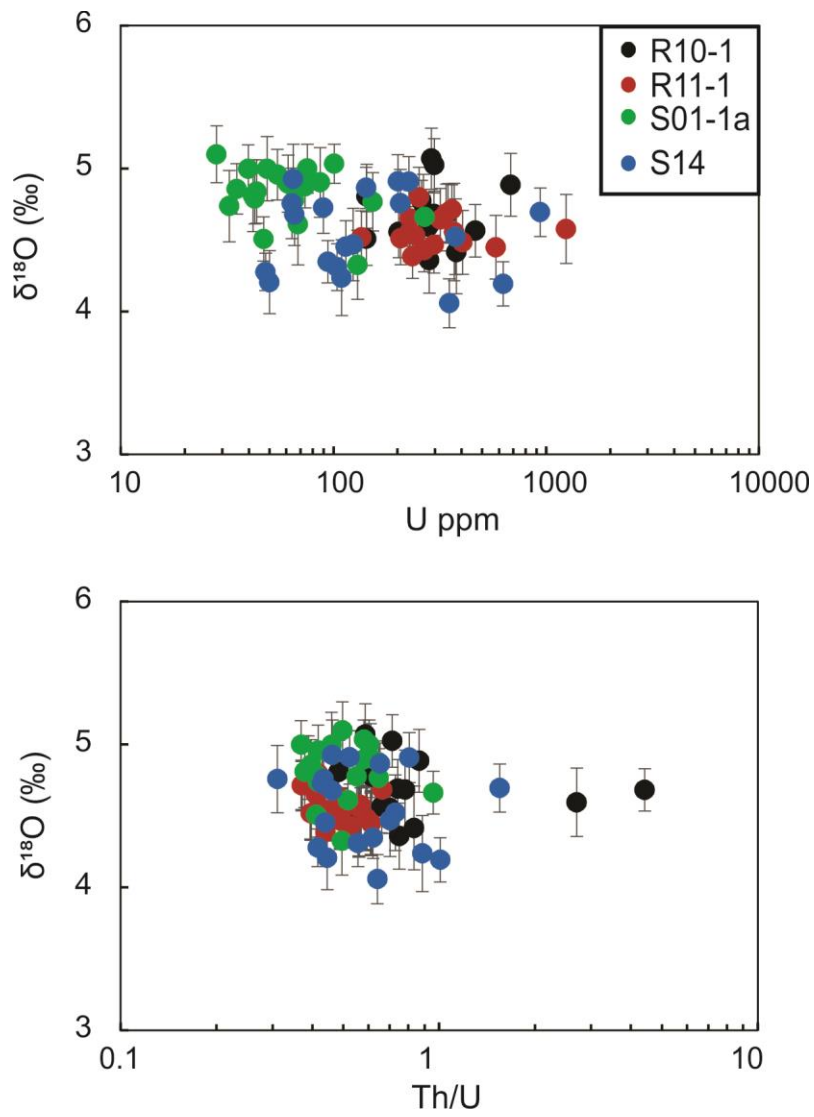


Figure B.3: Plot of $\delta^{18}\text{O}$ versus U content (a) and Th/U ratio (b) for zircon crystals of the studied samples.

Table B.1: Zircon U-Pb data of the studied rocks generated by SHRIMP.

Spot	U (ppm)	Th (ppm)	Th/U	²³² Th/ ²³⁸ U	±%	%com. ²⁰⁶ Pb	²³⁸ U/ ²⁰⁶ Pb ⁶ Pb*	±%	²⁰⁷ Pb* / ²⁰⁶ Pb	±%	²⁰⁷ Pb* / ²³⁵ U	±%	²⁰⁶ Pb* / ²³⁸ U	±%	err corr	²⁰⁶ Pb/ ²³⁸ U Age (Ma)	± 1σ	²⁰⁷ Pb*/ ²⁰⁶ Pb* Age (Ma)	± 1σ
Lat.	24°18'17"																		
Long.	35°08'15"																		
R10-1@1	202.85	141.81	0.70	0.72	0.62	0.31	8.75	2.23	0.06	3.28	0.95	3.97	0.11	2.23	0.56	697.23	14.76	620.85	70.78
R10-1@2	259.44	159.75	0.62	0.64	0.39	0.15	8.49	1.91	0.06	1.39	1.05	2.36	0.12	1.91	0.81	717.44	12.94	769.49	29.24
R10-1@3	378.01	315.51	0.83	0.86	0.34	0.27	8.46	1.87	0.06	1.40	1.04	2.34	0.12	1.87	0.80	720.20	12.77	743.30	29.52
R10-1@4	464.00	306.04	0.66	0.68	0.18	0.04	8.40	1.86	0.06	0.99	1.04	2.11	0.12	1.86	0.88	725.28	12.76	724.16	21.02
R10-1@5	142.89	81.00	0.57	0.59	0.37	0.54	8.36	2.21	0.06	5.80	0.95	6.21	0.12	2.21	0.36	728.16	15.21	519.40	127.34
R10-1@6	264.85	207.21	0.78	0.81	0.39	0.20	8.35	1.90	0.06	1.37	1.07	2.34	0.12	1.90	0.81	728.92	13.07	760.33	28.97
R10-1@7	279.61	755.92	2.70	2.79	0.38	0.12	8.10	1.89	0.07	1.12	1.12	2.19	0.12	1.89	0.86	750.58	13.39	790.39	23.42
R10-1@8	282.24	211.51	0.75	0.77	0.47	0.65	8.23	1.90	0.06	2.94	1.02	3.50	0.12	1.90	0.54	739.37	13.28	630.07	63.26
R10-1@9	143.41	69.40	0.48	0.50	0.34	0.26	8.36	1.97	0.07	1.85	1.07	2.70	0.12	1.97	0.73	728.35	13.55	776.80	38.97
R10-1@10	346.36	256.92	0.74	0.77	0.56	-0.11	8.10	1.89	0.06	1.59	1.05	2.47	0.12	1.89	0.76	750.86	13.39	664.57	34.12
R10-1@11	297.52	122.19	0.71	0.74	0.23	0.50	8.39	1.90	0.07	1.64	1.09	2.51	0.12	1.90	0.76	725.78	13.03	810.01	34.31
R10-1@12	296.81	1310.91	4.42	4.56	0.18	1.21	8.09	1.92	0.07	7.04	1.18	7.30	0.12	1.92	0.26	751.02	13.59	903.11	145.14
R10-1@13	288.45	169.32	0.59	0.61	0.39	0.26	8.25	1.91	0.07	2.47	1.11	3.12	0.12	1.91	0.61	737.20	13.31	816.14	51.57
R10-1@14	680.50	589.45	0.87	0.89	0.15	0.07	8.36	1.85	0.06	1.12	1.04	2.16	0.12	1.85	0.85	728.20	12.73	701.16	23.88
Lat.	24°18'13"																		
Long.	35°08'07"																		
R11-1@1	317.64	151.69	0.48	0.49	0.24	0.62	8.49	1.89	0.06	2.35	1.03	3.02	0.12	1.89	0.63	717.92	12.87	725.58	49.80
R11-1@2	242.33	119.47	0.49	0.51	0.26	0.12	8.33	1.91	0.06	1.74	1.05	2.58	0.12	1.91	0.74	730.98	13.18	713.91	36.87
R11-1@3	296.35	145.06	0.49	0.51	0.26	0.15	8.22	1.89	0.06	1.31	1.08	2.30	0.12	1.89	0.82	740.06	13.19	751.64	27.73
R11-1@4	404.47	239.60	0.59	0.61	1.08	0.11	8.39	2.06	0.06	1.35	1.04	2.46	0.12	2.06	0.84	726.09	14.13	709.02	28.81
R11-1@5	359.94	133.45	0.37	0.38	0.24	0.08	8.31	1.88	0.06	1.32	1.05	2.30	0.12	1.88	0.82	732.65	13.00	719.36	28.07
R11-1@6	267.02	140.48	0.53	0.54	0.54	0.10	8.17	1.90	0.06	1.69	1.07	2.54	0.12	1.90	0.75	744.05	13.36	716.13	35.83
R11-1@7	207.15	94.13	0.45	0.47	0.29	0.09	8.30	1.92	0.06	2.31	1.02	3.00	0.12	1.92	0.64	733.35	13.33	651.55	49.54
R11-1@8	580.02	354.87	0.61	0.63	0.51	0.03	8.24	1.85	0.06	1.02	1.06	2.12	0.12	1.85	0.88	738.63	12.93	715.68	21.71
R11-1@9	1241.80	703.39	0.57	0.59	0.33	0.16	8.15	1.86	0.06	0.90	1.07	2.07	0.12	1.86	0.90	746.13	13.12	719.30	19.15
R11-1@10	227.30	96.98	0.43	0.44	1.19	0.29	8.52	2.12	0.07	2.13	1.11	3.01	0.12	2.12	0.70	715.50	14.35	885.52	44.09
R11-1@11	369.02	206.68	0.56	0.58	0.46	0.20	8.34	1.88	0.06	2.08	1.05	2.81	0.12	1.88	0.67	730.28	12.97	715.74	44.26
R11-1@12	253.05	105.21	0.42	0.43	0.49	0.14	8.16	1.90	0.07	1.12	1.10	2.20	0.12	1.90	0.86	744.97	13.33	781.68	23.47
R11-1@13	235.39	103.49	0.44	0.45	0.28	0.14	8.26	1.93	0.06	1.86	1.05	2.68	0.12	1.93	0.72	736.33	13.45	711.73	39.54
R11-1@14	228.93	93.88	0.41	0.42	0.46	0.13	8.30	1.91	0.06	1.39	1.07	2.36	0.12	1.91	0.81	733.05	13.23	756.36	29.33
R11-1@15	135.32	53.47	0.40	0.41	0.37	0.66	8.29	1.98	0.07	3.70	1.09	4.20	0.12	1.98	0.47	734.48	13.76	784.94	77.70
R11-1@16	339.02	224.92	0.66	0.69	0.42	-0.01	8.17	1.88	0.06	2.17	1.04	2.87	0.12	1.88	0.66	744.12	13.22	664.90	46.38
Lat.	24°25'17"																		
Long.	34°35'38"																		
S01-1a@1	73.61	47.53	0.65	0.67	0.44	0.35	8.31	2.10	0.07	2.87	1.12	3.56	0.12	2.10	0.59	732.32	14.53	860.34	59.65
S01-1a@2	35.10	13.91	0.40	0.41	0.75	6.95	8.58	4.57	0.06	49.75	0.94	49.96	0.12	4.57	0.09	710.34	30.71	541.33	1087.79
S01-1a@3	130.00	64.35	0.50	0.51	0.38	0.91	8.44	2.05	0.07	3.21	1.10	3.81	0.12	2.05	0.54	721.92	13.99	848.40	66.73

S01-1a@4	65.40	35.99	0.55	0.57	0.48	0.00	8.40	2.13	0.06	3.94	1.00	4.48	0.12	2.13	0.48	724.78	14.62	635.40	84.71
S01-1a@5	46.95	19.34	0.41	0.43	0.65	0.71	8.40	2.29	0.07	4.97	1.20	5.47	0.12	2.29	0.42	725.14	15.71	1023.77	100.57
S01-1a@6	32.39	13.51	0.42	0.43	0.79	0.95	8.49	2.47	0.07	6.20	1.10	6.67	0.12	2.47	0.37	717.97	16.81	858.99	128.60
S01-1a@7	28.24	14.04	0.50	0.51	2.01	0.45	8.26	2.53	0.06	5.71	1.08	6.24	0.12	2.53	0.41	736.73	17.64	763.62	120.30
S01-1a@8	61.22	35.40	0.58	0.60	0.50	2.12	8.19	2.71	0.06	9.73	1.03	10.10	0.12	2.71	0.27	742.95	19.03	639.88	209.29
S01-1a@9	41.98	15.87	0.38	0.39	0.67	0.44	8.47	2.41	0.08	7.46	1.36	7.84	0.12	2.41	0.31	719.27	16.40	1281.71	145.43
S01-1a@10	75.37	45.47	0.60	0.62	0.49	0.61	8.33	2.15	0.07	4.34	1.21	4.85	0.12	2.15	0.44	731.08	14.86	1016.63	87.99
S01-1a@11	100.86	58.59	0.58	0.60	0.42	3.06	8.36	2.53	0.07	9.72	1.08	10.04	0.12	2.53	0.25	728.46	17.45	792.08	203.83
S01-1a@12	86.56	52.77	0.61	0.63	0.43	1.18	8.53	2.13	0.06	6.84	0.98	7.16	0.12	2.13	0.30	714.77	14.38	635.98	147.17
S01-1a@13	48.82	22.43	0.46	0.47	0.59	0.13	8.53	2.39	0.04	19.15	0.63	19.30	0.12	2.39	0.12	714.47	16.14	-432.33	502.71
S01-1a@14	43.51	16.92	0.39	0.40	0.66	0.98	8.35	2.33	0.08	5.27	1.28	5.76	0.12	2.33	0.40	729.42	16.04	1134.89	104.87
S01-1a@15	68.17	35.31	0.52	0.54	0.50	0.71	8.23	2.21	0.08	5.69	1.42	6.10	0.12	2.21	0.36	739.58	15.42	1305.71	110.45
S01-1a@16	39.72	14.66	0.37	0.38	0.71	0.75	8.33	2.32	0.07	3.43	1.15	4.14	0.12	2.32	0.56	730.55	16.01	919.07	70.58
S01-1a@17	153.00	98.92	0.65	0.67	0.32	0.11	8.23	1.97	0.07	2.77	1.15	3.40	0.12	1.97	0.58	739.63	13.77	888.15	57.22
S01-1a@18	268.13	257.08	0.96	0.99	0.70	0.07	8.27	1.91	0.06	2.79	1.03	3.38	0.12	1.91	0.57	735.96	13.30	668.92	59.61
S01-1a@19	42.69	17.57	0.41	0.43	0.66	0.32	8.16	2.37	0.08	6.66	1.30	7.07	0.12	2.37	0.33	745.56	16.66	1125.83	132.74
S01-1a@20	54.51	22.72	0.42	0.43	0.60	1.22	8.49	2.33	0.06	11.01	0.91	11.25	0.12	2.33	0.21	717.97	15.81	464.52	243.87

Lat.
Long.

24°18'45"
34°41'49"

S14@1	104.22	57.94	0.56	0.57	1.44	0.96	8.45	2.36	0.06	7.30	0.96	7.67	0.12	2.36	0.31	721.08	16.11	556.86	159.10
S14@2	65.48	30.15	0.46	0.48	0.51	-0.08	8.31	2.14	0.06	3.62	1.02	4.20	0.12	2.14	0.51	732.52	14.79	662.75	77.51
S14@3	374.86	273.14	0.73	0.75	0.32	0.32	8.32	1.89	0.06	1.41	1.08	2.36	0.12	1.89	0.80	731.53	13.06	772.05	29.72
S14@4	48.02	19.99	0.42	0.43	0.66	0.82	8.34	2.22	0.07	2.64	1.16	3.45	0.12	2.22	0.64	729.62	15.31	934.15	54.25
S14@5	63.80	27.70	0.43	0.45	0.53	0.96	8.42	2.17	0.08	4.08	1.24	4.62	0.12	2.17	0.47	723.54	14.84	1081.17	81.82
S14@6	206.35	64.11	0.31	0.32	0.33	0.56	8.81	1.93	0.06	3.71	0.99	4.18	0.11	1.93	0.46	693.18	12.68	715.85	78.73
S14@7	64.77	29.93	0.46	0.48	0.83	0.43	8.40	2.17	0.06	6.96	0.94	7.29	0.12	2.17	0.30	724.97	14.86	513.38	152.88
S14@8	142.55	93.07	0.65	0.67	0.31	0.31	8.46	1.96	0.06	2.35	1.04	3.06	0.12	1.96	0.64	719.85	13.37	741.83	49.77
S14@9	123.96	86.93	0.70	0.72	0.36	0.39	8.48	2.04	0.05	6.50	0.89	6.81	0.12	2.04	0.30	718.23	13.85	407.73	145.39
S14@10	50.10	22.32	0.45	0.46	0.62	1.59	8.31	2.42	0.05	15.47	0.84	15.66	0.12	2.42	0.15	732.39	16.76	229.98	357.26
S14@11	226.46	182.51	0.81	0.83	4.11	0.10	8.47	2.70	0.06	2.92	0.97	3.98	0.12	2.70	0.68	719.61	18.37	589.42	63.44
S14@12	350.87	224.50	0.64	0.66	0.38	0.39	8.56	1.88	0.06	1.60	1.04	2.47	0.12	1.88	0.76	712.39	12.68	751.69	33.87
S14@13	627.33	632.21	1.01	1.04	0.22	0.03	8.31	1.85	0.06	1.07	1.04	2.13	0.12	1.85	0.87	732.15	12.79	697.46	22.70
S14@14	109.41	96.93	0.89	0.92	1.06	1.33	8.68	2.34	0.06	5.87	1.01	6.31	0.12	2.34	0.37	703.07	15.56	723.78	124.45
S14@15	200.96	105.28	0.52	0.54	0.30	0.25	8.64	1.94	0.06	2.41	1.00	3.09	0.12	1.94	0.63	706.25	12.95	699.80	51.41
S14@16	94.05	58.36	0.62	0.64	0.42	0.35	8.49	2.45	0.07	3.67	1.14	4.41	0.12	2.45	0.56	718.10	16.67	928.39	75.28
S14@17	937.59	1451.94	1.55	1.60	0.30	-0.04	7.97	2.06	0.06	0.71	1.10	2.18	0.13	2.06	0.95	762.21	14.80	732.88	15.04
S14@18	89.70	38.48	0.43	0.44	0.48	0.55	8.48	2.07	0.07	2.81	1.08	3.50	0.12	2.07	0.59	718.40	14.09	825.49	58.74
S14@19	114.44	50.19	0.44	0.45	0.39	0.21	8.33	2.01	0.06	3.68	1.01	4.20	0.12	2.01	0.48	731.05	13.92	633.56	79.33

Table B.2: Zircon U-Pb-Hf-O and Trace element data of the studied rocks generated by LASS and SIMS.

Sample /Spot	207Pb/235U	$\pm 2\sigma$	206Pb/238U	$\pm 2\sigma$	206Pb/238U Age (Ma)	$\pm 2\sigma$	176Hf/177Hf	$\pm 2\sigma$	176Lu/177Hf	$\pm 2\sigma$	$\epsilon_{\text{Hf}}(t)$	$\pm 1\sigma$	TDM Crustal (Ga)	$\delta^{18}\text{O} (\text{‰})$	$\pm 2\sigma$
R10-1 - 1	1.114	0.058	0.1201	0.002	731	12	0.282747	7.5E-05	0.0076	0.0002	11.30	1.13	0.92	4.55	0.18
R10-1 - 2	1.066	0.055	0.1191	0.002	725	11	0.282772	8.2E-05	0.007197	3E-05	12.27	1.23	0.85	4.77	0.14
R10-1 - 3	1.019	0.047	0.1167	0.002	712	10	0.282729	7.5E-05	0.005393	7E-05	11.37	1.13	0.90	4.42	0.29
R10-1 - 4	1.015	0.049	0.1204	0.002	732.7	8.6	0.282729	7.7E-05	0.007873	2E-05	10.55	1.16	0.97	4.56	0.18
R10-1 - 5	0.994	0.044	0.1186	0.002	722	11	0.282749	8.1E-05	0.00572	0.0003	12.11	1.22	0.86	4.51	0.19
R10-1 - 6	0.99	0.042	0.1191	0.002	725.4	9.7	0.282753	6.6E-05	0.00483	0.0005	12.75	0.99	0.82	4.68	0.27
R10-1 - 7	1.275	0.059	0.1201	0.002	731	9.5	0.28266	6.2E-05	0.00432	0.0003	9.81	0.93	1.01	4.59	0.24
R10-1 - 8	1.056	0.049	0.1207	0.002	734.6	9.7	0.282715	6.5E-05	0.00583	0.0003	11.09	0.98	0.93	4.36	0.23
R10-1 - 9	1.05	0.058	0.1196	0.002	728	10	0.282739	7.3E-05	0.00762	0.0004	10.95	1.10	0.94	4.81	0.22
R10-1 - 10	1.061	0.045	0.1203	0.002	732	11	0.282803	7.5E-05	0.00743	0.0003	13.38	1.13	0.78	4.69	0.20
R10-1 - 11	1.029	0.046	0.1187	0.002	723.1	8.7	0.282795	7.7E-05	0.006413	1E-04	13.43	1.16	0.77	5.02	0.18
R10-1 - 12	1.048	0.052	0.1212	0.002	737.1	9.2	0.282733	6.2E-05	0.00573	0.0002	11.82	0.93	0.89	4.68	0.15
R10-1 - 13	1.094	0.053	0.1203	0.002	733	10	0.282676	6.4E-05	0.005784	6E-05	9.70	0.96	1.02	5.07	0.21
R10-1 - 14	1.072	0.032	0.12253	1E-03	745.1	5.6	0.282771	8.2E-05	0.008358	1E-04	12.02	1.23	0.88	4.88	0.22
R10-1 - 16	1.068	0.059	0.1247	0.002	757.5	9.1	0.282717	8.1E-05	0.005729	6E-05	11.64	1.22	0.92	4.81	0.15
R10-1 - 17	1.189	0.066	0.1219	0.002	742.4	9.7	0.282747	6.5E-05	0.0051	0.0006	12.73	0.98	0.83	4.88	0.18
R10-1 - 18	0.972	0.043	0.1197	0.001	728.7	7.7	0.282712	7.5E-05	0.00588	0.0002	10.85	1.13	0.94	5.09	0.24
R10-1 - 15	1.164	0.045	0.1183	0.001	720.9	7.9	0.282852	7.7E-05	0.00683	0.0002	15.21	1.16	0.66	4.33	0.29
R11-1 - 1	0.954	0.045	0.119	0.002	725	10	0.282666	6.8E-05	0.006666	9E-05	8.77	1.02	1.07	4.64	0.22
R11-1 - 2	0.97	0.048	0.1201	0.002	730.9	9	0.282706	7.7E-05	0.007526	5E-05	9.88	1.16	1.01	4.53	0.16
R11-1 - 3	1.02	0.041	0.1189	0.001	724.3	8.3	0.28279	8.6E-05	0.01162	0.0002	10.76	1.29	0.95	4.47	0.20
R11-1 - 4	1.048	0.044	0.1181	0.002	719.5	8.4	0.282713	6.9E-05	0.005508	5E-05	10.89	1.04	0.93	4.48	0.22
R11-1 - 5	0.985	0.038	0.1202	0.001	731.8	8.3	0.282738	7.2E-05	0.007351	3E-05	11.11	1.08	0.93	4.71	0.17
R11-1 - 6	1.01	0.044	0.1197	0.002	728.6	9.1	0.282706	8.9E-05	0.007582	5E-05	9.81	1.34	1.01	4.43	0.15
R11-1 - 7	1.062	0.054	0.1213	0.002	737.8	9.6	0.282704	5.5E-05	0.00776	0.0002	9.81	0.83	1.02		
R11-1 - 8	1.003	0.039	0.1199	0.001	731.1	6.9	0.282768	6.9E-05	0.006128	3E-05	12.76	1.04	0.82		
R11-1 - 9	1.043	0.025	0.1216	0.001	739.8	6.3	0.282785	0.00007	0.00834	0.0002	12.43	1.05	0.85		
R11-1 - 10	1.042	0.064	0.1222	0.003	743	14	0.282691	6.1E-05	0.00404	0.0004	11.28	0.92	0.93		
R11-1 - 11	1.024	0.045	0.1188	0.001	723.9	6.5	0.282693	5.8E-05	0.00586	0.0001	10.10	0.87	0.99		
R11-1 - 12	1.03	0.057	0.1198	0.002	729.1	9.7	0.282704	7.3E-05	0.00518	0.0001	10.91	1.10	0.94		
R11-1 - 13	0.994	0.044	0.1182	0.002	720	10	0.282721	6.4E-05	0.00648	0.0003	10.72	0.96	0.95		
R11-1 - 14	1.003	0.048	0.1203	0.002	732	11	0.282702	5.9E-05	0.004027	3E-05	11.46	0.89	0.91		
R11-1 - 15	1.003	0.07	0.1201	0.002	731	12	0.282734	7.2E-05	0.005897	3E-05	11.66	1.08	0.89		
R11-1 - 16	0.97	0.047	0.116	0.002	707.4	8.5	0.282801	6.8E-05	0.006847	7E-05	13.15	1.02	0.78		
R11-1 - 17	1.045	0.057	0.1178	0.002	717.8	9.3	0.282716	6.2E-05	0.0040701	9E-06	11.65	0.93	0.88		
R11-1 - 18	1.006	0.052	0.1171	0.002	714	11	0.282712	6.4E-05	0.005507	8E-05	10.75	0.96	0.94	4.51	0.18

R11-1 - 19	0.998	0.043	0.1181	0.002	720	11	0.282678	6.6E-05	0.003206	1E-05	10.76	0.99	0.94	4.45	0.22
R11-1 - 20	1.035	0.059	0.1189	0.002	727	11	0.282707	7.1E-05	0.00614	0.0001	10.51	1.07	0.96	4.58	0.24
R11-1 - 21	1.039	0.069	0.1224	0.002	744	11	0.282701	7.1E-05	0.004986	9E-05	11.19	1.07	0.93	4.55	0.20
R11-1 - 22	0.999	0.046	0.1183	0.002	720.4	9.6	0.28279	0.0001	0.00773	0.0001	12.57	1.50	0.83	4.56	0.34
R11-1 - 23	1.04	0.054	0.1197	0.002	730	10	0.282756	7.1E-05	0.00737	0.0001	11.71	1.07	0.89	4.80	0.21
R11-1 - 24	1.084	0.06	0.1188	0.002	724	11	0.282725	8.4E-05	0.005889	6E-05	11.22	1.26	0.92	4.39	0.15
R11-1 - 25	1.009	0.077	0.1203	0.002	732	14	0.282683	5.7E-05	0.00377	4E-05	10.91	0.86	0.94	4.65	0.20
R11-1 - 26	0.994	0.068	0.1192	0.002	726	11	0.282663	5.1E-05	0.00374	3E-05	10.10	0.77	0.99	4.52	0.18
R11-1 - 27	0.982	0.047	0.1207	0.001	734.3	7.7	0.282678	8.6E-05	0.00777	0.0001	8.83	1.29	1.08	4.68	0.21
R11-1 - 28	1.059	0.031	0.1199	0.001	730.2	7.6	0.282748	6.9E-05	0.00765	0.0003	11.29	1.04	0.92	4.47	0.30
R11-1 - 29	1.122	0.073	0.1195	0.002	727	12	0.282685	6.6E-05	0.0041	0.0001	10.72	0.99	0.95	4.59	0.21
R11-1 - 30	1.024	0.042	0.1195	0.001	727.7	7	0.282704	6.6E-05	0.00566	0.0001	10.65	0.99	0.96	4.53	0.27
R11-1 - 31	1.014	0.091	0.1222	0.003	743	15	0.282732	5.3E-05	0.00272	0.0001	13.39	0.80	0.79	4.88	0.16
R11-1 - 32	1.035	0.063	0.1193	0.001	726.5	7.7	0.282704	5.4E-05	0.00678	0.0003	10.09	0.81	0.99		
R11-1 - 33	1.068	0.057	0.1218	0.002	741	9.8	0.282692	8.1E-05	0.00557	0.0002	10.52	1.22	0.97		
R11-1 - 34	0.971	0.037	0.1167	0.001	711.7	8.2	0.282762	5.7E-05	0.007711	3E-05	11.44	0.86	0.89		
R11-1 - 35	1.023	0.039	0.1202	0.002	731.7	9.1	0.282667	9.4E-05	0.006639	1E-05	8.94	1.41	1.07		
R11-1 - 36	0.951	0.042	0.1177	0.002	717	10	0.282808	7.9E-05	0.009181	1E-04	12.46	1.19	0.83		
R11-1 - 37	1.012	0.059	0.1211	0.002	738	11	0.282705	8.3E-05	0.006831	7E-05	10.31	1.25	0.99		
R11-1 - 38	1.099	0.073	0.118	0.003	718	15	0.282615	6.7E-05	0.00285	0.0001	8.66	1.01	1.08		
S01-1a - 1	1.05	0.1	0.1234	0.003	750	15	0.28271	3.9E-05	0.002047	5E-05	13.09	0.59	0.82	4.87	0.15
S01-1a - 2	1.23	0.12	0.1159	0.003	706	20	0.282616	3.8E-05	0.001623	3E-05	9.03	0.57	1.04	4.86	0.18
S01-1a - 3	1.3	0.11	0.119	0.003	724	16	0.282711	4.8E-05	0.00331	0.0001	11.96	0.72	0.87	4.33	0.24
S01-1a - 4	1.1	0.13	0.117	0.003	713	18	0.282633	4.1E-05	0.0018044	9E-06	9.69	0.62	1.01	4.77	0.16
S01-1a - 5	1.45	0.18	0.1234	0.004	749	25	0.282675	3.9E-05	0.001614	6E-05	12.04	0.59	0.88	4.51	0.15
S01-1a - 6	1.06	0.12	0.1233	0.004	748	23	0.282624	3.6E-05	0.001796	1E-05	10.12	0.54	1.01	4.74	0.25
S01-1a - 7	1.035	0.097	0.1186	0.004	722	22	0.282679	3.9E-05	0.002262	5E-05	11.29	0.59	0.91	5.10	0.20
S01-1a - 8	1.01	0.12	0.1193	0.003	726	18	0.28263	4.1E-05	0.001864	6E-05	9.83	0.62	1.01	4.89	0.20
S01-1a - 9	1.55	0.18	0.1186	0.004	722	20	0.28266	4.5E-05	0.001999	2E-05	10.75	0.68	0.95	4.81	0.25
S01-1a - 10	2.39	0.34	0.1313	0.005	794	30	0.282698	4.1E-05	0.001688	2E-05	13.78	0.62	0.81	5.00	0.17
S01-1a - 11	1.1	0.11	0.1213	0.003	738	19	0.282665	3.4E-05	0.00184	5E-05	11.34	0.51	0.92	5.03	0.14
S01-1a - 12	1.12	0.14	0.1231	0.003	748	20	0.282666	4.1E-05	0.001817	6E-05	11.60	0.62	0.91	4.90	0.24
S01-1a - 13	1.11	0.12	0.1219	0.003	741	18	0.282642	4.3E-05	0.001797	3E-05	10.61	0.65	0.97	5.00	0.23
S01-1a - 14	1.87	0.18	0.1169	0.003	714	19	0.28266	4.2E-05	0.0021	4E-05	10.53	0.63	0.95	4.84	0.22
S01-1a - 15	1.164	0.094	0.1177	0.003	717	17	0.282659	4.5E-05	0.001886	3E-05	10.66	0.68	0.95	4.61	0.28
S01-1a - 16	1.17	0.14	0.1192	0.004	725	23	0.282667	0.00004	0.0017347	8E-06	11.19	0.60	0.92	5.00	0.17
S01-1a - 17	1.176	0.082	0.1159	0.002	707	13	0.282788	4.3E-05	0.0047	0.0002	13.69	0.65	0.74	4.77	0.20
S01-1a - 18	1.152	0.051	0.1221	0.002	743	10	0.282816	5.5E-05	0.00668	0.0002	14.40	0.83	0.73	4.66	0.15
S01-1a - 19	1.05	0.11	0.1165	0.003	710	18	0.282666	0.00004	0.0017985	6E-06	10.80	0.60	0.93	4.79	0.18
S01-1a - 20	0.989	0.088	0.1165	0.003	710	17	0.28265	4.6E-05	0.003	0.0003	9.67	0.69	1.01	4.96	0.18

S01-1a - 21	1	0.12	0.1174	0.004	715	20	0.282645	4.1E-05	0.002401	4E-05	9.88	0.62	1.00		
S01-1a - 22	1.79	0.23	0.1306	0.006	794	33	0.282637	4.4E-05	0.001634	2E-05	11.65	0.66	0.94		
S01-1a - 23	1.22	0.12	0.1194	0.004	730	22	0.282659	4.7E-05	0.001832	2E-05	10.96	0.71	0.94		
S01-1a - 24	1.09	0.13	0.122	0.003	742	20	0.282663	4.2E-05	0.001995	1E-05	11.28	0.63	0.93		
S01-1a - 25	0.96	0.12	0.1237	0.004	751	23	0.282642	0.00005	0.0019895	9E-06	10.73	0.75	0.97		
S01-1a - 26	0.99	0.12	0.1204	0.004	735	23	0.282644	0.00005	0.002313	5E-05	10.30	0.75	0.98		
S01-1a - 27	1.07	0.11	0.1192	0.003	728	15	0.282663	4.6E-05	0.0028	0.0001	10.59	0.69	0.96		
S01-1a - 28	0.91	0.12	0.1173	0.004	714	25	0.282657	4.6E-05	0.001776	1E-05	10.58	0.69	0.95		
S01-1a - 29	1.05	0.12	0.1191	0.003	727	20	0.282588	3.8E-05	0.001548	2E-05	8.52	0.57	1.09		
S01-1a - 30	1.186	0.065	0.1283	0.002	778	12	0.282662	5.4E-05	0.00368	0.0001	11.13	0.81	0.96		
S14 - 1	1.054	0.076	0.1231	0.002	748	13	0.282712	5.4E-05	0.003048	3E-05	12.62	0.81	0.85	4.31	0.16
S14 - 2	1.045	0.061	0.1225	0.002	748	13	0.282677	4.5E-05	0.002637	6E-05	11.58	0.68	0.91	4.68	0.21
S14 - 3	1.134	0.088	0.1148	0.005	700	28	0.282711	3.7E-05	0.001337	7E-05	12.39	0.56	0.82	4.52	0.26
S14 - 4	1.099	0.085	0.1258	0.003	763	18	0.282645	4.4E-05	0.001782	2E-05	11.19	0.66	0.95	4.28	0.13
S14 - 5	1.045	0.086	0.1132	0.003	691	16	0.282654	3.8E-05	0.00221	3E-05	9.78	0.57	0.98	4.76	0.25
S14 - 6	1.064	0.074	0.1122	0.002	685	11	0.282676	3.7E-05	0.0009361	9E-06	11.01	0.56	0.90	4.76	0.24
S14 - 7	1.102	0.093	0.1233	0.003	749	18	0.282607	4.1E-05	0.002103	4E-05	9.39	0.62	1.05	4.93	0.25
S14 - 8	1.104	0.091	0.1259	0.003	764	16	0.282673	3.3E-05	0.002083	9E-05	12.05	0.50	0.89	4.86	0.15
S14 - 9	1.108	0.087	0.1139	0.002	697	15	0.282688	0.00004	0.002187	8E-05	11.12	0.60	0.90	4.47	0.25
S14 - 10	1.01	0.11	0.1074	0.003	657	18	0.282748	4.5E-05	0.001974	7E-05	12.50	0.68	0.78	4.20	0.22
S14 - 11	1.067	0.067	0.1194	0.002	727	11	0.282725	3.7E-05	0.00239	0.0001	12.97	0.56	0.81	4.91	0.18
S14 - 12	1.209	0.078	0.1165	0.002	710	12	0.282695	4.5E-05	0.00323	0.0002	11.15	0.68	0.91	4.06	0.17
S14 - 13	1.071	0.065	0.1199	0.002	730	13	0.282727	5.4E-05	0.00282	0.0001	12.89	0.81	0.81	4.19	0.15
S14 - 14	1.195	0.088	0.12	0.003	732	14	0.282677	4.6E-05	0.002389	3E-05	11.37	0.69	0.91	4.24	0.27
S14 - 15	1.115	0.093	0.1206	0.002	734	14	0.282696	4.8E-05	0.002475	9E-05	12.04	0.72	0.87	4.91	0.19
S14 - 16	1.148	0.073	0.1142	0.002	697	12	0.282652	4.3E-05	0.00296	0.0001	9.49	0.65	1.01	4.35	0.15
S14 - 17	1.088	0.032	0.1191	0.001	725.2	7.5	0.282855	7.2E-05	0.011387	8E-05	13.19	1.08	0.79	4.69	0.17
S14 - 18	1.103	0.055	0.1168	0.002	712	12	0.282701	4.2E-05	0.00296	0.0001	11.53	0.63	0.89	4.73	0.18
S14 - 19	1.172	0.09	0.116	0.002	707	13	0.282643	4.5E-05	0.002323	6E-05	9.67	0.68	1.00	4.45	0.18

Table B.2: continue.

Sample /Spot	Nb	La	Ce	Pr	Nd	Sm	Eu	Gd	Tb	Dy	Ho	Er	Tm	Yb	Lu	Hf	Pb	Th	U	Ce/Ce*	Yb/Gd
R10-1 - 1	0.87		27.24	0.50	4.75	14.00	2.65	111.00	42.24	571.00	230.00	1101.00	234.90	2226.00	391.30	8467.00	564.00	163.60	170.00		26.70
R10-1 - 2	1.78		43.88	0.24	2.98	11.40	2.34	94.70	36.90	494.90	200.60	958.50	204.70	1964.00	354.10	7932.00	503.00	150.80	195.70		27.61
R10-1 - 3	1.07		31.73	0.43	4.13	12.08	2.08	84.50	32.04	441.70	178.90	854.90	183.70	1760.00	312.70	9410.00	579.00	182.20	200.70		27.73
R10-1 - 4	0.82		28.55	0.46	5.22	13.95	2.72	110.70	44.09	601.50	244.10	1161.50	249.00	2401.00	425.20	8721.00	614.00	185.50	202.00		28.87
R10-1 - 5	1.46		34.50	0.18	2.50	8.23	1.82	74.30	29.30	399.00	162.30	778.00	169.90	1653.00	299.00	8658.00	714.00	216.30	214.50		29.62
R10-1 - 6	0.60		21.50	0.57	3.95	10.10	1.94	70.80	27.30	369.00	151.00	721.00	157.00	1529.00	276.00	9630.00	586.00	182.60	205.60		28.75
R10-1 - 7	0.94		48.10	3.21	10.90	11.57	2.21	71.60	24.40	319.00	127.10	618.00	142.00	1459.00	272.00	10390.00	1670.00	485.00	182.00		27.13
R10-1 - 8	0.75		25.60	0.41	4.12	12.20	1.85	87.50	35.10	473.00	193.90	930.00	197.30	1902.00	339.00	9299.00	527.00	152.60	167.40		28.94
R10-1 - 9	0.87		29.70	0.53	5.44	14.60	3.36	120.10	46.00	608.00	245.50	1146.00	239.50	2239.00	394.00	8279.00	445.00	136.20	141.90		24.82
R10-1 - 10	0.71		21.92	0.43	3.67	9.70	2.02	82.10	32.37	451.00	188.80	933.00	204.60	2011.00	369.20	8026.00	483.00	147.90	171.80		32.61
R10-1 - 11	1.70		40.80	0.22	2.90	10.53	1.94	85.30	32.96	441.80	176.30	833.00	179.70	1722.00	313.20	7843.00	856.00	264.80	257.80		26.87
R10-1 - 12	0.85		23.38	0.35	3.35	10.35	2.02	82.50	32.34	430.80	175.80	846.00	185.30	1806.00	323.90	9216.00	496.00	146.80	166.40		29.14
R10-1 - 13	1.43		36.48	0.24	2.38	8.97	1.75	69.80	28.99	408.40	168.80	824.10	180.40	1772.00	318.40	8998.00	381.00	118.10	175.10		33.79
R10-1 - 14	2.46		69.30	0.68	5.88	18.91	2.29	136.50	53.72	719.00	290.00	1387.00	303.30	2949.00	525.20	10360.00	3290.00	999.00	684.00		28.76
R10-1 - 16	1.18		36.00	0.53	4.37	10.95	1.88	81.20	31.85	436.70	181.70	871.40	188.80	1816.00	328.60	9323.00	637.00	178.10	194.10		29.77
R10-1 - 17	0.69		16.30	0.53	3.76	6.70	1.53	50.00	20.60	303.00	133.00	684.00	158.00	1600.00	309.00	9596.00	572.00	161.00	206.00		42.60
R10-1 - 18	1.81		40.98	0.23	2.78	9.36	1.77	79.90	32.54	439.70	180.40	864.60	193.30	1864.00	333.30	9220.00	510.00	159.10	212.30		31.06
R10-1 - 15	2.36		66.90	2.16	10.70	17.94	4.24	114.50	42.91	559.00	221.60	1057.00	222.10	2142.00	380.00	8905.00	1367.00	400.70	352.80		24.90
R11-1 - 1	4.54		36.70	0.34	8.60	26.70	1.78	173.90	66.49	815.10	312.90	1374.00	259.60	2290.00	382.80	9373.00	373.00	118.30	204.00		17.53
R11-1 - 2	4.70		31.26	0.33	7.32	23.30	2.19	162.80	61.93	771.40	296.20	1310.00	251.00	2253.00	382.80	8331.00	346.00	106.20	178.40		18.42
R11-1 - 3	4.54		53.60	0.88	19.18	50.30	3.58	318.60	114.50	1379.00	516.90	2195.00	411.70	3544.00	582.30	8355.00	613.00	189.50	265.70		14.81
R11-1 - 4	6.02		34.38	0.16	3.85	14.65	1.22	119.80	46.34	586.50	227.00	1017.10	197.90	1781.00	303.60	9026.00	437.00	136.70	229.90		19.79
R11-1 - 5	10.06		59.25	0.21	5.47	22.74	1.50	171.60	66.34	832.30	322.10	1423.00	276.30	2456.00	414.00	9253.00	464.00	144.00	284.80		19.05
R11-1 - 6	3.78		33.43	0.37	9.71	28.90	2.51	197.50	71.97	870.40	330.70	1436.00	270.00	2377.00	399.20	8682.00	405.00	126.40	189.90		16.02
R11-1 - 7	4.38		35.44	0.38	9.87	30.10	2.48	200.20	71.95	887.00	337.60	1477.00	278.90	2469.00	412.60	8689.00	368.00	116.30	195.20		16.42
R11-1 - 8	10.99		61.50	0.22	6.17	21.13	1.29	168.40	62.32	772.00	293.40	1294.00	245.20	2149.00	355.30	9492.00	790.00	246.30	348.60		16.99
R11-1 - 9	17.80		124.30	1.64	18.02	32.60	1.94	193.40	78.20	1024.00	422.80	2065.00	430.50	3989.00	661.70	13098.00	2224.00	660.00	880.00		27.46
R11-1 - 10	2.92		17.21	0.14	2.90	11.10	0.89	85.70	31.40	405.00	159.00	719.00	142.00	1285.00	223.00	9183.00	153.00	49.70	110.90		19.96
R11-1 - 11	6.82		39.41	0.17	4.37	16.06	1.32	134.60	50.44	640.90	245.80	1100.00	211.30	1905.00	321.30	8944.00	491.00	159.10	243.50		18.84
R11-1 - 12	4.29		27.20	0.12	3.35	12.72	1.44	107.10	40.70	508.00	198.50	891.00	176.60	1577.00	271.80	8663.00	274.00	85.70	163.40		19.60
R11-1 - 13	3.57		24.99	0.26	6.72	21.20	1.53	155.60	55.90	706.00	277.00	1246.00	234.90	2118.00	357.00	9166.00	288.10	90.90	163.90		18.12
R11-1 - 14	4.42		23.37	0.09	3.09	10.70	0.87	89.70	33.20	426.70	165.50	746.30	146.60	1329.00	228.40	9330.00	260.70	83.50	162.80		19.72
R11-1 - 15	1.75		17.63	0.26	7.14	21.80	1.92	150.90	53.52	660.20	250.90	1113.70	209.80	1852.00	315.70	8740.00	212.90	65.97	118.76		16.34
R11-1 - 16	5.42		34.49	0.24	5.28	20.80	1.94	162.70	57.73	719.80	274.00	1197.00	229.00	2050.00	348.70	8333.00	544.00	179.00	225.40		16.77
R11-1 - 17	3.21		19.48	0.09	2.42	10.92	0.99	86.50	32.03	403.60	156.90	705.50	137.10	1263.90	217.40	8739.00	281.00	86.60	149.80		19.45
R11-1 - 18	2.98		22.98	0.27	6.03	20.00	1.52	144.30	50.60	631.00	240.20	1070.00	203.70	1825.00	309.20	9168.00	238.00	73.10	142.70		16.84
R11-1 - 19	3.63		19.55	0.07	2.19	8.98	0.59	74.60	27.37	351.00	137.70	622.20	121.29	1105.70	189.70	9686.00	257.60	81.83	161.80		19.73
R11-1 - 20	2.48		22.75	0.27	7.22	22.20	1.49	157.80	55.40	708.00	270.60	1200.00	229.80	2041.00	341.60	9115.00	269.30	82.20	150.40		17.22
R11-1 - 21	1.73		18.04	0.26	6.18	19.64	1.62	135.10	46.45	569.20	218.60	958.00	184.20	1628.00	273.80	9044.00	194.80	59.40	112.60		16.04
R11-1 - 22	3.23		25.80	0.38	8.57	25.00	1.71	185.20	66.70	829.00	319.60	1409.00	270.30	2362.00	397.30	8470.00	337.00	102.20	177.70		16.98
R11-1 - 23	2.75		37.80	2.12	18.90	31.80	2.56	201.70	68.03	850.30	323.10	1416.00	266.10	2340.00	393.60	8753.00	311.00	96.90	163.70		15.44

S14 - 1	1.61	3.71	21.11	2.99	9.63	11.11	1.20	57.10	22.93	285.80	114.30	525.80	111.60	1034.00	185.30	9846.00	215.40	67.92	86.80	1.52	24.11
S14 - 2	2.14	1.61	21.50	1.21	4.49	6.68	0.83	42.90	17.47	228.70	90.50	426.40	93.20	867.00	158.60	9851.00	337.00	100.80	115.10	3.70	26.90
S14 - 3	1.27	0.73	25.00	1.63	6.20	6.18	0.95	26.90	10.35	120.20	45.80	219.10	48.10	459.00	85.50	10241.00	182.00	49.30	102.00	5.50	22.71
S14 - 4	0.91	0.52	8.73	0.33	1.78	3.91	0.71	26.87	10.54	141.30	58.14	278.00	60.57	577.20	108.70	9703.00	113.50	34.90	51.90	5.06	28.60
S14 - 5	0.99	0.36	11.74	0.34	2.84	6.47	0.95	39.60	15.35	198.40	79.80	368.70	78.74	733.20	133.70	9796.00	154.50	47.01	66.50	8.01	24.65
S14 - 6	1.16	0.20	13.53	0.13	1.19	2.28	1.03	15.15	5.64	68.50	26.95	125.00	28.69	297.20	62.50	11322.00	255.00	80.60	140.90	20.34	26.11
S14 - 7	0.80	0.02	7.75	0.13	1.59	4.62	0.90	29.70	12.12	159.60	65.50	311.10	67.90	648.70	120.90	9265.00	134.90	37.60	50.60	36.50	29.08
S14 - 8	1.04	1.62	12.68	0.83	4.20	5.86	0.95	37.20	14.83	190.70	75.50	354.00	74.90	702.00	128.70	9858.00	219.00	61.80	68.10	2.63	25.12
S14 - 9	1.04	1.10	11.75	0.68	3.50	5.56	0.98	33.70	13.77	177.60	71.10	330.00	70.50	675.00	123.90	9440.00	141.40	44.70	59.10	3.26	26.66
S14 - 10	0.86	0.11	14.23	0.45	3.75	4.79	0.65	27.00	10.03	130.50	54.11	252.10	53.99	518.50	96.80	9585.00	122.00	35.81	54.59	15.06	25.56
S14 - 11	1.66	0.01	19.20	0.15	1.91	5.91	0.96	40.70	15.88	210.00	85.30	393.00	84.50	799.00	143.70	9657.00	459.00	133.00	126.00	114.2	26.13
																				9	
S14 - 12	2.19	5.10	32.20	2.22	12.10	13.27	1.50	66.50	24.10	304.00	119.90	546.00	116.30	1088.00	194.90	9766.00	402.00	112.70	137.60	2.30	21.78
S14 - 13	2.19	2.28	25.80	1.25	7.16	9.53	1.14	50.70	18.77	245.00	95.80	443.00	95.10	900.00	164.20	9476.00	464.00	127.00	134.30	3.67	23.63
S14 - 14	3.46	0.89	20.45	0.74	5.45	8.84	1.19	44.50	16.61	210.20	85.40	397.70	84.60	798.00	147.60	9850.00	217.00	52.90	87.60	6.05	23.87
S14 - 15	0.96	7.40	21.40	3.16	14.60	10.13	1.24	49.60	17.72	226.00	90.40	416.00	88.80	826.00	152.20	9822.00	187.60	55.10	70.10	1.06	22.17
S14 - 16	1.49	3.50	21.26	1.61	9.00	8.73	1.34	50.60	18.31	231.70	93.40	429.00	90.50	851.00	157.20	9206.00	332.00	93.70	97.00	2.15	22.39
S14 - 17	9.37	0.15	119.10	1.60	21.30	53.70	6.44	314.40	105.20	1253.00	459.00	1971.00	390.80	3457.00	588.90	8515.00	2613.00	727.00	482.10	58.51	14.64
S14 - 18	2.50	0.11	28.20	0.45	4.33	9.59	1.03	59.70	22.11	287.00	113.30	521.00	111.00	1027.00	185.70	10170.00	581.00	158.00	147.00	29.93	22.90
S14 - 19	1.23	0.51	14.87	0.38	3.18	6.81	0.93	43.80	16.03	208.20	83.40	392.10	82.30	774.00	142.10	9922.00	225.00	58.40	82.10	8.16	23.52

Chapter 4:

The El-Shadli bimodal volcanics, Eastern Desert, Egypt: Record of a 700 Ma rifting event during Rodinian break- up

Abstract

Island-arc accretion during the assembly of Gondwana has been recognized to be the main mechanism for Neoproterozoic crustal growth of the Arabian Nubian Shield (ANS). However, the size of the ANS and its Neoproterozoic growth rate significantly exceeds that of present-day examples of crustal generation via addition of juvenile mantle materials to arcs along subduction margins. Mantle plume-related magmatism has been proposed to represent an important alternative mechanism for the evolution of the ANS crust. Although Neoproterozoic plume and/or rifting magmatism is well developed globally during the fragmentation of the supercontinent Rodinia, direct record of such events is yet to be discovered in the ANS. Here, I identify that the El-Shadli volcanic province (80 km x 35 km and > 10 km thick) in the Eastern Desert of Egypt represents a Rodinian break-up-related bimodal volcanic event that may have been linked to mantle plume. The El-Shadli volcanic province mainly consists of a mafic-felsic bimodal suite and a subordinate amount of intermediate volcanic rocks that intruded the mafic rocks of the suite. The suite is characterized by a tholeiitic affinity with very low K₂O (< 1 wt.%) and flat-like REE patterns similar to N-MORB, whereas the intermediate rocks have a calc-alkaline affinity with arc-like REE patterns. Both the bimodal suite and the intermediate rocks give zircon U-Pb ages (using SHRIMP and LA-SS-ICPMS methods) of ~700 Ma. Whole-rock Nd-Sr isotopic data shows that the El-Shadli bimodal suite was extracted from a juvenile depleted mantle source. On the other hand, melts of the intermediate

rocks have undergone continental contamination. Nevertheless, Hafnium isotope data in zircon shows that both the bimodal suite (average $\epsilon\text{Hf}_{(t)} = +11.46$) and the intermediate rocks (average $\epsilon\text{Hf}_{(t)} = +9.76$) were derived from a depleted mantle source and have a juvenile nature. Oxygen isotope data for zircon shows low- $\delta^{18}\text{O}$ values for both the bimodal suite (average $\delta^{18}\text{O} = 4.94$ ‰) and intermediate rocks (average $\delta^{18}\text{O} = 4.79$ ‰). These values are lower than typical mantle values, indicating that the parental magma interacted with hydrothermal fluids. Collectively, field observations, whole-rock petrological, geochemical and isotopic data, and zircon U-Pb-Hf-O-trace element data, suggest that the El-Shadli bimodal suite and the intermediate rocks were produced by partial melting of MORB-like and arc-like gabbroic oceanic crust, respectively, during the break-up of Rodinia that might be related to mantle plume. The ~700 Ma El-Shadli bimodal volcanic province represents a major magmatic episode in the formation of the ANS crust. The recognition of the El-Shadli volcanic province as a rift-related product argue against the widely held believe that Neoproterozoic crustal growth in the ANS was primarily driven by arc magmatism; instead, magmatism formed in other tectonic settings such as mantle plume and continental rifting may also have played important roles.

4.1 Introduction

The Arabian Nubian Shield (ANS) forms one of the largest exposures of Neoproterozoic juvenile continental crust on Earth (Figure 3.1b; Pease and Johnson, 2013). Island-arc accretion during the assembly of Gondwana has been proposed to be the main mechanism for Neoproterozoic crustal growth in the ANS (Kröner *et al.*, 1991; Stern, 1994, 2002; Johnson and Woldehaimanot, 2003; Johnson *et al.*, 2011; Fritz *et al.*, 2013). However, the size of the ANS and its Neoproterozoic growth rate significantly exceed that of present-day examples of crustal generation via addition of juvenile mantle materials to arcs along subduction margins (Reymer and Schubert, 1984, 1986). As an alternative mechanism for Neoproterozoic crustal generation in the ANS, it has been proposed that mantle plume-related magmatism may also have played a major role (Stein and Goldstein, 1996; Stein, 2003). Nonetheless, so far no direct record of Neoproterozoic plume events have been reported in the ANS.

Bimodal volcanism represents intercalations between mafic and felsic rocks that are commonly found in magmatic rift systems above mantle plumes, such as the Cenozoic magmatism of the East-African rift (Rooney, 2017, 2020) and Neoproterozoic bimodal rift-related volcanism (Z. X. Li *et al.*, 1999, 2003; X. H. Li *et al.*, 2008; W. X. Li, X.H. Li and Z. X. Li, 2010; Lyu *et al.*, 2017; Kjølø *et al.*, 2019; Cheng *et al.*, 2020). In their paleogeographic reconstruction of the Neoproterozoic supercontinent Rodinia, Z. X. Li *et al.* (2008) and Z. X. Li, Evans, and Halverson (2013) suggest that the ANS terranes was likely located between India, Australia-East Antarctica, and the Sahara craton, on the fringe of the Rodinia superplume at ~825–680 Ma. This period has also been suggested to be the time of rifting and fragmentation of the supercontinent Rodinia (Z. X. Li *et al.*, 2008; Z. X. Li and Zhong, 2009; Z. X. Li, Evans and Halverson, 2013), and records of plume-related magmatism, including granitoids, mafic and ultramafic dikes, and rift-related bimodal volcanics, have been reported in places like South China (Z. X. Li *et al.*, 1999, 2003, 2008; X. H. Li *et al.*, 2003; Cheng *et al.*, 2020), Tarim (Zhang *et al.*, 2006), Australia (Wingate *et al.*, 1998), Southern Africa (Frimmel, Zartman and Späth, 2002) and Laurentia (Heaman, LeCheminant and Rainbird, 1992; Park, Buchan and Harlan, 1995).

Here, I describe the record of a rift-related magmatic event in the El-Shadli volcanic province (80 km x 35 km and > 10 km thick) of the Eastern Desert of Egypt, part of the ANS (Figures 4.1 and 4.2). The origin and tectonic setting of the rocks are

evaluated based on the whole-rock Sr-Nd isotopic and geochemical data, coupled with an integrated U-Pb-Hf-O isotopic and trace element analysis of magmatic zircons. I propose that the El-Shadli volcanic province represents a rift-related bimodal volcanism suite produced by partial melting of juvenile crust during Rodinian break-up around ~700 Ma which might be linked to mantle plume.

4.2 Geological setting

4.2.1 Geological background

The broad geological background about the ANS and the Eastern Desert of Egypt is provided in Chapter 3. Here I focus on the details of the volcanic rocks in the Eastern Desert of Egypt. Neoproterozoic volcanic rocks are widely distributed in the Eastern Desert (Stern and Hedge, 1985) (Figure 4.1). They mostly occur as metavolcanic-metasedimentary rock successions (Ali *et al.*, 2009). These volcanic rocks were initially interpreted as the first stage of eugeosynclinal filling (Akaad and El-Ramly, 1960). Based on field observations and petrological and geochemical data, Akaad and El-Ramly (1960) classified the Eastern Desert volcanics into (1) an older metavolcanic series (called the El-Shadli type) and (2) a non-metamorphosed younger volcanic series (called the Dokhan type). Stern (1981) divided the Eastern Desert volcanic rocks into two groups: (1) Old Metavolcanics (OMV) and (2) Young Metavolcanics (YMV). The OMV group corresponds to ophiolite-related volcanic rocks and consists of low-K tholeiitic pillow metabasalts and basaltic andesites such as the El-Fawakhir ophiolites. The YMV group corresponds to arc-related volcanics (i.e., non-ophiolitic) and is composed of a low- to medium-K calc-alkaline suite including andesitic flows with subordinate mafic and felsic rocks such as arc volcanics found in W. El-Dabbah and W. Arak.

According to a comprehensive geochemical data compilation, Khalil (1997) suggested that the Eastern Desert volcanic rocks comprise ocean-related ophiolitic volcanics (i.e., OMV), intra-oceanic island arc-related volcanics (i.e., YMV), and the Dokhan volcanics (DV). The DV group mostly occur in the northern part of the Eastern Desert (Figure 4.1) and are characterized by abundant felsic volcanics such as rhyolites, dacites and ignimbrites, with a small amount of mafic and intermediate rocks. The DV group is non-metamorphosed and has a medium- to high-K calc-

alkaline to alkaline affinity. The DV group is believed to have been formed in a continental arc (e.g., Khalil, 1997) or during post-orogenic extension i.e., post-collision (e.g. Eliwa, Kimura and Itaya, 2006; Eliwa, El-Bialy, and Murata, 2014).

Geochronological data show that the age relationships between the OMV and YMV are unclear and their age ranges largely overlap: while the ophiolite-related volcanic rocks (OMV) have an age range of ~750–730 Ma (e.g., Kröner *et al.*, 1992; Stern *et al.*, 2004; Ali *et al.*, 2010), the island arc metavolcanics (YMV) and associated metasedimentary rocks have an age range of ~770–720 Ma (e.g., Stern and Hedge, 1985; Kröner *et al.*, 1992; Ali *et al.*, 2009; Bühler *et al.*, 2014; Abd El-Rahman *et al.*, 2017). In contrast, the DV group is well distinguished from these two older groups by its younger age range of ~630–580 Ma (Wilde and Youssef, 2000; Breitzkreuz *et al.*, 2010) (Figure 4.1).

The relationships between the El-Shadli bimodal volcanic province and the OMV and YMV groups have been debated for a number of years (e.g., Ali *et al.*, 2009). Some consider the El-Shadli bimodal volcanic province to be related to the OMV group (Akaad and El-Ramly, 1960; Akaad and Noweir, 1969; El-Shazly and El-Sayed, 2000), whereas others classify it as a member of the YMV (Stern, 1981; El-gaby and El-nady, 1984; Khalil, 1997; Faisal *et al.*, 2020). Stern, Kröner, and Rashwan (1991) suggested that the El-Shadli bimodal volcanics formed at a magmatic rift, and are therefore unrelated to either metavolcanic groups. The age of the El-Shadli bimodal volcanics, determined by a Rb-Sr whole-rock isochron from mafic and felsic rocks around the Um Samiuki area (Figure 4.2), was reported as 712 ± 24 Ma (Stern, Kröner and Rashwan, 1991), younger than the previously reported ages of both the OMV and YMV. The most recent zircon LA-ICPMS U-Pb data, from felsic rocks around the Abu Hamamid area (Figure 4.2), yielded an age of 695 ± 6 Ma (Faisal *et al.*, 2020).

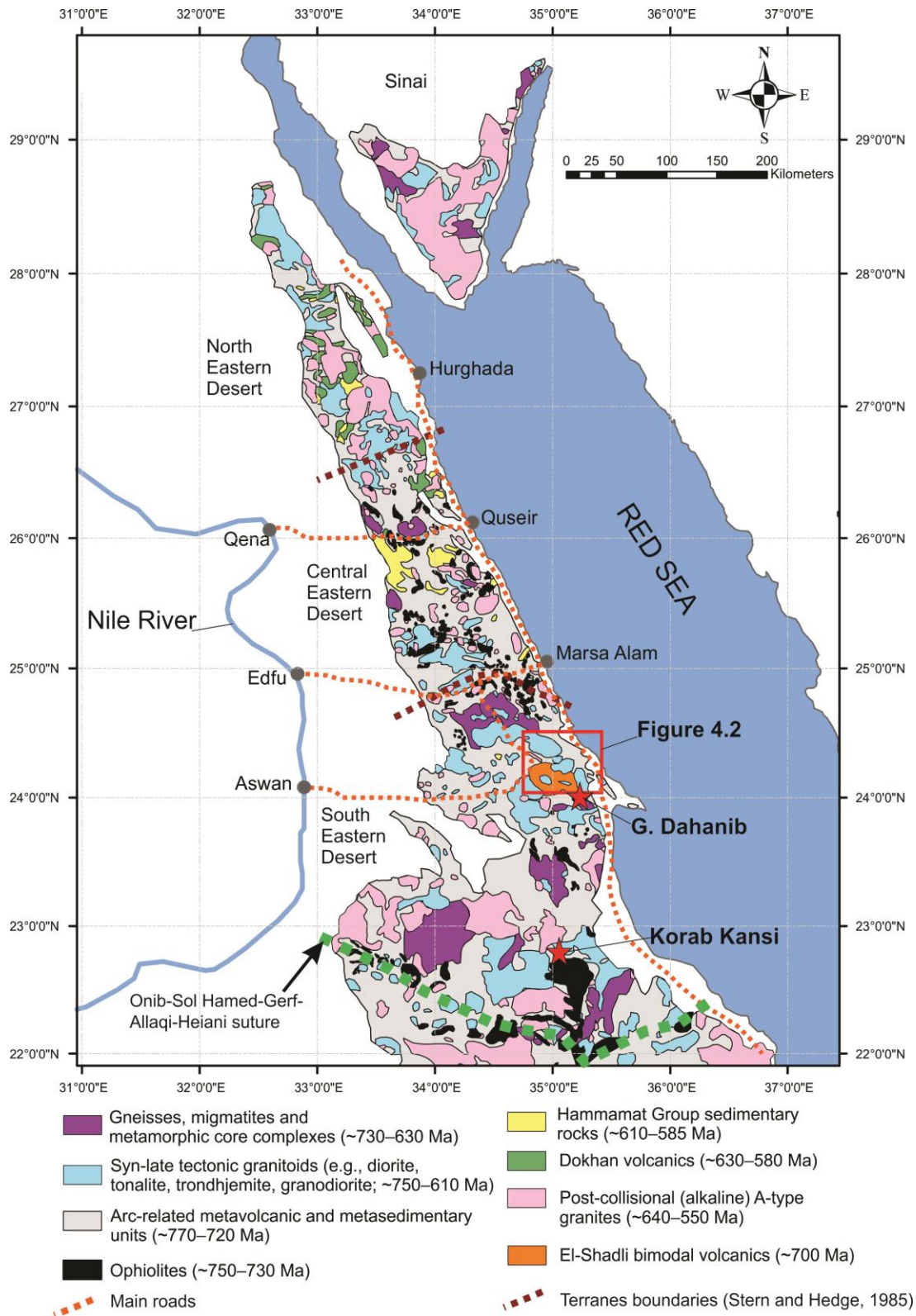
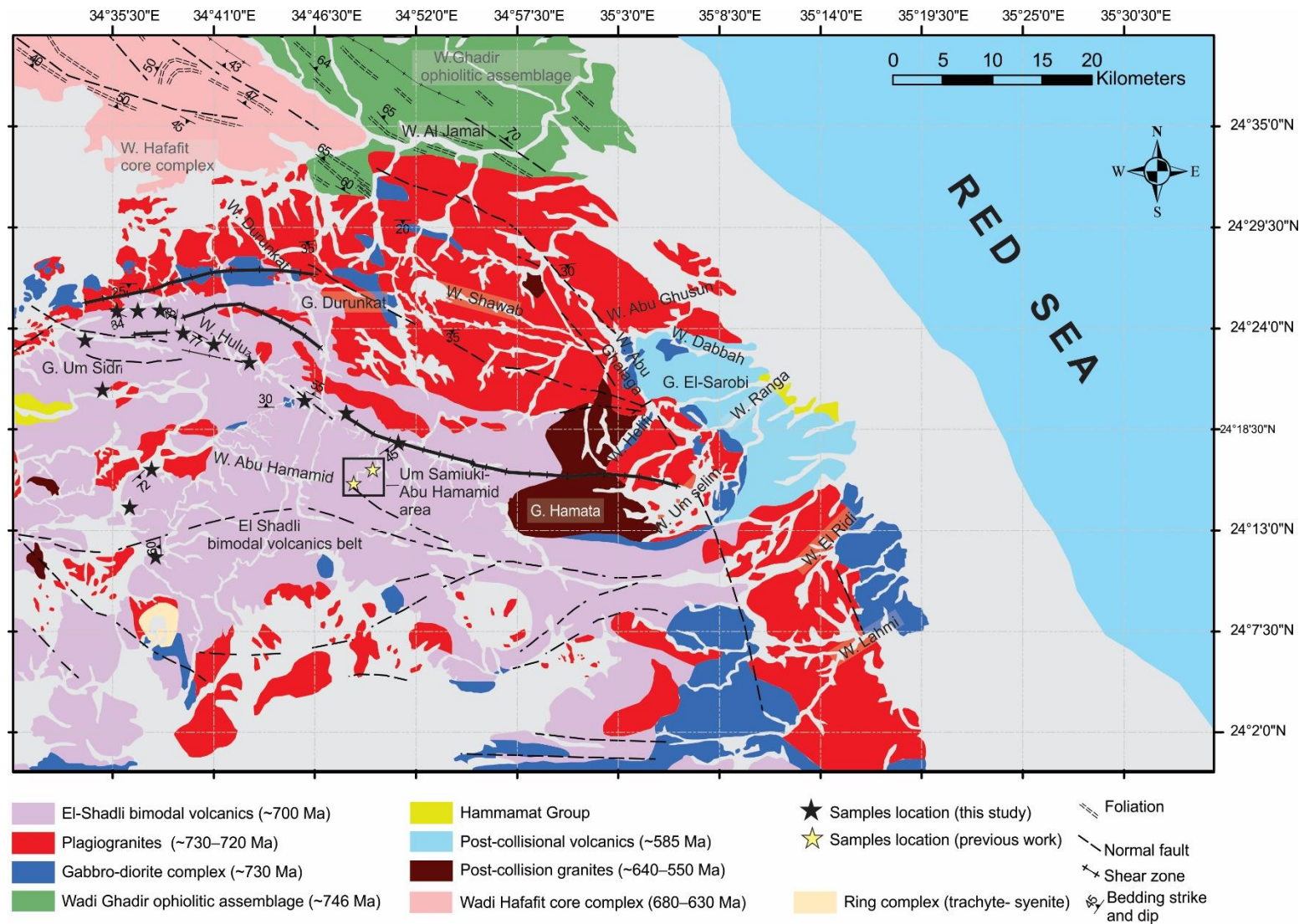


Figure 4.1: Geological map of the Eastern Desert showing the ages and distribution of the main Precambrian crustal basement rock units. Eastern Desert terrane boundaries are after Stern and Hedge (1985). The map is modified after Johnson *et al.* (2011).



4.2.2 Field observations and petrography

The El-Shadli area is located in the southern part of the Eastern Desert (Figures 4.1 and 4.2). Rocks exposed in this area include the El-Shadli bimodal volcanic rocks, the El-Shadli plagiogranite-gabbro association, the W. Ghadir ophiolitic assemblages, the W. Hafafit core complex, post-collisional alkaline granites, and post-collisional W. Ranga volcanics (Figure 4.2). The El-Shadli volcanic province represents the largest bimodal volcanic suite in the Eastern Desert of Egypt (80 km x 35 km and > 10 km thick) (Shukri and Mansour, 1980; Khudeir, Ali and El Habaak, 1988; Stern, Kröner and Rashwan, 1991). The province is roughly E-W trending and is surrounded by outcrops of the El-Shadli plagiogranite-gabbro association (Figure 4.2). The El-Shadli volcanic province consists of massive, dominantly submarine bimodal volcanics with several alternating layers of mafic and felsic lavas, tuffs, and their associated immature metasedimentary rocks, along with subordinate amounts of intermediate volcanic rocks (Figures 4.3-4.5). The province is characterized by upright folding, and is cut by several WNW-ESE-trending normal faults and shear zones (Shukri and Mansour, 1980; Stern, Kröner, and Rashwan, 1991) (Figure 4.2).

At the contact with the surrounding El-Shadli plagiogranites (sample S01-1a = 729 ± 7 Ma, see Chapter 3 for details), dyke swarms, interpreted as feeders for the mafic rocks of the bimodal volcanic suite (sample S01-2), are seen to intrude the plagiogranites (Figure 4) with well-developed chilled margins obviously in the field. These mafic dykes are up to 1 m in width. The plagiogranites and mafic dykes are intruded by small felsic rhyolite dykes (sample S01-3). The field relationships suggest that the El-Shadli bimodal volcanics are younger than the surrounding El-Shadli plagiogranite-gabbro association. This relationship is confirmed by new geochronological data from this study that shows that the El-Shadli bimodal volcanics (698 ± 6 Ma) are 30–20 Ma younger than the El-Shadli plagiogranite-gabbro association ($730 \pm 7 - 722 \pm 7$ Ma). Both the field relationships and geochronological data argue against the previous models that suggested that the El-Shadli plagiogranite-gabbro association intruded the volcanic province (Shukri and Mansour, 1980; Khudeir, Ali and El Habaak, 1988; Stern, Kröner and Rashwan, 1991; Faisal *et al.*, 2020). Previous works had primarily focused on an outcrop around the Um Samiuki-Abu Hamamid area (Figure 4.2), which is not in direct contact with the plagiogranite-gabbro association and may have thus led to those misinterpretations.

The bimodal volcanics consist of massive alternating sheets and layers that range in size from few to hundreds of metres in thickness, including some sills (Figure 4.3). The mafic rocks mainly consist of submarine tholeiitic basalts, basaltic andesites, and few dolerite sills (sample S04-2) with thin intercalations of tuffs and cherts (Figure 4.5a). These mafic rocks are generally massive and sometimes show pillow structures (Figures 4.3 and 4.5b). The pillows range in size from a few centimetres to metres in dimension with vesicular margins (Figure 4.5b). The felsic rocks mainly consist of massive rhyolitic lava flows (Figure 4.3). Minor intermediate rocks occur as small unmappable bodies that intrude the mafic rocks (Figure 4.5c, d). The volcanogenic sedimentary rocks mainly include tuffs and agglomerates (Figure 4.5a, f). The tuffs show well-developed sedimentary bedding and laminations (Figure 4.5a).

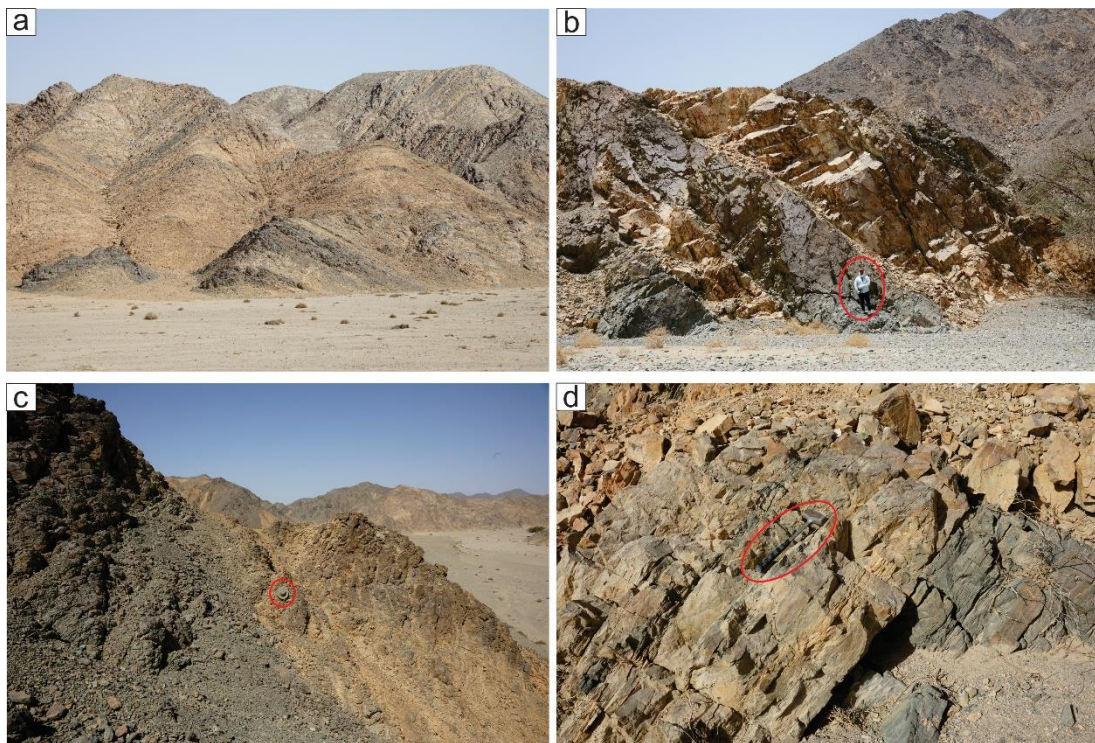


Figure 4.3: Field photos for the El-Shadli bimodal volcanic suite showing the cyclic intercalations between mafic and felsic rocks.

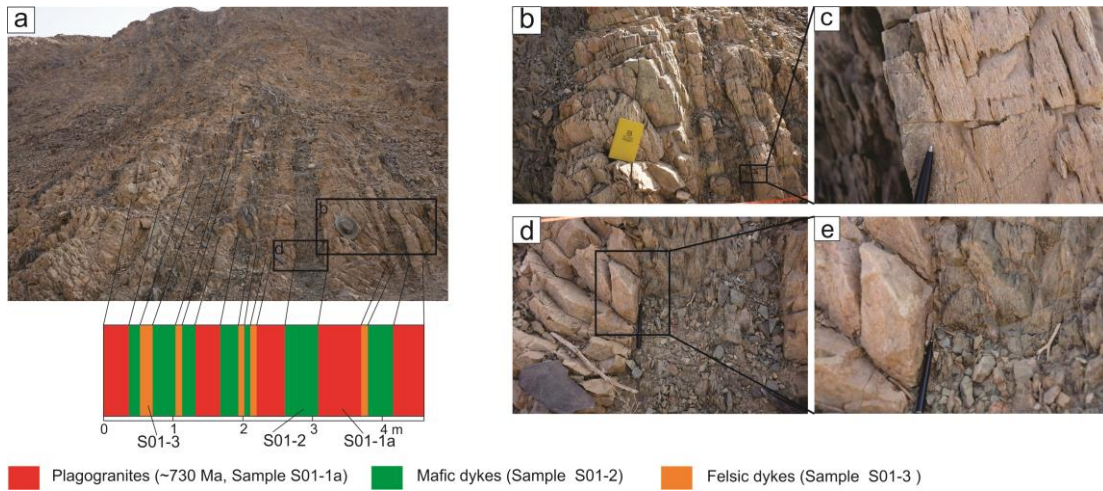


Figure 4.4: Field photos showing the field relationships between the surrounding plagiogranites (~730 Ma) and mafic and felsic dykes related to the bimodal volcanic suite (~700 Ma).



Figure 4.5: Field photos for the El-Shadli bimodal volcanic suite. (a) Pyroclastic layers intercalation with mafic rocks. (b) Pillow basalts of the mafic end-member. (c-e) intermediate rocks intruding the mafic rocks. (f) Associated agglomerates.

Petrographically, the mafic rocks show intergranular to porphyritic textures (Figure 4.6a-f). They are composed of plagioclase, clinopyroxene, and amphiboles (Figure 4.6a-f). Accessory minerals include opaque minerals such as Fe-Ti oxides, titanite, and apatite. Epidote, sericite, clay minerals, chlorite, and calcite are present as secondary minerals. Plagioclase occurs as fine-grained groundmass, small laths, and phenocrysts (Figure 4.6a-c). These phenocrysts are commonly euhedral with albite twinning and sometimes show secondary alteration to epidotes. Clinopyroxene is well preserved and ranges in sizes from small crystals to large phenocrysts, up to 1mm in dimension (Figure 4.6e). The clinopyroxene phenocrysts have small laths of plagioclase, forming ophitic and sub-ophitic textures (Figure 4.6e). The smaller clinopyroxene crystals are also seen to intercalate with the plagioclase groundmass (Figure 4.6c). Clinopyroxene is sometimes altered to amphibole and chlorite (Figure 4.6f). Amphiboles were pale green in color found either in the groundmass or as small phenocrysts (Figure 4.6f). Opaque minerals include magnetite, hematite and ilmenite, and they occur as fine subhedral grains randomly distributed in the groundmass (Figure 4.6f).

The felsic rocks are mainly rhyolites with reddish to pink-grey color (Figure 4.3). They are usually massive and composed of plagioclase, quartz, potash feldspar, and minor biotite (Figure 4.6g-j). Opaque minerals include magnetite, titanite, and zircon and occur as accessory minerals. Secondary minerals include chlorite, epidote, sericite, and clay minerals. Plagioclase, quartz, and potash feldspar occur either as euhedral to subhedral phenocrysts and/or small grains in the groundmass (Figure 4.6g-i). Plagioclase crystals are well preserved with albite twinning, sometimes displaying epidote alteration (Figure 4.6g). Some quartz crystals exhibit wavy extinction (Figure 4.6h). Potash feldspar phenocrysts show Carlsbad twinning (Figure 4.6i). Biotite is found in the groundmass and shows chlorite alteration along cleavage (Figures 4.6j).

The intermediate volcanics include andesitic rocks with grey color and a porphyritic texture (Figure 4.5c-e). They consist of plagioclase, quartz, hornblende, and biotite (Figure 4.6k, l). Opaque minerals include magnetite, ilmenite, titanite, and zircon, all as accessory minerals. Secondary minerals include chlorite, epidote, and sericite. Plagioclase, quartz, and biotite occur as large phenocrysts in the groundmass of the same minerals (Figure 4.6k). Hornblende occurs as small grains within the groundmass (Figure 4.6k). Chlorite represents an alteration product from biotite

(Figure 4.6l). Epidote and sericite are found disseminated in the groundmass as alteration products of parental plagioclase (Figure 4.6k).

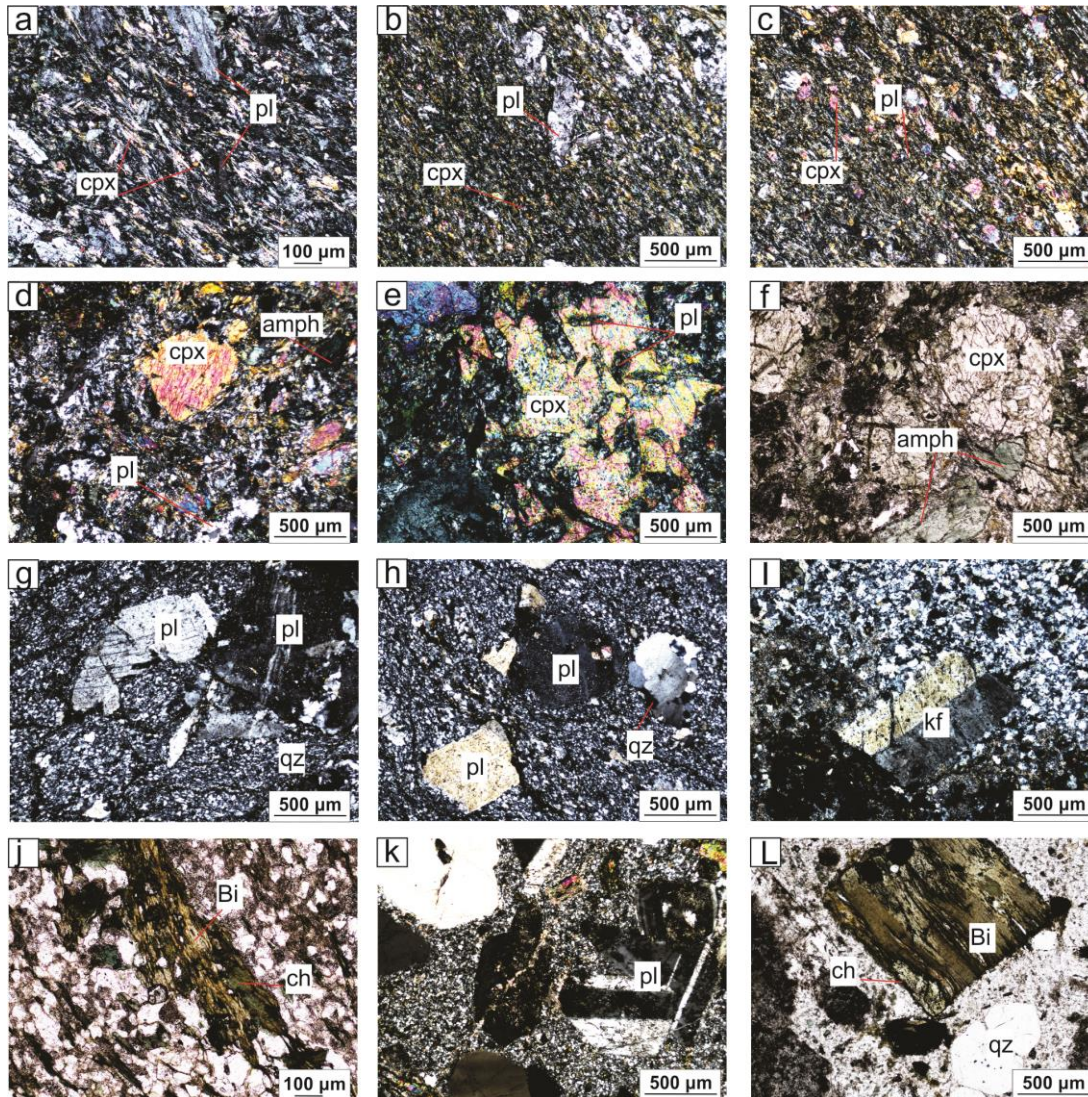


Figure 4.6: Photomicrographs of the El Shadli bimodal suite and associated intermediate rocks. (a-f) Crossed-polarized light images of the mafic rocks showing the porphyritic, ophitic, and sub-ophitic textures. The primary mineral (plagioclase and clinopyroxene) assemblage are well preserved. (g-j) Crossed-polarized light images of the felsic rocks showing porphyritic textures. The phenocrysts include quartz, plagioclase, and potash feldspar. (k-L) Crossed-polarized light images of the intermediate rocks showing porphyritic textures and phenocrysts include quartz, plagioclase, and biotite. Plagioclase= pl, clinopyroxene= cpx, quartz= qz, amphiboles= amph, potash feldspar= kf, biotite= Bi and chlorite= ch.

4.3 Analytical methods

Whole-rock major elements were determined for 18 samples (including 11 mafic, 5 felsic, and 2 intermediate rock samples) using X-ray fluorescence at the Bureau Veritas Lab, Perth (Table 4.1). Whole-rock trace elements and Sr-Nd isotope

data were determined using ICP-MS and TIMS, respectively, at the Macquarie (MQ) GeoAnalytical Lab, Macquarie University (Table 4.1). Zircon U-Pb dating was carried out using SHRIMP II at Curtin University (Table C1) for rhyolite sample S02-5 and andesitic sample S16. Zircon Hf isotope and trace element data were acquired using LASS-ICPMS at Curtin University (Table C2). Zircon O isotope data were acquired using SIMS at Guangzhou Institute of Geochemistry, China (Table C3). Analytical techniques are presented in more detail in Chapter 2 (Methodology).

4.4 Results

4.4.1 Whole-rock geochemical data

Samples of the El-Shadli volcanic rocks are fresh with minor alteration/weathering, as indicated by low loss on ignition (LOI) with values below 1 wt.% for felsic rocks and ranging between 1 to < 3 wt.% for the mafic and intermediate rocks (Table 4.1). It had been suggested that the mobile element content can be modified by alteration/weathering (Polat and Hofmann, 2003). Therefore, the effect of alteration on the mobility of the major and trace elements was first evaluated before discussing the geochemical and petrological characterizations of the studied volcanics. The LOI value was plotted against all major and some trace elements such as Cr, Ni, Rb, Sr, Y, Zr, Nb, Ba, La, and Ce (Figures C.1 and C.2). None of the major and trace elements shows any correlation with the LOI values, suggesting that there is no significant effect of alteration/weathering on the geochemical composition of the studied rocks.

The El-Shadli volcanic rocks have a wide range of SiO₂ contents (45.49–77.15 wt.%) that show a clear bimodal distribution (Figure 4.7). On a total alkali versus silica (TAS: Middlemost, 1994) plot (Figure 4.8a), two major subgroups are defined for the El-Shadli volcanic rocks (including data from this study and that of previous work by Stern, Kröner and Rashwan (1991) and Faisal *et al.* (2020)). The first group comprises basalts with a minor amount of basaltic andesite, and the other group consists of rhyolites along with a subordinate amount of intermediate rocks. The intermediate rocks include only andesitic samples from this study (S16 and S17-1) and three samples from the previous work of Stern, Kröner and Rashwan (1991) and Faisal *et*

al. (2020). The division of the two groups is consistent with the plot of Zr/Ti versus Nb/Y (Figure 4.8b) of Winchester and Floyd (1976).

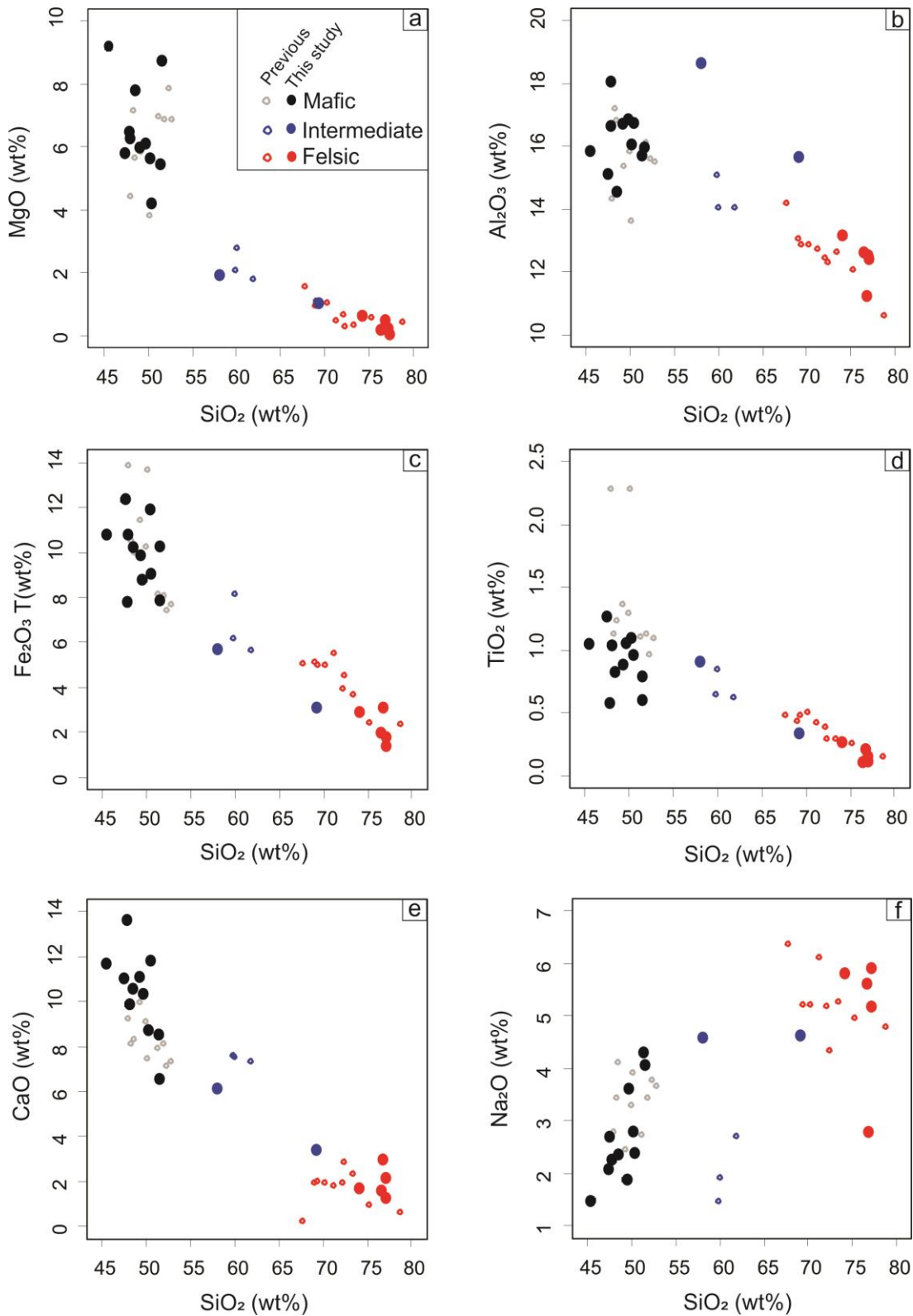


Figure 4.7: Harker plots showing the whole-rock major elements composition of the El-Shadli bimodal volcanic province. The previously published data are from Stern, Kröner, and Rashwan (1991) and Faisal *et al.* (2020).

Data from this study show that the mafic (i.e., basaltic) rocks have SiO₂ (45.49–51.50 wt.%), MgO (4.18–9.17 wt.%), Al₂O₃ (14.55–18.07 wt.%), Fe₂O₃^T (8.58–13.74 wt.%), and TiO₂ (0.59–1.27 wt.%) (Figure 4.7; Table 4.1). The felsic rocks have SiO₂ (74.14–77.15 wt.%), MgO (0.12–0.64 wt.%), Al₂O₃ (11.28–13.16 wt.%), Fe₂O₃^T (1.59–3.47 wt.%), and TiO₂ (0.13–0.27 wt.%) (Figure 4.7; Table 4.1). The two intermediate rocks (S16 and S17-1) have a composition of SiO₂ = 69.13 and 58.06 wt.%, MgO = 1.09 and 1.94 wt.%, Al₂O₃ = 15.66 and 18.63 wt.%, Fe₂O₃^T = 3.4 and 6.32 wt.%, and TiO₂ = 0.34 and 0.91 wt.%, respectively (Figure 4.7; Table 4.1). Overall, the basaltic and felsic rocks of this study have very low K₂O content (<1 wt.%), while the intermediate rocks have K₂O content of >1 wt.% (Figure 4.8d). For the basaltic samples the total alkalis (Na₂O + K₂O = 1.73–4.76) increase with increasing SiO₂ content (Figures 4.7 and 4.8a). In contrast, for the felsic rocks, the total alkalis (Na₂O + K₂O = 3.57–6.21) decreases with increasing SiO₂ content (Figures 4.7 and 4.8a). The intermediate rocks do not show any relationship between the total alkalis (Na₂O + K₂O = 5.7) and SiO₂ content (Figures 4.7 and 4.8a).

The basaltic rocks of this study show an evolved composition with Mg# [$\text{MgO}/(\text{MgO} + \text{FeO}^{\text{T}}) \times 100$] = 64–43 (Table 4.1). Cr (9–341 ppm) and Ni (3–120 ppm) contents of these basaltic rocks increase with increasing Mg# (Table 4.1). In Harker plots (Figure 4.7), the basaltic rocks show a decrease of MgO, Fe₂O₃^T, and CaO with increasing SiO₂, indicating significant fractional crystallization of olivine and clinopyroxene. Na₂O increases with increasing SiO₂, indicating plagioclase fractionation. On the other hand, for the felsic and intermediate rocks, almost all of the major elements, except Na₂O, show a decrease with increasing SiO₂ (Figure 4.7).

All of the studied rocks show sub-alkaline affinity according to the total alkalis (Middlemost, 1994) and Nb/Y ratios (Winchester and Floyd, 1976) (Figure 4.8a, b). On an AFM diagram, they plot on a tholeiitic series trend (Figure 4.8 c). The SiO₂ versus K₂O relationship (Peccerillo and Taylor, 1976) shows that the basaltic and felsic rocks belong to the tholeiitic series (Figure 4.8d), while the intermediate rocks are more akin to calc-alkaline series rocks. Accordingly, immobile elements and their ratios are more useful for defining the magmatic affinities of the sub-alkaline volcanic rocks. According to the Co-Th diagram of Hastie *et al.* (2007) and Th/Yb versus Zr/Y diagram of Ross and Bédard (2009), both the basaltic and felsic rocks are similar to the tholeiitic series, whereas the intermediate rocks show a calc-alkaline affinity.

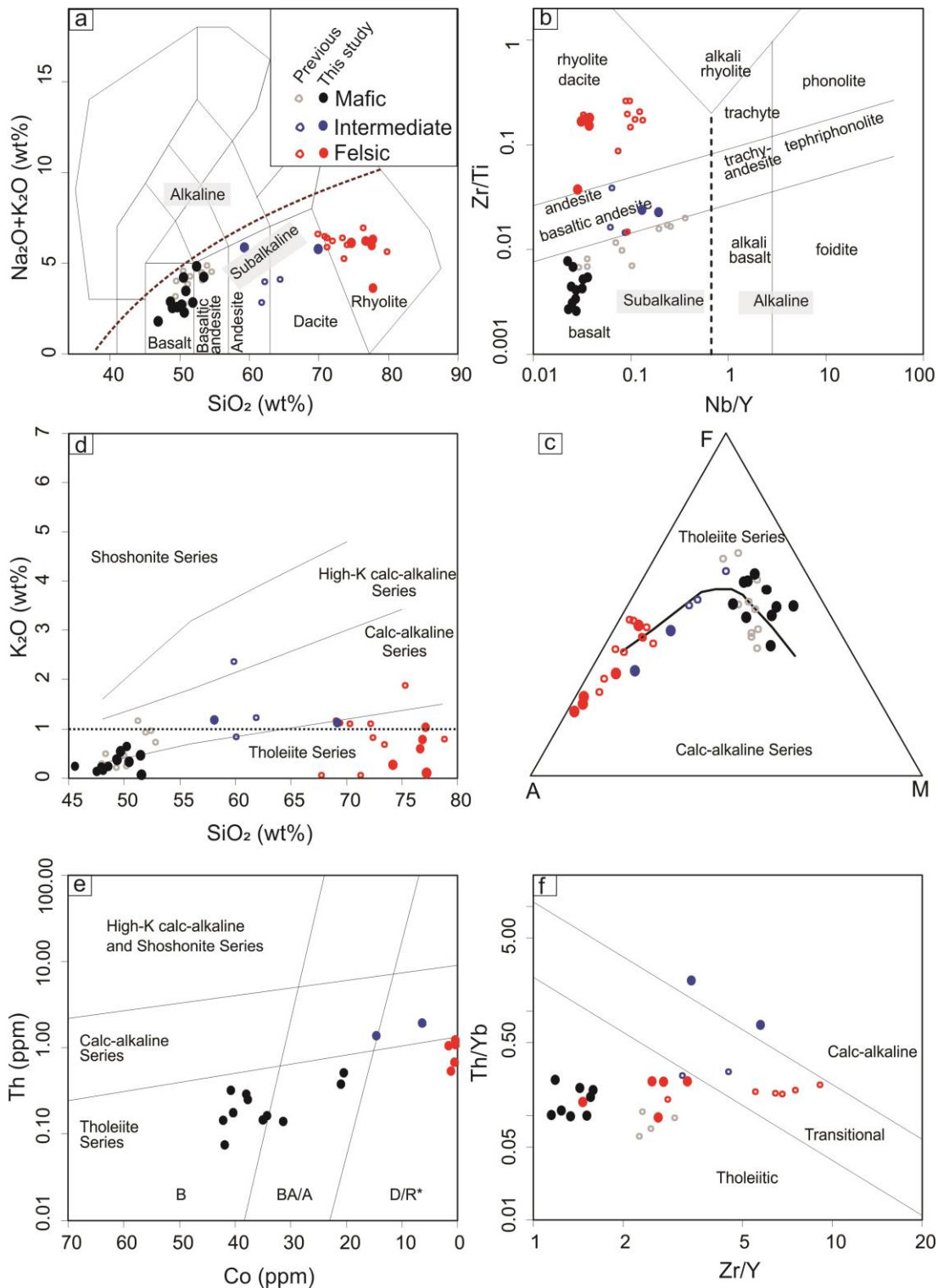


Figure 4.8: Chemical classification diagrams using the whole-rock major and trace element composition of the El-Shadli bimodal volcanic province. (a) Total alkali-silica diagram (TAS) of Middlemost (1994). (b) Zr/Ti versus Nb/Y of Winchester and Floyd (1976). (c-f) geochemical affinities plots including AFM diagram, SiO₂ versus K₂O relationship of Peccerillo and Taylor (1976), Co-Th diagram of Hastie *et al.* (2007) and Th/Yb versus Zr/Y diagram of Ross and Bédard (2009) showing that the El-Shadli bimodal suite belongs to the tholeiitic series and the intermediate rocks calc-alkaline series.

On the chondrite (CI)-normalized (Anders and Grevesse, 1989) rare earth element (REE) diagram (Figure 4.9a, b), the basaltic and felsic rocks commonly show distinct flat-like REE patterns with a slightly negative slope for the light REE (LREE) similar to MORB (Sun and McDonough, 1989). The basaltic rocks have uniform/tight REE patterns and show LREE-depletion with $La_N = 3.04\text{--}7.23$, $(La/Sm)_{CI} = 0.42\text{--}0.75$, $(La/Yb)_{CI} = 0.46\text{--}0.95$, heavy REE (HREE; $(Yb/Gd)_{CI} = 0.82\text{--}1.35$) and no significant Eu anomalies [$(Eu/Eu^*)_{CI} = 0.90\text{--}1.1$, where $Eu^* = \sqrt{(Sm \times Gd)}$] (Figure 4.9a). The felsic rocks have more evolved REE compositions, and mimic the REE patterns of the basaltic rocks, with $La_N = 11.54\text{--}24.93$, $(La/Sm)_{CI} = 0.63\text{--}1.12$, $(La/Yb)_{CI} = 0.64\text{--}1.07$ and $(Yb/Gd)_{CI} = 0.92\text{--}1.27$, but with negative Eu anomalies [$(Eu/Eu^*)_{CI} = 0.55\text{--}0.85$] (Figure 4.9b). The intermediate rocks show different REE patterns compared to those of the basaltic and felsic rocks, and display a positive trend from LREE to HREE with LREE-enrichment $La_N = 22.05\text{--}22.14$, $(La/Sm)_{CI} = 1.46\text{--}1.91$, and $(La/Yb)_{CI} = 2.89\text{--}5.49$.

On the Normal (N)-MORB-normalized trace elements diagram (Sun and McDonough, 1989) (Figure 4.9a) the basaltic rocks show depletion in Zr and Nb, but their large ion lithophile elements (LILE) such as Cs, Rb, Ba, Th, and U exhibit some enrichment relative to N-MORB (Sun and McDonough, 1989). The felsic rocks display strongly fractionated patterns relatively to N-MORB with significant negative Nb, P, and Ti anomalies (Figure 4.9b). The intermediate rocks show significant enrichments in almost all trace elements compared to N-MORB (Figure 4.9c).

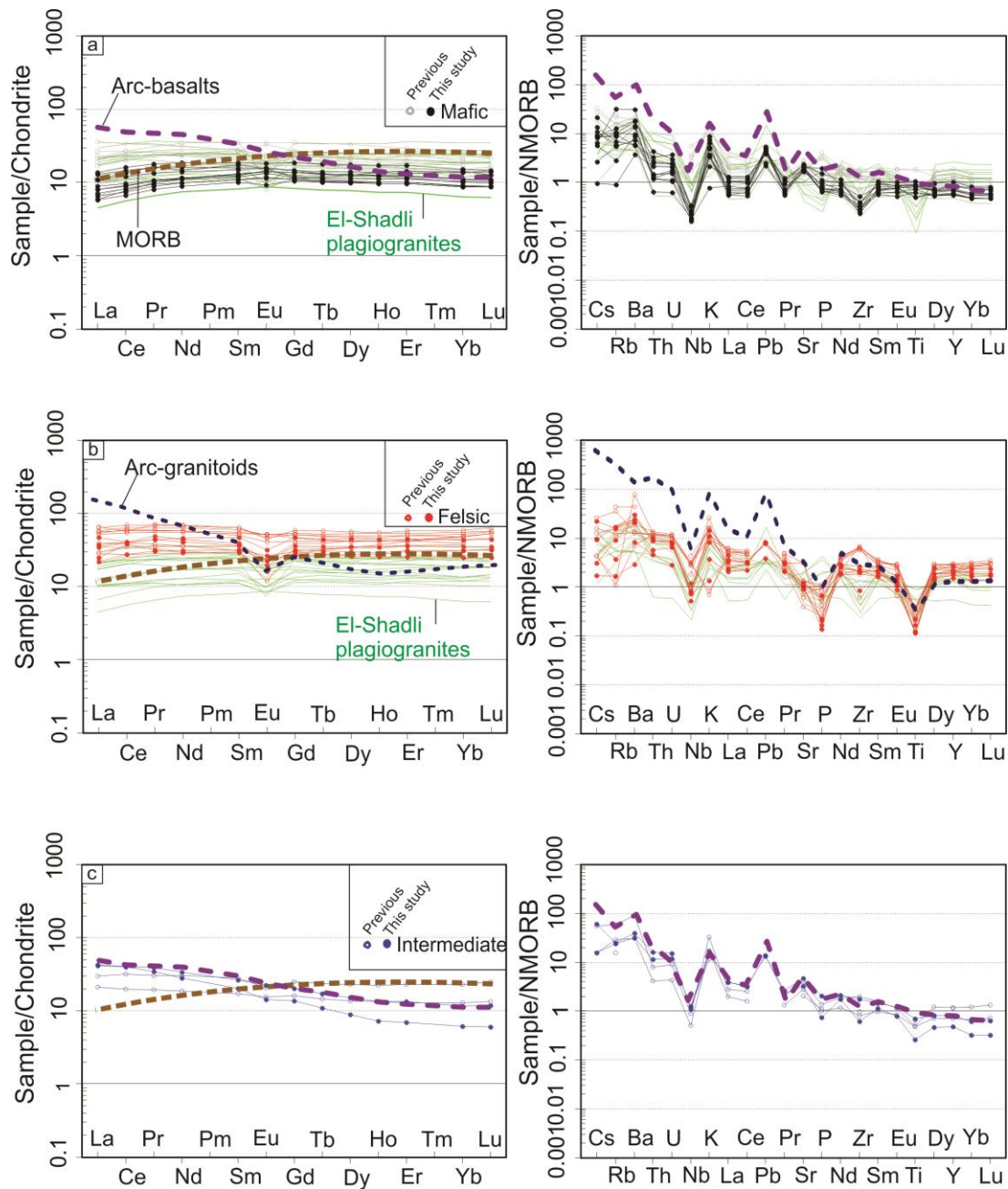


Figure 4.9: Chondrite-normalized REE patterns (Anders and Grevesse, 1989) and NMORB-normalized (Sun and McDonough, 1989) trace element diagram of the El-Shadli bimodal suite and intermediate rocks. MORB pattern is after Sun and McDonough (1989). Data of arc-basalts and granitoids are from GeoRoc (<http://georoc.mpch-mainz.gwdg.de/georoc/>). The previously published data are form Stern, Kröner, and Rashwan (1991) and Faisal *et al.* (2020). Open circle = pervious work, close circle = this study.

4.4.2 Whole-rock Sr-Nd isotopic data

The basaltic rocks show low concentration of Sr (149–209 ppm) and Rb (0.49–18.06 ppm), and their measured $^{87}\text{Sr}/^{86}\text{Sr}$ ratios range between 0.702503 ± 0.000005

and 0.705022 ± 0.000003 (Table 4.1). They also have a low concentration of Nd (4–16 ppm) and Sm (1.5–5.6 ppm), and their measured ratios of $^{143}\text{Nd}/^{144}\text{Nd}$ range from 0.512950 ± 0.000004 to 0.513135 ± 0.000002 (Table 4.1). The calculated initial ratios of $^{87}\text{Sr}/^{86}\text{Sr}$ have a range of 0.702219 ± 0.000003 – 0.702694 ± 0.000003 and $^{143}\text{Nd}/^{144}\text{Nd}$ have a range of 0.512030 ± 0.000005 – 0.512105 ± 0.000002 (Figure 4.10b and Table 4.1). The calculated $\epsilon\text{Nd}(t)$ values range from +5.84 to +7.31 (Figure 3.10b).

The felsic rocks show similar Sr and Nd isotopic composition to the basaltic rocks with initial ratios of $^{87}\text{Sr}/^{86}\text{Sr} = 0.702575 \pm 0.000004$ – 0.703043 ± 0.000003 , $^{143}\text{Nd}/^{144}\text{Nd} = 0.512065 \pm 0.000002$ – 0.512115 ± 0.000002 , and $\epsilon\text{Nd}(t)$ values ranging from +6.53 to +7.50 (Figure 4.10b and Table 4.1). The intermediate rocks display different isotopic composition when compared to the basaltic and felsic rocks, with initial ratios of $^{87}\text{Sr}/^{86}\text{Sr}$ in the range of 0.702527 ± 0.000004 – 0.702605 ± 0.000003 , $^{143}\text{Nd}/^{144}\text{Nd}$ 0.511677 ± 0.000001 – 0.511802 ± 0.000006 , and $\epsilon\text{Nd}(t)$ between +1.38 and –1.04 (Figure 4.10b and Table 4.1), indicating that their source underwent crustal contamination.

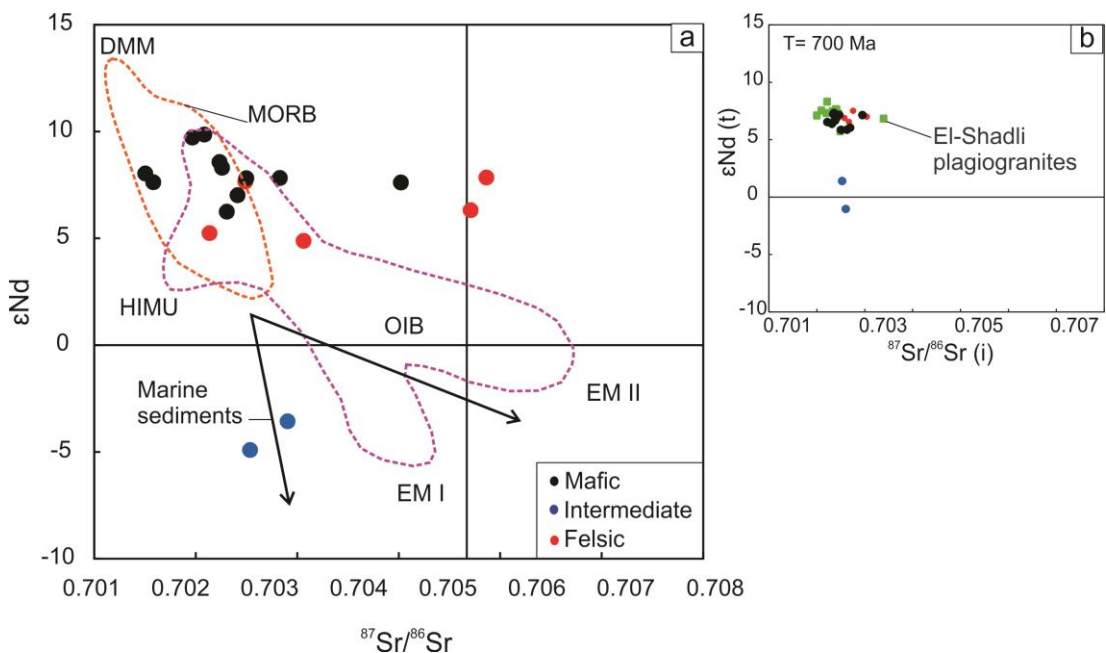


Figure 4.10: Sr-Nd isotopes of the El-Shadli bimodal volcanic province. MORB and OIB fields are after Hofmann (2013).

4.4.3 Zircon U-Pb-Hf-O isotopes and trace elements

4.4.3.1 Rhyolite sample S02-5

Zircon grains from sample S02-5 have euhedral equant to prismatic morphology and sizes of $< 100 \mu\text{m}$. In cathodoluminescence (CL) images, these zircons display well-developed oscillatory zoning, although some have unzoned homogenous cores (Figure 4.11a). Also, patch zoning is present (Figure 4.11a).

Twenty-seven U-Pb SHRIMP analyses were conducted on 27 grains. These analyses have variable U content (22–112 ppm), Th content (6–65 ppm), and Th/U ratios (0.23–0.58) (Table C.1) indicating a magmatic origin and crystallization from high SiO_2 content magma (Kirkland *et al.*, 2015). On the Tera-Wasserburg diagram, these 27 yield a weighted mean $^{206}\text{Pb}/^{238}\text{U}$ age of $698 \pm 11 \text{ Ma}$ ($\pm 95\%$ conf., MSWD = 1.19, N = 27; Figure 4.11a), interpreted to represent the crystallization age of the rhyolite sample S02-5.

Fifty-three laser ablation split stream (LASS) analyses were conducted on 53 grains from the same sample. Twenty-seven analyses were from the same 27 spots as the SHRIMP analyses, commonly over the SHRIMP spots, plus 26 additional LASS spots on 26 new grains. These LASS analyses yield a weighted mean $^{206}\text{Pb}/^{238}\text{U}$ age of $698 \pm 6 \text{ Ma}$ ($\pm 95\%$ conf., MSWD = 0.53, N = 46; Figure 4.11b and Table C.2), which is almost identical to the SHRIMP age. CI-normalized (Anders and Grevesse, 1989) zircon REE patterns show a negative slope from middle to heavy REE [$(\text{Yb}/\text{Gd})_{\text{CI}} = 12\text{--}32$], negative Eu anomalies [$(\text{Eu}/\text{Eu}^*)_{\text{CI}} = 0.12\text{--}0.41$], and variable Ce anomalies [$(\text{Ce}/\text{Ce}^*)_{\text{CI}} = 0.36\text{--}20$, where $\text{Ce}^* = \sqrt{(\text{La} \times \text{Pr})}$] that are characteristic of unaltered magmatic zircon (Belousova *et al.*, 2002; Grimes *et al.*, 2015) (Figure 4.12a and Table C.2). Zircon grains have Hf contents of 7975–8767 ppm, Nb contents of 0.56–6.16 ppm, U/Yb ratios of 0.04–0.11 (Figure 4.12C-d and Table C.2).

The Lu-Hf isotopes of these 53 spots yield $^{176}\text{Lu}/^{177}\text{Hf}$ ratios of 0.00191 ± 0.00001 – 0.00941 ± 0.00010 and $^{176}\text{Hf}/^{177}\text{Hf}_{(t)}$ ratios of 0.282517 ± 0.000028 – 0.282756 ± 0.000062 (Table C.2). The calculated $\epsilon\text{Hf}_{(t)}$ values range from $+7.38 \pm 0.42$ to $+15.14 \pm 0.93$ and give an average value of $+11.46$ (Figure 4.13 and Table C.2) that corresponds to T_{DM} Crustal ages of 0.70–1.19 Ga. Twenty-seven SIMS O isotope spots have $\delta^{18}\text{O}$ values within the range of 4.50 ± 0.18 – $5.24 \pm 0.18 \text{ ‰}$ and give an average value of 4.94 ‰ (Figure 4.13b and Table C.2).

4.4.3.2 Andesitic sample S16

Zircon grains from sample S16 are prismatic with euhedral rims and a size range of 100–200 μm . These zircons have homogenous textures and well-developed oscillatory zoning in CL images (Figure 4.11c). Some grains show only faint and broad zoning (Figure 4.11c).

Twenty U-Pb SHRIMP analyses were conducted on 20 grains. The analysed grains have variable U (33–300 ppm) and Th contents (19–150 ppm) and Th/U ratios (0.26–0.58) (Table C.1) that signify a magmatic origin (Kirkland *et al.*, 2015). On the Tera-Wasserburg diagram, 19 of the 20 analyses yield a weighted mean $^{206}\text{Pb}/^{238}\text{U}$ age of 698 ± 8 Ma (± 95 % conf., MSWD = 1.6, N = 19; Figure 4.11c), taken as the crystallization age of this andesitic sample.

Forty-three LASS analyses were conducted on 43 grains from the same sample. Twenty-six analyses were from the same 26 spots as the SHRIMP analyses, commonly over the SHRIMP spots, plus 17 additional LASS spots on 17 grains. Forty-two LASS analyses yield a weighted mean $^{206}\text{Pb}/^{238}\text{U}$ age of 707 ± 5 Ma (± 95 % conf., MSWD = 1.16, N = 42; Figure 4.11d and Table C.2) which is consistent with the SHRIMP age. One grain, S16@4, has an older $^{206}\text{Pb}/^{238}\text{U}$ age of 854 ± 25 Ma ($\pm 2\sigma$), and may represent a xenocryst from an older Neoproterozoic ANS rock such as the arc-related granitoids from Asir terrane, Saudi Arabia (845 ± 5 Ma; Robinson *et al.*, 2014) (Figure 4.11d and Table C.2). CI-normalized (Anders and Grevesse, 1989) zircon REE patterns show a negative slope from the middle to heavy REE [$(\text{Yb}/\text{Gd})_{\text{CI}} = 2.3\text{--}46$] and high negative Eu anomalies [$(\text{Eu}/\text{Eu}^*)_{\text{CI}} = 0.17\text{--}0.71$] which are characteristic of unaltered magmatic zircons (Belousova *et al.*, 2002; Grimes *et al.*, 2015) (Figure 4.12a and Table C.2). The zircon grains have Hf contents of 8768–12530 ppm, Nb contents of 0.27–2.14 ppm, and U/Yb ratios of 0.05–0.65 (Figure 4.12c-d and Table C.2).

The Lu-Hf isotopes of these 42 spots yield $^{176}\text{Lu}/^{177}\text{Hf}$ ratios of 0.00041 ± 0.00004 – 0.00198 ± 0.00001 and $^{176}\text{Hf}/^{177}\text{Hf}_{(t)}$ ratios of 0.282556 ± 0.000038 – 0.282686 ± 0.000047 (Table C.2). The calculated $\varepsilon\text{Hf}_{(t)}$ values range from $+7.38 \pm 0.57$ to $+11.96 \pm 0.81$ and give an average of $+9.76$ (Figure 4.13), corresponding to T_{DM} crustal ages of 0.85–1.14 Ga. Grain S16@4 has $^{176}\text{Lu}/^{177}\text{Hf}$ ratios of 0.000024 ± 0.000001 , $^{176}\text{Hf}/^{177}\text{Hf}_{(t)}$ ratio of 0.282625 ± 0.000061 and $\varepsilon\text{Hf}_{(t)}$ value of $+13.43 \pm 0.92$

corresponding to a T_{DM} crustal age of 0.88 Ga. A total of 20 SIMS O isotopes spots show $\delta^{18}O$ values ranging from 4.27 ± 0.16 ‰ to 5.23 ± 0.16 ‰ with an average of 4.79 ‰ (Figure 4.13b and Table C.2).

4.5. Discussion

4.5.1 Was the El-Shadli bimodal volcanic province formed at a convergent margin, or was it rift-related?

The tectonic affinity of the El-Shadli bimodal volcanic province remains controversial, with some arguing that the province was formed at a convergent margin, i.e. an island-arc (Shukri and Mansour, 1980; Khudeir, Ali and El Habaak, 1988; Faisal *et al.*, 2020), and others suggesting a continental rift-related origin (Stern, Kröner and Rashwan, 1991). The continental rift origin suggested by Stern, Kroner, and Rashwan (1991) was only supported by relatively few geochemical data from a small sampling area at W. Abu-Hamamid (Figure 4.2), within the El-Shadli bimodal volcanic province. The following section presents a detailed discussion with new evidence in support of a rift-related origin.

Field observations show clear intercalation between mafic and felsic rocks (Figure 4.3) which is characteristic of magmatic rift systems, i.e. the Cenozoic magmatism in the East-African rift (Rooney, 2017, 2020) and known Neoproterozoic bimodal rift volcanics (Z. X. Li *et al.*, 1999, 2003; X. H. Li *et al.*, 2008; W. X. Li, X. H. Li and Z. X. Li, 2010; Lyu *et al.*, 2017; Kjølล์ *et al.*, 2019; Cheng *et al.*, 2020). Also, there is no field evidence within the El-Shadli volcanic province of either upper mantle rocks such as peridotites and serpentinites, and/or sheeted dykes, which form part of the well-defined criteria for ophiolites (Furnes, De Wit and Dilek, 2014). The absence of these ophiolitic rock assemblages (e.g., upper mantle rocks such as peridotites and serpentinites, and/or sheeted dykes (Furnes, De Wit and Dilek, 2014) within the El-Shadli volcanic province also argues against it being a part of an ophiolitic section. This is in contrast to the well-defined and ~750-730 Ma ophiolites found both to the south of the study area, such as MORB-related Gerf ophiolites (Zimmer *et al.*, 1995), or to the north, such as the arc-related El-Fawakhir and W. Ghadir ophiolites (El-Sayed, Furnes and Mohamed, 1999; Abd El-Rahman, Polat, Dilek, *et al.*, 2009; Abd El-Rahman, Polat, Dilek, *et al.*, 2009; Basta *et al.*, 2011).

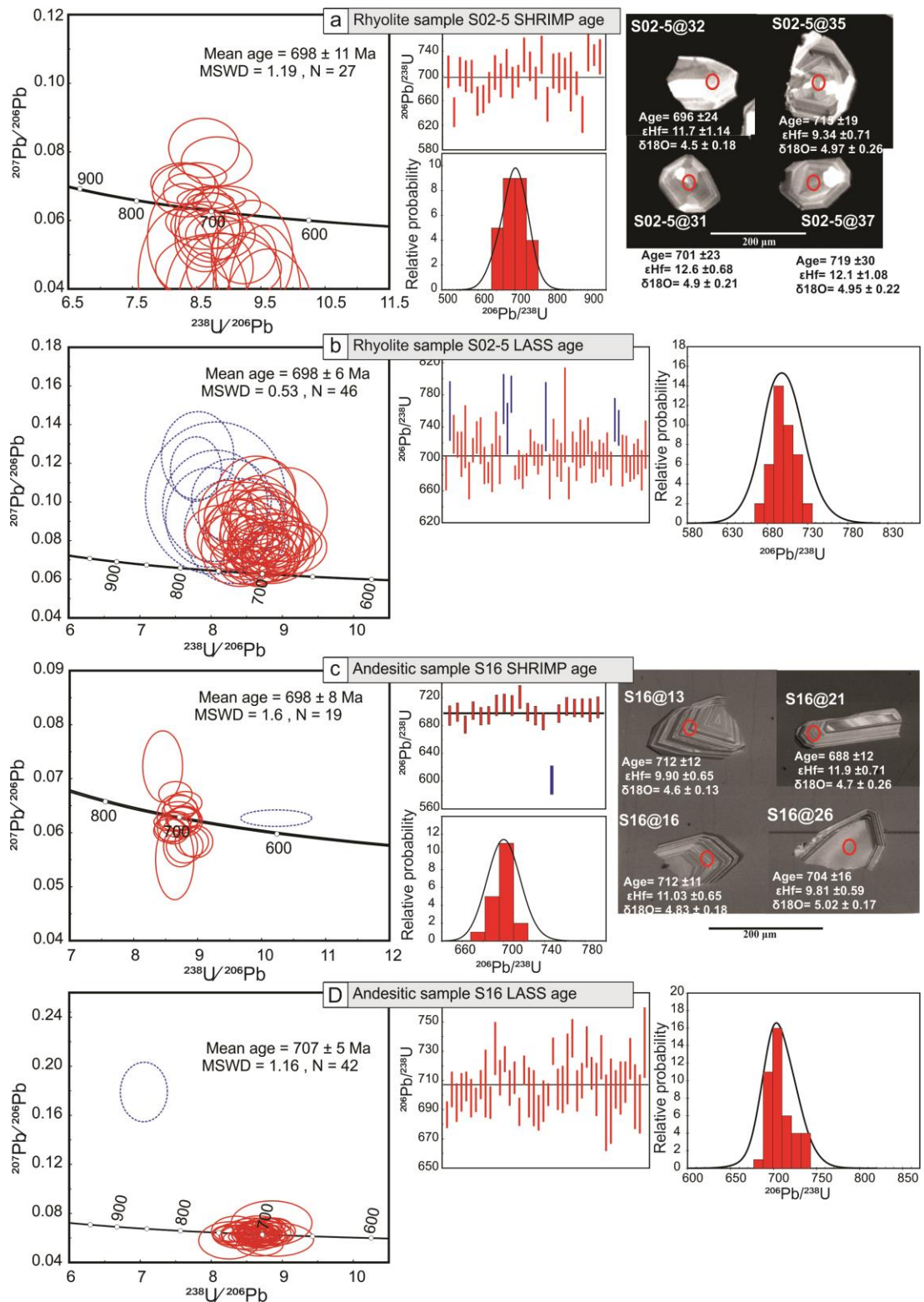


Figure 4.11: SHRIMP and LA-SS-ICPMS geochronological data and CL images of the El-Shadli volcanic province. (a, c) Zircon U-Pb SHRIMP Concordia diagrams showing the $^{206}\text{Pb}/^{238}\text{U}$ ages of the analysed zircons with 1 sigma errors. Weighted means, relative probability diagrams of $^{206}\text{Pb}/^{238}\text{U}$ ages and representative CL images are shown for each sample. The red circles on the CL images mark the place for SHRIMP, LASS, and SIMS spot analyses for the U-Pb age, Hf and O isotopes, and trace element data, respectively. (b, d) Zircon U-Pb LASS Concordia diagrams showing the $^{206}\text{Pb}/^{238}\text{U}$ ages of the analysed zircons with 1 sigma errors. Weighted means and relative probability diagrams of $^{206}\text{Pb}/^{238}\text{U}$ age are

shown for each sample. Red ellipse = data used to calculate the age. Blue ellipse = not included in age calculations.

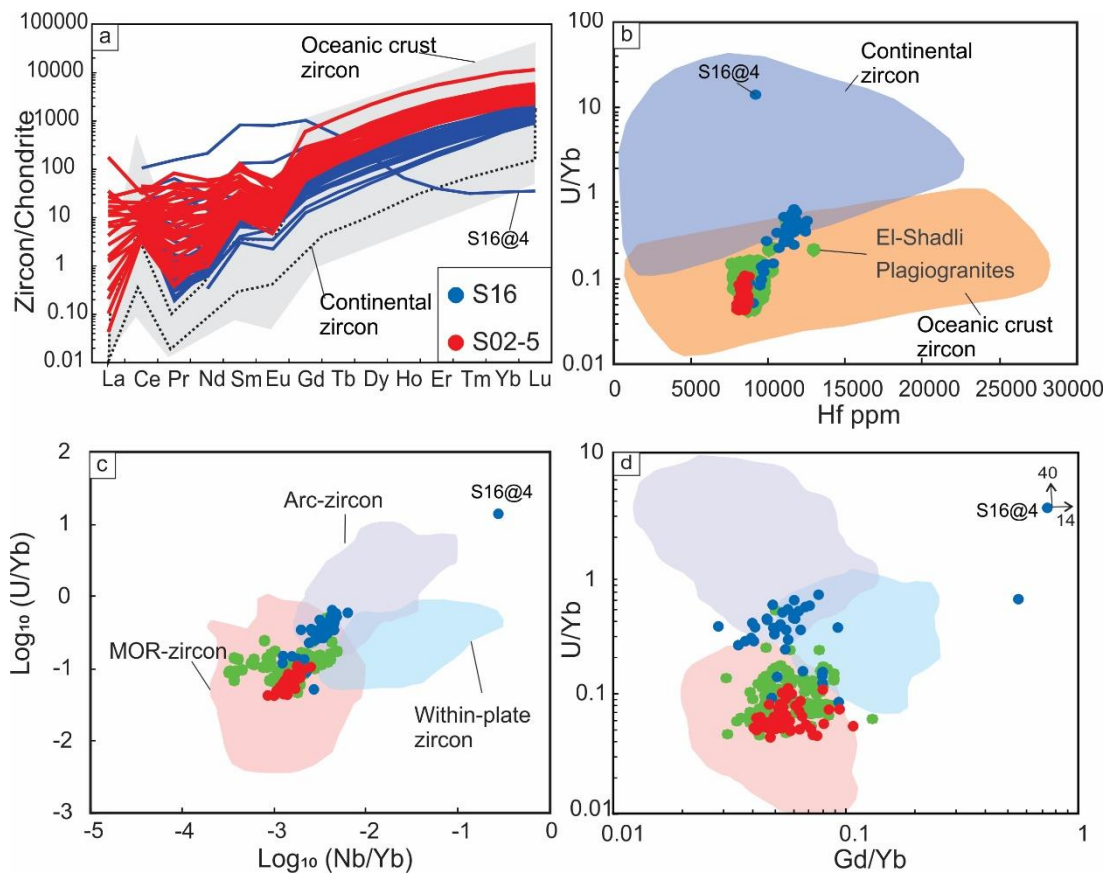


Figure 4.12: Zircon Chondrite-normalized REE patterns (Anders and Grevesse, 1989) and trace element composition tectono-magmatic classification of the El-Shadli volcanic province using the classification fields of Grimes *et al.* (2007, 2015).

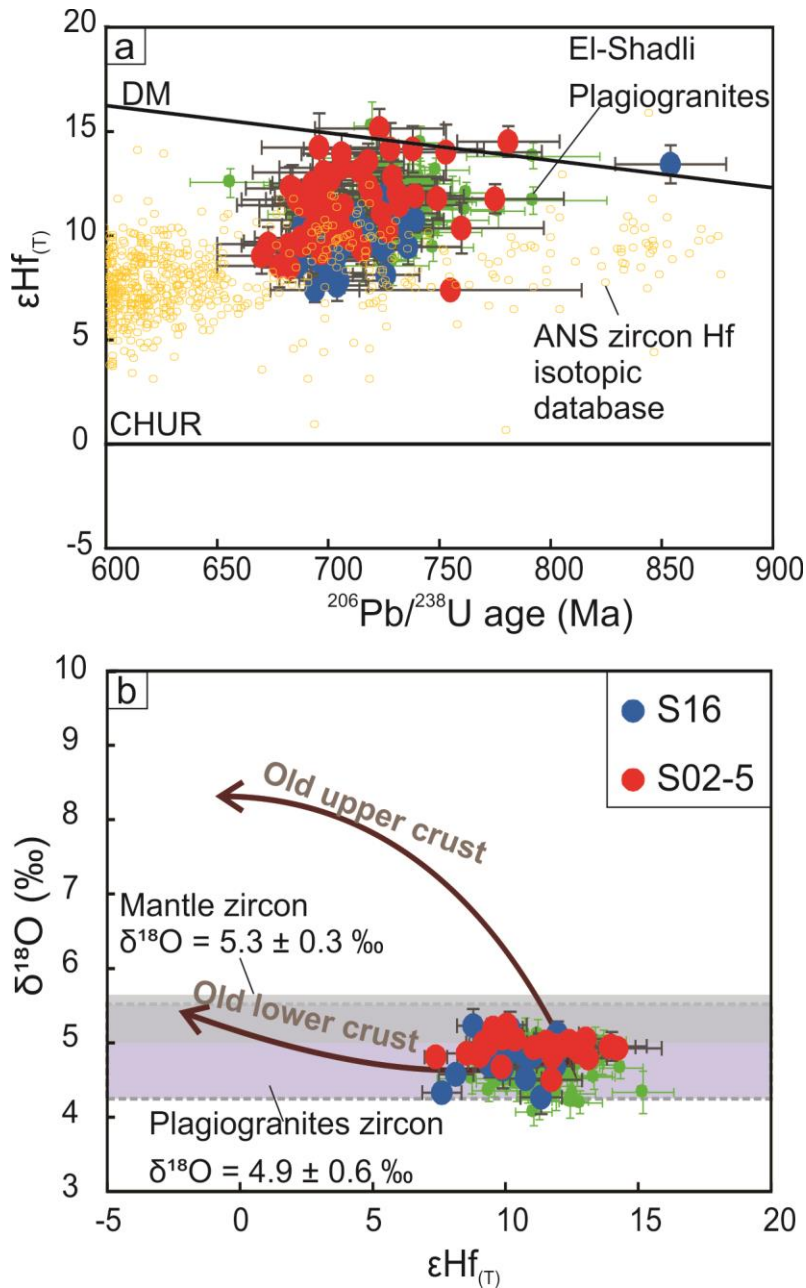


Figure 4.13: Age, Hf, and O isotopic data of zircon from the El-Shadli volcanic province. (a) $\epsilon\text{Hf}(t)$ vs $^{206}\text{Pb}/^{238}\text{U}$ age plot against the Chondritic uniform reservoir (CHUR) and depleted mantle (DM; Griffin *et al.*, 2002) lines. Hf isotopic data of ANS arc-related magmatism (e.g., Morag *et al.*, 2011, 2012; Robinson *et al.*, 2014) are used for comparison. (b) Plot of $\delta^{18}\text{O}$ vs $\epsilon\text{Hf}(t)$ for the studied zircons. Old upper and lower crust trends are from Kemp *et al.* (2007) and Wang *et al.* (2016). The zircon $\delta^{18}\text{O}$ mean value for ophiolitic plagiogranites (4.9 ± 0.6 ‰) is from Grimes *et al.* (2013) and that of typical mantle zircon (5.3 ± 0.3 ‰) is from Valley *et al.* (1998, 2005). Green dots are El-Shadli plagiogranites.

In general, there are characteristic geochemical and petrological features for magmatism formed in different tectonic environments. Martin and Piwinski (1972) proposed that the compressional/orogenic tectonic environments (oceanic- and

continental-arcs such as the Izu-Bonin-Marian (IBM) arc and the Andean arc, respectively) have different magmatic natures, as with extensional/non-orogenic tectonic environments (such as the East-African rift, Ethiopia). The approach of using geochemical and petrological methods to identify the tectonic environments of magmatism was further developed over the past decades, as exemplified for example by Pearce and co-workers (Pearce, Harris and Tindle, 1984; Pearce and Peate, 1995; Pearce, 1996, 2008; Pearce and Reagan, 2019). One distinct feature between magmatism of these three different tectonic environments is the distribution of their SiO₂ content.

To further verify this approach, I extracted the latest geochemical data related to the abovementioned tectonic environments (IBM, Andean arc, and the East-African rift) from the GEOROC repository and examined their differing characteristics. The SiO₂ content of the magma shows that the oceanic arc (IBM) and continental arc (Andean arc) have unimodal magmatic nature (basaltic and andesitic composition, respectively) whereas the East-African rift has a bimodal mafic and felsic magmatic nature (Figure 4.14e).

The SiO₂ content of the El-Shadli volcanic province (including data from both this study and previous work: Shukri and Mansour, 1980; Khudeir, Ali and El Habaak, 1988; Stern, Kröner and Rashwan, 1991; Faisal *et al.*, 2020) was compared with other Eastern Desert volcanics such as (1) ophiolite-related volcanics (Stern, 1981; El-Sayed, Furnes and Mohamed, 1999; Abd El-Rahman, Polat, Yildirim Dilek, *et al.*, 2009; Abd El-Rahman, Polat, Yildirim Dilek, *et al.*, 2009; Basta *et al.*, 2011), (2) arc-related volcanics (Ali *et al.*, 2009), and (3) the post-orogenic Dokhan volcanics (Eliwa, Kimura and Itaya, 2006; Eliwa, El-Bialy, and Murata, 2014) (Figure 4.14a-d). The El-Shadli volcanics display a distinct bimodal magmatic nature similar to that of the East-African rift-related volcanics which is different from that of ophiolite- or arc-related volcanics. This bimodal nature of the El-Shadli volcanics is also different from any other Eastern Desert volcanics as well as the well-known oceanic- and continental-arc volcanics (IBM and Andean arc, respectively) that have unimodal magmatism (Figure 4.14b-e).

In Harker variation diagrams (Figure C.3), SiO₂ content plotted against other major elements of rift-related (the East-African rift) and arc-related (the IBM and Andean arcs) volcanics. The arc-related volcanics display a constant, linear correlation with less dispersion; the East-African rift-related volcanics, on the other hand, mainly

show a continuous but non-linear (i.e., hyperbolic trend) correlation and more dispersion (Martin and Piwinski, 1972; Peccerillo *et al.*, 2003) (Figure C.3). The same data scatter/dispersion is observed in the El-Shadli volcanics. This is particularly evident in the Al_2O_3 , Na_2O , and K_2O contents of the El-Shadli volcanics between mafic and felsic rocks, and is shown in almost all major elements just within the mafic rocks (Figures 4.7 and 4.8). Overall, the El-Shadli bimodal volcanics display similar relationships between SiO_2 content versus other major elements (Figure 4.7) as for well-known rift-related volcanics (Figure C.3).

Whole-rock REE and Nd-Sr isotopic data together with zircon trace element data for the El-Shadli mafic and felsic rocks show a typical MORB-like composition that distinguishes them from arc-related basalts and granites, respectively (Figures 4.9a, b, 4.10, and 4.12). On the other hand, the whole-rock geochemical, isotopic, and zircon trace element data of the intermediate rocks show an arc-like signature (their origin will be discussed below).

The immobile trace element data from the basaltic rocks can help to further decipher their tectonic setting (X.-C. Wang *et al.*, 2016). Figure 4.15 shows plots for the different tectonic settings and enables a discrimination between arc-related volcanics and rift- or plume-related volcanics (including MORB and plume-related volcanics of oceanic-island basalts (OIB) and continental flood basalt (CFB)). In the V versus Ti (Shervais, 1982; X.-C. Wang *et al.*, 2016), ternary Sm-Ti-V (Vermeesch, 2006), Th/Yb versus Nb/Yb (Pearce, 2008), and TiO_2/Yb versus Nb/Yb (Pearce, 2008) diagrams, the El-Shadli mafic rocks plot in the MORB field and are similar to the Basin and Range rift-related basalts (X.-C. Wang *et al.*, 2016), suggesting that the formation of these rocks in a rift environment. Similarly, using geochemical classification diagrams of the felsic rocks such as the Ga/Al versus FeO_T/MgO ratio (Figure 4.16a) (Whalen, Currie, and Chappell, 1987) and SiO_2 versus $\text{FeO}_T/(\text{FeO}_T + \text{MgO})$ ratio (Figure 4.16b) (Frost *et al.*, 2001), the El-Shadli felsic rocks show similarities to A-type granites that generally form in non-orogenic, within plate/rift-related environments (Whalen, Currie, and Chappell, 1987; Bonin, 2007). On two of the key diagrams (Rb vs. (Y + Nb) and Nb vs. Y; Figure 4.16c, d) that link the magmatic source with the tectonic setting of the felsic rocks (Pearce, Harris and Tindle, 1984; Pearce, 1996), the El-Shadli felsic rocks plot close to ocean ridge granites (ORG) and slightly overlap with within-plate granites (WPG), supporting the rift-related origin interpretation.

In summary, based on field observations and geochemical data, the El-Shadli bimodal volcanics are typical rift-related volcanics (Stern, Kröner and Rashwan, 1991) and were not formed within convergent margins (i.e. arcs).

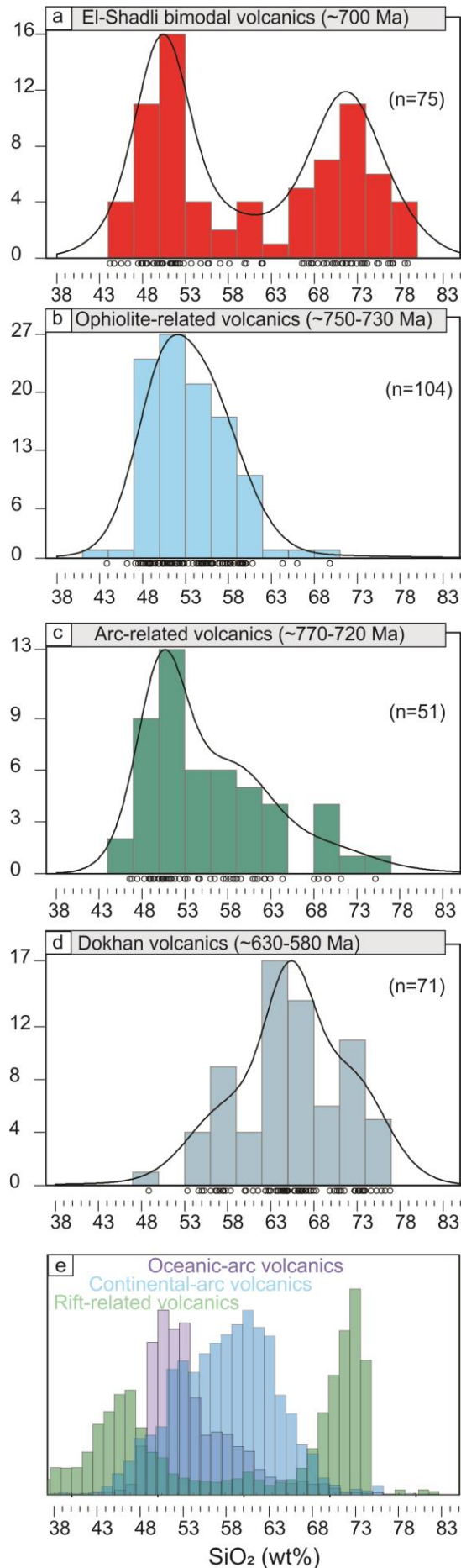


Figure 4.14: Density and histogram of silica contents of the El-Shadli bimodal volcanic province compared to that of the other Eastern Desert volcanics and well-studied arc- and rift-related volcanics. (a) The El-Shadli bimodal volcanic province data include that of this study, and of previous work (Shukri and Mansour, 1980; Khudeir, Ali and El Habaak, 1988; Stern, Kröner and Rashwan, 1991; Faisal *et al.*, 2020). (b-d) Data of other Eastern Desert volcanics including ophiolite-related volcanics (Stern, 1981; El-Sayed, Furnes and Mohamed, 1999; Abd El-Rahman, Polat, Yildirim Dilek, *et al.*, 2009; Abd El-Rahman, Polat, Yildirim Dilek, *et al.*, 2009; Basta *et al.*, 2011), arc-related volcanics (Ali *et al.*, 2009) and the Dokhan volcanics (Eliwa, Kimura and Itaya, 2006; Eliwa, El-Bialy, and Murata, 2014) (Figure 4.14a-d). (e) Global database (after GeoRoc: <http://georoc.mpch-mainz.gwdg.de/georoc/>) of oceanic arc (IBM) and continental arc (Andean arc) volcanics and rift-related volcanics (the East-African rift).

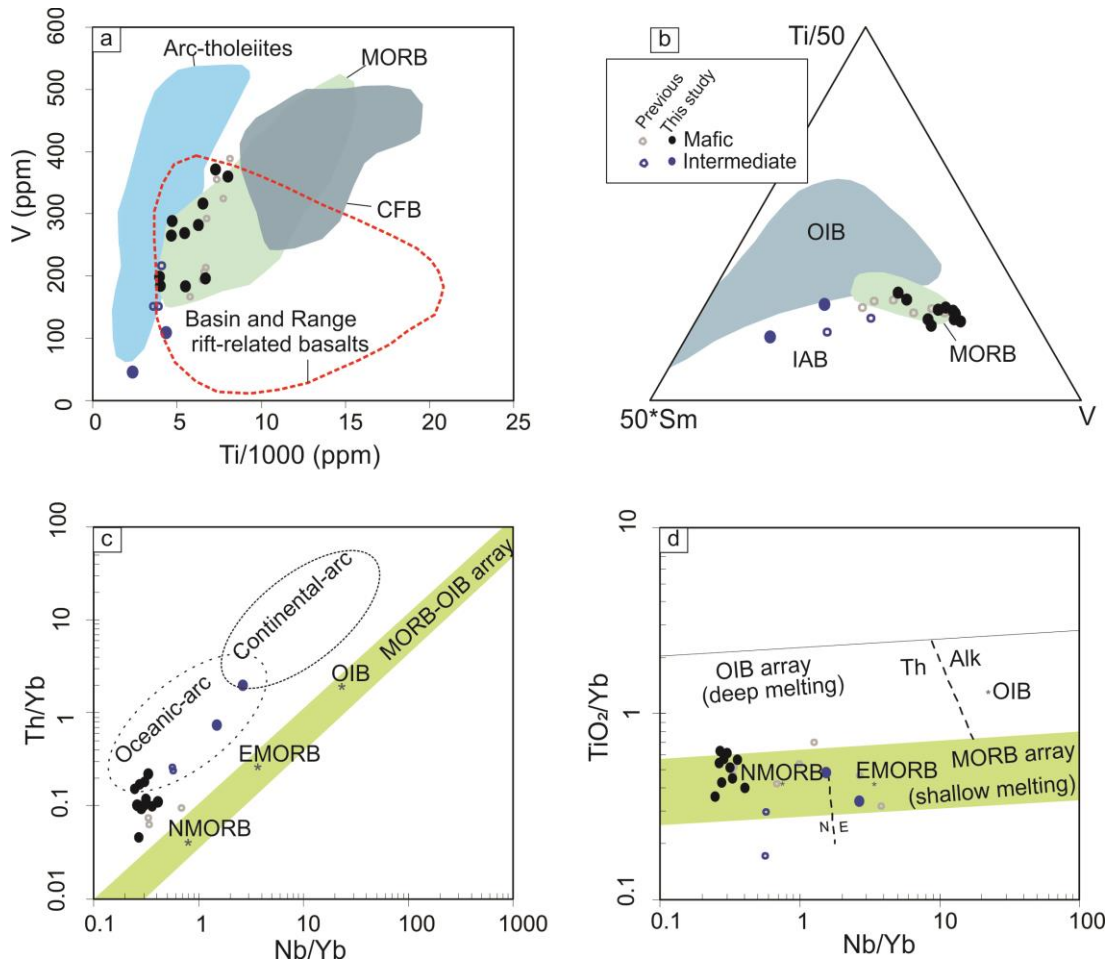


Figure 4.15: Tectonic discrimination diagrams for the El-Shadli mafic and intermediate rocks: (a) V versus Ti (Shervais, 1982; X.-C. Wang *et al.*, 2016); (b) ternary Sm-Ti-V (Vermeesch, 2006); (c) Th/Yb versus Nb/Yb (Pearce, 2008); and (d) TiO₂/Yb versus Nb/Yb (Pearce, 2008). The mafic rocks from the El-Shadli volcanic province plot in the MORB field similar to that of the Basin-and-Range rift-related basalts (X.-C. Wang *et al.*, 2016), and intermediate rocks plot in the arc-related volcanics field.

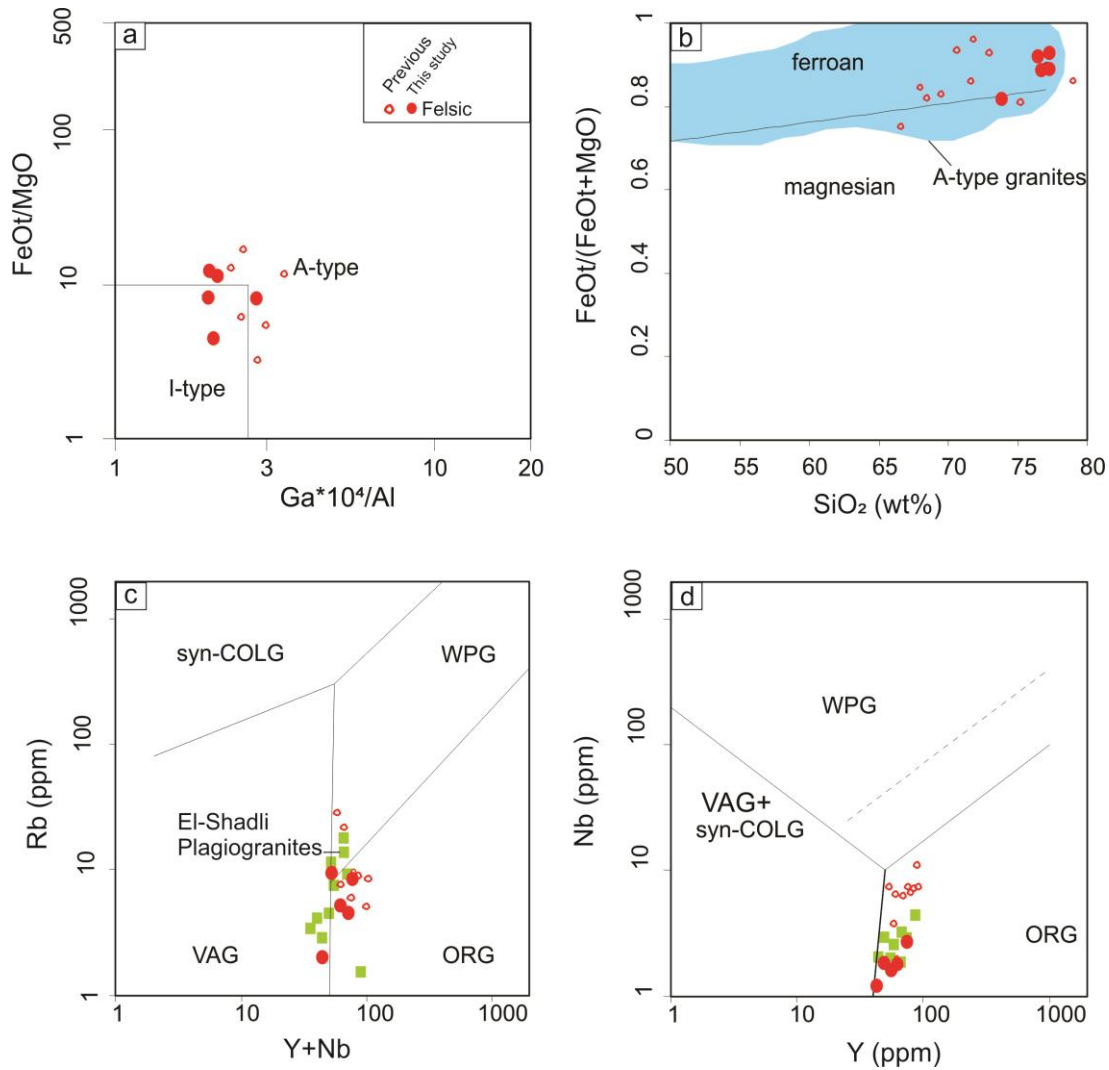


Figure 4.16: Tectonic discrimination diagrams for the El Shadli felsic rocks. (a) Ga/Al versus FeO_T/MgO ratio (Whalen, Currie, and Chappell, 1987) and (b) SiO_2 versus $FeO_T/(FeO_T + MgO)$ ratio (Frost *et al.*, 2001), where the felsic rocks show similarity to A-type granites. (c-d) Rb vs. Y + Nb and Nb vs. Y of Pearce, Harris, and Tindle, (1984) and Pearce (1996); the El Shadli felsic rocks are similar to ocean ridge granites (ORG) and show a slight overlap with within-plate granites (WPG), thus supporting a rift-related origin.

4.5.2 Origin of the El-Shadli bimodal suite

4.5.2.1 Nature of the parental magma and magma source

As mentioned above, the El-Shadli bimodal volcanics were interpreted to have been formed in a rift setting, thus the potential crustal contamination also needs to be assessed. The low initial $^{87}\text{Sr}/^{86}\text{Sr}$ ratios (0.702219–0.703043) and highly positive $\epsilon\text{Nd}(t)$ (from +5.84 to +7.50) of the El-Shadli mafic and felsic rocks (Figure 4.10b) indicate a juvenile nature for the parental magma, with no crustal contribution. This parental magma was likely extracted from a depleted MOR-like mantle source (Figures 4.9a, b, 4.10, and 4.12). The El-Shadli bimodal suite has a tholeiitic affinity with a parental magma characterized by very low K_2O content (Figure 4.8 and Table 4.1). The low abundance (<10 ppm) of Rb (a fluid-mobile element: FME) in the El-Shadli felsic rocks, or even in the mafic ones, indicates an inherited depleted mantle source and an absence of interaction/contamination with the continental crust (Pearce, Harris and Tindle, 1984; Pearce, 1996) (Figure 4.16c, d).

Zircon U-Pb analyses of rhyolite sample S02-5 indicate a lack of pre-Neoproterozoic inherited cores or zircon xenocrysts (Figure 4.11a), implying no interaction with old crustal materials (Carley *et al.*, 2014; Belousova *et al.*, 2015; Grimes *et al.*, 2015), consistent with the juvenile composition of the parental magma (i.e. a depleted mantle source). Variations of U/Yb in zircon reflect variations in the melt at the time of zircon crystallization (Grimes *et al.*, 2007). The U contents are enriched in continental crust relative to the oceanic crust (i.e., MORB); for example, U/Yb ratio for the bulk continental crust is 0.7 (Rudnick and Gao, 2014) compared to 0.02 for MORB (White and Klein, 2014). The low U/Yb ratios (typically < 0.1) of the studied zircons from rhyolite sample S02-5 are similar to those of modern ocean crust zircons formed from a depleted mantle-source, but are significantly different from continental and arc-related zircons (Grimes *et al.*, 2007, 2015; Carley *et al.*, 2014) (Figure 4.12). The low Nb/Yb and Gd/Yb ratios of these zircons are also a distinct feature for zircons extracted from a depleted MOR-like source (Grimes *et al.*, 2015) (Figure 4.12).

Hf isotopic compositions of zircons provide significant information about the nature and compositional evolution of the parental magma as well as the potential presence of mixed source components from the older continental crust and depleted mantle of different ages (Vervoort and Blichert-Toft, 1999; Griffin *et al.*, 2002;

Belousova *et al.*, 2010; Kemp and Hawkesworth, 2014). The highly positive zircon $\epsilon_{\text{Hf}(t)}$ values (from $+7.38 \pm 0.42$ to $+15.14 \pm 0.93$) of rhyolite sample S02-5 (Figure 4.13) indicate an extraction of the parental magma from a juvenile source with no involvement of old continental crust (Hawkesworth and Kemp, 2006; Belousova *et al.*, 2010). O isotopes in zircon are recognized as a powerful tool for tracing the parental magma contamination by continental and sedimentary materials (Valley, 2003). The $\delta^{18}\text{O}$ values of typical mantle-like magma ($5.3 \pm 0.3\text{‰}$) can be shifted to lower values due to interaction of the parental magma with hydrothermal fluids, or to higher values in rocks derived from a source that underwent sediment and/or crustal recycling (Valley *et al.*, 1998, 2005b; Valley, 2003; Hawkesworth and Kemp, 2006). The low $\delta^{18}\text{O}$ values ($4.50 \pm 0.18 - 5.24 \pm 0.18 \text{‰}$) of the examined zircons in rhyolite sample S02-5 indicate that the parental magma underwent interactions with high-temperature hydrothermal fluids (Grimes *et al.*, 2013; H. Wang *et al.*, 2016) (Figure 4.13).

Taken together, the whole-rock geochemical and isotopic compositions of the El-Shadli mafic and felsic rocks are consistent with a derivation from a depleted MOR-like mantle source instead of an arc-related source. The enrichments of the El-Shadli mafic and felsic rocks in some LILE such as Cs, Ba, and U relative to N-MORB (Figure 4.9) are likely an inherited feature and could be related to hydrothermal alteration of their MOR-like source (Koepke, Feig and Snow, 2005; Tao *et al.*, 2020), consistent with the zircon O isotopic data (Figure 4.13b). Finally, the whole-rock Nd-Sr isotopic and geochemical data, along with the zircon U-Pb-Hf-O-trace elements data suggest that the parental magma of the El-Shadli bimodal suite has a juvenile nature and was not affected by any continental crustal contamination. They were extracted from a depleted MOR-like source that had undergone alteration due to hydrothermal fluid circulation in an oceanic setting.

4.5.2.2 Petrogenesis

The similarity and complementary geochemical features between the El-Shadli mafic and felsic rocks suggest that the two types of rocks were fractionated from the same parental magma. The whole-rock major elements compositional variations between the mafic rocks and the felsic ones are consistent, both are generally non-

linear (Figure 4.7 and Figure C.3). Such compositional variations are consistent with an evolution from the same melt (Peccerillo *et al.*, 2003). This is also supported by the overlap between the mafic and felsic rocks in their K₂O and Nd-Sr isotopic data, and their similar tholeiitic affinities. The trace elements and REE trends between the mafic and felsic rocks are also very similar (Figures 4.7-4.10). The El-Shadli mafic rocks show positive Sr anomalies and higher Sr and Al₂O₃ contents than the felsic rocks (Figures 4.7 and 4.9), reflecting the removal of plagioclase in the early magmatic stage (Stern, Kröner and Rashwan, 1991; X. H. Li *et al.*, 2002; Zhang *et al.*, 2017). The felsic rocks show negative Eu anomalies and support the complementary plagioclase accumulation from a basaltic melt in the early-stage (Figure 4.9). The low Ti content and negative Ti anomalies of the El-Shadli felsic rocks compared to the mafic rocks indicate fractionation of Ti-Fe oxides in the early magmatic stage (Wang *et al.*, 2008; X. H. Li *et al.*, 2008) (Figure 4.8). Thus, the mafic rocks and associated felsic rocks are complementary to each other, with the basaltic rocks representing the mafic segregated melt and the rhyolites representing the evolved fractionated melt from the same parental magma (Figure 4.17a, b).

The El-Shadli mafic rocks have a very low content of Ni (3–120 ppm), Cr (9–341 ppm), and Mg# (64–43) lower than the primary mantle melt (Ni > 500 ppm, Cr > 1000 ppm, and Mg# > 72: Niu and O'hara, 2008). The highly evolved composition of the El-Shadli mafic rocks suggests a fractionation from a parental melt produced by the re-melting of a highly depleted source (Cheng *et al.*, 2020). Therefore, the El-Shadli bimodal suite does not represent direct fractional crystallization products from the primary mantle melt (i.e., one stage formation process after primary mantle partial melting).

Brophy (2009) suggested that fractionated felsic products from a melt produced by hydrous partial melting of a MORB-like source should (a) yield a flat or slightly decreasing REE trend with increasing SiO₂, and (b) show slightly higher and/or overlap REE patterns with coexisting mafic rocks. In contrast, felsic rocks produced through direct fractional crystallization of a primary mantle melt should yield a positive correlation between REE and SiO₂ over the entire mafic to the felsic range. The El-Shadli mafic and felsic rocks show flat REE patterns with some overlap (Figure 4.9) and a consistent flat correlation between La vs. SiO₂ (Figure 4.17c) similar to that of the associated El-Shadli plagiogranites, again demonstrating a hydrous

partial melting origin. This process is in contrast with that of the Iceland lavas thought to have been formed through fractional crystallization from primary mantle melt that display a positive correlation and steady increase of La from mafic to felsic end-member (Brophy, 2009).

The whole-rock geochemical and isotopic data, along with the Hf-O-trace element data of zircons, of the El-Shadli bimodal suite, suggest a genetic link with the underlying the El-Shadli plagiogranites and co-magmatic gabbros (plutonic complex). The El-Shadli plagiogranites and co-magmatic gabbros are suggested to have been crystallized from parental magma generated by partial melting of a hydrothermally altered, MOR-like gabbroic lower oceanic crust (see Chapter 3 for details). Such a genetic link between the El-Shadli bimodal suite and the plutonic complex is evidenced by both the bimodal nature, their low K₂O content pointing to tholeiitic MORB-like parental magma, and similar REE and trace element patterns (Figures 4.8 and 4.9). In addition, the compositions of the Hf-O-trace elements of zircons completely overlap between the El-Shadli bimodal suite and the plagiogranites (Figures 4.12 and 4.13), and they share the same T_{DM} crustal ages of 0.70–1.1 Ga, strongly indicating that they were extracted from the same mantle source. As the El-Shadli plagiogranites (~730-720 Ma) crystallized 20–30 Myr earlier than the bimodal suite (~700 Ma), they could represent the first stage of the magma extraction from the parental source. The bimodal suite, representing a later stage secondary extraction from the same source, should therefore show some depletion in their elemental compositions compared to the plagiogranites. Such a depletion is indeed evident in the REE and trace elements data of the mafic member of the El-Shadli volcanics (representing the first product of the second stage magma extraction) relative to that of the plagiogranites (Figure 4.9a).

In summary, The El-Shadli bimodal suite represents a coherent magmatic series that fractionated from a MORB-like melt, from the same source as the underlying El-Shadli plagiogranites which was created by partial melting of hydrothermally altered gabbroic lower crust.

4.5.3 Petrogenesis of the El-Shadli intermediate rocks

As mentioned above, field observations show that the minor intermediate rocks intrude the El-Shadli mafic rocks (Figure 4.5c-e). There is also a clear difference in the whole-rock geochemical and Nd-Sr isotopic data between them, as well as their U-Pb-Hf-O-trace element data from zircon. The following lines of evidence suggest that the El-Shadli intermediate rocks were derived from an arc-like parental magma. First, geochemically, these intermediate rocks have high K₂O contents (> 1 wt.%) and their trace element contents and ratios, particularly Th, Co, Th/Yb and Zr/Y, show a calc-alkaline affinity (Figure 4.8 d-f). In Figure 4.9c, the intermediate rocks are again characterized by arc-like signatures, i.e. their enrichment in LILE (e.g., Cs, Ba, Th, Pb, and U) and LREE (e.g., La and Ce) relative to HFSE (e.g., Nb, Zr, and Ti), which may indicate that the source underwent melt/fluid interaction during subduction (Pearce and Peate, 1995; Kessel *et al.*, 2005; X.-C. Wang *et al.*, 2016; Pearce and Reagan, 2019). The tectonic discrimination diagrams (Figure 4.15) also have these rocks plotting close to arc-like fields.

Second, the two intermediate rock samples have negative ϵNd (-3.57 and -4.91) and low $\epsilon\text{Nd}(t)$ (+1.38 and -1.04) values which indicate interaction of the parental magma with crustal and/or sedimentary materials, most likely occurred in an arc setting (Togashi *et al.*, 1992; Pearce and Peate, 1995; Li *et al.*, 2019) (Figures 4.10 and 4.17a). Finally, consistent with the geochemical and isotopic data, zircon U-Pb analyses of andesitic sample S16 show the presence of zircon xenocryst #S16@4 (Figure 4.11d), which indicates contamination of the parental magma by crustal components. The high U/Yb ratios (mostly > 0.1) of these zircons is also characteristic of arc-generated zircons (Grimes *et al.*, 2007, 2015; Carley *et al.*, 2014) (Figure 4.12).

Taking into account the above-mentioned arc signature for these intermediate rocks and the slightly low Hf and O isotopic values in zircon, that likely preserve the older lower crust features (H. Wang *et al.*, 2016) (Figure 4.13), these rocks may have originated from partial melting of arc-related (i.e., metasomatized) lower oceanic crust that had been modified by subduction (Figures 4. 13 and 4.17b).

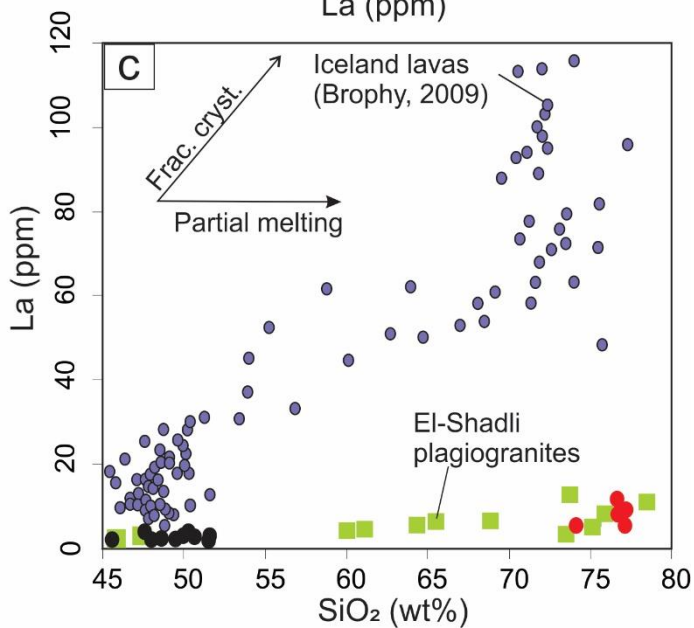
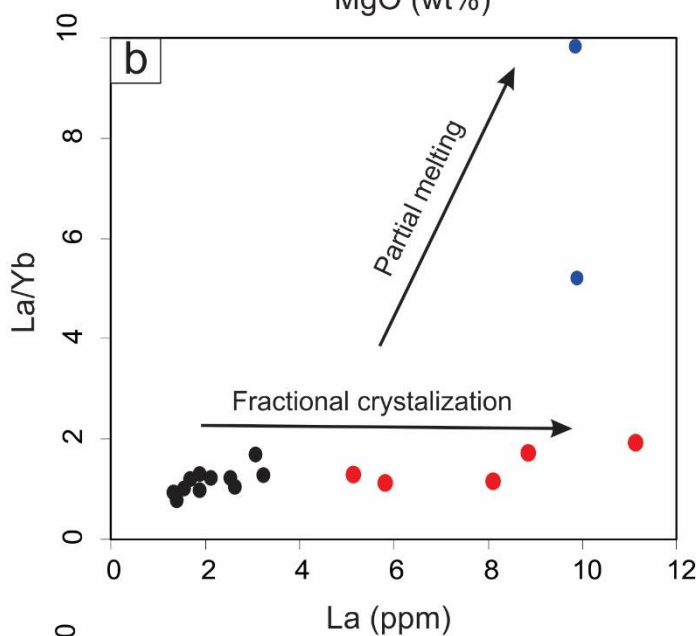
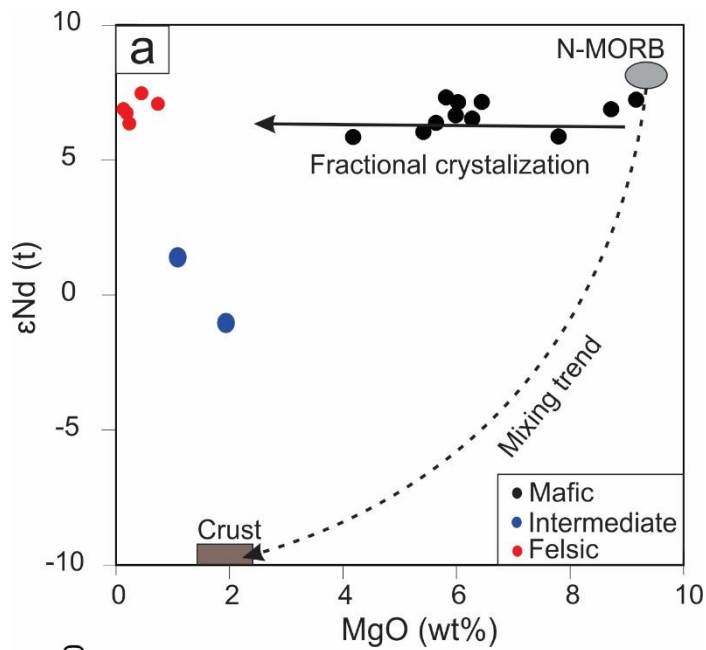


Figure 4.17: Whole-rock petrogenetic discrimination diagrams. (a) $\epsilon\text{Nd}(t)$ vs. MgO (wt. %) after W. X. Li, X. H. Li, and Z. X. Li (2005) and (b) La/Yb vs. La showing that the El-Shadli bimodal volcanic suite represents a coherent magmatic series fractionated from MORB-Like melts. (d) La vs. SiO_2 (wt. %) diagram modified after Brophy (2009) that suggests a partial melting origin.

4.5.4 Formation mechanism and tectonic implications

Field observations coupled with the whole-rock/zircon geochemical and isotopic data suggest that the El-Shadli volcanic province formed in a rift environment, not a volcanic arc (Stern, Kröner and Rashwan, 1991) (Figures 4.3, 4.9, 4.10, 4.12, 4.14-16). This rifting event represents a regional extension either in a back-arc environment or in a non-arc-related continental rifting environment (Tatsumi and Kimura, 1991).

Back-arc extension is by definition associated with subduction (Brooks *et al.*, 1984; Tatsumi and Kimura, 1991; Ohki, Shuto and Kagami, 1994; Taylor and Martinez, 2003; Pearce *et al.*, 2005; Tang *et al.*, 2014). However, the geochemical characteristics of the El-Shadli bimodal volcanics argue against such an origin. Bimodal volcanism generated in back-arc settings is commonly characterized by the presence of subduction zone geochemical signatures. For example, magmatism in Western Pacific back-arc basins (Ohki, Shuto and Kagami, 1994; Shinjo *et al.*, 1999; Shinjo and Kato, 2000; Pearce *et al.*, 2005; Tang *et al.*, 2014) is characterized by high LREE contents with $(La/Sm)_{CI} = 2-4$, $(La/Yb)_{CI} = 2-5$ (Shinjo *et al.*, 1999; Shinjo and Kato, 2000). This is in contrast to LREE depletion in the El-Shadli bimodal suite with $(La/Sm)_{CI} = 0.42-1.12$ and $(La/Yb)_{CI} = 0.46-1.07$. LILE in back-arc bimodal volcanism is also highly enriched relatively to N-MORB, such as having $Rb = \sim 20-200 \times N-MORB$, $Ba = \sim 10-80 \times N-MORB$, $Pb = \sim 10-50 \times N-MORB$, and $Sr = \sim 1-8 \times N-MORB$; Shinjo *et al.*, 1999; Shinjo and Kato, 2000). In contrast, the El-Shadli bimodal suite has significantly lower Rb ($\sim 1-20 \times N-MORB$), Ba ($\sim 3-40 \times N-MORB$), Pb ($\sim 2-6 \times N-MORB$), and Sr ($\sim 0.8-2 \times N-MORB$) contents (Figure 4.9). The felsic rocks of back-arc extension settings have medium-K contents ($\sim 2-3$ wt.%; Shinjo and Kato, 2000), which is in contrast to the low-K contents (<1 wt.%) of the El-Shadli bimodal suite (Figure 4.8d). Overall, the highly depleted source for the El-Shadli bimodal suite argue against it be related to a back-arc environment as bimodal volcanism of such an environment would reflect an enriched mantle source with a sub-arc mantle composition (Ohki, Shuto and Kagami, 1994; Shinjo *et al.*, 1999; Shinjo and Kato, 2000; Taylor and Martinez, 2003; Pearce *et al.*, 2005; Espinoza *et al.*, 2008; Bézos *et al.*, 2009; Tang *et al.*, 2014; Li *et al.*, 2016; Wei *et al.*, 2017).

The absence of significant deformation and metamorphism of the El-Shadli volcanics is consistent with an emplacement within a relatively stable environment i.e., a within-plate/continental rift-related tectonic setting (Stern, Kröner and Rashwan, 1991). Given the genetic link between the El Shadli bimodal suite and the older and likely underlying plagiogranites (Figures 4.9, 4.10, 4.12, 4.13, 4.16 and 4.17), with the latter intruding the strongly deformed and metamorphosed ophiolitic complexes, both the plagiogranites and the El-Shadli volcanism likely occurred post accretion. The highly depleted nature, the absence of crustal contamination, the tholeiitic affinities, and the N-MORB geochemical and isotopic signatures all indicate that the parental magma was likely derived from partial melting of a juvenile continental crust (i.e., accreted oceanic slabs) during a rifting event. The timing of the magmatism is consistent with that of global continental rifting and break-up of the supercontinent Rodinia (~825–600 Ma; Z. X. Li *et al.*, 2008; Z.X. Li, Evans and Halverson, 2013).

The rifting and fragmentation of Rodinia had been proposed to have been driven by either extensional resulted from subduction retreat (Cawood *et al.*, 2009, 2016) or mantle plumes (Z. X. Li *et al.*, 2008; Z. X. Li and Zhong, 2009; Z. X. Li, Evans and Halverson, 2013). Given that the ANS formed during terranes accretion (Stern, 1994; Fritz *et al.*, 2013) and field evidence suggests that the El Shadli bimodal suite form post-accretion, the ca. 700 Ma El-Shadli rifting event was more likely driven by mantle upwelling induced by either slab break-off or a mantle plume formed above the Rodinia superplume (Z. X. Li *et al.*, 2008; Z. X. Li and Zhong, 2009). The plume-induced model is slightly preferred based on the following arguments.

The El-Shadli volcanic province represents the largest bimodal volcanic suite in the Eastern Desert, and possibly in all of the ANS terranes, with an area of 80 km x 35 km and thickness of > 10 km (Shukri and Mansour, 1980; Khudeir, Ali and El Habaak, 1988; Stern, Kröner and Rashwan, 1991). Given this exceptional thickness and large lateral dimension, an enormous amount of heat (i.e. mantle plumes) would be required to remelt the already depleted mafic lower crust at such a large volume. This interpretation is consistent with the model proposed by Stern, Kröner and Rashwan (1991) in which the province was formed in a high volcanicity rift that was associated with extensive lithospheric extension and high-temperature melting might be driven by a mantle upwelling (i.e., plume). Other evidence for mantle plume activity in the region at that time include: (1) 710 ± 7 Ma G. Dahanib komatiitic

layered mafic-ultramafic intrusions (Figure 4.1; Dixon, 1981) located at the southern edge of the El-Shadli volcanic province (dated at 698 ± 6 Ma; this study); (2) slightly older 741 ± 24 Ma Korab Kansi ferropicritic layered mafic-ultramafic intrusions (Figure 4.1; Khedr *et al.*, 2020) found in the southern part of the El-Shadli volcanic province; (3) the apparent hiatus between the ~ 730 - 722 Ma plagiogranites and the ~ 700 Ma El-Shadli volcanic can be interpreted to represent plume-induced syn-magmatic doming and denudation as reported in Neoproterozoic South China (Z. X. Li *et al.*, 1999). It can thus be argued that mantle plume started in this region from ~ 740 Ma (immediately after accretion?) and lasted till ~ 700 Ma, which is in agreement with the location of the ANS in Rodinia construction at this time over the edge of the Rodinia superplume (Z. X. Li *et al.*, 2008; Z. X. Li and Zhong, 2009; Z. X. Li, Evans and Halverson, 2013).

The rifting and fragmentation timing (~ 825 – 680 Ma) of the supercontinent Rodinia have been associated with different plume-related magmatic events, with resulting igneous rocks including granitoids, mafic and ultramafic dikes, rift-related bimodal volcanics, and rare komatiitic basalts (e.g., Heaman, LeCheminant, and Rainbird, 1992; Z. X. Li *et al.*, 1999, 2008; Frimmel, Zartman, and Späth, 2002; X. H. Li *et al.*, 2003; Z. X. Li *et al.*, 2003; Zhang *et al.*, 2006; Wang *et al.*, 2007; Lyu *et al.*, 2017; Kjølล์ *et al.*, 2019; Cheng *et al.*, 2020). The field and geochemical characteristics of the El-Shadli bimodal volcanics province show similarity to other Neoproterozoic rift-related volcanics, believed to have formed above mantle plumes (e.g., Z. X. Li *et al.*, 1999, 2003; X. H. Li *et al.*, 2008; W. X. Li, X.H. Li and Z. X. Li, 2010; Lyu *et al.*, 2017; Kjølล์ *et al.*, 2019; Cheng *et al.*, 2020). The presence of rare intermediate rocks in the El-Shadli volcanic province is interpreted to represent partial melting of metasomatized slightly older arc-related crust that had been previous modified by the subduction.

To summarise, in the preferred tectonic model (Figure 4.18), both the ~ 730 - 722 Ma plagiogranite-gabbro suite (Chapter 3) and the ~ 700 Ma El-Shadli bimodal volcanic suite represent successive remelting products of an oceanic lower crust newly accreted to the ANS, and they both were important magmatic events contributing to the formation of the ANS crust (Stern and Hedge, 1985; Stern, 2018; this study).

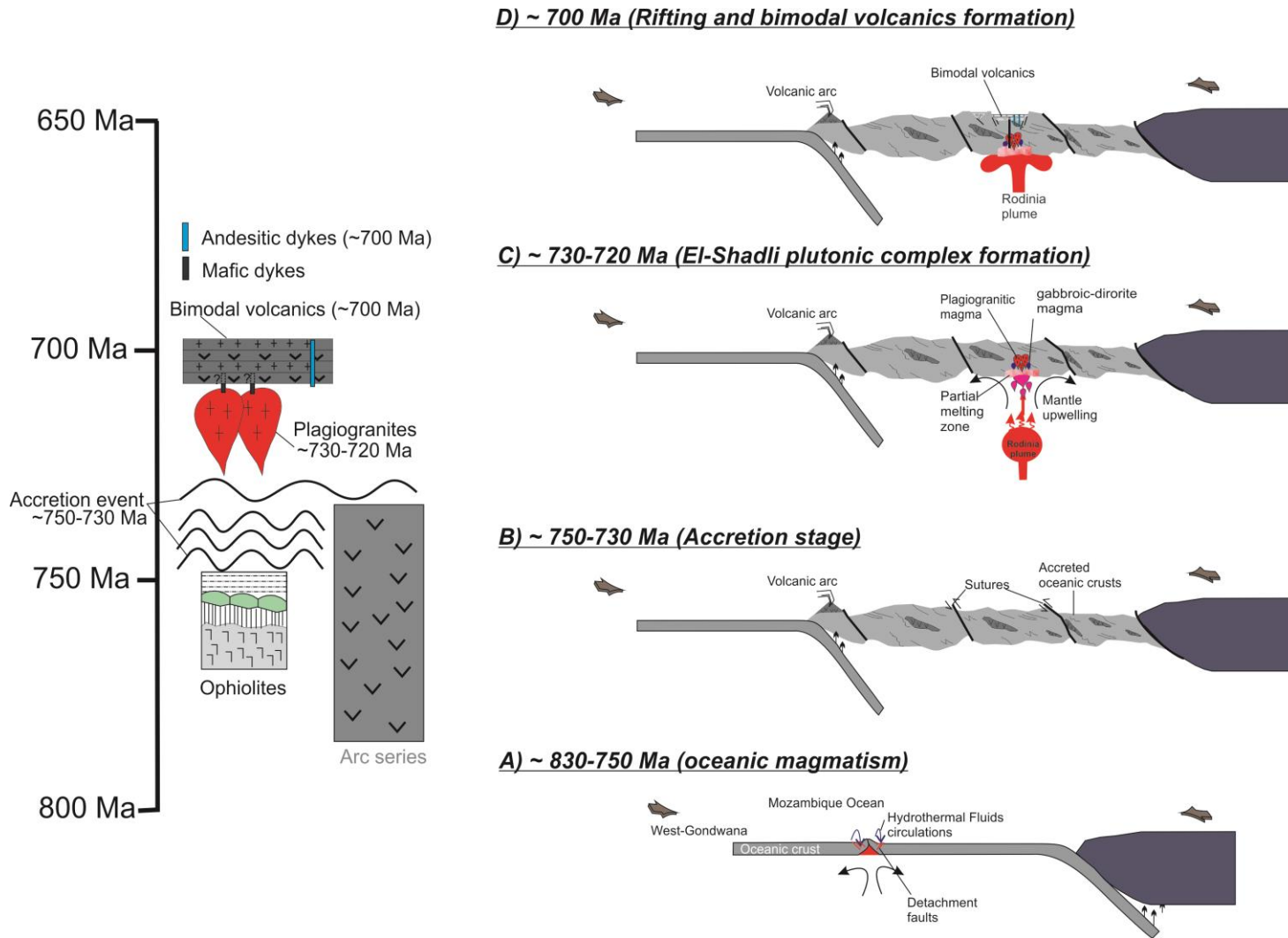


Figure 4.18: A proposed tectonic model for the genesis of the El-Shadli plutonic complex and bimodal volcanic province. (a) Oceanic spreading and ridge magmatism, and possible subduction at a continental arc during ~830–750 Ma with hydrothermal fluids circulating and altering the lower crust section of the oceanic crust near MOR. (b) Accretion of oceanic slabs along the subduction zone during ~750–730 Ma, forming a juvenile accreted terrane. (c) Formation of the El-Shadli plagiogranites and associated gabbros above asthenosphere upwelling possibly driven by a mantle plume at ~730–720 Ma by partial melting the lower crust of the accreted oceanic slabs. (d) Rifting and formation of the bimodal volcanic province from further remelting of the same (but slightly more depleted) lower crustal source at ~700 Ma.

Table 4.1: Whole-rock major and trace element and Sr-Nd isotopes of El-Shadli bimodal volcanic province.

Rock type	Felsic					Mafic					Intermediate							
Sample	S01-3	S02-5	S04-3	S07-2	S18-4	S01-2	S02-2	S04-2	S07-1	S09	S10	S15	S19	S21-2	S22-2	S25-3	S16	S17-1
Lat.	24°25'17"	24°24'57"	24°25'02"	24°24'13"	24°21'21"	24°25'17"	24°24'57"	24°25'02"	24°24'13"	24°23'33"	24°22'23"	24°12'06"	24°23'09"	24°20'17"	24°19'38"	24°17'40"	24°15'01"	24°16'17"
Long.	34°35'38"	34°35'53"	34°38'05"	34°39'02"	34°34'59"	34°35'38"	34°35'53"	34°38'05"	34°39'02"	34°40'11"	34°42'51"	34°37'49"	34°34'08"	34°46'21"	34°47'22"	34°50'13"	34°36'03"	34°36'47"
Major elements (wt %)																		
SiO ₂	74.14	77.15	77.06	76.57	76.81	49.64	50.20	49.27	51.41	45.49	50.37	47.46	48.50	47.89	47.81	51.50	69.13	58.06
TiO ₂	0.27	0.13	0.15	0.13	0.22	1.05	1.09	0.88	0.78	1.05	0.96	1.27	0.82	1.04	0.59	0.60	0.34	0.91
Al ₂ O ₃	13.16	12.40	12.45	12.63	11.28	16.81	16.03	16.78	15.74	15.81	16.78	15.13	14.55	16.63	18.07	15.91	15.66	18.63
MgO	0.64	0.12	0.21	0.17	0.39	6.03	5.64	5.99	5.42	9.17	4.18	5.82	7.80	6.45	6.28	8.73	1.09	1.94
Fe ₂ O ₃	3.19	1.59	1.93	2.13	3.47	9.75	13.31	11.00	11.39	11.95	10.06	13.74	11.37	11.94	8.58	8.80	3.40	6.32
CaO	1.69	2.13	1.28	1.52	2.99	10.37	8.70	11.05	8.47	11.63	11.87	11.01	10.55	9.90	13.66	6.61	3.42	6.12
Na ₂ O	5.80	5.90	5.17	5.59	2.79	3.60	2.78	1.87	4.30	1.49	2.39	2.69	2.35	2.25	2.21	4.04	4.61	4.59
K ₂ O	0.27	0.10	1.04	0.60	0.79	0.54	0.64	0.38	0.47	0.24	0.36	0.15	0.25	0.24	0.27	0.06	1.13	1.19
MnO	0.12	0.03	0.04	0.03	0.13	0.25	0.23	0.18	0.16	0.18	0.22	0.24	0.19	0.20	0.18	0.16	0.06	0.10
Cr ₂ O ₃		0.00					0.00	0.00	0.04	0.04		0.01	0.04	0.01	0.05	0.05	0.00	
P ₂ O ₅	0.08	0.02	0.02	0.02	0.03	0.23	0.13	0.09	0.08	0.12	0.10	0.17	0.08	0.08	0.08	0.09	0.09	0.24
LOI	0.63	0.48	0.62	0.63	0.93	0.79	1.29	2.44	1.61	2.96	2.72	2.38	3.55	3.25	2.19	3.71	1.16	2.06
TOTAL	99.99	100.05	99.97	100.02	99.83	99.06	100.05	99.93	99.86	100.13	100.01	100.08	100.05	99.89	99.97	100.25	100.09	100.16
Mg#	26.34	11.86	16.25	12.46	16.69	52.44	43.03	49.26	45.90	57.77	42.55	43.02	55.01	49.06	56.61	63.88	36.37	35.37
Trace elements (ppm)																		
Li	0.49	1.21	2.56	1.58	3.18	1.46	2.71	5.87	4.61	10.20	8.15	4.02	9.38	9.78	2.30	8.34	6.65	5.16
Be	0.75	0.97	1.11	0.94	1.31	0.94	0.38	0.23	0.29	0.21	0.31	0.43	0.23	0.40	0.33	0.42	1.08	1.01
Sc	16.74	8.88	8.66	8.05	9.52	27.74	39.35	43.30	39.25	45.55	31.32	48.99	42.09	41.64	34.48	41.91	5.50	13.46
Ti	1662.90	868.25	914.11	916.55	1257.52	6658.20	6770.58	5406.23	4628.67	6268.39	5451.28	8002.68	4679.37	6524.06	3811.29	3732.39	2006.99	5370.50
V	13.00	12.31	2.02	11.56	1.11	196.88	372.87	267.96	265.69	279.87	184.24	360.71	289.50	317.66	186.02	199.06	44.58	113.66
Cr	4.25	6.69	4.06	2.90	2.80	14.05	12.65	36.96	188.53	297.17	8.89	70.51	202.73	94.73	431.61	314.55	9.18	11.57
Mn	846.83	300.42	292.12	189.25	981.28	1974.15	1766.18	1400.06	1231.79	1407.39	1569.60	1880.38	1439.59	1563.61	1446.90	1227.22	444.70	699.64
Co	1.27	1.74	0.49	0.43	0.56	20.49	40.83	35.00	31.43	41.97	21.02	38.11	42.18	40.40	34.29	37.84	6.38	14.75
Ni	0.68	1.58	0.27	0.52	0.89	9.47	20.14	25.15	97.62	78.25	3.14	20.94	66.26	50.26	120.17	93.94	3.67	13.05
Cu	5.78	4.80	1.93	3.87	3.57	18.50	69.97	61.67	49.34	88.78	14.52	209.82	119.33	90.21	4.83	93.95	9.42	48.47

Zn	44.77	10.88	16.93	9.39	61.12	108.41	88.54	73.82	77.86	70.88	95.23	103.65	74.42	86.19	84.11	89.41	60.11	68.56
Ga	14.05	13.10	12.84	14.06	16.56	20.40	16.49	15.46	12.80	14.21	16.25	16.04	13.79	15.89	13.47	11.26	18.09	19.94
Rb	2.07	0.93	9.34	5.05	8.76	5.57	7.19	5.89	3.27	3.84	5.44	1.55	4.97	3.09	18.06	0.50	14.11	13.56
Sr	108.45	286.01	88.74	98.14	81.44	183.29	209.24	193.28	174.54	149.04	173.39	200.86	165.12	178.61	186.20	151.78	295.65	421.12
Y	42.84	54.45	49.74	61.24	74.47	24.10	19.70	15.89	15.41	19.41	23.85	28.55	16.16	21.00	16.59	18.71	13.71	22.77
Zr	62.32	147.95	162.79	152.37	194.53	28.38	28.05	18.13	20.41	16.99	37.60	20.77	24.27	20.26	20.50	28.90	46.13	130.06
Nb	1.20	1.70	1.77	1.88	2.75	0.76	0.54	0.42	0.37	0.44	0.61	0.78	0.51	0.52	0.59	0.41	2.63	2.89
Mo	0.13	1.66	0.17	0.06	-0.05	0.08	0.15	0.06	-0.01	-0.01	0.12	0.17	-0.03	0.04	0.02	0.02	-0.01	0.24
Cd	0.06	0.03	0.04	0.08	0.11	0.19	0.07	0.09	0.03	0.07	0.08	0.10	0.29	0.07	0.12	0.06	0.02	0.07
Cs	0.07	0.01	0.07	0.02	0.15	0.15	0.06	0.06	0.08	0.09	0.06	0.04	0.06	0.02	0.04	0.01	0.43	0.11
Ba	51.53	18.06	186.56	149.98	131.37	112.85	114.75	61.02	85.15	36.75	35.28	55.70	89.70	46.19	197.43	23.07	252.77	204.03
La	5.15	8.89	5.81	11.12	8.10	2.57	3.06	1.68	1.36	1.40	2.56	3.23	1.53	1.88	1.88	2.10	9.84	9.88
Ce	16.61	24.06	23.06	24.80	23.86	8.11	8.75	4.91	4.00	4.70	7.32	9.79	4.51	5.38	5.52	5.80	24.01	24.56
Pr	2.71	3.96	2.84	4.35	3.98	1.46	1.40	0.84	0.72	0.88	1.20	1.61	0.80	0.94	0.94	0.96	3.06	3.45
Nd	14.05	18.50	13.40	20.05	20.97	6.61	7.24	4.51	4.04	5.07	6.28	8.41	4.43	5.21	5.03	5.22	12.77	15.46
Sm	4.69	5.40	4.29	5.76	6.94	2.60	2.33	1.60	1.50	1.89	2.17	2.77	1.59	1.94	1.73	1.81	2.97	3.91
Eu	1.49	1.08	0.90	1.27	1.77	0.87	0.88	0.66	0.52	0.79	0.87	1.02	0.63	0.79	0.75	0.82	0.80	1.26
Tb	1.01	1.11	0.98	1.28	1.61	0.43	0.48	0.37	0.36	0.47	0.51	0.65	0.38	0.47	0.40	0.42	0.40	0.62
Gd	5.86	6.31	5.30	7.11	9.28	2.29	2.88	2.14	2.07	2.68	2.88	3.70	2.19	2.70	2.28	2.43	2.69	3.97
Dy	6.32	7.26	6.73	8.51	10.86	3.05	3.13	2.45	2.40	3.03	3.40	4.27	2.50	3.15	2.55	2.77	2.15	3.67
Ho	1.40	1.61	1.53	1.92	2.46	0.76	0.68	0.54	0.54	0.67	0.77	0.95	0.56	0.70	0.56	0.62	0.40	0.76
Er	4.01	4.96	4.75	5.77	7.19	2.08	1.94	1.53	1.53	1.85	2.26	2.72	1.59	1.96	1.59	1.79	1.11	2.12
Yb	4.03	5.08	5.07	5.77	7.03	2.34	1.78	1.42	1.42	1.65	2.22	2.47	1.44	1.82	1.47	1.69	1.00	1.90
Lu	0.61	0.78	0.79	0.86	1.06	0.31	0.27	0.22	0.21	0.24	0.34	0.36	0.22	0.26	0.22	0.26	0.15	0.29
Hf	1.58	4.08	4.53	4.21	5.15	1.04	0.89	0.61	0.69	0.64	1.03	0.85	0.77	0.70	0.69	0.86	1.60	3.31
Ta	0.14	0.13	0.13	0.15	0.18	0.12	0.03	0.03	0.02	0.03	0.04	0.05	0.03	0.04	0.04	0.03	0.23	0.20
Pb	1.14	2.47	2.29	2.37	2.38	1.38	1.28	1.50	1.34	0.67	1.14	1.18	0.74	1.42	1.29	1.60	4.17	4.03
Th	0.55	1.07	1.09	1.23	0.68	0.52	0.33	0.15	0.14	0.08	0.39	0.29	0.15	0.18	0.16	0.26	1.96	1.39
U	0.13	0.38	0.35	0.39	0.30	0.14	0.11	0.08	0.05	0.03	0.17	0.12	0.05	0.07	0.08	0.10	0.71	0.56

Sr-Nd isotopic data*

⁸⁷ Sr/ ⁸⁶ Sr	0.70349	0.70314	0.70571	0.70406	0.70587	0.70383	0.70331	0.70326	0.70324	0.70309	0.70341	0.70258	0.70350	0.70297	0.70502	0.70250	0.70391	0.70354
------------------------------------	---------	---------	---------	---------	---------	---------	---------	---------	---------	---------	---------	---------	---------	---------	---------	---------	---------	---------

⁸⁷ Rb/ ⁸⁶ Sr	0.05514	0.00943	0.30459	0.14899	0.31130	0.08792	0.09942	0.08815	0.05425	0.07445	0.09079	0.02233	0.08704	0.05004	0.28067	0.00952	0.13803	0.09316
⁸⁷ Sr/ ⁸⁶ Sr (i)	0.70294	0.70304	0.70267	0.70258	0.70276	0.70295	0.70231	0.70238	0.70269	0.70234	0.70251	0.70236	0.70263	0.70247	0.70222	0.70241	0.70253	0.70261
¹⁴³ Nd/ ¹⁴⁴ Nd	0.51302	0.51290	0.51295	0.51288	0.51303	0.51303	0.51295	0.51306	0.51307	0.51314	0.51299	0.51302	0.51303	0.51313	0.51302	0.51304	0.51245	0.51238
¹⁸⁷ Sm/ ¹⁴⁴ Nd	0.20172	0.17647	0.19364	0.17371	0.19996	0.20379	0.19463	0.21461	0.22436	0.22547	0.20917	0.19948	0.21785	0.22479	0.20810	0.20907	0.14058	0.15280
¹⁴³ Nd/ ¹⁴⁴ Nd (j)	0.51210	0.51209	0.51207	0.51208	0.51211	0.51210	0.51206	0.51207	0.51204	0.51210	0.51203	0.51211	0.51203	0.51210	0.51206	0.51208	0.51180	0.51168
εNd (t)	7.16	6.99	6.54	6.88	7.50	7.13	6.37	6.65	6.04	7.23	5.84	7.32	5.86	7.14	6.53	6.87	1.39	-1.05

-*The initial ⁸⁷Sr/⁸⁶Sr and ¹⁴³Nd/¹⁴⁴Nd ratios were calculated using $\lambda^{87}\text{Rb} = 1.42 \times 10^{-11}$ and $\lambda^{147}\text{Sm} = 6.55 \times 10^{-12}$ and the assigned U-Pb zircon ages were collected from SHRIMP and LASS for each sample. The ¹⁴³Nd/¹⁴⁴Nd isotopic ratios are given as epsilon (ε) notations relative to chondritic uniform reservoir (CHUR) (¹⁴³Nd/¹⁴⁴Nd = 0.512630 and ¹⁴⁷Sm/¹⁴⁴Nd = 0.196; Bouvier, Vervoort and Patchett, 2008):

$$\epsilon\text{Nd}_T = [({}^{143}\text{Nd}/{}^{144}\text{Nd}_{\text{sample}})/({}^{143}\text{Nd}/{}^{144}\text{Nd}_{\text{CHUR}}) - 1] \times 10000.$$

4.6 References

- Abd El-Rahman, Y., Polat, A., Dilek, Yildirim, *et al.* (2009) 'Geochemistry and tectonic evolution of the Neoproterozoic incipient arc-forearc crust in the Fawakhir area, Central Eastern Desert of Egypt', *Precambrian Research*, 175(1–4), pp. 116–134. doi: 10.1016/j.precamres.2009.09.008.
- Abd El-Rahman, Y., Polat, A., Dilek, Yildirim, *et al.* (2009) 'Geochemistry and tectonic evolution of the Neoproterozoic Wadi Ghadir ophiolite, Eastern Desert, Egypt', *Lithos*. Elsevier B.V., 113(1–2), pp. 158–178. doi: 10.1016/j.lithos.2008.12.014.
- Abd El-Rahman, Y. *et al.* (2017) 'The South Um Mongul Cu-Mo-Au prospect in the Eastern Desert of Egypt: From a mid-Cryogenian continental arc to Ediacaran post-collisional appinite-high Ba-Sr monzogranite', *Ore Geology Reviews*. Elsevier, 80, pp. 250–266. doi: 10.1016/J.OREGEOREV.2016.06.004.
- Akaad, M. and El-Ramly, M. (1960) 'Geological history and classification of the basement rocks of the Central Eastern Desert of Egypt', *Geological Survey of Egypt*, 9, pp. 1–15.
- Akaad, M. and Noweir, A. (1969) 'Lithostratigraphy of the Hammamat-Umm Seleimat district, Eastern Desert, Egypt.', *Nature*, 233(19), pp. 284–285.
- Ali, K. A. *et al.* (2009) 'Geochemistry, Nd isotopes and U-Pb SHRIMP zircon dating of Neoproterozoic volcanic rocks from the Central Eastern Desert of Egypt: New insights into the ~750 Ma crust-forming event', *Precambrian Research*, 171(1–4), pp. 1–22. doi: 10.1016/j.precamres.2009.03.002.
- Ali, K. A. *et al.* (2010) 'Age constraints on the formation and emplacement of Neoproterozoic ophiolites along the Allaqi-Heiani Suture, South Eastern Desert of Egypt', *Gondwana Research*, 18(4), pp. 583–595. doi: 10.1016/j.gr.2010.03.002.
- Anders, E. and Grevesse, N. (1989) 'Abundances of the elements: Meteoritic and solar', *Geochimica et Cosmochimica Acta*. Pergamon, 53(1), pp. 197–214. doi: 10.1016/0016-7037(89)90286-X.
- Basta, F. F. *et al.* (2011) 'Neoproterozoic contaminated MORB of Wadi Ghadir ophiolite, NE Africa: Geochemical and Nd and Sr isotopic constraints', *Journal of African Earth Sciences*. Pergamon, 59(2–3), pp. 227–242. doi: 10.1016/j.jafrearsci.2010.10.008.
- Belousova, E. *et al.* (2002) 'Igneous zircon: trace element composition as an indicator of source rock type', *Contributions to Mineralogy and Petrology*. Springer-Verlag, 143(5), pp. 602–622. doi: 10.1007/s00410-002-0364-7.
- Belousova, E. A. *et al.* (2010) 'The growth of the continental crust: Constraints from zircon Hf-isotope data', *Lithos*. Elsevier, 119(3–4), pp. 457–466. doi: 10.1016/J.LITHOS.2010.07.024.
- Belousova, E. A. *et al.* (2015) 'The enigma of crustal zircons in upper-mantle rocks: Clues from the Tumut ophiolite, Southeast Australia', *Geology*. Geological Society of America, 43(2), pp. 119–122. doi: 10.1130/G36231.1.

- Bézos, A. *et al.* (2009) 'Origins of chemical diversity of back-arc basin basalts: A segment-scale study of the Eastern Lau Spreading Center', *Journal of Geophysical Research*. Blackwell Publishing Ltd, 114(B6), p. B06212. doi: 10.1029/2008JB005924.
- Bonin, B. (2007) 'A-type granites and related rocks: Evolution of a concept, problems and prospects', *Lithos*. Elsevier, 97(1–2), pp. 1–29. doi: 10.1016/J.LITHOS.2006.12.007.
- Breitkreuz, C. *et al.* (2010) 'Neoproterozoic SHRIMP U–Pb zircon ages of silica-rich Dokhan Volcanics in the North Eastern Desert, Egypt', *Precambrian Research*. Elsevier, 182(3), pp. 163–174. doi: 10.1016/J.PRECAMRES.2010.06.019.
- Brooks, D. A. *et al.* (1984) 'Characteristics of back-arc regions', *Tectonophysics*, 102(1–4), pp. 1–16. doi: 10.1016/0040-1951(84)90005-2.
- Brophy, J. G. (2009) 'La-sio₂ and Yb-SiO₂ systematics in mid-ocean ridge magmas: Implications for the origin of oceanic plagiogranite', *Contributions to Mineralogy and Petrology*, 158(1), pp. 99–111. doi: 10.1007/s00410-008-0372-3.
- Bühler, B. *et al.* (2014) 'New insights into the accretion of the Arabian-Nubian Shield: Depositional setting, composition and geochronology of a Mid-Cryogenian arc succession (North Eastern Desert, Egypt)', *Precambrian Research*. Elsevier B.V., 243, pp. 149–167. doi: 10.1016/j.precamres.2013.12.012.
- Carley, T. L. *et al.* (2014) 'Iceland is not a magmatic analog for the Hadean: Evidence from the zircon record', *Earth and Planetary Science Letters*. Elsevier, 405, pp. 85–97. doi: 10.1016/j.epsl.2014.08.015.
- Cawood, P. A. *et al.* (2009) 'Accretionary orogens through Earth history', *Geological Society Special Publication*, 318, pp. 1–36. doi: 10.1144/SP318.1.
- Cawood, P. A. *et al.* (2016) 'Linking collisional and accretionary orogens during Rodinia assembly and breakup: Implications for models of supercontinent cycles', *Earth and Planetary Science Letters*. Elsevier, 449, pp. 118–126. doi: 10.1016/J.EPSL.2016.05.049.
- Cheng, J. X. *et al.* (2020) 'Petrogenesis of ca. 830 Ma Lushan bimodal volcanic rocks at the southeastern margin of the Yangtze Block, South China: Implications for asthenospheric upwelling and reworking of juvenile crust', *Precambrian Research*. Elsevier B.V., 342, p. 105673. doi: 10.1016/j.precamres.2020.105673.
- Dixon, T. H. (1981) 'Gebel Dahanib, Egypt: A Late Precambrian Layered Sill of Komatiitic Composition T.H.', *Contribution to Mineralogy and Petrology Mineral Petrol*, 76, pp. 42–52.
- El-gaby, S. and El-nady, O. (1984) 'Tectonic Evolution of the Basement Complex in the Central Eastern Desert of Egypt', pp. 1019–1036.
- El-Sayed, M. M., Furnes, H. and Mohamed, F. H. (1999) 'Geochemical constraints on the tectonomagmatic evolution of the late Precambrian Fawakhir ophiolite, Central Eastern Desert, Egypt', *Journal of African Earth Sciences*, 29(3), pp. 515–533. doi: 10.1016/S0899-5362(99)00113-X.
- El-Shazly, S. M. and El-Sayed, M. M. (2000) 'Petrogenesis of the Pan-African El-Bula igneous suite, central Eastern Desert, Egypt', *Journal of African Earth Sciences*, 31(2), pp.

317–336. doi: 10.1016/S0899-5362(00)00101-9.

Eliwa, H. A., El-Bialy, M. Z. and Murata, M. (2014) 'Edicaran post-collisional volcanism in the Arabian-Nubian Shield: The high-K calc-alkaline Dokhan Volcanics of Gabal Samr El-Qaa (592 ± 5 Ma), North Eastern Desert, Egypt', *Precambrian Research*. Elsevier, 246, pp. 180–207. doi: 10.1016/J.PRECAMRES.2014.03.015.

Eliwa, H. A., Kimura, J. I. and Itaya, T. (2006) 'Late Neoproterozoic Dokhan Volcanics, North Eastern Desert, Egypt: Geochemistry and petrogenesis', *Precambrian Research*, 151(1–2), pp. 31–52. doi: 10.1016/j.precamres.2006.08.005.

Espinoza, F. *et al.* (2008) 'Bimodal back-arc alkaline magmatism after ridge subduction: Pliocene felsic rocks from Central Patagonia (47° S)', *Lithos*. Elsevier, 101(3–4), pp. 191–217. doi: 10.1016/j.lithos.2007.07.002.

Faisal, M. *et al.* (2020) 'Geochronology and geochemistry of Neoproterozoic Hamamid metavolcanics hosting largest volcanogenic massive sulfide deposits in Eastern Desert of Egypt: Implications for petrogenesis and tectonic evolution', *Precambrian Research*. Elsevier, 344, p. 105751. doi: 10.1016/j.precamres.2020.105751.

Frimmel, H. E., Zartman, R. E. and Späth, A. (2002) 'The Richtersveld Igneous Complex, South Africa: U-Pb Zircon and Geochemical Evidence for the Beginning of Neoproterozoic Continental Breakup', *The Journal of Geology*, 109(4), pp. 493–508. doi: 10.1086/320795.

Fritz, H. *et al.* (2013) 'Orogen styles in the East African Orogen: A review of the Neoproterozoic to Cambrian tectonic evolution', *Journal of African Earth Sciences*. Elsevier Ltd, 86, pp. 65–106. doi: 10.1016/j.jafrearsci.2013.06.004.

Frost, B. R. *et al.* (2001) 'A Geochemical Classification for Granitic Rocks', *Journal of Petrology*. Oxford Academic, 42(11), pp. 2033–2048. doi: 10.1093/petrology/42.11.2033.

Furnes, H., De Wit, M. and Dilek, Y. (2014) 'Four billion years of ophiolites reveal secular trends in oceanic crust formation', *Geoscience Frontiers*. Elsevier Ltd, 5(4), pp. 571–603. doi: 10.1016/j.gsf.2014.02.002.

Griffin, W. . *et al.* (2002) 'Zircon chemistry and magma mixing, SE China: In-situ analysis of Hf isotopes, Tonglu and Pingtan igneous complexes', *Lithos*. Elsevier, 61(3–4), pp. 237–269. doi: 10.1016/S0024-4937(02)00082-8.

Grimes, C. B. *et al.* (2007) 'Trace element chemistry of zircons from oceanic crust: A method for distinguishing detrital zircon provenance', *Geology*, 35(7), pp. 643–646. doi: 10.1130/G23603A.1.

Grimes, C. B. *et al.* (2013) 'Perspectives on the origin of plagiogranite in ophiolites from oxygen isotopes in zircon', *Lithos*, 179, pp. 48–66. doi: 10.1016/j.lithos.2013.07.026.

Grimes, C. B. *et al.* (2015) "'Fingerprinting" tectono-magmatic provenance using trace elements in igneous zircon', *Contributions to Mineralogy and Petrology*. Springer Verlag, 170(5–6), pp. 1–26. doi: 10.1007/s00410-015-1199-3.

Hastie, A. R. *et al.* (2007) 'Classification of altered volcanic island arc rocks using immobile trace elements: Development of the Th-Co discrimination diagram', *Journal of Petrology*, 48(12), pp. 2341–2357. doi: 10.1093/petrology/egm062.

- Hawkesworth, C. J. and Kemp, A. I. S. (2006) 'Using hafnium and oxygen isotopes in zircons to unravel the record of crustal evolution', *Chemical Geology*. Elsevier, 226(3–4), pp. 144–162. doi: 10.1016/j.chemgeo.2005.09.018.
- Heaman, L. M., LeCheminant, A. N. and Rainbird, R. H. (1992) 'Nature and timing of Franklin igneous events, Canada: Implications for a Late Proterozoic mantle plume and the break-up of Laurentia', *Earth and Planetary Science Letters*. Elsevier, 109(1–2), pp. 117–131. doi: 10.1016/0012-821X(92)90078-A.
- Hofmann, A. W. (2014) 'Sampling Mantle Heterogeneity through Oceanic Basalts: Isotopes and Trace Elements', in *Treatise on Geochemistry*. Elsevier, pp. 67–101. doi: 10.1016/B978-0-08-095975-7.00203-5.
- Johnson, P. R. *et al.* (2011) 'Late Cryogenian-Ediacaran history of the Arabian-Nubian Shield: A review of depositional, plutonic, structural, and tectonic events in the closing stages of the northern East African Orogen', *Journal of African Earth Sciences*. Elsevier Ltd, 61(3), pp. 167–232. doi: 10.1016/j.jafrearsci.2011.07.003.
- Johnson, P. R. and Woldehaimanot, B. (2003) 'Development of the Arabian-Nubian Shield: perspectives on accretion and deformation in the northern East African Orogen and the assembly of Gondwana', *Geological Society, London, Special Publications*, 206(1), pp. 289–325. doi: 10.1144/GSL.SP.2003.206.01.15.
- Kemp, A. I. S. *et al.* (2007) 'Magmatic and crustal differentiation history of granitic rocks from Hf-O isotopes in zircon.', *Science (New York, N.Y.)*. American Association for the Advancement of Science, 315(5814), pp. 980–3. doi: 10.1126/science.1136154.
- Kemp, A. I. S. and Hawkesworth, C. J. (2014) 'Growth and Differentiation of the Continental Crust from Isotope Studies of Accessory Minerals', in *Treatise on Geochemistry*. Elsevier, pp. 379–421. doi: 10.1016/B978-0-08-095975-7.00312-0.
- Kessel, R. *et al.* (2005) 'Trace element signature of subduction-zone fluids, melts and supercritical liquids at 120–180 km depth', *Nature*. Nature Publishing Group, 437(7059), pp. 724–727. doi: 10.1038/nature03971.
- Khalil, E. (1997) 'Ocean-arc to continental margin volcanics sequences of the Pan- African Precambrian belt, Egypt: "geochemical approach"', *Egyptian Journal of Geology*, 41(2B), pp. 477–528.
- Khedr, M. Z. *et al.* (2020) 'Petrogenesis of the ~740 Korab Kansi mafic-ultramafic intrusion, South Eastern Desert of Egypt: Evidence of Ti-rich ferropicritic magmatism', *Gondwana Research*. Elsevier Inc., 82, pp. 48–72. doi: 10.1016/j.gr.2019.12.013.
- Khudeir, A., Ali, M. and El Habaak, G. (1988) 'The metavolcanics at Um Samiuku area, Egypt', *Bulletin Faculty of Science, Assuit University*, 17, pp. 73–101.
- Kirkland, C. L. *et al.* (2015) 'Zircon Th/U ratios in magmatic environs', *Lithos*. Elsevier, 212–215, pp. 397–414. doi: 10.1016/j.lithos.2014.11.021.
- Kjøll, H. J. *et al.* (2019) 'Timing of Breakup and Thermal Evolution of a Pre-Caledonian Neoproterozoic Exhumed Magma-Rich Rifted Margin', *Tectonics*. John Wiley & Sons, Ltd, 38(6), p. 2018TC005375. doi: 10.1029/2018TC005375.

- Koepke, J., Feig, S. T. and Snow, J. (2005) 'Hydrous partial melting within the lower oceanic crust', *Terra Nova*, 17(3), pp. 286–291. doi: 10.1111/j.1365-3121.2005.00613.x.
- Kröner, A. *et al.* (1991) 'Evolution of Pan-African island arc assemblages in the southern Red Sea Hills, Sudan, and in southwestern Arabia as exemplified by geochemistry and geochronology', *Precambrian Research*. Elsevier, 53(1–2), pp. 99–118. doi: 10.1016/0301-9268(91)90007-W.
- Kröner, A. *et al.* (1992) 'Dating of late Proterozoic ophiolites in Egypt and the Sudan using the single grain zircon evaporation technique', *Precambrian Research*, 59(1–2), pp. 15–32. doi: 10.1016/0301-9268(92)90049-T.
- Li, H.-Y. *et al.* (2019) 'Radiogenic isotopes document the start of subduction in the Western Pacific', *Earth and Planetary Science Letters*. Elsevier, 518, pp. 197–210. doi: 10.1016/J.EPSL.2019.04.041.
- Li, L. *et al.* (2016) 'Ca. 830 Ma back-arc type volcanic rocks in the eastern part of the Jiangnan orogen: Implications for the Neoproterozoic tectonic evolution of South China Block', *Precambrian Research*. Elsevier, 275, pp. 209–224. doi: 10.1016/j.precamres.2016.01.016.
- Li, W. X., Li, X. H. and Li, Z. X. (2005) 'Neoproterozoic bimodal magmatism in the Cathaysia Block of South China and its tectonic significance', *Precambrian Research*. Elsevier B.V., 136(1), pp. 51–66. doi: 10.1016/j.precamres.2004.09.008.
- Li, W. X., Li, X. H. and Li, Z. X. (2010) 'Ca. 850 Ma bimodal volcanic rocks in northeastern Jiangxi province, south China: Initial extension during the breakup of Rodinia?', *American Journal of Science*. American Journal of Science, 310(9), pp. 951–980. doi: 10.2475/09.2010.08.
- Li, X.-H. *et al.* (2008) '850–790 Ma bimodal volcanic and intrusive rocks in northern Zhejiang, South China: A major episode of continental rift magmatism during the breakup of Rodinia', *Lithos*. Elsevier, 102(1–2), pp. 341–357. doi: 10.1016/J.LITHOS.2007.04.007.
- Li, X. *et al.* (2002) 'U–Pb zircon geochronology, geochemistry and Nd isotopic study of Neoproterozoic bimodal volcanic rocks in the Kangdian Rift of South China: implications for the initial rifting of Rodinia', *Precambrian Research*. Elsevier, 113(1–2), pp. 135–154. doi: 10.1016/S0301-9268(01)00207-8.
- Li, X. H. *et al.* (2003) 'Neoproterozoic granitoids in South China: Crustal melting above a mantle plume at ca. 825 Ma?', *Precambrian Research*, 122(1–4), pp. 45–83. doi: 10.1016/S0301-9268(02)00207-3.
- Li, Z. . *et al.* (1999a) 'The breakup of Rodinia: did it start with a mantle plume beneath South China?', *Earth and Planetary Science Letters*. Elsevier, 173(3), pp. 171–181. doi: 10.1016/S0012-821X(99)00240-X.
- Li, Z. . *et al.* (1999b) 'The breakup of Rodinia: did it start with a mantle plume beneath South China?', *Earth and Planetary Science Letters*. Elsevier, 173(3), pp. 171–181. doi: 10.1016/S0012-821X(99)00240-X.
- Li, Z. X. *et al.* (2003) 'Geochronology of Neoproterozoic syn-rift magmatism in the Yangtze Craton, South China and correlations with other continents: Evidence for a mantle

- superplume that broke up Rodinia', *Precambrian Research*, 122(1–4), pp. 85–109. doi: 10.1016/S0301-9268(02)00208-5.
- Li, Z. X. *et al.* (2008) 'Assembly, configuration, and break-up history of Rodinia: A synthesis', *Precambrian Research*, 160(1–2), pp. 179–210. doi: 10.1016/j.precamres.2007.04.021.
- Li, Z. X., Evans, D. A. D. and Halverson, G. P. (2013) 'Neoproterozoic glaciations in a revised global palaeogeography from the breakup of Rodinia to the assembly of Gondwanaland', *Sedimentary Geology*. Elsevier B.V., 294, pp. 219–232. doi: 10.1016/j.sedgeo.2013.05.016.
- Li, Z. X. and Zhong, S. (2009) 'Supercontinent-superplume coupling, true polar wander and plume mobility: Plate dominance in whole-mantle tectonics', *Physics of the Earth and Planetary Interiors*, 176(3–4), pp. 143–156. doi: 10.1016/j.pepi.2009.05.004.
- Lyu, P. L. *et al.* (2017) 'Initial breakup of supercontinent Rodinia as recorded by ca 860–840 Ma bimodal volcanism along the southeastern margin of the Yangtze Block, South China', *Precambrian Research*. Elsevier B.V., 296, pp. 148–167. doi: 10.1016/j.precamres.2017.04.039.
- Martin, R. F. and Piwinski, A. J. (1972) 'Magmatism and tectonic settings', *Journal of Geophysical Research*, 77(26), pp. 4966–4975. doi: 10.1029/jb077i026p04966.
- Middlemost, E. A. K. (1994) 'Naming materials in the magma/igneous rock system', *Earth-Science Reviews*. Elsevier, 37(3–4), pp. 215–224. doi: 10.1016/0012-8252(94)90029-9.
- Morag, N. *et al.* (2011) 'Crustal evolution and recycling in the northern Arabian-Nubian Shield: New perspectives from zircon Lu–Hf and U–Pb systematics', *Precambrian Research*. Elsevier, 186(1–4), pp. 101–116. doi: 10.1016/J.PRECAMRES.2011.01.004.
- Morag, N. *et al.* (2012) '1000–580 Ma crustal evolution in the northern Arabian-Nubian Shield revealed by U–Pb–Hf of detrital zircons from late Neoproterozoic sediments (Elat area, Israel)', *Precambrian Research*. Elsevier, 208–211, pp. 197–212. doi: 10.1016/J.PRECAMRES.2012.04.009.
- Niu, Y. and O'hara, M. J. (2008) 'Global Correlations of Ocean Ridge Basalt Chemistry with Axial Depth: a New Perspective', *Journal of Petrology*. Oxford Academic, 49(4), pp. 633–664. doi: 10.1093/petrology/egm051.
- Ohki, J., Shuto, K. and Kagami, H. (1994) 'Middle Miocene bimodal volcanism by asthenospheric upwelling: Sr and Nd isotopic evidence from the back-arc region of the Northeast Japan arc.', *GEOCHEMICAL JOURNAL*. GEOCHEMICAL SOCIETY OF JAPAN, 28(6), pp. 473–487. doi: 10.2343/geochemj.28.473.
- Park, J. K., Buchan, K. L. and Harlan, S. S. (1995) 'A proposed giant radiating dyke swarm fragmented by the separation of Laurentia and Australia based on paleomagnetism of ca. 780 Ma mafic intrusions in western North America', *Earth and Planetary Science Letters*. Elsevier, 132(1–4), pp. 129–139. doi: 10.1016/0012-821X(95)00059-L.
- Pearce, J. (1996) 'Sources and settings of granitic rocks', *Episodes*, 19(4), pp. 120–125. doi: 10.18814/epiugs/1996/v19i4/005.

- Pearce, J. A. *et al.* (2005) 'Geochemical mapping of the Mariana arc-basin system: Implications for the nature and distribution of subduction components', *Geochemistry, Geophysics, Geosystems*, 6(7). doi: 10.1029/2004GC000895.
- Pearce, J. A. (2008) 'Geochemical fingerprinting of oceanic basalts with applications to ophiolite classification and the search for Archean oceanic crust', *Lithos*, 100(1–4), pp. 14–48. doi: 10.1016/j.lithos.2007.06.016.
- Pearce, J. A., Harris, N. B. W. and Tindle, A. G. (1984) 'Trace Element Discrimination Diagrams for the Tectonic Interpretation of Granitic Rocks', *Journal of Petrology*. Narnia, 25(4), pp. 956–983. doi: 10.1093/petrology/25.4.956.
- Pearce, J. A. and Peate, D. . (1995) 'Tectonic Implications of Volcanic Arc Magmas', *Annu. Rev. Earth Planet. Sci.*, 23, pp. 251–285.
- Pearce, J. A. and Reagan, M. K. (2019) 'Identification, classification, and interpretation of boninites from Anthropocene to Eoarchean using Si-Mg-Ti systematics', *Geosphere*. GeoScienceWorld, 15(4), pp. 1008–1037. doi: 10.1130/GES01661.1.
- Pease, V. and Johnson, P. R. (2013) 'Introduction to the JEBEL volume of Precambrian Research', *Precambrian Research*, 239, pp. 1–5. doi: 10.1016/j.precamres.2013.10.003.
- Peccerillo, A. *et al.* (2003) 'Relationships between Mafic and Peralkaline Silicic Magmatism in Continental Rift Settings: a Petrological, Geochemical and Isotopic Study of the Gedemsa Volcano, Central Ethiopian Rift', *Journal of Petrology*. Oxford Academic, 44(11), pp. 2003–2032. doi: 10.1093/petrology/egg068.
- Peccerillo, A. and Taylor, S. R. (1976) 'Geochemistry of eocene calc-alkaline volcanic rocks from the Kastamonu area, Northern Turkey', *Contributions to Mineralogy and Petrology*. Springer-Verlag, 58(1), pp. 63–81. doi: 10.1007/BF00384745.
- Polat, A. and Hofmann, A. W. (2003) 'Alteration and geochemical patterns in the 3.7-3.8 Ga Isua greenstone belt, West Greenland', in *Precambrian Research*. Elsevier B.V., pp. 197–218. doi: 10.1016/S0301-9268(03)00095-0.
- Reymer, A. and Schubert, G. (1984) 'Phanerozoic addition rates to the continental crust and crustal growth', *Tectonics*. John Wiley & Sons, Ltd, 3(1), pp. 63–77. doi: 10.1029/TC003i001p00063.
- Reymer, A. and Schubert, G. (1986) 'Rapid growth of some major segments of continental crust', *Geology*. GeoScienceWorld, 14(4), p. 299. doi: 10.1130/0091-7613(1986)14<299:RGOSMS>2.0.CO;2.
- Robinson, F. A. *et al.* (2014) 'Arabian Shield magmatic cycles and their relationship with Gondwana assembly: Insights from zircon U-Pb and Hf isotopes', *Earth and Planetary Science Letters*. Elsevier B.V., 408, pp. 207–225. doi: 10.1016/j.epsl.2014.10.010.
- Rooney, T. O. (2017) 'The Cenozoic magmatism of East-Africa: Part I — Flood basalts and pulsed magmatism', *Lithos*. Elsevier, 286–287, pp. 264–301. doi: 10.1016/J.LITHOS.2017.05.014.
- Rooney, T. O. (2020) 'The Cenozoic magmatism of East Africa: Part II – Rifting of the mobile belt', *Lithos*. Elsevier B.V., 360–361, p. 105291. doi: 10.1016/j.lithos.2019.105291.

Ross, P.-S. and Bédard, J. H. (2009) 'Magmatic affinity of modern and ancient subalkaline volcanic rocks determined from trace-element discriminant diagrams', *Canadian Journal of Earth Sciences*. Edited by A. Polat, 46(11), pp. 823–839. doi: 10.1139/E09-054.

Rudnick, R. L. and Gao, S. (2014) 'Composition of the Continental Crust', in *Treatise on Geochemistry*. Elsevier, pp. 1–51. doi: 10.1016/B978-0-08-095975-7.00301-6.

Shervais, J. W. (1982) 'TiV plots and the petrogenesis of modern and ophiolitic lavas', *Earth and Planetary Science Letters*. Elsevier, 59(1), pp. 101–118. doi: 10.1016/0012-821X(82)90120-0.

Shinjo, R. *et al.* (1999) 'Geochemical and Sr-Nd isotopic characteristics of volcanic rocks from the Okinawa Trough and Ryukyu Arc: Implications for the evolution of a young, intracontinental back arc basin', *Journal of Geophysical Research: Solid Earth*, 104(B5), pp. 10591–10608. doi: 10.1029/1999JB900040.

Shinjo, R. and Kato, Y. (2000) 'Geochemical constraints on the origin of bimodal magmatism at the Okinawa Trough, an incipient back-arc basin', *Lithos*. Elsevier, 54(3–4), pp. 117–137. doi: 10.1016/S0024-4937(00)00034-7.

Shukri, N. M. and Mansour, M. S. (1980) 'Lithostratigraphy of Um Samuiki District, Eastern Desert, Egypt', *Institute Applied Geology, University of Jeddah Bulletin*, 4, pp. 83–93. doi: 10.1016/b978-0-08-024481-5.50012-1.

Stein, M. (2003) 'Tracing the plume material in the Arabian-Nubian Shield', *Precambrian Research*, 123(2–4), pp. 223–234. doi: 10.1016/S0301-9268(03)00069-X.

Stein, M. and Goldstein, S. L. (1996) 'From plume head to continental lithosphere in the Arabian–Nubian shield', *Nature*, 382, pp. 773–778. Available at: <https://doi.org/10.1038/382773a0>.

Stern, R. J. (1981) 'Petrogenesis and tectonic setting of late Precambrian ensimatic volcanic rocks, central eastern desert of Egypt', *Precambrian Research*, 16(3), pp. 195–230. doi: 10.1016/0301-9268(81)90013-9.

Stern, R. J. (1994) 'ARC Assembly and Continental Collision in the Neoproterozoic East African Orogen: Implications for the Consolidation of Gondwanaland', *Annual Review of Earth and Planetary Sciences*, 22(1), pp. 319–351. doi: 10.1146/annurev.earth.22.050194.001535.

Stern, R. J. (2002) 'Crustal evolution in the East African Orogen: a neodymium isotopic perspective', *Journal of African Earth Sciences*. Pergamon, 34(3–4), pp. 109–117. doi: 10.1016/S0899-5362(02)00012-X.

Stern, R. J. *et al.* (2004) 'Neoproterozoic Ophiolites of the Arabian-Nubian Shield', *Developments in Precambrian Geology*, 13(C), pp. 95–128. doi: 10.1016/S0166-2635(04)13003-X.

Stern, R. J. (2018) 'Neoproterozoic formation and evolution of Eastern Desert continental crust – The importance of the infrastructure-superstructure transition', *Journal of African Earth Sciences*. Elsevier Ltd, 146, pp. 15–27. doi: 10.1016/j.jafrearsci.2017.01.001.

Stern, R. J. and Hedge, C. E. (1985) 'Geochronologic and isotopic constraints on late

Precambrian crustal evolution in the Eastern Desert of Egypt', *American Journal of Science*, 285, pp. 97–127. doi: 10.2475/ajs.285.2.97.

Stern, R. J., Kröner, A. and Rashwan, A. A. (1991) 'A late Precambrian (~ 710 Ma) high volcanicity rift in the southern Eastern Desert of Egypt', *Geologische Rundschau*, 80(1), pp. 155–170. doi: 10.1007/BF01828773.

Sun, S. -s. and McDonough, W. . (1989) 'Chemical and isotopic systematics of oceanic basalts: implications for mantle composition and processes', *Geological Society, London, Special Publications*, 42, pp. 313–345. doi: doi: 10.1144/GSL.SP.1989.042.01.19.

Tang, Y. *et al.* (2014) 'Changbaishan volcanism in northeast China linked to subduction-induced mantle upwelling', *Nature Geoscience*. Nature Publishing Group, 7(6), pp. 470–475. doi: 10.1038/ngeo2166.

Tao, C. *et al.* (2020) 'Deep high-temperature hydrothermal circulation in a detachment faulting system on the ultra-slow spreading ridge', *Nature Communications*. Springer US, 11(1), pp. 1–9. doi: 10.1038/s41467-020-15062-w.

Tatsumi, Y. and Kimura, N. (1991) 'Backarc extension versus continental breakup: petrological aspects for active rifting', *Tectonophysics*. Elsevier, 197(2–4), pp. 127–137. doi: 10.1016/0040-1951(91)90037-S.

Taylor, B. and Martinez, F. (2003) 'Back-arc basin basalt systematics', *Earth and Planetary Science Letters*. Elsevier B.V., 210(3–4), pp. 481–497. doi: 10.1016/S0012-821X(03)00167-5.

Togashi, S. *et al.* (1992) 'Trace elements and Nd-Sr isotopes of island arc tholeiites from frontal arc of Northeast Japan.', *Geochemical Journal*. GEOCHEMICAL SOCIETY OF JAPAN, 26(5), pp. 261–277. doi: 10.2343/geochemj.26.261.

Valley, J. W. *et al.* (1998) 'Zircon megacrysts from kimberlite: oxygen isotope variability among mantle melts', *Contributions to Mineralogy and Petrology*. Springer Berlin Heidelberg, 133(1–2), pp. 1–11. doi: 10.1007/s004100050432.

Valley, J. W. (2003) 'Oxygen Isotopes in Zircon', *Reviews in Mineralogy and Geochemistry*. GeoScienceWorld, 53(1), pp. 343–385. doi: 10.2113/0530343.

Valley, J. W. *et al.* (2005a) '4.4 billion years of crustal maturation: oxygen isotope ratios of magmatic zircon', *Contributions to Mineralogy and Petrology*. Springer-Verlag, 150(6), pp. 561–580. doi: 10.1007/s00410-005-0025-8.

Valley, J. W. *et al.* (2005b) '4.4 billion years of crustal maturation: oxygen isotope ratios of magmatic zircon', *Contributions to Mineralogy and Petrology*. Springer-Verlag, 150(6), pp. 561–580. doi: 10.1007/s00410-005-0025-8.

Vermeesch, P. (2006) 'Tectonic discrimination diagrams revisited', *Geochemistry, Geophysics, Geosystems*. John Wiley & Sons, Ltd, 7(6), p. n/a-n/a. doi: 10.1029/2005GC001092.

Vervoort, J. D. and Blichert-Toft, J. (1999) 'Evolution of the depleted mantle: Hf isotope evidence from juvenile rocks through time', *Geochimica et Cosmochimica Acta*. Pergamon, 63(3–4), pp. 533–556. doi: 10.1016/S0016-7037(98)00274-9.

- Wang, H. *et al.* (2016) ‘Continental growth through accreted oceanic arc: Zircon Hf-O isotope evidence for granitoids from the Qinling orogen’, *Geochimica et Cosmochimica Acta*. Elsevier Ltd, 182, pp. 109–130. doi: 10.1016/j.gca.2016.03.016.
- Wang, X.-C. *et al.* (2008) ‘The Bikou basalts in the northwestern Yangtze block, South China: Remnants of 820-810 Ma continental flood basalts?’, *Geological Society of America Bulletin*. GeoScienceWorld, 120(11–12), pp. 1478–1492. doi: 10.1130/B26310.1.
- Wang, X.-C. *et al.* (2016) ‘Origin of arc-like continental basalts: Implications for deep-Earth fluid cycling and tectonic discrimination’, *Lithos*. Elsevier B.V., 261, pp. 5–45. doi: 10.1016/j.lithos.2015.12.014.
- Wei, Y. *et al.* (2017) ‘Geochronology and geochemistry of the Early Jurassic Yeba Formation volcanic rocks in southern Tibet: Initiation of back-arc rifting and crustal accretion in the southern Lhasa Terrane’, *Lithos*. Elsevier B.V., 278–281, pp. 477–490. doi: 10.1016/j.lithos.2017.02.013.
- Whalen, J. B., Currie, K. L. and Chappell, B. W. (1987) ‘A-type granites: geochemical characteristics, discrimination and petrogenesis’, *Contributions to Mineralogy and Petrology*. Springer-Verlag, 95(4), pp. 407–419. doi: 10.1007/BF00402202.
- White, W. M. and Klein, E. M. (2014) ‘Composition of the Oceanic Crust’, *Treatise on Geochemistry*. Elsevier, pp. 457–496. doi: 10.1016/B978-0-08-095975-7.00315-6.
- Wilde, S. A. and Youssef, K. (2000) ‘Significance of SHRIMP U-Pb dating of the Imperial Porphyry and associated Dokhan Volcanics, Gebel Dokhan, north Eastern Desert, Egypt’, *Journal of African Earth Sciences*. Pergamon, 31(2), pp. 403–413. doi: 10.1016/S0899-5362(00)00096-8.
- Winchester, J. A. and Floyd, P. A. (1976) ‘Geochemical magma type discrimination: application to altered and metamorphosed basic igneous rocks’, *Earth and Planetary Science Letters*. Elsevier, 28(3), pp. 459–469. doi: 10.1016/0012-821X(76)90207-7.
- Wingate, M. T. *et al.* (1998) ‘Ion microprobe U–Pb ages for Neoproterozoic basaltic magmatism in south-central Australia and implications for the breakup of Rodinia’, *Precambrian Research*. Elsevier, 87(3–4), pp. 135–159. doi: 10.1016/S0301-9268(97)00072-7.
- Zhang, C. *et al.* (2017) ‘Felsic Plutonic Rocks from IODP Hole 1256D, Eastern Pacific: Implications for the Nature of the Axial Melt Lens at Fast-Spreading Mid-Ocean Ridges’, *Journal of Petrology*, 58(8), pp. 1535–1566. doi: 10.1093/petrology/egx064.
- Zhang, C. L. *et al.* (2006) ‘Neoproterozoic bimodal intrusive complex in the southwestern Tarim Block, northwest China: Age, geochemistry, and implications for the rifting of Rodinia’, *International Geology Review*. Taylor & Francis Group, 48(2), pp. 112–128. doi: 10.2747/0020-6814.48.2.112.
- Zimmer, M. *et al.* (1995) ‘The Gabal Gerf complex: A precambrian N-MORB ophiolite in the Nubian Shield, NE Africa’, *Chemical Geology*. Elsevier, 123(1–4), pp. 29–51. doi: 10.1016/0009-2541(95)00018-H.

“Every reasonable effort has been made to acknowledge the owners of copyright material. I would be pleased to hear from any copyright owner who has been omitted or incorrectly acknowledged.”

Appendix c:

Supplementary materials to Chapter 4

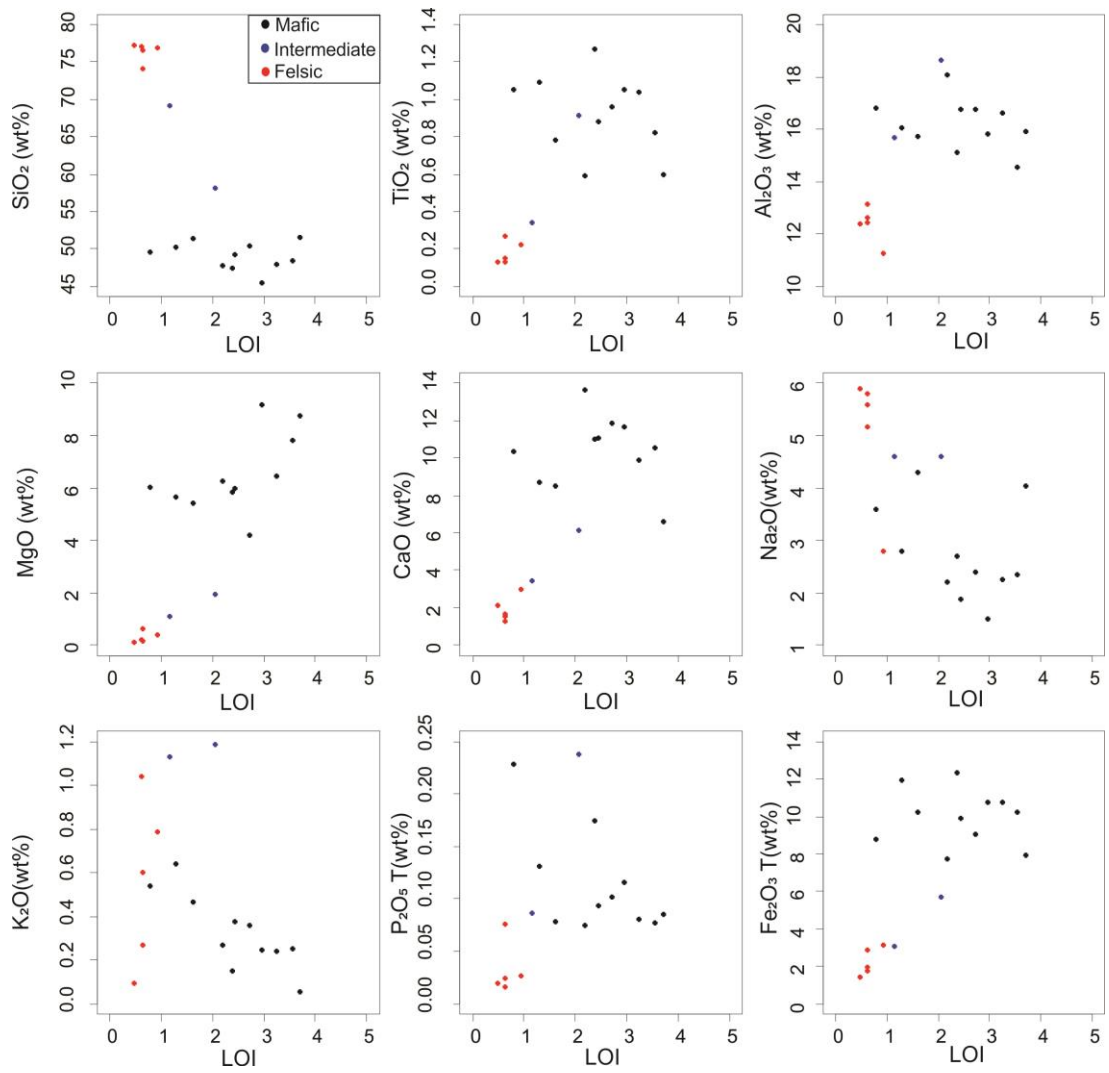


Figure C.1: Binary plots showing the relationship between the LOI and whole-rock major elements composition of the El-Shadli bimodal volcanic province.

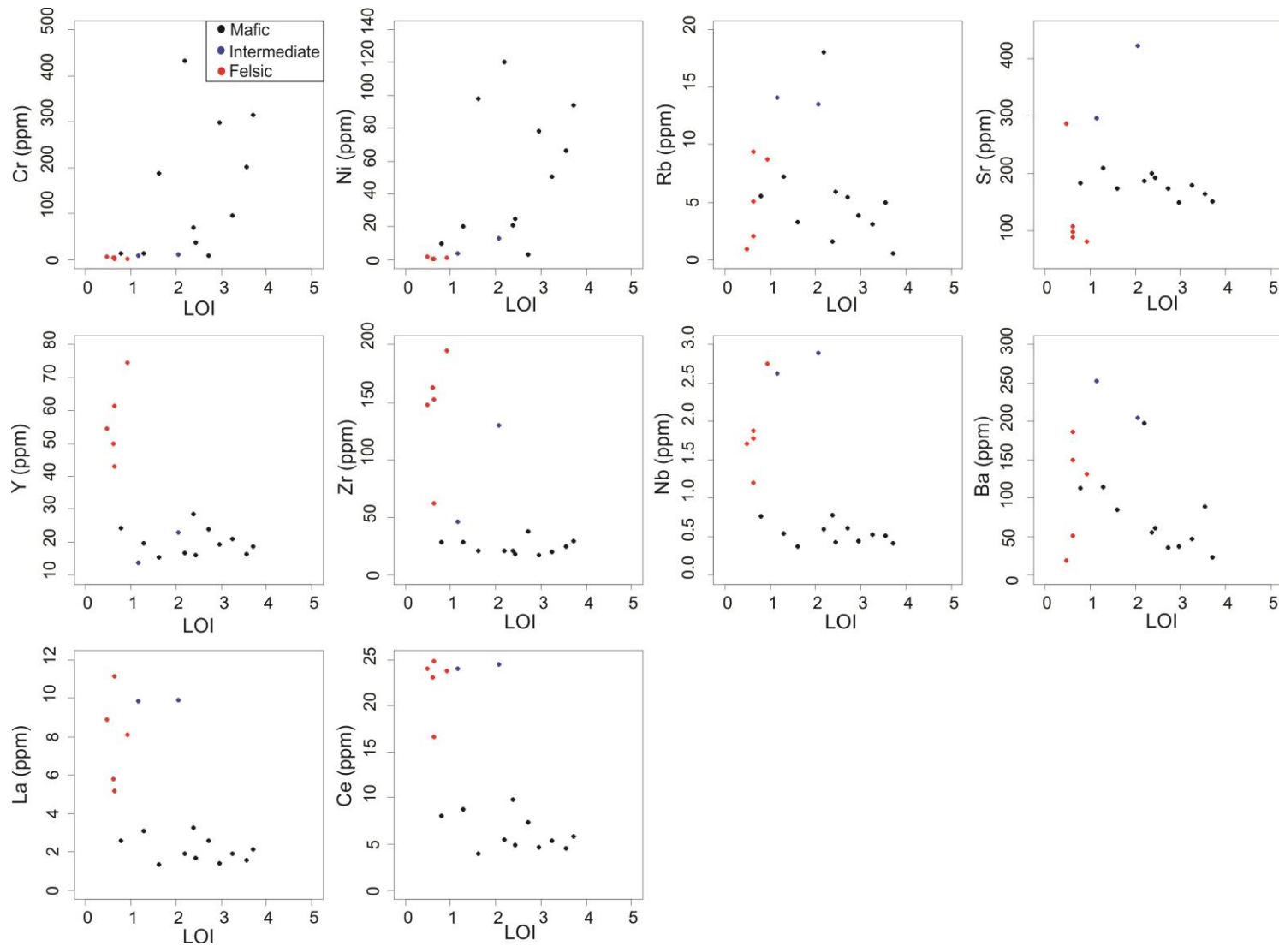


Figure C.2: Binary plots showing the relationship between the LOI and trace element composition of the El-Shadli bimodal volcanic province.

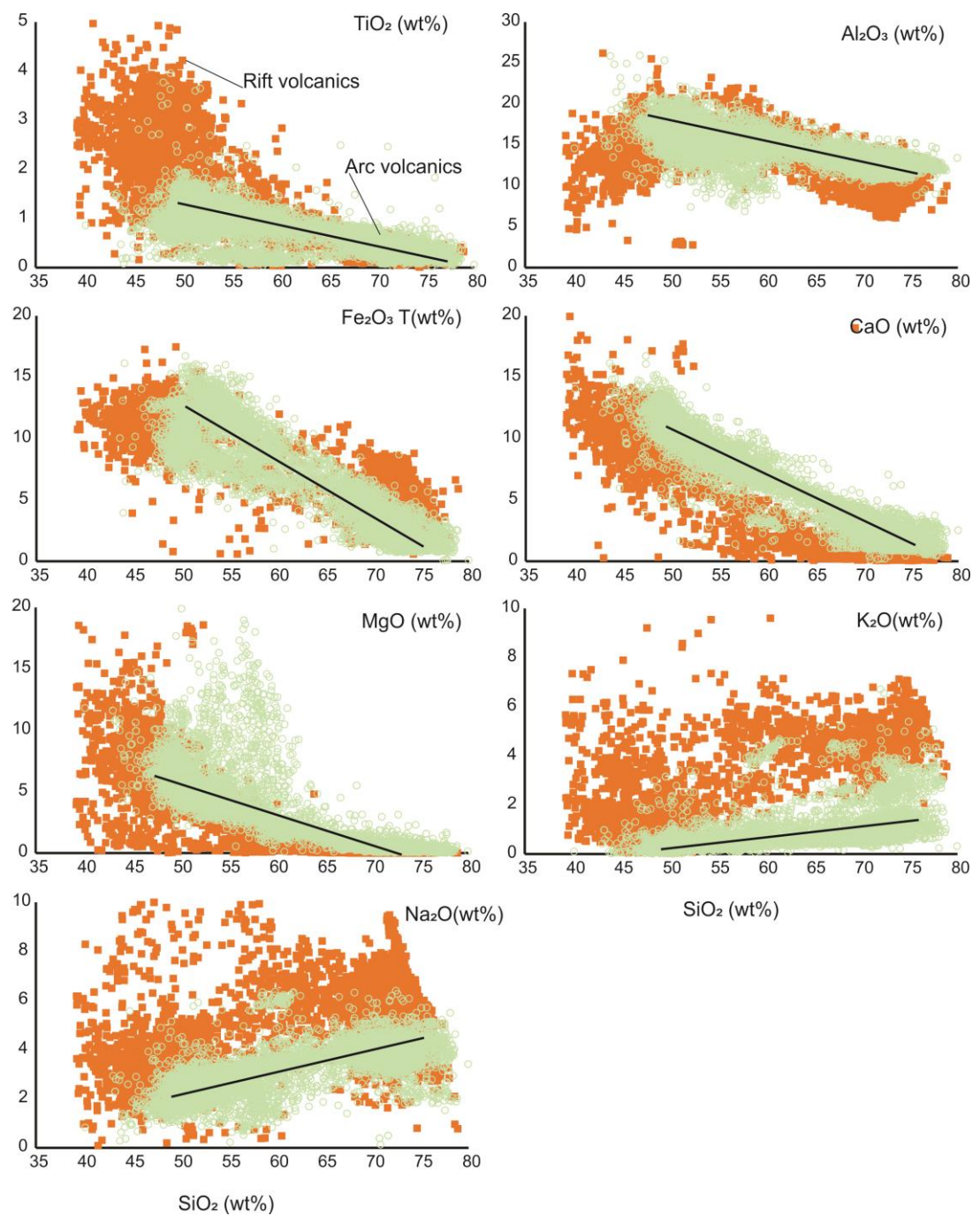


Figure C.3: Harker plots showing the differences between the whole-rock major elements composition of the rift-related volcanics (East-African rift) and arc volcanics (the Izu-Bonin-Marian (IBM) arc and the Andean arc). Data are from global database Georoc (<http://georoc.mpch-mainz.gwdg.de/georoc/>).

Table C.1: Zircon U-Pb age data of the studied rocks using SHRIMP.

Spot	U (ppm)	Th (ppm)	Th/U	232Th/238U	±%	%com. 206Pb	238U/206Pb*	±%	207Pb*/206Pb*	±%	207Pb*/235U	±%	206Pb*/238U	±%	err corr	206Pb/238U Age (Ma)	± 1σ	207Pb*/206Pb* Age (Ma)	± 1σ
Lat.	24°24'57"																		
Long.	34°35'53"																		
S02-5@1	38.86	14.16	0.36	0.38	1.80	2.38	8.63	3.89	0.02	84.51	0.35	84.60	0.12	3.89	0.05	706.88	26.06		
S02-5@2	36.18	10.89	0.30	0.31	1.92	4.13	9.56	3.90	0.04	38.82	0.53	39.02	0.10	3.90	0.10	641.43	23.83	-565.13	1047.63
S02-5@3	43.49	17.13	0.39	0.41	1.64	0.53	8.62	3.51	0.05	11.02	0.86	11.56	0.12	3.51	0.30	707.23	23.53	373.61	248.00
S02-5@4	35.99	12.15	0.34	0.35	1.90	1.23	8.72	3.80	0.06	11.46	0.92	12.07	0.11	3.80	0.31	699.65	25.21	527.86	251.18
S02-5@5	29.73	9.32	0.31	0.32	2.14	0.42	8.73	4.04	0.07	3.54	1.04	5.37	0.11	4.04	0.75	699.09	26.77	809.34	74.13
S02-5@6	39.81	14.04	0.35	0.36	1.82	1.60	9.28	3.73	0.04	24.63	0.61	24.91	0.11	3.73	0.15	659.44	23.38	-280.55	626.95
S02-5@7	44.58	17.43	0.39	0.40	1.61	0.40	9.23	3.58	0.05	11.80	0.75	12.33	0.11	3.58	0.29	662.80	22.55	220.61	273.00
S02-5@8	35.46	10.75	0.30	0.31	2.05	0.64	8.97	3.87	0.06	5.20	1.00	6.48	0.11	3.87	0.60	681.40	25.00	769.69	109.52
S02-5@9	29.02	9.85	0.34	0.35	2.05	0.13	8.64	4.16	0.06	7.84	0.93	8.88	0.12	4.16	0.47	705.72	27.83	547.91	171.28
S02-5@10	29.81	7.38	0.25	0.26	2.40	1.11	8.81	4.13	0.08	6.13	1.21	7.39	0.11	4.13	0.56	692.88	27.11	1125.22	122.27
S02-5@11	44.67	15.21	0.34	0.35	1.72	0.03	8.46	3.48	0.06	5.76	0.97	6.74	0.12	3.48	0.52	719.85	23.73	589.81	125.01
S02-5@12	35.31	11.61	0.33	0.34	1.94	-0.31	8.86	3.87	0.05	14.66	0.72	15.16	0.11	3.87	0.26	689.31	25.32	5.02	352.95
S02-5@13	112.07	64.62	0.58	0.60	0.95	0.48	8.72	2.70	0.07	2.31	1.04	3.56	0.11	2.70	0.76	699.89	17.92	797.94	48.49
S02-5@14	33.95	11.34	0.33	0.35	2.11	0.50	8.29	3.99	0.07	5.55	1.18	6.83	0.12	3.99	0.58	734.37	27.71	951.75	113.49
S02-5@15	31.35	11.63	0.37	0.38	4.53	1.20	8.52	3.48	0.07	3.58	1.18	4.99	0.12	3.48	0.70	715.72	23.57	1009.07	72.57
S02-5@16	35.75	11.70	0.33	0.34	2.07	-0.15	8.87	4.03	0.06	8.25	0.87	9.18	0.11	4.03	0.44	688.61	26.31	438.69	183.64
S02-5@17	27.05	10.50	0.39	0.40	2.13	1.43	8.29	4.39	0.05	19.24	0.91	19.73	0.12	4.39	0.22	734.51	30.49	402.10	430.90

S02-5@18	26.52	9.92	0.37	0.39	2.14	1.76	9.36	4.47	0.05	21.82	0.73	22.27	0.11	4.47	0.20	654.25	27.81	170.66	509.38
S02-5@19	28.78	8.65	0.30	0.31	2.19	1.15	8.61	4.20	0.08	7.06	1.30	8.21	0.12	4.20	0.51	708.06	28.14	1223.79	138.69
S02-5@20	22.04	6.01	0.27	0.28	2.70	0.16	8.65	4.85	0.04	31.71	0.60	32.08	0.12	4.85	0.15	705.22	32.43	-520.20	847.75
S02-5@21	36.81	14.53	0.39	0.41	1.82	1.72	8.67	3.84	0.06	13.31	0.92	13.86	0.12	3.84	0.28	703.82	25.62	534.80	291.41
S02-5@22	39.69	13.53	0.34	0.35	1.84	-0.03	8.84	7.31	0.05	14.73	0.72	16.44	0.11	7.31	0.44	690.81	47.88	-6.18	355.41
S02-5@23	92.72	54.02	0.58	0.60	1.06	0.09	8.87	2.89	0.06	5.54	0.88	6.24	0.11	2.89	0.46	688.59	18.86	471.45	122.49
S02-5@24	26.79	6.27	0.23	0.24	2.71	0.92	9.62	4.86	0.03	44.02	0.44	44.29	0.10	4.86	0.11	637.79	29.54	-1060.21	1322.61
S02-5@25	21.62	7.15	0.33	0.34	5.47	1.36	8.20	4.89	0.04	31.19	0.72	31.57	0.12	4.89	0.15	742.12	34.28	-177.14	777.99
S02-5@26	34.65	12.38	0.36	0.37	1.91	0.24	8.29	2.47	0.07	5.09	1.14	5.66	0.12	2.47	0.44	733.88	17.15	878.33	105.36
S02-5@27	31.48	9.73	0.31	0.32	2.23	-0.16	8.33	4.09	0.07	7.39	1.14	8.45	0.12	4.09	0.48	731.21	28.28	890.43	152.73
Lat.	24°15'01"																		
Long	34°36'03"																		
S16@1	194.04	80.47	0.41	0.43	0.32	0.07	8.80	2.15	0.06	3.61	0.90	4.20	0.11	2.15	0.51	693.93	14.13	512.33	79.25
S16@2	120.79	31.76	0.26	0.27	0.71	0.04	8.73	2.01	0.06	4.33	0.91	4.77	0.11	2.01	0.42	698.88	13.32	509.09	95.12
S16@3	213.24	75.20	0.35	0.36	0.32	0.20	8.97	1.93	0.06	3.35	0.90	3.86	0.11	1.93	0.50	681.03	12.48	541.97	73.14
S16@4	187.41	71.37	0.38	0.39	0.32	0.12	8.81	1.93	0.07	2.11	1.03	2.86	0.11	1.93	0.67	693.07	12.68	790.77	44.35
S16@5	180.28	55.56	0.31	0.32	0.36	0.31	8.79	1.94	0.06	2.55	0.98	3.21	0.11	1.94	0.61	694.39	12.80	686.68	54.45
S16@6	221.04	65.80	0.30	0.31	0.59	0.03	8.61	2.22	0.06	1.81	0.99	2.86	0.12	2.22	0.77	708.64	14.88	674.58	38.67
S16@7	282.76	142.17	0.50	0.52	2.59	-0.02	8.56	1.89	0.06	2.41	0.97	3.07	0.12	1.89	0.62	712.22	12.75	616.82	52.12
S16@8	195.44	83.35	0.43	0.44	0.31	0.17	8.61	2.16	0.06	2.59	0.97	3.37	0.12	2.16	0.64	708.38	14.51	632.06	55.79
S16@9	33.14	19.24	0.58	0.60	0.67	0.46	8.45	2.43	0.07	6.01	1.18	6.49	0.12	2.43	0.38	720.71	16.59	993.65	122.22

S16@10	167.12	51.30	0.31	0.32	0.37	0.46	8.73	1.95	0.06	2.24	1.02	2.97	0.11	1.95	0.66	698.94	12.91	764.29	47.20
S16@11	75.51	24.67	0.33	0.34	0.51	0.09	8.80	2.08	0.06	2.97	0.97	3.62	0.11	2.08	0.57	693.90	13.70	678.59	63.38
S16@12	193.90	59.16	0.31	0.32	0.34	0.05	8.91	1.94	0.06	3.06	0.90	3.62	0.11	1.94	0.53	685.79	12.59	541.38	66.85
S16@13	300.98	149.76	0.50	0.51	1.15	0.34	10.23	3.59	0.06	1.62	0.84	3.94	0.10	3.59	0.91	601.30	20.60	697.58	34.45
S16@14	154.10	43.53	0.28	0.29	0.38	0.20	8.76	1.95	0.06	2.28	0.98	3.00	0.11	1.95	0.65	696.82	12.90	693.32	48.66
S16@15	185.27	56.71	0.31	0.32	0.65	0.34	8.63	1.95	0.06	3.19	0.97	3.74	0.12	1.95	0.52	707.15	13.05	634.12	68.62
S16@16	219.63	98.71	0.45	0.46	0.27	0.14	8.65	1.91	0.06	1.93	0.99	2.72	0.12	1.91	0.70	704.98	12.76	678.75	41.24
S16@17	129.18	41.06	0.32	0.33	0.41	0.36	8.65	1.98	0.07	2.26	1.07	3.00	0.12	1.98	0.66	704.96	13.24	843.13	46.95
S16@18	88.11	34.18	0.39	0.40	0.48	0.58	8.70	2.51	0.06	4.18	1.00	4.87	0.11	2.51	0.51	701.56	16.66	712.33	88.85
S16@19	56.12	29.05	0.52	0.53	0.56	0.37	8.64	2.28	0.06	8.96	0.88	9.25	0.12	2.28	0.25	705.77	15.26	415.43	200.32
S16@20	203.65	76.23	0.37	0.39	0.92	0.49	9.25	2.94	0.07	1.69	0.98	3.40	0.11	2.94	0.87	661.93	18.51	791.76	35.55
S16@21	246.32	76.60	0.31	0.32	0.98	0.10	9.46	2.95	0.07	3.41	0.97	4.51	0.11	2.95	0.65	647.98	18.21	830.92	71.08
S16@22	126.73	38.27	0.30	0.31	1.01	0.01	7.98	2.97	0.07	1.90	1.13	3.52	0.13	2.97	0.84	760.80	21.28	784.25	39.95
S16@23	144.21	44.17	0.31	0.32	6.09	-0.08	8.52	2.70	0.06	2.26	0.99	3.52	0.12	2.70	0.77	715.25	18.27	636.11	48.67
S16@24	53.14	23.20	0.44	0.45	1.32	-0.36	7.97	3.37	0.05	10.14	0.83	10.68	0.13	3.37	0.32	762.36	24.25	92.67	240.14
S16@25	142.47	43.95	0.31	0.32	0.85	-0.14	8.31	2.89	0.06	2.66	0.99	3.92	0.12	2.89	0.74	732.44	20.00	586.62	57.65
S16@26	101.89	27.37	0.27	0.28	1.95	-0.35	8.18	2.96	0.06	1.99	1.04	3.56	0.12	2.96	0.83	743.48	20.77	670.52	42.54

Table C.2: Zircon U-Pb-Hf-O and Trace element data of the studied rocks generated using LASS and SIMS.

Sample #/Spot #	207Pb/235U	$\pm 2\sigma$	206Pb/238U	$\pm 2\sigma$	206Pb/238U Age (Ma)	$\pm 2\sigma$	176Hf/177Hf	$\pm 2\sigma$ INT	176Lu/177Hf	$\pm 2\sigma$ INT	$\epsilon_{\text{Hf}}(t)$	$\pm 1\sigma$	TDM Crustal (Ga)	$\delta^{18}\text{O}$ (‰)	$\pm 2\sigma$
S02-5 - 1	1.217	0.097	0.1118	0.0037	682	21	0.282662	0.000054	0.002965	0.000045	9.53	0.81	0.99		
S02-5 - 2	1.67	0.28	0.1253	0.0064	760	37	0.282642	0.000081	0.003079	0.000039	10.37	1.22	1.00		
S02-5 - 3	1.55	0.16	0.1198	0.0042	731	24	0.282695	0.000034	0.002263	0.000054	12.05	0.51	0.87		
S02-5 - 4	1.069	0.083	0.1175	0.0027	718	16	0.282763	0.000057	0.003578	0.000081	13.56	0.86	0.76		
S02-5 - 5	1.78	0.22	0.1159	0.0049	706	28	0.282747	0.00007	0.002482	0.000063	13.26	1.05	0.77		
S02-5 - 6	1.35	0.28	0.1199	0.0068	728	39	0.282763	0.000084	0.00277	0.0001	14.15	1.26	0.73		
S02-5 - 7	1.17	0.13	0.1098	0.0041	673	23	0.282662	0.000054	0.002403	0.000049	9.60	0.81	0.98		
S02-5 - 8	1.154	0.075	0.1166	0.0026	711	15	0.282674	0.000061	0.0041	0.000068	10.02	0.92	0.98		
S02-5 - 9	1.19	0.1	0.1195	0.0035	727	20	0.282648	0.000053	0.002357	0.000082	10.25	0.80	0.98		
S02-5 - 10	1.24	0.21	0.1189	0.0051	723	29	0.282798	0.000062	0.003073	0.000072	15.14	0.93	0.66		
S02-5 - 11	1.28	0.17	0.1134	0.004	692	23	0.282715	0.000057	0.00338	0.00014	11.42	0.86	0.88		
S02-5 - 12	1.052	0.081	0.1118	0.0023	683	13	0.282639	0.000047	0.00354	0.00018	8.48	0.71	1.06		
S02-5 - 13	1.19	0.18	0.113	0.0052	689	30	0.282711	0.000073	0.002863	0.000058	11.46	1.10	0.87		
S02-5 - 14	1.33	0.15	0.1204	0.0047	732	27	0.282688	0.000044	0.003004	0.000034	11.46	0.66	0.91		
S02-5 - 15	1.4	0.22	0.1147	0.0051	699	30	0.282687	0.000076	0.002987	0.000082	10.76	1.14	0.93		
S02-5 - 16	2.06	0.25	0.128	0.0055	775	31	0.282666	0.000047	0.002606	0.000091	11.77	0.71	0.92		
S02-5 - 17	1.74	0.24	0.1207	0.0054	738	32	0.282751	0.000074	0.002323	0.000023	14.15	1.11	0.74		
S02-5 - 18	2.12	0.2	0.1284	0.0039	781	23	0.282759	0.000049	0.0039	0.00011	14.52	0.74	0.75		
S02-5 - 19	1.08	0.056	0.1118	0.0015	682.9	8.9	0.282823	0.000065	0.00941	0.0001	12.33	0.98	0.81		

S02-5 - 20	1.11	0.11	0.1136	0.0032	693	18	0.282761	0.000088	0.004609	0.000043	12.51	1.32	0.81		
S02-5 - 21	1.16	0.12	0.112	0.0037	684	21	0.282754	0.000075	0.004215	0.000089	12.26	1.13	0.82		
S02-5 - 22	1.11	0.083	0.1133	0.0025	693	14	0.282682	0.000041	0.003228	0.00009	10.35	0.62	0.95		
S02-5 - 23	1.09	0.096	0.1182	0.003	720	17	0.282703	0.00005	0.002539	0.000021	11.97	0.75	0.86		
S02-5 - 24	1.125	0.078	0.116	0.0026	707	15	0.282714	0.000066	0.003951	0.00007	11.42	0.99	0.89		
S02-5 - 25	1.24	0.1	0.1148	0.0033	700	19	0.282688	0.000052	0.002506	0.000043	11.04	0.78	0.91		
S02-5 - 26	1.031	0.077	0.1156	0.0022	705	13	0.282691	0.00006	0.00341	0.000043	10.82	0.90	0.93		
S02-5 - 27	1.81	0.35	0.1241	0.0075	753	43	0.282749	0.000088	0.003109	0.000034	14.00	1.32	0.76	4.95	0.22
S02-5 - 28	1.35	0.22	0.1104	0.0046	678	28	0.282628	0.000069	0.002293	0.000033	8.55	1.04	1.05	4.86	0.18
S02-5 - 29	1.46	0.16	0.119	0.0045	724	26	0.282676	0.000061	0.00258	0.0001	11.08	0.92	0.93	4.94	0.15
S02-5 - 30	1.52	0.21	0.1151	0.004	701	23	0.282734	0.000057	0.00257	0.000082	12.66	0.86	0.81	4.92	0.21
S02-5 - 31	1.54	0.18	0.1142	0.0042	696	24	0.282727	0.000076	0.00378	0.00019	11.74	1.14	0.86	4.50	0.18
S02-5 - 32	1.7	0.38	0.124	0.01	755	59	0.28255	0.000028	0.002334	0.000025	7.38	0.42	1.19	4.81	0.23
S02-5 - 33	1.184	0.085	0.1096	0.0034	670	20	0.282654	0.000057	0.002888	0.00006	9.04	0.86	1.01	4.83	0.19
S02-5 - 34	1.31	0.14	0.1174	0.0032	715	19	0.282627	0.000047	0.002191	0.000019	9.34	0.71	1.03	4.97	0.26
S02-5 - 35	1.38	0.19	0.1144	0.0042	697	24	0.282634	0.000044	0.002247	0.000045	9.18	0.66	1.03	5.00	0.18
S02-5 - 36	1.42	0.18	0.1183	0.0052	719	30	0.282714	0.000072	0.002966	0.000088	12.13	1.08	0.85	4.95	0.22
S02-5 - 37	1.55	0.15	0.1167	0.0037	714	22	0.282739	0.000046	0.00253	0.00014	13.12	0.69	0.79	4.79	0.20
S02-5 - 38	1.38	0.2	0.1193	0.0039	729	23	0.282722	0.000054	0.002565	0.00005	12.82	0.81	0.82	4.87	0.26
S02-5 - 39	1.27	0.16	0.1142	0.0045	696	26	0.28281	0.00011	0.00477	0.00021	14.23	1.65	0.70	4.93	0.17
S02-5 - 40	1.12	0.12	0.1131	0.0034	690	19	0.282651	0.000029	0.002042	0.000072	9.73	0.44	0.99	5.15	0.21
S02-5 - 41	1.26	0.11	0.1158	0.0032	706	18	0.282779	0.000065	0.00349	0.00017	13.92	0.98	0.73	4.95	0.18
S02-5 - 42	1.25	0.11	0.1146	0.0037	699	21	0.282702	0.000041	0.002334	0.000068	11.59	0.62	0.87	4.93	0.22

S02-5 - 43	1.51	0.16	0.116	0.004	710	23	0.282644	0.000038	0.002155	0.00005	9.85	0.57	0.99	4.67	0.16
S02-5 - 44	1.16	0.13	0.1128	0.0037	688	21	0.282655	0.000042	0.001913	0.000015	9.89	0.63	0.97	5.06	0.21
S02-5 - 45	1.41	0.17	0.1234	0.0047	749	27	0.282681	0.000062	0.00256	0.00012	11.78	0.93	0.90	4.82	0.28
S02-5 - 46	1.54	0.19	0.1216	0.0039	739	22	0.282685	0.000037	0.002181	0.000017	11.90	0.56	0.88	4.96	0.19
S02-5 - 47	1.22	0.18	0.114	0.0056	698	32	0.282749	0.00006	0.002768	0.000073	13.03	0.90	0.78	5.05	0.13
S02-5 - 48	1.15	0.14	0.1159	0.004	706	23	0.282663	0.000047	0.002316	0.000015	10.36	0.71	0.96	5.05	0.18
S02-5 - 49	1.159	0.094	0.1127	0.0027	688	16	0.282665	0.000052	0.003446	0.000047	9.54	0.78	1.00	5.20	0.24
S02-5 - 50	1.7	0.18	0.1143	0.0038	697	22	0.282705	0.000049	0.002571	0.000078	11.55	0.74	0.87	5.01	0.24
S02-5 - 51	1.29	0.12	0.1153	0.0037	703	22	0.282655	0.00005	0.002234	0.000059	10.06	0.75	0.97	5.24	0.18
S02-5 - 52	1.25	0.13	0.1118	0.0041	686	25	0.282711	0.000047	0.002155	0.000055	11.72	0.71	0.85	4.93	0.18
S02-5 - 53	1.54	0.2	0.1181	0.0052	718	30	0.282713	0.000066	0.00229	0.000036	12.40	0.99	0.84	5.02	0.19
S16 - 1	0.927	0.052	0.1124	0.0015	686.7	9	0.282606	0.000038	0.000963	0.000012	8.56	0.57	1.06		
S16 - 2	0.992	0.07	0.1155	0.0021	704	12	0.282581	0.000042	0.000636	5.6E-06	8.20	0.63	1.09		
S16 - 3	1.002	0.062	0.1137	0.0021	695	13	0.282637	0.000049	0.001049	0.000057	9.80	0.74	0.98		
S16 - 4	3.6	0.39	0.1418	0.0044	854	25	0.282625	0.000061	0.000024	1.1E-06	13.43	0.92	0.88		
S16 - 5	0.999	0.076	0.1151	0.0022	702	13	0.282636	0.00004	0.000588	0.000024	10.13	0.60	0.97		
S16 - 6	0.992	0.058	0.1158	0.0017	706	10	0.282657	0.000046	0.001202	0.000021	10.68	0.69	0.94		
S16 - 7	0.988	0.072	0.1142	0.0021	698	13	0.282641	0.000029	0.000417	0.000042	10.30	0.44	0.95		
S16 - 8	0.979	0.051	0.1142	0.0014	696.9	8.2	0.282668	0.000049	0.000745	0.000015	11.08	0.74	0.90		
S16 - 9	1.004	0.052	0.116	0.0017	707.3	9.8	0.282669	0.000052	0.000752	0.000028	11.34	0.78	0.90	4.27	0.16
S16 - 10	1.01	0.14	0.1163	0.004	708	23	0.282646	0.000035	0.000701	0.000019	10.56	0.53	0.95		
S16 - 11	1.071	0.059	0.1138	0.0018	695	11	0.282658	0.000042	0.000699	0.000044	10.70	0.63	0.93		

S16 - 12	0.99	0.13	0.1199	0.0032	732	18	0.282671	0.000054	0.000749	0.000021	11.96	0.81	0.87	5.12	0.18
S16 - 13	0.975	0.069	0.1168	0.002	712	12	0.282629	0.000043	0.00102	0.000066	9.90	0.65	0.99	4.65	0.13
S16 - 14	0.988	0.044	0.119	0.0015	724.7	8.7	0.282687	0.000045	0.001709	0.00004	11.90	0.68	0.87	4.85	0.20
S16 - 15	0.936	0.053	0.1153	0.0022	705	12	0.282623	0.000026	0.000681	0.000012	9.69	0.39	1.00	4.77	0.28
S16 - 16	0.987	0.049	0.1169	0.0018	712	11	0.282661	0.000043	0.001025	0.000028	11.03	0.65	0.92	4.83	0.18
S16 - 17	0.944	0.04	0.1126	0.0016	688.7	9.5	0.282659	0.000043	0.000926	0.000026	10.50	0.65	0.93	4.90	0.23
S16 - 18	1.02	0.052	0.1177	0.0018	717	10	0.282636	0.000049	0.001021	6.3E-06	10.26	0.74	0.97	4.91	0.19
S16 - 19	0.857	0.09	0.1152	0.0029	702	17	0.282635	0.000032	0.00042	1.3E-06	10.17	0.48	0.97	5.20	0.21
S16 - 20	0.99	0.1	0.1144	0.0033	698	19	0.2826	0.000041	0.000555	9.6E-06	8.78	0.62	1.05	5.23	0.16
S16 - 21	1.049	0.058	0.1127	0.0021	688	12	0.282697	0.000047	0.000814	0.000037	11.88	0.71	0.85	4.69	0.26
S16 - 22	1.084	0.066	0.1141	0.0024	696	14	0.282625	0.000035	0.001028	8.8E-06	9.41	0.53	1.01	4.70	0.26
S16 - 23	0.984	0.054	0.1148	0.0013	700.4	7.6	0.282584	0.000043	0.000833	0.000014	8.14	0.65	1.10	4.57	0.18
S16 - 24	0.965	0.057	0.1199	0.0016	730.1	9.2	0.282641	0.00004	0.000939	0.00006	10.76	0.60	0.95	4.52	0.17
S16 - 25	0.981	0.061	0.1154	0.0025	704	14	0.282564	0.000049	0.000631	4.2E-06	7.61	0.74	1.13	4.33	0.26
S16 - 26	0.951	0.065	0.1155	0.0028	704	16	0.282629	0.000039	0.000836	0.000073	9.81	0.59	0.99	5.02	0.23
S16 - 27	0.97	0.11	0.1179	0.0042	718	24	0.282628	0.000063	0.001986	9.9E-06	9.53	0.95	1.02	4.73	0.22
S16 - 28	1.067	0.076	0.1212	0.0023	739	13	0.28263	0.00004	0.000564	0.000012	10.75	0.60	0.96	4.82	0.23
S16 - 29	1.022	0.076	0.1153	0.0024	703	14	0.282636	0.000039	0.001071	0.000052	9.93	0.59	0.98	4.79	0.15
S16 - 30	1.075	0.06	0.1163	0.0021	710	12	0.282621	0.000045	0.000945	0.000016	9.61	0.68	1.01	4.94	0.17
S16 - 31	1.056	0.063	0.1205	0.0025	733	14	0.28263	0.00004	0.000743	0.000023	10.53	0.60	0.97		
S16 - 32	1.05	0.067	0.1173	0.0019	715	11	0.282626	0.000041	0.00116	0.000032	9.79	0.62	1.00		
S16 - 33	1.04	0.12	0.1155	0.0031	704	18	0.282613	0.00007	0.001354	0.000037	9.00	1.05	1.04		
S16 - 34	0.999	0.092	0.1192	0.0026	726	15	0.282565	0.000042	0.000654	0.00003	8.12	0.63	1.12		

S16 - 35	0.9	0.14	0.1122	0.0044	688	26	0.282634	0.000046	0.00067	0.000027	9.71	0.69	0.98
S16 - 36	1.05	0.17	0.113	0.0048	696	29	0.282604	0.000059	0.000713	5.2E-06	8.81	0.89	1.05
S16 - 37	0.962	0.067	0.1155	0.0022	704	13	0.282577	0.000038	0.000712	0.000032	8.03	0.57	1.11
S16 - 38	0.99	0.1	0.1157	0.0031	705	18	0.282568	0.000039	0.000465	4.2E-06	7.85	0.59	1.12
S16 - 39	1.038	0.082	0.116	0.0023	709	14	0.282623	0.00004	0.000703	0.000019	9.77	0.60	1.00
S16 - 40	1.012	0.08	0.1191	0.0024	725	14	0.282601	0.000046	0.000755	0.000029	9.32	0.69	1.04
S16 - 41	0.98	0.11	0.1146	0.0038	699	22	0.282611	0.000044	0.000665	3.7E-06	9.14	0.66	1.03
S16 - 42	1.06	0.12	0.1138	0.0034	694	20	0.282566	0.000038	0.000787	0.000027	7.38	0.57	1.14
S16 - 43	0.91	0.16	0.1211	0.0042	736	24	0.282597	0.000055	0.000682	0.000019	9.46	0.83	1.04

Table C.2: continue

Sample #/Spot #	Nb	La	Ce	Pr	Nd	Sm	Eu	Gd	Tb	Dy	Ho	Er	Tm	Yb	Lu	Hf	Pb	Th	U	Eu/Eu*	Ce/Ce*	(Yb/Gd)N
S02-5 - 1	1.15	0.05	4.68	0.07	2.06	5.18	1.11	39.60	14.26	190.70	77.90	362.00	77.36	738.50	137.80	8211.00	117.50	24.97	41.38	0.23	20.25	24.83
S02-5 - 2	1.21	0.09	5.33	0.10	2.32	3.79	1.06	33.80	11.97	164.20	65.90	307.60	66.14	622.00	115.90	8194.00	170.00	33.03	46.78	0.28	13.48	24.50
S02-5 - 3	0.78	0.60	6.53	0.42	4.53	5.76	1.04	31.60	11.57	155.60	65.30	304.80	65.40	622.60	117.30	8523.00	104.30	17.78	35.89	0.23	3.14	26.23
S02-5 - 4	1.41	1.88	19.10	2.55	26.30	26.40	4.84	94.30	26.80	315.50	118.20	515.80	107.60	987.00	178.20	8428.00	194.00	49.30	71.70	0.29	2.10	13.93
S02-5 - 5	0.71	0.70	7.41	0.57	5.97	4.83	0.85	28.60	10.59	138.70	57.01	266.40	56.82	536.70	101.00	8388.00	115.00	21.10	37.11	0.22	2.82	24.98
S02-5 - 6	0.65	0.02	3.78		0.77	2.70	0.60	22.50	9.13	122.80	51.50	253.20	55.10	539.70	105.20	8207.00	62.00	10.85	26.14	0.23		31.93
S02-5 - 7	0.73	2.92	8.95	1.14	8.88	7.29	1.32	31.30	11.05	141.20	58.59	273.00	60.36	582.20	111.90	8287.00	56.90	15.02	29.32	0.26	1.18	24.76
S02-5 - 8	1.63	5.90	20.30	1.73	14.00	13.30	2.41	76.10	27.66	355.10	139.30	627.00	129.40	$\frac{1192.0}{0}$	214.70	8408.00	213.00	59.70	84.30	0.23	1.53	20.85
S02-5 - 9	0.82	9.50	23.00	3.04	22.90	15.00	2.57	45.10	14.90	178.10	70.80	324.00	69.50	659.30	121.20	8497.00	77.50	18.72	35.64	0.30	1.03	19.46
S02-5 - 10	0.75	$\frac{12.6}{0}$	13.30	2.07	13.20	7.10	1.00	38.30	13.34	177.80	70.40	326.10	69.70	658.00	123.00	7992.00	84.60	18.70	32.70	0.18	0.63	22.87
S02-5 - 11	0.95	1.22	8.19	0.34	3.64	7.22	1.34	42.00	15.57	198.50	79.60	365.70	77.50	723.00	135.00	8439.00	105.70	22.80	42.10	0.23	3.07	22.92
S02-5 - 12	1.54	5.00	13.11	0.91	7.10	7.04	1.12	49.10	19.13	251.40	99.80	443.90	93.10	859.00	154.90	8493.00	277.00	80.60	93.50	0.18	1.48	23.29
S02-5 - 13	0.62	0.55	3.99	0.17	1.74	4.39	0.90	27.40	10.31	140.70	58.26	278.20	59.70	573.40	108.70	8200.00	53.50	12.45	28.27	0.25	3.15	27.86
S02-5 - 14	0.94	0.24	5.19	0.07	1.64	5.18	0.93	33.30	13.19	177.20	72.90	344.90	74.52	704.30	131.30	8399.00	104.00	21.65	39.99	0.21	9.83	28.15
S02-5 - 15	0.72	0.14	3.86		1.06	2.80	0.72	23.30	9.67	132.90	55.50	267.50	59.56	573.60	111.20	8021.00	61.50	13.05	29.20	0.27		32.77
S02-5 - 16	0.84	$\frac{79.0}{0}$	36.90	7.60	37.00	13.90	1.47	37.90	11.60	143.20	58.20	275.90	60.40	590.00	111.20	8309.00	110.00	12.50	29.18	0.19	0.36	20.72
S02-5 - 17	0.80	7.60	17.72	1.67	15.10	14.70	2.47	42.20	12.60	144.10	54.80	248.00	54.20	517.00	97.00	8320.00	93.10	14.60	28.40	0.30	1.19	16.31
S02-5 - 18	1.36	3.41	12.42	0.75	9.39	15.24	3.22	73.40	24.56	301.60	114.20	499.60	105.10	962.00	172.30	7975.00	161.00	25.54	42.05	0.29	1.87	17.45

S02-5 - 19	6.16	11.60	43.70	1.37	16.14	33.80	3.31	196.00	70.20	860.00	325.30	1389.00	275.70	2427.00	419.50	8767.00	933.00	301.00	256.90	0.12	2.63	16.48
S02-5 - 20	2.33	1.90	16.18	0.23	2.91	9.26	1.39	64.00	25.60	320.20	128.20	568.30	119.90	1082.00	194.90	8484.00	291.00	86.80	106.00	0.17	5.84	22.51
S02-5 - 21	1.29	6.20	10.22	0.37	3.65	6.97	1.18	47.90	19.60	252.00	100.00	463.00	97.40	907.00	164.30	8200.00	179.00	51.00	72.70	0.19	1.62	25.21
S02-5 - 22	1.67	15.80	10.46	0.35	3.86	7.85	1.31	51.30	20.64	260.70	104.70	480.00	99.70	916.00	167.10	8493.00	226.00	69.90	81.30	0.20	1.08	23.77
S02-5 - 23	1.08		6.07	0.11	1.46	5.54	0.89	38.60	15.27	197.40	80.45	374.10	79.28	741.70	136.70	8578.00	96.20	31.24	50.65	0.18		25.58
S02-5 - 24	1.60		15.55	2.02	13.20	12.23	2.12	66.50	24.90	314.80	125.60	560.00	117.70	1082.00	196.50	8472.00	191.00	56.30	84.20	0.22		21.66
S02-5 - 26	0.88		11.00	2.29	15.50	11.50	2.17	38.20	13.95	182.50	73.60	341.00	73.25	693.00	129.80	8431.00	97.70	27.63	43.69	0.31		24.15
S02-5 - 27	1.39		10.75	0.68	4.42	7.47	1.28	50.90	20.97	271.50	108.90	497.30	105.30	978.00	180.20	8489.00	122.80	40.40	72.10	0.20		25.58
S02-5 - 28	0.61		4.12	0.36	2.92	4.89	1.06	28.80	11.69	153.00	61.68	293.60	62.90	602.00	115.10	8115.00	53.00	11.24	25.46	0.27		27.83
S02-5 - 29	0.67		14.00	0.71	5.60	7.10	1.67	27.60	10.20	125.80	52.10	240.90	52.09	492.30	92.10	8266.00	69.00	17.70	31.90	0.36		23.74
S02-5 - 30	0.78		7.71	1.66	9.30	8.60	1.85	32.20	12.54	161.20	65.70	308.70	67.59	636.80	118.60	8457.00	67.70	15.84	31.73	0.33		26.33
S02-5 - 31	0.83		4.67	0.72	4.65	4.55	1.03	26.80	10.55	137.80	56.90	278.10	60.30	581.30	111.10	8269.00	61.30	14.08	29.65	0.28		28.87
S02-5 - 32	1.03		8.52	0.76	5.43	6.42	1.37	40.10	15.33	203.90	82.30	379.00	80.60	753.00	140.20	8133.00	109.40	26.10	44.30	0.26		25.00
S02-5 - 33	1.00		16.80	4.13	27.60	27.30	5.70	63.60	17.70	178.10	62.00	284.60	61.40	581.00	110.00	8700.00	72.00	13.52	30.50	0.41		12.16
S02-5 - 34	1.12		6.60	0.10	1.68	4.97	0.93	35.10	14.69	199.10	80.70	372.80	80.09	742.50	138.62	8629.00	113.30	38.00	59.00	0.21		28.16
S02-5 - 35	0.89		4.47	0.18	1.78	3.80	0.83	25.20	10.53	139.90	59.10	281.50	61.80	591.10	113.50	8440.00	64.60	17.76	34.87	0.25		31.22
S02-5 - 36	0.65		17.10	5.30	26.10	12.20	1.67	34.50	11.67	143.60	58.80	279.60	60.70	590.00	111.00	8362.00	49.40	11.51	28.22	0.24		22.77
S02-5 - 37	0.85		4.18	0.18	1.44	4.68	0.79	27.20	11.26	149.50	62.69	300.30	66.00	628.60	118.50	8241.00	58.00	16.46	32.32	0.21		30.76
S02-5 - 38	1.02		6.59	2.25	14.50	11.60	2.24	39.60	12.79	156.30	61.46	286.20	62.60	603.00	112.90	8531.00	74.90	19.17	38.33	0.31		20.27
S02-5 - 39	0.65		5.54	0.37	2.75	4.71	0.81	27.20	10.32	137.40	56.26	264.20	57.71	557.20	104.50	8275.00	64.20	15.32	30.84	0.21		27.27

S02-5 - 40	1.72	11.85	0.13	2.10	6.48	1.24	51.30	20.54	274.60	111.00	496.30	104.40	954.00	175.10	8343.00	230.00	75.10	94.60	0.20	24.76
S02-5 - 41	0.79	3.79	0.07	1.09	4.11	0.60	24.90	10.27	136.00	56.50	269.20	58.00	562.00	106.10	8507.00	47.40	17.60	32.50	0.18	30.05
S02-5 - 42	1.34	24.50	8.40	40.00	24.30	4.49	71.30	22.10	249.00	96.30	434.00	89.30	831.00	152.20	8417.00	130.00	39.60	60.00	0.32	15.51
S02-5 - 43	1.02	4.31	0.06	1.20	3.37	0.68	27.60	10.82	152.80	64.10	306.70	67.20	638.00	121.10	8624.00	61.00	19.83	39.90	0.21	30.77
S02-5 - 44	0.72	6.74	2.61	14.90	14.70	3.04	41.10	12.63	144.30	55.60	261.30	57.89	561.00	107.40	8556.00	41.60	9.68	24.86	0.37	18.17
S02-5 - 45	0.65	3.55	0.10	0.81	2.61	0.46	19.52	8.27	107.50	46.04	222.10	48.90	468.90	89.91	8580.00	46.60	13.19	28.83	0.19	31.98
S02-5 - 46	0.80	35.30	13.80	49.00	18.00	1.78	42.50	12.97	162.20	63.50	297.50	62.89	591.60	111.50	8332.00	58.00	15.12	29.43	0.19	18.53
S02-5 - 47	0.86	8.87	1.70	6.80	6.87	1.11	29.70	10.92	142.80	59.54	279.90	61.55	597.40	111.90	8687.00	97.40	20.00	37.65	0.23	26.78
S02-5 - 48	0.70	4.87	0.34	2.79	5.07	0.95	30.80	11.02	151.00	62.40	296.70	62.90	606.60	113.80	8323.00	64.80	14.96	30.58	0.23	26.22
S02-5 - 49	0.56	3.69	0.37	2.46	4.97	0.88	30.80	12.01	158.00	65.90	308.40	67.30	642.70	120.60	8488.00	36.70	12.30	27.32	0.21	27.78
S02-5 - 50	1.23	19.40	5.70	20.80	11.50	1.63	55.20	20.02	252.80	99.60	445.50	92.70	853.00	155.70	8116.00	204.20	64.30	72.40	0.19	20.57
S02-5 - 51	0.83	6.89	2.17	7.99	6.85	1.36	29.60	10.75	139.50	57.50	274.20	60.00	579.00	108.30	8371.00	88.00	15.89	32.20	0.29	26.04
S02-5 - 52	0.66	5.12	0.86	4.09	4.66	0.90	29.20	11.04	147.90	61.02	289.40	62.50	600.80	114.60	8424.00	57.50	13.97	29.70	0.23	27.39
S02-5 - 53	0.79	9.23	2.37	7.40	5.28	0.82	27.20	10.27	132.90	55.59	262.80	58.00	551.20	104.30	8625.00	57.40	14.73	31.59	0.21	26.98
S02-5 - 54	0.75	4.35	0.24	1.35	3.10	0.72	23.00	9.00	123.70	52.65	252.60	56.07	540.20	101.70	8333.00	75.50	13.16	28.88	0.26	31.27
S16 - 1	1.61	15.81	0.16	1.09	3.21	1.68	23.60	7.83	93.80	33.99	154.60	33.46	333.10	66.76	11022.00	337.00	113.50	176.50	0.58	18.79
S16 - 2	0.99	10.14		0.83	2.02	0.83	14.33	4.84	56.50	20.89	95.50	21.51	233.90	48.72	12370.00	104.50	32.69	96.60	0.46	21.73
S16 - 3	1.38	14.48	0.13	0.94	2.25	0.96	16.10	5.84	72.90	29.60	143.20	32.50	346.00	73.50	11177.00	223.00	73.70	140.20	0.48	28.61
S16 - 4	2.29	119.10	25.70	#####	211.10	77.50	337.00	29.89	69.90	5.80	10.02	1.19	8.31	1.30	9186.00	1490.00	355.00	119.00	0.87	0.03
S16 - 5	0.84	11.06	0.53	1.83	1.67	0.55	9.86	3.48	43.40	17.13	81.00	18.53	200.90	42.50	11642.00	174.80	54.84	108.40	0.40	27.12

S16 - 6	1.66	15.90		1.15	3.10	1.26	23.10	7.81	97.30	38.60	180.80	39.65	412.10	84.60	11129.00	205.00	62.10	137.50	0.45	23.75
S16 - 7	1.07	21.60	2.52	21.30	34.20	13.5 0	95.00	14.70	88.10	20.90	81.80	16.80	167.00	32.10	11820.00	177.00	57.40	100.50	0.71	2.34
S16 - 8	1.13	41.40	10.6 0	24.40	6.50	1.64	20.30	6.14	68.90	25.37	115.20	26.07	262.10	54.41	11680.00	322.00	109.9 0	171.60	0.43	17.19
S16 - 9	1.26	13.57	0.07	0.68	2.22	0.92	16.12	5.47	67.80	25.13	117.70	26.05	265.10	54.90	11564.00	286.00	88.00	156.50	0.46	21.89
S16 - 10	0.27	25.50	5.20	12.10	4.47	1.51	17.50	5.39	61.20	22.10	99.90	21.58	216.80	42.62	9723.00	77.20	23.85	25.96	0.51	16.49
S16 - 11	1.08	12.12	0.15	0.98	2.09	0.87	14.13	4.85	62.60	23.28	108.90	24.44	248.00	51.60	11782.00	201.00	64.80	122.60	0.48	23.36
S16 - 12	0.38	8.34	0.19	2.07	4.63	1.37	19.50	6.30	71.50	25.40	112.50	24.27	241.60	46.55	9820.00	83.90	27.10	35.90	0.43	16.49
S16 - 13	1.08	10.73	0.10	0.77	1.91	0.72	13.55	5.12	65.30	27.00	136.30	31.80	343.00	72.80	11330.00	122.70	37.60	97.80	0.42	33.70
S16 - 14	2.14	22.53	0.11	1.27	4.10	1.77	27.40	10.38	126.10	49.50	235.40	52.16	546.20	113.20	10573.00	360.00	115.3 0	188.70	0.50	26.54
S16 - 15	1.00	10.62	0.05	0.63	1.89	0.82	13.37	4.67	58.40	22.59	105.30	23.09	247.00	51.60	11753.00	162.30	50.90	115.10	0.49	24.59
S16 - 16	1.49	14.31	0.09	1.00	2.29	0.99	16.27	6.15	79.30	30.88	146.20	33.84	351.70	72.60	11372.00	229.00	74.00	145.20	0.49	28.78
S16 - 17	1.52	16.57	0.11	1.10	3.18	1.48	21.94	7.73	89.00	32.57	147.30	32.16	322.90	65.00	11379.00	283.00	98.20	167.30	0.53	19.59
S16 - 18	1.49	14.63	0.10	0.81	2.42	1.12	16.34	6.23	77.70	30.69	146.80	33.57	352.00	71.91	11245.00	312.00	91.50	142.20	0.53	28.68
S16 - 19	0.37	6.74		0.28	0.79	0.22	4.13	1.52	20.47	8.73	46.42	12.05	144.80	33.13	12422.00	77.60	24.67	51.61	0.36	46.67
S16 - 20	0.45	12.70	1.17	3.47	2.50	0.72	10.36	3.36	39.24	15.45	74.90	17.36	186.40	37.19	10708.00	96.60	31.65	42.72	0.42	23.95
S16 - 21	0.94	11.81	0.28	1.25	2.56	1.13	15.30	6.00	71.10	26.40	125.90	27.16	289.00	59.10	11575.00	174.00	47.00	107.00	0.54	25.14
S16 - 22	1.05	10.87	0.17	0.79	1.96	0.83	13.43	5.10	64.93	26.50	130.60	30.67	330.50	70.49	11119.00	132.10	33.55	88.66	0.49	32.76
S16 - 23	1.01	18.33	0.73	3.11	4.18	1.27	20.28	6.86	80.50	29.72	138.30	30.87	319.20	64.70	12530.00	341.00	105.3 0	152.60	0.41	20.95
S16 - 24	1.18	12.65	0.11	1.04	2.32	0.97	16.20	5.97	76.60	29.80	141.30	31.50	325.00	66.30	11458.00	169.20	54.43	110.40	0.47	26.71
S16 - 25	1.03	10.69	0.03	0.74	2.06	0.99	13.78	4.96	58.30	21.27	95.70	21.70	228.80	48.53	12280.00	127.60	40.30	95.70	0.56	22.10

S16 - 26	0.91	10.02	0.06	0.59	1.87	0.68	11.25	4.36	54.50	22.40	108.20	25.20	274.00	58.20	11400.00	137.00	42.90	96.20	0.45	32.42
S16 - 27	1.74	5.81	0.15	1.40	4.36	0.69	34.10	14.11	184.30	72.97	338.30	68.62	636.00	112.01	9032.00	68.50	19.99	32.91	0.17	24.83
S16 - 28	0.74	7.93	0.05	0.50	1.05	0.56	8.04	3.19	42.40	16.57	81.80	18.86	201.00	42.49	11958.00	98.40	30.60	76.40	0.58	33.28
S16 - 29	1.00	10.77	0.07	1.10	2.84	1.35	18.80	6.96	85.80	32.00	145.50	32.20	329.00	66.40	9900.00	129.60	40.90	90.90	0.55	23.30
S16 - 30	1.48	14.52	0.15	1.14	3.14	1.25	19.60	7.20	85.70	32.41	145.40	32.10	324.80	65.65	11361.00	327.00	96.00	146.00	0.48	22.06
S16 - 31	0.69	8.20	0.04	0.59	2.04	0.96	13.29	4.92	60.40	23.63	109.50	24.72	259.50	54.10	11423.00	136.00	38.60	90.60	0.55	25.99
S16 - 32	1.32	11.42		0.52	1.80	0.86	14.25	5.66	75.20	30.71	151.70	35.08	382.60	80.60	11037.00	130.00	39.92	102.70	0.51	35.74
S16 - 33	0.88	12.11	0.17	1.41	3.17	1.26	18.85	7.18	88.20	36.94	180.90	39.34	388.50	75.70	8768.00	72.80	21.71	35.02	0.49	27.44
S16 - 34	0.59	9.52	0.14	1.73	2.95	1.19	14.70	5.11	58.90	21.25	98.10	21.97	227.00	46.50	11220.00	119.00	38.10	75.60	0.54	20.56
S16 - 35	0.41	9.80	1.12	3.10	2.22	0.75	9.66	2.97	36.00	13.80	68.80	16.77	188.40	40.30	9611.00	45.90	15.66	25.47	0.48	25.96
S16 - 36	0.40	8.82	0.09	1.37	3.91	1.31	21.91	7.31	82.30	29.23	123.80	24.76	231.30	42.73	9467.00	56.40	17.65	19.27	0.42	14.05
S16 - 37	0.53	10.10	0.16	2.26	5.21	2.03	24.80	8.14	87.00	30.40	129.10	26.82	264.30	52.70	11674.00	162.50	51.50	92.20	0.54	14.19
S16 - 38	0.43	7.68		0.56	0.95	0.34	5.30	2.06	24.66	9.98	53.49	13.60	152.30	33.90	11667.00	67.90	20.53	37.92	0.45	38.25
S16 - 39	0.92	8.99	0.06	0.73	1.89	0.88	12.01	4.61	57.40	22.29	103.30	23.44	240.60	48.50	11097.00	91.30	29.10	73.70	0.55	26.67
S16 - 40	1.17	9.65	0.07	0.69	1.96	0.83	12.78	5.06	61.60	23.86	111.60	24.94	259.00	55.20	11433.00	106.90	33.40	89.60	0.50	26.98
S16 - 41	0.27	8.40	0.08	1.68	2.80	1.30	14.16	4.56	52.90	19.88	90.40	20.45	214.00	43.16	10339.00	82.60	26.43	32.24	0.62	20.12
S16 - 42	0.45	8.66	0.19	2.21	4.39	1.29	20.10	6.79	75.10	27.07	121.30	25.95	250.00	48.10	9590.00	85.30	26.70	34.60	0.41	16.56
S16 - 43	0.45	9.29	0.21	1.17	2.09	0.65	12.55	4.71	57.40	22.05	100.90	21.79	211.70	40.34	9550.00	48.90	15.24	20.53	0.38	22.46

Chapter 5:

Nature of Neoproterozoic crustal growth in the Egyptian Nubian Shield: Geochronological and isotopic constraints

Abstract

The Neoproterozoic Arabian-Nubian Shield (ANS) consists of continental crust formed prior to and during the collision between East and West Gondwana. The Eastern Desert of Egypt (i.e., Egyptian Nubian Shield) constitutes the north-western part of the ANS. Magmatism in the Eastern Desert region have previously been subdivided into five or six episodes between ~800 Ma and ~540 Ma. However, the lack of precise geochronological and isotopic constraints has hampered a comprehensive understanding of the crustal growth and tectonic evolution of this region. This study presents a compilation of all previously published whole-rock Nd-Sr isotopes and zircon U-Pb-Hf-O-trace element of granitoids and volcanic rocks from the Eastern Desert, together with new and similar isotopic datasets obtained from the Genina Gharbia granitoid rocks in the south Eastern Desert. Based on the new and compiled datasets, I show that the Eastern Desert crust is characterised by juvenile crustal growth and reworking during ~800–650 Ma. During that time interval, magmatism is characterized by high $\epsilon\text{Nd}(t)$ (from +6.5 to +8.5), low initial $^{87}\text{Sr}/^{86}\text{Sr}$ (~0.702), high zircon $\epsilon\text{Hf}(t)$ (from +8.5 to +13), and mantle-like zircon $\delta^{18}\text{O}$ values (~+5‰), implying either a magmatic extraction from a depleted mantle or reworking of juvenile crust. In contrast, Nd-Sr-Hf-O isotopic data of the ~650–540 Ma magmatism show that the Eastern Desert crust experienced the crustal recycling/reworking during continental collision related to the formation of

Gondwana. The compiled data also show that the Eastern Desert crust evolved through three major episodes of magmatism with peaks at ~730 Ma, ~700 Ma, and ~600 Ma. The Eastern Desert magmatic activities reflect a fundamental transition in tectonic and magmatic styles around ~650 Ma, from pre-continental collision (~800–650 Ma, oceanic lithosphere-related magmatism, accretion, and reworking) to syn- and post-collision (~650–550 Ma). Collectively, the geochemical, isotopic, and geochronological data suggest that the Eastern Desert crustal growth has a protracted and episodic nature.

5.1 Introduction

The Arabian-Nubian Shield (ANS) forms one of the largest exposures of Neoproterozoic juvenile continental crust on Earth (Pease and Johnson, 2013; see Chapter 3 for the geological background, Figure 3.1b). The ANS crust is divided into different terranes by arc-arc suture zones that contain ophiolite belts (Figure 3.1b; Johnson *et al.*, 2011). The Eastern Desert of Egypt is located in the north-western part of the ANS (Figure 5.1) and is bounded to the south by the Onib-Sol Hamed-Gerf-Allaqi-Heiani suture, which is an ophiolitic belt thought to have been obducted during arc accretion between ~800 and 720 Ma (Ali *et al.*, 2010; Johnson *et al.*, 2011) (Figure 5.1).

Magmatism in the Eastern Desert has provided important constraints in crustal evolution models for the region (e.g., Stern and Hedge, 1985). The Neoproterozoic evolution of the Eastern Desert records successive major tectono-magmatic events that can be divided into (1) pre-accretionary and accretionary magmatism (~800–650 Ma; hereafter called pre-collisional magmatism), followed by (2) ~650–540 Ma syn- to post-continental collision magmatism (hereafter called collision-related magmatism) that led to the formation of Gondwana (Johnson *et al.*, 2011; Fritz *et al.*, 2013; Stern, 2018).

Pre-accretionary magmatism includes ~750–730 Ma ophiolites formed during mid-ocean ridge spreading and adjacent to oceanic arcs (Kröner *et al.*, 1992; Stern *et al.*, 2004; Ali *et al.*, 2010), as well as subduction-related metavolcanics that continued until syn-to post terranes accretion (~770–720 Ma: Stern and Hedge, 1985; Kröner *et al.*, 1992; Ali *et al.*, 2009; Bühler *et al.*, 2014; Abd El-Rahman *et al.*, 2017)

(Figure 5.2). Syn-to post-accretionary magmatism includes: (1) ~740–650 calc-alkali I-type granitoids including diorites, gabbroic diorites, tonalites, trondhjemites, and granodiorites (Stern and Hedge, 1985; Kroner *et al.*, 1994; Moussa *et al.*, 2008; Andresen *et al.*, 2009; Lundmark *et al.*, 2012; Augland *et al.*, 2012; Ali *et al.*, 2012a, 2015; Eliwa *et al.*, 2014; Abdel-Rahman, 2018; Stern *et al.*, 2020); (2) the ~730–700 Ma rift-related El-Shadli plutonic complex and bimodal volcanics (Chapters 3 and 4) related to re-working of accreted oceanic lithosphere; and (3) plume-related magmatism such as the ~740 Ma Korab Kansu layered ferropicritic mafic-ultramafic intrusions (Khedr *et al.*, 2020), and the ~710 Ma G. Dahanib komatiitic layered intrusions (Dixon, 1981; Azer *et al.*, 2017) (Figure 5.2).

The onset of continental-continental collision is heralded by ~655–620 Ma granulite-facies metamorphism in the southern ANS (Uganda, Kenya, Tanzania, and northern Mozambique; Coolen *et al.*, 1982; Johnson *et al.*, 2011; Fritz *et al.*, 2013). Collision-related magmatism includes (1) calc-alkaline to alkaline I-type granitoids including quartz diorites, tonalites, and granodiorites (~645–610: Zoheir *et al.*, 2019, 2020; El-Bialy *et al.*, 2020); (2) alkaline A-type granites (~645–550 Ma: Moussa *et al.*, 2008; Ali *et al.*, 2012b, 2013; Eliwa *et al.*, 2014; Lehmann *et al.*, 2020); and (3) Dokhan (alkaline) volcanics (~630–580 Ma: Wilde and Youssef, 2000; Breikreuz *et al.*, 2010) (Figure 5.2). Widespread ~650 to 580 Ma A-type granitic magmatism (Johnson *et al.*, 2011) and terrestrial-to-shallow marine strata deposited unconformable above strongly deformed and variably metamorphosed pre-650 Ma rocks (e.g. the ~620–585 Ma Hammamat molasse-type sedimentary rocks; Wilde and Youssef, 2002; Abd El-Rahman *et al.*, 2019) throughout the Eastern Desert indicate that the terranes accretion finished before ~650 Ma and continental collision started around that time (Johnson *et al.*, 2011).

However, the extent to which these pre-collisional (~800–650 Ma) and collision-related (~650–540 Ma) magmatic events have a juvenile nature or involved recycling/reworking of much older continental crust is actively debated (Stern, 2002; Ali *et al.*, 2009, 2013, 2015, 2016; Liégeois and Stern, 2010; Stern *et al.*, 2010; Li *et al.*, 2018).

Stern and Hedge (1985) have been proposed that Neoproterozoic magmatism in the Eastern Desert is occurred in five or six main magmatic episodes, starting before ~770 Ma and ending by ~540 Ma. However, the lack of precise and robust geochronological and isotopic data has hampered a comprehensive understanding of

the growth and evolution of the Eastern Desert crust. Tracking the evolution of these magmatic rocks (such as volcanics and granitoid rocks) is crucial for understanding the growth of continental crust (Kemp and Hawkesworth, 2014). As volcanic and granitic rocks are the most abundant lithological units in the Eastern Desert (Figure 5.1) (Stern and Hedge, 1985; Farahat *et al.*, 2007; Johnson *et al.*, 2011; Stern, 2018) and almost all geochronological and isotopic constraints are derived from them, they are the best targets for examining the magmatism and growth/evolution of the Eastern Desert crust.

In this chapter, I first compile all previously published geochronological data of granitoid and volcanic rocks from the Eastern Desert (see the following section for details; Table 5.1). In addition, I present new whole-rock Nd-Sr isotopic data and zircon U-Pb-Hf-O-trace elements data for the Genina Gharbia pluton, a granitoid body in the south Eastern Desert (Figures 5.1 and 5.3). The combination of new and compiled geochronological and isotopic data allow me to (1) assess the juvenile vs. recycled/reworking nature of crustal growth in the Eastern Desert, (2) evaluate the magmatic episodes recorded the Eastern Desert crust, and (3) detect the timing of the Neoproterozoic transition in tectonic and magmatic styles and track the evolution of the Eastern Desert crust.

In this Chapter, I will adopt the following definitions that consistent with Kemp and Hawkesworth (2014). Juvenile crust is generated by mantle-derived magmatism and has a sufficiently short residence time above the Moho that its radiogenic isotope ratios have not evolved significantly away from that of its contemporary mantle source. Crustal recycling is a term that encompasses processes through which older crustal materials are returned to the mantle, typically by subduction or delamination/foundering. This recycled crust is homogenized into the convective mantle, and may be sampled by younger magmatism which inherits significantly evolved radiogenic isotope ratios. Crustal reworking means physical reprocessing of pre-existing crust by melting (which may lead to evolve radiogenic isotope ratios in the resultant magmas), metamorphism, or rock-fluid interaction. Crustal growth means an increase in the overall volume of the continental crust. Crust generation means the addition of materials newly extracted from the mantle.

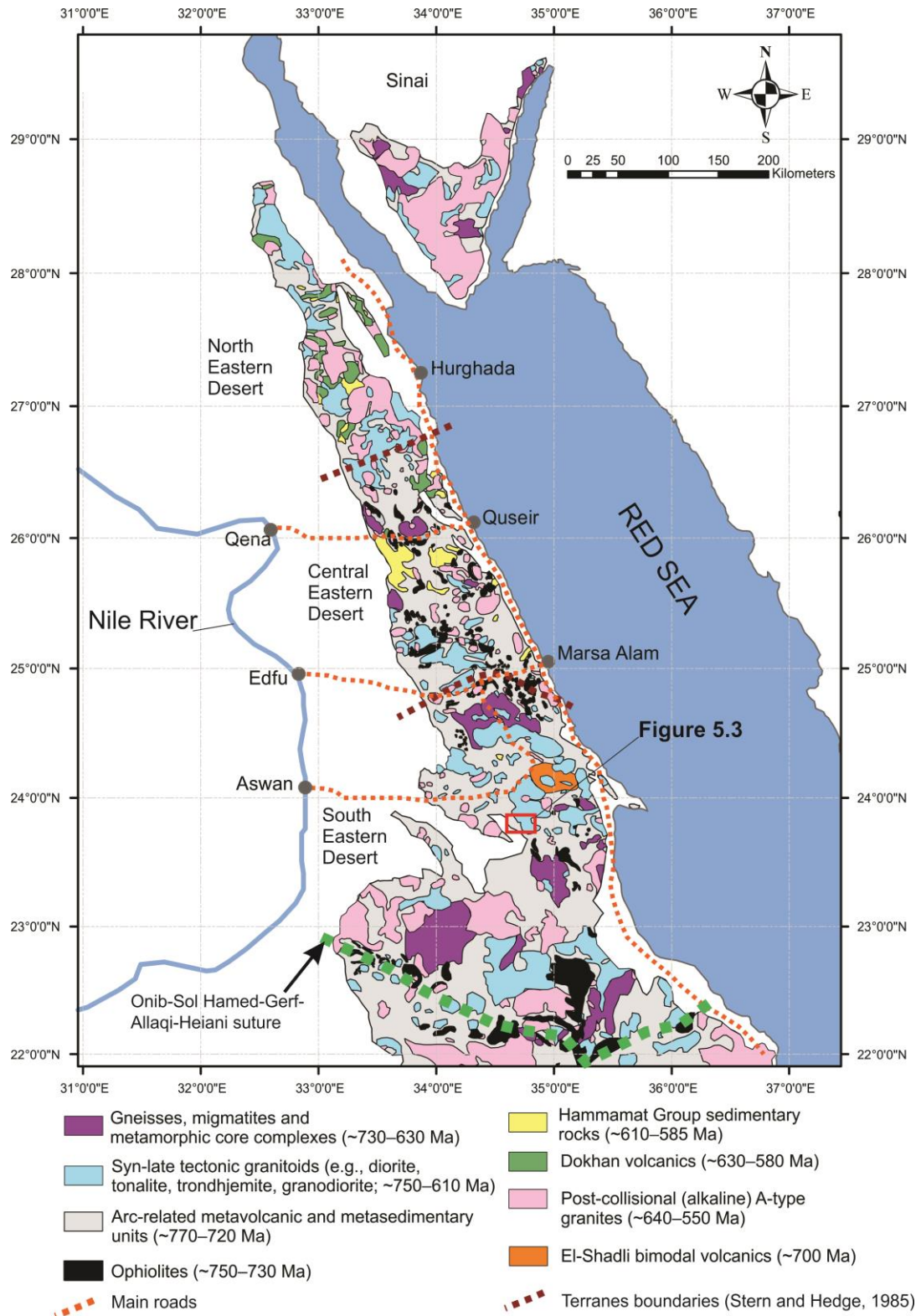


Figure 5.1: Geological map of the Eastern Desert showing the ages and distribution of the main rock Precambrian crustal basement rock units. Eastern Desert terranes boundaries are after Stern and Hedge (1985). The map is modified after Johnson *et al.*, (2011).

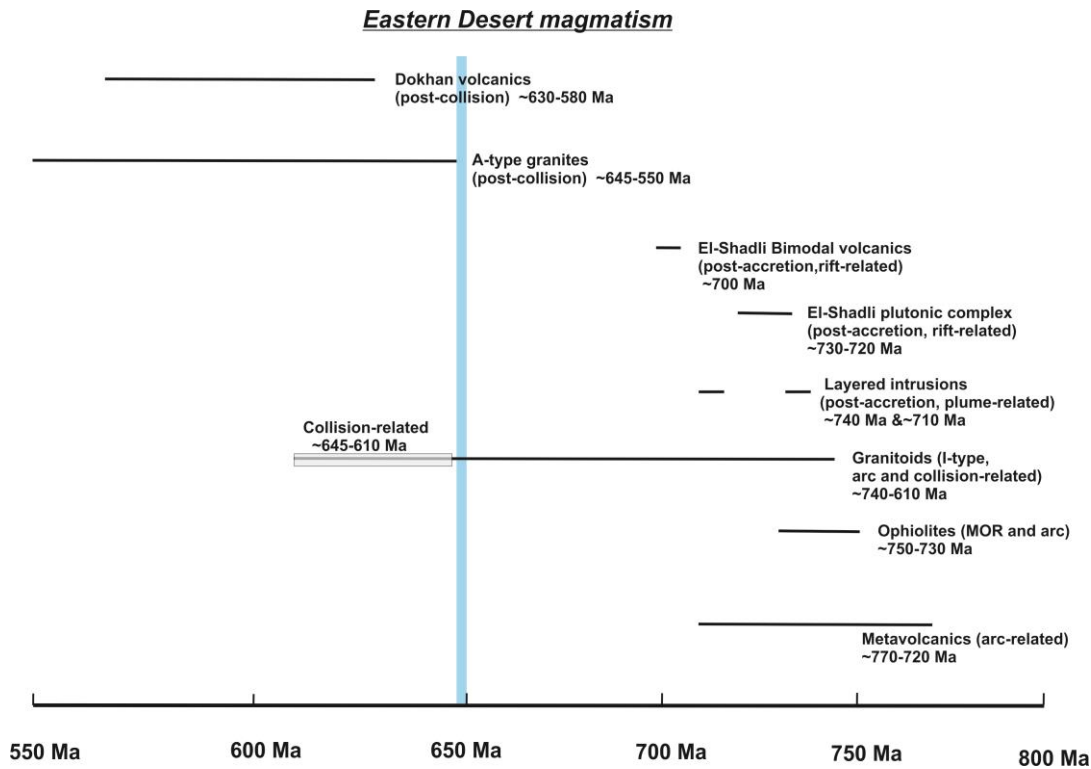


Figure 5.2: Timeline chart of the magmatic activities in the Eastern Desert crust.

5.2 Previous geochronological data of granitoid and volcanic rocks in the Eastern Desert

The crustal basement of the Eastern Desert consists of distinct geochemical and petrological rock assemblages (see Chapter 3 for the geological background about the Eastern Desert; Figure 5.1). In the following section, I will summarize the published U-Pb and Pb-Pb zircon/monazite geochronological data for the granitoids and volcanic rocks. All ages (and references) are given in Table 5.1.

According to diagnostic lithological characteristics and age constraints, Stern and Hedge (1985) subdivided the basement of the Eastern Desert into three domains, the North, Central, and South Eastern Desert (NED, CED, and SED) respectively (Figure 5.1). Applying the Pb-Pb single zircon evaporation technique to the Eastern Desert granitoids, Kröner *et al.* (1992) and Kröner, Kruger, and Rashwan (1994) reported U-Pb zircon ages of 746 ± 19 Ma (for granitoids from Wadi (W) Ghadir, CED), 736 ± 11 Ma (for granitoids from Abu Swayel, NED), 700 ± 12 Ma, 698 ± 14 Ma and 677 ± 9 Ma (for gneissose granites from Hafafit complex, SED), and $704 \pm$

8 Ma (for the Beitan granitic gneiss, SED) (Table 5.1). Bregar *et al.* (2002) also reported zircon evaporation U-Pb zircon ages ranging from 694 ± 27 Ma to 653 ± 15 Ma for the El Sibai granitic gneiss in the CED (Table 5.1).

U-Pb ID-TIMS zircon ages were first reported for the Eastern Desert (the Gabal (G) El Umra granodiorites in the CED) with a range of between 690 ± 21 Ma and 654 ± 5 Ma (Shalaby *et al.*, 2005). More precise ID-TIMS ages were reported by Andresen *et al.*, (2009) for granitoids from the Meatiq-Fawakhir region in the CED: 630 ± 2 Ma (Meatiq gneiss), 590 ± 3 Ma (Arieki granite), 606 ± 1 Ma (Abu Ziran diorites), 597 ± 3 Ma (Fawakhir monzogranites) and 596 ± 2 Ma (Um Had granites). Furthermore, using U-Pb ID-TIMS, Augland *et al.*, (2012) and Lundmark *et al.* (2012) reported ages ranging between 685 ± 3 and 679 ± 2 Ma for El Sibai granitoids gneiss in the CED, and between 689 ± 3 and 629 ± 5 for Hafafit granitoids in the SED (Table 5.1).

Moussa *et al.* (2008) reported the first U-Pb SHRIMP zircon ages for granites from the NED and CED, such as the G. Qattar A-type granites (604 ± 3 Ma), Abu Harba A-type granites (595 ± 3 Ma), G. Al Missikat A-type granites (597 ± 7 Ma), Um Taghir tonalites (653 ± 3 Ma) and Um Ara A-type granites (603 ± 14 Ma). Additional *in situ* age data on single zircons using SIMS, SHRIMP, or LA-ICPMS have been reported from the NED including the G. Dara granitoids (741 ± 3 , 720 ± 7 , 608 ± 3 , and 600 ± 3 Ma; Eliwa *et al.*, 2014) and W. Hawashiya granitoids (622 ± 4 and 589 ± 7 Ma; El-Bialy *et al.*, 2020). The ages presented by Ali (2015) from the NED include granitoids dated at G. Faliq El-Sahl (605 ± 10 Ma), G. Abu-Marwa (596 ± 8 Ma), G. El-Glouf (596 ± 11 Ma), and G. Qattar (580 ± 22 Ma). CED ages include the El Shalul gneissose granites (631 ± 6 Ma and 637 ± 5 Ma; Ali *et al.*, 2012a). SED ages include the Allaqi granodiorite (629 ± 5 Ma and 709 ± 4 Ma; Ali *et al.*, 2010), G. Humr Akarim A-type granites (633 ± 7 Ma and 603 ± 8 Ma; Ali *et al.*, 2012b), G. Humr Mukbid A-type granites (625 ± 8 Ma and 619 ± 8 Ma; Ali *et al.*, 2012b), W. Beitan granitic gneiss (744 ± 10 Ma, 725 ± 9 Ma and 791 ± 10 Ma; Ali *et al.*, 2015) and Hafafit gneiss (731 ± 3 Ma; Abu El-Enen *et al.*, 2016) (Table 5.1). Recently, new ages have been acquired on monazite for granites from the CED (B. Zoheir *et al.*, 2019; Lehmann *et al.*, 2020; Zoheir *et al.*, 2020): W. Atalla (615 ± 9 Ma), Um Rus (642 ± 9 Ma), and Abu Dabbab (644 ± 2 Ma).

There are very few geochronological data for volcanic rocks, and the majority of these data are from the NED (Table 5.1). They include: (1) arc-related volcanic

rocks from W. Um Mongol (773 ± 7 Ma; Abd El-Rahman *et al.*, 2017) and W. Malaak (725 ± 7 Ma and 717 ± 8 Ma; Bühler *et al.*, 2014), and (2) the Dokhan volcanic rocks from W. Abu Maamel (602 ± 9 Ma and 593 ± 13 Ma; Wilde and Youssef, 2000) and Ras Gharib area (from 630 ± 6 Ma to 601 ± 4 Ma; Breitzkreuz *et al.*, 2010). Ali *et al.* (2009) reported ages ranging from 769 ± 29 Ma to 730 ± 22 Ma for arc-related volcanics from W. Kareim in the CED. In the SED, reported ages for the volcanic rocks include the W. Shilman (733 ± 7 Ma; Ali *et al.*, 2010) and the El-Shadli volcanic province (695 ± 6 Ma; Faisal *et al.*, 2020 and ~ 700 Ma; this study, Chapter 4).

5.3 Description and sample localities of the Genina Gharbia pluton

The Genina Gharbia pluton is located in the southern part of the El-Shadli volcanics province in the SED (Figures 5.1 and 5.3a). Other rocks exposed in this area include gabbros, ultramafic rocks (i.e., pyroxenites and peridotites), and volcanic rocks. The Genina Gharbia pluton has suffered only minor deformation, has low relief, is highly eroded and is exposed as isolated outcrops (Figure 5.3). The pluton intrudes gabbros and ultramafic rocks with sharp contacts (Figure 5.3b). The area is dissected by two major WNW-ESE fault systems (Helmy *et al.*, 2014).

Tonalite G04-2 ($23^{\circ} 55' 49.9''$ N, $34^{\circ} 39' 20.95''$ E) and trondhjemite samples G04-1 ($23^{\circ} 55' 48.1''$ N, $44^{\circ} 39' 23.24''$ E) are both massive, medium-to coarse-grained and greyish-pink in colour (Figure 5.3c). They are hypidiomorphic, medium-to coarse-grained. Sample G04-2 is composed of 47% plagioclase, 39% quartz, 5% orthoclase, and 1.5% hornblende whereas Sample G04-1 contains 60% plagioclase, 24% quartz, 1.5% orthoclase, and 4.5% hornblende (Figure 5.4a, b). In both samples, opaque minerals (<2%), titanite, zircon, and apatite (<1%) are accessory minerals. Secondary minerals include clay minerals, chlorite, and sericite. Plagioclase occurs as a large subhedral to euhedral grains characterized by well-defined twinning and zoning and minor alteration. Quartz ranges in size from medium to coarse-grained, and occurs as interstitial aggregates within the plagioclase matrix (Figure 5.4a, b). Orthoclase occurs as small elongated crystals. Hornblende is distributed within the quartz-plagioclase dominated matrix. Opaque minerals consist of magnetite,

hematite, and ilmenite and are scattered randomly in the groundmass (Figure 5.4a, b).

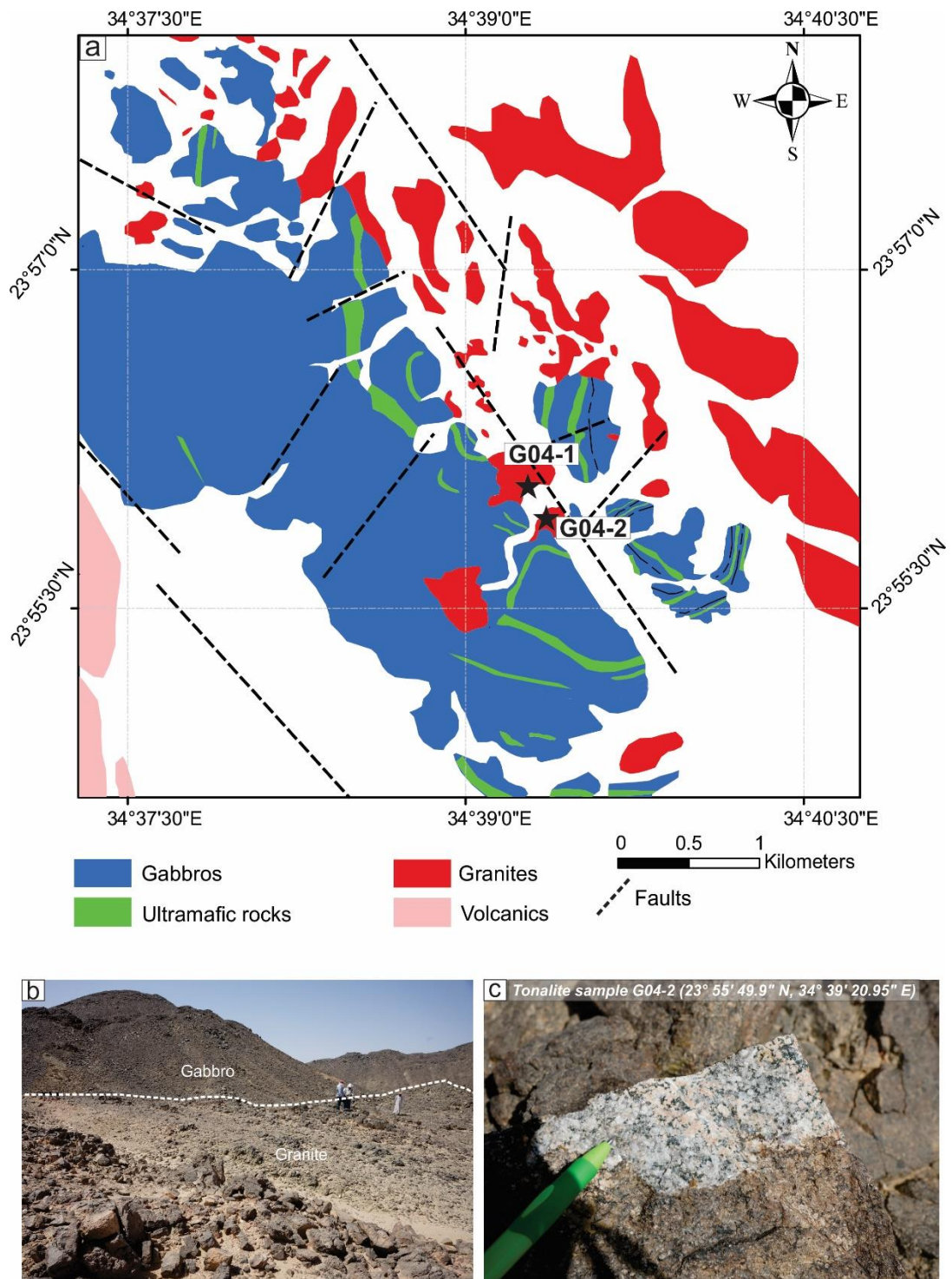


Figure 5.3: (a) Geological map of the Genina Gharbia area modified after Helmy *et al.* (2014) showing the major rock units. (b) The field photo displays the contact relationship between the granites and gabbros. (c) Close up view for sample G04-2.

5.4 Analytical techniques

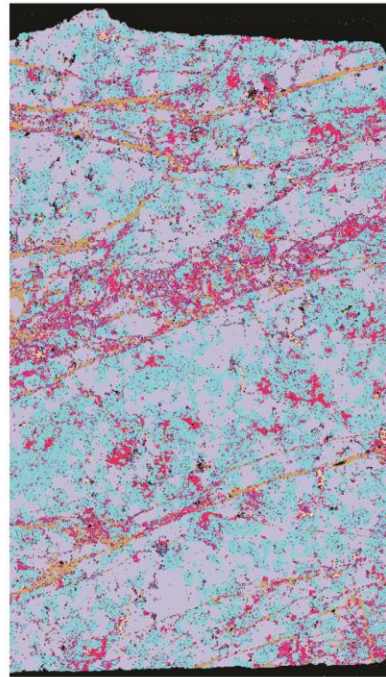
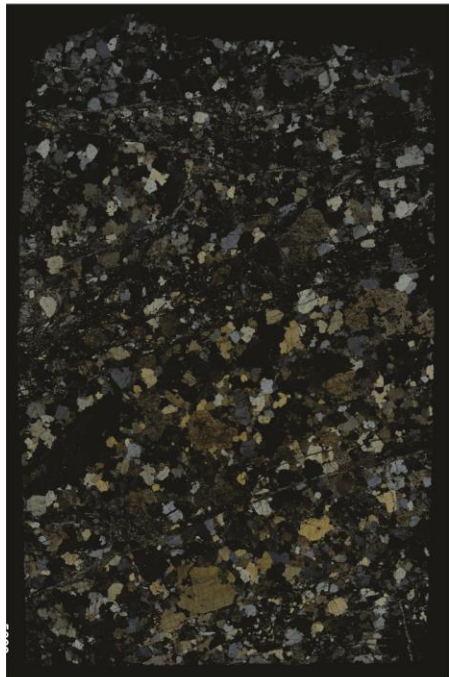
Phase mineral distribution maps for samples G04-2 and G04-1 (Figure 5.4) were acquired using a TESCAN Integrated Mineral Analyser (TIMA) housed at the John de Laeter Centre, Curtin University. Whole-rock major elements (Table D1) were determined using X-ray fluorescence at the Bureau Veritas Lab, Perth. Whole-rock trace elements and Sr-Nd isotope data (Table D1) were determined using ICP-MS and TIMS, respectively, at the Macquarie (MQ) GeoAnalytical Lab, Macquarie University. For sample G04-2, zircon U-Pb dating was carried out using SHRIMP II at Curtin University (Table D2). Zircon Hf isotope and trace element data (Table D2) were acquired using LASS-ICPMS at Curtin University, while zircon O isotope data (Table D3) were acquired using SIMS at Guangzhou Institute of Geochemistry, China. Analytical techniques for all methods used in this chapter are given in more detail in Chapter 2 (Methodology).

5.5 Results

5.5.1 Whole-rock geochemical and Sr-Nd isotopic data

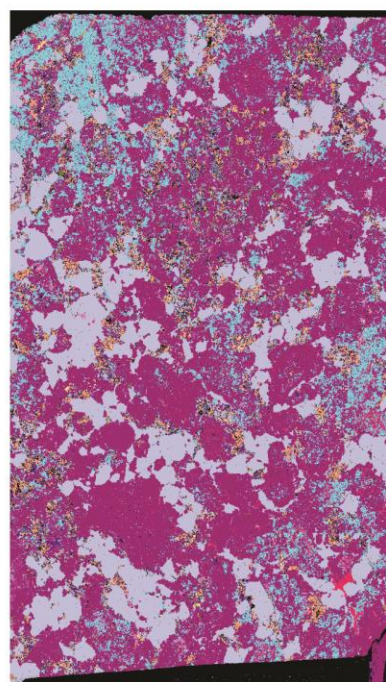
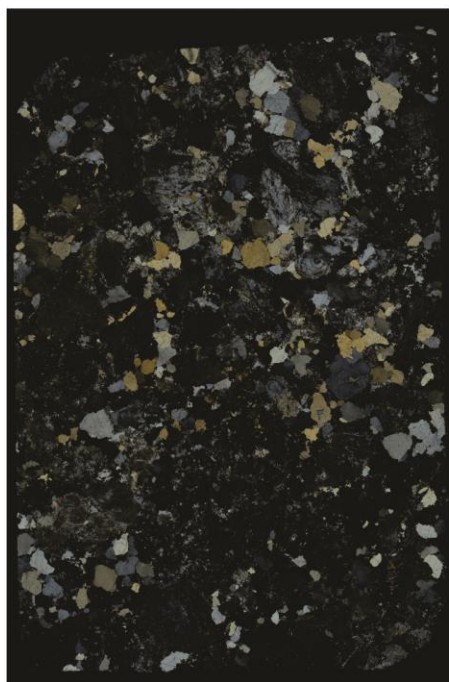
The Genina Gharbia pluton is generally fresh with no notable alteration/weathering, as indicated by low loss on ignition (LOI) values (typically below 1.5 wt.%, Table D1). Therefore, no significant alteration of its primary geochemical composition (including the petrogenetically indicative high field strength elements (HFSE) and rare earth elements (REE)) is expected. The Genina Gharbia pluton samples vary in SiO₂ (67.6 wt. % sample G04-1; 74.9 wt. % sample G04-2), Al₂O₃ (13.1 wt. % sample G04-2; 16.1 wt. % sample G04-1), MgO (0.29 wt. % sample G04-2; 1.2 wt. % sample G04-1) and Fe₂O_{3T} (1.4 wt. % sample G04-2; 3.5 wt. % sample G04-1) (Table D.1). The samples have low K₂O (0.97 wt. %, sample G04-2; 1.1 wt. % sample G04-1) and total alkali contents (<5.8 wt. %) (Figure 5.5a, c).

a- Sample G04-2



- Plagioclase (Ab2)
 - Quartz
 - Plagioclase (An2)
 - Plagioclase (Ab1)
 - Plagioclase (An1)
 - Orthoclase
 - Amph (hornblende)
 - Magnetite/hematite
 - Sericite
 - Clay
 - Titanite
 - Zircon
 - Ilmenite
 - Apatite
- 5 mm

b- Sample G04-1



- Plagioclase (An1)
 - Quartz
 - Plagioclase (Ab2)
 - Amph (hornblende)
 - Plagioclase (An2)
 - Orthoclase
 - Magnetite/hematite
 - Clay
 - Titanite
 - Ilmenite
 - Apatite
 - Zircon
- 5 mm

Figure 5.4: Mineralogical composition of the Genina Gharbia pluton including the crossed polar image (left) and TIMA phase map (right).

The Genina Gharbia samples plot in the granodiorite and granite fields on the total alkali-silica diagram (TAS; Figure 5.5a) (Middlemost, 1994). These samples are classified as tonalite (G04-2) and trondhjemite (G04-1) on the Ab-An-Or diagram (Figure 5.5b) (O'Connor, 1965; Barker, 1979). On the Ga/Al ratios versus total alkali (Figure 5.5c) and Y (Figure 5.5d) diagrams of Whalen, Currie, and Chappell (1987), the Genina Gharbia granite samples plot in the I- and S-type granite field. Ga/Al ratios, major oxide ratios, and some trace elements (such as Y, Zn, Nb, Ce, and Zr) have been widely used for petrogenetic studies and are insensitive to the degree of alteration (Whalen, Currie, and Chappell, 1987). To distinguish between I- and S-type for the Genina Gharbia samples, Shand's index A/NK (molar $\text{Al}_2\text{O}_3/(\text{NaO} + \text{K}_2\text{O})$) versus A/CNK (molar $\text{Al}_2\text{O}_3/(\text{CaO} + \text{Na}_2\text{O} + \text{K}_2\text{O})$) (Maniar and Piccoli, 1989) co-relationship is used. This co-relationship shows that the Genina Gharbia samples plot in the I-type field and have a metaluminous affinity (Figure 5.5e). The SiO_2 and K_2O plot (Peccerillo and Taylor, 1976) show that the Genina Gharbia samples belong to the tholeiitic series (Figure 5.5f).

The Genina Gharbia samples have higher concentrations of light rare earth elements (LREE) (La = 11.6 and 12.2 ppm) relative to the contents of heavy rare earth elements (HREE) (Yb = 0.7 and 1.4 ppm) (Figure 5.6). On the primitive mantle (PM)-normalized trace-element diagram (Figure 5.6), these samples exhibit negative Ti, Nb, and Ta anomalies and slightly positive U, Pb, and Ba anomalies, typical of arc settings.

The Genina Gharbia samples have low Sr (100.9 and 330.6 ppm) and Rb concentrations (13.8 and 17.6 ppm), whilst the measured $^{87}\text{Sr}/^{86}\text{Sr}$ ratios are 0.704054 ± 0.00002 and 0.707518 ± 0.000002 (Table D.1). These samples have a low Nd (9.2 and 10.2 ppm) and Sm concentration (1.7 and 2.1 ppm), and their $^{143}\text{Nd}/^{144}\text{Nd}$ ratios are 0.512501 ± 0.000002 and 0.512534 ± 0.000003 (Table D.1). The initial ratios (estimated using zircon ages) of $^{87}\text{Sr}/^{86}\text{Sr}_{(t)}$ and $^{143}\text{Nd}/^{144}\text{Nd}_{(t)}$ are 0.7025302–0.7028589 and 0.511981–0.511996, respectively (Figure 5.7). The latter correspond to $\epsilon\text{Nd}(t)$ values of +4.65 and +4.93 (Figure 5.7), and T_{DM} model ages of 1.0 and 0.95 Ga, respectively (Goldstein, O'Nions and Hamilton, 1984; Bouvier, Vervoort and Patchett, 2008).

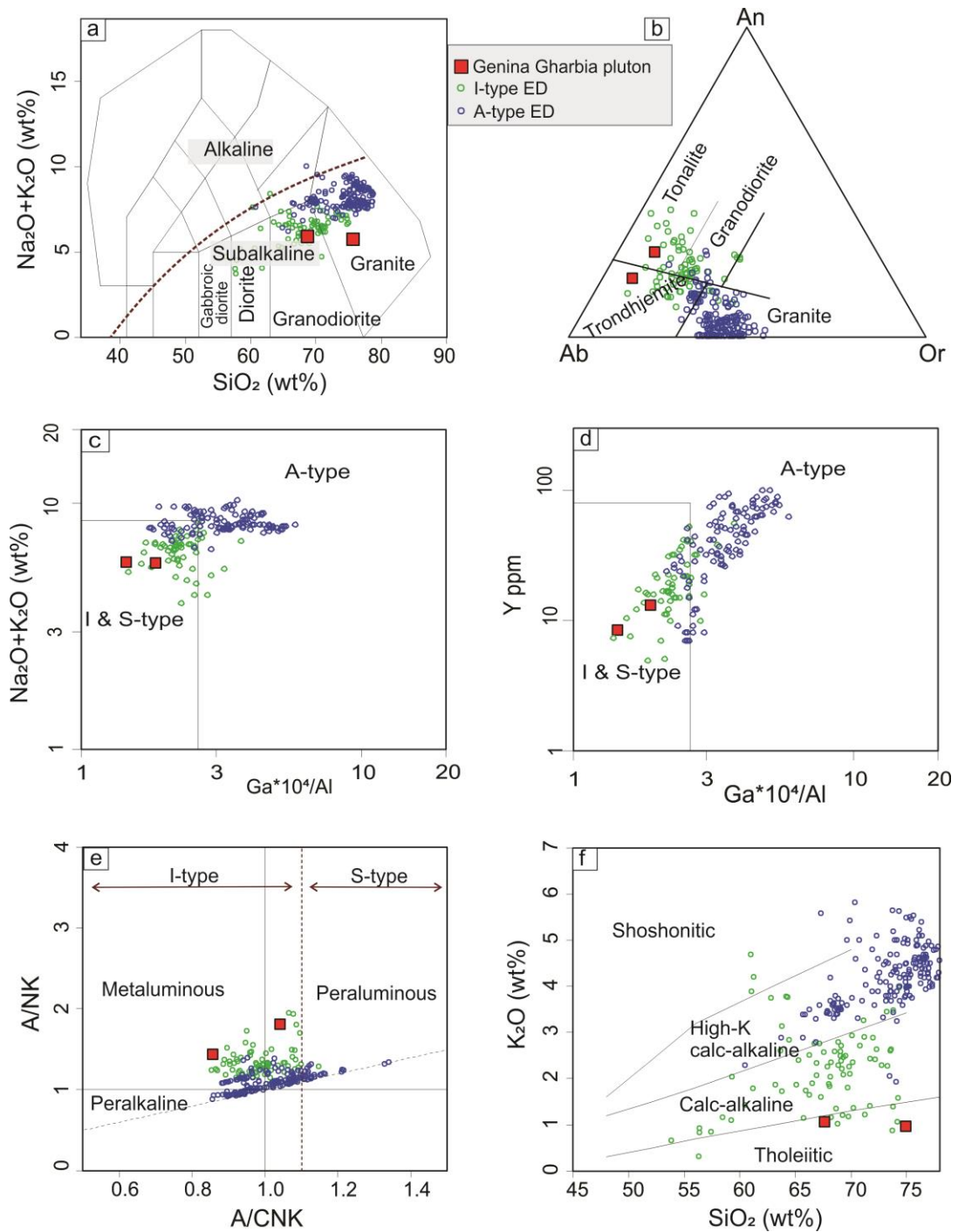


Figure 5.5: Chemical classification diagrams for whole-rock major and trace element compositions of the Genina Gharbia pluton. (a) Total alkali-silica diagram (TAS) of Middlemost (1994). (b) The Ab-An-Or diagram (O'Connor, 1965; Barker, 1979). (c, d) Ga/Al ratio versus $\text{Na}_2\text{O} + \text{K}_2\text{O}$ and Y plots (Whalen, Currie, and Chappell, 1987). (e) the plot of Shand's index A/NK (molar $\text{Al}_2\text{O}_3/(\text{NaO} + \text{K}_2\text{O})$) versus A/CNK (molar $\text{Al}_2\text{O}_3/(\text{CaO} + \text{Na}_2\text{O} + \text{K}_2\text{O})$) (Maniar and Piccoli, 1989). (f) SiO_2 versus K_2O relationship (Peccerillo and Taylor, 1976).

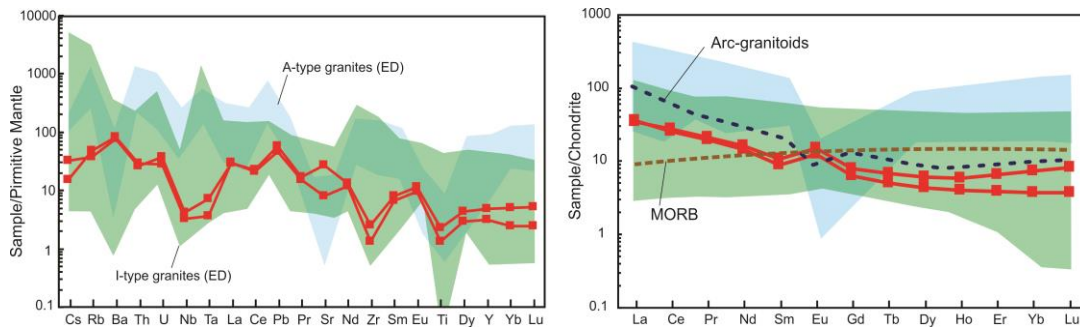


Figure 5.6: Chondrite-normalized REE patterns (Anders and Grevesse, 1989) and PM-normalized (McDonough and Sun, 1995) trace elements diagram of the Genina Gharbia pluton. I-and A-type granites database of the Eastern Desert used for comparison (e.g., Farahat *et al.*, 2007; Katzir *et al.*, 2007; Moussa *et al.*, 2008; Ali *et al.*, 2012a; Eliwa *et al.*, 2014; Ali *et al.*, 2015; Zoheir *et al.*, 2020). Arc-granitoids after GeoRoc (<http://georoc.mpch-mainz.gwdg.de/georoc/>) and MORB after Sun and McDonough (1989).

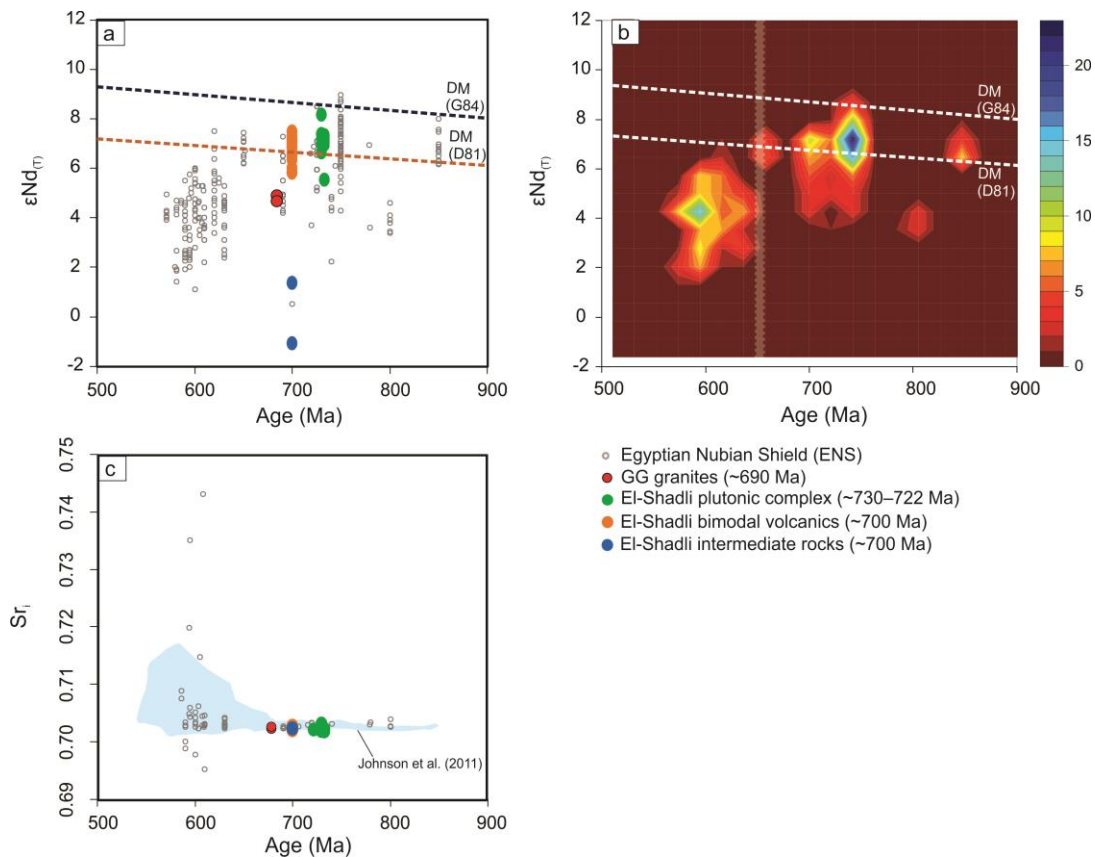


Figure 5.7: Sr-Nd isotopic data of the Eastern Desert magmatic activities (including the Genina Gharbia pluton and the El-Shadli plutonic complex-bimodal volcanic-intermediate rocks). The compiled data from the Egyptian Nubian Shield (ENS) after Zimmer *et al.* (1995), Katz *et al.* (2004), Moussa *et al.* (2008), Ali *et al.* (2009, 2012a, 2015), Be’eri-Shlevin *et al.* (2010), Liégeois and Stern (2010), Eyal *et al.* (2010), Basta *et al.* (2011), Eliwa *et al.* (2014), Sami *et al.* (2018) and Stern *et al.* (2020). Depleted mantle evolution curve after DePaolo (1981; DM(D81)) and Goldstein, O’Nions, and Hamilton (1984; DM (G84)). Panel (b) represents the density plot for all the data in panel (a).

5.5.2 Zircon U-Pb-Hf-O isotopes and trace elements

Zircon grains from sample G04-2 are equant to sub-rounded with euhedral rims and sizes of <100 μm (Figure 5.8a). On CL images, some zircon grains show well-developed oscillatory zoning but others show only faint and broad zoning (Figure 5.8a). The grains do not have any recrystallization or deformation features, indicating the absence of post-magmatic modification.

Thirty U-Pb SHRIMP analyses for sample G04-2 were conducted, one analysis on each of 30 grains. The analysed grains have variable U (48.9–269.8 ppm) and Th contents (34.4–192.9 ppm) and Th/U ratios (0.39–1.03) signifying their magmatic origin and crystallization from a high-SiO₂ magma (Kirkland *et al.*, 2015). These analyses yield a weighted mean ²⁰⁶Pb/²³⁸U age of 690 ± 5.6 Ma (± 95 % conf., MSWD = 0.48, N = 28; Figure 5.8a), which is interpreted as the crystallization age of the Genina Gharbia granitic pluton.

Thirty-one laser ablation split-stream (LASS) analyses on the same sample (G04-2) were conducted on 31 grains including the same 30 spots as the SHRIMP analyses, plus another analysis. These analyses yield a weighted mean ²⁰⁶Pb/²³⁸U age of 693 ± 2.6 Ma (± 95 % conf., MSWD = 0.97, N = 28; Figure 5.8b), indistinguishable, within error, to the SHRIMP age. Chondrite (CI)-normalized (Anders and Grevesse, 1989) zircon REE patterns have a negative slope from middle to heavy REE [(Yb/Gd)_{CI} = 16–33], and exhibit depleted light REE (La = 0.002–6.4 ppm), which is characteristic for unaltered magmatic zircons (Belousova *et al.*, 2002; Grimes *et al.*, 2015) (Figure 5.8b). These zircons show distinct negative Eu anomalies [(Eu/Eu*)_{CI} = 0.06–0.24, where Eu* = $\sqrt{(\text{Sm} \times \text{Gd})}$] and variable positive Ce anomalies [(Ce/Ce*)_{CI} = 1.86–224.80, where Ce* = $\sqrt{(\text{La} \times \text{Pr})}$], similar to zircons from I-type granitoids (Wang *et al.*, 2012). The analysed zircon grains have variable hafnium (9099–11484 ppm), niobium (0.68–2.68 ppm), and U/Nb ratios (54.25–93.92) (Figure 5.9).

The Lu-Hf isotopic analyses of these 31 spots yield ¹⁷⁶Lu/¹⁷⁷Hf ratios of 0.001261 ± 0.000082 – 0.002661 ± 0.000016 and ¹⁷⁶Hf/¹⁷⁷Hf_(t) ratios of 0.282516 ± 0.000049 – 0.282639 ± 0.000038 (Table D.3). The calculated $\epsilon\text{Hf}_{(t)}$ values range from +6.42 ± 0.57 to +10.12 ± 0.57, with a weighted mean of +8.01 ± 0.23 (MSWD = 1.53) (Figure 5.10a). Depleted mantle two-stage Hf model ages (T_{DM} crustal,

assuming $^{176}\text{Lu}/^{177}\text{Hf}$ value of 0.015 average value for the continental crust; Griffin *et al.*, 2002) yield ages between 0.96 and 1.2 Ga.

A total of 20 SIMS O isotope spots on these zircons yield mantle-like $\delta^{18}\text{O}$ values ranging from $4.73 \pm 0.28 \text{ ‰}$ to $5.51 \pm 0.19 \text{ ‰}$ with a weighted mean of $5.04 \pm 0.08 \text{ ‰}$ (MSWD = 0.71) (Figure 5.10c), indicating that these zircons crystallized from magma extracted from a juvenile source.

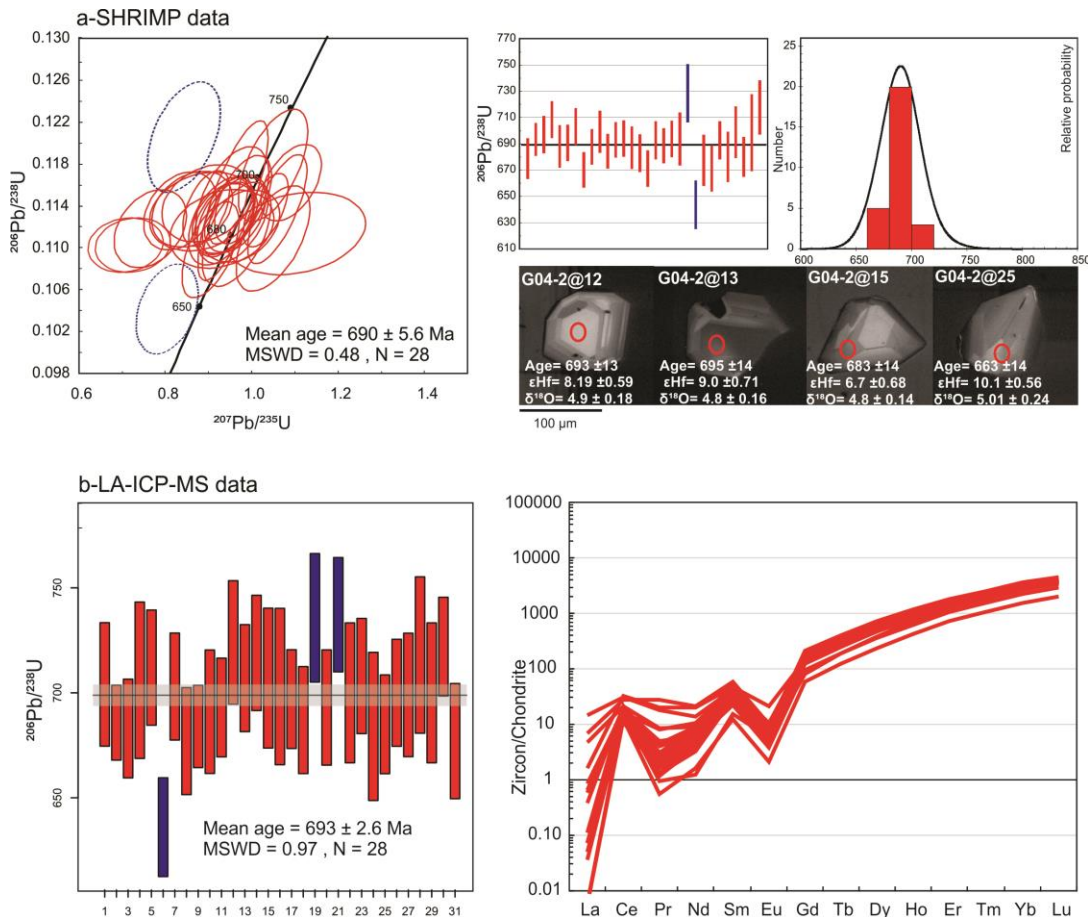


Figure 5.8: Zircon geochronological data of sample G04-2 from the Genina Gharbia pluton. (a) Zircon U-Pb SHRIMP Concordia diagrams show the $^{206}\text{Pb}/^{238}\text{U}$ ages of the analysed zircons with 1 sigma errors. Weight means relative probability diagrams of $^{206}\text{Pb}/^{238}\text{U}$ age and representative CL images are shown. The red circles on the CL images mark the place for SHRIMP, LASS, and SIMS spot analyses for the U-Pb age, Hf and O isotopes, and trace element data, respectively. (b) Zircon U-Pb Concordia diagrams show the $^{206}\text{Pb}/^{238}\text{U}$ ages of the studied zircons with 1 sigma errors (left) and zircon chondrite-normalized REE patterns (Anders and Grevesse, 1989) (right).

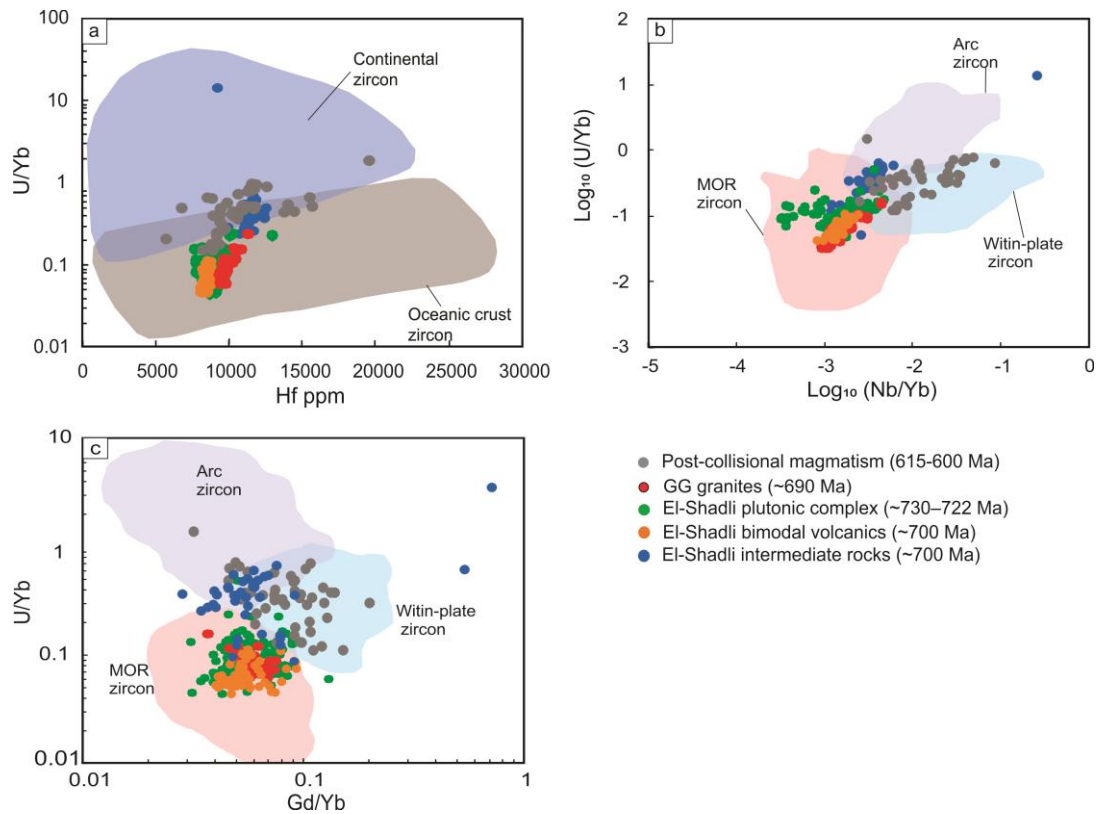


Figure 5.9: Trace element tectono-magmatic classification of the Genina Gharbia pluton including data from the El-Shadli plutonic complex-bimodal volcanics-intermediate rocks. Zircon fields after Grimes *et al.* (2007, 2015). The 600-615 Ma post-collision magmatism of the Eastern Desert (A-type granites and Dokhan alkaline volcanics) after El-Bialy and Ali (2013).

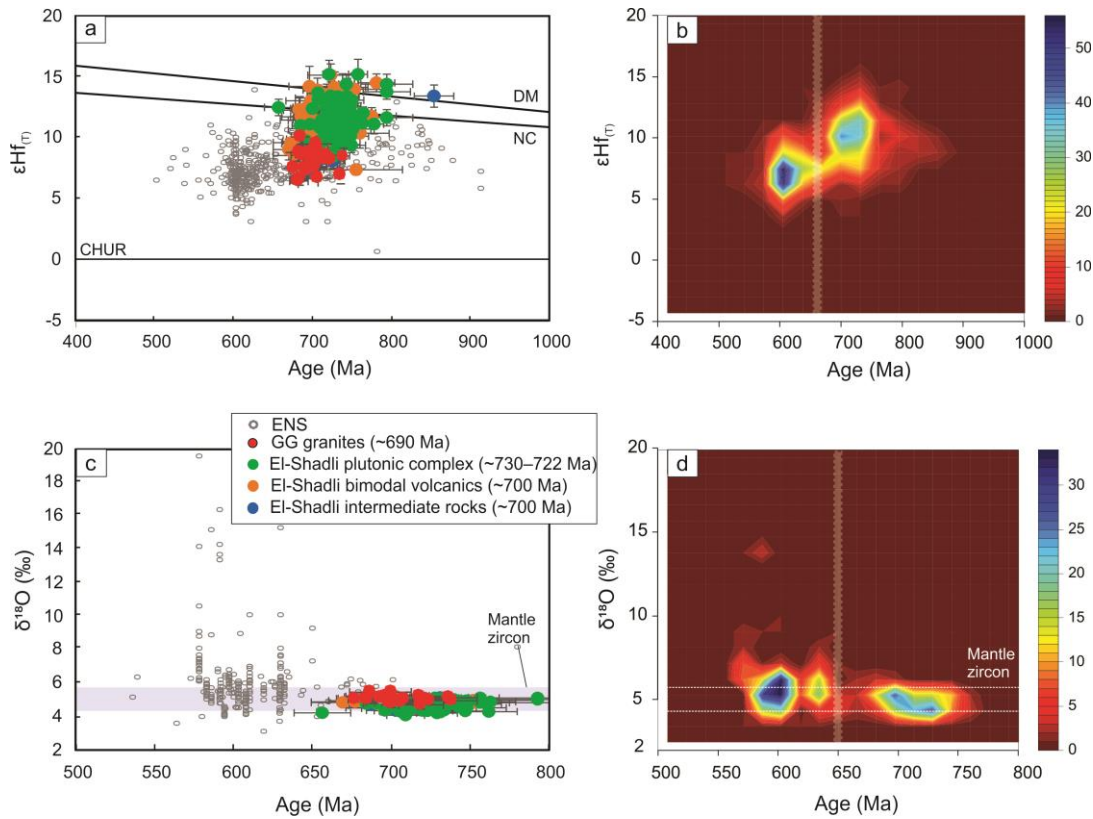


Figure 5.10: Age, Hf, and O isotopic data of the Eastern Desert magmatic activities (including the Genina Gharbia pluton and the El-Shadli plutonic complex-bimodal volcanics-intermediate rocks). ENS zircon Hf and O isotopic data used for comparison after Ali *et al.* (2013, 2014, 2015, 2016), Morag *et al.* (2011), Be’eri-Shlevin, Katzir, and Valley, (2009), Be’eri-Shlevin *et al.* (2010) and Stern *et al.* (2020). Chondritic uniform reservoir (CHUR), depleted mantle (DM; Griffin *et al.*, 2002), and new crust form at the island-arc (NC: Dhuime, Hawkesworth, and Cawood, 2011) lines are plotted. Panel (b) and (d) are density plots for panel (a) and (c), respectively.

5.6 Discussion

5.6.1 Petrogenesis of the Genina Gharbia pluton

The Genina Gharbia pluton has a tholeiitic affinity with a parental magma characterized by low K_2O content (Figure 5.5e, f). The low K_2O composition of the Genina Gharbia samples suggests that the magma was derived from partial melting of a low-K mafic source (Laurent *et al.*, 2014; Figure 5.11a). Samples from this pluton also show some arc-like signatures, i.e. negative anomalies of Nb, Ta, and Ti, and enrichment in LILE (Cs, Rb, Ba, Th, Pb, Sr, and U) and LREE (e.g., La and Ce) relative to HFSE (e.g., Nb, Zr, and Ti) (Figure 5.6), which indicate that the source likely underwent melt/fluid interaction during subduction (Pearce, Harris and Tindle,

1984; Pearce and Peate, 1995; Gamal El Dien *et al.*, 2019). On two of the key diagrams (Rb vs. (Y + Nb) and (Ta + Yb); Figure 5.11b, c) that distinguish the tectonic settings of granitic rocks (Pearce, Harris and Tindle, 1984; Pearce, 1996), the Genina Gharbia pluton plots in the volcanic-arc granitoids field (VAG), which suggests an arc-related origin. Overall, the Genina Gharbia samples have geochemical characteristics similar to the Eastern Desert I-type arc-related granitoids and are distinct from post-collision/within-plate A-type granites (Figures 5.5, 5.6, and 5.11).

The low $^{87}\text{Sr}/^{86}\text{Sr}(t)$ and positive $\epsilon\text{Nd}(t)$ of the Genina Gharbia pluton imply a juvenile composition for their parental magma (Figure 5.7). They have T_{DM} model ages of 1.0–0.95 Ga, which are within the range of previously reported T_{DM} model ages for arc-related magmatism in the Eastern Desert ($T_{\text{DM}} = \text{ca. } 0.80\text{--}1.30$ Ga and $\epsilon\text{Nd}(t) = +3 \text{ -- } +8$) (Stern, 2002; Ali *et al.*, 2013).

Consistent with the geochemical and Nd-Sr isotopic data, zircon U-Pb analyses of sample G04-2 show the absence of pre-Neoproterozoic inherited cores or zircon xenocrysts (Figure 5.8), suggesting that no older/pre-Neoproterozoic crustal materials was recycled into the parental magma. Taken together, the above-mentioned arc signatures for the pluton, the high $\epsilon\text{Hf}(t)$ values, and the mantle-like $\delta^{18}\text{O}$ values in zircon (Figure 5.10) that are similar to the isotopic features of the older mafic arc lower crust (Wang *et al.*, 2016) (Figure 5.11d), the Genina Gharbia pluton likely originated from partial melting of arc-related low-K mafic lower oceanic crust that had been modified by subduction (i.e., metasomatized).

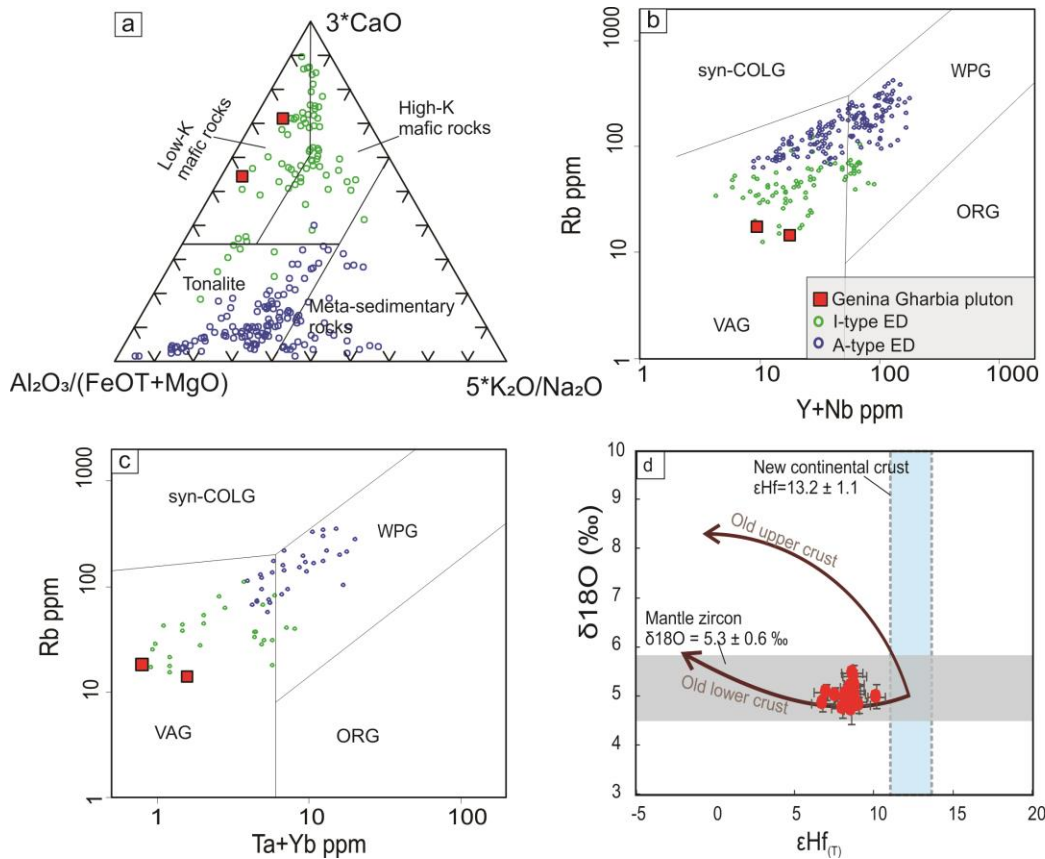


Figure 5.11: Chemical and isotopic compositions of the Genina Gharbia pluton. (a) Ternary diagram of $\text{Al}_2\text{O}_3/(\text{FeOT} + \text{MgO})$ - $3*\text{CaO}$ - $5*(\text{K}_2\text{O}/\text{Na}_2\text{O})$ after Laurent *et al.* (2014). (b, c) Granitoids source and tectonic setting plots of Pearce, Harris, and Tindle (1984). I and A-type granites database of the Eastern Desert used for comparison (e.g., Farahat *et al.*, 2007; Katzir *et al.*, 2007; Moussa *et al.*, 2008; Ali *et al.*, 2012a; Eliwa *et al.*, 2014; Ali *et al.*, 2015; Zoheir *et al.*, 2020). (d) The plot of $\delta^{18}\text{O}$ vs $\epsilon\text{Hf}(t)$ of sample G04-2 zircons from the Genina Gharbia pluton. Old upper and lower crust trends are from Kemp *et al.* (2007) and Wang *et al.* (2016). The $\delta^{18}\text{O}$ value of mantle zircons (5.3 ± 0.3 ‰) is from Valley *et al.* (1998, 2005) and ϵHf value (13.2 ± 1.1) of new crust form at the island-arc (NC) after Dhuime, Hawkesworth, and Cawood (2011).

5.6.2 Crustal growth of the Eastern Desert of Egypt: juvenile vs recycled/reworked nature

The Neoproterozoic formation and evolution of the Eastern Desert continental crust was mainly controlled by pre-continental collision magmatism (~800–650 Ma) followed by collision-related magmatism (~645–540 Ma) (Bentor, 1985; Johnson *et al.*, 2011; Fritz *et al.*, 2013; Stern, 2018). There is a general consensus that the ~800–650 Ma magmatism is the main contributor to crustal evolution of Eastern Desert (Bentor, 1985; Stern, 1994; Stein and Goldstein, 1996). However, it is still unclear whether all of these magmatic events had a juvenile nature, or if some involved the

recycling/reworking of much older continental crust (Stern, 2002; Ali *et al.*, 2009, 2013, 2015, 2016; Liégeois and Stern, 2010; Stern *et al.*, 2010; Li *et al.*, 2018). In the following section, I will discuss the nature of the evolution/growth of the Eastern Desert crust by investigating the whole-rock Sr-Nd isotopes and U-Pb-Hf-O-trace elements data in zircon from both the compilation of all previously published data and data present in this thesis in Chapters 3–5 from the Eastern Desert.

The combined new and compiled whole-rock Sr-Nd isotope data for the Eastern Desert pre-collisional magmatism (Figure 5.7) show that 70-90% of the $\epsilon\text{Nd}(t)$ values range between +6.5 and +8.5 (Figure 5.7b), plotting close to the Neoproterozoic depleted mantle evolution curve and are typical of juvenile magmas (DePaolo, 1981; Goldstein, O’Nions, and Hamilton, 1984) (Figure 5.7b). The very low $^{87}\text{Sr}/^{86}\text{Sr}(t)$ (i.e., Sr_i) ratios (~ 0.702) of this magmatic stage is also consistent with a juvenile composition (Figure 5.7c). A significant contribution of old continental crust, which would have shifted the $\epsilon\text{Nd}(t)$ toward lower values and $^{87}\text{Sr}/^{86}\text{Sr}(t)$ to higher values, is not evident in the data, with the exception of a few samples (Figure 5.7).

Variations of U/Yb in zircon reflect variations in the melt at the time of zircon crystallization (Grimes *et al.*, 2007). To the best of my knowledge, no zircon trace element data have been reported from the Eastern Desert pre-collisional magmatism before this study (Chapters 3–5; Figure 5.9). The low U/Yb ratios (0.05–0.24) and low Nb/Yb ratios (< 0.01) of zircons in the Genina Gharbia pluton, the El-Shadli plutonic complex, and the bimodal volcanics are similar to zircons in modern ocean crust which have a depleted mantle-source (Grimes *et al.*, 2007, 2015; Carley *et al.*, 2014) (Figure 5.9). On the other hand, high Nb content is a common characteristic of within-plate and alkaline magmatism (Pearce, Harris and Tindle, 1984) (Figure 5.9b). Thus, the high Nb contents of zircons of the 615-600 Ma post-collisional magmatism of the Eastern Desert (A-type granites and the Dokhan alkaline volcanics; El-Bialy and Ali, 2013) displays a continental characteristic and a within-plate tectonic setting (Figure 5.9).

These observations are further supported by Hf and O isotopic compositions of zircons, which reflect the juvenile nature of their parental magmas (Kemp and Hawkesworth, 2014). Because Hf is more incompatible than Lu, mantle partial melting enriches continental crust in Hf relative to Lu. This results in a depleted mantle with higher Lu/Hf and therefore higher (radiogenic) $^{176}\text{Hf}/^{177}\text{Hf}$ with time

compared to continental crust (Patchett *et al.*, 1981; Patchett, 1983; Kinny, Compston and Williams, 1991). As Hf substitutes for Zr, Hf content in zircon is typically much higher (0.5–2 %) than Lu, resulting in a Lu/Hf ratio in zircon close to 0 (< 0.001) (Patchett, 1983; Kemp and Hawkesworth, 2014). Therefore, zircon potentially preserves the initial $^{176}\text{Hf}/^{177}\text{Hf}$ of its magma source (Vervoort and Blichert-Toft, 1999; Hawkesworth and Kemp, 2006). Hf in zircon is also sensitive to the potential influences of mixed source components, such as from older continental crust (that may be related to crustal recycling/re-working) or depleted mantle sources of different ages (Kinny, Compston and Williams, 1991; Vervoort and Blichert-Toft, 1999; Griffin *et al.*, 2002; Kinny and Maas, 2003; Kemp *et al.*, 2006; Belousova *et al.*, 2010; Kemp and Hawkesworth, 2014). The Eastern Desert ~850-650 Ma pre-collision magmatic rocks are characterized by highly positive zircon $\epsilon\text{Hf}(t)$ values. More than 80% of the data range from $\sim+8.5$ to $+13$ (Figure 5.10b), implying that magma was primarily derived from a depleted mantle with no evidence of involvement of older continental crust (Hawkesworth and Kemp, 2006; Belousova *et al.*, 2010).

O isotopic values in zircon provide another powerful tool for tracking contamination of the parental magma by continental and sedimentary materials (Valley, 2003). Typical $\delta^{18}\text{O}$ values of zircon in mantle-derived magma have a narrow range (5.3 ± 0.3 ‰), with lower values attributed to interactions with hydrothermal fluids, and higher values to contamination of the source by sedimentary or crustal recycling (Valley *et al.*, 1998, 2005a; Valley, 2003; Hawkesworth and Kemp, 2006). To date, there are very few O isotopic data on the pre-collisional magmatism of the Eastern Desert, except for the Atud arc-related gabbroic diorites in the central Eastern Desert (Stern *et al.*, 2020). Here, I also report O isotopic data for both arc-related (the Genina Gharbia pluton) and rift-related magmatism (the El-Shadli plutonic complex and bimodal volcanics) from the Eastern Desert (Figure 5.10c). The uniform mantle-like $\delta^{18}\text{O}$ values (around ~ 5 ‰) for the zircons from the pre-collisional rocks (Figure 5.10d) indicate a juvenile source with no sign of interaction with supracrustal materials or sediments (Kemp *et al.*, 2006; Kemp and Hawkesworth, 2014; Wang *et al.*, 2016) (Figure 5.10b, c). The slightly lower $\delta^{18}\text{O}$ values of these pre-collisional rocks have been interpreted as their source having

undergone hydrothermal fluid circulation in the oceanic setting (see also Chapters 3 and 4 for more details).

The absence of pre-Neoproterozoic inherited zircon cores or zircon xenocrysts in almost all samples from the pre-collisional magmatic rocks of the Eastern Desert (e.g., Moussa *et al.*, 2008; Ali *et al.*, 2010, 2015; Stern *et al.*, 2010; Ali, 2015; this study; Figure 5.8 and Chapters 3 and 4) suggests no significant contribution from old crust to the crustal growth of the Eastern Desert during ~850–650 Ma magmatism. The only evidence for pre-Neoproterozoic inherited/xenocryst zircons (2730–1002 Ma) in magmatic rocks during this time interval is found in mafic metavolcanic rocks from W. El Dabbah and W. Kareim in the CED (Ali *et al.*, 2009; Table 5.1). However, Liégeois and Stern (2010), Stern *et al.* (2010), and Ali *et al.* (2013) interpret the presence of these zircon xenocrysts with mantle-like isotopic composition in mafic volcanics, and their absence from coeval felsic rocks to reflect (1) inheritance from the mantle source and/or (2) incorporation from subducted sediments from adjacent Archean crustal basement (i.e., Saharan Craton). In either case, these authors do not see the need for the presence of much older local continental crust during the crustal growth.

U-Pb analyses of detrital zircons from ~625 Ma post-collisional Hammamat Group sedimentary rocks in W. Iгла (Nasiri Bezenjani *et al.*, 2014) and W. Um Had (Abd El-Rahman *et al.*, 2019) of the CED yield a small proportion of zircons (less than 5% of the analysed zircons) with pre-Neoproterozoic ages. Previous studies (Nasiri Bezenjani *et al.*, 2014; Abd El-Rahman *et al.*, 2019) have suggested that these pre-Neoproterozoic zircons were likely derived by erosion of the flanked pre-Neoproterozoic basement. On the other hand, Li *et al.* (2018), based on zircon Hf-O isotopic data from a ~755 Ma felsic volcanic cobble (only one sample) in the ~720–700 Ma arc-related Atud greywacke in the CED, suggested the presence of a cryptic older continental crust underlying the Eastern Desert. Although these interesting results need more work to evaluate this possibility, such detrital zircons can also be explained by subduction recycling of nearby Archean crustal materials to the sub-arc mantle that would lead to highly evolved Hf isotopic ratios in younger magmatism (i.e., this ~755 Ma felsic volcanic magma). There is thus no need for a reworking of a hidden older continental crust beneath the Eastern Desert (Liégeois and Stern, 2010; Stern *et al.*, 2010).

In summary, Sr-Nd-Hf-O isotopic data of the ~800–650 Ma pre-collisional magmatism in the Eastern Desert indicates an overall juvenile nature of the crustal evolution and growth of the Eastern Desert crust. In contrast, the younger magmatism (<650 Ma, collision-related magmatism) shows very low $\epsilon\text{Nd}(t)$ values (down to +1; Figure 5.7b), high initial $^{87}\text{Sr}/^{86}\text{Sr}$ (Sr_i) ratios (up to ~0.75; Figure 5.7c), low zircon $\epsilon\text{Hf}(t)$ values (down to +2; Figure 5.10b), and high zircon $\delta^{18}\text{O}$ values (up to ~19‰; Figure 5.10c) compared to the pre-collisional magmatism. This is lower $\epsilon\text{Nd}(t)$ - $\epsilon\text{Hf}(t)$ and higher Sr_i and $\delta^{18}\text{O}$ of <650 Ma magmatism signifying the major role of processes, include both the crustal reworking (re-melting of pre-existing continental-like crust) and the crustal recycling through slab-break off, delamination, and orogenic collapse, that all linked to the continental collision stage that led to the final formation of Gondwana (Stern, 1994; Be'eri-Shlevin, Katzir and Valley, 2009; Be'eri-Shlevin, Katzir and Whitehouse, 2009; Be'eri-Shlevin *et al.*, 2010; Johnson *et al.*, 2011; Fritz *et al.*, 2013; Zoheir *et al.*, 2019).

5.6.3 Episodic magmatism during the growth of the Eastern Desert crust

Granitoid and volcanic rocks represent the major components of Neoproterozoic crust in the Eastern Desert (Bentor, 1985; Johnson *et al.*, 2011; Stern, 2018). Many detailed studies of these rocks have documented the relationship between magmatism and the crustal growth/evolution in the region (e.g., Bentor, 1985; Stern and Hedge, 1985; Stern, 2002; Johnson *et al.*, 2011; Fritz *et al.*, 2013). However, almost all previous zircon geochronological data for the Eastern Desert were obtained from granitic rocks and produced ages ranging between ~750 Ma and ~550 Ma (Table 5.1). Few zircon ages have been reported for volcanic rocks related to subduction (~770–720 Ma; Stern and Hedge, 1985; Kröner *et al.*, 1992; Ali *et al.*, 2009; Bühler *et al.*, 2014; Abd El-Rahman *et al.*, 2017), the post-accretionary El-Shadli volcanics province (~700 Ma: Faisal *et al.*, 2020; this study), or the post-collisional Dokhan volcanics (~630–580 Ma; Wilde and Youssef, 2000; Breikreuz *et al.*, 2010).

Based on twenty-four U-Pb single zircon evaporation ages and eighteen Rb-Sr whole-rock isochron ages of granitoid and volcanic rocks, Stern and Hedge (1985) proposed six magmatic episodes at ~770 Ma, 715–700 Ma, 685–665 Ma, 625–610

Ma, 600–575 Ma, and 555–540 Ma. More recently, Lundmark *et al.* (2012) hypothesised six magmatic episodes, based on the evolution of gneisses in the CED and the SED, at 705–680 Ma, ~660 Ma, 635–630 Ma, 610–604 Ma, 600–590 Ma and 550–540 Ma.

The new geochronological data from granitoid and volcanic rocks in the Eastern Desert (this thesis: Chapters 3–5), together with the data compilation presented here, suggest episodic magmatism during the growth of the Eastern Desert crust, involving three major magmatic episodes, with peaks at ~730 Ma, ~700 Ma, and ~630–600 Ma that increase in magnitude from oldest to youngest (Figure 5.12a). Episode 1 (peaks at ~730 Ma) is recorded by the ~770–720 Ma arc-related volcanic and granitoid rocks (Stern and Hedge, 1985; Kröner *et al.*, 1992; Ali *et al.*, 2009, 2015; Bühler *et al.*, 2014; Abd El-Rahman *et al.*, 2017), ~750–730 Ma ophiolitic rocks (Kröner *et al.*, 1992; Andresen *et al.*, 2009; Ali *et al.*, 2010), and the post-accretionary rift-related magmatism of the El-Shadli plutonic complex (~730–720 Ma; this study, Chapter 3) (Table 5.1). Episode 2 (peaks at ~700 Ma) is recorded by the post-accretionary, rift-related El-Shadli volcanics (this work; Chapter 4) and some other arc-related I-type granitoids (Table 5.1). Episode 2 currently lacks ophiolite or arc-related volcanic rocks, which may reflect a lack of data. Episode 3 (peaks at ~630–600 Ma) is recorded by collision-related magmatism (Stern, 1994; Johnson *et al.*, 2011; Fritz *et al.*, 2013; Robinson *et al.*, 2014, 2017; El-Bialy *et al.*, 2020) (Table 5.1).

The three crustal domains of the Eastern Desert (SED, CED, and NED) do not show consistent magmatic peaks (Figures 5.12b–d and 5.13). The SED domain is dominated by the oldest two episodes (Figure 5.12b, Table 5.1), whereas the youngest episode is only recorded by (1) within-plate/post-collisional A-type granites from the Um Ara area (603 ± 14 ; Moussa *et al.*, 2008) and G. Humr Mukbid and G. Humr Akarim ($633 \pm 7 - 603 \pm 8$; Ali *et al.*, 2012), and (2) syn-to post-collisional calc-alkaline to alkaline I-type granitoids from W. Shilman (629 ± 5 ; El-Kazzaz and Taylor, 2001; Ali *et al.*, 2010) and the Hafafit area ($646 \pm 12 - 629 \pm 5$; Lundmark *et al.*, 2012; Abu El-Enen *et al.*, 2016) (Table 5.1). The CED domain is characterised by three major magmatic pulses, with peaks at ~680 Ma, ~650 Ma, and ~600 Ma. The oldest magmatic activities in the CED domain comprise three subduction-related volcanic units at W. Kareim ($769 \pm 29 - 730 \pm 22$; Ali *et al.*, 2009) (Figures 5.11c and 5.12). The NED domain is dominated by the youngest magmatic episode with

only minor older peaks at (1) ~660 Ma (the Mons Claudianus I-type granitoids; Stern and Hedge, 1985; Abdel-Rahman, 2018), (2) $741 \pm 3 - 720 \pm 7$ Ma (G. Dara I-type granitoids; Eliwa *et al.*, 2014), and (3) $773 \pm 7 - 717 \pm 8$ Ma (arc-related volcanics at W. Um Mongol and W. Malaak; Bühler *et al.*, 2014; Abd El-Rahman *et al.*, 2017) (Figures 5.12d and 5.13).

The magmatic activities in the Eastern Desert show a general progression in ages from the SED domain through the CED to the NED domain (Stern and Hedge, 1985) (Figure 5.13). The data show that the bulk of the SED domain was formed before 650 Ma and was dominated by the pre-collisional juvenile magmatism (Table 5.1). The regionally most intense magmatic episode (~630–600) is more dominant northward (Figures 5.13 and 5.12d). Finally, the overall predominance of the ~630–600 Ma magmatic episode in the Eastern Desert crust (Figures 5.12a and 5.13) highlights the importance of this magmatic episode in consolidating of the Eastern Desert Neoproterozoic juvenile crust to form normal continental crust through intensive crustal reworking (likely accompanied by new melt additions from the mantle). Further detailed geochemical and isotopic studies are required to understand the nature of this episode.

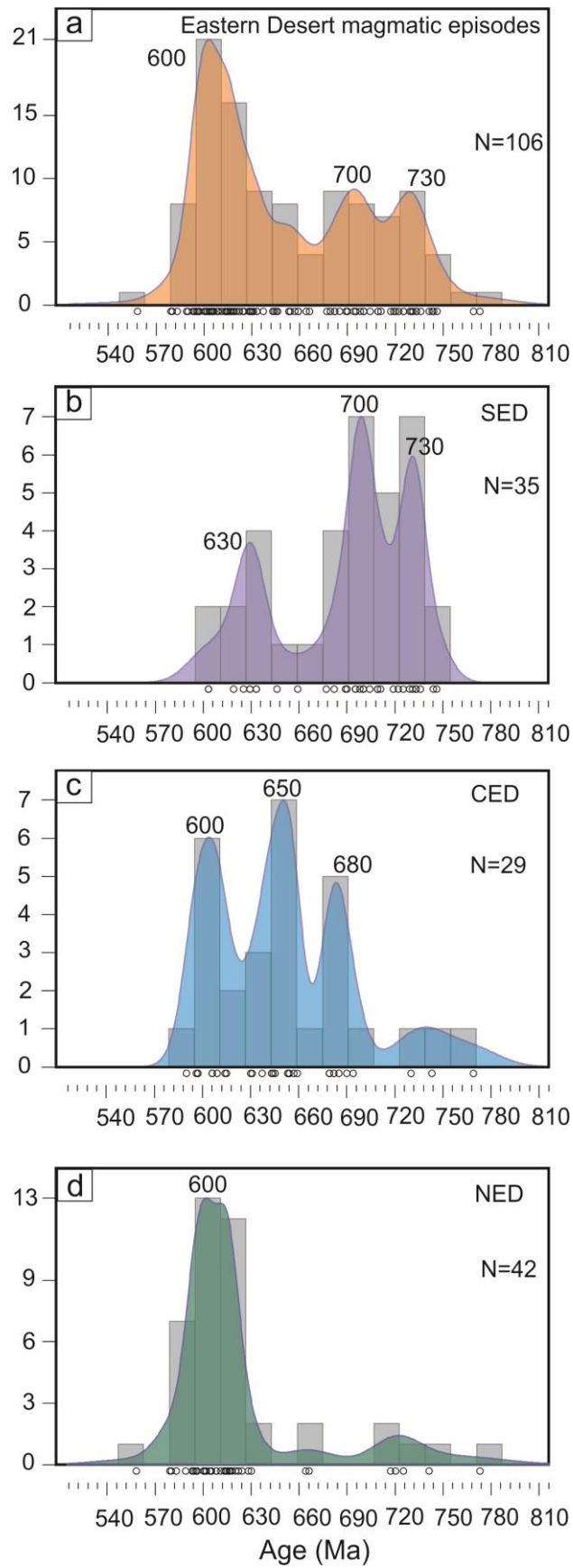


Figure 5.12: Histogram and Kernel density estimation for the Eastern Desert magmatic activities.

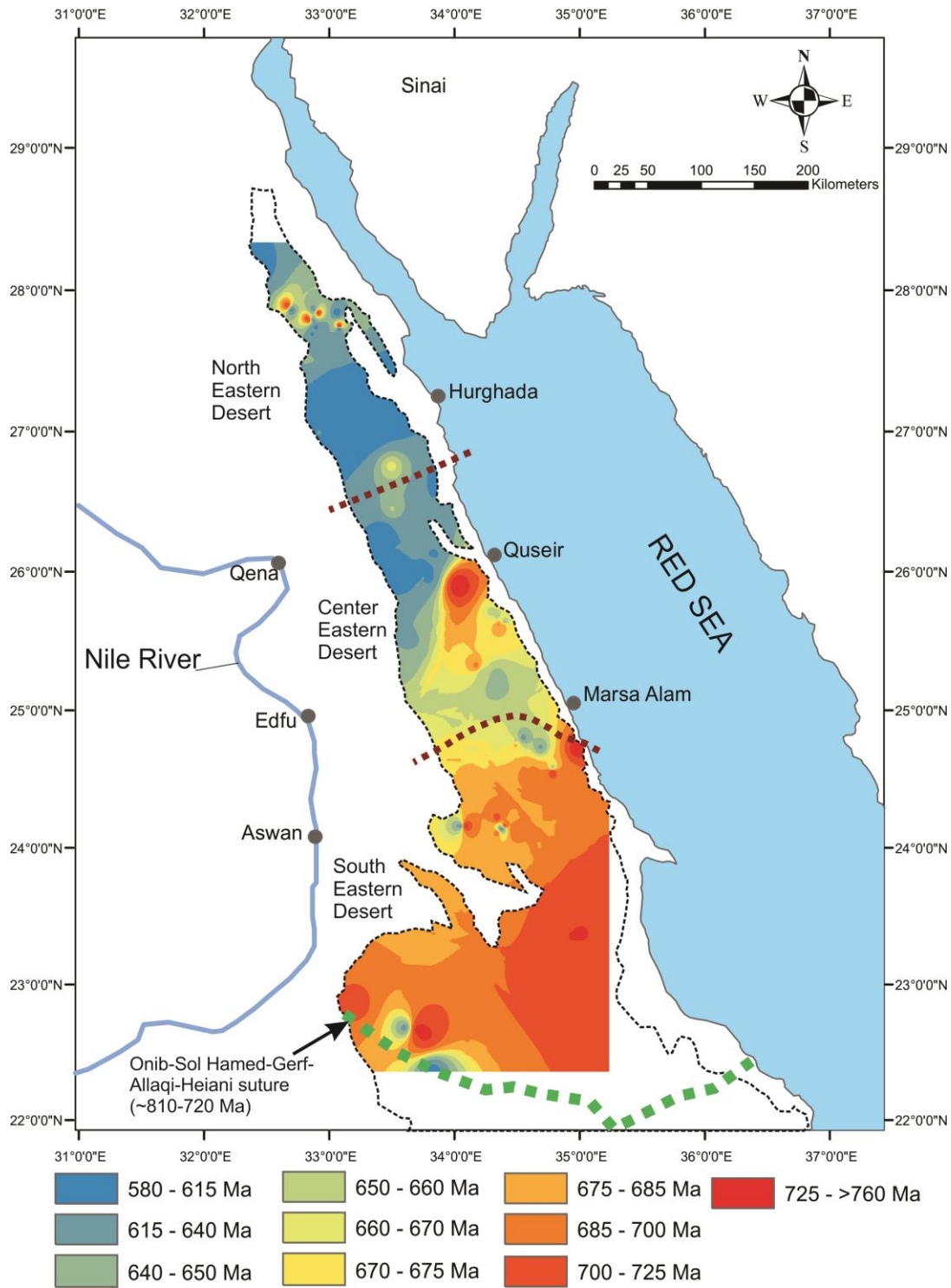


Figure 5.13: Geochronological map of the magmatic activities in the Eastern Desert crust. The age data was used to construct this map found in Table 5.1. The Eastern Desert terranes boundaries (dashed dark-red lines) are after Stern and Hedge (1985).

5.6.4 Transition of Neoproterozoic tectonic and magmatic styles: implications for the crustal evolution of the Eastern Desert

There is a general consensus that there are two main types of Neoproterozoic granitoids in the Eastern Desert: (1) pre-collisional tholeiitic and calc-alkaline assemblages of diorites, trondhjemites, granodiorites, and tonalites (called older/grey/I-type granitoids in the Egyptian literature) and (2) post-collision/within-plate alkaline suites of alkali granites, syenogranites, and monzogranites (called younger/pink/A-type granites in the Egyptian literature) (Bentor, 1985; Stern and Hedge, 1985; Farahat *et al.*, 2007; Moussa *et al.*, 2008; Johnson *et al.*, 2011; Ali *et al.*, 2012b; Fritz *et al.*, 2013; Eliwa *et al.*, 2014; Stern, 2018). Although the transition from I-type (pre-collision) to A-type (post-collision) magmatism proposed to be at ~630–610 Ma (Stern and Hedge, 1985; Beyth *et al.*, 1994; Johnson *et al.*, 2011), it is still a matter of debate when exactly the transition have been happened. On the other hand, there is no age overlap between the subduction-related volcanics (~770–720 Ma; Stern and Hedge, 1985; Kröner *et al.*, 1992; Ali *et al.*, 2009; Bühler *et al.*, 2014; Abd El-Rahman *et al.*, 2017), the post-accretionary rift-related El-Shadli volcanics (~700 Ma; this study), and the post-collisional Dokhan volcanics (~630–580 Ma; Wilde and Youssef, 2000; Breitzkreuz *et al.*, 2010). According to the available data, there may be a hiatus in volcanism between ~700 Ma and ~630 Ma in the Eastern Desert.

The new compilation of geochronological data from granitoid and volcanic rocks in the Eastern Desert shows that the pre-collisional magmatism ranges in ages between ~<800 Ma to ~650 Ma, including two main magmatic episodes at ~730 Ma (i.e., episode 1) and ~700 Ma (i.e., episode 2) (Figure 5.14a; Table 5.1). Collision-related magmatism ranges between ~650 Ma to ~550 Ma, with a well-defined magmatic peak at ~600 Ma (i.e., episode 3) (Figure 5.14b; Table 5.1). The collision-related magmatism include: (1) syn-continental collision magmatism (Figure 5.14c), and (2) post-collision/within-plate (Figure 5.14d). The syn-continental collision magmatism, features a major ~630–620 Ma magmatic pulse of calc-alkaline to alkaline I-type granitoid rocks such as the Um Rus (Zoheir *et al.*, 2020), and the W. Hawashiya granitoids (El-Bialy *et al.*, 2020) (Table 5.1). This I-type magmatism has geochemical characteristics transitional between arc- and within-plate origin which is a characteristic of orogenic granitoids (Pearce, Harris and Tindle, 1984; Pearce,

1996). The arc-like geochemical signature might be related to melting produced during the slab-beak off (e.g., Hildebrand, Whalen and Bowring, 2018) that consequently cause re-melting of thickened mafic lower crust to produce I-type magmatism (e.g., Johnson *et al.*, 2011; Zhu *et al.*, 2017) (Figure 5.15d). The post-collision/within-plate magmatism, has a major magmatic pulse at ~600 Ma and features alkaline A-type granites and the Dokhan volcanics (Table 5.1). Lehmann *et al.* (2020) recently documented the oldest post-collisional A-type granite (644 ± 2 Ma) from Abu Dabbab in the CED. While this age is older than the ~600 Ma peak of the post-collision/within-plate magmatic pulse, it is within the Eastern Desert collision-related magmatic range and supports the early start of this stage around ~650 Ma. The geochronological data compilation of magmatism in the Eastern Desert crust suggests that the transition between pre-collisional magmatism and collision-related magmatism takes place around ~650 Ma (Figures 5.2 and 5.14a, b)

Consistent with the geochronological data, the whole-rock Nd-Sr isotopes, and Hf-O isotopic data in zircon from the Eastern Desert show a major change in the composition of the magmatic activities and tectonic setting around ~650 Ma, from a juvenile to a more evolved isotopic composition, signifying an enhanced role of crustal reworking and recycling linked to the continental collision and the amalgamation of Gondwana (Figures 5.7, 5.9, and 5.10).

Figure 5.15 shows a proposed model for the Neoproterozoic evolution of the Eastern Desert region. Crustal evolution started with the generation of oceanic crust (at mid-ocean ridges) and oceanic arcs within the Mozambique Ocean (Bentor, 1985; Stern, 1994) (Figure 5.15a). This first phase is preserved as ophiolites and subduction-related metavolcanics (Ali *et al.*, 2010; Johnson *et al.*, 2011). The next phase (phase two) is represented by (1) the arc-related magmatism including metavolcanics and tholeiitic to calc-alkaline I-type granitoids that continued until ~650 Ma and (2) the accretion stage magmatism (Bentor, 1985; Stern and Hedge, 1985; Johnson *et al.*, 2011; Fritz *et al.*, 2013; Stern, 2018) (Figures 5.2 and 5.15b). The third phase represents the re-working of the accreted oceanic slabs by possibly plume-related re-melting, leading to the formation of the El-Shadli plutonic complex and bimodal volcanics (~730–700 Ma: Chapters 3 and 4) (Figures 5.2 and 5.15c). This third stage also includes interpreted plume products such as the ~740 Ma Korab Kansi ferropicritic layered mafic-ultramafic intrusions (Khedr *et al.*, 2020) and the ~710 Ma G. Dahanib komatiitic layered intrusions (Dixon, 1981; Azer *et al.*, 2017)

(Figures 5.2 and 5.15c). These three phases are consistent with the main proposed pre-collisional magmatism stage (~800–650 Ma) of the Eastern Desert that include the two oldest magmatic episodes, i.e., episode 1 peaks at ~730 Ma and episode 2 peaks at ~ 700 Ma (Figure 5.14a)

The final phase in the evolution of the Eastern Desert crust is represented by the collision-related magmatism stage (~650–550 Ma). This collision-related magmatism includes (1) syn-collisional calc-alkaline to alkaline I-type granitoids (~645–610: Zoheir *et al.*, 2019, 2020; El-Bialy *et al.*, 2020), (2) post-collisional alkaline A-type granites (~645–550 Ma: Moussa *et al.*, 2008; Ali *et al.*, 2012b, 2013; Eliwa *et al.*, 2014; Lehmann *et al.*, 2020), and (3) post-collisional Dokhan (alkaline) volcanics (~630–580 Ma: Stern and Gottfried, 1986; Wilde and Youssef, 2000; Breitzkreuz *et al.*, 2010) (Figures 5.2 and 5.15d). This collision-related magmatism is thought to be related to the crustal re-working through re-melting of the pre-existing crust, that could have been by mechanisms such as slab-break off, delamination, and orogenic collapse (Stern, 1994; Moussa *et al.*, 2008; Johnson *et al.*, 2011; Fritz *et al.*, 2013; Eliwa *et al.*, 2014; El-Bialy and Omar, 2015; Zoheir *et al.*, 2019; El-Bialy *et al.*, 2020). This final phase of crustal re-working played an important role in the crustal growth of the Egyptian Nubian Shield, involving further differentiating consolidating earlier formed juvenile crust into the Eastern Desert continental crust we see today.

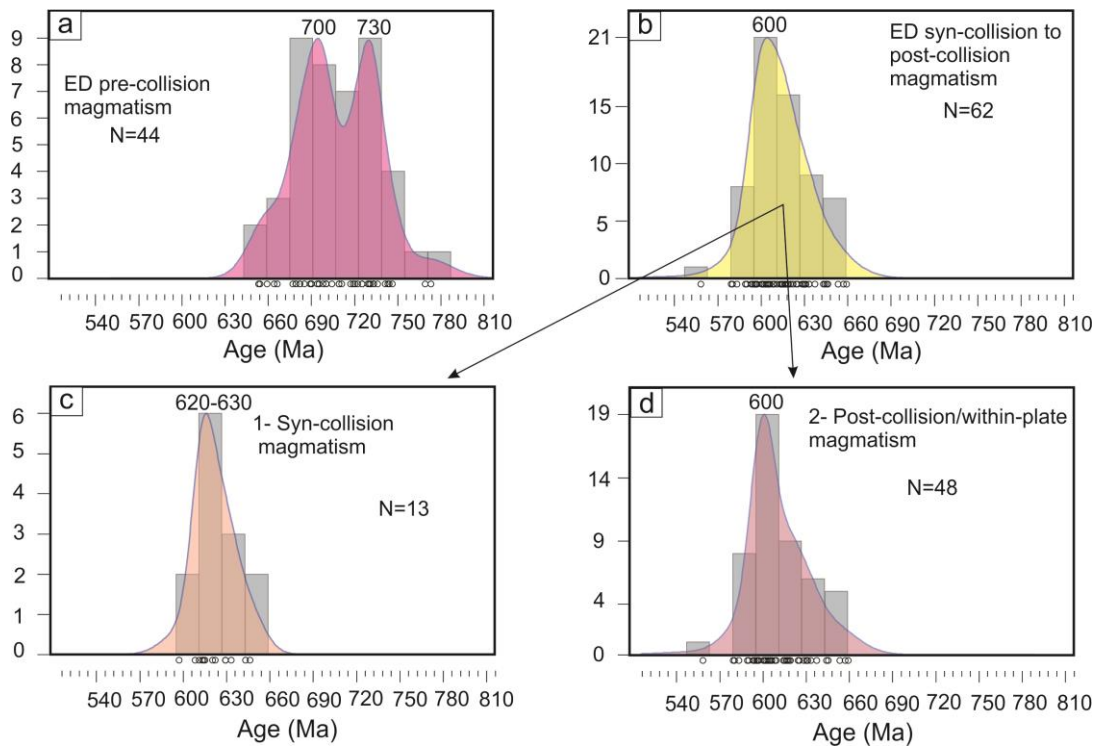
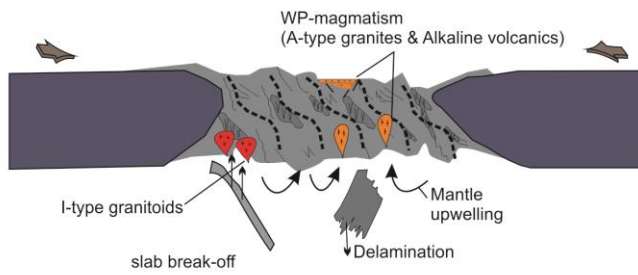
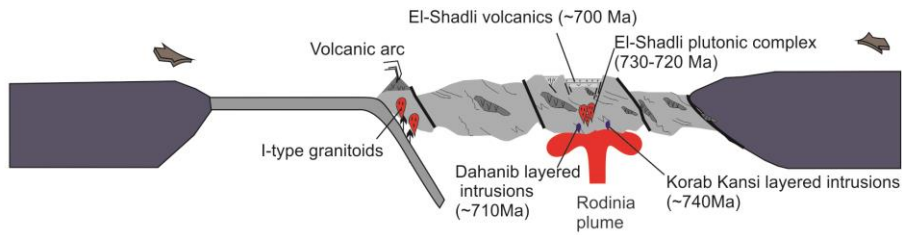


Figure 5.14: Histogram and Kernel density estimation for the Eastern Desert pre-collision magmatism and collision-related magmatism.

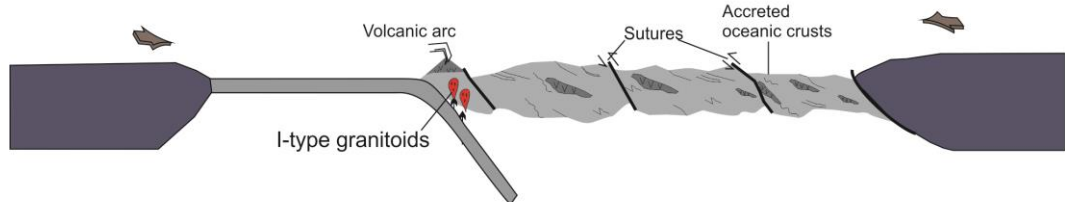
D) ~ 650-550 Ma (collision-related magmatism)



C) ~ 740-700 Ma (Accretion and post-accretion magmatism: plume?)



B) ~ 750-730 Ma (Accretion stage and arc-related magmatism)



A) ~ 800-750 Ma (MOR-spreading and oceanic-arc magmatism)

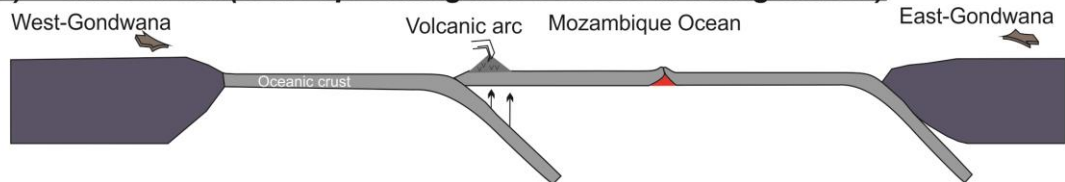


Figure 5.15: A proposed tectonic model for the evolution/growth of the Eastern Desert crust.

Table 5.1: List of all previously published U-Pb and Pb-Pb zircon/monazite geochronological data from granitoid and volcanic rocks of the Eastern Desert.

Location	Rock type	Lithology/Sample	Magmatism stage	Tectonic setting	Terranes	Lat	Long	Age (Ma)	±	Technique	Reference
Um Ara area	Granitoids	Pink granite	2	A-type (WPG)	SED	22.36	33.83	603	14	SHRIMP	Moussa et al (2008)
W. Shilman	Volcanics	Dacite	1	arc-related	SED	22.63	33.77	733	7	SHRIMP	Ali. K et al (2010)
W. Shilman	Granitoids	Granodiorite	2	I-type (syn))	SED	22.68	33.60	629	5	SHRIMP	Ali. K et al (2010)
W. Um Ashirah	Granitoids	Qz diorite	1	I-type (VAG)	SED	22.86	33.21	709	4	SHRIMP	Ali. K et al (2010)
Hafafit	Granitoids	Tonalite	1	I-type (VAG)	SED	24.78	34.50	682	2	U-Pb zircon evap.	Stern & Hedge (1985)
W. Keriga	Granitoids	Tonalite	1	I-type (VAG)	SED	22.85	35.25	709		U-Pb zircon evap.	Stern & Hedge (1985)
Abu Swayel	Granitoids	Tonalite	1	I-type (VAG)	SED	22.67	33.71	736	11	Pb-Pb zircon evap.	Kroner et al (1992)
W. Ghadir	Granitoids	Plagiogranite	1	I-type (VAG)	SED	24.75	35.00	746	19	Pb-Pb zircon evap.	Kroner et al (1992)
Beitan	Granitoids	Granitic gneiss (EG747)	1	I-type (VAG)	SED	23.31	35.00	704	8	Pb-Pb zircon evap.	Kroner et al (1994)
Hafafit	Granitoids	Granitoid gneiss EG 30)	1	I-type (VAG)	SED	24.61	34.60	677	9	Pb-Pb zircon evap.	Kroner et al (1994)
Hafafit	Granitoids	Granitoid gneiss (EG 27)	1	I-type (VAG)	SED	24.56	34.61	700	12	Pb-Pb zircon evap.	Kroner et al (1994)
Hafafit	Granitoids	Granitoid gneiss (EG 28)	1	I-type (VAG)	SED	24.60	34.60	698	14	Pb-Pb zircon evap.	Kroner et al (1994)
Beitan	Granitoids	Granodioritic gneiss (WB23)	1	I-type (VAG)	SED	23.28	35.00	725	9	SHRIMP	Ali. K et al (2015)
Beitan	Granitoids	Tonalitic gneiss (WB24)	1	I-type (VAG)	SED	23.35	35.00	744	10	SHRIMP	Ali. K et al (2015)
Beitan	Granitoids	Tonalitic gneiss (WB21)	1	I-type (VAG)	SED	23.45	34.93	719	10	SHRIMP	Ali. K et al (2015)
G. Danhib	Granitoids	Qz diorite	1	I-type (VAG)	SED	23.80	35.16	711	7	U-Pb zircon evap.	Dixon (1981)
El-Shadli	Volcanics	Dacite (EG-7)	1	rift-related	SED	24.12	34.49	695	9	LA-ICPMS	Faisal et al. (2020)
El-Shadli	Volcanics	Rhyolite (EG-11)	1	rift-related	SED	24.15	34.48	695	6	LA-ICPMS	Faisal et al. (2020)
G. Humr Mukbid	Granitoids	Pink granite (MK-19)	2	A-type (WPG)	SED	24.16	34.40	625	8	SHRIMP	Ali. K et al (2012b)
G. Humr Mukbid	Granitoids	Pink granite (MK-25)	2	A-type (WPG)	SED	24.16	34.38	619	8	SHRIMP	Ali. K et al (2012b)
G. Humr Akarim	Granitoids	Pink granite (AK-1)	2	A-type (WPG)	SED	24.18	34.03	633	7	SHRIMP	Ali. K et al (2012b)
G. Humr Akarim	Granitoids	Pink granite (AK-6)	2	A-type (WPG)	SED	24.18	34.06	603	8	SHRIMP	Ali. K et al (2012b)
Wadi Sikait	Granitoids	Syenogranite (Nu-10)	2	I-type (syn))	SED	24.61	34.80	646	12	SIMS	Abu-El-Enen et al. (2016)
Wadi Sikait	Granitoids	B H gneiss (Nu-2)	1	I-type (VAG)	SED	24.58	34.80	731	3	SIMS	Abu-El-Enen et al. (2016)
Hafafit	Granitoids	El Sukkari tonalite (AA06-15)	1	I-type (VAG)	SED	24.55	34.91	689	3	ID-TIMS	Lundmark et al (2012)
Hafafit	Granitoids	Zabara orthogenesis (AA06-16)	2	I-type (syn)	SED	24.76	34.70	633	5	ID-TIMS	Lundmark et al (2012)
Hafafit	Granitoids	Tonalite gneiss (AA06-6)	1	I-type (VAG)	SED	24.80	34.50	659	5	ID-TIMS	Lundmark et al (2012)
Hafafit	Granitoids	Hangalia granite (AA06-18/AA08-58)	2	I-type (syn)	SED	24.83	34.56	629	5	ID-TIMS	Lundmark et al (2012)
El Genina Gharbia	Granitoids	Tonalite (G04-2)	1	I-type (VAG)	SED	23.55	34.39	690	6	SHRIMP/LA-ICP-MS	This study
El-Shadli	Volcanics	Dacite (S16)	1	rift-related	SED	24.13	34.35	700	5	SHRIMP/LA-ICP-MS	This study
El-Shadli	Volcanics	Rhyolite (S05-2)	1	rift-related	SED	24.24	34.35	700	5	SHRIMP/LA-ICP-MS	This study
El-Shadli	plagiogranites	Diorite (R10-1)	1	rift-related	SED	24.18	34.10	733	7	SHRIMP/LA-ICP-MS	This study
El-Shadli	plagiogranites	Trondhjemitic (R11-1)	1	rift-related	SED	24.18	34.08	733	3	SHRIMP/LA-ICP-MS	This study
El-Shadli	plagiogranites	Trondhjemitic (S14)	1	rift-related	SED	24.18	34.41	722	7	SHRIMP/LA-ICP-MS	This study
El-Shadli	plagiogranites	Trondhjemitic (S01-1a)	1	rift-related	SED	24.24	34.35	729	7	SHRIMP/LA-ICP-MS	This study
Abu Dabbab	Granitoids	Granite	2	A-type (WPG)	CED	25.20	34.33	644	2	LA-ICPMS (Mz)	Lehmann et al (2020)
Um Rus	Granitoids	Granodiorite-tonalite (rus-g1, 25)	2	I-type (syn)	CED	25.28	34.34	643	9	SHRIMP (Mz)	Zoheir et al. (2020)
G. El Umra	Granitoids	Granodiorite	1	I-type (VAG)	CED	25.30	34.23	654	5	ID-TIMS	Shalaby et al. (2005)
G. El Umra	Granitoids	Granodiorite	1	I-type (VAG)	CED	25.36	34.18	690	21	ID-TIMS	Shalaby et al. (2005)
El Shalul	Granitoids	Granite (SH1)	2	A-type (WPG)	CED	25.55	33.66	637	5	LA-ICPMS	Ali. K et al (2012a)
El Shalul	Granitoids	Granitic gneiss (SH6)	2	A-type (WPG)	CED	25.55	33.66	631	6	LA-ICPMS	Ali. K et al (2012a)
El Sibai	Granitoids	El Shush granodiorite (AA07-16)	1	I-type (VAG)	CED	25.65	34.38	682	4	ID-TIMS	Augland et al. (2012)
El Sibai	Granitoids	El Shush granitic gneiss (AA07-17)	1	I-type (VAG)	CED	25.65	34.38	679	2	ID-TIMS	Augland et al. (2012)
El Sibai	Granitoids	El Shush granitic gneiss (AA07-18)	1	I-type (VAG)	CED	25.65	34.40	685	3	ID-TIMS	Augland et al. (2012)
El Sibai	Granitoids	El Shush gneiss (KP 273)	1	I-type (VAG)	CED	25.66	34.36	694	27	Pb-Pb zircon evap.	Bregar et al (2002)

El Sibai	Granitoids	El Shush gneiss (MB 320)	1	I-type (VAG)	CED	25.68	34.36	679	7	Pb-Pb zircon evap.	Bregar et al (2002)
El Sibai	Granitoids	Granite (AB 281)	2	A-type (WPG)	CED	25.68	34.41	645	5	Pb-Pb zircon evap.	Bregar et al (2002)
El Sibai	Granitoids	Central gneiss (MB 184)	2	A-type (WPG)	CED	25.70	34.35	659	14	Pb-Pb zircon evap.	Bregar et al (2002)
El Sibai	Granitoids	Granite (ED 151)	2	A-type (WPG)	CED	25.73	34.35	653	15	Pb-Pb zircon evap.	Bregar et al (2002)
El Sibai	Granitoids	Granite (MB 195)	2	A-type (WPG)	CED	25.75	34.30	657	24	Pb-Pb zircon evap.	Bregar et al (2002)
W. Kareim	Volcanics	Mafic (K11-9)	1	arc-related	CED	25.94	34.04	730	22	SHRIMP	Ali. K et al (2009)
W. Kareim	Volcanics	Mafic (K4G)	1	arc-related	CED	25.94	34.04	743	45	SHRIMP	Ali. K et al (2009)
W. Kareim	Volcanics	Felsic tuffs (K4K)	1	arc-related	CED	25.95	34.04	769	29	SHRIMP	Ali. K et al (2009)
Abu Ziran	Granitoids	Diorite (AA05-5)	2	I-type (WPG)	CED	26.00	33.80	606	1	ID-TIMS	Andresen et al (2009)
Fawakhir	Granitoids	Monzodiorite (AA05-3)	2	I-type (syn)	CED	26.00	33.60	597	3	ID-TIMS	Andresen et al (2009)
Um Had	Granitoids	Granite (AA05-14)	2	A-type (WPG)	CED	26.03	33.51	596	2	ID-TIMS	Andresen et al (2009)
Meatiq	Granitoids	Arieki granite (AA05-9)	2	A-type (WPG)	CED	26.06	33.78	590	3	ID-TIMS	Andresen et al (2009)
Meatiq	Granitoids	Um Baanib orthogenesis (AA05-11)	2	A-type (WPG)	CED	26.13	33.83	630	2	ID-TIMS	Andresen et al (2009)
Abu Fannani	Granitoids	Diorite lens (AA06-41)	2	I-type (WPG)	CED	26.16	33.83	609	1	ID-TIMS	Andresen et al (2009)
Abu Fannani	Granitoids	Diorite lens (AA06-42)	2	I-type (WPG)	CED	26.16	33.84	606	1	ID-TIMS	Andresen et al (2009)
W. Atalla	Granitoids	Monzogranite	2	I-type (syn)	CED	26.09	33.30	615	9	SHRIMP (Mz)	Zoheir et al. (2019)
Abu Ziran	Granitoids	Granodiorite	2	I-type (WPG)	CED	26.00	33.75	614	8	U-Pb zircon evap.	Stern & Hedge (1985)
G. Al Missikat	Granitoids	Pink granite	2	A-type (WPG)	CED	26.33	33.43	597	7	SHRIMP	Moussa et al (2008)
Um Taghir	Granitoids	Granodiorite	1	I-type (VAG)	CED	26.50	33.50	653	2.6	SHRIMP	Moussa et al (2008)
G. Qattar	Granitoids	Pink granite	2	A-type (WPG)	NED	27.06	33.36	579		U-Pb zircon evap.	Stern & Hedge (1985)
W. Dib	Granitoids	Granodiorite	2	I-type (syn)	NED	27.06	32.91	620		U-Pb zircon evap.	Stern & Hedge (1985)
Salah El Belih	Granitoids	pink granite	2	A-type (WPG)	NED	27.18	32.92	583		U-Pb zircon evap.	Stern & Hedge (1985)
Mons Claudianus	Granitoids	Granodiorite	1	I-type (VAG)	NED	26.81	33.50	666		U-Pb zircon evap.	Stern & Hedge (1985)
W. Hawashiya	Granitoids	Granodiorite	2	I-type (VAG)	NED	28.40	32.68	614		U-Pb zircon evap.	Stern & Hedge (1985)
G. Dara	Granitoids	Pink granite	2	A-type (WPG)	NED	27.91	33.05	596		U-Pb zircon evap.	Stern & Hedge (1985)
Mons Claudianus	Granitoids	Granodiorite	1	I-type (VAG)	NED	26.81	33.48	664	0.38	ID-TIMS	Abdel-Rahman (2018)
G. Gattar	Granitoids	Pink granite (E-17)	2	A type (WPG)	NED	27.03	33.22	580	22	SHRIMP	Ali.B et al (2015)
Faliq El-Sahl and			2								
El Waar	Granitoids	Pink granite (E-31)		A-type (WPG)	NED	27.08	33.53	605	10	SHRIMP	Ali.B et al (2015)
G.El-Glouf	Granitoids	Pink granite (E-21)	2	A-type (WPG)	NED	27.08	32.92	596	11	SHRIMP	Ali.B et al (2015)
G.Abu-Marwa	Granitoids	Pink granite (E-11)	2	A-type (WPG)	NED	27.37	33.08	596	8	SHRIMP	Ali.B et al (2015)
G. Qattar	Granitoids	Pink granite	2	A-type (WPG)	NED	27.16	33.33	604	3.3	SHRIMP	Moussa et al (2008)
Abu Harba	Granitoids	Pink granite	2	A-type (WPG)	NED	27.33	33.16	595	3.3	SHRIMP	Moussa et al (2008)
Um Mongol	Granitoids	Monzogranite	2	A-type (WPG)	NED	27.80	33.07	558	5	SHRIMP	Abd El-Rahman et al (2017)
Um Mongol	Volcanics	Dacite	1	arc-related	NED	27.81	33.07	773	7	LA-ICPMS	Abd El-Rahman et al (2017)
W. Abu Maamel	Volcanics	Dokhan Volcanics (V13)	2	WPG	NED	27.24	33.27	593	13	SHRIMP	Abd El-Rahman et al (2017)
W. Abu Maamel	Volcanics	Dokhan Volcanics (V16)	2	WPG	NED	27.24	33.29	602	9	SHRIMP	Wilde and Youssef (2000)
G. Mongol	Volcanics	Dokhan Volcanics (dacite, GM1)	2	WPG	NED	27.84	32.03	618	4	SHRIMP	Wilde and Youssef (2000)
G. Samr El-Qaa	Volcanics	Dokhan Volcanics (rhyolite, SQ1)	2	WPG	NED	28.23	32.43	594	5	SHRIMP	Breitkruez et al. (2010)
W. Malaak	Volcanics	Rhyodacitic ignimbrite (B-084)	1	arc-related	NED	27.86	32.83	725	7	LA-ICPMS	Breitkruez et al. (2010)
W. Malaak	Volcanics	Rhyodacitic ignimbrite (B-093)	1	arc-related	NED	27.87	32.81	717	8	LA-ICPMS	Bühler et al. (2014)
G. Nuqara	Volcanics	Dokhan Volcanics (ignimbrite, GN2)	2	WPG	NED	26.70	33.89	601	4	SHRIMP	Bühler et al. (2014)
W. Bali	Volcanics	Dokhan Volcanics (ignimbrite, WB1)	2	WPG	NED	27.39	33.57	608	4	SHRIMP	Breitkruez et al. (2010)
W. Dib	Volcanics	Dokhan Volcanics (ignimbrite,WD1)	2	WPG	NED	27.73	33.06	616	3	SHRIMP	Breitkruez et al. (2010)
W. Abu Mu'aymil	Volcanics	Dokhan Volcanics (ignimbrite, JM21)	2	WPG	NED	27.86	32.86	617	7	SHRIMP	Breitkruez et al. (2010)
G. El Urf	Volcanics	Dokhan Volcanics (ignimbrite, GU127)	2	WPG	NED	27.81	32.85	616	5	SHRIMP	Breitkruez et al. (2010)
G. El Urf	Volcanics	Dokhan Volcanics (ignimbrite, GU197)	2	WPG	NED	27.81	32.94	615	4	SHRIMP	Breitkruez et al. (2010)
G. El Kharaza	Volcanics	Dokhan Volcanics (ignimbrite, GK8)	2	WPG	NED	27.93	32.68	605	6	SHRIMP	Breitkruez et al. (2010)
G. El Kharaza	Volcanics	Dokhan Volcanics (ignimbrite, JK37)	2	WPG	NED	27.93	32.87	630	6	SHRIMP	Breitkruez et al. (2010)
W. Abu Hammad	Volcanics	Dokhan Volcanics (ignimbrite, GK4)	2	WPG	NED	27.94	32.86	628	7	SHRIMP	Breitkruez et al. (2010)

W. Abu Hammad	Volcanics	Dokhan Volcanics (ignimbrite,JK23)	2	WPG	NED	27.94	32.86	624	4	SHRIMP	Breitkruez et al. (2010)
G. Dara	Granitoids	Trondhjemite (D-42)	1	I-type (VAG)	NED	27.91	32.90	741	2.9	SIMS	Eliwa et al. (2014)
G. Dara	Granitoids	Granodiorite (D-16)	1	I-type (VAG)	NED	27.96	32.65	720	7	SIMS	Eliwa et al. (2014)
G. Dara	Granitoids	Granite (D-10)	2	A-type (WPG)	NED	27.81	32.88	600	3	SIMS	Eliwa et al. (2014)
G. Dara	Granitoids	Granite (S-71)	2	I-type (syn)	NED	27.76	32.85	608	2.9	SIMS	Eliwa et al. (2014)
W. Hawashiya	Granitoids	Monzogranite (WH-118)	2	A-type (WPG)	NED	28.17	32.30	589	8	LA-ICPMS	El-Baily et al. (2020)
W. Hawashiya	Granitoids	Monzogranite (WH-48)	2	A type (WPG)	NED	28.19	32.35	601	8	LA-ICPMS	El-Baily et al. (2020)
W. Hawashiya	Granitoids	Quartz diorite (WH-63)	2	I-type (syn)	NED	28.21	32.37	614	6	LA-ICPMS	El-Baily et al. (2020)
W. Hawashiya	Granitoids	Monzogranite (WH-30)	2	A-type (WPG)	NED	28.21	32.33	594	14	LA-ICPMS	El-Baily et al. (2020)
W. Hawashiya	Granitoids	Quartz diorite (WH-37)	2	I-type (syn)	NED	28.22	32.36	613	5	LA-ICPMS	El-Baily et al. (2020)
W. Hawashiya	Granitoids	Quartz diorite (WH-1)	2	I-type (syn)	NED	28.24	32.40	622	4	LA-ICPMS	El-Baily et al. (2020)
W. Hawashiya	Granitoids	Quartz diorite (WH-145)	2	I-type (syn)	NED	28.26	32.39	611	6	LA-ICPMS	El-Baily et al. (2020)

Note: 1= pre-collision magmatism and 2= collision-related magmatism. VAG = volcanics arc granites, WPG = within plate granites, syn = syn-collision.

5.7 References

- Abd El-Rahman, Y. *et al.* (2017) 'The South Um Mongul Cu-Mo-Au prospect in the Eastern Desert of Egypt: From a mid-Cryogenian continental arc to Ediacaran post-collisional appinite-high Ba-Sr monzogranite', *Ore Geology Reviews*. Elsevier, 80, pp. 250–266. doi: 10.1016/J.OREGEOREV.2016.06.004.
- Abd El-Rahman, Y. *et al.* (2019) 'The evolution of the Arabian-Nubian Shield and survival of its zircon U-Pb-Hf-O isotopic signature: A tale from the Um Had Conglomerate, central Eastern Desert, Egypt', *Precambrian Research*. Elsevier, 320, pp. 46–62. doi: 10.1016/J.PRECAMRES.2018.10.011.
- Abdel-Rahman, A.-F. M. (2018) 'Geochemistry, age and origin of the Mons Claudianus TTG batholith (Egypt): insight into the role of Pan-African magmatism in uniting plates of Gondwana', *Geological Magazine*. Cambridge University Press, pp. 1–20. doi: 10.1017/S0016756818000304.
- Abu El-Enen, M. M. *et al.* (2016) 'P–T path and timing of crustal thickening during amalgamation of East and West Gondwana: A case study from the Hafafit Metamorphic Complex, Eastern Desert of Egypt', *Lithos*. Elsevier, 263, pp. 213–238. doi: 10.1016/J.LITHOS.2016.01.001.
- Ali, B. H. (2015) 'SHRIMP U–Pb zircon geochronology: evidence for emplacement time of some granitoids north Eastern Desert, Egypt', *Arabian Journal of Geosciences*. Springer Verlag, 8(8), pp. 5465–5474. doi: 10.1007/s12517-014-1608-3.
- Ali, K. A. *et al.* (2009) 'Geochemistry, Nd isotopes and U-Pb SHRIMP zircon dating of Neoproterozoic volcanic rocks from the Central Eastern Desert of Egypt: New insights into the ~750 Ma crust-forming event', *Precambrian Research*, 171(1–4), pp. 1–22. doi: 10.1016/j.precamres.2009.03.002.
- Ali, K. A. *et al.* (2010) 'Age constraints on the formation and emplacement of Neoproterozoic ophiolites along the Allaqi-Heiani Suture, South Eastern Desert of Egypt', *Gondwana Research*, 18(4), pp. 583–595. doi: 10.1016/j.gr.2010.03.002.
- Ali, K. A., Moghazi, A.-K. M., *et al.* (2012) 'Composition, age, and origin of the ~620 Ma Humr Akarim and Humrat Mukbid A-type granites: no evidence for pre-Neoproterozoic basement in the Eastern Desert, Egypt', *International Journal of Earth Sciences*. Springer-Verlag, 101(7), pp. 1705–1722. doi: 10.1007/s00531-012-0759-2.
- Ali, K. A., Andresen, A., *et al.* (2012) 'U–Pb zircon dating and Sr–Nd–Hf isotopic evidence to support a juvenile origin of the ~ 634 Ma El Shalul granitic gneiss dome, Arabian–Nubian Shield', *Geological Magazine*. Cambridge University Press, 149(5), pp. 783–797. doi: 10.1017/S0016756811000975.
- Ali, K. A. *et al.* (2013) 'Hf isotopic composition of single zircons from Neoproterozoic arc volcanics and post-collision granites, Eastern Desert of Egypt: Implications for crustal growth and recycling in the Arabian-Nubian Shield', *Precambrian Research*. Elsevier B.V., 239, pp. 42–55. doi: 10.1016/j.precamres.2013.05.007.
- Ali, K. A. *et al.* (2014) 'U–Pb zircon geochronology and Nd–Hf–O isotopic systematics of the Neoproterozoic Hadb adh Dayheen ring complex, Central Arabian Shield, Saudi Arabia', *Lithos*. Elsevier, 206–207, pp. 348–360. doi: 10.1016/J.LITHOS.2014.07.030.

- Ali, K. A., Surour, A. A., *et al.* (2015) 'Single zircon Hf–O isotope constraints on the origin of A-type granites from the Jabal Al-Hassir ring complex, Saudi Arabia', *Precambrian Research*. Elsevier, 256, pp. 131–147. doi: 10.1016/J.PRECAMRES.2014.11.007.
- Ali, K. A., Kröner, A., *et al.* (2015) 'U–Pb zircon geochronology and Hf–Nd isotopic systematics of Wadi Beitan granitoid gneisses, South Eastern Desert, Egypt', *Gondwana Research*. Elsevier, 27(2), pp. 811–824. doi: 10.1016/J.GR.2013.11.002.
- Ali, K. A. *et al.* (2016) 'Lu–Hf and O isotopic compositions on single zircons from the North Eastern Desert of Egypt, Arabian–Nubian Shield: Implications for crustal evolution', *Gondwana Research*. Elsevier, 32, pp. 181–192. doi: 10.1016/J.GR.2015.02.008.
- Anders, E. and Grevesse, N. (1989) 'Abundances of the elements: Meteoritic and solar', *Geochimica et Cosmochimica Acta*. Pergamon, 53(1), pp. 197–214. doi: 10.1016/0016-7037(89)90286-X.
- Andresen, A. *et al.* (2009) 'U–Pb TIMS age constraints on the evolution of the Neoproterozoic Meatiq Gneiss Dome, Eastern Desert, Egypt', *International Journal of Earth Sciences*, 98(3), pp. 481–497. doi: 10.1007/s00531-007-0276-x.
- Augland, L. E., Andresen, A. and Boghdady, G. Y. (2012) 'U–Pb ID-TIMS dating of igneous and metaigneous rocks from the El-Sibai area: time constraints on the tectonic evolution of the Central Eastern Desert, Egypt', *International Journal of Earth Sciences*. Springer-Verlag, 101(1), pp. 25–37. doi: 10.1007/s00531-011-0653-3.
- Barker, F. (1979) 'Trondhjemite: Definition, Environment and Hypotheses of Origin', *Developments in Petrology*. Elsevier, 6, pp. 1–12. doi: 10.1016/B978-0-444-41765-7.50006-X.
- Basta, F. F. *et al.* (2011) 'Neoproterozoic contaminated MORB of Wadi Ghadir ophiolite, NE Africa: Geochemical and Nd and Sr isotopic constraints', *Journal of African Earth Sciences*. Pergamon, 59(2–3), pp. 227–242. doi: 10.1016/j.jafrearsci.2010.10.008.
- Be'eri-Shlevin, Y. *et al.* (2010) 'Nd–Sr–Hf–O isotope provinciality in the northernmost Arabian–Nubian Shield: implications for crustal evolution', *Contributions to Mineralogy and Petrology*. Springer-Verlag, 160(2), pp. 181–201. doi: 10.1007/s00410-009-0472-8.
- Be'eri-Shlevin, Y., Katzir, Y. and Valley, J. W. (2009) 'Crustal evolution and recycling in a juvenile continent: Oxygen isotope ratio of zircon in the northern Arabian Nubian Shield', *Lithos*. Elsevier, 107(3–4), pp. 169–184. doi: 10.1016/J.LITHOS.2008.10.001.
- Belousova, E. *et al.* (2002) 'Igneous zircon: trace element composition as an indicator of source rock type', *Contributions to Mineralogy and Petrology*. Springer-Verlag, 143(5), pp. 602–622. doi: 10.1007/s00410-002-0364-7.
- Belousova, E. A. *et al.* (2010) 'The growth of the continental crust: Constraints from zircon Hf-isotope data', *Lithos*. Elsevier, 119(3–4), pp. 457–466. doi: 10.1016/J.LITHOS.2010.07.024.
- Bentor, Y. K. (1985) 'The crustal evolution of the Arabo-Nubian Massif with special reference to the Sinai Peninsula', *Precambrian Research*. Elsevier, 28(1), pp. 1–74. doi: 10.1016/0301-9268(85)90074-9.

- Beyth, M. *et al.* (1994) 'The Late Precambrian Timna igneous complex, Southern Israel: Evidence for comagmatic-type sanukitoid monzodiorite and alkali granite magma', *Lithos*. Elsevier, 31(3–4), pp. 103–124. doi: 10.1016/0024-4937(94)90003-5.
- Bouvier, A., Vervoort, J. D. and Patchett, P. J. (2008) 'The Lu–Hf and Sm–Nd isotopic composition of CHUR: Constraints from unequilibrated chondrites and implications for the bulk composition of terrestrial planets', *Earth and Planetary Science Letters*. Elsevier, 273(1–2), pp. 48–57. doi: 10.1016/J.EPSL.2008.06.010.
- Bregar, M. *et al.* (2002) 'A late Neoproterozoic magmatic core complex in the Eastern Desert of Egypt: emplacement of granitoids in a wrench-tectonic setting', *Precambrian Research*. Elsevier, 118(1–2), pp. 59–82. doi: 10.1016/S0301-9268(02)00062-1.
- Breitkreuz, C. *et al.* (2010) 'Neoproterozoic SHRIMP U–Pb zircon ages of silica-rich Dokhan Volcanics in the North Eastern Desert, Egypt', *Precambrian Research*. Elsevier, 182(3), pp. 163–174. doi: 10.1016/J.PRECAMRES.2010.06.019.
- Bühler, B. *et al.* (2014) 'New insights into the accretion of the Arabian-Nubian Shield: Depositional setting, composition and geochronology of a Mid-Cryogenian arc succession (North Eastern Desert, Egypt)', *Precambrian Research*. Elsevier B.V., 243, pp. 149–167. doi: 10.1016/j.precamres.2013.12.012.
- Carley, T. L. *et al.* (2014) 'Iceland is not a magmatic analog for the Hadean: Evidence from the zircon record', *Earth and Planetary Science Letters*. Elsevier, 405, pp. 85–97. doi: 10.1016/j.epsl.2014.08.015.
- Coolen, J. J. M. M. M. *et al.* (1982) 'Possible zircon UPb evidence for Pan-African granulite-facies metamorphism in the Mozambique belt of southern Tanzania', *Precambrian Research*. Elsevier, 17(1), pp. 31–40. doi: 10.1016/0301-9268(82)90152-8.
- DePaolo, D. J. (1981) 'Neodymium isotopes in the Colorado Front Range and crust–mantle evolution in the Proterozoic', *Nature*. Nature Publishing Group, 291(5812), pp. 193–196. doi: 10.1038/291193a0.
- Dhuime, B., Hawkesworth, C. and Cawood, P. (2011) 'When Continents Formed', *Science*, 331(6014), pp. 155–156. doi: 10.1126/science.1200643.
- Dixon, T. H. (1981) 'Gebel Dahanib, Egypt: A Late Precambrian Layered Sill of Komatiitic Composition T.H.', *Contribution to Mineralogy and Petrology Mineral Petrol*, 76, pp. 42–52.
- El-Bialy, M. Z. *et al.* (2020) 'U-Pb zircon geochronology and geochemical constraints on the Ediacaran continental arc and post-collision Granites of Wadi Hawashiya, North Eastern Desert, Egypt: Insights into the ~600 Ma crust-forming Event in the northernmost part of Arabian-Nubian Shi', *Precambrian Research*. Elsevier, 345, p. 105777. doi: 10.1016/j.precamres.2020.105777.
- El-Bialy, M. Z. and Ali, K. A. (2013) 'Zircon trace element geochemical constraints on the evolution of the Ediacaran (600–614 Ma) post-collisional Dokhan Volcanics and Younger Granites of SE Sinai, NE Arabian–Nubian Shield', *Chemical Geology*. Elsevier, 360–361, pp. 54–73. doi: 10.1016/J.CHEMGEO.2013.10.009.
- El-Bialy, M. Z. and Omar, M. M. (2015) 'Spatial association of Neoproterozoic continental

arc I-type and post-collision A-type granitoids in the Arabian-Nubian Shield: The Wadi Al-Baroud Older and Younger Granites, North Eastern Desert, Egypt', *Journal of African Earth Sciences*. Elsevier Ltd, 103, pp. 1–29. doi: 10.1016/j.jafrearsci.2014.11.013.

El-Kazzaz, Y. A. H. A. and Taylor, W. E. G. (2001) 'Tectonic evolution of the Allaqi shear zone and implications for Pan-African terrane amalgamation in the south Eastern Desert, Egypt', *Journal of African Earth Sciences*. Elsevier Ltd, 33(2), pp. 177–197. doi: 10.1016/S0899-5362(01)80058-0.

Eliwa, H. A. *et al.* (2014) 'SIMS zircon U–Pb and mica K–Ar geochronology, and Sr–Nd isotope geochemistry of Neoproterozoic granitoids and their bearing on the evolution of the north Eastern Desert, Egypt', *Gondwana Research*. Elsevier, 25(4), pp. 1570–1598. doi: 10.1016/J.GR.2013.06.006.

Faisal, M. *et al.* (2020) 'Geochronology and geochemistry of Neoproterozoic Hamamid metavolcanics hosting largest volcanogenic massive sulfide deposits in Eastern Desert of Egypt: Implications for petrogenesis and tectonic evolution', *Precambrian Research*. Elsevier, 344, p. 105751. doi: 10.1016/j.precamres.2020.105751.

Farahat, E. S. *et al.* (2007) 'Origin of I- and A-type granitoids from the Eastern Desert of Egypt: Implications for crustal growth in the northern Arabian–Nubian Shield', *Journal of African Earth Sciences*. Pergamon, 49(1–2), pp. 43–58. doi: 10.1016/J.JAFREARSCI.2007.07.002.

Fritz, H. *et al.* (2013) 'Orogen styles in the East African Orogen: A review of the Neoproterozoic to Cambrian tectonic evolution', *Journal of African Earth Sciences*. Elsevier Ltd, 86, pp. 65–106. doi: 10.1016/j.jafrearsci.2013.06.004.

Gamal El Dien, H. *et al.* (2019) 'Origin of arc magmatic signature: A temperature-dependent process for trace element (re)-mobilization in subduction zones', *Scientific Reports*. Nature Publishing Group, 9(1), p. 7098. doi: 10.1038/s41598-019-43605-9.

Goldstein, S. L., O'Nions, R. K. and Hamilton, P. J. (1984) 'A Sm–Nd isotopic study of atmospheric dusts and particulates from major river systems', *Earth and Planetary Science Letters*. Elsevier, 70(2), pp. 221–236. doi: 10.1016/0012-821X(84)90007-4.

Griffin, W. . *et al.* (2002) 'Zircon chemistry and magma mixing, SE China: In-situ analysis of Hf isotopes, Tonglu and Pingtan igneous complexes', *Lithos*. Elsevier, 61(3–4), pp. 237–269. doi: 10.1016/S0024-4937(02)00082-8.

Grimes, C. B. *et al.* (2007) 'Trace element chemistry of zircons from oceanic crust: A method for distinguishing detrital zircon provenance', *Geology*, 35(7), pp. 643–646. doi: 10.1130/G23603A.1.

Grimes, C. B. *et al.* (2015) "'Fingerprinting" tectono-magmatic provenance using trace elements in igneous zircon', *Contributions to Mineralogy and Petrology*. Springer Verlag, 170(5–6), pp. 1–26. doi: 10.1007/s00410-015-1199-3.

Hawkesworth, C. J. and Kemp, A. I. S. (2006) 'Using hafnium and oxygen isotopes in zircons to unravel the record of crustal evolution', *Chemical Geology*. Elsevier, 226(3–4), pp. 144–162. doi: 10.1016/j.chemgeo.2005.09.018.

Helmy, H. M. *et al.* (2014) 'Petrology and Sm–Nd dating of the Genina Gharbia Alaskan-

type complex (Egypt): Insights into deep levels of Neoproterozoic island arcs', *Lithos*. Elsevier B.V., 198–199(1), pp. 263–280. doi: 10.1016/j.lithos.2014.03.028.

Hildebrand, R. S., Whalen, J. B. and Bowring, S. A. (2018) 'Resolving the crustal composition paradox by 3.8 billion years of slab failure magmatism and collisional recycling of continental crust', *Tectonophysics*. Elsevier, 734–735, pp. 69–88. doi: 10.1016/J.TECTO.2018.04.001.

Jarrar, G. H. *et al.* (2013) 'Geochemistry and P–T–t evolution of the Abu-Barqa Metamorphic Suite, SW Jordan, and implications for the tectonics of the northern Arabian–Nubian Shield', *Precambrian Research*. Elsevier, 239, pp. 56–78. doi: 10.1016/J.PRECAMRES.2013.08.003.

Johnson, P. R. *et al.* (2011) 'Late Cryogenian-Ediacaran history of the Arabian-Nubian Shield: A review of depositional, plutonic, structural, and tectonic events in the closing stages of the northern East African Orogen', *Journal of African Earth Sciences*. Elsevier Ltd, 61(3), pp. 167–232. doi: 10.1016/j.jafrearsci.2011.07.003.

Katzir, Y. *et al.* (2007) 'Petrogenesis of A-type granites and origin of vertical zoning in the Katharina pluton, Gebel Mussa (Mt. Moses) area, Sinai, Egypt', *Lithos*. Elsevier, 95(3–4), pp. 208–228. doi: 10.1016/J.LITHOS.2006.07.013.

Kemp, A. I. S. *et al.* (2006) 'Episodic growth of the Gondwana supercontinent from hafnium and oxygen isotopes in zircon', *Nature*. Nature Publishing Group, 439(7076), pp. 580–583. doi: 10.1038/nature04505.

Kemp, A. I. S. *et al.* (2007) 'Magmatic and crustal differentiation history of granitic rocks from Hf–O isotopes in zircon.', *Science (New York, N.Y.)*. American Association for the Advancement of Science, 315(5814), pp. 980–3. doi: 10.1126/science.1136154.

Kemp, A. I. S. and Hawkesworth, C. J. (2014) 'Growth and Differentiation of the Continental Crust from Isotope Studies of Accessory Minerals', in *Treatise on Geochemistry*. Elsevier, pp. 379–421. doi: 10.1016/B978-0-08-095975-7.00312-0.

Khedr, M. Z. *et al.* (2020) 'Petrogenesis of the ~740 Korab Kansi mafic-ultramafic intrusion, South Eastern Desert of Egypt: Evidence of Ti-rich ferropicritic magmatism', *Gondwana Research*. Elsevier Inc., 82, pp. 48–72. doi: 10.1016/j.gr.2019.12.013.

Kinny, P. D., Compston, W. and Williams, I. S. (1991) 'A reconnaissance ion-probe study of hafnium isotopes in zircons', *Geochimica et Cosmochimica Acta*. Pergamon, 55(3), pp. 849–859. doi: 10.1016/0016-7037(91)90346-7.

Kinny, P. D. and Maas, R. (2003) 'Lu–Hf and Sm–Nd isotope systems in zircon', *Reviews in Mineralogy and Geochemistry*. GeoScienceWorld, 53(1), pp. 327–341. doi: 10.2113/0530327.

Kirkland, C. L. *et al.* (2015) 'Zircon Th/U ratios in magmatic environs', *Lithos*. Elsevier, 212–215, pp. 397–414. doi: 10.1016/j.lithos.2014.11.021.

Kröner, A. *et al.* (1992) 'Dating of late Proterozoic ophiolites in Egypt and the Sudan using the single grain zircon evaporation technique', *Precambrian Research*, 59(1–2), pp. 15–32. doi: 10.1016/0301-9268(92)90049-T.

- Kroner, A., Kruger, J. and Rashwan, A. A. A. (1994) 'Age and tectonic setting of granitoid gneisses in the Eastern Desert of Egypt and south-west Sinai', *Geologische Rundschau*. Springer-Verlag, 83(3), pp. 502–513. doi: 10.1007/BF00194157.
- Laurent, O. *et al.* (2014) 'The diversity and evolution of late-Archean granitoids: Evidence for the onset of "modern-style" plate tectonics between 3.0 and 2.5 Ga', *Lithos*. Elsevier, 205, pp. 208–235. doi: 10.1016/J.LITHOS.2014.06.012.
- Lehmann, B. *et al.* (2020) 'Monazite and cassiterite U-Pb dating of the Abu Dabbab rare-metal granite, Egypt: Late Cryogenian metalliferous granite magmatism in the Arabian-Nubian Shield', *Gondwana Research*. Elsevier Inc., 84, pp. 71–80. doi: 10.1016/j.gr.2020.03.001.
- Li, X.-H. *et al.* (2018) 'Old Continental Crust Underlying Juvenile Oceanic Arc: Evidence From Northern Arabian-Nubian Shield, Egypt', *Geophysical Research Letters*. Wiley-Blackwell, 45(7), pp. 3001–3008. doi: 10.1002/2018GL077121.
- Liégeois, J. P. and Stern, R. J. (2010) 'Sr-Nd isotopes and geochemistry of granite-gneiss complexes from the Meatiq and Hafafit domes, Eastern Desert, Egypt: No evidence for pre-Neoproterozoic crust', *Journal of African Earth Sciences*. Elsevier Ltd, 57(1–2), pp. 31–40. doi: 10.1016/j.jafrearsci.2009.07.006.
- Lundmark, A. M. *et al.* (2012) 'Repeated magmatic pulses in the East African Orogen in the Eastern Desert, Egypt: An old idea supported by new evidence', *Gondwana Research*. International Association for Gondwana Research, 22(1), pp. 227–237. doi: 10.1016/j.gr.2011.08.017.
- Maniar, D. and Piccoli, M. (1989) 'Tectonic discrimination of granitoids', *Geological Society of America Bulletin*. GeoScienceWorld, 101(5), pp. 635–643. doi: 10.1130/0016-7606(1989)101<0635:TDOG>2.3.CO;2.
- McDonough, W. . and Sun, S. -. (1995) 'The composition of the Earth', *Chemical Geology*, 120, pp. 223–252. doi: doi.org/10.1016/0009-2541(94)00140-4.
- Middlemost, E. A. K. (1994) 'Naming materials in the magma/igneous rock system', *Earth-Science Reviews*. Elsevier, 37(3–4), pp. 215–224. doi: 10.1016/0012-8252(94)90029-9.
- Morag, N. *et al.* (2011) 'Crustal evolution and recycling in the northern Arabian-Nubian Shield: New perspectives from zircon Lu–Hf and U–Pb systematics', *Precambrian Research*. Elsevier, 186(1–4), pp. 101–116. doi: 10.1016/J.PRECAMRES.2011.01.004.
- Morag, N. *et al.* (2012) '1000–580 Ma crustal evolution in the northern Arabian-Nubian Shield revealed by U–Pb–Hf of detrital zircons from late Neoproterozoic sediments (Elat area, Israel)', *Precambrian Research*. Elsevier, 208–211, pp. 197–212. doi: 10.1016/J.PRECAMRES.2012.04.009.
- Moussa, E. M. M. *et al.* (2008) 'SHRIMP zircon dating and Sm/Nd isotopic investigations of Neoproterozoic granitoids, Eastern Desert, Egypt', *Precambrian Research*, 160(3–4), pp. 341–356. doi: 10.1016/j.precamres.2007.08.006.
- Nasiri Bezenjani, R. *et al.* (2014) 'Detrital zircon geochronology and provenance of the Neoproterozoic Hammamat Group (Igla Basin), Egypt and the Thalbah Group, NW Saudi

Arabia: Implications for regional collision tectonics', *Precambrian Research*. Elsevier, 245, pp. 225–243. doi: 10.1016/J.PRECAMRES.2013.12.002.

O'Connor, J. T. (1965) 'A classification of quartz rich igneous rock based on feldspar ratios.', *US Geological Survey*, 525B, pp. B79–B84. Available at: [https://www.scirp.org/\(S\(i43dyn45teexjx455qlt3d2q\)\)/reference/ReferencesPapers.aspx?ReferenceID=531502](https://www.scirp.org/(S(i43dyn45teexjx455qlt3d2q))/reference/ReferencesPapers.aspx?ReferenceID=531502) (Accessed: 3 September 2019).

Patchett, P. J. *et al.* (1981) 'Evolution of continental crust and mantle heterogeneity: Evidence from Hf isotopes', *Contributions to Mineralogy and Petrology*. Springer-Verlag, 78(3), pp. 279–297. doi: 10.1007/BF00398923.

Patchett, P. J. (1983) 'Importance of the Lu-Hf isotopic system in studies of planetary chronology and chemical evolution', *Geochimica et Cosmochimica Acta*. Pergamon, 47(1), pp. 81–91. doi: 10.1016/0016-7037(83)90092-3.

Pearce, J. (1996) 'Sources and settings of granitic rocks', *Episodes*, 19(4), pp. 120–125. doi: 10.18814/epiugs/1996/v19i4/005.

Pearce, J. A., Harris, N. B. W. and Tindle, A. G. (1984) 'Trace Element Discrimination Diagrams for the Tectonic Interpretation of Granitic Rocks', *Journal of Petrology*. Narnia, 25(4), pp. 956–983. doi: 10.1093/petrology/25.4.956.

Pearce, J. A. and Peate, D. . (1995) 'Tectonic Implications of Volcanic Arc Magmas', *Annu. Rev. Earth Planet. Sci.*, 23, pp. 251–285.

Pease, V. and Johnson, P. R. (2013) 'Introduction to the JEBEL volume of Precambrian Research', *Precambrian Research*, 239, pp. 1–5. doi: 10.1016/j.precamres.2013.10.003.

Peccerillo, A. and Taylor, S. R. (1976) 'Geochemistry of eocene calc-alkaline volcanic rocks from the Kastamonu area, Northern Turkey', *Contributions to Mineralogy and Petrology*. Springer-Verlag, 58(1), pp. 63–81. doi: 10.1007/BF00384745.

Robinson, F. A. *et al.* (2014) 'Arabian Shield magmatic cycles and their relationship with Gondwana assembly: Insights from zircon U-Pb and Hf isotopes', *Earth and Planetary Science Letters*. Elsevier B.V., 408, pp. 207–225. doi: 10.1016/j.epsl.2014.10.010.

Robinson, F. A. *et al.* (2017) 'A discussion on the tectonic implications of Ediacaran late-to post-orogenic A-type granite in the northeastern Arabian Shield, Saudi Arabia', *Tectonics*. John Wiley & Sons, Ltd, 36(3), pp. 582–600. doi: 10.1002/2016TC004320.

Robinson, F. A., Foden, J. D. and Collins, A. S. (2015) 'Geochemical and isotopic constraints on island arc, synorogenic, post-orogenic and anorogenic granitoids in the Arabian Shield, Saudi Arabia', *Lithos*. Elsevier B.V., 220–223, pp. 97–115. doi: 10.1016/j.lithos.2015.01.021.

Sami, M. *et al.* (2018) 'Petrogenesis and geodynamic implications of Ediacaran highly fractionated A-type granitoids in the north Arabian-Nubian Shield (Egypt): Constraints from whole-rock geochemistry and Sr-Nd isotopes', *Lithos*. Elsevier B.V., 304–307, pp. 329–346. doi: 10.1016/j.lithos.2018.02.015.

Shalaby, A. *et al.* (2005) 'The Wadi Mubarak belt, Eastern Desert of Egypt: a Neoproterozoic conjugate shear system in the Arabian–Nubian Shield', *Precambrian*

Research. Elsevier, 136(1), pp. 27–50. doi: 10.1016/J.PRECAMRES.2004.09.005.

Stein, M. and Goldstein, S. L. (1996) ‘From plume head to continental lithosphere in the Arabian–Nubian shield’, *Nature*, 382, pp. 773–778. Available at: <https://doi.org/10.1038/382773a0>.

Stern, R. J. (1994) ‘ARC Assembly and Continental Collision in the Neoproterozoic East African Orogen: Implications for the Consolidation of Gondwanaland’, *Annual Review of Earth and Planetary Sciences*, 22(1), pp. 319–351. doi: 10.1146/annurev.ea.22.050194.001535.

Stern, R. J. (2002) ‘Crustal evolution in the East African Orogen: a neodymium isotopic perspective’, *Journal of African Earth Sciences*. Pergamon, 34(3–4), pp. 109–117. doi: 10.1016/S0899-5362(02)00012-X.

Stern, R. J. *et al.* (2004) ‘Neoproterozoic Ophiolites of the Arabian-Nubian Shield’, *Developments in Precambrian Geology*, 13(C), pp. 95–128. doi: 10.1016/S0166-2635(04)13003-X.

Stern, R. J. *et al.* (2010) ‘Distribution and significance of pre-neoproterozoic zircons in juvenile neoproterozoic igneous rocks of the arabian-nubian shield’, *American Journal of Science*, 310(9), pp. 791–811. doi: 10.2475/09.2010.02.

Stern, R. J. (2018) ‘Neoproterozoic formation and evolution of Eastern Desert continental crust – The importance of the infrastructure-superstructure transition’, *Journal of African Earth Sciences*. Elsevier Ltd, 146, pp. 15–27. doi: 10.1016/j.jafrearsci.2017.01.001.

Stern, R. J. *et al.* (2020) ‘The Atud gabbro–diorite complex: glimpse of the Cryogenian mixing, assimilation, storage and homogenization zone beneath the Eastern Desert of Egypt’, *Journal of the Geological Society*. Geological Society of London, pp. jgs2019-199. doi: 10.1144/jgs2019-199.

Stern, R. J. and Hedge, C. E. (1985) ‘Geochronologic and isotopic constraints on late Precambrian crustal evolution in the Eastern Desert of Egypt’, *American Journal of Science*, 285, pp. 97–127. doi: 10.2475/ajs.285.2.97.

Sun, S. -s. and McDonough, W. . (1989) ‘Chemical and isotopic systematics of oceanic basalts: implications for mantle composition and processes’, *Geological Society, London, Special Publications*, 42, pp. 313–345. doi: 10.1144/GSL.SP.1989.042.01.19.

Valley, J. W. *et al.* (1998) ‘Zircon megacrysts from kimberlite: oxygen isotope variability among mantle melts’, *Contributions to Mineralogy and Petrology*. Springer Berlin Heidelberg, 133(1–2), pp. 1–11. doi: 10.1007/s004100050432.

Valley, J. W. (2003) ‘Oxygen Isotopes in Zircon’, *Reviews in Mineralogy and Geochemistry*. GeoScienceWorld, 53(1), pp. 343–385. doi: 10.2113/0530343.

Valley, J. W. *et al.* (2005a) ‘4.4 billion years of crustal maturation: oxygen isotope ratios of magmatic zircon’, *Contributions to Mineralogy and Petrology*. Springer-Verlag, 150(6), pp. 561–580. doi: 10.1007/s00410-005-0025-8.

Valley, J. W. *et al.* (2005b) ‘4.4 billion years of crustal maturation: oxygen isotope ratios of magmatic zircon’, *Contributions to Mineralogy and Petrology*. Springer-Verlag, 150(6),

pp. 561–580. doi: 10.1007/s00410-005-0025-8.

Vervoort, J. D. and Blichert-Toft, J. (1999) ‘Evolution of the depleted mantle: Hf isotope evidence from juvenile rocks through time’, *Geochimica et Cosmochimica Acta*. Pergamon, 63(3–4), pp. 533–556. doi: 10.1016/S0016-7037(98)00274-9.

Wang, H. *et al.* (2016) ‘Continental growth through accreted oceanic arc: Zircon Hf-O isotope evidence for granitoids from the Qinling orogen’, *Geochimica et Cosmochimica Acta*. Elsevier Ltd, 182, pp. 109–130. doi: 10.1016/j.gca.2016.03.016.

Wang, Q. *et al.* (2012) ‘Magmatic zircons from I-, S- and A-type granitoids in Tibet: Trace element characteristics and their application to detrital zircon provenance study’, *Journal of Asian Earth Sciences*, 53, pp. 59–66. doi: 10.1016/j.jseas.2011.07.027.

Whalen, J. B., Currie, K. L. and Chappell, B. W. (1987) ‘A-type granites: geochemical characteristics, discrimination and petrogenesis’, *Contributions to Mineralogy and Petrology*. Springer-Verlag, 95(4), pp. 407–419. doi: 10.1007/BF00402202.

Wilde, S. A. and Youssed, K. (2002) ‘A re-evaluation of the origin and setting of the Late Precambrian Hammamat Group based on SHRIMP U–Pb dating of detrital zircons from Gebel Umm Tawat, North Eastern Desert, Egypt’, *Journal of the Geological Society*, 159(5), pp. 595–604. doi: 10.1144/0016-764901-081.

Wilde, S. A. and Youssef, K. (2000) ‘Significance of SHRIMP U-Pb dating of the Imperial Porphyry and associated Dokhan Volcanics, Gebel Dokhan, north Eastern Desert, Egypt’, *Journal of African Earth Sciences*. Pergamon, 31(2), pp. 403–413. doi: 10.1016/S0899-5362(00)00096-8.

Zhu, K. Y. *et al.* (2017) ‘Revisiting Mesozoic felsic intrusions in eastern South China: spatial and temporal variations and tectonic significance’, *Lithos*. Elsevier B.V., 294–295, pp. 147–163. doi: 10.1016/j.lithos.2017.10.008.

Zimmer, M. *et al.* (1995) ‘The Gabal Gerf complex: A precambrian N-MORB ophiolite in the Nubian Shield, NE Africa’, *Chemical Geology*. Elsevier, 123(1–4), pp. 29–51. doi: 10.1016/0009-2541(95)00018-H.

Zoheir, B. *et al.* (2019) ‘Ediacaran (~ 600 Ma) orogenic gold in Egypt: age of the Atalla gold mineralization and its geological significance’, *International Geology Review*. Taylor and Francis Inc., 61(7), pp. 779–794. doi: 10.1080/00206814.2018.1463180.

Zoheir, B. *et al.* (2020) ‘Geochemical and geochronological characteristics of the Um Rus granite intrusion and associated gold deposit, Eastern Desert, Egypt’, *Geoscience Frontiers*. Elsevier B.V., 11(1), pp. 325–345. doi: 10.1016/j.gsf.2019.04.012.

Zoheir, B. A. *et al.* (2019) ‘Orogenic gold in the Egyptian Eastern Desert: Widespread gold mineralization in the late stages of Neoproterozoic orogeny’, *Gondwana Research*. Elsevier Inc., pp. 184–217. doi: 10.1016/j.gr.2019.06.002.

“Every reasonable effort has been made to acknowledge the owners of copyright material. I would be pleased to hear from any copyright owner who has been omitted or incorrectly acknowledged.”

Appendix D:

Supplementary materials to Chapter 5

Table D.1: Whole-rock major and trace elements and Sr-Nd isotopes of the Genina Gharbia granitoids.

	G04-1	G04-2		G04-1	G04-2
Lat.	23°55'48"	23°55'50"			
Long.	34°39'23"	34°39'20"			
Major elements (wt %)					
SiO₂	67.62	74.92	Nb	1.7	1.3
TiO₂	0.27	0.13	Mo	0.0	0.0
Al₂O₃	16.17	13.15	Cd	0.0	0.0
MgO	1.24	0.29	Cs	0.4	0.2
Fe₂O₃	3.57	1.4	Ba	309.2	342.0
CaO	3.63	3.51	La	11.6	12.2
Na₂O	4.7	4.82	Ce	23.8	21.7
K₂O	1.11	0.97	Pr	2.7	2.4
MnO	0.1	0.04	Nd	10.2	9.2
Cr₂O₃	0.002		Sm	2.1	1.7
P₂O₅	0.058	0.047	Eu	1.1	0.9
LOI	1.53	0.82	Tb	0.3	0.2
TOTAL	100	100.097	Gd	2.0	1.5
Trace elements (ppm)					
Li	9.0	4.1	Dy	1.8	1.3
Be	1.0	0.5	Ho	0.4	0.3
Sc	8.1	2.6	Er	1.2	0.7
Ti	1737.8	1008.0	Yb	1.4	0.7
V	40.6	13.0	Lu	0.2	0.1
Cr	6.4	6.1	Hf	0.6	0.3
Mn	717.3	275.9	Ta	0.2	0.1
Co	6.7	1.9	Pb	5.3	4.3
Ni	2.7	1.6	Th	1.3	1.4
Cu	6.5	2.7	U	0.5	0.4
Zn	50.8	17.1	Sr-Nd isotopic data*		
Ga	16.1	10.0	⁸⁷ Sr/ ⁸⁶ Sr	0.7040542	0.7075182
Rb	13.9	17.7	⁸⁷ Rb/ ⁸⁶ Sr	0.1214	0.5066
Sr	330.7	100.9	⁸⁷ Sr/ ⁸⁶ Sr (i)	0.702859	0.70253
Y	13.2	8.5	¹⁴³ Nd/ ¹⁴⁴ Nd	0.512535	0.512501
Zr	16.7	8.9	¹⁸⁷ Sm/ ¹⁴⁴ Nd	0.122216	0.111744
Nb	1.7	1.3	¹⁴³ Nd/ ¹⁴⁴ Nd (i)	0.511982	0.511996
Mo	0.0	0.0	εNd (t)	4.658076	4.934598

*The initial ⁸⁷Sr/⁸⁶Sr and ¹⁴³Nd/¹⁴⁴Nd ratios were calculated using $\lambda^{87}\text{Rb} = 1.42 \times 10^{-11}$ and $\lambda^{147}\text{Sm} = 6.55 \times 10^{-12}$ and the assigned U-Pb zircon ages were collected from SHRIMP and LASS for each sample. The ¹⁴³Nd/¹⁴⁴Nd isotopic ratios are given as epsilon (ε) notations relative to chondritic uniform reservoir (CHUR) (¹⁴³Nd/¹⁴⁴Nd = 0.512630 and ¹⁴⁷Sm/¹⁴⁴Nd = 0.196; Bouvier, Vervoort and Patchett, 2008):

$$\epsilon\text{Nd}_T = [({}^{143}\text{Nd}/{}^{144}\text{Nd}_{\text{sample}})/({}^{143}\text{Nd}/{}^{144}\text{Nd}_{\text{CHUR}}) - 1] \times 10000.$$

Table D.2: Zircon U-Pb of sample G04-2 generated by SHRIMP.

Spot	U (ppm)	Th (ppm)	Th/U	²³² Th/ ²³⁸ U	±%	²³⁸ U/ ²⁰⁶ Pb*	±%	²⁰⁷ Pb* / ²⁰⁶ Pb*	±%	²⁰⁷ Pb* / ²³⁵ U	±%	²⁰⁶ Pb*/ ²³⁸ U	±%	err corr	²³⁸ U/ ²⁰⁶ Pb* Age (Ma)	± 1σ	²⁰⁷ Pb*/ ²⁰⁶ Pb* Age (Ma)	± 1σ	
Lat.	23°55'50"																		
Long.	34°39'20"																		
G04-2@1	109.42	89.20	0.82	0.84	0.36	9.00	2.41	0.05	8.34	0.76	8.68	0.11	2.41	0.28	679.20	15.56	179.28	194.36	
G04-2@2	269.87	106.14	0.39	0.41	0.26	8.80	1.90	0.06	2.53	0.95	3.17	0.11	1.90	0.60	693.86	12.50	615.27	54.74	
G04-2@3	83.02	75.01	0.90	0.93	0.39	8.75	2.13	0.06	7.38	0.90	7.68	0.11	2.13	0.28	697.27	14.09	486.63	162.87	
G04-2@4	96.78	80.18	0.83	0.86	0.38	8.60	2.06	0.07	3.71	1.09	4.25	0.12	2.06	0.49	708.77	13.84	870.80	76.95	
G04-2@5	84.47	71.86	0.85	0.88	0.68	8.87	2.47	0.06	5.07	0.96	5.65	0.11	2.47	0.44	688.52	16.16	657.35	108.82	
G04-2@6	85.76	64.49	0.75	0.78	0.40	8.84	2.08	0.06	4.42	0.96	4.89	0.11	2.08	0.43	691.18	13.66	659.77	94.86	
G04-2@7	84.47	68.32	0.81	0.84	0.39	8.67	2.08	0.07	3.77	1.11	4.30	0.12	2.08	0.48	703.59	13.84	920.33	77.41	
G04-2@8	105.50	81.74	0.77	0.80	0.38	9.12	2.11	0.05	11.11	0.69	11.31	0.11	2.11	0.19	670.72	13.45	-27.86	269.14	
G04-2@9	97.46	100.05	1.03	1.06	0.34	8.88	2.05	0.06	4.43	0.94	4.88	0.11	2.05	0.42	688.19	13.36	611.77	95.63	
G04-2@10	95.49	60.17	0.63	0.65	0.68	8.72	2.41	0.06	3.78	0.98	4.48	0.11	2.41	0.54	699.60	15.98	674.20	80.81	
G04-2@11	123.60	92.38	0.75	0.77	0.34	8.92	2.01	0.06	5.68	0.97	6.03	0.11	2.01	0.33	684.76	13.09	710.25	120.73	
G04-2@12	97.68	73.08	0.75	0.77	0.38	8.81	2.05	0.07	2.65	1.03	3.35	0.11	2.05	0.61	693.45	13.45	803.97	55.52	
G04-2@13	194.54	192.89	0.99	1.02	3.04	8.79	2.09	0.06	3.43	0.89	4.02	0.11	2.09	0.52	694.51	13.77	491.16	75.73	
G04-2@14	83.01	72.28	0.87	0.90	0.40	8.89	2.47	0.06	4.87	0.93	5.46	0.11	2.47	0.45	687.46	16.11	601.65	105.51	
G04-2@15	58.11	36.19	0.62	0.64	0.49	8.94	2.21	0.06	8.22	0.93	8.51	0.11	2.21	0.26	683.38	14.30	617.18	177.50	
G04-2@16	83.23	56.01	0.67	0.70	0.41	9.11	2.16	0.04	12.38	0.66	12.56	0.11	2.16	0.17	671.73	13.76	-132.35	306.00	
G04-2@17	70.67	55.30	0.78	0.81	0.44	8.81	2.18	0.06	8.75	0.88	9.02	0.11	2.18	0.24	693.07	14.35	473.22	193.58	
G04-2@18	123.73	93.17	0.75	0.78	0.34	8.86	2.02	0.06	4.89	0.94	5.29	0.11	2.02	0.38	689.04	13.19	611.72	105.61	
G04-2@19	81.86	67.86	0.83	0.86	0.40	8.80	2.11	0.05	6.84	0.86	7.16	0.11	2.11	0.29	694.11	13.88	411.27	153.01	
G04-2@20	83.05	82.12	0.99	1.02	0.72	8.80	3.03	0.07	2.98	1.06	4.26	0.11	3.03	0.71	694.12	19.97	854.44	61.98	
G04-2@21	52.39	39.42	0.75	0.78	1.25	8.36	3.20	0.05	7.73	0.85	8.36	0.12	3.20	0.38	728.74	22.02	252.87	177.68	
G04-2@22	74.02	60.17	0.81	0.84	1.90	9.52	3.00	0.06	6.43	0.82	7.09	0.11	3.00	0.42	643.99	18.39	478.64	142.09	
G04-2@23	57.57	50.34	0.87	0.90	1.07	9.02	3.00	0.07	4.43	1.05	5.35	0.11	3.00	0.56	677.84	19.30	888.30	91.57	
G04-2@24	90.22	70.32	0.78	0.81	0.99	9.11	2.75	0.06	3.94	0.90	4.80	0.11	2.75	0.57	671.67	17.57	594.30	85.29	
G04-2@25	70.56	49.20	0.70	0.72	1.05	8.81	2.17	0.05	6.20	0.83	6.57	0.11	2.17	0.33	693.15	14.28	339.37	140.42	
G04-2@26	62.18	42.59	0.68	0.71	1.10	8.98	2.95	0.06	4.60	0.96	5.47	0.11	2.95	0.54	680.38	19.05	703.22	97.94	
G04-2@27	63.35	53.68	0.85	0.88	1.02	8.73	2.94	0.06	5.08	0.95	5.86	0.11	2.94	0.50	699.19	19.46	618.70	109.56	
G04-2@28	48.91	34.45	0.70	0.73	1.26	8.98	2.34	0.07	9.29	1.10	9.58	0.11	2.34	0.24	680.59	15.08	980.82	189.15	
G04-2@29	79.12	68.60	0.87	0.90	0.94	8.73	4.41	0.06	3.46	0.96	5.60	0.11	4.41	0.79	698.91	29.21	623.22	74.55	
G04-2@30	57.58	34.83	0.60	0.62	1.21	8.49	3.01	0.06	4.04	1.05	5.03	0.12	3.01	0.60	718.18	20.45	760.20	85.11	

Table D.3: Zircon U-Pb-Hf-O and trace element data of sample G04-2 generated by LASS and SIMS.

Sample #/Spot #	207Pb/235U	± 2σ	206Pb/238U	± 2σ	206Pb/238U Age (Ma)	± 2σ	176Hf/177Hf	±2σ INT	176Lu/177Hf	±2σ INT	εHf(t)	±1σ	T DM Crustal (Ga)	T NC Crustal (Ga)	δ18O (‰)	±2σ
G04-2 - 1	1.042	0.084	0.1155	0.0025	704	15	0.28259	0.000041	0.002588	0.000031	7.61	0.62	1.13	0.90		
G04-2 - 2	1.033	0.056	0.1123	0.0016	685.8	9.1	0.282565	0.000039	0.001795	6.9E-06	6.71	0.59	1.18	0.93		
G04-2 - 3	1.189	0.084	0.1118	0.0021	683	12	0.282567	0.000038	0.002458	0.00002	6.42	0.57	1.19	0.95		
G04-2 - 4	0.973	0.076	0.1158	0.0033	706	19	0.282624	0.000048	0.001261	0.000082	9.48	0.72	1.01	0.79		
G04-2 - 5	1.3	0.12	0.1169	0.0025	712	14	0.2826	0.000046	0.002384	0.000027	8.23	0.69	1.10	0.87		
G04-2 - 6	1.129	0.075	0.1038	0.0021	636	12	0.282628	0.000049	0.00238	0.00012	7.63	0.74	1.08	0.84		
G04-2 - 7	1.046	0.075	0.1153	0.0022	703	13	0.2826	0.00004	0.002169	0.000015	8.14	0.60	1.10	0.86		
G04-2 - 8	1.026	0.076	0.1107	0.0022	677	13	0.2826	0.000035	0.002303	0.000061	7.53	0.53	1.12	0.88		
G04-2 - 9	1.048	0.07	0.1119	0.0018	684	10	0.282572	0.000033	0.002496	9.7E-06	6.60	0.50	1.18	0.94		
G04-2 - 10	0.9	0.062	0.1133	0.0026	691	15	0.282591	0.000033	0.002285	0.000021	7.51	0.50	1.13	0.89		
G04-2 - 11	1.107	0.093	0.1136	0.0021	693	12	0.282585	0.000043	0.002292	0.000018	7.34	0.65	1.14	0.90		
G04-2 - 12	1.133	0.07	0.1189	0.0026	724	15	0.282588	0.000039	0.002104	6.4E-06	8.19	0.59	1.11	0.88	4.99	0.18
G04-2 - 13	1.011	0.074	0.1159	0.0022	707	13	0.282628	0.000047	0.00262	0.000056	9.00	0.71	1.05	0.82	4.85	0.16
G04-2 - 14	1.011	0.07	0.118	0.0024	719	14	0.282605	0.000032	0.00236	0.000022	8.56	0.48	1.08	0.85	4.73	0.28
G04-2 - 15	0.99	0.1	0.116	0.0029	707	17	0.282559	0.000045	0.002253	0.000015	6.73	0.68	1.19	0.95	4.87	0.16
G04-2 - 16	1.015	0.085	0.1148	0.0033	703	19	0.28261	0.000043	0.002557	0.000025	8.31	0.65	1.09	0.85	4.98	0.18
G04-2 - 17	1.276	0.099	0.1142	0.0021	697	12	0.282624	0.000038	0.002318	0.000013	8.79	0.57	1.05	0.82	5.23	0.20
G04-2 - 18	1.023	0.083	0.1125	0.0022	687	13	0.282627	0.000045	0.002513	0.000051	8.60	0.68	1.06	0.82	5.51	0.19
G04-2 - 19	1.158	0.093	0.1212	0.0031	737	18	0.282549	0.000049	0.002384	0.000011	6.94	0.74	1.20	0.96	5.11	0.17
G04-2 - 20	1.023	0.094	0.1135	0.0025	693	14	0.282626	0.000044	0.00262	4.4E-06	8.64	0.66	1.06	0.83	5.14	0.18
G04-2 - 21	1.28	0.1	0.1216	0.0028	739	16	0.282589	0.000041	0.002208	0.000018	8.49	0.62	1.10	0.87	4.99	0.19
G04-2 - 22	0.997	0.086	0.1147	0.0029	700	17	0.282621	0.000041	0.00237	0.000013	8.73	0.62	1.06	0.83	5.27	0.29
G04-2 - 23	0.924	0.09	0.1161	0.0025	708	14	0.282606	0.000036	0.002368	0.000013	8.36	0.54	1.09	0.86	5.08	0.17
G04-2 - 24	1.039	0.098	0.1116	0.0031	684	18	0.282635	0.000045	0.002661	0.000016	8.76	0.68	1.04	0.81	5.07	0.14
G04-2 - 25	1.155	0.07	0.1122	0.0021	685	12	0.282668	0.000038	0.002266	0.000025	10.12	0.57	0.96	0.73	5.01	0.24
G04-2 - 26	1.07	0.096	0.1148	0.0022	700	13	0.282624	0.000049	0.00259	0.000058	8.73	0.74	1.06	0.83	5.44	0.21
G04-2 - 27	1.39	0.12	0.1146	0.0025	699	15	0.28261	0.000056	0.00163	0.0001	8.66	0.84	1.06	0.83	4.91	0.18
G04-2 - 28	0.972	0.095	0.1179	0.0032	718	19	0.282605	0.000042	0.002512	0.000014	8.47	0.63	1.09	0.86	5.21	0.17
G04-2 - 29	1.165	0.094	0.1147	0.003	700	17	0.282598	0.000048	0.002203	0.000069	7.99	0.72	1.10	0.87	4.79	0.21
G04-2 - 30	0.956	0.09	0.1185	0.0022	722	12	0.282594	0.00004	0.002361	0.000011	8.23	0.60	1.11	0.87	5.06	0.19
G04-2 - 31	0.914	0.081	0.1105	0.0023	677	14	0.2826	0.000033	0.002248	0.000045	7.56	0.50	1.11	0.88	5.02	0.18

Sample #/Spot #	Nb	La	Ce	Pr	Nd	Sm	Eu	Gd	Tb	Dy	Ho	Er	Tm	Yb	Lu	Hf	Pb	Th	U	Eu/Eu*	Ce/Ce*	Yb/Gd
G04-2 - 1	0.90	0.00	15.81	0.41	4.41	9.75	0.55	54.50	19.61	234.40	89.10	403.10	85.31	820.70	153.40	9706.00	193.40	61.20	59.40	0.07	116.16	20.05
G04-2 - 2	2.68	0.02	18.15	0.16	1.03	4.01	0.56	27.20	11.48	151.60	64.20	309.80	68.22	668.40	125.70	11484.00	255.70	84.10	162.40	0.16	73.47	32.71
G04-2 - 3	1.41	0.28	21.63	0.81	4.96	9.25	0.65	52.10	18.27	220.30	84.28	387.60	83.65	813.20	150.30	10193.00	269.00	77.30	87.61	0.09	10.91	20.78
G04-2 - 4	1.08	0.00	13.68	0.09	1.31	3.25	0.20	19.70	7.55	94.60	37.50	178.80	39.00	384.00	73.10	10559.00	174.60	53.00	59.30	0.07	224.80	25.95
G04-2 - 5	1.03	2.97	30.40	4.70	17.30	14.90	0.99	61.20	19.73	229.60	84.65	373.30	77.78	745.50	138.10	9422.00	207.00	59.19	56.83	0.10	1.95	16.22
G04-2 - 6	1.59	0.73	37.00	3.26	16.50	12.34	1.99	49.10	16.48	193.10	74.10	341.80	72.37	710.10	133.00	10480.00	254.00	70.10	117.00	0.24	5.76	19.25
G04-2 - 7	0.97	0.38	19.86	0.65	5.35	9.49	0.49	48.40	17.04	202.80	77.25	349.90	73.74	714.80	133.70	9904.00	197.00	64.00	63.98	0.07	9.66	19.66
G04-2 - 8	1.76	0.05	24.30	0.32	2.98	7.12	0.43	41.30	15.18	193.40	74.47	347.50	76.86	734.60	138.40	10935.00	280.00	92.70	117.50	0.08	46.94	23.68
G04-2 - 9	0.94	0.26	22.42	0.74	7.52	14.50	0.90	67.40	23.20	264.00	96.06	423.30	86.21	817.00	148.80	9719.00	261.10	91.51	83.64	0.09	12.32	16.14
G04-2 - 10	1.24	0.03	19.97	0.26	3.43	8.31	0.48	44.00	16.63	203.70	79.63	362.90	78.47	762.40	142.40	10403.00	206.00	69.80	84.10	0.08	52.28	23.07
G04-2 - 11	1.43	6.40	34.10	3.00	11.60	11.00	0.61	51.20	17.71	211.30	81.13	367.90	78.04	758.40	140.70	10158.00	275.00	83.30	87.20	0.08	1.87	19.72
G04-2 - 12	0.90	0.02	16.71	0.20	3.07	7.22	0.47	41.70	15.34	183.20	71.45	325.70	69.47	680.30	128.43	9899.00	169.20	53.50	55.90	0.08	71.30	21.72
G04-2 - 13	0.97	0.17	23.79	0.51	5.76	12.75	0.79	69.50	24.55	285.30	104.60	459.00	95.00	891.00	161.00	10048.00	346.00	117.00	91.20	0.08	19.40	17.07
G04-2 - 14	0.96	2.03	23.35	1.38	7.52	12.51	0.74	58.90	20.18	235.00	86.90	385.30	80.92	772.40	143.30	9877.00	221.30	76.70	72.03	0.08	3.35	17.46
G04-2 - 15	0.73	0.03	12.26	0.22	2.63	7.41	0.38	42.00	15.40	188.10	74.88	338.80	73.12	719.30	136.30	9892.00	102.30	33.92	43.13	0.06	35.90	22.80
G04-2 - 16	0.85	0.03	15.09	0.33	4.66	11.01	0.63	57.90	19.81	236.10	89.73	399.00	84.69	815.70	152.20	9621.00	168.10	56.40	54.50	0.07	35.94	18.75
G04-2 - 17	1.05		20.55	0.32	4.06	9.30	0.57	50.70	18.22	220.60	84.30	382.00	80.61	776.60	144.20	10105.00	278.00	82.10	78.68	0.08		20.39
G04-2 - 18	0.86		19.13	0.73	7.16	12.48	0.64	58.40	20.59	235.00	88.40	390.00	80.95	781.00	145.10	9338.00	194.10	63.86	58.88	0.07		17.80
G04-2 - 19	0.82		17.99	1.32	8.80	11.55	1.01	52.20	18.55	218.50	81.47	368.70	79.35	758.50	141.90	9639.00	156.90	50.20	52.40	0.12		19.34
G04-2 - 20	0.89		16.30	0.35	5.29	10.90	0.67	55.80	20.01	236.70	88.56	399.00	83.96	800.20	150.00	9277.00	171.80	56.94	53.79	0.08		19.09
G04-2 - 21	0.94		14.07	0.35	4.18	8.35	0.62	44.20	15.45	188.20	72.34	329.90	70.21	686.20	129.40	9527.00	141.00	39.70	51.00	0.10		20.67
G04-2 - 22	0.72		15.11	0.20	3.66	8.49	0.61	49.60	17.72	210.00	79.95	366.20	77.23	750.90	139.50	9556.00	146.40	48.80	49.50	0.09		20.15
G04-2 - 23	0.68		13.47	0.21	3.25	9.10	0.54	47.40	17.82	209.40	80.52	364.70	78.76	754.50	142.21	9749.00	127.00	43.57	47.97	0.08		21.19
G04-2 - 24	0.70		15.39	0.28	5.07	11.48	0.80	61.40	21.05	242.40	89.98	397.50	84.13	805.20	149.60	9099.00	155.10	51.86	48.95	0.09		17.46
G04-2 - 25	1.16		19.45	0.45	5.38	9.51	0.54	48.50	17.69	210.90	79.45	355.90	76.25	734.00	136.40	9849.00	175.70	58.53	87.80	0.08		20.15
G04-2 - 26	0.78		18.33	0.50	6.93	12.87	0.76	61.80	21.64	247.80	92.40	408.70	85.50	813.00	150.10	9402.00	190.00	66.60	58.50	0.08		17.51
G04-2 - 27	0.98		19.40	0.75	4.41	5.87	0.37	30.40	11.56	144.80	56.30	262.00	57.00	553.00	105.60	10620.00	181.00	44.80	67.80	0.08		24.22
G04-2 - 28	0.76		13.90	0.22	3.66	8.89	0.56	49.70	18.34	219.50	82.69	381.60	81.13	783.30	147.40	9563.00	132.60	45.70	47.90	0.08		20.98
G04-2 - 29	0.78		18.19	0.45	5.62	10.96	0.69	50.10	17.96	213.40	78.50	350.10	73.50	710.00	129.80	9575.00	184.00	63.30	57.27	0.09		18.87
G04-2 - 30	0.94		17.06	0.20	3.95	9.39	0.55	48.40	17.89	215.60	81.99	366.80	78.89	763.30	142.68	9734.00	173.80	63.86	62.33	0.08		20.99
G04-2 - 31	1.03		19.20	0.72	5.90	8.31	0.70	42.70	15.72	196.20	74.60	346.10	75.80	738.00	139.50	9986.00	151.10	50.00	64.90	0.11		23.01

Part 2:

**Mantle partial
melting and
metasomatism:
Geochemical cycling
and subduction
polarity implications**

Chapter 6:

Cr-spinel records metasomatism not petrogenesis of mantle rocks

This chapter published as:

[Gamal El Dien, H., Arai, S., Doucet, L., Li, Z., Kil, Y., Fougereuse, D., Reddy, S.M., Saxey, D.W., and Hamdy, M., 2019a, Cr-spinel records metasomatism not petrogenesis of mantle rocks: *Nature Communications*, p. 5103, doi:10.1038/s41467-019-13117-1.](#)

Abstract

Mantle melts provide a window on processes related to global plate tectonics. The composition of chromian spinel (Cr-spinel) from mafic-ultramafic rocks has been widely used for tracing the geotectonic environments, the degree of mantle melting and the rate of mid-ocean ridge spreading. The assumption is that Cr-spinel's core composition ($Cr\# = Cr/(Cr + Al)$) is homogenous, insensitive to post-formation modification and therefore a robust petrogenetic indicator. However, we demonstrate that the composition of Cr-spinel can be modified by fluid/melt-rock interactions in both sub-arc and sub-mid oceanic mantle. Metasomatism can produce Al-Cr heterogeneity in Cr-spinel that lowers the Cr/Al ratio, and therefore modifies the Cr#, making Cr# ineffective as a geotectonic and mantle melting indicator. Our analysis also demonstrates that Cr-spinel is a potential sink for fluid-mobile elements, especially in subduction zone environments. The heterogeneity of Cr# in Cr-spinel can, therefore, be used as an excellent tracer for metasomatic processes.

6.1 Introduction

Mantle partial melting is a fundamental process that has contributed to the chemical stratification of the Earth and plays a key role in the long-term evolution of the lithosphere and Earth's tectonic and geodynamic processes in general (Albarède, 1998). Irvine (1965, 1967) first proposed to use chromian spinel ((Mg, Fe⁺²) (Cr, Al, Fe⁺³)₂O₄; hereafter Cr-spinel) in mafic-ultramafic rocks as a petrogenetic indicator because, at magmatic temperatures, this mineral is highly sensitive to the chemical conditions associated with melt generation in the mantle. Numerous subsequent studies have used the composition of Cr-spinel to estimate the degree of melt extraction, and therefore to discriminate among the different tectonic settings of ophiolitic complexes (Dick and Bullen, 1984). Arai (1994) systematically assessed spinel peridotites in terms of mantle melting conditions mainly based on the Cr# (Cr/(Cr + Al)) of Cr-spinel in combination with olivine composition. Cr-spinel has thus been established as a reliable indicator for studying mantle petrology (Hellebrand *et al.*, 2001), where the Cr# of Cr-spinel in residual peridotites has been viewed as a quantitative melting indicator for mantle residue based on the positive correlation between Cr# in Cr-spinel and degree of melting (see Figure 3 of Hellebrand *et al.* (2001).

However, mantle peridotites generally experienced complex metasomatic and metamorphic processes that can potentially obliterate their primary residual origin. Cr-spinel can exhibit a chemical classic (normal) zoning due to melting and fractional crystallization processes characterized by Mg-Al-rich core and Cr-Fe⁺²-rich rim (Dick and Bullen, 1984), or metamorphism that commonly removes almost all the Al from the outer parts of the crystal, leaving behind magnetite/ferritchromite rims (Barnes, 2000). Moreover, reverse zoning (Mg- and Al-rich rim and Fe⁺²- and Cr-rich core) can also occur, and it is usually regarded as a result of stress and deformation (Ozawa, 1989), elemental exchange with co-existing silicates (Bai *et al.*, 2018), or melt/rock interaction (Ceuleneer, 2004). Reverse zoning is undetectable under an optical microscope, and it appears either concentric and/or asymmetric when observed in atomic number contrast under backscattered electron (BSE) imaging (Bai *et al.*, 2018), or remains non-observable under both an optical microscope and BSE (this study).

Here, we conduct a correlative microanalysis workflow from the grain-scale to the nano-scale using X-ray elemental mapping, electron microprobe (EMP), laser-ablation inductively coupled plasma mass spectrometry (LA-ICPMS), electron backscattered diffraction (EBSD), and atom probe tomography (APT) in order to describe the Cr-spinel reverse zonation in mantle peridotites from the Arabian Nubian Shield. This type of reverse zoning “Al-Cr heterogeneity” is characterized by Al enrichment and Cr depletion in the rim compared to the core of the studied crystals. We demonstrate that this reverse zoning is unrelated to the magmatic or metamorphic/deformation history but is due to fluid/melt-rock interactions (i.e., metasomatism). The most striking feature is that such Cr-spinel Al-Cr heterogeneity is a widespread feature that affects the mantle rocks of various tectonic settings and ages (Figure E.1 and Supplementary Data 1). We therefore question the robustness of Cr-spinel during post-formation modification, and thus the suitability of Cr-spinel as a straightforward reliable indicator for tracing mantle melting conditions and tectonic environments.

6.2 Methods

6.2.1 Bulk rock chemical analysis

Whole rock geochemistry of major and trace (including rare earth) elements were carried out for some samples of serpentinized peridotites (Supplementary Data 2; all whole-rock results are reported on a volatile-free basis). Whole-rock samples were crushed with a polyethylene-wrapped hammer into <0.5 cm pieces and then grounded with ethyl alcohol in an agate mill to grain sizes below 50 μm . Major element compositions were analyzed using a X-ray fluorescence spectrometer (Shimadzu, XRF-1800) at the Pukyong National University, South Korea. Analytical conditions were 40 kV accelerating voltage and 70 mA beam current. Analytical precision is better than 2% for major elements. All glass beads were analysed three times and the averages are used. The trace and rare-earth elements of the studied samples were analysed using an ICP-MS (VG Elemental Ltd., PQ3) at the Korean Basic Science Institute (KBSI) at Ohchang, South Korea. Acid digestion with hydrofluoric acid is routinely used to digest geological materials for the trace-element determination. A

100 mg of powdered sample was accurately weighed into the PTFE digestion vessel, added with 5 ml mixed acid (HF: HNO₃: HClO₄ = 4:4:1). The sample vessel was tightly capped and placed on a hot plate for 24 hours at 190 °C and then cooled to room temperature. After opening the cap, the sample was subsequently evaporated to incipient dryness. The above process was repeated once more. The residue was dissolved in 10 ml of 1% HNO₃ with gentle heating, until a clear solution resulted. Determinations for USGS reference samples (BIR-1 and MUH-1) agree with recommended values within suggested tolerances. The precision of the measurements by repeated analyses of reference samples is better than ±5% for trace elements.

6.2.2 Electron probe micro analyses (EMPA)

Quantitative chemical analyses of major and some minor elements in Cr-spinel were carried out using a JEOL JXA-8800 electron-probe at Kanazawa University, Japan (Supplementary Data 2). The analytical conditions were 20 kV accelerating voltage, 20 nA probe current and 3 µm beam diameter. A ZAF-correction was made to correct the raw data. Ferric and ferrous iron redistribution from electron microprobe analyses was made using the charge balance equation of Droop (1987). Natural mineral standards were used for calibration: quartz for Si, corundum for Al, eskolaite for Cr, fayalite for Fe, periclase for Mg, manganosite for Mn, wollastonite for Ca, jadeite for Na and pentlandite for Ni. Si (<0.03 wt %) and Na (<0.02 wt %) for the studied Cr-spinel are below the detection limits.

6.2.3 X-ray mapping of Cr-Spinel

Al-Cr-Mg-Fe X-ray element distribution maps of Cr-spinel grains in the studied peridotites were acquired using a wavelength dispersive X-ray spectrometry (WDS) on a JEOL JXA-8800 electron-probe at Kanazawa University, Japan. The analytical conditions were 20 kV accelerating voltage, 20 nA probe current and <1 µm beam diameter. Dwell times on each spot were between 20 and 30 ms according to the analysed element and the sensitivity of the detector.

6.2.4 Electron back-scattered diffraction (EBSD)

EBSD data were collected at the Microscopy and Microanalysis Facility, John de Laeter Centre, Curtin University, using a Tescan MIRA3 SEM with Oxford Instruments Symmetry EBSD detector. Data were collected at 20 kV and ~1nA beam current, with an analytical step size of 2 μ m. EBSD data were collected using Oxford Aztec 4.1 acquisition software. Data were noise reduced using a wildspike and 5 nearest neighbor zero solution algorithm in Oxford Instruments Channel 5.12 software. Channel 5.12 was also used to create misorientation maps used to investigate the microstructural relationship between spinel core and rim. Relatively poor-indexing of the spinel represents the difficulty in polishing the analysed grains after laser-ablation analysis.

6.2.5 Laser ablation-inductively coupled plasma-mass spectrometry (LA-ICP-MS) micro analysis

Trace element compositions of Cr-spinel (Supplementary Data 2) were determined using a 193 nm ArF Excimer LA-ICP-MS at Korean Basic Science Institute (KBSI), South Korea (Teledyne Cetac Technologies equipped with Analyte Excite). Analyses were performed by ablating 30-50 μ m diameter spots at 10 Hz with an energy density of 5 J/cm² per pulse. Signal integration times were 60s for a gas background interval and 60s for an ablation interval. The NIST SRM 612 glass was used as the primary calibration standard and was analyzed at the beginning of each batch of <5 unknowns, with a linear drift correction applied between each calibration. The element concentration of NIST SRM 612 for the calibration is selected from the preferred values of Pearce *et al.* (1997). Each analysis was normalized using ⁵⁷Fe as internal standard elements, based on Fe contents obtained by Electron probe micro analysis. All minerals were analyzed multiple times and the averages were used. The relative standard deviations (RSD) of the trace elements in the minerals were mostly 5–10%. We used the Glitter software to process the data, which shows ablation profiles for elements and permits to reduce analytical contamination. The LA-ICP-MS ablation profiles of the intensity (counting) vs time for all analyses of the studied Cr-spinel are provided in supplementary information (Figure E.12). None of the calculated peaks has any significant spike signals for ²⁹Si and ⁵⁷Fe, which indicates that no silicate inclusion and/or magnetite was measured. The slight difference between EPMA and

LA-ICPMS data for trace elements such as Ni, Mn and Ti is due to matrix effect and the different standards used, but the LA-ICPMS data is more precise than the EMPA data especially for trace elements.

6.2.6 Atom probe tomography (APT)

Atom probe tomography has the ability to characterize and visualize the 3D distribution of atoms at sub-nanometer resolution (Saxey *et al.*, 2018). Recent advancements and the development of laser pulsing capabilities has made possible the analysis of non-conductive materials such as most rock-forming minerals. The technique is based on the field-evaporation of atoms from a needle-shaped specimen under a high electric field. The 3D position of atoms is given by the impact location on a position sensitive detector and the succession of detection events. The ions are identified using time-of-flight mass spectrometry by measuring the time between the laser pulse and the detection event. For more details about this technique see Larson *et al.* (2013) and Fougrouse *et al.* (2016). Four needle-shaped specimens (7 μm length and 2.5 μm depth for each one) for APT measurements were prepared with a Ga⁺ Tescan Lyra3 focused ion beam coupled with a scanning electron microscope (FIB-SEM) at Curtin University following the lift out method (Thompson *et al.*, 2007). The specimens were extracted from a polished thin section and their location is indicated on Figure 6.1b (Supplementary Data 2). The FIB was operated at 30 kV during the manufacturing of the specimen and a low kV (2 kV) clean-up was implemented to remove the surface layer affected by high-energy Ga⁺ ion implantation. APT measurements were performed on a CAMECA LEAP 4000X HR at Curtin University. The instrument was operated in laser mode ($\lambda = 355 \text{ nm}$) with a laser pulse energy of 150 pJ and a pulse frequency of 200 kHz. The specimens were kept at 60 K during analysis with a detection rate maintained at 1 detection event every 100 laser pulses. The specimens yielded between 100 million atoms (M5, M6 and M10) and 109 million atoms (M8) (See Supplementary Movies 1 and 2 for Al in M6 and M10 specimens). The mass spectra were characterised by large peak tails similar to other oxides such as rutile (Verberne *et al.*, 2019). In the mass spectra (Figure E.13), the cations are present as different molecular species with singly-charged to triply-charged ions. For example, Cr is present as Cr⁺, Cr⁺⁺, CrO⁺, CrO⁺⁺, CrO₂⁺, CrO₂⁺⁺, CrO₃⁺ and Cr₂O₃⁺; and Al is present as Al⁺, Al⁺⁺, Al⁺⁺⁺, AlO⁺, AlO⁺⁺, AlO₂⁺, Al₂O⁺⁺, and AlCrO₃⁺⁺. The combination of multiple ionic species for each element and large thermal peak tails

leads to difficulties in quantifying the composition of the analysed nano-scale domains. The estimation of the O composition from atom probe data is also renowned to be difficult (Gault *et al.*, 2016). These limitations indicate that the composition calculated from the atom probe data will differ from expected stoichiometry and other techniques that apply standardization protocols (i.e. EPMA and LA-ICPMS). However, the method used for the calculation of the composition in this study was consistent across all datasets, indicating that the differences between atom probe specimens are reliable.

6.2.7 Filter criteria for Cr-spinel data

Based on the available data, we filtered out modified Cr-spinel results that (1) show Al-Cr reverse/ asymmetric zoning “heterogeneity” in the same grain, (2) have high Al and Cr content range > 1.5 wt %, standard deviation >0.5 or > 5% variability percentage within a single sample, and (3) have Cr# variability greater than 1% or standard deviation > 0.01 within a single sample. In addition, we excluded samples that have Cr-spinel with only one analysis and no standard deviation or variability percentage.

6.3 Results

6.3.1 Al-Cr reverse zoning in spinel: An example from the Arabian-Nubian Shield

The Arabian-Nubian Shield (ANS) represents the largest Neoproterozoic juvenile continental crust formed through accretion of island arcs to continental margins by the closure of the Mozambique Ocean during the East-African orogeny (750–550 Ma) (Johnson *et al.*, 2011; Hamdy *et al.*, 2017). The peridotites in this study were sampled from serpentinite bodies at Wadi Alam in the Central Eastern Desert of Egypt (Figure E.2). Petrographic and textural investigations show that our peridotite samples consist of serpentine minerals, olivine relics, orthopyroxene bastites, carbonates, and Cr-spinels, with no amphiboles or chlorite. The samples have been affected by varying degrees of serpentinization. The predominance of pseudomorphic textures as mesh and bastite reflects a harzburgite protolith (Figure E.2). For more details about the geological background of the ANS see Gamal El Dien *et al.* (2016),

and for field observations and petrographical and mineralogical descriptions of the studied rocks see Hamdy and Gamal El Dien (2017).

The petrological and geochemical characteristics of the studied peridotites reveal a highly depleted origin, as shown by (1) a harzburgitic, clinopyroxene-free modal composition, (2) their low Al₂O₃ and high MgO bulk-rock content (<1 wt% and >44 wt %, respectively) (Figure E.3 and Supplementary Data 2) and (3) their low, heavy rare earth elements content (HREE; Yb_{N(CI-normalized value)} = 0.01-0.04) and low Y (<0.10 ppm) (Figure E.4). Melting models, using non-modal fractional melting, reproduced the HREE values of our samples with a 25–30% melt extraction from a depleted MORB mantle (DMM) source (Workman and Hart, 2005; De Hoog *et al.*, 2009) (Figures E.4, 5). This supports the highly refractory origin for the studied mantle peridotites. The bulk-rock major and trace element contents, and REE patterns, are similar to mantle wedge peridotites (Franz *et al.*, 2002; Ishimaru *et al.*, 2007; Ionov, 2010; Deschamps *et al.*, 2013) (Figures E.3, 4). Despite their refractory origin, the studied peridotites exhibit enrichment in incompatible trace elements and light REE (LREE) (Figure E.4). These enrichments are not correlated with either serpentinization (i.e., loss on ignition) (Figure E.6) or the different melting indices used (Figure E.3i), which indicates that the rocks underwent a post-melting metasomatic process (Bodinier *et al.*, 1990). This metasomatism process is believed to be due to fluid/melt-rock interaction between mantle wedge peridotites and slab-derived melts, as supported by a high enrichment of high field strengths elements (HFSE) (Figure E.7) and fluid-mobile elements (FME) in those rocks (Hamdy and Gamal El Dien, 2017). Generally, migration of aqueous fluids/melts from a subducting slab enriches the overlying mantle with incompatible elements (i.e., FME) and water, yielding metasomatized sub-arc mantle (Schiano *et al.*, 1995; Gamal El Dien *et al.*, 2019).

Cr-spinel represents up to 2 % of the mineral modal composition in our samples and exhibits a holly-leaf shape with a red color characteristic of residual peridotites (Hellebrand, Snow and Mühe, 2002). It presents as anhedral to subhedral grains of 50 µm to 2 mm in size. In BSE images, all Cr-spinel grains display small magnetite rims either surrounding a homogenous core and/or appearing in open cracks, indicating a late-stage modification (i.e., serpentinization and/or metamorphism; Figure 6.1a and Figure E.8). However, X-ray elemental mapping shows strongly heterogeneous and modified cores (Figure 6.1b-f). These cores display a concentric and gradual (Figure 6.1b, c, e, f) or asymmetrical (Figure 6.1d) reverse

zoning of highly Al-enriched and Cr-depleted rims and the opposite in the cores (we called this heterogeneity hereafter) with less variation in the distribution of Mg and Fe⁺² (Figure 6.2, Figure E.8, and Supplementary Data 2).

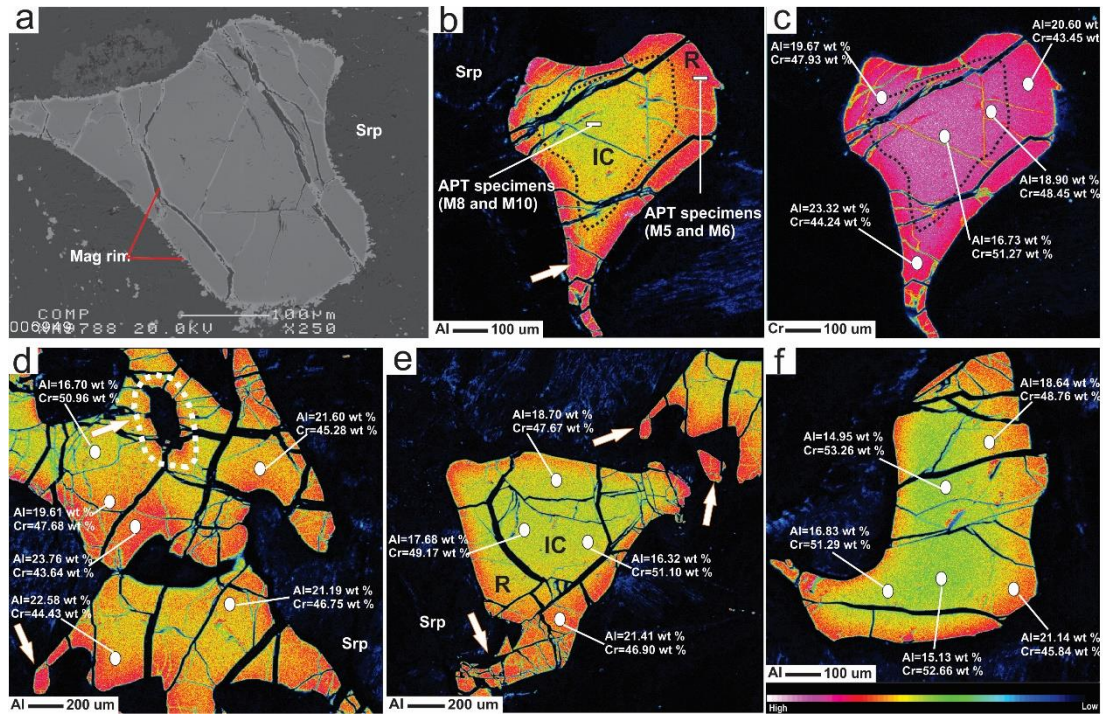


Figure 6.1: X-ray elemental map of the studied Cr-Spinel. (a) Backscattered electron (BSE) image of a Cr-spinel grain with a homogenous core surrounded by a small magnetite rim. Al (b) and Cr (c) X-ray map for the same grain show reverse zoning for Al and Cr. Asymmetrical and heterogeneous distribution of Al-Cr within the core (d) and gradual increase of Al-Cr from core to rim (b, c, e, f) of three different Cr-spinel grains. White arrows point to Al halos around inclusions within the Cr-spinel grains (d) and high Al content in small grains with tightly curved rims (b-e). The results of the Atom probe tomography (APT) specimens for the core (M8 and M10) and rim (M5 and M6) are shown in Figures 8.5. Mag = magnetite, Srp = serpentine, IC = inner core and R=rim.

The cores of Cr-spinels show a wide variation in compositions between grains from the same sample (core-to-core: Figures 6.1c, f and 2f), among samples (Figures 6.1c-f and 2c-e), and within the same grain (core to rim: Figures 6.1c-f, 2f and Supplementary Data 2). The Al₂O₃ content and Cr# display a continuous reverse variation trend from the cores (14.6–18.3 wt %, and 0.64–0.70, respectively) to the rims (19.6–26.1 wt % and 0.53–0.62, respectively) (Figures 6.1c-f and 2c-f). Al₂O₃ content shows different covariation trends, from the cores to the rims, with transition elements such as Sc (negative correlation), Ti and Ni (positive correlation), Cu and Ga (no correlation), whereas V, Mn, Co and Zn show V-shape covariation trends (Figure E.9). Fluid mobile elements (FME: Li, Rb, Sr, Cs, and Sb) increase with increasing

Al₂O₃ content from cores to rims (Figure 6.3). The opposite correlation is found between those elements and Cr₂O₃ content. We thus used Al content as a representative for these elemental variations in the following discussion.

Metasomatism is a ubiquitous phenomenon in the Earth's mantle and can be a protracted chemical process that modifies the primary chemical composition of pre-existing rocks and their composing minerals (Bailey, 1982). Metasomatism can be identified by drastic changes in the rocks' mineralogy (called modal metasomatism or refertilization) or by subtly incompatible trace element enrichment in the rocks and minerals, also called cryptic metasomatism (Harte, Hunter and Kinny, 1993). This process can happen in a sub-arc mantle (for example, arc-peridotites: Prouteau *et al.*, 2001; Arai and Ishimaru, 2008), and in a sub-oceanic mantle (i.e., Mid Ocean Ridge (MOR)-peridotites: Warren, 2016).

The most striking feature of the studied peridotites is the positive covariation between Al content and FME (Li, Rb, Sr, and Cs) contents in Cr-spinel (Figure 6.3a-d). This shows that slab-derived fluids-rock interactions were responsible for the Al-Cr heterogeneities (i.e., addition/depletion) in Cr-spinel, rather than fractional crystallization/melting (Sigurdsson and Schilling, 1976; Dick and Bullen, 1984), subsolidus elemental exchange (Bai *et al.*, 2018), or stress (Ozawa, 1989). The primitive mantle-normalized pattern of the FME of the studied Cr-spinel (Figure 6.3e) shows similarities to the average pattern of subduction inputs which includes altered oceanic crust (AOC) (Staudigel, 2013), global subducted sediments (GLOSS II) (Plank, 2013), and marine sediments (Li and Schoonmaker, 2013). The studied Cr-spinels also have similar FME contents as melt inclusions in Cr-spinels from the Avacha peridotite xenoliths, which experienced interactions with slab-derived melts (Ionov, Bénard and Plechov, 2011) (Figure 6.3e). Moreover, FME in the studied Cr-spinel cores and rims are highly enriched relatively to primitive mantle (McDonough and Sun, 1995), in contrast to Cr-spinel in refractory/depleted peridotites (Szilas *et al.*, 2018) (Figure 6.3e). This indicates that the compositions of both their cores and rims have been modified. We interpret the Al, Cr and FME zoning in Cr-spinel to be the result of cryptic metasomatism by interactions of hydrous Al-rich slab-derived melts with the host peridotites.

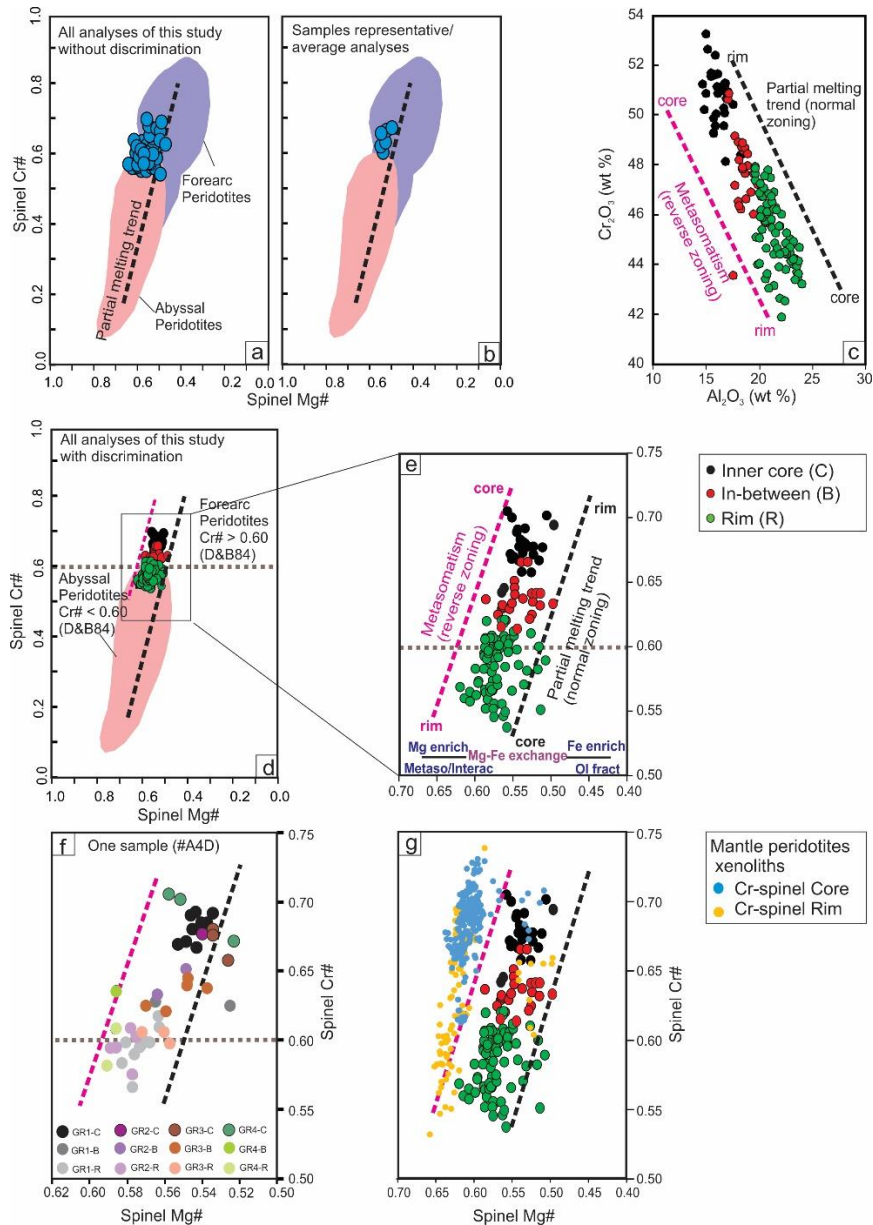


Figure 6.2: Plots of the studied Cr-Spinel chemical composition for different zones within the grains. (a) Cr# ($Cr/Cr + Al$) vs. Mg# ($Mg/Mg + Fe^{+2}$) plot of all the raw datasets for Cr-spinel grains in the studied rocks. Such data are usually not published in previous literature. The data span between recommended fields used in previous literature for abyssal peridotites (Dick and Bullen, 1984) and fore arc (FA)-peridotites (Ishii *et al.*, 1992; Parkinson and Pearce, 1998). (b) Representative/average Cr-spinel data for each sample. Such sample-average data are usually used in previous mantle petrology studies. This plot shows that our samples had a fore arc origin. (c) Al_2O_3 vs Cr_2O_3 and (d) Cr# vs Mg# plots of the studied Cr-spinel grains with low Al_2O_3 and high Cr_2O_3 and Cr# in their cores, and high Al_2O_3 and Low Cr_2O_3 and Cr# in their rims (reverse zoning). Partial melting trend and the brown line between abyssal peridotites ($Cr\# < 0.60$) and FA-peridotites ($Cr\# > 0.60$) are from Dick and Bullen (1984). (e) All datasets have trends parallel to both the melting trend and our newly defined metasomatism trend. (f) Datasets of different zones (from core to rim) from four grains from a single sample (sample # A4D) that show large Al-Cr heterogeneity. The data span across the whole range between abyssal peridotites and FA- peridotites. (g) Plots of the studied Cr-spinel grains compared with the compositions of both modified spinel/rims and non-modified spinel/cores of published mantle peridotite xenoliths (Franz *et al.*, 2002; Ishimaru *et al.*, 2007; Ishimaru and Arai, 2009; Ionov, Bénard and Plechov, 2011).

Deformation/stress can lead to Al and Cr crystal lattice diffusion resulting in Al-Cr dipolar zoning in elongated Cr-spinel grains in deformed peridotites (Ozawa, 1989). Contrary, the studied peridotites have massive textures at the field scale with no foliation/schistosity (Figure E.2c) and minerals aggregates have rounded shape and granular texture without any elongation and/or lineation arrangement (Figure 6.1 and Figure E.2d-h). In contrast to the dipolar zoning, the studied Cr-spinels show a concentric Al-Cr zonation (Figure 6.1 and Figure E.8). To test the effect of deformation/stress and microstructure of Cr-spinel grains, EBSD has been used to quantify the crystallographic orientation and microstructural characteristics of some Cr-spinel grains (Figure 6.4). The maximum misorientation in each grain from these points is 10° and 15° for grain 1 and 2, respectively (Figure 6.4a, b). This misorientation variation is spatially linked to the late brittle fractures that cut the grains (including the Al-Cr zoning seen in the X-ray elemental maps data (Figure 6.1b, f). Within individual, fracture-bound fragments of the grains, there is no evidence for any lattice orientation variation or significant plastic deformation. This includes fragments that contain the observed core to rim compositional variations. Hence, there is no relationship between the observed compositional Al-Cr heterogeneity in Cr-spinel and grain-scale deformation. In addition, the $\text{Fe}^{3+}/(\text{Fe}^{3+} + \text{Fe}^{2+})$ ratio, which is widely used as metamorphism-related enrichment indicator of the Cr-spinel (Barnes, 2000), has constant values between the Cr-spinel cores and rims and has no relationship with Al and FME (Figure E.10) giving a clear evidence that the enrichment process of those elements is not related to the late stage metamorphic processes.

On the crystal scale of the studied Cr-spinel, the interpreted metasomatism process is demonstrated by high Al content in fine-grained Cr-spinel and in tightly curved rims that would have been more affected by melt/rock interaction than coarser grains (Franz *et al.*, 2002; Arai, Ishimaru and Okrugin, 2003; Ionov, 2010) (Figure 6.1b-f); idiomorphic shapes for some grains (Figure 6.1b) that reflect high degrees of melt/rock interaction, where melt diffusion into the peridotites not only modified the composition of the Cr-spinel, but also corroded and modified the crystal morphology (Ohara and Ishii, 1998); and Al-rich halos around inclusions, which is expected to form during melt/rock interaction inside Cr-spinel grains, whereas the trapped melts modified the surrounding Cr-spinel (Figure 6.1d and Figure E.8c) similar to high Al

zone reported around melt inclusions in Cr-spinel from the Avacha peridotite xenoliths (Ishimaru and Arai, 2009; Ionov, B enard and Plechov, 2011).

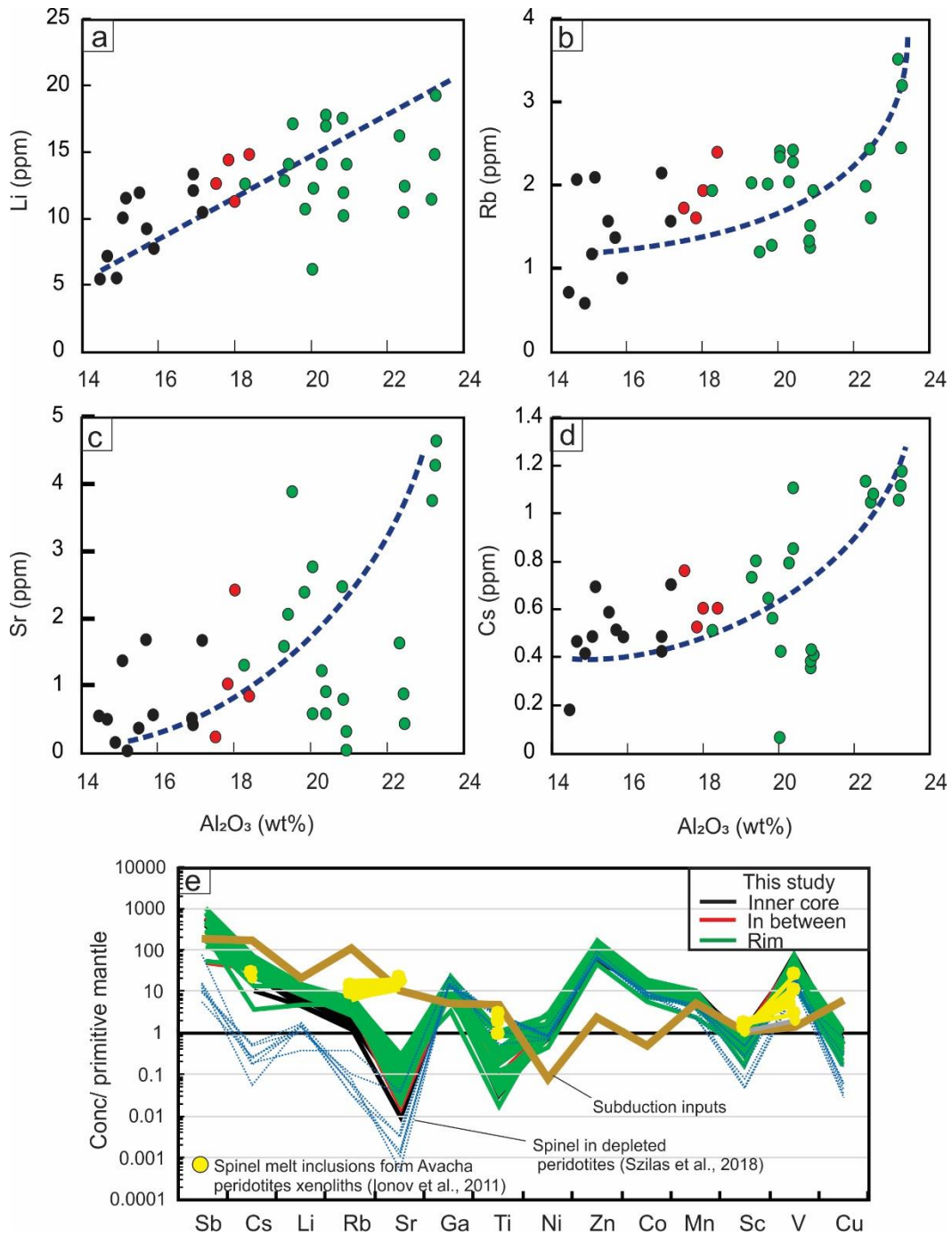


Figure 6.3: Trace elements concentration of different zones in the studied Cr-Spinel. (a- d) Covariation between Al₂O₃ (wt %) content and fluid-mobile elements (FME: Li, Rb, Sr and Cs). All the elements show positive a correlation with Al content and an increase from core to rim. (e) FME and transition elements normalized to primitive mantle(McDonough and Sun, 1995) compare with the average content of subduction inputs including altered oceanic crust (AOC) (Staudigel, 2013), global subducted sediments (GLOSS II) (Plank, 2013) and marine sediments (Li and Schoonmaker, 2013), melt inclusions in Cr-spinel from Avacha peridotite xenoliths (Ionov, B enard and Plechov, 2011), and spinel in refractory/depleted peridotites (Szilas *et al.*, 2018). The Cr-spinel show high enrichment in FME, attributed to slab-derived fluid/melt interaction with host peridotites.

The observation that some grains have Al-Cr heterogeneity extended inside the grain up to 200 μm (Figure 6.1) suggests that such heterogeneity in the grains is not an artifact of a deep embayment of Cr-spinel grains during cutting i.e. sectioning effect. In addition, LA-ICPMS data confirm the existence of such heterogeneity in different zones of the Cr-spinel (Figure 6.3). To further verify the 3D Al-Cr heterogeneity in the studied Cr-spinel, we applied Atom Probe Tomography (APT) advanced technique, which is a powerful tool to characterize and construct the 3D chemistry at the nanoscale (see methods for more details). Four needle-shaped specimens (Figure 6.5) from the core (M8 and M10) and the rim (M5 and M6) were extracted from sample A4D (Figure 6.1b). The specimens yielded between 100 million atoms (M5, M6 and M10) and 109 million atoms (M8). The core specimens M8 and M10 have Cr = 24.1 atomic % (at%) and 24.4 at%, respectively and Al = 9.0 at% and 8.9 at%, respectively (Figure 6.5 and Supplementary Data 2). On the other hand, the rim specimens M5 and M6 have Cr = 22.1 atomic % (at%) and 22.3 at%, respectively and Al = 10.7 at% and 10.6 at%, respectively (Figure 6.5, Supplementary Data 2 and Supplementary Movies 1 and 2 for Al in M6 and M10 specimens, respectively). Although the major element composition calculated from the APT data differs from EMPA and LA-ICPMS data due to the lack of standardization protocols, the APT results confirm the enrichment of Al and depletion in Cr in the rim, and the opposite for the core (Figure 6.5). Also, the detection limit of APT for the FME in Cr-spinel is too high to make meaningful measurements. The homogenous distribution of Al, Mg and Fe, non-detection of Si, and absence of any isolated clusters across the specimens, thus indicate that the high FME concentration in Cr-spinel is inherited and not related to silicate inclusions (i.e., serpentine phases), Fe-oxide nano-scale inclusions (magnetite) or low temperature alteration (Figure 6.5).

The above observations make the measured Cr-spinel composition unsuitable for deciphering the partial melting history of the studied peridotites. The melt/rock interaction between mantle peridotites and slab-derived fluids/melts may produce a strong heterogeneity that modifies the Al and Cr contents (i.e., Cr#) of primary Cr-spinel, and therefore produces a reverse trend/range (metasomatism trend) of Cr# in the studied mantle rocks, different from the melting trend. Plotted together on the Cr# vs. Mg# diagram (Figure 6.2d), the Cr# of the rims (mostly <0.6) are similar to MOR-peridotites, and the cores (with Cr# >0.60) are similar to Fore arc (FA)-peridotites (Dick and Bullen, 1984). This indicates that representative and/or average Cr# values

of Cr-spinel could give a misleading conclusion about the geotectonic setting of our samples (Figure 6.2a, b). For example, applying the equation of Hellebrand et al. (2001) [$F = 10 \ln (Cr\#) + 24$] to the studied Cr-spinel would indicate 17–18% melting if using the values from the rim, and > 20 % melting when using the values from the core. Such values are not consistent with the bulk rock data (Figures E.4, 5). We therefore conclude that for peridotites that experienced post-melting fluid/melt-rock interactions, their Cr-spinel data should not be used for determining the tectonic setting and melting history.

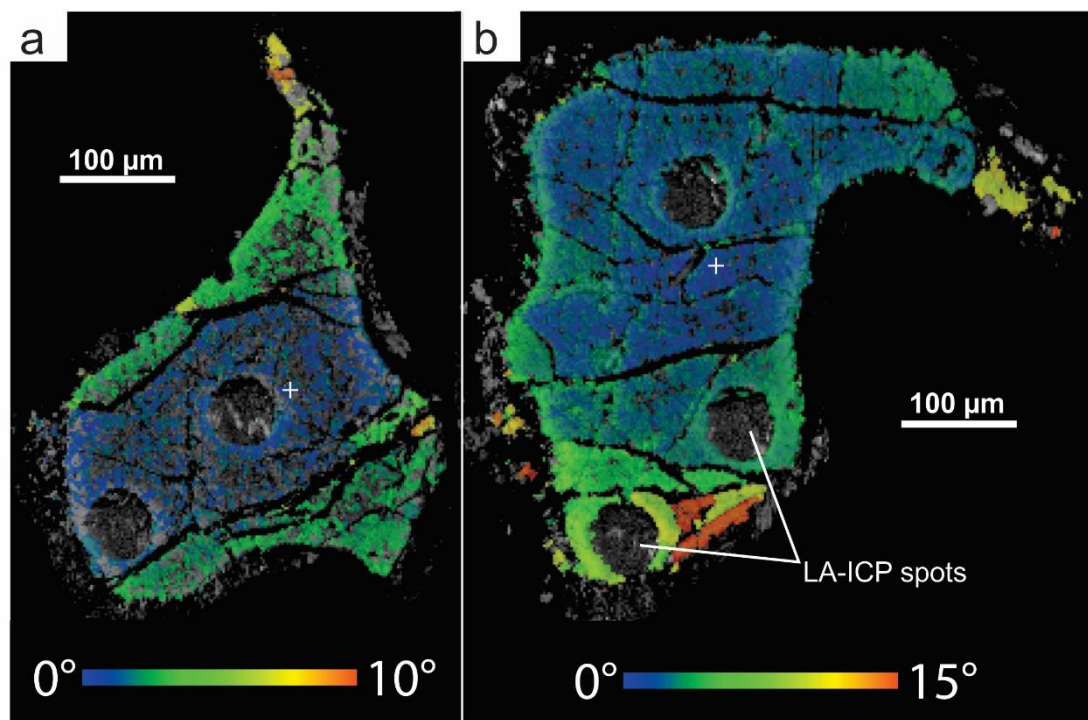


Figure 6.4: EBSD microstructural data from two Cr-spinel grains from sample A4D. Images comprise greyscale image of EBSD pattern quality overlain by misorientation maps measured relative to the orientation of spinel lattice at the position shown by the white cross. For grain (a) total misorientation is 10°, for (b) the total misorientation is 15°. The change in misorientation in each grain corresponds to presence of late fractures seen in the pattern quality image. Total misorientation within individual fracture-bound regions of the grain is <1°, indicating that there is no plastic deformation within the grains.

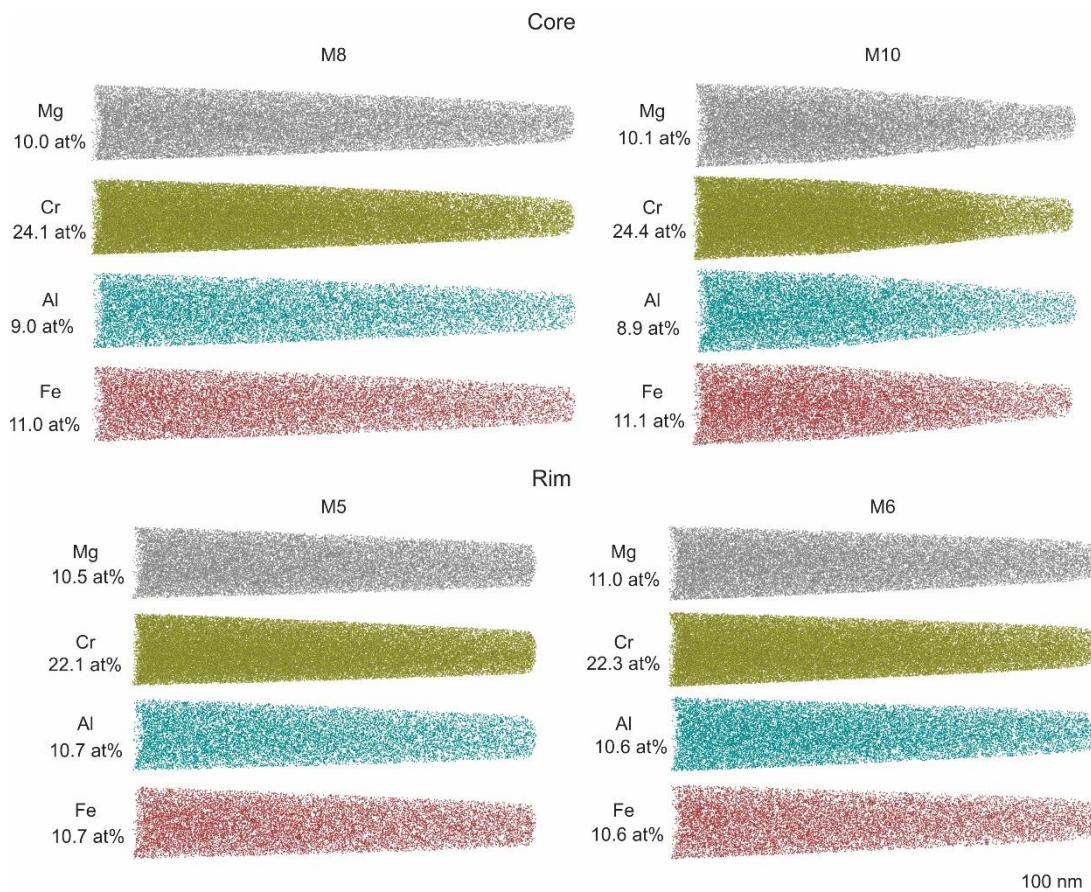


Figure 6.5: Atom probe tomography results. Atom maps of Mg, Cr, Al and Fe are presented for needle-shaped specimens from the core (M8 and M10) and the rim (M5 and M6). The specimens were extracted from sample A4D and their location is indicated on figure.1b. The composition in atomic % is indicated for each specimen (See Supplementary Data 2). The composition of the core is enriched in Cr and depleted in Al compared to the rim.

6.3.2 A re-evaluation of Al-Cr heterogeneity in Cr-spinel from previous studies

Our study shows that metasomatism can dramatically change the composition of Cr-spinel (i.e., Cr#). A careful literature review revealed that Cr-spinel compositional heterogeneity can be found in most mantle rocks of various tectonic environments and ages (Figure E.1 and Supplementary Data 1). These include all available Cr-spinel data from arc-peridotites composed of FA-peridotites (including dredged samples from the present-day oceanic arc, e.g., the Izu-Bonin-Mariana arc, and mantle wedge xenoliths such as those from the Kamchatka arc) and back-arc peridotites (i.e., Mariana Trough), plus abyssal/MOR-peridotites (Supplementary Data 3).

Strikingly, even though some of the reported Cr-spinel have homogeneous compositions, the majority of the reported Cr-spinel from arc-peridotites, FA-

peridotites in particular, show high heterogeneity in Al and Cr contents both within single grains (with core-rim structures) (Bloomer and Fisher, 1987; Parkinson and Pearce, 1998; Franz *et al.*, 2002) and within a single sample (from core to core) (Ishii *et al.*, 1992; Ohara *et al.*, 2002, 2003), which we hereafter refer to as modified Cr-spinel. Based on the available data from arc-peridotites (Figure 6.6a), we filtered the modified/non-modified Cr-spinel using the Al-Cr variability between the core and rim of a single grain, and between cores of grains from the same sample (see methods). The non-modified Cr-spinel grains that have tight Cr# for a single sample display a different Cr# range of ~0.45–0.70 (Figure 6.6d) for FA-peridotites from that of the accepted range used in previous studies (~0.30–0.85) (Figure 6.6a), and back arc-peridotites have Cr# range of ~0.15–0.65 that significantly overlapped with FA-peridotites (Figure 6.6a, c).

In contrast, metasomatism is slightly different in abyssal/MOR-peridotites due to the rarity of hydrous fluids. It is driven by a melt-rock interaction that causes veined peridotites (Warren, 2016), LREE enrichment in clinopyroxene (Seyler *et al.*, 2001; Warren and Shimizu, 2010), and Ti enrichment in Cr-spinel (Dick, Johan Lissenberg and Warren, 2010; Warren, 2016). MOR-peridotites can be divided into two main types residual rocks (not affected by any melt-rock interaction process) and non-residual rocks (including dunites, plagioclase peridotites, gabbroic-pyroxenite veined samples, and metasomatized ones) (Warren, 2016). However, both rock types share the same range of spinel Cr# (~ 0.1–0.6) (Figure 6.6b) following the melting trend (Dick and Bullen, 1984) (Figure E.11) and the non-residual rocks are present in all the ridges. This indicates that the Cr-spinel from sub-oceanic mantle beneath all ridge systems is likely to have been affected by similar melt-rock interaction processes.

Representative Cr# of Cr-spinel composition for a given location or dredge base has been used for mitigating the effect of Cr-spinel heterogeneity and high compositional variations (Zhou and Dick, 2013; Warren, 2016). However, this approach overlooked the elemental compositional variability of the Cr-spinel affected by melt-rock interaction. To further illustrate this point, we discuss below and give specific examples, according to available published datasets, of Cr-spinel heterogeneity due to metasomatism at different scales, from dredge sites to samples (core-core Al-Cr heterogeneity) and single grains (within core and core-rim Al-Cr heterogeneity) (see Supplementary Data 1 for more details and summary of Cr-spinel heterogeneity for each individual ridge at different scales, and Supplementary Data 3

for the complete datasets). Here we emphasize that using representative or average data for Cr-spinel made it very difficult (or even impossible) to investigate the variation in Cr-spinel of those rocks. Hence, we only considered the samples that have at least two grains analysed (see Supplementary Data 3). In addition, there have been only rare cases where studies traced core to rim chemical variation within individual grains (Brunelli *et al.*, 2006; Cipriani, Bonatti, Brunelli, *et al.*, 2009; Cipriani, Bonatti, Seyler, *et al.*, 2009; Dick, Johan Lissenberg and Warren, 2010).

Dredge sites scale: There is a large variation in Al and Cr contents in Cr-spinel from a given dredge site, for example, section #V3306-IN18 (Owen FZ, Central Indian Ridge – CIR) has Al content = 32.20 – 52.90 wt % and Cr# = 0.15 – 0.42 (Hamlyn and Bonatti, 1980); section #ANTP-89-HD (Marie Celeste TF-CIR: Al= 28.4-46.9 wt% and Cr# = 0.23-0.50) (Hellebrand *et al.*, 2002); section #PS55-89 (Lena trough-Arctic Ridge: Al= 25-55 wt% and Cr# = 0.14-0.54) (Lassiter *et al.*, 2014); section #S1905 (Vema TF- Mid Atlantic Ridge, MAR: Al= 27.1-48.2 wt% and Cr# = 0.22-0.49) (Brunelli *et al.*, 2006; Cipriani, Bonatti, Brunelli, *et al.*, 2009; Cipriani, Bonatti, Seyler, *et al.*, 2009) and section #Van7-85 (Oblique Segment, South Western Indian Ridge – SWIR) has Al content = 24.41– 54.87 wt % and Cr# = 0.16 – 0.52 (Warren, 2007). For more examples and details, see Supplementary Data 1.

Sample scale: Similar ranges of Cr# variation exist at the sample scale. For example, Hamlyn and Bonatti (Hamlyn and Bonatti, 1980) analyzed four grains from the same peridotite sample (#V3306-IN18I-Owen FZ, CIR) and found inter-grain variations in Cr# spreading the range of 0.2 to 0.4 (mainly the entire range for CIR residual peridotites). Also, sample # AII32-8-6 (residual harzburgite-Ridge at 43°N, MAR: Al= 26.8-38.1 wt% and Cr# = 0.34-0.52) (Shibata and Thompson, 1986), sample # 1274A-14R-1/76-82 (residual harzburgite-Fifteen-Twenty TF, MAR: Al= 32.4-41 wt% and Cr# = 0.32-0.44) (Vils *et al.*, 2008), sample #G9604-4 (residual peridotite-Conrad FZ, American Antarctic Ridge (AAR): Al= 23-40 wt% and Cr# = 0.29-0.53) (Brunelli *et al.*, 2003) and sample #895D-4R2-45-49 (Hess Deep, East Pacific Rise (EPR): Al= 17.5-25.2 wt% and Cr# = 0.51-0.58) (Arai and Matsukage, 1996). Dick *et al.* (2010) published a Cr-spinel dataset from residual peridotites from Kane Megamullion (MAR), typically with data of one grain only per samples except for sample Kn180-2-4-2 that has two grains with a large range of Al content = 40.0 – 36.5 wt % and Cr# = 0.30 – 0.36 (Supplementary Data 3). In the Warren (2007) study, there are also a variation of Al-Cr content within the same sample of cryptic

metasomatized peridotite from the Atlantis II fracture zone (SWIR), such as sample #6K-465-2 that has a Al range of 28.89 – 46.54 wt % and Cr# of 0.22 – 0.46, and sample #RC27-9-6-5 that has a Al range of 27.59-46.58 wt % and Cr# of 0.22 – 0.48. For more examples and details, see Supplementary Data 1.

Grain scale: At the grain scale, data reported in Brunelli *et al.* (2006), Cipriani *et al.* (2009b, 2009a) and Dick *et al.* (2010) have some grains showing within-grain core-rim Al-Cr reverse variation. For example, sample #Kn180-214-44 (residual peridotite- Kane Megamullion) has rim showing high Al = 39.5 wt % and core showing low Al = 36.8 wt% (Dick, Johan Lissenberg and Warren, 2010), sample #L2627-04B (residual peridotite- Vema TF) has rim showing high Al = 48.5 wt % and core showing low Al = 44.5 wt% (Cipriani, Bonatti, Brunelli, *et al.*, 2009), sample #L2630-01D (residual peridotite- Vema TF) has rim showing high Al = 32.2 wt % and core showing low Al = 27.8 wt% (Cipriani, Bonatti, Brunelli, *et al.*, 2009). For more examples and details, see Supplementary Data 1.

These examples, together with the comprehensive compilation (Supplementary Data 1), show that the majority (~ 85%) of Cr-spinel from MOR-peridotites exhibit heterogeneity, indicating that it is a widespread feature in sub-oceanic mantle (Figure E.1 and Supplementary Data 1). Moreover, such large variations in Cr# featuring Al enrichment and Cr depletion are most likely the results of melt-rock interaction/metasomatism, consistent with cryptic metasomatic that led to LREE enrichments in Cpx of the same rocks (e.g., Hellebrand *et al.*, 2002a; Dick *et al.*, 2010; Warren and Shimizu, 2010). For example, Warren (2007) reported a similarly large compositional variation in Cpx from MOR-peridotites in the scales of dredge sites, samples, and individual grains, and interpreted it as the result of widespread melt-rock interaction. Indeed, some non-residual/impregnated samples have high Al content and low Cr# than residual samples from the same section, for example, sections # 6K-458 and Kn162-19 from SWIR (Supplementary Data 3) (Warren, 2007). Moreover, Constantin *et al.* (1995) documented that the Terevaka TF cryptic harzburgite samples have lower Cr# (~0.35) compared to harzburgites free of impregnation (Cr# = ~0.45; see their figure. 2). Additionally, the orogenic replacive dunites (melt-rock interaction origin) have low Cr# than the residual origin dunites (see Figure 8 of Su *et al.* (2016)). Our re-interpretation of high Al-Cr heterogeneity in Cr-spinel from MOR-peridotites as a melt-rock interaction/metasomatism origin is supported the new geochemical modelling and observations of Brunelli *et al.* (2018)

from Vema at MAR where veined peridotites have lower Cr# than residual/vein-free ones.

We distinguished modified from non-modified Cr-spinel in MOR-peridotites, as we did for arc-peridotites, using our filter criteria (see methods). The data show a large overlap in Cr# of Cr-spinel between MOR-peridotites and arc-peridotites (~75% of all FA-peridotite data, ~90% of all MOR-peridotite data and 100% of back arc-peridotites data fall inside the common field of $\text{Cr\#} = \sim 0.15\text{-}0.65$) (Figure 6.6c, d). Furthermore, Arai and co-workers (Arai and Ishimaru, 2008; Arai *et al.*, 2018; Payot *et al.*, 2018) suggested that the lithospheric mantle beneath arcs (such as the Western Pacific arcs) have peridotites with a chemical and mineralogical composition comparable to that of MOR/abyssal peridotites. In addition, Cr-spinel datasets of both modified and non-modified MOR-peridotites fall entirely within the field of mantle wedge peridotites (Arai and Ishimaru, 2008) (Figure 6.6b), rendering the application of Cr# as a geotectonic indicator ineffective, and $\text{Cr\#} < 0.6$ is not a unique feature of MOR-peridotites.

6.4 Discussion

Our new analyses and a careful review of published results show that the chemical composition of Cr-spinel can be easily and severely modified by cryptic metasomatism through fluid/melt-rock interaction involving slab-derived fluids in the sub-arc mantle, or even by small volumes of melts in the sub-oceanic mantle. We also demonstrate that the wide range of Cr# of Cr-spinel in mantle rocks is a function of melt-rock interaction (Ceuleneer, 2004; Ceuleneer and Le Sueur, 2008; Kaczmarek and Müntener, 2008; Abily and Ceuleneer, 2013; Rospabé *et al.*, 2018) rather than partial melting. In addition, we identify Cr-spinel as a carrier of fluid-mobile elements especially in subduction zone environments, where Al is easily mobilised by fluids and melts and therefore cannot be used as a melting degree indicator at least at the mineral scale. Furthermore, the heterogeneity of Cr# in Cr-spinel can be used as a powerful tracer for Cr-spinel metasomatic modification.

Our findings, therefore, provide a framework for a re-evaluation of Cr-spinel compositions in mantle rocks. They will also have numerous new applications. These include using Cr-spinel composition as a melt-rock interaction indicator, and as a

tracer of mantle heterogeneity. In addition, Cr-spinel as a FME-carrying mineral may also provide a feeding mechanism for FME into the deep mantle chemical cycle because it breaks down at >1000 km depth (Ringwood, 1962). The present findings will thus help to develop a new way of deciphering deep mantle metasomatism and heterogeneity through analysing non-traditional isotopes (e.g., Li, Zn, Ti and Ni) in Cr-spinel.

Finally, we suggest that future studies of Cr-spinel chemistry need to first carry out systematic microanalyses in order to detect any heterogeneity of trace elements (including fluid mobile elements) using methods such as X-ray elemental mapping, electron microprobe (at least 3-5 spots within the same grain spreading from the inner to outer core, and at least 3 grains per sample), and LA-ICPMS. More advanced methods such as EBSD and APT, plus careful interpretation of the obtained results, will help to detect modified/heterogeneous Cr-spinels. Whereas altered Cr-spinels may help to address post-melting metasomatic process, non-modified/homogenous ones can then be used for tracking partial melting.

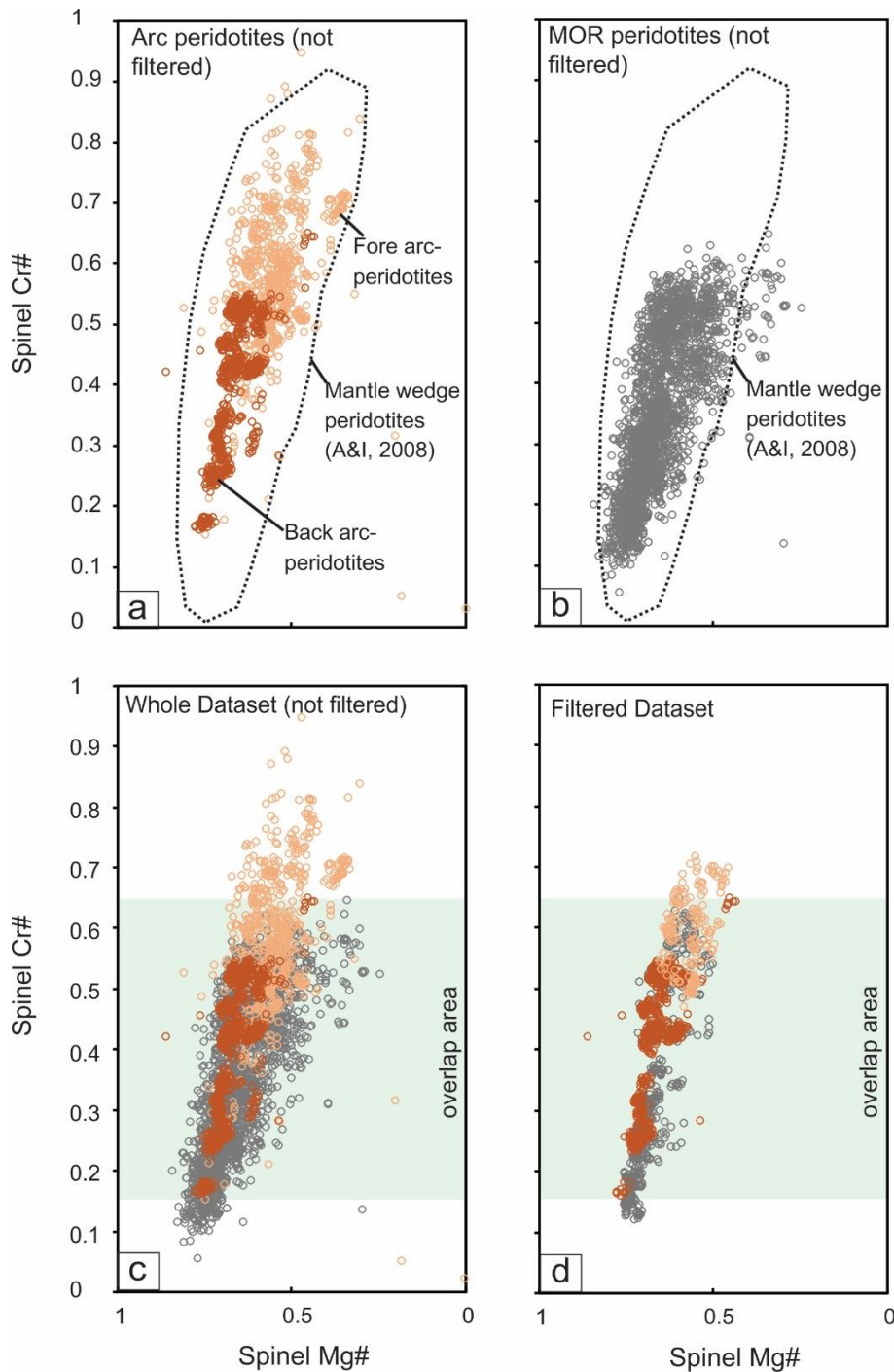


Figure 6.6: Spinel Cr# and Mg# for the arc and MOR peridotites. (a) Cr-spinel database from arc-peridotites including forearc settings (composed of mantle wedge xenoliths (e.g., the Kamchatka arc) (Ishimaru *et al.*, 2007; Ionov, 2010) and dredged samples from present-day oceanic arcs (e.g., the Izu-Bonin-Mariana arc) (Ishii *et al.*, 1992; Parkinson and Pearce, 1998)) and back arc-peridotites (i.e., Mariana Trough) (Ohara *et al.*, 2002, 2003). (b) Cr-spinel database from abyssal/ Mid-ocean ridge (MOR) peridotites. See Supplementary Data 3 for the arc and MOR-Cr-spinel datasets. All the arc and MOR-peridotites dataset plot within the Cr-spinel from mantle wedge peridotites (Arai and Ishimaru, 2008). (c) All arc peridotite Cr-spinel datasets (without filtering) plotted against MOR-peridotite one, showing their overlapping fields. (d) Filtered dataset for both arc- and MOR-peridotite are still completely overlapping. For filter details, see the methods. The shaded area in (c, d) marks the overlapping range of Cr# (0.15-0.65) between the arc-peridotite and MOR-peridotite fields.

6.5 References

- Abily, B. and Ceuleneer, G. (2013) 'The dunitic mantle-crust transition zone in the Oman ophiolite: Residue of melt-rock interaction, cumulates from high-mg melts, or both?', *Geology*, 41(1), pp. 67–70. doi: 10.1130/G33351.1.
- Albarède, F. (1998) 'The growth of continental crust', *Tectonophysics*, 296(1–2), pp. 1–14. doi: 10.1016/S0040-1951(98)00133-4.
- Anders, E. and Grevesse, N. (1989) 'Abundances of the elements: Meteoritic and solar', *Geochimica et Cosmochimica Acta*. Pergamon, 53(1), pp. 197–214. doi: 10.1016/0016-7037(89)90286-X.
- Arai, S. (1994) 'Characterization of spinel peridotites by olivine-spinel compositional relationships: Review and interpretation', *Chemical Geology*, 113(3–4), pp. 191–204. doi: 10.1016/0009-2541(94)90066-3.
- Arai, S. *et al.* (2018) 'Abyssal Peridotite as a Component of Forearc Mantle: Inference from a New Mantle Xenolith Suite of Bankawa in the Southwest Japan Arc', *Minerals*. Multidisciplinary Digital Publishing Institute, 8(11), p. 540. doi: 10.3390/min8110540.
- Arai, S. and Ishimaru, S. (2008) 'Insights into Petrological Characteristics of the Lithosphere of Mantle Wedge beneath Arcs through Peridotite Xenoliths : a Review', *JOURNAL OF PETROLOGY*, 49(4), pp. 665–695. doi: 10.1093/petrology/egm069.
- Arai, S., Ishimaru, S. and Okrugin, V. M. (2003) 'Metasomatized hazburgite xenoliths from Avacha volcano as fragments of mantle wedge of the Kamchatka arc: Implication for the metasomatic agent', *Island Arc*, 12(2), pp. 233–246. doi: 10.1046/j.1440-1738.2003.00392.x.
- Arai, S. and Matsukage, K. (1996) 'Petrology of Gabbro-Troctolite-Peridotite Complex from Hess Deep, Equatorial Pacific: Implications for Mantle-Melt Interaction within the Oceanic Lithosphere', *Proceedings of the Ocean Drilling Program, 147 Scientific Results*, 147, pp. 135–155. doi: 10.2973/odp.proc.sr.147.008.1996.
- Bai, Y. *et al.* (2018) 'Origin of Reverse Zoned Cr-Spinels from the Paleoproterozoic Yanmenguan Mafic-Ultramafic Complex in the North China Craton', *Minerals*, 8(2), p. 62. doi: 10.3390/min8020062.
- Bailey, D. (1982) 'Mantle metasomatism-continuing chemical change within the Earth', *Nature*, 296, pp. 525–530. doi: 10.1038/296525a0.
- Barnes, S. J. (2000) 'Chromite in komatiites, II. Modification during greenschist to mid-amphibolite facies metamorphism', *Journal of Petrology*, 41(3), pp. 387–409. doi: 10.1093/petrology/41.3.387.
- Bloomer, S. H. and Fisher, R. L. (1987) 'Petrology and Geochemistry of Igneous Rocks from the Tonga Trench: A Non-Accreting Plate Boundary', *JOURNAL OF GEOLOGY*, 95(4), pp. 469–495.
- Bodinier, J. L. *et al.* (1990) 'Mechanisms of Mantle Metasomatism: Geochemical Evidence from the Lherz Peridotite', *Journal of Petrology*, 31(3), pp. 597–628.

Brunelli, D. *et al.* (2003) 'Mantle peridotites from the Bouvet Triple Junction Region, South Atlantic', *Terra Nova*, 15(3), pp. 194–203. doi: 10.1046/j.1365-3121.2003.00482.x.

Brunelli, D. *et al.* (2006) 'Discontinuous melt extraction and weak refertilization of mantle peridotites at the vema lithospheric section (mid-atlantic ridge)', *Journal of Petrology*, 47(4), pp. 745–771. doi: 10.1093/petrology/egi092.

Brunelli, D., Cipriani, A. and Bonatti, E. (2018) 'Thermal effects of pyroxenites on mantle melting below mid-ocean ridges', *Nature Geoscience*. Springer US, 11(7), pp. 520–525. doi: 10.1038/s41561-018-0139-z.

Ceuleneer, G. (2004) 'Mantle mapped in the desert', *Nature*. Nature Publishing Group, 432(7014), pp. 156–157. doi: 10.1038/432156a.

Ceuleneer, G. and Le Sueur, E. (2008) 'The Trinity ophiolite (California): the strange association of fertile mantle peridotite with ultra-depleted crustal cumulates', *Bulletin de la Societe Geologique de France*. GeoScienceWorld, 179(5), pp. 503–518. doi: 10.2113/gssgfbull.179.5.503.

Cipriani, A., Bonatti, E., Brunelli, D., *et al.* (2009) '26 million years of mantle upwelling below a segment of the Mid Atlantic Ridge: The Vema Lithospheric Section revisited', *Earth and Planetary Science Letters*. Elsevier B.V., 285(1–2), pp. 87–95. doi: 10.1016/j.epsl.2009.05.046.

Cipriani, A., Bonatti, E., Seyler, M., *et al.* (2009) 'A 19 to 17 Ma amagmatic extension event at the Mid-Atlantic Ridge: Ultramafic mylonites from the Vema Lithospheric Section', *Geochemistry, Geophysics, Geosystems*, 10(10). doi: 10.1029/2009GC002534.

Constantin, M. *et al.* (1995) *Mafic and ultramafic intrusions into upper mantle peridotites from fast spreading centers of the Easter Microplate (South East Pacific)*. In: Vissers, R.L.M., Nicolas, A. (Eds.), *Mantle and Lower Crust Exposed in Oceanic Ridges and in Ophiolites*. Kluwer Aca. doi: 10.1007/978-94-015-8585-9.

Deschamps, F. *et al.* (2013) 'Geochemistry of subduction zone serpentinites: A review', *Lithos*, 178(APRIL), pp. 96–127. doi: 10.1016/j.lithos.2013.05.019.

Dick, H. J. B. and Bullen, T. (1984) 'Chromian spinel as a petrogenetic indicator in abyssal and alpine-type peridotites and spatially associated lavas', *Contributions to Mineralogy and Petrology*, 86(1), pp. 54–76. doi: 10.1007/BF00373711.

Dick, H. J. B., Johan Lissenberg, C. and Warren, J. M. (2010) 'Mantle melting, melt transport, and delivery beneath a slow-spreading ridge: The paleo-MAR from 23°15'N to 23°45'N', *Journal of Petrology*, 51(1–2), pp. 425–467. doi: 10.1093/petrology/egp088.

Fougerouse, D. *et al.* (2016) 'Nanoscale gold clusters in arsenopyrite controlled by growth rate not concentration: Evidence from atom probe microscopy', *American Mineralogist*. GeoScienceWorld, 101(8), pp. 1916–1919. doi: 10.2138/am-2016-5781CCBYNCND.

Franz, L. *et al.* (2002) 'Metasomatic Mantle Xenoliths from the Bismarck Microplate (Papua New Guinea)--Thermal Evolution, Geochemistry and Extent of Slab-induced Metasomatism', *Journal of Petrology*, 43(2), pp. 315–343. doi: 10.1093/petrology/43.2.315.

Gamal El Dien, H. *et al.* (2016) 'Neoproterozoic serpentinites from the Eastern Desert of

Egypt: Insights into Neoproterozoic mantle geodynamics and processes beneath the Arabian-Nubian Shield', *Precambrian Research*. Elsevier B.V., 286, pp. 213–233. doi: 10.1016/j.precamres.2016.10.006.

Gamal El Dien, H. *et al.* (2019) 'Origin of arc magmatic signature: A temperature-dependent process for trace element (re)-mobilization in subduction zones', *Scientific Reports*. Nature Publishing Group, 9(1), p. 7098. doi: 10.1038/s41598-019-43605-9.

Gault, B. *et al.* (2016) 'Behavior of molecules and molecular ions near a field emitter', *New Journal of Physics*. IOP Publishing, 18(3), p. 033031. doi: 10.1088/1367-2630/18/3/033031.

Hamdy, M. M. *et al.* (2017) 'Garnet hornblendite in the Meatiq Core Complex, Central Eastern Desert of Egypt: Implications for crustal thickening preceding the ~600 Ma extensional regime in the Arabian-Nubian Shield', *Precambrian Research*. Elsevier B.V., 298, pp. 593–614. doi: 10.1016/j.precamres.2017.07.002.

Hamdy, M. M. and Gamal El Dien, H. (2017) 'Nature of serpentinization and carbonation of ophiolitic peridotites (Eastern Desert, Egypt): constrains from stable isotopes and whole-rock geochemistry', *Arabian Journal of Geosciences*. Arabian Journal of Geosciences, 10(19). doi: 10.1007/s12517-017-3215-6.

Hamdy, M. M., Harraz, H. Z. and Aly, G. A. (2013) 'Pan-African (intraplate and subduction-related?) metasomatism in the Fawakhir ophiolitic serpentinites, Central Eastern Desert of Egypt: mineralogical and geochemical evidences', *Arabian Journal of Geosciences*. Springer-Verlag, 6(1), pp. 13–33. doi: 10.1007/s12517-011-0319-2.

Hamlyn, P. R. and Bonatti, E. (1980) 'Petrology of mantle-derived ultramafics from the Owen fracture zone, northwest Indian ocean: Implications for the nature of the oceanic upper mantle', *Earth and Planetary Science Letters*, 48(1), pp. 65–79. doi: 10.1016/0012-821X(80)90171-5.

Harte, B., Hunter, R. H. and Kinny, P. D. (1993) 'Melt geometry, movement and crystallization, in relation to mantle dykes, veins and metasomatism', *Philosophical Transactions of the Royal Society of London. Series A: Physical and Engineering Sciences*, 342(1663), pp. 1–21. doi: 10.1098/rsta.1993.0001.

Hellebrand, E. *et al.* (2001) 'Coupled major and trace elements as indicators of the extent of melting in mid-ocean-ridge peridotites', *Nature*, 410(6829), pp. 677–681. doi: 10.1038/35070546.

Hellebrand, E. *et al.* (2002) 'Garnet-field Melting and Late-stage Refertilization in "Residual" Abyssal Peridotites from the Central Indian Ridge', *Journal of Petrology*, 43(12), pp. 2305–2338. doi: 10.1093/petrology/43.12.2305.

Hellebrand, E., Snow, J. E. and Mühe, R. (2002) 'Mantle melting beneath Gakkel Ridge (Arctic Ocean): Abyssal peridotite spinel compositions', *Chemical Geology*, 182(2–4), pp. 227–235. doi: 10.1016/S0009-2541(01)00291-1.

De Hoog, J. C. M. *et al.* (2009) 'Serpentinised peridotites from an ultrahigh-pressure terrane in the Pohorje Mts. (Eastern Alps, Slovenia): Geochemical constraints on petrogenesis and tectonic setting', *Lithos*. Elsevier B.V., 109(3–4), pp. 209–222. doi: 10.1016/j.lithos.2008.05.006.

Ionov, D. A. (2010) 'Petrology of mantle wedge lithosphere: New data on supra-subduction zone peridotite xenoliths from the andesitic Avacha volcano, Kamchatka', *Journal of Petrology*, 51(1–2), pp. 327–361. doi: 10.1093/petrology/egp090.

Ionov, D. A., Bénard, A. and Plechov, P. Y. (2011) 'Melt evolution in subarc mantle: Evidence from heating experiments on spinel-hosted melt inclusions in peridotite xenoliths from the andesitic Avacha volcano (Kamchatka, Russia)', *Contributions to Mineralogy and Petrology*, 162(6), pp. 1159–1174. doi: 10.1007/s00410-011-0645-0.

Irvine, T. N. (1965) 'Chromian Spinel As a Petrogenetic Indicator: Part 1. Theory', *Canadian Journal of Earth Sciences*, 4(1), pp. 71–103. doi: 10.1139/e67-004.

Irvine, T. N. (1967) 'Chromian Spinel As a Petrogenetic Indicator: Part 2. Petrologic Applications', *Canadian Journal of Earth Sciences*, 4(1), pp. 71–103. doi: 10.1139/e67-004.

Ishii, T. *et al.* (1992) 'Petrological studies of peridotites from diapiric serpentinite seamounts in the Izu-Ogasawara-Mariana Forearc, Leg 125', *Proceedings of the Ocean Drilling Program, Scientific Results*, 125, pp. 445–485. doi: 10.2973/odp.proc.sr.125.129.1992.

Ishimaru, S. *et al.* (2007) 'Melting and multi-stage metasomatism in the mantle wedge beneath a frontal arc inferred from highly depleted peridotite xenoliths from the avacha volcano, Southern Kamchatka', *Journal of Petrology*, 48(2), pp. 395–433. doi: 10.1093/petrology/egl065.

Ishimaru, S. and Arai, S. (2009) 'Highly silicic glasses in peridotite xenoliths from Avacha volcano, Kamchatka arc; implications for melting and metasomatism within the sub-arc mantle', *Lithos*. Elsevier B.V., 107(1–2), pp. 93–106. doi: 10.1016/j.lithos.2008.07.005.

Johnson, P. R. *et al.* (2011) 'Late Cryogenian-Ediacaran history of the Arabian-Nubian Shield: A review of depositional, plutonic, structural, and tectonic events in the closing stages of the northern East African Orogen', *Journal of African Earth Sciences*. Elsevier Ltd, 61(3), pp. 167–232. doi: 10.1016/j.jafrearsci.2011.07.003.

Kaczmarek, M.-A. and Müntener, O. (2008) 'Juxtaposition of Melt Impregnation and High-Temperature Shear Zones in the Upper Mantle; Field and Petrological Constraints from the Lanzo Peridotite (Northern Italy)', *Journal of Petrology*. Oxford University Press, 49(12), pp. 2187–2220. doi: 10.1093/petrology/egn065.

Larson, D. J. *et al.* (2013) *Local Electrode Atom Probe Tomography*. New York, NY: Springer New York. doi: 10.1007/978-1-4614-8721-0.

Lassiter, J. C. *et al.* (2014) 'Constraints from Os-isotope variations on the origin of Lena Trough abyssal peridotites and implications for the composition and evolution of the depleted upper mantle', *Earth and Planetary Science Letters*. Elsevier B.V., 403, pp. 178–187. doi: 10.1016/j.epsl.2014.05.033.

Lee, C.-T. A., Brandon, A. D. and Norman, M. (2003) 'Vanadium in peridotites as a proxy for paleo-fO₂ during partial melting: prospects, limitations, and implications', *Geochimica et Cosmochimica Acta*. Pergamon, 67(16), pp. 3045–3064. doi: 10.1016/S0016-7037(03)00268-0.

Li, Y. H. and Schoonmaker, J. E. (2013) *Chemical Composition and Mineralogy of Marine Sediments, Treatise on Geochemistry: Second Edition*. doi: 10.1016/B978-0-08-095975-

7.00701-4.

McDonough, W. . and Sun, S. -. (1995) 'The composition of the Earth', *Chemical Geology*, 120, pp. 223–252. doi: doi.org/10.1016/0009-2541(94)00140-4.

Le Mée, L., Girardeau, J. and Monnier, C. (2004) 'Mantle segmentation along the Oman ophiolite fossil mid-ocean ridge', *Nature*, 432(7014), pp. 167–172. doi: 10.1038/nature03075.

Ohara, Y. *et al.* (2002) 'Peridotites from the Mariana Trough: First look at the mantle beneath an active back-arc basin', *Contributions to Mineralogy and Petrology*, 143(1), pp. 1–18. doi: 10.1007/s00410-001-0329-2.

Ohara, Y. *et al.* (2003) 'Peridotites and gabbros from the Parece Vela backarc basin: Unique tectonic window in an extinct backarc spreading ridge', *Geochemistry, Geophysics, Geosystems*. John Wiley & Sons, Ltd, 4(7). doi: 10.1029/2002GC000469.

Ohara, Y. and Ishii, T. (1998) 'Peridotites from the southern Mariana forearc: Heterogeneous fluid supply in mantle wedge', *Island Arc*, 7(3), pp. 541–558. doi: 10.1111/j.1440-1738.1998.00209.x.

Ozawa, K. (1989) 'Stress-induced Al-Cr zoning of spinel in deformed peridotites', *Nature*, pp. 141–144. doi: 10.1038/338141a0.

Parkinson, I. J. and Pearce, J. A. (1998) 'Peridotites from the Izu – Bonin – Mariana Forearc (ODP Leg 125): Evidence for Mantle Melting and Melt – Mantle Interaction in a Supra-Subduction Zone Setting', *Journal of Petrology*, 39(9), pp. 1577–1618.

Paulick, H. *et al.* (2006) 'Geochemistry of abyssal peridotites (Mid-Atlantic Ridge, 15°20'N, ODP Leg 209): Implications for fluid/rock interaction in slow spreading environments', *Chemical Geology*, 234(3–4), pp. 179–210. doi: 10.1016/j.chemgeo.2006.04.011.

Payot, B. *et al.* (2018) 'Mantle Evolution from Ocean to Arc: The Record in Spinel Peridotite Xenoliths in Mt. Pinatubo, Philippines', *Minerals*. Multidisciplinary Digital Publishing Institute, 8(11), p. 515. doi: 10.3390/min8110515.

Pearce, N. J. G. *et al.* (1997) 'A Compilation of New and Published Major and Trace Element Data for NIST SRM 610 and NIST SRM 612 Glass Reference Materials', *Geostandards and Geoanalytical Research*. Wiley/Blackwell (10.1111), 21(1), pp. 115–144. doi: 10.1111/j.1751-908X.1997.tb00538.x.

Peters, D. *et al.* (2017) 'Fluid-mobile elements in serpentinites: Constraints on serpentinitisation environments and element cycling in subduction zones', *Chemical Geology*. Elsevier, 466(July), pp. 654–666. doi: 10.1016/j.chemgeo.2017.07.017.

Plank, T. (2013) *The Chemical Composition of Subducting Sediments*. 2nd edn, *Treatise on Geochemistry: Second Edition*. 2nd edn. Elsevier Ltd. doi: 10.1016/B978-0-08-095975-7.00319-3.

Prouteau, G. *et al.* (2001) 'Evidence for mantle metasomatism by hydrous silicic melts derived from subducted oceanic crust', *Nature*, 410(March), pp. 197–200.

Ringwood, A. E. (1962) 'Mineralogical constitution of the deep mantle', *Journal of*

Geophysical Research. Wiley-Blackwell, 67(10), pp. 4005–4010. doi: 10.1029/JZ067i010p04005.

Rospabé, M. *et al.* (2018) 'Extreme geochemical variability through the dunitic transition zone of the Oman ophiolite: Implications for melt/fluid-rock reactions at Moho level beneath oceanic spreading centers', *Geochimica et Cosmochimica Acta*. Pergamon, 234, pp. 1–23. doi: 10.1016/J.GCA.2018.05.012.

Saxey, D. W. *et al.* (2018) 'Atomic worlds: Current state and future of atom probe tomography in geoscience', *Scripta Materialia*. Pergamon, 148, pp. 115–121. doi: 10.1016/J.SCRIPTAMAT.2017.11.014.

Schiano, P. *et al.* (1995) 'Hydrous, silica-rich melts in the sub-arc mantle and their relationship with erupted arc lavas', *Nature*, 377(6550), pp. 595–600. doi: 10.1038/377595a0.

Seyler, M. *et al.* (2001) 'Clinopyroxene microtextures reveal incompletely extracted melts in abyssal peridotites', *Geology*, 29(2), pp. 155–158. doi: 10.1130/0091-7613(2001)029<0155:CMRIEM>2.0.CO;2.

Shibata, T. and Thompson, G. (1986) 'Peridotites from the Mid-Atlantic Ridge at 43° N and their petrogenetic relation to abyssal tholeiites', *Contributions to Mineralogy and Petrology*, 93(2), pp. 144–159. doi: 10.1007/BF00371316.

Sigurdsson, H. and Schilling, J. G. (1976) 'Spinel in Mid-Atlantic Ridge basalts: Chemistry and occurrence', *Earth and Planetary Science Letters*, 29(1), pp. 7–20. doi: 10.1016/0012-821X(76)90021-2.

Staudigel, H. (2013) *Chemical Fluxes from Hydrothermal Alteration of the Oceanic Crust*. 2nd edn, *Treatise on Geochemistry: Second Edition*. 2nd edn. Elsevier Ltd. doi: 10.1016/B978-0-08-095975-7.00318-1.

Su, B. *et al.* (2016) 'Origins of orogenic dunites: Petrology, geochemistry, and implications', *Gondwana Research*. International Association for Gondwana Research, 29(1), pp. 41–59. doi: 10.1016/j.gr.2015.08.001.

Szilas, K. *et al.* (2018) 'Highly refractory Archaean peridotite cumulates: Petrology and geochemistry of the Seqi Ultramafic Complex, SW Greenland', *Geoscience Frontiers*. Elsevier Ltd, 9(3), pp. 689–714. doi: 10.1016/j.gsf.2017.05.003.

Thompson, K. *et al.* (2007) 'In situ site-specific specimen preparation for atom probe tomography', *Ultramicroscopy*. North-Holland, 107(2–3), pp. 131–139. doi: 10.1016/J.ULTRAMIC.2006.06.008.

Verberne, R. *et al.* (2019) 'Analysis of Natural Rutile (TiO₂) by Laser-assisted Atom Probe Tomography', *Microscopy and Microanalysis*. Cambridge University Press, 25(02), pp. 539–546. doi: 10.1017/S1431927618015477.

Vils, F. *et al.* (2008) 'The Lithium, Boron and Beryllium content of serpentinized peridotites from ODP Leg 209 (Sites 1272A and 1274A): Implications for lithium and boron budgets of oceanic lithosphere', *Geochimica et Cosmochimica Acta*. Pergamon, 72(22), pp. 5475–5504. doi: 10.1016/J.GCA.2008.08.005.

Warren, J. M. (2007) ‘Geochemical and rheological constraints on the dynamics of the oceanic upper mantle’, *PhD Thesis, MIT/WHOI Joint Program*, p. 282. doi: 10.1575/1912/2030.

Warren, J. M. (2016) ‘Global variations in abyssal peridotite compositions’, *Lithos*. The Author, 248–251, pp. 193–219. doi: 10.1016/j.lithos.2015.12.023.

Warren, J. M. and Shimizu, N. (2010) ‘Cryptic variations in abyssal peridotite compositions: Evidence for shallow-level melt infiltration in the oceanic lithosphere’, *Journal of Petrology*, 51(1–2), pp. 395–423. doi: 10.1093/petrology/egp096.

Workman, R. K. and Hart, S. R. (2005) ‘Major and trace element composition of the depleted MORB mantle (DMM)’, *Earth and Planetary Science Letters*, 231(1–2), pp. 53–72. doi: 10.1016/j.epsl.2004.12.005.

Zhou, H. and Dick, H. J. B. (2013) ‘Thin crust as evidence for depleted mantle supporting the Marion Rise’, *Nature*. Nature Publishing Group, 494(7436), pp. 195–200. doi: 10.1038/nature11842.

“Every reasonable effort has been made to acknowledge the owners of copyright material. I would be pleased to hear from any copyright owner who has been omitted or incorrectly acknowledged.”

Appendix E:
Supplementary materials to Chapter 6

**Supplementary Data Tables and movies related to this chapter
can be found [here](#).**

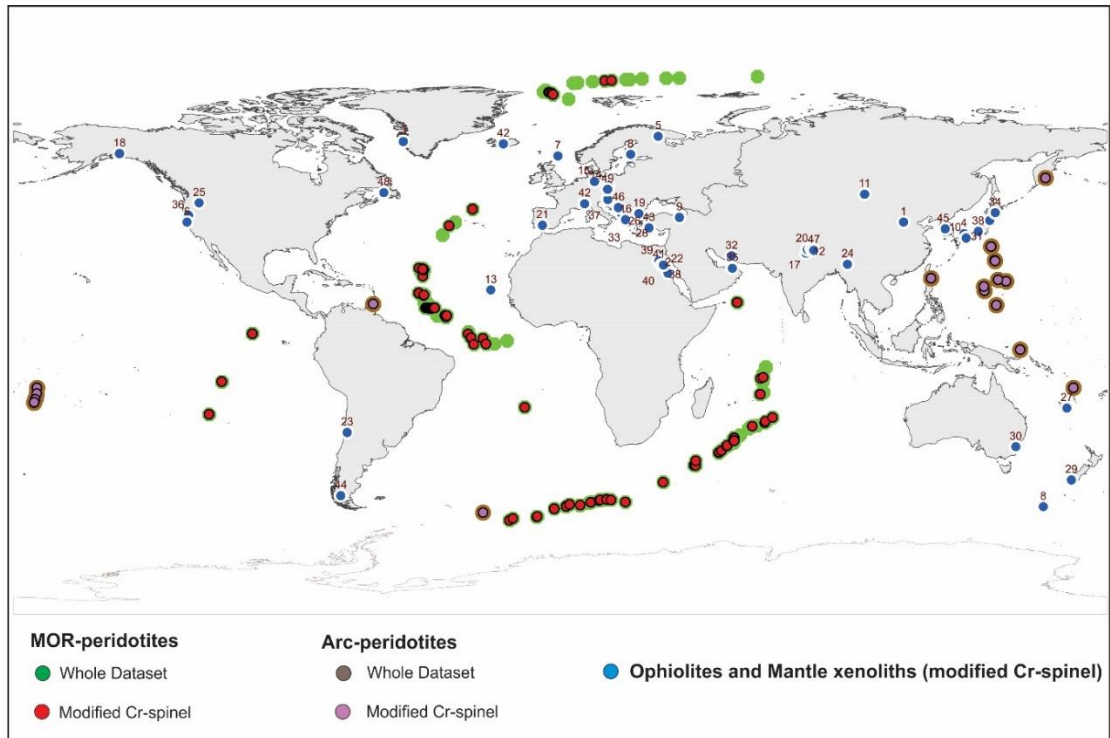


Figure E.1: Samples location of peridotite rocks that have modified spinel. The map shows the distribution of mid-ocean ridge (MOR) and arc-peridotites whole dataset used in this study and ones that have Al-Cr reverse zoning in spinel and modified spinel that passed our filter. In addition to some examples of on-land ophiolites and mantle xenoliths that also have modified Cr-spinel. Only a small proportion of the original authors clearly stated spinel heterogeneity. The on-land ophiolites samples have ages ranging from Archean to the Present. See Supplementary Data 1 for more details about this record. Our compilation is certainly not an exhaustive one of all results on modified spinel as such features have commonly been ignored in previous studies, but it does illustrate how widespread such a feature is, and forms a base for future data addition.

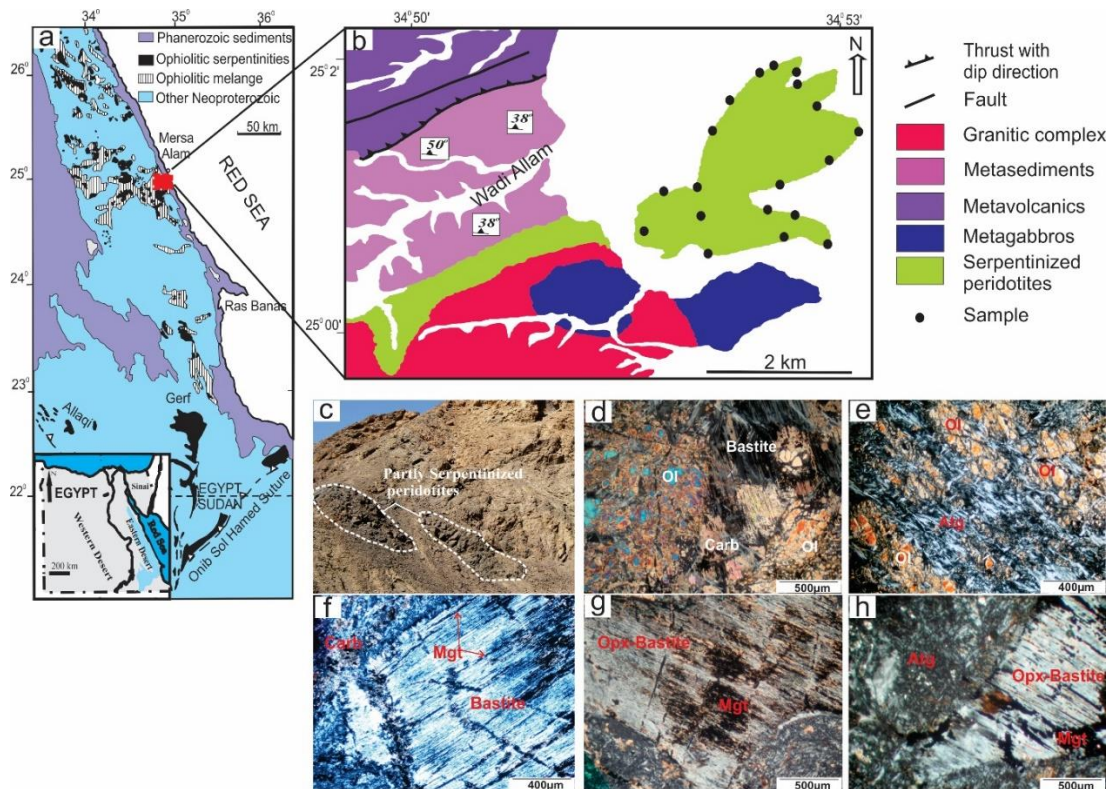


Figure E.2: Simplified geological maps of the Eastern Desert region in Egypt and study area with sampling locations. (a) Distribution of ophiolitic rocks in the Eastern Desert of Egypt (Johnson *et al.*, 2011). (b) Geological map of the Wadi Alam serpentinized peridotites (Hamdy and Gamal El Dien, 2017). (c) Partially serpentinized peridotites showing lensoidal bodies. (d) Olivine (Ol) relicts forming mesh texture and bastite texture, with oriented magnetite grains along cleave planes (e) Olivine cracked crystals dissected by antigorite (Atg) serpentine network. (f-h) Orthopyroxene (Opx) bastite texture has small magnetite (Mgt) grains distributed along original pyroxene cleavage. Carb = Carbonates.

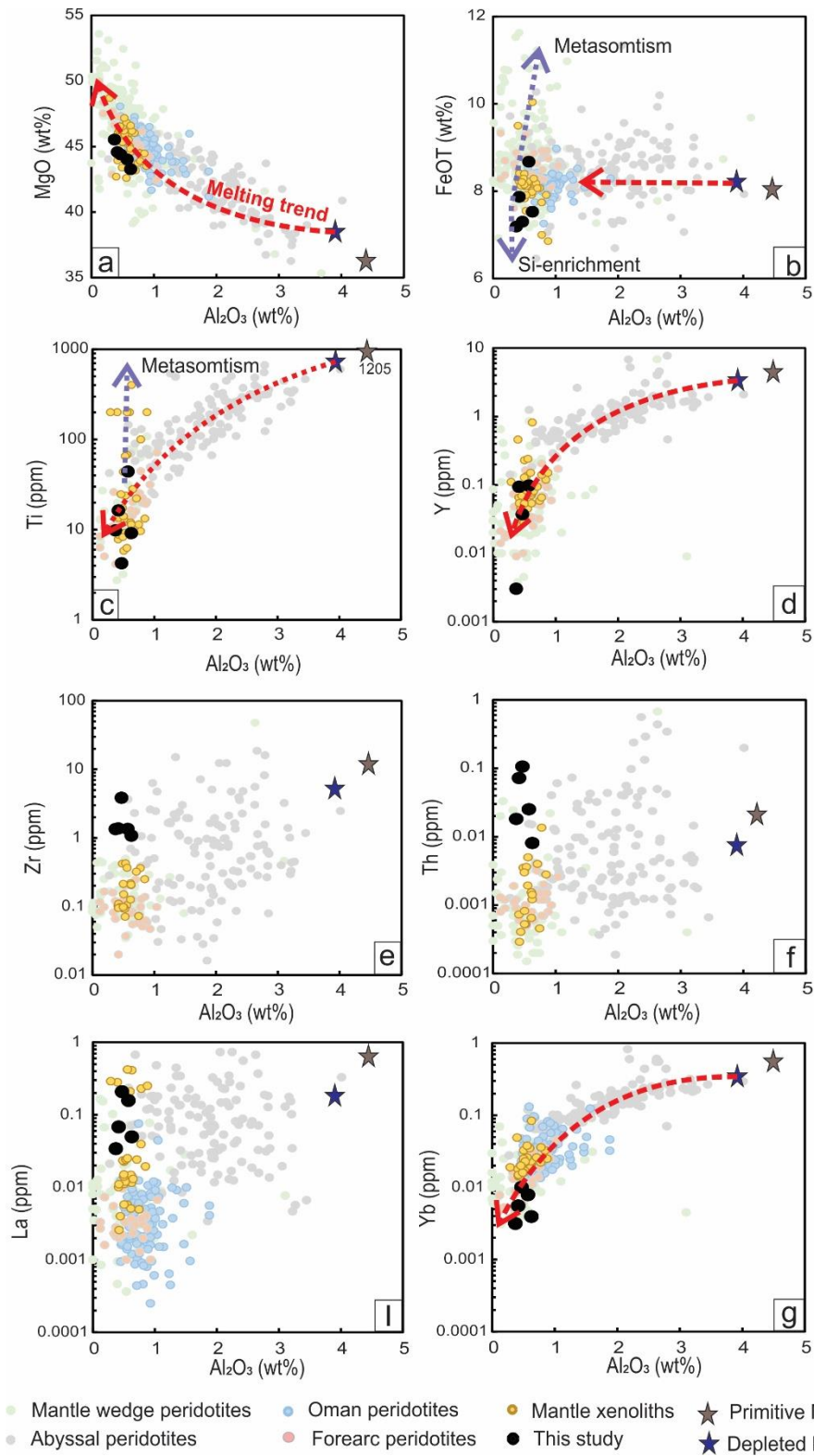


Figure E.3: Whole-rock Al_2O_3 (wt %) vs. selected major, trace and rare earth elements variation of the studied peridotites. Fields of abyssal peridotites (Deschamps *et al.*, 2013; Peters *et al.*, 2017), forearc peridotites (Parkinson and Pearce, 1998), Oman peridotites (Le Mée, Girardeau and Monnier, 2004), mantle wedge peridotites (Deschamps *et al.*, 2013) and mantle xenoliths (Ionov, 2010). Composition of primitive mantle (McDonough and Sun, 1995) and depleted MORB mantle (DMM) (Workman and Hart, 2005) is plotted for comparison.

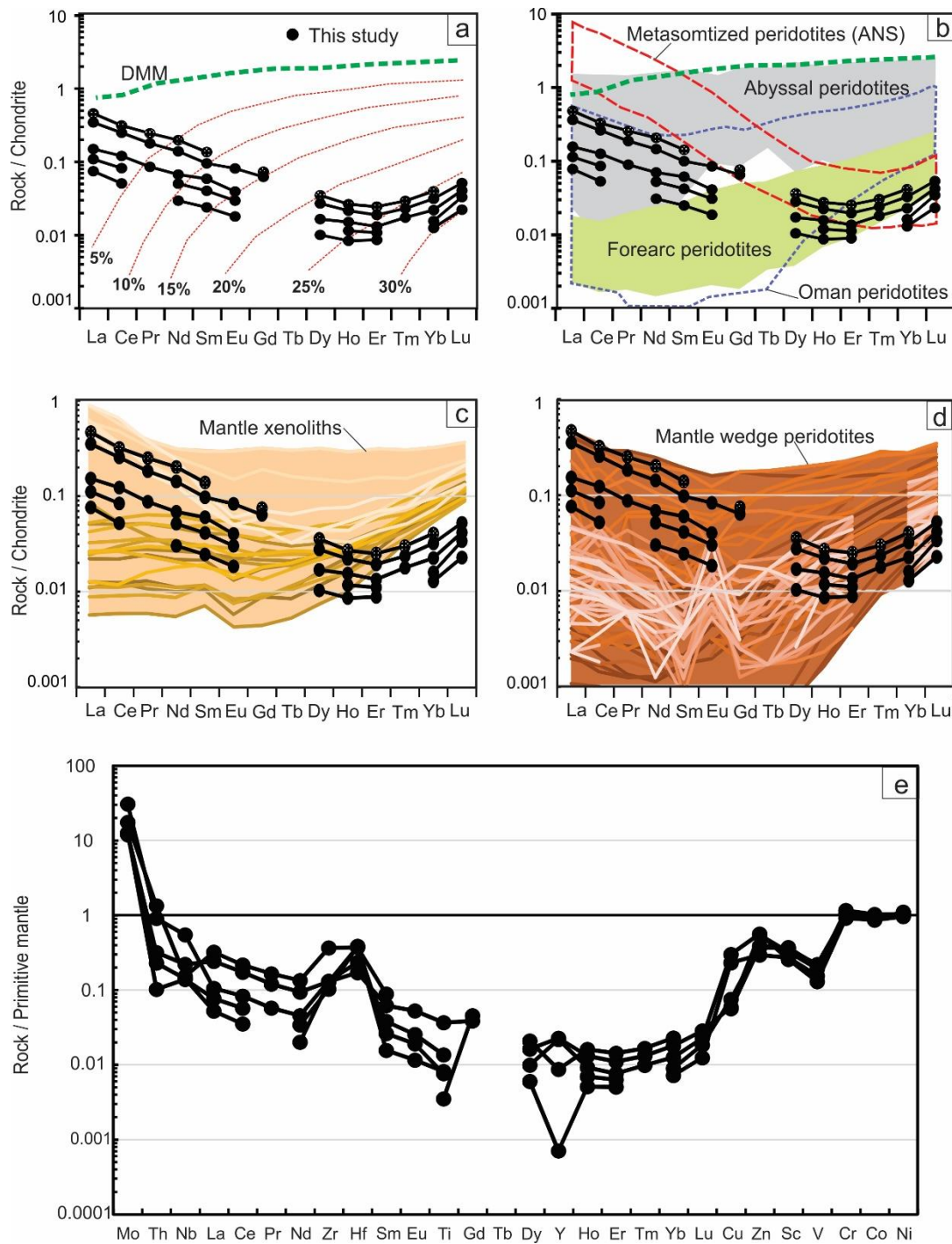


Figure E.4: Primitive mantle-normalized (McDonough and Sun, 1995) multi-element and rare earth element patterns normalized to chondrite (Anders and Grevesse, 1989) of the studied peridotites. (a) Estimation of degree of partial melting for the studied rocks by using the non-modal fractional melting model of a source of depleted MORB mantle (DMM) (Workman and Hart, 2005), with melting curves based on an assumed source of DMM composition in the spinel stability field (De Hoog *et al.*, 2009). (b-c) A comparison our studied rocks with that of different tectonic settings and metasomatized peridotites from Arabian-Nubian Shield (ANS; after Hamdy *et al.* (2013)). (e) Primitive mantle normalized elements for the studied rock showing a gradual increase from rare earth elements to high field strength elements and high enrichment in Mo.

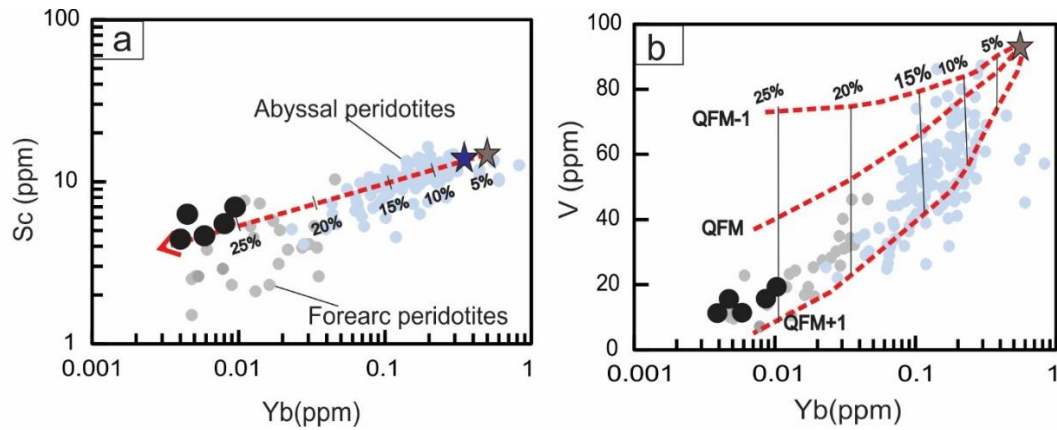


Figure E.5: A determination of the degree of partial melting of the studied rocks based on bulk-rock chemistry. The plots of Yb (ppm) vs. Sc ppm (a) and V ppm (b) are for residual peridotites according to Lee et al. (2003), with annotated degrees of mantle melting (in %). Diagrams contain fractional melting trends for different oxygen fugacities. FMM = Fertile MORB mantle. Vanadium behaves as a moderately incompatible element while melting under reducing conditions (QFM-1; this refers to $\log fO_2$ (QFM) = log units relative to quartz-fayalite-magnetite buffer), resulting in low depletion of V; under oxidizing conditions (QFM+1), the ratio of $V^{3+}/(V^{4+}+V^{5+})$ is low and partition coefficients are high. Thus vanadium as a highly incompatible element is readily depleted in the mantle during partial melting. Legends for symbols are the as in Figure E.3

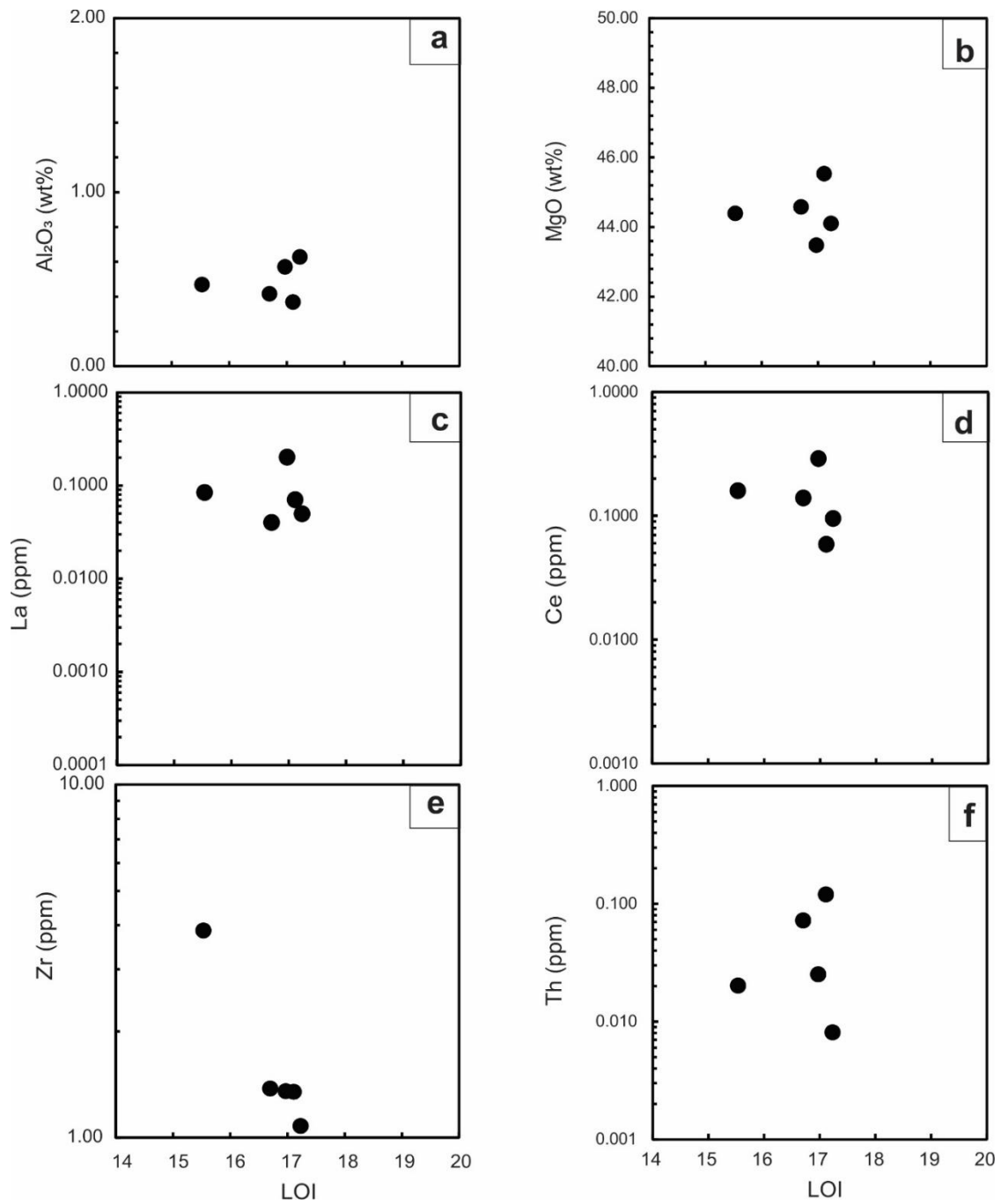


Figure E.6: Variation diagrams of LOI (wt%) vs. selected major, trace and rare earth elements of bulk composition of the studied peridotites. The plots show no correlation between LOI and the selected elements.

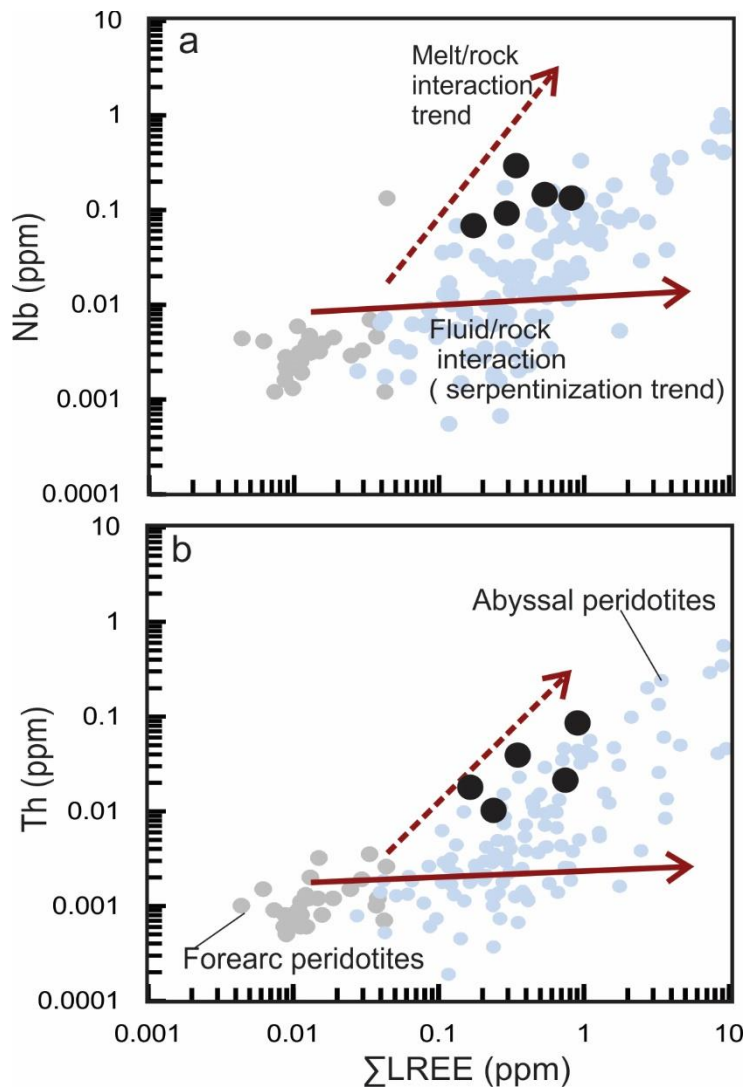


Figure E.7: Co-variation of HFSE and LREE. (a) Nb vs Σ LREE and (b) Th vs Σ LREE. The plots show the melt-rock interaction and fluid-rock interaction (serpentinization-related) trends (Paulick *et al.*, 2006). The studied peridotites have been affected by post melting melt/rock interactions process that led to HFSE enrichments. Legends for symbols are the as in Figure E.3.

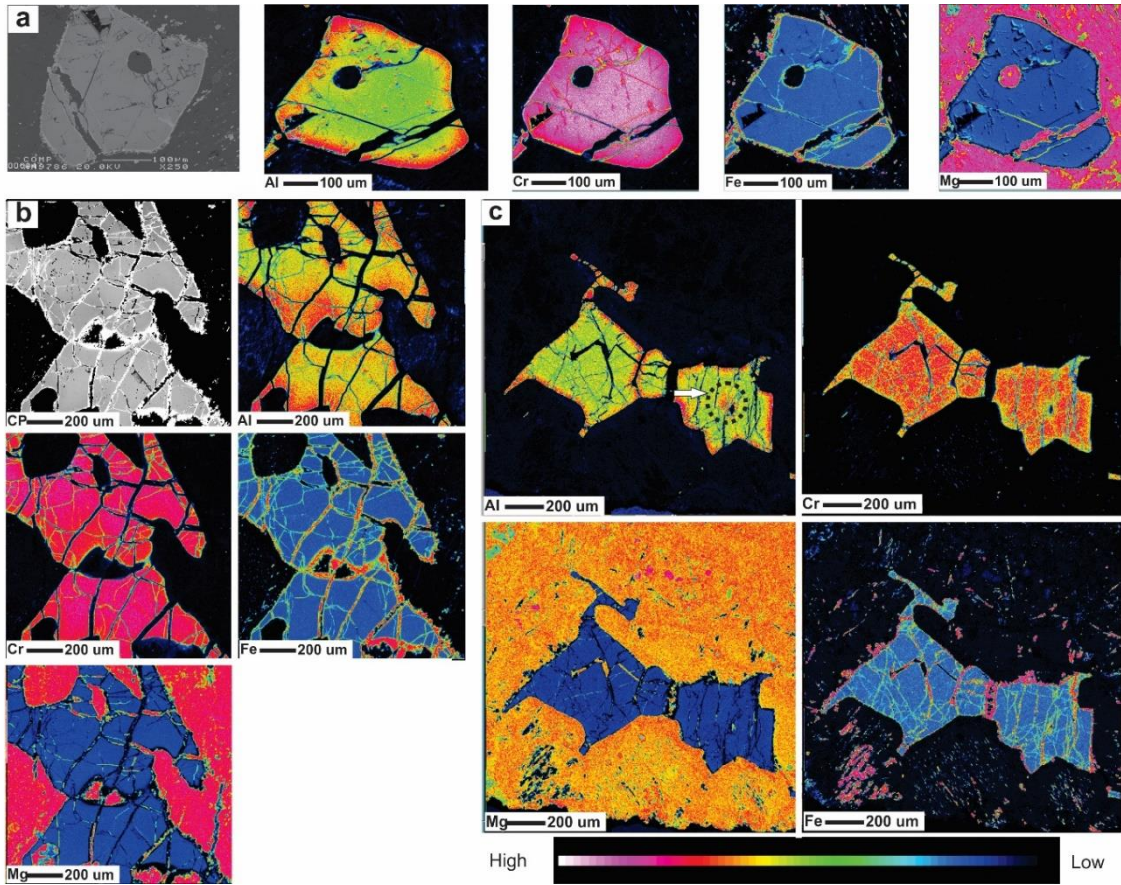


Figure E.8: Al-Cr-Fe-Mg X-ray elemental maps for the studied Cr-Spinel. The maps show heterogeneity in Al-Cr content distribution within the grains, but relatively homogenous Fe and Mg distribution between the cores and the rims.

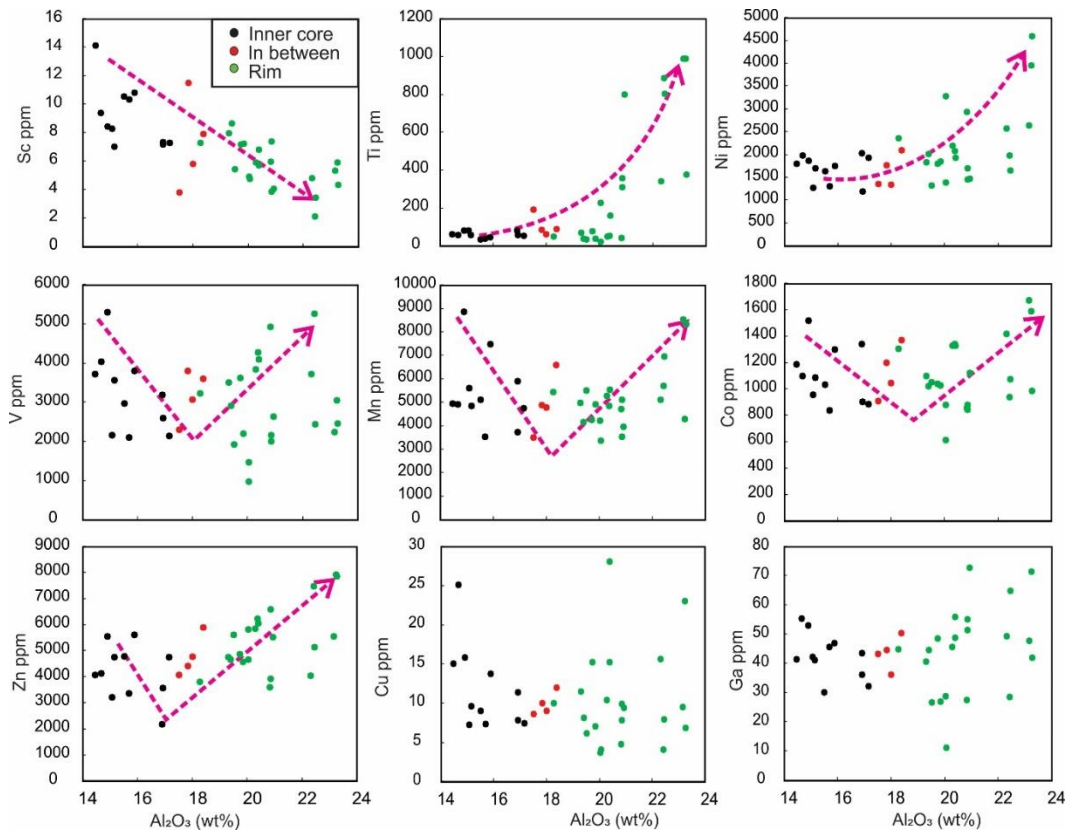


Figure E.9: Binary plots of Al₂O₃ (wt %) vs. transitions elements for the studied Cr-spinel. Sc shows negative relation, Ti and Ni show positive relation, V, Mn, Co and Zn show a V-shape relation, whereas Cu and Ga show no relation.

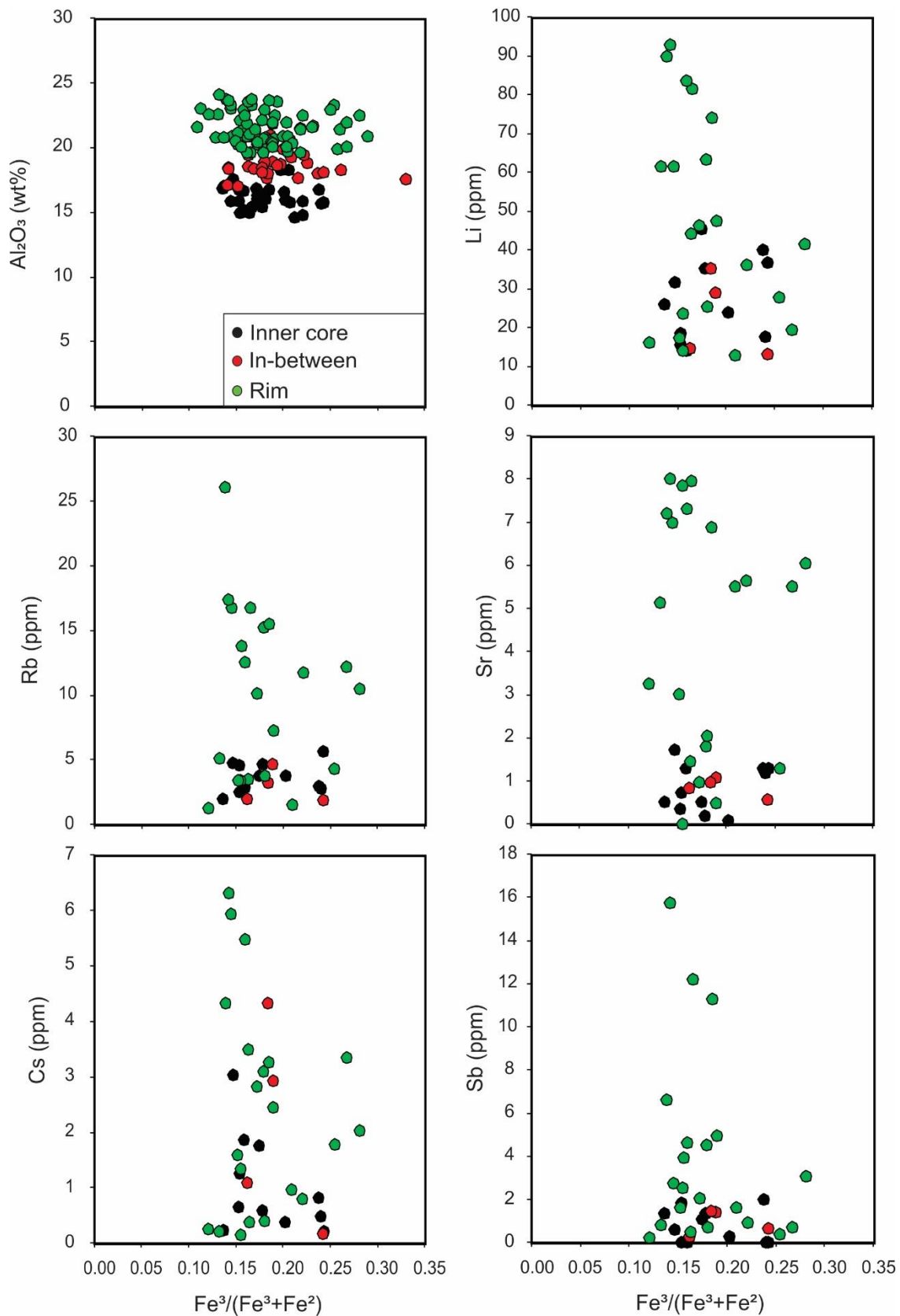


Figure E.10: Binary plots of $Fe^{3+}/(Fe^{3+} + Fe^{2+})$ ratio vs Al_2O_3 (wt %) and FME (ppm) for the studied Cr-spinel. The plot show that $Fe^{3+}/(Fe^{3+} + Fe^{2+})$ ratio has a constant values between the Cr-spinel cores and rims and has no relationship with Al and FME.

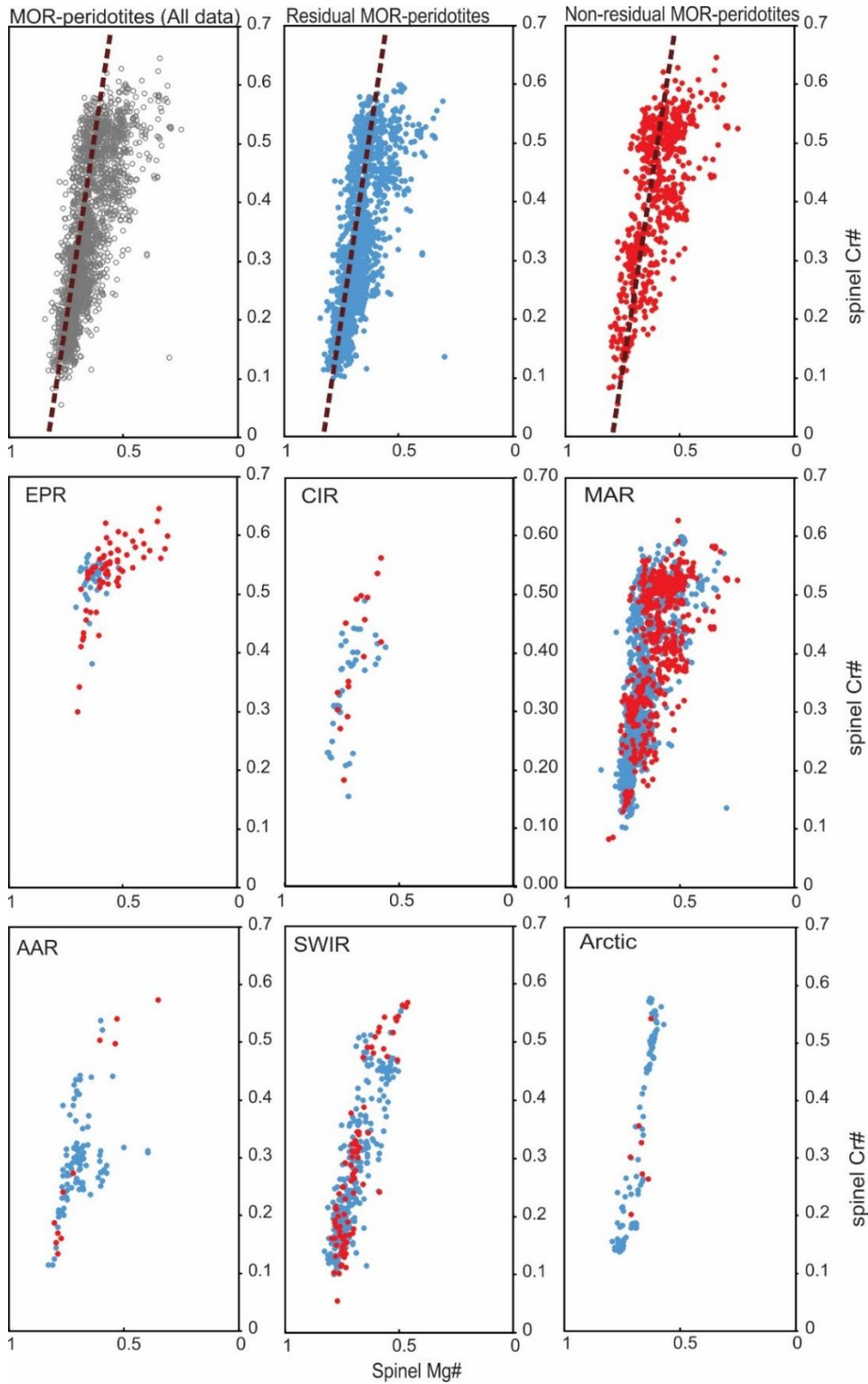


Figure E.11: Compositional variation for Cr-spinel in the global datasets for abyssal peridotites. The plots show Cr-spinel Cr# and Mg# in different mid-ocean ridges peridotites and defined as residual and non-residual peridotites. Red dash line represents melting trend from Dick and Bullen (1984). EPR= East Pacific Rise, CIR= Central Indian Ridge, MAR= Mid-Atlantic Ridge, AAR= American-Antarctic Ridge, SWIR= Southwest Indian Ridge and Arctic including Gakkel ridge, Lena trough and Molloy ridge.

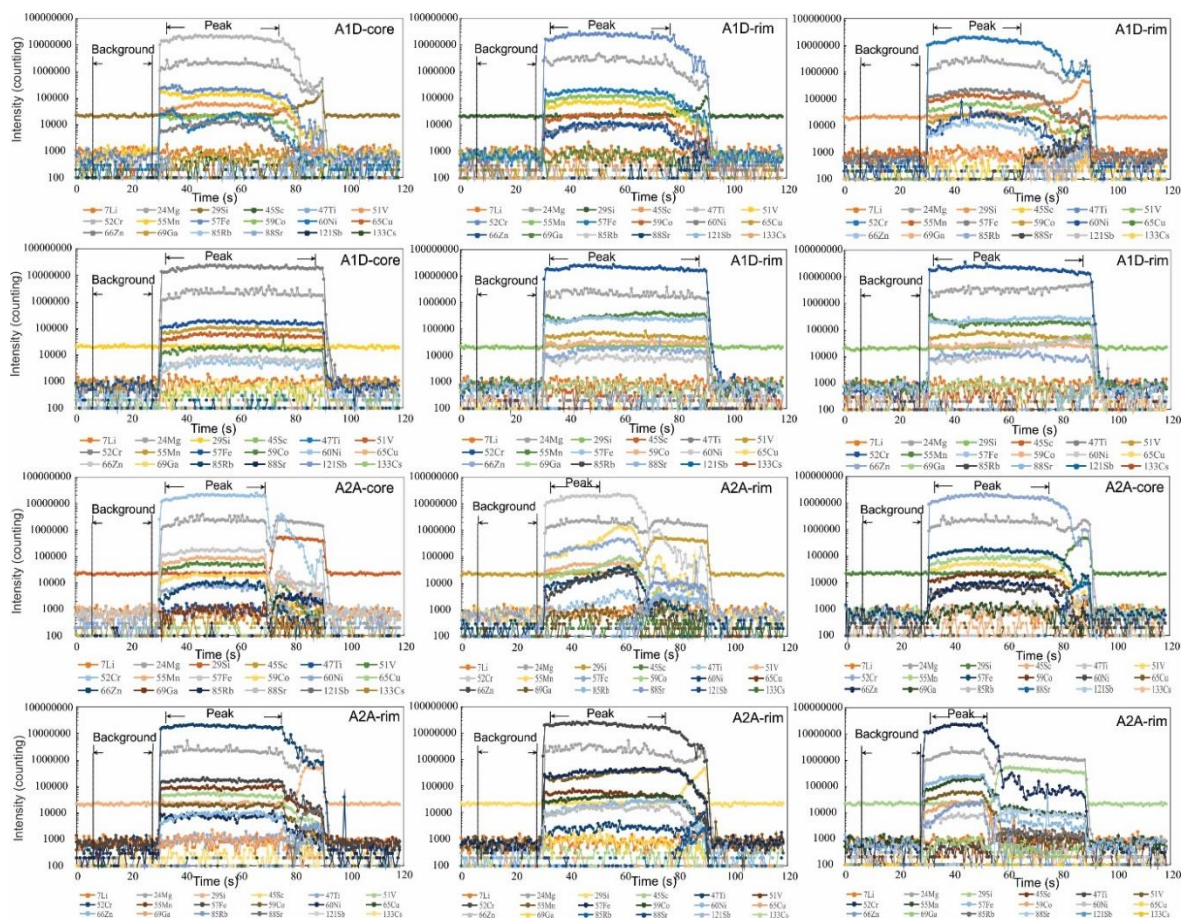


Figure E.12: LA-ICP-MS ablation profiles of the counting vs time (s) for trace element analyses for the studied Cr-spinel. All the calculated peaks area do not have any significant positive peaks for ^{29}Si and ^{57}Fe which indicated that there are no silicate inclusions and/or magnetite measured.

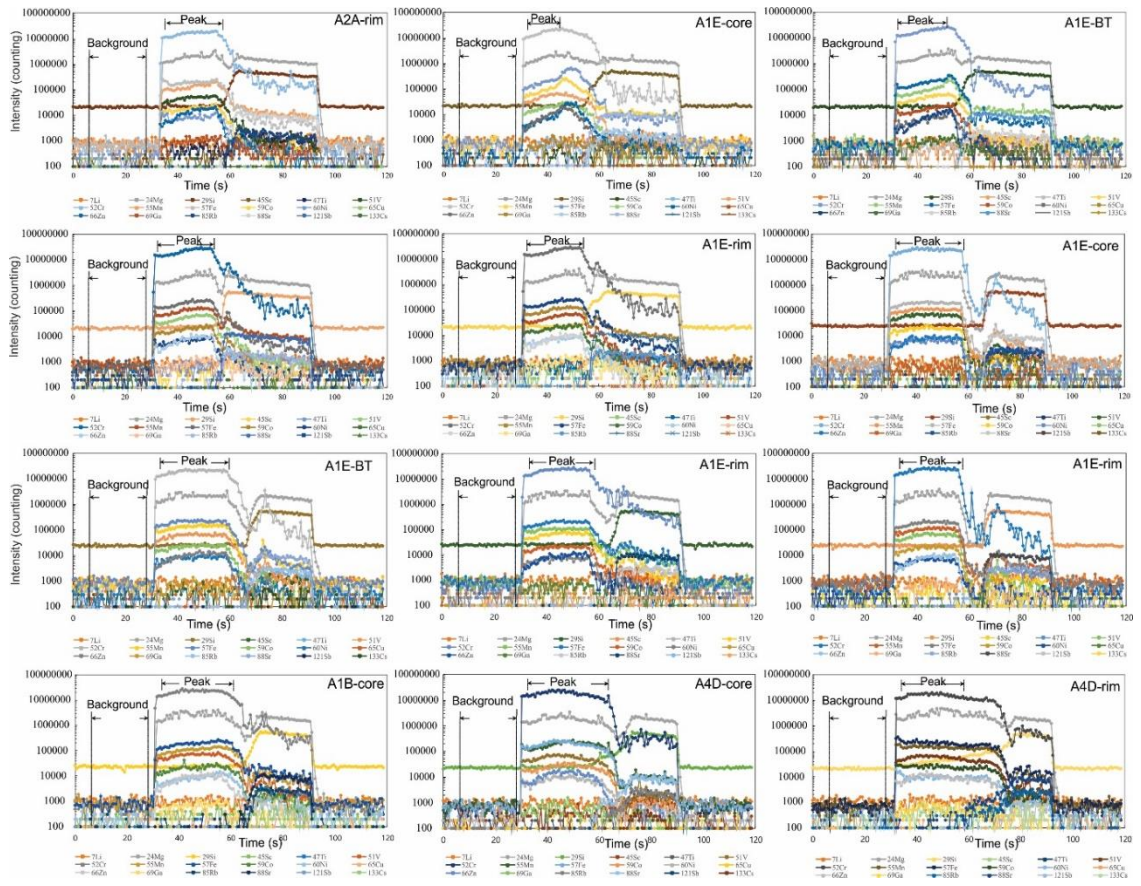


Figure E.12 continue

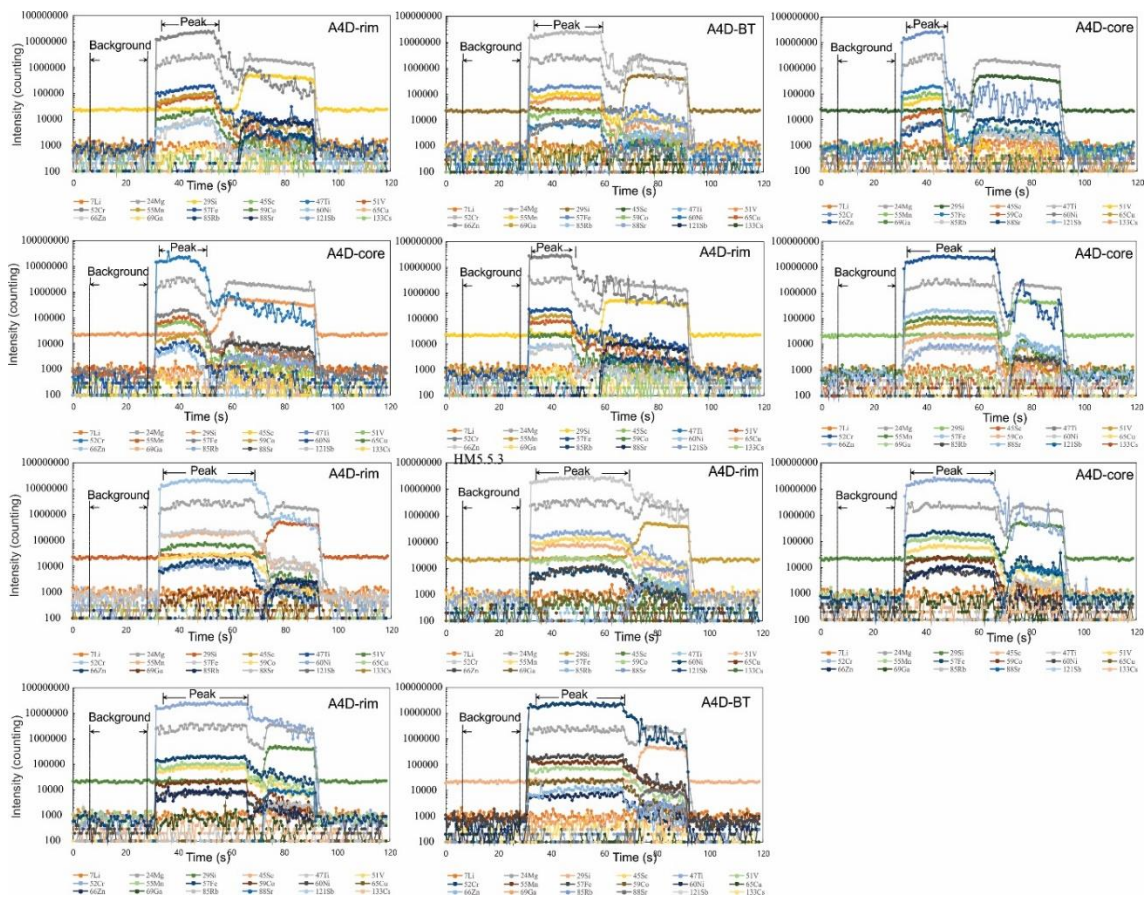


Figure E.12 continue

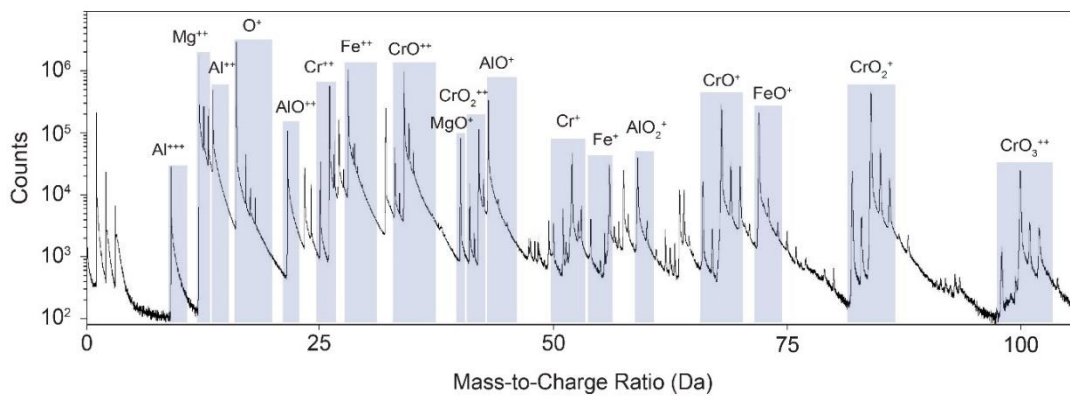


Figure E.13: Atom probe mass spectrum of the studied Cr-spinel. The cations are present as different molecular species with singly-charged to triply-charged ions. For example, Cr is present as Cr^+ , Cr^{2+} , CrO^+ , CrO^{2+} , CrO_2^+ , CrO_2^{2+} , CrO_3^+ and Cr_2O_3^+ ; and Al is present as Al^+ , Al^{2+} , Al^{3+} , AlO^+ , AlO^{2+} , AlO_2^+ , Al_2O^{2+} , and AlCrO_3^+ .

References (Appendix E)

- Anders, E. and Grevesse, N. (1989) 'Abundances of the elements: Meteoritic and solar', *Geochimica et Cosmochimica Acta*, Pergamon, 53(1), pp. 197–214. doi: 10.1016/0016-7037(89)90286-X.
- Arai, S., Ishimaru, S. and Okrugin, V. M. (2003) 'Metasomatized hazburgite xenoliths from Avacha volcano as fragments of mantle wedge of the Kamchatka arc: Implication for the metasomatic agent', *Island Arc*, 12(2), pp. 233–246. doi: 10.1046/j.1440-1738.2003.00392.x.
- Deschamps, F. *et al.* (2013) 'Geochemistry of subduction zone serpentinites: A review', *Lithos*, 178(APRIL), pp. 96–127. doi: 10.1016/j.lithos.2013.05.019.
- Dick, H. J. B. and Bullen, T. (1984) 'Chromian spinel as a petrogenetic indicator in abyssal and alpine-type peridotites and spatially associated lavas', *Contributions to Mineralogy and Petrology*, 86(1), pp. 54–76. doi: 10.1007/BF00373711.
- Franz, L. *et al.* (2002) 'Metasomatic Mantle Xenoliths from the Bismarck Microplate (Papua New Guinea)--Thermal Evolution, Geochemistry and Extent of Slab-induced Metasomatism', *Journal of Petrology*, 43(2), pp. 315–343. doi: 10.1093/petrology/43.2.315.
- Hamdy, M. M. and Gamal El Dien, H. (2017) 'Nature of serpentinitization and carbonation of ophiolitic peridotites (Eastern Desert, Egypt): constrains from stable isotopes and whole-rock geochemistry', *Arabian Journal of Geosciences*. Arabian Journal of Geosciences, 10(19). doi: 10.1007/s12517-017-3215-6.
- Hamdy, M. M., Harraz, H. Z. and Aly, G. A. (2013) 'Pan-African (intraplate and subduction-related?) metasomatism in the Fawakhir ophiolitic serpentinites, Central Eastern Desert of Egypt: mineralogical and geochemical evidences', *Arabian Journal of Geosciences*. Springer-Verlag, 6(1), pp. 13–33. doi: 10.1007/s12517-011-0319-2.
- De Hoog, J. C. M. *et al.* (2009) 'Serpentinised peridotites from an ultrahigh-pressure terrane in the Pohorje Mts. (Eastern Alps, Slovenia): Geochemical constraints on petrogenesis and tectonic setting', *Lithos*. Elsevier B.V., 109(3–4), pp. 209–222. doi: 10.1016/j.lithos.2008.05.006.
- Ionov, D. A. (2010) 'Petrology of mantle wedge lithosphere: New data on supra-subduction zone peridotite xenoliths from the andesitic Avacha volcano, Kamchatka', *Journal of Petrology*, 51(1–2), pp. 327–361. doi: 10.1093/petrology/egp090.
- Ishimaru, S. *et al.* (2007) 'Melting and multi-stage metasomatism in the mantle wedge beneath a frontal arc inferred from highly depleted peridotite xenoliths from the avacha volcano, Southern Kamchatka', *Journal of Petrology*, 48(2), pp. 395–433. doi: 10.1093/petrology/egl065.
- Johnson, P. R. *et al.* (2011) 'Late Cryogenian-Ediacaran history of the Arabian-Nubian Shield: A review of depositional, plutonic, structural, and tectonic events in the closing stages of the northern East African Orogen', *Journal of African Earth Sciences*. Elsevier Ltd, 61(3), pp. 167–232. doi: 10.1016/j.jafrearsci.2011.07.003.
- Lee, C.-T. A., Brandon, A. D. and Norman, M. (2003) 'Vanadium in peridotites as a proxy for paleo-fO₂ during partial melting: prospects, limitations, and implications', *Geochimica et Cosmochimica Acta*. Pergamon, 67(16), pp. 3045–3064. doi: 10.1016/S0016-

7037(03)00268-0.

McDonough, W. . and Sun, S. -. (1995) ‘The composition of the Earth’, *Chemical Geology*, 120, pp. 223–252. doi: doi.org/10.1016/0009-2541(94)00140-4.

Le Mée, L., Girardeau, J. and Monnier, C. (2004) ‘Mantle segmentation along the Oman ophiolite fossil mid-ocean ridge’, *Nature*, 432(7014), pp. 167–172. doi: 10.1038/nature03075.

Parkinson, I. J. and Pearce, J. A. (1998) ‘Peridotites from the Izu – Bonin – Mariana Forearc (ODP Leg 125): Evidence for Mantle Melting and Melt – Mantle Interaction in a Supra-Subduction Zone Setting’, *Journal of Petrology*, 39(9), pp. 1577–1618.

Paulick, H. *et al.* (2006) ‘Geochemistry of abyssal peridotites (Mid-Atlantic Ridge, 15°20’N, ODP Leg 209): Implications for fluid/rock interaction in slow spreading environments’, *Chemical Geology*, 234(3–4), pp. 179–210. doi: 10.1016/j.chemgeo.2006.04.011.

Peters, D. *et al.* (2017) ‘Fluid-mobile elements in serpentinites: Constraints on serpentinitisation environments and element cycling in subduction zones’, *Chemical Geology*. Elsevier, 466(July), pp. 654–666. doi: 10.1016/j.chemgeo.2017.07.017.

Workman, R. K. and Hart, S. R. (2005) ‘Major and trace element composition of the depleted MORB mantle (DMM)’, *Earth and Planetary Science Letters*, 231(1–2), pp. 53–72. doi: 10.1016/j.epsl.2004.12.005.

“Every reasonable effort has been made to acknowledge the owners of copyright material. I would be pleased to hear from any copyright owner who has been omitted or incorrectly acknowledged.”

Chapter 7:

Origin of arc magmatic signature: A temperature-dependent process for trace element (re)-mobilization in subduction zones

This chapter published as:

[Gamal El Dien, H., Li, Z.-X., Kil, Y., and Abu-Alam, T., 2019, Origin of arc magmatic signature: A temperature-dependent process for trace element \(re\)-mobilization in subduction zones: *Scientific Reports*, v. 9, p. 7098, doi:10.1038/s41598-019-43605-9.](https://doi.org/10.1038/s41598-019-43605-9)

Abstract

Serpentinite is a major carrier of fluid-mobile elements in subduction zones, which influences the geochemical signature of arc magmatism (e.g. high abundances of Li, Ba, Sr, B, As, Mo and Pb). Based on results from Neoproterozoic serpentinites in the Arabian-Nubian Shield, we herein report the role of antigorite in the transportation of fluid-mobile elements (FME) and light rare earth elements (LREE) from the subducted slab to arc-related magma during subduction. The serpentinites contain two generations of antigorites: the older generation is coarse-grained, formed at a temperature range of 165–250 °C and is enriched in Li, Rb, Ba and Cs, whereas the younger generation is finer-grained, formed at higher temperature conditions (425–475 °C) and has high concentrations of B, As, Sb, Mo, Pb, Sr and LREE. Magnesite, on the other hand, remains stable at sub-arc depths beyond the stability field of both antigorites, and represents a potential reservoir of FME and LREE for deeper mantle melts. Magnesite has high FME and LREE absorbing capacity (over 50–60%) higher than serpentine phases. Temperature is the main controlling factor for stability of these minerals and therefore the release of these elements from subducted

slabs into arc magmatism. As the liberation of these elements varies along the length of the slab, the resulting cross-arc geochemical variation trend can help to determine the subduction polarity of ancient arcs.

7.1 Introduction

Regardless of the tectonic setting in which they form, serpentinites are a major potential carrier of water (up to 15 %) and incompatible fluid-mobile elements (FME) such as Li, B, As, Sb, Pb, Ba, Cs, U and Sr (Rüpke *et al.*, 2004; Deschamps *et al.*, 2013; Kendrick *et al.*, 2017) into the subduction zone and the overlying mantle wedge. Serpentinites can be stable to high temperatures (620 °C) and pressures (5 GPa) at depths of up to 150–200 km (Ulmer and Trommsdorff, 1995), and their hydration and subsequent dehydration critically influence the generation and chemistry of arc-related magmas (Tatsumi, 1989; Hattori and Guillot, 2003; Pagé and Hattori, 2017). Thus, understanding the role of serpentinites (i.e., dehydration/devolatilization) in trace element geochemical cycles in subduction zones can discriminate between arc-related (i.e., high abundances of FME), plume-related, and mid-ocean ridge (MOR) basalts, and can track the cross-arc geochemical variations (Walowski *et al.*, 2015). Currently, the factors and mechanisms that control the transfer of these elements from oceanic environments through subducting serpentinites to arc magmatism are still unclear.

Numerous *in situ* studies were previously carried out on serpentinites with the aim of defining the behavior of fluid-mobile elements and rare earth elements (REE) during subduction. These studies highlighted the role of the original minerals (i.e., olivine vs. pyroxene) and temperature on trace element distributions during the subduction process (Deschamps *et al.*, 2010, 2011; Kodolányi *et al.*, 2012; Lafay *et al.*, 2013; Pagé and Hattori, 2017) but did not consider the distribution of trace elements at higher-temperature conditions within the stability field of antigorite. Instead, they concentrated on the lizardite/antigorite transition. In addition, they did not provide enough constraints on the temperatures range beyond which FME and REE are uptaken/released from the serpentines to arc magma. Although subducted carbonates are recognized to be a potential source of C for deep mantle melts through subduction (Galvez *et al.*, 2013; Liu, Lin and Prakapenka, 2015), the role of carbonate

minerals in serpentinite-bearing rocks as a reservoir for FME and REE has not been adequately considered.

Here, we use the results of a detailed petrological, mineralogical and geochemical study from selected Neoproterozoic serpentinite bodies in the Arabian-Nubian Shield (a typical arc-accretion orogen) (Stern *et al.*, 2004) to constrain the role of temperature within the stability field of antigorite on the distribution of FME and REE in subduction zones. In addition to antigorite, mineral chemistry of carbonate minerals indicates that magnesite is a potential reservoir for these elements during the subduction process. Our work argues against the prevailing view that original minerals (olivine and pyroxene) are the main factors controlling the trace element distribution. Instead, we provide evidence for the systematic distribution of FME and REE in subduction zones that depends on temperature conditions of the subducting slab, and we illustrate how the resultant cross-arc geochemical trends may help to determine the subduction polarity of ancient arcs in Earth's history.

7.2 Geological background and sample description

The Arabian-Nubian Shield (ANS) represents the largest Neoproterozoic juvenile continental crust. ANS formed through accretion of island arcs to the Gondwanan continental margins by the closure of the Mozambique Ocean during the East-African orogeny (750–550 Ma) (Johnson *et al.*, 2011). ANS ophiolites (which include abundant serpentinites) mark the suture zones between the accreted arcs (Stern *et al.*, 2004). Egyptian ophiolites, including ultramafic bodies, occur mainly in the central and southern parts of the Eastern Desert, extending across the border with Sudan (Figure F.1a). They were intensely deformed in the late Neoproterozoic during oblique collision (Abu-Alam and Stuwe, 2009) and accretion of island arcs onto the Saharan Metacraton, forming ophiolitic mélanges (Stern *et al.*, 2004). Although, some ophiolites were previously thought to have formed in mid-ocean ridges (Zimmer *et al.*, 1995), there is a general consensus that the majority of the ANS ophiolites formed in subduction-related tectonic settings (Stern *et al.*, 2004; Azer and Stern, 2007; Abd El-Rahman *et al.*, 2009; Abu-Alam and Hamdy, 2014; Gamal El Dien *et al.*, 2015, 2016; Hamdy and Gamal El Dien, 2017; Hamdy *et al.*, 2017).

Serpentinite samples were collected from Wadi Muweilih in the Central Eastern Desert of Egypt (Figure F.1b, c). This area is part of the Um Esh-Um Seleimat tectonic ophiolitic mélangé (Fowler and El Kalioubi, 2004) (Figure F.1b), and consists of highly sheared mélangé rocks containing many isolated masses of serpentinites, metagabbros, pillowed metabasalts, schistose rocks, metasedimentary rocks including metaconglomerates (Abu El Ela, 1996) (Figure F.1c and F2a, b). These serpentinized bodies crop out either as large lenticular blocks about 1–3 km in size, or as small thrust sheets in a tectonic mélangé with small amounts of talc-carbonate rocks. The contacts of the serpentinites with metasedimentary and metagabbroic rocks in the east and with metaconglomerates in the west are both SW-dipping thrusts (Figure F.1c). Along the faults, sheared serpentinites have been altered to talc-carbonates.

Petrographic investigations and Raman spectral analyses reveal that the protolith of the studied peridotites was suffered variable degrees of serpentinization and carbonation. Primary minerals olivine and pyroxene are completely serpentinized and chrome-spinel is the only primary relict phase. The studied serpentinites are composed mainly of antigorite, magnesite \pm dolomite, magnetite, small amounts of chrome-spinel, and minor amounts of chlorite and talc (Figure F.2d, e). Antigorite exhibits a predominantly a non-pseudomorphic, interpenetrating texture (Figure 7.1a-c) and mainly occurs in two distinct crystal sizes: fine aggregate grains (20–50 μm) and coarse radiating fibrous (100–150 μm) (Figure 7.1a-c). The fine antigorites commonly overprint the coarse ones (Figure 7.1a-c). Magnesite is present in two forms: either as anhedral clusters (Figure 7.1d) or in small veinlets associated with fine dolomite (Figure F.2c, d). Magnesite, magnetite, chrome-spinel, chlorite and talc occur as randomly distributed grains among antigorite-dominated groundmass.

7.3 Methods

7.3.1 Raman Spectroscopy analysis

Raman spectra of serpentines and carbonates (Figure 7.1e) were obtained by a micro-Raman system (HORIBA Jobin Yvon, Lab-RAM HR-800) equipped with a 514 nm Ar^+ laser (melles Griot, 43 series Ion Laser, 543-GS-A02) and an optical microscope (Olympus, BX41) at Kanazawa university, Japan. The Ar^+ laser has an irradiation power at 50 mW with a spectral resolution of about ± 2.5 to ± 3.5 cm^{-1} . The

Raman signal was acquired between 50 and 120 sec. Scattered light was collected in a backscattered geometry, using a pinhole (300 μm), slit (100 μm) and a grating (600 groves/ μm). A Si-based CCD (charge-coupled device) was used to record the Raman spectra. Based on OH stretching mode regions and lattice vibrational modes of the serpentine species (Groppo *et al.*, 2006), the spectral regions (0 to 1500 cm^{-1} and 3400 to 3900 cm^{-1}) were investigated. The LabSpec software was used to determine the band position of each spectrum.

7.3.2 Bulk rock chemical analysis

Major and trace element bulk-rock geochemistry was carried out for 8 serpentinite samples (Table F.1; all whole-rock data is reported on a volatile-free basis). Whole-rock samples were crushed with a polyethylene-wrapped hammer into <0.5 cm pieces and then were ground with ethyl alcohol in an agate mill to a grain size below 50 μm . Major element compositions were analysed by X-ray fluorescence spectrometer (Shimadzu, XRF-1800) at the Pukyong National University, South Korea. Analytical conditions were 40 kV accelerating voltage and 70 mA beam current. Analytical precision is better than 2% for major elements. All glass beads were analysed three times and the averages were taken. Certified Reference Materials (CRMs), BIR-1 and JG-2, were used to determine the accuracy of the major element compositions. For detailed method for trace and rare earth element analyses see Gamal El Dien Et al. (2016). Analytical values for USGS reference samples (BIR-1 and MUH-1) agree with recommended values within suggested tolerances. The precision of the measurements by repeated analyses of reference samples is better than $\pm 5\%$ for trace elements.

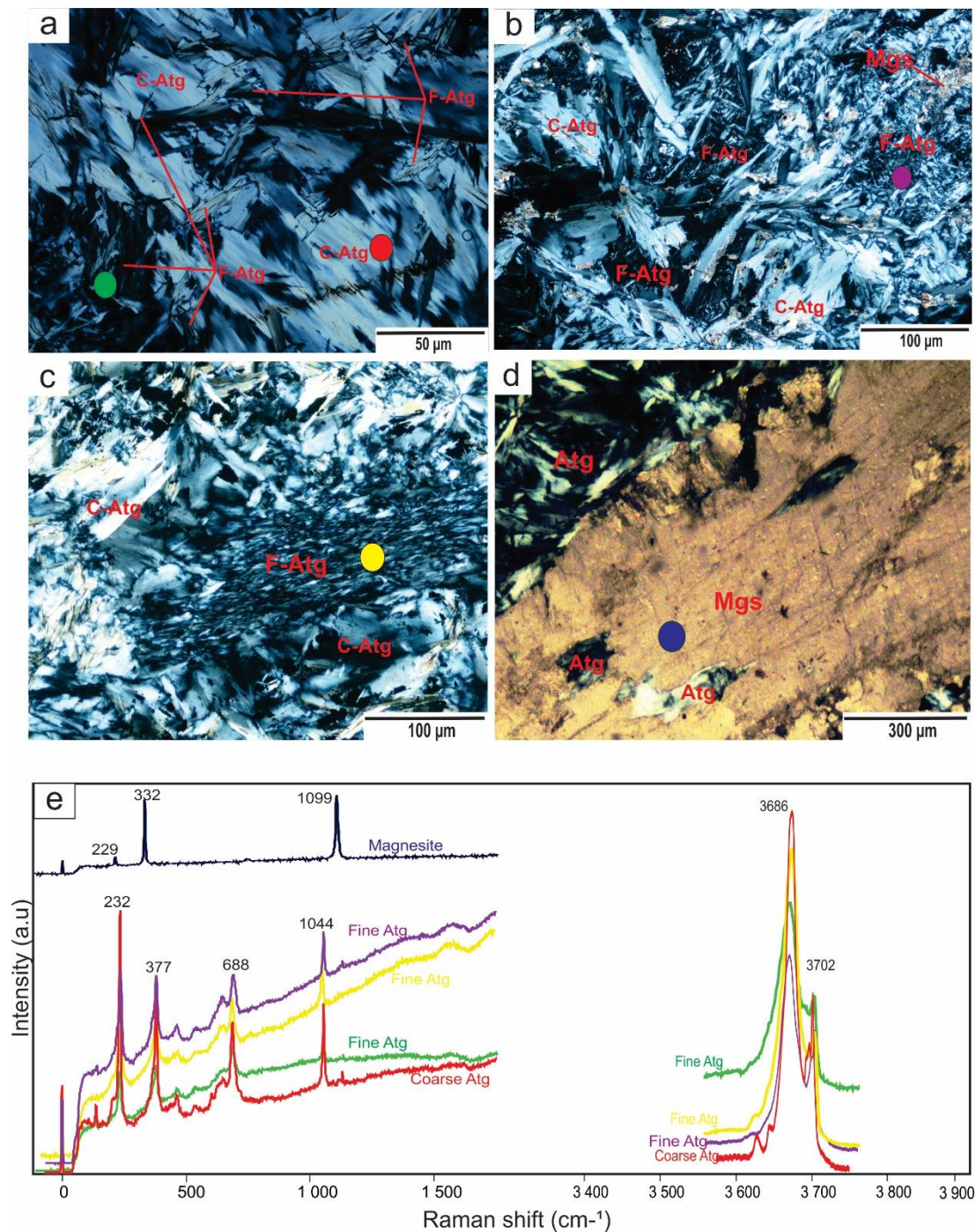


Figure 7.1: Photomicrographs of the studied serpentinites. (a-c) Interpenetrating texture of antigorite (Atg). (d) Magnesite (Mgs) clast containing antigorite relics. (e) Raman spectra of fine (F) and coarse (C)-grained antigorites in the studied serpentinites in low frequency (0–1500 cm^{-1}) and OH stretching (3350–3900 cm^{-1}) ranges. Antigorite shows discrete peaks at 232, 377, 688 and 1044 cm^{-1} in the low wavenumber region and 3686 and 3702 cm^{-1} in the OH-band region. The Raman spectra of magnesite show peaks at 229, 332 and 1099 cm^{-1} in the low wavenumber region.

7.3.3 Electron probe micro analysis (EMPA)

Major and some minor elements in antigorites and carbonates were acquired using a JEOL JXA-8800 electron-probe at Kanazawa University, Japan (Table F.2). The analytical conditions were 15 kV accelerating voltage, 20 nA probe current and 3 μm beam diameter. The ZAF-correction was performed to correct the raw data. Ferric and ferrous iron redistribution from electron microprobe analyses was made using the charge balance equation (Droop, 1987). Natural minerals standards were used for calibration (JEOL Kanazawa STD1) such as Q17-quartz for Si, O16-corundum for Al, O19-eskolaite for Cr, M6-fayalite for Fe, O15-periclase for Mg, O20-manganosite for Mn, M8-wollastonite for Ca, M3-jadeite for Na, M13-KTiPO₅ for K, Ti and O24-pentlandite for Ni. Olivine, clinopyroxene and spinel standard reference minerals, separated from Kurose peridotites xenoliths, were used.

7.3.4 Laser ablation-inductively coupled plasma-mass spectrometry (LA-ICP-MS) micro analysis

Trace element compositions of serpentine and magnesite (Table F.3, 4) were determined by 193 nm ArF Excimer LA-ICP-MS at Korean Basic Science Institute (KBSI), South Korea (Teledyne Cetac Technologies equipped with Analyte Excite). Analyses were performed by ablating 110 μm diameter spots at 10 Hz with an energy density of 5 J/cm² per pulse. Signal integration times were 60s for a gas background interval and 60s for an ablation interval. The NIST SRM 612 glass was used as the primary calibration standard and was analysed at the beginning of each batch of <5 unknowns, with a linear drift correction applied between each calibration. The element concentration of NIST SRM 612 for the calibration is selected from the preferred values of Pearce et al. (1997). Each analysis was normalized using ²⁹Si for serpentine and ²⁴Mg for magnesite as internal standard elements, based on Si and Mg contents obtained by Electron probe micro analysis (EMPA). All minerals were analysed multiple times and the average taken. The relative standard deviations (RSD) of the trace and rare earth elements in the minerals were mostly 5–10%. To improve precision and accuracy of the trace elements data, we analysed the NIST612 CRM before and after each 5 unknown samples. High RSD is found only for ¹³⁷Ba

(10.7%). We analysed some clear homogenous areas of antigorite aggregates, but some area may contain dusty magnetite or other minor phases which may influence the actual antigorite trace elements values. Thus, we used the Glitter software, which shows ablation profile for element and permits to reduction of analytical contamination.

7.3.5 Thermodynamic modelling

Thermodynamic modelling was calculated in a FMCASH-CO₂ system (i.e., FeO-MgO-CaO-Al₂O₃-SiO₂-H₂O-CO₂). Different pseudosections were constructed using *Perple_X* (Connolly and Kerrick, 1987) and the internally consistent dataset of Holland and Powell (2011). We assumed that local equilibrium, when chemical potentials are equalized (Evans, Powell and Frost, 2013), was obtained at a length scale of millimetres. The solution model of (antigorite, chlorite, olivine and garnet, orthopyroxene, clinopyroxene, spinel, carbonate (magnesite) and fluid) (Connolly and Trommsdorff, 1991; Holland and Powell, 2011; Padrón-Navarta *et al.*, 2013; Jennings and Holland, 2015) was used. Ideal mixing is assumed for anthophyllite, brucite and talc. Lizardite and chrysotile were used without solution models. Equilibrium thermodynamics is widely used to study the tectonic evolution of the metamorphic rocks (Holland and Powell, 2011). However, for serpentinite where mineralogical change is driven primary by fluid infiltration processes and to a lesser extent by changes in pressure and temperature, the thermodynamic techniques have been applied less commonly. Fluid infiltration process, in general, causes changes in the bulk rock composition, therefore the changes in the bulk chemistry of the system are considered in all the calculated pseudosections. All the major elements of the modelled chemical system show linear relations with the H₂O content (Figure F.3). Al₂O₃, SiO₂ and FeO show negative correlations while MgO shows a positive correlation. The concentrations of these elements were shifted from the original composition of the rock during partial melting and serpentinization process (Gamal El Dien *et al.*, 2016). For the modelling, the x-axes of the pseudosections are assigned to the composition of the system. The value zero of the x-axes indicates the less modified amounts of the oxides while the value one indicates the maximum modification recorded in the studied rock samples.

7.4 Results

7.4.1 Geochemical composition

All the studied serpentinite samples have high-water contents (i.e., high LOI values), ranging from 12.54 to 14.93 wt% (for details on the bulk-rock compositions see Supplementary Information). The Raman spectra of the examined serpentinite samples identify antigorite as the only serpentine phase (Figure 7. 1e). Two groupings of antigorite are distinguished based on their different textures (grain sizes) and chemical compositions (Figures 7.1 and 7.2a; Table F.2). The first group is coarse-grained (100–150 μm), and the second group is fine-grained (20–50 μm) (Figure 7.1a–c). The coarse-antigorite (CA) group has higher SiO_2 content (43.01–45.86 wt%) and lower Al_2O_3 content (0.02–0.97 wt%) compared to the fine-antigorite (FA) group which range in SiO_2 from 39.52–42.95 wt% and in Al_2O_3 from 1.16–3.38 wt% (Figure 7.2a). MgO and FeO contents do not show systematic variation between the two groups (Figure 7.2a). NiO (up to 0.92 wt %) and Cr_2O_3 (up to 1.06 wt %) contents show no notable difference, and both groups plot in the serpentine fields of olivine and orthopyroxene, reflecting a harzburgite protolith (Figure 7.2b). *In situ* trace element analyses reveal a heterogeneous distribution of FME between the CA- and FA-groups. FME such as B have higher contents in the FA-group (40.89–49.87 ppm) than in the CA-group (15.32–24.50 ppm), whereas Li has higher contents in the CA-group (3.44–3.95 ppm) than in the FA-group (2.03–2.73 ppm) (Figures 7.3, F.7, and F.6; Table F.3). Moreover, the CA-group has lower contents of As, Sb, Pb, Mo, Sr and higher contents of Rb, Cs and Ba (Figures 7.3, F.7, and F.6; Table F.3). Th, U, P and high-field strength elements (HFSE: Nb, Ta, Zr and Hf) show no obvious difference between the two groups, but Ta and Hf show positive spikes compared to elements of the same compatibility in both groups (Figure 7. 3). REE normalized to (CI)-Chondrite (Anders and Grevesse, 1989) patterns have a U-shape pattern, and the light rare earth elements (LREE) contents higher in the FA-group ($\text{La} = 0.074\text{--}0.127$ ppm, $\text{La}_\text{N}/\text{Sm}_\text{N} = 1.96\text{--}3.29$) compared to the CA-group ($\text{La} = 0.031\text{--}0.047$ ppm, $\text{La}_\text{N}/\text{Sm}_\text{N} = 1.88\text{--}2.79$) (Figure 7.3). The middle rare earth elements (MREE) to heavy rare earth elements (HREE) show a slight negative slope. The HREE concentrations of the FA and CA- groups are indistinguishable ($\text{Yb}_{\text{N(CI-normalized value)}} = 0.47\text{--}0.57$) (Figure 7.3).

Magnesite is the main carbonate mineral, representing 5–10 % of the modal mineral composition in the studied samples, although minor thin veinlets of dolomite also occur (Figure 7.1d; Figure F.2c, d). Magnesite composition varies in MgO (37.72–40.49 wt %), FeO (1.88–5.77 wt %) and MnO (0.32–2.74 wt %). Dolomite has variable contents of MgO (14.83–20.21 wt %), CaO (21.44–27.54 wt %), FeO (0.44–5.65 wt %) and MnO (0.09–1.15 wt %). A Primitive Mantle (PM)-normalized (McDonough and Sun, 1995) trace element diagram of analysed magnesite shows a significant enrichment in incompatible elements (Figure 7.3). Almost all FME, such as Sb (1.55–17.83 ppm), B (59.06–170.96 ppm), As (25.31–46.30 ppm), Mo (1.89–2.28 ppm), Cs (0.28–0.72 ppm), Li (13.90–36.01 ppm) and Pb (1.63–2.86 ppm) are enriched in magnesite (Figure 7.3; Table F.3). Rb (0.70–0.91 ppm) is slightly enriched and both Sr (5.48–9.04 ppm) and Ba (0.56–4.32 ppm) are slightly depleted relative to primitive mantle but are slightly enriched relative to elements with similar compatibility (Figure 7.3). HFSE such as Ti (11.62–20.39 ppm), Zr (~0.31 ppm), Hf (0.14–0.15 ppm), Nb (0.08–0.09 ppm) and Y (0.57–1.44 ppm) are highly depleted. Chondrite (Anders and Grevesse, 1989)-normalized REE pattern shows the same U-shape like antigorites, but with higher LREE contents ($La_N = 5.04–5.80$) (Figure 7.3). HREE are highly enriched, with Yb up to 3 times of that of Chondrite, and show a slight negative slope to MREE.

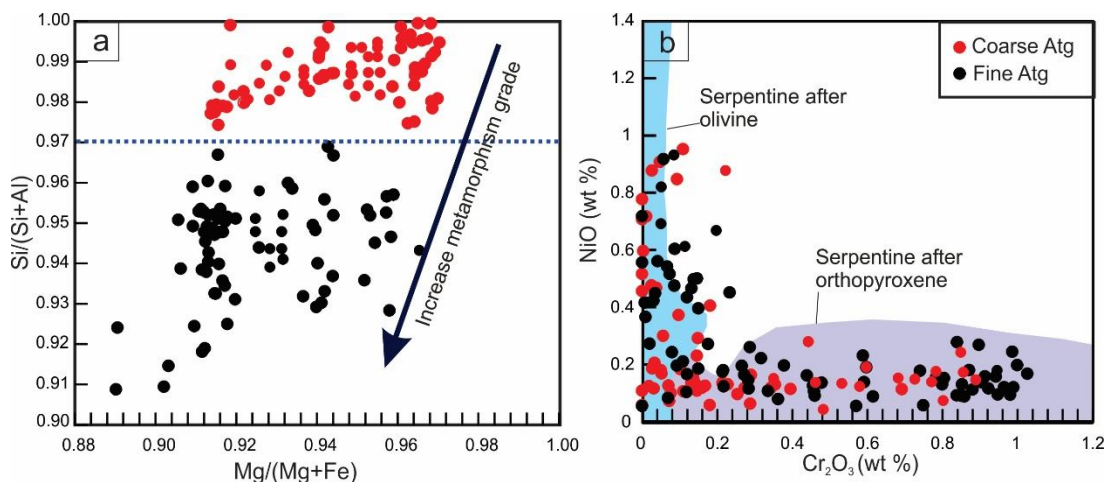


Figure 7.2: Mineral chemistry of antigorites from the studied samples. (a) $Si/(Si+Al)$ vs. $Mg/(Mg+Fe)$. The variation of $Mg/(Mg+Fe)$ indicates different bulk chemistry of the rocks while the variation of $Si/(Si+Al)$ is due to increase in the metamorphic grade. (b) NiO vs. Cr_2O_3 (wt %). Data used to create olivine and orthopyroxene fields collected from Kodolányi et al. (2012).

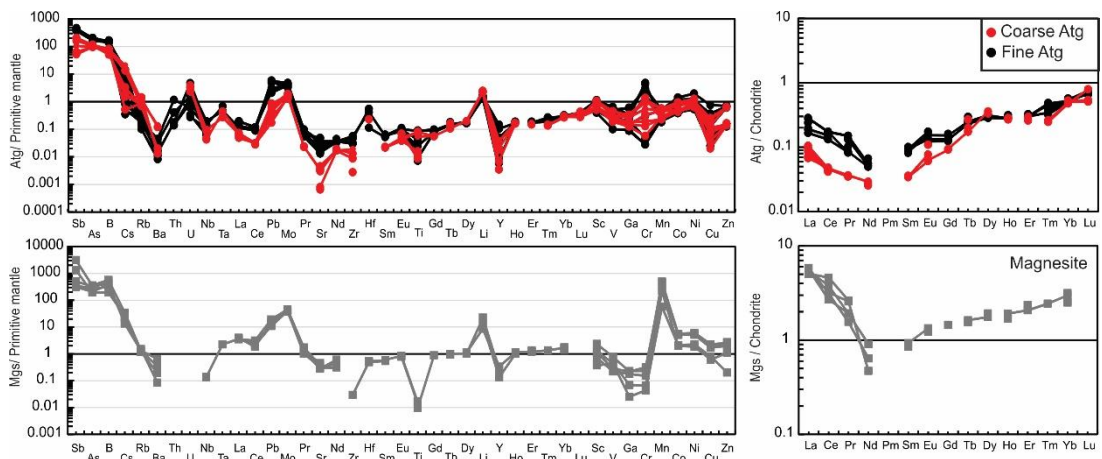


Figure 7.3: Primitive mantle (McDonough and Sun, 1995) normalized multielement and rare earth element patterns normalized to chondrite (Anders and Grevesse, 1989) of the studied antigorite and magnesite.

7.4.2 Thermodynamic modelling

A series of T-X pseudosections at different pressures were calculated to estimate the pressure-temperature conditions of the serpentinization. All the T-X pseudosections show stability of the spinel mineral at high-temperatures (> 670 °C; Figure F.7). These temperature estimates indicate that the observed spinel in the studied samples is a metastable phase with respect to the surrounded low-grade assemblages (Arai, 1994). Figure 7.4 shows two T-X pseudosections at 1 and 8 kbar, respectively. These pseudosections have similar topology but dolomite is unstable at low pressure conditions (i.e., 1 kbar) within the studied T-X range. At higher pressure conditions (i.e., 8 kbar; Figure 7.4), however, dolomite is stable within the temperature range of 325–550 °C. The observed mineral assemblages, i.e., chlorite-talc-antigorite-magnesite-fluid \pm dolomite, are thermodynamically stable at the bulk composition range of between 0.15–1 and 0–1 for pressures of 1 and 8 kbar, respectively (Figure 7.4). The upper temperature limits for the stability of the observed assemblages are marked by the anthophyllite-in boundaries. At low pressure conditions (e.g. 1 kbar), the anthophyllite-in boundaries appear in the temperature range of 360–375 °C, but at 8 kbar the boundaries shift to the higher temperature (450–475 °C). Figure 5a shows

the shift of anthophyllite-in boundaries toward higher temperature with an increase in pressure from 1 kbar to 9 kbar.

The antigorites display an increase in SiO₂ content and decrease in Al₂O₃ content from the FA-group to the CA-group (Figure 7.2a; Table F.2). Tschermak's substitution in antigorites is proposed to occur following the equation of $M^{2+} + Si^{4+} = Al^{3+} + M^{3+}$, where M²⁺ resides in the octahedral site (Mg, Fe²⁺, Mn and Ni) and M³⁺ in the tetrahedral site (Fe³⁺, Cr, Al) (Li, Rahn and Bucher, 2004). Thus, Al³⁺ is incorporated in antigorite through a coupled exchange when one Mg and one Si cation are substituted by two Al cations (Li, Rahn and Bucher, 2004; Padrón-Navarta *et al.*, 2013). The Si/(Al+Si) ratio of antigorite has been used as a non-linear potential geothermometer for serpentinite rocks, due to its sensitivity to temperature (Eggler and Ehmann, 2010; Padrón-Navarta *et al.*, 2013). In the current study, the Si/(Al+Si) ratios are insensitive to changes in pressure but are sensitive to changes in temperature (Figure 7.5).

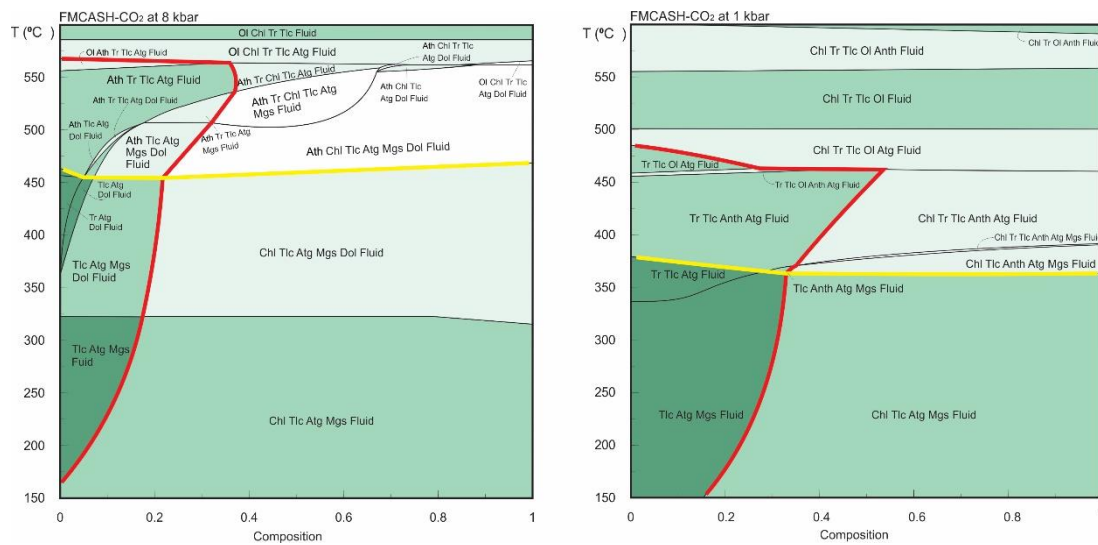


Figure 7.4: T-X pseudosections. The two pseudosections constructed at pressure 8 kbar (a) and 1 kbar (b) in the chemical system FMCASH-CO₂ using the activity models cited in the methods section. The x-axes represent a range of the bulk composition in wt% where 0 is equivalent to bulk of: FeO: 4.157, MgO: 47.13, CaO: 0.001, Al₂O₃: 0.715, SiO₂: 40.524, H₂O: 8.89, CO₂: 0.001, and 1 is equivalent to bulk of: FeO: 7.00, MgO: 35.00, CaO: 0.04, Al₂O₃: 3.00, SiO₂: 50.00, H₂O: 18.00, CO₂: 0.8. The red isochemical lines represent the chlorite-in boundaries. The studied mineral assemblages are stable to right-side of the chlorite-in boundaries. The yellow line shows the anthophyllite-in boundary. The studied assemblages are stable to the lower temperature part of the anthophyllite-in boundaries.

Although the difference in Si/(Al+Si) between the two groups is relatively small (Figure 7. 5b, c), a gap in the mineralogical composition is clearly observed at

Si/(Al+Si) between 0.965 and 0.975 (Figure 7.2a and Figure 7.5b, c) which corresponds with the petrographic transition from the CA to the FA-group. Also, this gap corresponds with the isopleth line (with value 0.965) which is observed in the temperature range of 250–425 °C (Figure 7. 5a). The CA-group has Si/(Al+Si) in the range of 0.975 – 1 (apfu; atoms per formula unit), corresponding with a temperature range of ca. 200 to 250 °C (Figure 7.5). The FA-group has a Si/(Al+Si) content range of 0.92 – 0.96 which indicates higher temperature conditions (425–475 °C). Such temperatures cannot be achieved unless the system attains local equilibrium at pressure > 9 kbar.

7.5 Discussion

7.5.1 Origin of the protolith

Field, petrographical and geochemical characteristics of the studied serpentinites suggest a subduction channel origin for the protolith. A subduction channel typically consists of fragments of subducted oceanic serpentinites, metasediments, and altered mafic crust that can be later accreted to the arc system to form a mélangé zone (Saumur, Hattori and Guillot, 2010; Blanco-Quintero *et al.*, 2011; Deschamps *et al.*, 2012). Such serpentinites are typically strongly sheared and dominated by antigorite (Guillot *et al.*, 2015). All of these features are present in the studied region (Figure F.1 and F2a, b) and most of the ANS ophiolites (Stern *et al.*, 2004). The studied serpentinites occur in one of the well-developed suture zones in the Eastern Desert of Egypt, i.e., the Um Esh-Um Seleimat tectonic mélangé (Fowler and El Kalioubi, 2004) (Figure F.1b, c). Furthermore, these rocks are similar to some subducted serpentinites in Mesozoic ophiolites such as those of the Zagros suture zone in Iraq (Aziz, Aswad and Koyi, 2011) and ophiolite complexes of Northwest Anatolia in Turkey (Aldanmaz and Koprubasi, 2006). Previous work (e.g., Abd El-Rahman *et al.*, 2009; Hamdy *et al.*, 2017) on ophiolites in the vicinity also suggest a subduction-related origin.

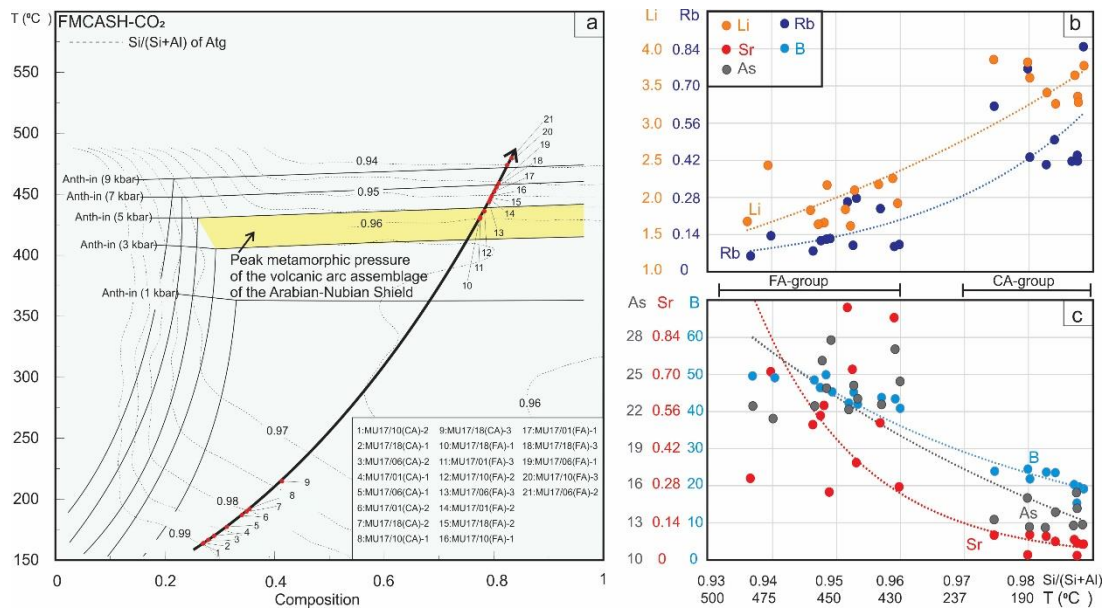


Figure 7.5: P-T-X pseudosection showing the shift of the anthophyllite-in boundaries toward higher temperature conditions when the pressure increases. The yellow area represents the anthophyllite-in boundaries at pressure of ca. 4 kbar which is equivalent to the peak metamorphic pressure of the volcanic arc assemblages of the Arabian-Nubian Shield (Abu-Alam *et al.*, 2014). The pressure represents a combination of lithostatic and hydrostatic pressures. The vertical isochemical solid lines show the shifting in the chlorite-in boundary with pressure change. Contour lines are the Si/(Si+Al) ratio of the antigorite chemistry in the T-X space. The solid black arrow represents the P-T-X path of the studied rocks. The red dots along the P-T-X path represent some of the analysed antigorites (CA at the low temperature conditions) and (FA at the high temperature conditions). The right hand plots shows the variations of Li and Rb (b) B, Sr and As (c) contents of the two group antigorites with the temperature changing along the P-T-X path. The x-axes represents temperature and Si/(Si+Al).

The harzburgite protolith of the studied serpentinites suggests that the peridotite parents have a refractory origin, and clinopyroxenes were almost completely exhausted by pre-serpentinization partial melting (for details on the nature of the protolith see Supplementary information). Moreover, mineralogical (spinel Cr# > 0.6) (Arai, 1994) and geochemical characteristics such as low Al_2O_3/SiO_2 (≤ 0.04), strong depletion in compatible trace elements (i.e., HREE and Y), over-enrichment of As, Pb, Mo and nearly flat REE patterns, also point to a subducting-slab origin (Deschamps *et al.*, 2012, 2013; Lafay *et al.*, 2013) for the studied serpentinites and distinguishes them from mantle wedge/fore-arc serpentinites (e.g., Izu-Bonin-Mariana) (Savov *et al.*, 2005; Kodolányi *et al.*, 2012) (Figure F.4 and F.5).

The high field strength element (HFSE: Nb, Th, Hf and Ti) contents of the studied rocks (Figure F.5b) differ significantly from patterns expected of a melt residue (Paulick *et al.*, 2006). In addition, the absence of any correlation between these elements and LOI indicates that the enrichment processes were not related to the

serpentinization; instead, they were more likely caused by melt-rock interaction (Paulick *et al.*, 2006; Kodolányi *et al.*, 2012). The high Ti content (150–360 ppm) of the studied serpentinites that plot above the melting trend (Figure F.5b) suggests interaction of the subducting serpentinite mainly with Ti-rich melts (Ti= 30–500 ppm) (Deschamps *et al.*, 2013). On the other hand, the positive correlations of LREE and FME with LOI point to the enrichment of these elements during serpentinization process of the protolith through fluid/rock interactions (Figure F.3).

7.5.2 Two-stage serpentinization and geochemical consequences

We suggest that the studied rocks experienced two stages of serpentinization which correspond to the different temperature ranges associated with the formation of CA- and FA-group antigorites (Figure 7.5). The first stage resulted in the formation of coarse antigorites at 200–250 °C that may have grown directly from the original olivine and orthopyroxene (Muntener, Hermann and Trommsdorff, 2000) during the initial stage of subduction. During this stage, the slab-derived fluids caused strong hydration of the subducted peridotites protolith forming CA-group, such as the antigorite serpentinites (≥ 200 °C) (Evans, 2004; Hilairret, Daniel and Reynard, 2006) in the Happono-O'ne area in Japan (Khedr and Arai, 2010) and some of the other antigorite serpentinites in Eastern Desert, Egypt (Gamal El Dien *et al.*, 2016; Hamdy and Gamal El Dien, 2017). Although the coarse antigorites could also have crystallized by progressive replacement of lizardite formed during low-temperature oceanic serpentinization (Mével, 2003; Evans, 2004), we favour the former explanation due to the absences of lizardite relics (i.e., mesh cells) (Guillot *et al.*, 2015) in the studied serpentinites. The second serpentinization stage occurred at increased subduction depths with elevated metamorphic temperatures of 425–475 °C (Deschamps *et al.*, 2011; Lafay *et al.*, 2013) (Figure 7.5), resulting in the formation of the fine antigorites which overprinted and replaced some of the coarse ones (Figure 7.1a-c).

During subduction, oceanic lithosphere gets serpentinized through interactions with circulating fluids released from the subduction channel (Gerya, Stöckhert and Perchuk, 2002; Rüpke *et al.*, 2004; Li and Lee, 2006; Blanco-Quintero *et al.*, 2011; Bebout, 2014; Guillot *et al.*, 2015). Although some studies show that the oceanic lithosphere can be serpentinized before it enters the subduction zone (Alt *et al.*, 2013),

the primitive mantle-normalized pattern of the FME and LREE of the studied serpentinites (Figure 7.6) and their rock-forming minerals (antigorites and magnesites) have significant similarity to the subduction inputs components that include mainly altered oceanic crust (AOC) (Staudigel, 2013), global subducted sediments (GLOSS II) (Plank, 2013) and marine sediments (Li and Schoonmaker, 2013). These elements, with the exception of Sr, Rb and Li, are more highly enriched than seawater-derived hydrothermal fluids in spreading mid-ocean ridges (MOR: Logatchev, Rainbow, Snake Pit) (Schmidt *et al.*, 2007). Moreover, the over-enrichments of As, Sb, B and Mo in the studied serpentinites and their rock-forming minerals support an important role for sediment-derived fluids (Plank and Langmuir, 1993; Bebout, 2014; Gaschnig *et al.*, 2017) which are characteristic of subduction-related serpentinites (Deschamps *et al.*, 2012, 2013; Lafay *et al.*, 2013). The similarities in Li, Sr and Rb contents between the serpentinites and seawater-derived hydrothermal fluids suggest contribution of seawater either through direct infiltration into fractures and faults that formed during the bending of a subducted slab (Faccenda, Gerya and Burlini, 2009) as it entered the subduction channel, or through the circulation of water/fluids in the subduction channel that were released from the subducted oceanic lithosphere and marine sediments (Kerrick, 2002).

To further test our interpretation, we calculated the FME composition of the fluids that interacted with the studied rocks during serpentinization. There are only a few experimental studies focused on FME (i.e., B, Li, As, Sb and Cs) partitioning during progressive serpentinization (Lafay *et al.*, 2014, 2016) and those studies are limited to the low temperature serpentine phase (200–300 °C). Here we used the partitioning coefficient of those elements (Lafay *et al.*, 2014, 2016) to estimate the fluid composition in equilibrium with the CA-group antigorites. The estimated composition of those elements in the equilibrated fluids have B = 26.41–42.24 ppm, Li = 0.40–0.46 ppm, Sb = 0.03–0.09 ppm, As = 3.26–3.96 ppm and Cs = 0.07–0.23 ppm. With the exception of Li, these estimates are similar to the subduction input components compositions of GLOSS II and AOC (e.g., B = 26.6–67.9 ppm and Cs = 0.15–4.9 ppm) (Plank, 2013; Staudigel, 2013), but are higher than seawater-derived hydrothermal fluids in MOR (B = 3.35 ppm, Cs = 0.03 ppm, As = 0.009 ppm and Sb = 0.0008 ppm) (Li, 1982; Schmidt *et al.*, 2007). Therefore, we conclude that the studied serpentinites were formed in a subduction-related environment where

serpentinization was caused mainly by fluids from the subduction channel with sedimentary input.

The studies of Bebout (2014) and Marschall *et al.* (2007) demonstrated the release of B, Li, As, Sb and Cs from sedimentary and mafic rocks via prograde metamorphism and increasing pressure-temperature conditions within the subduction channel. *In situ* B and Li analyses in the studied antigorites indicate, based on thermodynamic modelling (Figures 7.4, 7.5), that the different distributions in B and Li between the two antigorite groups (CA- av. = 21.29, 3.69 ppm, respectively; FA- av. = 45.61, 2.30 ppm, respectively) (Figure 7.5b, c; Figure 7.6) are related to different temperature conditions. The enrichment of B at high temperature and Li at low temperature contrasts with some previous studies (Vils *et al.*, 2011; Deschamps *et al.*, 2012, 2013; Kodolányi *et al.*, 2012) which argue that B enrichment occurs in the low temperature serpentine phase and is depleted at high temperature conditions. However, it is in agreement with the reported retention of B at higher metamorphic grade phase (Scambelluri and Tonarini, 2012; Pagé and Hattori, 2017). Our interpretation is also supported by a continuous loss of B from the subducting slab (i.e., low B at high temperature) during the progression of subduction (Bebout, 2014). The behaviour of Li, on the other hand, is in agreement with previous studies that revealed the loss of Li during the lizardite/antigorite transition and increasing temperature of serpentinization. Furthermore, As, Sb, Pb and Mo contents are higher in the high temperature FA-group (Av. As = 23.16 ppm, Sb = 2.04 ppm, Pb = 0.61 ppm, Mo = 0.20 ppm) compared to the low temperature CA-group (Av. As = 13.36 ppm, Sb = 0.77 ppm, Pb = 0.08 ppm, Mo = 0.06 ppm) (Figure 7.5c; Figure 7.6), suggesting addition/incorporation of those elements to the FA-group at higher temperatures. These trends are consistent with a continuous release of those elements from subducted sediments and from AOC during prograde metamorphism (Bebout, 2014; Gaschnig *et al.*, 2017). Whereas B, As and Sb are preferentially incorporated into tetrahedral Si in sheet silicates (Hattori and Guillot, 2003; Pagé and Hattori, 2017) (i.e., antigorite), they are likely to increase from CA- to FA-group with decreasing Si/(Al+Si) and increasing temperature (Figure 7.5b, c).

Contrary to the aforementioned elements, large ion lithophile elements (LILE) such as Rb, Ba, Cs and U are more enriched in the low temperature CA-group (Av. Rb = 0.55 ppm, Ba = 0.48 ppm, Cs = 0.17 ppm, U = 0.06 ppm) than in the high

temperature FA-group (Av. Rb = 0.15 ppm, Ba = 0.14 ppm, Cs = 0.08 ppm, U = 0.02 ppm), consistent with the enrichment of these elements at low-temperature conditions (Bebout, 2013; Deschamps *et al.*, 2013) (Figures 7.5b and 7.6). This enrichment suggests the release of these elements during the high-temperature serpentinization process (Deschamps *et al.*, 2012; Kodolányi *et al.*, 2012; Lafay *et al.*, 2013). However, Sr has higher content in the high temperature FA-group (Av. = 0.56 ppm compared to Av = 0.06) indicating continuously addition of Sr to the antigorite from the subduction channel-derived fluids and retention at higher temperatures. This result is contrary to previous studies that argue against Sr enrichment at high temperature (Vils *et al.*, 2009; Deschamps *et al.*, 2012, 2013; Kodolányi *et al.*, 2012; Lafay *et al.*, 2013), although those studies concentrated only on lizardite/antigorite transition without determining the formation temperature for each phase or distinguishing between the two temperature-dependant phases of antigorite. Moreover, our results support Kodolányi *et al.*'s (2012) observation that the distribution of B and Sr is controlled by the same mechanisms, which we suggest to be temperature- and fluid-dependent processes.

The REE contents of the serpentine phases are commonly assumed to be an inherited feature from the original minerals (olivine and pyroxene) (Deschamps *et al.*, 2010, 2013; Kodolányi *et al.*, 2012; Lafay *et al.*, 2013). Here, the studied antigorite (both the CA- and FA- groups) displays interpenetrating textures with no preservation of the primary minerals, arguing against the role of the parent minerals in the trace element concentrations of antigorite. Although, the two groups have similar HREE contents, the high temperature FA-group have higher LREE (La = 0.074–0.127 ppm) than the low temperature CA-group (La = 0.030–0.047 ppm) (Figure 7.6). Our data suggest re-mobilization of LREE with increasing serpentinization temperature.

7.5.3 Carbonates formation and trace elements budget

The predominance of magnesite in the studied serpentinites also indicates a paleo-subduction zone origin (Grozeva *et al.*, 2017) as magnesite is rarely found in carbonate-related ultramafic rocks in normal oceanic settings (Grozeva *et al.*, 2017). Magnesite can be formed directly from (1) olivine or orthopyroxene-dominated ultramafic rocks (i.e., $Ol + 2CO_{2aq} = 2 Mgs + SiO_2$) (Kelemen and Matter, 2008;

Grozeva *et al.*, 2017) or by (2) replacing antigorite ($2\text{Atg} + 3\text{CO}_2 = 3\text{Mgs} + \text{Tlc} + 3\text{H}_2\text{O}$) (Hamdy and Gamal El Dien, 2017; Sieber, Hermann and Yaxley, 2018). We favour the second mechanism for our study because of a complete absence of quartz in the studied samples. This interpretation is supported by (1) the presence of fractures and veinlets of magnesite that crosscut serpentinites and antigorite groundmass (Figure F.2c, d), which represent CO_2 -rich fluids pathways, (2) the presence of antigorite relics inside magnesite clasts (Figure 7.1d), (3) the presence of minor talc associated with magnesite (Figure F.2d), (4) strong similarities between the trace element patterns of magnesite and antigorite (Figure 7.6), and (5) high trace element contents of magnesite over antigorite that support the formation of magnesite at higher temperature and depth (~ 60 -70 km) (Poli and Schmidt, 2002; Sieber, Hermann and Yaxley, 2018) compared to the formation condition of antigorite. The carbon may have come from metamorphic decarbonation of subducted sediments (Kerrick and Connolly, 1998; Liu, Lin and Prakapenka, 2015) as supported by similar FME and LREE patterns between the magnesite and subducted sediments, AOC and marine sediments. The presence of dolomite with magnesite indicates percolation of moderate to high flow of CO_2 -Mg-rich and Ca-poor fluids from the subducted sediments (Kelemen and Matter, 2008; Grozeva *et al.*, 2017). Generally, Mg-rich and Ca-poor fluids are associated with peridotites when they undergo complete or near-complete serpentinization (Kelemen and Matter, 2008). Therefore, we suggest that magnesite formed after antigorites at higher temperatures and depths during subduction.

Although antigorite is the major carrier of trace elements in serpentinite, we note that magnesite has higher contents of FME of B, Li, As, Sb, Pb, Mo, Cs and LREE than antigorite and primitive mantle (Figures 7.3 and 7.6), which suggests that magnesite is a potential carrier of, as well as, a reservoir for these elements. In addition, magnesite is also a sink for Mn (Figure 7.3). On the other hand, magnesite is depleted in Sr, Ba and U. In summary, we suggest that magnesite has high FME and LREE absorbing capacity of over 50–60% higher than serpentine phases (calculated according to differences in the contents of those elements between magnesite and antigorite). Based on our petrographic observations and previous experimental studies (Sieber, Hermann and Yaxley, 2018), we argue that magnesite forms as a result of

antigorite transformation, where the parent antigorite contributes a considerable amount of FME and LREE to the newly formed magnesite.

7.5.4 Implications for arc magmatism and subduction polarity geochemical fingerprinting

The thermodynamic modelling results (Figures 7.4 and 7.5) demonstrate that the formation of two types of antigorite is a temperature-dependent process. The first serpentinization stage and formation of coarse antigorite is estimated at 200–250 °C and the second serpentinization stage and formation of fine antigorite occurred at 425–475 °C (Figure 7.7). According to different FME and LREE contents of the two types of antigorite groups, we suggest that these elements mainly redistributed (uptaken, trapped and released) as a result of varying temperature. During the first serpentinization stage, the LILE such as Rb, Ba, Cs and Li and U are released from the subducted slab at low temperatures (200–250 °C) and shallow depths and incorporated into coarse antigorites (CA). These result are consistent with previous reported high enrichment of LILE in fluids released from subducting slabs at shallow depths and lower temperatures (~200 °C) directly beneath the forearc region (Hyndman and Peacock, 2003; Bebout, 2014). The second serpentinization stage is represented by the release of higher amounts of B, As, Sb, Mo, Pb, Sr and LREE from the subducting slab at higher temperatures (425–475 °C) and greater depths, and their incorporation into the fine antigorites (FA) (Figure 7.7).

Finally, we suggest that serpentinites remain stable at high sub-arc depths and represent a potential carrier of FME such as B, As, Sb, Sr, Mo, Pb and LREE that get recycled back into the mantle wedge through the so-called “antigorite breakdown” (600–700 °C) (Ulmer and Trommsdorff, 1995). The similarities of the FME (B, As, Sb, and Li) patterns between the studied serpentinites (including rock forming minerals) and volcanic arc basalts (Figure 7.6c) demonstrate how dehydration of serpentinites during subduction plays a principle role in the generation of arc-related magmatism (Figure 7.7), in addition to the commonly considered dehydration of subducted sediments and AOC (Marschall, Altherr and Rüpke, 2007; Bebout, 2014). The high enrichment of these elements in the arc-related basalts can therefore be used to distinguish them from non-arc basalts such as plume-related basalt and MORB. The

model also predicts that arc magmatism closest to the trench should have higher LILE such as Li, Rb and Cs, released during the first serpentinization stage, whereas those landward from the trench should be more enriched in B, As, Sb, Pb and LREE, released during the second serpentinization stage and after antigorite breakdown (Ulmer and Trommsdorff, 1995). Such a cross-arc geochemical variation pattern has indeed been reported in some previous studies of arc volcanic rocks (Macdonald, Hawkesworth and Heath, 2000; Singer *et al.*, 2007). This cross-arc FME and LREE variation pattern, along with previously reported K_2O/SiO_2 cross-arc variation pattern (Gill, 1981), can be powerful tools for the identification of subduction polarities of ancient arc systems.

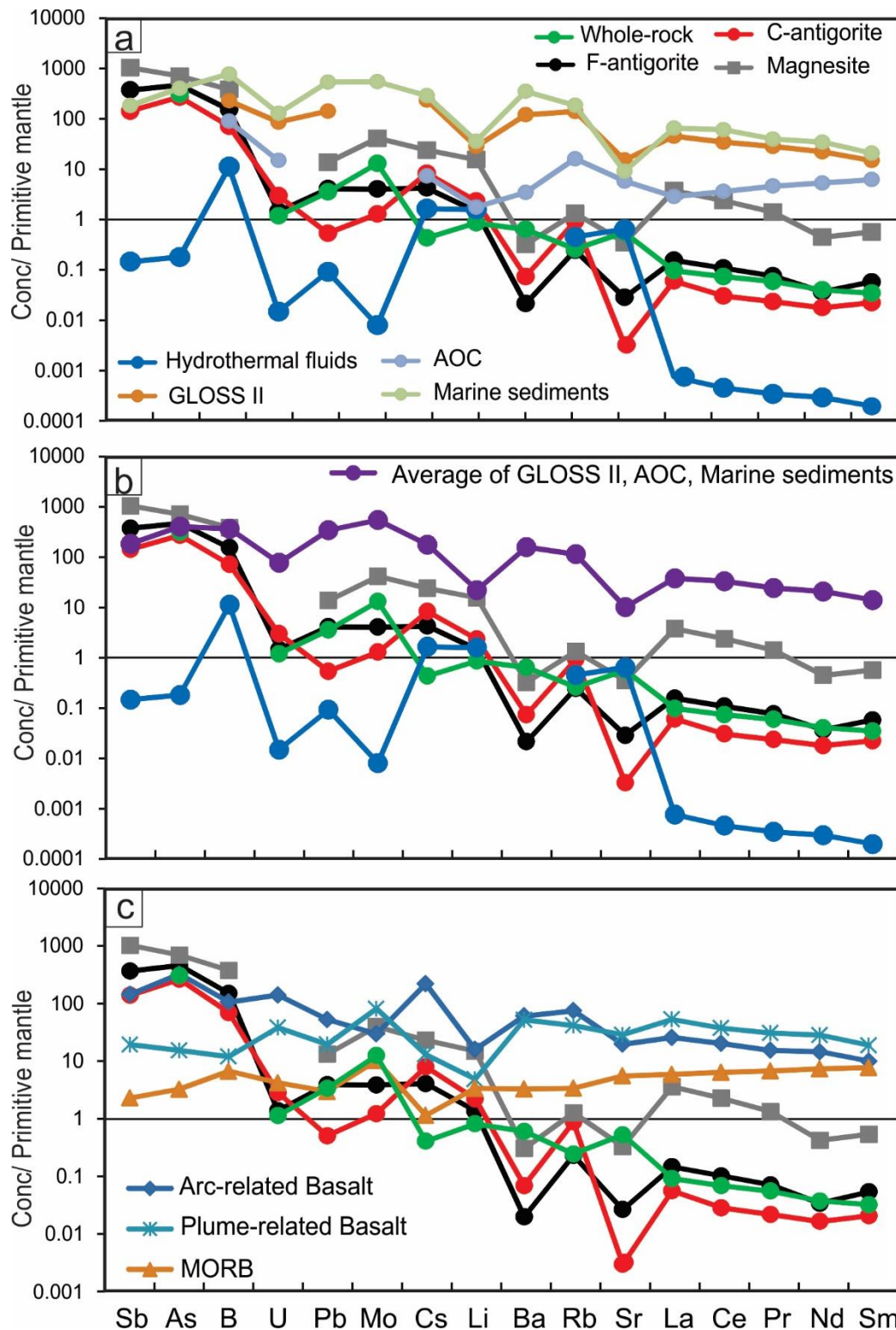


Figure 7.6: The average contents of fluid-mobile element and light rare earth element patterns of the studied serpentinites and rock forming minerals (antigorite and magnesite) normalized to the Primitive Mantle (McDonough and Sun, 1995). (a, b) plotted against the composition of hydrothermal fluids (Logatchev, Rainbow, Snake Pit) (Schmidt *et al.*, 2007) and the contents of subduction inputs including altered oceanic crust (AOC) (Staudigel, 2013), global subduction sediments (GLOSS II) (Plank, 2013) and marine sediments pattern (Li and Schoonmaker, 2013) are reported for comparison; (c) plotted against the average compositions of arc-related basalts, plume-related basalts and mid ocean ridge basalts (MORB) after Georoc repository (<http://georoc.mpch-mainz.gwdg.de/georoc/>) .

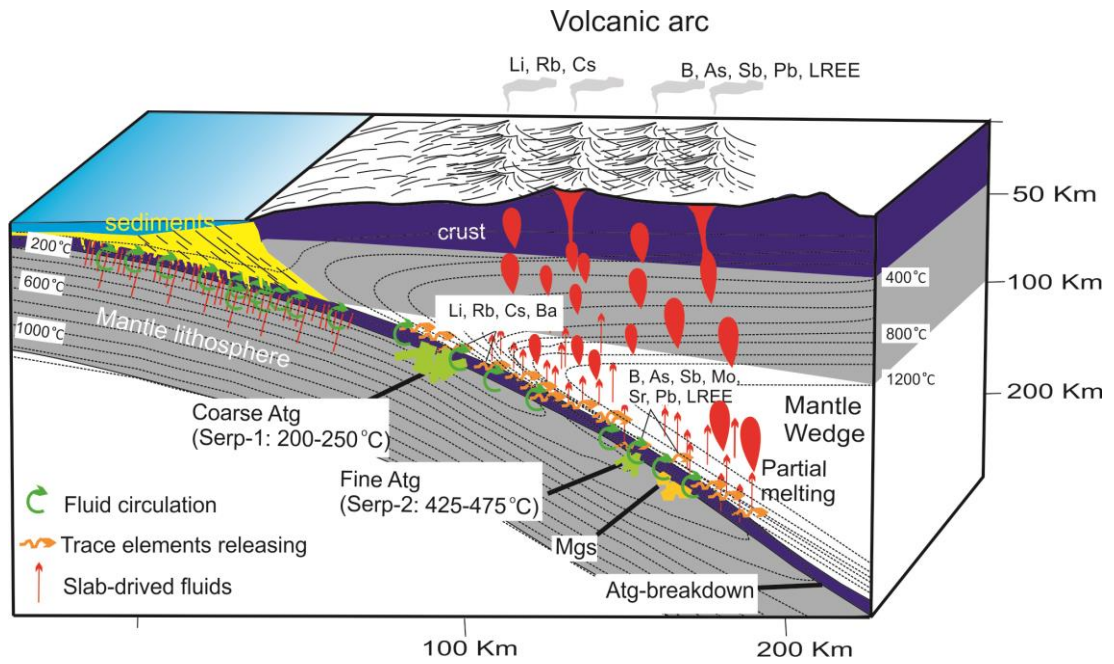


Figure 7.7: A cross-section sketch of a subduction zone complex showing the position of the first serpentinization stage (Serp-1) and formation of coarse antigorites (Atg) at 200–250 °C, the second serpentinization stage (Serp-2) and formation of fine antigorites at 425–475 °C and magnesite formation (Mgs).

7.6 References

- Abd El-Rahman, Y. *et al.* (2009) 'Geochemistry and tectonic evolution of the Neoproterozoic incipient arc-forearc crust in the Fawakhir area, Central Eastern Desert of Egypt', *Precambrian Research*, 175(1–4), pp. 116–134. doi: 10.1016/j.precamres.2009.09.008.
- Abd El-Wahed, M. A. and Kamh, S. Z. (2010) 'Pan-African dextral transpressive duplex and flower structure in the Central Eastern Desert of Egypt', *Gondwana Research*. International Association for Gondwana Research, 18(2–3), pp. 315–336. doi: 10.1016/j.gr.2010.02.007.
- Abu-Alam, T. S. *et al.* (2014) 'Multistage Tectonism and Metamorphism During Gondwana Collision: Baladiyah Complex, Saudi Arabia', *Journal of Petrology*. Oxford University Press, 55(10), pp. 1941–1964. doi: 10.1093/petrology/egu046.
- Abu-Alam, T. S. and Hamdy, M. M. (2014) 'Thermodynamic modelling of Sol Hamed serpentinite, south eastern Desert of Egypt: Implication for fluid interaction in the Arabian-Nubian shield ophiolites', *Journal of African Earth Sciences*, 99(PA1), pp. 7–23. doi: 10.1016/j.jafrearsci.2014.06.001.
- ABU-ALAM, T. S. and STÜWE, K. (2009) 'Exhumation during oblique transpression: The Feiran-Solaf region, Egypt', *Journal of Metamorphic Geology*. Wiley/Blackwell (10.1111), 27(6), pp. 439–459. doi: 10.1111/j.1525-1314.2009.00827.x.
- Abu El Ela, A. . (1996) 'Contribution to the mineralogy and chemistry of some serpentinites from the Eastern Desert of Egypt', *MERC Ain. Shams Univ. Earth Sci.*, 10, pp. 1–25.
- Aldanmaz, E. and Koprubasi, N. (2006) 'Platinum-Group-Element Systematics of Peridotites from Ophiolite Complexes of Northwest Anatolia, Turkey: Implications for Mantle Metasomatism by Melt Percolation in a Supra-subduction Zone Environment', *International Geology Review*. Taylor & Francis Group , 48(5), pp. 420–442. doi: 10.2747/0020-6814.48.5.420.
- Alt, J. C. *et al.* (2013) 'The role of serpentinites in cycling of carbon and sulfur: Seafloor serpentinitization and subduction metamorphism', *Lithos*. Elsevier, 178, pp. 40–54. doi: 10.1016/J.LITHOS.2012.12.006.
- Anders, E. and Grevesse, N. (1989) 'Abundances of the elements: Meteoritic and solar', *Geochimica et Cosmochimica Acta*. Pergamon, 53(1), pp. 197–214. doi: 10.1016/0016-7037(89)90286-X.
- Arai, S. (1994) 'Characterization of spinel peridotites by olivine-spinel compositional relationships: Review and interpretation', *Chemical Geology*, 113(3–4), pp. 191–204. doi: 10.1016/0009-2541(94)90066-3.
- Azer, M. K. and Stern, R. J. (2007) 'Neoproterozoic (835 – 720 Ma) Serpentinites in the Eastern Desert , Egypt: Fragments of Forearc Mantle', *The Journal of Geology*, 115(4), pp. 457–472. doi: 10.1086/518052.
- Aziz, N. R. H., Aswad, K. J. A. and Koyi, H. A. (2011) 'Contrasting settings of serpentinite bodies in the northwestern Zagros Suture Zone, Kurdistan Region, Iraq', *Geological Magazine*, 148(5–6), pp. 819–837. doi: 10.1017/S0016756811000409.

- El Bahariya, G. A. (2012) 'Classification and origin of the Neoproterozoic ophiolitic mélanges in the Central Eastern Desert of Egypt', *Tectonophysics*. Elsevier B.V., 568–569, pp. 357–370. doi: 10.1016/j.tecto.2012.03.020.
- Bebout, G. E. (2013) *Chemical and Isotopic Cycling in Subduction Zones, Treatise on Geochemistry: Second Edition*. Elsevier Ltd. doi: 10.1016/B978-0-08-095975-7.01401-7.
- Bebout, G. E. (2014) 'Chemical and Isotopic Cycling in Subduction Zones', *Treatise on Geochemistry*. Elsevier, pp. 703–747. doi: 10.1016/B978-0-08-095975-7.00322-3.
- Blanco-Quintero, I. F. *et al.* (2011) 'Serpentinites and serpentinites within a fossil subduction channel: La Corea mélange, eastern Cuba', *Geologica Acta*, 9(3), pp. 389–405. doi: 10.1344/105.00000166.
- Connolly, J. A. D. and Kerrick, D. M. (1987) 'An algorithm and computer program for calculating composition phase diagrams', *Calphad*. Pergamon, 11(1), pp. 1–55. doi: 10.1016/0364-5916(87)90018-6.
- Connolly, J. A. D. and Trommsdorff, V. (1991) 'Petrogenetic grids for metacarbonate rocks: pressure-temperature phase-diagram projection for mixed-volatile systems', *Contributions to Mineralogy and Petrology*. Springer-Verlag, 108(1–2), pp. 93–105. doi: 10.1007/BF00307329.
- Deschamps, F. *et al.* (2010) 'In situ characterization of serpentinites from forearc mantle wedges: Timing of serpentinitization and behavior of fluid-mobile elements in subduction zones', *Chemical Geology*, 269(3–4), pp. 262–277. doi: 10.1016/j.chemgeo.2009.10.002.
- Deschamps, F. *et al.* (2011) 'Serpentinites act as sponges for fluid-mobile elements in abyssal and subduction zone environments', *Terra Nova*, 23(3), pp. 171–178. doi: 10.1111/j.1365-3121.2011.00995.x.
- Deschamps, F. *et al.* (2012) 'Behavior of fluid-mobile elements in serpentinites from abyssal to subduction environments: Examples from Cuba and Dominican Republic', *Chemical Geology*, 312–313(June 2016), pp. 93–117. doi: 10.1016/j.chemgeo.2012.04.009.
- Deschamps, F. *et al.* (2013) 'Geochemistry of subduction zone serpentinites: A review', *Lithos*, 178(APRIL), pp. 96–127. doi: 10.1016/j.lithos.2013.05.019.
- Droop, G. T. R. (1987) 'A general equation for estimating Fe³⁺ concentrations in ferromagnesian silicates and oxides from microprobe analyses, using stoichiometric criteria', *Mineralogical Magazine*, 51, pp. 431–435. doi: 10.1180/minmag.1987.051.361.10.
- Eggler, D. H. and Ehmann, A. N. (2010) 'Rate of antigorite dehydration at 2 GPa applied to subduction zones', *American Mineralogist*. GeoScienceWorld, 95(5–6), pp. 761–769. doi: 10.2138/am.2010.3227.
- Evans, B. W. (2004) 'The Serpentinite Multisystem Revisited: Chrysotile Is Metastable', *International Geology Review*, 46(6), pp. 479–506. doi: 10.2747/0020-6814.46.6.479.
- Evans, K. A., Powell, R. and Frost, B. R. (2013) 'Using equilibrium thermodynamics in the study of metasomatic alteration, illustrated by an application to serpentinites', *Lithos*. Elsevier B.V., 168–169, pp. 67–84. doi: 10.1016/j.lithos.2013.01.016.

Faccenda, M., Gerya, T. V. and Burlini, L. (2009) 'Deep slab hydration induced by bending-related variations in tectonic pressure', *Nature Geoscience*. Nature Publishing Group, 2(11), pp. 790–793. doi: 10.1038/ngeo656.

Fowler, A. R. and El Kalioubi, B. (2004) 'Gravitational collapse origin of shear zones, foliations and linear structures in the Neoproterozoic cover nappes, Eastern Desert, Egypt', *Journal of African Earth Sciences*, 38(1), pp. 23–40. doi: 10.1016/j.jafrearsci.2003.09.003.

Fritz, H. *et al.* (2013) 'Orogen styles in the East African Orogen: A review of the Neoproterozoic to Cambrian tectonic evolution', *Journal of African Earth Sciences*. Elsevier Ltd, 86, pp. 65–106. doi: 10.1016/j.jafrearsci.2013.06.004.

Galvez, M. E. *et al.* (2013) 'Graphite formation by carbonate reduction during subduction', *Nature Geoscience*. Nature Publishing Group, 6(6), pp. 473–477. doi: 10.1038/ngeo1827.

Gamal El Dien, H. *et al.* (2015) 'A Window into Neoproterozoic Mantle and its Development: Observations from Ophiolitic Serpentinites in the Eastern Desert of Egypt', *Acta Geologica Sinica*, 89(Supp.2), pp. 22–24.

Gamal El Dien, H. *et al.* (2016) 'Neoproterozoic serpentinites from the Eastern Desert of Egypt: Insights into Neoproterozoic mantle geodynamics and processes beneath the Arabian-Nubian Shield', *Precambrian Research*. Elsevier B.V., 286, pp. 213–233. doi: 10.1016/j.precamres.2016.10.006.

Gaschnig, R. M. *et al.* (2017) 'The Molybdenum Isotope System as a Tracer of Slab Input in Subduction Zones: An Example From Martinique, Lesser Antilles Arc', *Geochemistry, Geophysics, Geosystems*, 18(12), pp. 4674–4689. doi: 10.1002/2017GC007085.

Gerya, T. V., Stöckhert, B. and Perchuk, A. L. (2002) 'Exhumation of high-pressure metamorphic rocks in a subduction channel: A numerical simulation', *Tectonics*. John Wiley & Sons, Ltd, 21(6), pp. 6–16–19. doi: 10.1029/2002TC001406.

Gill, J. B. (1981) *Orogenic Andesites and Plate Tectonics*. Springer Berlin Heidelberg.

Groppo, C. *et al.* (2006) 'Micro-Raman spectroscopy for a quick and reliable identification of serpentine minerals from ultramafics', *European Journal of Mineralogy*, 18(3), pp. 319–329. doi: 10.1127/0935-1221/2006/0018-0319.

Grozeva, N. G. *et al.* (2017) 'Experimental study of carbonate formation in oceanic peridotite', *Geochimica et Cosmochimica Acta*. Elsevier Ltd, 199, pp. 264–286. doi: 10.1016/j.gca.2016.10.052.

Guillot, S. *et al.* (2015) 'Tectonic significance of serpentinites', *Tectonophysics*. Elsevier, 646, pp. 1–19. doi: 10.1016/J.TECTO.2015.01.020.

Hamdy, M. M. *et al.* (2017) 'Garnet hornblendite in the Meatiq Core Complex, Central Eastern Desert of Egypt: Implications for crustal thickening preceding the ~600 Ma extensional regime in the Arabian-Nubian Shield', *Precambrian Research*. Elsevier B.V., 298, pp. 593–614. doi: 10.1016/j.precamres.2017.07.002.

Hamdy, M. M. and Gamal El Dien, H. (2017) 'Nature of serpentinization and carbonation of ophiolitic peridotites (Eastern Desert, Egypt): constraints from stable isotopes and whole-rock geochemistry', *Arabian Journal of Geosciences*. Arabian Journal of Geosciences,

10(19). doi: 10.1007/s12517-017-3215-6.

Hattori, K. H. and Guillot, S. (2003) 'Volcanic fronts as a consequence of serpentinite dehydration in the mantle wedge', *Geology*, 31, pp. 525–528. doi: 10.1130/0091-7613(2003)031<0525:vffaac>2.0.co;2.

Hilairt, N., Daniel, I. and Reynard, B. (2006) 'Equation of state of antigorite, stability field of serpentines, and seismicity in subduction zones', *Geophysical Research Letters*, 33(2). doi: 10.1029/2005GL024728.

Holland, T. J. B. and Powell, R. (2011) 'An improved and extended internally consistent thermodynamic dataset for phases of petrological interest, involving a new equation of state for solids', *Journal of Metamorphic Geology*. Wiley/Blackwell (10.1111), 29(3), pp. 333–383. doi: 10.1111/j.1525-1314.2010.00923.x.

De Hoog, J. C. M. *et al.* (2009) 'Serpentinised peridotites from an ultrahigh-pressure terrane in the Pohorje Mts. (Eastern Alps, Slovenia): Geochemical constraints on petrogenesis and tectonic setting', *Lithos*. Elsevier B.V., 109(3–4), pp. 209–222. doi: 10.1016/j.lithos.2008.05.006.

Hyndman, R. D. and Peacock, S. M. (2003) 'Serpentinization of the forearc mantle', *Earth and Planetary Science Letters*, 212(3–4), pp. 417–432. doi: 10.1016/S0012-821X(03)00263-2.

Jennings, E. S. and Holland, T. J. B. (2015) 'A Simple Thermodynamic Model for Melting of Peridotite in the System NCFMASOCr', *Journal of Petrology*. Oxford University Press, 56(5), pp. 869–892. doi: 10.1093/petrology/egv020.

Johnson, P. R. *et al.* (2011) 'Late Cryogenian-Ediacaran history of the Arabian-Nubian Shield: A review of depositional, plutonic, structural, and tectonic events in the closing stages of the northern East African Orogen', *Journal of African Earth Sciences*. Elsevier Ltd, 61(3), pp. 167–232. doi: 10.1016/j.jafrearsci.2011.07.003.

Kelemen, P. B. and Matter, J. (2008) 'In situ carbonation of peridotite for CO₂ storage', *Proceedings of the National Academy of Sciences*. National Academy of Sciences, 105(45), pp. 17295–17300. doi: 10.1073/PNAS.0805794105.

Kendrick, M. A. *et al.* (2017) 'Seawater cycled throughout Earth's mantle in partially serpentinitized lithosphere', *Nature Geoscience*. Nature Publishing Group, 10(3), pp. 222–228. doi: 10.1038/ngeo2902.

Kerrick, D. M. (2002) 'Serpentinite Seduction', *Science*, 298, pp. 1344–1345.

Kerrick, D. M. and Connolly, J. A. D. (1998) 'Subduction of ophicarbonates and recycling of CO₂ and H₂O', *Geology*. GeoScienceWorld, 26(4), p. 375. doi: 10.1130/0091-7613(1998)026<0375:SOOARO>2.3.CO;2.

Khedr, M. Z. and Arai, S. (2010) 'Hydrous peridotites with Ti-rich chromian spinel as a low-temperature forearc mantle facies: evidence from the Happo-O'ne metaperidotites (Japan)', *Contributions to Mineralogy and Petrology*. Springer-Verlag, 159(2), pp. 137–157. doi: 10.1007/s00410-009-0420-7.

Kodolányi, J. *et al.* (2012) 'Geochemistry of ocean floor and fore-arc serpentinites:

- Constraints on the ultramafic input to subduction zones', *Journal of Petrology*, 53(2), pp. 235–270. doi: 10.1093/petrology/egr058.
- Lafay, R. *et al.* (2013) 'High-pressure serpentinites, a trap-and-release system controlled by metamorphic conditions: Example from the Piedmont zone of the western Alps', *Chemical Geology*, 343(July), pp. 38–54. doi: 10.1016/j.chemgeo.2013.02.008.
- Lafay, R. *et al.* (2014) 'Influence of trace elements on the textural properties of synthetic chrysotile: Complementary insights from macroscopic and nanoscopic measurements', *Microporous and Mesoporous Materials*. Elsevier, 183, pp. 81–90. doi: 10.1016/J.MICROMESO.2013.08.032.
- Lafay, R. *et al.* (2016) 'Experimental investigation of As, Sb and Cs behavior during olivine serpentinization in hydrothermal alkaline systems', *Geochimica et Cosmochimica Acta*. Elsevier Ltd, 179, pp. 177–202. doi: 10.1016/j.gca.2016.02.014.
- Lee, C.-T. A., Brandon, A. D. and Norman, M. (2003) 'Vanadium in peridotites as a proxy for paleo-fO₂ during partial melting: prospects, limitations, and implications', *Geochimica et Cosmochimica Acta*. Pergamon, 67(16), pp. 3045–3064. doi: 10.1016/S0016-7037(03)00268-0.
- Li, X. P., Rahn, M. and Bucher, K. (2004) 'Serpentinites of the Zermatt-Saas ophiolite complex and their texture evolution', *Journal of Metamorphic Geology*, 22(3), pp. 159–177. doi: 10.1111/j.1525-1314.2004.00503.x.
- Li, Y.-H. (1982) 'A brief discussion on the mean oceanic residence time of elements', *Geochimica et Cosmochimica Acta*. Pergamon, 46(12), pp. 2671–2675. doi: 10.1016/0016-7037(82)90386-6.
- Li, Y. H. and Schoonmaker, J. E. (2013) *Chemical Composition and Mineralogy of Marine Sediments, Treatise on Geochemistry: Second Edition*. doi: 10.1016/B978-0-08-095975-7.00701-4.
- Li, Z. X. A. and Lee, C. T. A. (2006) 'Geochemical investigation of serpentinized oceanic lithospheric mantle in the Feather River Ophiolite, California: Implications for the recycling rate of water by subduction', *Chemical Geology*, 235(1–2), pp. 161–185. doi: 10.1016/j.chemgeo.2006.06.011.
- Liu, J., Lin, J.-F. and Prakapenka, V. B. (2015) 'High-Pressure Orthorhombic Ferromagnesite as a Potential Deep-Mantle Carbon Carrier', *Scientific Reports*. Nature Publishing Group, 5(1), p. 7640. doi: 10.1038/srep07640.
- Macdonald, R., Hawkesworth, C. J. and Heath, E. (2000) 'The Lesser Antilles volcanic chain: a study in arc magmatism', *Earth-Science Reviews*. Elsevier, 49(1–4), pp. 1–76. doi: 10.1016/S0012-8252(99)00069-0.
- Marschall, H. R., Altherr, R. and Rüpke, L. (2007) 'Squeezing out the slab — modelling the release of Li, Be and B during progressive high-pressure metamorphism', *Chemical Geology*. Elsevier, 239(3–4), pp. 323–335. doi: 10.1016/J.CHEMGEO.2006.08.008.
- McDonough, W. . and Sun, S. -. (1995) 'The composition of the Earth', *Chemical Geology*, 120, pp. 223–252. doi: doi.org/10.1016/0009-2541(94)00140-4.

- Mével, C. (2003) 'Serpentinization of abyssal peridotites at mid-ocean ridges', *Comptes Rendus Geoscience*. Elsevier Masson, 335(10–11), pp. 825–852. doi: 10.1016/J.CRTE.2003.08.006.
- Muntener, O., Hermann, J. and Trommsdorff, V. (2000) 'Cooling History and Exhumation of Lower-Crustal Granulite and Upper Mantle (Malenco, Eastern Central Alps)', *Journal of Petrology*. Oxford University Press, 41(2), pp. 175–200. doi: 10.1093/petrology/41.2.175.
- Niu, Y. (2004) 'Bulk-rock major and trace element compositions of abyssal peridotites: Implications for mantle melting, melt extraction and post-melting processes beneath Mid-Ocean ridges', *Journal of Petrology*, 45(12), pp. 2423–2458. doi: 10.1093/petrology/egh068.
- Padrón-Navarta, J. A. *et al.* (2013) 'Tschermak's substitution in antigorite and consequences for phase relations and water liberation in high-grade serpentinites', *Lithos*, 178(MAY 2013), pp. 186–196. doi: 10.1016/j.lithos.2013.02.001.
- Pagé, L. and Hattori, K. (2017) 'Tracing halogen and B cycling in subduction zones based on obducted, subducted and forearc serpentinites of the Dominican Republic', *Scientific Reports*, 7(1), pp. 1–9. doi: 10.1038/s41598-017-18139-7.
- Parkinson, I. J. and Pearce, J. A. (1998) 'Peridotites from the Izu – Bonin – Mariana Forearc (ODP Leg 125): Evidence for Mantle Melting and Melt – Mantle Interaction in a Supra-Subduction Zone Setting', *Journal of Petrology*, 39(9), pp. 1577–1618.
- Paulick, H. *et al.* (2006) 'Geochemistry of abyssal peridotites (Mid-Atlantic Ridge, 15°20'N, ODP Leg 209): Implications for fluid/rock interaction in slow spreading environments', *Chemical Geology*, 234(3–4), pp. 179–210. doi: 10.1016/j.chemgeo.2006.04.011.
- Pearce, J. A. *et al.* (2000) 'Geochemistry and tectonic significance of peridotites from the South Sandwich arc-basin system, South Atlantic', *Contributions to Mineralogy and Petrology*, 139(1), pp. 36–53. doi: 10.1007/s004100050572.
- Pearce, N. J. G. *et al.* (1997) 'A Compilation of New and Published Major and Trace Element Data for NIST SRM 610 and NIST SRM 612 Glass Reference Materials', *Geostandards and Geoanalytical Research*. Wiley/Blackwell (10.1111), 21(1), pp. 115–144. doi: 10.1111/j.1751-908X.1997.tb00538.x.
- Plank, T. (2013) *The Chemical Composition of Subducting Sediments*. 2nd edn, *Treatise on Geochemistry: Second Edition*. 2nd edn. Elsevier Ltd. doi: 10.1016/B978-0-08-095975-7.00319-3.
- Plank, T. and Langmuir, C. H. (1993) 'Tracing trace elements from sediment input to volcanic output at subduction zones', *Nature*. Nature Publishing Group, 362(6422), pp. 739–743. doi: 10.1038/362739a0.
- Poli, S. and Schmidt, M. W. (2002) 'Petrology of Subducted Slabs', *Annual Review of Earth and Planetary Sciences*, 30(1), pp. 207–235. doi: 10.1146/annurev.earth.30.091201.140550.
- Rüpke, L. H. *et al.* (2004) 'Serpentine and the subduction zone water cycle', *Earth and Planetary Science Letters*. Elsevier, 223(1–2), pp. 17–34. doi: 10.1016/J.EPSL.2004.04.018.
- Saumur, B. M., Hattori, K. H. and Guillot, S. (2010) 'Contrasting origins of serpentinites in a subduction complex, northern Dominican Republic', *Bulletin of the Geological Society of*

America, 122(1–2), pp. 292–304. doi: 10.1130/B26530.1.

Savov, I. P. *et al.* (2005) ‘Geochemistry of serpentinized peridotites from the Mariana Forearc Conical Seamount, ODP Leg 125: Implications for the elemental recycling at subduction zones’, *Geochemistry, Geophysics, Geosystems*. John Wiley & Sons, Ltd, 6(4), p. n/a-n/a. doi: 10.1029/2004GC000777.

Scambelluri, M. and Tonarini, S. (2012) ‘Boron isotope evidence for shallow fluid transfer across subduction zones by serpentinized mantle’, *Geology*, 40(10), pp. 907–910. doi: 10.1130/G33233.1.

Schmidt, K. *et al.* (2007) ‘Geochemistry of hydrothermal fluids from the ultramafic-hosted Logatchev hydrothermal field, 15°N on the Mid-Atlantic Ridge: Temporal and spatial investigation’, *Chemical Geology*, 242(1–2), pp. 1–21. doi: 10.1016/j.chemgeo.2007.01.023.

Sieber, M. J., Hermann, J. and Yaxley, G. M. (2018) ‘An experimental investigation of C–O–H fluid-driven carbonation of serpentinites under forearc conditions’, *Earth and Planetary Science Letters*, 496, pp. 178–188. doi: 10.1016/j.epsl.2018.05.027.

Singer, B. S. *et al.* (2007) ‘Along-strike trace element and isotopic variation in Aleutian Island arc basalt: Subduction melts sediments and dehydrates serpentine’, *Journal of Geophysical Research: Solid Earth*, 112(6). doi: 10.1029/2006JB004897.

Staudigel, H. (2013) *Chemical Fluxes from Hydrothermal Alteration of the Oceanic Crust*. 2nd edn, *Treatise on Geochemistry: Second Edition*. 2nd edn. Elsevier Ltd. doi: 10.1016/B978-0-08-095975-7.00318-1.

Stern, R. J. *et al.* (2004) ‘Neoproterozoic Ophiolites of the Arabian-Nubian Shield’, *Developments in Precambrian Geology*, 13(C), pp. 95–128. doi: 10.1016/S0166-2635(04)13003-X.

Tatsumi, Y. (1989) ‘Migration of fluid phases and genesis of basalt magmas in subduction zones’, *Journal of Geophysical Research: Solid Earth*. John Wiley & Sons, Ltd, 94(B4), pp. 4697–4707. doi: 10.1029/JB094iB04p04697.

Ulmer, P. and Trommsdorff, V. (1995) ‘Serpentine stability to mantle depths and subduction-related magmatism.’, *Science (New York, N.Y.)*. American Association for the Advancement of Science, 268(5212), pp. 858–61. doi: 10.1126/science.268.5212.858.

Uysal, I. *et al.* (2016) ‘Multiple episodes of partial melting, depletion, metasomatism and enrichment processes recorded in the heterogeneous upper mantle sequence of the Neotethyan Eldivan ophiolite, Turkey’, *Lithos*, 246–247, pp. 228–245. doi: 10.1016/j.lithos.2016.01.004.

Vail, J. R. (1983) ‘Pan-African crustal accretion in north-east Africa’, *Journal of African Earth Sciences (1983)*. Pergamon, 1(3–4), pp. 285–294. doi: 10.1016/S0731-7247(83)80013-5.

Vils, F. *et al.* (2009) ‘Boron, lithium and strontium isotopes as tracers of seawater-serpentine interaction at Mid-Atlantic ridge, ODP Leg 209’, *Earth and Planetary Science Letters*. Elsevier B.V., 286(3–4), pp. 414–425. doi: 10.1016/j.epsl.2009.07.005.

Vils, F. *et al.* (2011) ‘Implications of the serpentine phase transition on the behaviour of

beryllium and lithium-boron of subducted ultramafic rocks', *Geochimica et Cosmochimica Acta*, 75(5), pp. 1249–1271. doi: 10.1016/j.gca.2010.12.007.

Walowski, K. J. *et al.* (2015) 'Slab melting beneath the Cascade Arc driven by dehydration of altered oceanic peridotite', *Nature Geoscience*. Nature Publishing Group, 8(5), pp. 404–408. doi: 10.1038/ngeo2417.

Workman, R. K. and Hart, S. R. (2005) 'Major and trace element composition of the depleted MORB mantle (DMM)', *Earth and Planetary Science Letters*, 231(1–2), pp. 53–72. doi: 10.1016/j.epsl.2004.12.005.

Zimmer, M. *et al.* (1995) 'The Gabal Gerf complex: A precambrian N-MORB ophiolite in the Nubian Shield, NE Africa', *Chemical Geology*. Elsevier, 123(1–4), pp. 29–51. doi: 10.1016/0009-2541(95)00018-H.

"Every reasonable effort has been made to acknowledge the owners of copyright material. I would be pleased to hear from any copyright owner who has been omitted or incorrectly acknowledged."

Appendix F:
Supplementary materials to Chapter 7

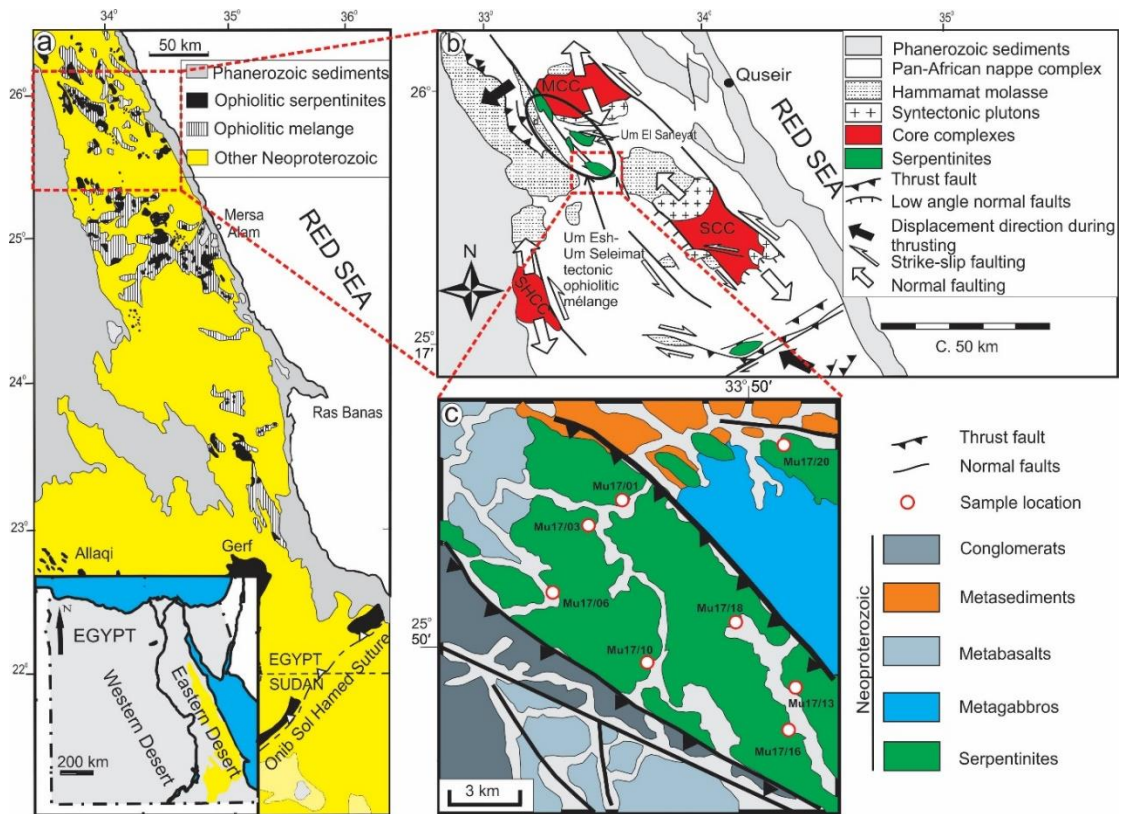


Figure F.1: (a) Distribution of the ophiolites in the Arabian-Nubian Shield (modified after Vail (1983)). (b) Location of the studied serpentinite masses and their relations, with the major structural trends and younger metamorphic and magmatic core complexes (MCC, Meatiq and SCC, Sibai) in the East-African Orogen, central Eastern Desert of Egypt (major structures are after Fritz et al. (2013) and Abd El-Wahed and Kamh (2010)). (c) Geologic map of the Muweilih serpentinites in the Wadi Muweilih area (modified after El Bahariya (2012)).

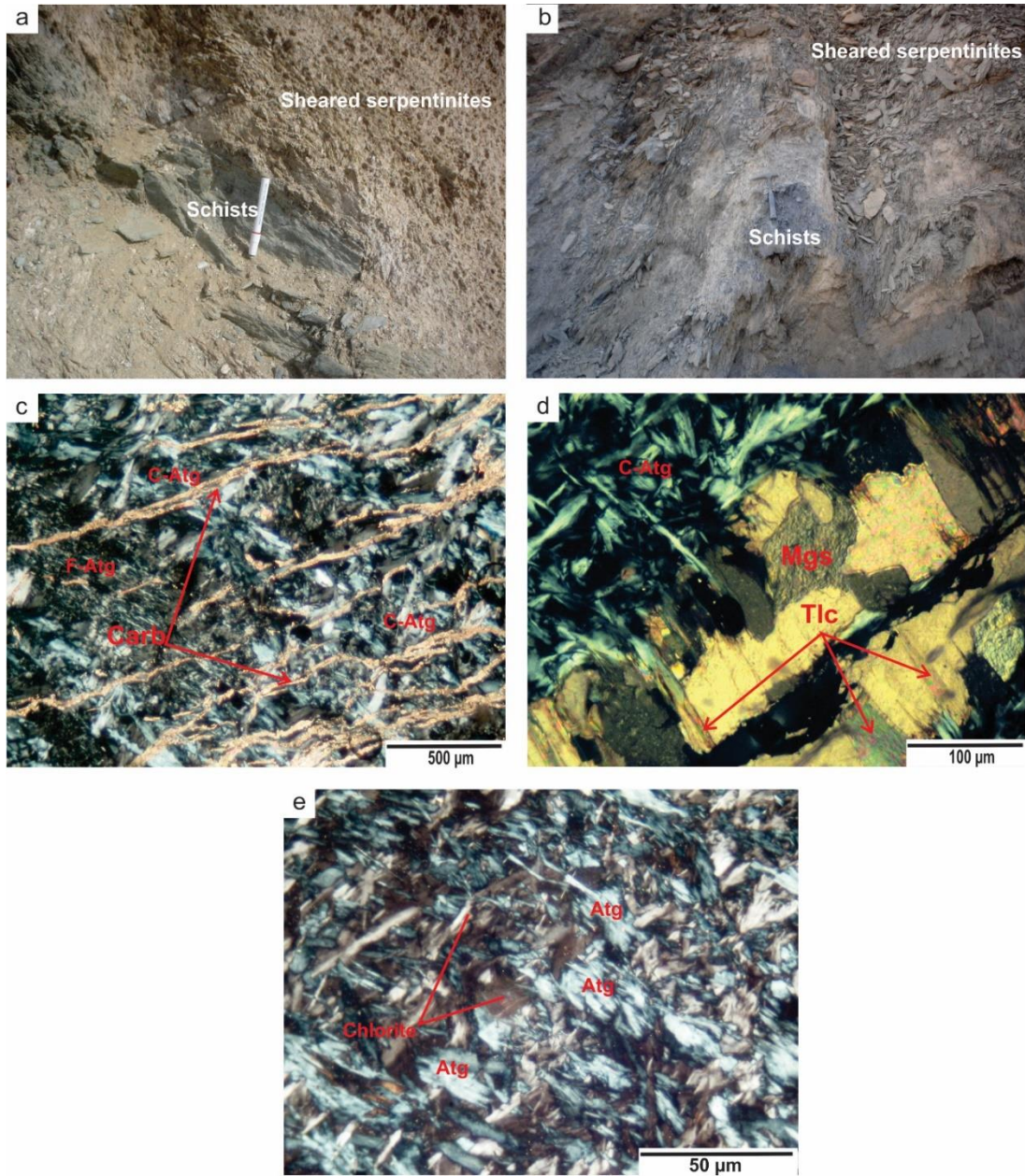


Figure F.2: (a, b) Field photos showing a tectonic melange consisting of highly sheared serpentinites and schists. Photomicrographs of the studied serpentinites. (c) Carbonates (Carb) veins crosscut the antigorite (F-Atg and C-Atg) groundmass, indicating a later formation age after antigorite. (d) Magnesite (Mgs) veins with small amounts of talc (Tlc). (e) Chlorite aggregates disseminated in the antigorite groundmass.

Bulk-rock composition

All the examined rocks are completely serpentinized with high-water contents (i.e., high LOI values of 12.54 to 14.93 wt%) (Figure F.3). The MgO contents of the studied samples show a range of 40.47 wt % (sample # MU17/06) to 45.67 wt% (sample # MU17/16) (Figure F.3). Al₂O₃ and SiO₂ contents have ranges of 0.64–1.81 wt. % and 44.85–46.84 wt%, respectively. Fe₂O₃ and MnO contents are in the ranges of 8.49–10.20 wt% and 0.04–0.35 wt%, respectively (Table F.1). Trace elements spider-diagram, normalized to Primitive Mantle (PM) of McDonough and Sun (1995), displays low contents of highly and moderately compatible elements relatively to the high incompatible elements (Figure F.4). Trace elements concentrations vary among the samples. All the studied serpentinite rocks show decreasing slope from the fluid mobile elements (FME) to rare earth elements (REE) (Fig. S4). As, Ba, Cs, U, Pb, Sr, Li, Mo and Hf show positive spikes relative to elements of the same compatibility. Chondrite (CI)-normalized REE patterns in all the studied serpentinites, using the normalizing values of Anders and Grevesse (1989), display nearly-flat shapes (Figure F.4). Light rare earth elements (LREE) are enriched in comparison to middle rare earth elements (MREE), and there is a slight enrichment from Sm to La ($La_N/Sm_N = 1.92–3.91$; $La_N/Yb_N = 0.17–4.50$ CI-Chondrite). Heavy rare earth elements (HREE) show a slight negative slope to MREE. The HREE concentrations reflect the fertility of the samples ($Yb_{N(CI-normalized\ value)} = 0.01–0.31$).

Nature of protolith

To trace the primary mantle processes in ultramafic rocks that underwent intense serpentinization and subduction metamorphism, we checked the whole-rock trace (i.e., HREE) element compositions of the samples because they are fluid immobile HREE of the whole-rock composition, particular Yb, are highly immobile during post-melting processes and fluid circulation in mantle peridotite (Pearce *et al.*, 2000; Niu, 2004; De Hoog *et al.*, 2009). Their contents are commonly used to estimate melting degrees of the original fertile source (Parkinson and Pearce, 1998). The co-variations between Yb and some major and trace elements such as Al, Y, Sc, V, Cr and Zr are almost the same during partial melting and have lower contents than the

primitive mantle (McDonough and Sun, 1995) and the depleted MORB mantle (DMM) (Workman and Hart, 2005) (Figure F.5). This suggests a residual origin of mantle protolith of the studied serpentinites. The correlations between Yb and Cr, Sc and V (Figure F.5c, d, e) demonstrate that the mantle protolith of the studied serpentinites have high melting degrees ranging between ~16% and 27%. Such estimated melting degrees agree with our results of non-modal fractional melting modelling in the spinel stability field (Workman and Hart, 2005) using the HREE of the studied samples and the DMM (Figure F.4) and unaltered spinel core Cr-numbers. Generally, V values record the fO_2 during mantle melting (Lee, Brandon and Norman, 2003). The V values from the studied serpentinite rocks plot around the QFM+1 curve indicating oxidizing conditions (Figure F.5e).

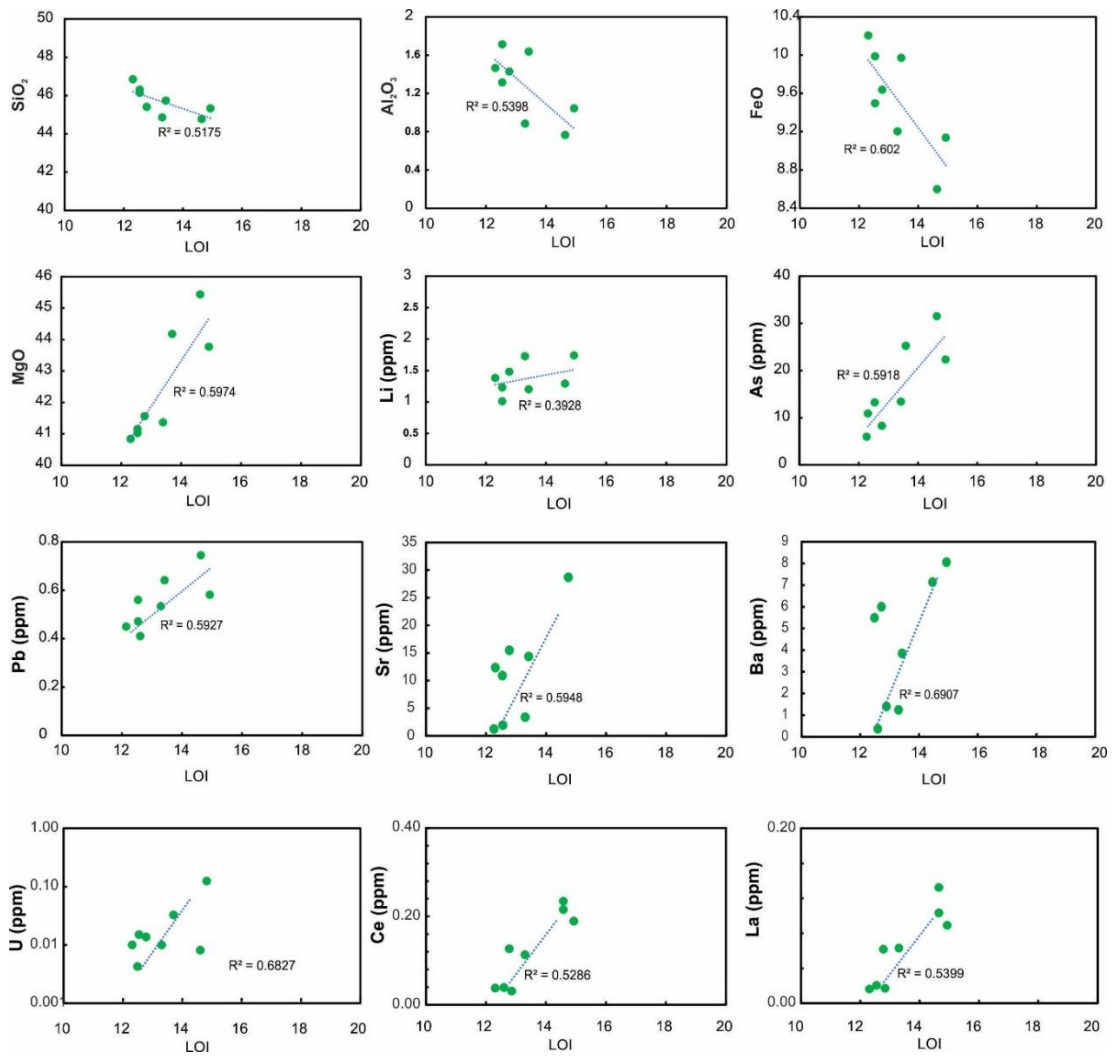


Figure F.3: Variation diagrams of LOI (wt%) vs. selected major, trace and rare earth elements of bulk composition of the serpentinites.

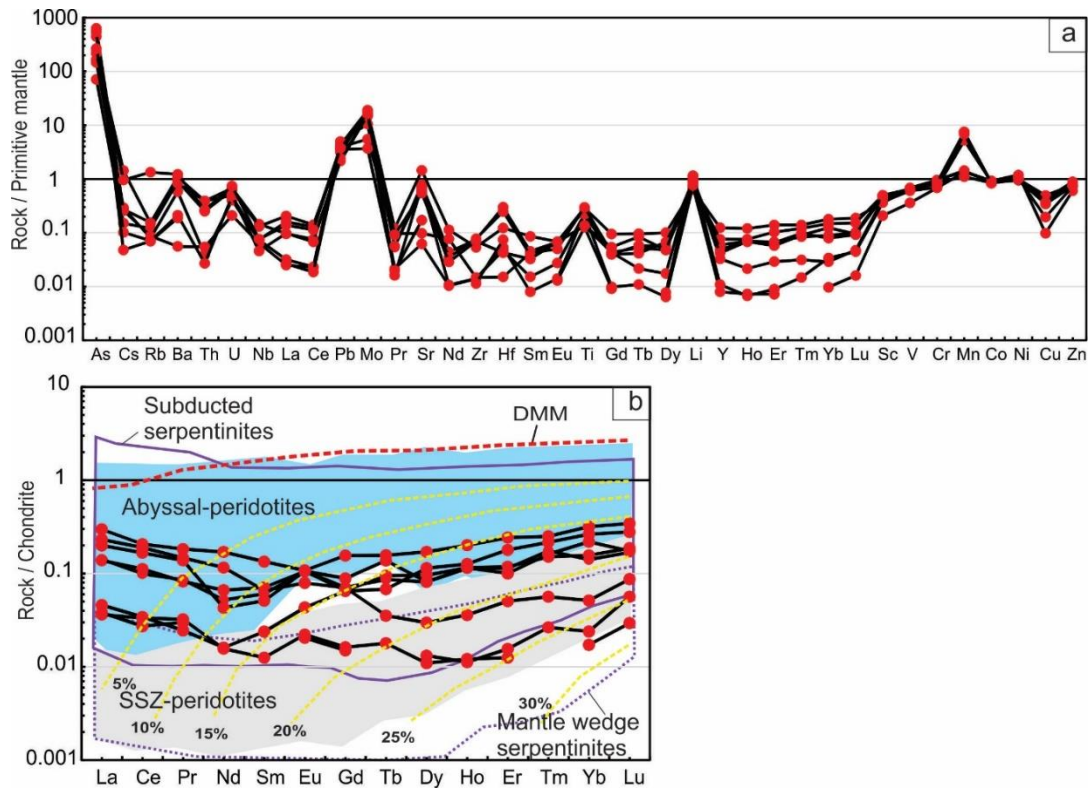


Figure F.4: Primitive mantle (McDonough and Sun, 1995) normalized multielement and rare earth element patterns normalized to chondrite (Anders and Grevesse, 1989) of the studied serpentinites. Fields of Abyssal peridotites are from Niu (2004), supra subduction zone (SSZ; Izu-Bonin-Mariana) peridotites from Parkinson and Pearce (1998) and Subducted and mantle wedge serpentinites from Deschamps et al. (2013). The non-modal fractional melting model of a depleted MORB mantle (DMM) source (Workman and Hart, 2005) is used, with melting curves assumed of a DMM source in the spinel stability field (De Hoog *et al.*, 2009).

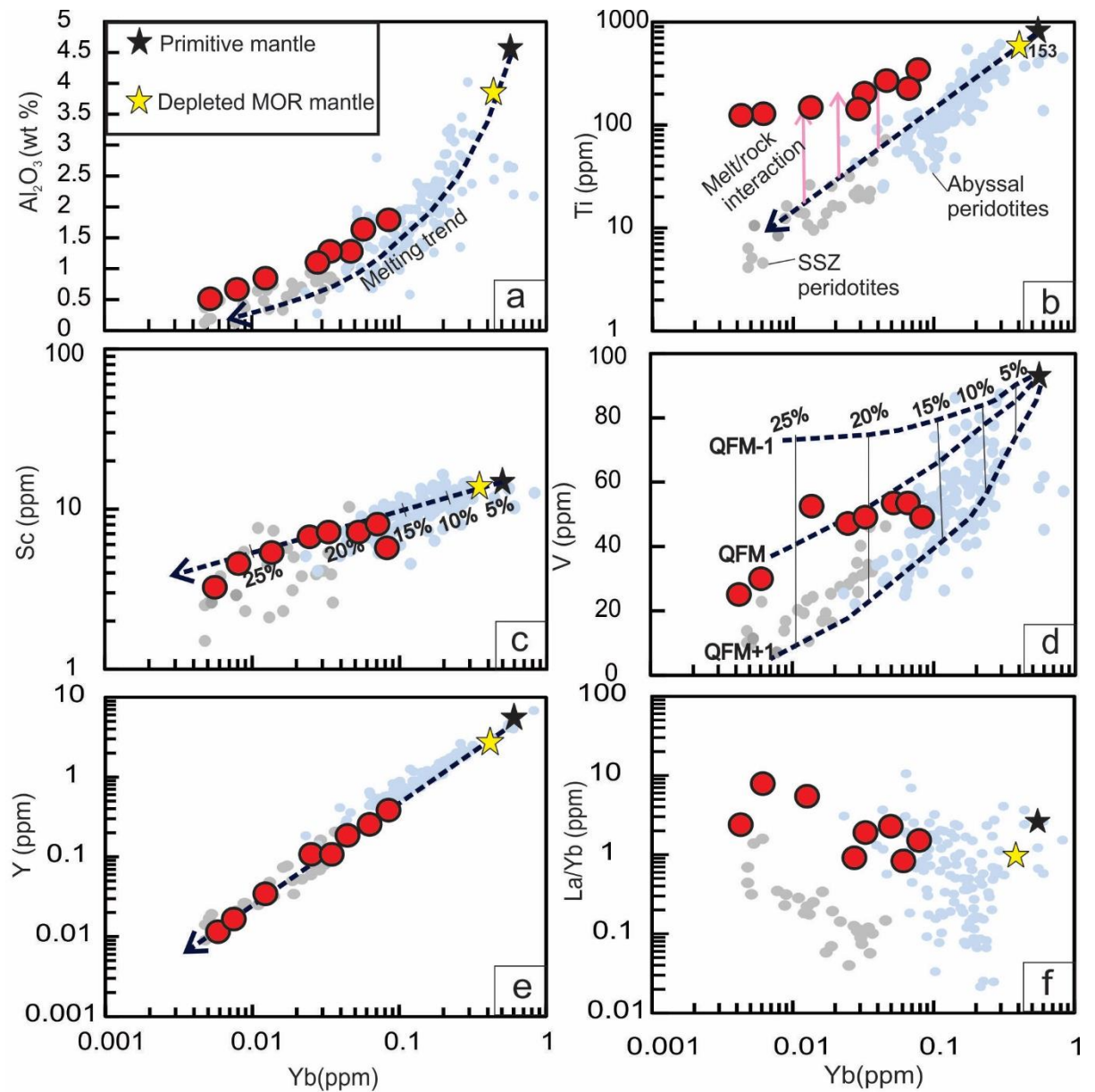


Figure F.5: Whole-rock Yb (ppm) vs. selected major, trace and rare earth elements variation of the studied serpentinites. Fields of abyssal peridotites are from Niu (2004), and supra subduction zone (SSZ; Izu-Bonin-Mariana) peridotites from Parkinson and Pearce (1998). Compositions of the primitive mantle (McDonough and Sun, 1995) and depleted MORB mantle (DMM) (Workman and Hart, 2005) is plotted for comparison.. Determination of the degree of partial melting was based on bulk-rock chemistry showing in figures (c, d) according to the biviariates of Yb (ppm) vs. Cr and V (ppm) for residual peridotites, according to Lee et al. (2003), with annotated degrees of mantle melting (in %). Fractional melting trends for different oxygen fugacities are also shown. FMM = fertile MORB mantle. Vanadium behaves as a moderately incompatible element when melting occurs under reducing conditions (QFM–1; this refers to $\log f_{O_2}$ (QFM) = log units relative to quartz–fayalite–magnetite buffer), resulting in low depletion of V. Under oxidizing conditions (QFM+1), the ratio of $V^{3+}/(V^{4+}+V^{5+})$ become lower whereas partition coefficients are higher causing vanadium to become a highly incompatible element and readily depleted in the mantle during partial melting. The melt/rock interaction trend in (b) after Deschamps et al. (2013) Depletion trends are after Uysal et al. (2016) and Gamal El Dien et al. (2016).

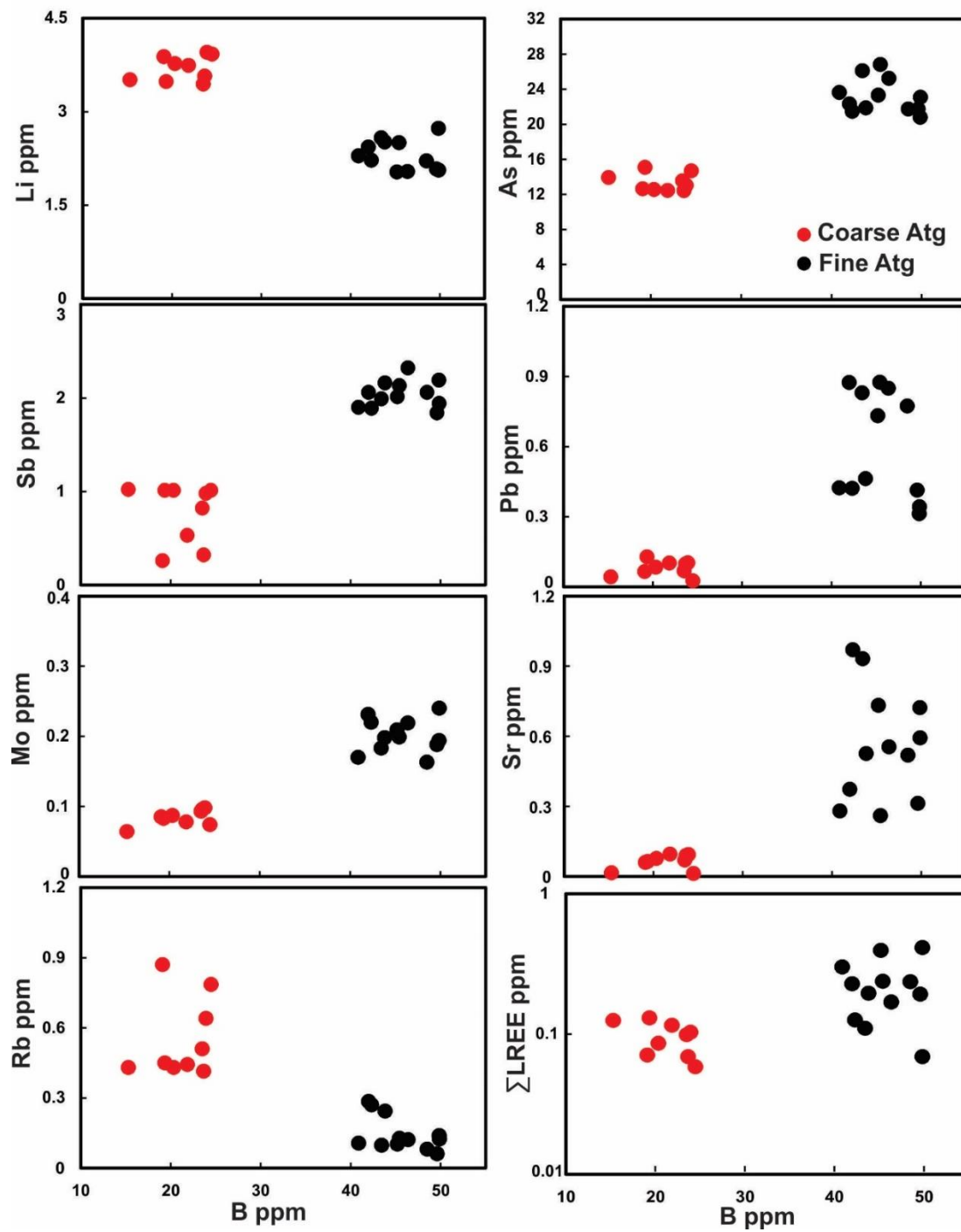


Figure F.6: Binary plots of B and various trace elements in the studied antigorites showing the different contents between the two antigorites groups. All concentrations are in ppm.

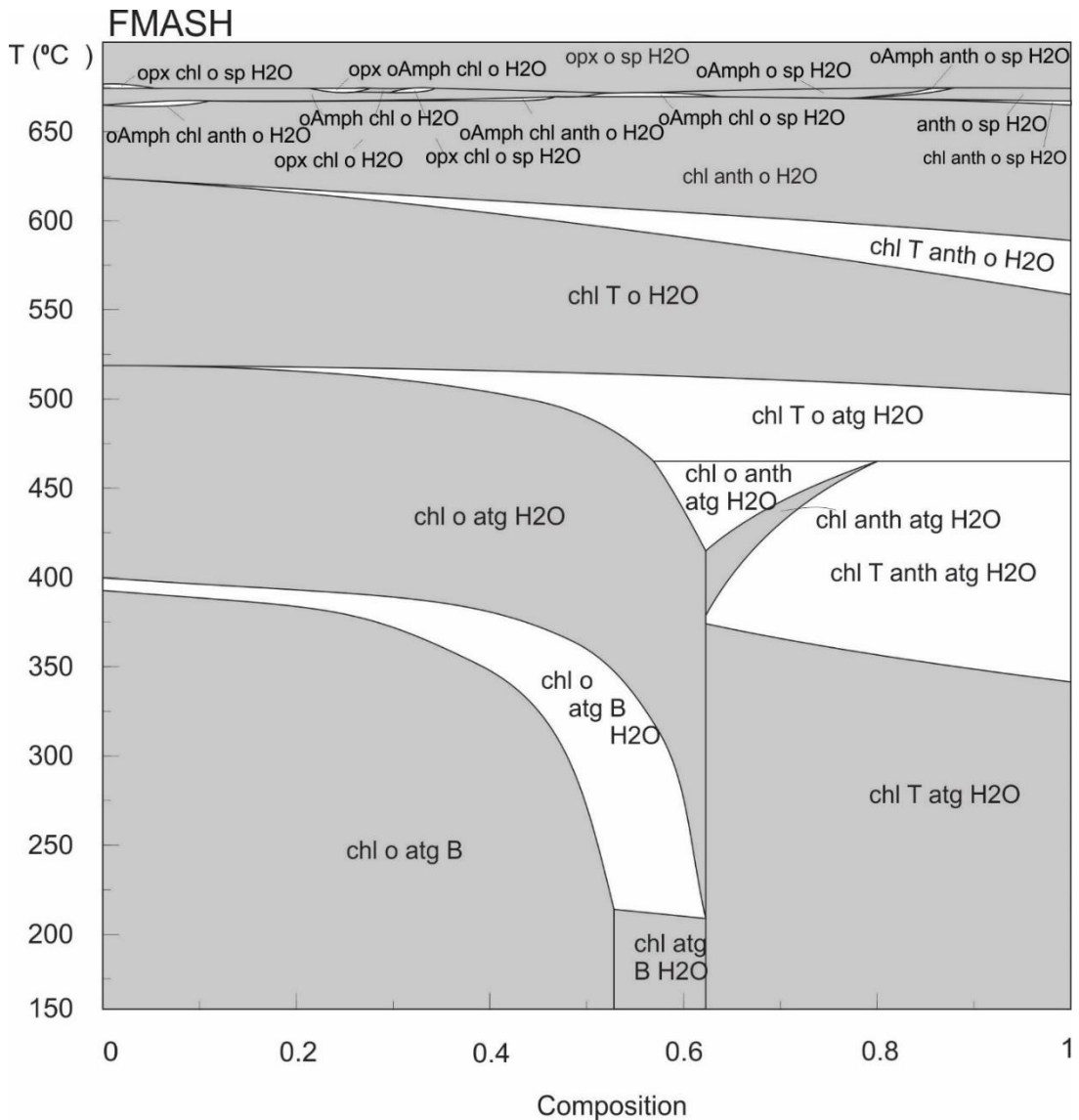


Figure F.7: A T-X pseudosection at 2 kbar shows the stability range of the spinel mineral up to > 670 °C. This indicates that the observed spinel in the studied samples are a metastable phase with respect to the surrounding low-grade assemblage. The x-axis is the bulk composition which is similar to that in Figures. 4 and 5 in the main text with the exception of reducing the system to FMASH.

Table F.1: Major oxides (anhydrous) and trace elements (including REEs) compositions of the studied serpentinites.

Sample #	Mu17/0 1	Mu17/0 3	Mu17/0 6	Mu17/1 0	Mu17/1 3	Mu17/1 6	Mu17/1 8	Mu17/2 0
Major Elements (wt %)								
SiO ₂	45.402	46.130	45.730	46.847	46.304	44.769	44.851	45.326
Al ₂ O ₃	1.427	1.813	1.738	1.464	1.314	0.642	0.761	1.043
TiO ₂	0.032	0.035	0.027	0.027	0.036	0.015	0.016	0.016
FeO	9.637	9.494	9.970	10.204	9.986	8.596	9.201	9.136
MnO	0.104	0.143	0.130	0.356	0.144	0.136	0.046	0.353
MgO	41.563	41.021	40.475	40.835	41.152	45.674	44.316	43.526
CaO	1.168	0.961	2.012	0.164	0.966	0.090	0.227	0.162
Na ₂ O	0.002	0.002	0.002	0.002	0.002	0.002	0.002	0.001
K ₂ O	0.003	0.003	0.003	0.003	0.003	0.003	0.003	0.003
P ₂ O ₅	0.004	0.003	0.004	0.007	0.003	0.002	0.003	0.007
Total	99.340	99.605	100.090	99.908	99.910	99.930	99.425	99.573
LOI	12.781	12.544	13.425	12.313	12.544	14.636	13.303	14.931
Trace Elements (ppm)								
Ti	318.00	349.00	265.00	267.00	358.00	153.00	160.00	163.00
Li	1.48	1.01	1.08	1.38	1.23	1.17	1.85	1.74
Sc	7.91	6.07	8.02	7.34	8.01	3.36	5.90	6.78
Mn	1035.00	1434.00	1304.00	3560.00	1437.00	1362.00	461.00	3531.00
V	51.78	49.22	52.93	50.98	53.01	29.39	32.28	55.68
Cr	2198.03	2229.32	2509.59	2243.98	2150.93	1793.52	1835.00	2490.11
Co	89.85	93.22	96.24	88.34	87.23	96.65	87.77	87.64
Ni	1852.81	2054.63	1908.20	2010.32	1983.43	2323.25	2010.59	1940.48
Cu	10.23	12.07	12.69	11.82	10.98	2.93	5.85	14.76
Zn	40.55	44.79	48.59	40.55	41.31	33.17	40.05	41.73
As	8.26	3.54	7.32	10.87	13.23	31.50	27.04	22.32
Rb	0.09	0.07	0.05	0.09	0.80	0.05	0.04	0.04
Sr	15.45	28.68	14.35	12.34	10.89	1.23	3.39	1.94
Y	0.26	0.53	0.32	0.21	0.18	0.03	0.05	0.14
Zr	0.78	0.56	0.15	0.81	0.73	0.14	0.12	0.15
Nb	0.09	0.09	0.05	0.03	0.05	0.04	0.00	0.05
Mo	0.77	0.91	0.95	0.74	0.82	0.52	0.18	0.27
Cd	0.03	0.02	0.03	0.04	0.02	0.03	0.08	0.03
Cs	0.01		0.01	0.03	0.02	0.01		
Ba	7.14	5.99	3.85	5.49	8.05	0.37	1.24	1.40
La	0.0617	0.1324	0.0205	0.0162	0.1033	0.0170	0.0631	0.0892
Ce	0.1269	0.2343	0.0389	0.0378	0.2152	0.0310	0.1131	0.1893
Pr	0.0137	0.0305	0.0041	0.0054	0.0245	0.0050	0.0143	0.0231
Nd	0.0549	0.1408	0.0133	0.0129	0.0959		0.0431	0.0356
Sm	0.0183	0.0347	0.0061	0.0032	0.0170		0.0156	0.0132
Eu	0.0103	0.0105	0.0042	0.0104	0.0103	0.0022	0.0020	0.0077
Gd	0.0217	0.0514	0.0214	0.0234	0.0292	0.0053	0.0050	0.0232
Tb	0.0057	0.0095	0.0041	0.0052	0.0083	0.0011		0.0021
Dy	0.0377	0.0672	0.0450	0.0320	0.0321	0.0043	0.0052	0.0117
Ho	0.0103	0.0179	0.0113	0.0101	0.0102	0.0011	0.0010	0.0032
Er	0.0296	0.0608	0.0449	0.0285	0.0251	0.0031	0.0039	0.0127
Tm	0.0057	0.0095	0.0082	0.0066	0.0061		0.0010	0.0021
Yb	0.0388	0.0788	0.0654	0.0350	0.0543	0.0043	0.0059	0.0127

Lu	0.0069	0.0126	0.0102	0.0062	0.0064	0.0011	0.0021	0.0032
Hf	0.08	0.03	0.01	0.07	0.01	0.02	0.02	
Pb	0.32	0.47	0.64	0.36	0.56	0.74	0.53	0.58
Th	0.03	0.02	0.00	0.03	0.02	0.00	0.00	0.00
U	0.01	0.12	0.01	0.01	0.02	0.00	0.01	0.01

Table F.2: EMP data of the studied antigorites.

Sample #	Mu17/01	Mu17/01	Mu17/01	Mu17/01	Mu17/01	Mu17/01	Mu17/03	Mu17/03
Mineral	Coarse	Coarse	Coarse	Coarse	Coarse	Coarse	Coarse	Coarse
	(CA)	(CA)	(CA)	(CA)	(CA)	(CA)	(CA)	(CA)
SiO ₂	44.03	43.31	44.33	44.53	44.40	44.00	44.56	44.18
TiO ₂	0.01							0.02
Al ₂ O ₃	0.49	0.65	0.31	0.34	0.53	0.54	0.25	0.51
FeO	4.02	4.41	4.22	4.24	4.21	4.20	4.20	4.20
MnO	0.03	0.06	0.06	0.04	0.08	0.08	0.06	0.00
MgO	37.73	37.47	37.61	37.61	38.22	37.39	38.05	37.97
CaO			0.12	0.01	0.01	0.02		
Na ₂ O			0.02		0.01	0.02		
K ₂ O		0.02				0.02		
Cr ₂ O ₃	0.03	0.00	0.22		0.03	0.01		
NiO	0.19	0.78	0.88	0.52	0.21	0.72	0.46	0.88
Total	86.54	86.68	87.78	87.30	87.70	87.00	87.58	87.76
LOI	13.46	13.32	12.22	12.70	12.30	13.01	12.42	12.24
Si/Si+Al	0.99	0.98	0.99	0.99	0.99	0.99	0.99	0.99
Mg/Mg+Fe	0.94	0.94	0.94	0.94	0.94	0.94	0.94	0.94

Sample #	Mu17/03	Mu17/03	Mu17/03	Mu17/03	Mu17/03	Mu17/06	Mu17/06	Mu17/06
Mineral	Coarse	Coarse	Coarse	Coarse	Coarse	Coarse	Coarse	Coarse
	(CA)	(CA)	(CA)	(CA)	(CA)	(CA)	(CA)	(CA)
SiO ₂	44.52	44.85	44.11	45.18	44.27	44.28	44.80	45.08
TiO ₂	0.02		0.01	0.00	0.05			
Al ₂ O ₃	0.21	0.05	0.40	0.41	0.37	0.60	0.43	0.02
FeO	4.28	4.16	2.40	2.43	2.95	2.60	2.58	2.48
MnO	0.00	0.09	0.11	0.08	0.06	0.07	0.10	0.06
MgO	38.24	38.38	38.92	39.57	38.98	39.31	39.18	38.26
CaO					0.01	0.01		
Na ₂ O							0.01	
K ₂ O	0.01				0.01		0.02	
Cr ₂ O ₃			0.10	0.16	0.40	0.28	0.07	0.07
NiO	0.60	0.72	0.38	0.12	0.12	0.16	0.08	0.13
Total	87.86	88.25	86.43	87.97	87.20	87.31	87.28	86.10
LOI	12.14	11.75	13.57	12.03	12.80	12.69	12.72	13.90
Si/Si+Al	0.99	1.00	0.99	0.99	0.99	0.98	0.99	1.00
Mg/Mg+Fe	0.94	0.94	0.97	0.97	0.96	0.96	0.96	0.97

Sample #	Mu17/06	Mu17/06	Mu17/10	Mu17/10	Mu17/10	Mu17/10	Mu17/13	Mu17/13
Mineral	Coarse	Coarse	Coarse	Coarse	Coarse	Coarse	Coarse	Coarse
	(CA)	(CA)	(CA)	(CA)	(CA)	(CA)	(CA)	(CA)
SiO ₂	45.22	45.52	45.38	44.15	43.92	44.31	44.59	43.97
TiO ₂	0.04		0.03	0.01	0.02			
Al ₂ O ₃	0.63	0.05	0.16	0.47	0.76	0.21	0.32	0.82
FeO	2.97	2.83	2.80	2.47	2.87	2.60	2.29	2.29
MnO	0.01	0.03	0.03	0.06	0.06	0.00	0.05	0.05

MgO	38.82	38.94	38.77	39.19	39.13	38.73	39.43	39.70
CaO	0.01		0.00	0.01				
Na2O		0.02						
K2O	0.01	0.00	0.01	0.01				0.01
Cr2O3	0.69	0.23	0.27	0.00	0.09	0.29	0.05	0.05
NiO	0.12	0.14	0.12	0.71	0.85	0.07	0.91	0.19
Total	88.52	87.74	87.57	87.07	87.70	86.20	87.64	87.08
LOI	11.49	12.26	12.43	12.93	12.30	13.80	12.36	12.92
Si/Si+Al	0.98	1.00	1.00	0.99	0.98	0.99	0.99	0.98
Mg/Mg+Fe	0.96	0.96	0.96	0.97	0.96	0.96	0.97	0.97

Sample #	Mu17/13 Coarse (CA)	Mu17/16 Coarse (CA)	Mu17/16 Coarse (CA)	Mu17/16 Coarse (CA)	Mu17/16 Coarse (CA)	Mu17/16 Coarse (CA)	Mu17/18 Coarse (CA)	Mu17/18 Coarse (CA)
SiO2	43.64	44.34	45.16	43.92	44.35	45.86	45.20	45.18
TiO2		0.02	0.03	0.01	0.03	0.01	0.02	
Al2O3	0.94	0.52	0.16	0.72	0.29	0.26	0.17	0.75
FeO	2.59	2.60	2.40	2.18	2.20	2.82	2.80	2.22
MnO	0.10	0.07	0.07	0.07	0.05	0.11	0.03	0.03
MgO	38.99	39.59	39.69	39.32	38.90	38.95	38.98	37.95
CaO			0.00		0.01		0.01	0.02
Na2O			0.03			0.01		0.01
K2O				0.01	0.02	0.01		0.01
Cr2O3	0.21	0.25	0.08		0.25	0.34	0.16	0.15
NiO	0.14	0.10	0.11	0.11	0.41	0.12	0.13	0.24
Total	86.61	87.48	87.71	86.35	86.51	88.49	87.49	86.55
LOI	13.39	12.52	12.29	13.65	13.49	11.51	12.51	13.45
Si/Si+Al	0.98	0.99	1.00	0.98	0.99	0.99	1.00	0.98
Mg/Mg+Fe	0.96	0.96	0.97	0.97	0.97	0.96	0.96	0.97

Sample #	Mu17/18 Coarse (CA)	Mu17/18 Coarse (CA)	Mu17/18 Coarse (CA)	Mu17/18 Coarse (CA)	Mu17/18 Coarse (CA)	Mu17/18 Coarse (CA)	Mu17/20 Coarse (CA)	Mu17/20 Coarse (CA)
SiO2	44.78	45.43	45.27	44.19	44.20	44.02	43.34	43.96
TiO2	0.01	0.03	0.01					0.04
Al2O3	0.20	0.13	0.18	0.96	0.47	0.49	0.79	0.04
FeO	2.13	2.65	2.42	2.65	2.55	3.96	5.90	5.74
MnO	0.13	0.05	0.04	0.10	0.09	0.03	0.03	0.00
MgO	39.32	38.74	38.72	38.29	38.85	37.52	36.45	36.32
CaO	0.01		0.01	0.01				0.03
Na2O				0.02			0.01	0.03
K2O	0.01	0.01		0.01	0.01		0.00	0.04
Cr2O3	0.13	0.18	0.35	0.18	0.02	0.03	0.15	0.63
NiO	0.12	0.06	0.13	0.41	0.13	0.48	0.11	0.21
Total	86.84	87.27	87.14	86.81	86.31	86.52	86.77	87.04
LOI	13.16	12.73	12.87	13.19	13.69	13.48	13.23	12.96
Si/Si+Al	0.99	1.00	1.00	0.97	0.99	0.99	0.98	1.00

Mg/Mg+Fe 0.97 0.96 0.97 0.96 0.96 0.94 0.92 0.92

Sample #	Mu17/20	Mu17/20	Mu17/20	Mu17/20	Mu17/20	Mu17/20	Mu17/20	Mu17/20
Mineral	Coarse	Coarse	Coarse	Coarse	Coarse	Coarse	Coarse	Coarse
	(CA)	(CA)	(CA)	(CA)	(CA)	(CA)	(CA)	(CA)
SiO2	43.53	43.43	43.01	43.40	44.61	43.23	43.24	43.37
TiO2								
Al2O3	0.80	0.86	0.76	0.84	0.77	0.61	0.97	0.91
FeO	5.69	6.13	5.96	6.09	5.62	5.91	5.99	5.85
MnO	0.02	0.03	0.04	0.01			0.02	
MgO	35.63	36.34	35.98	36.65	35.68	35.98	36.40	36.32
CaO	0.14	0.01	0.02	0.03	0.06	0.03	0.01	0.01
Na2O	0.04	0.02	0.03	0.03	0.01	0.01	0.01	0.01
K2O	0.05	0.04	0.02	0.04	0.03	0.05	0.03	0.02
Cr2O3	0.14	0.05	0.17	0.29	0.03	0.06	0.14	0.11
NiO	0.16	0.17	0.13	0.17	0.12	0.30	0.15	0.11
Total	86.20	87.07	86.11	87.55	86.92	86.18	86.96	86.70
LOI	13.81	12.94	13.89	12.45	13.08	13.82	13.05	13.30
Si/Si+Al	0.98	0.98	0.98	0.98	0.98	0.98	0.97	0.98
Mg/Mg+Fe	0.92	0.91	0.92	0.91	0.92	0.92	0.92	0.92

Sample #	Mu17/0	Mu17/0	Mu17/0	Mu17/0	Mu17/0	Mu17/0	Mu17/0	Mu17/0
Mineral	1	1	1	1	1	3	3	3
	Fine	Fine	Fine	Fine	Fine	Fine	Fine	Fine
	(FA)	(FA)	(FA)	(FA)	(FA)	(FA)	(FA)	(FA)
SiO2	42.54	41.74	42.67	40.98	41.00	42.95	40.59	42.22
TiO2			0.01	0.02			0.03	
Al2O3	1.17	1.48	1.25	1.89	1.76	1.95	2.36	2.63
FeO	4.06	4.44	3.92	4.28	3.99	4.36	4.16	4.51
MnO	0.03	0.05	0.04	0.05	0.01	0.07	0.04	0.04
MgO	37.55	34.52	37.28	37.38	37.75	37.72	37.87	37.35
CaO	0.02	0.04			0.01			0.02
Na2O	0.02				0.01			
K2O		0.02					0.01	
Cr2O3	0.02	0.22	0.06	0.12	0.00	0.57	0.75	0.85
NiO	0.28	0.13	0.92	0.11	0.72	0.06	0.06	0.10
Total	85.69	82.64	86.14	84.82	85.25	87.68	85.87	87.71
LOI	14.31	17.36	13.86	15.18	14.75	12.32	14.13	12.29
Si/Si+Al	0.97	0.96	0.97	0.95	0.95	0.95	0.96	0.93
Mg/Mg+Fe	0.94	0.93	0.94	0.94	0.94	0.94	0.94	0.94

Sample #	Mu17/0	Mu17/0	Mu17/0	Mu17/0	Mu17/0	Mu17/0	Mu17/0	Mu17/0
Mineral	3	3	3	3	3	3	6	6
	Fine	Fine	Fine	Fine	Fine	Fine	Fine	Fine
	(FA)	(FA)	(FA)	(FA)	(FA)	(FA)	(FA)	(FA)
SiO2	42.06	41.29	41.94	40.66	39.80	41.98	42.35	40.85
TiO2	0.02		0.05		0.02	0.01	0.01	
Al2O3	2.71	1.75	2.17	1.74	1.96	1.62	1.42	1.48

FeO	4.25	3.02	2.03	3.29	3.22	3.01	3.95	4.10
MnO	0.04	0.07	0.08	0.10	0.05	0.04	0.03	0.04
MgO	37.17	38.01	38.62	37.62	37.94	37.77	37.25	37.31
CaO	0.03			0.01	0.16	0.01	0.01	
Na2O					0.03		0.02	0.11
K2O	0.01	0.01	0.00	0.01	0.03	0.01		0.03
Cr2O3	0.91	0.27	0.28	0.32	0.46	0.33	0.01	0.00
NiO	0.16	0.17	0.12	0.23	0.10	0.37	0.37	0.56
Total	87.37	84.59	85.29	83.98	83.76	85.15	85.42	84.47
LOI	12.63	15.41	14.71	16.02	16.24	14.85	14.58	15.53
Si/Si+Al	0.93	0.95	0.94	0.95	0.95	0.96	0.94	0.93
Mg/Mg+Fe	0.94	0.96	0.97	0.95	0.95	0.96	0.94	0.94

Sample #	Mu17/0 6	Mu17/0 6	Mu17/0 6	Mu17/0 6	Mu17/0 6	Mu17/1 0	Mu17/1 0	Mu17/1 0
Mineral	Fine (FA)	Fine (FA)	Fine (FA)	Fine (FA)	Fine (FA)	Fine (FA)	Fine (FA)	Fine (FA)
SiO2	39.78	42.34	41.19	42.00	40.77	42.64	41.89	42.04
TiO2	0.02	0.01						0.01
Al2O3	1.53	1.75	2.69	2.45	2.95	2.63	2.26	1.91
FeO	4.22	3.39	2.96	3.37	3.02	2.94	4.23	5.98
MnO	0.03	0.07	0.04	0.06	0.06	0.05	0.02	0.00
MgO	37.75	38.10	37.75	37.30	38.78	38.38	37.29	35.16
CaO	0.02	0.01			0.02		0.02	0.03
Na2O	0.03	0.02	0.01		0.01		0.02	0.06
K2O	0.01	0.00	0.01	0.02			0.01	0.03
Cr2O3	0.01	0.44	0.95	0.84	0.86	0.78	0.80	0.79
NiO	0.42	0.17	0.10	0.28	0.09	0.16	0.16	0.23
Total	83.81	86.29	85.69	86.31	86.55	87.57	86.69	86.24
LOI	16.19	13.71	14.32	13.69	13.45	12.43	13.31	13.76
Si/Si+Al	0.93	0.95	0.93	0.94	0.95	0.96	0.94	0.95
Mg/Mg+Fe	0.94	0.95	0.96	0.95	0.96	0.96	0.94	0.91

Sample #	Mu17/1 0	Mu17/1 0	Mu17/1 0	Mu17/1 3	Mu17/1 3	Mu17/1 3	Mu17/1 3	Mu17/1 3
Mineral	Fine (FA)	Fine (FA)	Fine (FA)	Fine (FA)	Fine (FA)	Fine (FA)	Fine (FA)	Fine (FA)
SiO2	39.87	42.43	42.39	42.21	42.77	42.20	42.56	40.61
TiO2		0.02			0.02		0.01	
Al2O3	1.67	2.01	1.99	1.95	1.83	1.74	1.94	1.98
FeO	6.20	5.85	6.10	5.73	5.95	6.18	6.43	6.11
MnO	0.00	0.03	0.05	0.02	0.02	0.03	0.02	0.01
MgO	36.13	35.13	35.44	35.37	35.93	35.46	36.06	35.61
CaO		0.01	0.05	0.03	0.05	0.09	0.01	0.01
Na2O	0.01	0.04	0.01	0.03	0.01	0.04		
K2O		0.03	0.01	0.05	0.04	0.07		
Cr2O3	0.60	0.60	0.74	0.34	0.07	0.25	0.28	0.48
NiO	0.20	0.37	0.18	0.11	0.09	0.50	0.48	0.14

Total	84.67	86.51	86.96	85.84	86.77	86.57	87.79	84.94
LOI	15.33	13.49	13.04	14.16	13.23	13.43	12.21	15.06
Si/Si+Al	0.95	0.95	0.95	0.95	0.95	0.95	0.95	0.95
Mg/Mg+Fe	0.91	0.91	0.91	0.92	0.91	0.91	0.91	0.91

Sample #	Mu17/1 6	Mu17/1 6	Mu17/1 6	Mu17/1 6	Mu17/1 6	Mu17/1 6	Mu17/1 6	Mu17/1 6
Mineral	Fine (FA)	Fine (FA)	Fine (FA)	Fine (FA)	Fine (FA)	Fine (FA)	Fine (FA)	Fine (FA)
SiO2	42.69	41.18	42.67	39.94	42.45	42.88	39.81	40.69
TiO2					0.01	0.01		
Al2O3	1.81	2.87	2.21	2.21	1.88	1.83	1.16	2.81
FeO	5.92	7.45	6.07	6.11	5.70	5.98	5.36	6.26
MnO	0.00	0.07	0.03	0.05	0.00	0.00	0.00	0.03
MgO	36.00	33.99	35.85	33.19	35.45	35.80	32.64	35.35
CaO	0.03	0.03	0.01	0.12		0.02	0.06	
Na2O	0.03	0.07	0.04	0.24	0.01	0.01	0.15	0.04
K2O	0.02	0.06	0.01	0.22	0.01	0.03	0.11	0.02
Cr2O3	0.07	0.72	0.74	0.28	0.21	0.38	0.68	0.80
NiO	0.52	0.45	0.21	0.15	0.18	0.20	0.22	0.14
Total	87.08	86.90	87.82	82.51	85.90	87.13	80.17	86.13
LOI	12.92	13.10	12.18	17.49	14.10	12.87	19.83	13.87
Si/Si+Al	0.95	0.92	0.94	0.94	0.95	0.95	0.97	0.92
Mg/Mg+Fe	0.92	0.89	0.91	0.91	0.92	0.91	0.92	0.91

Sample #	Mu17/1 6	Mu17/1 8	Mu17/1 8	Mu17/1 8	Mu17/1 8	Mu17/1 8	Mu17/1 8	Mu17/1 8
Mineral	Fine (FA)	Fine (FA)	Fine (FA)	Fine (FA)	Fine (FA)	Fine (FA)	Fine (FA)	Fine (FA)
SiO2	41.91	42.21	42.30	42.43	41.71	42.61	42.62	41.30
TiO2								0.01
Al2O3	1.74	1.83	1.78	1.83	1.76	1.85	1.86	1.81
FeO	5.81	5.76	6.17	5.78	6.04	5.59	5.86	6.03
MnO	0.04	0.05	0.02	0.04	0.01	0.02	0.02	0.05
MgO	35.59	36.13	35.31	35.48	35.04	36.00	35.66	32.41
CaO	0.01		0.03		0.04		0.18	0.13
Na2O	0.02	0.01	0.04	0.01	0.02	0.03		0.11
K2O	0.03	0.02	0.03	0.01	0.02	0.03	0.01	0.10
Cr2O3	0.59	0.46	0.46	0.61	0.70	0.36	0.29	0.11
NiO	0.14	0.13	0.11	0.40	0.30	0.08	0.27	0.22
Total	85.87	86.61	86.26	86.58	85.64	86.56	86.76	82.26
LOI	14.13	13.39	13.74	13.42	14.36	13.44	13.24	17.74
Si/Si+Al	0.95	0.95	0.95	0.95	0.95	0.95	0.95	0.95
Mg/Mg+Fe	0.92	0.92	0.91	0.92	0.91	0.92	0.92	0.91

Sample #	Mu17/1 8	Mu17/1 8	Mu17/1 8	Mu17/1 8	Mu17/1 8	Mu17/2 0	Mu17/2 0	Mu17/2 0
Mineral	Fine (FA)	Fine (FA)	Fine (FA)	Fine (FA)	Fine (FA)	Fine (FA)	Fine (FA)	Fine (FA)
SiO2	41.91	42.21	42.30	42.43	41.71	42.61	42.62	41.30
TiO2								0.01
Al2O3	1.74	1.83	1.78	1.83	1.76	1.85	1.86	1.81
FeO	5.81	5.76	6.17	5.78	6.04	5.59	5.86	6.03
MnO	0.04	0.05	0.02	0.04	0.01	0.02	0.02	0.05
MgO	35.59	36.13	35.31	35.48	35.04	36.00	35.66	32.41
CaO	0.01		0.03		0.04		0.18	0.13
Na2O	0.02	0.01	0.04	0.01	0.02	0.03		0.11
K2O	0.03	0.02	0.03	0.01	0.02	0.03	0.01	0.10
Cr2O3	0.59	0.46	0.46	0.61	0.70	0.36	0.29	0.11
NiO	0.14	0.13	0.11	0.40	0.30	0.08	0.27	0.22
Total	85.87	86.61	86.26	86.58	85.64	86.56	86.76	82.26
LOI	14.13	13.39	13.74	13.42	14.36	13.44	13.24	17.74
Si/Si+Al	0.95	0.95	0.95	0.95	0.95	0.95	0.95	0.95
Mg/Mg+Fe	0.92	0.92	0.91	0.92	0.91	0.92	0.92	0.91

SiO2	41.82	42.02	42.03	42.66	41.16	41.61	41.29	42.30
TiO2								
Al2O3	2.34	2.25	1.52	1.99	3.12	3.12	2.53	2.30
FeO	6.08	5.99	5.70	5.86	6.24	6.17	5.98	5.83
MnO	0.02	0.00	0.00	0.00	0.02	0.02	0.03	0.03
MgO	35.18	35.32	35.44	35.83	36.04	35.93	36.02	35.61
CaO	0.02	0.02	0.01		0.01	0.01		0.01
Na2O	0.03	0.01	0.02	0.03	0.01	0.01	0.01	0.01
K2O	0.04	0.02	0.01	0.02	0.02	0.02	0.02	0.03
Cr2O3	0.90	0.85	0.99	0.87	1.00	0.99	1.06	0.91
NiO	0.27	0.14	0.13	0.19	0.20	0.25	0.26	0.35
Total	86.69	86.63	85.85	87.44	87.83	88.12	87.20	87.37
LOI	13.31	13.37	14.15	12.56	12.17	11.88	12.80	12.63
Si/Si+Al	0.94	0.94	0.96	0.95	0.92	0.92	0.93	0.94
Mg/Mg+Fe	0.91	0.91	0.92	0.92	0.91	0.91	0.91	0.92

Sample #	Mu17/2 0	Mu17/2 0	Mu17/2 0	Mu17/2 0	Mu17/2 0	Mu17/2 0	Mu17/2 0	Mu17/2 0
Mineral	Fine (FA)	Fine (FA)	Fine (FA)	Fine (FA)	Fine (FA)	Fine (FA)	Fine (FA)	Fine (FA)
SiO2	40.68	41.85	39.64	39.52	41.69	40.75	40.97	41.90
TiO2			0.02	0.01				
Al2O3	2.80	2.70	3.38	3.14	2.43	2.50	3.48	2.75
FeO	5.75	5.61	6.32	6.04	5.84	5.82	6.15	6.07
MnO	0.02	0.03	0.01	0.06	0.02	0.00	0.04	0.01
MgO	36.07	36.01	28.80	31.64	36.02	35.13	34.52	35.48
CaO	0.03	0.01	0.69	0.35		0.01	0.01	
Na2O		0.02	0.53	0.32			0.01	
K2O		0.00	0.31	0.38			0.01	0.01
Cr2O3	0.98	0.98	1.03	0.92	0.88	0.94	1.02	0.92
NiO	0.10	0.55	0.17	0.38	0.12	0.16	0.33	0.12
Total	86.43	87.75	80.90	82.77	86.99	85.32	86.53	87.27
LOI	13.57	12.25	19.10	17.23	13.01	14.69	13.47	12.73
Si/Si+Al	0.92	0.93	0.91	0.91	0.94	0.93	0.96	0.94
Mg/Mg+Fe	0.92	0.92	0.89	0.90	0.92	0.91	0.91	0.91

Table F.3: EMP data of the studied carbonates.

Sample #	Mu17/01	Mu17/01	Mu17/01	Mu17/03	Mu17/03	Mu17/06	Mu17/06	Mu17/06
Mineral	Magnesite	Magnesite	Magnesite	Magnesite	Magnesite	Magnesite	Magnesite	Magnesite
SiO ₂		0.03	0.14	0.01	3.60	0.03	0.81	0.21
TiO ₂	0.01					0.01		0.02
Al ₂ O ₃	0.01	0.01			0.13		0.02	0.00
FeO	5.77	3.22	3.51	2.96	3.00	2.36	4.14	2.15
MnO	0.32	1.30	0.89	2.41	1.61	2.07	1.03	2.20
MgO	40.06	40.21	37.72	39.73	39.88	39.57	39.90	39.76
CaO	0.16	0.16	0.27	0.60	0.08	0.20	0.17	0.14
K ₂ O		0.01	0.02	0.01	0.01	0.01		
Cr ₂ O ₃	0.02	0.03			0.02	0.01	0.03	
NiO	0.01	0.03	0.03		0.20	0.01	0.05	
Total	46.36	44.99	42.62	45.73	48.54	44.28	46.16	44.48

Sample #	Mu17/06	Mu17/10	Mu17/10	Mu17/10	Mu17/10	Mu17/10	Mu17/13	Mu17/13
Mineral	Magnesite	Magnesite	Magnesite	Magnesite	Magnesite	Magnesite	Magnesite	Magnesite
SiO ₂	0.52	0.01	0.07	0.08	0.06	0.03	0.23	0.14
TiO ₂		0.02	0.01					
Al ₂ O ₃	0.03	0.00		0.02	0.02	0.01	0.02	
FeO	2.88	1.86	3.46	1.88	1.90	2.19	3.80	3.10
MnO	1.93	2.55	1.07	2.74	2.73	2.31	0.33	0.99
MgO	40.49	39.13	39.19	39.81	40.34	39.91	40.08	38.80
CaO	0.21	0.36	0.19	0.30	0.27	0.20	0.23	0.15
K ₂ O	0.07	0.00		0.02	0.02	0.00	0.03	
Cr ₂ O ₃	0.02	0.02					0.01	0.01
NiO	0.00	0.04		0.03			0.04	
Total	46.21	44.00	44.03	44.89	45.35	44.64	44.77	43.19

Sample #	Mu17/13	Mu17/16	Mu17/16	Mu17/18	Mu17/18	Mu17/18	Mu17/18	Mu17/18
Mineral	Magnesite	Magnesite	Magnesite	Magnesite	Magnesite	Magnesite	Magnesite	Magnesite
SiO ₂	0.14	0.16	0.66	0.33	0.30	1.20	1.18	1.93
TiO ₂		0.03	0.09			0.17	0.01	
Al ₂ O ₃		0.00	0.00					
FeO	3.10	3.06	3.40	2.50	2.63	2.89	2.79	2.89
MnO	0.99	1.01	0.88	1.04	0.95	0.99	1.09	0.98
MgO	38.80	38.83	38.01	38.77	39.69	38.89	38.03	39.94
CaO	0.15	0.11	0.23	0.14	0.11	0.23	0.19	0.19
K ₂ O						0.00	0.02	0.00
Cr ₂ O ₃	0.01	0.01	0.01	0.07		0.14	0.06	0.00
NiO						1.16	0.00	0.00
Total	43.19	43.21	43.28	42.85	43.68	45.67	43.37	45.93

Sample #	Mu17/20	Mu17/20	Mu17/20	Mu17/01	Mu17/01	Mu17/01	Mu17/06	Mu17/06
Mineral	Magnesite	Magnesite	Magnesite	Dolomite	Dolomite	Dolomite	Dolomite	Dolomite
SiO ₂	1.45	1.22	0.84	0.60	0.27	0.31	1.49	0.19
TiO ₂	0.02	0.05	0.00	0.08			0.08	
Al ₂ O ₃						0.03	0.76	
FeO	2.93	2.99	2.95	5.65	0.49	2.01	4.96	0.44
MnO	0.97	0.94	1.06	0.86	0.13	0.42	0.88	0.09

MgO	39.06	38.86	39.50	15.88	19.76	17.63	14.83	20.13
CaO	0.12	0.07	0.04	21.93	27.06	24.30	21.44	27.43
K2O	0.00	0.02		0.04	0.01		0.12	0.05
Cr2O3	0.04	0.05		0.12	0.01		0.34	
NiO	0.01	0.00	0.00	0.87	0.23	0.30	0.70	0.14
Total	44.60	44.20	44.39	46.03	47.96	45.00	45.60	48.47

Sample #	Mu17/16	Mu17/16	Mu17/16	Mu17/18	Mu17/18	Mu17/18	Mu17/18	Mu17/18
Mineral	Dolomite	Dolomite	Dolomite	Dolomite	Dolomite	Dolomite	Dolomite	Dolomite
SiO2	0.28	1.08	1.08	1.19	0.12	0.34	0.21	0.17
TiO2			0.02	0.02				
Al2O3								
FeO	1.51	3.66	1.77	1.67	0.94	1.91	0.66	1.51
MnO	0.35	1.15	0.57	0.89	0.29	0.49	0.31	0.53
MgO	19.64	19.33	19.55	18.46	19.23	20.21	19.75	18.79
CaO	26.81	24.73	25.77	23.20	26.97	26.39	27.54	26.46
K2O		0.02	0.03	0.01	0.06		0.02	0.01
Cr2O3	0.02	0.11	0.04	8.20	0.03	0.02	0.03	0.05
NiO	0.38	0.48	0.41	0.55	0.20	0.41	0.10	
Total	48.99	50.56	49.24	54.19	47.84	49.77	48.62	47.52

Table F.4: *In situ* LA-ICP-MS data of the studied antigorites and carbonates.

Sample #	Mu17/01	Mu17/01	Mu17/01	Mu17/06	Mu17/06	Mu17/06	Mu17/10	Mu17/10
Mineral	fine antigorite (FA)	fine antigorite (FA)	fine antigorite (FA)	fine antigorite (FA)	fine antigorite (FA)	fine antigorite (FA)	fine antigorite (FA)	fine antigorite (FA)
B	49.870	42.330	40.890	48.520	49.620	42.010	45.440	43.830
Li	2.060	2.220	2.290	2.210	2.080	2.430	2.500	2.510
P	56.190	39.420	47.480	75.230	86.850	81.680	73.370	106.450
Sb	1.940	1.890	1.900	2.060	1.840	2.060	2.130	2.160
As	23.080	21.470	23.620	21.730	21.730	22.300	26.800	21.850
Cs	0.182	0.027	0.011	0.028	0.235	0.007	0.024	0.058
Rb	0.124	0.270	0.106	0.081	0.061	0.285	0.127	0.244
Ba					0.054	0.117	0.074	
Mo	0.240	0.220	0.170	0.163	0.188	0.231	0.199	0.198
Th								0.011
U	0.020		0.012	0.006	0.007	0.028	0.067	0.026
Nb				0.073	0.040	0.051	0.128	0.071
Ta							0.017	
La	0.125	0.086	0.085		0.107		0.074	0.127
Ce	0.195		0.173	0.198		0.173	0.150	
Pb	0.342	0.421	0.423	0.773	0.413	0.874	0.875	0.463
Pr	0.025	0.017		0.014	0.022		0.014	
Sr	0.593	0.970	0.280	0.519	0.313	0.373	0.260	0.526
Nd	0.046		0.043		0.042	0.055		0.045
Zr						0.330	0.486	0.590
Hf					0.032		0.155	0.118
Sm	0.022	0.023		0.024	0.021			0.023
Eu	0.015		0.012	0.017		0.012	0.015	
Ti	19.210	8.690	10.770	12.970	10.440	10.630	108.220	106.210
Gd			0.043			0.041	0.050	0.053
Tb	0.014		0.014	0.016	0.016		0.015	
Dy			0.113	0.112			0.123	0.124
Y	0.025	0.034	0.015	0.217	0.181	0.179	0.446	0.637
Ho		0.026		0.025	0.026		0.025	
Er			0.075			0.082		0.075
Tm	0.012	0.015	0.013	0.016			0.018	0.017
Yb	0.126	0.127	0.126	0.127		0.136	0.129	
Lu	0.025		0.027		0.028	0.028		0.028
Sc	8.2	6.5	7.7	14.6	15.6	16.8	17.0	17.9
V	19.7	8.2	17.7	50.1	52.3	52.7	41.4	41.3
Cr	123.1	73.2	5032.1	12483.8	11564.4	11520.2	7825.3	6981.9
Mn	214.6	264.4	236.0	195.0	197.8	212.0	564.3	556.7
Co	40.4	43.2	41.5	80.4	88.3	84.5	124.4	92.1
Ni	1151.3	1052.1	1372.5	1962.9	2287.3	1888.4	2510.7	2482.9
Cu	1.6	0.7	2.6	7.1	11.1	5.5	7.1	3.8
Zn	9.0	9.0	7.1	38.2	37.2	40.6	36.2	34.0
Ga	0.8	0.4	0.7	1.2	1.1	1.3	2.4	2.2

Sample #	Mu17/10	Mu17/18	Mu17/18	Mu17/18	Mu17/01	Mu17/01	Mu17/06	Mu17/06
Mineral	fine antigorite (FA)	fine antigorite (FA)	fine antigorite (FA)	fine antigorite (FA)	coarse antigorite (CA)	coarse antigorite (CA)	coarse antigorite (CA)	coarse antigorite (CA)
B	49.850	43.450	45.210	46.380	20.350	23.680	23.530	19.120
Li	2.730	2.580	2.030	2.040	3.770	3.570	3.440	3.880
P	117.990	112.490	74.090	57.870	61.010	44.150	47.130	17.330
Sb	2.190	1.990	2.012	2.321	1.010	0.320	0.820	0.260
As	20.770	26.090	23.310	25.220	12.560	12.410	13.560	12.630
Cs	0.017	0.092	0.301	0.083	0.282		0.011	0.032
Rb	0.139	0.098	0.103	0.121	0.430	0.414	0.510	0.870
Ba		0.214	0.092	0.293		0.130		0.087
Mo	0.194	0.183	0.209	0.219	0.087	0.096	0.093	0.085
Th	0.011	0.032	0.014	0.092				
U	0.018	0.032	0.094	0.012			0.047	
Nb	0.096	0.073	0.092	0.074	0.031			
Ta	0.025							
La		0.086	0.126	0.088	0.038		0.032	0.039
Ce			0.198		0.048	0.047	0.052	
Pb	0.313	0.830	0.732	0.849	0.084	0.098	0.068	0.065
Pr	0.023		0.025	0.014			0.006	
Sr	0.722	0.931	0.732	0.554	0.077	0.090	0.070	0.060
Nd	0.046		0.046	0.041		0.022		0.023
Zr	0.315	0.540	0.313	0.520				
Hf					0.065			
Sm		0.024		0.026			0.009	0.009
Eu		0.013	0.015		0.011	0.011		0.006
Ti	66.360	29.300	49.920	92.030	10.480	12.520	16.700	19.020
Gd		0.044						
Tb	0.018		0.015	0.015	0.016		0.016	
Dy				0.123				
Y	0.154	0.214	0.044	0.026	0.000	0.000	0.015	0.029
Ho	0.028				0.025	0.025		0.024
Er		0.075						
Tm		0.018	0.018	0.017	0.009	0.009		0.010
Yb	0.142	0.124		0.131	0.118		0.132	
Lu	0.024			0.026	0.029		0.019	0.020
Sc	17.0	18.0	18.4	17.1	9.3	9.1	10.7	8.2
V	27.3	49.2	51.0	49.1	15.2	18.5	23.5	21.2
Cr	817.0	12433.8	73.2	123.1	151.5	338.9	3604.4	504.0
Mn	546.9	199.4	245.4	244.6	312.1	268.0	248.7	248.5
Co	148.3	80.5	43.4	40.3	54.5	45.1	49.4	47.1
Ni	3867.6	1932.9	1042.1	1153.3	1254.0	1240.2	1788.1	1331.1
Cu	22.6	7.5	0.8	1.6	2.4	1.1	2.1	0.6
Zn	39.8	38.1	9.0	8.9	9.3	8.2	8.7	7.7
Ga	0.6	1.3	0.3	0.9	0.5	0.6	1.2	0.7

Sample #	Mu17/10	Mu17/10	Mu17/18	Mu17/18	Mu17/18
Mineral	coarse antigorite (CA)	coarse antigorite (CA)	coarse antigorite (CA)	coarse antigorite (CA)	coarse antigorite (CA)
B	24.500	15.320	19.370	21.870	23.940
Li	3.920	3.510	3.480	3.740	3.950
P	75.150	97.730	144.530	113.540	114.930
Sb	1.010	1.020	1.010	0.530	0.980
As	14.670	13.910	15.080	12.450	13.020
Cs		0.069	0.037	0.350	0.430
Rb	0.785	0.430	0.450	0.443	0.640
Ba	0.790				0.930
Mo	0.074	0.064	0.083	0.078	0.098
Th					
U		0.060	0.077		0.056
Nb		0.061	0.028	0.054	0.056
Ta		0.010	0.016		
La		0.043	0.047	0.030	0.043
Ce	0.049	0.052	0.053	0.055	0.051
Pb	0.026	0.042	0.128	0.102	0.103
Pr			0.006		
Sr	0.013	0.016	0.064	0.096	0.094
Nd		0.021	0.024	0.021	
Zr	0.029	0.091	0.136	0.198	0.198
Hf					
Sm	0.009	0.009		0.009	0.009
Eu		0.008	0.006		
Ti	17.920	93.540	97.370	66.630	64.930
Gd			0.030	0.031	
Tb	0.012	0.011		0.011	0.010
Dy			0.131		0.142
Y		0.089	0.076	0.166	0.016
Ho	0.024	0.024		0.025	
Er			0.065		0.074
Tm	0.010	0.010		0.009	
Yb		0.122	0.126		0.125
Lu	0.019		0.020	0.019	0.019
Sc	9.6	16.0	17.3	16.7	8.0
V	17.9	34.9	36.8	26.8	25.0
Cr	909.3	3198.6	2442.9	1446.9	1443.2
Mn	484.2	603.7	613.0	512.0	539.5
Co	52.7	93.3	98.4	73.8	77.0
Ni	1388.1	2061.4	2492.6	1845.5	1983.8
Cu	3.4	7.5	3.9	6.8	7.5
Zn	8.4	35.2	36.0	33.7	34.6
Ga	0.6	1.3	1.2	1.1	1.0

Sample #	Mu17/06	Mu17/10	Mu17/10	Mu17/18	Mu17/18
Mineral	Magnesite	Magnesite	Magnesite	Magnesite	Magnesite
B	112.590	95.860	59.060	170.960	130.010
Li	13.900	17.500	20.440	36.010	35.140
P	138.090	226.460	556.980	1227.680	1185.100
Sb	1.550	1.780	6.560	15.830	2.540
As	27.040	34.240	25.310	46.300	41.500
Cs		0.460	0.530	0.720	0.280
Rb	0.910	0.790	0.700	0.790	0.770
Ba	0.560		1.280	4.320	2.270
Mo	1.940	1.890	2.040	2.280	2.060
Th					
U					
Nb	0.087	0.091			
Ta	0.083				
La	2.346	2.420	2.590	2.250	2.510
Ce	3.638	4.290	3.550	5.240	3.060
Pb	1.630	1.790	1.670	2.860	2.250
Pr	0.430	0.320	0.260	0.440	0.320
Sr	6.010	5.480	6.420	7.560	9.040
Nd	0.390	0.750	0.530		
Zr					0.310
Hf	0.150				0.140
Sm	0.230	0.240			0.220
Eu		0.130	0.120		
Ti	11.620	19.070	16.910	20.390	19.330
Gd	0.479				
Tb		0.093			0.098
Dy	0.756				0.693
Y	1.150	1.440	0.570	1.070	0.850
Ho		0.170	0.151		
Er		0.520		0.590	
Tm		0.092			
Yb		0.740	0.630	0.780	0.620
Lu					
Sc	21.6	37.8	6.0	18.6	11.5
V	34.9	63.7	35.8	22.2	18.1
Cr	114.3	826.3	171.1	613.8	398.3
Mn	62926.7	343033.6	238638.4	515058.8	534852.1
Co	218.5	548.0	211.5	581.8	531.9
Ni	4486.0	10021.6	3607.1	11905.6	10611.9
Cu	23.7	50.4	18.2	68.0	51.1
Zn	11.3	152.4	61.1	143.6	111.5
Ga	0.1	0.8	0.3	0.9	0.7

References (Appendix F)

- Abd El-Wahed, M. A. and Kamh, S. Z. (2010) 'Pan-African dextral transpressive duplex and flower structure in the Central Eastern Desert of Egypt', *Gondwana Research*. International Association for Gondwana Research, 18(2–3), pp. 315–336. doi: 10.1016/j.gr.2010.02.007.
- Anders, E. and Grevesse, N. (1989) 'Abundances of the elements: Meteoritic and solar', *Geochimica et Cosmochimica Acta*. Pergamon, 53(1), pp. 197–214. doi: 10.1016/0016-7037(89)90286-X.
- El Bahariya, G. A. (2012) 'Classification and origin of the Neoproterozoic ophiolitic mélanges in the Central Eastern Desert of Egypt', *Tectonophysics*. Elsevier B.V., 568–569, pp. 357–370. doi: 10.1016/j.tecto.2012.03.020.
- Deschamps, F. *et al.* (2013) 'Geochemistry of subduction zone serpentinites: A review', *Lithos*, 178(APRIL), pp. 96–127. doi: 10.1016/j.lithos.2013.05.019.
- Fritz, H. *et al.* (2013) 'Orogen styles in the East African Orogen: A review of the Neoproterozoic to Cambrian tectonic evolution', *Journal of African Earth Sciences*. Elsevier Ltd, 86, pp. 65–106. doi: 10.1016/j.jafrearsci.2013.06.004.
- Gamal El Dien, H. *et al.* (2016) 'Neoproterozoic serpentinites from the Eastern Desert of Egypt: Insights into Neoproterozoic mantle geodynamics and processes beneath the Arabian-Nubian Shield', *Precambrian Research*. Elsevier B.V., 286, pp. 213–233. doi: 10.1016/j.precamres.2016.10.006.
- De Hoog, J. C. M. *et al.* (2009) 'Serpentinised peridotites from an ultrahigh-pressure terrane in the Pohorje Mts. (Eastern Alps, Slovenia): Geochemical constraints on petrogenesis and tectonic setting', *Lithos*. Elsevier B.V., 109(3–4), pp. 209–222. doi: 10.1016/j.lithos.2008.05.006.
- Lee, C.-T. A., Brandon, A. D. and Norman, M. (2003) 'Vanadium in peridotites as a proxy for paleo-fO₂ during partial melting: prospects, limitations, and implications', *Geochimica et Cosmochimica Acta*. Pergamon, 67(16), pp. 3045–3064. doi: 10.1016/S0016-7037(03)00268-0.
- McDonough, W. . and Sun, S. –. (1995) 'The composition of the Earth', *Chemical Geology*, 120, pp. 223–252. doi: doi.org/10.1016/0009-2541(94)00140-4.
- Niu, Y. (2004) 'Bulk-rock major and trace element compositions of abyssal peridotites: Implications for mantle melting, melt extraction and post-melting processes beneath Mid-Ocean ridges', *Journal of Petrology*, 45(12), pp. 2423–2458. doi: 10.1093/petrology/egh068.
- Parkinson, I. J. and Pearce, J. A. (1998) 'Peridotites from the Izu – Bonin – Mariana Forearc (ODP Leg 125): Evidence for Mantle Melting and Melt – Mantle Interaction in a Supra-Subduction Zone Setting', *Journal of Petrology*, 39(9), pp. 1577–1618.
- Pearce, J. A. *et al.* (2000) 'Geochemistry and tectonic significance of peridotites from the South Sandwich arc-basin system, South Atlantic', *Contributions to Mineralogy and Petrology*, 139(1), pp. 36–53. doi: 10.1007/s004100050572.
- Uysal, I. *et al.* (2016) 'Multiple episodes of partial melting, depletion, metasomatism and

enrichment processes recorded in the heterogeneous upper mantle sequence of the Neotethyan Eldivan ophiolite, Turkey’, *Lithos*, 246–247, pp. 228–245. doi: 10.1016/j.lithos.2016.01.004.

Vail, J. R. (1983) ‘Pan-African crustal accretion in north-east Africa’, *Journal of African Earth Sciences* (1983). Pergamon, 1(3–4), pp. 285–294. doi: 10.1016/S0731-7247(83)80013-5.

Workman, R. K. and Hart, S. R. (2005) ‘Major and trace element composition of the depleted MORB mantle (DMM)’, *Earth and Planetary Science Letters*, 231(1–2), pp. 53–72. doi: 10.1016/j.epsl.2004.12.005.

“Every reasonable effort has been made to acknowledge the owners of copyright material. I would be pleased to hear from any copyright owner who has been omitted or incorrectly acknowledged.”

Part 3:

Geochemical records linking mantle plumes, supercontinent cycles, and plate tectonics

Chapter 8:

Global geochemical fingerprinting of plume intensity suggests coupling with the supercontinent cycle

This chapter published as:

[Gamal EL Dien, H., Doucet, L.S., Li, Z.-X., Cox, G., and Mitchell, R., 2019, Global geochemical fingerprinting of plume intensity suggests coupling with the supercontinent cycle: *Nature Communications*, v. 10, p. 5270, doi:10.1038/s41467-019-13300-4.](#)

Abstract

Plate tectonics and mantle plumes are two of the most fundamental solid-Earth processes that have operated through much of Earth history. For the past 300 million years, mantle plumes are known to derive mostly from two large low shear velocity provinces (LLSVPs) above the core-mantle boundary, referred to as the African and Pacific superplumes, but their possible connection with plate tectonics is debated. Here, we demonstrate that transition elements (Ni, Cr, and Fe/Mn) in basaltic rocks can be used to trace plume-related magmatism through Earth history. Our analysis indicates the presence of a direct relationship between the intensity of plume magmatism and the supercontinent cycle, suggesting a possible dynamic coupling between supercontinent and superplume events. In addition, our analysis shows a consistent sudden drop in MgO, Ni and Cr at ~3.2–3.0 billion years ago, possibly indicating an abrupt change in mantle temperature at the start of global plate tectonics.

8.1 Introduction

The plate tectonic theory developed last century works well on Earth's outer shell, but how this system interacts with mantle plumes, and if they are part of the same geodynamic system in Earth history, remains unclear. Seismic studies have revealed that Earth's present-day lower mantle is dominated by two antipodal large low shear velocity provinces (LLSVPs), also known as the African and Pacific superplumes, surrounded by high-velocity zones with subducted cold slabs (Dziewonski, Lekic and Romanowicz, 2010). It has been further shown that almost all known mantle plumes since around 300 million years ago (Ma) were generated atop or near the edges of these two LLSVPs (Burke *et al.*, 2008; Torsvik *et al.*, 2014). On the other hand, the assembly and breakup of supercontinents are controlled by global-scale mantle dynamics and constant feedback between surface and deep mantle processes (Anderson, 1994). It has been further established that the African LLSVP (whether or not in its present geometry) was located underneath the supercontinent Pangaea ca. 300 Ma (Burke and Torsvik, 2004), and that there was a close link between mantle plumes and Pangaea breakup (Courillot *et al.*, 1999). However, how long the LLSVPs have been present, how such LLSVPs interact with tectonic plates in Earth history, and whether they are fixed in the deep mantle (Dziewonski, Lekic and Romanowicz, 2010; Torsvik *et al.*, 2010, 2014) or part of a dynamic system associated with the supercontinent cycle since at least the Proterozoic (Zhong *et al.*, 2007; Li *et al.*, 2008, 2019; Li and Zhong, 2009), remain topics of debate. Tracing mantle plume signatures throughout Earth history is fundamental for answering those questions and testing the stable vs. dynamic/cyclic nature of the LLSVPs, and thus achieving a better understanding of the coupling between Earth's mantle dynamics and plate tectonics.

Basaltic magmatism can be used to probe mantle evolution throughout Earth history (Herzberg, 2011; White, 2015). Such mafic magmatism is mostly generated in three main tectonic settings: mantle plume, mid-ocean ridge, and subduction zone (arc). Geochemical and isotopic characteristics of basalts generated in such settings can identify, or “fingerprint”, the processes and sources of magma generation from different parts of the mantle (White, 2015). Where mid-ocean ridge basalts (MORBs) and arc-related basalts (ARBs) represent melts generated within the sub-oceanic and sub-arc upper mantle, respectively (Pearce and Peate, 1995; Herzberg *et al.*, 2007; Condie, Aster and Van Hunen, 2016; Gamal El Dien *et al.*, 2019), plume basalts, such as oceanic island basalts (OIBs), oceanic flood basalts, and continental large igneous provinces (LIPs) commonly involve deeper mantle processes in which LLSVPs

may provide both additional heat and some melt materials (Condie, 2003; Wang *et al.*, 2013; White, 2015).

Incompatible trace elements, particularly high field strength elements (HFSEs) and their ratios, are widely used to monitor and discriminate between mantle domains and tectonic environments for basaltic magmatism, and to trace plume signatures (Pearce and Peate, 1995; Condie, Aster and Van Hunen, 2016; Condie and Shearer, 2017). However, as HFSEs can be affected by various processes such as source contamination, magma mixing, crust-magma interaction and high-grade metamorphism, the validity of using such an approach to discriminate tectonic settings has been questioned (Pearce, 2008; Condie, 2015). One reason for this is that the low partition coefficients (<1) of HFSEs with Fe-Mg silicate minerals and spinel (White, 2013, 2015)—the main components of basaltic magmatism—make HFSEs easily redistributed by the aforementioned processes. On the other hand, transition elements have partition coefficients with Fe-Mg silicate minerals and spinel >1 , making them highly insensitive to post-formation processes (Leeman and Scheidegger, 1977; Horn *et al.*, 1994; White, 2013). The behavior of the first-row transition elements, especially Ni and Cr (highly compatible) and their ratios to less compatible ones (Co and Zn), is strongly melt-composition dependent (White, 2013, 2015) and highly sensitive to the earliest magmatic differentiation stages (Tang, Chen and Rudnick, 2016). Thus, the abundance of Ni and Cr may track the nature of basaltic magmatism generated from different parts of the mantle.

Here, we demonstrate that Ni and Cr contents constitute an excellent tool for discriminating between plume- and non-plume-related (MORBs and ARBs) magmatism. In addition, by using the statistical bootstrapping method on the global geochemical database of basaltic rocks, we show that the transition elements (Ni, Cr, and Fe/Mn, i.e., plume intensity) exhibit systematic short-term variations that coincide with the supercontinent cycle, which could potentially suggest a dynamic coupling between first-order mantle structure (e.g., LLSVPs) and plate tectonics.

8.2 Methods

8.2.1 Database compilation

We compiled a global database of komatiites (~ 3,000 samples) and picrites (~ 1,650 samples), covering major- and trace elements (particular transition elements such as Ni, Cr,

Co, Zn, Cu, and Sc) from the Georoc (<http://georoc.mpch-mainz.gwdg.de/georoc/>) and EarthChem (<https://www.earthchem.org/>) repositories (Supplementary Data 1). The komatiite and picrite samples in the database have ages ranging from Archean to present-day. We made a manual double-check of data quality against the original references to choose only komatiite (>18 wt% MgO, SiO₂ <52 wt% and total alkali (K₂O+Na₂O) <2 wt%) and picrite (>12 wt% MgO, SiO₂ <52 wt% and total alkali (K₂O+Na₂O) <3 wt%) compositions (Le Bas, 2000; Herzberg *et al.*, 2007; Arndt *et al.*, 2008; Condie *et al.*, 2016) for the plots of Figure G.1. The present-day mid-ocean ridge basalts (MORBs) and arc-related basalts (ARBs), used in Figures 8.1, 8.2 and Figure G.1 and G.2 , are assembled from the same repositories and filtered for samples with basaltic composition (i.e. 45-53 wt % SiO₂ , MgO < 12 wt% and total alkali (K₂O+Na₂O)<5 wt % (Le Bas, 2000; Le Maitre and International Union of Geological Sciences, 2002; Herzberg *et al.*, 2007; Condie *et al.*, 2016) and comprehensive major- and transition elements datasets including Ni, Cr, Co, Zn, Cu and Sc. The present-day MORBs whole rock and glass database (~1,200 samples) includes Atlantic, Pacific, and Indian mid-ocean ridges; the ARBs database (~5,300 samples) includes oceanic-arc basalts such as the Izu-Bonin-Mariana, Tonga, Sunda, Aleutian, Kermadec, New Hebrides, Kurile, and Lesser Antilles arcs, and continental-arc basalts such as that of the Andean, Cascades, and Central American arcs (Supplementary Data 1). The oceanic island basalts, oceanic flood basalts, and large igneous provinces database (~ 6, 200 samples) includes mainly Cenozoic basalts such as the Hawaiian islands, Canary islands, Cape Verde islands, Society islands, St. Helena Chain, Deccan, Afro-Arabia, North Atlantic, Columbia River, Caribbean-Colombian, Hess rise and Manihiki Plateau basalts (Supplementary Data 1).

8.2.2 Data bootstrap resampling

A geochemical database of major and transition elements of basalts (~41,000 samples), with ages ranging from 3.8 Ga to present-day, was extracted from the Georoc and EarthChem repositories (Figures 8.3, 4 and Supplementary Data 2), including age estimates and geospatial sample locations for each sample. Data with unknown age or sample location, suspicious data with major elements totalling more than 100%, and data from ultramafic cumulates or komatiites, have been manually filtered out. The database mainly consists of samples with a basaltic composition (i.e. 45-53 wt % SiO₂ and total alkali (K₂O+Na₂O)<5 wt % (Le Bas, 2000) and age uncertainties below 50% relative standard deviation (RSD). To obtain an optimal

estimate of composition distribution of Ni, Cr and MgO in mantle-derived melts and minimize sampling and preservation bias, we did a weighted bootstrap resampling of the database following the method of Keller and Schoene (2012) using the Matlab MIT open-source code available at <https://github.com/brenhinkeller/StatisticalGeochemistry>.

8.3 Results

8.3.1 Ni and Cr as tracers for mantle plume products

Magnesium content and its ratio to other elements (i.e., Mg/Fe) are commonly used as tracers for the differentiation of silicate rocks and an indicator for mantle temperature (Herzberg *et al.*, 2007; Lee *et al.*, 2009; Condie, Aster and Van Hunen, 2016). Geochemical modelling using MgO content revealed the ambient mantle temperature below the ridges and sub-arc to be ~1350 °C, but typically thermal anomalies of ~200–300 °C over the ambient mantle temperature are expected for mantle plumes (Herzberg *et al.*, 2007; Lee *et al.*, 2009; Herzberg, Condie and Korenaga, 2010; Condie, Aster and Van Hunen, 2016; Keller and Schoene, 2018). As transition elements (i.e., Ni and Cr) behave similarly to Mg during mantle melting, Ni and Cr should also be highly sensitive to mantle temperature, and can thus be used for distinguishing between plume and non-plume mantle melt products. To illustrate this point, we compare the global databases (see methods and Supplementary Data 1) of mantle melts with a range of MgO content and potential mantle temperature of melting (Herzberg *et al.*, 2007) such as komatiites (>18 wt% MgO and T~ 1600 °C), picrites (> 12 wt % MgO and T ~ 1500 °C; from OIBs and LIPs) and normal basalts (< 12 wt % MgO and T ~ 1350 °C; from present-day MORBs and ARBs) (Le Bas, 2000; Herzberg *et al.*, 2007; Arndt *et al.*, 2008; Condie *et al.*, 2016) to their corresponding Ni, Cr, Ni/Co and Cr/Zn contents and ratios respectively (Figure G.1). Strikingly, those transition elements have a positive correlation with MgO content and can, therefore, be used for discriminating komatiites and picrites (representing plume magmatism) from normal basalts (representing non-plume magmatism). Plume magmatism is characterized by Ni > 200 ppm, Cr > 500 ppm, and Ni/Co and Cr/Zn both >8 (Figure G. 1).

To further verify the inferred plume characteristics, we produced covariation plots for Ni and Cr, and Mg# ($100 \cdot \text{MgO} / (\text{MgO} + \text{FeO}_T)$) vs. Ni and Cr of basalt datasets (45 wt% < SiO₂ < 53 wt% and Na₂O+K₂O <5 wt %) (Le Maitre and International Union of Geological

Sciences, 2002) from Cenozoic OIBs and LIPs and present-day MORBs and ARBs (Figure 8.1, Figure G.2 and Supplementary Data 1). Much like komatiites and picrites, 70 % of the plume basalt (PB) datasets have Ni > 150 ppm and Cr > 300 ppm whereas non-plume magmatism (MORBs and ARBs) are mostly below these limits. Thus, we argue that high Ni and Cr contents in basalts implies a plume signature. In addition, consistent with previous studies of some OIBs from the Pacific superplume (Humayun, Qiu and Norman, 2004; Qin and Humayun, 2008), we found that plume basalts (OIBs and LIPs) generally have Fe/Mn > 65, clearly higher than that of MORBs and ARBs (Figure 8.2).

Based on these observations, we use MgO, Cr and Ni contents to filter data from ~41,000 samples (Figure G.3, 4 and Supplementary Data 2) in the global databases (Georoc and EarthChem repositories) in order to trace plume signature throughout Earth history (see methods). The bootstrapped data (see methods) reveal a first-order decrease in MgO, Cr and Ni content in basalts since the Archean eon (Keller and Schoene, 2012, 2018) (Figure 8.3), plus second-order variations within the Proterozoic and the Phanerozoic (Figure 8.4). To further interrogate the second-order variations, we detrended the linear secular decreases in each dataset (Figure 8.4a-c, Figure G.4 and Table G.1).

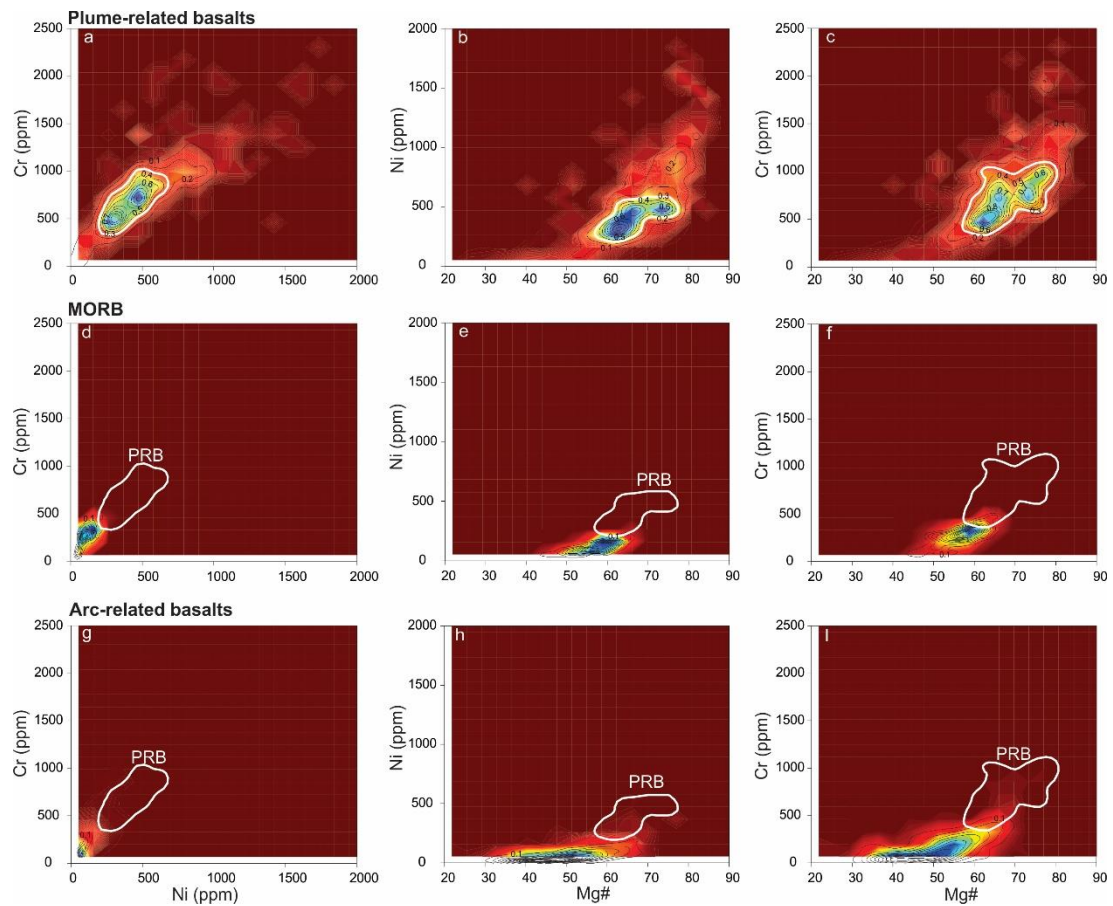


Figure 8.1: Density plot of Ni, Cr, and Mg# for different basaltic magmatism types. Panels a, b and c are density plots of plume-related basalts (PRB) for Ni (ppm) vs. Cr (ppm) and Mg# ($100 \cdot \text{MgO} / (\text{MgO} + \text{FeO})$) vs. Ni (ppm) and Cr (ppm), respectively. Panels d-f are density plots for mid-ocean ridge basalts (MORB) and g-i panels are for arc-related basalts. Data sources: Georoc and EarthChem (see Methods and Supplementary Data 1). Black contours define the data density values from high density (blue) to low density (red). The white contour represents 70% of PRB data.

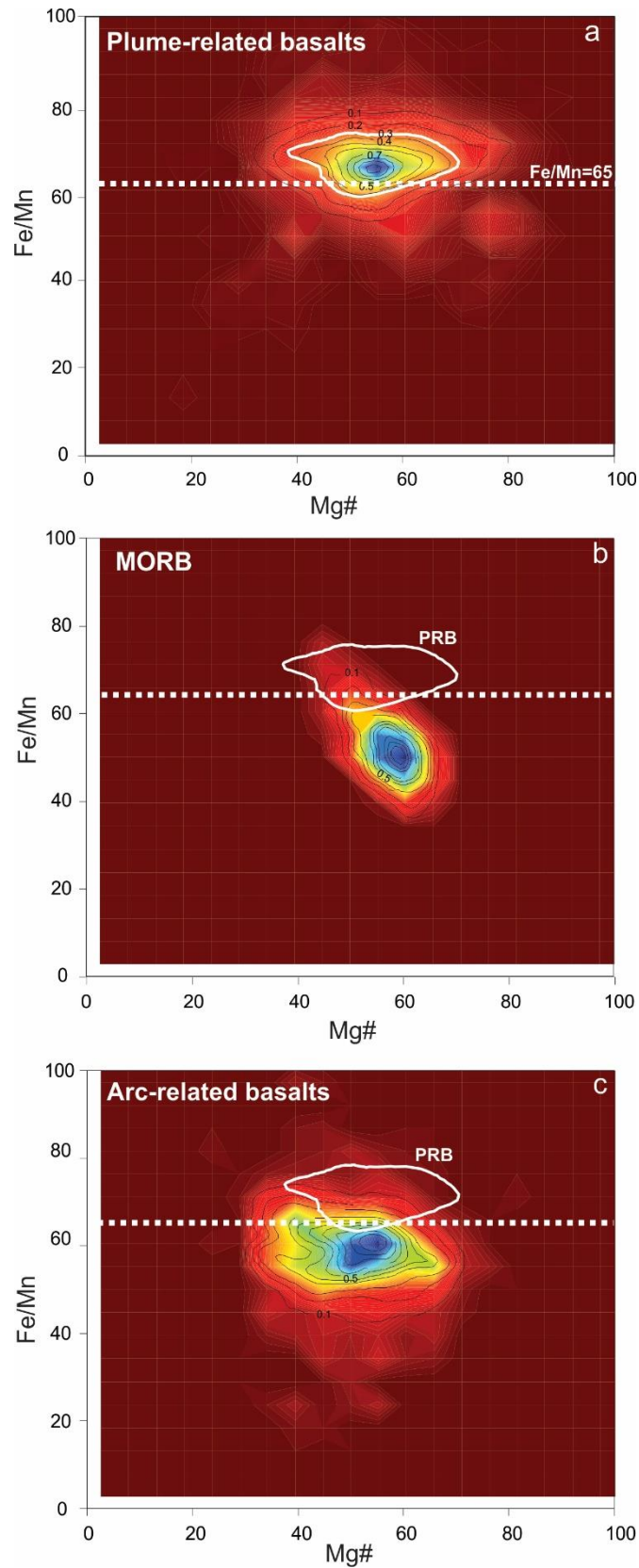


Figure 8.2: Density plot of Fe/Mn vs. Mg# for different basaltic types. (a) Plume-related basalts (PRB); (b) mid-ocean ridge basalts (MORB); (c) arc-related basalts. Data sources: Georoc and EarthChem (see Methods). Black contours define the data density values from high density (blue) to low density (red). The white contour represents 70% of PRB data.

8.4 Discussion

8.4.1 Time variations in mantle plume intensity

The highly compatible transition elements Ni and Cr and their ratios to less compatible ones (e.g., Ni/Co and Cr/Zn), plus Fe/Mn and the previously widely used MgO, are good discriminants for mantle plume magmatism because they all indicate higher mantle melt temperature. As basaltic magmatism represents the direct melt products of Earth's mantle, its composition potentially records Earth's mantle evolution since 4 billion years ago (Ga). Our analysis revealed a first-order decrease in MgO, Ni and Cr since the Archean similar to that shown by Keller and Schoene (2012, 2018) (Figure 8.3a-c), readily explainable by Earth's secular cooling (including the lowering of the mantle potential temperature) (Herzberg, Condie and Korenaga, 2010; Keller and Schoene, 2012, 2018; Condie, Aster and Van Hunen, 2016).

The second-order variability of MgO, Ni and Cr, previously largely ignored (Keller and Schoene, 2012, 2018; Condie, 2018), is more intriguing. The curves consistently show major positive peaks at ~2.8–2.3 Ga, ~1.6–1.3 Ga, ~1.0–0.7 Ga, and ~0.3–0.0 Ga. The most straightforward interpretation of these second-order variations is that they reflect changes in mantle potential temperature/degree of melting (see figure 4 of Keller and Schoene (2018), which may be a consequence of either mantle plumes, or thermal insulation in the upper mantle (Anderson, 2000), or both. Plumes are possibly a more dominant factor because they allow the higher Ni (>150 ppm) and Cr (>300 ppm) contents of the basalts to be sourced from the fertile lower mantle peridotites (i.e., Ni = 2,500 – 3,200 ppm and Cr = 2,600 – 7,500 ppm) (Herzberg *et al.*, 2007, 2013; Ionov and Hofmann, 2007) (Figure 8.1a-c) rather than the depleted upper mantle peridotites (i.e., Ni = 1,960 ppm and Cr = 2,500 ppm) (Salters and Stracke, 2004) (Figure 8.1d-f). This interpretation is supported by their anomalously high Fe/Mn of >65 (Figure 8.2), a well-accepted characteristic of plume basalts (Humayun, Qiu and Norman, 2004; Qin and Humayun, 2008), as well as high abundances of Ni and Cr (Figure 8.1).

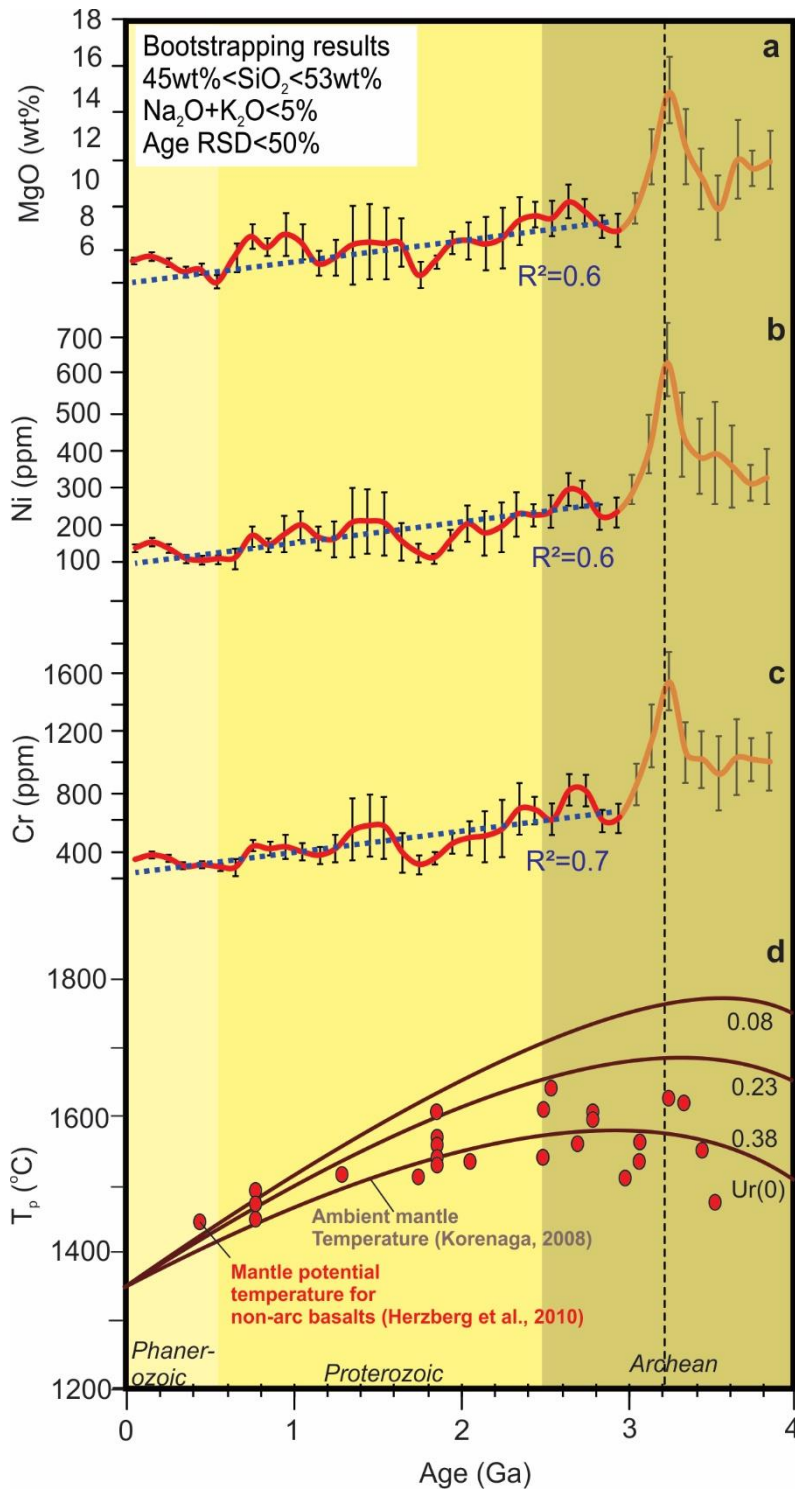


Figure 8.3: Time evolution of global mean MgO, Ni and Cr contents after a bootstrap resampling of the selected basaltic database. The blue dashed lines in a–c are regression lines for data between 0 to 3.0 Ga that reveal first-order secular decreases. Error bars in a–c show 2-s.e.m. (standard error of the mean) uncertainties. (d) Secular cooling of Earth’s mantle based on non-arc basalts (Herzberg, Condie and Korenaga, 2010) and thermal modelling (Korenaga, 2008). Urey ratios (Ur) are shown: 0.08 (upper curve), 0.23 (middle curve) and 0.38 (lower curve).

8.4.2 Implications for mantle dynamics coupled with the supercontinent cycle

Our results show a general temporal consistency between the MgO, Ni and Cr peaks/anomalies (i.e., plume intensity/activities) and the occurrence of known supercontinents, suggesting a clear positive correlation between mantle plume intensity and supercontinent tenure (Figure 8.4). Such results allow us to speculate on the fixed vs. dynamic models for the two LLSVPs in the lower mantle. In the fixed LLSVPs model (Dziewonski, Lekic and Romanowicz, 2010; Torsvik *et al.*, 2010, 2014), the LLSVPs are stable features anchored to the core-mantle boundary (CMB) since early Earth. Their positions and shapes would therefore not have been linked to the subduction girdle and thus to plate motion in general (Zhong *et al.*, 2007; Li *et al.*, 2008, 2019; Li and Zhong, 2009). As such, one would expect the formation of plume basalts to be stochastic in Earth history, implying a semi-uniform occurrence of plume magmatism over geological time, i.e., plume intensity unrelated to the supercontinent cycle. Alternatively, if supercontinents indeed preferentially form on the global subduction girdle (cold downwelling mantle) as suggested by some (e.g., Mitchell *et al.*, 2012), and both the antipodal LLSVPs and the subduction girdle are fixed and long-lived features, then one would expect an anticorrelation between plume intensity and supercontinental tenure (we note that the pre-Cretaceous global plume record is dominated by continental LIPs). In contrast, according to the dynamic LLSVPs model (Zhong *et al.*, 2007; Li and Zhong, 2009), the formation of antipodal LLSVPs is linked to circum-supercontinent subduction that leads to the formation of the subduction girdle; the subduction girdle subsequently divides the hot and dense lower mantle into the two antipodal LLSVPs (Zhong *et al.*, 2007; Li and Zhong, 2009). Such a dynamic LLSVP model therefore predicts an increase in the intensity of plume magmatism during the tenure and breakup stage of the supercontinent cycle, and thus a periodicity positively correlated with the supercontinent cycle.

The global plume intensity record we reported here (Figure 8.4) is inconsistent with either predictions of the fixed LLSVPs model, i.e., it shows neither a semi-uniform time distribution, nor an anticorrelation with the supercontinent tenure. The observed positive correlation between plume intensity and supercontinent cycle cannot be viewed as mere coincidence. In the absence of viable alternative explanations, we suggest the coupled supercontinent-mantle plume records as evidence supporting the dynamic LLSVP model. Indeed, it would be challenging to keep the LLSVPs fixed to the CMB because a constantly evolving subduction geometry changes the deposition of the subducted slabs above the CMB (Tan *et al.*, 2011).

Furthermore, our analysis shows a consistent sudden drop in MgO, Ni, and Cr at ~3.2–3.0 Ga (Figure 8.3a-c), interpreted to indicate an abrupt change in mantle temperature. These results are comparable to the petrological estimation of mantle potential temperature using non-arc basalts (Herzberg, Condie and Korenaga, 2010), as well as Earth’s secular cooling predicted by parameterized convection models (Korenaga, 2008) (Figure 8.3d). We speculate that this interpreted dramatic drop in mantle temperature may indicate the initiation of global plate tectonics, where the subduction-driven whole-mantle convection enhanced the heat flux out of the core and mantle. The sharp peaks at ca. 3.2 Ga (Figure 8.3a-c), also shown in the mantle potential temperature estimations based on non-arc basalts (red dots in Figure 8.3d) (Herzberg, Condie and Korenaga, 2010), possibly reflect a dramatic build-up in mantle temperature before the initiation of plate tectonics, when there was a lack of a mechanism for efficient heat flux out of the mantle. A ~3.2–3.0 Ga emergence of plate tectonics would be broadly consistent with the sedimentary, igneous, metamorphic and palaeomagnetic records (Tang, Chen and Rudnick, 2016; Cawood *et al.*, 2018; Condie, 2018).

To summarise, geochemical tracers for plume basalts (Ni, Cr, and Fe/Mn) indicate the presence of a coupling between global plume intensity and supercontinent cycle. Such results are consistent with the suggested dynamic LLSVP model (Zhong *et al.*, 2007; Li *et al.*, 2008; Li and Zhong, 2009) that links the formation, position and evolution of LLSVPs with that of supercontinents. Recent numerical modelling (Zhang *et al.*, 2010; Simmons *et al.*, 2015; Hassan *et al.*, 2016; Flament *et al.*, 2017), paleomagnetic (Li, Evans and Zhang, 2004; Bono, Tarduno and Bunge, 2019), and seismic (Forte *et al.*, 2010; Koelemeijer, Deuss and Ritsema, 2017) work are also in general agreements with the geodynamic LLSVP model.

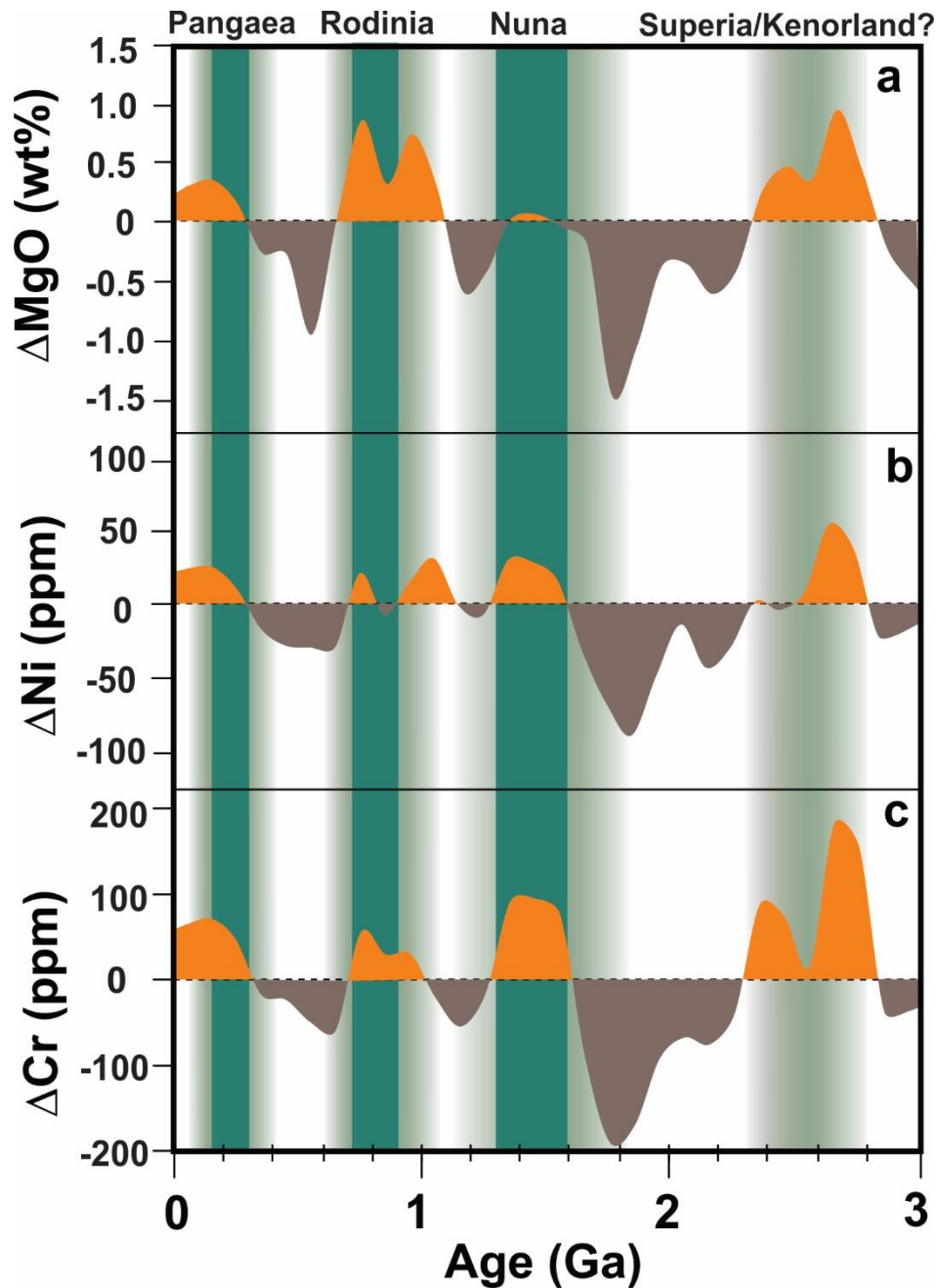


Figure 8.4: Variability of global mean MgO, Ni and Cr in basalts after detrending the linear secular decreases. The linear secular decreases used are those shown with blue dash lines in Figure 8.3. The plot shows major positive peaks at $\sim 2.8\text{--}2.3$ Ga, $\sim 1.6\text{--}1.3$ Ga, $\sim 1.0\text{--}0.7$ Ga, and $\sim 0.3\text{--}0.0$ Ga, broadly consistent with the tenures and break-up times of post-2 Ga supercontinents. The durations of supercontinent tenure (Evans, Li and Murphy, 2016; Pourteau *et al.*, 2018) are marked with solid green vertical bars, e.g., at ca. 320–170 Ma (Pangea), 900–700 Ma (Rodinia), 1600–1300 Ma (Nuna), but the occurrence of Kenorland during 2700–2300 Ma is highly uncertain (thus shown in faded green). The assembly and break-up of supercontinents are generally prolonged and multistage processes, which are marked by gradual green shading.

8.5 References

Anderson, D. L. (1994) 'Superplumes or supercontinents?', *Geology*. GeoScienceWorld, 22(1), p. 39. doi: 10.1130/0091-7613(1994)022<0039:SOS>2.3.CO;2.

Anderson, D. L. (2000) 'The thermal state of the upper mantle; No role for mantle plumes', *Geophysical Research Letters*. Wiley-Blackwell, 27(22), pp. 3623–3626. doi: 10.1029/2000GL011533.

Arndt, N., Leshner, C. M. and Barnes, S. J. (2008) *Komatiite*. Cambridge: Cambridge University Press. doi: 10.1017/CBO9780511535550.

LE BAS, M. J. (2000) 'IUGS Reclassification of the High-Mg and Picritic Volcanic Rocks', *Journal of Petrology*. Oxford University Press, 41(10), pp. 1467–1470. doi: 10.1093/petrology/41.10.1467.

Bono, R. K., Tarduno, J. A. and Bunge, H.-P. (2019) 'Hotspot motion caused the Hawaiian-Emperor Bend and LLSVPs are not fixed', *Nature Communications*. Nature Publishing Group, 10(1), p. 3370. doi: 10.1038/s41467-019-11314-6.

Burke, K. *et al.* (2008) 'Plume Generation Zones at the margins of Large Low Shear Velocity Provinces on the core-mantle boundary', *Earth and Planetary Science Letters*, 265(1–2), pp. 49–60. doi: 10.1016/j.epsl.2007.09.042.

Burke, K. and Torsvik, T. H. (2004) 'Derivation of Large Igneous Provinces of the past 200 million years from long-term heterogeneities in the deep mantle', *Earth and Planetary Science Letters*, 227(3–4), pp. 531–538. doi: 10.1016/j.epsl.2004.09.015.

Cawood, P. A. *et al.* (2018) 'Geological archive of the onset of plate tectonics', *Philosophical Transactions of the Royal Society A: Mathematical, Physical and Engineering Sciences*, 376(2132), p. 20170405. doi: 10.1098/rsta.2017.0405.

Condie, K. (2015) 'Changing tectonic settings through time: Indiscriminate use of geochemical discriminant diagrams', *Precambrian Research*. Elsevier B.V., 266, pp. 587–591. doi: 10.1016/j.precamres.2015.05.004.

Condie, K. C. (2003) 'Incompatible element ratios in oceanic basalts and komatiites: Tracking deep mantle sources and continental growth rates with time', *Geochemistry, Geophysics, Geosystems*, 4(1), pp. 1–28. doi: 10.1029/2002GC000333.

Condie, K. C. (2018) 'A planet in transition: The onset of plate tectonics on Earth between 3 and 2 Ga?', *Geoscience Frontiers*, 9(1), pp. 51–60. doi: 10.1016/j.gsf.2016.09.001.

Condie, K. C., Aster, R. C. and Van Hunen, J. (2016) 'A great thermal divergence in the mantle beginning 2.5 Ga: Geochemical constraints from greenstone basalts and komatiites', *Geoscience Frontiers*. Elsevier Ltd, 7(4), pp. 543–553. doi: 10.1016/j.gsf.2016.01.006.

Condie, K. C. and Shearer, C. K. (2017) 'Tracking the evolution of mantle sources with incompatible element ratios in stagnant-lid and plate-tectonic planets', *Geochimica et Cosmochimica Acta*. Elsevier Ltd, 213, pp. 47–62. doi: 10.1016/j.gca.2017.06.034.

Courtillot, V. *et al.* (1999) 'On causal links between flood basalts and continental breakup', *Earth and Planetary Science Letters*, 166(3–4), pp. 177–195. doi: 10.1016/S0012-821X(98)00282-9.

Dziewonski, A. M., Lekic, V. and Romanowicz, B. A. (2010) 'Mantle Anchor Structure: An argument for bottom up tectonics', *Earth and Planetary Science Letters*. Elsevier B.V., 299(1–2), pp. 69–79. doi: 10.1016/j.epsl.2010.08.013.

Evans, D. A. D., Li, Z. X. and Murphy, J. B. (2016) 'Four-dimensional context of Earth's supercontinents', in Li, Z., Evans, David A.D., and Murphy, J. B. (eds) *Geological Society Special Publication*. Geological Society of London, pp. 1–14. doi: 10.1144/SP424.12.

Flament, N. *et al.* (2017) 'Origin and evolution of the deep thermochemical structure beneath Eurasia', *Nature Communications*. Nature Publishing Group, 8(1), p. 14164. doi: 10.1038/ncomms14164.

Forte, A. M. *et al.* (2010) 'Joint seismic–geodynamic–mineral physical modelling of African geodynamics: A reconciliation of deep-mantle convection with surface geophysical constraints', *Earth and Planetary Science Letters*. Elsevier, 295(3–4), pp. 329–341. doi: 10.1016/J.EPSL.2010.03.017.

Gamal El Dien, H. *et al.* (2019) 'Origin of arc magmatic signature: A temperature-dependent process for trace element (re)-mobilization in subduction zones', *Scientific Reports*, 9(1), p. 7098. doi: 10.1038/s41598-019-43605-9.

Hassan, R. *et al.* (2016) 'A rapid burst in hotspot motion through the interaction of tectonics and deep mantle flow', *Nature*. Nature Publishing Group, 533(7602), pp. 239–242. doi: 10.1038/nature17422.

Herzberg, C. *et al.* (2007) 'Temperatures in ambient mantle and plumes: Constraints from basalts, picrites, and komatiites', *Geochemistry, Geophysics, Geosystems*, 8(2). doi: 10.1029/2006GC001390.

Herzberg, C. (2011) 'Basalts as temperature probes of Earth's mantle', *Geology*, 39(12), pp. 1179–1180. doi: 10.1130/focus122011.1.

Herzberg, C. *et al.* (2013) 'Nickel and helium evidence for melt above the core-mantle boundary', *Nature*. Nature Publishing Group, 493(7432), pp. 393–397. doi: 10.1038/nature11771.

Herzberg, C., Condie, K. and Korenaga, J. (2010) 'Thermal history of the Earth and its petrological expression', *Earth and Planetary Science Letters*. Elsevier B.V., 292(1–2), pp. 79–88. doi: 10.1016/j.epsl.2010.01.022.

Horn, I. *et al.* (1994) 'Experimentally determined partitioning of high field strength-and selected transition elements between spinel and basaltic melt', *Chemical Geology*, 117(2), pp. 193–218.

Humayun, M., Qiu, L. and Norman, M. D. (2004) 'Geochemical evidence for excess iron in the Hawaiian mantle: Implications for mantle dynamics', *Science (New York, N.Y.)*, 306(October), pp. 91–94.

Ionov, D. A. and Hofmann, A. W. (2007) 'Depth of formation of subcontinental off-craton peridotites'. doi: 10.1016/j.epsl.2007.07.036.

Keller, B. and Schoene, B. (2018) 'Plate tectonics and continental basaltic geochemistry throughout Earth history', *Earth and Planetary Science Letters*. Elsevier B.V., 481, pp. 290–304. doi: 10.1016/j.epsl.2017.10.031.

Keller, C. B. and Schoene, B. (2012) 'Statistical geochemistry reveals disruption in secular lithospheric evolution about 2.5Gyr ago', *Nature*. Nature Publishing Group, 485(7399), pp. 490–493.

doi: 10.1038/nature11024.

Koelemeijer, P., Deuss, A. and Ritsema, J. (2017) 'Density structure of Earth's lowermost mantle from Stoneley mode splitting observations', *Nature Communications*. Nature Publishing Group, 8(1), p. 15241. doi: 10.1038/ncomms15241.

Korenaga, J. (2008) 'Urey Ratio and the Structure and Evolution of Earth ' S Mantle', *American Geophysical Union*, (2007), pp. 1–32. doi: 10.1029/2007RG000241.1.

Lee, C.-T. A. *et al.* (2009) 'Constraints on the depths and temperatures of basaltic magma generation on Earth and other terrestrial planets using new thermobarometers for mafic magmas', *Earth and Planetary Science Letters*, 279, pp. 20–33. doi: 10.1016/j.epsl.2008.12.020.

Leeman, W. P. and Scheidegger, K. . (1977) 'OLIVINE/LIQUID DISTRIBUTION COEFFICIENTS AND A TEST FOR CRYSTAL-LIQUID EQUILIBRIUM', *Earth and Planetary Science Letters*, 35, pp. 247–257.

Li, Z. X. *et al.* (2008) 'Assembly, configuration, and break-up history of Rodinia: A synthesis', *Precambrian Research*, 160(1–2), pp. 179–210. doi: 10.1016/j.precamres.2007.04.021.

Li, Z. X. *et al.* (2019) 'Decoding Earth's rhythms: Modulation of supercontinent cycles by longer superocean episodes', *Precambrian Research*. Elsevier, 323, pp. 1–5. doi: 10.1016/J.PRECAMRES.2019.01.009.

Li, Z. X., Evans, D. A. D. and Zhang, S. (2004) 'A 90° spin on Rodinia: Possible causal links between the Neoproterozoic supercontinent, superplume, true polar wander and low-latitude glaciation', *Earth and Planetary Science Letters*, 220(3–4), pp. 409–421. doi: 10.1016/S0012-821X(04)00064-0.

Li, Z. X. and Zhong, S. (2009) 'Supercontinent-superplume coupling, true polar wander and plume mobility: Plate dominance in whole-mantle tectonics', *Physics of the Earth and Planetary Interiors*, 176(3–4), pp. 143–156. doi: 10.1016/j.pepi.2009.05.004.

Le Maitre, R. W. (Roger W. and International Union of Geological Sciences. Subcommittee on the Systematics of Igneous Rocks. (2002) *Igneous rocks : a classification and glossary of terms : recommendations of the International Union of Geological Sciences, Subcommittee on the Systematics of Igneous Rocks*. Cambridge University Press.

Mitchell, R. N., Kilian, T. M. and Evans, D. A. D. (2012) 'Supercontinent cycles and the calculation of absolute palaeolongitude in deep time', *Nature*. Nature Publishing Group, 482(7384), pp. 208–211. doi: 10.1038/nature10800.

Pearce, J. A. (2008) 'Geochemical fingerprinting of oceanic basalts with applications to ophiolite classification and the search for Archean oceanic crust', *Lithos*, 100(1–4), pp. 14–48. doi: 10.1016/j.lithos.2007.06.016.

Pearce, J. A. and Peate, D. . (1995) 'Tectonic Implications of Volcanic Arc Magmas', *Annu. Rev. Earth Planet. Sci.*, 23, pp. 251–285.

Pourteau, A. *et al.* (2018) '1.6 Ga crustal thickening along the final Nuna suture', *Geological Society of America | GEOLOGY*, 46(11). doi: 10.1130/G45198.1.

Qin, L. and Humayun, M. (2008) 'The Fe/Mn ratio in MORB and OIB determined by ICP-MS', *Geochimica et Cosmochimica Acta*. Elsevier Ltd, 72(6), pp. 1660–1677. doi:

10.1016/j.gca.2008.01.012.

Salters, V. J. M. and Stracke, A. (2004) 'Composition of the depleted mantle', *Geochemistry, Geophysics, Geosystems*. John Wiley & Sons, Ltd, 5(5), p. n/a-n/a. doi: 10.1029/2003GC000597.

Simmons, N. A. *et al.* (2015) 'Evidence for long-lived subduction of an ancient tectonic plate beneath the southern Indian Ocean', *Geophysical Research Letters*. John Wiley & Sons, Ltd, 42(21), pp. 9270–9278. doi: 10.1002/2015GL066237.

Tan, E. *et al.* (2011) 'On the location of plumes and lateral movement of thermochemical structures with high bulk modulus in the 3-D compressible mantle', *Geochemistry, Geophysics, Geosystems*. Wiley-Blackwell, 12(7), p. n/a-n/a. doi: 10.1029/2011GC003665.

Tang, M., Chen, K. and Rudnick, R. L. (2016) 'Archean upper crust transition from mafic to felsic marks the onset of plate tectonics', *Science*, 351(6271), pp. 372–375. doi: 10.1126/science.aad5513.

Torsvik, T. H. *et al.* (2010) 'Diamonds sampled by plumes from the core-mantle boundary', *Nature*. Nature Publishing Group, 466(7304), pp. 352–355. doi: 10.1038/nature09216.

Torsvik, T. H. *et al.* (2014) 'Deep mantle structure as a reference frame for movements in and on the Earth', *Proceedings of the National Academy of Sciences*, 111(24), pp. 8735–8740. doi: 10.1073/pnas.1318135111.

Wang, X.-C. *et al.* (2013) 'Identification of an ancient mantle reservoir and young recycled materials in the source region of a young mantle plume: Implications for potential linkages between plume and plate tectonics', *Earth and Planetary Science Letters*. Elsevier, 377–378, pp. 248–259. doi: 10.1016/J.EPSL.2013.07.003.

White, W. (2015) 'Probing the Earth's Deep Interior Through Geochemistry', *Geochemical Perspectives*, 4(2), pp. 95–251. doi: 10.7185/geochempersp.4.2.

White, W. M. (2013) 'Trace Elements in Igneous Processes', in *Geochemistry*. Wiley-Blackwell, pp. 259–313. Available at: <https://www.imwa.info/geochemistry/Chapters/Chapter07.pdf> (Accessed: 1 October 2018).

Zhang, N. *et al.* (2010) 'A model for the evolution of the Earth's mantle structure since the Early Paleozoic', *Journal of Geophysical Research*, 115(B6), p. B06401. doi: 10.1029/2009JB006896.

Zhong, S. *et al.* (2007) 'Supercontinent cycles, true polar wander, and very long-wavelength mantle convection', *Earth and Planetary Science Letters*, 261(3–4), pp. 551–564. doi: 10.1016/j.epsl.2007.07.049.

"Every reasonable effort has been made to acknowledge the owners of copyright material. I would be pleased to hear from any copyright owner who has been omitted or incorrectly acknowledged."

Appendix G:
Supplementary materials to Chapter 8

Supplementary Data Tables related to this chapter can be found [here](#).

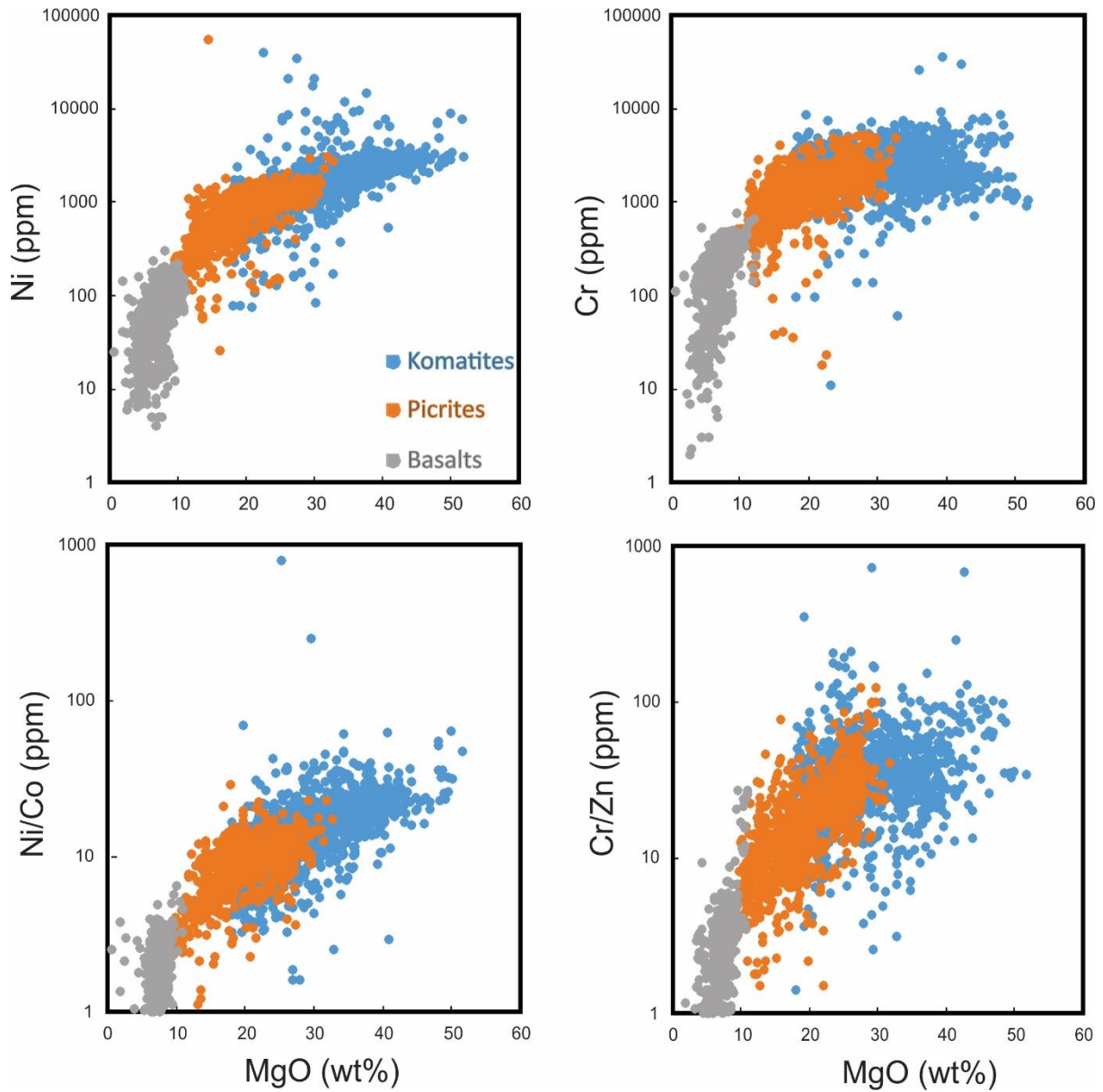


Figure G.1: Covariation of MgO vs Ni, Cr, Ni/Co and Cr/Zn for different mantle magmatic products (komatiites, picrites and basalts). Data source: Georoc and EarthChem.

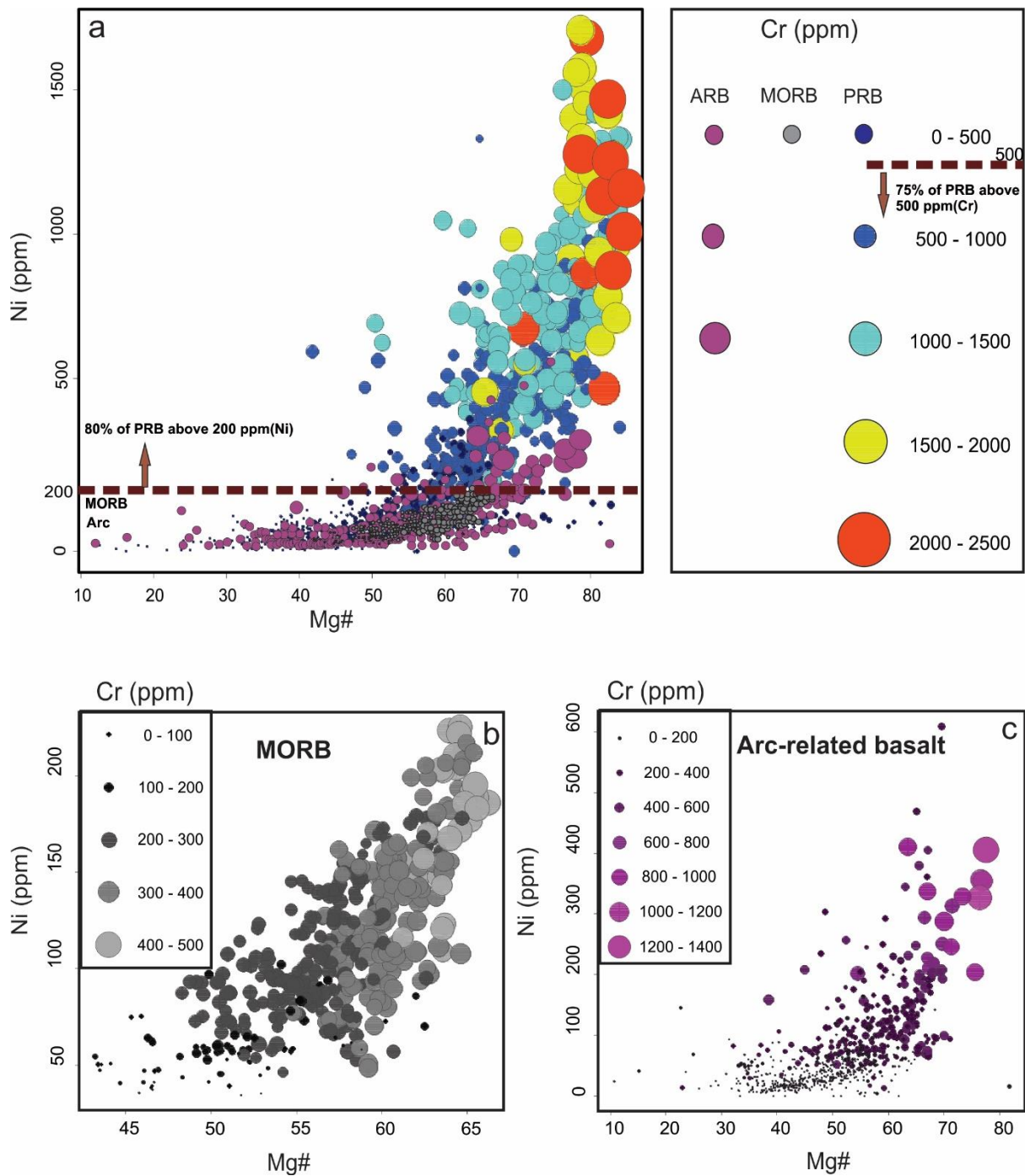


Figure G.2: Covariation plots of Mg# ($100 \cdot \text{MgO} / (\text{MgO} + \text{FeO})$) vs. Ni with the size of the symbol proportional to Cr content in each samples for plume-related basalts (PRB) (a), mid-ocean ridge basalts (MORB) (b) and arc-related basalts (c). Data sources: Georoc and EarthChem.

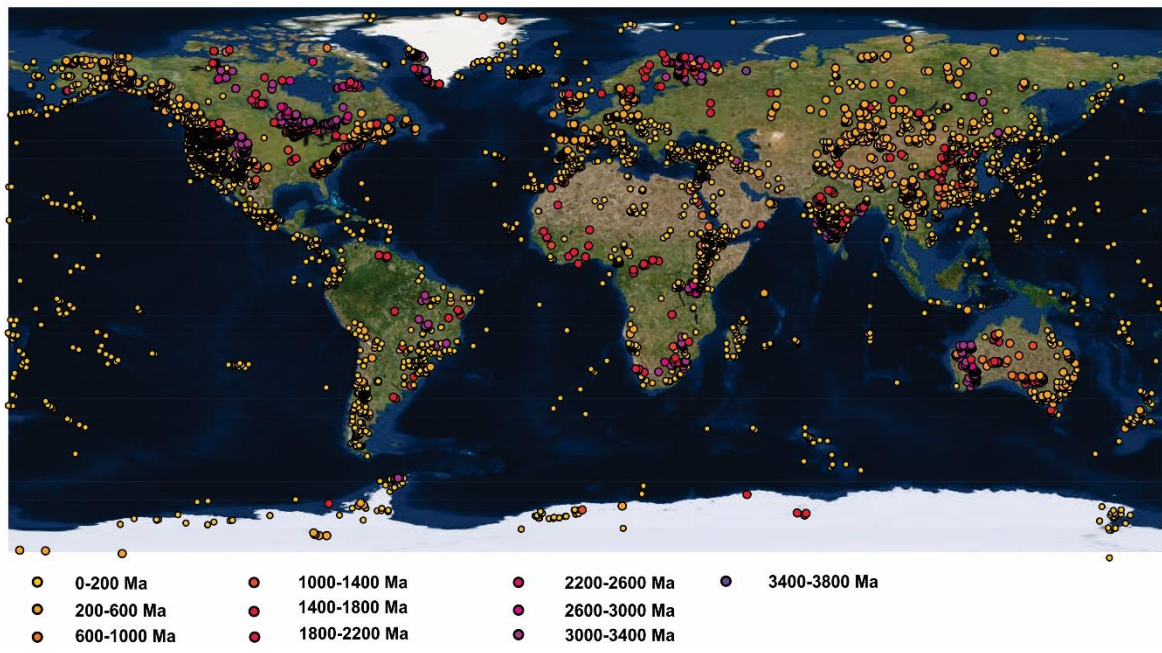


Figure G.3: Geographic distribution map of basaltic datasets used for bootstrap resampling and the plots in Figures 3a-c and 4. The basaltic datasets have an age range of 3.8 to 0 Ga, sourced from the Georoc and EarthChem community data repositories.

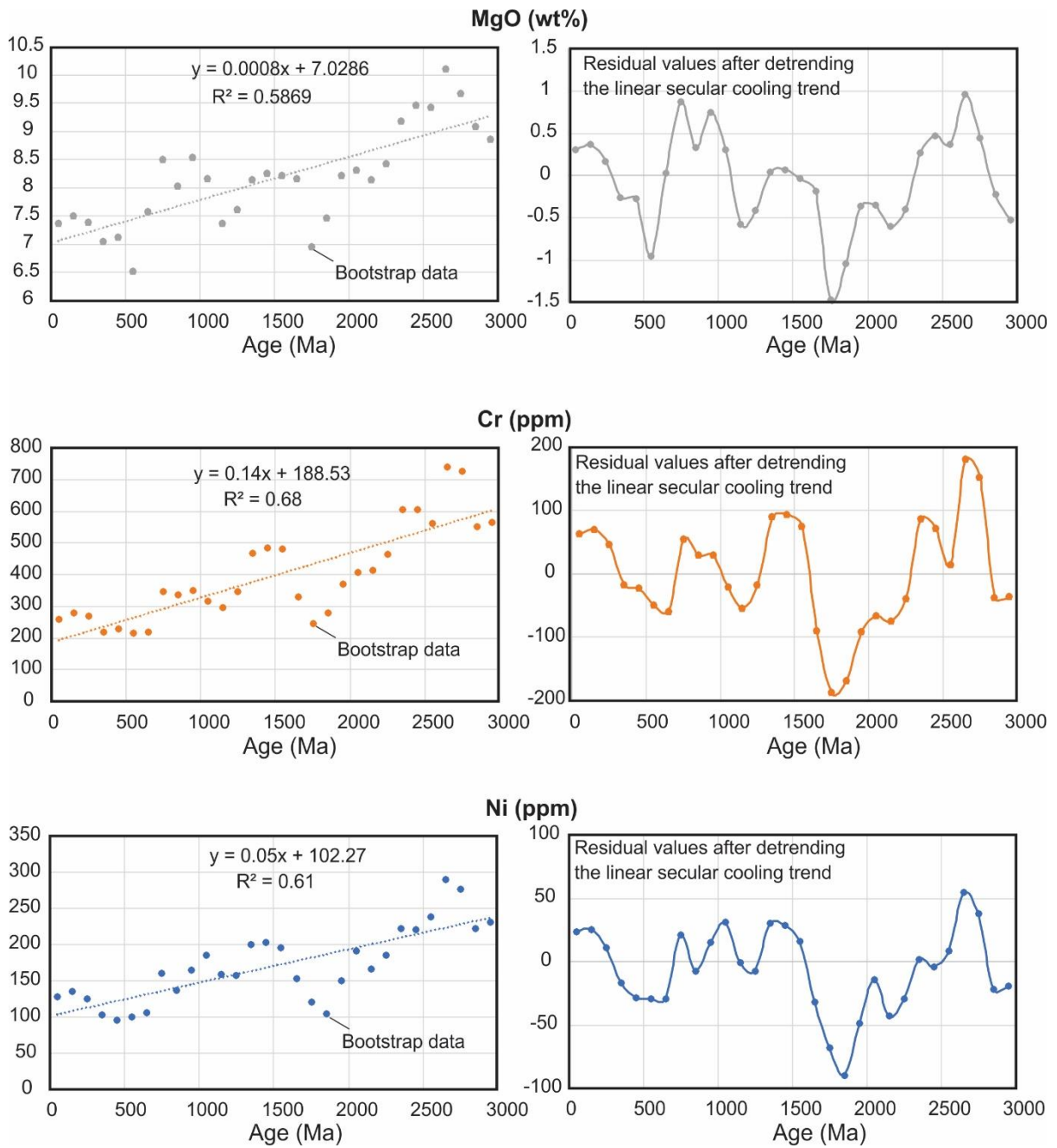


Figure G.4: Variability of global mean of bootstrap data of MgO, Cr and Ni in basalts from the global database (left hand plots), and plots of the same dataset after detrending the linear secular decreases (dashed lines) (right hand plots).

Table G.1: The average bootstrapped values used to create Figures 8.3 and 8.4 and the normalized values to the secular decrease.

Age	Ni (ppm)	Cr (ppm)	MgO (wt.%)	Ni secular	Ni subtract	Cr secular	Cr subtract	MgO secular	MgO subtract
50	128.868	259.382	7.37601	104.77	24.098	195.83	63.552	7.07	0.30601
150	135.395	280.1	7.51192	109.77	25.625	209.83	70.27	7.15	0.36192
250	125.809	269.702	7.39924	114.77	11.039	223.83	45.872	7.23	0.16924
350	102.895	220.686	7.05096	119.77	-16.875	237.83	-17.144	7.31	-0.25904
450	96.6094	228.531	7.11686	124.77	-28.1606	251.83	-23.299	7.39	-0.27314
550	100.338	216.341	6.52004	129.77	-29.432	265.83	-49.489	7.47	-0.94996
650	105.476	220.801	7.58095	134.77	-29.294	279.83	-59.029	7.55	0.03095
750	161.004	347.986	8.49647	139.77	21.234	293.83	54.156	7.63	0.86647
850	137.524	336.766	8.03617	144.77	-7.246	307.83	28.936	7.71	0.32617
950	164.648	351.43	8.53782	149.77	14.878	321.83	29.6	7.79	0.74782
1050	186.009	314.992	8.17058	154.77	31.239	335.83	-20.838	7.87	0.30058
1150	158.908	295.723	7.37644	159.77	-0.862	349.83	-54.107	7.95	-0.57356
1250	157.666	346.648	7.61674	164.77	-7.104	363.83	-17.182	8.03	-0.41326
1350	199.933	467.83	8.1537	169.77	30.163	377.83	90	8.11	0.0437
1450	203.584	485.196	8.25727	174.77	28.814	391.83	93.366	8.19	0.06727
1550	196.282	480.751	8.22847	179.77	16.512	405.83	74.921	8.27	-0.04153
1650	152.822	330.395	8.16305	184.77	-31.948	419.83	-89.435	8.35	-0.18695
1750	121.504	245.873	6.96043	189.77	-68.266	433.83	-187.957	8.43	-1.46957
1850	105.403	279.864	7.46371	194.77	-89.367	447.83	-167.966	8.51	-1.04629
1950	150.906	370.832	8.22228	199.77	-48.864	461.83	-90.998	8.59	-0.36772
2050	191.028	408.983	8.31674	204.77	-13.742	475.83	-66.847	8.67	-0.35326
2150	166.766	414.954	8.14365	209.77	-43.004	489.83	-74.876	8.75	-0.60635
2250	185.205	464.542	8.4351	214.77	-29.565	503.83	-39.288	8.83	-0.3949
2350	221.733	603.983	9.17702	219.77	1.963	517.83	86.153	8.91	0.26702
2450	220.962	604.084	9.46374	224.77	-3.808	531.83	72.254	8.99	0.47374
2550	237.968	560.8	9.43902	229.77	8.198	545.83	14.97	9.07	0.36902
2650	289.505	740.433	10.1045	234.77	54.735	559.83	180.603	9.15	0.9545
2750	277.392	725.925	9.67061	239.77	37.622	573.83	152.095	9.23	0.44061
2850	222.943	550.612	9.08734	244.77	-21.827	587.83	-37.218	9.31	-0.22266
2950	230.905	565.4	8.86807	249.77	-18.865	601.83	-36.43	9.39	-0.52193
3050	288.32	775.972	9.78203						

3150	392.479	1055.14	11.6683
3250	590.063	1390.2	14.2681
3350	417.756	958.609	12.1733
3450	367.437	921.68	10.9689
3550	375.708	835.83	9.78972
3650	346.972	949.448	11.7559
3750	305.528	945.795	11.4923
3850	314.816	922.046	11.7328
Average >3Ga	378	973	12
Average <3Ga	171	400	8

Chapter 9:

Geochemical evidence for a widespread mantle re-enrichment 3.2 billion years ago: implications for global-scale plate tectonics

This chapter published as:

[Gamal EL Dien, H., Doucet, L.S., Murphy, J.B., and Li, Z-X., 2020, Geochemical evidence for a widespread mantle re-enrichment 3.2 billion years ago : implications for global-scale plate tectonics: *Scientific Reports*, p. 1–7, doi:10.1038/s41598-020-66324-y](#)

Abstract

Progressive mantle melting during the Earth's earliest evolution led to the formation of a depleted mantle and a continental crust enriched in highly incompatible elements. Re-enrichment of Earth's mantle can occur when continental crustal materials begin to founder into the mantle by either subduction or, to a lesser degree, by delamination processes, profoundly affecting the mantle's trace element and volatile compositions. Deciphering when mantle re-enrichment/refertilization became a global-scale process would reveal the onset of efficient mass transfer of crust to the mantle and potentially when plate tectonic processes became operative on a global-scale. Here we document the onset of mantle re-enrichment/refertilization by comparing the abundances of petrogenetically significant isotopic values and key ratios of highly incompatible elements compared to lithophile elements in Archean to Early-Proterozoic mantle-derived melts (i.e., basalts and komatiites). Basalts and komatiites both record a rapid-change in mantle chemistry around 3.2 billion years ago (Ga) signifying a fundamental change in Earth geodynamics. This rapid-change is recorded in Nd isotopes and in key trace element ratios that reflect a fundamental shift in the balance between fluid-mobile and incompatible elements (i.e., Ba/La, Ba/Nb, U/Nb, Pb/Nd and Pb/Ce) in basaltic and komatiitic rocks. These geochemical

proxies display a significant increase in magnitude and variability after ~3.2 Ga. We hypothesize that rapid increases in mantle heterogeneity indicate the recycling of supracrustal materials back into Earth's mantle via subduction. Our new observations thus point to a ≥ 3.2 Ga onset of global subduction processes via plate tectonics.

9.1 Introduction

Although plate tectonics is now well accepted as the paradigm for Earth's evolution in the Phanerozoic eon, the question of when these processes began is still controversial (Korenaga, 2013). Estimates are based mainly on crustal observations, and range from early Archean to the late Neoproterozoic (Korenaga, 2013). Resolution of this debate is fundamental to our understanding of the evolution of Earth systems. A key process of plate tectonics is widespread subduction (Clift and Vannucchi, 2004; Sobolev and Brown, 2019). Subduction zones recycle terrestrial materials back into Earth's mantle as the subducting slab sinks and re-equilibrates within Earth's interior (Stern, 2002; Clift and Vannucchi, 2004; Willbold and Stracke, 2010). Fluids and magmas released from sediments and crustal materials in the vicinity of the subducting slab facilitate melting of the upper mantle wedge creating arc basalts with specific trace element signatures (such as elevated large ion lithophile elements (LILE): Ba, Pb, U, Sr, As, B, and Cs) (Poli and Schmidt, 2002; Gamal El Dien, Li, *et al.*, 2019) that reflect enrichment of the sub-arc mantle source (compared to mid-ocean ridge basalts (Kessel *et al.*, 2005; Hofmann, 2013). Some of these recycled terrestrial materials also invade the deeper mantle (Patchett *et al.*, 1982), causing enrichment of the deep mantle in LILE and light rare earth elements (LREE) and promoting a geochemical and isotopic heterogeneity that characterizes basalts derived from mantle plumes (White and Hofmann, 1982; Hofmann, 1997, 2013; Mazza *et al.*, 2019). It is commonly believed that before the plate tectonics regime, a chemically stratified Earth had a relatively homogeneous mantle composition (Condie, 2018; Moyen and Laurent, 2018) (due to the lack of large/global-scale recycling of terrestrial materials into the upper and lower mantle) that was depleted in highly incompatible elements (e.g. Ba, Pb, Rb, Cs, Sr, and U) but enriched in high field strength elements (e.g. Nb and Ta) (Hofmann, 1988). So, a globally- detectable large change in the mantle heterogeneity

(Hofmann, 1997, 2013; Bennett, 2003), caused by a refertilization/re-enrichment in incompatible and fluid mobile elements, and a step-change in Nd isotope systematics of the upper and lower mantle-derived materials, could identify the onset of global-scale subduction and plate tectonic processes. Thus, tracking the isotopic and chemical heterogeneities of the Earth's upper and lower mantle through the Archean and Early Proterozoic may provide a new way of identifying when plate tectonics started.

9.2 Geochemical tracer for crustal recycling

Most previous estimates of when plate tectonics commenced were based on proxies recorded in continental crustal rocks (Dhuime *et al.*, 2012; Naeraa *et al.*, 2012; Nagel, Hoffmann and Münker, 2012; Tang, Chen and Rudnick, 2016; Reimink *et al.*, 2019) which are only indirectly related to mantle processes, and may intrinsically have a preservation bias and/or reflect regional rather than global processes (Furnes *et al.*, 2007; Shirey and Richardson, 2011; Naeraa *et al.*, 2012; Komiya *et al.*, 2014; Turner *et al.*, 2014; Blichert-Toft *et al.*, 2015a; Kaczmarek *et al.*, 2016; Sobolev *et al.*, 2019). In order to identify when widespread global-scale mantle refertilization/re-enrichment occurred, we investigate the composition of the mantle directly by examining the global database of Archean-Early Proterozoic mafic-ultramafic rocks focusing on their Sm-Nd isotopic systematics and on petrogenetically-sensitive trace element ratios.

Samarium and Neodymium have very similar chemical behaviour (i.e., similar ionic radii and the same valency). As the Sm/Nd ratio is robust to the effects of alteration and metamorphism and is not significantly affected by crystal fractionation, this ratio typically reflects source composition (DePaolo and Wasserburg, 1976; White and Hofmann, 1982; Murphy and Nance, 2002; Chauvel *et al.*, 2008). As the depleted mantle reservoir retains Sm over Nd, its Sm/Nd ratio (~ 0.5) is greater than the bulk earth chondritic (~ 0.32) and typical continental crust (~ 0.2) values (DePaolo and Wasserburg, 1976; Murphy and Nance, 2002). Thus, ^{147}Sm to ^{143}Nd decay over geological time would yield a significantly higher $^{143}\text{Nd}/^{144}\text{Nd}$ ratio in magmas derived from depleted mantle compared to contemporary magmas derived from a crustal reservoir (Murphy and Nance, 2002). As magmas passively acquire the $^{143}\text{Nd}/^{144}\text{Nd}$ initial ratio of their source (Murphy and Nance, 2002), differences in ϵ_{Nd} (the relative deviation of the $^{143}\text{Nd}/^{144}\text{Nd}$ initial ratio from the chondritic value, $\epsilon_{\text{Nd}} =$

0) in mafic/ultramafic rocks constrain the evolution of the mantle source. Over geological time, the depleted mantle isotopically evolves toward more positive ϵ_{Nd} values but the crust evolves towards negative values (DePaolo and Wasserburg, 1976; Murphy and Nance, 2002). Thus, shifting of ϵ_{Nd} of mafic-ultramafic rocks to less positive values identifies when a significant contribution of terrestrial materials to the mantle source occurred (White and Hofmann, 1982; Hofmann, 1997; Murphy and Nance, 2002; Chauvel *et al.*, 2008).

In addition, the ratios of incompatible fluid-mobile elements (FMEs: Ba, Pb, Rb, Sr, and U) to relatively immobile elements such as high field strength elements (HFSEs: Nb and Ta) and rare earth elements (REE) are excellent tracers for the invasion of fluids and magmas derived from the recycling of sediments (such as Ba/La and Ba/Nb) (Plank and Langmuir, 1993; Kelley and Cottrell, 2009; Nielsen *et al.*, 2018) and of continental crust materials (such as U/Nb) (Hofmann, 1997, 2013) into mantle sources (Miller, Goldstein and Langmuir, 1994; Kessel *et al.*, 2005). FMEs are transferred to the crust during subduction dehydration and arc magmatism (Gamal El Dien, Arai, *et al.*, 2019; Gamal El Dien, Li, *et al.*, 2019), but HFSEs are retained in the mantle source by minerals such as amphibole and rutile (Keppler, 1996). Such trace element pairs/ratios, with similar incompatibility but with very distinct chemical behaviours, are particularly useful because they are insensitive to alteration/metamorphism, and are less fractionated during partial melting (Hofmann, 1997, 2013; Condie, 2018). Thus, tracking ratios such as Ba/La, Ba/Nb, U/Nb, Pb/Nd and Pb/Ce in addition to Nd isotopes in mafic and ultramafic magmatic products during the Archean and Proterozoic eons could precisely identify the time when heterogeneities in their respective upper and lower mantle sources originated, as well as source chemistry differences and the change of mantle trace element budget.

9.3 Methods

We compiled a database of basaltic rocks ($n = 3,127$) and komatiites ($n = 2,740$) for major and trace elements (including rare earth elements) mainly using the Georoc repository (Supplementary Data 1, 2). We cross-checked every sample with their original reference to verify its magmatic age and location (continent, craton and formation). Samples with no age constraints were excluded. All the selected samples

have age estimates and age error less than ± 100 Myr, sample ID and geospatial sample locations. The basaltic and komatiitic rocks in the selected database range in age of 3.8–2.4 Ga and 3.8–2.0 Ga, respectively. The basaltic rock database is composed mainly of basalts and basaltic andesites with 40–55 wt % SiO₂, MgO < 12 wt% and total alkali (K₂O+Na₂O) < 5 wt %. To obtain an optimal distribution estimate of trace element ratios for mantle-derived melts (basalts and komatiites) and minimize sampling and preservation bias, we performed a weighted bootstrap resampling of the selected database following the method of Keller and Schoene (2012) using the Matlab MIT open-source code, available at <https://github.com/brenhinkeller/StatisticalGeochemistry>. All the fluid-mobile-elements/immobile-elements plots for basalts and komatiites in this paper were made using bootstrap-resampled data.

Nd isotopes database of Archaean and Proterozoic basaltic rocks and komatiites were taken from Spencer *et al.* (2018). Nd data were filtered, and only analyses with magmatic age constraints better than ± 100 Myr were used. Only Georoc analyses that included ¹⁴³Nd/¹⁴⁴Nd along with Sm and Nd concentrations were used. The ¹⁴⁷Sm/¹⁴⁴Nd ratio was determined using the atomic weights and abundances with the following equation:

$$^{147}\text{Sm}/^{143}\text{Nd} = \frac{\text{Sm ppm}}{\text{Nd ppm}} * \frac{\text{Abs.}^{147}\text{Sm} * \text{At. wt. Nd}}{\text{Abs.}^{144}\text{Nd} * \text{At. wt. Sm}}$$

The tonalite-trondhjemite-granodiorite rock database (TTG; sample number = 1,230) was collected from Johnson *et al.* (2019). The change in the median data range before and after 3.3–3.2 Ga is highlighted by rectangular shades of different colours (Figure 9.ure I. 9). Also, the average of medians for data within each rectangular shade is shown with horizontal bar. As many samples do not contain all the ratios used, the density of the data differs between plots.

9.4 Results

We compiled a database consisting of major and trace element whole-rock and Nd isotopes (Spencer *et al.*, 2018) of ~6,250 analyses from mafic and ultramafic rocks

with reliable crystallization age and geospatial location for each sample (see methods). The studied samples are widely representative of all the continents and cratons, and span the Archean–Early Proterozoic time range (3.8–2.2 Ga) (Figures H.1–4 and Supplementary Tables 1 and 2). The database includes primary mantle melts represented by basaltic rocks and komatiites. Using the variation of the means of Nd isotopes (as ϵ_{Nd}) in samples of the same age, and a statistical bootstrapping method (Keller and Schoene, 2012) on the basaltic and komatiitic rocks focusing on Ba/La, Ba/Nb, U/Nb, Pb/Nd and Pb/Ce ratios, we identify a significant change in mantle geochemical composition after ~3.25 Ga for basaltic rocks and after ~3.15 Ga for komatiites (Figures 9.1–3 and Figure H. 5).

Figure 9.1 displays a significant shift in the range of ϵ_{Nd} values of basaltic rocks and komatiites that span the Paleo- to Meso-Archean transition (~3.2 Ga). Although specific suites may show a range in values implying the shift may occur locally at earlier times, these shifts are not recognizable when viewed from the perspective of the global database, indicating they are probably local in scale. For example, Nd isotopic data of the Greenland Eoarchean (3.8–3.7 Ga) basaltic rocks extend to negative ϵ_{Nd} (attributed to mantle contamination (Blichert-Toft *et al.*, 1999; Rizo *et al.*, 2013) although on average, the data from that time interval plot at positive ϵ_{Nd} (Bennett, Brandon and Nutman, 2007; Hoffmann *et al.*, 2011; O’Neil *et al.*, 2016; Carlson *et al.*, 2019). More generally, the averages of ϵ_{Nd} in basaltic and komatiitic suites before ~3.2 Ga show little variation, ranging between +0.02 and +2.2. After ~3.2 Ga, however, ϵ_{Nd} averages for basaltic and komatiitic rocks show an abrupt decrease from -1.5 (at ~ 3.0 Ga) to -8.0 (at ~ 1.7 Ga), which we interpret to reflect the onset of global-scale heterogeneity in their upper and lower (respectively) mantle sources (Figure 9.1). This analysis provides robust evidence for global-scale, pene-contemporaneous contamination/refertilization of the mantle source for both mafic and ultramafic rocks, beginning after ~ 3.2 Ga in the upper mantle (inferred from basaltic rocks) but also affecting the lower mantle (inferred by komatiites) as the influx of LREE-enriched crustal materials yield negative ϵ_{Nd} values (White and Hofmann, 1982; Murphy and Nance, 2002).

Trace element ratios (i.e., Ba/La, Ba/Nb, U/Nb, Pb/Nd and Pb/Ce) of basalts and komatiites are widely accepted to track the recycling of terrestrial materials into mantle sources (Hofmann, 1997, 2013). Figures 9.2 and 3 monitor the best estimate of

the average composition of these trace element ratios through time, and are reported as means with associated 2-standard-error (95% confidence interval) uncertainties of intervals between 2.2 and 4.0 Ga. These ratios display a systematic increase in both magnitude and variability, mainly after ~3.2 Ga. In general, Figure 9.2 and Figure H.5a both display abrupt increases in the moving means of Ba/La, Ba/Nb, U/Nb, Pb/Nd and Pb/Ce ratios in basaltic rocks after ~3.25 Ga. In addition, the average mean values of all ratios of komatiites after ~3.15 Ga are highly enriched compared to komatiites older than ~3.15 Ga (Figure 9.3 and Figure H.5b).

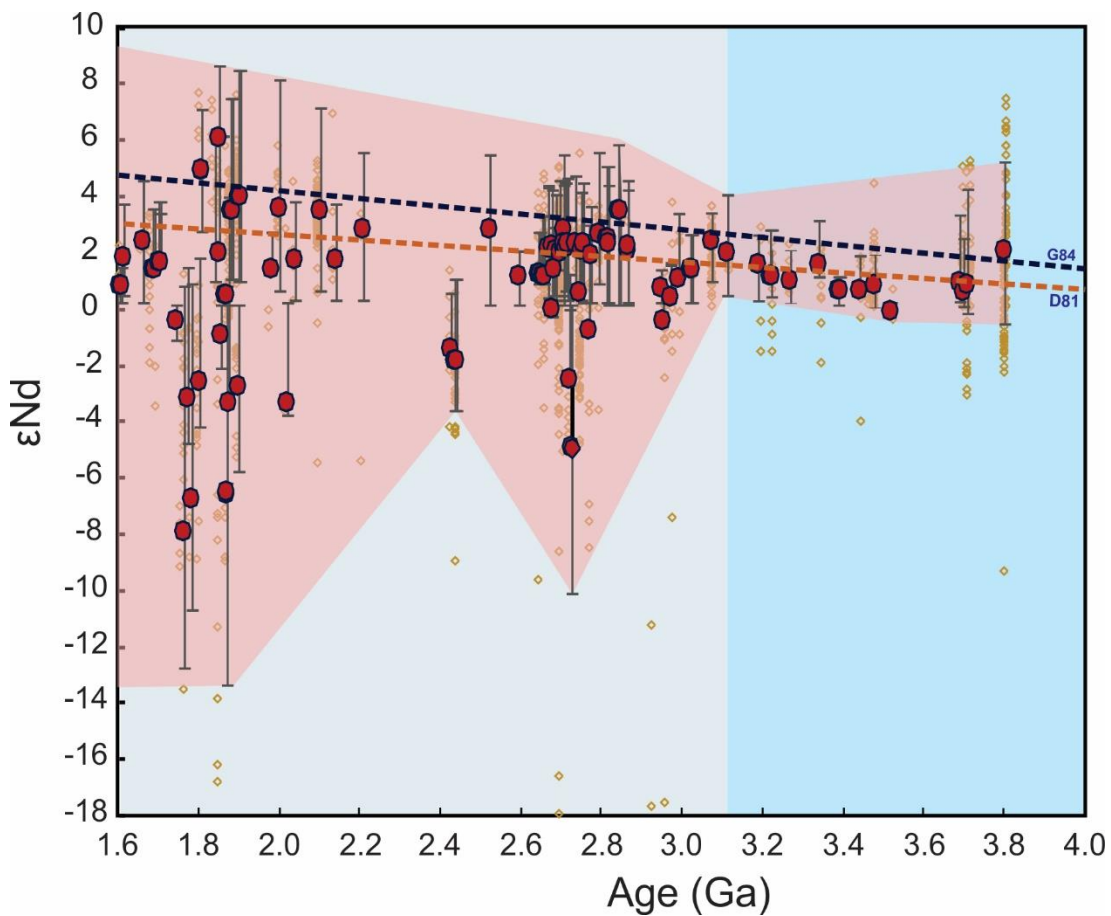


Figure 9.1: $^{143}\text{Nd}/^{144}\text{Nd}$ ratio (represented as ϵNd) vs. age for Archaean and Proterozoic basaltic rocks and komatiites (data from Spencer *et al.* (2018)). Brown circles represent individual samples. Red dots represent the median of samples with the same age, and the associated error bars spans across the middle 50% of the data, called the median data range here. The red field represents the envelope for the median range. The large variation in the mean ϵNd values after ~3.2–3.0 Ga suggests an isotopic shift in the mantle source of the basaltic rocks and the komatiites. The depleted mantle curves are shown for comparison (DePaolo, 1981; Goldstein, O’Nions and Hamilton, 1984).

There is some evidence supporting localized subduction in specific suites before ca. 3.2 Ga. For example at 3.8–3.7 Ga, some ratios such as Ba/La (20.15–19.43) and U/Nb (0.08–0.05) are somewhat higher than estimates of equivalent ratios in the primitive mantle (PM) (McDonough and Sun, 1995) (Ba/La = 10.81 and U/Nb = 0.03, respectively (Figure 9.2 a,c). These higher values may reflect subduction zone-like signature such as that proposed for the Isua greenstone belt, SW Greenland according to field and geochemical data interpretations (Hanmer and Greene, 2002; Polat *et al.*, 2003; Furnes *et al.*, 2007; Jenner *et al.*, 2009; Kaczmarek *et al.*, 2016). Also, at 3.4–3.3 Ga, U/Nb (0.04) and Pb/Nd (0.14) are slightly higher than PM values (0.03 and 0.12, respectively) (McDonough and Sun, 1995) (Figure 9.2c, d) which may reflect crustal contamination of the mantle source for the Barberton greenstone belt, the Kaapvaal craton (Furnes, de Wit and Robins, 2013; Blichert-Toft *et al.*, 2015b; Smart *et al.*, 2016; Sobolev *et al.*, 2019). However, when viewed from the perspective of the global database, these ratios become statistically detectable only around 3.25 Ga (e.g. Ba/La = 96.31, Ba/Nb = 53.32, U/Nb = 0.24 and Pb/Nd = 0.45 compared to the PM-like values and those before 3.25 Ga (Figure 9.2). From this perspective, contamination of the mantle by LILE- and LREE-enriched recycled continental materials during subduction would have been localized and relatively minor in the Palaeoarchaeon and the Eoarchaeon, but became a global process at ca. 3.2 Ga. The observed time lag (~100 Ma) in the increase in those ratios between basalts and komatiites could reflect the transit time of subducted slabs from upper mantle (contaminated basaltic rocks) to the lower mantle (contaminated komatiites). Taken together, these results suggest a fundamental and global change in the upper and lower mantle source composition of basalts and komatiites through refertilization/replenishment of fluid-mobile elements at the start of the Mesoarchean, which is consistent with the negative ϵNd values after ~3.2–3.0 Ga (Figure 9.1).

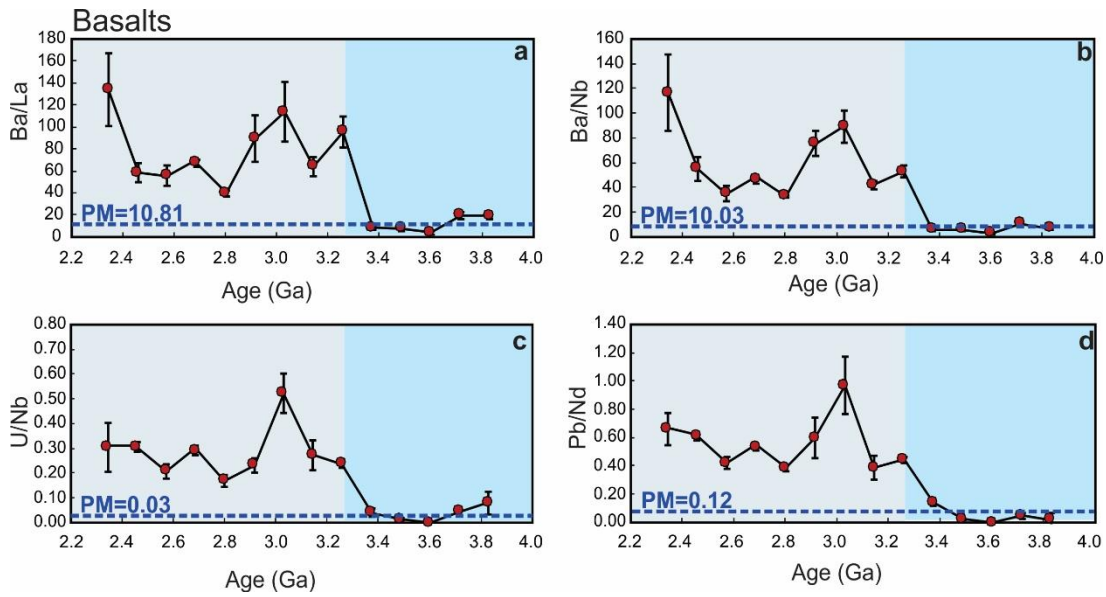


Figure 9.2: Time evolution of fluid-mobile-elements/immobile-elements in the basaltic rock datasets. Ba/La (a), Ba/Nb (b), U/Nb (c), and Pb/Nd (d). All ratios show an abrupt increase at ~ 3.25 Ga. Dotted horizontal lines are the primitive mantle values (PM; Ba/La = 10.81, Ba/Nb = 10.03, U/Nb = 0.03, Pb/Nd = 0.12) (McDonough and Sun, 1995). Error bars in a–d show the 2-standard errors of the means.

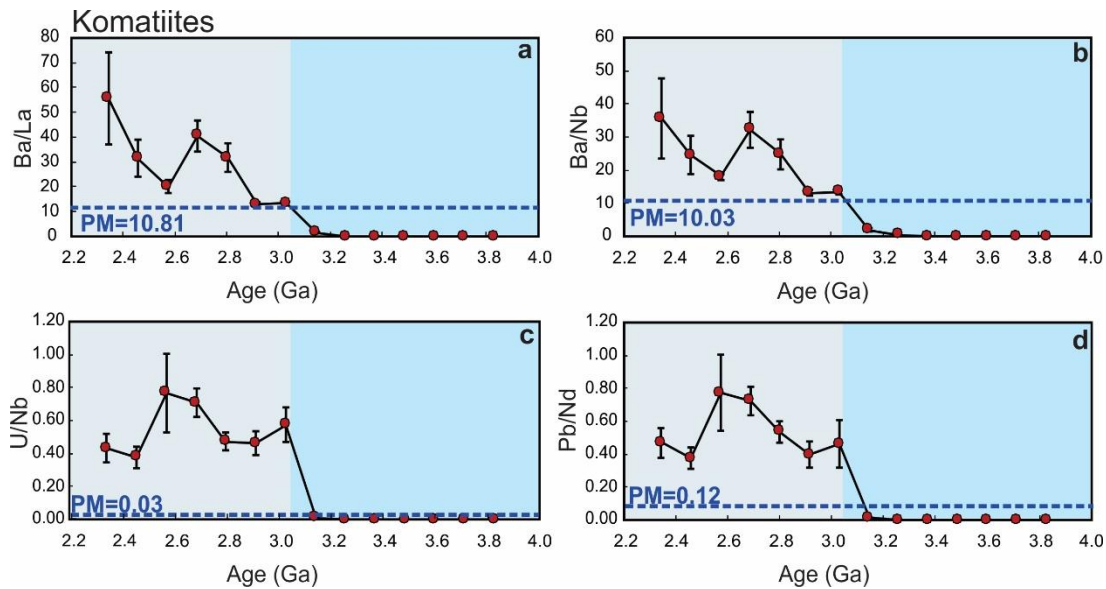


Figure 9.3: Time evolution of fluid-mobile-elements/immobile-elements in the komatiite datasets. Ba/La (a), Ba/Nb (b), U/Nb (c), and Pb/Nd (d). All ratios show an abrupt increase at ~ 3.15 Ga. Dotted horizontal lines are the primitive mantle values (PM; Ba/La = 10.81, Ba/Nb = 10.03, U/Nb = 0.03, Pb/Nd = 0.12) (McDonough and Sun, 1995). Error bars show 2-standard error of the mean.

9.5 Discussion

Our observed abrupt changes could be attributed to either (1) crustal contamination of ascending mantle-derived magma (van Hunen and Moyen, 2012) or (2) contamination of the mantle source by either subduction or delamination (van Hunen and Moyen, 2012; Bédard, 2018; Moyen and Laurent, 2018). Crustal contamination/mixing of mafic and ultramafic magmas during their emplacement can be evaluated using the Th/Yb ratio, which is widely accepted as a powerful tracer of this process (Pearce, 2008). Figures I.6 and 7 show the covariation between the studied ratios and Th/Yb in both basaltic rocks and komatiites before and after 3.25 Ga and 3.15 Ga, respectively, compared with such ratios in Archean continental crust (i.e., tonalite-trondhjemite-granodiorite (TTGs) dataset) (Johnson *et al.*, 2019). These plots show that Th/Yb has no relationship with Ba/La, Ba/Nb, U/Nb, Pb/Nd and Pb/Ce in either basaltic rocks (Figure H.6) or komatiites (Figure H.7). In addition, the Th/Yb values are very low compared to those typical of TTGs, providing clear evidence that no significant contamination of basaltic or komatiitic rocks by Archean crust occurred during their emplacement. Moreover, Archean basaltic and komatiitic rocks plot on an array that is parallel to the oceanic mantle array (MORB-OIB array) on the Th/Yb vs. Nb/Yb diagram (Figure H.8) (Pearce, 2008). This trend is similar to that of a modern-arc array, suggesting derivation of those rocks from a metasomatized/re-enriched mantle source (Pearce, 2008), and contrasts with the oblique trend displayed by TTGs (Figure H.8). The similarly low Th/Yb in post-3.2 Ga komatiites and basalts compares favourably with modern-arc basalts (Figure H.8), suggesting that the enrichment in these ratios was source-dependent and the mantle inherited these features before the generation of these mafic and ultramafic magmas.

The similarity between the average mean values of the studied trace element ratios in basalts and komatiites before ~3.25–3.15 Ga with primitive mantle estimates (PM) (McDonough and Sun, 1995) (Figure 9.2, 3 and Figure H.5, 8) indicates the existence of a primitive-like and/or quasi-homogeneous mantle with only minor and local terrestrial inputs before ~3.25–3.15 Ga. In contrast, the average mean values of the studied ratios of basalts and komatiites after ~3.25–3.15 Ga are highly enriched compared to the primitive mantle (Figure 9.2, 3 and Figure H.5, 8). Such an interpreted abrupt change in mantle composition is also reflected in the source of TTGs, generally considered to be juvenile crust newly extracted from the upper mantle (Johnson *et al.*,

2019). As shown in Figure H.9, the same ratios (except for U/Nb) in TTGs not only have the same contents as their parent mafic rocks (Figure H.6) but also show the same abrupt change after ~3.3–3.2 Ga (Johnson *et al.*, 2019). Similarly, a recent study on Jack Hills zircons (4.3–3.3 Ga) suggests a small yet notable change in Earth’s crustal composition between the Hadean and the Mesoarchean (Turner *et al.*, 2020).

Mantle refertilization/re-enrichment at ~3.2 Ga could have occurred by two major processes — sagduction/delamination (Bédard, 2018) or subduction (van Hunen and Moyen, 2012). Sagduction/delamination of dense residue after TTG formation would have facilitated the refertilization of the upper mantle with crust-like chemical and isotopic signatures (Bédard, 2018; Moyen and Laurent, 2018), but this process would have had less influence on the composition of the lower mantle (Bédard, 2018; Condie, 2018). Therefore, a sagduction/delamination scenario is not consistent with our analysis of komatiites (Figure 9.3) which are thought to have been derived from the lower mantle, and represent the products of mantle plumes (Bennett, 2003). Komatiites younger than ~3.15 Ga are enriched in petrogenetically-indicating trace element ratios suggesting a re-enriched/metasomatized mantle source. Consistent with trace element results, ϵNd values of komatiites and basaltic rocks both show a pronounced abrupt-shift to lower values at ~3.0 Ga (Figure 9.1). This shift is powerful evidence that recycling of subducted sediments and crust affected the composition of both the upper mantle and the deep mantle plume source on a global scale (White and Hofmann, 1982; Hofmann, 1997; Chauvel *et al.*, 2008), indicating that subduction into the lower mantle was widely/globally operative by ~3.2 Ga. These results are consistent with oxygen and hydrogen isotopes studies of the 3.2 Ga Barberton komatiites, South Africa that suggest mantle source heterogeneity by then (Byerly *et al.*, 2017; Sobolev *et al.*, 2019).

Some previous work (Shirey and Richardson, 2011; Dhuime *et al.*, 2012; Naeraa *et al.*, 2012), though based on more indirect measures of global mantle composition than we present here, support our first-order conclusions. Shirey and Richardson (2011) interpret the appearance at ca. 3.2 Ga of eclogitic inclusions in diamonds from kimberlite pipes of the Kaapvaal craton to require subduction processes. Analysis of Hf-O zircon data in crustal rocks, which tracks the recycling of supracrustal materials, provides evidence for a step change at ca. 3 Ga indicative of the onset of subduction (Dhuime *et al.*, 2012; Naeraa *et al.*, 2012). Recently, Sobolev

and Brown (2019) hypothesize that the evolution and start of plate tectonics on Earth were facilitated by accumulation of sediments at the continental edges and trenches, which acted as a lubricant for the emergence and stabilization of subduction processes since the Mesoarchean (3.2–2.8 Ga). Our new observations, based on direct products of mantle melting, identify geochemical tracers of sediments recycling into both the upper and lower mantle (i.e., Ba/La and Ba/Nb) in both basaltic and komatiitic rocks, show that the abrupt increase occurred at ~3.2 Ga (Figures 9.2 and 3). In addition, Gamal EL Dien *et al.* (2019c), using Mg, Ni and Cr elements in basaltic rocks show a consistent and rapid drop at ~3.2–3.0 Ga that indicates an abrupt change in mantle potential temperature at the start of global-scale plate tectonics. Although we cannot rule out the presence of intermittent stagnant lid tectonics along with plate tectonics after ~3.2 Ga (Wyman, 2018), our analysis suggests mass transfer from the surface to the deep mantle from ~3.2 Ga, a process most feasibly accomplished through subduction and plate tectonics.

Our interpretation assumes no dramatic continental crustal growth at around 3.2 Ga (Armstrong, 1981; Dewey and Windley, 1981; Pujol *et al.*, 2013). However, if there was a spike of global continental crustal growth at ca. 3.2 Ga (as argued by some Taylor and McLennan, 1995; Belousova *et al.*, 2010; Dhuime *et al.*, 2012), then global plate tectonics could have started earlier than 3.2 Ga but mantle re-enrichment may not be as pronounced due to the relatively small amount of continental crust (Hurley and Rand, 1969; Allègre and Rousseau, 1984; Condie and Aster, 2010).

Overall, our work points to a profound mantle re-enrichment event at ca. 3.2 billion years ago, interpreted to indicate the start of global-scale plate tectonics no later than that time.

9.6 References

- Allègre, C. J. and Rousseau, D. (1984) 'The growth of the continent through geological time studied by Nd isotope analysis of shales', *Earth and Planetary Science Letters*. Elsevier, 67(1), pp. 19–34. doi: 10.1016/0012-821X(84)90035-9.
- Armstrong, R. L. (1981) 'Radiogenic Isotopes: The Case for Crustal Recycling on a Near-Steady-State No-Continental-Growth Earth', *Philosophical Transactions of the Royal Society A: Mathematical, Physical and Engineering Sciences*. The Royal Society, 301(1461), pp. 443–472. doi: 10.1098/rsta.1981.0122.
- Bédard, J. H. (2018) 'Stagnant lids and mantle overturns: Implications for Archaean tectonics, magmagenesis, crustal growth, mantle evolution, and the start of plate tectonics', *Geoscience Frontiers*. Elsevier, 9(1), pp. 19–49. doi: 10.1016/J.GSF.2017.01.005.
- Belousova, E. A. *et al.* (2010) 'The growth of the continental crust: Constraints from zircon Hf-isotope data', *Lithos*. Elsevier, 119(3–4), pp. 457–466. doi: 10.1016/J.LITHOS.2010.07.024.
- Bennett, V. C. (2003) 'Compositional Evolution of the Mantle', *Treatise on Geochemistry*. Pergamon, pp. 493–519. doi: 10.1016/B0-08-043751-6/02013-2.
- Bennett, V. C., Brandon, A. D. and Nutman, A. P. (2007) 'Coupled ^{142}Nd - ^{143}Nd isotopic evidence for hadean mantle dynamics', *Science*, 318(5858), pp. 1907–1910. doi: 10.1126/science.1145928.
- Blichert-Toft, J. *et al.* (1999) 'The Nd and Hf isotopic evolution of the mantle through the Archean. Results from the Isua supracrustals, West Greenland, and from the Birimian terranes of West Africa', *Geochimica et Cosmochimica Acta*. Elsevier Ltd, 63(22), pp. 3901–3914. doi: 10.1016/S0016-7037(99)00183-0.
- Blichert-Toft, J. *et al.* (2015a) 'Hf and Nd isotope systematics of early Archean komatiites from surface sampling and ICDP drilling in the Barberton Greenstone Belt, South Africa', *American Mineralogist*. Walter de Gruyter GmbH, 100(11–12), pp. 2396–2411. doi: 10.2138/am-2015-5325.
- Blichert-Toft, J. *et al.* (2015b) 'Hf and Nd isotope systematics of early Archean komatiites from surface sampling and ICDP drilling in the Barberton Greenstone Belt, South Africa', *American Mineralogist*, 100(11–12), pp. 2396–2411. doi: 10.2138/am-2015-5325.
- Brenhin Keller, C. and Schoene, B. (2012) 'Statistical geochemistry reveals disruption in secular lithospheric evolution about 2.5Gyr ago', *Nature*. Nature Publishing Group, 485(7399), pp. 490–493. doi: 10.1038/nature11024.
- Byerly, B. L. *et al.* (2017) 'Early Earth mantle heterogeneity revealed by light oxygen isotopes of Archean komatiites', *Nature Geoscience*. Nature Publishing Group, 10(11), pp. 871–875. doi: 10.1038/ngeo3054.
- Carlson, R. W. *et al.* (2019) 'The nature of Earth's first crust', *Chemical Geology*. Elsevier B.V., 530, p. 119321. doi: 10.1016/j.chemgeo.2019.119321.
- Chauvel, C. *et al.* (2008) 'Role of recycled oceanic basalt and sediment in generating the Hf–Nd mantle array', *Nature Geoscience*. Nature Publishing Group, 1(1), pp. 64–67. doi:

10.1038/ngeo.2007.51.

Clift, P. and Vannucchi, P. (2004) 'Controls on tectonic accretion versus erosion in subduction zones: Implications for the origin and recycling of the continental crust', *Reviews of Geophysics*. John Wiley & Sons, Ltd, 42(2), p. RG2001. doi: 10.1029/2003RG000127.

Condie, K. C. (2018) 'A planet in transition: The onset of plate tectonics on Earth between 3 and 2 Ga?', *Geoscience Frontiers*, 9(1), pp. 51–60. doi: 10.1016/j.gsf.2016.09.001.

Condie, K. C. and Aster, R. C. (2010) 'Episodic zircon age spectra of orogenic granitoids: The supercontinent connection and continental growth', *Precambrian Research*. Elsevier B.V., 180(3–4), pp. 227–236. doi: 10.1016/j.precamres.2010.03.008.

DePaolo, D. J. (1981) 'Neodymium isotopes in the Colorado Front Range and crust–mantle evolution in the Proterozoic', *Nature*. Nature Publishing Group, 291(5812), pp. 193–196. doi: 10.1038/291193a0.

DePaolo, D. J. and Wasserburg, G. J. (1976) 'Nd isotopic variations and petrogenetic models', *Geophysical Research Letters*. John Wiley & Sons, Ltd, 3(5), pp. 249–252. doi: 10.1029/GL003i005p00249.

Dewey, J. . and Windley, B. F. (1981) 'Growth and differentiation of the continental crust', *Philosophical Transactions of the Royal Society of London. Series A, Mathematical and Physical Sciences*. The Royal Society, 301(1461), pp. 189–206. doi: 10.1098/rsta.1981.0105.

Dhuime, B. *et al.* (2012) 'A change in the geodynamics of continental growth 3 billion years ago.', *Science (New York, N.Y.)*. American Association for the Advancement of Science, 335(6074), pp. 1334–6. doi: 10.1126/science.1216066.

Furnes, H. *et al.* (2007) 'A Vestige of Earth ' s Oldest Ophiolite', *Science (New York, N.Y.)*, 315(March), pp. 2001–2004. doi: 10.1126/science.1139170.

Furnes, H., de Wit, M. and Robins, B. (2013) 'A review of new interpretations of the tectonostratigraphy, geochemistry and evolution of the Onverwacht Suite, Barberton Greenstone Belt, South Africa', *Gondwana Research*. Elsevier, pp. 403–428. doi: 10.1016/j.gr.2012.05.007.

Gamal El Dien, H., Arai, S., *et al.* (2019) 'Cr-spinel records metasomatism not petrogenesis of mantle rocks', *Nature Communications*. Springer US, (10), p. 5103. doi: 10.1038/s41467-019-13117-1.

Gamal El Dien, H., Li, Z.-X., *et al.* (2019) 'Origin of arc magmatic signature: A temperature-dependent process for trace element (re)-mobilization in subduction zones', *Scientific Reports*, 9(1), p. 7098. doi: 10.1038/s41598-019-43605-9.

Gamal EL Dien, H. *et al.* (2019) 'Global geochemical fingerprinting of plume intensity suggests coupling with the supercontinent cycle', *Nature Communications*. Nature Research, 10(1), p. 5270. doi: 10.1038/s41467-019-13300-4.

Goldstein, S. L., O'Nions, R. K. and Hamilton, P. J. (1984) 'A Sm-Nd isotopic study of atmospheric dusts and particulates from major river systems', *Earth and Planetary Science Letters*. Elsevier, 70(2), pp. 221–236. doi: 10.1016/0012-821X(84)90007-4.

Hanmer, S. and Greene, D. C. (2002) 'A modern structural regime in the Paleoproterozoic (~ 3.64 Ga); Isua Greenstone Belt, southern West Greenland', *Tectonophysics*. Elsevier, 346(3–4), pp. 201–222. doi: 10.1016/S0040-1951(02)00029-X.

Hoffmann, J. E. *et al.* (2011) 'The origin of decoupled Hf–Nd isotope compositions in Eoarchean rocks from southern West Greenland', *Geochimica et Cosmochimica Acta*. Pergamon, 75(21), pp. 6610–6628. doi: 10.1016/J.GCA.2011.08.018.

Hofmann, A. W. (1988) 'Chemical differentiation of the Earth: the relationship between mantle, continental crust, and oceanic crust', *Earth and Planetary Science Letters*. Elsevier, 90(3), pp. 297–314. doi: 10.1016/0012-821X(88)90132-X.

Hofmann, A. W. (1997) 'Mantle geochemistry: the message from oceanic volcanism', *Nature*. Nature Publishing Group, 385(6613), pp. 219–229. doi: 10.1038/385219a0.

Hofmann, A. W. (2013) 'Sampling Mantle Heterogeneity through Oceanic Basalts: Isotopes and Trace Elements', *Treatise on Geochemistry*. Elsevier, pp. 67–101. doi: 10.1016/B978-0-08-095975-7.00203-5.

van Hunen, J. and Moyen, J.-F. (2012) 'Archean Subduction: Fact or Fiction?', *Annual Review of Earth and Planetary Sciences*, 40(1), pp. 195–219. doi: 10.1146/annurev-earth-042711-105255.

Hurley, P. M. and Rand, J. R. (1969) *Pre-Drift Continental Nuclei*, *Science*.

Jenner, F. E. *et al.* (2009) 'Evidence for subduction at 3.8 Ga: Geochemistry of arc-like metabasalts from the southern edge of the Isua Supracrustal Belt', *Chemical Geology*. Elsevier B.V., 261(1–2), pp. 82–97. doi: 10.1016/j.chemgeo.2008.09.016.

Johnson, T. E. *et al.* (2019) 'Secular change in TTG compositions: Implications for the evolution of Archaean geodynamics', *Earth and Planetary Science Letters*. Elsevier, 505, pp. 65–75. doi: 10.1016/J.EPSL.2018.10.022.

Kaczmarek, M. A. *et al.* (2016) 'Earth's oldest mantle fabrics indicate Eoarchean subduction', *Nature Communications*. Nature Publishing Group, 7(1), pp. 1–7. doi: 10.1038/ncomms10665.

Kelley, K. A. and Cottrell, E. (2009) 'Water and the oxidation state of subduction zone magmas.', *Science (New York, N.Y.)*. American Association for the Advancement of Science, 325(5940), pp. 605–7. doi: 10.1126/science.1174156.

Keppler, H. (1996) 'Constraints from partitioning experiments on the composition of subduction-zone fluids', *Nature*. Nature Publishing Group, 380(6571), pp. 237–240. doi: 10.1038/380237a0.

Kessel, R. *et al.* (2005) 'Trace element signature of subduction-zone fluids, melts and supercritical liquids at 120–180 km depth', *Nature*. Nature Publishing Group, 437(7059), pp. 724–727. doi: 10.1038/nature03971.

Komiya, T. *et al.* (2014) 'Geology of the Eoarchean, >3.95 Ga, Nulliak supracrustal rocks in the Saglek Block, northern Labrador, Canada: The oldest geological evidence for plate tectonics', *Tectonophysics*. Elsevier B.V., 662, pp. 40–66. doi: 10.1016/j.tecto.2015.05.003.

- Korenaga, J. (2013) 'Initiation and Evolution of Plate Tectonics on Earth: Theories and Observations', *Annual Review of Earth and Planetary Sciences*, 41(1), pp. 117–151. doi: 10.1146/annurev-earth-050212-124208.
- Mazza, S. E. *et al.* (2019) 'Sampling the volatile-rich transition zone beneath Bermuda', *Nature*. Nature Publishing Group, 569(7756), pp. 398–403. doi: 10.1038/s41586-019-1183-6.
- McDonough, W. . and Sun, S. -. (1995) 'The composition of the Earth', *Chemical Geology*, 120, pp. 223–252. doi: doi.org/10.1016/0009-2541(94)00140-4.
- Miller, D. M., Goldstein, S. L. and Langmuir, C. H. (1994) 'Cerium/lead and lead isotope ratios in arc magmas and the enrichment of lead in the continents', *Nature*. Nature Publishing Group, 368(6471), pp. 514–520. doi: 10.1038/368514a0.
- Moyen, J. F. and Laurent, O. (2018) 'Archaean tectonic systems: A view from igneous rocks', *Lithos*. Elsevier B.V., 302–303, pp. 99–125. doi: 10.1016/j.lithos.2017.11.038.
- Murphy, J. B. and Nance, R. D. (2002) 'Sm–Nd isotopic systematics as tectonic tracers: an example from West Avalonia in the Canadian Appalachians', *Earth-Science Reviews*. Elsevier, 59(1–4), pp. 77–100. doi: 10.1016/S0012-8252(02)00070-3.
- Naeraa, T. *et al.* (2012) 'Hafnium isotope evidence for a transition in the dynamics of continental growth 3.2 Gyr ago', *Nature*. Nature Publishing Group, 485(7400), pp. 627–630. doi: 10.1038/nature11140.
- Nagel, T. J., Hoffmann, J. E. and Münker, C. (2012) 'Generation of Eoarchean tonalite-trochilite-granodiorite series from a thickened mafic arc crust', *Geology*. GeoScienceWorld, 40(4), pp. 375–378. doi: 10.1130/G32729.1.
- Nielsen, S. G. *et al.* (2018) 'Barium isotope evidence for pervasive sediment recycling in the upper mantle', *Science Advances*. American Association for the Advancement of Science, 4(7), p. eaas8675. doi: 10.1126/sciadv.aas8675.
- O'Neil, J. *et al.* (2016) 'Geochemistry and Nd isotopic characteristics of Earth's Hadean mantle and primitive crust', *Earth and Planetary Science Letters*. Elsevier B.V., 442, pp. 194–205. doi: 10.1016/j.epsl.2016.02.055.
- Patchett, P. J. *et al.* (1982) 'Evolution of continental crust and mantle heterogeneity: Evidence from Hf isotopes', *Contributions to Mineralogy and Petrology*. Springer-Verlag, 78(3), pp. 279–297. doi: 10.1007/BF00398923.
- Pearce, J. A. (2008) 'Geochemical fingerprinting of oceanic basalts with applications to ophiolite classification and the search for Archean oceanic crust', *Lithos*, 100(1–4), pp. 14–48. doi: 10.1016/j.lithos.2007.06.016.
- Plank, T. and Langmuir, C. H. (1993) 'Tracing trace elements from sediment input to volcanic output at subduction zones', *Nature*. Nature Publishing Group, 362(6422), pp. 739–743. doi: 10.1038/362739a0.
- Polat, A. *et al.* (2003) 'Contrasting geochemical patterns in the 3.7–3.8 Ga pillow basalt cores and rims, Isua greenstone belt, Southwest Greenland: Implications for postmagmatic alteration processes', *Geochimica et Cosmochimica Acta*. Pergamon, 67(3), pp. 441–457.

doi: 10.1016/S0016-7037(02)01094-3.

Poli, S. and Schmidt, M. W. (2002) 'Petrology of Subducted Slabs', *Annual Review of Earth and Planetary Sciences*, 30(1), pp. 207–235. doi: 10.1146/annurev.earth.30.091201.140550.

Pujol, M. *et al.* (2013) 'Argon isotopic composition of Archaean atmosphere probes early Earth geodynamics', *Nature*. Nature Publishing Group, 498(7452), pp. 87–90. doi: 10.1038/nature12152.

Reimink, J. R. *et al.* (2019) 'Onset of new, progressive crustal growth in the central Slave craton at 3.55 Ga', *Geochem. Persp. Lett.*, 10, pp. 8–13. doi: 10.7185/geochemlet.1907.

Rizo, H. *et al.* (2013) 'Early mantle dynamics inferred from ^{142}Nd variations in Archean rocks from southwest Greenland', *Earth and Planetary Science Letters*. Elsevier, 377–378, pp. 324–335. doi: 10.1016/j.epsl.2013.07.012.

Shirey, S. B. and Richardson, S. H. (2011) 'Start of the Wilson cycle at 3 Ga shown by diamonds from subcontinental mantle.', *Science (New York, N.Y.)*. American Association for the Advancement of Science, 333(6041), pp. 434–6. doi: 10.1126/science.1206275.

Smart, K. A. *et al.* (2016) 'Early Archaean tectonics and mantle redox recorded in Witwatersrand diamonds', *Nature Geoscience*. Nature Publishing Group, 9(3), pp. 255–259. doi: 10.1038/ngeo2628.

Sobolev, A. V. *et al.* (2019) 'Deep hydrous mantle reservoir provides evidence for crustal recycling before 3.3 billion years ago', *Nature*. Nature Publishing Group, p. 1. doi: 10.1038/s41586-019-1399-5.

Sobolev, S. V. and Brown, M. (2019) 'Surface erosion events controlled the evolution of plate tectonics on Earth', *Nature*. Nature Publishing Group, 570(7759), pp. 52–57. doi: 10.1038/s41586-019-1258-4.

Spencer, C. J. *et al.* (2018) 'A Palaeoproterozoic tectono-magmatic lull as a potential trigger for the supercontinent cycle', *Nature Geoscience*. Nature Publishing Group, 11(2), pp. 97–101. doi: 10.1038/s41561-017-0051-y.

Stern, R. J. (2002) 'Subduction zones', *Reviews of Geophysics*, 40(4). doi: 10.1029/2001RG000108.

Tang, M., Chen, K. and Rudnick, R. L. (2016) 'Archean upper crust transition from mafic to felsic marks the onset of plate tectonics', *Science*, 351(6271), pp. 372–375. doi: 10.1126/science.aad5513.

Taylor, S. R. and McLennan, S. M. (1995) 'The geochemical evolution of the continental crust', *Reviews of Geophysics*, 33(2), p. 241. doi: 10.1029/95RG00262.

Turner, S. *et al.* (2014) 'Heading down early on? Start of subduction on earth', *Geology*. Geological Society of America, 42(2), pp. 139–142. doi: 10.1130/G34886.1.

Turner, S. *et al.* (2020) 'An andesitic source for Jack Hills zircon supports onset of plate tectonics in the Hadean', *Nature Communications*. Nature Publishing Group, 11(1), p. 1241. doi: 10.1038/s41467-020-14857-1.

White, W. M. and Hofmann, A. W. (1982) 'Sr and Nd isotope geochemistry of oceanic basalts and mantle evolution', *Nature*. Nature Publishing Group, 296(5860), pp. 821–825. doi: 10.1038/296821a0.

Willbold, M. and Stracke, A. (2010) 'Formation of enriched mantle components by recycling of upper and lower continental crust', *Chemical Geology*. Elsevier, 276(3–4), pp. 188–197. doi: 10.1016/J.CHEMGEO.2010.06.005.

Wyman, D. (2018) 'Do cratons preserve evidence of stagnant lid tectonics?', *Geoscience Frontiers*. Elsevier, 9(1), pp. 3–17. doi: 10.1016/J.GSF.2017.02.001.

“Every reasonable effort has been made to acknowledge the owners of copyright material. I would be pleased to hear from any copyright owner who has been omitted or incorrectly acknowledged.”

Appendix H:
Supplementary materials to Chapter 9

Supplementary Data Tables related to this chapter can be found [here](#).

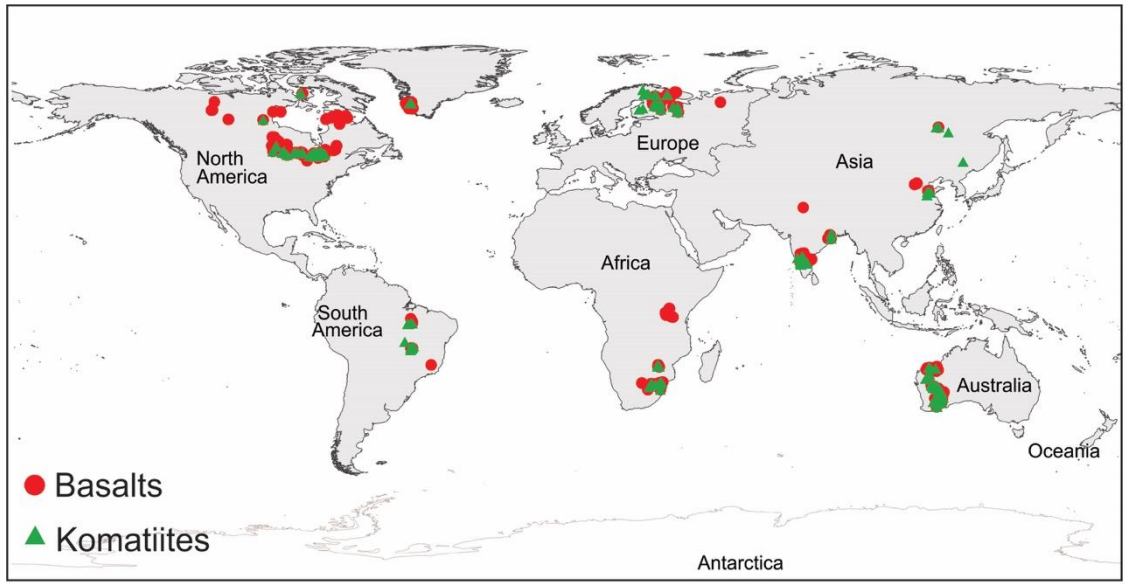


Figure H. 1: Sample locations of basaltic rocks and komatiites used in this study. The map shows that the samples covered all the continents. This map created using ArcGIS Desktop 10.7 final-Curtin university licenced version (<https://www.arcgis.com/home/index.html>).

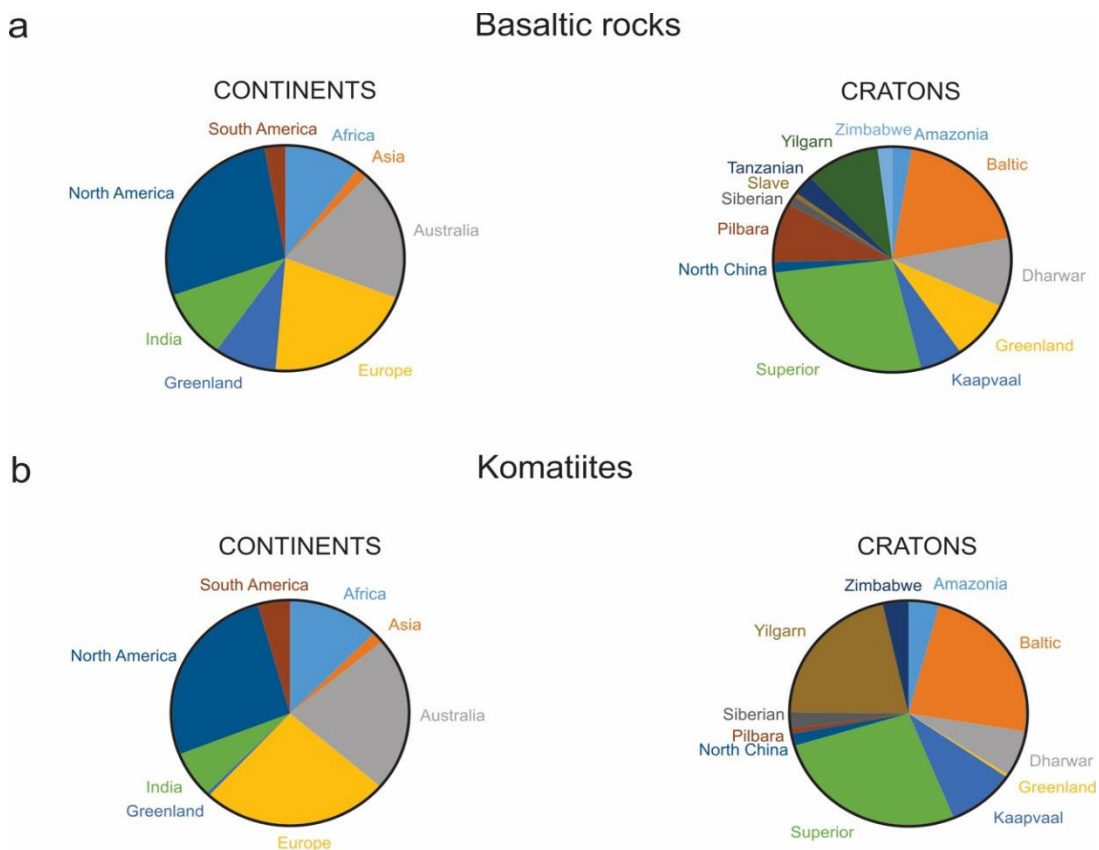
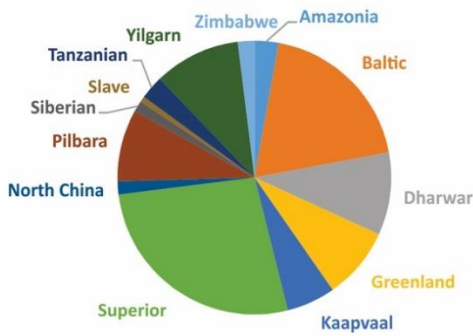


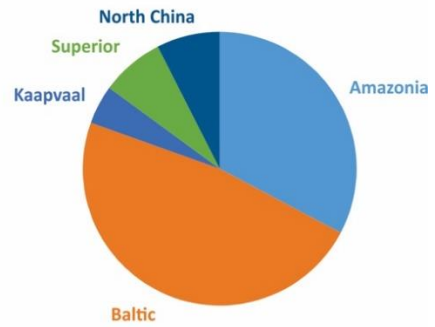
Figure H. 2: 2D Pie-charts show that the distribution of the studied samples of basaltic rocks and komatiites is representative for all continents and cratons.

Basaltic rocks

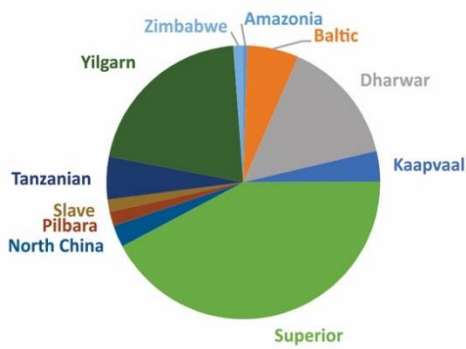
a- All data (3.8–2.4 Ga)



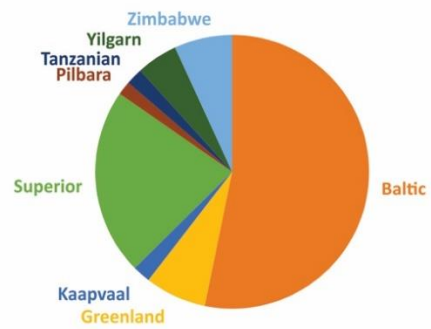
b- 2.6–2.4 Ga



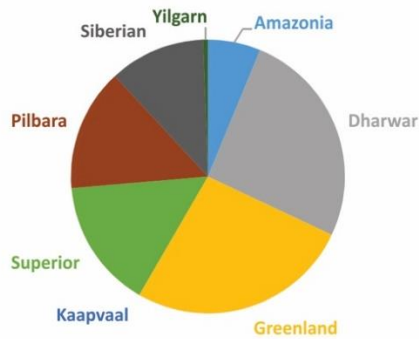
c- 2.8–2.6 Ga



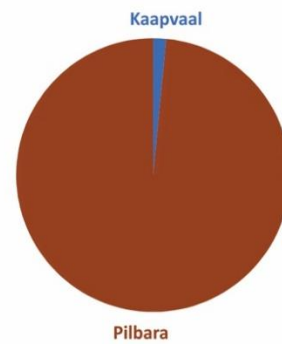
d- 3.0–2.8 Ga



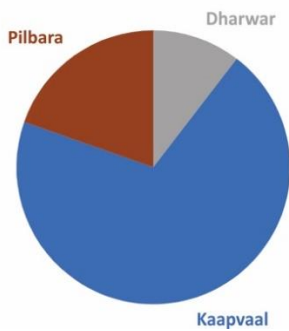
e- 3.2–3.0 Ga



f- 3.4–3.2 Ga



g- 3.6–3.4 Ga



h- 3.8–3.6 Ga

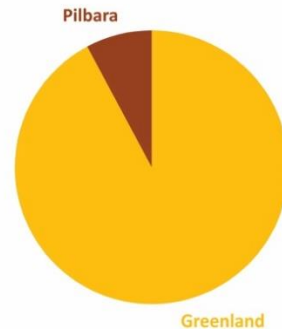


Figure H. 3: 2D Pie-charts show that the distribution of the studied basalt samples is representative of all the cratons for the time range of 3.8–2.4 Ga.

Komatiites

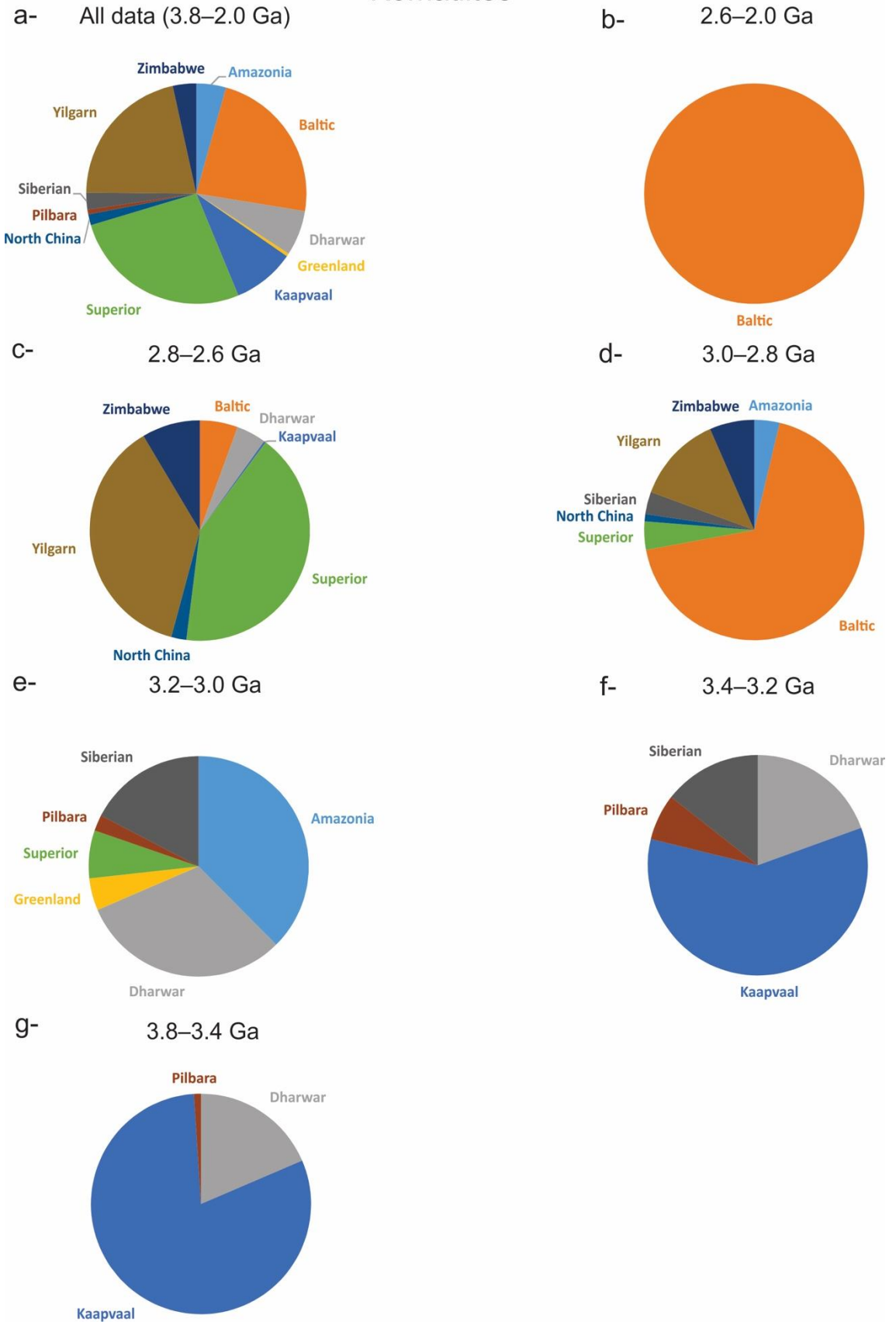


Figure H. 4: 2D Pie-charts show that the distribution of the studied komatiite samples is representative of all the cratons for the time range of 3.8–2.0 Ga.

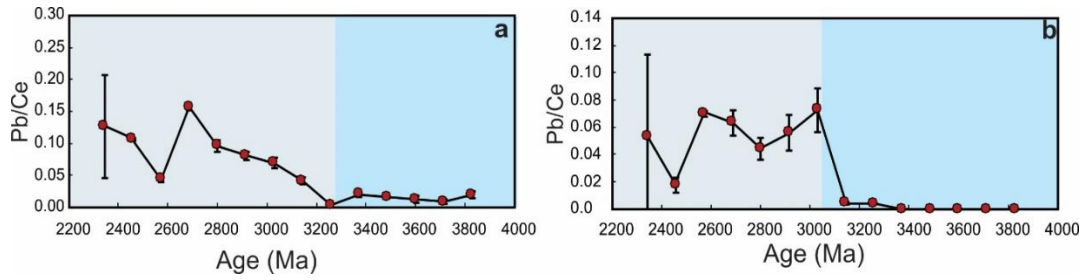


Figure H. 5: Time evolution of Pb/Ce ratios for basaltic rocks (a) and komatiites (b). Pb/Ce ratio shows an abrupt increase after ~3.25 Ga for basalts and after ~3.15 Ga for komatiites. Error bars show the 2-s.e.m. (standard error of the mean) uncertainties.

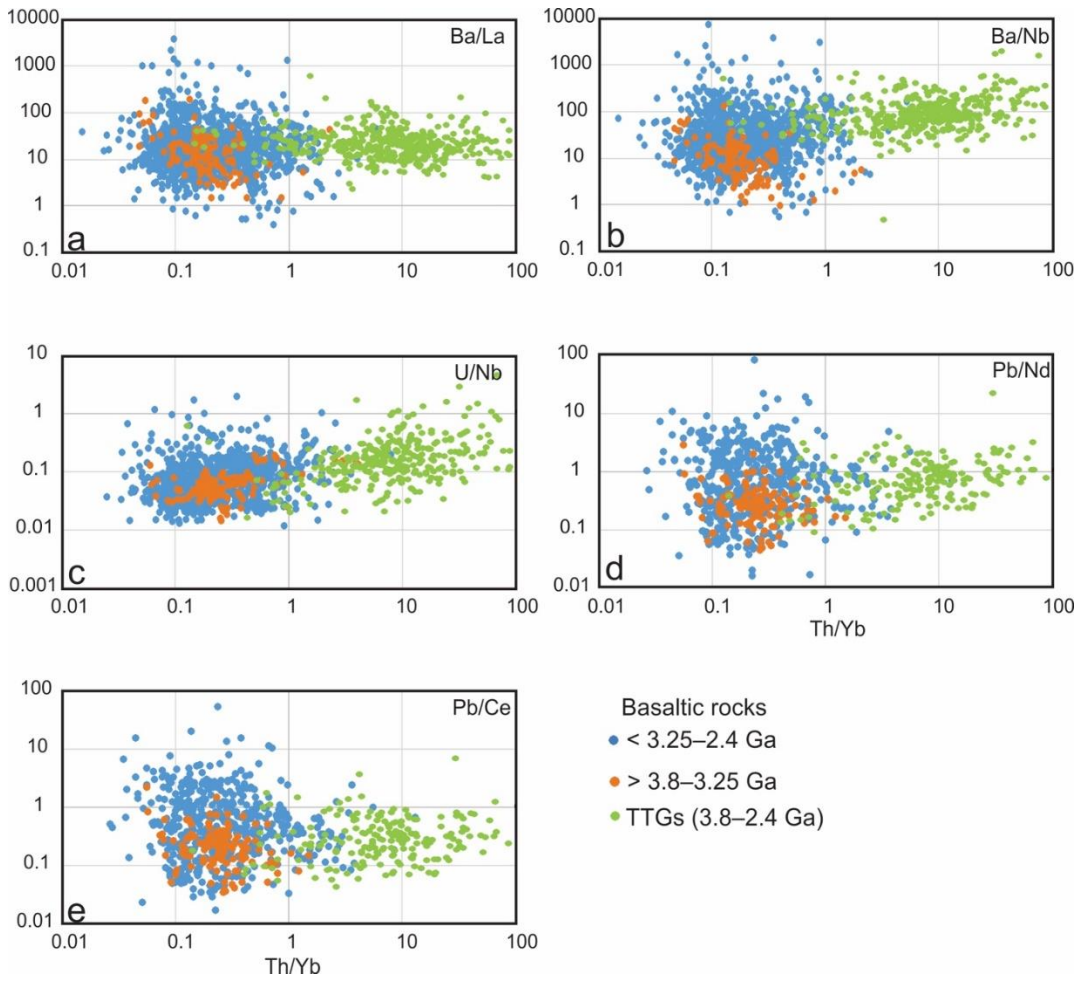


Figure H.6: Plots of Th/Yb vs Ba/La (a), Ba/Nb (b), U/Nb (c), Pb/Nd (d), and Pb/Ce (e) for basaltic rocks and TTGs. The basalts datasets are split into two age ranges <math>< 3.25-2.4</math> Ga and $> 3.8-3.25$ Ga. Th/Yb is significantly higher for TTGs than for basalts, indicating no crustal contamination in the basalts.

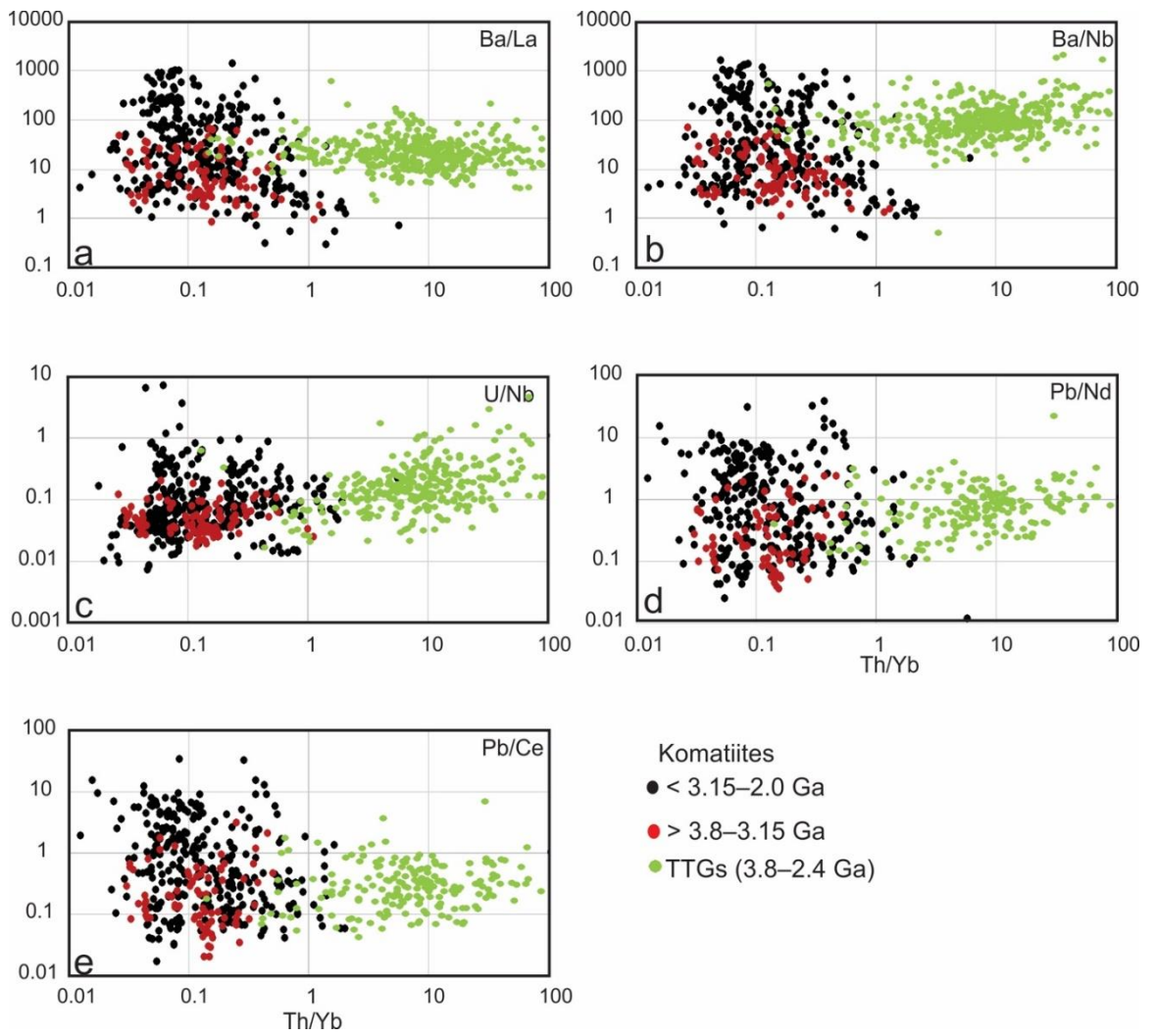


Figure H.7: Plots of Th/Yb vs Ba/La (a), Ba/Nb (b), U/Nb (c), Pb/Nd (d), and Pb/Ce (e) for komatiites. The datasets are split into two ranges as <math>< 3.15\text{--}2.0</math> and $> 3.8\text{--}3.15$ Ga. Th/Yb is significantly higher in TTGs than in komatiites, indicating no crustal contamination in the komatiites.

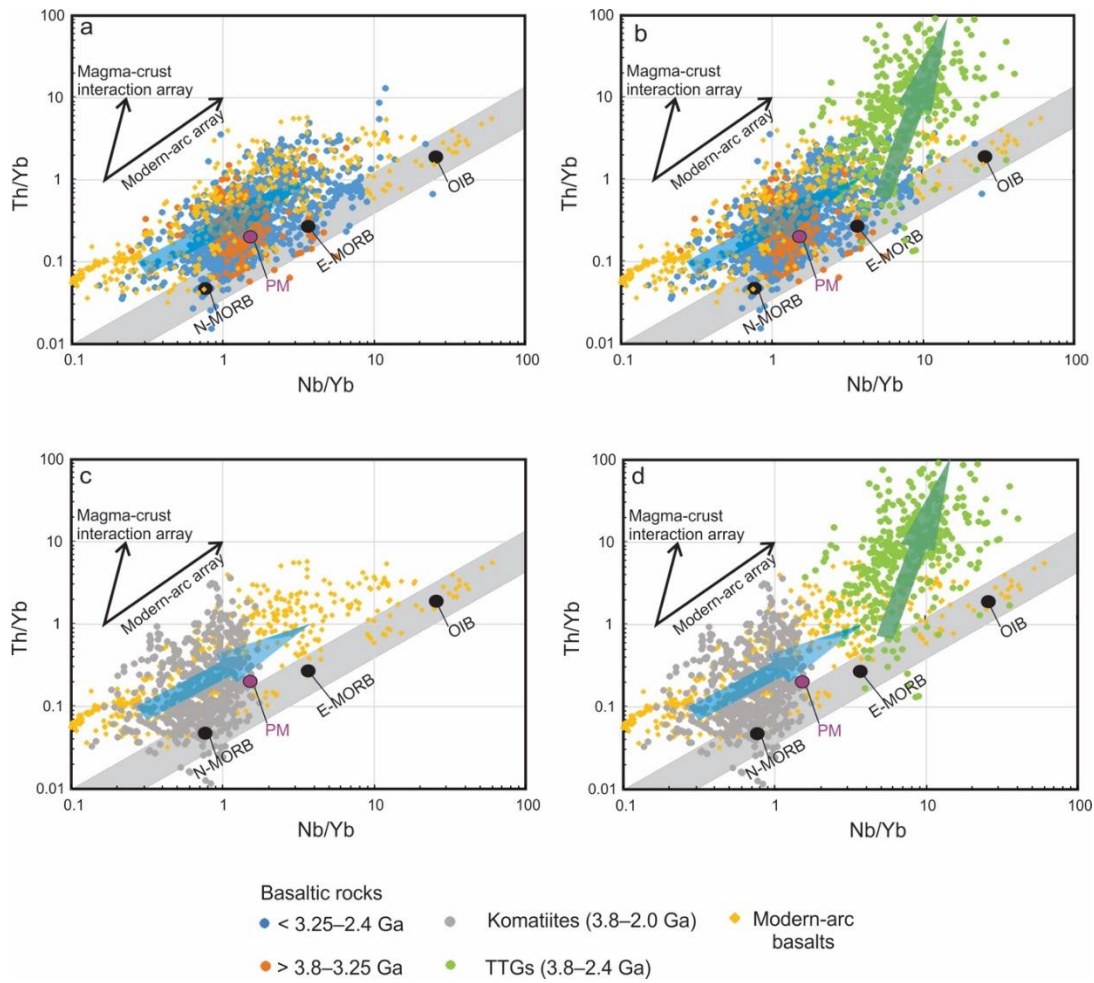


Figure H. 8: Nb/Yb-Th/Yb plots Pearce (2008) for the studied basalts (a, b), komatiites (c, d) and TTGs. The primitive mantle value is from McDonough and Sun (1995), and the modern-arc basalts datasets are collected from Georoc. The basalt and komatiite datasets define a trend (bold blue arrows) parallel to the oceanic mantle array (grey field), as do modern arc-basalts. In contrast, TTGs have an oblique trend (bold green arrow). Moreover, the Th/Yb ratios of the TTGs are significantly higher than that of the basalts and komatiites, indicating no crustal contamination.

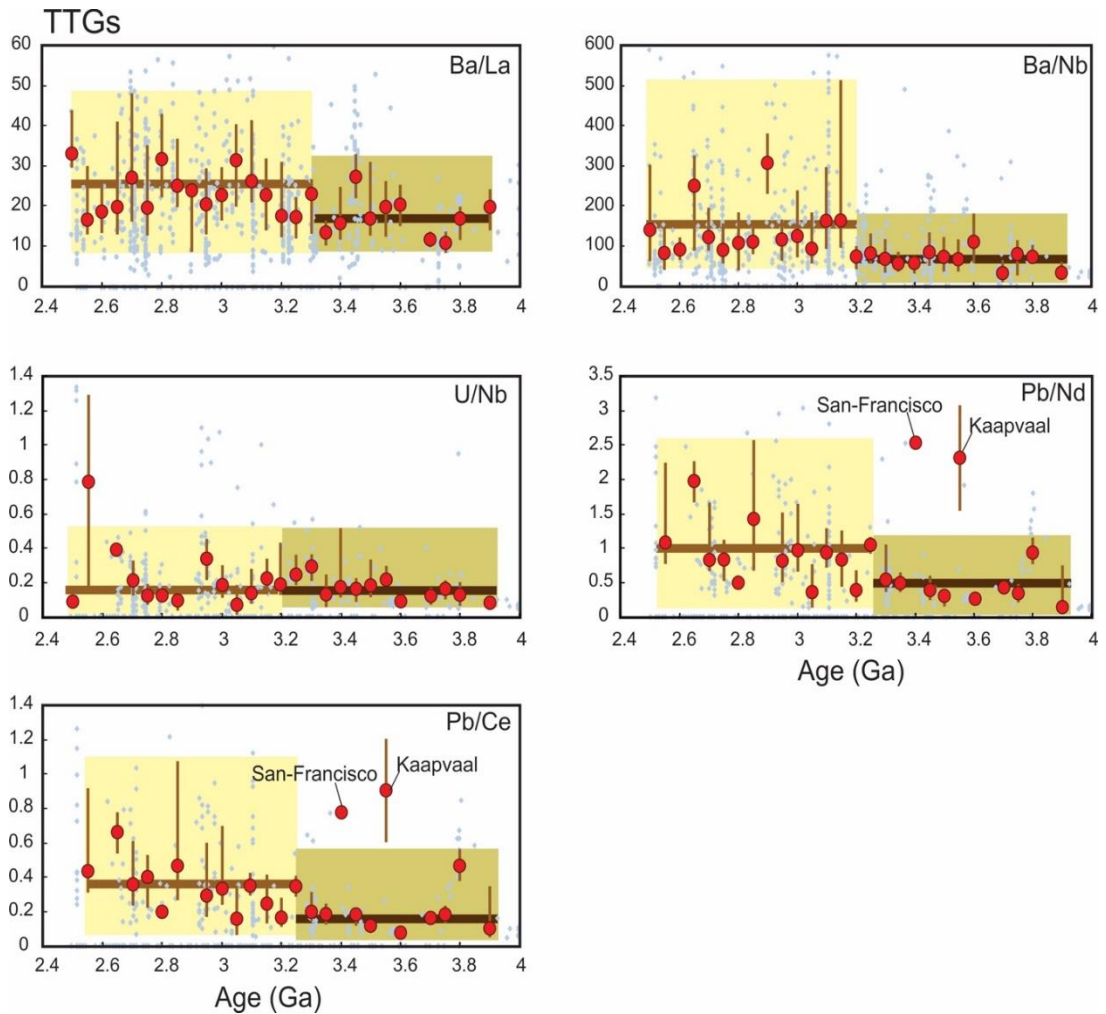


Figure H. 9. Plots of selected fluid-mobile/immobile elements ratios of tonalite-trondhjemite-granodiorite (TTG) rocks. Ba/La (a), Ba/Nb (b), U/Nb (c), Pb/Nd (d), and Pb/Ce. Grey dots represent the entire data compiled from Johnson et al. (2019). Red dots represent the medians using 50 Myr windows, and vertical bars span across the middle 50% of the data, called here the median data range. The rectangular shades of different colours represent the median data range before and after $\sim 3.3\text{--}3.2$ Ga. Solid horizontal lines are the average of medians for data within each rectangular shade. For Pb/Nd and Pb/Ce, datasets from the Kaapvaal and San-Francisco cratons show abnormal increase at 3.55 and 3.4 Ga which we take as representing local events. All but the U/Nb ratios show a step change to a higher value after $\sim 3.3\text{--}3.2$ Ga.

References (Appendix H)

Johnson, T. E. *et al.* (2019) 'Secular change in TTG compositions: Implications for the evolution of Archaean geodynamics', *Earth and Planetary Science Letters*. Elsevier, 505, pp. 65–75. doi: 10.1016/j.epsl.2018.10.022.

McDonough, W. . and Sun, S. –. (1995) 'The composition of the Earth', *Chemical Geology*, 120, pp. 223–252. doi: doi.org/10.1016/0009-2541(94)00140-4.

Pearce, J. A. (2008) 'Geochemical fingerprinting of oceanic basalts with applications to ophiolite classification and the search for Archean oceanic crust', *Lithos*, 100(1–4), pp. 14–48. doi: 10.1016/j.lithos.2007.06.016.

“Every reasonable effort has been made to acknowledge the owners of copyright material. I would be pleased to hear from any copyright owner who has been omitted or incorrectly acknowledged.”

Chapter 10:

Summary and future perspective: Geochemical records of the Earth's Mantle evolution from global- to nano- scale

This thesis set out to decipher the processes that played a significant role in Earth's dynamic evolution through geological time by studying the geochemical record of mantle-derived/related rocks, for example, ultramafic rocks, basalts, and juvenile granitoids. In this thesis, I focused on (1) an early start of global subduction and its influence on the deep mantle composition, (2) feedback mechanisms between plate tectonics and the first-order mantle structure, superplumes, and supercontinent cycles, (3) crustal growth and the extraction of juvenile continental crust from the Neoproterozoic mantle, using the Egyptian Nubian Shield as an example, and (4) the effect of subduction zones on the geochemical cycle and mantle heterogeneity. To explore these processes, I combined different approaches ranging from global-scale to nano-scale perspectives. For the global-scale approach, I have extracted, filtered, and analysed mafic-ultramafic rock (basalts, picrites, and komatiites) datasets from a global database for the entirety of Earth's history. I also studied the minerals using the cutting-edge atom probe tomography (APT) technique to investigate the mantle heterogeneities at the atomic-scale (see chapter 2 for methodology).

The following headlines are the major outcomes and findings of this Ph.D. thesis. I begin by addressing how the global processes (global-scale) affect the Earth's dynamic evolution by discussing the above-mentioned points 1 and 2. I then move to the regional-scale by addressing point 3, and finally the micro- to nano-scale through discussing point 4.

10.1 Mantle re-fertilization and the start of global subduction at ~3.2 Ga

Progressive mantle melting during the Earth's earliest evolution led to the formation of a depleted mantle and a continental crust enriched in highly incompatible elements (Figure 1.2b). It is commonly believed that before the plate tectonics regime, a chemically stratified Earth had a relatively homogeneous mantle composition (Condie, 2018; Moyen and Laurent, 2018) (due to the lack of large/global-scale recycling of terrestrial materials into the upper and lower mantle) that was depleted in highly incompatible elements (e.g. Ba, Pb, Rb, Cs, Sr, and U) but enriched in high field strength elements (e.g. Nb and Ta) (Hofmann, 1988). Re-enrichment/re-fertilization of Earth's mantle can occur when continental crustal materials begin to founder into the mantle, mainly through subduction profoundly affecting the mantle's trace element and volatile compositions (Stern, 2002b). The key process of plate tectonics is widespread subduction (Clift and Vannucchi, 2004; Sobolev and Brown, 2019). Subduction zones recycle terrestrial materials back into Earth's mantle as the subducting slab sinks and re-equilibrates within Earth's interior (Stern, 2002b; Clift and Vannucchi, 2004; Willbold and Stracke, 2010). So, a globally-detectable large change in the mantle heterogeneity (Hofmann, 1997, 2014; Bennett, 2003), caused by a refertilization/re-enrichment in incompatible and fluid mobile elements, could identify the onset of global-scale subduction and plate tectonic processes.

In Chapter 9, I used a global geochemical database of the Archean to Early-Proterozoic mantle-derived melts (i.e., basalts and komatiites) to detect the onset of global mantle re-enrichment/refertilization. This was achieved through tracking the change of the abundances of petrogenetically significant isotopic values (Nd isotopes) and key ratios of highly incompatible elements compared to lithophile elements (i.e., Ba/La, Ba/Nb, U/Nb, Pb/Nd, and Pb/Ce) in basaltic and komatiitic rocks (Figures 9.1-3). The results showed a significant increase in magnitude and variability of these geochemical proxies after ~3.2 Ga, whereas the mantle before that time displayed a primitive-like composition.

I hypothesize that the rapid increases in mantle heterogeneity indicate the recycling of supracrustal materials back into Earth's mantle via subduction, leading to a significant change in the upper and lower mantle composition. The notable change in komatiites' composition highlights the role of deep subduction in

modifying the mantle at this time. These new observations thus point to a ≥ 3.2 Ga onset of global subduction processes via plate tectonics.

In Chapter 8, by using the statistical bootstrapping method on the global geochemical database of basaltic rocks, I show a consistent sudden drop in MgO, Ni, and Cr at $\sim 3.2\text{--}3.0$ Ga (Figure 8.3a-c), interpreted to indicate an abrupt change in mantle temperature which may indicate the initiation of global plate tectonics (which is in agreement with the detecting mantle global re-enrichment event at ~ 3.2 Ga), where the subduction-driven whole-mantle convection enhanced the heat flux out of the core and mantle.

Then, I suggested ~ 3.2 Ga as a pivotal moment in Earth's history, with the emergence of global (and potentially deep) subduction processes and the beginning of the plate tectonics, which plays a key role in shaping the Earth's interior structure and composition.

10.2 Plate tectonics and superplumes-supercontinental coupling

The Earth's mantle structure, composition, and dynamics are controlled by plate tectonics and subduction (Bennett, 2003; Condie, 2016). The present Earth's interior structure, particularly the lower mantle, is dominated by two antipodal large low shear velocity provinces (LLSVPs), known as the African and Pacific superplumes (Dziewonski, Lekic, and Romanowicz, 2010) (Figure 1.3). However, how plate tectonics interact with mantle processes and influence the lower mantle structure, i.e. LLSVPs, remains unclear. Mantle plumes, since around 200 Ma, have been suggested to be generated and closely related to these two LLSVPs (Burke et al., 2008; Torsvik et al., 2014). It has been established that the African LLSVP was located underneath the supercontinent Pangaea ca. 200 Ma (Burke and Torsvik, 2004), and there was a close link between mantle plumes and Pangaea breakup (Courtillot *et al.*, 1999). Li and Zhong (2009) analysed the evolution of supercontinents and superplumes throughout geological history and, combined with three-dimensional numerical simulations, proposed that ongoing peripheral subduction after supercontinent assembly leads to the accumulation of oceanic slabs at the mantle transition zone. The accumulated slabs avalanche and sink to the core-mantle boundary, inducing the rise of a mantle superplume (i.e. LLSVPs), which

could potentially lead to the breakup of the supercontinent. However, nature and evolution histories of these two LLSVPs, including how long the LLSVPs have been present, how such LLSVPs interact with tectonic plates in Earth history, and whether they are fixed in the deep mantle (Dziwonski, Lekic, and Romanowicz, 2010; Torsvik *et al.*, 2010, 2014) or part of a dynamic system associated with the supercontinent cycle since at least the Proterozoic (Zhong *et al.*, 2007; Li *et al.*, 2008, 2019; Li and Zhong, 2009), remain topics of debate. Thus, tracking mantle plume activities/signatures throughout Earth's history is fundamental to answering those questions.

In Chapter 8, I used global geochemical analyses of basaltic magmatism to investigate the stable vs. dynamic/cyclic nature of the LLSVPs. I demonstrated that the transition elements (Ni, Cr, and Fe/Mn) represent an excellent tool for discriminating between plume- (oceanic island basalts, oceanic flood basalts, and continental large igneous provinces) and non-plume-related (mid-ocean ridge basalts and arc-related basalts) magmatism. These elements can also be used to trace plume-related magmatism throughout Earth's history.

The analyses (using the statistical bootstrapping method) suggest a direct relationship between the intensity of plume magmatism and the supercontinent cycle and therefore support a dynamic coupling between first-order mantle structures (e.g., LLSVPs) and plate tectonics. So, these results suggest a possible dynamic coupling between superplume events and supercontinent cycles.

There are three Pre-Cambrian and Phanerozoic supercontinents called Nuna, Rodinia, and Pangea (Evans, Li, and Murphy, 2016; Nance and Murphy, 2018; Pastor-Galán *et al.*, 2018; Li *et al.*, 2019). The episodic assembly, tenure, and breakup (termed the supercontinent cycle), and the transition from one supercontinent to another, are closely related to global orogenesis and crustal growth and have an important impact on the mantle composition (Doucet *et al.*, 2020). Because the transition between the breakup of a supercontinent and the assembly of the next supercontinent has a deep effect on crustal growth, and the mantle structure and composition, we need to study such transitions. The best way to do so is to study geological regions that are relics of such transitions, i.e. regional-scale studies. The Arabian-Nubian Shield (ANS) is a typical example of continental crust generation

that formed during the transition between the breakup of Rodinia through to Gondwana assembly, which then led to the assembly of Pangea (Stern, 1994; Fritz *et al.*, 2013). Studying the ANS, particularly the Egyptian Nubian Shield as an example, can then provide the opportunity to address the crustal growth process and the effect of extraction of juvenile continental crust on the Neoproterozoic mantle evolution/nature.

10.3 Crustal evolution of the Egyptian Nubian Shield

The ANS represents one of the largest exposures of Neoproterozoic juvenile continental crust on Earth (Figure 3.1b; Pease and Johnson, 2013). The Eastern Desert of Egypt (i.e., Egyptian Nubian Shield) constitutes the north-western part of the ANS (Figure 3.2). Island-arc accretion during the assembly of Gondwana has been proposed to be the main mechanism for the Neoproterozoic crustal growth of the ANS (Kröner *et al.*, 1991; Stern, 1994, 2002a; Johnson and Woldehaimanot, 2003; Johnson *et al.*, 2011; Fritz *et al.*, 2013). However, the size of the ANS and its Neoproterozoic growth rate significantly exceeds that of present-day examples of crustal generation via the addition of juvenile mantle materials to arcs along subduction margins (Reymer and Schubert, 1984, 1986). As an alternative mechanism for Neoproterozoic crustal generation in the ANS, it has been proposed that mantle plume-related magmatism may also have played a major role (Stein and Goldstein, 1996; Stein, 2003). Although Neoproterozoic plume- and/or rift-related magmatism is well developed globally during the fragmentation of the supercontinent Rodinia (Li *et al.*, 2008), there is currently no direct record of such magmatism in all ANS terranes. Also, the lack of adequate precise geochronological and isotopic constraints of the magmatic activities hampered a comprehensive understanding of the crustal growth and evaluate the possibility of the presence of plume and/or rifting magmatism.

In this Ph.D. thesis, I reported the occurrence of the largest known plagiogranitic pluton on Earth (the El-Shadli plutonic complex) (~5,000 km²) (Chapter 3) and the El-Shadli bimodal volcanic suite (80 km x 35 km and >10 km-thick) (Chapter 4), discovered in the southern Eastern Desert of Egypt. These are interpreted to have occurred during Rodinia break-up, which may have been linked

to a mantle plume. The El-Shadli plutonic complex (plagiogranites and associated gabbroic rocks) and bimodal volcanic suite are characterized by a tholeiitic affinity with very low K₂O (< 1 wt.%) and flat-like REE patterns similar to N-MORB. Zircon U-Pb ages (using SHRIMP and LA-SS-ICPMS methods) of the El-Shadli plutonic complex range from ~730 to ~722 Ma; whereas the volcanics have an age of ~700 Ma. Whole-rock geochemical and Nd-Sr isotopic data coupled with zircon U-Pb-Hf-O-trace element data suggest that the El-Shadli plutonic complex and volcanics rocks were derived from a juvenile parental magma that was produced by partial melting of the gabbroic oceanic lower crust. Finally, the geochemical and geological data suggest that both the El-Shadli plutonic complex and the overlaying bimodal volcanic suite formed by extensive partial melting of a juvenile continental crust (i.e., accreted oceanic slabs) during Rodinia break-up/rifting. These results argue against the widely held belief that the Neoproterozoic crustal growth in the ANS, particularly the Egyptian Nubian Shield, was only driven by arc magmatism; instead, magmatism formed in other tectonic settings such as mantle plume and continental rifting may also have played important roles.

In Chapter 5, I addressed the magmatic activities and the crustal evolution of the Eastern Desert. This study presents a complication of all previously published whole-rock Nd-Sr isotopes and zircon U-Pb-Hf-O and trace elements of granitoids and volcanic rocks from the Eastern Desert, together with new and similar isotopic datasets obtained from the Genina Gharbia granitoid in the south Eastern Desert and also similar datasets from the post-accretion rifting magmatism of the El-Shadli plutonic complex and volcanics. I demonstrated that the crustal growth and reworking of the Eastern Desert are characterized by an overall juvenile nature. I reported that Neoproterozoic crustal growth in the Eastern Desert evolved through three major episodes at ~730 Ma, ~700 Ma, and ~600 Ma, respectively. This process involved the changing of the magmatic activities at ~650 Ma from pre-collision (~800–650 Ma, oceanic lithosphere-related magmatism, accretion, and reworking) to syn- to post-collision (~650–550 Ma).

As the ANS represents a typical arc-accretion orogen (Stern et al., 2004), the ongoing subductions during this orogen would affect the geochemical cycle of the sub-arc mantle. Also, the subduction polarity during this accretionary orogen is still a matter of debate and needed to be addressed (Abd El-Rahman *et al.*, 2009). I tackled

those points through the study of selected Neoproterozoic subduction-related peridotites (i.e., serpentinites) from the Eastern Desert.

10.4 Sub-arc mantle geochemical cycle and subduction polarity: implication for temperature control on trace elements (re)-mobilization

Subduction zones are the largest recycling system, where sediments, oceanic crust, and mantle lithosphere return to and re-equilibrate with Earth's mantle leading to a significant influence on its geochemical cycle in general (Stern, 2002b). Serpentinites/serpentinitized peridotites are a major potential carrier of water (up to 15 %) and incompatible fluid-mobile elements (FME) such as Li, B, As, Sb, Pb, Ba, Cs, U, and Sr into the subduction zone and the overlying mantle wedge (Rüpke et al., 2004; Deschamps et al., 2013; Kendrick et al., 2017). Serpentinites can be stable to high temperatures (620 °C) and pressures (5 GPa) at depths of up to 150–200 km (Ulmer and Trommsdorff, 1995), and their hydration and subsequent dehydration critically influence the sub-arc mantle composition and the generation and chemistry of the arc magmas (Tatsumi, 1989; Hattori and Guillot, 2003; Pagé and Hattori, 2017). Thus, deciphering the dehydration/devolatilization processes of serpentinites represents a critical role in understanding trace element geochemical cycles in subduction zones and their feedback on mantle chemistry. However, the factors and mechanisms that control the transfer of the trace elements from oceanic environments through subducting serpentinites to the sub-arc mantle (i.e., mantle wedge) and then to arc magmatism are still unclear.

In Chapter 7, using a detailed micro-scale *in situ* LA-ICP-MS trace elements analyses for serpentine and carbonate minerals coupled with thermodynamic modelling from serpentinite bodies in the Eastern Desert, I reported the role of antigorite (a serpentine mineral phase) in the transportation of FME and light rare earth elements (LREE) from the subducted slab to the mantle wedge and arc-related magma during subduction. In addition to antigorite, the mineral chemistry of carbonate minerals indicates that magnesite represents a potential reservoir for transferring the FME and LREE to the deep mantle. I identified that temperature is the main controlling factor for the stability of these minerals and therefore the release of these elements from subducted slabs into arc magmatism. As the liberation of these

elements varies along the length of the slab, the resulting cross-arc geochemical variation trend can help to determine the subduction polarity of ancient arcs (Figure 7.7).

The subduction inputs to the sub-arc mantle or even to the deep mantle have a great impact on the mantle processes and its heterogeneity (Stern, 2002b; Schmidt and Poli, 2013). I addressed this point at a nano-scale through studying the Cr-spinel, the most resistant mineral in mantle-derived peridotites.

10.5 Mantle melting and metasomatism: Cr-spinel a new tool to decipher the mantle heterogeneity

Mantle partial melting, at the sub-arc mantle and in the mantle away from subduction zones, is a fundamental process that has an impact on geochemical cycling between the crust and the mantle, chemical stratification of the Earth, and therefore the evolution of both the crust and the mantle. Cr-spinel (i.e., Cr# ($\text{Cr}/(\text{Cr} + \text{Al})$)) in mantle peridotites (including mantle xenoliths, abyssal peridotites, and ophiolitic peridotites) has been widely used for determining mantle partial melting processes (Irvine, 1967; Dick and Bullen, 1984; Hellebrand et al., 2001). However, mantle peridotites generally experience complex metasomatic and metamorphic processes that can potentially obliterate their primary residual origin. These post-formation processes play a significant role in the modification of Cr-spinel composition, i.e. heterogeneity.

In Chapter 6, I conduct, for the first time, a correlative microanalysis workflow from the grain-scale to the nano-scale using X-ray elemental mapping, EMP, LA-ICP-MS, EBSD, and atom probe tomography to describe the Cr-spinel heterogeneity in mantle peridotites from the ANS. The result demonstrates that there is significant Al-Cr heterogeneity, which is characterized by Al enrichment and Cr depletion in the rim compared to the core of the studied crystals (Figure 6.1). The new analyses and a careful review of published results of Cr-spinel from different tectonic settings showed that the chemical composition of Cr-spinel can be easily and severely modified by cryptic metasomatism through fluid/melt-rock interactions involving slab-derived fluids in the sub-arc mantle, or even by small volumes of melts in the sub-oceanic mantle. I also identified Cr-spinel as a carrier of FME, especially

in subduction zone environments where Al is easily mobilised by fluids and melts and therefore cannot be used as a melting degree indicator, at least at the mineral scale. Furthermore, the heterogeneity of Cr# in Cr-spinel can be used as a powerful tracer for Cr-spinel metasomatic modification.

These findings will have new applications in (1) providing a framework for a re-evaluation of Cr-spinel compositions in mantle rocks, (2) using Cr-spinel composition as a melt-rock interaction indicator and as a tracer of mantle heterogeneity, and (3) Cr-spinel as an FME-carrying mineral may also provide a feeding mechanism for FME into the deep mantle chemical cycle. The present findings will also help to develop a new way of deciphering deep mantle metasomatism and heterogeneity through analysing non-traditional isotopes (e.g., Li, Zn, Ti, and Ni) in Cr-spinel.

10.6 Future work

This study sheds light on some of the main processes that play a significant role in the evolution of Earth's dynamics. This study suggests that plate tectonics has a major impact on changing the Earth's mantle composition and dynamics at different scales ranging from the global-, regional- to the micro- and nano-scale. However, the outcomes of this thesis present new findings that have a lot of further applications and provide even more questions that need to be explored in future work. Regarding the early evolution of the Earth's mantle, more isotopic and geochemical investigation of the mantle-derived rocks (komatiites and basalts), for example from the Pilbara and Singhbhum cratons, will help to answer when exactly the mantle composition started to be re-enriched after the early depletion/stratification, when did whole mantle convection start, including the lower mantle, and at what depth did the Archaean komatiites and plume-related basalts form. Future studies on the Archaean komatiites and plume-related basalts can also help to address when the LLSVPs started to form. Regarding the crustal growth of the ANS, further studies should address the possibility for the presence of other rift- and plume-related magmatism before ~730 Ma in the Eastern Desert or even throughout all of the ANS. These studies should include detailed fieldwork and geochemical and isotopic data to investigate the origin of the mafic-ultramafic layered intrusions that are highly abundant in the south Eastern Desert around the El-Shadli area. Also, more studies

can be done on the post-collision magmatism (such as A-type granites and within-plate alkaline volcanics) to assess the nature of the collision that starts around ~650 Ma, how it occurred and what other geological evidence is there for such a collision. The future work related to subduction zone geochemical cycles and deep mantle heterogeneity will include (1) characterization of the fluid inclusions of different serpentine phases to understand the nature of subduction zone fluids at different temperature and depth, (2) atom probe exploration of serpentinites, and magnesite to trace which FME are found within their structure, (3) thermodynamic modelling to explore at which pressure and temperature magnesite can be stable in the lower mantle, (4) using Cr-spinel in Archean mantle xenoliths to track the mantle heterogeneity at this time, and (5) developing an *in situ* isotopic analyses (such as Li and O) for the Cr-spinel to track the recycling of the subduction materials that lead to the deep mantle enrichments.

10.7 References

- Abd El-Rahman, Y. *et al.* (2009) 'Geochemistry and tectonic evolution of the Neoproterozoic incipient arc-forearc crust in the Fawakhir area, Central Eastern Desert of Egypt', *Precambrian Research*, 175(1–4), pp. 116–134. doi: 10.1016/j.precamres.2009.09.008.
- Bennett, V. C. (2003) 'Compositional Evolution of the Mantle', *Treatise on Geochemistry*. Pergamon, pp. 493–519. doi: 10.1016/B0-08-043751-6/02013-2.
- Burke, K. *et al.* (2008) 'Plume Generation Zones at the margins of Large Low Shear Velocity Provinces on the core-mantle boundary', *Earth and Planetary Science Letters*, 265(1–2), pp. 49–60. doi: 10.1016/j.epsl.2007.09.042.
- Burke, K. and Torsvik, T. H. (2004) 'Derivation of Large Igneous Provinces of the past 200 million years from long-term heterogeneities in the deep mantle', *Earth and Planetary Science Letters*, 227(3–4), pp. 531–538. doi: 10.1016/j.epsl.2004.09.015.
- Clift, P. and Vannucchi, P. (2004) 'Controls on tectonic accretion versus erosion in subduction zones: Implications for the origin and recycling of the continental crust', *Reviews of Geophysics*. John Wiley & Sons, Ltd, 42(2), p. RG2001. doi: 10.1029/2003RG000127.
- Condie, K. C. (2016) *Earth as an Evolving Planetary System*. Elsevier. doi: 10.1016/C2015-0-00179-4.
- Condie, K. C. (2018) 'A planet in transition: The onset of plate tectonics on Earth between 3 and 2 Ga?', *Geoscience Frontiers*, 9(1), pp. 51–60. doi: 10.1016/j.gsf.2016.09.001.
- Courtillot, V. *et al.* (1999) 'On causal links between flood basalts and continental breakup', *Earth and Planetary Science Letters*, 166(3–4), pp. 177–195. doi: 10.1016/S0012-821X(98)00282-9.
- Deschamps, F. *et al.* (2013) 'Geochemistry of subduction zone serpentinites: A review', *Lithos*, 178(APRIL), pp. 96–127. doi: 10.1016/j.lithos.2013.05.019.
- Dick, H. J. B. and Bullen, T. (1984) 'Chromian spinel as a petrogenetic indicator in abyssal and alpine-type peridotites and spatially associated lavas', *Contributions to Mineralogy and Petrology*, 86(1), pp. 54–76. doi: 10.1007/BF00373711.
- Doucet, L. S. *et al.* (2020) 'Distinct formation history for deep-mantle domains reflected in geochemical differences', *Nature Geoscience*. Springer US, 13(July). doi: 10.1038/s41561-020-0599-9.
- Dziewonski, A. M., Lekic, V. and Romanowicz, B. A. (2010) 'Mantle Anchor Structure: An argument for bottom up tectonics', *Earth and Planetary Science Letters*. Elsevier B.V., 299(1–2), pp. 69–79. doi: 10.1016/j.epsl.2010.08.013.
- Evans, D. A. D., Li, Z. X. and Murphy, J. B. (2016) 'Four-dimensional context of Earth's supercontinents', in Li, Z., Evans, David A.D., and Murphy, J. B. (eds) *Geological Society Special Publication*. Geological Society of London, pp. 1–14. doi: 10.1144/SP424.12.
- Fritz, H. *et al.* (2013) 'Orogen styles in the East African Orogen: A review of the

- Neoproterozoic to Cambrian tectonic evolution', *Journal of African Earth Sciences*. Elsevier Ltd, 86, pp. 65–106. doi: 10.1016/j.jafrearsci.2013.06.004.
- Hattori, K. H. and Guillot, S. (2003) 'Volcanic fronts as a consequence of serpentinite dehydration in the mantle wedge', *Geology*, 31, pp. 525–528. doi: 10.1130/0091-7613(2003)031<0525:vffaac>2.0.co;2.
- Hellebrand, E. *et al.* (2001) 'Coupled major and trace elements as indicators of the extent of melting in mid-ocean-ridge peridotites', *Nature*, 410(6829), pp. 677–681. doi: 10.1038/35070546.
- Hofmann, A. W. (1988) 'Chemical differentiation of the Earth: the relationship between mantle, continental crust, and oceanic crust', *Earth and Planetary Science Letters*. Elsevier, 90(3), pp. 297–314. doi: 10.1016/0012-821X(88)90132-X.
- Hofmann, A. W. (1997) 'Mantle geochemistry: the message from oceanic volcanism', *Nature*. Nature Publishing Group, 385(6613), pp. 219–229. doi: 10.1038/385219a0.
- Hofmann, A. W. (2014) 'Sampling Mantle Heterogeneity through Oceanic Basalts: Isotopes and Trace Elements', in *Treatise on Geochemistry*. Elsevier, pp. 67–101. doi: 10.1016/B978-0-08-095975-7.00203-5.
- Irvine, T. N. (1967) 'Chromian Spinel As a Petrogenetic Indicator: Part 2. Petrologic Applications', *Canadian Journal of Earth Sciences*, 4(1), pp. 71–103. doi: 10.1139/e67-004.
- Johnson, P. R. *et al.* (2011) 'Late Cryogenian-Ediacaran history of the Arabian-Nubian Shield: A review of depositional, plutonic, structural, and tectonic events in the closing stages of the northern East African Orogen', *Journal of African Earth Sciences*. Elsevier Ltd, 61(3), pp. 167–232. doi: 10.1016/j.jafrearsci.2011.07.003.
- Johnson, P. R. and Woldehaimanot, B. (2003) 'Development of the Arabian-Nubian Shield: perspectives on accretion and deformation in the northern East African Orogen and the assembly of Gondwana', *Geological Society, London, Special Publications*, 206(1), pp. 289–325. doi: 10.1144/GSL.SP.2003.206.01.15.
- Kendrick, M. A. *et al.* (2017) 'Seawater cycled throughout Earth's mantle in partially serpentinized lithosphere', *Nature Geoscience*. Nature Publishing Group, 10(3), pp. 222–228. doi: 10.1038/ngeo2902.
- Kröner, A. *et al.* (1991) 'Evolution of Pan-African island arc assemblages in the southern Red Sea Hills, Sudan, and in southwestern Arabia as exemplified by geochemistry and geochronology', *Precambrian Research*. Elsevier, 53(1–2), pp. 99–118. doi: 10.1016/0301-9268(91)90007-W.
- Li, Z. X. *et al.* (2008) 'Assembly, configuration, and break-up history of Rodinia: A synthesis', *Precambrian Research*, 160(1–2), pp. 179–210. doi: 10.1016/j.precamres.2007.04.021.
- Li, Z. X. *et al.* (2019) 'Decoding Earth's rhythms: Modulation of supercontinent cycles by longer superocean episodes', *Precambrian Research*. Elsevier, 323, pp. 1–5. doi: 10.1016/J.PRECAMRES.2019.01.009.

- Li, Z. X. and Zhong, S. (2009) 'Supercontinent-superplume coupling, true polar wander and plume mobility: Plate dominance in whole-mantle tectonics', *Physics of the Earth and Planetary Interiors*, 176(3–4), pp. 143–156. doi: 10.1016/j.pepi.2009.05.004.
- Moyen, J. F. and Laurent, O. (2018) 'Archaean tectonic systems: A view from igneous rocks', *Lithos*. Elsevier B.V., 302–303, pp. 99–125. doi: 10.1016/j.lithos.2017.11.038.
- Nance, R. D. and Murphy, J. B. (2018) 'Supercontinents and the case for Pannotia', *Geological Society, London, Special Publications*, p. SP470.5. doi: 10.1144/SP470.5.
- Pagé, L. and Hattori, K. (2017) 'Tracing halogen and B cycling in subduction zones based on obducted, subducted and forearc serpentinites of the Dominican Republic', *Scientific Reports*, 7(1), pp. 1–9. doi: 10.1038/s41598-017-18139-7.
- Pastor-Galán, D. *et al.* (2018) 'Supercontinents: myths, mysteries, and milestones', *Geological Society, London, Special Publications*. Geological Society of London, 470, p. SP470.16. doi: 10.1144/SP470.16.
- Pease, V. and Johnson, P. R. (2013) 'Introduction to the JEBEL volume of Precambrian Research', *Precambrian Research*, 239, pp. 1–5. doi: 10.1016/j.precamres.2013.10.003.
- Reymer, A. and Schubert, G. (1984) 'Phanerozoic addition rates to the continental crust and crustal growth', *Tectonics*. John Wiley & Sons, Ltd, 3(1), pp. 63–77. doi: 10.1029/TC003i001p00063.
- Reymer, A. and Schubert, G. (1986) 'Rapid growth of some major segments of continental crust', *Geology*. GeoScienceWorld, 14(4), p. 299. doi: 10.1130/0091-7613(1986)14<299:RGOSMS>2.0.CO;2.
- Rüpke, L. H. *et al.* (2004) 'Serpentine and the subduction zone water cycle', *Earth and Planetary Science Letters*. Elsevier, 223(1–2), pp. 17–34. doi: 10.1016/J.EPSL.2004.04.018.
- Schmidt, M. W. and Poli, S. (2013) 'Devolatilization During Subduction', in *Treatise on Geochemistry: Second Edition*. Elsevier Inc., pp. 669–701. doi: 10.1016/B978-0-08-095975-7.00321-1.
- Sobolev, S. V. and Brown, M. (2019) 'Surface erosion events controlled the evolution of plate tectonics on Earth', *Nature*. Nature Publishing Group, 570(7759), pp. 52–57. doi: 10.1038/s41586-019-1258-4.
- Stein, M. (2003) 'Tracing the plume material in the Arabian-Nubian Shield', *Precambrian Research*, 123(2–4), pp. 223–234. doi: 10.1016/S0301-9268(03)00069-X.
- Stein, M. and Goldstein, S. L. (1996) 'From plume head to continental lithosphere in the Arabian–Nubian shield', *Nature*, 382, pp. 773–778. Available at: <https://doi.org/10.1038/382773a0>.
- Stern, R. J. (1994) 'ARC Assembly and Continental Collision in the Neoproterozoic East African Orogen: Implications for the Consolidation of Gondwanaland', *Annual Review of Earth and Planetary Sciences*, 22(1), pp. 319–351. doi: 10.1146/annurev.earth.22.050194.001535.

- Stern, R. J. (2002a) 'Crustal evolution in the East African Orogen: a neodymium isotopic perspective', *Journal of African Earth Sciences*. Pergamon, 34(3–4), pp. 109–117. doi: 10.1016/S0899-5362(02)00012-X.
- Stern, R. J. (2002b) 'Subduction zones', *Reviews of Geophysics*. John Wiley & Sons, Ltd, 40(4), pp. 1–38. doi: 10.1029/2001RG000108.
- Stern, R. J. *et al.* (2004) 'Neoproterozoic Ophiolites of the Arabian-Nubian Shield', *Developments in Precambrian Geology*, 13(C), pp. 95–128. doi: 10.1016/S0166-2635(04)13003-X.
- Tatsumi, Y. (1989) 'Migration of fluid phases and genesis of basalt magmas in subduction zones', *Journal of Geophysical Research: Solid Earth*. John Wiley & Sons, Ltd, 94(B4), pp. 4697–4707. doi: 10.1029/JB094iB04p04697.
- Torsvik, T. H. *et al.* (2010) 'Diamonds sampled by plumes from the core-mantle boundary', *Nature*. Nature Publishing Group, 466(7304), pp. 352–355. doi: 10.1038/nature09216.
- Torsvik, T. H. *et al.* (2014) 'Deep mantle structure as a reference frame for movements in and on the Earth', *Proceedings of the National Academy of Sciences*, 111(24), pp. 8735–8740. doi: 10.1073/pnas.1318135111.
- Ulmer, P. and Trommsdorff, V. (1995) 'Serpentine stability to mantle depths and subduction-related magmatism.', *Science (New York, N.Y.)*. American Association for the Advancement of Science, 268(5212), pp. 858–61. doi: 10.1126/science.268.5212.858.
- Willbold, M. and Stracke, A. (2010) 'Formation of enriched mantle components by recycling of upper and lower continental crust', *Chemical Geology*. Elsevier, 276(3–4), pp. 188–197. doi: 10.1016/J.CHEMGEO.2010.06.005.
- Zhong, S. *et al.* (2007) 'Supercontinent cycles, true polar wander, and very long-wavelength mantle convection', *Earth and Planetary Science Letters*, 261(3–4), pp. 551–564. doi: 10.1016/j.epsl.2007.07.049.

**ATTRIBUTION
STATEMENTS AND
COPYRIGHTS
INFORMATION**



RightsLink®

?
Help

✉
Email Support

SPRINGER NATURE

Cr-spinel records metasomatism not petrogenesis of mantle rocks

Author: Hamed Gamal El Dien et al

Publication: Nature Communications

Publisher: Springer Nature

Date: Nov 8, 2019

Copyright © 2019, The Author(s)

Creative Commons

This is an open access article distributed under the terms of the [Creative Commons CC BY](#) license, which permits unrestricted use, distribution, and reproduction in any medium, provided the original work is properly cited.

You are not required to obtain permission to reuse this article.

To request permission for a type of use not listed, please contact [Springer Nature](#)

© 2020 Copyright - All Rights Reserved | [Copyright Clearance Center, Inc.](#) | [Privacy statement](#) | [Terms and Conditions](#)
Comments? We would like to hear from you. E-mail us at customer care@copyright.com

ATTRIBUTION STATEMENTS

Table i: Attribution statement table for published -Chapter 6: *Cr-spinel records metasomatism not petrogenesis of mantle rocks*







	Conception and Design	Acquisition of Data and Method	Data Conditioning and Manipulation	Analysis and Statistical Method	Interpretation and Discussion	Final Approval	Total % contribution
Co-Author 1 (Hamed Gamal El Dien)	85	50	65	55	60	40	60
Co Author 1 Acknowledgment: I acknowledge that these represent my contribution to the above research output				Signed: 03/11/2020			
Co-Author 2 (Shoji Arai)	5				10	10	8
Co Author 2 Acknowledgment: I acknowledge that these represent my contribution to the above research output				Signed:			
Co-Author 3 (Luc-Serge Doucet)	5		20		10	10	7
Co Author 3 Acknowledgment: I acknowledge that these represent my contribution to the above research output				Signed: 04/11/2020			
Co-Author 4 (Zheng-Xiang Li)	5				10	20	5
Co Author 4 Acknowledgment: I acknowledge that these represent my contribution to the above research output				Signed:			
Co-Author 5 (Youngwoo Kil)		15		20			5
Co Author 5 Acknowledgment: I acknowledge that these represent my contribution to the above research output				Signed: 03/11/2020			
Co-Author 6 (Denis Fougerouse)		10	5	10	5	10	5
Co Author 6 Acknowledgment: I acknowledge that these represent my contribution to the above research output				Signed: 04/11/2020			
Co-Author 7 (Steven M. Reddy)		10	5	10	5	10	4
Co Author 7 Acknowledgment: I acknowledge that these represent my contribution to the above research output				Signed:			
Co-Author 8 (David W. Saxey)		10		5			3
Co Author 8 Acknowledgment: I acknowledge that these represent my contribution to the above research output				Signed: 04/11/2020			
Co-Author 9 (Mohamed Hamdy)		5	5				3
Co Author 9 Acknowledgment: I acknowledge that these represent my contribution to the above research output				Signed:			
Total %	100	100	100	100	100	100	100

ARTICLE

<https://doi.org/10.1038/s41467-019-13117-1>

OPEN

Cr-spinel records metasomatism not petrogenesis of mantle rocks

Hamed Gamal El Dien ^{1,2*}, Shoji Arai³, Luc-Serge Doucet¹, Zheng-Xiang Li ¹, Youngwoo Kil⁴, Denis Fougerouse ^{5,6}, Steven M. Reddy ^{5,6}, David W. Saxey ⁶ & Mohamed Hamdy ²

Mantle melts provide a window on processes related to global plate tectonics. The composition of chromian spinel (Cr-spinel) from mafic-ultramafic rocks has been widely used for tracing the geotectonic environments, the degree of mantle melting and the rate of mid-ocean ridge spreading. The assumption is that Cr-spinel's core composition ($Cr\# = Cr/(Cr + Al)$) is homogenous, insensitive to post-formation modification and therefore a robust petrogenetic indicator. However, we demonstrate that the composition of Cr-spinel can be modified by fluid/melt-rock interactions in both sub-arc and sub-mid oceanic mantle. Metasomatism can produce Al-Cr heterogeneity in Cr-spinel that lowers the Cr/Al ratio, and therefore modifies the Cr#, making Cr# ineffective as a geotectonic and mantle melting indicator. Our analysis also demonstrates that Cr-spinel is a potential sink for fluid-mobile elements, especially in subduction zone environments. The heterogeneity of Cr# in Cr-spinel can, therefore, be used as an excellent tracer for metasomatic processes.

¹Earth Dynamics Research Group, The Institute for Geoscience Research (TIGeR), School of Earth and Planetary Sciences, Curtin University, GPO Box U1987Perth, WA 6845, Australia. ²Geology Department, Faculty of Science, Tanta University, 31527 Tanta, Egypt. ³Department of Earth Science, School of Natural System, Kanazawa University, Kanazawa 920-1192, Japan. ⁴Department of Energy and Resources Engineering, College of Engineering, Chonnam National University, Yongbong-ro, Buk-gu, Gwangju, South Korea. ⁵School of Earth and Planetary Sciences, The Institute for Geoscience Research (TIGeR), Curtin University, GPO Box U1987Perth, WA 6845, Australia. ⁶Geoscience Atom Probe, Advanced Resource Characterisation Facility, John de Laeter Centre, Curtin University, GPO Box U1987Perth, WA 6845, Australia. *email: hamed.gamaleldien@postgrad.curtin.edu.au

Mantle partial melting is a fundamental process that has contributed to the chemical stratification of the Earth and plays a key role in the long-term evolution of the lithosphere and Earth's tectonic and geodynamic processes in general¹. Irvine^{2,3} first proposed to use chromian spinel ($(\text{Mg}, \text{Fe}^{+2})(\text{Cr}, \text{Al}, \text{Fe}^{+3})_2\text{O}_4$; hereafter Cr-spinel) in mafic-ultramafic rocks as a petrogenetic indicator because, at magmatic temperatures, this mineral is highly sensitive to the chemical conditions associated with melt generation in the mantle. Numerous subsequent studies have used the composition of Cr-spinel to estimate the degree of melt extraction, and therefore to discriminate among the different tectonic settings of ophiolitic complexes⁴. Arai⁵ systematically assessed spinel peridotites in terms of mantle melting conditions mainly based on the Cr# ($\text{Cr}/(\text{Cr} + \text{Al})$) of Cr-spinel in combination with olivine composition. Cr-spinel has thus been established as a reliable indicator for studying mantle petrology⁶, where the Cr# of Cr-spinel in residual peridotites has been viewed as a quantitative melting indicator for mantle residue based on the positive correlation between Cr# in Cr-spinel and degree of melting (see Fig. 3 of Hellebrand et al.⁶).

However, mantle peridotites generally experienced complex metasomatic and metamorphic processes that can potentially obliterate their primary residual origin. Cr-spinel can exhibit a chemical classic (normal) zoning due to melting and fractional crystallization processes characterized by Mg-Al-rich core and Cr-Fe⁺²-rich rim⁴, or metamorphism that commonly removes almost all the Al from the outer parts of the crystal, leaving behind magnetite/ferritichromite rims⁷. Moreover, reverse zoning (Mg- and Al-rich rim and Fe⁺²- and Cr-rich core) can also occur, and it is usually regarded as a result of stress and deformation⁸, elemental exchange with co-existing silicates⁹, or melt/rock interaction¹⁰. Reverse zoning is undetectable under an optical microscope, and it appears either concentric and/or asymmetric when observed in atomic number contrast under backscattered electron (BSE) imaging⁹, or remains non-observable under both an optical microscope and BSE (this study).

Here, we conduct a correlative microanalysis workflow from the grain-scale to the nano-scale using X-ray elemental mapping, electron microprobe (EMP), laser-ablation-inductively coupled plasma mass spectrometry (LA-ICPMS), electron backscattered diffraction (EBSD), and atom probe tomography (APT) in order to describe the Cr-spinel reverse zonation in mantle peridotites from the Arabian Nubian Shield. This type of reverse zoning “Al-Cr heterogeneity” is characterized by Al enrichment and Cr depletion in the rim compared to the core of the studied crystals. We demonstrate that this reverse zoning is unrelated to the magmatic or metamorphic/deformation history but is due to fluid/melt-rock interactions (i.e., metasomatism). The most striking feature is that such Cr-spinel Al-Cr heterogeneity is a widespread feature that affects the mantle rocks of various tectonic settings and ages (Supplementary Fig. 1 and Supplementary Data 1). We therefore question the robustness of Cr-spinel during post-formation modification, and thus the suitability of Cr-spinel as a straightforward reliable indicator for tracing mantle melting conditions and tectonic environments.

Results

Al-Cr reverse zoning in spinel: An example from the Arabian-Nubian Shield. The Arabian-Nubian Shield (ANS) represents the largest Neoproterozoic juvenile continental crust formed through accretion of island arcs to continental margins by the closure of the Mozambique Ocean during the East-African orogeny (750–550 Ma)^{11,12}. The peridotites in this study were sampled from serpentinite bodies at Wadi Alam in the Central Eastern

Desert of Egypt (Supplementary Fig. 2). Petrographic and textural investigations show that our peridotite samples consist of serpentine minerals, olivine relics, orthopyroxene bastites, carbonates, and Cr-spinels, with no amphiboles or chlorite. The samples have been affected by varying degrees of serpentinization. The predominance of pseudomorph textures as mesh and bastite reflects a harzburgite protolith (Supplementary Fig. 2). For more details about the geological background of the ANS see Gamal El Dien et al.¹³, and for field observations and petrographical and mineralogical descriptions of the studied rocks see Hamdy and Gamal El Dien¹⁴.

The petrological and geochemical characteristics of the studied peridotites reveal a highly depleted origin, as shown by (1) a harzburgitic, clinopyroxene-free modal composition, (2) their low Al_2O_3 and high MgO bulk-rock content (<1 wt% and >44 wt%, respectively) (Supplementary Fig. 3 and Supplementary Data 2) and (3) their low, heavy rare earth elements content (HREE; $\text{Yb}_{\text{N(CI-normalized value)}} = 0.01\text{--}0.04$) and low Y (<0.10 ppm) (Supplementary Fig. 4). Melting models, using non-modal fractional melting, reproduced the HREE values of our samples with a 25–30% melt extraction from a depleted MORB mantle (DMM) source^{15,16} (Supplementary Figs. 4, 5). This supports the highly refractory origin for the studied mantle peridotites. The bulk-rock major and trace element contents, and REE patterns, are similar to mantle wedge peridotites^{17–20} (Supplementary Figs. 3, 4). Despite their refractory origin, the studied peridotites exhibit enrichment in incompatible trace elements and light REE (LREE) (Supplementary Fig. 4). These enrichments are not correlated with either serpentinization (i.e., loss on ignition) (Supplementary Fig. 6) or the different melting indices used (Supplementary Fig. 3i), which indicates that the rocks underwent a post-melting metasomatic process²¹. This metasomatism process is believed to be due to fluid/melt-rock interaction between mantle wedge peridotites and slab-derived melts, as supported by a high enrichment of high field strengths elements (HFSE) (Supplementary Fig. 7) and fluid-mobile elements (FME) in those rocks¹⁴. Generally, migration of aqueous fluids/melts from a subducting slab enriches the overlying mantle with incompatible elements (i.e., FME) and water, yielding metasomatized sub-arc mantle^{22,23}.

Cr-spinel represents up to 2% of the mineral modal composition in our samples and exhibits a holly-leaf shape with a red color characteristic of residual peridotites²⁴. It presents as anhedral to subhedral grains of 50 μm to 2 mm in size. In BSE images, all Cr-spinel grains display small magnetite rims either surrounding a homogenous core and/or appearing in open cracks, indicating a late-stage modification (i.e., serpentinization and/or metamorphism; Fig. 1a and Supplementary Fig. 8). However, X-ray elemental mapping shows strongly heterogeneous and modified cores (Fig. 1b–f). These cores display a concentric and gradual (Fig. 1b, c, e, f) or asymmetrical (Fig. 1d) reverse zoning of highly Al-enriched and Cr-depleted rims and the opposite in the cores (we called this heterogeneity hereafter) with less variation in the distribution of Mg and Fe⁺² (Fig. 2, Supplementary Fig. 8, and Supplementary Data 2).

The cores of Cr-spinels show a wide variation in compositions between grains from the same sample (core-to-core: Figs. 1c, f and 2f), among samples (Figs. 1c–f and 2c–e), and within the same grain (core to rim: Figs. 1c–f, 2f and Supplementary Data 2). The Al_2O_3 content and Cr# display a continuous reverse variation trend from the cores (14.6–18.3 wt%, and 0.64–0.70, respectively) to the rims (19.6–26.1 wt % and 0.53–0.62, respectively) (Figs. 1c–f and 2c–f). Al_2O_3 content shows different covariation trends, from the cores to the rims, with transition elements such as Sc (negative correlation), Ti and Ni (positive correlation), Cu and Ga (no correlation), whereas V, Mn, Co, and Zn show V-shape

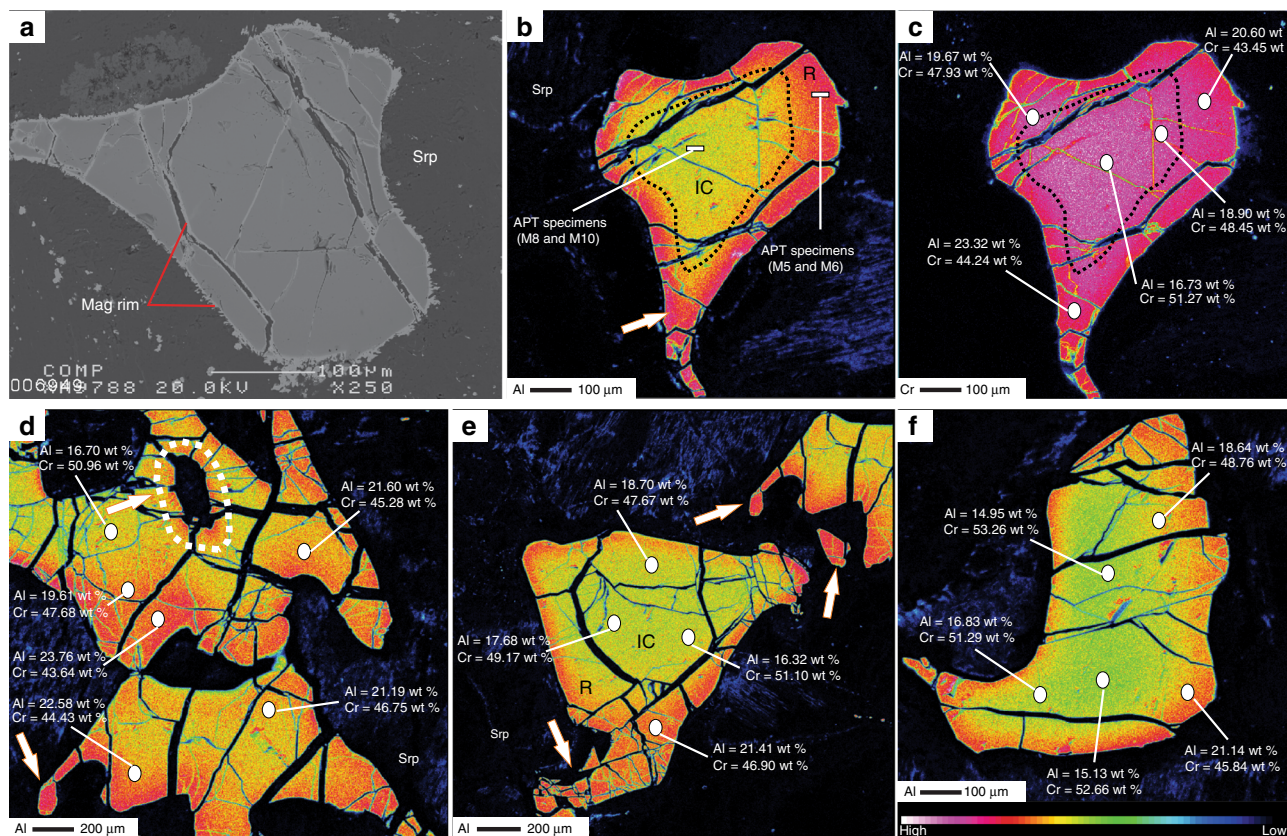


Fig. 1 X-ray elemental map of the studied Cr-Spinel. **a** Backscattered electron (BSE) image of a Cr-spinel grain with a homogenous core surrounded by a small magnetite rim. Al **(b)** and Cr **(c)** X-ray map for the same grain show reverse zoning for Al and Cr. Asymmetrical and heterogeneous distribution of Al-Cr within the core **(d)** and gradual increase of Al-Cr from core to rim **(b, c, e, f)** of three different Cr-spinel grains. White arrows point to Al halos around inclusions within the Cr-spinel grains **(d)** and high Al content in small grains with tightly curved rims **(b-e)**. The results of the Atom probe tomography (APT) specimens for the core (M8 and M10) and rim (M5 and M6) are shown in Fig. 5. Mag = magnetite, Srp = serpentine, IC = inner core and R = rim

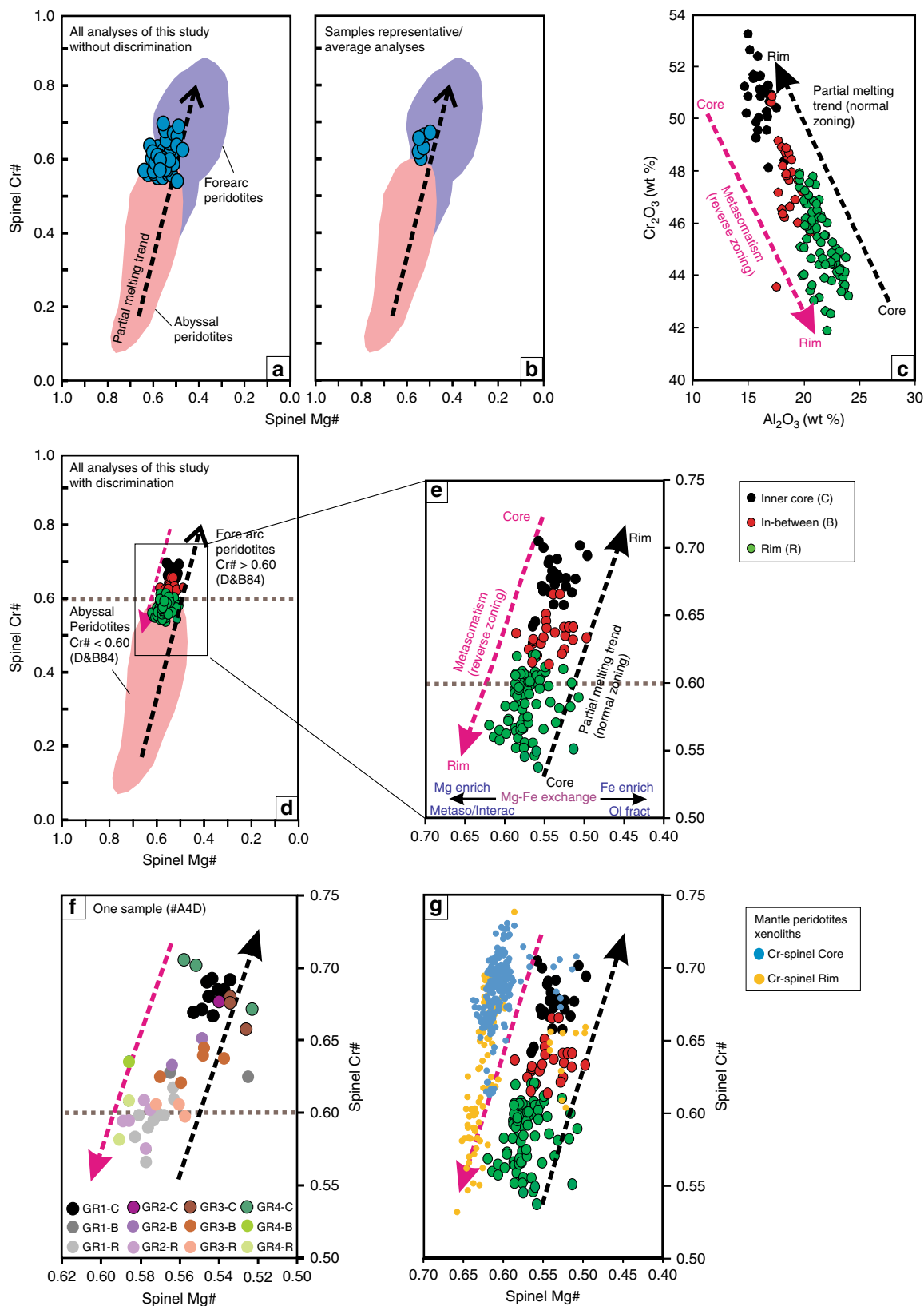
covariation trends (Supplementary Fig. 9). Fluid mobile elements (FME: Li, Rb, Sr, Cs, and Sb) increase with increasing Al_2O_3 content from cores to rims (Fig. 3). The opposite correlation is found between those elements and Cr_2O_3 content. We thus used Al content as a representative for these elemental variations in the following discussion.

Metasomatism is a ubiquitous phenomenon in the Earth's mantle and can be a protracted chemical process that modifies the primary chemical composition of pre-existing rocks and their composing minerals²⁵. Metasomatism can be identified by drastic changes in the rocks' mineralogy (called modal metasomatism or refertilization) or by subtly incompatible trace element enrichment in the rocks and minerals, also called cryptic metasomatism²⁶. This process can happen in a sub-arc mantle (for example, arc-peridotites^{27,28}), and in a sub-oceanic mantle (i.e., Mid Ocean Ridge (MOR)-peridotites²⁹).

The most striking feature of the studied peridotites is the positive covariation between Al content and FME (Li, Rb, Sr, and Cs) contents in Cr-spinel (Fig. 3a-d). This shows that slab-derived fluids-rock interactions were responsible for the Al-Cr heterogeneities (i.e., addition/depletion) in Cr-spinel, rather than fractional crystallization/melting^{4,30}, subsolidus elemental exchange⁹, or stress⁸. The primitive mantle-normalized pattern of the FME of the studied Cr-spinel (Fig. 3e) shows similarities to the average pattern of subduction inputs which includes altered oceanic crust (AOC)³¹, global subducted sediments (GLOSS II)³², and marine sediments³³. The studied Cr-spinels also have similar FME contents as melt inclusions in Cr-spinels from the Avacha peridotite xenoliths, which experienced interactions with slab-

derived melts³⁴ (Fig. 3e). Moreover, FME in the studied Cr-spinel cores and rims are highly enriched relatively to primitive mantle³⁵, in contrast to Cr-spinel in refractory/depleted peridotites³⁶ (Fig. 3e). This indicates that the compositions of both their cores and rims have been modified. We interpret the Al, Cr and FME zoning in Cr-spinel to be the result of cryptic metasomatism by interactions of hydrous Al-rich slab-derived melts with the host peridotites.

Deformation/stress can lead to Al and Cr crystal lattice diffusion resulting in Al-Cr dipolar zoning in elongated Cr-spinel grains in deformed peridotites⁸. Contrary, the studied peridotites have massive textures at the field scale with no foliation/schistosity (Supplementary Fig. 2c) and minerals aggregates have rounded shape and granular texture without any elongation and/or lineation arrangement (Fig. 1 and Supplementary Fig. 2d-h). In contrast to the dipolar zoning, the studied Cr-spinels show a concentric Al-Cr zonation (Fig. 1 and Supplementary Fig. 8). To test the effect of deformation/stress and microstructure of Cr-spinel grains, EBSD has been used to quantify the crystallographic orientation and microstructural characteristics of some Cr-spinel grains (Fig. 4). The maximum misorientation in each grain from these points is 10° and 15° for grain 1 and 2, respectively (Fig. 4a, b). This misorientation variation is spatially linked to the late brittle fractures that cut the grains (including the Al-Cr zoning seen in the X-ray elemental maps data (Fig. 1b, f)). Within individual, fracture-bound fragments of the grains, there is no evidence for any lattice orientation variation or significant plastic deformation. This includes fragments that contain the observed core to rim compositional variations. Hence, there is no



relationship between the observed compositional Al-Cr heterogeneity in Cr-spinel and grain-scale deformation. In addition, the $Fe^{3+}/(Fe^{3+} + Fe^{2+})$ ratio, which is widely used as a metamorphism-related enrichment indicator of the Cr-spinel⁷, has constant values between the Cr-spinel cores and rims and has no relationship with Al and FME (Supplementary Fig. 10) giving a

clear evidence that the enrichment process of those elements is not related to the late stage metamorphic processes.

On the crystal scale of the studied Cr-spinel, the interpreted metasomatism process is demonstrated by high Al content in fine-grained Cr-spinel and in tightly curved rims that would have been more affected by melt/rock interaction than coarser

Fig. 2 Plots of the studied Cr-Spinel chemical composition for different zones within the grains. **a** Cr# ($\text{Cr}/(\text{Cr} + \text{Al})$) vs. Mg# ($\text{Mg}/(\text{Mg} + \text{Fe}^{+2})$) plot of all the raw datasets for Cr-spinel grains in the studied rocks. Such data are usually not published in previous literature. The data span between recommended fields used in previous literature for abyssal peridotites⁴ and fore arc (FA)-peridotites^{40,42}. **b** Representative/average Cr-spinel data for each sample. Such sample-average data are usually used in previous mantle petrology studies. This plot shows that our samples had a fore arc to abyssal peridotite origin. **c** Al_2O_3 vs Cr_2O_3 and **d** Cr# vs Mg# plots of the studied Cr-spinel grains with low Al_2O_3 and high Cr_2O_3 and Cr# in their cores, and high Al_2O_3 and Low Cr_2O_3 and Cr# in their rims (reverse zoning). Partial melting trend and the brown line between abyssal peridotites (Cr# < 0.60) and FA-peridotites (Cr# > 0.60) are from Dick and Bullen⁴. **e** All datasets have trends parallel to both the melting trend and our newly defined metasomatism trend. **f** Datasets of different zones (from core to rim) from four grains from a single sample (sample # A4D) that show large Al-Cr heterogeneity. The data span across the whole range between abyssal peridotites and FA- peridotites. **g** Plots of the studied Cr-spinel grains compared with the compositions of both modified spinel/rims and non-modified spinel/cores of published mantle peridotite xenoliths^{17,18,34,39}

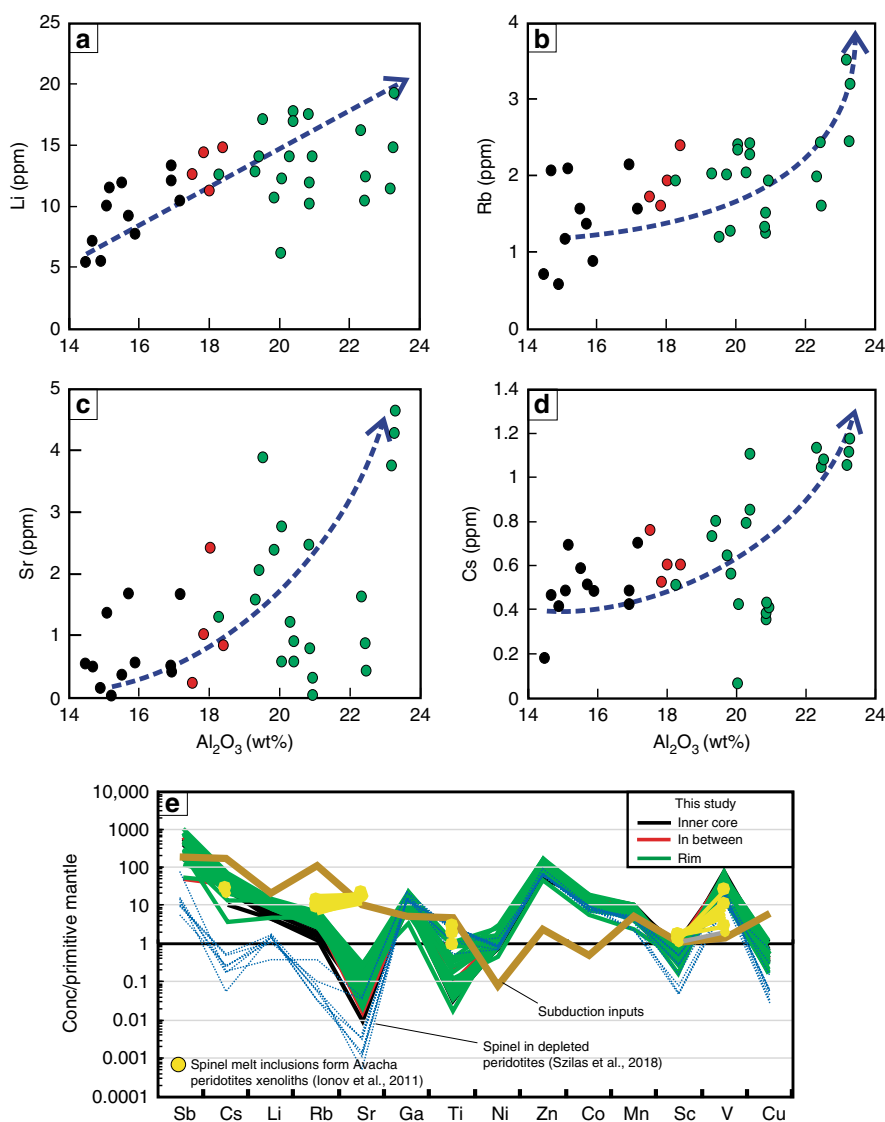


Fig. 3 Trace elements concentration of different zones in the studied Cr-Spinel. **a-d** Covariation between Al_2O_3 (wt %) content and fluid-mobile elements (FME: Li, Rb, Sr, and Cs). All the elements show positive a correlation with Al content and an increase from core to rim. **e** FME and transition elements normalized to primitive mantle³⁵ compare with the average content of subduction inputs including altered oceanic crust (AOC)³¹, global subducted sediments (GLOSS II)³² and marine sediments³³, melt inclusions in Cr-spinel from Avacha peridotite xenoliths³⁴, and spinel in refractory/depleted peridotites³⁶. The Cr-spinel show high enrichment in FME, attributed to slab-derived fluid/melt interaction with host peridotites

grains^{17,19,37} (Fig. 1b-f); idiomorphic shapes for some grains (Fig. 1b) that reflect high degrees of melt/rock interaction, where melt diffusion into the peridotites not only modified the composition of the Cr-spinel, but also corroded and modified the crystal morphology;³⁸ and Al-rich halos around inclusions, which is expected to form during melt/rock interaction inside Cr-

spinel grains, whereas the trapped melts modified the surrounding Cr-spinel (Fig. 1d and Supplementary Fig. 8c) similar to high Al zone reported around melt inclusions in Cr-spinel from the Avacha peridotite xenoliths^{34,39}.

The observation that some grains have Al-Cr heterogeneity extended inside the grain up to 200 μm (Fig. 1) suggests that such

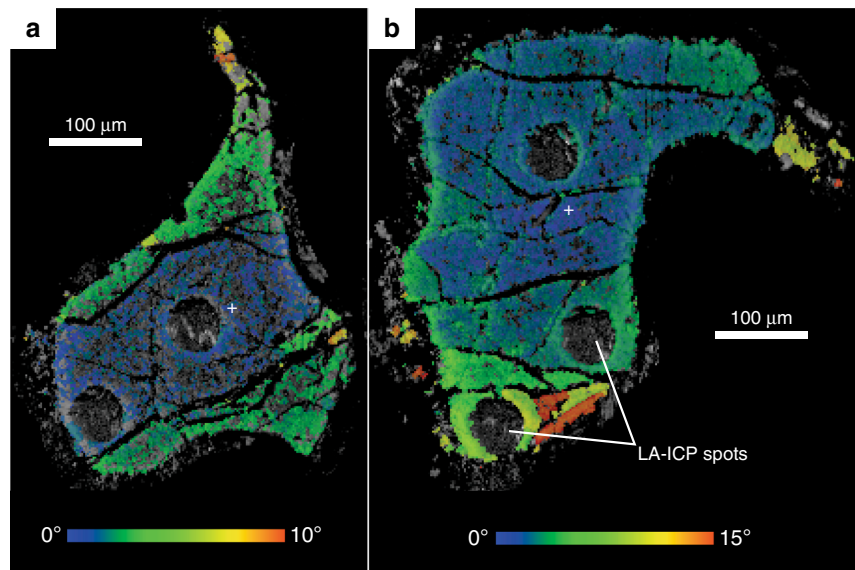


Fig. 4 EBSD microstructural data from two Cr-spinel grains from sample A4D. Images comprise greyscale image of EBSD pattern quality overlain by misorientation maps measured relative to the orientation of spinel lattice at the position shown by the white cross. For grain **a** total misorientation is 10°, for **b** the total misorientation is 15°. The change in misorientation in each grain corresponds to presence of late fractures seen in the pattern quality image. Total misorientation within individual fracture-bound regions of the grain is <1°, indicating that there is no plastic deformation within the grains

heterogeneity in the grains is not an artifact of a deep embayment of Cr-spinel grains during cutting, i.e., sectioning effect. In addition, LA-ICPMS data confirm the existence of such heterogeneity in different zones of the Cr-spinel (Fig. 3). To further verify the 3D Al-Cr heterogeneity in the studied Cr-spinel, we applied APT advanced technique, which is a powerful tool to characterize and construct the 3D chemistry at the nanoscale (see methods for more details). Four needle-shaped specimens (Fig. 5) from the core (M8 and M10) and the rim (M5 and M6) were extracted from sample A4D (Fig. 1b). The specimens yielded between 100 million atoms (M5, M6 and M10) and 109 million atoms (M8). The core specimens M8 and M10 have Cr = 24.1 atomic % (at%) and 24.4 at%, respectively and Al = 9.0 at% and 8.9 at%, respectively (Fig. 5 and Supplementary Data 2). On the other hand, the rim specimens M5 and M6 have Cr = 22.1 atomic % (at%) and 22.3 at%, respectively and Al = 10.7 at% and 10.6 at %, respectively (Fig. 5, Supplementary Data 2 and Supplementary Movies 1 and 2 for Al in M6 and M10 specimens, respectively). Although the major element composition calculated from the APT data differs from EMPA and LA-ICPMS data due to the lack of standardization protocols, the APT results confirm the enrichment of Al and depletion in Cr in the rim, and the opposite for the core (Fig. 5). Also, the detection limit of APT for the FME in Cr-spinel is too high to make meaningful measurements. The homogenous distribution of Al, Mg and Fe, non-detection of Si, and absence of any isolated clusters across the specimens, thus indicate that the high FME concentration in Cr-spinel is inherited and not related to silicate inclusions (i.e., serpentine phases), Fe-oxide nano-scale inclusions (magnetite) or low temperature alteration (Fig. 5).

The above observations make the measured Cr-spinel composition unsuitable for deciphering the partial melting history of the studied peridotites. The melt/rock interaction between mantle peridotites and slab-derived fluids/melts may produce a strong heterogeneity that modifies the Al and Cr contents (i.e., Cr#) of primary Cr-spinel, and therefore produces a reverse trend/range (metasomatism trend) of Cr# in the studied mantle rocks, different from the melting trend. Plotted together on the Cr# vs. Mg# diagram (Fig. 2d), the Cr# of the rims (mostly <0.6) are similar to MOR-peridotites, and the cores (with Cr# >0.60) are

similar to Fore arc (FA)-peridotites⁴. This indicates that representative and/or average Cr# values of Cr-spinel could give a misleading conclusion about the geotectonic setting of our samples (Fig. 2a, b). For example, applying the equation of Hellebrand et al.⁶ [$F = 10 \ln(Cr\#) + 24$] to the studied Cr-spinel would indicate 17–18% melting if using the values from the rim, and >20% melting when using the values from the core. Such values are not consistent with the bulk rock data (Supplementary Figs. 4, 5). We therefore conclude that for peridotites that experienced post-melting fluid/melt-rock interactions, their Cr-spinel data should not be used for determining the tectonic setting and melting history.

A re-evaluation of Al-Cr heterogeneity in Cr-spinel from previous studies. Our study shows that metasomatism can dramatically change the composition of Cr-spinel (i.e., Cr#). A careful literature review revealed that Cr-spinel compositional heterogeneity can be found in most mantle rocks of various tectonic environments and ages (Supplementary Fig. 1 and Supplementary Data 1). These include all available Cr-spinel data from arc-peridotites composed of FA-peridotites (including dredged samples from the present-day oceanic arc, e.g., the Izu-Bonin-Mariana arc, and mantle wedge xenoliths such as those from the Kamchatka arc) and back-arc peridotites (i.e., Mariana Trough), plus abyssal/MOR-peridotites (Supplementary Data 3).

Strikingly, even though some of the reported Cr-spinel have homogeneous compositions, the majority of the reported Cr-spinel from arc-peridotites, FA-peridotites in particular, show high heterogeneity in Al and Cr contents both within single grains (with core-rim structures)^{17,40,41} and within a single sample (from core to core)^{42–44}, which we hereafter refer to as modified Cr-spinel. Based on the available data from arc-peridotites (Fig. 6a), we filtered the modified/non-modified Cr-spinel using the Al-Cr variability between the core and rim of a single grain, and between cores of grains from the same sample (see methods). The non-modified Cr-spinel grains that have tight Cr# for a single sample display a different Cr# range of ~0.45–0.70 (Fig. 6d) for FA-peridotites from that of the accepted range used in previous studies (~0.30–0.85) (Fig. 6a), and back

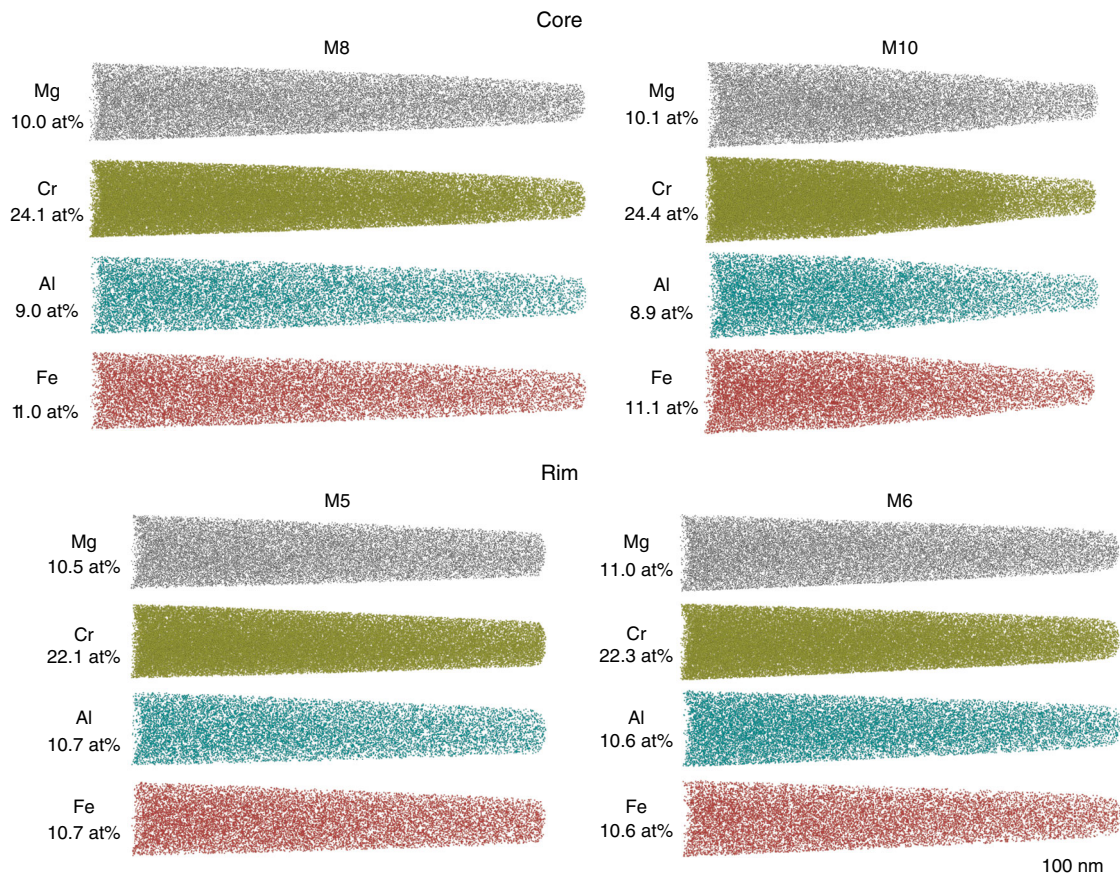


Fig. 5 Atom probe tomography results. Atom maps of Mg, Cr, Al, and Fe are presented for needle-shaped specimens from the core (M8 and M10) and the rim (M5 and M6). The specimens were extracted from sample A4D and their location is indicated on Fig. 1b. The composition in atomic % is indicated for each specimen (See Supplementary Data 2). The composition of the core is enriched in Cr and depleted in Al compared to the rim

arc-peridotites have Cr# range of ~ 0.15 – 0.65 that significantly overlapped with FA-peridotites (Fig. 6a, c).

In contrast, metasomatism is slightly different in abyssal/MOR-peridotites due to the rarity of hydrous fluids. It is driven by a melt-rock interaction that causes veined peridotites²⁹, LREE enrichment in clinopyroxene^{45,46}, and Ti enrichment in Cr-spinel^{29,47}. MOR-peridotites can be divided into two main types residual rocks (not affected by any melt-rock interaction process) and non-residual rocks (including dunites, plagioclase peridotites, gabbroic-pyroxenite veined samples, and metasomatized ones)²⁹. However, both rock types share the same range of spinel Cr# (~ 0.1 – 0.6) (Fig. 6b) following the melting trend⁴ (Supplementary Fig. 11) and the non-residual rocks are present in all the ridges. This indicates that the Cr-spinel from sub-oceanic mantle beneath all ridge systems is likely to have been affected by similar melt-rock interaction processes.

Representative Cr# of Cr-spinel composition for a given location or dredge base has been used for mitigating the effect of Cr-spinel heterogeneity and high compositional variations^{29,48}. However, this approach overlooked the elemental compositional variability of the Cr-spinel affected by melt-rock interaction. To further illustrate this point, we discuss below and give specific examples, according to available published datasets, of Cr-spinel heterogeneity due to metasomatism at different scales, from dredge sites to samples (core-core Al-Cr heterogeneity) and single grains (within core and core-rim Al-Cr heterogeneity) (see Supplementary Data 1 for more details and summary of Cr-spinel heterogeneity for each individual ridge at different scales, and Supplementary Data 3 for the complete datasets). Here we emphasize that using representative or average data for Cr-spinel

made it very difficult (or even impossible) to investigate the variation in Cr-spinel of those rocks. Hence, we only considered the samples that have at least two grains analyzed (see Supplementary Data 3). In addition, there have been only rare cases where studies traced core to rim chemical variation within individual grains^{47,49–51}.

There is a large variation in Al and Cr contents in Cr-spinel from a given dredge site, for example, section #V3306-IN18 (Owen FZ, Central Indian Ridge – CIR) has Al content = 32.20–52.90 wt% and Cr# = 0.15–0.42,⁵² section #ANTP-89-HD (Marie Celeste TF-CIR: Al = 28.4–46.9 wt% and Cr# = 0.23–0.50);⁵³ section #PS55-89 (Lena trough- Arctic Ridge: Al = 25–55 wt% and Cr# = 0.14–0.54);⁵⁴ section # S1905 (Vema TF- Mid Atlantic Ridge, MAR: Al = 27.1–48.2 wt% and Cr# = 0.22–0.49)^{49–51} and section #Van7–85 (Oblique Segment, South Western Indian Ridge – SWIR) has Al content = 24.41–54.87 wt% and Cr# = 0.16–0.52⁵⁵. For more examples and details, see Supplementary Data 1.

Similar ranges of Cr# variation exist at the sample scale. For example, Hamlyn and Bonatti⁵² analyzed four grains from the same peridotite sample (#V3306-IN18I-Owen FZ, CIR) and found inter-grain variations in Cr# spreading the range of 0.2 to 0.4 (mainly the entire range for CIR residual peridotites). Also, sample # AII32-8-6 (residual harzburgite-Ridge at 43°N, MAR: Al = 26.8–38.1 wt% and Cr# = 0.34–0.52)⁵⁶, sample # 1274A-14R-1/76-82 (residual harzburgite-Fifteen-Twenty TF, MAR: Al = 32.4–41 wt% and Cr# = 0.32–0.44)⁵⁷, sample # G9604-4 (residual peridotite-Conrad FZ, American Antarctic Ridge (AAR): Al = 23–40 wt% and Cr# = 0.29–0.53)⁵⁸ and sample #895D-4R2-45-49 (Hess Deep, East Pacific Rise (EPR): Al = 17.5–25.2 wt% and Cr# = 0.51–0.58)⁵⁹. Dick et al.⁴⁷ published a

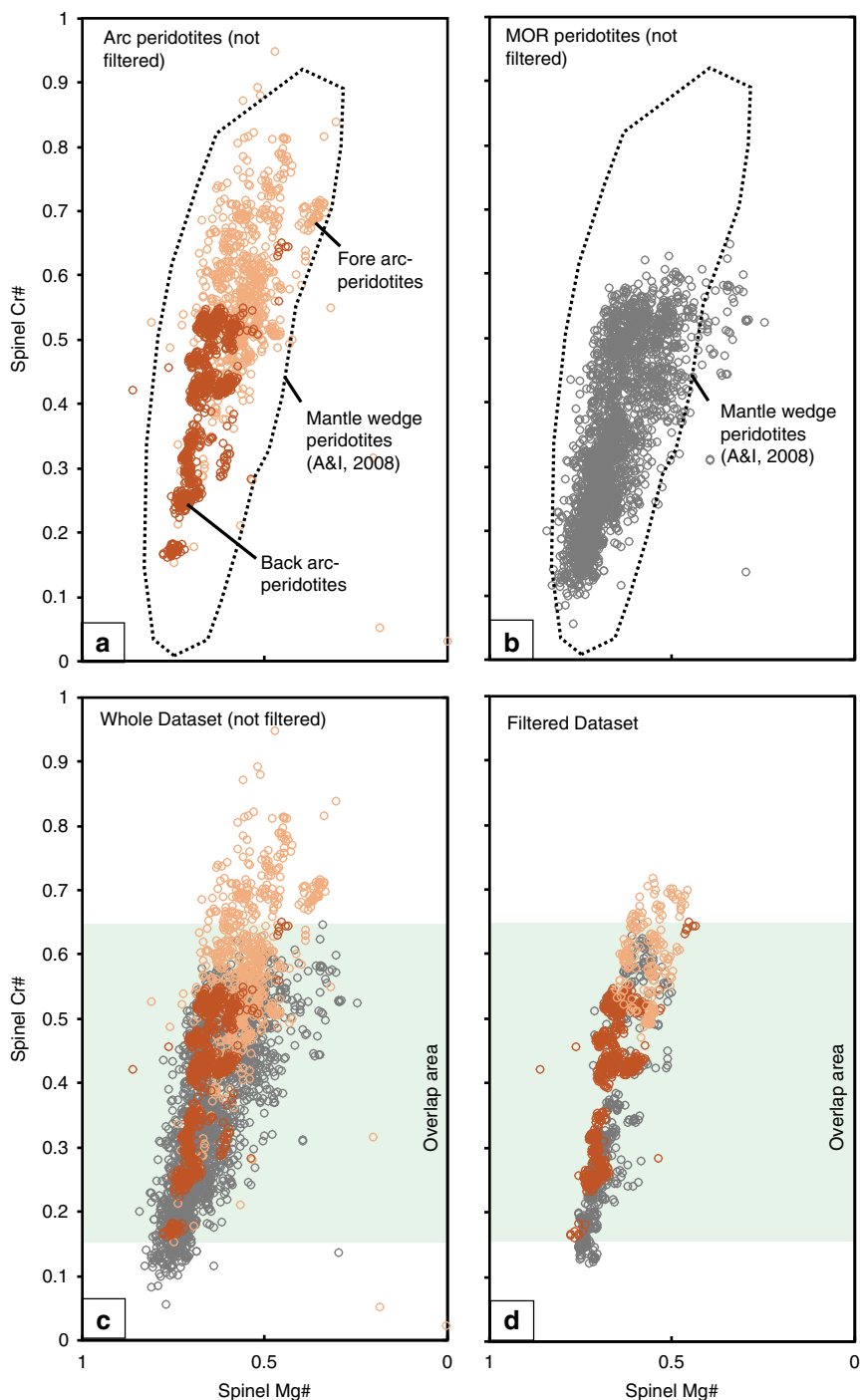


Fig. 6 Spinel Cr# and Mg# for the fore arc peridotites. **a** Cr-spinel database from arc-peridotites including fore arc settings (composed of mantle wedge xenoliths (e.g., the Kamchatka arc)^{18,19} and dredged samples from present-day oceanic arcs (e.g., the Izu-Bonin-Mariana arc)^{40,42}) and back arc-peridotites (i.e., Mariana Trough)^{43,44}. **b** Cr-spinel database from abyssal/ Mid-ocean ridge (MOR) peridotites. See Supplementary Data 3 for the arc and MOR-Cr-spinel datasets. All the arc and MOR-peridotites dataset plot within the Cr-spinel from mantle wedge peridotites²⁸. **c** All arc peridotite Cr-spinel datasets (without filtering) plotted against MOR-peridotite one, showing their overlapping fields. **d** Filtered dataset for both arc- and MOR-peridotite are still completely overlapping. For filter details, see the methods. The shaded area in **(c, d)** marks the overlapping range of Cr# (0.15–0.65) between the arc-peridotite and MOR-peridotite fields

Cr-spinel dataset from residual peridotites from Kane Megamullion (MAR), typically with data of one grain only per samples except for sample Kn180-2-4-2 that has two grains with a large range of Al content = 40.0–36.5 wt% and Cr# = 0.30–0.36 (Supplementary Data 3). In the Warren⁵⁵ study, there are also a variation of Al-Cr content within the same sample of cryptic metasomatized peridotite from the Atlantis II fracture

zone (SWIR), such as sample #6K-465-2 that has a Al range of 28.89–46.54 wt% and Cr# of 0.22–0.46, and sample #RC27-9-6-5 that has a Al range of 27.59–46.58 wt% and Cr# of 0.22–0.48. For more examples and details, see Supplementary Data 1.

At the grain scale, data reported in Brunelli et al.⁴⁹, Cipriani et al.^{50,51} and Dick et al.⁴⁷ have some grains showing within-grain

core-rim Al-Cr reverse variation. For example, sample #Kn180-214-44 (residual peridotite- Kane Megamullion) has rim showing high Al = 39.5 wt% and core showing low Al = 36.8 wt%⁴⁷, sample # L2627-04B (residual peridotite- Vema TF) has rim showing high Al = 48.5 wt% and core showing low Al = 44.5 wt%⁵¹, sample # L2630-01D (residual peridotite- Vema TF) has rim showing high Al = 32.2 wt% and core showing low Al = 27.8 wt%⁵¹. For more examples and details, see Supplementary Data 1.

These examples, together with the comprehensive compilation (Supplementary Data 1), show that the majority (~85%) of Cr-spinel from MOR-peridotites exhibit heterogeneity, indicating that it is a widespread feature in sub-oceanic mantle (Supplementary Fig. 1 and Supplementary Data 1). Moreover, such large variations in Cr# featuring Al enrichment and Cr depletion are most likely the results of melt-rock interaction/metamorphism, consistent with cryptic metasomatic that led to LREE enrichments in Cpx of the same rocks (e.g., refs. 46,47,53). For example, Warren⁵⁵ reported a similarly large compositional variation in Cpx from MOR-peridotites in the scales of dredge sites, samples, and individual grains, and interpreted it as the result of widespread melt-rock interaction. Indeed, some non-residual/impregnated samples have high Al content and low Cr# than residual samples from the same section, for example, sections # 6K-458 and Kn162-19 from SWIR (Supplementary Data 3)⁵⁵. Moreover, Constantin et al.⁶⁰ documented that the Terevaka TF cryptic harzburgite samples have lower Cr# (~0.35) compared to harzburgites free of impregnation (Cr# = ~0.45; see their Fig. 2). Additionally, the orogenic replacive dunites (melt-rock interaction origin) have low Cr# than the residual origin dunites (see Fig. 8 of Su et al.⁶¹). Our re-interpretation of high Al-Cr heterogeneity in Cr-spinel from MOR-peridotites as a melt-rock interaction/metamorphism origin is supported the new geochemical modeling and observations of Brunelli et al.⁶² from Vema at MAR where veined peridotites have lower Cr# than residual/vein-free ones.

We distinguished modified from non-modified Cr-spinel in MOR-peridotites, as we did for arc-peridotites, using our filter criteria (see methods). The data show a large overlap in Cr# of Cr-spinel between MOR-peridotites and arc-peridotites (~75% of all FA-peridotite data, ~90% of all MOR-peridotite data and 100% of back arc-peridotites data fall inside the common field of Cr# = ~0.15–0.65) (Fig. 6c, d). Furthermore, Arai and co-workers^{28,63,64} suggested that the lithospheric mantle beneath arcs (such as the Western Pacific arcs) have peridotites with a chemical and mineralogical composition comparable to that of MOR/abyssal peridotites. In addition, Cr-spinel datasets of both modified and non-modified MOR-peridotites fall entirely within the field of mantle wedge peridotites²⁸ (Fig. 6b), rendering the application of Cr# as a geotectonic indicator ineffective, and Cr# < 0.6 is not a unique feature of MOR-peridotites.

Discussion

Our new analyses and a careful review of published results show that the chemical composition of Cr-spinel can be easily and severely modified by cryptic metasomatism through fluid/melt-rock interaction involving slab-derived fluids in the sub-arc mantle, or even by small volumes of melts in the sub-oceanic mantle. We also demonstrate that the wide range of Cr# of Cr-spinel in mantle rocks is a function of melt-rock interaction^{10,65–68} rather than partial melting. In addition, we identify Cr-spinel as a carrier of FME especially in subduction zone environments, where Al is easily mobilized by fluids and melts and therefore cannot be used as a melting degree indicator at least at the mineral scale. Furthermore, the heterogeneity of Cr# in Cr-spinel can be used as a powerful tracer for Cr-spinel metasomatic modification.

Our findings, therefore, provide a framework for a re-evaluation of Cr-spinel compositions in mantle rocks. They will also have numerous new applications. These include using Cr-spinel composition as a melt-rock interaction indicator, and as a tracer of mantle heterogeneity. In addition, Cr-spinel as a FME-carrying mineral may also provide a feeding mechanism for FME into the deep mantle chemical cycle because it breaks down at >1000 km depth⁶⁹. The present findings will thus help to develop a new way of deciphering deep mantle metasomatism and heterogeneity through analysing non-traditional isotopes (e.g., Li, Zn, Ti, and Ni) in Cr-spinel.

Finally, we suggest that future studies of Cr-spinel chemistry need to first carry out systematic microanalyses in order to detect any heterogeneity of trace elements (including FME) using methods such as X-ray elemental mapping, EMP (at least 3–5 spots within the same grain spreading from the inner to outer core, and at least three grains per sample), and LA-ICPMS. More advanced methods such as EBSD and APT, plus careful interpretation of the obtained results, will help to detect modified/heterogeneous Cr-spinels. Whereas altered Cr-spinels may help to address post-melting metasomatic process, non-modified/homogenous ones can then be used for tracking partial melting.

Methods

Bulk rock chemical analysis. Whole rock geochemistry of major and trace (including rare earth) elements were carried out for some samples of serpentinized peridotites (Supplementary Data 2; all whole-rock results are reported on a volatile-free basis). Whole-rock samples were crushed with a polyethylene-wrapped hammer into <0.5 cm pieces and then grounded with ethyl alcohol in an agate mill to grain sizes below 50 μm . Major element compositions were analyzed using a X-ray fluorescence spectrometer (Shimadzu, XRF-1800) at the Pukyong National University, South Korea. Analytical conditions were 40 kV accelerating voltage and 70 mA beam current. Analytical precision is better than 2% for major elements. All glass beads were analyzed three times and the averages are used. The trace and rare-earth elements of the studied samples were analyzed using an ICP-MS (VG Elemental Ltd., PQ3) at the Korean Basic Science Institute (KBSI) at Ohchang, South Korea. Acid digestion with hydrofluoric acid is routinely used to digest geological materials for the trace-element determination. A 100 mg of powdered sample was accurately weighed into the PTFE digestion vessel, added with 5 ml mixed acid ($\text{HF}:\text{HNO}_3:\text{HClO}_4 = 4:4:1$). The sample vessel was tightly capped and placed on a hot plate for 24 h at 190 °C and then cooled to room temperature. After opening the cap, the sample was subsequently evaporated to incipient dryness. The above process was repeated once more. The residue was dissolved in 10 ml of 1% HNO_3 with gentle heating, until a clear solution resulted. Determinations for USGS reference samples (BIR-1 and MUH-1) agree with recommended values within suggested tolerances. The precision of the measurements by repeated analyses of reference samples is better than $\pm 5\%$ for trace elements.

Electron probe micro analyses (EMPA). Quantitative chemical analyses of major and some minor elements in Cr-spinel were carried out using a JEOL JXA-8800 electron-probe at Kanazawa University, Japan (Supplementary Data 2). The analytical conditions were 20 kV accelerating voltage, 20 nA probe current and 3 μm beam diameter. A ZAF-correction was made to correct the raw data. Ferric and ferrous iron redistribution from EMP analyses was made using the charge balance equation of Droop⁷⁰. Natural mineral standards were used for calibration: quartz for Si, corundum for Al, eskolaite for Cr, fayalite for Fe, periclase for Mg, manganosite for Mn, wollastonite for Ca, jadeite for Na and pentlandite for Ni. Si (<0.03 wt%) and Na (<0.02 wt%) for the studied Cr-spinel are below the detection limits.

X-ray mapping of Cr-Spinel. Al-Cr-Mg-Fe X-ray element distribution maps of Cr-spinel grains in the studied peridotites were acquired using a wavelength dispersive X-ray spectrometry (WDS) on a JEOL JXA-8800 electron-probe at Kanazawa University, Japan. The analytical conditions were 20 kV accelerating voltage, 20 nA probe current and <1 μm beam diameter. Dwell times on each spot were between 20 and 30 ms according to the analyzed element and the sensitivity of the detector.

Electron back-scattered diffraction (EBSD). EBSD data were collected at the Microscopy and Microanalysis Facility, John de Laeter Centre, Curtin University, using a Tescan MIRA3 SEM with Oxford Instruments Symmetry EBSD detector. Data were collected at 20 kV and ~1 nA beam current, with an analytical step size of 2 μm . EBSD data were collected using Oxford Aztec 4.1 acquisition software. Data were noise reduced using a wildspike and 5 nearest neighbor zero solution

algorithm in Oxford Instruments Channel 5.12 software. Channel 5.12 was also used to create misorientation maps used to investigate the microstructural relationship between spinel core and rim. Relatively poor-indexing of the spinel represents the difficulty in polishing the analyzed grains after laser-ablation analysis.

Laser ablation-inductively coupled plasma-mass spectrometry (LA-ICP-MS) micro analysis. Trace element compositions of Cr-spinel (Supplementary Data 2) were determined using a 193 nm ArF Excimer LA-ICP-MS at Korean Basic Science Institute (KBSI), South Korea (Teledyne Cetac Technologies equipped with Analyte Excite). Analyses were performed by ablating 30–50 μm diameter spots at 10 Hz with an energy density of 5 J/cm² per pulse. Signal integration times were 60 s for a gas background interval and 60 s for an ablation interval. The NIST SRM 612 glass was used as the primary calibration standard and was analyzed at the beginning of each batch of <5 unknowns, with a linear drift correction applied between each calibration. The element concentration of NIST SRM 612 for the calibration is selected from the preferred values of Pearce et al.⁷¹. Each analysis was normalized using ⁵⁷Fe as internal standard elements, based on Fe contents obtained by Electron probe micro analysis. All minerals were analyzed multiple times and the averages were used. The relative standard deviations (RSD) of the trace elements in the minerals were mostly 5–10%. We used the Glitter software to process the data, which shows ablation profiles for elements and permits to reduce analytical contamination. The LA-ICP-MS ablation profiles of the intensity (counting) vs time for all analyses of the studied Cr-spinel are provided in supplementary information (Supplementary Fig. 12). None of the calculated peaks has any significant spike signals for ²⁹Si and ⁵⁷Fe, which indicates that no silicate inclusion and/or magnetite was measured. The slight difference between EPMA and LA-ICPMS data for trace elements such as Ni, Mn, and Ti is due to matrix effect and the different standards used, but the LA-ICPMS data is more precise than the EMPA data especially for trace elements.

Atom probe tomography (APT). APT has the ability to characterize and visualize the 3D distribution of atoms at sub-nanometer resolution⁷². Recent advancements and the development of laser pulsing capabilities has made possible the analysis of non-conductive materials such as most rock-forming minerals. The technique is based on the field-evaporation of atoms from a needle-shaped specimen under a high electric field. The 3D position of atoms is given by the impact location on a position sensitive detector and the succession of detection events. The ions are identified using time-of-flight mass spectrometry by measuring the time between the laser pulse and the detection event. For more details about this technique see Ref. 73,74. Four needle-shaped specimens (7 μm length and 2.5 μm depth for each one) for APT measurements were prepared with a Ga⁺ Tescan Lyra3 focused ion beam coupled with a scanning electron microscope (FIB-SEM) at Curtin University following the lift out method⁷⁵. The specimens were extracted from a polished thin section and their location is indicated on Fig. 1b (Supplementary Data 2). The FIB was operated at 30 kV during the manufacturing of the specimen and a low kV (2 kV) clean-up was implemented to remove the surface layer affected by high-energy Ga⁺ ion implantation. APT measurements were performed on a CAMECA LEAP 4000X HR at Curtin University. The instrument was operated in laser mode ($\lambda = 355 \text{ nm}$) with a laser pulse energy of 150 pJ and a pulse frequency of 200 kHz. The specimens were kept at 60 K during analysis with a detection rate maintained at 1 detection event every 100 laser pulses. The specimens yielded between 100 million atoms (M5, M6 and M10) and 109 million atoms (M8) (See Supplementary Movies 1 and 2 for Al in M6 and M10 specimens). The mass spectra were characterized by large peak tails similar to other oxides such as rutile⁷⁶. In the mass spectra (Supplementary Fig. 13), the cations are present as different molecular species with singly-charged to triply-charged ions. For example, Cr is present as Cr⁺, Cr²⁺, CrO⁺, CrO²⁺, CrO₂⁺, CrO₂²⁺, CrO₃⁺ and Cr₂O₃⁺; and Al is present as Al⁺, Al²⁺, Al³⁺, AlO⁺, AlO²⁺, AlO₂⁺, Al₂O²⁺, and AlCrO₃²⁺. The combination of multiple ionic species for each element and large thermal peak tails leads to difficulties in quantifying the composition of the analyzed nano-scale domains. The estimation of the O composition from atom probe data is also renowned to be difficult⁷⁷. These limitations indicate that the composition calculated from the atom probe data will differ from expected stoichiometry and other techniques that apply standardization protocols (i.e., EPMA and LA-ICPMS). However, the method used for the calculation of the composition in this study was consistent across all datasets, indicating that the differences between atom probe specimens are reliable.

Filter criteria for Cr-spinel data. Based on the available data, we filtered out modified Cr-spinel results that (1) show Al-Cr reverse/ asymmetric zoning “heterogeneity” in the same grain, (2) have high Al and Cr content range >1.5 wt%, standard deviation >0.5 or >5% variability percentage within a single sample, and (3) have Cr# variability greater than 1% or standard deviation >0.01 within a single sample. In addition, we excluded samples that have Cr-spinel with only one analysis and no standard deviation or variability percentage.

Data availability

All the data that are necessary for evaluating the findings of this study are available within this article and its Supplementary Information.

Received: 27 November 2018; Accepted: 21 October 2019;

Published online: 08 November 2019

References

- Albarède, F. The growth of continental crust. *Tectonophysics* **296**, 1–14 (1998).
- Irvine, T. N. Chromian spinel as a petrogenetic indicator: Part 1. Theory. *Can. J. Earth Sci.* **4**, 71–103 (1965).
- Irvine, T. N. Chromian spinel as a petrogenetic indicator: Part 2. Petrologic applications. *Can. J. Earth Sci.* **4**, 71–103 (1967).
- Dick, H. J. B. & Bullen, T. Chromian spinel as a petrogenetic indicator in abyssal and alpine-type peridotites and spatially associated lavas. *Contrib. Mineral. Petrol.* **86**, 54–76 (1984).
- Arai, S. Characterization of spinel peridotites by olivine-spinel compositional relationships: Review and interpretation. *Chem. Geol.* **113**, 191–204 (1994).
- Hellebrand, E., Snow, J. E., Dick, H. J. B. & Hofmann, A. W. Coupled major and trace elements as indicators of the extent of melting in mid-ocean-ridge peridotites. *Nature* **410**, 677–681 (2001).
- Barnes, S. J. Chromite in komatiites. II. Modification during greenschist to mid-amphibolite facies metamorphism. *J. Petrol.* **41**, 387–409 (2000).
- Ozawa, K. Stress-induced Al-Cr zoning of spinel in deformed peridotites. *Nature* **338**, 141–144 (1989).
- Bai, Y. et al. Origin of reverse zoned Cr-spinels from the Paleoproterozoic Yanmenguan mafic-ultramafic complex in the North China Craton. *Minerals* **8**, 62 (2018).
- Ceuleneer, G. Mantle mapped in the desert. *Nature* **432**, 156–157 (2004).
- Johnson, P. R. et al. Late Cryogenian-Ediacaran history of the Arabian-Nubian Shield: a review of depositional, plutonic, structural, and tectonic events in the closing stages of the northern East African Orogen. *J. Afr. Earth Sci.* **61**, 167–232 (2011).
- Hamdy, M. M., Abd El-Wahed, M. A., Gamal El Dien, H. & Morishita, T. Garnet hornblende in the Meatiq Core Complex, Central Eastern Desert of Egypt: implications for crustal thickening preceding the ~600 Ma extensional regime in the Arabian-Nubian Shield. *Precambrian Res.* **298**, 593–614 (2017).
- Gamal El Dien, H. et al. Neoproterozoic serpentinites from the Eastern Desert of Egypt: insights into Neoproterozoic mantle geodynamics and processes beneath the Arabian-Nubian Shield. *Precambrian Res.* **286**, 213–233 (2016).
- Hamdy, M. M. & Gamal El Dien, H. Nature of serpentinization and carbonation of ophiolitic peridotites (Eastern Desert, Egypt): constrains from stable isotopes and whole-rock geochemistry. *Arab. J. Geosci.* **10**: 429, <https://doi.org/10.1007/s12517-017-3215-6> (2017).
- Workman, R. K. & Hart, S. R. Major and trace element composition of the depleted MORB mantle (DMM). *Earth Planet. Sci. Lett.* **231**, 53–72 (2005).
- De Hoog, J. C. M., Janák, M., Vrabec, M. & Froitzheim, N. Serpentinized peridotites from an ultrahigh-pressure terrane in the Pohorje Mts. (Eastern Alps, Slovenia): geochemical constraints on petrogenesis and tectonic setting. *Lithos* **109**, 209–222 (2009).
- Franz, L., Becker, K.-P., Kramer, W. & Herzog, A. P. M. Metasomatic Mantle Xenoliths from the Bismarck Microplate (Papua New Guinea)—Thermal Evolution, Geochemistry and Extent of Slab-induced Metasomatism. *J. Petrol.* **43**, 315–343 (2002).
- Ishimaru, S., Arai, S., Ishida, Y., Shirasaka, M. & Okrugin, V. M. Melting and multi-stage metasomatism in the mantle wedge beneath a frontal arc inferred from highly depleted peridotite xenoliths from the avacha volcano, Southern Kamchatka. *J. Petrol.* **48**, 395–433 (2007).
- Ionov, D. A. Petrology of mantle wedge lithosphere: new data on supra-subduction zone peridotite xenoliths from the andesitic Avacha volcano, Kamchatka. *J. Petrol.* **51**, 327–361 (2010).
- Deschamps, F., Godard, M., Guillot, S. & Hattori, K. Geochemistry of subduction zone serpentinites: a review. *Lithos* **178**, 96–127 (2013).
- Bodinier, J. L., Vasseur, G., Vernieres, J., Dupuy, C. & Fabries, J. Mechanisms of Mantle Metasomatism: Geochemical Evidence from the Lherz Peridotite. *J. Petrol.* **31**, 597–628 (1990).
- Schiano, P. et al. Hydrous, silica-rich melts in the sub-arc mantle and their relationship with erupted arc lavas. *Nature* **377**, 595–600 (1995).
- Gamal El Dien, H., Li, Z.-X., Kil, Y. & Abu-Alam, T. Origin of arc magmatic signature: a temperature-dependent process for trace element (re-)mobilization in subduction zones. *Sci. Rep.* **9**, 7098 (2019).
- Hellebrand, E., Snow, J. E. & Mühe, R. Mantle melting beneath Gakkel Ridge (Arctic Ocean): Abyssal peridotite spinel compositions. *Chem. Geol.* **182**, 227–235 (2002).
- Bailey, D. Mantle metasomatism-continuing chemical change within the Earth. *Nature* **296**, 525–530 (1982).

26. Harte, B., Hunter, R. H. & Kinny, P. D. Melt geometry, movement and crystallization, in relation to mantle dykes, veins and metasomatism. *Philos. Trans. R. Soc. Lond. Ser. A Phys. Eng. Sci.* **342**, 1–21 (1993).
27. Prouteau, G., Davidson, B., Burbank, D. & Maury, R. C. Evidence for mantle metasomatism by hydrous silicic melts derived from subducted oceanic crust. *Nature* **410**, 197–200 (2001).
28. Arai, S. & Ishimaru, S. Insights into Petrological Characteristics of the Lithosphere of Mantle Wedge beneath Arcs through Peridotite Xenoliths: a review. *J. Petrol.* **49**, 665–695 (2008).
29. Warren, J. M. Global variations in abyssal peridotite compositions. *Lithos* **248–251**, 193–219 (2016).
30. Sigurdsson, H. & Schilling, J. G. Spinel in Mid-Atlantic Ridge basalts: chemistry and occurrence. *Earth Planet. Sci. Lett.* **29**, 7–20 (1976).
31. Staudigel, H. *Chemical Fluxes from Hydrothermal Alteration of the Oceanic Crust. Treatise on Geochemistry*, 2nd edn. **4**, (Elsevier Ltd., 2014).
32. Plank, T. *The Chemical Composition of Subducting Sediments. Treatise on Geochemistry*, 2nd edn. **4**, (Elsevier Ltd., 2014).
33. Li, Y. H. & Schoonmaker, J. E. *Chemical Composition and Mineralogy of Marine Sediments. Treatise on Geochemistry*, 2nd edn. **9**, (Elsevier, 2014).
34. Ionov, D. A., Bénard, A. & Plechov, P. Y. Melt evolution in subarc mantle: Evidence from heating experiments on spinel-hosted melt inclusions in peridotite xenoliths from the andesitic Avacha volcano (Kamchatka, Russia). *Contrib. Mineral. Petrol.* **162**, 1159–1174 (2011).
35. McDonough, W. & Sun, S. – The composition of the Earth. *Chem. Geol.* **120**, 223–252 (1995).
36. Szilas, K. et al. Highly refractory Archaean peridotite cumulates: Petrology and geochemistry of the Seqi Ultramafic Complex, SW Greenland. *Geosci. Front.* **9**, 689–714 (2018).
37. Arai, S., Ishimaru, S. & Okrugin, V. M. Metasomatized harzburgite xenoliths from Avacha volcano as fragments of mantle wedge of the Kamchatka arc: implication for the metasomatic agent. *Isl. Arc* **12**, 233–246 (2003).
38. Ohara, Y. & Ishii, T. Peridotites from the southern Mariana forearc: heterogeneous fluid supply in mantle wedge. *Isl. Arc* **7**, 541–558 (1998).
39. Ishimaru, S. & Arai, S. Highly silicic glasses in peridotite xenoliths from Avacha volcano, Kamchatka arc; implications for melting and metasomatism within the sub-arc mantle. *Lithos* **107**, 93–106 (2009).
40. Parkinson, I. J. & Pearce, J. A. Peridotites from the Izu – Bonin – Mariana Forearc (ODP Leg 125): Evidence for Mantle Melting and Melt – Mantle Interaction in a Supra-Subduction Zone Setting. *J. Petrol.* **39**, 1577–1618 (1998).
41. Bloomer, S. H. & Fisher, R. L. Petrology and Geochemistry of Igneous Rocks from the Tonga Trench: A Non-Accreting Plate Boundary. *J. Geol.* **95**, 469–495 (1987).
42. Ishii, T., Robinson, P. T., Maekawa, H. & Fiske, R. Petrological studies of peridotites from diapiric serpentinite seamounts in the Izu-Ogasawara-Mariana Forearc, Leg 125. *Proc. Ocean Drill. Program, Sci. Results* **125**, 445–485 (1992).
43. Ohara, Y., Stern, R. J., Ishii, T., Yurimoto, H. & Yamazaki, T. Peridotites from the Mariana Trough: first look at the mantle beneath an active back-arc basin. *Contrib. Mineral. Petrol.* **143**, 1–18 (2002).
44. Ohara, Y., Fujioka, K., Ishii, T. & Yurimoto, H. Peridotites and gabbros from the Parece Vela backarc basin: unique tectonic window in an extinct backarc spreading ridge. *Geochem., Geophys. Geosyst.* **4(7)**, 8611, <https://doi.org/10.1029/2002GC000469> (2003).
45. Seyler, M., Toplis, M. J., Lorand, J. P., Lugué, A. & Cannat, M. Clinopyroxene microtextures reveal incompletely extracted melts in abyssal peridotites. *Geology* **29**, 155–158 (2001).
46. Warren, J. M. & Shimizu, N. Cryptic variations in abyssal peridotite compositions: evidence for shallow-level melt infiltration in the oceanic lithosphere. *J. Petrol.* **51**, 395–423 (2010).
47. Dick, H. J. B., Johan Lissenberg, C. & Warren, J. M. Mantle melting, melt transport, and delivery beneath a slow-spreading ridge: the paleo-MAR from 23°15'N to 23°45'N. *J. Petrol.* **51**, 425–467 (2010).
48. Zhou, H. & Dick, H. J. B. Thin crust as evidence for depleted mantle supporting the Marion Rise. *Nature* **494**, 195–200 (2013).
49. Brunelli, D., Seyler, M., Cipriani, A., Ottolini, L. & Bonatti, E. Discontinuous melt extraction and weak refertilization of mantle peridotites at the vema lithospheric section (mid-atlantic ridge). *J. Petrol.* **47**, 745–771 (2006).
50. Cipriani, A. et al. A 19 to 17 Ma amagmatic extension event at the Mid-Atlantic Ridge: ultramafic mylonites from the Vema Lithospheric Section. *Geochem., Geophys. Geosyst.* **10**, Q10011, <https://doi.org/10.1029/2009GC002534> (2009).
51. Cipriani, A., Bonatti, E., Brunelli, D. & Ligi, M. 26 million years of mantle upwelling below a segment of the Mid Atlantic Ridge: The Vema Lithospheric Section revisited. *Earth Planet. Sci. Lett.* **285**, 87–95 (2009).
52. Hamlyn, P. R. & Bonatti, E. Petrology of mantle-derived ultramafics from the Owen fracture zone, northwest Indian ocean: Implications for the nature of the oceanic upper mantle. *Earth Planet. Sci. Lett.* **48**, 65–79 (1980).
53. Hellebrand, E., Snow, J. E., Hoppe, P. & Hofmann, A. W. Garnet-field Melting and Late-stage Refertilization in 'Residual' Abyssal Peridotites from the Central Indian Ridge. *J. Petrol.* **43**, 2305–2338 (2002).
54. Lassiter, J. C., Byerly, B. L., Snow, J. E. & Hellebrand, E. Constraints from Os-isotope variations on the origin of Lena Trough abyssal peridotites and implications for the composition and evolution of the depleted upper mantle. *Earth Planet. Sci. Lett.* **403**, 178–187 (2014).
55. Warren, J. M. Geochemical and rheological constraints on the dynamics of the oceanic upper mantle. *PhD Thesis, MIT/WHOI Jt. Progr.* **282**. <https://doi.org/10.1575/1912/2030> (2007).
56. Shibata, T. & Thompson, G. Peridotites from the Mid-Atlantic Ridge at 43° N and their petrogenetic relation to abyssal tholeiites. *Contrib. Mineral. Petrol.* **93**, 144–159 (1986).
57. Vils, F., Pelletier, L., Kalt, A., Müntener, O. & Ludwig, T. The Lithium, Boron and Beryllium content of serpentinized peridotites from ODP Leg 209 (Sites 1272A and 1274A): Implications for lithium and boron budgets of oceanic lithosphere. *Geochim. Cosmochim. Acta* **72**, 5475–5504 (2008).
58. Brunelli, D., Cipriani, A., Ottolini, L., Peyve, A. & Bonatti, E. Mantle peridotites from the Bouvet Triple Junction Region, South Atlantic. *Terra Nov.* **15**, 194–203 (2003).
59. Arai, S. & Matsukage, K. Petrology of Gabbro-Troctolite-Peridotite Complex from Hess Deep, Equatorial Pacific: Implications for Mantle-Melt Interaction within the Oceanic Lithosphere. *Proc. Ocean Drill. Program, 147 Sci. Results* **147**, 135–155 (1996).
60. Constantin, M., Hékinian, R., Ackermann, D. & Stoffers, P. in *Mantle and Lower Crust Exposed in Oceanic Ridges and in Ophiolites*. (eds Vissers, R. L. M. & Nicolas, A.) (Kluwer Academic, 1995).
61. Su, B., Chen, Y., Guo, S. & Liu, J. Origins of orogenic dunites: petrology, geochemistry, and implications. *Gondwana Res.* **29**, 41–59 (2016).
62. Brunelli, D., Cipriani, A. & Bonatti, E. Thermal effects of pyroxenites on mantle melting below mid-ocean ridges. *Nat. Geosci.* **11**, 520–525 (2018).
63. Payot, B. et al. Mantle Evolution from Ocean to Arc: The Record in Spinel Peridotite Xenoliths in Mt. Pinatubo, Philippines. *Minerals* **8**, 515 (2018).
64. Arai, S. et al. Abyssal Peridotite as a Component of Forearc Mantle: Inference from a New Mantle Xenolith Suite of Bankawa in the Southwest Japan Arc. *Minerals* **8**, 540 (2018).
65. Abily, B. & Ceuleneer, G. The dunitic mantle-crust transition zone in the Oman ophiolite: residue of melt-rock interaction, cumulates from high-mgO melts, or both? *Geology* **41**, 67–70 (2013).
66. Ceuleneer, G. & Le Sueur, E. The Trinity ophiolite (California): the strange association of fertile mantle peridotite with ultra-depleted crustal cumulates. *Bull. la Soc. Geol. Fr.* **179**, 503–518 (2008).
67. Rospabé, M., Benoit, M., Ceuleneer, G., Hodel, F. & Kaczmarek, M.-A. Extreme geochemical variability through the dunitic transition zone of the Oman ophiolite: implications for melt/fluid-rock reactions at Moho level beneath oceanic spreading centers. *Geochim. Cosmochim. Acta* **234**, 1–23 (2018).
68. Kaczmarek, M.-A. & Müntener, O. Juxtaposition of Melt Impregnation and High-Temperature Shear Zones in the Upper Mantle; Field and Petrological Constraints from the Lanzo Peridotite (Northern Italy). *J. Petrol.* **49**, 2187–2220 (2008).
69. Ringwood, A. E. Mineralogical constitution of the deep mantle. *J. Geophys. Res.* **67**, 4005–4010 (1962).
70. Droop, G. T. R. A general equation for estimating Fe³⁺ concentrations in ferromagnesian silicates and oxides from microprobe analyses, using stoichiometric criteria. *Mineral. Mag.* **51**, 431–435 (1987).
71. Pearce, N. J. G. et al. A Compilation of New and Published Major and Trace Element Data for NIST SRM 610 and NIST SRM 612 Glass Reference Materials. *Geostand. Geoanalytical Res.* **21**, 115–144 (1997).
72. Saxey, D. W., Moser, D. E., Piazzolo, S., Reddy, S. M. & Valley, J. W. Atomic worlds: current state and future of atom probe tomography in geoscience. *Scr. Mater.* **148**, 115–121 (2018).
73. Fougereuse, D. et al. Nanoscale gold clusters in arsenopyrite controlled by growth rate not concentration: evidence from atom probe microscopy. *Am. Mineral.* **101**, 1916–1919 (2016).
74. Larson, D. J., Prosa, T. J., Ulfig, R. M., Geiser, B. P. & Kelly, T. F. *Local Electrode Atom Probe Tomography*. (Springer New York, 2013).
75. Thompson, K. et al. In situ site-specific specimen preparation for atom probe tomography. *Ultramicroscopy* **107**, 131–139 (2007).
76. Verberne, R. et al. Analysis of Natural Rutile (TiO₂) by Laser-assisted Atom Probe Tomography. *Microsc. Microanal.* **25**, 539–546 (2019).
77. Gault, B. et al. Behavior of molecules and molecular ions near a field emitter. *New J. Phys.* **18**, 033031 (2016).

Acknowledgements

We thank A. Cipriani, D. Brunelli, M. Seyler, M. D'Errico, S. Mallick, L. Franz, J. Warren, D. Ionov, A. Bénard, Y. Ohara, and Y. Bai for sharing their research results and for

their helpful discussion, A. Abu El-Ela and A. Hassan are thanked for assistance with field work and regional geology, T. Morishita for assisting with the Electron Microprobe analyses, X-ray mapping and suggestions, Nguyen The Cong for helping with the LA-ICPMS analyses. Field work was supported by Tanta University, Egypt. Financial support by the Australian Research Council (grant FL150100133 to Z.X.L.) is acknowledged. This is a contribution to IGCP648: Supercontinent Cycles and Global Geodynamics.

Author contributions

H.G. establish the idea, collect all the data, prepare the figures, and wrote the first draft of the manuscript. Y.K. did the LA-ICPMS analyses. D.F. and D.S. perform APT. S.R. did EBSD. M.H. help in collecting samples. S.A., L.S.D. and Z.X.L. designed the paper and clarify the concepts. All the authors participated in the interpretation of the results and preparation of the final version of the manuscript.

Competing interests

The authors declare no competing interests.

Additional information

Supplementary information is available for this paper at <https://doi.org/10.1038/s41467-019-13117-1>.

Correspondence and requests for materials should be addressed to H.G.E.D.

Peer review information *Nature Communications* thanks George Ceuleneer, Emily Cooperdock, Michel Gregoire and the other, anonymous, reviewer for their contribution to the peer review of this work. Peer reviewer reports are available.

Reprints and permission information is available at <http://www.nature.com/reprints>

Publisher's note Springer Nature remains neutral with regard to jurisdictional claims in published maps and institutional affiliations.



Open Access This article is licensed under a Creative Commons Attribution 4.0 International License, which permits use, sharing, adaptation, distribution and reproduction in any medium or format, as long as you give appropriate credit to the original author(s) and the source, provide a link to the Creative Commons license, and indicate if changes were made. The images or other third party material in this article are included in the article's Creative Commons license, unless indicated otherwise in a credit line to the material. If material is not included in the article's Creative Commons license and your intended use is not permitted by statutory regulation or exceeds the permitted use, you will need to obtain permission directly from the copyright holder. To view a copy of this license, visit <http://creativecommons.org/licenses/by/4.0/>.

© Crown 2019



RightsLink®

?
Help

✉
Email Support

Origin of arc magmatic signature: A temperature-dependent process for trace element (re)-mobilization in subduction zones

SPRINGER NATURE

Author: Hamed Gamal El Dien et al

Publication: Scientific Reports

Publisher: Springer Nature

Date: May 8, 2019

Copyright © 2019, The Author(s)

Creative Commons

This is an open access article distributed under the terms of the [Creative Commons CC BY](#) license, which permits unrestricted use, distribution, and reproduction in any medium, provided the original work is properly cited.

You are not required to obtain permission to reuse this article.

To request permission for a type of use not listed, please contact [Springer Nature](#)

© 2020 Copyright - All Rights Reserved | [Copyright Clearance Center, Inc.](#) | [Privacy statement](#) | [Terms and Conditions](#)
Comments? We would like to hear from you. E-mail us at customercare@copyright.com

ATTRIBUTION STATEMENTS

Table ii: Attribution statement table for published -Chapter 7: *Origin of arc magmatic signature: A temperature-dependent process for trace element (re)-mobilization in subduction zones*

	Conception and Design	Acquisition of Data and Method	Data Conditioning and Manipulation	Analysis and Statistical Method	Interpretation and Discussion	Final Approval	Total % contribution
Co-Author 1 (Hamed Gamal El Dien)	70	50	70	60	70	60	70
Co Author 1 Acknowledgment: I acknowledge that these represent my contribution to the above research output					Signed: 03/11/2020		
Co-Author 2 (Zheng-Xiang Li)	15				10	20	10
Co Author 2 Acknowledgment: I acknowledge that these represent my contribution to the above research output					Signed:		
		40	10	20			10
Co Author 3 Acknowledgment: I acknowledge that these represent my contribution to the above research output					Signed: 03/11/2020		
Co-Author 4 (Tamer Abu-Alam)	15	10	20	20	20	20	10
Co Author 4 Acknowledgment: I acknowledge that these represent my contribution to the above research output					Signed: 04/11/2020		
Total %	100	100	100	100	100	100	100

SCIENTIFIC REPORTS



OPEN

Origin of arc magmatic signature: A temperature-dependent process for trace element (re)-mobilization in subduction zones

Hamed Gamal El Dien^{1,2}, Zheng-Xiang Li¹ , Youngwoo Kil³ & Tamer Abu-Alam⁴

Serpentinite is a major carrier of fluid-mobile elements in subduction zones, which influences the geochemical signature of arc magmatism (e.g. high abundances of Li, Ba, Sr, B, As, Mo and Pb). Based on results from Neoproterozoic serpentinites in the Arabian-Nubian Shield, we herein report the role of antigorite in the transportation of fluid-mobile elements (FME) and light rare earth elements (LREE) from the subducted slab to arc-related magma during subduction. The serpentinites contain two generations of antigorites: the older generation is coarse-grained, formed at a temperature range of 165–250 °C and is enriched in Li, Rb, Ba and Cs, whereas the younger generation is finer-grained, formed at higher temperature conditions (425–475 °C) and has high concentrations of B, As, Sb, Mo, Pb, Sr and LREE. Magnesite, on the other hand, remains stable at sub-arc depths beyond the stability field of both antigorites, and represents a potential reservoir of FME and LREE for deeper mantle melts. Magnesite has high FME and LREE absorbing capacity (over 50–60%) higher than serpentine phases. Temperature is the main controlling factor for stability of these minerals and therefore the release of these elements from subducted slabs into arc magmatism. As the liberation of these elements varies along the length of the slab, the resulting cross-arc geochemical variation trend can help to determine the subduction polarity of ancient arcs.

Regardless of the tectonic setting in which they form, serpentinites are a major potential carrier of water (up to 15%) and incompatible fluid-mobile elements (FME) such as Li, B, As, Sb, Pb, Ba, Cs, U and Sr^{1–3} into the subduction zone and the overlying mantle wedge. Serpentinites can be stable to high temperatures (620 °C) and pressures (5 GPa) at depths of up to 150–200 km⁴, and their hydration and subsequent dehydration critically influence the generation and chemistry of arc-related magmas^{5–7}. Thus, understanding the role of serpentinites (i.e., dehydration/devolatilization) in trace element geochemical cycles in subduction zones can discriminate between arc-related (i.e., high abundances of FME), plume-related, and mid-ocean ridge (MOR) basalts, and can track the cross-arc geochemical variations⁸. Currently, the factors and mechanisms that control the transfer of these elements from oceanic environments through subducting serpentinites to arc magmatism are still unclear.

Numerous *in situ* studies were previously carried out on serpentinites with the aim of defining the behavior of fluid-mobile elements and rare earth elements (REE) during subduction. These studies highlighted the role of the original minerals (i.e., olivine vs. pyroxene) and temperature on trace element distributions during the subduction process^{5,9–12} but did not consider the distribution of trace elements at higher-temperature conditions within the stability field of antigorite. Instead, they concentrated on the lizardite/antigorite transition. In addition, they did not provide enough constraints on the temperatures range beyond which FME and REE are uptaken/released from the serpentines to arc magma. Although subducted carbonates are recognized to be a potential source of C

¹Earth Dynamics Research Group, The Institute for Geoscience Research (TIGeR) and ARC Centre of Excellence for Core to Crust Fluid Systems (CCFS), School of Earth and Planetary Sciences, Curtin University, GPO Box U1987, Perth, WA 6845, Australia. ²Geology Department, Faculty of Science, Tanta University, 31527, Tanta, Egypt. ³Department of Energy and Resources Engineering, College of Engineering, Chonnam National University, Yongbong-ro, Buk-gu, Gwangju, South Korea. ⁴Universitetsbiblioteket, University of Tromsø - The Arctic University of Norway, 9037, Tromsø, Norway. Correspondence and requests for materials should be addressed to H.G.E.D. (email: hamed.gamaleldien@postgrad.curtin.edu.au)

for deep mantle melts through subduction^{13,14}, the role of carbonate minerals in serpentinite-bearing rocks as a reservoir for FME and REE has not been adequately considered.

Here, we use the results of a detailed petrological, mineralogical and geochemical study from selected Neoproterozoic serpentinite bodies in the Arabian-Nubian Shield (a typical arc-accretion orogen)¹⁵ to constrain the role of temperature within the stability field of antigorite on the distribution of FME and REE in subduction zones. In addition to antigorite, mineral chemistry of carbonate minerals indicates that magnesite is a potential reservoir for these elements during the subduction process. Our work argues against the prevailing view that original minerals (olivine and pyroxene) are the main factors controlling the trace element distribution. Instead, we provide evidence for the systematic distribution of FME and REE in subduction zones that depends on temperature conditions of the subducting slab, and we illustrate how the resultant cross-arc geochemical trends may help to determine the subduction polarity of ancient arcs in Earth's history.

Geological background and sample description. The Arabian-Nubian Shield (ANS) represents the largest Neoproterozoic juvenile continental crust. ANS formed through accretion of island arcs to the Gondwanan continental margins by the closure of the Mozambique Ocean during the East-African orogeny (750–550 Ma)¹⁶. ANS ophiolites (which include abundant serpentinites) mark the suture zones between the accreted arcs¹⁵. Egyptian ophiolites, including ultramafic bodies, occur mainly in the central and southern parts of the Eastern Desert, extending across the border with Sudan (Supplementary Fig. S1a). They were intensely deformed in the late Neoproterozoic during oblique collision¹⁷ and accretion of island arcs onto the Saharan Metacraton, forming ophiolitic mélanges¹⁵. Although, some ophiolites were previously thought to have formed in mid-ocean ridges¹⁸, there is a general consensus that the majority of the ANS ophiolites formed in subduction-related tectonic settings^{15,19–25}.

Serpentinite samples were collected from Wadi Muweilih in the Central Eastern Desert of Egypt (Supplementary Fig. S1b,c). This area is part of the Um Esh-Um Seleimat tectonic ophiolitic mélange²⁶ (Supplementary Fig. S1b), and consists of highly sheared mélange rocks containing many isolated masses of serpentinites, metagabbros, pillowed metabasalts, schistose rocks, metasedimentary rocks including metaconglomerates²⁷ (Supplementary Figs S1c, S2a,b). These serpentinitized bodies crop out either as large lenticular blocks about 1–3 km in size, or as small thrust sheets in a tectonic mélange with small amounts of talc-carbonate rocks. The contacts of the serpentinites with metasedimentary and metagabbroic rocks in the east and with metaconglomerates in the west are both SW-dipping thrusts (Fig. S1c). Along the faults, sheared serpentinites have been altered to talc-carbonates.

Petrographic investigations and Raman spectral analyses reveal that the protolith of the studied peridotites was suffered variable degrees of serpentinization and carbonation. Primary minerals olivine and pyroxene are completely serpentinized and chrome-spinel is the only primary relict phase. The studied serpentinites are composed mainly of antigorite, magnesite ± dolomite, magnetite, small amounts of chrome-spinel, and minor amounts of chlorite and talc (Supplementary Fig. S2d,e). Antigorite exhibits a predominantly a non-pseudomorphic, interpenetrating texture (Fig. 1a–c) and mainly occurs in two distinct crystal sizes: fine aggregate grains (20–50 µm) and coarse radiating fibrous (100–150 µm) (Fig. 1a–c). The fine antigorites commonly overprint the coarse ones (Fig. 1a–c). Magnesite is present in two forms: either as anhedral clusters (Fig. 1d) or in small veinlets associated with fine dolomite (Supplementary Fig. S2c,d). Magnesite, magnetite, chrome-spinel, chlorite and talc occur as randomly distributed grains among antigorite-dominated groundmass.

Results

Geochemical composition. All the studied serpentinite samples have high-water contents (i.e., high LOI values), ranging from 12.54 to 14.93 wt% (for details on the bulk-rock compositions see Supplementary Information). The Raman spectra of the examined serpentinite samples identify antigorite as the only serpentine phase (Fig. 1e). Two groupings of antigorite are distinguished based on their different textures (grain sizes) and chemical compositions (Figs. 1 and 2a; Supplementary Table). The first group is coarse-grained (100–150 µm), and the second group is fine-grained (20–50 µm) (Fig. 1a–c). The coarse-antigorite (CA) group has higher SiO₂ content (43.01–45.86 wt%) and lower Al₂O₃ content (0.02–0.97 wt%) compared to the fine-antigorite (FA) group which range in SiO₂ from 39.52–42.95 wt% and in Al₂O₃ from 1.16–3.38 wt% (Fig. 2a). MgO and FeO contents do not show systematic variation between the two groups (Fig. 2a). NiO (up to 0.92 wt %) and Cr₂O₃ (up to 1.06 wt %) contents show no notable difference, and both groups plot in the serpentine fields of olivine and orthopyroxene, reflecting a harzburgite protolith (Fig. 2b). *In situ* trace element analyses reveal a heterogeneous distribution of FME between the CA- and FA-groups. FME such as B have higher contents in the FA-group (40.89–49.87 ppm) than in the CA-group (15.32–24.50 ppm), whereas Li has higher contents in the CA-group (3.44–3.95 ppm) than in the FA-group (2.03–2.73 ppm) (Fig. 3; Supplementary Fig. S6, Table). Moreover, the CA-group has lower contents of As, Sb, Pb, Mo, Sr and higher contents of Rb, Cs and Ba (Fig. 3; Supplementary Fig. S6, Table). Th, U, P and high-field strength elements (HFSE: Nb, Ta, Zr and Hf) show no obvious difference between the two groups, but Ta and Hf show positive spikes compared to elements of the same compatibility in both groups (Fig. 3). REE normalized to (CI)-Chondrite²⁸ patterns have a U-shape pattern, and the light rare earth elements (LREE) contents higher in the FA-group (La = 0.074–0.127 ppm, La_N/Sm_N = 1.96–3.29) compared to the CA-group (La = 0.031–0.047 ppm, La_N/Sm_N = 1.88–2.79) (Fig. 3). The middle rare earth elements (MREE) to heavy rare earth elements (HREE) show a slight negative slope. The HREE concentrations of the FA and CA- groups are indistinguishable (Yb_{N(CI-normalized value)} = 0.47–0.57) (Fig. 3).

Magnesite is the main carbonate mineral, representing 5–10% of the modal mineral composition in the studied samples, although minor thin veinlets of dolomite also occur (Fig. 1d; supplementary Fig. S2c,d). Magnesite composition varies in MgO (37.72–40.49 wt %), FeO (1.88–5.77 wt %) and MnO (0.32–2.74 wt %). Dolomite has variable contents of MgO (14.83–20.21 wt %), CaO (21.44–27.54 wt %), FeO (0.44–5.65 wt %) and MnO (0.09–1.15 wt %). A Primitive Mantle (PM)-normalized²⁹ trace element diagram of analysed magnesite shows a significant enrichment in incompatible elements (Fig. 3). Almost all FME, such as Sb (1.55–17.83 ppm), B

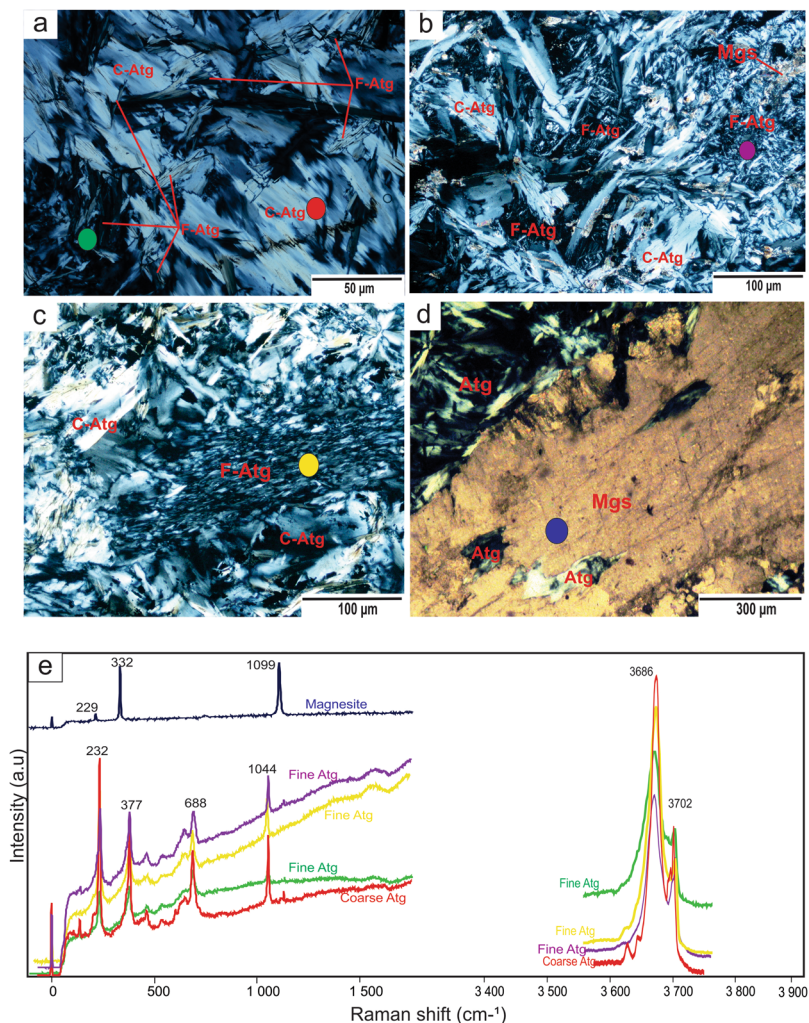


Figure 1. Photomicrographs of the studied serpentinites. (a–c) Interpenetrating texture of antigorite (Atg). (d) Magnesite (Mgs) clast containing antigorite relics. (e) Raman spectra of fine (F) and coarse (C)-grained antigorites in the studied serpentinites in low frequency (0–1500 cm^{-1}) and OH stretching (3350–3900 cm^{-1}) ranges. Antigorite shows discrete peaks at 232, 377, 688 and 1044 cm^{-1} in the low wavenumber region and 3686 and 3702 cm^{-1} in the OH-band region. The Raman spectra of magnesite show peaks at 229, 332 and 1099 cm^{-1} in the low wavenumber region.

(59.06–170.96 ppm), As (25.31–46.30 ppm), Mo (1.89–2.28 ppm), Cs (0.28–0.72 ppm), Li (13.90–36.01 ppm) and Pb (1.63–2.86 ppm) are enriched in magnesite (Fig. 3; Supplementary Table). Rb (0.70–0.91 ppm) is slightly enriched and both Sr (5.48–9.04 ppm) and Ba (0.56–4.32 ppm) are slightly depleted relative to primitive mantle but are slightly enriched relative to elements with similar compatibility (Fig. 3). HFSE such as Ti (11.62–20.39 ppm), Zr (–0.31 ppm), Hf (0.14–0.15 ppm), Nb (0.08–0.09 ppm) and Y (0.57–1.44 ppm) are highly depleted. Chondrite²⁸-normalized REE pattern shows the same U-shape like antigorites, but with higher LREE contents ($\text{La}_N = 5.04\text{--}5.80$) (Fig. 3). HREE are highly enriched, with Yb up to 3 times of that of Chondrite, and show a slight negative slope to MREE.

Thermodynamic modelling. A series of T-X pseudosections at different pressures were calculated to estimate the pressure-temperature conditions of the serpentinization. All the T-X pseudosections show stability of the spinel mineral at high-temperatures (>670 °C; Supplementary Fig. S7). These temperature estimates indicate that the observed spinel in the studied samples is a metastable phase with respect to the surrounded low-grade assemblages³⁰. Figure 4 shows two T-X pseudosections at 1 and 8 kbar, respectively. These pseudosections have similar topology but dolomite is unstable at low pressure conditions (i.e., 1 kbar) within the studied T-X range. At higher pressure conditions (i.e., 8 kbar; Fig. 4), however, dolomite is stable within the temperature range of 325–550 °C. The observed mineral assemblages, i.e., chlorite-talc-antigorite-magnesite-fluid \pm dolomite, are thermodynamically stable at the bulk composition range of between 0.15–1 and 0–1 for pressures of 1 and 8 kbar, respectively (Fig. 4). The upper temperature limits for the stability of the observed assemblages are marked by the anthophyllite-in boundaries. At low pressure conditions (e.g. 1 kbar), the anthophyllite-in boundaries appear in the temperature range of 360–375 °C, but at 8 kbar the boundaries shift to the higher temperature (450–475 °C).

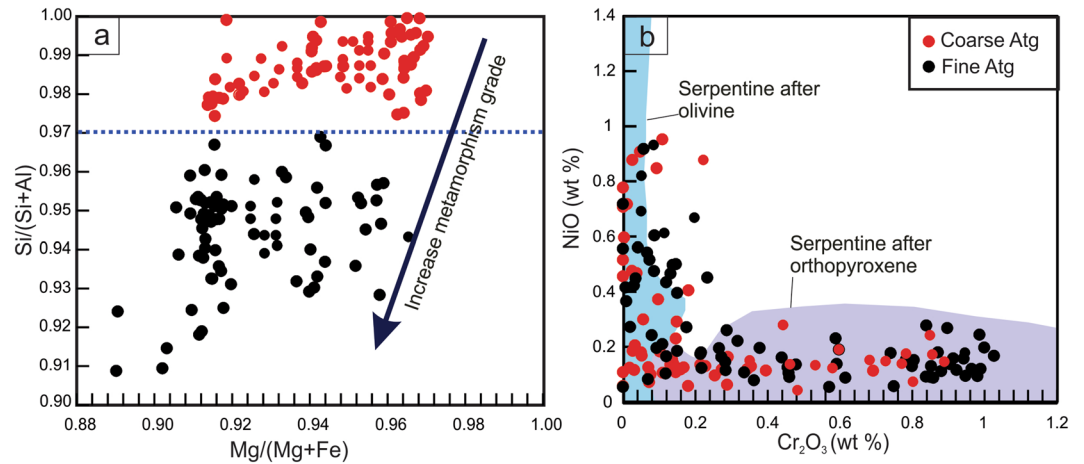


Figure 2. Mineral chemistry of antigorites from the studied samples. (a) $\text{Si}/(\text{Si} + \text{Al})$ vs. $\text{Mg}/(\text{Mg} + \text{Fe})$. The variation of $\text{Mg}/(\text{Mg} + \text{Fe})$ indicates different bulk chemistry of the rocks while the variation of $\text{Si}/(\text{Si} + \text{Al})$ is due to increase in the metamorphic grade. (b) NiO vs. Cr_2O_3 (wt %). Data used to create olivine and orthopyroxene fields collected from Kodolányi *et al.*¹².

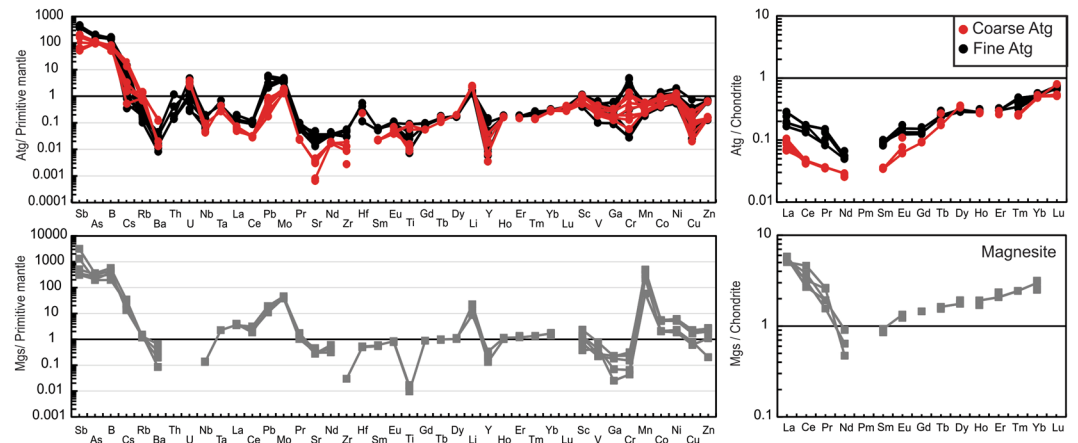


Figure 3. Primitive mantle²⁹ normalized multielement and rare earth element patterns normalized to chondrite²⁸ of the studied antigorite and magnesite.

Figure 5a shows the shift of anthophyllite-in boundaries toward higher temperature with an increase in pressure from 1 kbar to 9 kbar.

The antigorites display an increase in SiO_2 content and decrease in Al_2O_3 content from the FA-group to the CA-group (Fig. 2a; Supplementary Table). Tschermak's substitution in antigorites is proposed to occur following the equation of $\text{M}^{2+} + \text{Si}^{4+} = \text{Al}^{3+} + \text{M}^{3+}$, where M^{2+} resides in the octahedral site (Mg, Fe^{2+} , Mn and Ni) and M^{3+} in the tetrahedral site (Fe^{3+} , Cr, Al)³¹. Thus, Al^{3+} is incorporated in antigorite through a coupled exchange when one Mg and one Si cation are substituted by two Al cations^{31,32}. The $\text{Si}/(\text{Al} + \text{Si})$ ratio of antigorite has been used as a non-linear potential geothermometer for serpentinite rocks, due to its sensitivity to temperature^{32,33}. In the current study, the $\text{Si}/(\text{Al} + \text{Si})$ ratios are insensitive to changes in pressure but are sensitive to changes in temperature (Fig. 5).

Although the difference in $\text{Si}/(\text{Al} + \text{Si})$ between the two groups is relatively small (Fig. 5b,c), a gap in the mineralogical composition is clearly observed at $\text{Si}/(\text{Al} + \text{Si})$ between 0.965 and 0.975 (Figs. 2a and 5b,c) which corresponds with the petrographic transition from the CA to the FA-group. Also, this gap corresponds with the isopleth line (with value 0.965) which is observed in the temperature range of 250–425 °C (Fig. 5a). The CA-group has $\text{Si}/(\text{Al} + \text{Si})$ in the range of 0.975–1 (apfu; atoms per formula unit), corresponding with a temperature range of ca. 200 to 250 °C (Fig. 5). The FA-group has a $\text{Si}/(\text{Al} + \text{Si})$ content range of 0.92–0.96 which indicates higher temperature conditions (425–475 °C). Such temperatures cannot be achieved unless the system attains local equilibrium at pressure >9 kbar.

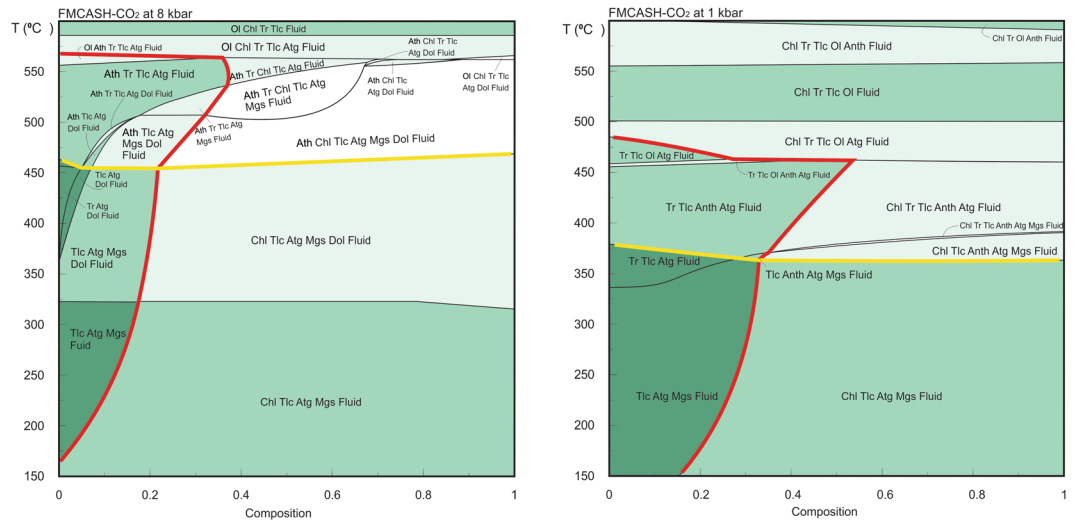


Figure 4. T-X pseudosections. The two pseudosections constructed at pressure 8 kbar and 1 kbar in the chemical system FMCASH-CO₂ using the activity models cited in the methods section. The x-axes represent a range of the bulk composition in wt% where 0 is equivalent to bulk of: FeO: 4.157, MgO: 47.13, CaO: 0.001, Al₂O₃: 0.715, SiO₂: 40.524, H₂O: 8.89, CO₂: 0.001, and 1 is equivalent to bulk of: FeO: 7.00, MgO: 35.00, CaO: 0.04, Al₂O₃: 3.00, SiO₂: 50.00, H₂O: 18.00, CO₂: 0.8. The red isochemical lines represent the chlorite-in boundaries. The studied mineral assemblages are stable to right-side of the chlorite-in boundaries. The yellow line shows the anthophyllite-in boundary. The studied assemblages are stable to the lower temperature part of the anthophyllite-in boundaries.

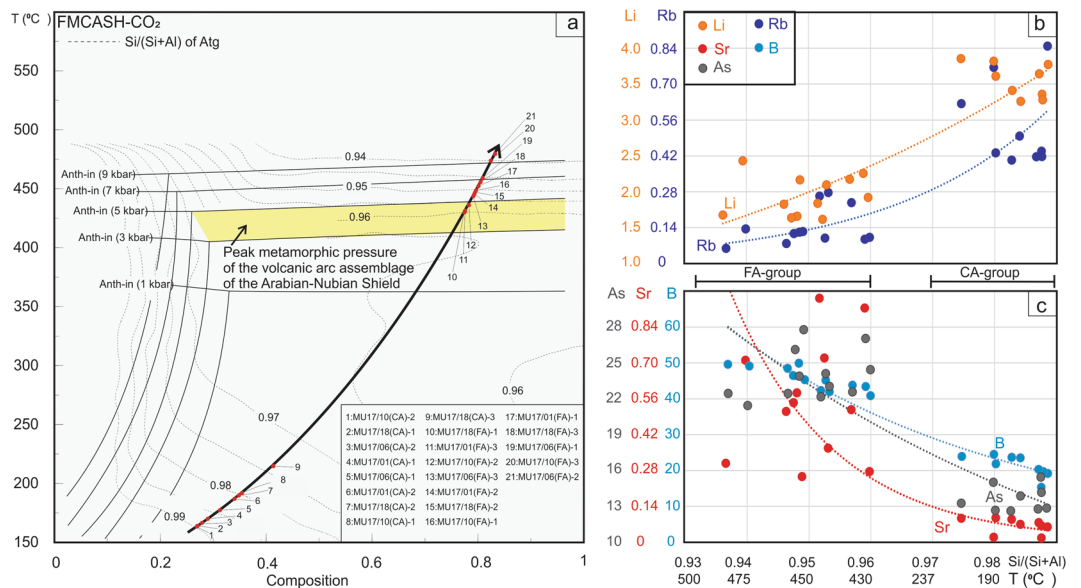


Figure 5. P-T-X pseudosection showing the shift of the anthophyllite-in boundaries toward higher temperature conditions when the pressure increases (a). The yellow area represents the anthophyllite-in boundaries at pressure of ca. 4 kbar which is equivalent to the peak metamorphic pressure of the volcanic arc assemblages of the Arabian-Nubian Shield⁸³. The pressure represents a combination of lithostatic and hydrostatic pressures. The vertical isochemical solid lines show the shifting in the chlorite-in boundary with pressure change. Contour lines are the Si/ (Si + Al) ration of the antigorite chemistry in the T-X space. The solid black arrow represents the P-T-X path of the studied rocks. The red dots along the P-T-X path represent some of the analysed antigorites (CA at the low temperature conditions) and (FA at the high temperature conditions). The right hand plots shows the variations of Li and Rb (b) B, Sr and As (c) contents of the two group antigorites with the temperature changing along the P-T-X path. The x-axes represents temperature and Si/(Si + Al).

Discussion

Origin of the protolith. Field, petrographical and geochemical characteristics of the studied serpentinites suggest a subduction channel origin for the protolith. A subduction channel typically consists of fragments of subducted oceanic serpentinites, metasediments, and altered mafic crust that can be later accreted to the arc system to form a mélange zone^{34–36}. Such serpentinites are typically strongly sheared and dominated by antigorite³⁷. All of these features are present in the studied region (Supplementary Figs. S1, S2a,b) and most of the ANS ophiolites¹⁵. The studied serpentinites occur in one of the well-developed suture zones in the Eastern Desert of Egypt, i.e., the Um Esh-Um Seleimat tectonic mélange²⁶ (Supplementary Fig. S1b,c). Furthermore, these rocks are similar to some subducted serpentinites in Mesozoic ophiolites such as those of the Zagros suture zone in Iraq³⁸ and ophiolite complexes of Northwest Anatolia in Turkey³⁹. Previous work (e.g.^{20,24}) on ophiolites in the vicinity also suggest a subduction-related origin.

The harzburgite protolith of the studied serpentinites suggests that the peridotite parents have a refractory origin, and clinopyroxenes were almost completely exhausted by pre-serpentinization partial melting (for details on the nature of the protolith see Supplementary information). Moreover, mineralogical (spinel Cr# >0.6)³⁰ and geochemical characteristics such as low Al₂O₃/SiO₂ (<0.04), strong depletion in compatible trace elements (i.e., HREE and Y), over-enrichment of As, Pb, Mo and nearly flat REE patterns, also point to a subducting-slab origin^{2,11,34} for the studied serpentinites and distinguishes them from mantle wedge/fore-arc serpentinites (e.g., Izu-Bonin-Mariana)^{12,40} (Supplementary Figs. S4, S5).

The high field strength element (HFSE: Nb, Th, Hf and Ti) contents of the studied rocks (Supplementary Fig. S5b) differ significantly from patterns expected of a melt residue⁴¹. In addition, the absence of any correlation between these elements and LOI indicates that the enrichment processes were not related to the serpentinization; instead, they were more likely caused by melt-rock interaction^{12,41}. The high Ti content (150–360 ppm) of the studied serpentinites that plot above the melting trend (Supplementary Fig. S5b) suggests interaction of the subducting serpentinite mainly with Ti-rich melts (Ti = 30–500 ppm)². On the other hand, the positive correlations of LREE and FME with LOI point to the enrichment of these elements during serpentinization process of the protolith through fluid/rock interactions (Supplementary Fig. S3).

Two-stage serpentinization and geochemical consequences. We suggest that the studied rocks experienced two stages of serpentinization which correspond to the different temperature ranges associated with the formation of CA- and FA-group antigorites (Fig. 5). The first stage resulted in the formation of coarse antigorites at 200–250 °C that may have grown directly from the original olivine and orthopyroxene⁴² during the initial stage of subduction. During this stage, the slab-derived fluids caused strong hydration of the subducted peridotites protolith forming CA-group, such as the antigorite serpentinites (>200 °C)^{43,44} in the Happo-O'ne area in Japan⁴⁵ and some of the other antigorite serpentinites in Eastern Desert, Egypt^{21,23}. Although the coarse antigorites could also have crystallized by progressive replacement of lizardite formed during low-temperature oceanic serpentinization^{43,46}, we favour the former explanation due to the absence of lizardite relics (i.e., mesh cells)³⁷ in the studied serpentinites. The second serpentinization stage occurred at increased subduction depths with elevated metamorphic temperatures of 425–475 °C^{10,11} (Fig. 5), resulting in the formation of the fine antigorites which overprinted and replaced some of the coarse ones (Fig. 1a–c).

During subduction, oceanic lithosphere gets serpentinized through interactions with circulating fluids released from the subduction channel^{3,36,37,47–49}. Although some studies show that the oceanic lithosphere can be serpentinized before it enters the subduction zone⁵⁰, the primitive mantle-normalized pattern of the FME and LREE of the studied serpentinites (Fig. 6) and their rock-forming minerals (antigorites and magnesites) have significant similarity to the subduction inputs components that include mainly altered oceanic crust (AOC)⁵¹, global subducted sediments (GLOSS II)⁵² and marine sediments⁵³. These elements, with the exception of Sr, Rb and Li, are more highly enriched than seawater-derived hydrothermal fluids in spreading mid-ocean ridges (MOR: Logatchev, Rainbow, Snake Pit)⁵⁴. Moreover, the over-enrichments of As, Sb, B and Mo in the studied serpentinites and their rock-forming minerals support an important role for sediment-derived fluids^{48,55,56} which are characteristic of subduction-related serpentinites^{2,11,34}. The similarities in Li, Sr and Rb contents between the serpentinites and seawater-derived hydrothermal fluids suggest contribution of seawater either through direct infiltration into fractures and faults that formed during the bending of a subducted slab⁵⁷ as it entered the subduction channel, or through the circulation of water/fluids in the subduction channel that were released from the subducted oceanic lithosphere and marine sediments⁵⁸.

To further test our interpretation, we calculated the FME composition of the fluids that interacted with the studied rocks during serpentinization. There are only a few experimental studies focused on FME (i.e., B, Li, As, Sb and Cs) partitioning during progressive serpentinization^{59,60} and those studies are limited to the low temperature serpentine phase (200–300 °C). Here we used the partitioning coefficient of those elements^{59,60} to estimate the fluid composition in equilibrium with the CA-group antigorites. The estimated composition of those elements in the equilibrated fluids have B = 26.41–42.24 ppm, Li = 0.40–0.46 ppm, Sb = 0.03–0.09 ppm, As = 3.26–3.96 ppm and Cs = 0.07–0.23 ppm. With the exception of Li, these estimates are similar to the subduction input components compositions of GLOSS II and AOC (e.g. B = 26.6–67.9 ppm and Cs = 0.15–4.9 ppm)^{51,52}, but are higher than seawater-derived hydrothermal fluids in MOR (B = 3.35 ppm, Cs = 0.03 ppm, As = 0.009 ppm and Sb = 0.0008 ppm)^{54,61}. Therefore, we conclude that the studied serpentinites were formed in a subduction-related environment where serpentinization was caused mainly by fluids from the subduction channel with sedimentary input.

The studies of Bebout⁴⁸ and Marschall *et al.*⁶² demonstrated the release of B, Li, As, Sb and Cs from sedimentary and mafic rocks via prograde metamorphism and increasing pressure-temperature conditions within the subduction channel. *In situ* B and Li analyses in the studied antigorites indicate, based on thermodynamic modelling (Figs. 4, 5), that the different distributions in B and Li between the two antigorite groups (CA- av. = 21.29,

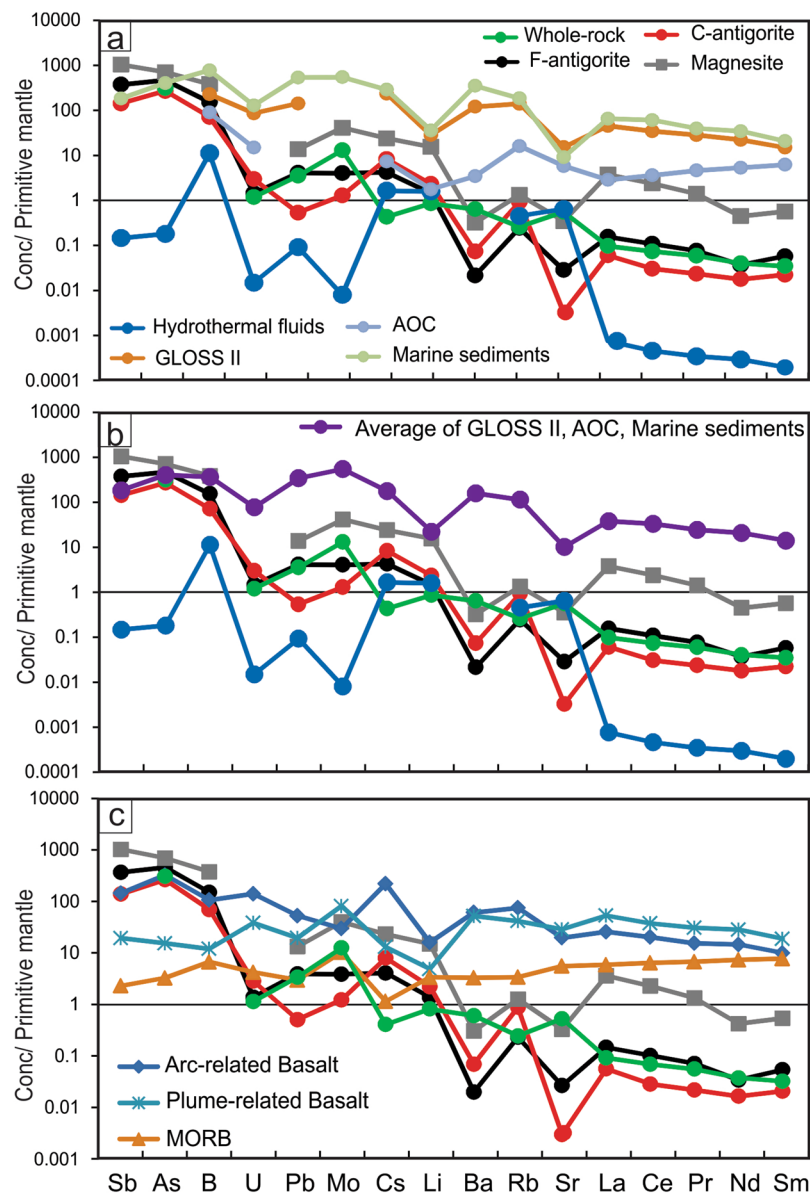


Figure 6. The average contents of fluid-mobile element and light rare earth element patterns of the studied serpentinites and rock forming minerals (antigorite and magnesite) normalized to the Primitive Mantle²⁹. (a,b) plotted against the composition of hydrothermal fluids (Logatchev, Rainbow, Snake Pit)⁵⁴ and the contents of subduction inputs including altered oceanic crust (AOC)⁵¹, global subduction sediments (GLOSS II)⁵² and marine sediments pattern⁵³ are reported for comparison; (c) plotted against the average compositions of arc-related basalts, plume-related basalts and mid ocean ridge basalts (MORB) after Georoc repository (<http://georoc.mpch-mainz.gwdg.de/georoc/>).

3.69 ppm, respectively; FA- av. = 45.61, 2.30 ppm, respectively) (Figs. 5b,c and 6) are related to different temperature conditions. The enrichment of B at high temperature and Li at low temperature contrasts with some previous studies^{2,12,34,63} which argue that B enrichment occurs in the low temperature serpentine phase and is depleted at high temperature conditions. However, it is in agreement with the reported retention of B at higher metamorphic grade phase^{5,64}. Our interpretation is also supported by a continuous loss of B from the subducting slab (i.e., low B at high temperature) during the progression of subduction⁴⁸. The behaviour of Li, on the other hand, is in agreement with previous studies that revealed the loss of Li during the lizardite/antigorite transition and increasing temperature of serpentinization. Furthermore, As, Sb, Pb and Mo contents are higher in the high temperature FA-group (Av. As = 23.16 ppm, Sb = 2.04 ppm, Pb = 0.61 ppm, Mo = 0.20 ppm) compared to the low temperature CA-group (Av. As = 13.36 ppm, Sb = 0.77 ppm, Pb = 0.08 ppm, Mo = 0.06 ppm) (Figs. 5c and 6), suggesting addition/incorporation of those elements to the FA-group at higher temperatures. These trends are consistent with a continuous release of those elements from subducted sediments and from AOC during prograde metamorphism^{48,56}. Whereas B, As and Sb are preferentially incorporated into tetrahedral Si in sheet silicates^{5,6}

(i.e., antigorite), they are likely to increase from CA- to FA-group with decreasing Si/(Al + Si) and increasing temperature (Fig. 5b,c).

Contrary to the aforementioned elements, large ion lithophile elements (LILE) such as Rb, Ba, Cs and U are more enriched in the low temperature CA-group (Av. Rb = 0.55 ppm, Ba = 0.48 ppm, Cs = 0.17 ppm, U = 0.06 ppm) than in the high temperature FA-group (Av. Rb = 0.15 ppm, Ba = 0.14 ppm, Cs = 0.08 ppm, U = 0.02 ppm), consistent with the enrichment of these elements at low-temperature conditions² (Figs. 5b, 6). This enrichment suggests the release of these elements during the high-temperature serpentinization process^{11,12,34}. However, Sr has higher content in the high temperature FA-group (Av. = 0.56 ppm compared to Av = 0.06) indicating continuously addition of Sr to the antigorite from the subduction channel-derived fluids and retention at higher temperatures. This result is contrary to previous studies that argue against Sr enrichment at high temperature^{2,11,12,34,65}, although those studies concentrated only on lizardite/antigorite transition without determining the formation temperature for each phase or distinguishing between the two temperature-dependant phases of antigorite. Moreover, our results support Kodolányi *et al.*'s¹² observation that the distribution of B and Sr is controlled by the same mechanisms, which we suggest to be temperature- and fluid-dependent processes.

The REE contents of the serpentine phases are commonly assumed to be an inherited feature from the original minerals (olivine and pyroxene)^{2,9,11,12}. Here, the studied antigorite (both the CA- and FA- groups) displays interpenetrating textures with no preservation of the primary minerals, arguing against the role of the parent minerals in the trace element concentrations of antigorite. Although, the two groups have similar HREE contents, the high temperature FA-group have higher LREE (La = 0.074–0.127 ppm) than the low temperature CA-group (La = 0.030–0.047 ppm) (Fig. 6). Our data suggest re-mobilization of LREE with increasing serpentinization temperature.

Carbonates formation and trace element budget. The predominance of magnesite in the studied serpentinites also indicates a paleo-subduction zone origin⁶⁶ as magnesite is rarely found in carbonate-related ultramafic rocks in normal oceanic settings⁶⁶. Magnesite can be formed directly from (1) olivine or orthopyroxene-dominated ultramafic rocks (i.e., $\text{Ol} + 2\text{CO}_{2\text{aq}} = 2\text{Mgs} + \text{SiO}_2$ ^{66,67} or by (2) replacing antigorite ($2\text{Atg} + 3\text{CO}_2 = 3\text{Mgs} + \text{Tlc} + 3\text{H}_2\text{O}$)^{23,68}. We favour the second mechanism for our study because of a complete absence of quartz in the studied samples. This interpretation is supported by (1) the presence of fractures and veinlets of magnesite that crosscut serpentinites and antigorite groundmass (Supplementary Fig. S2c,d), which represent CO₂-rich fluids pathways, (2) the presence of antigorite relics inside magnesite clasts (Fig. 1d), (3) the presence of minor talc associated with magnesite (Supplementary Fig. S2d), (4) strong similarities between the trace element patterns of magnesite and antigorite (Fig. 6), and (5) high trace element contents of magnesite over antigorite that support the formation of magnesite at higher temperature and depth (~60–70 km)^{68,69} compared to the formation condition of antigorite. The carbon may have come from metamorphic decarbonation of subducted sediments^{13,70} as supported by similar FME and LREE patterns between the magnesite and subducted sediments, AOC and marine sediments. The presence of dolomite with magnesite indicates percolation of moderate to high flow of CO₂-Mg-rich and Ca-poor fluids from the subducted sediments^{66,67}. Generally, Mg-rich and Ca-poor fluids are associated with peridotites when they undergo complete or near-complete serpentinization⁶⁷. Therefore, we suggest that magnesite formed after antigorites at higher temperatures and depths during subduction.

Although antigorite is the major carrier of trace elements in serpentine, we note that magnesite has higher contents of FME of B, Li, As, Sb, Pb, Mo, Cs and LREE than antigorite and primitive mantle (Figs. 3, 6), which suggests that magnesite is a potential carrier of, as well as, a reservoir for these elements. In addition, magnesite is also a sink for Mn (Fig. 3). On the other hand, magnesite is depleted in Sr, Ba and U. In summary, we suggest that magnesite has high FME and LREE absorbing capacity of over 50–60% higher than serpentine phases (calculated according to differences in the contents of those elements between magnesite and antigorite). Based on our petrographic observations and previous experimental studies⁶⁸, we argue that magnesite forms as a result of antigorite transformation, where the parent antigorite contributes a considerable amount of FME and LREE to the newly formed magnesite.

Implications for arc magmatism and subduction polarity geochemical fingerprinting. The thermodynamic modelling results (Figs. 4, 5) demonstrate that the formation of two types of antigorite is a temperature-dependent process. The first serpentinization stage and formation of coarse antigorite is estimated at 200–250 °C and the second serpentinization stage and formation of fine antigorite occurred at 425–475 °C (Fig. 7). According to different FME and LREE contents of the two types of antigorite groups, we suggest that these elements mainly redistributed (uptaken, trapped and released) as a result of varying temperature. During the first serpentinization stage, the LILE such as Rb, Ba, Cs and Li and U are released from the subducted slab at low temperatures (200–250 °C) and shallow depths and incorporated into coarse antigorites (CA). These result are consistent with previous reported high enrichment of LILE in fluids released from subducting slabs at shallow depths and lower temperatures (~200 °C) directly beneath the forearc region^{48,71}. The second serpentinization stage is represented by the release of higher amounts of B, As, Sb, Mo, Pb, Sr and LREE from the subducting slab at higher temperatures (425–475 °C) and greater depths, and their incorporation into the fine antigorites (FA) (Fig. 7).

Finally, we suggest that serpentinites remain stable at high sub-arc depths and represent a potential carrier of FME such as B, As, Sb, Sr, Mo, Pb and LREE that get recycled back into the mantle wedge through the so-called “antigorite breakdown” (600–700 °C)⁴. The similarities of the FME (B, As, Sb, and Li) patterns between the studied serpentinites (including rock forming minerals) and volcanic arc basalts (Fig. 6c) demonstrate how dehydration of serpentinites during subduction plays a principle role in the generation of arc-related magmatism (Fig. 7), in addition to the commonly considered dehydration of subducted sediments and AOC^{48,62}. The high enrichment of these elements in the arc-related basalts can therefore be used to distinguish them from non-arc basalts such as

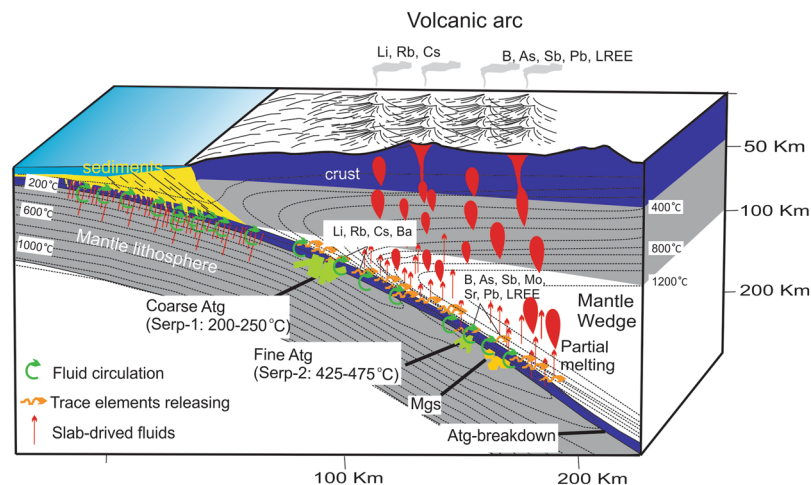


Figure 7. A cross-section sketch of a subduction zone complex showing the position of the first serpentinization stage (Serp-1) and formation of coarse antigorites (Atg) at 200–250 °C, the second serpentinization stage (Serp-2) and formation of fine antigorites at 425–475 °C and magnesite formation (Mgs).

plume-related basalt and MORB. The model also predicts that arc magmatism closest to the trench should have higher LILE such as Li, Rb and Cs, released during the first serpentinization stage, whereas those landward from the trench should be more enriched in B, As, Sb, Pb and LREE, released during the second serpentinization stage and after antigorite breakdown⁴. Such a cross-arc geochemical variation pattern has indeed been reported in some previous studies of arc volcanic rocks^{72,73}. This cross-arc FME and LREE variation pattern, along with previously reported K_2O/SiO_2 cross-arc variation pattern⁷⁴, can be powerful tools for the identification of subduction polarities of ancient arc systems.

Methods

Raman spectroscopy analysis. Raman spectra of serpentines and carbonates (Fig. 1e) were obtained by a micro-Raman system (HORIBA Jobin Yvon, Lab-RAM HR-800) equipped with a 514 nm Ar^+ laser (melles Griot, 43 series Ion Laser, 543-GS-A02) and an optical microscope (Olympus, BX41) at Kanazawa university, Japan. The Ar^+ laser has an irradiation power at 50 mW with a spectral resolution of about ± 2.5 to ± 3.5 cm^{-1} . The Raman signal was acquired between 50 and 120 sec. Scattered light was collected in a backscattered geometry, using a pin-hole (300 μm), slit (100 μm) and a grating (600 grooves/ μm). A Si-based CCD (charge-coupled device) was used to record the Raman spectra. Based on OH stretching mode regions and lattice vibrational modes of the serpentine species⁷⁵, the spectral regions (0 to 1500 cm^{-1} and 3400 to 3900 cm^{-1}) were investigated. The LabSpec software was used to determine the band position of each spectrum.

Bulk rock chemical analysis. Major and trace element bulk-rock geochemistry was carried out for 8 serpentine samples (Supplementary Table; all whole-rock data is reported on a volatile-free basis). Whole-rock samples were crushed with a polyethylene-wrapped hammer into <0.5 cm pieces and then were ground with ethyl alcohol in an agate mill to a grain size below 50 μm . Major element compositions were analysed by X-ray fluorescence spectrometer (Shimadzu, XRF-1800) at the Pukyong National University, South Korea. Analytical conditions were 40 kV accelerating voltage and 70 mA beam current. Analytical precision is better than 2% for major elements. All glass beads were analysed three times and the averages were taken. Certified Reference Materials (CRMs), BIR-1 and JG-2, were used to determine the accuracy of the major element compositions. For detailed method for trace and rare earth element analyses see ref.²¹. Analytical values for USGS reference samples (BIR-1 and MUH-1) agree with recommended values within suggested tolerances. The precision of the measurements by repeated analyses of reference samples is better than $\pm 5\%$ for trace elements.

Electron probe micro analysis (EMPA). Major and some minor elements in antigorites and carbonates were acquired using a JEOL JXA-8800 electron-probe at Kanazawa University, Japan (Supplementary Table). The analytical conditions were 15 kV accelerating voltage, 20 nA probe current and 3 μm beam diameter. The ZAF-correction was performed to correct the raw data. Ferric and ferrous iron redistribution from electron microprobe analyses was made using the charge balance equation⁷⁶. Natural minerals standards were used for calibration (JEOL Kanazawa STD1) such as Q17-quartz for Si, O16-corundum for Al, O19-eskolaite for Cr, M6-fayalite for Fe, O15-periclase for Mg, O20-manganosite for Mn, M8-wollastonite for Ca, M3-jadeite for Na, M13-KTiPO5 for K, Ti and O24-pentlandite for Ni. Olivine, clinopyroxene and spinel standard reference minerals, separated from Kurose peridotites xenoliths, were used.

Laser ablation-inductively coupled plasma-mass spectrometry (LA-ICP-MS) micro analysis. Trace element compositions of serpentine and magnesite (Supplementary Table) were determined by 193 nm ArF Excimer LA-ICP-MS at Korean Basic Science Institute (KBSI), South Korea (Teledyne Cetac Technologies equipped with Analyte Excite). Analyses were performed by ablating 110 μm diameter spots at 10 Hz with an

energy density of 5 J/cm² per pulse. Signal integration times were 60 s for a gas background interval and 60 s for an ablation interval. The NIST SRM 612 glass was used as the primary calibration standard and was analysed at the beginning of each batch of <5 unknowns, with a linear drift correction applied between each calibration. The element concentration of NIST SRM 612 for the calibration is selected from the preferred values of Pearce *et al.*⁷⁷. Each analysis was normalized using ²⁹Si for serpentine and ²⁴Mg for magnesite as internal standard elements, based on Si and Mg contents obtained by Electron probe micro analysis (EMPA). All minerals were analysed multiple times and the average taken. The relative standard deviations (RSD) of the trace and rare earth elements in the minerals were mostly 5–10%. To improve precision and accuracy of the trace elements data, we analysed the NIST612 CRM before and after each 5 unknown samples. High RSD is found only for ¹³⁷Ba (10.7%). We analysed some clear homogenous areas of antigorite aggregates, but some area may contain dusty magnetite or other minor phases which may influence the actual antigorite trace elements values. Thus, we used the Glitter software, which shows ablation profile for element and permits to reduction of analytical contamination.

Thermodynamic modelling. Thermodynamic modelling was calculated in a FMCASH-CO₂ system (i.e., FeO-MgO-CaO-Al₂O₃-SiO₂-H₂O-CO₂). Different pseudosections were constructed using *Perple_X*⁷⁸ and the internally consistent dataset of Holland and Powell⁷⁹. We assumed that local equilibrium, when chemical potentials are equalized⁸⁰, was obtained at a length scale of millimetres. The solution model of (antigorite, chlorite, olivine and garnet, orthopyroxene, clinopyroxene, spinel, carbonate (magnesite) and fluid)^{32,79,81,82} was used. Ideal mixing is assumed for anthophyllite, brucite and talc. Lizardite and chrysotile were used without solution models. Equilibrium thermodynamics is widely used to study the tectonic evolution of the metamorphic rocks⁷⁹. However, for serpentinite where mineralogical change is driven primary by fluid infiltration processes and to a lesser extent by changes in pressure and temperature, the thermodynamic techniques have been applied less commonly. Fluid infiltration process, in general, causes changes in the bulk rock composition, therefore the changes in the bulk chemistry of the system are considered in all the calculated pseudosections. All the major elements of the modelled chemical system show linear relations with the H₂O content (Supplementary Fig. S3). Al₂O₃, SiO₂ and FeO show negative correlations while MgO shows a positive correlation. The concentrations of these elements were shifted from the original composition of the rock during partial melting and serpentinization process²¹. For the modelling, the x-axes of the pseudosections are assigned to the composition of the system. The value zero of the x-axes indicates the less modified amounts of the oxides while the value one indicates the maximum modification recorded in the studied rock samples.

References

- Kendrick, M. A. *et al.* Seawater cycled throughout Earth's mantle in partially serpentinized lithosphere. *Nat. Geosci.* **10**, 222–228 (2017).
- Deschamps, F., Godard, M., Guillot, S. & Hattori, K. Geochemistry of subduction zone serpentinites: A review. *Lithos* **178**, 96–127 (2013).
- Rüpke, L. H., Morgan, J. P., Hort, M. & Connolly, J. A. Serpentine and the subduction zone water cycle. *Earth Planet. Sci. Lett.* **223**, 17–34 (2004).
- Ulmer, P. & Trommsdorff, V. Serpentine stability to mantle depths and subduction-related magmatism. *Science* **268**, 858–61 (1995).
- Pagé, L. & Hattori, K. Tracing halogen and B cycling in subduction zones based on obducted, subducted and forearc serpentinites of the Dominican Republic. *Sci. Rep.* **7**, 1–9 (2017).
- Hattori, K. H. & Guillot, S. Volcanic fronts as a consequence of serpentinite dehydration in the mantle wedge. *Geology* **31**, 525–528 (2003).
- Tatsumi, Y. Migration of fluid phases and genesis of basalt magmas in subduction zones. *J. Geophys. Res. Solid Earth* **94**, 4697–4707 (1989).
- Walowski, K. J., Wallace, P. J., Hauri, E. H., Wada, I. & Clyne, M. A. Slab melting beneath the Cascade Arc driven by dehydration of altered oceanic peridotite. *Nat. Geosci.* **8**, 404–408 (2015).
- Deschamps, F. *et al.* *In situ* characterization of serpentinites from forearc mantle wedges: Timing of serpentinization and behavior of fluid-mobile elements in subduction zones. *Chem. Geol.* **269**, 262–277 (2010).
- Deschamps, F., Guillot, S., Godard, M., Andreani, M. & Hattori, K. Serpentinites act as sponges for fluid-mobile elements in abyssal and subduction zone environments. *Terra Nov.* **23**, 171–178 (2011).
- Lafay, R. *et al.* High-pressure serpentinites, a trap-and-release system controlled by metamorphic conditions: Example from the Piedmont zone of the western Alps. *Chem. Geol.* **343**, 38–54 (2013).
- Kodolányi, J., Pettké, T., Spandler, C., Kamber, B. S. & Ling, K. G. Geochemistry of ocean floor and fore-arc serpentinites: Constraints on the ultramafic input to subduction zones. *J. Petrol.* **53**, 235–270 (2012).
- Liu, J., Lin, J.-F. & Prakapenka, V. B. High-Pressure Orthorhombic Ferromagnesite as a Potential Deep-Mantle Carbon Carrier. *Sci. Rep.* **5**, 7640 (2015).
- Galvez, M. E. *et al.* Graphite formation by carbonate reduction during subduction. *Nat. Geosci.* **6**, 473–477 (2013).
- Stern, R. J., Johnson, P. R., Kröner, A. & Yibas, B. Neoproterozoic Ophiolites of the Arabian-Nubian Shield. *Dev. Precambrian Geol.* **13**, 95–128 (2004).
- Johnson, P. R. *et al.* Late Cryogenian-Ediacaran history of the Arabian-Nubian Shield: A review of depositional, plutonic, structural, and tectonic events in the closing stages of the northern East African Orogen. *J. African Earth Sci.* **61**, 167–232 (2011).
- Abu-Alam, T. S. & Stüwe, K. Exhumation during oblique transpression: The Feiran-Solaf region, Egypt. *J. Metamorph. Geol.* **27**, 439–459 (2009).
- Zimmer, M., Kröner, A., Jochum, K. P., Reischmann, T. & Todt, W. The Gabal Gerf complex: A precambrian N-MORB ophiolite in the Nubian Shield, NE Africa. *Chem. Geol.* **123**, 29–51 (1995).
- Azer, M. K. & Stern, R. J. Neoproterozoic (835–720 Ma) Serpentinites in the Eastern Desert, Egypt: Fragments of Forearc Mantle. *J. Geol.* **115**, 457–472 (2007).
- Abd El-Rahman, Y. *et al.* Geochemistry and tectonic evolution of the Neoproterozoic incipient arc-forearc crust in the Fawakhr area, Central Eastern Desert of Egypt. *Precambrian Res.* **175**, 116–134 (2009).
- Gamal El Dien, H. *et al.* Neoproterozoic serpentinites from the Eastern Desert of Egypt: Insights into Neoproterozoic mantle geodynamics and processes beneath the Arabian-Nubian Shield. *Precambrian Res.* **286**, 213–233 (2016).
- Gamal El Dien, H., Hamdy, M., El-ela, A. S. A., Hassan, A. & Kil, Y. A Window into Neoproterozoic Mantle and its Development: Observations from Ophiolitic Serpentinites in the Eastern Desert of Egypt. *Acta Geol. Sin.* **89**, 22–24 (2015).

23. Hamdy, M. M. & Gamal El Dien, H. Nature of serpentinization and carbonation of ophiolitic peridotites (Eastern Desert, Egypt): constrains from stable isotopes and whole-rock geochemistry. *Arab. J. Geosci.* **10** (2017).
24. Hamdy, M. M., Abd El-Wahed, M. A., Gamal El Dien, H. & Morishita, T. Garnet hornblende in the Meatiq Core Complex, Central Eastern Desert of Egypt: Implications for crustal thickening preceding the ~600 Ma extensional regime in the Arabian-Nubian Shield. *Precambrian Res.* **298**, 593–614 (2017).
25. Abu-Alam, T. S. & Hamdy, M. M. Thermodynamic modelling of Sol Hamed serpentinite, south eastern Desert of Egypt: Implication for fluid interaction in the Arabian-Nubian shield ophiolites. *J. African Earth Sci.* **99**, 7–23 (2014).
26. Fowler, A. R. & El Kalioubi, B. Gravitational collapse origin of shear zones, foliations and linear structures in the Neoproterozoic cover nappes, Eastern Desert, Egypt. *J. African Earth Sci.* **38**, 23–40 (2004).
27. Abu El Ela, A. Contribution to the mineralogy and chemistry of some serpentinites from the Eastern Desert of Egypt. *MERC Ain. Shams Univ. Earth Sci.* **10**, 1–25 (1996).
28. Anders, E. & Grevesse, N. Abundances of the elements: Meteoritic and solar. *Geochim. Cosmochim. Acta* **53**, 197–214 (1989).
29. McDonough, W. & Sun, S. The composition of the Earth. *Chem. Geol.* **120**, 223–252 (1995).
30. Arai, S. Characterization of spinel peridotites by olivine-spinel compositional relationships: Review and interpretation. *Chem. Geol.* **113**, 191–204 (1994).
31. Li, X. P., Rahn, M. & Bucher, K. Serpentinities of the Zermatt-Saas ophiolite complex and their texture evolution. *J. Metamorph. Geol.* **22**, 159–177 (2004).
32. Padrón-Navarta, J. A. *et al.* Tschermak's substitution in antigorite and consequences for phase relations and water liberation in high-grade serpentinites. *Lithos* **178**, 186–196 (2013).
33. Eggler, D. H. & Ehmann, A. N. Rate of antigorite dehydration at 2 GPa applied to subduction zones. *Am. Mineral.* **95**, 761–769 (2010).
34. Deschamps, F. *et al.* Behavior of fluid-mobile elements in serpentines from abyssal to subduction environments: Examples from Cuba and Dominican Republic. *Chem. Geol.* **312–313**, 93–117 (2012).
35. Saumur, B. M., Hattori, K. H. & Guillot, S. Contrasting origins of serpentinites in a subduction complex, northern Dominican Republic. *Bull. Geol. Soc. Am.* **122**, 292–304 (2010).
36. Blanco-Quintero, I. F., Proenza, J. A., García-Casco, A., Tauler, E. & Galí, S. Serpentinities and serpentinites within a fossil subduction channel: La Corea mélange, eastern Cuba. *Geol. Acta* **9**, 389–405 (2011).
37. Guillot, S., Schwartz, S., Reynard, B., Agard, P. & Prigent, C. Tectonic significance of serpentinites. *Tectonophysics* **646**, 1–19 (2015).
38. Aziz, N. R. H., Aswad, K. J. A. & Koyi, H. A. Contrasting settings of serpentinite bodies in the northwestern Zagros Suture Zone, Kurdistan Region, Iraq. *Geol. Mag.* **148**, 819–837 (2011).
39. Aldanmaz, E. & Koprubasi, N. Platinum-Group-Element Systematics of Peridotites from Ophiolite Complexes of Northwest Anatolia, Turkey: Implications for Mantle Metasomatism by Melt Percolation in a Supra-subduction Zone Environment. *Int. Geol. Rev.* **48**, (420–442) (2006).
40. Savov, I. P., Ryan, J. G., D'Antonio, M., Kelley, K. & Mattie, P. Geochemistry of serpentinized peridotites from the Mariana Forearc Conical Seamount, ODP Leg 125: Implications for the elemental recycling at subduction zones. *Geochemistry, Geophys. Geosystems* **6**, n/a–n/a (2005).
41. Paulick, H. *et al.* Geochemistry of abyssal peridotites (Mid-Atlantic Ridge, 15°20'N, ODP Leg 209): Implications for fluid/rock interaction in slow spreading environments. *Chem. Geol.* **234**, 179–210 (2006).
42. Muntener, O., Hermann, J. & Trommsdorff, V. Cooling History and Exhumation of Lower-Crustal Granulite and Upper Mantle (Malenco, Eastern Central Alps). *J. Petrol.* **41**, 175–200 (2000).
43. Evans, B. W. The Serpentine Multisystem Revisited: Chrysotile Is Metastable. *Int. Geol. Rev.* **46**, 479–506 (2004).
44. Hilaret, N., Daniel, I. & Reynard, B. Equation of state of antigorite, stability field of serpentines, and seismicity in subduction zones. *Geophys. Res. Lett.* **33** (2006).
45. Khedr, M. Z. & Arai, S. Hydrous peridotites with Ti-rich chromian spinel as a low-temperature forearc mantle facies: evidence from the Happo-O'ne metaperidotites (Japan). *Contrib. to Mineral. Petrol.* **159**, 137–157 (2010).
46. Mével, C. Serpentinization of abyssal peridotites at mid-ocean ridges. *Comptes Rendus Geosci.* **335**, 825–852 (2003).
47. Li, Z. X. A. & Lee, C. T. A. Geochemical investigation of serpentinized oceanic lithospheric mantle in the Feather River Ophiolite, California: Implications for the recycling rate of water by subduction. *Chem. Geol.* **235**, (161–185) (2006).
48. Bebout, G. E. Chemical and Isotopic Cycling in Subduction Zones. *Treatise on Geochemistry: Second Edition 15*, (Elsevier Ltd., 2014).
49. Gerya, T. V., Stöckhert, B. & Perchuk, A. L. Exhumation of high-pressure metamorphic rocks in a subduction channel: A numerical simulation. *Tectonics* **21**, 6-1-6–19 (2002).
50. Alt, J. C. *et al.* The role of serpentinites in cycling of carbon and sulfur: Seafloor serpentinization and subduction metamorphism. *Lithos* **178**, 40–54 (2013).
51. Staudigel, H. *Chemical Fluxes from Hydrothermal Alteration of the Oceanic Crust. Treatise on Geochemistry: Second Edition 4*, (Elsevier Ltd., 2014).
52. Plank, T. *The Chemical Composition of Subducting Sediments. Treatise on Geochemistry: Second Edition 4*, (Elsevier Ltd., 2014).
53. Li, Y. H. & Schoonmaker, J. E. *Chemical Composition and Mineralogy of Marine Sediments. Treatise on Geochemistry: Second Edition 9*, (2014).
54. Schmidt, K., Koschinsky, A., Garbe-Schönberg, D., de Carvalho, L. M. & Seifert, R. Geochemistry of hydrothermal fluids from the ultramafic-hosted Logatchev hydrothermal field, 15°N on the Mid-Atlantic Ridge: Temporal and spatial investigation. *Chem. Geol.* **242**, 1–21 (2007).
55. Plank, T. & Langmuir, C. H. Tracing trace elements from sediment input to volcanic output at subduction zones. *Nature* **362**, 739–743 (1993).
56. Gaschnig, R. M. *et al.* The Molybdenum Isotope System as a Tracer of Slab Input in Subduction Zones: An Example From Martinique, Lesser Antilles Arc. *Geochemistry, Geophys. Geosystems* **18**, 4674–4689 (2017).
57. Faccenda, M., Gerya, T. V. & Burlini, L. Deep slab hydration induced by bending-related variations in tectonic pressure. *Nat. Geosci.* **2**, 790–793 (2009).
58. Kerrick, D. M. Serpentine Seduction. *Science* (80). **298**, 1344–1345 (2002).
59. Lafay, R. *et al.* Experimental investigation of As, Sb and Cs behavior during olivine serpentinization in hydrothermal alkaline systems. *Geochim. Cosmochim. Acta* **179**, 177–202 (2016).
60. Lafay, R. *et al.* Influence of trace elements on the textural properties of synthetic chrysotile: Complementary insights from macroscopic and nanoscopic measurements. *Microporous Mesoporous Mater.* **183**, 81–90 (2014).
61. Li, Y.-H. A brief discussion on the mean oceanic residence time of elements. *Geochim. Cosmochim. Acta* **46**, 2671–2675 (1982).
62. Marschall, H. R., Altherr, R. & Rüpke, L. Squeezing out the slab — modelling the release of Li, Be and B during progressive high-pressure metamorphism. *Chem. Geol.* **239**, 323–335 (2007).
63. Vils, F., Muntener, O., Kalt, A. & Ludwig, T. Implications of the serpentine phase transition on the behaviour of beryllium and lithium-boron of subducted ultramafic rocks. *Geochim. Cosmochim. Acta* **75**, 1249–1271 (2011).
64. Scambelluri, M. & Tonarini, S. Boron isotope evidence for shallow fluid transfer across subduction zones by serpentinized mantle. *Geology* **40**, 907–910 (2012).

65. Vils, F., Tonarini, S., Kalt, A. & Seitz, H. M. Boron, lithium and strontium isotopes as tracers of seawater-serpentinite interaction at Mid-Atlantic ridge, ODP Leg 209. *Earth Planet. Sci. Lett.* **286**, 414–425 (2009).
66. Grozeva, N. G., Klein, F., Seewald, J. S. & Sylva, S. P. Experimental study of carbonate formation in oceanic peridotite. *Geochim. Cosmochim. Acta* **199**, 264–286 (2017).
67. Kelemen, P. B. & Matter, J. *In situ* carbonation of peridotite for CO₂ storage. *Proc. Natl. Acad. Sci.* **105**, 17295–17300 (2008).
68. Sieber, M. J., Hermann, J. & Yaxley, G. M. An experimental investigation of C–O–H fluid-driven carbonation of serpentinites under forearc conditions. *Earth Planet. Sci. Lett.* **496**, 178–188 (2018).
69. Poli, S. & Schmidt, M. W. Petrology of Subducted Slabs. *Annu. Rev. Earth Planet. Sci.* **30**, 207–235 (2002).
70. Kerrick, D. M. & Connolly, J. A. D. Subduction of ophiocarbonates and recycling of CO₂ and H₂O. *Geology* **26**, 375 (1998).
71. Hyndman, R. D. & Peacock, S. M. Serpentinization of the forearc mantle. *Earth Planet. Sci. Lett.* **212**, 417–432 (2003).
72. Macdonald, R., Hawkesworth, C. J. & Heath, E. The Lesser Antilles volcanic chain: a study in arc magmatism. *Earth-Science Rev.* **49**, 1–76 (2000).
73. Singer, B. S. *et al.* Along-strike trace element and isotopic variation in Aleutian Island arc basalt: Subduction melts sediments and dehydrates serpentine. *J. Geophys. Res. Solid Earth* **112** (2007).
74. Gill, J. B. *Orogenic Andesites and Plate Tectonics*. (Springer Berlin Heidelberg, 1981).
75. Groppo, C., Rinaudo, C., Cairo, S., Gastaldi, D. & Compagnoni, R. Micro-Raman spectroscopy for a quick and reliable identification of serpentine minerals from ultramafics. *Eur. J. Mineral.* **18**, 319–329 (2006).
76. Droop, G. T. R. A general equation for estimating Fe³⁺ concentrations in ferromagnesian silicates and oxides from microprobe analyses, using stoichiometric criteria. *Mineral. Mag.* **51**, 431–435 (1987).
77. Pearce, N. J. G. *et al.* A Compilation of New and Published Major and Trace Element Data for NIST SRM 610 and NIST SRM 612 Glass Reference. *Materials. Geostand. Geoanalytical Res.* **21**, 115–144 (1997).
78. Connolly, J. A. D. & Kerrick, D. M. An algorithm and computer program for calculating composition phase diagrams. *Calphad* **11**, 1–55 (1987).
79. Holland, T. J. B. & Powell, R. An improved and extended internally consistent thermodynamic dataset for phases of petrological interest, involving a new equation of state for solids. *J. Metamorph. Geol.* **29**, 333–383 (2011).
80. Evans, K. A., Powell, R. & Frost, B. R. Using equilibrium thermodynamics in the study of metasomatic alteration, illustrated by an application to serpentinites. *Lithos* **168–169**, 67–84 (2013).
81. Jennings, E. S. & Holland, T. J. B. A Simple Thermodynamic Model for Melting of Peridotite in the System NCFMASOCr. *J. Petrol.* **56**, 869–892 (2015).
82. Connolly, J. A. D. & Trommsdorff, V. Petrogenetic grids for metacarbonate rocks: pressure-temperature phase-diagram projection for mixed-volatile systems. *Contrib. to Mineral. Petrol.* **108**, 93–105 (1991).
83. Abu-Alam, T. S., Hassan, M., Stuwe, K., Meyer, S. E. & Passchier, C. W. Multistage Tectonism and Metamorphism During Gondwana Collision: Baladiyah Complex, Saudi Arabia. *J. Petrol.* **55**, 1941–1964 (2014).

Acknowledgements

We are appreciative of Prof. Abdel Salam Abu El-Ela from Tanta University for support with some rock samples and valuable discussion about the geological and field observations. We are grateful to Prof. T. Morishita and Prof. T. Mizukami from Kanazawa University for their kind assistance to carry out the Electron Microprobe and Raman analyses, respectively. Mr. Nguyen The Cong is thanked for his helping in LA-ICP-MS analyses. Prof. Brendan Murphy and Dr. Josh Beardmore is appreciated for proofreading the paper. Field work was supported by Tanta University, Egypt, which is appreciatively acknowledged. Financial support by the Australian Research Council (grant FL150100133 to ZXL) is acknowledged. This is a contribution to IGCP648: Supercontinent Cycles and Global Geodynamics.

Author Contributions

H.G. established the idea and was responsible for all the data collection and figures preparation. T.A. performed the thermodynamic modelling and the chemical formula of the minerals. H.G. wrote the manuscript with contributions and revisions by Z.-X.L., Y.K. and T.A.

Additional Information

Supplementary information accompanies this paper at <https://doi.org/10.1038/s41598-019-43605-9>.

Competing Interests: The authors declare no competing interests.

Publisher's note: Springer Nature remains neutral with regard to jurisdictional claims in published maps and institutional affiliations.



Open Access This article is licensed under a Creative Commons Attribution 4.0 International License, which permits use, sharing, adaptation, distribution and reproduction in any medium or format, as long as you give appropriate credit to the original author(s) and the source, provide a link to the Creative Commons license, and indicate if changes were made. The images or other third party material in this article are included in the article's Creative Commons license, unless indicated otherwise in a credit line to the material. If material is not included in the article's Creative Commons license and your intended use is not permitted by statutory regulation or exceeds the permitted use, you will need to obtain permission directly from the copyright holder. To view a copy of this license, visit <http://creativecommons.org/licenses/by/4.0/>.

© The Author(s) 2019



RightsLink®

?
Help

✉
Email Support

Global geochemical fingerprinting of plume intensity suggests coupling with the supercontinent cycle

SPRINGER NATURE

Author: Hamed Gamal EL Dien et al

Publication: Nature Communications

Publisher: Springer Nature

Date: Nov 21, 2019

Copyright © 2019, Crown

Creative Commons

This is an open access article distributed under the terms of the [Creative Commons CC BY](#) license, which permits unrestricted use, distribution, and reproduction in any medium, provided the original work is properly cited.

You are not required to obtain permission to reuse this article.

To request permission for a type of use not listed, please contact [Springer Nature](#)

© 2020 Copyright - All Rights Reserved | [Copyright Clearance Center, Inc.](#) | [Privacy statement](#) | [Terms and Conditions](#)
Comments? We would like to hear from you. E-mail us at customercare@copyright.com

ATTRIBUTION STATEMENTS

Table iii: Attribution statement table for published -Chapter 8: *Global geochemical fingerprinting of plume intensity suggests coupling with the supercontinent cycle*

	Conception and Design	Acquisition of Data and Method	Data Conditioning and Manipulation	Analysis and Statistical Method	Interpretation and Discussion	Final Approval	Total % contribution
Co-Author 1 (Hamed Gamal El Dien)	50	50	65	60	50	40	60
Co Author 1 Acknowledgment: I acknowledge that these represent my contribution to the above research output					Signed: 03/11/2020		
Co-Author 2 (Luc-Serge Doucet)	10	40	15	40	10	10	20
Co Author 2 Acknowledgment: I acknowledge that these represent my contribution to the above research output					Signed: 04/11/2020		
Co-Author 3 (Zheng-Xiang Li)	40	10	10		40	50	15
Co Author 3 Acknowledgment: I acknowledge that these represent my contribution to the above research output					Signed:		
Co-Author 4 (Grant Cox)			5				3
Co Author 4 Acknowledgment: I acknowledge that these represent my contribution to the above research output					Signed:		
Co-Author 5 (Ross Mitchell)			5				2
Co Author 5 Acknowledgment: I acknowledge that these represent my contribution to the above research output					Signed:		
Total %	100	100	100	100	100	100	100

ARTICLE

<https://doi.org/10.1038/s41467-019-13300-4>

OPEN

Global geochemical fingerprinting of plume intensity suggests coupling with the supercontinent cycle



Hamed Gamal EL Dien ^{1,2*}, Luc S. Doucet¹, Zheng-Xiang Li ¹, Grant Cox¹ & Ross Mitchell¹

Plate tectonics and mantle plumes are two of the most fundamental solid-Earth processes that have operated through much of Earth history. For the past 300 million years, mantle plumes are known to derive mostly from two large low shear velocity provinces (LLSVPs) above the core-mantle boundary, referred to as the African and Pacific superplumes, but their possible connection with plate tectonics is debated. Here, we demonstrate that transition elements (Ni, Cr, and Fe/Mn) in basaltic rocks can be used to trace plume-related magmatism through Earth history. Our analysis indicates the presence of a direct relationship between the intensity of plume magmatism and the supercontinent cycle, suggesting a possible dynamic coupling between supercontinent and superplume events. In addition, our analysis shows a consistent sudden drop in MgO, Ni and Cr at ~3.2–3.0 billion years ago, possibly indicating an abrupt change in mantle temperature at the start of global plate tectonics.

¹Earth Dynamics Research Group, The Institute for Geoscience Research (TIGeR), School of Earth and Planetary Sciences, Curtin University, GPO Box U1987, Perth, WA 6845, Australia. ²Geology Department, Faculty of Science, Tanta University, 31527 Tanta, Egypt. *email: hamed.gamaleldien@postgrad.curtin.edu.au

The plate tectonic theory developed last century works well on Earth's outer shell, but how this system interacts with mantle plumes, and if they are part of the same geodynamic system in Earth history, remains unclear. Seismic studies have revealed that Earth's present-day lower mantle is dominated by two antipodal large low shear velocity provinces (LLSVPs), also known as the African and Pacific superplumes, surrounded by high-velocity zones with subducted cold slabs¹. It has been further shown that almost all known mantle plumes since ~300 million years ago (Ma) were generated atop or near the edges of these two LLSVPs^{2,3}. On the other hand, the assembly and breakup of supercontinents are controlled by global-scale mantle dynamics and constant feedback between surface and deep mantle processes⁴. It has been further established that the African LLSVP (whether or not in its present geometry) was located underneath the supercontinent Pangaea ca. 300 Ma⁵, and that there was a close link between mantle plumes and Pangaea breakup⁶. However, how long the LLSVPs have been present, how such LLSVPs interact with tectonic plates in Earth history, and whether they are fixed in the deep mantle^{1,3,7} or part of a dynamic system associated with the supercontinent cycle since at least the Proterozoic^{8–11}, remain topics of debate. Tracing mantle plume signatures throughout Earth history is fundamental for answering those questions and testing the stable vs. dynamic/cyclic nature of the LLSVPs, and thus achieving a better understanding of the coupling between Earth's mantle dynamics and plate tectonics.

Basaltic magmatism can be used to probe mantle evolution throughout Earth history^{12,13}. Such mafic magmatism is mostly generated in three main tectonic settings: mantle plume, mid-ocean ridge, and subduction zone (arc). Geochemical and isotopic characteristics of basalts generated in such settings can identify, or “fingerprint”, the processes and sources of magma generation from different parts of the mantle¹². Where mid-ocean ridge basalts (MORBs) and arc-related basalts (ARBs) represent melts generated within the sub-oceanic and sub-arc upper mantle, respectively^{14–17}, plume basalts, such as oceanic island basalts (OIBs), oceanic flood basalts, and continental large igneous provinces (LIPs) commonly involve deeper mantle processes in which LLSVPs may provide both additional heat and some melt materials^{12,18,19}.

Incompatible trace elements, particularly high-field strength elements (HFSEs) and their ratios, are widely used to monitor and discriminate between mantle domains and tectonic environments for basaltic magmatism, and to trace plume signatures^{15,16,20}. However, as HFSEs can be affected by various processes, such as source contamination, magma mixing, crust-magma interaction, and high-grade metamorphism, the validity of using such an approach to discriminate tectonic settings has been questioned^{21,22}. One reason for this is that the low partition coefficients (<1) of HFSEs with Fe–Mg silicate minerals and spinel^{12,23}—the main components of basaltic magmatism—make HFSEs easily redistributed by the aforementioned processes. On the other hand, transition elements have partition coefficients with Fe–Mg silicate minerals and spinel >1, making them highly insensitive to post-formation processes^{23–25}. The behavior of the first-row transition elements, especially Ni and Cr (highly compatible) and their ratios to less compatible ones (Co and Zn), is strongly melt-composition dependent^{12,23} and highly sensitive to the earliest magmatic differentiation stages²⁶. Thus, the abundance of Ni and Cr may track the nature of basaltic magmatism generated from different parts of the mantle.

Here, we demonstrate that Ni and Cr contents constitute an excellent tool for discriminating between plume- and non-plume-related (MORBs and ARBs) magmatism. In addition, by using the statistical bootstrapping method on the global geochemical

database of basaltic rocks, we show that the transition elements (Ni, Cr, and Fe/Mn, i.e., plume intensity) exhibit systematic short-term variations that coincide with the supercontinent cycle, which could potentially suggest a dynamic coupling between first-order mantle structure (e.g., LLSVPs) and plate tectonics.

Results

Ni and Cr as tracers for mantle plume products. Magnesium content and its ratio to other elements (i.e., Mg/Fe) are commonly used as tracers for the differentiation of silicate rocks and an indicator for mantle temperature^{14,15,27}. Geochemical modeling using MgO content revealed the ambient mantle temperature below the ridges and sub-arc to be ~1350 °C, but typically thermal anomalies of ~200–300 °C over the ambient mantle temperature are expected for mantle plumes^{14,15,27–29}. As transition elements (i.e., Ni and Cr) behave similarly to Mg during mantle melting, Ni and Cr should also be highly sensitive to mantle temperature, and can thus be used for distinguishing between plume and non-plume mantle melt products. To illustrate this point, we compare the global databases (see the Methods section and Supplementary Data 1) of mantle melts with a range of MgO content and potential mantle temperature of melting¹⁴, such as komatiites (>18 wt% MgO and T ~1600 °C), picrites (>12 wt % MgO and T ~1500 °C; from OIBs and LIPs), and normal basalts (<12 wt % MgO and T ~1350 °C; from present-day MORBs and ARBs)^{14,15,30,31} to their corresponding Ni, Cr, Ni/Co, and Cr/Zn contents and ratios, respectively (Supplementary Fig. 1). Strikingly, those transition elements have a positive correlation with MgO content and can, therefore, be used for discriminating komatiites and picrites (representing plume magmatism) from normal basalts (representing non-plume magmatism). Plume magmatism is characterized by Ni > 200 ppm, Cr > 500 ppm, and Ni/Co and Cr/Zn both >8 (Supplementary Fig. 1).

To further verify the inferred plume characteristics, we produced covariation plots for Ni and Cr, and Mg# ($100 \times \text{MgO}/(\text{MgO} + \text{FeO}_T)$) vs. Ni and Cr of basalt datasets (45 wt% <SiO₂ <53 wt% and Na₂O + K₂O < 5 wt%)³² from Cenozoic OIBs and LIPs and present-day MORBs and ARBs (Fig. 1; Supplementary Fig. 2 and Supplementary Data 1). Much like komatiites and picrites, 70% of the plume basalt (PB) datasets have Ni >150 ppm and Cr > 300 ppm, whereas non-plume magmatism (MORBs and ARBs) are mostly below these limits. Thus, we argue that high Ni and Cr contents in basalts implies a plume signature. In addition, consistent with previous studies of some OIBs from the Pacific superplume^{33,34}, we found that plume basalts (OIBs and LIPs) generally have Fe/Mn > 65, clearly higher than that of MORBs and ARBs (Fig. 2).

Based on these observations, we use MgO, Cr, and Ni contents to filter data from ~41,000 samples (Supplementary Figs. 3, 4 and Supplementary Data 2) in the global databases (Georoc and EarthChem repositories) in order to trace plume signature throughout Earth history (see the Methods section). The bootstrapped data (see Methods) reveal a first-order decrease in MgO, Cr, and Ni content in basalts since the Archean eon^{29,35} (Fig. 3), plus second-order variations within the Proterozoic and the Phanerozoic (Fig. 4). To further interrogate the second-order variations, we detrended the linear secular decreases in each dataset (Fig. 4a–c; Supplementary Fig. 4 and Supplementary Table 1).

Discussion

Time variations in mantle plume intensity. The highly compatible transition elements Ni and Cr and their ratios to less compatible ones (e.g., Ni/Co and Cr/Zn), plus Fe/Mn and the previously widely used MgO, are good discriminants for mantle

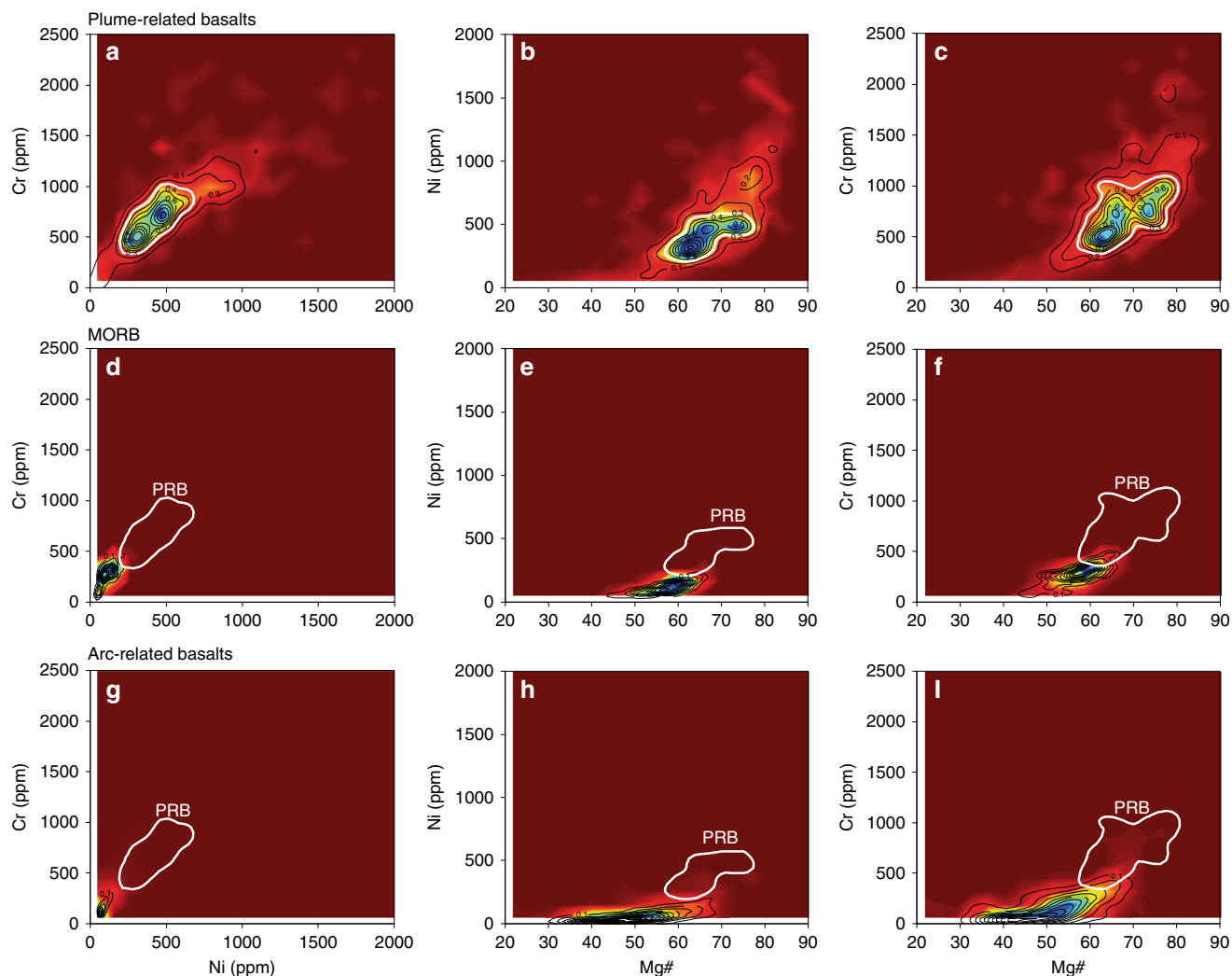


Fig. 1 Density plot of Ni, Cr, and Mg# for different basaltic magmatism types. Panels **a**, **b**, and **c** are density plots of plume-related basalts (PRB) for Ni (ppm) vs. Cr (ppm) and Mg# ($100 \times \text{MgO} / (\text{MgO} + \text{FeO}_7)$) vs. Ni (ppm) and Cr (ppm), respectively. Panels **d–f** are density plots for mid-ocean ridge basalts (MORB) and **g–i** panels are for arc-related basalts. Data sources: Georoc and EarthChem (see Methods and Supplementary Data 1). Black contours define the data density values from high density (blue) to low density (red). The white contour represents 70% of the PRB data

plume magmatism because they all indicate higher mantle melt temperature. As basaltic magmatism represents the direct melt products of Earth's mantle, its composition potentially records Earth's mantle evolution since 4 billion years ago (Ga). Our analysis revealed a first-order decrease in MgO, Ni and Cr since the Archean similar to that shown by Keller and Schoene^{29,35} (Fig. 3a–c), readily explainable by Earth's secular cooling (including the lowering of the mantle potential temperature)^{15,28,29,35}.

The second-order variability of MgO, Ni, and Cr, previously largely ignored^{29,35,36}, is more intriguing. The curves consistently show major positive peaks at ~ 2.8 – 2.3 Ga, ~ 1.6 – 1.3 Ga, ~ 1.0 – 0.7 Ga, and ~ 0.3 – 0.0 Ga. The most straightforward interpretation of these second-order variations is that they reflect changes in mantle potential temperature/degree of melting (see Fig. 4 of Ref. 29), which may be a consequence of either mantle plumes, or thermal insulation in the upper mantle³⁷, or both. Plumes are possibly a more dominant factor because they allow the higher Ni (>150 ppm) and Cr (>300 ppm) contents of the basalts to be sourced from the fertile lower mantle peridotites (i.e., Ni = 2500–3200 ppm and Cr = 2600–7500 ppm)^{14,38,39} (Fig. 1a–c) rather than the depleted upper mantle peridotites (i.e., Ni = 1960 ppm and Cr = 2500 ppm)⁴⁰ (Fig. 1d–f). This interpretation is supported by their anomalously high Fe/Mn of >65 (Fig. 2), a

well-accepted characteristic of plume basalts^{33,34}, as well as high abundances of Ni and Cr (Fig. 1).

Implications for mantle dynamics coupled with the supercontinent cycle.

Our results show a general temporal consistency between the MgO, Ni, and Cr peaks/anomalies (i.e., plume intensity/activities) and the occurrence of known supercontinents, suggesting a clear positive correlation between mantle plume intensity and supercontinent tenure (Fig. 4). Such results allow us to speculate on the fixed vs. dynamic models for the two LLSVPs in the lower mantle. In the fixed LLSVPs model^{1,3,7}, the LLSVPs are stable features anchored to the core-mantle boundary (CMB) since early Earth. Their positions and shapes would therefore not have been linked to the subduction girdle and thus to plate motion in general^{8–11}. As such, one would expect the formation of plume basalts to be stochastic in Earth history, implying a semi-uniform occurrence of plume magmatism over geological time, i.e., plume intensity unrelated to the supercontinent cycle. Alternatively, if supercontinents indeed preferentially form on the global subduction girdle (cold downwelling mantle) as suggested by some⁴¹, and both the antipodal LLSVPs and the subduction girdle are fixed and long-lived features, then one would expect an anticorrelation between

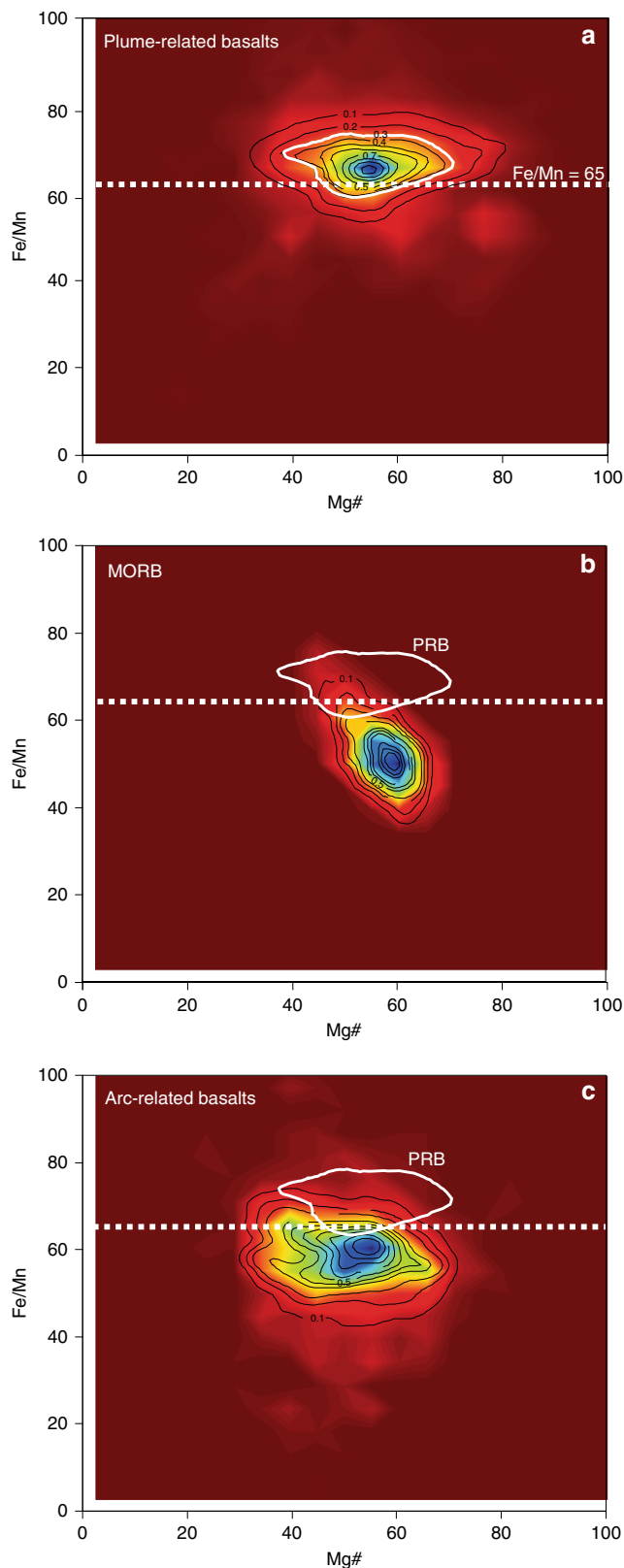


Fig. 2 Density plot of Fe/Mn vs. Mg# for different basaltic types. **a** Plume-related basalts (PRB); **b** mid-ocean ridge basalts (MORB); **c** arc-related basalts. Data sources: Georoc and EarthChem (see Methods). Black contours define the data density values from high density (blue) to low density (red). The white contour represents 70% of the PRB data

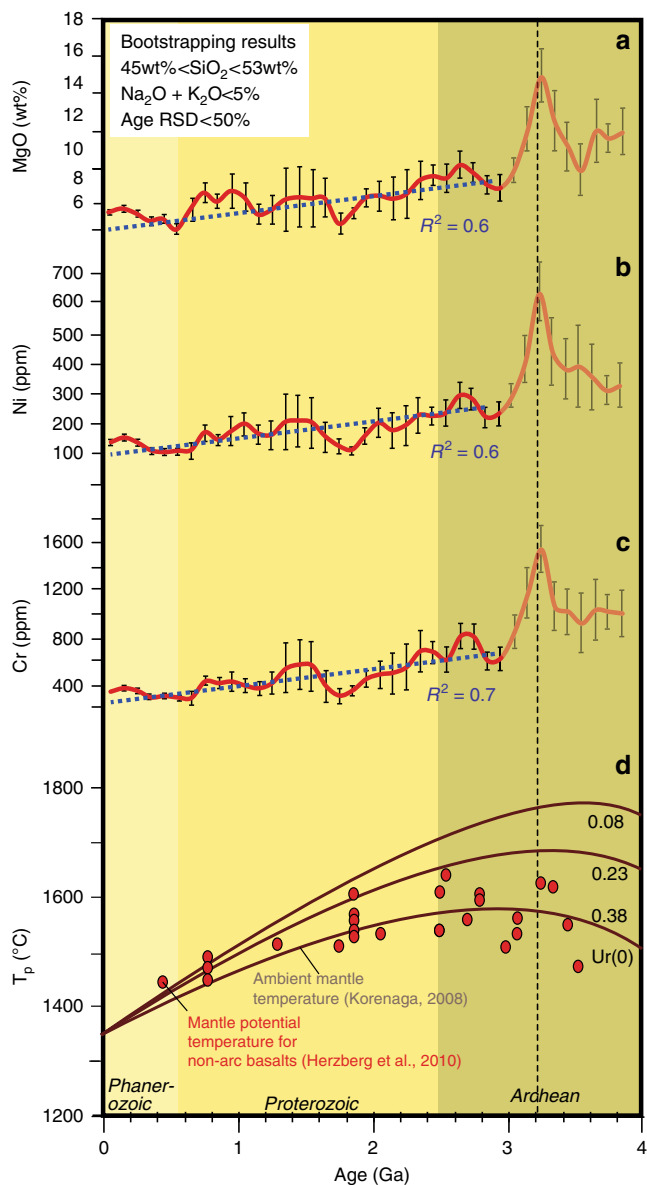


Fig. 3 Time evolution of global mean MgO, Ni, and Cr contents after a bootstrap resampling of the selected basaltic database. The blue dashed lines in **a–c** are regression lines for data between 0 to 3.0 Ga that reveal first-order secular decreases. Error bars in **a–c** show 2 s.e.m. (standard error of the mean) uncertainties. **d** Secular cooling of Earth’s mantle based on non-arc basalts²⁸ and thermal modeling⁴³. Urey ratios (Ur) are shown: 0.08 (upper curve), 0.23 (middle curve), and 0.38 (lower curve)

plume intensity and supercontinental tenure (we note that the pre-Cretaceous global plume record is dominated by continental LIPs). In contrast, according to the dynamic LLSVPs model^{8,9}, the formation of antipodal LLSVPs is linked to circum-supercontinent subduction that leads to the formation of the subduction girdle; the subduction girdle subsequently divides the hot and dense lower mantle into the two antipodal LLSVPs^{8,9}. Such a dynamic LLSVP model therefore predicts an increase in the intensity of plume magmatism during the tenure and breakup stage of the supercontinent, and thus a periodicity positively correlated with the supercontinent cycle.

The global plume intensity record we reported here (Fig. 4) is inconsistent with either predictions of the fixed LLSVPs model,

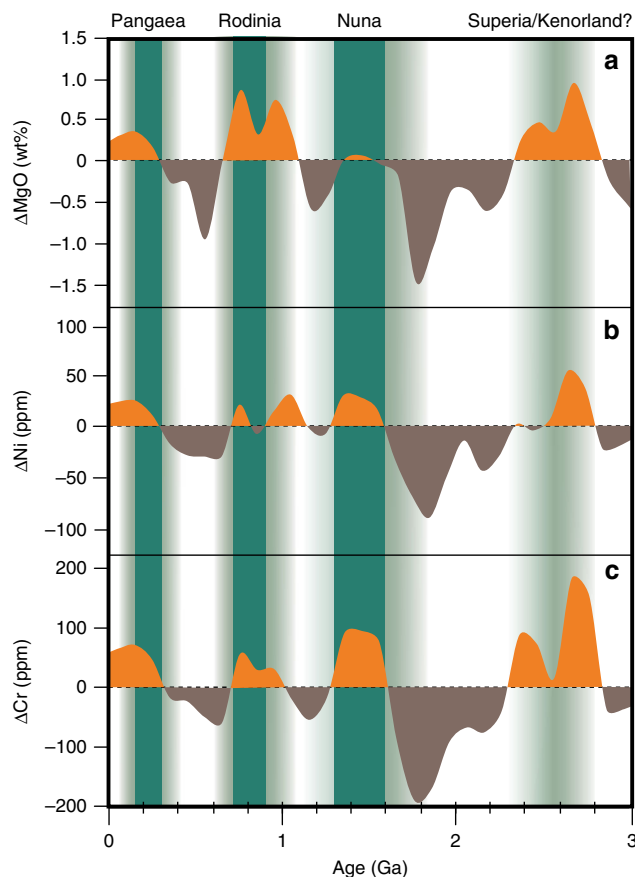


Fig. 4 Variability of global mean MgO, Ni, and Cr in basalts after detrending the linear secular decreases. The linear secular decreases used are those shown with blue dash lines in Fig. 3. The plot shows major positive peaks at $\sim 2.8\text{--}2.3$ Ga, $\sim 1.6\text{--}1.3$ Ga, $\sim 1.0\text{--}0.7$ Ga, and $\sim 0.3\text{--}0.0$ Ga, broadly consistent with the tenures and break-up times of post-2 Ga supercontinents. The durations of supercontinent tenure^{53,54} are marked with solid green vertical bars, e.g., at ca. 320–170 Ma (Pangea), 900–700 Ma (Rodinia), 1600–1300 Ma (Nuna), but the occurrence of Kenorland during 2700–2300 Ma is highly uncertain (thus shown in faded green). The assembly and break-up of supercontinents are generally prolonged and multistage processes, which are marked by gradual green shading

i.e., it shows neither a semi-uniform time distribution, nor an anticorrelation with the supercontinent tenure. The observed positive correlation between plume intensity and supercontinent cycle cannot be viewed as mere coincidence. In the absence of viable alternative explanations, we suggest the coupled supercontinent-mantle plume records as evidence supporting the dynamic LLSVP model. Indeed, it would be challenging to keep the LLSVPs fixed to the CMB because a constantly evolving subduction geometry changes the deposition of the subducted slabs above the CMB⁴².

Furthermore, our analysis shows a consistent sudden drop in MgO, Ni, and Cr at $\sim 3.2\text{--}3.0$ Ga (Fig. 3a–c), interpreted to indicate an abrupt change in mantle temperature. These results are comparable with the petrological estimation of mantle potential temperature using non-arc basalts²⁸, as well as Earth's secular cooling predicted by parameterized convection models⁴³ (Fig. 3d). We speculate that this interpreted dramatic drop in mantle temperature may indicate the initiation of global plate tectonics, where the subduction-driven whole-mantle convection enhanced the heat flux out of the core and mantle. The sharp peaks at ca. 3.2 Ga (Fig. 3a–c), also shown in the mantle potential

temperature estimations based on non-arc basalts (red dots in Fig. 3d)²⁸, possibly reflect a dramatic build-up in mantle temperature before the initiation of plate tectonics, when there was a lack of a mechanism for efficient heat flux out of the mantle. A $\sim 3.2\text{--}3.0$ Ga emergence of plate tectonics would be broadly consistent with the sedimentary, igneous, metamorphic, and palaeomagnetic records^{26,36,44}.

To summarize, geochemical tracers for plume basalts (Ni, Cr, and Fe/Mn) indicate the presence of a coupling between global plume intensity and supercontinent cycle. Such results are consistent with the suggested dynamic LLSVP model^{8–10} that links the formation, position, and evolution of LLSVPs with that of supercontinents. Recent numerical modeling^{45–48}, paleomagnetic^{49,50}, and seismic^{51,52} work are also in general agreements with the geodynamic LLSVP model.

Methods

Database compilation. We compiled a global database of komatiites (~ 3000 samples) and picrites (~ 1650 samples), covering major- and trace elements (particular transition elements such as Ni, Cr, Co, Zn, Cu, and Sc) from the Georoc (<http://georoc.mpch-mainz.gwdg.de/georoc/>) and EarthChem (<https://www.earthchem.org/>) repositories (Supplementary Data 1). The komatiite and picrite samples in the database have ages ranging from Archean to present-day. We made a manual double-check of data quality against the original references to choose only komatiite (>18 wt% MgO, $\text{SiO}_2 < 52$ wt%, and total alkali ($\text{K}_2\text{O} + \text{Na}_2\text{O}$) < 2 wt%) and picrite (>12 wt% MgO, $\text{SiO}_2 < 52$ wt% and total alkali ($\text{K}_2\text{O} + \text{Na}_2\text{O}$) < 3 wt%) compositions^{14,15,30,31} for the plots of Supplementary Fig. 1. The present-day mid-ocean ridge basalts (MORBs) and arc-related basalts (ARBs), used in Figs. 1, 2 and Supplementary Figs. 1, 2, are assembled from the same repositories and filtered for samples with basaltic composition (i.e., 45–53 wt% SiO_2 , MgO < 12 wt%, and total alkali ($\text{K}_2\text{O} + \text{Na}_2\text{O}$) < 5 wt%)^{14,15,31,32} and comprehensive major- and transition elements datasets including Ni, Cr, Co, Zn, Cu, and Sc. The present-day MORBs whole rock and glass database (~ 1200 samples) includes Atlantic, Pacific, and Indian mid-ocean ridges; the ARBs database (~ 5300 samples) includes oceanic-arc basalts, such as the Izu–Bonin–Mariana, Tonga, Sunda, Aleutian, Kermadec, New Hebrides, Kurile, and Lesser Antilles arcs, and continental-arc basalts such as that of the Andean, Cascades, and Central American arcs (Supplementary Data 1). The oceanic island basalts, oceanic flood basalts, and large igneous provinces database (~ 6200 samples) includes mainly Cenozoic basalts, such as the Hawaiian islands, Canary islands, Cape Verde islands, Society islands, St. Helena Chain, Deccan, Afro-Arabia, North Atlantic, Columbia River, Caribbean–Colombian, Hess rise, and Manihiki Plateau basalts (Supplementary Data 1).

Data bootstrap resampling. A geochemical database of major and transition elements of basalts ($\sim 41,000$ samples), with ages ranging from 3.8 Ga to present-day, was extracted from the Georoc and EarthChem repositories (Figs. 3, 4; Supplementary Data 2), including age estimates and geospatial sample locations for each sample. Data with unknown age or sample location, suspicious data with major elements totaling $>100\%$, and data from ultramafic cumulates or komatiites, have been manually filtered out. The database mainly consists of samples with a basaltic composition (i.e., 45–53 wt% SiO_2 and total alkali ($\text{K}_2\text{O} + \text{Na}_2\text{O}$) < 5 wt%)³¹ and age uncertainties below 50% relative standard deviation (RSD). To obtain an optimal estimate of composition distribution of Ni, Cr, and MgO in mantle-derived melts and minimize sampling and preservation bias, we did a weighted bootstrap resampling of the database following the method of Keller and Schoene³⁵ using the Matlab MIT open-source code available at <https://github.com/brenhinkeller/StatisticalGeochemistry>.

Data availability

All the data that are necessary for evaluating the findings of this study are available within this article and its Supplementary Information.

Received: 5 October 2019; Accepted: 1 November 2019;

Published online: 21 November 2019

References

- Dziewonski, A. M., Lekic, V. & Romanowicz, B. A. Mantle anchor structure: an argument for bottom up tectonics. *Earth Planet. Sci. Lett.* **299**, 69–79 (2010).
- Burke, K., Steinberger, B., Torsvik, T. H. & Smethurst, M. A. Plume generation zones at the margins of large low shear velocity provinces on the core-mantle boundary. *Earth Planet. Sci. Lett.* **265**, 49–60 (2008).

3. Torsvik, T. H. et al. Deep mantle structure as a reference frame for movements in and on the Earth. *Proc. Natl. Acad. Sci. USA* **111**, 8735–8740 (2014).
4. Anderson, D. L. Superplumes or supercontinents? *Geology* **22**, 39 (1994).
5. Burke, K. & Torsvik, T. H. Derivation of large igneous provinces of the past 200 million years from long-term heterogeneities in the deep mantle. *Earth Planet. Sci. Lett.* **227**, 531–538 (2004).
6. Courtillot, V., Jaupart, C., Manighetti, I., Tapponnier, P. & Besse, J. On causal links between flood basalts and continental breakup. *Earth Planet. Sci. Lett.* **166**, 177–195 (1999).
7. Torsvik, T. H., Burke, K., Steinberger, B., Webb, S. J. & Ashwal, L. D. Diamonds sampled by plumes from the core-mantle boundary. *Nature* **466**, 352–355 (2010).
8. Li, Z. X. & Zhong, S. Supercontinent-superplume coupling, true polar wander and plume mobility: plate dominance in whole-mantle tectonics. *Phys. Earth Planet. Inter.* **176**, 143–156 (2009).
9. Zhong, S., Zhang, N., Li, Z. X. & Roberts, J. H. Supercontinent cycles, true polar wander, and very long-wavelength mantle convection. *Earth Planet. Sci. Lett.* **261**, 551–564 (2007).
10. Li, Z. X. et al. Assembly, configuration, and break-up history of Rodinia: a synthesis. *Precambrian Res.* **160**, 179–210 (2008).
11. Li, Z. X. et al. Decoding Earth's rhythms: modulation of supercontinent cycles by longer superocean episodes. *Precambrian Res.* **323**, 1–5 (2019).
12. White, W. Probing the Earth's deep interior through geochemistry. *Geochemical Perspect.* **4**, 95–251 (2015).
13. Herzberg, C. Basalts as temperature probes of Earth's mantle. *Geology* **39**, 1179–1180 (2011).
14. Herzberg, C. et al. Temperatures in ambient mantle and plumes: constraints from basalts, picrites, and komatiites. *Geochemistry, Geophys. Geosystems* **8**, Q02006 <https://doi.org/10.1029/2006GC001390> (2007).
15. Condie, K. C., Aster, R. C. & Van Hunen, J. A great thermal divergence in the mantle beginning 2.5 Ga: geochemical constraints from greenstone basalts and komatiites. *Geosci. Front.* **7**, 543–553 (2016).
16. Pearce, J. A. & Peate, D. Tectonic implications of volcanic Arc magmas. *Annu. Rev. Earth Planet. Sci.* **23**, 251–285 (1995).
17. Gamal El Dien, H., Li, Z. X., Kil, Y. & Abu-Alam, T. Origin of arc magmatic signature: a temperature-dependent process for trace element (re-)mobilization in subduction zones. *Sci. Rep.* **9**, 7098 (2019).
18. Condie, K. C. Incompatible element ratios in oceanic basalts and komatiites: tracking deep mantle sources and continental growth rates with time. *Geochem., Geophys. Geosystems* **4**, 1–28 (2003).
19. Wang, X.-C. et al. Identification of an ancient mantle reservoir and young recycled materials in the source region of a young mantle plume: implications for potential linkages between plume and plate tectonics. *Earth Planet. Sci. Lett.* **377–378**, 248–259 (2013).
20. Condie, K. C. & Shearer, C. K. Tracking the evolution of mantle sources with incompatible element ratios in stagnant-lid and plate-tectonic planets. *Geochim. Cosmochim. Acta* **213**, 47–62 (2017).
21. Condie, K. Changing tectonic settings through time: indiscriminate use of geochemical discriminant diagrams. *Precambrian Res.* **266**, 587–591 (2015).
22. Pearce, J. A. Geochemical fingerprinting of oceanic basalts with applications to ophiolite classification and the search for Archean oceanic crust. *Lithos* **100**, 14–48 (2008).
23. White, W. M. *Geochemistry*. <https://doi.org/10.1017/S0016756813000708> (Wiley-Blackwell, 2013).
24. Leeman, W. P. & Scheidegger, K. Olivine/liquid distribution coefficients and a test for crystal-liquid equilibrium. *Earth Planet. Sci. Lett.* **35**, 247–257 (1977).
25. Horn, I., Foley, S., Jakson, S. & Jenner, G. Experimentally determined partitioning of high field strength and selected transition elements between spinel and basaltic melt. *Chem. Geol.* **117**, 193–218 (1994).
26. Tang, M., Chen, K. & Rudnick, R. L. Archean upper crust transition from mafic to felsic marks the onset of plate tectonics. *Science* **351**, 372–375 (2016).
27. Lee, C.-T. A., Luffi, P., Plank, T., Dalton, H. & Leeman, W. P. Constraints on the depths and temperatures of basaltic magma generation on Earth and other terrestrial planets using new thermobarometers for mafic magmas. *Earth Planet. Sci. Lett.* **279**, 20–33 (2009).
28. Herzberg, C., Condie, K. & Korenaga, J. Thermal history of the Earth and its petrological expression. *Earth Planet. Sci. Lett.* **292**, 79–88 (2010).
29. Keller, B. & Schoene, B. Plate tectonics and continental basaltic geochemistry throughout Earth history. *Earth Planet. Sci. Lett.* **481**, 290–304 (2018).
30. Arndt, N., Leshar, C. M. & Barnes, S. J. *Komatiite*. <https://doi.org/10.1017/CBO9780511535550> (Cambridge University Press, 2008).
31. Le Bas, M. J. IUGS reclassification of the high-Mg and picritic volcanic rocks. *J. Pet.* **41**, 1467–1470 (2000).
32. Le Maitre, R.W., Streckeisen, A., Zanettin, B., Le Bas, M.J., Bonin, B. & Bateman, P., editors. *Igneous Rocks: A Classification and Glossary of Terms: Recommendations of the International Union of Geological Sciences Subcommission on the Systematics of Igneous Rocks*. 2nd ed. <https://doi.org/10.1017/CBO9780511535581> (Cambridge University Press, 2002).
33. Humayun, M., Qiu, L. & Norman, M. D. Geochemical evidence for excess iron in the Hawaiian mantle: implications for mantle dynamics. *Science* **306**, 91–94 (2004).
34. Qin, L. & Humayun, M. The Fe/Mn ratio in MORB and OIB determined by ICP-MS. *Geochim. Cosmochim. Acta* **72**, 1660–1677 (2008).
35. Keller, C. B. & Schoene, B. Statistical geochemistry reveals disruption in secular lithospheric evolution about 2.5Gyr ago. *Nature* **485**, 490–493 (2012).
36. Condie, K. C. A planet in transition: the onset of plate tectonics on Earth between 3 and 2 Ga? *Geosci. Front.* **9**, 51–60 (2018).
37. Anderson, D. L. The thermal state of the upper mantle; no role for mantle plumes. *Geophys. Res. Lett.* **27**, 3623–3626 (2000).
38. Ionov, D. A. & Hofmann, A. W. Depth of formation of subcontinental off-craton peridotites. *Earth Planet. Sci. Lett.* **261**, 620–634 (2007).
39. Herzberg, C. et al. Nickel and helium evidence for melt above the core-mantle boundary. *Nature* **493**, 393–397 (2013).
40. Salters, V. J. M. & Stracke, A. Composition of the depleted mantle. *Geochem., Geophys. Geosystems* **5**, n/a–n/a (2004).
41. Mitchell, R. N., Kilian, T. M. & Evans, D. A. D. Supercontinent cycles and the calculation of absolute palaeolongitude in deep time. *Nature* **482**, 208–211 (2012).
42. Tan, E., Leng, W., Zhong, S. & Gurnis, M. On the location of plumes and lateral movement of thermochemical structures with high bulk modulus in the 3-D compressible mantle. *Geochem., Geophys. Geosystems* **12**, Q07005 <https://doi.org/10.1029/2011GC003665> (2011).
43. Korenaga, J. Urey ratio and the structure and evolution of Earth's mantle. *Am. Geophys. Union* 1–32 <https://doi.org/10.1029/2007RG000241.1> (2008).
44. Cawood, P. A. et al. Geological archive of the onset of plate tectonics. *Philos. Trans. R. Soc. A Math. Eng. Sci.* **376**, 20170405 (2018).
45. Flament, N., Williams, S., Müller, R. D., Gurnis, M. & Bower, D. J. Origin and evolution of the deep thermochemical structure beneath Eurasia. *Nat. Commun.* **8**, 14164 (2017).
46. Hassan, R., Müller, R. D., Gurnis, M., Williams, S. E. & Flament, N. A rapid burst in hotspot motion through the interaction of tectonics and deep mantle flow. *Nature* **533**, 239–242 (2016).
47. Zhang, N., Zhong, S., Leng, W. & Li, Z.-X. A model for the evolution of the Earth's mantle structure since the Early Paleozoic. *J. Geophys. Res.* **115**, B06401 (2010).
48. Simmons, N. A., Myers, S. C., Johannesson, G., Matzel, E. & Grand, S. P. Evidence for long-lived subduction of an ancient tectonic plate beneath the southern Indian Ocean. *Geophys. Res. Lett.* **42**, 9270–9278 (2015).
49. Bono, R. K., Tarduno, J. A. & Bunge, H.-P. Hotspot motion caused the Hawaiian-Emperor Bend and LLSVPs are not fixed. *Nat. Commun.* **10**, 3370 (2019).
50. Li, Z. X., Evans, D. A. D. & Zhang, S. A 90° spin on Rodinia: possible causal links between the neoproterozoic supercontinent, superplume, true polar wander and low-latitude glaciation. *Earth Planet. Sci. Lett.* **220**, 409–421 (2004).
51. Koelemeijer, P., Deuss, A. & Ritsema, J. Density structure of Earth's lowermost mantle from Stoneley mode splitting observations. *Nat. Commun.* **8**, 15241 (2017).
52. Forte, A. M. et al. Joint seismic-geodynamic-mineral physical modelling of African geodynamics: a reconciliation of deep-mantle convection with surface geophysical constraints. *Earth Planet. Sci. Lett.* **295**, 329–341 (2010).
53. Evans, D. A. D., Li, Z. X. & Murphy, J. B. Four-dimensional context of Earth's supercontinents. In *Geological Society Special Publication* (eds Li, Z. X., Evans, D. A. D. & Murphy, J. B.) 424, 1–14 (Geological Society of London, 2016).
54. Pourteau, A. et al. 1.6 Ga crustal thickening along the final Nuna suture. *Geol.* **46**, 959–962 (2018).

Acknowledgements

We appreciate helpful comments and discussions with Brendan Murphy. We thank C.B. Keller for discussions regarding the bootstrap resampling method. Dr. Josh Beardmore is appreciated for proofreading the paper. Financial support by the Australian Research Council (grant FL150100133 to Z.X.L.) is acknowledged. This is a contribution to IGCP648: Supercontinent Cycles and Global Geodynamics.

Author contributions

H.G. conducted the data evaluation and analyses and designed the paper. L.S.D. did the bootstrap resampling for the database (Figs. 3, 4). Z.X.L. designed the study and clarified the concepts. H.G., L.S.D., and Z.X.L. participated in the interpretation of the results and preparation of the paper. G.M.C. and R.M. were involved in an early attempt of this study.

Competing interests

The authors declare no competing interests.

Additional information

Supplementary information is available for this paper at <https://doi.org/10.1038/s41467-019-13300-4>.

Correspondence and requests for materials should be addressed to H.G.E.D.

Peer review information *Nature Communications* thanks the anonymous reviewer(s) for their contribution to the peer review of this work. Peer reviewer reports are available.

Reprints and permission information is available at <http://www.nature.com/reprints>

Publisher's note Springer Nature remains neutral with regard to jurisdictional claims in published maps and institutional affiliations.



Open Access This article is licensed under a Creative Commons Attribution 4.0 International License, which permits use, sharing, adaptation, distribution and reproduction in any medium or format, as long as you give appropriate credit to the original author(s) and the source, provide a link to the Creative Commons license, and indicate if changes were made. The images or other third party material in this article are included in the article's Creative Commons license, unless indicated otherwise in a credit line to the material. If material is not included in the article's Creative Commons license and your intended use is not permitted by statutory regulation or exceeds the permitted use, you will need to obtain permission directly from the copyright holder. To view a copy of this license, visit <http://creativecommons.org/licenses/by/4.0/>.

© Crown 2019



RightsLink®

?
Help

✉
Email Support

Geochemical evidence for a widespread mantle re-enrichment 3.2 billion years ago: implications for global-scale plate tectonics

SPRINGER NATURE

Author: Hamed Gamal El Dien et al

Publication: Scientific Reports

Publisher: Springer Nature

Date: Jun 11, 2020

Copyright © 2020, The Author(s)

Creative Commons

This is an open access article distributed under the terms of the [Creative Commons CC BY](#) license, which permits unrestricted use, distribution, and reproduction in any medium, provided the original work is properly cited.

You are not required to obtain permission to reuse this article.

To request permission for a type of use not listed, please contact [Springer Nature](#)

© 2020 Copyright - All Rights Reserved | [Copyright Clearance Center, Inc.](#) | [Privacy statement](#) | [Terms and Conditions](#)
Comments? We would like to hear from you. E-mail us at customercare@copyright.com

ATTRIBUTION STATEMENTS

Table iv: Attribution statement table for published -Chapter 9: *Geochemical evidence for a widespread mantle re-enrichment 3.2 billion years ago: implications for global-scale plate tectonics*

	Conception and Design	Acquisition of Data and Method	Data Conditioning and Manipulation	Analysis and Statistical Method	Interpretation and Discussion	Final Approval	Total % contribution
Co-Author 1 (Hamed Gamal El Dien)	70	90	65	60	70	40	70
Co Author 1 Acknowledgment: I acknowledge that these represent my contribution to the above research output					Signed: 03/11/2020		
Co-Author 2 (Luc-Serge Doucet)	10	10	25	40	10	10	10
Co Author 2 Acknowledgment: I acknowledge that these represent my contribution to the above research output					Signed: 04/11/2020		
Co-Author 3 (J. Brendan Murphy)	10		5		10	25	10
Co Author 3 Acknowledgment: I acknowledge that these represent my contribution to the above research output					Signed: 03/11/2020		
Co-Author 4 (Zheng-Xiang Li)	10		5		10	25	10
Co Author 4 Acknowledgment: I acknowledge that these represent my contribution to the above research output					Signed:		
Total %	100	100	100	100	100	100	100



OPEN

Geochemical evidence for a widespread mantle re-enrichment 3.2 billion years ago: implications for global-scale plate tectonics

Hamed Gamal El Dien^{1,2}✉, Luc S. Doucet¹, J. Brendan Murphy^{1,3} & Zheng-Xiang Li¹

Progressive mantle melting during the Earth's earliest evolution led to the formation of a depleted mantle and a continental crust enriched in highly incompatible elements. Re-enrichment of Earth's mantle can occur when continental crustal materials begin to founder into the mantle by either subduction or, to a lesser degree, by delamination processes, profoundly affecting the mantle's trace element and volatile compositions. Deciphering when mantle re-enrichment/refertilization became a global-scale process would reveal the onset of efficient mass transfer of crust to the mantle and potentially when plate tectonic processes became operative on a global-scale. Here we document the onset of mantle re-enrichment/refertilization by comparing the abundances of petrogenetically significant isotopic values and key ratios of highly incompatible elements compared to lithophile elements in Archean to Early-Proterozoic mantle-derived melts (i.e., basalts and komatiites). Basalts and komatiites both record a rapid-change in mantle chemistry around 3.2 billion years ago (Ga) signifying a fundamental change in Earth geodynamics. This rapid-change is recorded in Nd isotopes and in key trace element ratios that reflect a fundamental shift in the balance between fluid-mobile and incompatible elements (i.e., Ba/La, Ba/Nb, U/Nb, Pb/Nd and Pb/Ce) in basaltic and komatiitic rocks. These geochemical proxies display a significant increase in magnitude and variability after ~3.2 Ga. We hypothesize that rapid increases in mantle heterogeneity indicate the recycling of supracrustal materials back into Earth's mantle via subduction. Our new observations thus point to a ≥ 3.2 Ga onset of global subduction processes via plate tectonics.

Although plate tectonics is now well accepted as the paradigm for Earth's evolution in the Phanerozoic eon, the question of when these processes began is still controversial¹. Estimates are based mainly on crustal observations, and range from early Archean to the late Neoproterozoic¹. Resolution of this debate is fundamental to our understanding of the evolution of Earth systems. A key process of plate tectonics is widespread subduction^{2,3}. Subduction zones recycle terrestrial materials back into Earth's mantle as the subducting slab sinks and re-equilibrates within Earth's interior^{2,4,5}. Fluids and magmas released from sediments and crustal materials in the vicinity of the subducting slab facilitate melting of the upper mantle wedge creating arc basalts with specific trace element signatures (such as elevated large ion lithophile elements (LILE): Ba, Pb, U, Sr, As, B, and Cs)^{6,7} that reflect enrichment of the sub-arc mantle source (compared to mid-ocean ridge basalts^{8,9}). Some of these recycled terrestrial materials also invade the deeper mantle¹⁰, causing enrichment of the deep mantle in LILE and light rare earth elements (LREE) and promoting a geochemical and isotopic heterogeneity that characterizes basalts derived from mantle plumes^{9,11–13}. It is commonly believed that before the plate tectonics regime, a chemically stratified Earth had a relatively homogeneous mantle composition^{14,15} (due to the lack of large/global-scale recycling of terrestrial materials into the upper and lower mantle) that was depleted in highly incompatible elements (e.g. Ba, Pb, Rb, Cs, Sr, and U) but enriched in high field strength elements (e.g. Nb and Ta)¹⁶. So, a globally-detectable large change in the mantle heterogeneity^{9,12,17}, caused by a refertilization/re-enrichment in incompatible and fluid mobile elements, and a step-change in Nd isotope systematics of the upper and lower mantle-derived materials,

¹Earth Dynamics Research Group, The Institute for Geoscience Research (TIGeR), School of Earth and Planetary Sciences, Curtin University, GPO Box U1987, Perth, WA, 6845, Australia. ²Geology Department, Faculty of Science, Tanta University, 31527, Tanta, Egypt. ³Department of Earth Sciences, St. Francis Xavier University, Antigonish, Nova Scotia, Canada. ✉e-mail: hamed.gamaleldien@postgrad.curtin.edu.au

could identify the onset of global-scale subduction and plate tectonic processes. Thus, tracking the isotopic and chemical heterogeneities of the Earth's upper and lower mantle through the Archean and Early Proterozoic may provide a new way of identifying when plate tectonics started.

Geochemical tracer for crustal recycling. Most previous estimates of when plate tectonics commenced were based on proxies recorded in continental crustal rocks^{18–22} which are only indirectly related to mantle processes, and may intrinsically have a preservation bias and/or reflect regional rather than global processes^{18,23–29}. In order to identify when widespread global-scale mantle refertilization/re-enrichment occurred, we investigate the composition of the mantle directly by examining the global database of Archean–Early Proterozoic mafic-ultramafic rocks focusing on their Sm–Nd isotopic systematics and on petrogenetically-sensitive trace element ratios.

Samarium and Neodymium have very similar chemical behaviour (i.e., similar ionic radii and the same valency). As the Sm/Nd ratio is robust to the effects of alteration and metamorphism and is not significantly affected by crystal fractionation, this ratio typically reflects source composition^{11,30–32}. As the depleted mantle reservoir retains Sm over Nd, its Sm/Nd ratio (~0.5) is greater than the bulk earth chondritic (~0.32) and typical continental crust (~0.2) values^{31,32}. Thus, ¹⁴⁷Sm to ¹⁴³Nd decay over geological time would yield a significantly higher ¹⁴³Nd/¹⁴⁴Nd ratio in magmas derived from depleted mantle compared to contemporary magmas derived from a crustal reservoir³¹. As magmas passively acquire the ¹⁴³Nd/¹⁴⁴Nd initial ratio of their source³¹, differences in ϵ Nd (the relative deviation of the ¹⁴³Nd/¹⁴⁴Nd initial ratio from the chondritic value, ϵ Nd = 0) in mafic/ultramafic rocks constrain the evolution of the mantle source. Over geological time, the depleted mantle isotopically evolves toward more positive ϵ Nd values but the crust evolves towards negative values^{31,32}. Thus, shifting of ϵ Nd of mafic-ultramafic rocks to less positive values identifies when a significant contribution of terrestrial materials to the mantle source occurred^{11,12,30,31}.

In addition, the ratios of incompatible fluid-mobile elements (FMEs: Ba, Pb, Rb, Sr, and U) to relatively immobile elements such as high field strength elements (HFSEs: Nb and Ta) and rare earth elements (REE) are excellent tracers for the invasion of fluids and magmas derived from the recycling of sediments (such as Ba/La and Ba/Nb)^{33–35} and of continental crust materials (such as U/Nb)^{9,12} into mantle sources^{8,36}. FMEs are transferred to the crust during subduction dehydration and arc magmatism^{6,37}, but HFSEs are retained in the mantle source by minerals such as amphibole and rutile³⁸. Such trace element pairs/ratios, with similar incompatibility but with very distinct chemical behaviours, are particularly useful because they are insensitive to alteration/metamorphism, and are less fractionated during partial melting^{9,12,15}. Thus, tracking ratios such as Ba/La, Ba/Nb, U/Nb, Pb/Nd and Pb/Ce in addition to Nd isotopes in mafic and ultramafic magmatic products during the Archean and Proterozoic eons could precisely identify the time when heterogeneities in their respective upper and lower mantle sources originated, as well as source chemistry differences and the change of mantle trace element budget.

Results

We compiled a database consisting of major and trace element whole-rock and Nd isotopes³⁹ of ~6,250 analyses from mafic and ultramafic rocks with reliable crystallization age and geospatial location for each sample (see methods). The studied samples are widely representative of all the continents and cratons, and span the Archean–Early Proterozoic time range (3.8–2.2 Ga) (Supplementary Figures 1–4 and Supplementary Tables 1 and 2). The database includes primary mantle melts represented by basaltic rocks and komatiites. Using the variation of the means of Nd isotopes (as ϵ Nd) in samples of the same age, and a statistical bootstrapping method⁴⁰ on the basaltic and komatiitic rocks focusing on Ba/La, Ba/Nb, U/Nb, Pb/Nd and Pb/Ce ratios, we identify a significant change in mantle geochemical composition after ~3.25 Ga for basaltic rocks and after ~3.15 Ga for komatiites (Figs. 1–3 and Supplementary Figure 5).

Figure 1 displays a significant shift in the range of ϵ Nd values of basaltic rocks and komatiites that span the Paleo- to Meso-Archean transition (~3.2 Ga). Although specific suites may show a range in values implying the shift may occur locally at earlier times, these shifts are not recognizable when viewed from the perspective of the global database, indicating they are probably local in scale. For example, Nd isotopic data of the Greenland Eoarchean (3.8–3.7 Ga) basaltic rocks extend to negative ϵ Nd (attributed to mantle contamination^{41,42}) although on average, the data from that time interval plot at positive ϵ Nd^{43–46}. More generally, the averages of ϵ Nd in basaltic and komatiitic suites before ~3.2 Ga show little variation, ranging between +0.02 and +2.2. After ~3.2 Ga, however, ϵ Nd averages for basaltic and komatiitic rocks show an abrupt decrease from –1.5 (at ~3.0 Ga) to –8.0 (at ~1.7 Ga), which we interpret to reflect the onset of global-scale heterogeneity in their upper and lower (respectively) mantle sources (Fig. 1). This analysis provides robust evidence for global-scale, pene-contemporaneous contamination/refertilization of the mantle source for both mafic and ultramafic rocks, beginning after ~3.2 Ga in the upper mantle (inferred from basaltic rocks) but also affecting the lower mantle (inferred by komatiites) as the influx of LREE-enriched crustal materials yield negative ϵ Nd values^{11,31}.

Trace element ratios (i.e., Ba/La, Ba/Nb, U/Nb, Pb/Nd and Pb/Ce) of basalts and komatiites are widely accepted to track the recycling of terrestrial materials into mantle sources^{9,12}. Figures 2 and 3 monitor the best estimate of the average composition of these trace element ratios through time, and are reported as means with associated 2-standard-error (95% confidence interval) uncertainties of intervals between 2.2 and 4.0 Ga. These ratios display a systematic increase in both magnitude and variability, mainly after ~3.2 Ga. In general, Figure 2 and supplementary Figure 5a both display abrupt increases in the moving means of Ba/La, Ba/Nb, U/Nb, Pb/Nd and Pb/Ce ratios in basaltic rocks after ~3.25 Ga. In addition, the average mean values of all ratios of komatiites after ~3.15 Ga are highly enriched compared to komatiites older than ~3.15 Ga (Fig. 3 and Supplementary Figure 5b).

There is some evidence supporting localized subduction in specific suites before ca. 3.2 Ga. For example at 3.8–3.7 Ga, some ratios such as Ba/La (20.15–19.43) and U/Nb (0.08–0.05) are somewhat higher than estimates of equivalent ratios in the primitive mantle (PM)⁴⁷ (Ba/La = 10.81 and U/Nb = 0.03, respectively (Fig. 2a,c). These

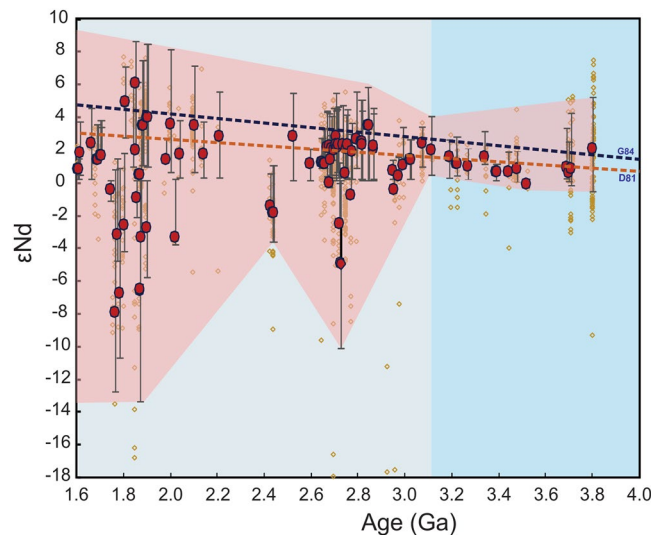


Figure 1. $^{143}\text{Nd}/^{144}\text{Nd}$ ratio (represented as ϵNd) vs. age plot for Archean and Proterozoic basaltic rocks and komatiites (data from Spencer *et al.*³⁹). Brown circles represent individual samples. Red dots represent the median of samples with the same age, and the associated error bars spans across the middle 50% of the data, called the median data range here. The red field represents the envelope for the median range. The large variation in the mean ϵNd values after ~ 3.2 – 3.0 Ga suggests an isotopic shift in the mantle source of the basaltic rocks and the komatiites. The depleted mantle curves are shown for comparison^{70,71}.

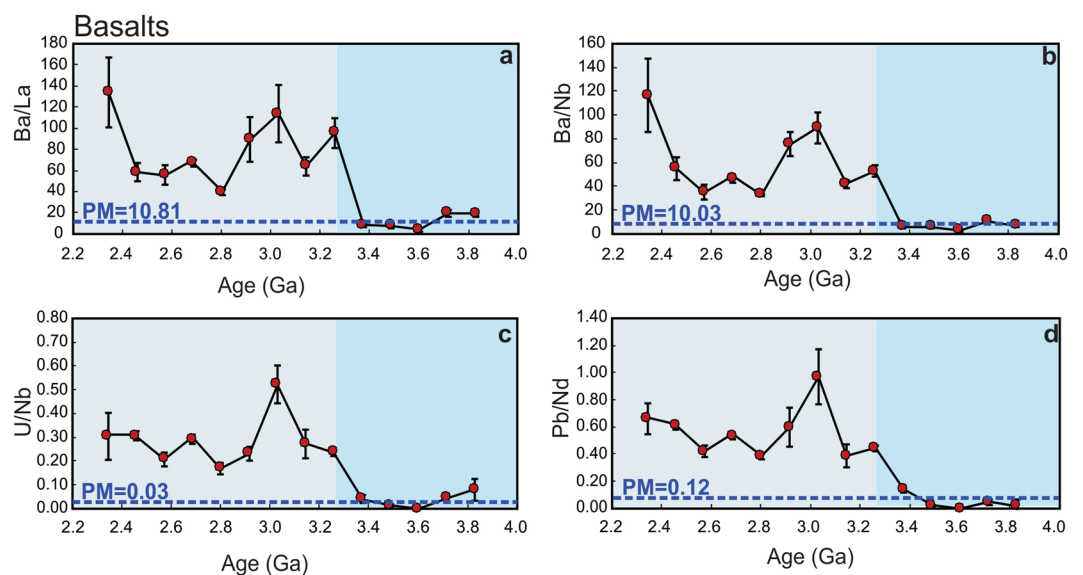


Figure 2. Time evolution of fluid-mobile-elements/immobile-elements in the basaltic rock datasets. Ba/La (a), Ba/Nb (b), U/Nb (c), and Pb/Nd (d). All ratios show an abrupt increase at ~ 3.25 Ga. Dotted horizontal lines are the primitive mantle values (PM; Ba/La = 10.81, Ba/Nb = 10.03, U/Nb = 0.03, Pb/Nd = 0.12)⁴⁷. Error bars in a–d show the 2-standard errors of the means.

higher values may reflect a subduction zone-like signature such as that proposed for the Isua greenstone belt, SW Greenland according to field and geochemical data interpretations^{24,26,48–50}. Also, at 3.4–3.3 Ga, U/Nb (0.04) and Pb/Nd (0.14) are slightly higher than PM values (0.03 and 0.12, respectively)⁴⁷ (Fig. 2c,d) which may reflect crustal contamination of the mantle source for the Barberton greenstone belt, the Kaapvaal craton^{28,51–53}. However, when viewed from the perspective of the global database, these ratios become statistically detectable only around 3.25 Ga (e.g. Ba/La = 96.31, Ba/Nb = 53.32, U/Nb = 0.24 and Pb/Nd = 0.45 compared to the PM-like values and those before 3.25 Ga (Fig. 2). From this perspective, contamination of the mantle by LILE- and LREE-enriched recycled continental materials during subduction would have been localized and relatively minor in the Palaeoarchaeon and the Eoarchaeon, but became a global process at ca. 3.2 Ga. The observed time lag (~ 100 Ma) in the increase in those ratios between basalts and komatiites could reflect the transit time of subducted slabs from upper mantle

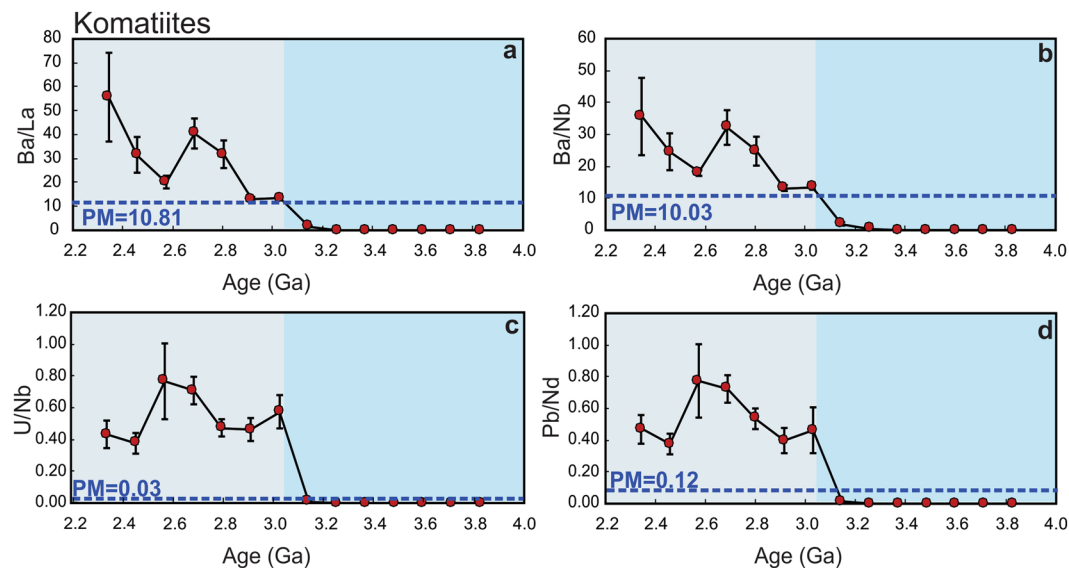


Figure 3. Time evolution of fluid-mobile-elements/immobile-elements in the komatiite datasets. Ba/La (a), Ba/Nb (b), U/Nb (c), and Pb/Nd (d). All ratios show an abrupt increase at ~ 3.15 Ga. Dotted horizontal lines are the primitive mantle values (PM; Ba/La = 10.81, Ba/Nb = 10.03, U/Nb = 0.03, Pb/Nd = 0.12)⁴⁷. Error bars show 2-standard errors of the means.

(contaminated basaltic rocks) to the lower mantle (contaminated komatiites). Taken together, these results suggest a fundamental and global change in the upper and lower mantle source composition of basalts and komatiites through refertilization/replenishment of fluid-mobile elements at the start of the Mesoarchean, which is consistent with the negative ϵNd values after ~ 3.2 – 3.0 Ga (Fig. 1).

Discussion

Our observed abrupt changes could be attributed to either (1) crustal contamination of ascending mantle-derived magma⁵⁴ or (2) contamination of the mantle source by either subduction or delamination^{14,54,55}. Crustal contamination/mixing of mafic and ultramafic magmas during their emplacement can be evaluated using the Th/Yb ratio, which is widely accepted as a powerful tracer of this process⁵⁶. Supplementary Figures 6 and 7 show the covariation between the studied ratios and Th/Yb in both basaltic rocks and komatiites before and after 3.25 Ga and 3.15 Ga, respectively, compared with such ratios in Archean continental crust (i.e., tonalite-trondhjemite-granodiorite (TTGs) dataset)⁵⁷. These plots show that Th/Yb has no relationship with Ba/La, Ba/Nb, U/Nb, Pb/Nd and Pb/Ce in either basaltic rocks (Supplementary Figure 6) or komatiites (Supplementary Figure 7). In addition, the Th/Yb values are very low compared to those typical of TTGs, providing clear evidence that no significant contamination of basaltic or komatiitic rocks by Archean crust occurred during their emplacement. Moreover, Archean basaltic and komatiitic rocks plot on an array that is parallel to the oceanic mantle array (MORB-OIB array) on the Th/Yb vs. Nb/Yb diagram (Supplementary Figure 8)⁵⁶. This trend is similar to that of a modern-arc array, suggesting derivation of those rocks from a metasomatized/re-enriched mantle source⁵⁶, and contrasts with the oblique trend displayed by TTGs (Supplementary Figure 8). The similarly low Th/Yb in post-3.2 Ga komatiites and basalts compares favourably with modern-arc basalts (Supplementary Figure 8), suggesting that the enrichment in these ratios was source-dependent and the mantle inherited these features before the generation of these mafic and ultramafic magmas.

The similarity between the average mean values of the studied trace element ratios in basalts and komatiites before ~ 3.25 – 3.15 Ga with primitive mantle estimates (PM)⁴⁷ (Figs. 2, 3 and Supplementary Figures 5, 8) indicates the existence of a primitive-like and/or quasi-homogeneous mantle with only minor and local terrestrial inputs before ~ 3.25 – 3.15 Ga. In contrast, the average mean values of the studied ratios of basalts and komatiites after ~ 3.25 – 3.15 Ga are highly enriched compared to the primitive mantle (Figs. 2, 3 and Supplementary Figures 5, 8). Such an interpreted abrupt change in mantle composition is also reflected in the source of TTGs, generally considered to be juvenile crust newly extracted from the upper mantle⁵⁷. As shown in Supplementary Figure 9, the same ratios (except for U/Nb) in TTGs not only have the same contents as their parent mafic rocks (Supplementary Figure 6) but also show the same abrupt change after ~ 3.3 – 3.2 Ga⁵⁷. Similarly, a recent study on Jack Hills zircons (4.3–3.3 Ga) suggests a small yet notable change in Earth's crustal composition between the Hadean and the Mesoarchean⁵⁸.

Mantle refertilization/re-enrichment at ~ 3.2 Ga could have occurred by two major processes — sagduction/delamination⁵⁵ or subduction⁵⁴. Sagduction/delamination of dense residue after TTG formation would have facilitated the refertilization of the upper mantle with crust-like chemical and isotopic signatures^{14,55}, but this process would have had less influence on the composition of the lower mantle^{15,55}. Therefore, a sagduction/delamination scenario is not consistent with our analysis of komatiites (Fig. 3) which are thought to have been derived from the lower mantle, and represent the products of mantle plumes¹⁷. Komatiites younger than ~ 3.15 Ga are enriched

in petrogenetically-indicating trace element ratios suggesting a re-enriched/metasomatized mantle source. Consistent with trace element results, ϵNd values of komatiites and basaltic rocks both show a pronounced abrupt-shift to lower values at ~ 3.0 Ga (Fig. 1). This shift is powerful evidence that recycling of subducted sediments and crust affected the composition of both the upper mantle and the deep mantle plume source on a global scale^{11,12,30}, indicating that subduction into the lower mantle was widely/globally operative by ~ 3.2 Ga. These results are consistent with oxygen and hydrogen isotopes studies of the 3.2 Ga Barberton komatiites, South Africa that suggest mantle source heterogeneity by then^{28,59}.

Some previous work^{18,19,23}, though based on more indirect measures of global mantle composition than we present here, support our first-order conclusions. Shirey and Richardson²³ interpret the appearance at ca. 3.2 Ga of eclogitic inclusions in diamonds from kimberlite pipes of the Kaapvaal craton to require subduction processes. Analysis of Hf-O zircon data in crustal rocks, which tracks the recycling of supracrustal materials, provides evidence for a step change at ca. 3 Ga indicative of the onset of subduction^{18,19}. Recently, Sobolev and Brown³ hypothesize that the evolution and start of plate tectonics on Earth were facilitated by accumulation of sediments at the continental edges and trenches, which acted as a lubricant for the emergence and stabilization of subduction processes since the Mesoarchean (3.2–2.8 Ga). Our new observations, based on direct products of mantle melting, identify geochemical tracers of sediments recycling into both the upper and lower mantle (i.e., Ba/La and Ba/Nb) in both basaltic and komatiitic rocks, show that the abrupt increase occurred at ~ 3.2 Ga (Figs. 2 and 3). In addition, Gamal El Dien *et al.*⁶⁰, using Mg, Ni and Cr elements in basaltic rocks show a consistent and rapid drop at ~ 3.2 – 3.0 Ga that indicates an abrupt change in mantle potential temperature at the start of global-scale plate tectonics. Although we cannot rule out the presence of intermittent stagnant lid tectonics along with plate tectonics after ~ 3.2 Ga⁶¹, our analysis suggests mass transfer from the surface to the deep mantle from ~ 3.2 Ga, a process most feasibly accomplished through subduction and plate tectonics.

Our interpretation assumes no dramatic continental crustal growth at around 3.2 Ga^{62–64}. However, if there was a spike of global continental crustal growth at ca. 3.2 Ga (as argued by some^{19,65,66}), then global plate tectonics could have started earlier than 3.2 Ga but mantle re-enrichment may not be as pronounced due to the relatively small amount of continental crust^{67–69}.

Overall, our work points to a profound mantle re-enrichment event at ca. 3.2 billion years ago, interpreted to indicate the start of global-scale plate tectonics no later than that time.

Methods

We compiled a database of basaltic rocks ($n = 3,127$) and komatiites ($n = 2,740$) for major and trace elements (including rare earth elements) mainly using the Georoc repository (Supplementary Data 1, 2). We cross-checked every sample with their original reference to verify its magmatic age and location (continent, craton and formation). Samples with no age constraints were excluded. All the selected samples have age estimates and age error less than ± 100 Myr, sample ID and geospatial sample locations. The basaltic and komatiitic rocks in the selected database range in age of 3.8–2.4 Ga and 3.8–2.0 Ga, respectively. The basaltic rock database is composed mainly of basalts and basaltic andesites with 40–55 wt % SiO_2 , $\text{MgO} < 12$ wt% and total alkali ($\text{K}_2\text{O} + \text{Na}_2\text{O}$) < 5 wt %. To obtain an optimal distribution estimate of trace element ratios for mantle-derived melts (basalts and komatiites) and minimize sampling and preservation bias, we performed a weighted bootstrap resampling of the selected database following the method of Keller and Schoene⁴⁰ using the Matlab MIT open-source code, available at <https://github.com/brenhinkeller/StatisticalGeochemistry>. All the fluid-mobile-elements/immobile-elements plots for basalts and komatiites in this paper were made using bootstrap-resampled data.

Nd isotopes database of Archaean and Proterozoic basaltic rocks and komatiites were taken from Spencer *et al.*³⁹. Nd data were filtered, and only analyses with magmatic age constraints better than ± 100 Myr were used. Only Georoc analyses that included $^{143}\text{Nd}/^{144}\text{Nd}$ along with Sm and Nd concentrations were used. The $^{147}\text{Sm}/^{144}\text{Nd}$ ratio was determined using the atomic weights and abundances with the following equation:

$$^{147}\text{Sm}/^{143}\text{Nd} = \frac{\text{Sm ppm}}{\text{Nd ppm}} * \frac{\text{Abs.}^{147} \text{ Sm} * \text{At. wt. Nd}}{\text{Abs.}^{144} \text{ Nd} * \text{At. wt. Sm}}$$

The tonalite-trondhjemitic-granodiorite rock database (TTG; sample number = 1,230) was collected from Johnson *et al.*⁵⁷ The change in the median data range before and after 3.3–3.2 Ga is highlighted by rectangular shades of different colours (Supplementary Figure 9). Also, the average of medians for data within each rectangular shade is shown with horizontal bar. As many samples do not contain all the ratios used, the density of the data differs between plots.

Data availability

All the data that are necessary for evaluating the findings of this study are available within this article and its Supplementary Information

Received: 13 February 2020; Accepted: 12 May 2020;

Published online: 11 June 2020

References

1. Korenaga, J. Initiation and Evolution of Plate Tectonics on Earth: Theories and Observations. *Annu. Rev. Earth Planet. Sci.* **41**, 117–151 (2013).
2. Clift, P. & Vannucchi, P. Controls on tectonic accretion versus erosion in subduction zones: Implications for the origin and recycling of the continental crust. *Rev. Geophys.* **42**, RG2001 (2004).
3. Sobolev, S. V. & Brown, M. Surface erosion events controlled the evolution of plate tectonics on Earth. *Nature* **570**, 52–57 (2019).

4. Willbold, M. & Stracke, A. Formation of enriched mantle components by recycling of upper and lower continental crust. *Chem. Geol.* **276**, 188–197 (2010).
5. Stern, R. J. Subduction zones. *Rev. Geophys.* **40**, (2002).
6. Gamal El Dien, H., Li, Z.-X., Kil, Y. & Abu-Alam, T. Origin of arc magmatic signature: A temperature-dependent process for trace element (re)-mobilization in subduction zones. *Sci. Rep.* **9**, 7098 (2019).
7. Poli, S. & Schmidt, M. W. Petrology of Subducted Slabs. *Annu. Rev. Earth Planet. Sci.* **30**, 207–235 (2002).
8. Kessel, R., Schmidt, M. W., Ulmer, P. & Pettko, T. Trace element signature of subduction-zone fluids, melts and supercritical liquids at 120–180 km depth. *Nature* **437**, 724–727 (2005).
9. Hofmann, A. W. Sampling Mantle Heterogeneity through Oceanic Basalts: Isotopes and Trace Elements. *Treatise on Geochemistry* 67–101 (2014). <https://doi.org/10.1016/B978-0-08-095975-7.00203-5>
10. Patchett, P. J., Kouvo, O., Hedge, C. E. & Tatsumoto, M. Evolution of continental crust and mantle heterogeneity: Evidence from Hf isotopes. *Contrib. to Mineral. Petrol.* **78**, 279–297 (1982).
11. White, W. M. & Hofmann, A. W. Sr and Nd isotope geochemistry of oceanic basalts and mantle evolution. *Nature* **296**, 821–825 (1982).
12. Hofmann, A. W. Mantle geochemistry: the message from oceanic volcanism. *Nature* **385**, 219–229 (1997).
13. Mazza, S. E. *et al.* Sampling the volatile-rich transition zone beneath Bermuda. *Nature* **569**, 398–403 (2019).
14. Moya, J. F. & Laurent, O. Archaean tectonic systems: A view from igneous rocks. *Lithos* **302–303**, 99–125 (2018).
15. Condie, K. C. A planet in transition: The onset of plate tectonics on Earth between 3 and 2 Ga? *Geosci. Front.* **9**, 51–60 (2018).
16. Hofmann, A. W. Chemical differentiation of the Earth: the relationship between mantle, continental crust, and oceanic crust. *Earth Planet. Sci. Lett.* **90**, 297–314 (1988).
17. Bennett, V. C. Compositional Evolution of the Mantle. *Treatise on Geochemistry* 493–519 (2003). <https://doi.org/10.1016/B0-08-043751-6/02013-2>
18. Naeraa, T. *et al.* Hafnium isotope evidence for a transition in the dynamics of continental growth 3.2 Gyr ago. *Nature* **485**, 627–630 (2012).
19. Dhuime, B., Hawkesworth, C. J., Cawood, P. A. & Storey, C. D. A change in the geodynamics of continental growth 3 billion years ago. *Science* **335**, 1334–6 (2012).
20. Tang, M., Chen, K. & Rudnick, R. L. Archean upper crust transition from mafic to felsic marks the onset of plate tectonics. *Science* (80-). **351**, 372–375 (2016).
21. Nagel, T. J., Hoffmann, J. E. & Münker, C. Generation of Eoarchean tonalite-trondhjemite-granodiorite series from a thickened mafic arc crust. *Geology* **40**, 375–378 (2012).
22. Reimink, J. R., Pearson, D. G., Shirey, S. B., Carlson, R. W. & Ketchum, J. W. F. Onset of new, progressive crustal growth in the central Slave craton at 3.55 Ga. *Geochem. Persp. Lett.* **10**, 8–13 (2019).
23. Shirey, S. B. & Richardson, S. H. Start of the Wilson cycle at 3 Ga shown by diamonds from subcontinental mantle. *Science* **333**, 434–6 (2011).
24. Furnes, H. *et al.* A Vestige of Earth's Oldest Ophiolite. *Science* **315**, 2001–2004 (2007).
25. Komiya, T. *et al.* Geology of the Eoarchean, >3.95 Ga, Nulliak supracrustal rocks in the Saglek Block, northern Labrador, Canada: The oldest geological evidence for plate tectonics. *Tectonophysics* **662**, 40–66 (2014).
26. Kaczmarek, M. A., Reddy, S. M., Nutman, A. P., Friend, C. R. L. & Bennett, V. C. Earth's oldest mantle fabrics indicate Eoarchean subduction. *Nat. Commun.* **7**, 1–7 (2016).
27. Turner, S., Rushmer, T., Reagan, M. & Moya, J. F. Heading down early on? Start of subduction on earth. *Geology* **42**, 139–142 (2014).
28. Sobolev, A. V. *et al.* Deep hydrous mantle reservoir provides evidence for crustal recycling before 3.3 billion years ago. *Nature* **1**, <https://doi.org/10.1038/s41586-019-1399-5> (2019).
29. Blichert-Toft, J., Arndt, N. T., Wilson, A. & Coetzee, G. Hf and Nd isotope systematics of early Archean komatiites from surface sampling and ICDP drilling in the Barberton Greenstone Belt, South Africa. *Am. Mineral.* **100**, 2396–2411 (2015).
30. Chauvel, C., Lewin, E., Carpentier, M., Arndt, N. T. & Marini, J.-C. Role of recycled oceanic basalt and sediment in generating the Hf–Nd mantle array. *Nat. Geosci.* **1**, 64–67 (2008).
31. Murphy, J. B. & Nance, R. D. Sm–Nd isotopic systematics as tectonic tracers: an example from West Avalonia in the Canadian Appalachians. *Earth-Science Rev.* **59**, 77–100 (2002).
32. DePaolo, D. J. & Wasserburg, G. J. Nd isotopic variations and petrogenetic models. *Geophys. Res. Lett.* **3**, 249–252 (1976).
33. Nielsen, S. G. *et al.* Barium isotope evidence for pervasive sediment recycling in the upper mantle. *Sci. Adv.* **4**, eaas8675 (2018).
34. Plank, T. & Langmuir, C. H. Tracing trace elements from sediment input to volcanic output at subduction zones. *Nature* **362**, 739–743 (1993).
35. Kelley, K. A. & Cottrell, E. Water and the oxidation state of subduction zone magmas. *Science* **325**, 605–7 (2009).
36. Miller, D. M., Goldstein, S. L. & Langmuir, C. H. Cerium/lead and lead isotope ratios in arc magmas and the enrichment of lead in the continents. *Nature* **368**, 514–520 (1994).
37. Gamal El Dien, H. *et al.* Cr-spinel records metasomatism not petrogenesis of mantle rocks. *Nat. Commun.* **5103** (2019). <https://doi.org/10.1038/s41467-019-13117-1>
38. Keppler, H. Constraints on partitioning experiments on the composition of subduction-zone fluids. *Nature* **380**, 237–240 (1996).
39. Spencer, C. J., Murphy, J. B., Kirkland, C. L., Liu, Y. & Mitchell, R. N. A Palaeoproterozoic tectono-magmatic lull as a potential trigger for the supercontinent cycle. *Nat. Geosci.* **11**, 97–101 (2018).
40. Brenhin Keller, C. & Schoene, B. Statistical geochemistry reveals disruption in secular lithospheric evolution about 2.5 Gyr ago. *Nature* **485**, 490–493 (2012).
41. Blichert-Toft, J., Albarède, F., Rosing, M., Frei, R. & Bridgwater, D. The Nd and Hf isotopic evolution of the mantle through the Archean. Results from the Isua supracrustals, West Greenland, and from the Birimian terranes of West Africa. *Geochim. Cosmochim. Acta* **63**, 3901–3914 (1999).
42. Rizo, H., Boyet, M., Blichert-Toft, J. & Rosing, M. T. Early mantle dynamics inferred from ¹⁴²Nd variations in Archean rocks from southwest Greenland. *Earth Planet. Sci. Lett.* **377–378**, 324–335 (2013).
43. Carlson, R. W., Garçon, M., O'Neil, J., Reimink, J. & Rizo, H. The nature of Earth's first crust. *Chem. Geol.* **530**, 119321 (2019).
44. Bennett, V. C., Brandon, A. D. & Nutman, A. P. Coupled ¹⁴²Nd–¹⁴³Nd isotopic evidence for Hadean mantle dynamics. *Science* (80-). **318**, 1907–1910 (2007).
45. Hoffmann, J. E., Münker, C., Polat, A., Rosing, M. T. & Schulz, T. The origin of decoupled Hf–Nd isotope compositions in Eoarchean rocks from southern West Greenland. *Geochim. Cosmochim. Acta* **75**, 6610–6628 (2011).
46. O'Neil, J., Rizo, H., Boyet, M., Carlson, R. W. & Rosing, M. T. Geochemistry and Nd isotopic characteristics of Earth's Hadean mantle and primitive crust. *Earth Planet. Sci. Lett.* **442**, 194–205 (2016).
47. McDonough, W. & Sun, S. – The composition of the Earth. *Chem. Geol.* **120**, 223–252 (1995).
48. Polat, A., Hofmann, A. W., Münker, C., Regelous, M. & Appel, P. W. U. Contrasting geochemical patterns in the 3.7–3.8 Ga pillow basalt cores and rims, Isua greenstone belt, Southwest Greenland: Implications for postmagmatic alteration processes. *Geochim. Cosmochim. Acta* **67**, 441–457 (2003).
49. Jenner, F. E. *et al.* Evidence for subduction at 3.8 Ga: Geochemistry of arc-like metabasalts from the southern edge of the Isua Supracrustal Belt. *Chem. Geol.* **261**, 82–97 (2009).

50. Hanmer, S. & Greene, D. C. A modern structural regime in the Paleoproterozoic (~ 3.64 Ga); Isua Greenstone Belt, southern West Greenland. *Tectonophysics* **346**, 201–222 (2002).
51. Blichert-Toft, J., Arndt, N. T., Wilson, A. & Coetsee, G. Hf and Nd isotope systematics of early Archean komatiites from surface sampling and ICDP drilling in the Barberton Greenstone Belt, South Africa. *Am. Mineral.* **100**, 2396–2411 (2015).
52. Furnes, H., de Wit, M. & Robins, B. A review of new interpretations of the tectonostratigraphy, geochemistry and evolution of the Onverwacht Suite, Barberton Greenstone Belt, South Africa. *Gondwana Research* **23**, 403–428 (2013).
53. Smart, K. A., Tappe, S., Stern, R. A., Webb, S. J. & Ashwal, L. D. Early Archean tectonics and mantle redox recorded in Witwatersrand diamonds. *Nat. Geosci.* **9**, 255–259 (2016).
54. van Hunen, J. & Moyen, J.-F. Archean Subduction: Fact or Fiction? *Annu. Rev. Earth Planet. Sci.* **40**, 195–219 (2012).
55. Bédard, J. H. Stagnant lids and mantle overturns: Implications for Archean tectonics, magmatogenesis, crustal growth, mantle evolution, and the start of plate tectonics. *Geosci. Front.* **9**, 19–49 (2018).
56. Pearce, J. A. Geochemical fingerprinting of oceanic basalts with applications to ophiolite classification and the search for Archean oceanic crust. *Lithos* **100**, 14–48 (2008).
57. Johnson, T. E. *et al.* Secular change in TTG compositions: Implications for the evolution of Archean geodynamics. *Earth Planet. Sci. Lett.* **505**, 65–75 (2019).
58. Turner, S., Wilde, S., Wörner, G., Schaefer, B. & Lai, Y.-J. An andesitic source for Jack Hills zircon supports onset of plate tectonics in the Hadean. *Nat. Commun.* **11**, 1241 (2020).
59. Byerly, B. L., Kareem, K., Bao, H. & Byerly, G. R. Early Earth mantle heterogeneity revealed by light oxygen isotopes of Archean komatiites. *Nat. Geosci.* **10**, 871–875 (2017).
60. Gamal EL Dien, H., Doucet, L. S. & Li, Z.-X. Global geochemical fingerprinting of plume intensity suggests coupling with the supercontinent cycle. *Nat. Commun.* **10**, 5270 (2019).
61. Wyman, D. Do cratons preserve evidence of stagnant lid tectonics? *Geosci. Front.* **9**, 3–17 (2018).
62. Armstrong, R. L. Radiogenic Isotopes: The Case for Crustal Recycling on a Near-Steady-State No-Continental-Growth Earth. *Philos. Trans. R. Soc. A Math. Phys. Eng. Sci.* **301**, 443–472 (1981).
63. Pujol, M., Marty, B., Burgess, R., Turner, G. & Philippot, P. Argon isotopic composition of Archean atmosphere probes early Earth geodynamics. *Nature* **498**, 87–90 (2013).
64. Dewey, J. & Windley, B. F. Growth and differentiation of the continental crust. *Philos. Trans. R. Soc. London. Ser. A, Math. Phys. Sci.* **301**, 189–206 (1981).
65. Belousova, E. A. *et al.* The growth of the continental crust: Constraints from zircon Hf-isotope data. *Lithos* **119**, 457–466 (2010).
66. Taylor, S. R. & McLennan, S. M. The geochemical evolution of the continental crust. *Rev. Geophys.* **33**, 241 (1995).
67. Allègre, C. J. & Rousseau, D. The growth of the continent through geological time studied by Nd isotope analysis of shales. *Earth Planet. Sci. Lett.* **67**, 19–34 (1984).
68. Condie, K. C. & Aster, R. C. Episodic zircon age spectra of orogenic granitoids: The supercontinent connection and continental growth. *Precambrian Res.* **180**, 227–236 (2010).
69. Hurlley, P. M. & Rand, J. R. *Pre-Drift Continental Nuclei*. *Science* **164**, (1969).
70. Goldstein, S. L., O’Nions, R. K. & Hamilton, P. J. A Sm-Nd isotopic study of atmospheric dusts and particulates from major river systems. *Earth Planet. Sci. Lett.* **70**, 221–236 (1984).
71. DePaolo, D. J. Neodymium isotopes in the Colorado Front Range and crust–mantle evolution in the Proterozoic. *Nature* **291**, 193–196 (1981).

Acknowledgements

We would like to thank Chris Spencer for providing Nd isotopic data related to Spencer *et al.*³⁹, discussions and suggestions and the insightful suggestions of two journal reviewers. Financial support by the Australian Research Council (grant FL150100133 to ZXL) is acknowledged. This is a contribution to IGCP648: Supercontinent Cycles and Global Geodynamics.

Author contributions

H.G. conceived the idea, collected the data and wrote the first draft of the manuscript. L.S.D. and H.G. did the statistical testing. B.M. and Z.X.L. designed the paper and clarified the concepts. All the authors participated in the interpretation of the results and preparation of the final manuscript.

Competing interests

The authors declare no competing interests.

Additional information

Supplementary information is available for this paper at <https://doi.org/10.1038/s41598-020-66324-y>.

Correspondence and requests for materials should be addressed to H.G.E.D.

Reprints and permissions information is available at www.nature.com/reprints.

Publisher’s note Springer Nature remains neutral with regard to jurisdictional claims in published maps and institutional affiliations.



Open Access This article is licensed under a Creative Commons Attribution 4.0 International License, which permits use, sharing, adaptation, distribution and reproduction in any medium or format, as long as you give appropriate credit to the original author(s) and the source, provide a link to the Creative Commons license, and indicate if changes were made. The images or other third party material in this article are included in the article’s Creative Commons license, unless indicated otherwise in a credit line to the material. If material is not included in the article’s Creative Commons license and your intended use is not permitted by statutory regulation or exceeds the permitted use, you will need to obtain permission directly from the copyright holder. To view a copy of this license, visit <http://creativecommons.org/licenses/by/4.0/>.

© The Author(s) 2020